

DE GRUYTER

INTEGRATED CHEMICAL PROCESSES IN LIQUID MULTI- PHASE SYSTEMS

FROM CHEMICAL REACTION TO PROCESS DESIGN
AND OPERATION

*Edited by Matthias Kraume, Sabine Enders, Anja
Drews, Reinhard Schomäcker, Sebastian Engell and
Kai Sundmacher*



DE
G

Matthias Kraume, Sabine Enders, Anja Drews, Reinhard Schomäcker,
Sebastian Engell, Kai Sundmacher (Eds.)

Integrated Chemical Processes in Liquid Multiphase Systems

Also of interest



*Biorefinery: From Biomass to Chemicals and Fuels.
Towards Circular Economy*

Edited by Michele Aresta, Angela Dibenedetto, Franck Dumeignil,
2022

ISBN 978-3-11-070536-2, e-ISBN (PDF) 978-3-11-070538-6,
e-ISBN (EPUB) 978-3-11-070541-6



Process Engineering.

Addressing the Gap between Study and Chemical Industry

Michael Kleiber, 2020

ISBN 978-3-11-065764-7, e-ISBN (PDF) 978-3-11-065768-5,
e-ISBN (EPUB) 978-3-11-065807-1



The Autotrophic Biorefinery.

Raw Materials from Biotechnology

Edited by Robert Kourist and Sandy Schmidt, 2021

ISBN 978-3-11-054988-1, e-ISBN (PDF) 978-3-11-055060-3,
e-ISBN (EPUB) 978-3-11-054995-9



Process Systems Engineering.

For a Smooth Energy Transition

Edited by Edwin Zondervan, planned for 2022

ISBN 978-3-11-070498-3, e-ISBN (PDF) 978-3-11-070520-1,
e-ISBN (EPUB) 978-3-11-070531-7



Sustainable Process Engineering

Gyorgy Szekely, 2021

ISBN 978-3-11-071712-9, e-ISBN (PDF) 978-3-11-071713-6,
e-ISBN (EPUB) 978-3-11-071730-3

Integrated Chemical Processes in Liquid Multiphase Systems

From Chemical Reaction to Process Design
and Operation

Edited by

Matthias Kraume, Sabine Enders, Anja Drews,
Reinhard Schomäcker, Sebastian Engell,
Kai Sundmacher

DE GRUYTER

Editors

Prof. Dr.-Ing. Matthias Kraume
Technische Universität Berlin
Fachgebiet Verfahrenstechnik
Straße des 17. Juni 135
10623 Berlin, Germany
Matthias.Kraume@tu-berlin.de

Prof. Dr. rer. nat. Sabine Enders
Karlsruher Institut für Technologie KIT
Institut für Technische Thermodynamik und
Kältetechnik
Engler-Bunte-Ring 21
76131 Karlsruhe, Germany
Sabine.enders@kit.edu

Prof. Dr.-Ing. Anja Drews
Hochschule für Technik und Wirtschaft Berlin
Fachgebiet Verfahrenstechnik in Life Science
Engineering
Wilhelminenhofstr. 75A
12459 Berlin, Germany
Anja.drews@htw-berlin.de

Prof. Dr. nat. Reinhard Schomäcker
Technische Universität Berlin
Institut für Chemie
Straße des 17. Juni 135
10623 Berlin, Germany
schomaecker@tu-berlin.de

Prof. Dr.-Ing. Sebastian Engell
Technische Universität Dortmund
Lehrstuhl für Systemdynamik und
Prozessführung
Emil-Figge-Straße 70
44227 Dortmund, Germany
sebastian.engell@bci.tu-dortmund.de

Prof. Dr. Kai Sundmacher
Otto-von-Guericke-Universität
Institut für Verfahrenstechnik
Universitätsplatz 2
39106 Magdeburg, Germany
kai.sundmacher@ovgu.de

Graphics and images by: Editienne, Constantin Karl

ISBN 978-3-11-070943-8

e-ISBN (PDF) 978-3-11-070985-8

e-ISBN (EPUB) 978-3-11-070991-9

DOI <https://doi.org/10.1515/9783110709858>



This work is licensed under the Creative Commons Attribution 4.0 International License. For details go to <https://creativecommons.org/licenses/by/4.0/>.

Library of Congress Control Number: 2021952231

Bibliographic information published by the Deutsche Nationalbibliothek

The Deutsche Nationalbibliothek lists this publication in the Deutsche Nationalbibliografie; detailed bibliographic data are available on the Internet at <http://dnb.dnb.de>.

© 2022 with the authors, editing © 2022 Matthias Kraume, Sabine Enders, Anja Drews, Reinhard Schomäcker, Sebastian Engell, Kai Sundmacher, published by Walter de Gruyter GmbH, Berlin/Boston
The book is published open access at www.degruyter.com.

Cover image: Gettyimages/MACIEJ NOSKOWSKI

Typesetting: Integra Software Services Pvt. Ltd.

Printing and binding: CPI books GmbH, Leck

www.degruyter.com

Contents

Foreword — XIII

List of Authors — XV

Abbreviations — XXI

List of Symbols — XXVII

Matthias Kraume

1 Motivation and Objectives — 1

- 1.1 Goals and Scientific Concept — 3
 - 1.2 Advanced Phase Systems — 5
 - 1.2.1 Thermomorphic Multiphase Systems — 6
 - 1.2.2 Microemulsion Systems — 7
 - 1.2.3 Pickering Emulsions — 7
 - 1.3 Material Basis and Reactions — 9
 - 1.4 Model Process — 11
 - 1.5 Challenges of the Fundamental Investigations — 12
 - 1.5.1 Chemical–Physical Fundamentals — 13
 - 1.5.2 Process Technology — 15
 - 1.5.3 Systems Technology — 18
 - 1.6 Structure of the Book — 20
- References — 21

Matthias Kraume

2 State of the Art of the Investigated Phase Systems — 23

- 2.1 Thermomorphic Multiphase Systems — 24
 - 2.1.1 Introduction — 24
 - 2.1.2 Fundamentals and Thermodynamics — 25
 - 2.1.3 Reactions in TMS and Remaining Challenges — 31
- 2.2 Microemulsion Systems — 32
 - 2.2.1 Introduction — 32
 - 2.2.2 Fundamentals — 33
 - 2.2.2.1 Properties and Phase Behavior of Microemulsion Systems — 33
 - 2.2.2.2 Features and Description of the Three-Phase Body — 35
 - 2.2.2.3 Coalescence Behavior and Separation Dynamics — 36
 - 2.2.3 Industrial Applications and Remaining Challenges — 39

- 2.3 Pickering Emulsions — **40**
 - 2.3.1 Introduction — **40**
 - 2.3.2 Fundamentals — **40**
 - 2.3.2.1 Stabilizing Mechanism — **40**
 - 2.3.2.2 Properties of Pickering Emulsions — **41**
 - 2.3.3 Reactions in Pickering Emulsions — **42**
 - 2.3.4 Remaining Challenges — **42**
 - 2.3.4.1 Pickering Emulsion Characterization and Properties — **43**
 - 2.3.4.2 Mass Transfer and Location of Catalyst — **44**
 - 2.3.4.3 Continuous L/L Separation for Catalyst Retention — **44**
- 2.4 Reaction Indicators — **45**
- References — **48**

Sabine Enders

3 Thermodynamics, Kinetics, and Mass Transfer — 55

- 3.1 Thermodynamics — **55**
 - 3.1.1 Heterosegmented Perturbed-Chain Statistical Associating Fluid Theory — **56**
 - 3.1.2 Lattice Cluster Theory — **57**
 - 3.1.3 Phase Equilibria — **58**
 - 3.1.4 Interfacial Properties — **71**
 - 3.1.5 Reaction Equilibria — **84**
 - 3.1.6 Aggregation Formation of Aqueous Surfactant Solutions — **90**
 - 3.1.7 Solubilization of Weak Polar Molecules in Aqueous Surfactant Solutions — **96**
 - 3.1.8 Conclusion — **100**
- 3.2 Kinetic Modeling of Complex Catalytic Reactions in Multiphase Systems — **101**
 - 3.2.1 Introduction — **101**
 - 3.2.2 Methodological Approach — **102**
 - 3.2.2.1 Reaction Network Investigation — **102**
 - 3.2.2.2 Derivation of Explicit Rate Equations — **108**
 - 3.2.2.3 Reduction of Kinetic Models — **117**
 - 3.2.3 Demonstration of Concept for Coupled Networks — **136**
 - 3.2.3.1 Isomerizing Hydroformylation — **137**
 - 3.2.3.2 Overall Reaction Network of Tandem Hydroaminomethylation — **142**

3.2.4	Thermodynamic Outlook —	144
3.2.5	Summary —	148
3.3	Mass Transfer Processes —	149
3.3.1	Introduction —	149
3.3.2	Experimental Characterization of Multiphase Liquid–Liquid Mass Transport —	150
3.3.2.1	Single Drop Experiments —	150
3.3.2.2	Modified Nitsch Cell —	153
3.3.2.3	Stirred Tank Reactor —	155
3.3.3	Experimental Characterization of Multiphase Gas-Liquid Mass Transport —	156
3.3.3.1	Determination of $k_L a$ from Pressure Decrease in a Closed System —	156
3.3.3.2	Stirred Tank Reactor —	159
3.3.3.3	Falling Film Contactor —	160
3.3.4	Gas–Liquid Mass Transfer —	162
3.3.5	Effect of Mass Transfer on Reaction Selectivity —	170
	References —	175

Anja Drews, Reinhard Schomäcker

4 Phase Systems Characterization and Process Development — 189

4.1	Thermomorphic Multiphase Systems —	190
4.1.1	Phase System Characterization —	190
4.1.2	Mass Transfer in Thermomorphic Multiphase Systems —	192
4.1.3	Applications —	197
4.1.4	Recent Developments in TMSs —	219
4.1.4.1	Combination of TMSs with Other Reactor Types —	222
4.1.4.2	Improved Online Analytics —	223
4.1.4.3	Application of TMSs for Complex Reactions in Continuous Operation —	224
4.1.4.4	Combined Reaction Separation Processes —	229
4.1.5	Summary and Outlook —	234
4.2	Microemulsion Systems —	236
4.2.1	Phase System Characterization and Systematic Analysis of MES for the Selected Reaction —	239
4.2.1.1	Dispersion Types in Micellar Multiphase Systems —	239
4.2.1.2	Localization of the Catalyst Complex —	241
4.2.1.3	Mass Transfer in Microemulsion Systems —	242

	4.2.1.4	Micellar-Enhanced Ultrafiltration and Organic Solvent Nanofiltration — 252
	4.2.1.5	Systematic Development and Analysis of Microemulsions for Process Application — 254
	4.2.2	Applications — 263
	4.2.3	Application Case Study: Hydroformylation of 1-Dodecene — 268
	4.2.4	Concluding Remarks — 302
4.3		Pickering Emulsions — 304
	4.3.1	Phase System Characterization — 304
	4.3.1.1	Particle Types and Characterization — 304
	4.3.1.2	Particles at the Liquid/Liquid Interface — 309
	4.3.1.3	Drop Size Distributions and Stability — 310
	4.3.1.4	Rheology of Pickering Emulsions — 315
	4.3.1.5	Mass Transfer in Pickering Emulsions — 317
	4.3.1.6	Filterability of Pickering Emulsions — 322
	4.3.2	Applications — 329
	4.3.3	Application Case Study — 330
	4.3.3.1	Influence of the Catalyst (Rh-SX) on the Pickering Emulsion Properties — 331
	4.3.3.2	Emulsions Stabilized by HNT (o/w) — 332
	4.3.3.3	Reaction in and Filtration of Pickering Emulsions Using Tailored Nanospheres (w/o) — 333
	4.3.3.4	Reaction in and Filtration of Pickering Emulsions Using a Commercial Particle System (w/o) — 335
	4.3.4	Concluding Remarks — 336
4.4		Summary and Comparison of Phase Systems — 338
		References — 342

Sebastian Engell

5		Tools for Systems Engineering — 361
	5.1	Overview — 361
	5.2	Modeling and Simulation — 364
	5.2.1	A Framework for Process Modeling and Simulation — 364
	5.2.1.1	Requirements for Collaborative Modeling — 365
	5.2.1.2	Data Model for Modeling at the Documentation Level and Hierarchical Modeling — 368
	5.2.1.3	Collaborative Modeling and Web Technologies — 376

- 5.2.1.4 Specification of Simulation and Optimization Problems — **377**
- 5.2.1.5 Model-Based Code Implementation of Models — **378**
- 5.2.1.6 Examples of Models Developed and Managed in MOSAICmodeling — **380**
- 5.2.1.7 Outlook on Model Development and Collaboration — **383**
- 5.2.2 Fluid-Dynamic Investigations of Multiphase Processes — **383**
 - 5.2.2.1 Introduction — **383**
 - 5.2.2.2 Numerical Flow Simulations of Reactor and Settler for the MES Process — **384**
 - 5.2.2.3 Fluid-Dynamic Investigation of Gas-Liquid-Liquid Continuous Helical Flow Reactors — **392**
- 5.2.3 Surrogate Models for Thermodynamic Equilibria of Gas-Liquid and Liquid-Liquid Systems — **400**
- 5.3 Process Optimization — **413**
 - 5.3.1 Optimal Design of Reactors for Complex Reaction Systems — **413**
 - 5.3.1.1 Reactor-Network Synthesis — **414**
 - 5.3.1.2 Elementary Process Functions Methodology — **415**
 - 5.3.1.3 EPF Application to the Hydroformylation of Long-Chain Olefins — **421**
 - 5.3.1.4 Proof of Concept: Optimal Reactor-Design Hydroformylation of 1-Dodecene — **424**
 - 5.3.1.5 Summary — **433**
 - 5.3.2 Global Optimization for Process Design — **433**
 - 5.3.2.1 Introduction — **433**
 - 5.3.2.2 Distillation and Hybrid Separations — **437**
 - 5.3.2.3 Multi-stage Separation Networks — **443**
 - 5.3.2.4 Combined Reaction and Catalyst Recycling — **445**
 - 5.3.2.5 Liquid-Liquid Extraction — **446**
 - 5.3.2.6 Summary — **449**
 - 5.3.3 Optimization under Uncertainties in Process Development — **451**
- 5.4 Model-Based Process Monitoring and Operation — **461**
 - 5.4.1 Online Monitoring and Online Optimization in the Development of Multiphase Processes — **461**

- 5.4.2 Iterative Real-Time Optimization Applied to a Hydroformylation Process on Miniplant Scale — **463**
 - 5.4.2.1 Real-Time Optimization and Approaches to Handle the Plant-Model Mismatch — **463**
 - 5.4.2.2 Iterative Real-Time Optimization by Modifier Adaptation — **466**
 - 5.4.2.3 Application of Real-Time Optimization with Modifier Adaptation to the Hydroformylation of 1-Dodecene in a TMS-system on Miniplant Scale — **472**
 - 5.4.2.4 Conclusion and Outlook — **480**
- 5.4.3 State Estimation for Reactions and Separations in a MES System in a Mini plant — **481**
- 5.4.4 Optimal Operation of Reaction-Separation Processes in a MES Miniplant — **489**
- References — **497**

Kai Sundmacher

- 6 Integrated Process Design — 509**
 - 6.1 Introduction — **509**
 - 6.2 Selection Criteria for Liquid Multiphase Systems — **510**
 - 6.2.1 Introduction — **510**
 - 6.2.2 General Criteria for Phase System Selection — **512**
 - 6.2.3 Feasibility and Constraints for Phase Systems Application and Key Experiments — **514**
 - 6.2.3.1 Thermomorphic Multiphase System — **514**
 - 6.2.3.2 Microemulsion Systems — **516**
 - 6.2.3.3 Pickering Emulsions — **517**
 - 6.2.4 Systematic Phase System Selection and Process Design — **519**
 - 6.3 Solvent Selection for Reactions in Liquid Phases — **523**
 - 6.3.1 Standard Gibbs Energies of Chemical Reactions and Transition State Barriers — **524**
 - 6.3.2 Introducing a Three-Level Description of Chemical Reactions in Solution — **524**
 - 6.3.2.1 Taking Quantum Chemical Calculations from the Gas Phase to Infinitely Diluted Solution — **526**
 - 6.3.2.2 From Infinite Dilution to Real Solutions with Thermodynamic Activities of Reacting Species — **526**

- 6.3.3 Solvent Selection for Chemical Equilibria and Reaction Rates — **528**
 - 6.3.3.1 Modeling Solvent Effects on Standard Gibbs Energies and Chemical Equilibria — **528**
 - 6.3.3.2 Model-Based Screening to Predict Solvent Effects on Reaction Kinetics — **530**
 - 6.3.3.3 Beyond Implicit Solvation: The Many Roles of Solvent Molecules — **532**
- 6.3.4 Conclusions — **535**
- 6.4 Integrated Solvent and Process Design — **535**
 - 6.4.1 Introduction to Integrated Solvent and Process Design — **536**
 - 6.4.2 Survey of Integrated Solvent and Process Design Methodologies — **538**
 - 6.4.2.1 Approaches Using Alternative Thermodynamic Models — **540**
 - 6.4.2.2 Most Recent Contributions — **541**
 - 6.4.2.3 Direct Optimization of Thermodynamic Parameters: Continuous Molecular Targeting — **541**
 - 6.4.2.4 Integrated Solvent and Process Design for the Kinetics of Chemical Reactions — **543**
 - 6.4.2.5 Genetic Optimization Approach for Complex Solvent-Process Optimization Problems — **545**
 - 6.4.3 Integrated Solvent and Process Design for Thermomorphic Multiphase Systems — **546**
 - 6.4.4 Conclusions — **551**
- 6.5 Integrated Model-Based Process Design Methodology — **552**
 - 6.5.1 Experimental Design for Efficient and Accurate Parameter Identification — **553**
 - 6.5.2 Integrated Process Design — **555**
 - 6.5.2.1 Methodology — **556**
 - 6.5.2.2 Methods for Sensitivity Analysis in Process Synthesis — **557**
 - 6.5.2.3 Case Study I: Hydroaminomethylation of 1-Decene — **559**
 - 6.5.2.4 Case Study II: Hydroformylation of 1-Dodecene — **562**
 - 6.5.3 Advanced Integration Potential for Systematic Multiphase Process Design — **564**

XII — Contents

6.5.3.1	Model-Based Solvent Selection —	565
6.5.3.2	Model-Based Optimal Reactor Design —	566
6.5.4	Summary —	568
	References —	568

Matthias Kraume

7	Résumé —	575
----------	-----------------	------------

Index —	583
----------------	------------

Foreword

The increasingly visible consequences of the wasteful use of natural resources, such as climate change, biodiversity loss, or shrinking forests, force humankind to consume the earth's resources less extensively. To fulfill this, extensive innovations and high-tech solutions are required in all sectors, from private households to the transport sector to the manufacturing industry. Faced with these challenges, academia, industry, and society are currently developing strategies for structural change toward a circular economy. For the process industry, this results in the need to reduce the consumption of fossil raw materials, which affects both the energy and raw material consumption for the manufacturing of valuable products. For the chemical industry, this creates, among others, the challenge of converting the raw material base for chemical production from fossil to renewable feedstocks. Accordingly, modern, efficient production concepts must be implemented, based, for example, on the ideas of Green Chemistry, and aim for the most environmentally friendly production of chemical products. In addition to using renewable raw materials, the essential principles of this chemistry are the application of highly efficient catalysts, the use of harmless solvents, energy efficiency, and process optimization in real time. However, concerning the implementation in large-scale processes, these goals are currently still of a visionary nature.

To develop such novel, efficient production processes, all levels of the processes must be viewed from the molecular elementary steps up to the design and operation of the entire plant. Therefore, an intense interdisciplinary collaboration is necessary to realize such processes. This background led to the joint collaboration between researchers from Technische Universität Berlin, Technische Universität Dortmund, Otto-von-Guericke-Universität Magdeburg, Technische Universität Darmstadt, Karlsruhe Institute of Technology, Hochschule für Technik und Wirtschaft Berlin, Anhalt University of Applied Sciences, and Max Planck Institute for Dynamics of Complex Technical Systems. The German Research Foundation (Deutsche Forschungsgemeinschaft e.V. (DFG)) funded this activity in the framework of the Collaborative Research Centre/Transregio 63 "Integrated Chemical Processes in Liquid Multiphase Systems" (InPROMPT/56091768) from 2010 to 2022.

The CRC/TR 63 focused on the necessary methods for developing homogeneously catalyzed processes in liquid multiphase systems. Together with chemical-physical fundamentals, process and systems technology formed the scientific foundation. Thus, fundamental investigations were conducted to gain a deeper understanding of the processes and their modeling. In addition to the reaction steps, separation processes were also developed, modeled, and optimized as part of the overall process synthesis to develop technical processes. Finally, the developed processes were implemented and validated in two miniplants.

This volume presents the final scientific report of the CRC/TR 63. Over the total funding period, 46 tightly interlocked projects were carried out by 36 principal

investigators strongly supported by 131 young scientists. This volume is not the only result of our scientific activities. A total of 103 doctoral theses were written, and 387 papers were published. The successful support of the young scientists, together with a productive environment, is reflected by seven appointments to full professorships received by members of the CRC/TR 63.

The editors like to express their sincere appreciation for the long-lasting funding by DFG. Without them, such an extensive collaboration would not have been possible. Special thanks also go to all 15 members of our industrial board. With their industrial perspective and experience, they supported our scientific work and gave valuable hints for technological aspects that should be considered. We are obviously greatly indebted to all 62 authors of this volume for their individual contributions. We also owe plenty of thanks to the numerous employees in the workshops, laboratories, and administration who have substantially supported the CRC/TR 63. Particular thanks are due to Alexandra Vetter, who successfully managed all organizational issues, especially the time schedule.

List of Authors

Nona Afraz

Otto-von-Guericke-Universität Magdeburg,
Institute of Apparatus and Environmental
Technology,
Universitätsplatz 2,
39106 Magdeburg, Germany

Jonas Bianga

Technische Universität Dortmund,
Department of Biochemical and Chemical
Engineering, Industrial Chemistry Laboratory,
Emil-Figge-Str. 66,
44227 Dortmund, Germany

Lutz Böhm

Technische Universität Berlin,
Faculty III Process Sciences,
Institute for Chemical and Process
Engineering,
Straße des 17. Juni,
10623 Berlin, Germany

Saskia Bublitz

Technische Universität Berlin,
Faculty III Process Sciences,
Institute for Chemical and Process
Engineering, Process Dynamics and
Operations Group,
Straße des 17. Juni,
10623 Berlin, Germany

Jens M. Dreimann

Technische Universität Dortmund,
Department of Biochemical and Chemical
Engineering, Industrial Chemistry Laboratory,
Emil-Figge-Str. 66,
44227 Dortmund, Germany

Anja Drews

HTW Berlin - University of Applied Sciences,
Chemical Engineering in Life Science
Engineering,
Wilhelminenhofstr. 75A,
12459 Berlin, Germany

Karsten Duch

Technische Universität Berlin,
Faculty III Process Sciences,
Institute for Chemical and Process
Engineering,
Process Dynamics and Operations Group,
Straße des 17. Juni,
10623 Berlin, Germany

Sabine Enders

Karlsruhe Institute of Technology,
Institute of Technical Thermodynamics and
Refrigeration Technology,
Engler-Bunte-Ring 21,
76131 Karlsruhe, Germany

Sebastian Engell

Technische Universität Dortmund,
Department of Biochemical and Chemical
Engineering,
Process Dynamics and Operations Group
Emil-Figge-Str. 70,
44221 Dortmund, Germany

Erik Esche

Technische Universität Berlin,
Faculty III Process Sciences,
Institute for Chemical and Process
Engineering,
Process Dynamics and Operations Group,
Straße des 17. Juni,
10623 Berlin, Germany

Tom Gaide

Technische Universität Dortmund,
Department of Biochemical and Chemical
Engineering,
Industrial Chemistry Laboratory,
Emil-Figge-Str. 66,
44227 Dortmund, Germany

Martin Gerlach

Otto-von-Guericke-Universität Magdeburg,
Institute of Process Engineering,
Chemical Process Engineering Group,
Universitätsplatz 2,
39106 Magdeburg, Germany

Anwesh R. Gottu Mukkula

Technische Universität Dortmund,
Department of Biochemical and Chemical
Engineering, Process Dynamics and
Operations Group,
Emil-Figge-Str. 70,
44221 Dortmund, Germany

Niklas Haarmann

Technische Universität Dortmund,
Department of Biochemical and Chemical
Engineering,
Thermodynamics Laboratory,
Emil-Figge-Str. 70,
44221 Dortmund, Germany

Christof Hamel

Otto-von-Guericke-Universität Magdeburg,
Institute of Process Engineering,
Chemical Process Engineering Group,
Universitätsplatz 2,
39106 Magdeburg, Germany

Hochschule Anhalt - University of Applied
Sciences, Applied Biosciences and Process
Technology,
Bernburger Straße 55,
06366 Koethen, Germany

Kristin Hecht

Otto-von-Guericke-Universität Magdeburg,
Institute of Apparatus and Environmental
Technology,
Universitätsplatz 2,
39106 Magdeburg, Germany

Reinaldo Hernandez

Technische Universität Dortmund,
Department of Biochemical and Chemical
Engineering,
Process Dynamics and Operations Group,
Emil-Figge-Str. 70,
44221 Dortmund, Germany

Lena Hohl

Technische Universität Berlin,
Faculty III Process Sciences,
Institute for Chemical and Process Engineering,
Straße des 17. Juni,
10623 Berlin, Germany

Fabian Huxoll

Technische Universität Dortmund,
Department of Biochemical and Chemical
Engineering, Thermodynamics Laboratory,
Emil-Figge-Str. 70,
44227 Dortmund, Germany

Markus Illner

Technische Universität Berlin,
Faculty III Process Sciences,
Institute for Chemical and Process
Engineering,
Process Dynamics and Operations Group,
Straße des 17. Juni 135,
10623 Berlin, Germany

Froze Jameel

Max Planck Institute for Dynamics of Complex
Technical Systems,
Molecular Simulations and Design Group,
Sandtorstraße 1,
39106 Magdeburg, Germany

Gábor Janiga

Otto-von-Guericke-Universität Magdeburg,
Laboratory of Fluid Dynamics and Technical
Flows, Faculty of Process & Systems
Engineering,
Universitätsplatz 2,
39106 Magdeburg, Germany

Tim Janus

Technische Universität Dortmund,
Department of Biochemical and Chemical
Engineering, Process Dynamics and
Operations Group,
Emil-Figge-Str. 70,
44221 Dortmund, Germany

Michael Jokiel

Max Planck Institute for Dynamics of Complex
Technical Systems,
Process Systems Engineering,
Sandtorstraße 1,
39106 Magdeburg, Germany

Stefanie Kaiser

Technische Universität Dortmund,
Department of Biochemical and Chemical
Engineering,
Process Dynamics and Operations Group,
Emil-Figge-Str. 70,
44221 Dortmund, Germany

Anna Kampwerth

Technische Universität Dortmund,
Department of Biochemical and Chemical
Engineering,
Industrial Chemistry Laboratory,
Emil-Figge-Str. 66,
44227 Dortmund, Germany

Maresa V. Kempin

HTW Berlin - University of Applied Sciences,
Chemical Engineering in Life Science
Engineering,
Wilhelminenhofstr. 75A,
12459 Berlin, Germany

Tobias Keßler

Otto-von-Guericke-Universität Magdeburg,
Faculty of Electrical Engineering and
Information Technology,
Universitätsplatz 2,
39106 Magdeburg, Germany

Achim Kienle

Otto-von-Guericke-Universität Magdeburg,
Faculty of Electrical Engineering and
Information Technology,
Universitätsplatz 2,
39106 Magdeburg, Germany

Max Planck Institute for Dynamics of Complex
Technical Systems,
PSD Group,
Sandtorstraße 1,
39106 Magdeburg, Germany

Sabine Kirschtowski

Otto-von-Guericke-Universität Magdeburg,
Institute of Process Engineering,
Chemical Process Engineering Group,
Universitätsplatz 2,
39106 Magdeburg, Germany

Regine von Klitzing

Technische Universität Darmstadt,
Institute for Condensed Matter Physics,
Soft Matter at Interfaces,
Hochschulstraße 8,
64289 Darmstadt, Germany

Matthias Kraume

Technische Universität Berlin,
Faculty III Process Sciences,
Institute for Chemical and Process
Engineering,
Straße des 17. Juni,
10623 Berlin, Germany

Kai Uwe Künnemann

Technische Universität Dortmund,
Department of Biochemical and Chemical
Engineering,
Industrial Chemistry Laboratory,
Emil-Figge-Str. 66,
44227 Dortmund, Germany

Péter Kováts

Otto-von-Guericke-Universität Magdeburg,
Laboratory of Fluid Dynamics and Technical
Flows, Faculty of Process & Systems
Engineering,
Universitätsplatz 2,
39106 Magdeburg, Germany

Volodymyr Kozachynskyi

Technische Universität Berlin,
Faculty III Process Sciences,
Institute for Chemical and Process
Engineering, Process Dynamics and
Operations Group,
Straße des 17. Juni,
10623 Berlin, Germany

Christian Kunde

Otto von Guericke Universität Magdeburg,
Faculty of Electrical Engineering and
Information Technology,
Universitätsplatz 2,
39106 Magdeburg, Germany

Steffen Linke

Otto-von-Guericke-Universität Magdeburg,
Faculty of Process- and Systems Engineering,
Process Systems Engineering Group,
Universitätsplatz 2,
39106 Magdeburg, Germany

Michael Mansour

Otto-von-Guericke-Universität Magdeburg,
Laboratory of Fluid Dynamics and Technical
Flows, Faculty of Process & Systems
Engineering,
Universitätsplatz 2,
39106 Magdeburg, Germany

Anurag Misra

Otto-von-Guericke-Universität Magdeburg,
Laboratory of Fluid Dynamics and Technical
Flows, Faculty of Process & Systems
Engineering,
Universitätsplatz 2,
39106 Magdeburg, Germany

Corina Nentwich

Technische Universität Dortmund,
Department of Biochemical and Chemical
Engineering, Process Dynamics and
Operations Group,
Emil-Figge-Str. 70,
44221 Dortmund, Germany

Marc Petzold

Technische Universität Berlin,
Faculty III Process Sciences,
Institute for Chemical and Process
Engineering,
Straße des 17. Juni,
10623 Berlin, Germany

Karsten H.G. Rätze

Otto-von-Guericke-Universität Magdeburg,
Faculty of Process- and Systems Engineering,
Process Systems Engineering Group,
Universitätsplatz 2,
39106 Magdeburg, Germany

Annika Reinhardt

Karlsruhe Institute of Technology,
Institute of Technical Thermodynamics and
Refrigeration Technology,
Engler-Bunte-Ring 21,
76131 Karlsruhe, Germany

Jens-Uwe Repke

Technische Universität Berlin,
Faculty III Process Sciences,
Institute for Chemical and Process Engineering,
Process Dynamics and Operations Group,
Straße des 17. Juni 135,
10623 Berlin, Germany

Gabriele Sadowski

Technische Universität Dortmund,
Department of Biochemical and Chemical
Engineering, Thermodynamics Laboratory,
Emil-Figge-Str. 70,
44227 Dortmund, Germany

Stefan Schlüter

Technische Universität Dortmund,
Department of Biochemical and Chemical
Engineering,
Fluid Separations Laboratory,
Emil-Figge-Str. 70,
44227 Dortmund, Germany

Reinhard Schomäcker

Technische Universität Berlin,
Faculty II Mathematics and Natural Sciences,
Institute of Chemistry, Chemical Reaction
Engineering,
Straße des 17. Juni 124,
10623 Berlin, Germany

Andreas Seidel-Morgenstern

Otto-von-Guericke-Universität Magdeburg,
Institute of Process Engineering,
Chemical Process Engineering Group,
Universitätsplatz 2,
39106 Magdeburg, Germany

Max Planck Institute for Dynamics of Complex
Technical Systems, Physical and Chemical
Foundations of Process Engineering,
Sandtorstrasse 1,
39106 Magdeburg, Germany

Thomas Seidensticker

Technische Universität Dortmund,
Department of Biochemical and Chemical
Engineering, Industrial Chemistry Laboratory,
Emil-Figge-Str. 66,
44227 Dortmund, Germany

Mirko Skiborowski

Technische Universität Dortmund,
Department of Biochemical and Chemical
Engineering, Fluid Separations Laboratory,
Emil-Figge-Str. 70,
44221 Dortmund, Germany

Technische Universität Hamburg,
Institute of Process Systems Engineering,
Am Schwarzenberg-Campus 4 (C),
21073 Hamburg, Germany

Jochen Steimel

Technische Universität Dortmund,
Department of Biochemical and Chemical
Engineering,
Process Dynamics and Operations Group,
Emil-Figge-Str. 70,
44221 Dortmund, Germany

Matthias Stein

Max Planck Institute for Dynamics of Complex
Technical Systems,
Molecular Simulations and Design Group,
Sandtorstraße 1,
39106 Magdeburg, Germany

Sebastian Stock

Technische Universität Darmstadt,
Institute for Condensed Matter Physics,
Soft Matter at Interfaces Hochschulstraße 8,
64289 Darmstadt, Germany

Kai Sundmacher

Max Planck Institute for Dynamics of Complex
Technical Systems,
Process Systems Engineering,
Sandtorstraße 1,
39106 Magdeburg, Germany

Otto-von-Guericke-Universität Magdeburg,
Faculty of Process- and Systems Engineering,
Process Systems Engineering Group,
Universitätsplatz 2,
39106 Magdeburg, Germany

Dominique Thévenin

Otto-von-Guericke-Universität Magdeburg,
Laboratory of Fluid Dynamics and Technical
Flows, Faculty of Process & Systems
Engineering,
Universitätsplatz 2,
39106 Magdeburg, Germany

Reddy Velagala

Otto-von-Guericke-Universität Magdeburg,
Laboratory of Fluid Dynamics and Technical
Flows, Faculty of Process & Systems
Engineering,
Universitätsplatz 2,
39106 Magdeburg, Germany

Dieter Vogt

Technische Universität Dortmund,
Department of Biochemical and Chemical
Engineering, Industrial Chemistry Laboratory,
Emil-Figge-Str. 66,
44227 Dortmund, Germany

Andreas J. Vorholt

Max Planck Institute for Chemical Energy
Conversion,
Stiftstrasse 34 – 36,
45470 Mülheim an der Ruhr, Germany

Ariane Weber

Technische Universität Berlin,
Faculty II Mathematics and Natural Sciences,
Institute of Chemistry, Chemical Reaction
Engineering,
Straße des 17. Juni 124,
10623 Berlin, Germany

Günter Wozny

Technische Universität Berlin,
Faculty III Process Sciences,
Institute for Chemical and Process
Engineering,
Process Dynamics and Operations Group,
Straße des 17. Juni,
10623 Berlin, Germany

Katharina Zähringer

Otto-von-Guericke-Universität Magdeburg,
Laboratory of Fluid Dynamics and Technical
Flows, Faculty of Process & Systems
Engineering,
Universitätsplatz 2,
39106 Magdeburg, Germany

Tim Zeiner

Technische Universität Dortmund,
Department of Biochemical and
Chemical Engineering, Fluid Separations
Laboratory,
Emil-Figge-Straße 70,
44227 Dortmund, Germany

Abbreviations

1,2-DTBPMB	1,2-Bis(di-tert-butylphosphinomethyl)benzene
4-DPBA	4-Diphenylphosphinobenzoic acid
10-UME	Methyl 10-undecenoate
acac	Acetylacetonate
ACN	Acetonitrile
AE	Atom economy
AFM	Atomic force microscopy
ANN	Artificial neural network
APTES	Aminopropyltrimethoxysilane
AR	Attainable region
aux	Auxiliary
BARON	Branch-and-reduce optimization navigator
BET	Brunauer–Emmett–Teller
BIPHEPHOS	6,6'-[(3,3'-Di-tert-butyl-5,5'-dimethoxy-1,1'-biphenyl-2,2'-diyl)bis(oxy)]bis(dibenzo[d,f][1,3,2]dioxaphosphepin)
BTEM	Band target entropy minimization
C _i E _j	Poly(oxyethylene) alkyl ethers
CALM	Chemical association lattice model
CAMD	Computer-aided molecular design
CAMPD	Computer-aided molecular and process design
caPSS	Computer-aided phase system selection
cat	Catalyst
CMC	Critical micelle concentration
CO	Carbon monoxide
CO ₂	Carbon dioxide
cod	1,5-Cyclooctadiene
COSMO	Conductor-like screening model
COSMO-SAC	Conductor-like screening model segment activity coefficient
COSMO-RS	Conductor-like screening model for real solvents
CSTR	Continuous stirred-tank reactor
CVE	Cross-validation error
dba	Dibenzylideneacetone
DDDME	Dodecanedioic acid dimethyl ester
DDoF	Design degrees of freedom
DFO	Derivative free optimization
dppb	1,4-Bis(diphenylphosphino)butane
DESO	Diethyl sulfoxide
DFT	Density functional theory
DGT	Density gradient theory
DMA	<i>N,N</i> -Dimethylacetamide
DMF	<i>N,N</i> -Dimethylformamide
DMG	Dimethyl glutarate
DMSU	Dimethylsuccinate
DoE	Statistical design of experiments
DoF	Degrees of freedom
dppf	1,1'-Bis(-diphenylphosphino)ferrocene
DSR	Distributed side stream reactor

XXII — Abbreviations

DTBPMB	1,2-Bis(di-tert-butylphosphino-methyl)benzene
EC	Ethylene carbonate
EHS	Environmental, health, safety
ELL	Ethyl levulinate
EMM	1-Ethyl 4-methyl 2-methylsuccinate
Enamine	<i>N,N</i> -Diethylundecylamine
EoS	Equation of state
EPF	Elementary process functions
EtAc	Ethyl acetate
EtOH	Ethanol
FH	Flory–Huggins theory
FIM	Fisher information matrix
Fmoc	Fluorenylmethyloxycarbonyl
FPA	Flux profile analysis
FTIR	Fourier-transform infrared
GA	Genetic algorithm
GC	Group contribution
GC	Gas chromatograph
G/L	Gas–liquid
G/L/S	Gas–liquid–solid
G/S	Gas–solid
H ₂	Hydrogen
HAM	Hydroaminomethylation
HCTR	Helically coiled tubular reactor
hfacac	Hexafluoroacetylacetonate
HNEt ₂	Diethylamine
HNT	Halloysite nanotubes
HSi(OEt) ₃	Triethoxysilane
HYD	Hydrogenation
iC12en	Dodecene isomers
iC13al	Branched aldehydes
ICP	Inductively coupled plasma
ICP-AES	Inductively coupled plasma – atomic emission spectroscopy
ICP-MS	Inductively coupled plasma – mass spectroscopy
ICP-OES	Inductively coupled plasma – optical emission spectroscopy
ID	1-Dodecene
IL	Ionic liquid
inh	Inherent
InPROMPT	Integrated chemical processes in liquid multiphase systems
IR	Infrared
ISO	Isomerization of 1- and internal iso-decenes (2-, 3-, 4-, 5-decene)
isoHYFO	Hydroformylation to the branched aldehyde
KPI	Key performance indicator
L	Ligand
LACS	Least abundant catalyst-containing species
LCST	Lower critical solution temperature
LCT	Lattice cluster theory
LCT-EOS	Lattice cluster theory – equation of state
LHS	Latin hypercube sampling

L/L	Liquid–liquid
LLE	Liquid–liquid equilibrium
lig	Ligand
MA	Modifier adaptation
MACS	Most abundant catalyst containing species
MAE	Mean absolute error
MAWQA	Modifier adaptation with quadratic approximation
mbOED	Model-based optimal experimental design
MEA	Methyl 2-ethylacetoacetate
MeCN	Acetonitrile
MeOH	Methanol
MES	Microemulsion system
Mes	1,3,5-Trimethylbenzol
MEUF	Micellar-enhanced ultrafiltration
MHE	Moving horizon estimation
MIDO	Mixed-integer dynamic optimization
MINLP	Mixed-integer nonlinear problem
MisC	Percentage of misclassified test set samples
MP2	Second-order Møller–Plesset perturbation theory
MPC	Model predictive controller
MSE	Mean squared error
MSA	Methanesulfonic acid
MSDS	Material and safety data sheet
MW	Molecular weight
MWCO	Molecular weight cutoff
n/iso	Linear-to-branched ratio
nC12an	Dodecane
nC12en	1-Dodecene
nC13al	Linear aldehyde (tridecanal)
NCP	<i>N</i> -Cyclohexylpyrrolidone
NEP	<i>N</i> -Ethylpyrrolidone
NEt ₃	Triethylamine
NHC	<i>N</i> -Heterocyclic carbene
nHYFO	Hydroformylation to the linear aldehyde
NLP	Nonlinear optimization problem
NLP	Nonlinear program
N(<i>n</i> Bu) ₂ H	Di- <i>n</i> -butylamine
NMP	<i>N</i> -Methyl-2-pyrrolidone
NMR	Nuclear magnetic resonance
NOP	<i>N</i> -Octylpyrrolidone
NRTL	Nonrandom two-liquid
OCP	Optimal control problem
OCP	Optimal control profile
ODE	Ordinary differential equation
ODoF	Operational degrees of freedom
OFAT	One factor at a time
OPEX	Operating expenses
OSN	Organic solvent nanofiltration
o/w	Oil in water

XXIV — Abbreviations

PADA	Pyridine-2-azo-dimethylaniline
PC	Propylene carbonate
PC1	Rh-precursor Rh(acac)(CO) ₂
PC2	Rh-precursor Rh-center (Rh(acac)(P∩P)
PC-SAFT	Perturbed-chain statistical associating fluid theory
PDAE	Partial differential algebraic equation
PDF	Probability density function
PE	Pickering emulsion
PEG	Poly(ethylene glycol)
PETPP	Polyether-substituted triphenyl phosphine
PNIPAM	Poly(<i>N</i> -isopropylacrylamide)
ppm	Parts per million
pro	Product
PFR	Plug flow reactor
QM	Quantum mechanics
QRD	QR decomposition
QSPR	Quantitative structure–property relationship
RA	Reductive amination
RAST	Real adsorbed solution theory
RDS	Rate-determining step
rea	Reactant
REACH	Registration, Evaluation, Authorisation and Restriction of Chemicals
RS	Resting state, rhodium hydrido-dicarbonyl complex
RSBR	Repeatedly operated semibatch reactor
RTO	Real-time optimization
SAFT-VR	Statistical associating fluid theory with attractive potential of variable range
SE	State estimation
SEM	Scanning electron microscopy
SLE	Solid–liquid equilibrium
SLLE	Solid–liquid–liquid equilibrium
SRC	Standardized regression coefficients
SULFOXANTPHOS	[Rh(acac)(CO) ₂]/4,5-bis(diphenylphosphino)-9,9-dimethyl-2,7-disulfoxanthene disodium salt
SVD	Singular value decomposition
SVM	Support vector machine
SX	Sulfoxantphos
TAC	Total annual cost
TC	Rh-tetracarbonyl
TEM	Transmission electron microscopy
THF	Tetrahydrofuran
THPO	Tetrahydropyranone
TMS	Thermomorphic multiphase system
TMPGP	Tri-(methoxyl polyethylene glycol)-phosphite
TPP	Triphenylphosphine
TPPTS	Trisodium 3,3',3"-phosphinetriyltribenzenesulfonate
<i>tt</i> -telomer	Tail-to-tail telomer
TRL	Technology readiness level
TST	Transition state theory
UCST	Upper critical solution temperature

UF	Ultrafiltration
UNIFAC	Universal functional activity coefficient
UNIFAC-DO	Universal quasichemical functional group activity coefficients Dortmund
UNIFAC-IL	Universal functional activity coefficient for ionic liquids
UT	ULTRA-TURRAX [®]
VLE	Vapor–liquid equilibrium
VLLE	Vapor–liquid–liquid equilibrium
w/o	Water in oil
WP	Working point
WPC	Weak-polar components
XANTPHOS	4,5-Bis-(diphenylphosphino)-9,9-dimethylxanthene

List of Symbols

Latin Letters

Symbol	Unit	Property
A	J mol^{-1}	Helmholtz energy
a	m^2	Area
A_c	m^2	Cross-sectional area
A_i	–	Antoine A parameter of component i
A_{void}	m^2	Total void area
A_{tot}	m^2	Total oil contact area
A_{\emptyset}	m^2	Total cross-sectional area of particles
a	$\text{m}^2 \text{s}^{-1}$	Thermal diffusivity
a	–	Thermodynamic activity
a	$\text{m}^2 \text{m}^{-3}$	Volume specific transfer area
a_{\emptyset}	$\text{m}^2 \text{kg}^{-1}$	Specific particle cross section
B_i	K	Antoine B parameter of component i
C	Various	Capacity matrix
C	Various	Objective function
C_D	–	Drag coefficient
C_i	K	Antoine C parameter of component i
C_i	mol m^{-3}	Molar concentration of the i th component in the reactor
$C_{i,\text{polar}}$	mol m^{-3}	Molar concentration of the i th component in the polar phase
$C_{i,\text{nonpolar}}$	mol m^{-3}	Molar concentration of the i th component in the nonpolar phase
$\dot{C}_{i,\text{out,polar}}$	$\text{mol m}^{-3} \text{s}^{-1}$	Molar concentration of the i th component in the polar outflow of the decanter
$\dot{C}_{i,\text{out,nonpolar}}$	$\text{mol m}^{-3} \text{s}^{-1}$	Molar concentration of the i th component in the nonpolar outflow of the decanter
C_{invest}	€	Investment costs
C_{op}	€ year $^{-1}$	Operational costs
CPT	€ t $^{-1}$	Cost per ton of tridecanal
c	mol m^{-3}	Concentration
c	various	Constant vector
c_{add}	–	Number of selected points
$c_{\text{Rh(acac)(CO}_2)}$	mol m^{-3}	Concentration of the precursor
c^*	mol m^{-3}	Equilibrium concentration
CRAA	$\text{nm}^{-2} \text{h}^{-1}$	Conversion rate per active area
D	m	Tank/reactor diameter
$D_{AB}/D_{a,b}$	$\text{m}^2 \text{s}^{-1}$	Diffusion coefficient
d	m	Diameter
d	–	Design variable
d_{gap}	m	Gap size
$d_j(\text{Euclidean})$	Various	Minimum Euclidean distance
$d_j(\text{Manhattan})$	Various	Minimum Manhattan distance
$d_{3,2}$	m	Sauter mean diameter
E	–	Expectation value
E_i	J mol^{-1}	Activation energy for the reaction r_i

(continued)

Symbol	Unit	Property
E'	N m^{-1}	Elastic dilational modulus
E''	N m^{-1}	Viscous dilational modulus
E^+	N m^{-1}	Dilational viscoelasticity
F	Various	Weight factor matrix
F_θ	Various	Fisher information matrix
$F_{\theta,\text{prior}}$	Various	Fisher information matrix prior
\tilde{F}_θ	Various	Weighted Fisher information matrix
f	–	Discretized system of differential equations
f	–	Function
f	Pa	Fugacity
f	–	Model for the prediction of molecular properties
f_{acc}	–	Part of the molecule that can serve as an acceptor for hydrogen bonding
f_p	–	True description of the process
f_m	–	Nominal model of the process
f_V	N m^{-3}	Volume forces
G	–	Geometrical state of the fluid element
G	J mol^{-1}	Gibbs free energy
G	–	Constraint functions of the optimization problem
G_{ad}^k	–	Adapted constraint functions for the k th iteration
G'	Pa	Storage modulus
G''	Pa	Loss modulus
g	–	Equation
g	m s^{-2}	Gravitational constant
g	s^{-1}	Matter element geometry variation rate
g_E	J	Excess Gibbs energy
H	mol m^{-3}	Henry's constant
	Pa^{-1}	
H	m	Tank/reactor filling height
H	–	Steady-state model equations
h	Various	Equality constraints
h	m	Height
h	–	Inequality constraint
$h(\sigma)$	–	σ -Profile – a fingerprint of a molecule according to the COSMO theory
h_c	m	Stirrer clearance
h_1	–	Inequality constraints for integrated solvent and process design
h_2	–	Equality constraints for integrated solvent and process design
\tilde{h}	Various	Inequality constraints
J	$\text{L m}^{-2} \text{h}^{-1}$	Flux
J	Various	Generalized flux vector
J	–	Objective function of the optimization problem
J_{ad}^k	–	Adapted objective function for the k th iteration
J_j	mol s^{-1}	Molar flux of the j th gas component into the liquid phase of the reactor
j	$\text{mol m}^{-2} \text{s}^{-1}$	Diffusion flux density vector

(continued)

Symbol	Unit	Property
j_{mix}	$\text{mol m}^{-2} \text{s}^{-1}$	Axial dispersion fluxes
K_a	–	Thermodynamic equilibrium constant
K_f	–	Thermodynamic equilibrium constant
K_i	–	Distribution coefficient
K_x	–	Mole-fraction-based apparent equilibrium constant
K_y	–	Activity-coefficient-based apparent equilibrium constant
K_φ	–	Fugacity-coefficient-based apparent equilibrium constant
k	–	Discrete time point
k	Various	Reaction rate constant
k_B	J K^{-1}	Boltzmann constant
k_{ij}	–	Binary interaction parameter
k_L	m s^{-1}	Mass transfer coefficient
$k_L a$	s^{-1}	Volumetric mass transfer coefficient
k_N	m^{-2}	Amount of SX molecules per particle surface
L	–	Catalyst leaching new
L	m	Length
L	mol mol^{-1}	Loss
l/b	–	Linear to branched
M_{acc}	e \AA^{-1}	First-order σ -moment for the part of the molecule that can serve as an acceptor for hydrogen bonding
M_c	–	Mixing coefficient
M^k	$(\text{e \AA}^{-1})^k$	σ -Moment of order k
MW	kg mol^{-1}	Molecular weight
m	kg	Mass
m	€	Revenue margin
m_{cat}	kg	Mass of active catalyst in the reactor
m_i^{seg}	–	Segment number
\dot{m}	kg s^{-1}	Mass flow
\dot{m}_A	$\text{kg m}^{-2} \text{s}^{-1}$	Mass flux
N	–	Number of samples
N	–	Set of auxiliary degrees of freedom
N_i	–	Max. value for index i
N_j	–	Max. value for index j
N^A	–	Number of electron donors
N^B	–	Number of electron acceptors
NSS	–	Number of subsets
N_{test}	–	Number of samples in the test set
\dot{N}	mol s^{-1}	Molar flow rate
n	–	Number of auxiliary degrees of freedom
n	mol	Molar amount
n	s^{-1}	Stirring frequency
n	–	Vector with structure information of a solvent
n_{Exp}	–	Number of experiments
$n_{i,\text{liq}}$	mol	Number of moles of the i th liquid component in the reactor
$n_{j,\text{gas}}$	mol	Number of moles of the j th gas component in the reactor
n_u	–	Number of input variables

(continued)

Symbol	Unit	Property
n_y	–	Number of measured variables
n_θ	–	Number of uncertain parameters
n^L	–	Lower bounds for the structure of a solvent in integrated solvent and process design
n^U	–	Upper bounds for the structure of a solvent in integrated solvent and process design
\dot{n}	mol s^{-1}	Molar flow rate
$\dot{n}_{i,A}$	mol s^{-1}	Molar flow rate of component i in phase A
$\dot{n}_{i,\text{in}}$	mol s^{-1}	Molar flow rate of component i in the feed
$\dot{n}_{j,\text{off-gas}}$	mol s^{-1}	Molar outflow rate of the j th gas component as an off-gas
O	Various	Criterion space
P	$\text{kg m}^2 \text{s}^{-3}$	Power
P	€ mol^{-1}	Price per mole
P	Various	Space of time-constant controls
P_{12}	mol mol^{-1}	Partition coefficient of a solute between two liquid phases
p	–	Parameter
p	Pa	Pressure
p	–	Property vector for a solvent
$p_{0,i}^{LV}$	Pa	Vapor pressure of component i
p^L	–	Lower bounds for properties of a solvent in integrated solvent and process design
p^U	–	Upper bounds for properties of a solvent in integrated solvent and process design
Q	–	Covariance matrix
Q_0	–	Cumulative number based size distribution
q	–	Corresponding catalyst component
\dot{q}	$\text{J m}^{-2} \text{s}^{-1}$	Heat flux
R	–	Covariance matrix
R	–	Real numbers
R	m^{-1}	Resistance
R	$\text{J mol}^{-1} \text{K}^{-1}$	Universal gas constant
r	m	Radius
r	–	Number of repetitive reaction runs
r	$\text{mol m}^{-3} \text{s}^{-1}$	Reaction rate
r	m	Spatial variable
r_V	$\text{mol m}^{-3} \text{s}^{-1}$	Internal volumetric reaction flux
S	mol mol^{-1}	Selectivity
S_i	–	Effect of a single parameter i
S_j	$\text{e}/\text{Å}$	Partial section of a σ -profile
$S_{T,i}$	–	Total effect of parameter i
SF	–	Selection factor
SFC	–	Set of all species
SRC	Various	Standardized regression coefficient
STY	$\text{kg L}^{-1} \text{s}^{-1}$	Space–time–yield
s	–	Packing parameter

(continued)

Symbol	Unit	Property
s_j^2 (Jackknife)	Various	Jackknife variance
s_j^2 (Bootstrap)	Various	Bootstrap variance
s_1	–	Inequality constraints for solvent structure in integrated solvent and process design
s_2	–	Equality constraints for solvent structure in integrated solvent and process design
T	K	Temperature
T_{ref}	K	Reference temperature
TOF	s^{-1}	Turnover frequency
TON	–	Turnover number
TON	–	Total turnover number
t	s	Time
t_f	s	Final time
t_0	s	Initial time
U	Various	Space of the dynamic control variables
u	$m s^{-1}$	Velocity magnitude
u	–	Control variable
$u(t)$	Various	Dynamic control vector
u^k	–	Input for the k th iteration
u^L	–	Lower bound of the manipulated variables
u^U	–	Upper bound of the manipulated variables
u^*	–	Optimum of the optimization problem
u_p^*	–	Process optimum
u_m^*	–	Nominal model optimum
$u_i k_B^{-1}$	K	Dispersion energy parameter
V	m^3	Volume
V	m^3	Molar volume
V_{decanter}	m^3	Decanter volume
V_L	m^3	Liquid volume
$V_{R,\text{liq}}$	m^3	Liquid volume in the reactor
Var	–	Variance
\dot{V}	$m^3 s^{-1}$	Volumetric flow rate
\dot{V}_{in}	$m^3 s^{-1}$	Inlet volumetric flow rate
$\dot{V}_{\text{nonpolar}}$	$m^3 h^{-1}$	Volume flow rate of the nonpolar outlet stream from decanter
\dot{V}_{out}	$m^3 s^{-1}$	Outlet volumetric flow rate
\dot{V}_{polar}	$m^3 h^{-1}$	Volume flow rate of the polar outlet stream from decanter
v	–	Random Gaussian white noise variable
v	$m s^{-1}$	Velocity
v_g	$m s^{-1}$	Superficial gas velocity
$v_{i,l}$	–	Molar coefficients of the i th component in the l th reaction
W	–	Catalyst leaching old
W	–	Weight matrix
w	$kg kg^{-1}$	Mass fraction
w	–	Random Gaussian white noise variable
w	$m s^{-1}$	Velocity
w	m	Width

(continued)

Symbol	Unit	Property
$w_{i,\text{product}}$	kg kg^{-1}	Mass fraction of component i in the product stream
w_t	J	Technical work
w_{tip}	m s^{-1}	Tip speed
X	mol mol^{-1}	Conversion
X	Various	Space of the state variables
x	Various	State vector, molar fraction
y_p	–	Vector of n_y plant measurements
y_m	–	Vector of n_y model-simulated measurements
x^{eq}	Various	Equilibrium values of states
X_ω	Various	Operational degrees of freedom
x^{I}	mol mol^{-1}	Molar fraction of a phase in liquid–liquid equilibrium with another phase II
x^{II}	mol mol^{-1}	Molar fraction of a phase in liquid–liquid equilibrium with another phase I
Y	mol mol^{-1}	Yield
y	Various	Measured variables
y	–	Measurement
y_c	Various	Continuous design degrees of freedom
y_{class}	–	True class
y_d	Various	Discrete design degrees of freedoms
y_p^k	–	Process measurements for the input u^k
y_m^k	–	Nominal model-simulated measurements for the input u^k
\tilde{y}_{class}	–	Classifier output
\tilde{y}_{ij}	Various	Weighted average of the jackknife pseudovalues
Z_i	Various	Regressed objective value
z	–	Noncatalyst phase
z	m	Spatial variable
z_ω	Various	Uncertain parameters

Greek Letters

Symbol	Unit	Property
α	–	Independent phase
α	–	Volume fraction
α	kg kg^{-1}	Weight ratio of oil to oil and water
α_k	–	Value of the slope criterion
β	–	Independent phase
β_i	Various	Regression coefficient
Γ	kg m^{-2}	Surface concentration
γ	–	Activity coefficient
γ	Nm^{-1}	Surface tension
$\dot{\gamma}$	s^{-1}	Shear rate
δ	m	Film thickness
δ_{eff}	m	Effective active membrane layer thickness
ε	–	Dielectric constant
ε	W kg^{-1}	Energy dissipation rate
$\varepsilon^{A_i B_i} k_B^{-1}$	K	Association-energy parameter
$\varepsilon_j^k, \varepsilon_G^k$	–	Bias correction modifiers
ζ	V	Zeta potential
ζ_i	–	Split factor of the i th component in the decanter
η	Pa s	Dynamic viscosity
η	–	Sampling criterion
η_A	–	Relative saturation
Θ	Various	Parameter space
θ	–	contact angle
θ	s	Average time at surface
θ	Various	Time-constant control vector
θ	Various	Uncertain parameter vector
θ^*	Various	True parameter vector
$\hat{\theta}$	Various	Best parameter guess
κ	–	Coefficient in eq. (3.3.1)
$\kappa(T)$	Various	Collision frequency factor
$\kappa^{A_i B_i}$	–	Association-volume parameter
μ	J mol^{-1}	Chemical potential
μ	Pa s	Dynamic viscosity of fluid
μ	–	Process variables in integrated solvent and process design
μ^L	–	Lower bound for a process variable in integrated solvent and process design
μ^U	–	Upper bound for a process variable in integrated solvent and process design
μ_i	D	Dipole moment
μ^*	–	Viscosity ratio
ν	$\text{m}^2 \text{s}^{-1}$	Kinematic viscosity
ν	–	Stoichiometric matrix
ν_i	–	Stoichiometric coefficient
π	Pa	Osmotic pressure
π_ω	–	Probability of scenario ω
ρ	kg m^{-3}	Density
σ	Nm^{-1}	Surface tension
σ_i	Å	Segment diameter

(continued)

Symbol	Unit	Property
σ	$e \text{ \AA}^{-1}$	Charge of a surface segment of a molecule according to the COSMO theory
σ	$e \text{ \AA}^{-1}$	Charge of a surface segment of a molecule according to the COSMO theory
σ_{hb}	$e \text{ \AA}^{-1}$	Threshold value for the surface charge of a molecule above which hydrogen bonding is possible
τ	s	Residence time
τ_A	N m^{-2}	Surface stress
ϕ	–	Arrival cost
ϕ	Various	Objective function
ϕ	Various	Objective function metrics
φ	Various	Differential reaction flux
φ	–	Disperse phase fraction
φ	–	Volume fraction
φ_i	–	Fugacity coefficient
Ψ	–	Dimensionless ratio
Ψ_j^k, Ψ_G^k	–	Gradient correction modifiers
Ω	–	Number of discrete scenarios

Subscripts

A	Component A
Ald	Aldehyde
abs	Absorption
BzCl	Benzoyl chloride
b	Bubble
b	At conditions before start
C	Cake
dod	Dodecene
CO	Carbon monoxide
c	Contact
c	Continuous
dod	Dodecene
d	Disperse
f	Fluid
G	Gas
g	Gas
H	Hydrodynamic
H	Hydrogen
HYD	Hydration
HYFO	Hydroformylation
i	Index of disperse phase
i	Solvent (1-dodecene)
i	Substrate
j	Particle type

(continued)

L	Liquid
M	Membrane
NaOH	Sodium hydroxide
PE	Pickering emulsion
p	Product
p	Particle
surf	Surfactant
tot	Total
w	Water
wash	Washing during membrane pretreatment
react	Reaction
s	Surface
st	Stirrer
tip	At the tip of the stirrer
0	At starting conditions
0	Reference state

Dimensionless Numbers

$Fo = \frac{D_{AB} \cdot t}{d^2}$	Fourier number
$Fr = \frac{n^2 \cdot d_{st}}{g}$	Froude number
$Pe = \frac{w \cdot d}{D_{AB}}$	Péclet number
$Pr = \frac{\nu}{a}$	Prandtl number
$Q = \frac{\dot{V}_G}{n \cdot d^3}$	Dimensionless gas flow number
$Re = \frac{w \cdot d}{\nu}$	Reynolds number
$Sh = \frac{k_L \cdot d}{D_{AB}}$	Sherwood number
$We = \frac{\rho \cdot w^2 \cdot d}{\sigma}$	Weber number

1 Motivation and Objectives

Matthias Kraume

In 2020, humankind used up the resources that nature can restore in a single year in just under 8 months [7]. However, the increasingly visible consequences of this wasteful use of resources, such as climate change, biodiversity loss, or shrinking forests, are forcing humankind to consume the Earth's resources less extensively. For that, the restoration of a balance between renewable and consumed resources is a minimum requirement. To fulfill this demands extensive innovations and high-tech solutions in all sectors, from private households to the transport sector to the manufacturing industry. Faced with these challenges, science, industry, and society are currently developing strategies for structural change toward a circular economy.

For the process industry, this results in the need to reduce the consumption of fossil raw materials, which affects both the consumption of energy and raw materials used to manufacture valuable products. For the chemical industry, this results, among other things, in the challenge of changing the raw material base for chemical production from fossil to renewable feedstocks. As a result, the products based on renewable raw materials should be either fed as intermediate products directly into the existing production networks or used as chemical end products for further processing. Additionally, modern, efficient production concepts must be implemented based on, for example, the ideas of Green Chemistry and aim for the most environmentally friendly production of chemical products [1]. In addition to using renewable raw materials, the essential principles of this chemistry are the application of highly efficient catalysts, the use of harmless solvents, energy efficiency, and process optimization in real time.

Given the lack of large-scale industrial processes, these goals are currently still of a visionary nature. However, several classes of renewable raw materials are now being examined regarding their suitability for substituting fossil raw materials. Unsaturated oleo compounds, obtained as renewable raw materials from animal fats and oils, constitute one such class of potential raw materials. Their very defined structures make them closely related to basic chemicals. Ideally, the feedstocks are not cracked into individual short-chain components first but used as unaltered as possible. For example, end products such as biosurfactants or biopolymers are made from fats or carbohydrates. Nature's synthesis effectiveness can thus be fully exploited, and renewable raw materials converted into valuable products in an energetically advantageous manner.

The program of the research project presented in this book addresses the substance group of long-chain unsaturated olefins and oleo compounds and dealt with the task of introducing polar functional groups containing oxygen and nitrogen into the feedstocks with the help of various catalytic reactions. The aim was to manufacture essential basic chemicals that can, later on, be fed into the existing production networks.

Since renewable raw materials have different structures, molecular compositions, and physical properties from petrochemicals and, additionally, a production that is as environmentally friendly as possible was to be achieved, and new, efficient production processes had to be developed. To this end, not only new methodological approaches had to be worked out, but an innovative path that has not yet been technically implemented was to be pursued by using phase systems with partially tunable properties. Furthermore, the aim was to utilize the advantages of homogeneous catalysis while avoiding the problems usually associated with it, namely the recovery and recycling of the highly efficient but mostly very expensive catalyst complexes. The application of liquid multiphase systems was the specific approach of the research program to reach this goal.

Owing to the complexity of the task, the research approach pursued was strongly interdisciplinary as it went far beyond the exclusively experimental investigation of the central chemical reactions. The extensive method development was based on selected reactions, including the associated processing steps, to design complete processes. In addition to the elucidation of reaction networks and kinetics, the thermodynamic properties of the phase systems that had not yet been adequately analyzed had to be better understood and modeled. In addition to quantifying their physical properties, this task also included processes such as mixing, separation, and mass transfer. Ultimately, it was necessary to implement methods for efficient, integrated process design. The designed processes were technically implemented on a miniplant scale, including catalyst and educt recycling, and optimized systematically based on models. For this project, methods from the disciplines of technical chemistry, thermodynamics, fluid dynamics, process engineering, and systems engineering were either newly or further developed and brought together to synthesize efficient integrated entire processes. Overall, a comprehensive understanding of the process and a model-based approach for process development in iterations between experiments and model-based optimization were generated for the selected advanced phase systems through this interdisciplinary research.

The handling of such a global task required an extensive network in which numerous individual investigations and developments could be carried out in parallel over a sufficiently long time. Furthermore, diverse competencies in the field of fundamental research had to be brought together and coordinated. With the SFB/Transregios, the German Research Foundation offers a funding instrument that enables establishing such a research network. In this way, scientists from several universities and research institutions have worked for 12 years within the SFB/TR 63 (integrated chemical processes in liquid multiphase systems) to develop efficient chemical processes in liquid multiphase systems. The resulting method reservoir was designed in a manner that is as generally applicable as possible and is now also available for other processes. For a better first overview, the closely interlinked research work and its objectives are presented in this chapter in a condensed form.

1.1 Goals and Scientific Concept

The overarching goal of the research program was the technical development of multiphase systems for the catalytic conversion of biogenic raw materials with efficient catalyst separation and recycling to substitute conventional petrochemicals with a high level of environmental friendliness and sustainability. A research program for the development of the associated processes which follow the principles of Green Chemistry, for example, must cover all levels of chemical processes from the molecular elementary steps of the reaction via the individual process steps to the design and operation of the entire plant. The scope of such a program requires boundaries that keep the effort within manageable limits. Therefore, the SFB/TR 63 focused on the necessary methods for the development of homogeneously catalyzed processes in liquid multiphase systems. Chemical–physical fundamentals, together with process and systems technology, formed the scientific foundation. The applied methods can be assigned to three thematic focal points (Figure 1.1).

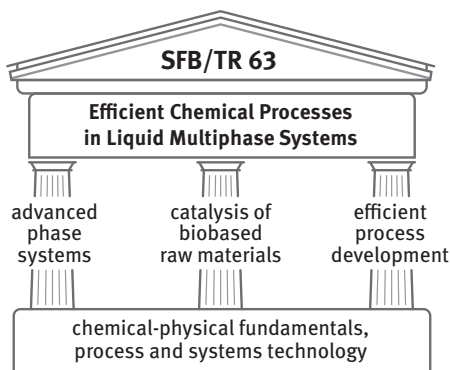


Figure 1.1: Foundation, pillars, and roof of the research program.

Innovative phase systems formed the first pillar of the research program of the SFB/TR 63: thermomorphic multiphase system (TMS), microemulsion systems (MES), and Pickering emulsions (PE). These phase systems were chosen because they promise homogeneously catalyzed reactions with high conversions and selectivities with simultaneously highly efficient catalyst separation. Furthermore, the reaction and separation steps were considered in an integrated manner to achieve the optimum of the overall process instead of local optima for individual process steps. However, despite the great interest from the chemical industry, these novel phase systems have little been used on an industrial scale so far. On the one hand, this is due to a lack of the required chemical–physical and process-engineering fundamentals. On the other hand, the evidence is missing that these phase systems can be used to implement economically and ecologically attractive overall processes.

The second pillar represented the homogeneously catalyzed treatment of long-chain olefins and unsaturated oleo compounds as typical representatives of biobased raw materials. Polar functional groups containing oxygen or nitrogen were to be introduced into these molecules with high selectivity. This requires highly developed homogeneous catalyst–ligand systems. Because of the high costs of the catalysts and ligands, the development of processes that enable almost complete catalyst recycling is a central challenge for the profitability of such operations.

Methodological gaps for the design of efficient processes were closed through an integrated research approach as a third pillar. New methods of reaction management, together with special (partially) integrated reaction and separation processes, were investigated, and the results merged in an overall process simulation and optimization. With the aim of holistic and rapid process development, the entire process from basic or platform chemicals to the pure product was considered.

The objective of the research program required the creation of relevant knowledge and methods for the design of efficient chemical production processes based on liquid, reactive multiphase systems, and new types of phase systems. This resulted in three essential subgoals:

1. Significant deepening and broadening of the chemical–physical and process engineering fundamentals of complete, homogeneously catalyzed processes with several fluid phases.
2. Further development, integration, and sample application as well as validation of the methods for fast, systematic, model-based process development using challenging new reaction systems.
3. Accelerated process development from first laboratory experiments for catalyst and phase system selection up to the demonstration of the operation of the process with optimized process control in miniplants within four years as a challenging period.

As a result of the SFB/TR 63, an elaborated, integrated procedure for rapid process development from the first theoretical concept to the overall process selection, overall process simulation, and process optimization is available. To this end, numerous methodological developments were united, tested, and validated using sample reactions. Thus, the whole development chain from the first reaction-related investigations in the laboratory up to the technological realization in feedback controlled miniplants was implemented. Furthermore, based on the experiences of the entire duration of the SFB/TR 63, a classification was developed for an efficient selection of a suitable phase system for the broadest possible spectrum of homogeneously catalyzed reactions based on orienting key experiments and the assessment of fundamental properties of substances and mixtures.

1.2 Advanced Phase Systems

A fundamental task of the project was the research on promising novel types of phase systems for homogeneously catalyzed, multiphase production processes in the spirit of Green Chemistry, together with the development and validation of efficient processes applying them. Since the start of the research project in January 2010, national and international interest in innovative phase systems has grown significantly. This is demonstrated, for example, by the rapidly increasing number of scientific papers on the subjects “advanced fluids,” “tunable solvents,” or “switchable solvents.” In 2010, 92 articles with one of the three terms in their title were published; in 2020, there were already 348 (source: Google Scholar).

Figure 1.2 illustrates the properties of the phase systems and their importance for homogeneously catalyzed liquid–liquid reactions combined with the subsequent catalyst separation. Conventionally, such processes are often carried out with a purely mechanical dispersion of the reaction components. The other extreme alternative consists of providing single-phase reaction conditions, for example, by adding solvents. In catalytic processes, efficient catalyst recovery is usually indispensable for economic reasons. For an entire process, therefore, not only the efficiency of the reaction stage is decisive, but also that of the subsequent catalyst retention. The single-phase state leads to highly efficient reaction conditions, but the subsequent separation of the catalyst systems is complex.

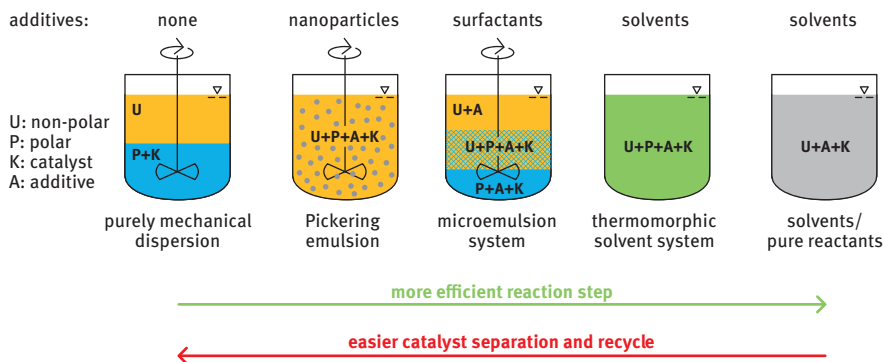


Figure 1.2: Phase systems for liquid–liquid reactions.

On the other hand, with a purely mechanical dispersion, the reaction is less efficient due to the mass transfer resistance and the small interfacial area. Still, the subsequent separation step becomes efficient and straightforward. The phase systems currently intensively investigated range between the two extremes of purely mechanical dispersion and single-phase reaction. They represent attractive but so far hardly developed alternatives to the conventional concepts. From a large number of possible

such phase systems, three different systems were selected and examined as typical representatives: thermomorphic solvent systems, MES, and PE. Many results of these investigations should be transferable to other phase systems.

Developing a method for the uncomplicated and quick identification of the best-suited phase system constituted a superordinate task in the phase system investigations. This should open up the possibilities for industrial users to make a reliable selection of a phase system very early on with correspondingly little information and low experimental effort. The strategies required for this were to be developed based on a combination of a few key experiments and model concepts to keep the expenditure for selecting phase systems within an economic limit.

1.2.1 Thermomorphic Multiphase Systems

In TMS (Section 2.1), the use of multicomponent solvent systems can influence the phase behavior. The systems basically consist of two components (polar and nonpolar) with a corresponding miscibility gap. The phase behavior, especially the temperature dependency of the width of the miscibility gap, can be varied by adding a third, medium-polar substance (additional additive or feedstock or product). A single-phase reaction can thus be carried out at an elevated temperature (Figure 1.3). The reaction, therefore, takes place with a molecular disperse distribution of the reaction components and thus ideal mass transport conditions. When the temperature drops, two phases form again. In this way, simple separation and recycling of the catalyst by simple phase separation due to gravity are made possible after the reaction step. Concepts for the realization of homogeneously catalyzed reactions in two-phase systems are based on the specific adjustment of the solubility of the catalyst, the feedstocks, and the products in the phases that coexist at low temperatures. A suitable choice of pure solvents or solvent mixtures must be used to find an appropriate system for both the reaction and subsequent separations.

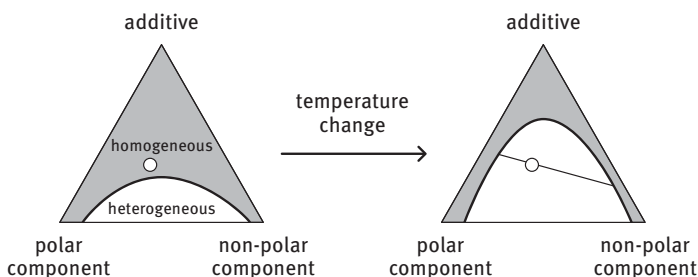


Figure 1.3: Schematic representation of the concept for the use of thermomorphic systems.

1.2.2 Microemulsion Systems

As a second phase system to intensify the contact between the starting materials and the catalyst complex, MES (Section 2.2) were used to carry out homogeneously catalyzed reactions. Adding surfactants reduces the interfacial tension between the organic and the aqueous catalyst phase, and the interfacial area caused by dispersion increases dramatically. In contrast to classic homogeneous catalysis, as in thermomorphic solvent systems, where there is only one phase, in MES, mass transfer resistances appear between the phases. Different phase states that depend on composition and temperature may occur when adding a nonionic surfactant to an oil–water mixture (Figure 1.4). The strong temperature dependence of the phase equilibria in these multicomponent systems can be used for catalyst recovery and product isolation, analogous to TMS. However, so far, catalysis in MES has only rarely gone beyond the laboratory scale so that only a single industrial application is known [5]. One reason for this is the complex interrelationship between the numerous physical properties and process parameters and their effects on the entire process, which have only been partially understood. Furthermore, the procedures for processing the product stream of MES have not yet been systematically developed to process maturity.

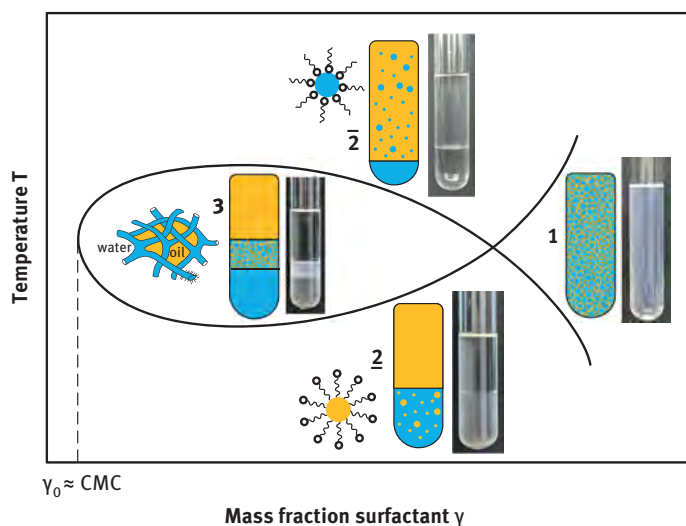


Figure 1.4: Phase behavior of ternary mixtures of oil, water, and surfactant.

1.2.3 Pickering Emulsions

In PE (Section 2.3), drops are stabilized by partially wetted nano- or microparticles, and the formed emulsion type (w/o or o/w) mainly depends on the contact angle of

the particles (Figure 1.5). PE have been known for a long time. Today, they are already used industrially, for example, for the formulation of active ingredients in food technology and drug delivery. In contrast, their application in chemical production on an industrial scale is not known. Although PEs have also been used in connection with chemical reactions in the last 10 years in academic research, mainly batch processes and no continuous processes on a laboratory scale have been investigated.

In PEs, the intensity of the dispersion lies between that of MES and that resulting from purely mechanical dispersion, which leads to larger interfacial areas compared to systems without additives and thus better mass transfer. At the same time, however, the stability of the emulsions is too high for phase separation in a liquid–liquid gravity settler but – in contrast to TMS and MES – facilitates mechanical separation of the catalyst containing droplets from the product containing phase (Figure 1.5) without having to disperse/emulsify/dissolve the aqueous phase again. The challenges for using PE in liquid multiphase systems result, on the one hand, from the lack of validated technological concepts for separating the phase containing particles and catalysts from the organic product phase. On the other hand, by selecting particles of suitable size and suitable wetting properties, a system that is equally well suited for reaction and separation must be found. Ultimately, completely new continuous processes must be developed in system technology.

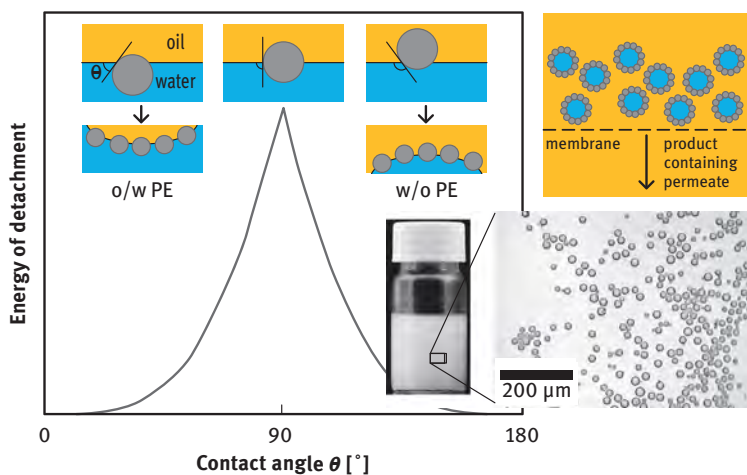


Figure 1.5: Schematic representation of how particle contact angle θ influences the formed type of Pickering emulsion, adapted from Binks [2], photographs/micrographs of a w/o PE and envisaged separation in continuous reactions.

1.3 Material Basis and Reactions

The method development was based on selected feedstocks and reactions, including the associated processing steps of an entire chemical process and the internal recycling flows that occur. Long-chain, unsaturated compounds that can also be obtained from renewable raw materials formed the material basis. The feedstocks used were 1-decene and 1-dodecene, two linear olefins with a terminal double bond, and two biobased unsaturated oleo compounds with 10-undecenoic acid methyl ester and oleic acid methyl ester.

For the selection of the investigated reactions (Figure 1.6), their model character and technical relevance for the chemical industry and the substitution of petrochemicals by renewable raw materials were decisive criteria. For the model character of the reactions, it was crucial that other types of reactions also catalyzed by transition metals behave very similarly. The results obtained in the research project can, therefore, apply to these types of reactions. Ultimately, the same basic principle can be used to carry out numerous reactions with long-chain, unsaturated molecules. These include essential addition reactions with olefins with the formation of new C–C, C–O, C–N, or C–Si bonds such as hydroformylation, hydroesterification, hydroaminomethylation, hydrocarboxylation, amination, and hydrosilylation.

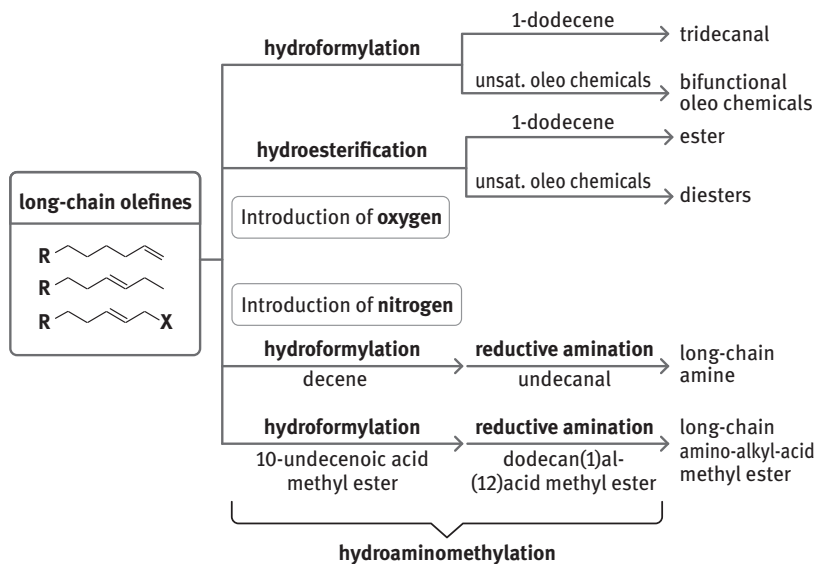


Figure 1.6: Material basis and reactions of the research program.

With the help of homogeneous catalysis, functional groups were introduced into the feedstocks to convert them into valuable intermediate products by introducing heteroatom-containing substituents. Processes for the introduction of oxygen and nitrogen were developed and validated in miniplants in feedback-controlled operation. The hydroformylation and hydroesterification of 1-dodecene and methyl undecenoate, and methyl oleate were selected for the introduction of oxygen-containing groups.

The introduction of nitrogen into petrochemical and renewable basic chemicals was investigated to enable access to amines and amides from these raw materials. For this purpose, the reductive amination of long-chain aldehydes and the hydroaminomethylation of long-chain olefins and oleo compounds were treated. These reactions were also chosen because they lead to increased complexity, which is more common in homogeneously catalyzed reactions. The water formed as a by-product in the reaction is soluble in the catalyst phase and must be continuously removed from the process. Due to the high reaction rate, the gas–liquid–liquid mass transfer is essential for macro kinetics.

As homogeneous catalysts, in most of our studies, rhodium complexes with diphosphine or diphosphite ligands were chosen. The design and selection of a suitable ligand for a homogeneous catalyst is a research field of its own. This is covered in other references [6]. The versatility of ligands is governed by the molecular architecture, electronic properties, and stereogenic behavior. In comparison to ligand-free metals, the ligand-modified catalysts show higher activity and selectivity for the desired products due to a modification of the electron density of the metal centers and steric control of the reactant binding. In comparison to monodentate ligands, a smaller metal to ligand ratio is needed for the formation of stable and selective catalysts from bidentate ligands due to the stabilizing chelate effect. The “construction” of combinations of central metal atoms and ligands depends on a firm foundation of mechanistic studies, including thermodynamic considerations. This is a proven concept which ought to be complemented by in situ spectroscopic studies and kinetic analysis. Such data will pave the way toward a mechanistic understanding and will eventually, through accurate mechanistic studies, emerge with *new* catalysts.

Out of a huge pool of available ligands, BIPHEPHOS and SULFO-XANTPHOS were chosen as representative examples for well-established, high-performance catalysts that are frequently applied in research and industry [3]. From BIPHEPHOS, a non-charged catalyst complex is obtained that proved to be well compatible with different thermomorphic solvent systems. For aqueous systems, the sulfonated version of XANTPHOS was applied, because only this bidentate phosphine ligand is stable enough for a sulfonation reaction. This is not the case for BIPHEPHOS. Due to their different electronic properties. The similar molecular architecture, expressed in a similar “bite angle” of both ligands results in a comparable selectivity of Rh-catalyst formed with these ligands. The stronger electron donation of BIPHEPHOS to Rh causes a somewhat higher activity of the Rh-BIPHEPHOS compared to Rh-XANTPHOS, independent of the

used reaction medium. Therefore, observed differences between studies with these different catalysts always need to be analyzed for the ligand effects as well as the solvent effects.

1.4 Model Process

The three-phase systems used for the reaction step differ in the intensity of the dispersion of the reaction components and the phase separation process. This variety opens a spectrum of options for possible industrial implementations. From these, a phase system optimally suited from an entire process perspective can be selected depending on the requirements of the individual reactions and the further process steps. All phase systems considered here are based on the addition of additives. These components may influence the chemical kinetics, the thermodynamic properties, and the mass transport processes coinciding inside the reactor. The choice of the phase system aims to intensify the contact between the reaction components and the catalyst complex. At the same time, almost complete separation and recycling of the catalyst complex and the additives from the product stream into the reactor are indispensable for economic reasons. These contradicting requirements inevitably necessitate a simultaneous treatment of the reaction stage and the necessary separation operations during the process design.

Due to many possible additives, their systematic selection with simultaneous consideration of reaction and separation is of outstanding importance. The additives are usually selected based on expert knowledge or heuristics. This procedure was to be replaced by systematic, experimental, and model-based selection processes in the present research project. The integrated consideration of reaction and separation stages for removing additives was essential for developing such methods. The overarching goal of these methods has always been to optimize the environmental friendliness and economic efficiency of the overall processes. For this reason, the general model process shown in Figure 1.7 was developed and experimentally investigated with the phase systems. A selective reaction procedure and efficient catalyst recovery were essential here. The further processing of the product-containing phase after the removal of additives and catalysts was beyond the scope as this product separation chain can usually be designed and optimized reliably using existing methods of thermal process engineering. For the design of entire industrial processes, however, in addition to the reaction steps, the complete separation processes were also worked out, modeled, and optimized as part of the overall process synthesis.

For all phase systems, developed process steps of the model process were implemented and operated in miniplants. The necessity of this validation resulted from the fact that for the selected reaction and separation concepts, due to their complexity, it was not sufficient to successfully implement them independently

from one another on a laboratory scale. This statement particularly applies to the transition from batch to continuous reactor operation and the closure of recycling flows. Using complex phase systems, economical overall processes can only be developed by taking a holistic view of the reaction and all other process steps. As a unique feature of the practiced process development, miniplants were already used in a very early phase of the process development. This procedure enabled critical process steps to be identified early and thus a more targeted and accelerated process development as well as the consideration of the optimizing process control already in an early development phase.

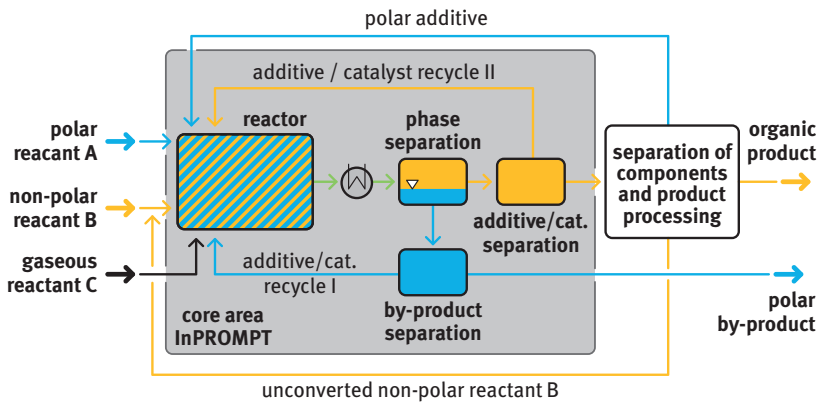


Figure 1.7: General flow diagram showing the process steps to be examined for the various phase systems with their links.

1.5 Challenges of the Fundamental Investigations

So far, complete industrial processes based on the phase systems considered in SFB/TR 63 are only rarely implemented. This is due to the lack of the necessary chemical–physical, process, and systems technology fundamentals. In addition, the complex interrelationships in liquid multiphase systems require numerous efficient methods for investigating process alternatives, optimizing the process structure, and determining the process parameters, including alternative phase systems and additives. The concepts and methodical approaches pursued within the SFB/TR 63 in basic investigations are related to three subject areas. The work is motivated in this section as an overview and explained briefly.

1.5.1 Chemical–Physical Fundamentals

The design of the process steps requires extensive knowledge and methods for characterizing the reaction kinetics as well as the substance and mixture behavior in connection with the phase systems. The associated investigations consist of experiments and modeling or simulations that aim at the molecular level. As part of feasibility studies, the fundamental suitability of the three-phase systems for the selected reactions had to be demonstrated. For this purpose, systematic batch tests were carried out on a laboratory scale, quantifying the achievable conversions and yields. In addition, different additives and catalyst systems had to be tested for their efficiency. Sequential tests answered the question of the recyclability of the catalyst system. In this way, on the one hand, it was possible to select particularly suitable additives and their optimal concentrations for the respective phase systems. On the other hand, the results allowed us to compare the phase systems concerning their efficiency. As a result of the systematic selection of the additives for the phase systems, a general catalog of criteria for choosing a suitable phase system for any catalytic reaction with practically immiscible feedstocks was to be developed.

The kinetic modeling of the investigated reactions is the basis for any design of reactors and processes. For this purpose, experimental and theoretical investigations were carried out on the mechanisms and kinetics to systematically elucidate the reaction networks and catalytic cycles, derive and reduce kinetic models, and determine the model parameters accurately. For all phase systems, the kinetic modeling was based on mechanistic, reversible models that had to be developed from the reaction mechanisms. Subsequently, the model parameters were used for the work on model-based reactor design and process optimization. In addition, the influence of impurities unavoidable in industrial applications on the kinetics of the reactions had to be assessed quantitatively as well as the catalyst deactivation processes.

Methods for determining the thermodynamic equilibrium data, which are indispensable for process design, partially had to be newly developed for the present systems. Furthermore, there was no thermodynamically consistent modeling of chemical equilibria and reaction kinetics in such systems. First of all, knowledge about the effects of solvents/solvent mixtures and temperature on solubilities, interfacial tensions, reaction equilibria, reaction kinetics, and the transition states of complex reactions was collected. This expertise enabled an influence on reactions in a targeted manner and the development of a new approach for the optimal solvent selection for chemical reactions in liquid phases. Conceptually, this methodology combines quantum chemical calculations of reaction equilibria and transition states with a modeling of the non-ideal thermodynamic activities of reactants and products of a chemical reaction. Experimental kinetic data were measured to validate the results. By combining experiments and theory, the systematic determination of the most favorable solvent from a thermodynamic and kinetic point of view was sought. Depending on the process

conditions, different isomers can be produced. Therefore, a separation based on crystallization or adsorption must be developed. The corresponding design requires a thermodynamics description of linear and branched isomers. A new modeling strategy based on the lattice cluster theory without the need for pure-component thermodynamic data had to be developed.

The level of knowledge about MESs and PEs was initially significantly lower than that of thermomorphic systems. Therefore, these had to be investigated more intensively concerning thermodynamic data and other properties as well as mass transfer processes. Thus, the thermodynamic behavior of MES was examined, with ternary phase diagrams for pure and technical nonionic surfactants being recorded using a novel analysis method. In addition to measuring the tie lines, the aim was to determine the position of the three-phase area, as this was of great importance for the separation. Another task was to model the solubilization of weakly polar components in micellar, aqueous systems. Such constituents arise in reactions like hydroformylations, hydroesterifications, and hydroaminations, where polar functional groups with heteroatoms such as oxygen or nitrogen are introduced into the feedstocks. Existing micelle formation models were previously only applicable to nonpolar or strongly polar components. Therefore, the micelle formation model was to be extended to weakly polar molecules by combining the PC-SAFT equation of state with the density gradient theory. The primary goals of this modeling were the determination of the critical micelle concentration of the surfactants in the presence of various concentrations of the weakly polar components, micelle size and shape, and, as an essential contribution to the kinetic modeling of catalytic reactions in micellar solutions, the determination of the local concentrations of the reactants near the catalyst.

In contrast to thermomorphic systems, the convective mass transport between the liquid phases affects the space-time yield in microemulsions and PEs. Thus, a deeper physical understanding of the mass transfer in these phase systems had to be developed. Furthermore, the different phases occurring in MES lead to an enormous degree of complexity in the mass transport that occurs in reactive surfactant-containing systems. Therefore, new methodical approaches had to be found to characterize mass transport in microemulsions. Additionally, a better understanding of the experimental results required the rheological characterization of the MES and PE. For both systems, the interfacial area had to be characterized by determining the drop size distributions. In PEs, surface coverage by nanoparticles together with the location of the catalyst was to be determined.

In all reactions, oxygen or nitrogen was added via gaseous components. In particular, at higher reaction rates, the gas–liquid mass transport must always be taken into account as it also determines the rate of reaction independently of the phase system. The measurements had to consider the chemical reaction, as this can significantly accelerate the mass transfer. The particular challenge with the considered systems lay in the complex interplay of up to four phases (gas, liquid, liquid, and solid) and the quantitative measurement under reaction conditions. The volume-related mass transfer

coefficient $k_L a$ was determined as the quantitative variable in a laboratory reactor for all phase systems. To differentiate between the influences of the various process parameters on the mass transfer coefficient k_L and the volume-specific interfacial area a , mass transport studies were also carried out in a micro falling film contactor with a defined interface. The experimental findings aimed to clarify the transport routes for the multiphase reactor and quantify the gas–liquid mass transport dependency, characterized by the $k_L a$ value, on all crucial influencing parameters and the phase state or particle fraction. The results summarized utilizing modeling were then available for the reactor design.

1.5.2 Process Technology

In addition to the processes that primarily occur on the molecular scale, numerous process-engineering questions related to individual process steps (reaction; separation of catalysts, additives, products, and by-products) had to be answered for process development on the scale of the technical apparatus. The research work aimed to achieve an extensive generalization of the developed experimental and theoretical methods. The common goal was to make these methods usable for the analysis and design of individual unit operations and the coupling of process steps for as broad a spectrum of material systems as possible. Finally, the question of how to realize a rational selection of the components of a phase system in connection with the design of the separation processes using computer-aided optimization methods was also taken up. In accomplishing these tasks, the results of the fundamental chemical–physical investigations were used. On the other hand, the data, models, and methods of the process engineering work for the functional description and optimization of individual process steps as well as groups of process steps were passed on to the area of system engineering investigations, in which the development of integrated overall processes was advanced.

A model-based design methodology for optimal reactors was to be developed in reactor design for liquid multiphase systems. Thereby, the best process route inside the reactor concerning several control variables can be found using a sequential optimization strategy. The methodology should be so general that it can be used for reaction networks of different complexity, various phase combinations (gas–liquid, liquid–liquid, gas–liquid–liquid), and different phase systems. Going beyond the classic reactor design, the methodology should support the synthesis of integrated reactor–separator systems, especially reactors with integrated separation functions. The apparatus implementation of the reactor systems was planned in the form of apparatus modules, which should be characterized in detail using experimental and numerical methods. Selected modules were integrated into the miniplants and evaluated experimentally concerning their performance while closing the main recycle flows. As an overarching goal, a model-based design methodology should be established and experimentally validated, with which optimal reactor–separator

systems for liquid multiphase systems can be reliably developed based on thermodynamic and chemical kinetics information.

Various separation tasks specific to the phase systems, some of which only became apparent in the course of the investigations, had to be examined more closely and methodologically developed. Especially the separation of additives and catalysts from the organic product containing phase after the reactor is essential. For TMS and MES, gravity settlers were applied for this first separation step. The droplet sizes occurring inside the reactor (MES and PE) are essential for the liquid–liquid interfacial area and thus influence mass transfer. Additionally, drop sizes also affect the phase separation after the reaction stage in a gravity settler (TMS and MES). Hence, they were to be quantified experimentally for appropriate designs and correlations with power inputs needed to generate targeted sizes. In MES, depending on the process conditions, complex drop interactions (e.g., drop-in-drop configurations as shown in Figure 1.8) occur, mainly influenced by the interfacial tensions. These interactions significantly affect the separation time of the systems. Drop-in-drop configurations cause a change in the stability of the systems, which can lead to a complete reversal of the separation process. Due to this, the phases separate in a different order which may either accelerate or delay the separation by orders of magnitude. Overall, there was a need for systematic quantification of the separation process of MES, including the determination of the state of dispersion. These requirements also included detailed modeling of the settling process of MES via the expansion of semiempirical separator models and numerical simulations based on population balances coupled with CFD models. The previously limited validity of CFD models had to be extended to a more extensive process window by considering all central influencing variables, particularly the third liquid phase and the droplet interactions. Subsequently, these models and simulations were to be used to design and optimize the phase separation of MES systems in the context of process design and process control.

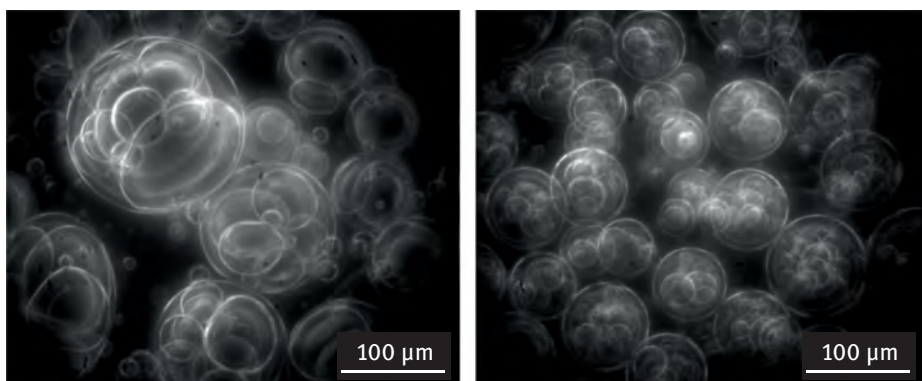


Figure 1.8: Endoscopic photographs of the three-phase system with two dispersed phases in stirred microemulsion systems at a low (left) and a higher rotational frequency (right).

When separating the reactor discharge from MES in a gravity settler, the catalyst separation from the product phase turned out to be surprisingly uncomplicated and efficient. In contrast, the occurrence of high surfactant concentrations in the product phase after the settler proved to be problematic. As a consequence of these findings from miniplant experiments, a separation method for the surfactant removal from the organic phase with sufficient surfactant retention had to be developed.

Since some of the components emerging from the reaction stages have only minor boiling point differences, simple rectification as the sole separation process is not always economical because of increasing investment and energy costs. The separation of higher boiling by-products utilizing rectification is also energy intensive since the products present in larger quantities have to be evaporated. Hybrid processes are becoming attractive for both applications, in which rectification is combined on the one hand with melt crystallization and on the other hand with organic solvent nanofiltration. For the design of hybrid separation methods, a design methodology was to be developed that can be applied in an early project phase if, for example, experimental data, precise mathematical models, and detailed cost parameters are not available. As an optimization goal, the minimum total costs must be achieved.

For PEs, the behavior of the nanoparticle stabilized droplets under process conditions had to be studied. Additionally, a novel separation process for the catalyst-containing, aqueous phase by membrane filtration had to be developed before the interactions between the reaction step and the subsequent separation, including the catalyst recycling to the reactor, could be investigated. Various nanoparticles used as additives, varying in shape and surface properties, had to be tested in different concentrations concerning their influence on both the reaction and the catalyst separation. Novel processes for separation and recycling the catalyst-containing dispersed aqueous phase and the removal of polar components were to be developed and evaluated. The result was a transferable concept for continuous multiphase reactions in PE.

In terms of methodical systematization, model-based methods for the integrated design of thermomorphic solvent systems and the associated purification processes for the efficient separation of homogeneous catalysts and solvents from reaction mixtures had to be developed. In this way, the aim was to identify new solvent systems and structures of separation processes to reduce the energy requirement and the equipment required for the catalyst separation and to improve the environmental compatibility of the solvents used significantly. The most efficient separation process for catalyst and solvent recovery was to be identified by simultaneous optimization of the molecular structure of the solvent components and the process design while sensibly weighing economic and ecological targets. The results were to be integrated into the process development and the overall process optimization.

1.5.3 Systems Technology

For the desired accelerated design of efficient chemical processes based on liquid, reactive multiphase systems, and novel phase systems, the development of new methods and tools for the systematic, model-based design of complex multiphase processes and optimal process control was required. The basic approach in process design was to develop mathematical models based on first orienting and then quantitative chemical studies of the phase system and the catalyst–ligand system. Subsequently, these models were used to determine promising flow diagrams and operating points of a possible industrial process based on optimization. After that, the quantitative statements and modeling in these relevant process windows were refined in more detailed experimental work. Based on the first models and flow diagrams, tests in miniplants provided data that could be used to improve the models. Additional early testings of high-quality control structures and optimizations carried out in miniplant scale allowed a more precise estimate of the achievable yields and optimization potential together with a more rapid subsequent implementation of the process design on an industrial scale. Finally, based on the method and tool development in the field of chemical–physical fundamentals and process technology, the developed integrated model, optimization, and miniplant-supported process design should be thoroughly tested and demonstrated using two example processes, reductive amination, and hydroaminomethylation.

A central focus of work in the area of system technology was the coordination of process development. In this way, the methods designed within the SFB/TR 63 were used in the model-based development of new multiphase processes and validated by applying them to exemplary reactions. For this purpose, the methods and tools developed in the course of the project for process design under uncertainties, for determining optimal reaction control, and for measuring and modeling thermodynamic equilibria and reaction kinetics were integrated into an iterative, model-based approach to process development driven by economic optimization. In close contact, reaction-engineering experiments, physical properties modeling, and optimizations of reactor design and flow diagrams were carried out in iteration loops. Based on the first experiments and first empirical process models, the relevant operating windows were narrowed down. The required chemical–physical models were developed and experimentally validated within these operating windows. A significant reduction in experimental effort and process development time was sought through the close interdisciplinary link of test planning, model development, and design optimization. As a result, an exemplary integrated procedure and optimized flow charts for the rhodium-catalyzed reductive amination of undecanal with diethylamine and an estimate of the resulting production costs for the phase systems were developed. As a validation, the overall process of hydroaminomethylation based on technical mixtures of decenes should be treated and experimentally investigated in the miniplant.

A unique feature of the entire research program was the early inclusion of mini-plant experiments. The investigations aimed to check individual unit operations and connections of process steps. The operated miniplants were highly instrumented and equipped with control systems to enable partially automated operation. Reactions in the various phase systems were successfully transferred from batch to continuous processes and operated for several days. Similar conversions and selectivities as in the laboratory reactors were achieved in the miniplants. The continuous operation also included catalyst separation and checking of catalyst activity. Thus, concepts from process development could be tested at an early stage, or unexpected problems in process management could be identified. For example, a predicted increase in yield through the recycling of internal 1-dodecenes during the hydroformylation in TMS could be quantified utilizing a downstream continuous rectification in an appropriately configured miniplant (Figure 1.9). In contrast, in the MES process, the liquid–liquid phase separation for catalyst recycling proved to be demanding. So, additional work in the area of process technology to master this separation step could be initiated at an early stage. Finally, the developed process management strategies could be checked. Using the example of the demanding reductive amination, the success of the integrated process development was to be demonstrated in long-term campaigns in the miniplants.

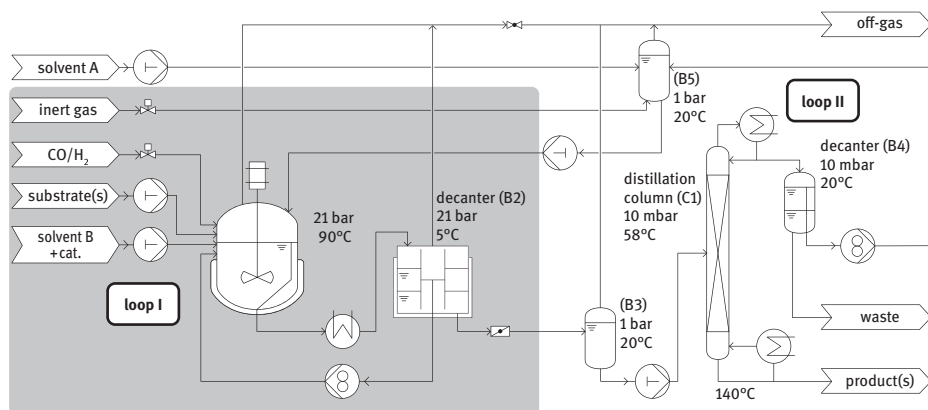


Figure 1.9: Flow diagram of the continuous-flow process of the rhodium-catalyzed hydroformylation of 1-dodecene in a TMS with DMF and *n*-decane. TMS miniplant expanded by a continuously operated distillation (white background) [4].

To support the process development, hierarchical modeling of the entire process was created based on a web-based simulation environment. This also enabled a centralized collaboration of locally distributed workgroups by using the internet. In this way, a basis for a central model filing and data storage was created, whereby an integrated model development could be realized. Furthermore, by considering and including

various submodels and process models for individual process steps, applying a hierarchical modeling system to characterize the phenomena that predominantly occur in the process became possible. The intended result was a model structure optimal in terms of various criteria for describing each unit operation and the entire process.

For the process classes considered within the SFB/TR 63, the development of new deterministic global optimization methods proved necessary because the local or stochastic solution methods usually used in process systems engineering cannot generally ensure that the solution found represents a global optimum. On the other hand, it was shown that currently available standard software for deterministic global optimization is often unable to solve relatively simple problems from a process engineering point of view globally in an optimal way. Therefore, efficient methods for global optimization had to be developed for multistage separation processes, which play an essential role in processing reaction mixtures and can significantly influence the total costs. The investigations also included global optimization under uncertainties. The starting point was the two-stage approach pursued in the process development to optimize flow diagram superstructures with uncertain model parameters.

By developing process control concepts as early as the miniplant phase, which could then be transferred directly to the production scale, the potential of the processes and possible problems during the operation were assessed at an early stage. To stabilize the function of the miniplants and optimize them online, model and data-based control and process management concepts were developed. This procedure significantly supported the testing of the process concepts in the miniplants. In particular, the MES miniplant, which was very complex in terms of both equipment and processes, could only be operated with advanced control concepts. During the implementation of these concepts, the behavior of the actual processes in the miniplants sometimes deviated significantly from the model predictions. Therefore, the consideration of model uncertainties in the model-based process management proved to be necessary. The prerequisite for these developments was designing dynamic models for the selected process concepts and operating conditions, relying on experimental data and simulation results from the investigations on the chemical–physical and process-engineering fundamentals. In this way, control and optimization strategies were targeted that can be applied to complex, highly efficient, but not precisely model-based, multiphase processes and achieve optimal economic efficiency and ecologically friendly operation.

1.6 Structure of the Book

The assembly of the investigations outlined in this chapter corresponds to the structure of the detailed result presentation in the following chapters. Due to their essential importance for the entire project, the behavior and the fundamental physical

properties of all used phase systems are explained first (Chapter 2). The presentation of the basic chemical–physical investigations on thermodynamics, kinetic modeling, and mass transfer phenomena follows (Chapter 3). Then the process steps required to carry out the reactions and the catalyst recovery together with their process engineering characterization are presented for the phase systems in detail (Chapter 4). The methodical developments for the optimized process design and process control for system development are subsequently presented (Chapter 5). Finally, all of the methods and knowledge acquired in this way were applied in the context of the integrated process design developed, implemented, and operated in an exemplary way (Chapter 6).

In summary, the capability for realizing efficient and fast process development for liquid multiphase processes based on the derived methods is presented in this book.

References

- [1] Anastas PT, Warner JC. 1998: *Green Chemistry: Theory and Practice*. New York: Oxford University Press, p.30
- [2] Binks BP. 2002: Particles as surfactants – similarities and differences. *Curr. Opin. Colloid Interf. Sci.* 7: 21–41.
- [3] Cornils B, Herrmann W. 2003: Concepts in homogeneous catalysis: the industrial view. *J. Catal.* 216: 23–31.
- [4] Dreimann JM, Warmeling H, Weimann JN, Künnemann K, Behr A, Vorholt AJ. 2016: Increasing selectivity of the hydroformylation in a miniplant. Catalyst, solvent, and olefin recycle in two loops. *AIChE J.* 62: 4377–4383.
- [5] Gallou F, Isley NA, Ganic A, Onken U, Parmentier M. 2016: Surfactant technology applied toward an active pharmaceutical ingredient: more than a simple green chemistry advance. *Green Chem.* 18: 14–19.
- [6] van Leeuwen PWNM. 2004: *Homogeneous Catalysis*. Dordrecht, Boston, London: Kluwer Academic Publishers.
- [7] UBA 2020: <https://www.umweltbundesamt.de/themen/earth-overshoot-day-2020-ressourcenbudget>, downloaded on 23. 12.20.

2 State of the Art of the Investigated Phase Systems

Matthias Kraume

While catalysts are applied in more than 80% of the chemical production processes, only a small number of processes take advantage of homogeneous catalysts, such as transition-metal complexes. Most often, heterogeneous catalysts are preferred over homogeneous ones because the separation of catalyst and product and unconverted feed is simple. However, several beneficial aspects come with homogeneous transition-metal catalysts, such as high activities under mild reaction conditions and high selectivities. Nevertheless, because the recovery of these catalysts is an issue, only a limited number of homogeneously catalyzed reactions are currently applied in the chemical industry [17]. In these instances (cases), individual solutions were developed to achieve high productivity combined with a high separation efficiency. One prominent example is the Ruhrchemie/Rhône-Poulenc process in which propene is hydroformylated to butanals. In this process, a rhodium catalyst complexed with a water-soluble phosphine ligand is applied in the aqueous phase. Sufficient solubility of propene in the catalyst solution and poor solubility of the products leads to high conversion and efficient separation of catalyst and product. However, this process relies on the solubility of the substrate, and thus only short-chain alkenes up to butenes can efficiently be hydroformylated with this process concept [33, 39].

The development of solutions for the efficient application and recovery of homogeneous transition-metal catalysts is an important means of enabling sustainable production processes with small waste streams and low energy consumption. Therefore, a broad variety of strategies to combine efficient reactions and catalyst recovery are very much desired [32].

Because homogeneous transition-metal catalysts are versatile in their applications, a toolbox comprising different catalyst applications and recovery strategies should be available. As demonstrated in Figure 2.1, homogeneously catalyzed reaction systems can be divided into two basic classes, which are distinguished by the number of liquid phases that are present in the reaction vessel. On the one hand, permanently monophasic systems achieve the best reaction performance because all components are well mixed. To recover the transition-metal catalyst after monophasic reactions, conventional separation techniques, such as distillation and extraction, are usually applied [17]. Also, innovative separation techniques, such as organic solvent nanofiltration, can be applied for the recovery of transition-metal catalysts from a monophasic reaction mixture [34, 43, 64, 96]. In contrast, liquid multiphase systems are very efficient for the recovery of homogeneous transition-metal catalysts because the two phases are selected in such a way that the products

are (mostly) present in one phase and the catalyst is only present in the other and can be recycled, often together with unconverted feed streams [20, 78]. Unfortunately, the existence of the liquid–liquid interface will usually impede the reaction performance due to mass transfer limitations.

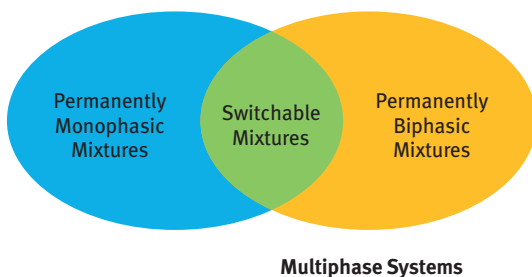


Figure 2.1: Phase conditions of reaction mixtures for homogeneous catalysis. Here, the liquid phases in the reaction vessel are considered [23].

As a combination of the two cases, switchable reaction systems exist by which one can achieve high productivity of the reaction and efficient recovery of the catalyst. Under the reaction conditions, the systems contain substrates and catalyst in one certain liquid phase, whereas under separation conditions, products and catalyst are contained in two different liquid phases.

2.1 Thermomorphic Multiphase Systems

Jonas Bianga, Kai Uwe Künnemann, Anna Kampwerth, Tom Gaide,
Andreas J. Vorholt, Thomas Seidensticker, Jens M. Dreimann, Dieter Vogt

2.1.1 Introduction

Among these switchable reaction systems, thermomorphic multiphase systems (TMSs) are a simple and promising approach¹. In these, the temperature is used as a trigger to switch from monophasic reaction to biphasic separation conditions so that both the contact of the substrates and the catalyst and the recovery of the catalyst can be achieved effectively.

¹ This section is based on the following paper: “Thermomorphic Multiphase Systems: Switchable Solvent Mixtures for the Recovery of Homogeneous Catalysts in Batch and Flow Processes” in *Chemistry – A European Journal* [23]. For this publication, parts of the content have been rewritten by the authors. All of the figures come from the previous publication and have been slightly altered for this section.

TMSs are mixtures of at least two solvents with a highly temperature-dependent miscibility gap. In most cases, these mixtures behave in a way that two liquid phases are present at lower temperatures (i.e., separation conditions) and one single phase is present at elevated temperatures (i.e., reaction conditions). Commonly, a TMS consists of a polar solvent and a nonpolar solvent. A closer look into the mechanism of these thermoregulated properties is provided in Section 2.1.2. Different terms and definitions of TMSs can be found in the literature. Among others, these mixtures have been referred to as thermomorphic solvent systems [9, 85], thermomorphic multicomponent solvent systems [15, 84], thermomorphic solvent mixtures [20, 79], thermomorphic multicomponent solvents [86, 93], temperature-dependent solvent system [11, 16], temperature-dependent multicomponent solvent system [10], thermoregulated biphasic system [50, 107], biphasic thermomorphic systems [31, 44], thermoregulated solvent system [65], and temperature-controlled solvents [18]. Other related recovery strategies by using ionic liquids [73], supercritical liquids [61], or fluorinated solvents [48, 49] also meet these requirements. However, these strategies usually require sophisticated solvents or specific catalysts [65]. The advantages of TMSs compared with other recycling strategies for homogeneous transition-metal catalysts are the applicability of standard solvents and readily available catalyst systems (precursors and ligands) [35].

In what follows, we give an introductory description of TMSs discussing their physical background, as well as challenges (e.g., product purification and cross-dissolubility of the product) and opportunities for the application of these systems (Sections 2.1.2, 3.1.3, and 4.1).

2.1.2 Fundamentals and Thermodynamics

TMSs are a specialized extraction technology that was developed for the recovery of homogeneous catalysts. Essentially, TMSs are mixtures of at least two liquid solvents of different polarities with a highly temperature-dependent miscibility gap, which can be used to switch from homogeneous to heterogeneous mixtures. To achieve both high reactivity in a single liquid phase and good recovery of the valuable components through phase separation, compounds that are practically immiscible at low temperature (T_0) and completely miscible at elevated temperatures (T_1) are applied. The general principle of the application of TMSs in homogeneous catalysis is visualized in Figure 2.2. For instance, the catalyst can be soluble in the polar liquid (blue), whereas the substrate and additional reactants are dissolved in the nonpolar liquid (yellow), or vice versa. By increasing the temperature, a homogeneous mixture (green) is obtained under reaction conditions.

The main challenge considering TMSs in homogeneous catalysis is to find the best compromise between the reaction objectives, such as high selectivity and high

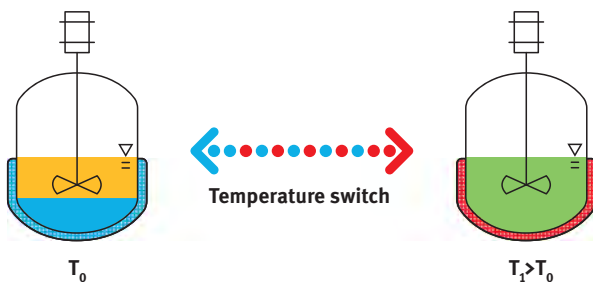


Figure 2.2: The working principle of TMSs [23].

yield, as well as the separation objectives, such as low catalyst leaching and suitable downstream processing [12, 19].

TMSs are governed by thermodynamic fundamentals, i.e., liquid–liquid equilibria (LLE). By combining homogeneously catalyzed reactions with conventional extraction, as presented in Figure 2.3a, there is only one single liquid phase present during the reaction and an extraction agent is added subsequently to selectively extract one component from the reaction mixture so that the recovery and recycling of the catalyst are enabled. The solute is transferred from the liquid reaction mixture into the extraction agent because of its affinity to it, as described by the distribution coefficient, K_i (eq. (2.5)). The exiting lean feed stream is called the raffinate, whereas the rich extracting agent stream leaving the unit is called the extract [66]. To minimize the loss of components (leaching) and to increase the efficiency, the miscibility of both solvents should be as small as possible. In contrast, with a TMS (Figure 2.3b), the extracting agent is already present during the reaction and by the change of the temperature, a switch from mono- to biphasic conditions is realized [7, 13, 14, 48, 99]. Both catalyst recovery strategies (Figure 2.3a, b) are based on liquid–liquid extraction, which is a separation process that exploits the different solubility of a solute (product) in two partially miscible solvents.

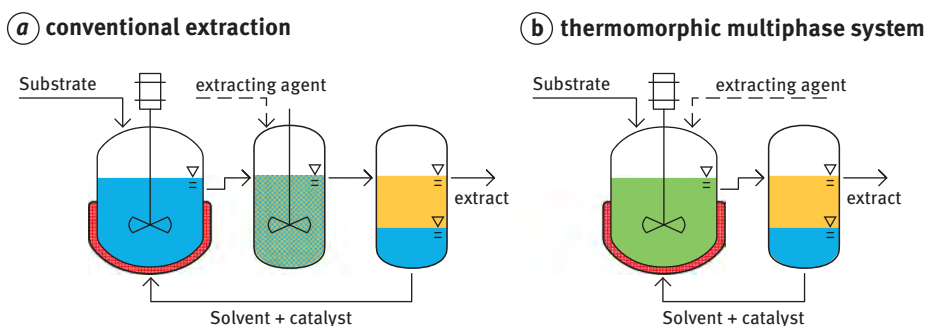


Figure 2.3: Catalyst recovery/product separation through conventional extraction (a) and TMS (b) [23].

Figure 2.4 shows a simplified system consisting of two components in a T, x_i diagram (temperature T , mole fraction x) that illustrates the phase behavior of the two solvents in a TMS. Herein, the working point is either in the monophasic region under the reaction conditions (Figure 2.4b) or in the biphasic region under the separation conditions (Figure 2.4a).

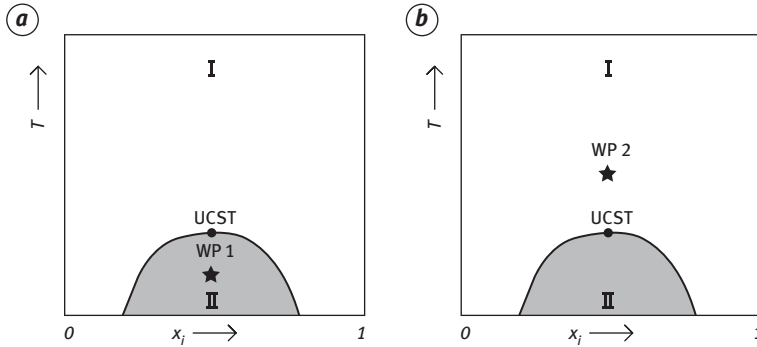


Figure 2.4: Schematic T, x diagram representing the temperature dependency of the working point (WP) in an LLE: (a) at low temperatures and (b) at high temperatures; I = monophasic; II = biphasic [23].

Usually, the mutual solubility increases with increasing temperature until the system becomes homogeneous above a certain temperature (Figure 2.5a). The upper critical solution temperature (UCST) determines the temperature at which the solvent mixture of any composition is homogeneous. In other cases (Figure 2.5b), the mutual solubility increases with decreasing temperature until the two-phase region completely disappears below the lower critical solution temperature (LCST). Rarely, both the UCST and LCST exist for a specific system (Figure 2.5c). The binodal curve encloses the area of compositions that result in a biphasic system. The UCST and LCST are located as the maximum or minimum of the binodal curve, respectively. The tie-lines (horizontal lines) connect the compositions of the two coexisting phases. Those compositions determine the distribution coefficient (eq. (2.5)).

For a proper understanding of the operating principle of TMS, thermodynamics needs to be taken into account. In particular, LLE data are necessary to describe the phase behavior of liquid–liquid extractions because the disintegration of a mixed homogenous liquid phase into two liquid phases occurs if a liquid phase is thermodynamically unstable or metastable. In terms of TMS, the two phases are formed due to the existence of two local minima in the Gibbs energy. The basic thermodynamic principles of LLE are explained below using binary systems. This information is based on reports by the groups of Lüdecke [63] and Gmehling [42].

Figure 2.6 schematically shows the Gibbs energy of a binary mixture at constant pressure and constant temperature, depending on the concentration in three different cases. The blue line in Figure 2.6 shows in contrast to the black line an inflection

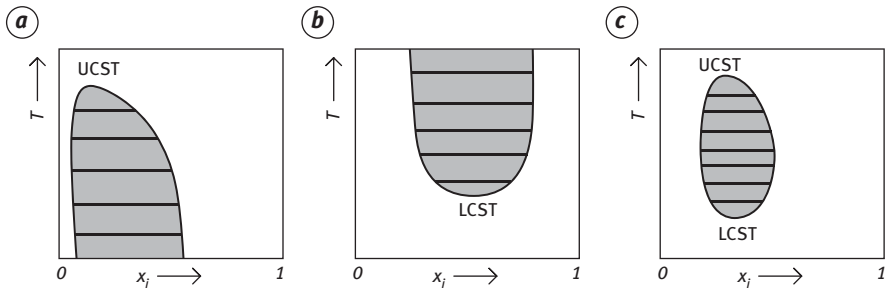


Figure 2.5: Temperature dependency of reaction mixtures with (a) an UCST, (b) an LCST, and (c) both UCST and LCST [23].

point. Whether the Gibbs energy follows the blue or the black line depends on the activity coefficients, γ_i (eq. (2.7)), of its components in the mixture or the free excess enthalpy of the mixture (last term in eq. (2.6)). The same mixture can show different behaviors at different temperatures. For a binary mixture with composition x_1 in TMS, the curve of the free enthalpy often resembles that of the blue line. To reduce its free enthalpy, the homogeneous mixture breaks down into two phases x_1^α and x_1^β .

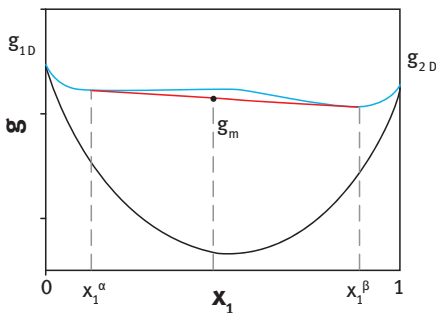


Figure 2.6: The Gibbs energy, g , of a binary mixture, depending on the composition at constant pressure and constant temperature (black line: complete miscibility, blue line: miscibility gap). In the case of miscibility gap, the mixture with composition x_1 separates into two coexisting phases, with compositions of x_1^α and x_1^β according to the tie-line (red line).

The formation of two liquid phases can only occur if the shape of the Gibbs energy curve as a function of composition shows an inflection point, i.e., if the condition given by eq. (2.1) is valid at some point

$$\left(\frac{\partial^2 g}{\partial x^2}\right)_{T,P} = 0 \tag{2.1}$$

Phase equilibrium exists if the components are in mechanical equilibrium and thermal equilibrium, and have identical chemical potentials in the coexisting phases α and β :

$$\mu_i^\alpha = \mu_i^\beta \quad (2.2)$$

The chemical potential of a component, i , can be expressed by

$$\mu_i = \mu_{i,0} + RT \ln(x_i \gamma_i) \quad (2.3)$$

where $\mu_{i,0}$ is the chemical potential of the component, i , in its pure state, x_i is the mole fraction, and γ_i is the activity coefficient of the component, i . The activity coefficient describes the deviation of a real mixture from an ideal mixture. Inserting eq. (2.3) into eq. (2.2) leads to

$$x_i^\alpha \gamma_i^\alpha = x_i^\beta \gamma_i^\beta \quad (2.4)$$

The distribution of a component, i , between the two coexisting phases, α and β , can be expressed by the distribution coefficient, K_i :

$$K_i = \frac{x_i^\beta}{x_i^\alpha} \quad (2.5)$$

The distribution coefficients are not constant. They strongly depend on the concentrations and temperature. The concentration and temperature dependence of LLEs are defined by the activity coefficients. The chemical potential, μ_i , is connected to the Gibbs energy, g , being the partial molar quantity of g . The Gibbs energy of a mixture with N components reads:

$$g = \sum_i^N x_i g_{i,0} + g^{\text{ideal}} + g^E \quad (2.6)$$

where the first term is related to the pure components, the second term represents the properties of an ideal mixture, and the last term takes the effects resulting from the real mixtures into account. Using standard thermodynamics [42], eq. (2.6) for a binary mixture can also be formulated by

$$g = x_1 g_{1,0} + x_2 g_{2,0} + RT(x_1 \ln(x_1) + x_2 \ln(x_2)) + RT(x_1 \ln(\gamma_1) + x_2 \ln(\gamma_2)) \quad (2.7)$$

The activity coefficients can be calculated using a g^E model or an equation of state. The most important difference between these two methods consists in the possibility to take into account the pressure dependency by using an equation of state.

Although a large number of phase equilibrium data are available for binary systems, much less or almost no data have been published on ternary and multicomponent systems [42]. Especially in homogeneous catalysis, TMSs consist of more than two components (Section 4.1.3). Therefore, it is necessary to look at least at the

characteristics of ternary diagrams (Figure 2.7). With the following assumptions and constraints regarding the chemical components in a given mixture, ternary diagrams are a tool for the description of the liquid–liquid phase behavior of TMS:

- 1) The mixture has three components: solvent I (polar), solvent II (nonpolar), and substrate or product.
- 2) The catalyst is neglected due to its comparably low concentration.
- 3) The influence of byproducts and coproducts is neglected due to their comparatively low concentration or their similarity to the product.
- 4) The LLE is pressure independent.
- 5) The influence of solubilized gasses in different phases is neglected.

The properties of the polar and nonpolar solvents are the most important factors for describing the LLE because these liquids often make up more than 80 wt% of the TMS mixture. Additionally, the consideration of the substrate is important to describe the phase behavior at the start of reaction, when a TMS is expected to be monophasic at the reaction temperature. Moreover, the consideration of the product is important to describe the phase behavior for the separation (after the reaction), when a TMS is expected to be biphasic at the separation temperature. Therefore, both ternary diagrams have to be considered (one for the reaction mixture before and one for the reaction mixture after the reaction) for implementing a new TMS. The first diagram should include the polar solvent, nonpolar solvent, and substrate (composition before the start of reaction), whereas the second diagram should include the polar solvent, nonpolar solvent, and product (composition after reaction, assuming full conversion and perfect selectivity).

In the past, a classification of different TMSs based on the number of solvents and the corresponding appearance of their miscibility gaps was discussed in the literature. Therein, different TMSs are grouped into three different types (TMS types I, II, and III). In contrast to the previous description of TMSs, TMS type I and II consist of three solvents: one polar solvent containing the catalyst (A), one nonpolar solvent containing the product (B), and one mediator solvent (C). TMS type I has a closed miscibility gap (Figure 2.7a or b) at the separation and reaction temperatures. For efficient catalyst separation, the miscibility gap at low temperatures should be as large as possible. In contrast to TMS type I, TMS type II systems show an open miscibility gap (Figure 2.7c) at the separation temperature and a closed miscibility gap at the reaction temperature. By choosing a proper mediator solvent, the shape of the miscibility gap can be tuned to fulfill a certain target (e.g., to increase the solubility of the catalyst in the polar liquid phase or to reduce the switching temperature from bi- to monophasic). TMS type III is in accordance with the basic definition of the TMS above. These TMSs consist of two solvent components: one polar solvent containing the catalyst and one nonpolar solvent containing the product in the separation stage. These TMS type III systems are beneficial from a process development point of view due to their lower complexity compared to those of TMS type I or II systems [14].

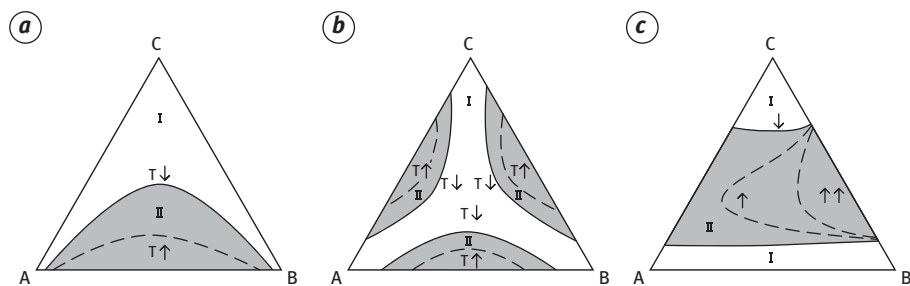


Figure 2.7: Different ternary phase diagrams for LLE and their potential temperature dependency: (a), (b) systems with a closed miscibility gap and (c) a system with an open miscibility gap; I = monophasic; II = biphasic; A–C describe chemical components; T describes the temperature, and the dashed lines indicate the temperature dependency of the miscibility gap. An upward arrow indicates a temperature increase and vice versa [23].

However, the differentiation between the three types of TMSs is not expedient because real systems are typically more complex than just a three-component system.

To be able to describe and carry out the calculations of phase behavior for different multicomponent systems, laboratory experiments are necessary, but these are very time-consuming [42]. To reduce the experimental effort, reliable thermodynamic models are required, which allow the calculation of the phase equilibrium behavior of multicomponent systems from only a limited number of experimental data, for example, only for binary systems. For the measurements often computer-driven lab facilities with various highly sophisticated experimental methods are available today. From the theoretical point of view, it is more complicated to accurately calculate LLE in multicomponent systems than to describe vapor–liquid or solid–liquid equilibria [98]. The reason is that LLE occurs only in real mixtures, in contrast to VLE or LLE. Despite the fact that modeling these LLEs for multicomponent systems is challenging, successful approaches, e.g., by PC-SAFT (Sections 3.1.3 and 4.1.1) have been demonstrated. PC-SAFT can be used to describe ternary systems well based on binary parameters. Additionally, PC-SAFT allows extrapolation over wide ranges of temperature and pressure. However, experimental studies still play an important role to investigate the performance of TMSs for various applications. These systems are still a niche topic in academia and industry, but Section 4.1.3 shows that these systems were already successfully used in several different research fields.

2.1.3 Reactions in TMS and Remaining Challenges

Since their first application for catalyst recycling in homogeneous catalysis by Bergbreiter's group in 1998, TMSs have aroused increasing interest for further applications. A large number of successful examples in the literature demonstrate the suitability of

TMS for homogeneous catalyst recycling. Mostly, the feasibility of separating the catalyst from the product has been investigated. In some cases, the reuse of the catalyst was also achieved. However, a continuous process has been realized only rarely. In Section 4.1.3, application examples can be found sorted by the reaction carried out in the TMS, e.g., hydrogenation and hydroformylation. In addition, the recent developments in TMS can be found in Section 4.1.4. Although there are many application examples for TMS in homogeneous catalysis, no industrial applications of TMS are known so far.

To enable industrial application, some challenges still need to be overcome. Currently, the concept of TMS for most examples corresponds more to a technology readiness level (TRL) of 1–2, while a smaller number can be assigned to TRLs 4–5. Within TRL 5, the next step in TMS technology development is the application of a TMS against an industrially established process, followed by the construction of a pilot plant (TRL 6) that demonstrates large-scale operational capability. An overview of the remaining challenges and what additional work needs to be done for industry adoption of TMS is provided in Section 4.1.5.

2.2 Microemulsion Systems

Markus Illner, Reinhard Schomäcker

2.2.1 Introduction

The idea of a switchable solvent system combines contradicting design features of a reaction mixture: perfect miscibility for good mass transfer leading to fast reactions, and easy separability for product isolation as well as catalyst recycling. The latter is attainable using biphasic mixtures which, however, do not provide sufficient reaction rates due to the missing contact, e.g., of catalysts dissolved in a polar phase and substrates located in a nonpolar phase. To stabilize a dispersion of such practically immiscible fluids, amphiphilic substances can be used. Given a sufficient amount of a suitable amphiphile, a sufficiently large interface area between the two phases is obtained, and optically homogeneous and stable emulsions are formed. Schulman et al. [82] characterized these systems as optically isotropic transparent oil and water dispersions and coined the term “micro-emulsion”. Later, investigations emphasized this by finding average droplet diameters from 10 to 200 nm [89]. Hence, a drastic reduction of the interfacial tension is obtained, and a large interfacial area between nonpolar hydrophilic and hydrophobic compounds is formed.

This enables a variety of technical applications ranging from enhanced oil recovery (see reviews by Abe [1]; Bera and Mandal [6]) over cosmetics and pharmaceuticals [29, 46, 47] to chemical reaction media [58, 81, 83].

2.2.2 Fundamentals

For the application of microemulsion (ME) systems as switchable liquid reaction media, insights into their thermodynamic and physical properties, as well as the system dynamics are required. Regarding the desired process applications, the specific phase separation behavior, relevant influences and control parameters, and the connection between emulsion configurations and chemical reactions are of interest.

Remark: In the following deliberations on ME systems, ranging from theory, development of methodologies and models, to process development and operation, only the application of nonionic surfactants is considered. With ionic surfactants, a similar general pattern of the phase behavior is observed, but with a different sequence of phases, which is controlled by different molecular interactions.

2.2.2.1 Properties and Phase Behavior of Microemulsion Systems

Surfactant Molecules, Interfaces, and Micelle Formation

Surfactant molecules are amphiphiles that are active at the interface between hydrophobic and hydrophilic substances, which alter several fluid properties, such as interfacial tension, conductivity, and turbidity. To analyze the effect on the interfacial tension, the Gibbs surface energy $G(\sigma)$ is used. It expresses the deviation of the Gibbs free energy of a system consisting of two contacting phases and surfactant molecules present at the interface, from the sum of the free energies G_i of the individual phases. This can be used to derive the surface excess concentration Γ for the sorption of components at an interface [3]:

$$\Gamma_i = -\frac{1}{RT} \cdot \frac{d\sigma}{d \ln c_i} \quad (2.8)$$

Hence, if a surfactant i adsorbs at an interface starting at $c_i = 0 \text{ mol L}^{-1}$, first, the interfacial tension σ of the binary system is present and slowly decreases with increasing c_i (Figure 2.8). Surfactant molecules then start to aggregate at the interface until at approx. 60% surface coverage a significant drop of the interfacial tension occurs, as the molecules start to align their heads with the hydrophilic phase and form a new interface. After passing a specific value of the concentration – the critical micelle concentration (CMC) – the interface is fully covered and the interfacial tension remains constant. A further increase in the surfactant concentration then leads to the formation of energetically favorable spherical aggregates (micelles) in the bulk phase, which can, e.g., trap oil in water (o/w). The resulting structural elements and the relevant aggregation number depend on several influences [67].

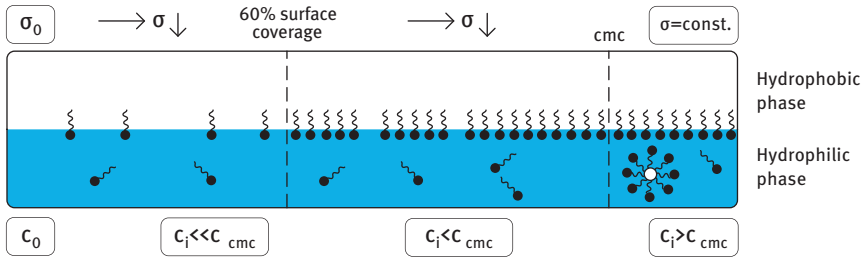


Figure 2.8: Qualitative representation of the interfacial tension depending on the surfactant concentration and the corresponding coordination of the surfactant molecules at the interface of a two-phase system.

General Phase Behavior of Microemulsion Systems

The identification of the phase behavior and of advantageous phase states are of general interest for process applications. To obtain a general description, a ternary system of water (**A**), oil (**B**), and a nonionic amphiphile (**C**) is assumed. Typically, the composition variables are chosen as the oil-to-water ratio α and the surfactant mass fraction γ :

$$\alpha = \frac{m_{Oil}}{m_{Water} + m_{Oil}} \quad (2.9)$$

$$\gamma = \frac{m_{Surfactant}}{m_{Water} + m_{Oil} + m_{Surfactant}} \quad (2.10)$$

The general phase behavior of MEs is mainly dictated by the miscibility gaps that are present in the corresponding binary systems. Typically, water and nonionic surfactants show good mutual solubility at low temperatures but form a miscibility gap with an LCST at elevated temperatures. The inverted case applies to oil–surfactant mixtures because the surfactant solubility in oil increases with temperature [53]. As the influence of pressure is generally found to be low, the phase behavior of the ternary system can then be represented by the Gibbs phase prism, with the temperature T as the ordinate for stacked ternary composition diagrams [54].

Figure 2.9 depicts a two-dimensional cut through this phase prism at a constant oil-to-water ratio of 50% (Kahlweit’s fish diagram) on the left, as well as the corresponding ternary diagrams at different temperatures on the right. From this figure, several observations can be made:

- A ME phase is only formed if the CMC is exceeded.
- Starting at low temperatures, a two-phasic miscibility gap (2) is formed, showing an oily excess phase (B^{ex}) and a surfactant-rich aqueous phase (A^{em}) as the emulsion phase.

- At high temperatures, again a two-phasic miscibility gap ($\bar{2}$) is formed, showing an aqueous excess phase (A^{ex}) and a surfactant-rich oil phase (B^{em}) as the emulsion phase.
- Inside a constrained temperature window $[T_l; T_u]$ the three-phase region 3 is formed, characterized by a surfactant-rich bicontinuous emulsion phase (ME) and aqueous and oily excess phases (A^{ex} and B^{ex}).
- A homogeneous and stable emulsion phase (1) is formed if the surfactant concentration exceeds the plait point at $\tilde{\gamma}$. At the plait point, a minimum amount of surfactant $\tilde{\gamma}$ is required to form a stable ME, while also defining the phase inversion temperature \tilde{T} .
- At very high surfactant concentrations, liquid crystals or lyotropic mesophases can occur which are of high viscosity [59].

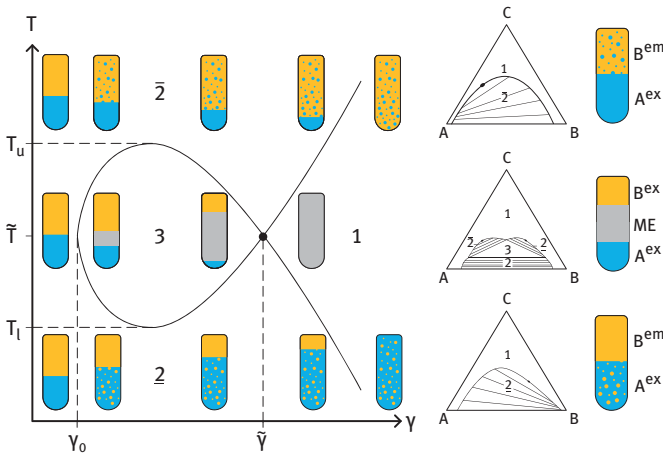


Figure 2.9: Left: Phase state and evolution of volumes of phase fractions for different temperatures and surfactant concentrations. Right: Isothermal Gibbs triangle diagrams for mixtures of oil (B), water (A), and surfactant (C). Phase equilibria: $\bar{2}$; 3; $\bar{2}$; 1. Phases are labeled: B (oil), A (water), and ME (bicontinuous microemulsion phase); with superscripts $^{\text{ex}}$ (excess phase) and $^{\text{em}}$ (emulsion phase). The figure is adapted from Sottmann and Stubenrauch [88].

2.2.2.2 Features and Description of the Three-Phase Body

Looking at the complex phase behavior of microemulsion systems (MES), the three-phase region is of special interest for process applications as rather pure excess phases of oil and water are obtained which can be used for catalyst recycling and product isolation. Hence, it is further discussed regarding its characteristic features. Figure 2.10 shows an isothermal Gibbs triangle with a ternary miscibility gap, as well as qualitative phase distributions and phase volume fractions at different temperatures. It is now assumed that an initial mixture at a set point SP1 in the middle of the ternary miscibility gap is prepared and separated into the ME phase and the adjacent excess phases.

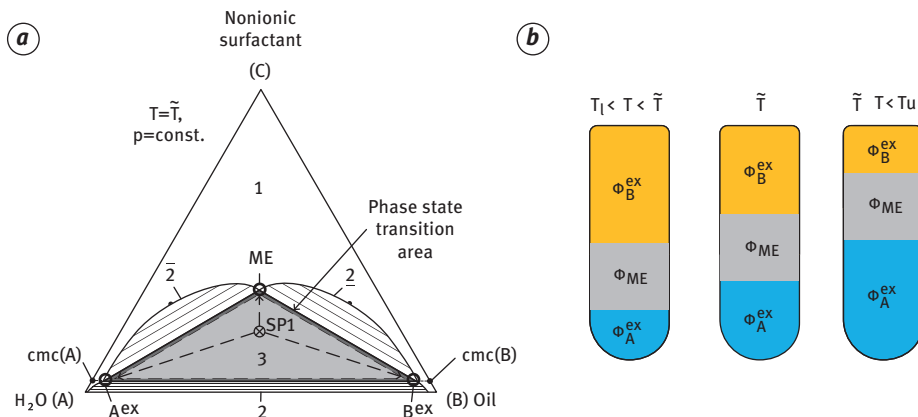


Figure 2.10: Left: Schematic isothermal triangle of the ternary system at \tilde{T} with miscibility gaps. Right: Schematic evolution of the volume fractions of the developed phases over temperature within the three-phase body. Taken from Illner [51].

The following features of such a system can then be observed:

- The phase volume fractions of each phase depend on the initial mixture and the location of the corners of the miscibility gap. Hence, for constant temperature, pressure, and other external influences, always the same compositions of the developed phases are observed for any chosen SP1, but phase volume fractions are changing.
- With increasing temperature, the ME corner of the ternary miscibility gap moves toward the oil side of the triangle. For constant SP1, increasing aqueous excess phases and decreasing oil phases are observed.
- The surfactant concentration in the excess phases is at the level of the corresponding CMC of the binary systems and rather low [77].
- The composition of the excess phases is then mainly dictated by the binary miscibility gap of oil and water.
- CMCs in oil and water are temperature-dependent and increase with temperature for oil while decreasing in water.

2.2.2.3 Coalescence Behavior and Separation Dynamics

Aiming at process applications, the separation dynamics is of high interest. This is closely connected to the preferential contact between the phases present, their interfacial tensions, and the resulting coalescence behavior. For MEs, several phase states and transitions between them are possible. For the emerging three-phase body at low temperatures, a separation of the surfactant-rich aqueous phase into an emulsion and an aqueous excess phase occurs. Referring to Figure 2.11, the interfacial tension $\sigma_A^{\text{ex-ME}}$ hence rises from zero (at phase region boundary) to high values within the three-phase region (3). Likewise, the same behavior is found at the

upper temperature boundary of the three-phase region and for the emerging oily excess phase. This directly affects the separation dynamics as, for the near-critical phases in the boundary regions of the three-phase body, a maximum of the required separation time is observed (interfacial tension near zero). Likewise, a minimum separation time is found within the three-phase body at the phase inversion temperature [56].

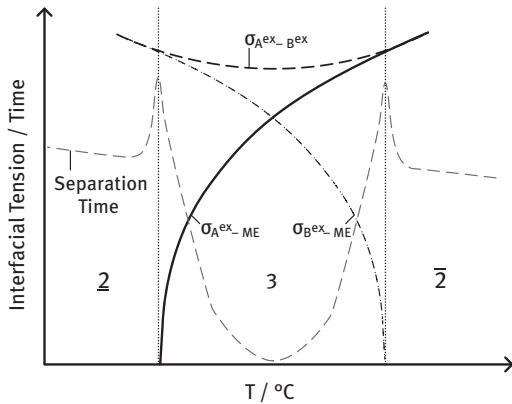


Figure 2.11: Temperature-dependent evolution of the interfacial tension and separation time for phase states of a microemulsion. Phases are labeled: A (water), B (oil), ME (bicontinuous microemulsion phase), and ex (excess phase). Taken from [52].

The evolution of the interfacial tension for the ME phases additionally dictates the coalescence behavior of MEs and the dynamics of the development of the individual phases. Up to now, MESs lack a profound description of their coalescence behavior, which is mainly due to their inherent complexity. Hence, extended experimental studies and a deep understanding of such systems are required. Figure 2.12 is used for a general discussion of the coalescence characteristics of MESs, specifically for the three-phase region. The following statements can be made:

- At the lower temperature boundary of the three-phase region ($\underline{2}/3$ transition), dispersed droplets of the oily excess phase and a surfactant-rich emulsion phase are present in a continuous aqueous surfactant-rich phase. The interfacial tension between the aqueous excess phase and the emulsion phase is almost zero and the phase separation is thus inhibited (Figure 2.11). The aqueous excess phase and the ME phase are therefore formed slowly. In contrast, oil droplets rise quickly and coalesce as the oily excess phase. Additionally, the surfactant may accumulate at the interface of the oil and the ME phase.
- Increasing the temperature leads to an accelerated separation within the three-phase body, as different emulsion states are present. These may have the character of a droplet in droplet emulsions or dual droplets [55]. Droplets will rise in the aqueous phase due to density differences and disrupt at the interface of the

- aqueous and emulsion phases. Due to larger interfacial tensions, the emulsion part of the droplets quickly coalesces, while oil droplets also rise fast and coalesce.
- Above the phase inversion temperature, the continuous phase is switched to the oily phase due to the higher surfactant solubility in oil at elevated temperatures. Here, dual droplets consisting of water and of the ME phase are found in an oily continuous phase, descending and disrupting at the oil–emulsion interface. With the interfacial tensions still being large, separation into the three phases still is fast.
 - In the upper transition zone ($3/2$ transition), the interfacial tension of the ME and of the oil phase vanishes. Single droplets are present as a disperse phase in an oily continuous phase. During the separation, falling water droplets dragging surfactant with them are observed. The separation of the oil and emulsion phases is very slow and again surfactant accumulation can occur at the interface of the aqueous and emulsion phases.

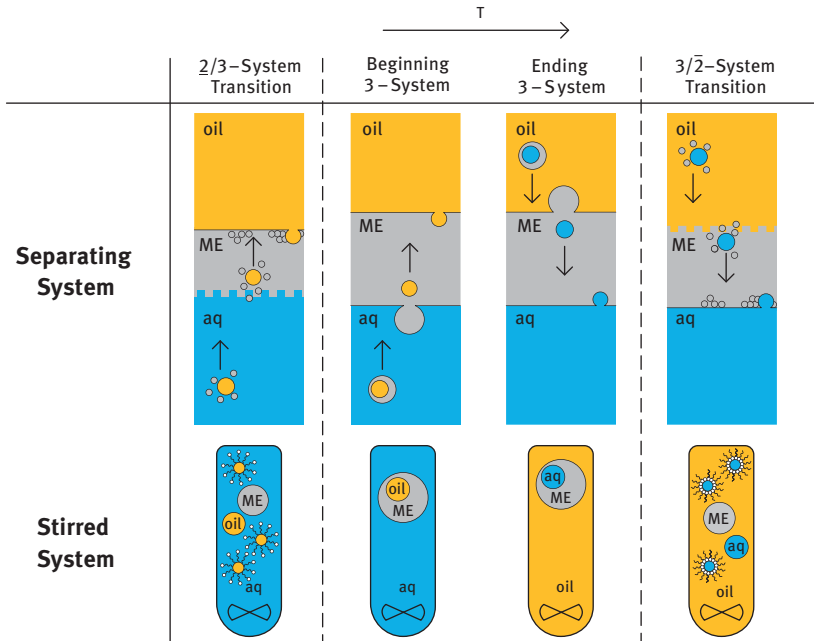


Figure 2.12: Schematic illustration of the coalescence behavior along the three-phase body. The upper section shows separating systems with droplet configurations and coalescence. The lower part sketches the situation of continuous and disperse phases in the stirred system. Oil, oil-rich phase; aq, aqueous phase; ME, microemulsion phase. Taken from Illner [51].

2.2.3 Industrial Applications and Remaining Challenges

Surfactants are widely used in processes like emulsion polymerization or product formulations like cosmetics and pharmaceutical products. Also, the stabilization of dispersions for variable applications is based on the surface activity of surfactants. Reduction of surface tension and increase of interfacial areas by the addition of surfactants in two-phase systems greatly accelerate mass transfer and with this the rates of chemical reactions. A systematic investigation and utilization of these phenomena in industrial applications have only started recently. This development is supported by the idea of using water as a green solvent for organic synthesis. Researchers of the Novartis Pharma AG and their collaboration partner from Scripps Research Institute perfectly showed the potential of aqueous micellar solutions as reaction media for the synthesis of active pharmaceutical ingredients (API) [40] based on the pioneering work of Lipshutz [62, 68]. All these applications have in common that no separation of the emulsion is intended, and the surfactants are an integral part of the final products. Although these advantages have been recognized also for the formation of switchable solvent systems for industrial syntheses, no process development has reached the required maturity for industrial implementation so far. Most emulsion systems are considered to be too stable for efficient separation and workup procedures. Also, product contamination by difficult to separate surfactants is often suspected in practice.

This also widely holds for MESs, where industrial applications are scarce, despite their remarkable performance features as switchable solvent systems [81]. This is mainly caused by the inherent complexity of these systems demanding knowledge which is typically out of scope for reaction engineering practitioners. Colloidal science and surface chemistry have to be taken into account for the design of suitable reaction mixtures, as well as reaction and separation processes. Moreover, (thermodynamic) model descriptions of MES are scarce and are limited to idealized equilibrium state calculations [41] or still require extended experimental studies [94]. Although the general thermodynamics is well investigated and heuristics-based methodologies on the selection of MES components are available, the design and operation of processes using MES remain challenging. Central to this is the complex phase behavior, which is influenced by virtually all thermodynamic states and components in a reactive system. Thus, close interactions between the reactions and the MES have to be expected, posing also operational challenges when aiming at continuous production processes. Therefore, Section 4.2 aims at addressing these major obstacles by presenting an integrated process development methodology, which combines the design and the optimization of MES as switchable reaction media with the development of suitable process concepts and units, as well as an analysis of process operability. Therein, key experiments and systematic guidelines based on the fundamental thermodynamics of MEs are used to limit the experimental effort and ensure applicability by reaction engineering practitioners. The methodology is outlined based on a larger case study for

the homogeneously catalyzed hydroformylation of 1-dodecene. The performance of MES will then be compared to that of TMS and Pickering emulsion (PE) in Section 4.4.

2.3 Pickering Emulsions

Anja Drews

2.3.1 Introduction

In Pickering emulsions (PEs), typically micro-sized droplets are stabilized by micro- or nanoparticles. PEs are commonly used in cosmetics and food formulations and in pharmaceutical, biomedical, and drug delivery applications [22, 30, 71, 103], where the use of synthetic surfactants has to be avoided. Despite having first been discovered and described more than a hundred years ago [72, 74], fundamental investigations on their properties and further applications have been rare until a rise in attention in the 2000s [26, 27]. Through the choice or design of the properties of the particles, the composition of the PE, and the conditions under which it is prepared, the opportunity arises to tailor PEs for a wide variety of desired applications.

Due to their high adsorption energy (of up to 100,000 kT), once adsorbed, the particles are kept almost irreversibly at the interface, thus preventing drop coalescence and in turn leading to very stable emulsions [24, 25, 30]. This high stability makes PEs interesting candidates for industrial processes where media are subjected to temperature changes and mechanical stress from stirring or pumping. This includes catalytic liquid/liquid (L/L) reactions where mechanical separation of the catalyst containing droplets from the product containing phase is a promising option for simple continuous operation with efficient recovery of the catalyst and stabilizing additives.

2.3.2 Fundamentals

2.3.2.1 Stabilizing Mechanism

A large variety of organic or inorganic particles can be used to stabilize PEs. Besides the often studied spherical or fumed silica nanoparticles [24, 101], e.g., clay platelets [100], clay, or carbon nanotubes [28, 69], various food-grade particles [36] or even microbial cells [76] have been utilized.

The hydrophobicity of the particles, i.e., the three-phase contact angle θ_{ow} , defines their ability to adsorb at the interface. Ideal stabilization can be achieved with particles that have a contact angle close to 90° . If the contact angle is too small ($\ll 90^\circ$), the particle will be wetted mainly by the aqueous phase, if it is too high ($\gg 90^\circ$), it will be wetted by the oil phase. In both extreme cases, the particles will

not bind to the interface and thus cannot prevent coalescence. Additionally, the particle radius r [27] and the oil/water interfacial tension γ_{ow} influence the stabilization energy [24]:

$$E = \pi r^2 \gamma_{ow} (1 - |\cos \theta_{ow}|)^2 \quad (2.11)$$

The contact angle in most cases defines the resulting emulsion type: oil in water (o/w) or water in oil (w/o) (see Figure 1.5). Similar to the Bancroft rule for surfactants, the phase that favorably wets the particle constitutes the continuous phase. However, exceptions, e.g., at certain oil/water ratios are possible.

In recent years, stimuli-responsive PEs were developed that can be demulsified or inverted by an external trigger such as temperature or pH shift [90], N_2 bubbling [104], or other means [4]. To achieve this, e.g., stimuli-sensitive polymer particles [75] or surfactant-modified particles [104] can be used whose hydrophobicity can be altered in situ.

2.3.2.2 Properties of Pickering Emulsions

A large number of publications on the properties of PEs deals with o/w rather than w/o PEs [30, 38] due to their traditional applications or because they were studied in the context of the remediation of oil spills [69, 91].

PE properties such as drop size distribution, rheology, and stability depend on the viscosities and the interfacial tension of the used liquid phases, their phase fraction, as well as on the particle type and content, and the presence of other additives, e.g., salt or proteins [24, 38, 45, 95, 100]. Assuming complete coverage of the interface with particles and a constant interfacial area per particle mass ratio $a_{dp/NP}$, the theoretical drop diameter d is inversely proportional to the mass of nanoparticles M_{NP} that is used to stabilize a given dispersed volume V_{dp} [38]:

$$d = 6 \cdot \frac{V_{dp}}{A_{dp}} = \frac{6}{\rho_{dp} \cdot a_{dp/NP}} \cdot \frac{M_{dp}}{M_{NP}} \quad (2.12)$$

Like other emulsions, PEs typically exhibit shear thinning behavior [30], although Newtonian behavior has also been observed for certain particles [45]. The shear thinning behavior can be explained by the tendency of nanoparticles to form a three-dimensional network between particles and stabilized droplets [30, 57] which can additionally increase the emulsion stability. These aggregates may reorient or break up under shear. The droplets themselves remain intact which is a precondition for the intended application of PEs as reaction media.

In addition to the above-mentioned PE composition, the resulting PE properties depend on the dispersion device used in their preparation [95]. Generally, PEs can be prepared using ultrasonication, high-pressure homogenizers, rotor-stator devices, stirrers, or membrane emulsification [2, 30]. The higher the energy input, the larger

the produced interfacial area where particles can adsorb and stabilize the droplets. In contrast to surfactants, nanoparticles do not reduce the interfacial tension between the liquid phases [80]. Hence, higher energy inputs are needed to create PEs of the desired drop size in comparison to, e.g., micellar multiphase systems. With ultrasonication, around 10^9 W kg⁻¹ can be achieved, while the power input of high-speed rotor-stator devices ranges from 10^3 to 10^5 W kg⁻¹ and that of stirred tanks from 10^{-1} to 10^2 W kg⁻¹ [70].

2.3.3 Reactions in Pickering Emulsions

Since the first reported biocatalytic reaction in w/o PEs [102] where they were shown to increase the performance of both stable and sensitive biocatalysts in organic media, PEs have attracted increasing interest for their use in two-phase reactions. Since then, numerous different (bio)catalytic reactions in PEs have been reported [4, 71, 97, 107] with catalysts either dissolved in the dispersed phase or anchored/grafted onto the stabilizing particles, such as the epoxidation of cyclic alkenes [60], the etherification of glycerol with dodecanol [37], the acetalization of long-chain fatty aldehydes with ethylene glycol [106], the formation of disulfide bonds in peptides [87], the hydrolysis of olive oil, and the esterification of octanol [104] (see also Section 4.3.2). The hydroformylation of long-chain olefins has also been demonstrated using mesoporous nanospheres [92, 106]. The potential of PEs to exceed the productivity of stirred dispersions was demonstrated, e.g., using catalytically active microbial whole cells for both PE stabilization and catalysis of a carbonylation reaction [76].

PEs are promising reaction phase system candidates wherever the use of synthetic surfactants [71] or elaborate purification steps shall be avoided, or where sensitive catalysts need to be protected [4]. Published reactions in PEs are limited mainly to batch processes since the continuous separation of the liquid phases for catalyst reuse remained an unsolved challenge up until recently [71]. Attempts to enable reuse of the catalyst included repeated batches with demulsification between reaction cycles, induced by either centrifugation [97], shear-induced coalescence [100], or N₂ trigger [104], which, however, can damage the catalyst and require multiple energy inputs for re-emulsification.

2.3.4 Remaining Challenges

As outlined above, further to their traditional use as a mere replacement for surfactants, the high stability of PEs presents better opportunities for catalyst protection as well as a more robust mechanical L/L separation and thus simpler flow sheets with only one step for simultaneous catalyst, water, and additive retention (Figures 2.13

and 1.7). For certain applications, such advantages can outweigh the expected lower reaction rates in comparison to even more intensely dispersed systems such as TMS and MES. However, with just a decade of research on their application for catalysis, PEs are the least mature of the three phase systems that are considered in this volume. Their behavior and properties under process conditions are the least well understood, and options for the separation of the reaction mixture have not been comprehensively explored.

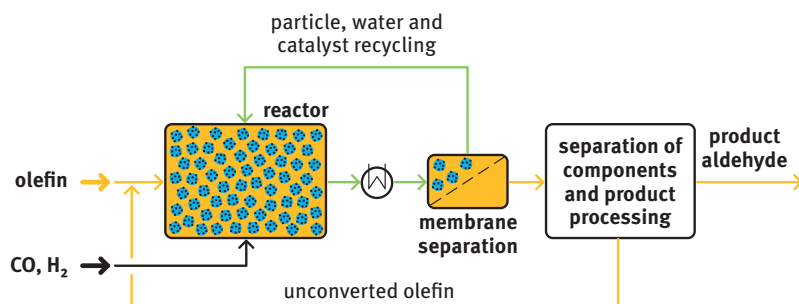


Figure 2.13: Envisaged flow sheet for continuous reactions (e.g., hydroformylation) in w/o Pickering emulsions.

2.3.4.1 Pickering Emulsion Characterization and Properties

Despite the fact that many influences on the properties of PEs are already well understood, detailed knowledge on their behavior under reaction conditions is scarce. Most fundamental studies have dealt with ideal spherical particles instead of the more industrially relevant and commercially available, irregularly shaped particles. Little is known on the effect of potentially unadsorbed particles present in the continuous phase or partial/multilayer coverage on drop size, rheology, mass transfer, and thus reaction rates.

Such knowledge, however, is crucial in order to prepare PEs with tailor-made characteristics [2], as well as for the design of mixing, pumping, and separation steps in the envisaged overall continuous process. For a given dispersed volume, the reaction rate is likely to increase with decreasing drop size as shown for, e.g., the lipase-catalyzed esterification of 1-hexanol with hexanoic acid or the hydrogenation of benzene [4]. However, opposing trends have also been reported in the lipid oxidation in o/w PEs [21], and the authors concluded that such discrepancies might arise from an incomplete characterization of the properties of the system and that the underlying mechanisms are far from being understood or quantified.

2.3.4.2 Mass Transfer and Location of Catalyst

In addition to drop size, the gas/liquid and liquid/liquid mass transfer will strongly influence the reaction rate. The presence of particles at the interface reduces the available mass transfer area of a given drop, but the overall effect of particles on mass transfer rates has not been comprehensively investigated yet [4]. The presence of the particles in the continuous phase is likely to influence both the diffusivity of reactants and the liquid viscosity which will, in turn, affect the mass transfer coefficients. Such relationships so far have mainly been described for unwanted particulate impurities, e.g., in extraction columns but not for reacting systems. An optimum particle concentration is likely to exist, which balances the positive and the negative effects of the presence of particles.

Quantifying the influence of the occupancy of the L/L interface by the particles and the catalyst in relation to the physical properties of the PEs is essential for optimizing and predicting the productivity of PEs and for optimizing processes but has not been studied before for w/o PEs.

2.3.4.3 Continuous L/L Separation for Catalyst Retention

An efficient phase separation step for catalyst retention is crucial in order to design economically feasible homogeneously catalyzed processes. While published PE separations typically rely on demulsification, which, on the one hand, might damage sensitive catalysts and, on the other hand, enables only repeated batch processes, membrane filtration appears to be a promising alternative as it maintains the integrity of the droplets and can be operated continuously. Through the selection of appropriate pore size or cutoff, it can retain small drops as required for high reaction rates and also has the potential to safely retain residual particles. Due to the novelty of this application, suitable membranes have to be identified first and potential membrane-particle interactions need to be investigated. To design an efficient process, knowledge on the influence of the properties of the PE, especially of the drop sizes, and the residual particles which will constitute the filter cake on the filtration performance is required. Once these relationships are established, a permeability model can be developed for process optimization.

Finally, the feasibility of a continuous reaction in PEs using membrane filtration to retain the catalyst containing droplets should be demonstrated for example applications, and the benefits need to be evaluated.

All these challenges will be addressed in Section 4.3, and the performance and features of PE will be compared to those of TMS and MES in Section 4.4.

2.4 Reaction Indicators

Jonas Bianga, Kai U. Künnemann, Anna Kampwerth, Tom Gaide,
Andreas J. Vorholt, Thomas Seidensticker, Jens M. Dreimann, Dieter Vogt

Apart from thermodynamic equilibrium parameters, also other process characteristics are very important indicators for describing the effectiveness of reactions conducted in the investigated phase systems². Therefore, common indicators, such as conversion (X), yield (Y), and selectivity (S), as well as catalyst stability determined by the turnover number (TON) and activity determined by the turnover frequency (TOF), are very useful and can be found in the relevant literature [5, 8]. For some indicators, a differentiation between batch and continuous reactions is necessary because the reference values for the calculations are different. For the efficiency of separation, the contamination of the product mixture is most important. Indicators such as catalyst loss (leaching), solvent loss, and product purity have to be taken into account.

The conversion, X , as a measure of the reaction progress of a chemical reaction, indicates the ratio of the amount of substrate i converted at time t ($n_{i,0} - n_i(t)$) to the initial amount of substrate $n_{i,0}$ at time t_0 (eq. (2.13)). Most commonly, the limiting component of a reaction is used to calculate the conversion:

$$X_B(t) = \frac{n_{i,0} - n_i(t)}{n_{i,0}} \quad (2.13)$$

For continuous experiments (eq. (2.14)), the amount of substrate in the input stream, $\dot{n}_{i,\text{in}}$, has to be related to the amount of substrate in the output stream, $\dot{n}_{i,\text{out}}$:

$$X_C(t) = \frac{\dot{n}_{i,\text{in}} - \dot{n}_{i,\text{out}}(t)}{\dot{n}_{i,\text{in}}} \quad (2.14)$$

To characterize the production of byproducts of the reaction, the yield is an important criterion. It establishes a relationship between the product, p , formed and the substrate, i , that is consumed at a specific reaction time. The yield of a batch reaction can be calculated from the amount of p formed by the reaction at time t ($n_p(t) - n_{p,0}$) with an initial amount $n_{i,0}$ of substrate i :

$$Y_B(t) = \frac{n_p(t) - n_{p,0}}{n_{i,0}} \frac{|v_i|}{|v_p|} \quad (2.15)$$

² This section is based on the following paper: “Thermomorphic Multiphase Systems: Switchable Solvent Mixtures for the Recovery of Homogeneous Catalysts in Batch and Flow Processes” in *Chemistry – A European Journal* [23]. For this publication, parts of the content have been rewritten by the authors. All of the figures come from the previous publication and have been slightly altered for this section.

The stoichiometric factors ν_i and ν_p indicate the ratios of the moles of products formed per mole of the starting material. For calculations of continuous experiments (eq. (2.16)), the input stream of the substrate $\dot{n}_{i,\text{in}}$ has to be considered, as well as the input and output streams of the product $\dot{n}_{p,\text{out}}$:

$$Y_C(t) = \frac{\dot{n}_{p,\text{out}}(t) - \dot{n}_{p,\text{in}}(t)}{\dot{n}_{i,\text{in}}} \frac{|\nu_i|}{|\nu_p|} \quad (2.16)$$

The selectivity, $S(t)$, determines how much of the consumed substrate is converted into the product p , as given by

$$S(t) = \frac{Y_{p,i}(t)}{X(t)} \quad (2.17)$$

TON characterizes the performance of a catalyst. The relationship between the amount of converted substrate at a certain time, the amount of used catalyst, and the selectivity to the desired product reflects the catalytic productivity:

$$\text{TON}(t) = \frac{n_{i,0} - n_i(t)}{n_{\text{cat}}} S(t) \quad (2.18)$$

After a certain reaction time when the applied amount of catalyst does not show any catalytic activity anymore, the TON determines the largest number of possible turnovers. TOF indicates the actual activity of the catalyst:

$$\text{TOF}(t) = \frac{n_p}{n_{\text{cat}} \cdot t} \quad (2.19)$$

The amount of product formed is related to the reaction time and to the amount of catalyst applied. Because the TOF is a time-dependent indicator, a defined time or turnover point at which the TOF was determined for a particular reaction must be specified. Typically, the TOF should be determined at low conversions, for example, at 20% conversion. TON and TOF are crucial indicators for the economics of the reaction because these indicators can be used to estimate the cost of the catalyst that is incurred for a process. Another important indicator, especially for continuous flow processes, is catalyst leaching, which is based on the distribution coefficient (eq. (2.5)). In the literature, catalyst leaching, W , is often reported as the concentration of catalyst in the noncatalyst phase:

$$W = \frac{n_{q,z}}{n_z} \quad (2.20)$$

The catalyst leaching is determined as the number of catalyst molecules in the non-catalyst liquid phase, $n_{q,z}$, over the total number of molecules in the same liquid phase, n_z (eq. (2.20)), where q indicates the corresponding catalyst component and z indicates the corresponding liquid phase. Most often, this value is reported in

ppm. Unfortunately, this value is not presented in a fully consistent manner in the literature because different reference units (volume, mass, molar) are considered. We would like to point out that a pure indication of the loss of catalyst via its concentration in the product phase (typically in ppm) is not sufficient and a direct reference to the quantity of catalyst used in an experiment is absolutely essential. Therefore, we propose definitions of leaching, L , for batch and continuous processes, as shown in the following equations:

$$L_B = \frac{n_{q,z,r}}{n_{q,c,0}} = \frac{n_{q,c,0} - n_{q,c,r}}{n_{q,c,0}} \quad (2.21)$$

$$L_C(t) = \int \frac{\dot{n}_{q,z}(t)}{\dot{n}_{q,c,0}} = \frac{\dot{n}_{q,c,0} - \dot{n}_{q,c}(t)}{\dot{n}_{q,c,0}} \quad (2.22)$$

It is based on the ratio of the amount of lost catalyst q (either the catalytic metal or the surrounding ligands) in the product/nonpolar phase and any other phase than the catalyst phase z , and the initially applied amount of catalyst in the catalyst phase c . In eq. (2.21), r represents discrete values of the number of repetitive reaction runs, while in eq. (2.22), t represents the specific time of process operation at which L is determined.

For multiple consecutive recycling runs of the catalyst in batch experiments, the value defined by eq. (2.21) approaches the value provided by eq. (2.22). This effect is graphically represented in Figure 2.14. In this manner, it is possible to calculate the relative loss of catalyst, with regard to the initial amount of catalyst, to every point in time in batch and in continuous experiments.

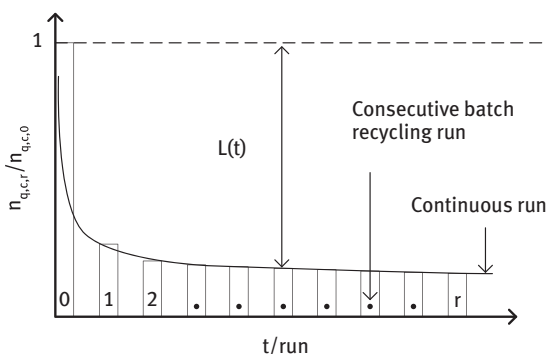


Figure 2.14: Catalyst leaching behavior in multiple consecutive batch recycling runs and continuous experiments, depending on time [23].

References

- [1] Abe M. 1996: Microemulsions in enhanced oil recovery – middle-phase microemulsion formation with some typical anionic surfactants. In: Solans C, Kunieda H, (Eds.) *Industrial Applications of Microemulsions*. 1st ed. CRC Press; p. 279–304.
- [2] Albert C, Beladjine M, Tsapis N., Fattal E, Agnely F, Huang N. 2019: Pickering emulsions: preparation processes, key parameters governing their properties and potential for pharmaceutical applications. *J. Controlled Release* 309: 302–332.
- [3] Atkins PW, Paula J. (Eds.) 2010: *Physikalische Chemie*. Wiley-VCH Verlag GmbH.
- [4] Bago Rodriguez AM, Binks B. 2020: Catalysis in Pickering emulsions. *Soft Matter*. 16: 10221–10243.
- [5] Baerns M, Behr A, Brehm A, Gmehling J, Hinrichsen KO, Hofmann H, Palkowitz R, Onken U, Renken A. 2013: *Technische Chemie*. Weinheim, Wiley-VCH.
- [6] Bera A, Mandal A. 2014: Microemulsions: a novel approach to enhanced oil recovery: a review. *J. Petrol. Expl. Prod. Techn.* 5: 255–268.
- [7] Behr A. 1998: Technische Konzepte zum Recycling von Homogenkatalysatoren. *Chem. Ing. Tech.* 70: 685–695.
- [8] Behr A. 2008: *Angewandte Homogene Katalyse*. Weinheim, Wiley-VCH.
- [9] Behr A, Brunsch Y, Lux A. 2012: Rhodium nanoparticles as catalysts in the hydroformylation of 1-dodecene and their recycling in thermomorphic solvent systems. *Tetrahedron Lett.* 53: 2680–2683.
- [10] Behr A, Fängewisch C. 2002: Temperature-dependent multicomponent solvent systems – an alternative concept for recycling homogeneous catalysts. *Chem. Eng. Technol.* 25: 143–147.
- [11] Behr A, Fängewisch C. 2003: Rhodium-catalysed synthesis of branched fatty compounds in temperature-dependent solvent systems. *J. Mol. Catal. A: Chem.* 197: 115–126.
- [12] Behr A, Henze G, Obst D, Turkowski B. 2005: Selection process of new solvents in temperature-dependent multi-component solvent systems and its application in isomerising hydroformylation. *Green Chem.* 7: 645–649.
- [13] Behr A, Henze G, Schomäcker R. 2006: Thermoregulated liquid/liquid catalyst separation and recycling. *Adv. Synth. Catal.* 348: 1485–1495.
- [14] Behr A, Henze G, Johnen L, Awungacha C. 2008: Advances in thermomorphic liquid/liquid recycling of homogeneous transition metal catalysts. *J. Mol. Catal. A: Chem.* 285: 20–28.
- [15] Behr A, Johnen L, Rentmeister N. 2010: Novel palladium-catalysed hydroamination of myrcene and catalyst separation by thermomorphic solvent systems. *Adv. Synth. Catal.* 352: 2062–2072.
- [16] Behr A, Miao Q. 2004: A new temperature-dependent solvent system based on polyethylene glycol 1000 and its use in rhodium catalyzed cooligomerization. *J. Mol. Catal. A: Chem.* 222: 127–132.
- [17] Behr A, Neubert P. 2012: *Applied Homogeneous Catalysis*. Weinheim, Wiley-VCH.
- [18] Behr A, Schöbel R. 2006: Katalysatorrecycling mit temperaturgesteuerten Lösungsmitteln. *Nachr. Chem.* 54: 20–23.
- [19] Behr A, Wintzer A. 2011: Baukastensystem zur Auswahl von Lösungsmitteln in homogenkatalytischen Reaktionen. *Chem. Ing. Tech.* 83: 1356–1370.
- [20] Bergbreiter DE, Sung SD. 2006: Liquid/liquid biphasic recovery/reuse of soluble polymer-supported catalysts. *Adv. Synth. Catal.* 348: 1352–1366.
- [21] Berton-Carabin CC, Ropers MH, Genot C. 2014: Lipid oxidation in oil-in-water emulsions: involvement of the interfacial layer. *Compr. Rev. Food Sci. Food Saf.* 13: 945–977.
- [22] Berton-Carabin CC, Schroën, K. 2015: Pickering emulsions for food applications: background, trends, and challenges. *Annu. Rev. Food Sci. Technol.* 6: 263–297.

- [23] Bianga J, Künnemann KU, Gaide T, Vorholt AJ, Seidensticker T, Dreimann JM, Vogt D. 2019: Thermomorphic multiphase systems: switchable solvent mixtures for the recovery of homogeneous catalysts in batch and flow processes. *Chem. Eur. J.* 25: 11586–11608.
- [24] Binks BP. 2002: Particles as surfactants – similarities and differences. *Curr. Opin. Colloid Interf. Sci.* 7: 21–41.
- [25] Binks BP, Horozov TS. 2006: *Colloidal Particles at Liquid Interfaces*. 1st ed. Cambridge University Press.
- [26] Binks BP, Lumsdon, SO. 2000: Influence of particle wettability on the type and stability of surfactant-free emulsions. *Langmuir* 16: 8622–8631.
- [27] Binks BP, Lumsdon, SO. 2001: Pickering emulsions stabilized by monodisperse latex particles: effects of particle size. *Langmuir* 17: 4540–4547.
- [28] Briggs NM, Weston JS, Li B, Venkataramani, D, Aichele, CP, Harwell JH, Crossley, SP. 2015: Multiwalled carbon nanotubes at the interface of Pickering emulsions. *Langmuir* 31: 13077–13084.
- [29] Boonme P. 2007: Applications of microemulsions in cosmetics. *J. Cosm. Dermatol.* 6: 223–228.
- [30] Chevalier Y, Bolzinger, MA. 2013: Emulsions stabilized with solid nanoparticles: Pickering emulsions. *Colloids Surf. A Physicochem. Eng. Asp.* 439: 23–34.
- [31] Chiba K, Kono Y, Kim S, Nishimoto K, Kitano Y, Tada M. 2002: A liquid-phase peptide synthesis in cyclohexane-based biphasic thermomorphic systems. *Chem. Commun.* 16: 1766–1767.
- [32] Cole-Hamilton DJ, Tooze RP. 2006: *Catalyst Separation, Recovery and Recycling: Chemistry and Process Design*. Dordrecht, Springer Verlag.
- [33] Cornils B, Herrmann WA, Rasch M. 1994: Otto Roelen, pioneer in industrial homogeneous catalysis. *Angew. Chem. Int. Ed. Engl.* 33: 2144–2163.
- [34] Dreimann JM, Skiborowski M, Behr A, Vorholt AJ. 2016: Recycling homogeneous catalysts simply by organic solvent nanofiltration: new ways to efficient catalysis. *ChemCatChem*. 8: 3330–3333.
- [35] Dreimann JM, Faßbach TA, Fuchs S, Fürst MRL, Gaide T, Kuhlmann R, Ostrowski KA, Stadler A, Seidensticker T, Vogelsang D, Warmeling HWF, Vorholt AJ. 2017: Vom Laborcuriosum zum kontinuierlichen Prozess: Die Entwicklung thermomorpher Lösungsmittelsysteme. *Chem. Ing. Tech.* 89: 252–262.
- [36] Duffus LJ, Norton, JE, Smith P, Norton, IT, Spyropoulos, F. 2016: A comparative study on the capacity of a range of food-grade particles to form stable O/W and W/O Pickering emulsions. *J. Colloid Interf. Sci.* 473: 9–21.
- [37] Fan Z, Tay A, Pera-Titus M, Zhou WJ, Benhabbari S, Feng X, Malcouronne G, Bonneviot L, De Campo F, Wang L, Clacens, JM. 2014: Pickering interfacial catalysts for solvent-free biomass transformation: physicochemical behaviour of nonaqueous emulsions. *J. Colloid Interf. Sci.* 427: 80–90.
- [38] Frelichowska J, Bolzinger MA, Chevalier, Y. 2010: Effects of solid particle content on properties of o/w Pickering emulsions. *J. Colloid Interf. Sci.* 351: 348–356.
- [39] Frey G, Dämbkes G. (Eds.) 2013: *75 Jahre Oxo-Synthese: 75 Years of Oxo Synthesis*. 1st ed. Essen, Klartext.
- [40] Gallou F, Isley NA, Ganic A, Onken U, Parmentier M. 2016: Surfactant technology applied toward an active pharmaceutical ingredient: more than a simple green chemistry advance. *Green Chem.* 18: 14–19.
- [41] García-Sánchez F, Eliosa-Jiménez G, Salas-Padrón A, Hernández-Garduza O, Ápam-Martínez D. 2001: Modeling of microemulsion phase diagrams from excess Gibbs energy models. *Chem. Eng. J.* 84: 257–274.

- [42] Gmehling J, Kolbe B, Kleiber M, Rarey JR. 2012: *Chemical Thermodynamics for Process Simulation*. Weinheim, Wiley-VCH.
- [43] Güven S, Hamers B, Franke R, Priske M, Becker M, Vogt D. 2014: Kinetics of cyclooctene hydroformylation for continuous homogeneous catalysis. *Catal. Sci. Technol.* 4: 524–530.
- [44] Hayashi K, Kim S, Kono Y, Tamura M, Chiba K. 2006: Microwave-promoted Suzuki–Miyaura coupling reactions in a cycloalkane-based thermomorphic biphasic system. *Tetrahedron Lett.* 47: 171–174.
- [45] Heyse A, Kraume M, Drews A. 2020: The impact of lipases on the rheological behavior of colloidal silica nanoparticle stabilized Pickering emulsions for biocatalytical applications. *Colloids Surf. B Biointerf.* 185: 110580.
- [46] Hloucha M, Küsters E, Schorb J, Prinz D, Seipel W, Wirtz M. 2014: Use of microemulsions in cosmetic cleaning compositions. Patent US9656104B2.
- [47] Hong CI, Kim JW, Choi NH, Shin HJ, Yang SG, Kim JH, Lim JL, Kim CK. 2001: Microemulsions and uses thereof as nanoreactors or delivery vehicles. Patent US10384178B2. 2001 Oct 23.
- [48] Horváth IT, Rábai J. 1994: Facile catalyst separation without water: fluororous biphasic hydroformylation of olefins. *Science* 266: 72–75.
- [49] Horváth IT. 1998: Fluororous biphasic chemistry. *Acc. Chem. Res.* 31: 641–650.
- [50] Huang TS, Wang YH, Jiang JY, Jin ZL. 2008: PEG-stabilized palladium nanoparticles: an efficient and recyclable catalyst for the selective hydrogenation of 1,5-cyclooctadiene in thermoregulated PEG biphasic system. *Chin. Chem. Lett.* 19: 102–104.
- [51] Illner M. 2020: Rigorous analysis of reactive microemulsion systems for process design and operation. Ph.D. dissertation, Technische Universität Berlin.
- [52] Illner M, Kozachynskiy V, Esche E, Repke J.-U. 2021: Fast-track realization of reactive microemulsion systems – Systematic system analysis and tailored application of PSE methods. *Chem. Eng. Sc.*: 117290.
- [53] Kahlweit M, Strey R. 1985: Phasenverhalten ternärer Systeme des Typs $H_2O - \text{Öl} - \text{nichtionisches Amphiphil}$ (Mikroemulsionen). *Angew. Chem.* 97: 655–669.
- [54] Kahlweit M, Strey R, Busse G. 1990: Microemulsions: a qualitative thermodynamic approach. *J. Phys. Chem.* 94: 3881–3894.
- [55] Kahlweit M, Strey R, Firman P, Haase D, Jen J, Schomaecker R. 1988: General patterns of the phase behavior of mixtures of water, nonpolar solvents, amphiphiles, and electrolytes. 1. *Langmuir* 4: 499–511.
- [56] Kahlweit M, Strey R, Haase D, Kunieda H, Schmeling T, Faulhaber B, Borkovec M, Eicke HF, Busse G, Eggers F, Funck T, Richmann H, Magid L, Sodermann O, Stilbs P, Winkler J, Dittrich A, Jahn, W. 1987: How to study microemulsions. *J. Coll. Interf. Sci.* 118: 436–453.
- [57] Katepalli H., John VT, Tripathi A, Bose A. 2017: Microstructure and rheology of particle stabilized emulsions: effects of particle shape and inter-particle interactions. *J. Colloid Interf. Sci.* 485: 11–17.
- [58] Klier J, Tucker CJ, Kalantar TH, Green DP. 2000: Properties and applications of microemulsions. *Adv. Mater.* 12: 1751–1757.
- [59] Langevin D. 1986: Microemulsions and liquid crystals. *Mol. Cryst. Liq. Cryst.* 138: 259–305.
- [60] Leclercq L, Mouret A, Proust A, Schmitt V, Bauduin P, Aubry JM, Nardello-Rataj V. 2012: Pickering emulsion stabilized by catalytic polyoxometalate nanoparticles: a new effective medium for oxidation reactions. *Chem. A. Eur. J.* 18: 14352–14358.
- [61] Leitner W, Jessop PG. (Eds.) 2010: *Supercritical Solvents*. Weinheim, Wiley-VCH.
- [62] Lipshutz BH. 2018: Synthetic chemistry in a water world. New rules ripe for discovery. *Curr. Opin. Green Sust. Chem.* 11: 1–8.
- [63] Lüdecke D, Lüdecke C. 2000: *Thermodynamik: Physikalisch-chemische Grundlagen der Thermischen Verfahrenstechnik*. Berlin, Springer.

- [64] Marchetti P, Jimenez Solomon MF, Szekely G, Livingston AG. 2014: Molecular separation with organic solvent nanofiltration: a critical review. *Chem. Rev.* 114: 10735–10806.
- [65] Molnár Á, Papp A. 2017: Catalyst recycling – a survey of recent progress and current status. *Coord. Chem. Rev.* 349: 1–65.
- [66] Müller E, Berger R, Blass E, Sluyts D, Pfennig A. 2008: Liquid-Liquid extraction. In: *Ullmann's Encyclopedia of Industrial Chemistry*. Weinheim, Wiley-VCH.
- [67] Myers D. (Ed.) 2005: Surfactants in solution: monolayers and micelles. *Surfactant Science and Technology*. John Wiley & Sons, Inc.; pp. 107–159.
- [68] Nishikata T, Abela AR, Lipshutz BH. 2010: Room temperature C-H activation and cross-coupling of aryl ureas in water. *Angewandte Chemie (International Ed. in English)*. 49: 781–784.
- [69] Owoseni O, Nyankson E, Zhang Y, Adams SJ, He J, McPherson GL, Bose A, Guptaand RB, John VT. 2014: Release of surfactant cargo from interfacially-active halloysite clay nanotubes for oil spill remediation. *Langmuir* 30: 13533–13541.
- [70] Paul EL, Atiemo-Obeng VA, Kresta SM. 2004: *Handbook of Industrial Mixing: Science and Practice*. John Wiley & Sons, Inc.
- [71] Pera-Titus M, Leclercq L, Clacens JM, De Campo F, Nadrello-Rataj, V. 2015: Pickering interfacial catalysis for biphasic systems: from emulsion design to green reactions. *Angew. Chem. Int. Ed.* 54: 2006–2021.
- [72] Pickering SU. 1907: Emulsions. *J. Chem. Soc., Trans.* 91: 2001–2021.
- [73] Qiao Y, Ma W, Theyssen N, Chen C, Hou Z. 2017: Temperature-responsive ionic liquids: fundamental behaviors and catalytic applications. *Chem. Rev.* 117: 6881–6928.
- [74] Ramsden W. 1903: Separation of solids in the surface-layers of solutions and “suspensions” (observations on surface-membranes, bubbles, emulsions, and mechanical coagulation) – preliminary account. *Proc. Roy. Soc. Lond.* 72: 156–164.
- [75] Richtering W. 2012: Responsive emulsions stabilized by stimuli-sensitive microgels: emulsions with special non-Pickering properties. *Langmuir* 28: 17218–17229.
- [76] Röllig R, Plikat C, Ansorge-Schumacher MB. 2019: Efficient and selective carboligation with whole-cell biocatalysts in Pickering emulsion. *Angew. Chemie Int. Ed.* 58: 12960–12963.
- [77] Rosen MJ, Cohen AW, Dahanayake M, Hua XY. 1982: Relationship of structure to properties in surfactants. 10. Surface and thermodynamic properties of 2-dodecyloxypoly-(ethenoxy-ethanol)s, $C_{12}H_{25}(OC_2H_4)_xOH$ in aqueous solution. *J. Phys. Chem.* 86: 541–545.
- [78] Rösler T, Faßbach TA, Schrimpf M, Vorholt AJ, Leitner W. 2019: Toward water-based recycling techniques: methodologies for homogeneous catalyst recycling in liquid/liquid multiphase media and their implementation in continuous processes. *Ind. Eng. Chem. Res.* 58: 2421–2436.
- [79] Rost A, Brunsch Y, Behr A, Schomäcker R. 2014: Comparison of the activity of a rhodium-biphenos catalyst in thermomorphic solvent mixtures and microemulsions. *Chem. Eng. Technol.* 37: 1055–1064.
- [80] Saïen J, Bamdadi H. 2012: Mass transfer from nanofluid single drops in liquid–liquid extraction process. *Ind. Eng. Chem. Res.* 51: 5157–5166.
- [81] Schomäcker R, Holmberg K. 2009: Reactions in organised surfactant systems. In: Stubenrauch C, (Ed.). *Microemulsions: Background, New Concepts, Applications, Perspectives*. John Wiley & Sons, Ltd; p. 148–179.
- [82] Schulman JH, Stoeckenius W, Prince LM. 1959: Mechanism of formation and structure of micro emulsions by electron microscopy. *J. Phys. Chem.* 63: 1677–1680.
- [83] Schwuger MJ, Stickdorn K, Schomäcker R. 1995: Microemulsions in technical processes. *Chem. Rev.* 95: 849–864.

- [84] Shaharun MS, Mukhtar H, Dutta BK. 2008: Solubility of carbon monoxide and hydrogen in propylene carbonate and thermomorphic multicomponent hydroformylation solvent. *Chem. Eng. Sci.* 63: 3024–3035.
- [85] Shaharun MS, Mukhtar H, Dutta BK. 2011: Selectivity of rhodium-catalyzed hydroformylation of 1-octene in a thermomorphic solvent system. *J. Appl. Sci.* 11: 1157–1163.
- [86] Sharma S, Basavaraju KC, Singh AK, Kim DP. 2014: Continuous recycling of homogeneous Pd/Cu catalysts for cross-coupling reactions. *Org. Lett.* 16: 3974–3977.
- [87] Shen X, Huang C, Shinde S, Jagadeesan KK, Ekström S, Fritz E, Sellergren B. 2016: Catalytic formation of disulfide bonds in peptides by molecularly imprinted microgels at oil/water interfaces. *ACS Appl. Mater. Interf.* 8: 30484–30491.
- [88] Sottmann T, Stubenrauch C. 2009: Phase behaviour, interfacial tension and microstructure of microemulsions. In: Stubenrauch C, (Ed.) *Microemulsions: Background, New Concepts, Applications, Perspectives*. John Wiley & Sons, Ltd; p. 1–47.
- [89] Tadros TF. 2013: Emulsion formation, stability, and rheology. In: *Emulsion Formation and Stability*. Wiley-VCH Verlag GmbH & Co. KGaA; p. 1–75.
- [90] Tang J, Quinlan PJ, Tam KC. 2015: Stimuli responsive Pickering emulsions: recent advances and potential applications, *Soft Matter* 11: 3512–3529.
- [91] Tanudjaja HJ, Tarabara VV, Fane AG, Chew JW. 2017: Effect of cross-flow velocity, oil concentration and salinity on the critical flux of an oil-in-water emulsion in microfiltration. *J. Membr. Sci.* 530: 11–19.
- [92] Tao L, Zhong M, Chen J, Jayakumar S, Liu L, Li H, Yang Q. 2018: Heterogeneous hydroformylation of long-chain alkenes in IL-in-oil Pickering emulsion. *Green Chem.* 20: 188–196.
- [93] Ternel J, Couturier JL, Dubois JL, Carpentier JF. 2013: Rhodium-catalyzed tandem isomerization/hydroformylation of the bio-sourced 10-undecenenitrile: selective and productive catalysts for production of polyamide-12 precursor. *Adv. Synth. Catal.* 355: 3191–3204.
- [94] Torrealba VA, Johns RT. 2018: Microemulsion phase-behavior equation-of-state model using empirical trends in chemical potentials. *SPE J.* 23: 0819–0830.
- [95] Tsabet E, Fradette L. 2015: Effect of processing parameters on the production of Pickering emulsions. *Ind. Eng. Chem. Res.* 54: 2227–2236.
- [96] Vandezande P, Gevers LEM, Vankelecom IFJ. 2008: Solvent resistant nanofiltration: separating on a molecular level. *Chem. Soc. Rev.* 37: 365–405.
- [97] Wei L, Zhang M, Zhang X, Xin H, Yang H. 2016: Pickering emulsion as an efficient platform for enzymatic reactions without stirring. *ACS Sus. Chem. Eng.* 4: 6838–6843.
- [98] Weir RD, de Loos TW. (Eds.) 2005: *Measurement of the Thermodynamic Properties of Multiple Phases*. 1st ed. Amsterdam, Elsevier.
- [99] Wende M, Gladysz JA. 2003: Fluorous catalysis under homogeneous conditions without fluorous solvents: a “greener” catalyst recycling protocol based upon temperature-dependent solubilities and liquid/solid phase separation. *J. Am. Chem. Soc.* 125: 5861–5872.
- [100] Whitby CP, Fischer FE, Fornasiero D, Ralston J. 2011: Shear-induced coalescence of oil-in-water Pickering emulsions. *J. Colloid Interf. Sci.* 361: 170–177.
- [101] Whitby CP, Anwar HK, Hughes J. 2016: Destabilising Pickering emulsions by drop flocculation and adhesion. *J. Colloid Interf. Sci.* 465: 158–164.
- [102] Wu C, Bai S, Ansoorge-Schumacher MB, Wang D. 2011: Nanoparticle cages for enzyme catalysis in organic media. *Adv. Mater.* 23: 5694–5699.
- [103] Wu J, Ma GH. 2016: Recent studies of Pickering emulsions: particles make the difference. *Small* 12: 4633–4648.

- [104] Yu S, Zhang D, Jiang J, Cui Z, Xia W, Binks BP, Yang H. 2019: Biphasic biocatalysis using a CO₂-switchable Pickering emulsion. *Green Chem.* 21: 4062–4068.
- [105] Zhang M, Wei L, Chen H, Du Z, Binks BP, Yang, H. 2016: Compartmentalized droplets for continuous flow liquid-liquid interface catalysis. *J. Am. Chem. Soc.* 138: 10173–10183.
- [106] Zhao Y, Zhang X, Sanjeevi J, Yang Q. 2016: Hydroformylation of 1-octene in Pickering emulsion constructed by amphiphilic mesoporous silica nanoparticles. *J. Catal.* 334: 52–59.
- [107] Zeng Y, Wang Y, Xu Y, Song Y, Zhao J, Jiang J, Jin Z. 2012: Rh nanoparticles catalyzed hydroformylation of olefins in a thermoregulated ionic liquid/organic biphasic system. *Chin. J. Catal.* 33: 402–406.
- [108] Zhou WJ, Fang L, Fan Z, Albela B, Bonneviot L, De Campo F, Pera-Titus M, Clacens JM. 2014: Tunable catalysts for solvent-free biphasic systems: Pickering interfacial catalysts over amphiphilic silica nanoparticles. *J. Am. Chem. Soc.* 136: 4869–4872.

3 Thermodynamics, Kinetics, and Mass Transfer

Sabine Enders

3.1 Thermodynamics

Sabine Enders, Niklas Haarmann, Fabian Huxoll, Annika Reinhardt,
Gabriele Sadowski, Tim Zeiner

Thermodynamic phenomena form the physical fundament of the chemical reactions as well as of all separation steps necessary for the reconditioning of the feedstock or isolation of the final product. For the development of new processes or the improvement of known processes, thermodynamic data should be known. However, a high experimental effort is usually required. The most important goal of thermodynamic research activities is the prediction of all thermodynamic data. This goal cannot be reached due to the complexity and the required properties of the mixtures involved. Therefore, we paid our attention to increasing the predictive power of the thermodynamic tools. We focus our attention on two physically-based models, namely the Perturbed-Chain Statistical Associating Fluid Theory (PC-SAFT) [85–87] and the Lattice Cluster Theory (LCT) [55, 64, 141, 249]. The PC-SAFT permits the detailed description of different types of interaction. The LCT includes the molecular architecture in the thermodynamic equations and can be used as an activity coefficient model or as an equation of state (LCT-EOS). The PC-SAFT as well as the LCT-EOS requires pure-component parameters and mostly a binary interaction parameter for every binary subsystem. The application of the LCT as an activity coefficient model needs only binary parameters. Consequently, both models should be able to predict the thermodynamic behavior of ternary mixtures. For the minimization of the number of adjustable parameters, the properties of the homologues series are used, allowing the extrapolation of the parameters to other components belonging to the same homologues series.

Using standard thermodynamics (Section 2.1), different types of phase equilibria, where two or three phases coexist, can be calculated using one of the two models. With the combination of the thermodynamic models with the Density Functional Theory (DFT) for inhomogeneous system or with the Density Gradient Theory (DGT) [96] that is the first approach of DFT, additional interfacial properties can be calculated. Interfacial properties of fluid interphases must be distinguished from those between a fluid and a solid for the calculation of interfacial properties. The first case can be treated with DGT, and the second case can be examined only with DFT.

The phase behavior of surfactant-containing mixtures cannot be modelled, because different nanostructures will be formed. For this type of mixture, the relevant phase diagrams must be measured. However, the aggregation behavior of aqueous surfactant solutions can be modelled using a detailed aggregation formation model

[60, 170]. Moreover, the solubilization of weak polar components (n-aldehydes, n-amines, or esters) acting as the reaction product can be modeled.

3.1.1 Heterosegmented Perturbed-Chain Statistical Associating Fluid Theory

The PC-SAFT [85–87] is formulated in terms of the residual Helmholtz energy, a^{res} , which is obtained as a superposition of multiple contributions accounting for different molecular interactions.

$$a^{res} = a^{hc} + a^{disp} + a^{dipol} + a^{assoc} \quad (3.1)$$

Molecules are considered as chains of m spherical segments of diameter σ . Repulsive interactions between these molecules are accounted for by the hard-chain contribution, a^{hc} , whereas a^{disp} accounts for attractive interactions via a dispersive energy, u . If the component is of polar nature, the resulting polar interactions between the molecules are taken into account by the dipole moment, μ and the corresponding dipolar contribution, a^{dipol} . Furthermore, the association contribution, a^{assoc} considers associative interactions such as hydrogen bonding. For that purpose, association sites, namely a number of N^A electron donors (A) and a number of N^B electron acceptors (B), are mounted onto the chain and the associative interactions are characterized by the association energy, ε^{AB} and the association volume, κ^{AB} . Consequently, a nonpolar, nonassociating component is fully characterized using the PC-SAFT pure-component parameter set, m , σ , and u . Depending on the nature of the component, the additional parameters, μ , N^A , N^B , ε^{AB} , and κ^{AB} can be taken into account.

The so-called homo-segmental approach assumes that all segments of a chain are identical (cf. n-hexylamine on the right-hand side of Figure 3.1) [85–87]. In contrast, a component can also be described in a hetero-segmental manner as a chain of segments that differ in diameter and interaction parameters. This approach is particularly useful for molecules of a homologous series, which comprise a functional head group connected to an n-alkyl residue, e.g., aldehydes, alcohols, or amines. Hence, a representative of the homologous series is considered to be composed of two types of segments, each of them representing the functional head domain and the n-alkyl tail domain, respectively (cf. n-hexylamine on the left-hand side of Figure 3.1) [90, 91]. In contrast to the homo-segmental approach, only the functional head domain and not the whole molecule is described as being dipolar or associative, whereas the tail domain is treated as being nonpolar and does not carry any association sites. The advantage of this approach is that there is only one PC-SAFT pure-component parameter set for a functional head domain, which is identical for all species of a homologous series, whereas the n-alkyl tail domains

can conveniently be described using the PC-SAFT pure-component parameters of the corresponding n-alkanes.

For mixtures, a binary interaction parameter, k_{ij} between segments of a different kind can be applied for both the homo-segmental and the hetero-segmental approaches of PC-SAFT. As illustrated in Figure 3.1, for the homo-segmental case, a binary parameter is applied for each binary mixture long-chain compound + water (k_{iW}) as well as for mixtures long-chain compound + n-alkane (k_{iA}). For the hetero-segmental approach, there is only one binary parameter between the head domain + water (k_{HW}), which holds for all molecules of this homologous series. Furthermore, the binary parameter between tail domain + water (k_{TW}) is set equal to that between the real binary mixture n-alkane + water. Hence, this binary parameter can be determined from experimental data, which are independent of the homologous series under consideration.

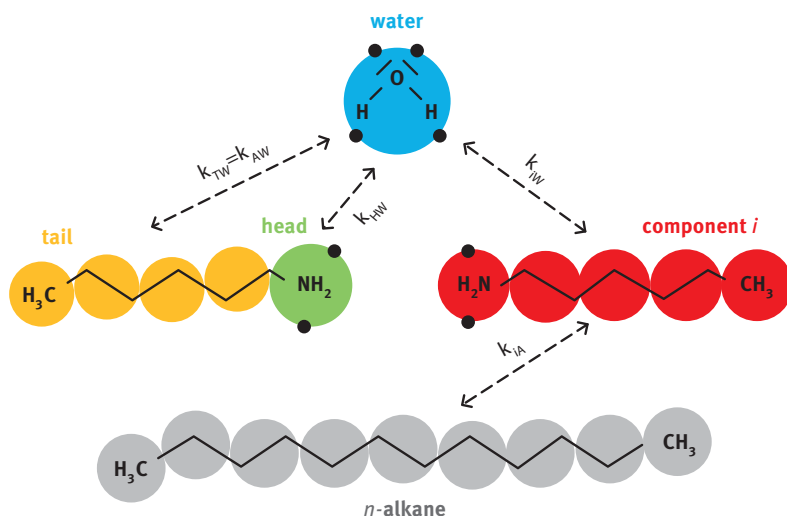


Figure 3.1: Schematic representation of a long-chain compound modeled in a hetero-segmental (middle left) and homo-segmental (middle right) manner. Moreover, the binary interaction parameters k_{ij} for the binary mixtures, water + long-chain compound (upper part) and n-alkane + long-chain compound (lower part) are shown. While the binary interaction parameters, k_{TW} and k_{HW} are identical for all long-chain compounds, the binary interaction parameters, k_{iW} , k_{TW} , and k_{iA} vary for different long-chain compounds, i .

3.1.2 Lattice Cluster Theory

Dudowicz and Freed [55] have developed a perturbative method to systematically derive corrections to the well-known Flory-Huggins theory describing polymer-containing mixtures [68]. This Lattice Cluster Theory (LCT) allows the description of

the molecular architecture, for example, branching, directly in the thermodynamic relations. The Gibbs free energy for a binary system according to the LCT can be derived [64, 249]:

$$\frac{\Delta G_s^{LCT}}{RTN_L} = \frac{\phi_A}{N_A} \ln \phi_A + \frac{\phi_B}{N_B} \ln \phi_B + \sum_{i=1}^6 \alpha_i \phi_B^i \quad (3.2)$$

where R denotes the universal gas constant and T denotes the temperature. From eq. (3.2) it can be seen that the LCT is based on the Flory-Huggins theory [68], since the first two terms equal the entropic part of Flory-Huggins theory (FH). The quantities, α_i , within the sum, include corrections to the FH mean field theory taking into account the molecular architecture. The α_i -values depend on the interaction energy, ε_{ij} , which has to be fitted to experimental data and on the architectural parameters. These architectural parameters can be determined only by the chemical structure of the molecules. If compressibility must be included, voids are introduced in the lattice. In this case, the Gibbs free energy is replaced by the Helmholtz free energy [64, 141].

Equation (3.2) includes only dispersion interactions. For the description of associating molecules an additional contribution must be added, for instance, the Chemical Association Lattice Model (CALM) [25]. Within CALM, the self-association of the solvent, A, is regarded as a chemical equilibrium:



Two associating chains with degrees, r and r' , respectively, are in equilibrium with one chain of degree, $r+r'$. This approach leads to a distribution of association chain lengths ranging from 1 to infinity. Similar to chemical reactions, Browarzik [25] introduced the equilibrium association constant, wherein the temperature dependence of the association is described by an Arrhenius approach. Examples of the combination of LCT and CALM can be found in the literature [64, 250].

3.1.3 Phase Equilibria

Vapor–Liquid Equilibria (VLEs)

Figure 3.2 shows, for example, the VLE modeling of n-dodecane + dodecanedioic acid dimethyl ester (DDDME) [144], (Figure 3.2a), methanol + n-hexene [114], and methanol + n-octene [114], (Figure 3.2b). PC-SAFT is able to describe the VLE of these three systems in almost quantitative agreement with experimental data from the literature [27, 28]. The systems methanol + n-hexene and methanol + n-octene show an azeotropic phase behavior. For increasing the C chain length of the n-alkene, the azeotropic composition shifts towards higher mole fractions of methanol. Using the same and temperature-independent binary interaction parameters

for the two methanol + n-alkene systems, PC-SAFT can predict the azeotropic phase behavior as well as the azeotropic composition [114], quantitatively.

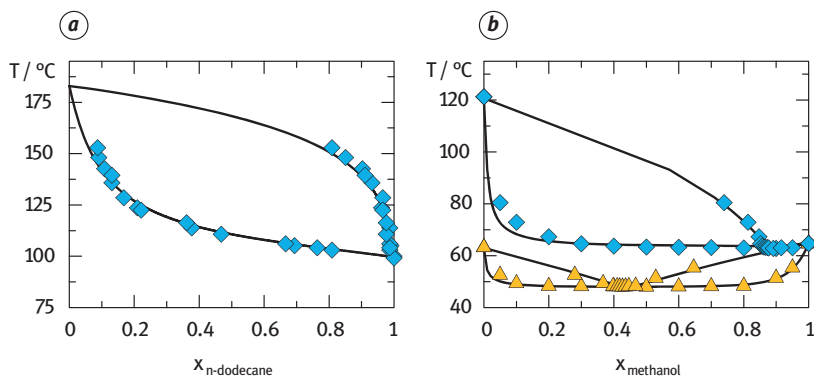


Figure 3.2: Examples for vapor–liquid equilibria of binary systems. Symbols represent experimental VLE data. (a) n-Dodecane + DDDME [144] (diamonds) at 0.02 bar, (b) Methanol + n-hexene [28] (triangles) at 1 bar and methanol + n-octene [27] (diamonds) at 1 bar. Lines are calculations using PC-SAFT. All PC-SAFT pure-component parameters and binary parameters used for the calculations were taken from the literature [114, 144].

Gas Solubilities

Complex reactions with gaseous reactants depend on the solubility of the gas(es) in the multicomponent reaction systems. Syngas is a key for hydroformylation, where CO and H_2 react with olefins to aldehydes. Therefore, the syngas solubility in the liquid determines the amounts of the gases available for the reaction. The calculation of gas solubilities can be performed using the iso-fugacity condition, which requires the identical fugacity of every component, i , in the liquid and the gas phase.

Figure 3.3 shows PC-SAFT modeling results for syngas solubilities in different solvent mixtures consisting of n-decane + DMF compared to experimental data. Syngas solubilities were measured in a high-pressure variable-volume view cell applying a visual synthetic method, at pressures ranging from 1.5 MPa to 12.8 MPa [238]. The PC-SAFT prediction (all $k_{ij} = 0$) shows only small deviations from the experimental data (Figure 3.3a). Moreover, the influences of temperature and varying solvent composition on the gas solubility can be correctly predicted. The modeling could be further improved by applying linear temperature-dependent binary interaction parameters, which have been fitted to the solubilities of the pure gases in the pure solvents only (Figure 3.3b).

The gas solubilities depend not only on the solvents but also on the reactants/products. This is particularly important for reactions, as, due to the changing composition of the reaction mixture, the gas solubility in the liquid changes during the reaction. For example, in case of the hydroformylation, the gas solubility in the

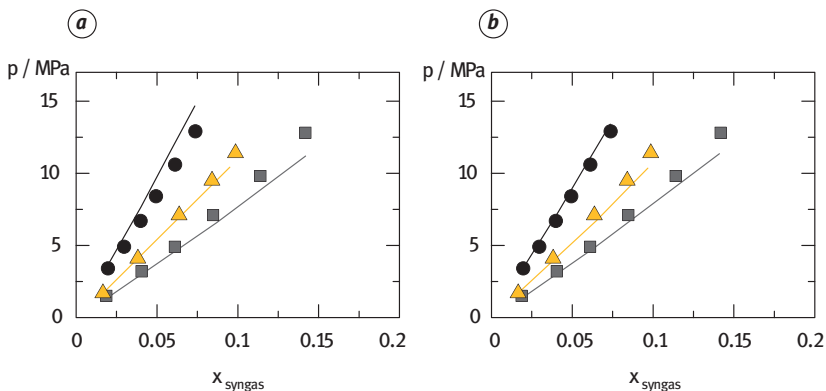


Figure 3.3: Syngas solubility in different n-decane + DMF mixtures. Symbols represent measured syngas solubility data in mixture 1 ($x_{n\text{-decane}}/x_{DMF} = 1/4$) at 93.15 °C (circles), 2 ($x_{n\text{-decane}}/x_{DMF} = 1/1$) at 93.75 °C (triangles) and 3 ($x_{n\text{-decane}}/x_{DMF} = 4/1$) at 93.45 °C (squares). Lines are fully-predicted (all $k_{ij} = 0$) PC-SAFT modeling results (a) and using k_{ij} 's from literature [239] (b). All pure-component parameters used for the calculations can be found in the literature [239].

reactant (olefin) is significantly higher than the one in the product (aldehyde). PC-SAFT can also quantitatively describe the syngas solubility in the hydroformylation multicomponent system, consisting of six components, namely H_2 , CO, 1-dodecene, n-dodecane, n-decane, and DMF [239]. The maximum deviation compared to the measured solubility in mole fraction was only 2.2%. Concluding, PC-SAFT is a valuable modeling tool, which allows predicting gas solubilities in complex multicomponent systems over wide ranges of temperature and pressure, based on few data points only, thus reducing the experimental effort to a minimum.

Liquid–Liquid Equilibria (LLEs)

A strong deviation from ideal phase behavior, e.g., for mixtures of strongly polar and nonpolar solvents, might result in the formation of two liquid phases with different compositions [79]. Such an LLE can be modeled using eq. (2.4). Most often, the miscibility gap decreases with increasing temperature, until the upper critical solution temperature (UCST) is reached, above which the system becomes homogeneous (Section 2.1.2).

Figure 3.4 shows various LLE examples for binary mixtures relevant for the hydroformylation and the reductive amination, particularly the solvent systems DMF + 1-dodecene, DMF + n-decane, and methanol + n-dodecene. All studied systems show a UCST behavior, i.e., miscibility increases with increasing temperature. If not already reported in the literature, LLE data of the binary mixtures were determined experimentally. Using a binary interaction parameter, k_{ij} , which linearly depends on temperature, it was possible to describe the miscibility gaps of the considered binary systems with satisfactory accuracy, over the considered temperature range.

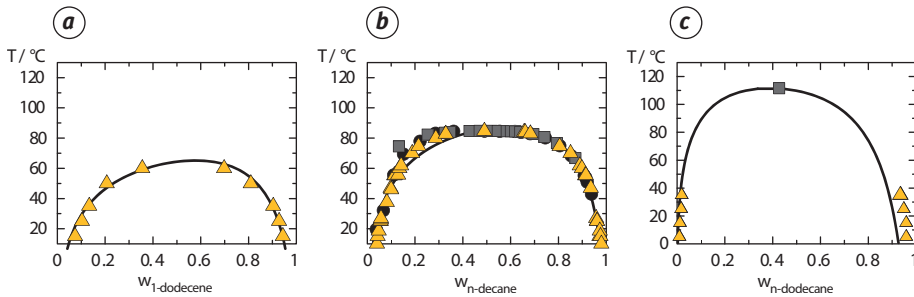


Figure 3.4: LLE of 1-dodecene + DMF (a), n-decane + DMF (b) and n-dodecane + methanol (c). Symbols represent experimental data at 1 bar for 1-dodecene + DMF (triangles) [214], n-decane + DMF (circles) [8], (squares) [112], (triangles) [214], and methanol + n-dodecane (triangles) [34], (square) [35]. Lines are calculations using PC-SAFT. All PC-SAFT pure-component parameters and k_{ij} s used for the calculations can be found in the literature [114, 214].

Furthermore, Figure 3.5 shows the mutual solubilities of some binary mixtures of water + n-alkane. These mixtures show a wide miscibility gap, whereas the mole-fraction solubility of water in the organic phase is several orders of magnitude higher than the one of the n-alkane in the aqueous phase. Moreover, the solubility of water in the organic phase monotonically increases with increasing temperature, T , and is almost independent of the chain length of the n-alkane. In contrast, the solubility of the n-alkanes in the aqueous phase shows a minimum as a function of temperature and decreases with an increasing chain length of the n-alkane. PC-SAFT is capable of representing this behavior in excellent agreement with the experimental data n-alkanes ranging from n-pentane to n-pentadecane [89], which is depicted for a few even-numbered n-alkanes in Figure 3.5.

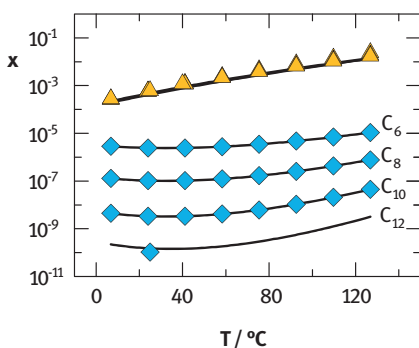


Figure 3.5: Mutual mole-fraction solubilities of binary mixtures water + n-alkane (n-hexane, n-octane, n-decane, and n-dodecane) as a function of temperature, T at atmospheric pressure. The symbols represent experimental data [159, 219, 235], where triangles show the solubility, x , of water in the organic phase, and diamonds represent the solubility, x , of the n-alkane in the aqueous phase. Moreover, the lines show the modeling results obtained with PC-SAFT [89].

As mentioned in Section 3.1.1, the accurate description of the mutual solubilities of the binary mixtures water + n-alkane is a prerequisite for modeling the phase behavior of the binary mixtures water + long-chain compound, when applying the hetero-segmental approach of PC-SAFT. That is, the PC-SAFT binary interaction parameters of the binary mixtures water + n-alkane are applied in the hetero-segmental approach of PC-SAFT for prediction of the mutual solubilities of the binary mixtures water + long-chain compounds [90, 91]. As an example, Figure 3.6a illustrates the hetero-segmental PC-SAFT predictions for the mutual solubility of the binary mixture water + n-hexylamine [91]. Despite the different orders of magnitude of the solubilities in the organic and the aqueous phases, the predictions were found to satisfactorily agree with the experimental data [90, 91].

Next to the representation of the mutual solubilities in water/long-chain compound mixtures, the hetero-segmental approach of PC-SAFT can also successfully be applied to model excess properties of binary mixtures n-alkane + long-chain compound [90–92]. In general, these mixtures show endothermic mixing behavior and, thus, positive molar excess enthalpies h^E . For a given long-chain compound, the molar excess enthalpies of these mixtures increase with an increasing chain length of the n-alkane [90–92]. In contrast, for a given n-alkane, the molar excess enthalpies of the mixtures decrease with an increasing chain length of the long-chain compound. As it becomes obvious from Figure 3.6b for a few binary mixtures n-dodecane + n-amine, the hetero-segmental approach of PC-SAFT fully predicts this behavior in remarkable accordance with the experimental data.

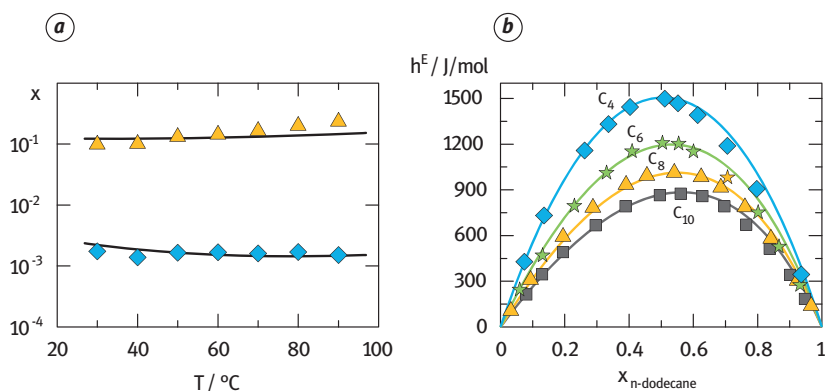


Figure 3.6: Mutual solubility of the binary mixture water + n-hexylamine as a function of temperature (a) and molar excess enthalpies of the binary mixtures n-dodecane + n-amine (n-butylamine, n-hexylamine, n-octylamine, and n-decylamine) as a function of the mole fraction of n-dodecane (b). While symbols represent the experimental data ((a) [232]; (b) [183]), lines show the predictions applying the hetero-segmental approach of PC-SAFT [91].

The developed model can also be applied for the modeling of LLE in ternary mixtures. In the literature, several examples can be found [214]. Figure 3.7 shows the phase behavior for the system DMF + decane + butanal as an example. The binary subsystem DMF + butanal has a large miscibility gap. This miscibility gap of the binary subsystem can be used to estimate the binary interaction parameter between DMF and butanal. The other two subsystems are miscible over the entire concentration range. Therefore, the binary parameters between decane + DMF and between butanal + DMF must be fitted to ternary LLE data. As can be seen from Figure 3.7, modeled and experimentally determined LLE data coincide well. According to Figure 3.7, butanal, which is the product of the hydroformylation, acts as a strong solubilizer for the system DMF/decane. Thus, the miscibility gap between the decane-rich and the DMF-rich phases shrinks for increasing weight fractions of butanal.

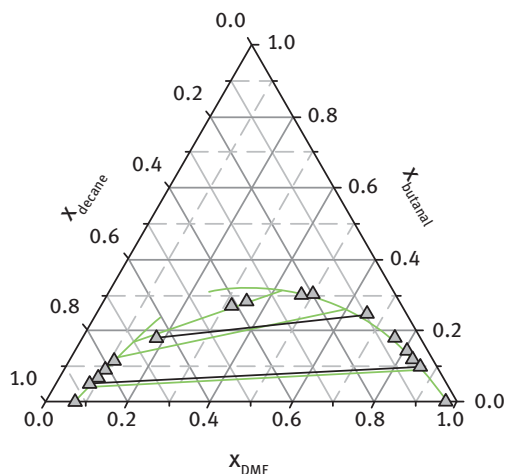


Figure 3.7: LLE of the system DMF/n-decane/n-butanal at 25°C. Black triangles are experimental data, black lines are the experimental tie lines, and the green lines are modeling results [214].

The principle phase behavior of surfactant-containing mixtures was explained in Section 2.2. The calculation of phase diagrams for surfactant-containing mixtures relevant for the MES is not possible by just using a thermodynamic model, such as PC-SAFT or LCT. The reason for this is the occurring nanostructures (aggregation, microemulsions with bicontinuous structures) in these mixtures. Therefore, the phase behavior can only be estimated by experiments. The experimental methods were explained in the literature [220–222]. As an example, the phase behavior of the system water + n-dodecene + dodecyl octaethylene glycol ether ($C_{12}E_8$) and the influence of the product formation, as well as the influence of the catalyst on the phase behavior were discussed [221, 222]. The concentrations in the surfactant-containing solutions can be characterized in the following way:

$$\alpha = \frac{m_{water}^F}{m_{oil}^F + m_{water}^F} \quad \gamma = \frac{m_{surfactant}^F}{\sum_i m_i^F} \quad \beta = \frac{W_{aldehyde}^F}{W_{aldehyde}^F + W_{oil}^F} \quad (3.4)$$

where the superscript, F stands for the feed phase.

At temperatures above the melting point of the surfactant, the binary subsystem n-dodecane + $C_{12}E_8$ is completely miscible [220]. The binary subsystem water + surfactant having a lower critical solution point (LCST) shows demixing at high temperatures (Figure 3.8a). The large scattering of the experimental data is caused by different experimental methods. Fujimatsu et al. [71] and Michell et al. [165] used a measurement technique with constant heating rates (1.3 Kmin^{-1} and 2 Kmin^{-1}). The large heating rates can only be used for roughly detecting LLEs. Unfortunately, Shinoda [225] gave no information about the experimental details. For this reason, the further use of these data is questionable. Good agreement between the data of Schrader et al. [220] and the data of Degiorgio et al. [49] can be found in the diluted and concentrated regions of the LLE. However, near the critical point, these data differ a lot. Schrader et al. [220] used the visual method, and Degiorgio et al. [49] used a light scattering method with a very low heating rate (0.1 Kmin^{-1}). Close to the critical point, critical fluctuations appear, which can lead to critical opalescence having a strong impact on the light scattering intensity and, therefore, lead to a large scattering.

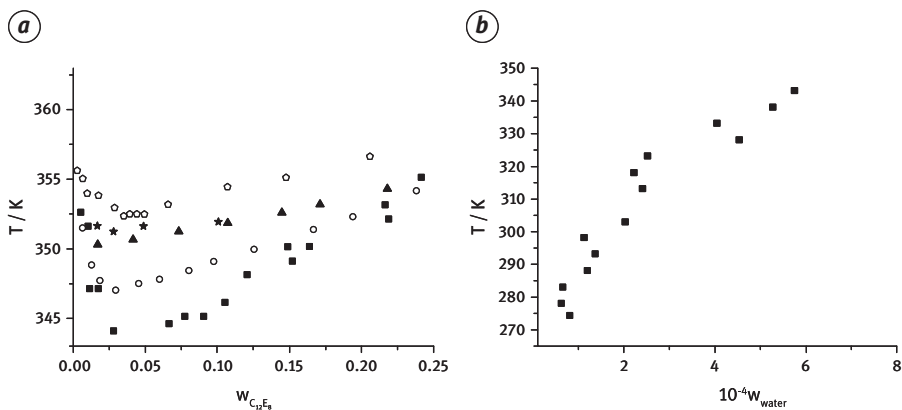


Figure 3.8: (a) LLE of water + $C_{12}E_8$ [open pentagons: [71], stars: [225], triangles: [165], open circles: [49], squares: [220] of water + $C_{12}E_8$. (b) Water solubility of 1-dodecene [220].

The third binary subsystem, namely water + 1-dodecene, shows a broad miscibility gap. The water solubility of 1-dodecene is depicted in Figure 3.8b. The solubility of 1-dodecene at $T = 298.15 \text{ K}$ in water is $w_{1-dodecene} = 1.8 \cdot 10^{-7}$ [220].

Figure 3.9a depicts the Kahlweit's fish (Section 2.2) for the ternary system $C_{12}E_8$ + water + 1-dodecene. At low temperatures, a Winsor I system is existing; the amphiphilic surfactant is mainly dissolved in the water-rich phase. When the mass fraction

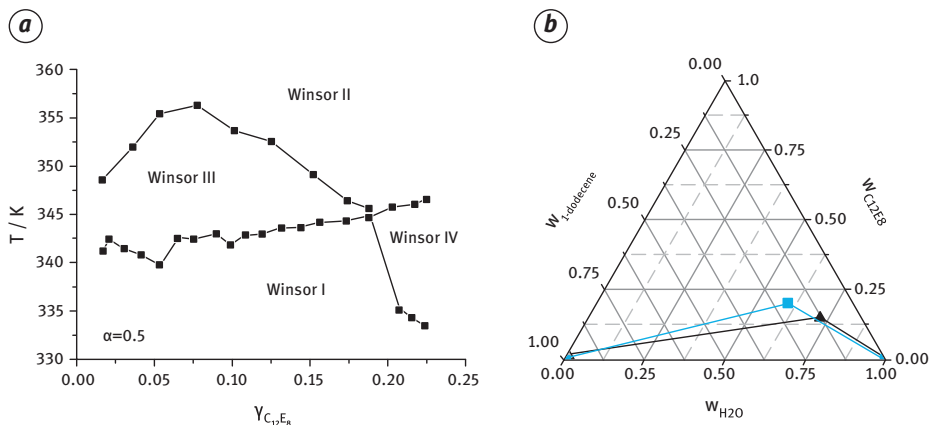


Figure 3.9: (a) Kahlweit's fish for the system 1-dodecene + water + $C_{12}E_8$ at $\alpha = 0.5$. The symbols are experimental data [220], and the lines guide the eyes. (b) Concentrations in the three coexisting phases at two different temperatures ($T = 343.15$ K: black triangles and black lines; $T = 353.15$ K: blue squares and blue lines).

of surfactant ($C_{12}E_8$), γ , is increasing, the phase behavior changes into the one-phase Winsor IV system. If the temperature increases at a certain $C_{12}E_8$ concentration, a three-phase region appears with the microemulsion (Winsor III). Microemulsions are of interest, because unlike oil and water, they solubilize molecules in a single, thermodynamically stable, liquid phase. Microemulsions are macroscopically homogeneous mixtures of water, oil, and surfactant. On a microscopic level, however, the mixtures are structured into water-rich and oil-rich domains separated by an amphiphilic film. At high temperatures, the solubility of the surfactant changes, and there, it is mostly dissolved in the oil-rich phase. The compositions of the three-coexisting phases can be seen in the Gibbs triangle (Figure 3.9b). Raising the temperature to 353 K enhances the surfactant solubility in the oil-rich phase, moving the top of the 3-phase area to the 1-dodecene site of the Gibbs triangle. Increasing the temperature leads to an increase in surfactant concentration and, hence, of the water concentration in the middle-phase. In order to perform the hydroformylation of 1-dodecene, a high amount of the latter as well as a high amount of water containing the polar catalyst is preferable. Using $C_{12}E_8$ as surfactant and 353.15 K as reaction temperature, a 1-dodecene mass fraction of approximately 0.2 and a water mass fraction of approximately 0.6 in the microemulsion can be achieved.

During the hydroformylation of 1-dodecene, tridecanal will be formed. The influence of tridecanal on Kahlweit fish is depicted in Figure 3.10a. With increasing aldehyde concentration, β , the Winsor III system is shifted to lower temperatures. This behavior is in good agreement with the results obtained by Hamerla et al. [99] and Rost et al. [209]. The Winsor III phase temperature decreases to about 40 °C, if β increases up to 0.5. For $\beta = 1$, the three-phase area moves below the surfactant's

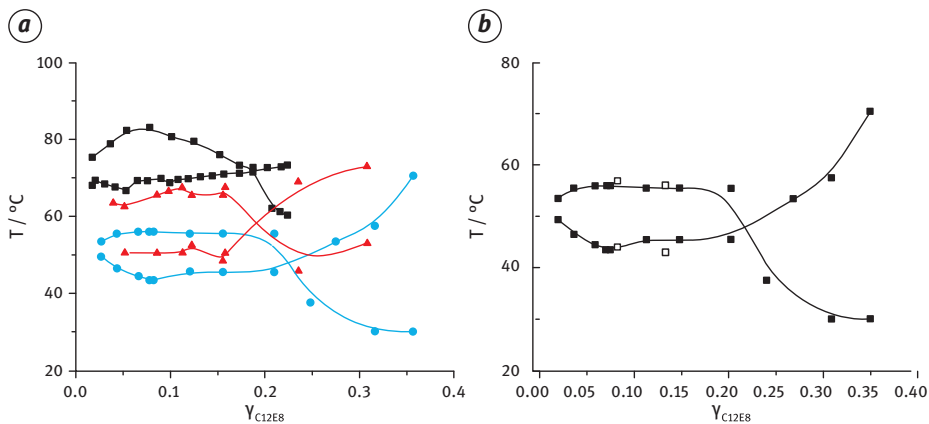


Figure 3.10: (a) Kahlweit's fish for the system 1-dodecene + water + C₁₂E₈ + tridecanal at α = 0.5 and different values of β (β = 0: black symbols and lines; β = 0.25: red symbols and lines; β = 0.5: blue symbols and lines). (b) Kahlweit's fish for the system 1-dodecene + water + C₁₂E₈ + tridecanal + Rh – TTPS catalyst (solid symbols: without catalyst; empty symbols: w_{cat} = 2 · 10⁻⁵). The symbols are experimental data [221], and the lines guide the eyes.

melting point. Additionally, the used catalyst/ligand system Rh-TIPS has a complex amphiphilic structure, which can also influence the LLE. For α = 0.5 and β = 0.5, the influence of the catalyst is negligible (Figure 3.10b).

Most scientific studies were performed using analytical-grade chemicals. However, for technical applications, technical-grade substances are used. Therefore, additional experiments were carried out using technical-grade 1-dodecene, and pure C₁₂E₈ was replaced by technical-grade Genapol X080 [222]. It turned out that the solubility of water in technical 1-dodecene is slightly better than the solubility of water in pure 1-dodecene. Cloud point curves of aqueous technical-surfactant solutions and those of pure surfactants show extreme differences in temperature and also in shape [222] (Figure 3.11a). The cloud point curve is shifted to lower temperatures, if C₁₂E₈ is replaced by technical grade Genapol X080. Consequently, the Kahlweit fish is also shifted to lower temperatures when Genapol X080 is applied (Figure 3.11b). The temperature range, in which the microemulsion is formed, is also shifted to lower temperatures. This is an unwanted effect, as the chemical reaction must be performed at lower temperatures. Usually, at high surfactant concentrations, a homogeneous mixture, the so-called Winsor IV system, is established. However, for the technical-grade mixture, this does not happen. Instead, a four-phase liquid equilibrium was observed [222]. This situation is shown in Figure 3.12, which clearly shows a four-phase equilibrium.

Vapor–Liquid–Liquid Equilibria (VLLEs)

Some n-alkane + DMF systems show a complex phase behavior caused by the overlap of liquid–liquid demixing and VLEs leading to VLLEs [216]. To account for that,

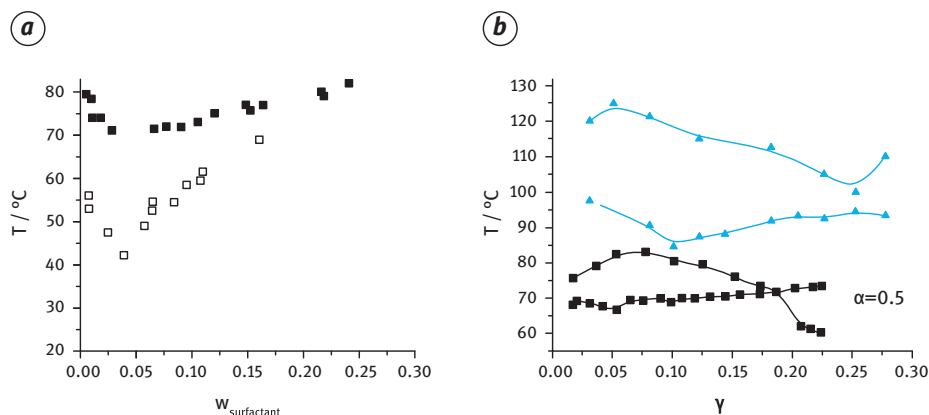


Figure 3.11: (a) Cloud point curve of water + surfactant [solid symbols: pure $C_{12}E_8$, open symbols: technical grade Genapol X080, 222]. (b) Kahlweit's fish for the system 1-dodecene + water + surfactant at $\alpha = 0.5$ (blue symbols and lines: pure $C_{12}E_8$, black symbols, and lines: technical grade Genapol X080). The symbols are experimental data [222], and the lines guide the eyes.

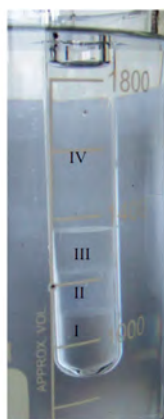


Figure 3.12: Four-phase equilibrium for the mixture water + 1-dodecene + Genapol X080 $T = 363.15 \text{ K}$ [222].

VLEs, as well as LLEs were investigated over wide pressure and temperature ranges for different n-alkanes. Particularly, the azeotropic behavior was considered in more detail.

For n-alkane + DMF mixtures, strong deviations from the ideal phase behavior are expected, since DMF is a polar component, whereas n-alkanes are non-polar molecules. To describe their phase behavior using PC-SAFT, a temperature-dependent binary interaction parameter was used. This parameter was determined via fitting to experimental LLE data of binary systems n-alkane (C_6 - C_{12}) + DMF [215] and then, extrapolating to predict VLE and VLLE data of n-alkane + DMF systems not used for parameter fitting.

PC-SAFT modeling results revealed that n-alkane + DMF systems with n-alkanes longer than n-hexane show a temperature-dependent change from hetero-azeotropic to homo-azeotropic behavior, meaning that the hetero-azeotrope is found at low temperatures and disappears at higher temperatures. This is shown for n-heptane + DMF in Figure 3.13a, where, at 5 °C and 25 °C, the existence of a hetero-azeotrope can be observed, whereas a homo-azeotrope is found at 65 °C (Figure 3.13b). This finding is in perfect agreement with the experimental data [216]. Furthermore, an increasing DMF concentration in the vapor phase was observed for increasing n-alkane chain lengths, which is caused by a change in the vapor–pressure difference of the pure components.

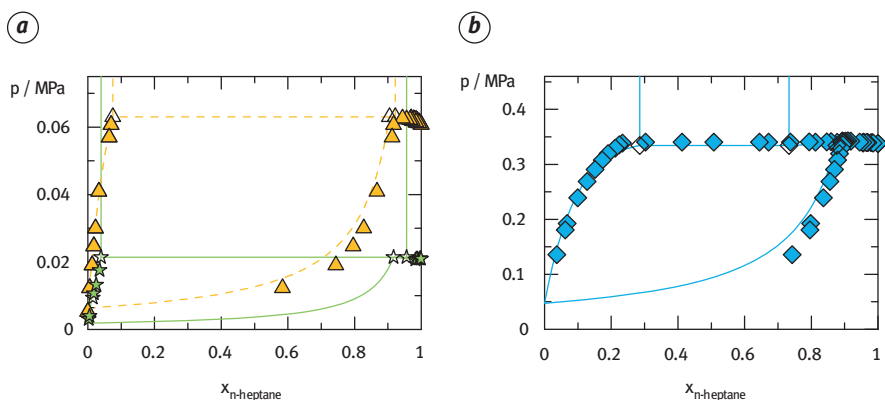


Figure 3.13: VLE of n-heptane + DMF at 5 °C (a), 25 °C (a), and 65 °C (b). Filled Symbols represent experimental data from the literature [197]. Lines and open symbols represent PC-SAFT VLE modeling results at 5 °C (solid lines, open stars), 25 °C (dashed lines, open triangles), and 65 °C (solid lines, open diamonds) [216].

A comparison of experimental VLE data and the modeling results demonstrates that PC-SAFT predicts the VLE and the VLLE behavior almost quantitatively in the considered temperature and pressure range. It should be emphasized that the binary parameter, k_{ij} was only fitted to LLE data of n-alkane + DMF systems, but no VLE data nor VLLE data were included in the parameter fitting. Based on that, VLE and VLLE data of various n-alkane (C5-C10) + DMF systems were satisfactorily predicted, even correctly reporting the presence of either homo-azeotropic or hetero-azeotropic behavior [216].

Solid–Liquid–Liquid Equilibria (SLEs)

Crystallization can be used for purification if a high purity is required. There is a possibility that the necessary SLE could be superposed by an LLE. This unwanted situation leads to oiling-out effects. Assuming that the compressibility has no impact on

LLE and SLE, the LCT based on the Gibbs free energy (eq. (3.2)) can be used for the calculation of these equilibria, if the model parameters are available. However, for branched molecules, the parameter fitting can cause problems, especially if the pure isomers are not available with high purity and, consequently, no high-quality data can be measured. To overcome this limitation, a methodology that enables the prediction of the phase behavior of systems containing branched isomers was developed [80]. An overview of the methodology is shown in Figure 3.14.

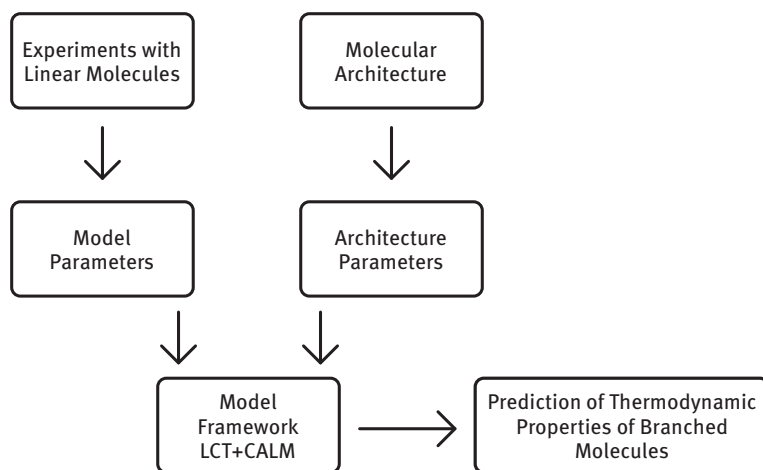


Figure 3.14: Overview of the methodology for the prediction of phase equilibria of branched molecules [80].

The new methodology requires only experiments using linear molecules. The fitted model parameters for the linear molecules are combined with the prior known architecture parameters, which were determined by the molecular architecture, for the prediction of the phase diagram of systems containing the branched isomers. The method will be demonstrated for the ternary system containing an associating solvent, branched alkane, and linear alkane. First of all, the two association parameters of the solvent as well as the interaction energy ε_{ij} between solvent and linear isomers, are simultaneously fitted to LLE data of one binary system with three different chain lengths of the *n*-alkane. The results are depicted in Figure 3.15. It was figured out that the interaction energy, ε_{ij} , depends linearly on the chain length of the *n*-alkane. Next, the prediction of the LLE of the system 2,2,4,4,6,8,8-heptamethylnonane and ethanol will be investigated (Figure 3.16). The chain length of the backbone of 2,2,4,4,6,8,8-heptamethylnonane is 9. Using the linear relationship mentioned above leads to the binary interaction parameter. Having in mind that no experimental data of the branched isomer was used for the parameter fitting procedure, the agreement between the predictions and the experimental data is very satisfying.

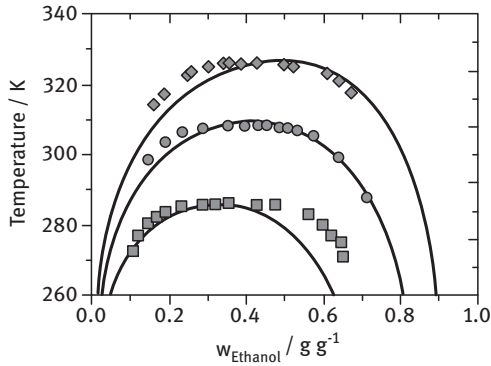


Figure 3.15: LLE of the binary systems n-dodecane (squares), n-tetradecane (circles), and n-hexadecane (diamonds) all with the solvent ethanol. The experimental data were taken from the literature [46]. The solid lines were calculated using the LCT in combination with CALM [80].

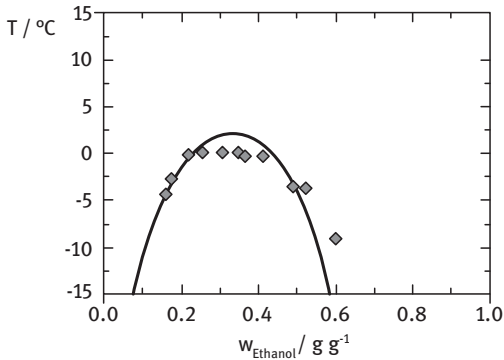


Figure 3.16: Predicted LLE of the binary system 2,2,4,4,6,8,8-heptamethylnonane + ethanol. Experimental data were taken from the literature [46]; solid lines were calculated using the LCT in combination with CALM [80].

After successfully showing the possibility of predicting binary LLE of systems containing a branched molecule, the prediction of ternary phase equilibria of systems containing branched alkanes can be discussed. This implies that no experimental data of the ternary system was used for adjusting model parameters. The ternary system n-hexadecane + 2,2,4,4,6,8,8-heptamethylnonane + ethanol was chosen for the prediction (Figure 3.17). Regarding predicted binodal curve and tie lines, an excellent agreement with the experimental data can be found for the compositions on the ethanol-rich side. Now, it can be checked whether the superposition of ternary LLE and SLE, which is essential for the design of crystallization processes, can be predicted correctly. The already-determined model parameters were used for the prediction of both phase equilibria, and the same melting temperature and enthalpy of fusion of

n-hexadecane were used [82]. It was assumed that the solid phase only contains n-hexadecane.

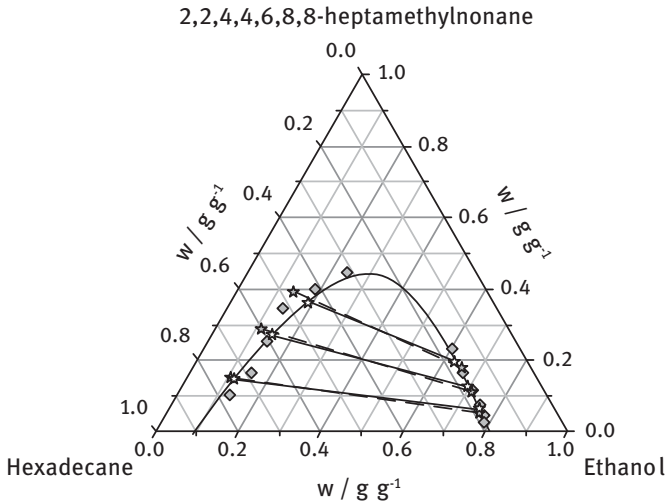


Figure 3.17: LLE of the ternary system n-hexadecane + 2,2,4,4,6,8,8-heptamethylnonane + ethanol at a temperature of 25 °C. Experimental points on the binodal curve are shown as diamonds; experimental tie lines are shown as grey stars connected by dashed lines. The binodal curve, as well as the tie lines (white stars connected by solid lines), was calculated using the LCT in combination with CALM [81].

The results depicted in Figure 3.18 show that the model can be used to predict the SLLE very close to experimental data. Below the SLE curve, the LLE is shown as a dashed line indicating the metastable state. The obtained phase behavior gives valuable information for the design of the crystallization.

3.1.4 Interfacial Properties

Besides the phase equilibrium, information about interfacial properties is essential to design, operate, and optimize unit operations such as separation or reaction processes. The liquid–liquid extraction operation, for instance, is based on mass transfer between two liquid phases in contact. Devising an efficient extraction column requires not only knowledge of the liquid–liquid phase behavior of the components; interfacial tension data are also important to describe the fluid dynamic characteristics of the process, which have a direct influence, e.g., the diameter and height of the column as well as the selection of appropriate contacting devices.

The interfacial properties can be obtained experimentally or by theoretical tools. Regarding modeling of interfacial properties, the Density Gradient Theory (DGT),

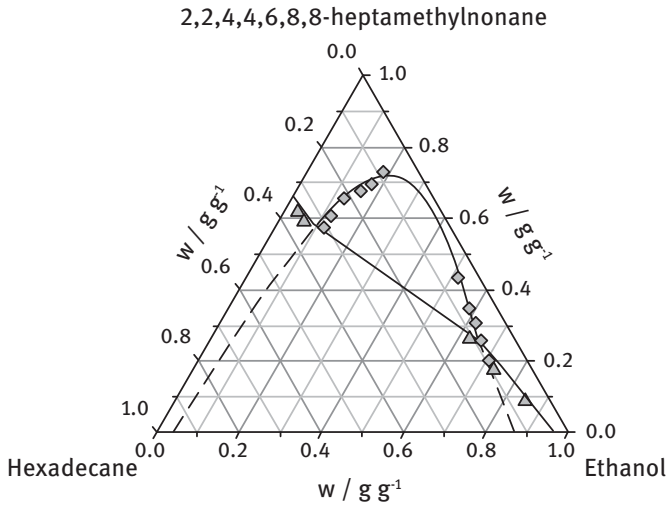


Figure 3.18: Superposition of LLE (diamonds) and SLE (triangles) of the ternary system n-hexadecane + 2,2,4,4,6,8,8-heptamethylnonane + ethanol at a temperature of 5 °C. Lines were calculated using the LCT in combination with CALM. The dashed lines denote the metastable LLE [81].

originally developed by van der Waals and rediscovered by Cahn and Hilliard [32] is a widely used method [61]. The DGT has the advantage that the developed models including the model parameters can directly be used for the calculation of the interfacial properties between fluid phases. The characteristic feature of a phase in terms of physical science is that the values of the properties of a phase are uniform within that phase. The DGT is based on the idea that concentrations and, accordingly, densities change gradually across an interface between two phases. That is, density gradients occur in the interface that has to be accounted for in the calculation of interfacial properties. Composition and density changes across the interface are assumed to be one-dimensional in the direction of z , perpendicular to the interface. The Helmholtz free energy, A , of a system exhibiting an interface is then expressed in terms of a Taylor series expansion. The expansion is around the local Helmholtz free energy density, $a_0(z)$, in the interface of thickness, L , which belongs to a hypothetical system of the same density and composition, but without an interface. The expression for A is given as:

$$A = S_0 \int a_0(z) + \frac{1}{2} \sum_i \sum_j \kappa_{ij} \left(\frac{d\rho_i}{dz} \right) \left(\frac{d\rho_j}{dz} \right) dz \quad (3.5)$$

where S_0 is the interfacial area and κ_{ij} are the so-called influence parameters of the pure components, (κ_{ii}), and corresponding cross terms for mixtures (κ_{ij}), respectively.

The cross term is commonly determined using the geometric mean of κ_{ii} and κ_{jj} modified by a binary parameter β_{ij} [193]:

$$\kappa_{ij} = \beta_{ij} \sqrt{\kappa_{ii} \kappa_{jj}} \quad (3.6)$$

The pure-component value for the influence parameter, κ_{ii} , can be fitted to the surface tension of the pure component at one temperature. Within a homologous series, a correlation between κ_{ii} and the carbon number can be found [93, 178]. Figure 3.19 demonstrates the dependence of κ_{ii} on the carbon number for four different homologous series. This situation allows the calculation of the surface tension for all members of the homologous series.

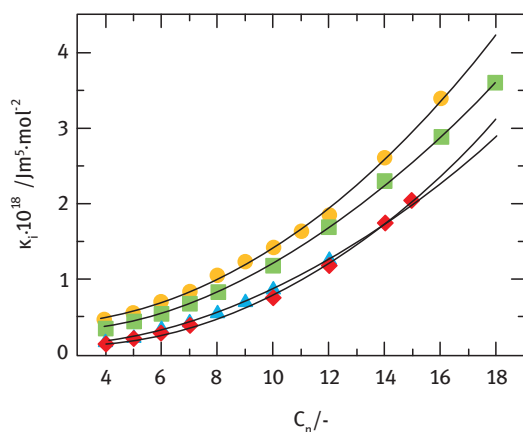


Figure 3.19: Dependence of the DGT pure-component influence parameters, κ_i , on the carbon number, C_n , within a homologous series. The symbols show the actual values for methyl alkanooates (squares), ethyl alkanooates (circles), n-alcohols (triangles), and n-alkyl carboxylic acids (diamonds), whereas solid lines represent their respective second-order polynomial correlations [93].

For mixtures containing only nonpolar components, it could often be shown that the prediction of surface tensions of mixtures using the geometrical mixing rule (eq. (3.6)), applying $\beta_{ij} = 1$ is possible [29, 178, 231]. If the parameter β_{ij} in eq. (3.6) is needed, binary surface or interfacial data must also be included in the parameter-fitting procedure. The Helmholtz free energy and the densities can be calculated using the equations of state and the involved parameters introduced in Sections 3.1.1. We would like to discuss three examples, namely, the binary mixture n-heptane + DMF [217], where the phase equilibria are depicted in Figure 3.13, the mixtures composed of water + n-alkane [201], where the LLE is shown in Figure 3.5, and the interfacial properties of ternary mixtures. Other examples can be found in the literature [17, 37, 47, 48, 70, 82, 93, 158, 179, 180, 210, 218, 231].

The mixture, n-heptane + DMF, shows a complex phase behavior including an azeotropic point and a superposition of a VLE and LLE, depending on system temperature and pressure (Figure 3.13). Due to the presence of the LLE, the interfacial tension, σ^{VLE} , cannot be estimated over the whole concentration range, but only at very low and at very high n-alkane concentrations. This situation leads to two different interfacial tensions, namely, the interfacial tension between the two coexisting liquid phases, σ^{LLE} , and the surface tension related to the VLE, σ^{VLE} . DMF carries a dipole momentum, and therefore, the parameter β_{ij} in eq. (3.6) is required. The adjustment of this value can be done using a value of σ^{LLE} or σ^{VLE} . Having in mind that the modeling of σ^{LLE} is more challenging than the modeling of σ^{VLE} , a value of σ^{LLE} at one temperature for the system n-heptane + DMF was selected for this purpose, resulting in $\beta_{ij} = 0.675$.

Figure 3.20A demonstrates the comparison between experimental data and modeling results using $\beta_{ij} = 0.675$ for all mixtures considered. First, it can be concluded that the theory allows the description of the experimental data with high accuracy. Second, the fitted β_{ij} value can be transferred to other n-alkane + DMF mixtures. For the experiments, the spinning drop method [217] or the pendant drop method [128] was used. Both methods required the measurement of the density difference of both coexisting phases. On the other side, this density difference can also be calculated using PC-SAFT [217]. A detailed discussion about this issue can be found in the literature [47, 217, 218]. Figure 3.20B shows that the estimated β_{ij} value can also be transferred from LLE to VLE. A similar behavior could be found for mixtures of n-alkane and other components carrying a dipole momentum [217].

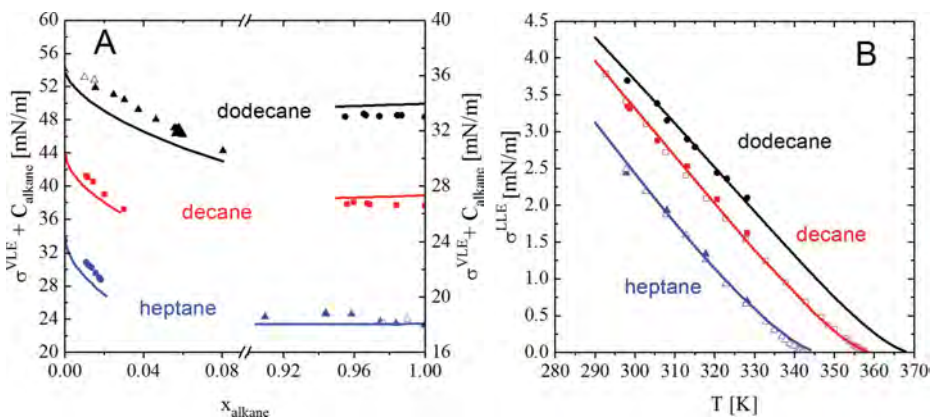


Figure 3.20: Comparison between experimental [solid symbols: 217, open stars, circles, and squares: 128, open triangles: 241] and calculated interfacial tension [lines with $\beta_{ij} = 0.675$, 217] for DMF + n-alkane mixtures. C_{alkane} is an alkane-specific, fictitious constant added to experimental and modeled surface tensions for a clear representation of the data.

The DGT also permits the calculation of the partial density profiles across the interface. The density profiles at 298.15 K in Figure 3.21 for the mixture n-heptane + DMF reveal that heptane accumulates in the DMF-rich region and that DMF accumulates in the alkane-rich region at the interface. Usually, the component having a higher vapor pressure enriches at the interface [17, 61, 178–180, 193]. Thereby, the accumulation of the n-alkanes is, in general, larger than that of DMF. Furthermore, accumulation of DMF in the dodecane-rich region is larger than in the heptane-rich region [217]. The reason for this observation is the difference in the vapor pressures. In the case of the DMF/n-heptane system, n-heptane is the more volatile component regarding pure-component vapor pressures. For the DMF/n-dodecane system, it is the other way round. The vapor pressure of DMF is higher than that of n-dodecane. This explains why the accumulation of DMF in the DMF/n-dodecane system is larger. Still, both systems behave the same in the general trend that the n-alkane accumulates in the DMF-rich region, whereas DMF accumulates in the alkane-rich region. These characteristic phenomena can be explained if the VLE behavior of the DMF/n-alkane systems is taken into account (Figure 3.13). Due to limited miscibility of the DMF/n-alkane mixtures, heteroazeotropes occur at 298.15 K. In Figure 3.22, a schematic p, x_i -diagram is presented, which illustrates the VLE behavior including a heteroazeotrope of a fictitious binary system, A/B, where A represents the n-alkane and B the polar solvent, for instance, DMF. x_i is the mole fraction of component, i in the liquid phase and y_i is the mole fraction of the same component in the coexisting vapor phase. Due to the heteroazeotrope, the relation x_i/y_i changes in a certain way, with the overall concentration of the component, i . While x_i/y_i is smaller than one before the azeotrope for one component, it is larger than one beyond the azeotrope. The relation x_i/y_i of the second component of a binary system changes thereby, contrariwise. The DMF-rich region of the DMF/n-alkane systems is located on the side of the heteroazeotrope, where $x_A/y_A < 1$. The alkane-rich region is located on the other side, where $x_B/y_B < 1$. That is, the alkane accumulates in the DMF-rich region with $x_A/y_A < 1$ and DMF accumulates in the n-alkane-rich region, where $x_B/y_B < 1$ occurs. Based on these findings, the following conclusion can be drawn for the DMF/n-alkane systems exhibiting heteroazeotropes: the accumulation occurs for the component i , if $x_i/y_i < 1$ is valid (Figure 3.22).

For the development of suitable TMS, the interfacial properties of ternary mixtures are important. The theoretical details, as well as the description of the numerical procedure, can be found in the literature [218]. As an example, the mixture composed of DMF + n-decane + butanal will be investigated [215], where the phase behavior is depicted in Figure 3.7. Within the DGT framework, the parameter, β_{ij} is required for all binary subsystems. Figure 3.7 shows that only the binary subsystem n-decane + DMF possess a miscibility gap. In this case, the corresponding β_{ij} can be fitted to the interfacial tension of the binary subsystem. The other two values must be fitted to the ternary mixture. Following the concept of homologous series, the β_{ij} values were estimated for DMF-aldehyde mixtures and n-decane + aldehyde

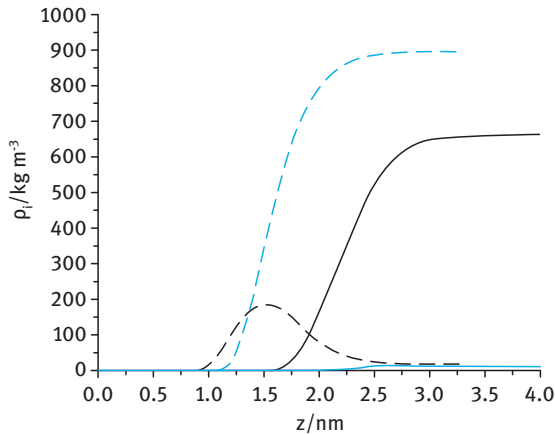


Figure 3.21: Modeled density profiles across the interface phases for n-heptane + DMF in the DMF-rich region $x_{n\text{-heptane}}^F = 0.015$ (solid lines) and in the n-heptane-rich region $>x_{n\text{-heptane}}^F = 0.978$ (broken line) at 298.15 K, where the blue lines represent DMF and the black line represents n-heptane [217].

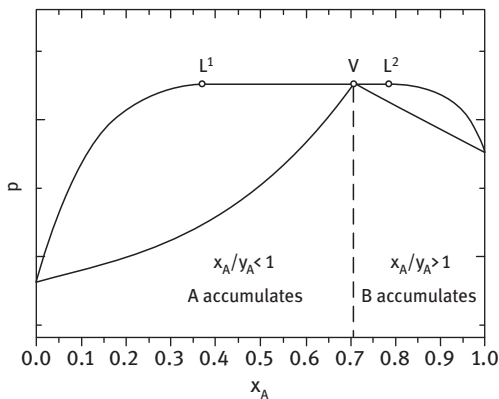


Figure 3.22: Schematic VLE p , x -diagram for constant, T of a fictitious binary system, A/B exhibiting a VLE, where x_A is the composition of the liquid phase and y_A is the composition in the vapor phase. The solid lines are the equilibrium concentrations of coexisting vapor and liquid phases. The dashed line marks the boundary between the areas left and right from the heteroazeotrope, and the open circles represent the equilibrium concentrations at the VLE.

mixtures [218]. Figure 3.23 demonstrates the comparison of the experimental and modeled interfacial tensions for mixtures composed of the polar solvent DMF, n-decane, and the reaction product of the hydroformylation, an aldehyde, where the experimental data are obtained using the spinning drop method. From the data in Figure 3.23, it can be concluded that the used approach works and allows the calculation of the interfacial tension very close to the experimental values. The calculated concentration

profiles across the interface are also depicted in Figure 3.23. The concentration profiles show clearly, that the aldehyde acting as solubilizer accumulates at the interface. This effect increases with an increasing chain length of the aldehyde.

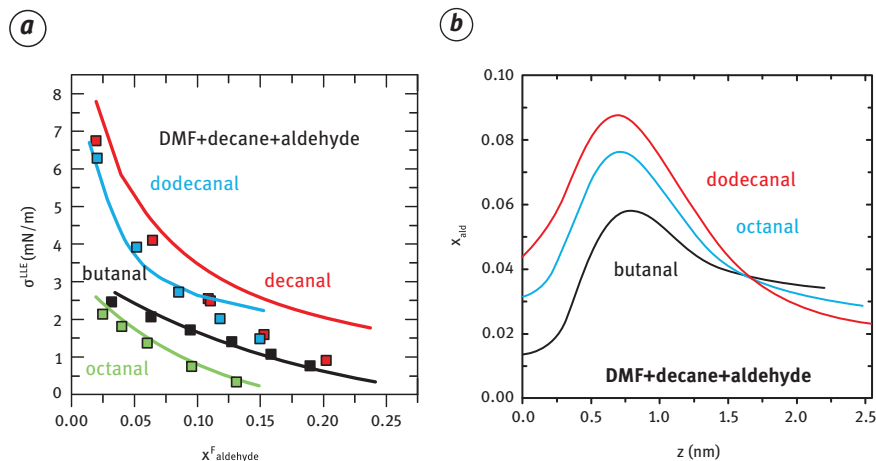


Figure 3.23: Interfacial properties (a) interfacial tension; b) interfacial concentration profiles) for ternary mixtures of DMF + n-decane + different aldehydes at $T = 298.15$ K. The symbols represent experimental data, and the lines, calculations, using $\beta_{12} = 0.913$, $\beta_{23} = 0.95$, and $\beta_{13} = 0.75$ [218].

The calculation of interfacial properties of the water-containing mixture is an outstanding challenge caused by the complex association effects of water. The demixing behavior of water + n-alkane mixtures is shown in Figure 3.5. The accurate description of the composition of the coexisting phases as a function of temperature is a necessary condition for the calculation of the interfacial tension using DGT. If water is involved in the mixture, it is not possible to transfer the κ_w -adjusted utilizing surface tensions of pure water to mixtures [47, 93]. This problem can be solved by the introduction of a β_{ij} value, according to eq. (3.6). However, this approach leads to a high numerical effort. Another possibility, suggested by Danzer and Enders [47], is the refitting of the κ_w -value, using binary data. For the mixtures of water + n-alkane, we assume the following temperature dependency of κ_w [201].

$$\kappa_w = a_n + b_n(T/K) \quad (3.7)$$

where n represents the carbon number of the n-alkane. Both parameters depend on the carbon number of the considered n-alkane in a quadratic way. This approach has the advantage that all β_{ij} values can be set to unity. Additionally, the interfacial tension of water + n-alkane can be calculated, using one set of model parameters. The influence parameters of the pure n-alkane were taken from the literature [178]. Figure 3.24 depicts a comparison between experimental data taken from the literature and the

modeled interfacial tensions for selected n-alkane + water mixtures. It can be recognized that the mentioned approach can be applied for modeling very close to the experimental data over the entire temperature range. The trend of increasing interfacial tension with an increasing carbon number of the n-alkane was calculated correctly. It should be mentioned that the suggested strategy allows calculation of the interfacial tension of these mixtures correctly, for the first time.

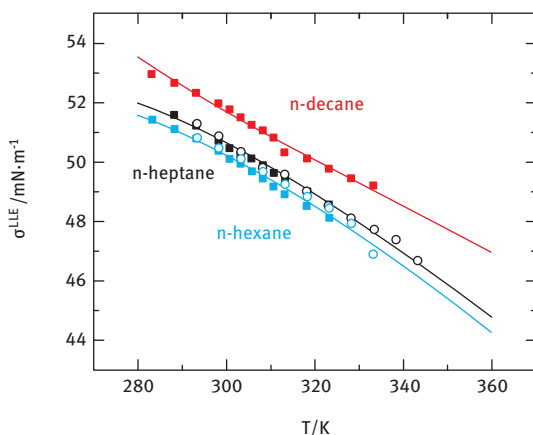


Figure 3.24: Comparison of the experimental interfacial tensions [solid squares: 251, open circles: 234] and calculated interfacial tension, using PC-SAFT and DGT [202] for n-alkane + water mixtures.

One of the major separation problems is the separation of isomers. For this purpose, the adsorption in porous solid can be applied. This situation requires knowledge of adsorption isotherms. The state of the art of experimental as well as theoretical work for adsorption isotherms related to the separation of isomers is reviewed by Zimmermann et al. [255]. It turns out that the calculation of the adsorption isotherms for isomer mixtures is a very challenging task, because there are two major problems: a) the correct thermodynamic description of the isomers and their mixtures and b) the correct description of the solids, including the pore network. We focus our attention on the correct thermodynamic modeling of the isomers, having in mind the problems related to the availability of reliable pure-component data. For the modeling of adsorption isotherms of linear aldehydes, it was figured out that the used thermodynamic model has an important impact [31, 253]. Therefore, we would like to combine the density function theory (DFT) [57, 96] approach with the LCT-EOS [55, 64, 141, 249], which permits to distinguish between different isomers, using the architecture parameters. Within the LCT framework, the molecules have to be divided into segments of equal size, and hence, all thermodynamic quantities are segment-molar quantities. The size of the lattice sites is quantified by

the side length, σ . The compressibility is introduced by empty lattice sites and, consequently, the grand potential functional must be rewritten in the following way:

$$\begin{aligned} \Omega(T; \phi_i(z_L)) = & A(T; \phi_i(z_L)) - \int_{H/\sigma} \sum_i \phi_i(z_L) (\mu_i - V_i^{ext}(z_L)) dz_L \\ & - \int_{H/\sigma} \left(1 - \sum_i \phi_i(z_L)\right) \mu_v dz_L \end{aligned} \quad (3.8)$$

In eq. (3.8), $A(T; \phi_i(z_L))$ represents the functional of the segment molar Helmholtz energy, and ϕ_i is the volume fraction of component, i , characterized by μ_i , its segment molar chemical potential $\mu_i = (\partial A / \partial (n_i M_i))_{T, V, i \neq j}$, where T is the temperature, V is the volume, M_i is the segment number, and n_i is the amount of mole. $V_i^{ext}(z_L)$ is the segment molar external potential, and the quantity $\mu_v = (\partial A / \partial n_v)_{T, n_i}$ describes the chemical potential of the empty lattice sites (voids). The variable, $z_L = x/\sigma$ indicates that the integration runs over a certain number of lattice sites, H/σ , perpendicular to the wall, where H is the pore width. Minimization of eq. (3.8) leads to $\phi_i(z_L)$. The original LCT was developed to model polymer-containing mixtures [55] and, consequently, the compressibility is quite low and the dispersion interaction is much smaller than for low molecular compounds. Therefore, the LCT was developed further, by extending the series development by one additional order [256]. These extensions lead to a better description of the thermodynamic properties of low-molecular-weight components, for instance, the vapor pressure and the saturated liquid density [256]. As external potentials characterizing the solid-fluid interactions, Steele 10-4-3 potential [230] or the classical Lenard-Jones potential was selected in eq. (3.8).

First, the new theoretical framework (eq. (3.8)) in combination with the extended LCT should be verified. For this purpose, the calculation results were compared with experimental data taken from the literature [15]. Figure 3.25 shows an example; however, more examples can be found elsewhere [254]. The calculations require the parameters of the solid-fluid interaction potential. These values were fitted to the experimental data at $T = 423$ K. The calculated adsorption isotherms at the other temperatures are predictions. It can be concluded that the new theoretical framework can be used to model pure-component adsorption isotherms at different temperatures that are very close to the experimental data.

Model calculations of the adsorption isotherms of pure isomers (for example n-hexane, 3-methyl pentane, and 2,3-dimethyl butane) from the gas phase were performed [255]. It turned out that the calculated density profiles were practically the same. Therefore, no separation effect could be found. In contrast, the calculated pure-component adsorption isotherm from the liquid phase shows a small separation effect (Figure 3.26).

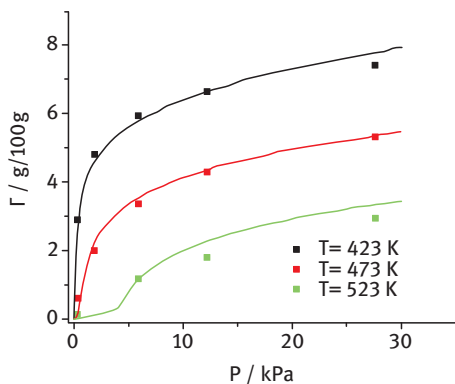


Figure 3.25: Comparison of experimental [symbols: 15] and calculated adsorption isotherms [lines, 254] for the adsorption of n-hexane at β -zeolites at different temperatures, where the Lenard-Jones potential was applied.

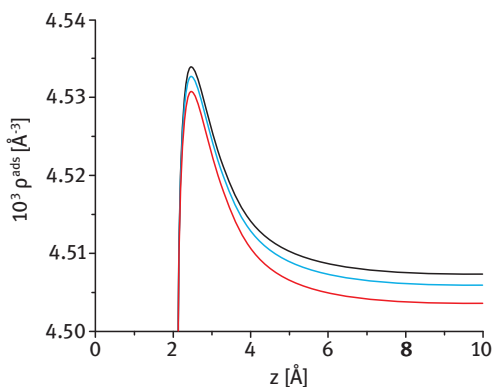


Figure 3.26: Predicted density profiles of the three liquid hexane isomers, n-hexane (black line), 3-methyl pentane (blue line), and 2,3-dimethyl butane (red line) at $T = 273 \text{ K}$ and $p = 0.1 \text{ MPa}$ [255].

Figure 3.27 shows the predicted adsorption isotherms of the binary mixtures n-hexane + 3-methyl pentane and n-hexane + 2,3-dimethyl butane at two different temperatures and a pore width of 200 nm. For both mixtures, n-hexane will be preferentially adsorbed in the narrow pore, independently of temperature. Due to the capillary condensation occurring at lower pressure for lower temperatures, more material can be adsorbed at lower temperatures. The composition of the adsorbed mixture differs from the bulk composition. The adsorbed partial density of hexane does not depend on the nature of branched molecules present in the mixture. Since n-hexane and 3-methyl pentane do not differ in shape as much as n-hexane and 2,3-dimethyl butane, with the latter having a more sphere-like shape, the packing in the first mixture without steric hindrances can be higher than the second mixture (Figure 3.27). This difference increases with increasing temperature. Therefore, the separation effect should also increase with increasing temperature. One possible explanation can be the different heat of adsorption. The differences between adsorbent and bulk compositions shown in Figure 3.27 are too small to be promising

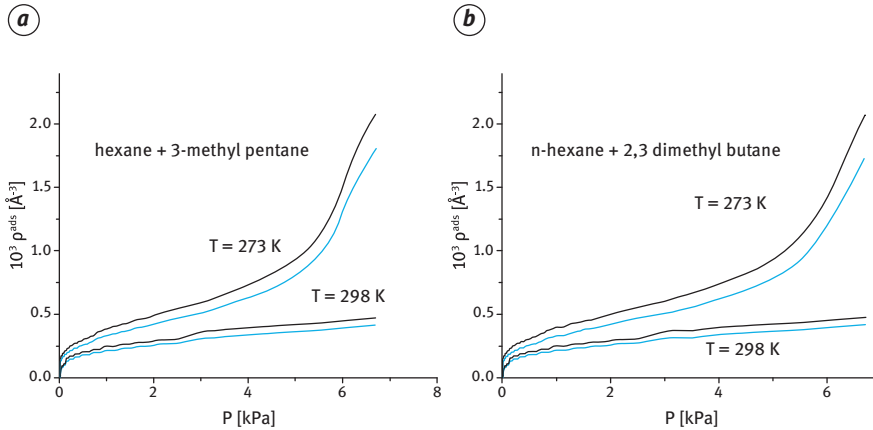


Figure 3.27: Predicted adsorption isotherms of equimolar binary mixtures: (a) n-hexane (black line) + 3-methyl pentane (blue line) and (b) n-hexane (black line) + 2,3-dimethyl butane (blue line) at different temperatures and a pore width of 200 nm [254].

for a technical adsorption process. To evaluate the possibilities to increase the separation, the influence of pore diameters and the solid–fluid interaction were studied [255]. The differences between adsorbed and bulk compositions increase with decreasing pore diameter, which is an indicator of the importance of pore size distributions, when separating isomers. Here again, for each pore diameter, higher temperature leads to better results. Another possible influence on the adsorption process is the choice of the adsorbent itself. The solid–fluid interaction characterized by the Steele potential has the best effects on adsorption. The increase of interaction strength has a large effect on separation.

The numerical results obtained with the DFT reveal that the separation of isomers should be performed in the liquid phase. However, the DFT calculations imply high numerical effort. For the process design, a much simpler model is desirable. Therefore, a new approach based on the real adsorbed solution theory (RAST) [198] introduces an activity coefficient for the adsorbed phase. However, the new approach also introduces activity coefficients for the corresponding bulk phase, where the activity coefficients are calculated using LCT in its incompressible version [83]. Additionally, the new model takes the swelling of the adsorbent into account, because expansion and contraction of porous solids caused by solid–fluid intermolecular forces during fluid adsorption were observed [84]. The adsorbents investigated are supposed to not swell that much; therefore, the affine network theory introduced by Flory [68] was used. The porous adsorbent is assumed to be present only in the adsorbed phase. Besides the adsorbent, all molecules adsorbed within the pores and on the surface of the adsorbent are related to the adsorbed phase (phase I). All remaining molecules, which are not adsorbed, are assumed to build the bulk phase (phase II). The linear

molecules can more easily enter the pores than their branched isomers because of the smaller kinetic diameter.

From the thermodynamic point of view, a ternary system containing linear alkane (A), adsorbent (B), and branched alkane (C) must be considered; hereby, the adsorbent (B) is immobilized as solid and regarded as a network of linear carbon chains. Regarding the calculation of the binary adsorption isotherms, it was assumed that bulk phase and adsorbed phase are in equilibrium [83]:

$$\mu_i^I + \Delta\mu_{network} = \mu_i^{II} \quad i = A, C \quad (3.9)$$

where $\Delta\mu_{network}$ takes the swelling of the adsorbent into account, and according to the affine network theory [68] it is given by:

$$\Delta\mu_{network} = RTc_{network} \left(\phi_B^{1/3} - \frac{\phi_B}{2} \right) \quad (3.10)$$

where ϕ_B is the segment fraction of the adsorbent and equals the mass fraction of the adsorbent in phase I, and hence this quantity corresponds to the degree of swelling. The quantity, $c_{network}$ is an adjustable parameter. The solution of eq. (3.9) in combination with eq. (3.10) and the material balance results in the adsorption isotherm.

In Figure 3.28a, the calculated adsorption isotherms of a binary mixture composed of n-octane and 2,2,4-trimethyl pentane as well as the calculated swelling degree of activated carbon are compared with experimental data. Regarding the experimental data, it is obvious that the temperature affects the separation efficiency. The higher the temperature, the better is the separation efficiency indicated by a larger concentration difference of the coexisting phases (Figure 3.28a). The fact that the separation efficiency increases with increasing temperature was also predicted by the DFT in combination with the LCT-EOS [254]. The comparison of the experimental adsorption isotherms and the calculated isotherms shows that the model can describe the different adsorption efficiencies in good agreement with experimental data (Figure 3.28a). The degree of swelling of activated carbon is also dependent on temperature (Figure 3.28b). This means that, in total, fewer molecules are adsorbed at higher temperatures. In contrast to the adsorption on activated carbon, the adsorption, as well as the swelling of zeolites or silica gel does not depend on temperature [83].

All three adsorbents possessed a different pore size distribution, leading to different adsorption efficiencies (Figure 3.29). Zeolite showed an almost perfect separation of linear and branched alkane, whereas silica gel achieved no separation. Activated carbon showed a separation efficiency that is between those two values, and the adsorption depends on temperature. Within the model, the adsorption efficiency can be described by interaction energies between the adsorbent and the individual alkane isomers. A good agreement between experimental adsorption isotherms and calculated

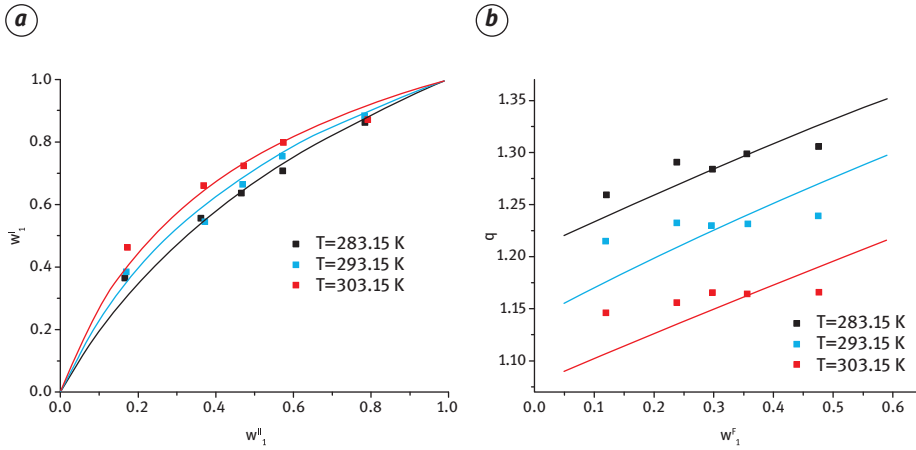


Figure 3.28: (a) Adsorption isotherms of the binary system n-octane – 2,2,4-trimethylpentane on activated carbon and (b) degree of swelling at different temperatures, where the experiments are represented by symbols and the calculation results by lines. The lines were calculated by the adsorption model. The mass fraction of activated carbon was always 0.4 [83].

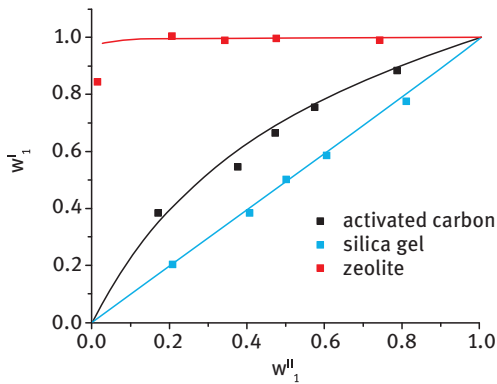


Figure 3.29: Adsorption isotherms of the binary system n-octane – 2,2,4-trimethylpentane on different adsorbents at $T = 293.15 \text{ K}$ [83].

ones could be observed for all systems (Figure 3.29). Thus, the model can describe all kinds of separation efficiencies between no separation and nearly ideal separation. Besides the binary system n-octane – 2,2,4-trimethylpentane, the binary system n-hexane – 2,3-dimethylbutane was also investigated [83], and it was figured out that both mixtures behave very similarly.

3.1.5 Reaction Equilibria

The thermodynamic equilibrium of a chemical reaction is characterized by

$$\Delta^R G^{0,id}(T, p^0) = \sum_i \nu_i \cdot \Delta^F G_i^{0,id}(T, p^0) = -RT \cdot \ln K_f \quad (3.11)$$

Here, $\Delta^R G^{0,id}$ is the standard Gibbs energy of reaction referring to the ideal-gas standard state (0,id) at the reference pressure $p^0 = 1.013$ bar. It can be obtained from the stoichiometric coefficients of the reactants/products, ν_i and their Gibbs energies of formation, $\Delta^F G_i^{0,id}$. The thermodynamic equilibrium constant, K_f is obtained from the mole-fraction-based apparent equilibrium constant, K_x and the fugacity-coefficient-based K_φ (eq. (3.12)) [79, 145].

$$K_f = K_x \cdot K_\varphi \cdot \left(\frac{p}{p^0}\right)^{\sum_i \nu_i} = \prod_i (x_i)^{\nu_i} \cdot \prod_i (\varphi_i)^{\nu_i} \cdot \left(\frac{p}{p^0}\right)^{\sum_i \nu_i} \quad (3.12)$$

K_f depends only on temperature and does not depend on pressure or on the concentrations of the reactants/products nor on the solvents. At constant temperature, K_f is constant. In contrast, K_φ depends on all components present in the reaction medium (including the solvents) and on their concentrations. K_φ is calculated from the fugacity coefficients of the reactants/products that can be obtained using PC-SAFT. According to eq. (3.12), at constant temperature, T and pressure, p , K_x needs to change as soon as K_φ changes, to assure that K_f remains constant. Thus, the fugacity-based approach can predict solvent-induced changes of K_φ and, therewith, also allows predicting changes of K_x as a function of solvents. It is worth mentioning that assuming the reactants and products are ideal gases and neglecting any interactions of these components with the solvents, K_f would be equal to the apparent equilibrium constant, K_x , if $\sum_i \nu_i = 0$ is also valid. However, this would mean neglecting the entire solvent effect on the reaction equilibrium, which is obviously wrong for most reactions and solvents.

Another standard state often used for liquid reactions is the standard state of the liquid pure component (0,oi). Then, eq. (3.11) can be rewritten as:

$$\Delta^R G^{0,oi}(T, p) = \sum_i \nu_i \cdot \Delta^F G_i^{0,oi}(T, p) = -RT \cdot \ln K_a \quad (3.13)$$

The thermodynamic equilibrium constant, K_a does not depend on temperature, or on the concentrations of the reactants/products, or on the solvents. In contrast to K_f , K_a depends on pressure, which, however, can be neglected in most cases, as K_a is only used for liquid-phase reactions. K_a is based on the thermodynamic activities, a_i of the reactants/products and is calculated according to eq. (3.14) instead of eq. (3.12).

$$K_a = \prod_i a_i^{v_i} = K_x \cdot K_y = \prod_i x_i^{v_i} \cdot \prod_i \gamma_i^{v_i} \quad (3.14)$$

In the following, the thermodynamic influence of the solvents on the reaction equilibrium, i.e., on K_x , is discussed for the example reactions of esterification, hydroformylation, and reductive amination. Fugacity coefficients and activity coefficients for predicting K_ϕ and K_y respectively, were obtained from PC-SAFT.

Solvent Effects on the Esterification Reaction Equilibrium

The esterification of acetic acid and ethanol was experimentally investigated at 40 °C and ambient pressure [205]. To determine the thermodynamic equilibrium constant, K_a , experiments with varying initial reactant concentrations were performed. Thereby, equilibrium concentrations (mole fractions) were obtained and further used to calculate the corresponding activity coefficients of the reactant and the products, using PC-SAFT (Table 3.1).

Table 3.1: Measured equilibrium concentrations (mole fractions), x , for the esterification of acetic acid and ethanol at 40 °C and at ambient pressure for varying mole ratios of ethanol/acetic acid in the initial reaction mixture. Corresponding activity coefficients, γ , of the reactants/products were obtained from PC-SAFT [205].

Initial mole-fraction ratio ethanol/acetic acid	1/3		1/1		3/1	
	x	$\gamma_{PC-SAFT}$	x	$\gamma_{PC-SAFT}$	x	$\gamma_{PC-SAFT}$
Ethanol	0.014	1.255	0.146	1.256	0.542	1.054
Acetic acid	0.512	0.766	0.190	0.533	0.035	0.517
Water	0.241	1.767	0.382	1.842	0.228	2.147
Ethyl acetate	0.234	1.268	0.283	1.960	0.196	2.089

Using the equilibrium mole fractions and the corresponding activity coefficients of reactant and products (Table 3.1), K_x and K_y were calculated according to eq. (3.14). They can be found in Table 3.2. As can be seen, high product concentrations (mole fractions) were achieved for an initial excess of acetic acid compared to ethanol, which is consistent with the experimental findings for the esterification of acetic acid with 1-butanol [88]. In contrast, a high initial excess of ethanol leads to low product concentrations. The thermodynamic equilibrium constant, K_a , which is expected to be the same in all cases, was obtained according to eq. (3.14), with the average value being 19.4 ± 1.3 . The standard Gibbs energy of reaction was then calculated according to eq. (3.11) ($\Delta^R G^{0,0i} = -7.7 \pm 0.2 \text{ kJ mol}^{-1}$) and found in good agreement with available literature data ($\Delta^R G^{0,0i} = -6.2 \pm 1.4 \text{ kJ mol}^{-1}$ [245], $\Delta^R G^{0,0i} = -6.5 \text{ kJ mol}^{-1}$ [88]).

Using $K_a = 19.4$, the solvent effect on the reaction equilibrium of the same esterification reaction was afterward successfully predicted for acetone, acetonitrile (ACN), DMF, and tetrahydrofuran (THF) using eq. (3.14) and reactant/product activity coefficients

Table 3.2: Calculated values for K_x , K_y , and K_a according to eq. (3.14), using data from Table 3.1 [205].

Initial mole-fraction ratio ethanol/acetic acid	1/3	1/1	3/1
K_x	7.7	3.9	2.32
K_y	2.33	5.40	8.23
K_a	17.95	21.05	19.09

obtained from PC-SAFT (Figure 3.30). The predictions revealed quite different effects of the solvents on the esterification reaction equilibrium (yield). While acetone and ACN were predicted to promote the esterification leading to high K_x values, DMF and THF were predicted to suppress the reaction compared to the solvent-free system. As can be seen in Figure 3.30, the experimentally determined equilibrium concentrations were found in almost quantitative agreement with the PC-SAFT predictions.

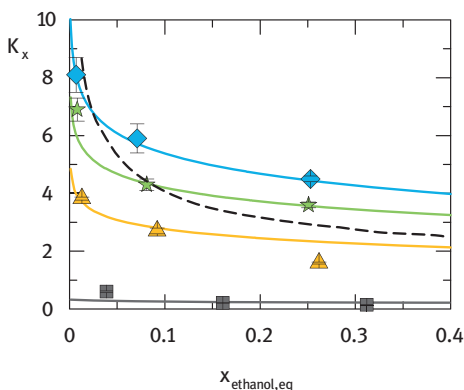


Figure 3.30: K_x of the esterification reaction of ethanol and acetic acid as a function of the equilibrium ethanol mole fraction at 40 °C and atmospheric pressure, in different solvents ($x_{solvent} = 0.5$). Symbols represent measured ethanol mole fractions in acetone (stars), ACN (diamonds), DMF (squares), and THF (triangles). Solid lines are PC-SAFT predictions using $K_a = 19.4$. The dashed line is the PC-SAFT prediction for the solvent-free system [205].

In the next step, the presented approach was applied to esterification reactions in solvent mixtures. For that purpose, solvent systems consisting of ACN mixed with acetone and THF and those consisting of DMF mixed with ACN, acetone, and THF were investigated. The overall solvent concentration was again chosen to be $x_{solvent} = 0.5$ for all systems. A comparison of the PC-SAFT predictions with the experimental data is shown for the ACN mixtures in Figure 3.31a and the DMF mixtures in Figure 3.31b.

In both cases, the PC-SAFT predictions are in very good agreement with the experimental data.

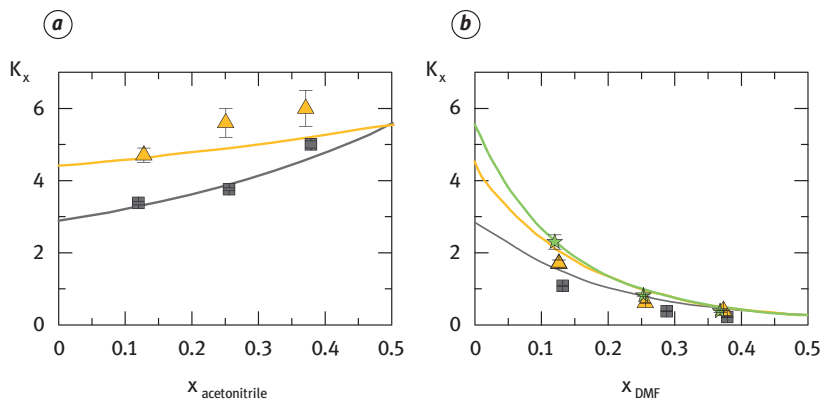


Figure 3.31: K_x of the esterification reaction of ethanol and acetic acid as a function of the solvent in the reaction mixture ($x_{\text{solvents}} = 0.5$) at 40 °C and atmospheric pressure. The symbols are experimental data: (a) Solvent mixtures of ACN + acetone (triangles) and ACN + THF (squares). (b) Solvent mixtures of DMF + ACN (stars), DMF + acetone (triangles), and DMF + THF (squares). Solid lines are PC-SAFT predictions using $K_a = 19.4$ [205].

Solvent Effects on the Hydroformylation Reaction Equilibrium

The solvent effect on the reaction equilibrium of the hydroformylation of 1-dodecene with CO/H_2 to n-tridecanal was investigated for different n-decane + DMF solvent mixtures ($w_{\text{decane}}/w_{\text{DMF}} = 80/20, 60/40, 0/100$) [145]. In contrast to the esterification reaction discussed earlier, the solvents not only affect the reaction equilibrium but also have a significant influence on the solubility of the gaseous reactants in the liquid reaction medium. According to eq. (3.12), the thermodynamic equilibrium constant, K_f for the hydroformylation was calculated using eq. (3.15):

$$K_f = \underbrace{\frac{x_{n\text{-tridecanal}}^{(l)}}{x_{1\text{-dodecene}}^{(l)} \cdot x_{\text{CO}}^{(l)} \cdot x_{\text{H}_2}^{(l)}}}_{K_x} \cdot \underbrace{\frac{\varphi_{n\text{-tridecanal}}^{(l)}}{\varphi_{1\text{-dodecene}}^{(l)} \cdot \varphi_{\text{CO}}^{(l)} \cdot \varphi_{\text{H}_2}^{(l)}}}_{K_\varphi} \cdot \left(\frac{p}{p^0}\right)^{-2} \quad (3.15)$$

Reaction experiments were performed between 95 °C and 115 °C for different n-decane/DMF solvent mixtures [145]. To determine K_x , PC-SAFT was first used to calculate the CO/H_2 solubility in the liquid phase containing the solvents, the 1-dodecene, and n-tridecanal at reaction equilibrium. Based on quantum mechanical (QM) calculations (Sections 3.2.2.2 and Section 6.3.1) of the standard Gibbs energy of reaction $\Delta^R G^{0,id}$, K_f was determined at 95 °C, 105 °C, and 115 °C (eq. (3.11)). The resulting K_f values, the experimentally-determined K_x values, as well as the K_φ and K_x values

obtained from PC-SAFT according to eq. (3.15) are listed in Table 3.3. The apparent equilibrium constant, $K_{x,exp}$, differs from the thermodynamic equilibrium constant, K_f by seven orders of magnitude. Consequently, if the nonideality was neglected ($K_\phi = 1$), according to the K_f value, the reaction would not happen at all. However, taking into account the PC-SAFT predicted fugacity coefficients and using K_ϕ , the equilibrium (K_x) was found to be almost completely on the product side, which perfectly agrees with the experimental results (Figure 3.32). This emphasizes the significant effect of the fugacity coefficients for modeling the hydroformylation reaction equilibrium.

Table 3.3: Calculated values for K_f , K_ϕ , $K_{x,PC-SAFT}$, and $K_{x,exp}$ for the hydroformylation of 1-dodecene with CO/H₂ to n-tridecanal at different temperatures and in varying solvent mixtures, according to eq. (3.15). K_f values were obtained from QM calculations, and $K_{x,exp}$ values were calculated based on experimentally determined equilibrium concentrations [145].

T / °C	$w_{n-decane}/w_{DMF}$ / (wt% wt% ⁻¹)	p_{eq} / bar	K_f	$K_{\phi,PC-SAFT}$ / 10 ⁸	$K_{x,PC-SAFT}$ / 10 ⁻⁸	$K_{x,exp}$ / 10 ⁻⁸
95	80/20	0.4	848.85	3.36	38.45	18.69 ± 4.4
	60/40	0.35	848.85	1.54	65.52	76.34 ± 18.7
	0/100	0.29	848.85	0.18	369.62	441.52 ± 137.2
105	80/20	0.74	292.97	13.81	11.36	7.64 ± 1.6
	60/40	0.58	292.97	5.17	18.77	20.92 ± 1.7
	0/100	0.57	292.97	0.97	97.15	99.02 ± 12.0
115	80/20	1.11	106.65	36.82	3.50	2.18 ± 0.4
	60/40	0.98	106.65	17.49	5.73	7.02 ± 0.6
	0/100	0.81	106.65	2.54	26.71	45.43 ± 11.2

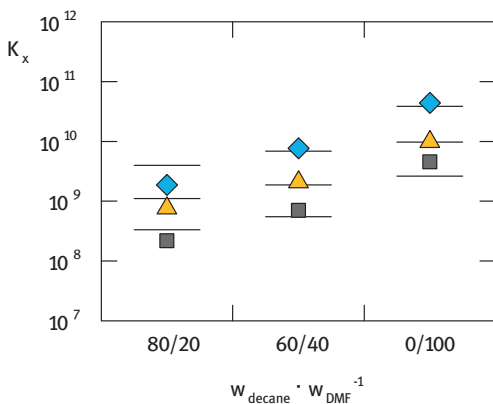


Figure 3.32: K_x values of the 1-dodecene hydroformylation in different n-decane/DMF ($w_{n-decane}/w_{DMF}$) solvent mixtures. Symbols are experimental data at 95 °C (diamonds), 105 °C (triangles), and 115 °C (squares). Solid lines are PC-SAFT predictions based on QM calculations of $\Delta^R G^{0,id}$ [145].

As shown in Figure 3.32, the experimental K_x values rise with decreasing temperature and increase with increasing DMF concentration in the solvent mixture, both of which are perfectly covered by the predictions. Thus, for complex reactions involving gaseous reactants too, PC-SAFT can predict the solvent effect on the reaction equilibrium in very good agreement with the experimental data.

Solvent Effects on the Reductive Amination Reaction Equilibrium

PC-SAFT was further used to predict the solvent effect on the reductive amination of *n*-undecanal with diethylamine and H_2 to *N,N*-diethyldecylenamine and water at 100 °C. To obtain the thermodynamic equilibrium constant K_f , the standard Gibbs energy of reaction, $\Delta^R G^{0,id}$, was calculated using the Gibbs energies of formation, $\Delta^F G_i^{0,id}$ (see eq. (3.11)) [245]. The resulting value ($\Delta^R G^{0,id} = -43.2 \text{ kJ mol}^{-1}$) was found to be in good agreement with K_f obtained from QM calculations ($\Delta^R G^{0,id} = -46.5 \pm 4.0 \text{ kJ mol}^{-1}$ [117]) (Section 6.3.1). Taking into account the interactions between the reactants/products and the solvents using fugacity coefficients obtained by PC-SAFT and simultaneously calculating the H_2 solubility in the reaction medium ($x_{H_2}^{(l)}$), K_x was predicted for different methanol/*n*-dodecane solvent mixtures using eq. (3.16).

$$K_x = \frac{x_{N,N\text{-diethyldecylenamine}}^{(l)} \cdot x_{\text{water}}^{(l)}}{x_{n\text{-undecanal}}^{(l)} \cdot x_{\text{diethylamine}}^{(l)} \cdot x_{H_2}^{(l)}} = K_f \cdot \frac{\varphi_{N,N\text{-diethyldecylenamine}}^{(l)} \cdot \varphi_{\text{water}}^{(l)}}{\varphi_{n\text{-undecanal}}^{(l)} \cdot \varphi_{\text{diethylamine}}^{(l)} \cdot \varphi_{H_2}^{(l)}} \cdot \left(\frac{p}{p^0}\right)^{-1} \quad (3.16)$$

Based on the predictions, the reaction equilibrium of the reductive amination at 100 °C and 20 bar was expected to be far on the product side ($K_{x,PC-SAFT} > 10^{11}$ for $w_{MeOH}/w_{n\text{-dodecane}} = 99/1$). Moreover, an increase in the *n*-dodecane weight fraction in the solvent mixture was predicted to result in a significant decrease of K_x and, thus, in lower product yields. To validate the PC-SAFT predictions, the reductive amination of *n*-undecanal with diethylamine was experimentally performed at 100 °C and 20 bar in different MeOH/*n*-dodecane solvent mixtures ($w_{MeOH}/w_{n\text{-dodecane}} = 99/1, 80/20$). Very low initial reactant concentrations (4 w% *n*-undecanal) combined with a reaction equilibrium being far on the product side resulted in extremely low *n*-undecanal equilibrium mole fractions ($< 3 \cdot 10^{-3}$), which could hardly be detected very accurately. However, the experimental results [134] confirm that an increase of the *n*-dodecane weight fraction in the solvent mixture leads to a decrease of K_x and, thus, to decreasing reaction yields. This agrees with the predictions using PC-SAFT, where the K_x value was found to be smaller for the 80/20 solvent mixture compared to the 99/1 solvent mixture. It should be emphasized that this qualitative agreement between the PC-SAFT predictions and experimental data was achieved without fitting any model parameters to the experimental reaction data.

Concluding, it was shown that solvents might have a significant impact on reaction equilibrium concentrations. Using an activity-based approach combined with PC-SAFT accounting for the occurring interactions between the reactants/products and the solvents, the solvent effect on the reaction equilibrium concentrations can be predicted in almost quantitative agreement to the experimental data.

3.1.6 Aggregation Formation of Aqueous Surfactant Solutions

Amphiphilic surfactants display characteristic molecular self-assembly behavior in solutions, at interfaces, and in bulk, generating nanoscale structures of different shapes. These nanoscale features determine many characteristics of these amphiphiles, relevant for their practical applications in materials, chemical engineering, and pharmaceutical and biomedical technologies. Critical to achieving this goal is an understanding of the link between the molecular structure of the amphiphiles and their self-assembly behavior. The main emphasis is on demonstrating how general principles of thermodynamics and considerations of molecular packing together help predict the self-assembled morphologies, given the amphiphilic molecular structure. The self-assembly of surfactants in solution has been widely investigated both experimentally and theoretically [60, 63, 170, 171, 173, 174, 195, 196, 257], because numerous practical applications take advantage of the resulting multimolecular aggregates. The structure of these aggregates influences the properties of surfactant solutions, as their solubilization capacity for hydrophobic substances or their viscous and viscoelastic properties, and consequently, the performance of surfactants in various applications. To select molecules that would yield desired structures such as spherical, globular, or rod like micelles, or spherical bilayer vesicles (Figure 3.33), or to custom-design novel amphiphiles to generate desired aggregate morphologies, it is necessary to know how the molecular structure of the surfactant controls the shape and size of the resulting aggregate.



Figure 3.33: Schematic representation of surfactant aggregates (spherical, globular or rod like micelles, or spherical bilayer vesicles) in dilute aqueous solutions [170].

Nagarajan and Ruckenstein [170] formulated an explicit expression for the standard free energy difference between a nonionic surfactant molecule present in an aggregate and the one present in the singly dispersed state in water:

$$\Delta\mu_{g,shape}^0 = \mu_{g,shape}^0 - g\mu_1^0 = \Delta\mu_{g,Tr}^0 + \Delta\mu_{g,shape,Int}^0 + \Delta\mu_{g,shape,Def}^0 + \mu_{g,shape,Ster}^0 \quad (3.17)$$

When aggregation occurs, the hydrophobic tail of the surfactant is transferred from its contact with water to the hydrophobic core of the aggregate. The contribution to the free energy from this transfer process, $\Delta\mu_{g,Tr}^0$, is estimated by considering the aggregate core to be like a liquid hydrocarbon. The formation of surfactant aggregates generates an interface between the hydrophobic core region consisting of the surfactant tails and the surrounding water medium ($\Delta\mu_{g,shape,Int}^0$). The surfactant tails inside the hydrophobic core of the aggregate are not in a state identical to that in liquid hydrocarbons. This is because one end of the surfactant tail in the aggregate is constrained to remain at the aggregate-water interface, while the entire tail has to assume a conformation consistent with the maintenance of a uniform density equal to that of liquid hydrocarbon in the aggregate core ($\Delta\mu_{g,Def}^0$). The formation of the surfactant aggregate brings the polar head groups of the surfactant molecules to the surface of the aggregate, where they are crowded, when compared to their isolated states as singly dispersed surfactant molecules. The area occupied by the head groups at the aggregate surface is excluded for the translational motion of the surfactant molecules constituting the aggregate. This generates steric repulsions among the head groups ($\Delta\mu_{g,shape,Ster}^0$). Originally, the detailed expressions for the different contributions in eq. (3.17) were developed based on thermodynamic principles and experimental data [170]. The use of eq. (3.17) requires the knowledge of the carbon number of the hydrophobic tail of the surfactant and the effective cross-sectional area of the polar head group, a_p . The quantity, a_p , can be estimated using the slope of surface tension versus the logarithm of the surface concentration. The minimization of eq. (3.17) leads to the aggregation form and the geometrical properties of the formed aggregate.

Knowing $\Delta\mu_{g,shape}^0$ as a function of temperature, aggregation size, and aggregation shape and calculating the aggregation-size distribution function via the principle of multiple chemical equilibria between aggregates of different sizes and monomers, that is $\mu_{g,shape} = g\mu_1$, allows the calculation of the micellar-size distribution, where g is the number of surfactant molecules forming an aggregate. The chemical potential, $\mu_{g,shape}$ can be derived by the first derivative of the total Gibbs energy of a dilute surfactant solution with respect to N_g . The chemical potential of a single dispersed surfactant molecule can be obtained by setting $g=1$ in the obtained expression. Since the critical micellar concentration (CMC) is characterized by a sudden change of properties of the aqueous surfactant solution, the CMC can be obtained at the sharp increase of the number-average aggregation number, g_N , or the mass-average aggregation number, g_M , as a function of the monomer concentration of surfactants, X_1 . The original model could be applied to the self-

assembly of sugar surfactants, where several properties could be predicted close to experimental data [60, 63, 126, 127].

Recently, the empirical correlations involved in different contributions in eq. (3.17) were replaced by more physical-based approaches [200, 202]. First, the contribution, $\Delta\mu_{g,Tr}^0$, will be considered. Nagarajan and Ruckenstein [170] suggested the calculation of the transfer contribution, $\Delta\mu_{g,Tr}^0$. For this purpose, they used the following theoretical pathway: first, an n-alkane molecule dispersed in a saturated aqueous phase is transferred to the ideal-gas state, and second, it is transferred from the ideal-gas state into the liquid phase of the pure n-alkane. To obtain the first contribution, they used experimental aqueous-solubility data of n-alkane vapors ranging from methane to n-octane as function of temperature [1, 2]. The difference between the free enthalpy for n-alkanes in their ideal-gas state and the one in their pure liquid state was obtained from the vapor-pressure data of the n-alkanes. The drawbacks of this approach are threefold: first, the expressions depend on the data which were available at that time; second, the mutual solubility of the n-alkanes and water was not taken into account; third, the hydrophobic tail of the surfactant molecules needs to be a hydrocarbon. For other hydrophobic tails, this expression must be revised [229]. To overcome these drawbacks, the following thermodynamic approach is used [200]. As an n-alkane with the carbon number, C_n , comprises two methyl groups and $C_n - 2$ methylene groups, the transfer contribution of the hydrophobic tail can be obtained by:

$$\frac{\Delta\mu_{g,Tr}^0}{k_B T} = \frac{1}{2} \left(\left(\frac{\mu_{A,Tr}}{k_B T} \right) - (C_n - 2) \left(\frac{\mu_{CH_2,Tr}}{k_B T} \right) \right) \quad (3.18)$$

The quantity, $\mu_{A,Tr}$, can be calculated by the following thermodynamic relation:

$$\frac{\mu_{A,Tr}}{k_B T} = \frac{\mu_{0A}^L}{k_B T} - \frac{\mu_A^{\infty,aq}}{k_B T} = -\ln(\gamma_A^{\infty,aq}) \quad (3.19)$$

where A represents the n-alkane acting as the hydrophobic tail of the surfactant. The quantities in eq. (3.19) have the following meaning: μ_{0A}^L is the chemical potential of pure A at system temperature and pressure, and $\mu_{0A}^{\infty,aq}$ is the chemical potential of A in the water phase at infinite dilution. $\gamma_A^{\infty,aq}$ is the activity coefficient of the n-alkane at infinite dilution in water and at system pressure and temperature. The quantity, $\mu_{CH_2,Tr}/k_B T$, can be estimated by the slope of $\mu_{A,Tr}/k_B T$ versus the carbon number, C_n . Consequently, a correlation, based on experimental data, is not required anymore to obtain the transfer free energy since $\gamma_A^{\infty,aq}$ can be calculated using a thermodynamic model, e.g., PC-SAFT. Figure 3.34 illustrates the transfer contributions of the octyl residue in the temperature range of 280–360 K calculated using eqs. (3.18) and (3.19), compared to the transfer contribution retrieved using the original model [60]. While the transfer contribution of the original model increases continuously with temperature, the transfer contribution computed with PC-SAFT exhibits a minimum, which is connected to the solubility minimum of n-octane in water

at $T = 318$ K (Figure 3.5). The reason for this minimum in solubility is still controversially discussed in the literature [89]. The data depicted in Figure 3.34 clearly shows that the description of the hydrophobic effect including the minima in $\mu_{g,Tr}^0/k_B T$ is now possible because experimental data related to the LLE rather than related to the VLE of n-alkane + water mixtures were used for estimating the binary interaction parameters of PC-SAFT [89].

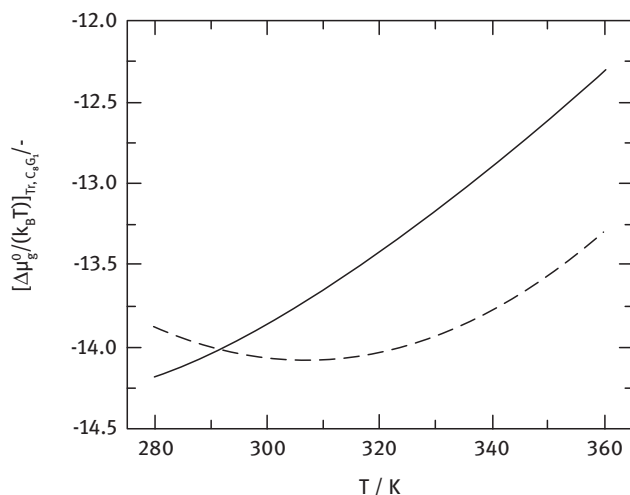


Figure 3.34: Transfer contribution, $\Delta\mu_{g,Tr}$ in eq. (3.17) of n-octyl- β -D glycopyranosid (C_8G_1) as a function of temperature. The solid line shows the results of the original model [60], while the dashed line indicates the results of the modified transfer contribution obtained from eqs. (3.18) and (3.19), applying PC-SAFT [200].

The modification of the interfacial contribution consists in the use of the interfacial tension, σ^{LL} , obtained by combining PC-SAFT with the DGT [201], rather than using the empirical correlations based on the surface tensions, σ^{VLE} , of pure water and pure n-alkanes, as done in the original model [200]. The empirical correlation underestimates the interfacial tension clearly, whereas the values calculated using PC-SAFT + DGT nicely agree with the experimental data over the whole temperature range (Figure 3.24). The interfacial tensions estimated by applying the empirical correlation depended only very slightly on the n-alkane chain length, whereas the experimental interfacial tensions [234, 251] and the ones calculated using PC-SAFT + DGT increase with increasing molecular weight of the n-alkanes (Figure 3.24). The reason for the strong molecular-weight dependence of σ^{LLE} is the strong dependence of the aqueous solubility on the molecular weight of the n-alkane, which is calculated via PC-SAFT in excellent agreement with the experimental data (Figure 3.5). Aveyard

and Haydon [11] compared interfacial tensions, σ^{LLE} , and the surface tensions, σ^{VLE} , for different water + n-alkane mixtures at the same temperature and figured out that the interfacial tension was always higher than the surface tension. The empirical correlation [170] was fitted to surface tensions, which explains that the interfacial tensions obtained from the empirical model are too small (Figure 3.35).

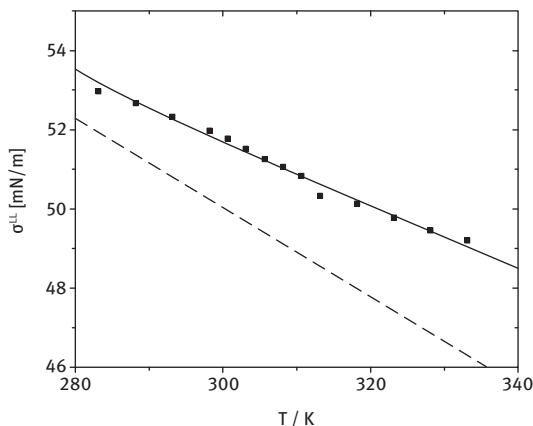


Figure 3.35: Comparison between the experimental liquid–liquid interfacial tension [solid squares: 251] with calculation results (solid line: PC-SAFT + DGT [201], dotted line: original model [60] for n-decane + water.

Figure 3.36 shows the impact of the suggested modifications on the minimum value of $\Delta\mu_{g,shape}^0/k_B T$ [200]. The original model predicts that at small aggregation numbers, spherical micelles are favored, and at a certain surfactant concentration, very close to the CMC, spherical bilayer vesicles are formed [60]. This holds true for all applied modeling approaches. The change from a spherical micelle to a spherical bilayer vesicle takes place when 28 surfactant molecules form an aggregate. The rearrangement from spherical micelles to spherical bilayer vesicles is characterized by the discontinuity in $\Delta\mu_{g,shape}^0/k_B T$ (Figure 3.36). Comparing the different modeling approaches, it can be observed that the modification of the interface Gibbs energy causes an upward shift of $\Delta\mu_{g,shape}^0/k_B T$, while applying the modification of the transfer free energy leads to a lower $\Delta\mu_{g,shape}^0/k_B T$, compared to the results of the original model [60]. Since the total difference in chemical potential is the sum of the different contributions, the result was to be expected from the impact of the different modifications, as discussed earlier. However, the resulting difference in $\Delta\mu_{g,shape}^0/k_B T$ is still slightly lower than the one calculated with the original model.

Although the impact of the modifications appears to be small for $\Delta\mu_{g,shape}^0/k_B T$, it can lead to significant changes when calculating aggregation properties as the size

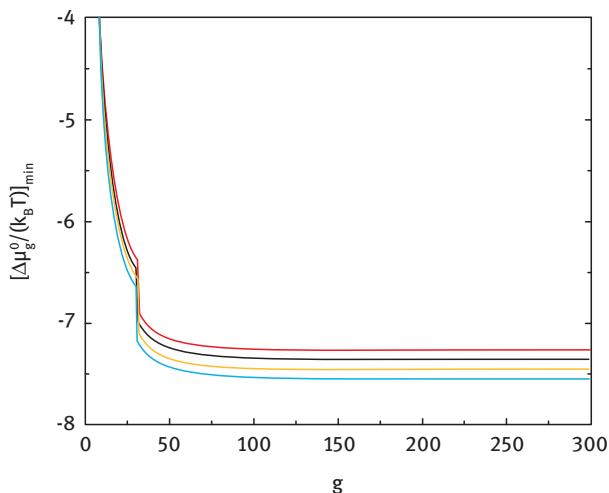


Figure 3.36: Impact of different modeling approaches (black line: original model, magenta line: interface modification; blue line: transfer modification; red line: a combination of interface and transfer modification) on the calculation of the minimal value of $\Delta\mu_{g,shape}^0/k_B T$ in eq. (3.17) for C_8G_1 surfactant solutions at $T=298.15$ K [200].

distribution or critical micelle concentration. Since the aggregation-size distribution, X_g , is an exponential function of $\Delta\mu_{g,shape}^0/k_B T$, the resulting distribution functions are very sensitive about $\Delta\mu_{g,shape}^0/k_B T$.

Comparing the predicted CMCs with the experimental data, it can be concluded that all versions predict the CMCs in a reasonable concentration range (Figure 3.37). Different experimental methods were used for the CMC measurements. From a theoretical point of view, there is no single CMC, but a concentration range, where the self-assembling starts. Caused by the polydispersity with respect to the aggregation size, different experimental methods lead to different experimental results, since the detection depends on the number of molecules (e.g., time-resolved fluorescence quenching) or on the mass of the formed aggregates (e.g., light scattering). Moreover, some other methods, such as surface-tension measurements or speed-of-sound measurement cannot even be clearly correlated to g_N or to g_M . This also raises the question about which CMC criterion should be used for comparison. The current approach for $\Delta\mu_{g,Ster}^0/k_B T$ relies on the simple van der Waals repulsion. For future work, the term $\Delta\mu_{g,Ster}^0/k_B T$ too should be replaced, using a more realistic theoretical picture.

In the case of aggregates formed by nonionic surfactants belonging to the class of poly(oxyethylene) alkyl ethers (C_iE_j) the steric repulsion of the polar head groups cannot be described by the simple van der Waals term for the repulsion of hard spheres (eq. (3.17)) as suggested in the original model [170]. The reason for this situation is that

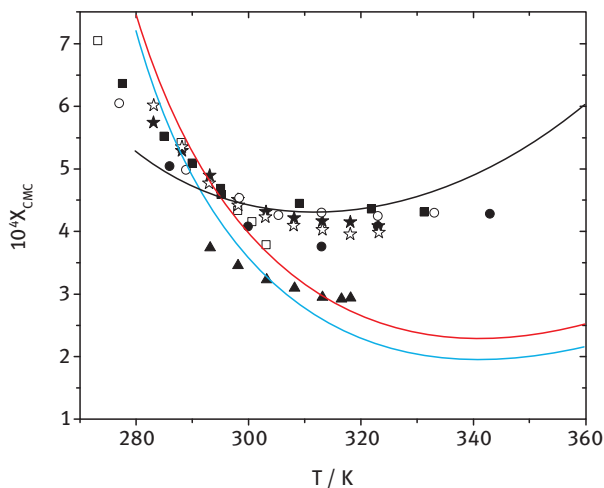


Figure 3.37: CMC for aqueous C_8G_1 solutions as a function of temperature. Experimental data [solid squares: [131], open squares: [7], solid triangles: [62], solid circles: [160], solid and open stars: [36], open circles: [9]] and predicted results (black line: original model, red line: modified transfer contribution, blue line: modified transfer and interfacial contribution) [200].

the diameter of hard spheres does not depend on temperature. However, the volume of the polar head group made of oxyethylene depends on temperature for two reasons. First, the polar heads are hydrated, the hydration number decreasing with increasing temperature [157, 177]. This leads to a decrease in the effective cross-sectional area of the polar head group, a_p , with temperature. Second, the volume of the polar head group increases with increasing temperature. This effect leads to an increase of the a_p value with temperature. Recently, a correlation of the a_p values as a function of the number of head groups (j), the tail length (i), and the temperature was developed [202]. This new approach allows the description of the CMC for all members of this surfactant class as a function of temperature, where the CMC runs through a minimum [202]. Similar to the C_iG_j surfactants, C_iE_j surfactants also form vesicles in aqueous solutions.

3.1.7 Solubilization of Weak Polar Molecules in Aqueous Surfactant Solutions

One of the most useful properties of vesicles is their ability to enhance the aqueous solubility of hydrophobic substances. This phenomenon, referred to as solubilization, is made possible by the incorporation of the solubilizates in the hydrophobic microenvironment offered by the micellar core. This effect can be modeled based on the detailed aggregation model [172], where the aggregates were modeled as spherical micelles. From the thermodynamic point of view, an aqueous solution containing two surfactants is considered. In this solution, singly dispersed surfactant molecules

of all components and aggregates of all possible sizes, as well as compositions, are present. The formed aggregates are described by a two-dimensional distribution function, $W(g, \alpha)$, where g is the number of molecules that form the aggregates, and α represents the chemical composition of the formed aggregates:

$$\alpha = \frac{N_{\text{Surfactant}, A}}{N_{\text{Surfactant}, A} + N_{\text{surfactant}, B}} \quad (3.20)$$

The reaction products of the studied chemical reactions (Chapter 2) are weak polar components (WPC) and the formed aggregates without the WPC are spherical vesicles. The polar group of the WPC will accumulate in the corona layer of the aggregate and the nonpolar tail will remain in the aggregate core. Taking advantage of the hetero-segmental version of the PC-SAFT, the thermodynamic properties of the polar head and the tails of the WPC can be modeled close to the experimental data. The already-obtained parameters for these components, namely n-amines [91], n-aldehydes [215], and esters [90] can be used directly in the aggregation formation model. The WPC can be handled in such a way that this component acts as a seconded surfactant and, consequently, contributes to the aggregation and, hence, mixed aggregates will be formed. Nagarajan [168, 169] developed a molecular theory for the formation of mixed micelles as an extension of the theory for single-component micelles. The theory permits the calculation of the CMC, the average micelle size, and the average micelle composition as well as the size and the composition distribution of micelles in mixed surfactant systems. However, only spherical micelles were considered [168; 169], and the corresponding contributions were modeled using the empirical expressions, as discussed in Section 3.1.6.

Recently [203], a new theoretical framework was developed with the following new features:

- 1) The possible shapes of globular or rodlike micelles and spherical bilayer vesicles (Figure 3.33) were included.
- 2) The transfer term is modeled via the activity coefficients at infinite dilution using PC-SAFT (eq. (3.19)).
- 3) The interfacial tension occurring in the interfacial contribution was calculated using PC-SAFT in combination with the DGT.
- 4) The effective cross-sectional area of the polar head group for the surfactant is calculated by the correlation developed in the literature [202], and the temperature-dependent a_P value for WPC is calculated via PC-SAFT, using the parameter provided in the literature [91, 215].
- 5) The activity coefficients describing the interaction between both tails were calculated via PC-SAFT rather than applying the Hildebrand approach.

- 6) The polydispersities with respect to the aggregation number, $g = N_{Surfactant} + N_{WPC}$, and with respect to the chemical composition, α , (eq. (3.20)) are taken into account completely, rather than the use of the maximal term, as suggested by Nagarajan and Ruckenstein [170].

The mixture $C_{10}E_8 + n\text{-octylamine} + \text{water}$ serves as an example for the discussion of the modeling results [203], where $n\text{-octylamine}$ is a possible reaction product of the reductive amination. The solubility of $n\text{-octylamine}$ in water [91] is very low; therefore, the number of singly dispersed WPC molecules will be quite low. The ability of alkylamines to form aggregates has been widely demonstrated in the literature [10, 13, 75]. According to fluorescence probe measurements, the aggregates contain 140 molecules [10]. Binary surfactant systems consisting of cationic surfactants and alkylamines exhibit a nonideal behavior associated with a negative synergistic phenomenon [75]. The model predicts the self-assembly of $n\text{-octylamine}$ in water [203]. Similar to the formed aggregate without WPC (Figure 3.36), the model predicts the formation of spherical micelles at low aggregation numbers, followed by spherical vesicles at higher aggregation numbers. An example of the two-dimensional distribution function is depicted in Figure 3.38. These data show clearly that $n\text{-octylamine}$ acts as a co-surfactant because it will be incorporated in the formed aggregates. The average composition of the aggregates is close to 0.7. The points of discontinuities of the distribution function designate the change of the aggregation shape from spherical micelles to spherical vesicles (Figure 3.33). The establishment of the inner surfactant layer leads to a volatile increase in the number of molecules forming the aggregate. The integration of the $n\text{-octylamine}$ into the aggregates permits higher solubility in the surfactant solution, compared to pure water.

The incorporation of the $n\text{-octylamine}$ in the aggregates also yields a decrease in the CMC in comparison to the pure surfactant solution (Figure 3.39), even if only a small amount of $n\text{-octylamine}$ is added. The special shape of the curve in Figure 3.39 can be explained in the following way: At low $n\text{-octylamine}$ concentrations, the properties of the water are changed by single dispersed $n\text{-octylamine}$ molecules. At a certain $n\text{-octylamine}$ concentration ($X_{n\text{-octylamine}} = 6.83 \cdot 10^{-5}$) $n\text{-octylamine}$ starts to form aggregates. This concentration is close to the solubility of $n\text{-octylamine}$ in water, which was measured by McBain and Richards [164] to be $X_{n\text{-octylamine}} = 2.8 \cdot 10^{-5}$ at $T = 298.15 \text{ K}$. At an $n\text{-octylamine}$ concentration of $X_{n\text{-octylamine}} = 6.83 \cdot 10^{-5}$, the average aggregation number also begins to increase strongly from approximately $g \approx 60$ to $g \approx 300$. The composition of the formed aggregates also changes in this concentration range from $\alpha = 1$ to $\alpha = 0.65$, if the $C_{10}E_8$ concentrations keep constant. The data in Figure 3.39 show clearly that binary surfactant systems consisting of nonionic surfactants and alkylamines exhibit a nonideal behavior associated with a positive synergistic phenomenon, in contrast to the behavior of $n\text{-alkylamines}$ in mixtures with cationic surfactants [75].

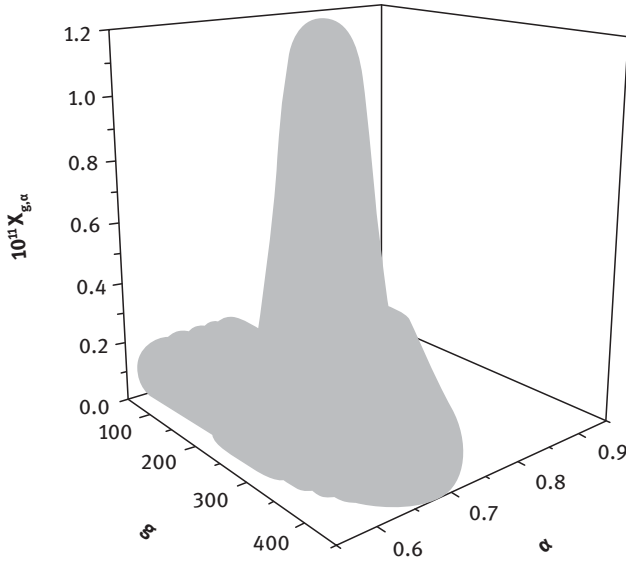


Figure 3.38: Predicted two-dimensional distribution function of the formed aggregates for the aqueous solution containing $C_{10}E_8$ ($X_{C_{10}E_8} = 1.68 \cdot 10^{-5}$) and n-octylamine ($X_{n-octyla\ min} = 1 \cdot 10^{-5}$) at $T = 298.15$ K [203].

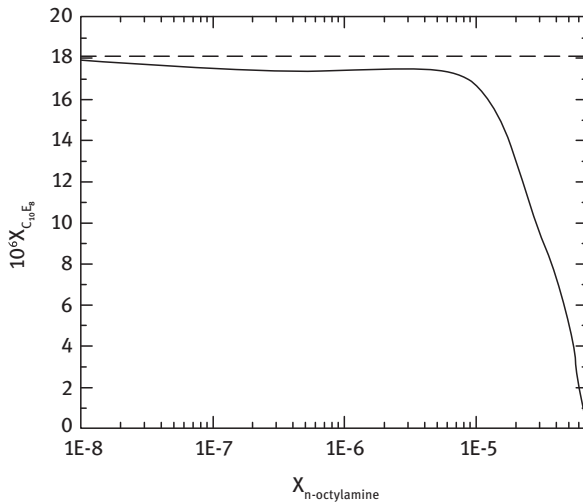


Figure 3.39: Predicted CMC for the aqueous solution containing $C_{10}E_8$ and n-octylamine at $T = 298.15$ K. The dashed line represents the CMC for the aqueous solution containing only $C_{10}E_8$ [203].

Knowing the composition of the formed aggregates allows the calculation of the distribution coefficient, K , defined as the number of n-octylamine molecules in the formed aggregates and the number of single dispersed n-octylamine molecules. At low n-octylamine concentrations, the distribution coefficient decreases until the calculated CMC of n-octylamine (Figure 3.39). At n-octylamine concentrations above this value, the distribution coefficient increases with increasing of the n-octylamine concentration, because mixed aggregates were formed. Consequently, the solubility of n-octylamine in the surfactant solution is enhanced in comparison with pure water.

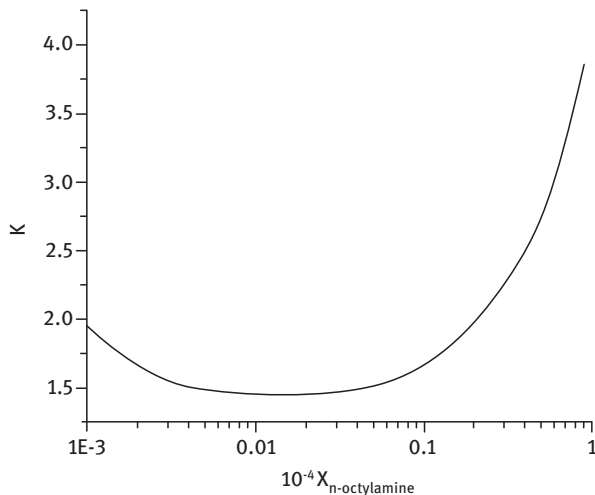


Figure 3.40: Predicted distribution coefficient, K , of n-octylamine between the formed aggregates and the aqueous surroundings for the aqueous solution containing $C_{10}E_8$ and n-octylamine at $T = 298.15$ K, where the $C_{10}E_8$ mole fraction is $X_{C_{10}E_8} = 1.75 \cdot 10^{-5}$ [203].

3.1.8 Conclusion

Both the thermodynamics models (PC-SAFT and LCT) that were used were able to describe the phase equilibria of the studied mixture close to the experimental data. In PC-SAFT, the new heterosegmented approach leads to a noticeable improvement of the prediction power. Some model parameters can be correlated with the carbon number within a homologous series. As regards LCT, an improvement in the description of small molecules could be achieved. Besides the phase behavior, the interfacial properties, such as interfacial tension, surface tension, and adsorption isotherms could also be modeled in agreement with experimental data. This was possible by a combination of the thermodynamic models with the DFT for inhomogeneous systems. Additionally, PC-SAFT could also be used to investigate chemical reactions; especially, the impact of

solvents on the reaction equilibrium could be predicted in agreement with experimental findings.

Although many approaches to model the phase behavior of surfactant solutions have been developed so far, this research field still shows potential for improvement. This is mainly due to the formation of nanostructures. For mixtures containing surfactants, only experimental investigations lead to trusted phase diagrams. For the description of the aggregation behavior in aqueous surfactant solutions, the aggregation model could be improved by the replacement of empirical correlation with PC-SAFT in combination with DGT. The increased solubility of n-octylamine in surfactant solutions compared to the solubility in pure water could be predicted by extending the aggregation formation model to the modeling of mixed micelles. The new model can predict the distribution of n-octylamine between the surrounding water and the formed aggregates. Verification by experiments is a challenging task for the future.

3.2 Kinetic Modeling of Complex Catalytic Reactions in Multiphase Systems

Martin Gerlach, Sabine Kirschtowski, Froze Jameel, Fabian Huxoll,
Matthias Stein, Gabriele Sadowski, Andreas Seidel-Morgenstern,
Christof Hamel

3.2.1 Introduction

The essential basis for a rational design of chemical reactors is the availability of a suitable model-based description of the reaction kinetics. Depending on the phases involved, homogeneous and heterogeneous reactions [12, 20, 148] can be distinguished. In the latter type, the reactor performance is often strongly influenced by interphase mass transport limitations [104, 148].

Due to the complexity of parallel and series reactions that proceed simultaneously in complex reaction networks, the kinetics are often described by simple empirical rate expressions like power laws. However, there are clear limitations of such nonmechanistic rate equations. Consequently, extrapolations beyond the experimental range covered during parametrization are highly uncertain, and global process optimization is not possible.

In this chapter, a general strategy for deriving and parametrizing mechanistically based reaction kinetics, evaluating underlying catalytic cycles, is presented. As an example, a homogeneously catalyzed tandem reaction, namely the hydroaminomethylation (HAM) of long-chain olefins (Figure 3.41) [4–6, 18, 40, 45, 58, 95, 129, 204, 224] performed in a thermomorphic multiphase system (TMS) [21] is considered. In homogeneous catalysis, the identification of reaction mechanisms in terms of underlying

catalytic cycle(s) may be supported by spectroscopy. For this purpose, spectroscopic methods such as UV/VIS, infrared, mass, and nuclear magnetic resonance (NMR) spectroscopy could be applied experimentally [19, 20]. On a theoretical level, DFT calculations are a powerful support [135] for the elucidation of reaction pathways [20].

The key of an extrapolatable kinetic model based on **catalytic cycles** lies in the corresponding **mechanistically-based rate equations** [42, 104, 161, 167]. In the following, a methodical approach to **derive**, initially, a general but overparametrized model and an approach to **reduce it systematically** [136, 161] will be reported. The following specific steps will be discussed in detail:

- **reaction network elucidation**
- **mechanistic kinetic modeling**
- reduction of **kinetic models** exploiting **3 strategies** (a mathematical approach, operando spectroscopic techniques and quantum mechanics (QM))

This conceptual approach will be applied and “trained” first for selected subnetworks of the hydroformylation reaction network (see subset in Figure 3.41) as a part of the total reaction network of HAM illustrated in Figure 3.41. Finally, the methods applied and the mechanistic kinetic models developed will be validated and proven by describing the overall tandem reaction system of the HAM.

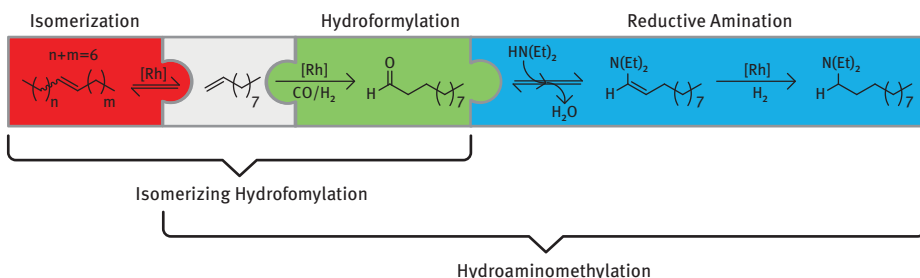


Figure 3.41: Rh-catalyzed HAM of 1-decene and Rh-catalyzed isomerizing hydroformylation of decenes coupled in a tandem reaction sequence scheme [18, 22, 40, 45, 58, 129, 133, 134, 140, 204, 224].

3.2.2 Methodological Approach

3.2.2.1 Reaction Network Investigation

In the first step of the strategy applied to identify and parametrize mechanistic reaction kinetic models, the investigation of the reaction network is essential, as it reveals the number of reaction rates that need to be quantified mathematically. A sequence of reactions is illustrated for the subnetwork of the isomerizing hydroformylation (Figure 3.42) of 1-decene to undecanal. Due to its relative simplicity, this individual reaction was initially investigated in preliminary experiments under typical process

conditions to analyze the formation of the main and side reaction products that may enter in more complex situations to other reaction subnetworks. Based on experimental observations, a reaction network is deduced and a reaction mechanism is postulated, which serves as the basis for kinetic modeling.

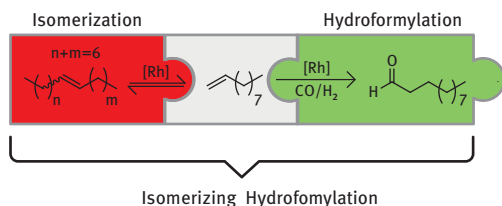


Figure 3.42: Reaction scheme of the subnetwork of the Rh-catalyzed isomerizing hydroformylation of 1-decene coupling the isomerization and hydroformylation in a reaction sequence.

Experimental Investigations

An analysis of the reaction network of the Rh/BIPHEPHOS (6,6'-[(3,3'-Di-*tert*-butyl-5,5'-dimethoxy-1,1'-biphenyl-2,2'-diyl)bis(oxy)]bis(dibenzo[*d,f*] [1,3,2]dioxaphosphepin)-catalyzed hydroformylation of 1-decene to undecanal (Figure 3.42) was performed in preliminary kinetic experiments. A TMS consisting of dodecane and *N,N*-dimethylformamide (DMF) as nonpolar and polar solvents, respectively, was used. The TMS was one phasic in a temperature range of 95–135 °C to avoid liquid–liquid mass transport limitations. Kinetic hydroformylation experiments with different CO:H₂ gas compositions were conducted. Detailed information about the general procedure using 1-dodecene is provided in [132, 162]. As limiting cases, the gaseous reactants CO and/or H₂ were excluded from the reaction to study the reaction subnetworks individually.

Different reactor setups were used that enabled the investigation of the hydroformylation reaction upon variation of the reactor scale, the gas/liquid mass transport and the possibility to apply process control trajectories (Figure 3.43a). An important feature to study the reaction kinetics was the developed load–lock system of the laboratory reactor (Figure 3.43b), which enabled inert handling of all chemicals, especially the sensitive catalyst and a well-defined starting point of the kinetic experiment. Thus, the catalyst pretreatment under syngas atmosphere (CO:H₂ = 1:1) could be performed independently, while the substrate 1-decene was loaded initially into a PTFE-coated gas cylinder and injected afterwards to start the kinetic experiment. In addition, to study the reaction mechanism using *operando* FTIR (Fourier-transform infrared)-spectroscopy (vide infra), one reactor was equipped with a Si-ATR (attenuated total reflection)-probe, which was attached to a FTIR spectrometer (Mettler Toledo, ReactIR, resolution 8 cm⁻¹, recorded wavelength 700–2280 cm⁻¹) (Figure 3.43c) [123].

Typical experimentally determined concentration profiles are shown in Figure 3.44 [122]. Besides the hydroformylation of 1-decene to undecanal (Figure 3.44a), the double-bond isomerization to internal decenes (Figure 3.44b) and hydrogenation (Figure 3.44c) turned out to be the most important side reactions influencing the

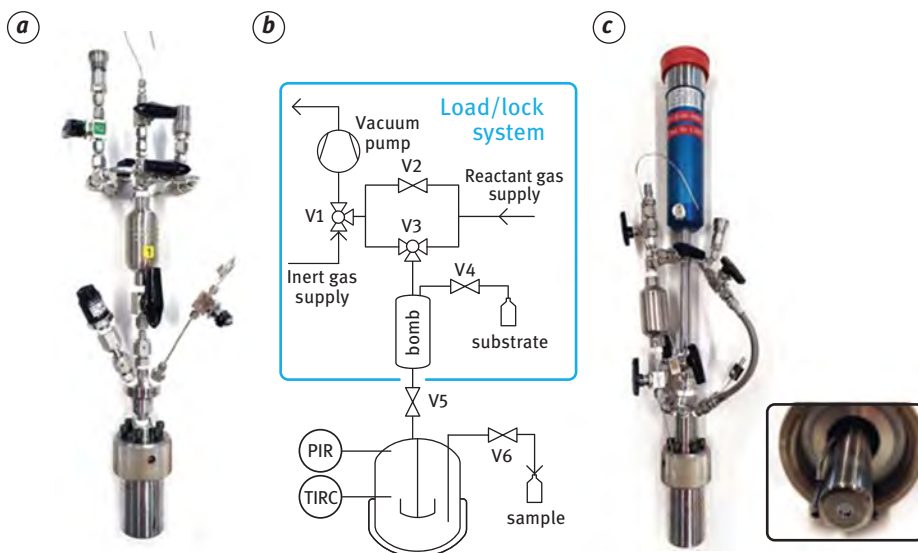


Figure 3.43: Experimental setup for the investigation of reaction kinetics of homogeneously catalyzed liquid phase reactions: a) 75 mL reactor, b) process flow diagram and c) customized 75 mL reactor equipped with a Si-ATR-probe for *operando* FTIR measurements.

chemoselectivity of the target hydroformylation. For certain conditions, the isomerization of the double bond could be observed up to 5-decene including *cis/trans*-configurations. The challenging quantification of all *cis/trans*-decenes was realized by gas chromatography, using a highly polar stationary phase [119, 120] and could be validated by quantitative ^{13}C -NMR-spectroscopy [94]. Under typical hydroformylation conditions, using an equimolar mixture of CO and H_2 , hydrogenation was of minor importance, with a yield of about 3% alkane. Due to the possibility of internal, iso-selective hydroformylation leading to undesired branched iso-aldehydes, the regioselectivity is an important parameter that determines the ratio of the desired *n*-aldehyde to all aldehydes. High regioselectivity >95% could be achieved in all experiments, which is a characteristic outcome for bulky diphosphite ligand BIPHEPHOS catalysts [240]. Thus, the production of branched iso-aldehydes was found to be of minor importance for further kinetic studies.

Postulation of the Reaction Network

Evaluating the presented experimental results and further investigations of the related hydroformylation of 1-dodecene [132, 162], the detailed reaction network for the Rh/BIPHEPHOS-catalyzed hydroformylation of 1-decene shown in Figure 3.45 was postulated. This network consists of eight reactions in three subnetworks. In the discussion of the side reactions, the isomerization of 1- and internal iso-decenes

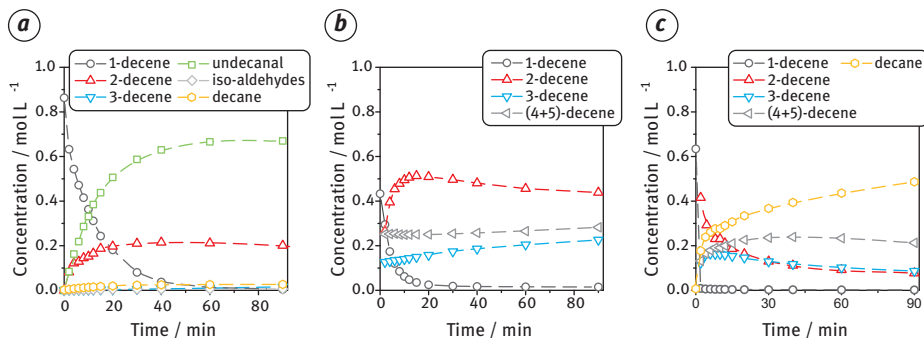


Figure 3.44: Experimental results for the reaction network elucidation of the Rh/BIPHEPHOS-catalyzed hydroformylation of 1-decene at 105°C: a) isomerization in absence of CO and H₂, b) hydrogenation in absence of CO, c) hydroformylation under CO:H₂ = 1:1. Compositions of the reaction mixtures can be found in [120].

(2-,3-,4-,5-decene) (designated as **ISO**) is most important. During isomerization, the double bond migrates reversibly along the chain from terminal 1-decene to internal 5-decene, whereby cis/trans isomers are formed for all internal decenes. The cis/trans isomers of a single iso-decene are lumped together for simplification, as it was not possible to determine the interconversion of the same. Thus, the isomerization sub-network constitutes four reactions ($r_{\text{ISO},1}, \dots, r_{\text{ISO},4}$). To determine the thermodynamic equilibrium of decene isomerization, individual experiments and calculations based on minimization of the Gibbs energy were carried out and experimentally validated [119]. The necessary thermodynamic properties such as heats of formation were determined, based on both Benson's group contribution method and quantum mechanical calculations [121]. The good agreement between the experimental and predicted data revealed the suitability of these methods to determine the equilibrium constants of alkene isomerization reactions, in general.

The hydrogenation (**HYD**), as a further side reaction, was assumed to exclusively exploit 1-decene. This assumption was verified by additional hydroformylation experiments using mixtures of internal decenes [122].

For the main hydroformylation reaction, 1-decene can be converted to the desired linear aldehyde undecanal (**nHYFO**) and also to the undesired branched iso-aldehyde 2-methyl-decanal (**isoHYFO**, **1**). Since the formation of branched iso-aldehydes is also possible from internal iso-decenes, all corresponding products have been lumped into iso-aldehydes (designated as **isoHYFO**, **2**).

Reaction Mechanism

Although the reaction network described above already appears to be rather detailed, it does not completely represent the underlying reaction mechanisms of the

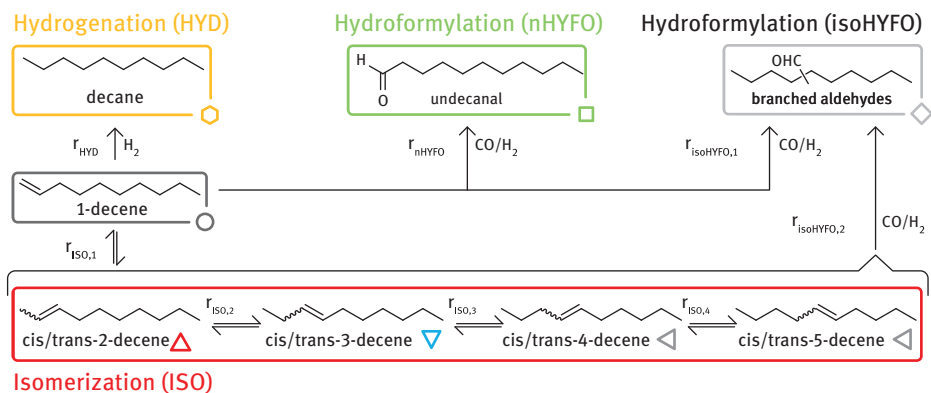


Figure 3.45: Identified detailed reaction network of the Rh/BIPHEPHOS-catalyzed hydroformylation of 1-decene.

specific reactions. For the discussed *n*-selective hydroformylation (**nHYFO**), the reaction scheme is still only a simplified, condensed description of the numerous elementary reactions that take place.

A more detailed reaction mechanism of the Rh/BIPHEPHOS-catalyzed hydroformylation of long-chain olefins (Figure 3.46) is typically based on the postulated mechanism of Evans et al [65]. Here, it was extended for the first time by the most common side reactions, namely iso-selective hydroformylation, double-bond isomerization, and hydrogenation observed in the kinetic experiments [132, 162] starting from the same active catalyst species. In addition, the formation of the catalyst from its resting state and chemical equilibria of catalytically inactive species were considered, based on the performed experimental analysis.

As starting point for all coupled reaction cycles, the electronically and coordinately unsaturated hydrido-carbonyl complex **1** is assumed, which is in equilibrium with the hydrido-dicarbonyl complex **RS** by CO dissociation. The catalyst pre-equilibrium is of central importance, as it influences the availability of the entire catalyst mass for the productive catalyst cycles and may be dependent on the metal and ligand concentration as well as the substrate concentrations in a complex manner. It is characterized by several Rh species (catalyst precursors) that are assumed to be catalytically inactive. Starting with the Rh-precursor $\text{Rh}(\text{acac})(\text{CO})_2$ (**PC1**), the addition of the diphosphite ligand BIPHEPHOS ($\text{P}\cap\text{P}$) substitutes both carbonyl ligands at the Rh-centre ($\text{Rh}(\text{acac})(\text{P}\cap\text{P})$, **PC2**). Upon further addition of CO and H_2 , the hydrido-dicarbonyl complex, **RS**, is formed, which is assumed to be the resting state for all reactions. Depending on the concentration of CO, a carbonyl saturated species (Rh-tetracarbonyl, **TC**) was reported [150] and high concentrations of **TC** may facilitate the formation of Rh-dimers [166].

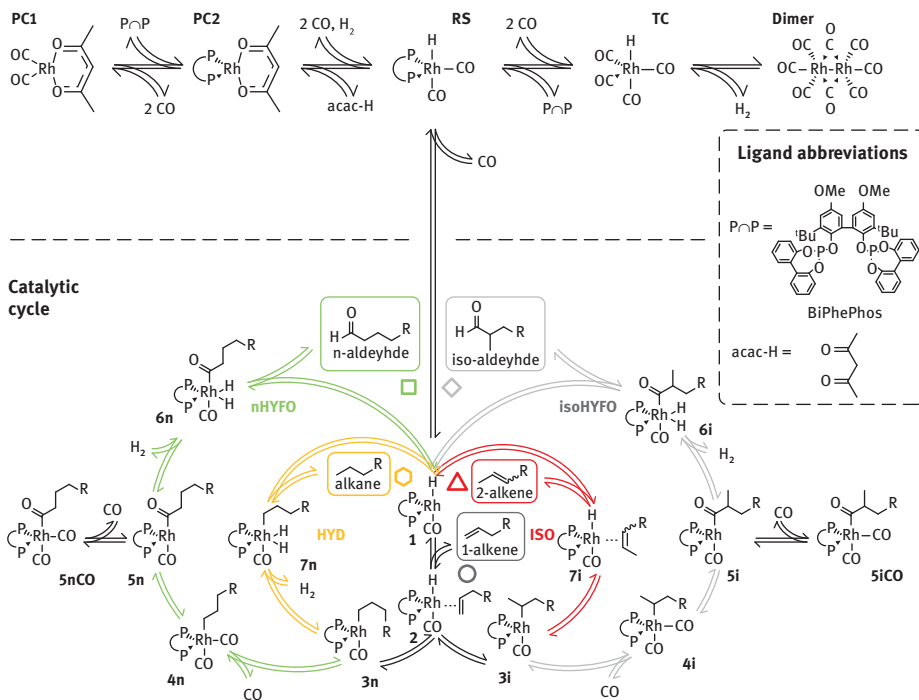
Catalyst
pre-equilibrium

Figure 3.46: Postulated catalytic cycle for the Rh/BIPHEPHOS-catalyzed isomerizing hydroformylation of long-chain alkenes as basis for the mechanistic modeling of reaction kinetics [122, 132, 162].

In the catalytic cycle, the catalytically active hydrido-carbonyl complex **1** coordinates and, thus, activates the 1-alkene forming the hydrido-alkene complex **2**. The subsequent insertion of the 1-alkene into the Rh-H bond can form either the linear Rh alkyl complex, **3n** (anti-Markovnikov product) or the branched Rh alkyl complex, **3i** (Markovnikov product). This is an important reaction sequence that determines the chemo- and regioselectivity of the coupled reaction network (**nHYFO-isoHYFO**).

For the n-selective hydroformylation cycle (**nHYFO**), starting from the linear Rh alkyl complex **3n**, CO coordinates (dicarbonyl alkyl complex, **4n**) to form the acyl complex, **5n** by insertion into the Rh alkyl bond. For **5n**, CO competes with H₂ to form the inactive saturated acyl complex, **5nCO**. In the oxidative addition of H₂ to **5n**, the dihydrido-carbonyl complex, **6n** is formed, which releases the linear n-aldehyde by reductive elimination and reforms the catalytically active hydrido-carbonyl complex **1**. In the iso-selective hydroformylation cycle (**isoHYFO**), starting

from the branched Rh alkyl complex, **3i**, the same elementary steps hold as in the *n*-selective hydroformylation cycle, and the branched iso-aldehyde is released.

The chemoselectivity of **nHYFO** is influenced by several side reactions. Starting from the linear Rh alkyl complex, **3n**, in addition to the coordination of CO in the **nHYFO** cycle, the direct oxidative addition of H₂ to the dihydrido-alkyl complex, **7n**, to follow the hydrogenation (**HYD**) cycle is also possible, which, in turn, can release the alkane in subsequent reductive elimination. Starting from the branched Rh alkyl complex, **3i**, in addition to the coordination of CO in the **isoHYFO** cycle, β-H elimination to the hydrido-alkene complex, **7i**, in the **ISO** cycle is also possible, which releases the 2-alkene as an isomerization product and reforms the catalytically active hydrido-carbonyl complex **1**. The 2-alkene can enter the catalytic cycle as substrate again.

All the mentioned elementary steps contribute to the overall reaction progress. Dynamic changes in macroscopic states as substrate concentrations and temperatures perturb the postulated equilibria between the catalytic intermediates and, thus, influence the chemoselectivity of the reaction process. For this reason, the mathematical description of these effects by mechanistic kinetic model equations is very valuable for process development and optimization, for example, to enhance the yield for the desired reaction product. This objective is not achievable by applying the frequently used simple empirical power law kinetic models.

3.2.2.2 Derivation of Explicit Rate Equations

The main objective of this section is to derive a mechanistic kinetic model for the Rh/BIPHEPHOS-catalyzed hydroformylation of alkenes, which describes the observed complex reaction network for a broad range of process conditions by the implementation of the more detailed reaction mechanism. Since it includes the elementary steps in the catalytic cycles, it should possess the potentials to be valid in a wide range of reaction conditions (temperature, pressure, gas composition, etc.) and to increase the extrapolability as the main objective.

Concept of Mechanistic Kinetic Modeling

The Basic Idea and “Recipe” for the Derivation of Mechanistic Rate Equations

Mechanistic models are a powerful possibility for the mathematical description of reaction rates. A postulated reaction mechanism can be evaluated to generate microkinetic models, which consider the corresponding elementary reactions and the concentrations of the individual catalyst species. Based on mathematical algorithms developed already in 1931 by Christiansen [42], kinetic models can be derived, considering single and multistep reactions as well as catalyst cycles, external catalyst equilibria and possible inhibition steps [104]. In the following section, the derivation of such models is explained in short, for a simple cycle based on [104]. More theoretical background and examples are available in [104, 167].

reverse $\lambda_{i+1,i}$ coefficients. The denominator, D_{0k} , elements are calculated by constructing a square matrix of order k , with unity on the diagonal, with forward-coefficients, $\lambda_{i,i+1}$, in all rows above the diagonal and with reverse, $\lambda_{i+1,i}$, coefficients in all rows below the diagonal. D_{0k} results from the sum of the products of the elements in each row (eq. (3.24)) [104].

$$\begin{bmatrix} 1 & & & \lambda^+ \\ & 1 & & \\ & & \ddots & \\ \lambda^- & & & 1 \end{bmatrix} D_{0k} = \sum_{j=1}^k \left(\prod_{i=1}^{j-1} \lambda_{i,i-1} \prod_{i=j}^{k-1} \lambda_{i,i+1} \right) \quad (3.24)$$

This methodology can be extended in a straightforward fashion to describe catalytic cycles. In this case, eq. (3.25) applies to quantify the reaction rate. Here, the total catalytic mass, $c_{cat,tot}$, as well as its distribution is considered in the reaction rates expressed by the Christiansen matrix, \mathcal{C} . Christiansen mathematics offer a general, flexible tool and allow considering the distribution of the catalyst species in a catalytic cycle.

$$r_p = \left(\prod_{i=0}^{k-1} \frac{\lambda_{i,i+1}}{\mathcal{C}_{\mathcal{S}}} - \prod_{i=0}^{k-1} \frac{\lambda_{i+1,i}}{\mathcal{C}_{\mathcal{S}}} \right) c_{cat,tot} = \frac{(\lambda^+ - \lambda^-) c_{cat,tot}}{\mathcal{C}_{\mathcal{S}}} \quad (3.25)$$

The indices 0 and k refer to the free catalyst. The denominator, $\mathcal{C}_{\mathcal{S}}$, is the sum of all elements of the Christiansen matrix, \mathcal{C} . The Christiansen matrix, \mathcal{C} , contains the concentration of an intermediate in one row. This leads directly to one of Christiansen's key conclusions: The sum of the elements of each row is proportional to the concentration of one species involved in the catalytic cycle [104]. Consequently, concentration ratios between an intermediate, c_j , and the total catalytic mass, $c_{cat,tot}$, can be easily formulated (eq. (3.26)). The detailed composition of the Christiansen matrix, \mathcal{C} , will be exemplified later in Section 3.2.2.2.

$$\frac{c_j}{c_{cat,tot}} = \frac{D_{jj}}{\mathcal{C}_{\mathcal{S}}} = \frac{\text{sum of the row } (j+1)}{\text{sum of all elements}} \quad (3.26)$$

Extension of the Concept to Combine Catalytic Cycles with External Equilibrium Reactions

Catalytic cycles are often connected with additional external equilibrium reactions such as inhibitions, with external catalyst equilibria, or with multiple cycles originating from the same catalytic species in different side reactions. Thus, the total catalyst mass in the cycle is affected and must be considered in the reaction rate model. In Figure 3.48a, a network combined with an external reaction is shown. X_j or any other intermediate can form an inactive catalyst species, and the external path can consist of one or more reactions. Based on eq. (3.25) the total catalyst

concentration must be replaced by the concentration of the active catalyst in the respective cycle, $c_{cat,\omega}$ [104].

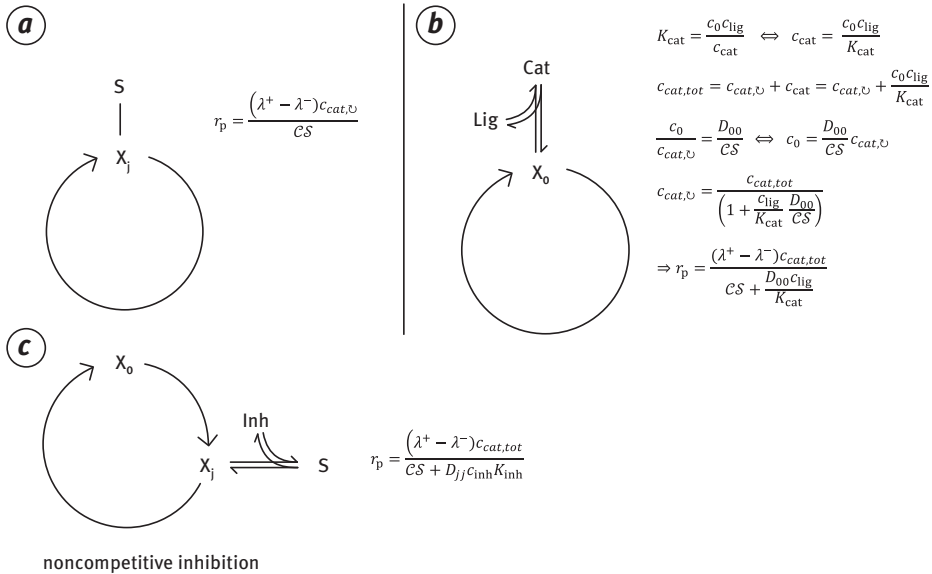


Figure 3.48: Catalyst cycle with external reactions and connected a) with random intermediate; b) with one external equilibrium and c) with non-competitive inhibition [104].

In catalysis, the formation of an active catalytic species from a resting state often requires the decooordination of a ligand. This can be represented by an external catalytic equilibrium, so that the active catalytic mass in the cycle, $c_{cat,\omega}$ could be described by an equilibrium constant, K_{cat} . For the total catalytic mass balance, $c_{cat,tot} = c_{cat,\omega} + c_{cat}$ (Figure 3.48b) holds. The relation of the concentration of the active catalyst material in the cycle and of the free catalyst, X_0 , is given in eq. (3.26). External reactions with more than one equilibrium could be described by considering each equilibrium separately. By introducing the coefficient, \mathfrak{R}'_{i0} , the ratio of the product of co-reactants to the product of co-products, eq. (3.27) results for any number of external equilibria, m [104]:

$$r_p = \frac{(\lambda^+ - \lambda^-) c_{cat,tot}}{C_S + \frac{D_{00}}{\sum_{i=1}^m (\mathfrak{R}'_{i0} K'_{i0})}} \quad \text{with} \quad \mathfrak{R}'_{i0} = \frac{\prod \text{co-reactant}}{\prod \text{co-product}} \quad (3.27)$$

where m is the number of species along the external pathway.

Special forms of external equilibria are often related to inhibitions of catalyst species in the cycle that can reduce the active catalyst mass. Two cases can be distinguished: In the case of *competitive inhibition*, the inhibitor reacts with the catalyst species, X_0 , that initiates the reaction through the binding of the substrate, C . In the case of *noncompetitive inhibition*, the inhibitor reacts with another species of the catalytic cycle, X_j [104] (Figure 3.48c). Both cases are covered by the more general equation given in Figure 3.48c, where K_{inh} is the equilibrium constant of the inhibition reaction $inh + X_j S$ [104].

Reduction of the Christiansen Matrix

The description of multistep catalyst cycles with the approach discussed above is complex due to the large number of intermediates considered for a general kinetic description. A systematic analysis could be used to reduce the Christiansen matrix. Important useful concepts are:

- the evaluation of the relative abundance of catalyst-containing species
- the specification of a rate-determining step
- considering certain steps as irreversible

If the catalyst is present in a cycle almost completely in the form of just one species, this species is called the “most abundant catalyst-containing species” (MACS). Then, the catalyst cycle can be reduced into an imaginary simple pathway that starts and ends with the MACS and one row of the Christiansen matrix becomes dominant [104].

In contrast, only one row can be neglected if an intermediate is deficient (least abundant catalyst-containing species, LACS). In this case, all other intermediates dominate the reaction rate [104].

By identifying a rate-determining step in the catalytic cycle, the corresponding λ -coefficients of the step are neglectable, compared to the coefficients of the other reaction steps. Thus, all terms of the Christiansen matrix that contain the rate-determining step can be disregarded for specifying the reaction rate (Figure 3.49) [122, 132]. Whenever a certain step in the catalytic cycle is chemically irreversible, the respective reverse reaction and all corresponding terms become zero (Figure 3.49).

Illustration for the Hydroformylation Reaction

Based on the postulated catalytic cycle (Figure 3.46), rate equations for the hydroformylation reaction will be derived. The main reaction of hydroformylation of the 1-alkene to the linear aldehyde (**nHYFO**) is selected as an example.

The **nHYFO** cycle in Figure 3.46 consists of six intermediates and several external equilibria, among which the total amount of catalyst, $c_{Rh, tot}$, is distributed. As external equilibria, the inhibition of intermediate **5n** by CO is considered, as well as the catalyst distribution in the catalyst pre-equilibrium. For the latter, three catalyst

species, namely a Rh-hydrido-dicarbonyl complex (**RS**), Rh-tetracarbonyl (**TC**) and Rh-dimer (**Dimer**), are considered in the model derivation. By combining eq. (3.27) with $m = 3$ species along the external pathway and the equation given in Figure 3.48c for a single inhibition step, the following reaction equation results for the hydroformylation to the linear aldehyde:

$$r_{\text{nHYFO}} = \frac{(\lambda^+ - \lambda^-)c_{\text{Rh,tot}}}{c_{\text{nHYFO}} + \frac{D_{11}}{\sum_{i=1}^3 \left(\frac{c_{i0}}{K_{i0}} \right)} + D_{jj}c_{\text{inh}}K_{\text{inh}}} \quad (3.28)$$

Incorporation of the equilibrium constant, $K_{\text{inh}} = K_{5\text{nCO}}$, leads to:

$$r_{\text{nHYFO}} = \frac{(\lambda^+ - \lambda^-)c_{\text{Rh,tot}}}{c_{\text{nHYFO}} + D_{11} \left[\left(\frac{c_{\text{CO}}}{K_{\text{RS},1}} \right) + \left(\frac{c_{\text{BPP}}}{c_{\text{CO}}K_{\text{TC},1}} \right) + \left(\frac{c_{\text{BPP}}c_{\text{H}_2}}{c_{\text{CO}}c_{\text{TC}}K_{\text{dimer}}} \right) \right] + D_{55}c_{\text{CO}}K_{5\text{nCO}}} \quad (3.29)$$

The forward and reverse λ -coefficients involve the product of the reaction rate constant, k , and the co-reactants (eq. (3.30)) based on Table 3.4.

$$r_{\text{nHYFO}} = \frac{(\lambda_{12}\lambda_{23n}\lambda_{3n4n}\lambda_{4n5n}\lambda_{5n6n}\lambda_{6n1} - \lambda_{21}\lambda_{3n2}\lambda_{4n3n}\lambda_{5n4n}\lambda_{6n5n}\lambda_{16n})c_{\text{Rh,tot}}}{c_{\text{nHYFO}} + D_{11} \left[\left(\frac{c_{\text{CO}}}{K_{\text{RS},1}} \right) + \left(\frac{c_{\text{BPP}}}{c_{\text{CO}}K_{\text{TC},1}} \right) + \left(\frac{c_{\text{BPP}}c_{\text{H}_2}}{c_{\text{CO}}c_{\text{TC}}K_{\text{dimer}}} \right) \right] + D_{55}c_{\text{CO}}K_{5\text{nCO}}} \quad (3.30)$$

Table 3.4: Derivation of the λ -coefficients for the hydroformylation to the linear aldehyde (nHYFO), according to the reaction mechanism illustrated in Figure 3.46.

Forward reaction		Backward reaction	
Olefin coordination (1 → 2)	$\lambda_{12} = k_{12}c_{1D}$	Olefin decoordination (2 → 1)	$\lambda_{21} = k_{21}$
Olefin insertion (2 → 3n)	$\lambda_{23n} = k_{23n}$	β -H-elimination (3n → 2)	$\lambda_{3n2} = k_{3n2}$
CO coordination (3n → 4n)	$\lambda_{3n4n} = k_{3n4n}c_{\text{CO}}$	CO decoordination (4n → 3n)	$\lambda_{4n3n} = k_{4n3n}$
CO insertion (4n → 5n)	$\lambda_{4n5n} = k_{4n5n}$	CO extrusion (5n → 4n)	$\lambda_{5n4n} = k_{5n4n}$
Oxidative addition of H ₂ (5n → 6n)	$\lambda_{5n6n} = k_{5n6n}c_{\text{H}_2}$	Reductive elimination of H ₂ (6n → 5n)	$\lambda_{6n5n} = k_{6n5n}$
Reductive elimination of prod. (6n → 1)	$\lambda_{6n1} = k_{6n1}$	Oxidative addition of prod. (1 → 6n)	$\lambda_{16n} = k_{16n}c_{\text{nAld}}$

The Christiansen matrix, c_{nHYFO} , (eq. (3.31)) for a cycle of six intermediates consists of a 6×6-matrix, which is represented as a composition of six column vectors, A_1 to A_6 , for a clearer presentation. The derived products of λ -coefficients are summarized in the following:

$$\begin{aligned}
 c_{nHYFO} &= (A_1 \ A_2 \ A_3 \ A_4 \ A_5 \ A_6) \\
 A_1 &= \begin{pmatrix} \lambda_{23n} \lambda_{3n4n} \lambda_{4n5n} \lambda_{5n6n} \lambda_{6n1} \\ \lambda_{3n4n} \lambda_{4n5n} \lambda_{5n6n} \lambda_{6n1} \lambda_{12} \\ \lambda_{4n5n} \lambda_{5n6n} \lambda_{6n1} \lambda_{12} \lambda_{23n} \\ \lambda_{5n6n} \lambda_{6n1} \lambda_{12} \lambda_{23n} \lambda_{3n4n} \\ \lambda_{6n1} \lambda_{12} \lambda_{23n} \lambda_{3n4n} \lambda_{4n5n} \\ \lambda_{12} \lambda_{23n} \lambda_{3n4n} \lambda_{4n5n} \lambda_{5n6n} \end{pmatrix}; \quad A_2 = \begin{pmatrix} \lambda_{21} \lambda_{3n4n} \lambda_{4n5n} \lambda_{5n6n} \lambda_{6n1} \\ \lambda_{3n2} \lambda_{4n5n} \lambda_{5n6n} \lambda_{6n1} \lambda_{12} \\ \lambda_{4n3n} \lambda_{5n6n} \lambda_{6n1} \lambda_{12} \lambda_{23n} \\ \lambda_{5n4n} \lambda_{6n1} \lambda_{12} \lambda_{23n} \lambda_{3n4n} \\ \lambda_{6n5n} \lambda_{12} \lambda_{23n} \lambda_{3n4n} \lambda_{4n5n} \\ \lambda_{16n} \lambda_{23n} \lambda_{3n4n} \lambda_{4n5n} \lambda_{5n6n} \end{pmatrix} \\
 A_3 &= \begin{pmatrix} \lambda_{21} \lambda_{3n2} \lambda_{4n5n} \lambda_{5n6n} \lambda_{6n1} \\ \lambda_{3n2} \lambda_{4n3n} \lambda_{5n6n} \lambda_{6n1} \lambda_{12} \\ \lambda_{4n3n} \lambda_{5n4n} \lambda_{6n1} \lambda_{12} \lambda_{23n} \\ \lambda_{5n4n} \lambda_{6n5n} \lambda_{12} \lambda_{23n} \lambda_{3n4n} \\ \lambda_{6n5n} \lambda_{16n} \lambda_{23n} \lambda_{3n4n} \lambda_{4n5n} \\ \lambda_{16n} \lambda_{21} \lambda_{3n4n} \lambda_{4n5n} \lambda_{5n6n} \end{pmatrix}; \quad A_4 = \begin{pmatrix} \lambda_{21} \lambda_{3n2} \lambda_{4n3n} \lambda_{5n6n} \lambda_{6n1} \\ \lambda_{3n2} \lambda_{4n3n} \lambda_{5n4n} \lambda_{6n1} \lambda_{12} \\ \lambda_{4n3n} \lambda_{5n4n} \lambda_{6n5n} \lambda_{12} \lambda_{23n} \\ \lambda_{5n4n} \lambda_{6n5n} \lambda_{16n} \lambda_{23n} \lambda_{3n4n} \\ \lambda_{6n5n} \lambda_{16n} \lambda_{21} \lambda_{3n4n} \lambda_{4n5n} \\ \lambda_{16n} \lambda_{21} \lambda_{3n2} \lambda_{4n5n} \lambda_{5n6n} \end{pmatrix} \\
 A_5 &= \begin{pmatrix} \lambda_{21} \lambda_{3n2} \lambda_{4n3n} \lambda_{5n4n} \lambda_{6n1} \\ \lambda_{3n2} \lambda_{4n3n} \lambda_{5n4n} \lambda_{6n5n} \lambda_{12} \\ \lambda_{4n3n} \lambda_{5n4n} \lambda_{6n5n} \lambda_{16n} \lambda_{23n} \\ \lambda_{5n4n} \lambda_{6n5n} \lambda_{16n} \lambda_{21} \lambda_{3n4n} \\ \lambda_{6n5n} \lambda_{16n} \lambda_{21} \lambda_{3n2} \lambda_{4n5n} \\ \lambda_{16n} \lambda_{21} \lambda_{3n2} \lambda_{4n3n} \lambda_{5n6n} \end{pmatrix}; \quad A_6 = \begin{pmatrix} \lambda_{21} \lambda_{3n2} \lambda_{4n3n} \lambda_{5n4n} \lambda_{6n5n} \\ \lambda_{3n2} \lambda_{4n3n} \lambda_{5n4n} \lambda_{6n5n} \lambda_{16n} \\ \lambda_{4n3n} \lambda_{5n4n} \lambda_{6n5n} \lambda_{16n} \lambda_{21} \\ \lambda_{5n4n} \lambda_{6n5n} \lambda_{16n} \lambda_{21} \lambda_{3n2} \\ \lambda_{6n5n} \lambda_{16n} \lambda_{21} \lambda_{3n2} \lambda_{4n3n} \\ \lambda_{16n} \lambda_{21} \lambda_{3n2} \lambda_{4n3n} \lambda_{5n4n} \end{pmatrix} \quad (3.31)
 \end{aligned}$$

The denominator of the reaction rate, c_{nHYFO}^{\ominus} , is formed by the sum of all elements in the Christiansen matrix (eq. (3.32)).

$$\begin{aligned}
 c_{nHYFO}^{\ominus} &= D_{11} + D_{22} + D_{33} + D_{44} + D_{55} + D_{66} \\
 D_{11} &= \lambda_{23n} \lambda_{3n4n} \lambda_{4n5n} \lambda_{5n6n} \lambda_{6n1} + \lambda_{21} \lambda_{3n4n} \lambda_{4n5n} \lambda_{5n6n} \lambda_{6n1} + \lambda_{21} \lambda_{3n2} \lambda_{4n5n} \lambda_{5n6n} \lambda_{6n1} \\
 &\quad + \lambda_{21} \lambda_{3n2} \lambda_{4n3n} \lambda_{5n6n} \lambda_{6n1} + \lambda_{21} \lambda_{3n2} \lambda_{4n3n} \lambda_{5n4n} \lambda_{6n5n} \\
 D_{22} &= \lambda_{3n2} \lambda_{4n3n} \lambda_{5n6n} \lambda_{6n1} \lambda_{12} + \lambda_{3n2} \lambda_{4n5n} \lambda_{5n6n} \lambda_{6n1} \lambda_{12} + \lambda_{3n2} \lambda_{4n3n} \lambda_{5n6n} \lambda_{6n1} \lambda_{12} \\
 &\quad + \lambda_{3n2} \lambda_{4n3n} \lambda_{5n4n} \lambda_{6n1} \lambda_{12} + \lambda_{3n2} \lambda_{4n3n} \lambda_{5n4n} \lambda_{6n5n} \lambda_{12} + \lambda_{3n2} \lambda_{4n3n} \lambda_{5n4n} \lambda_{6n5n} \lambda_{16n} \\
 D_{33} &= \lambda_{4n5n} \lambda_{5n6n} \lambda_{6n1} \lambda_{12} \lambda_{23n} + \lambda_{4n3n} \lambda_{5n6n} \lambda_{6n1} \lambda_{12} \lambda_{23n} + \lambda_{4n3n} \lambda_{5n4n} \lambda_{6n1} \lambda_{12} \lambda_{23n} \\
 &\quad + \lambda_{4n3n} \lambda_{5n4n} \lambda_{6n5n} \lambda_{12} \lambda_{23n} + \lambda_{4n3n} \lambda_{5n4n} \lambda_{6n5n} \lambda_{16n} \lambda_{23n} + \lambda_{4n3n} \lambda_{5n4n} \lambda_{6n5n} \lambda_{16n} \lambda_{21} \\
 D_{44} &= \lambda_{5n6n} \lambda_{6n1} \lambda_{12} \lambda_{23n} \lambda_{3n4n} + \lambda_{5n6n} \lambda_{6n1} \lambda_{12} \lambda_{23n} \lambda_{3n4n} + \lambda_{5n4n} \lambda_{6n5n} \lambda_{12} \lambda_{23n} \lambda_{3n4n} \\
 &\quad + \lambda_{5n4n} \lambda_{6n5n} \lambda_{16n} \lambda_{23n} \lambda_{3n4n} + \lambda_{5n4n} \lambda_{6n5n} \lambda_{16n} \lambda_{23n} \lambda_{3n4n} + \lambda_{5n4n} \lambda_{6n5n} \lambda_{16n} \lambda_{21} \lambda_{3n2} \\
 D_{55} &= \lambda_{6n1} \lambda_{12} \lambda_{23n} \lambda_{3n4n} \lambda_{4n5n} + \lambda_{6n5n} \lambda_{12} \lambda_{23n} \lambda_{3n4n} \lambda_{4n5n} + \lambda_{6n5n} \lambda_{16n} \lambda_{23n} \lambda_{3n4n} \lambda_{4n5n} \\
 &\quad + \lambda_{6n5n} \lambda_{16n} \lambda_{21} \lambda_{3n4n} \lambda_{4n5n} + \lambda_{6n5n} \lambda_{16n} \lambda_{21} \lambda_{3n2} \lambda_{4n5n} + \lambda_{6n5n} \lambda_{16n} \lambda_{21} \lambda_{3n2} \lambda_{4n3n}
 \end{aligned}$$

$$D_{66} = \lambda_{12}\lambda_{23n}\lambda_{3n4n}\lambda_{4n5n}\lambda_{5n6n} + \lambda_{16n}\lambda_{23n}\lambda_{3n4n}\lambda_{4n5n}\lambda_{5n6n} + \lambda_{16n}\lambda_{21}\lambda_{3n4n}\lambda_{4n5n}\lambda_{5n6n} \\ + \lambda_{16n}\lambda_{21}\lambda_{3n2}\lambda_{4n5n}\lambda_{5n6n} + \lambda_{16n}\lambda_{21}\lambda_{3n2}\lambda_{4n5n}\lambda_{5n6n} + \lambda_{16n}\lambda_{21}\lambda_{3n2}\lambda_{4n3n}\lambda_{5n4n} \quad (3.32)$$

In the next step, the pseudo first-order rate coefficients, λ , are replaced by the product of the true reaction rate constants, k , and the corresponding co-reactant concentrations given in Table 3.4. To improve clarity, the reaction rate constants are lumped into coefficients Ω to visualize the connection as factors to the co-reactant concentrations, c_{CO} , c_{H_2} and c_{1D} [124]. Subsequently, all matrices can be introduced into the reaction rate expression (eq. 3.30), resulting in the following equation:

$$r_{nHYFO} = \frac{\left(k_{12}k_{23n}k_{3n4n}k_{4n5n}k_{5n6n}k_{6n1}c_{H_2}c_{CO}c_{1D} \right) C_{Rh,tot} - K_{21}k_{3n2}k_{4n3n}k_{5n4n}k_{6n5n}k_{16n}c_{nAld}}{c_{S_{nHYFO}} + \Omega_1 \left[\left(\frac{c_{co}}{K_{RS,1}} \right) + \left(\frac{c_{BPP}}{c_{co}K_{TC,1}} \right) + \left(\frac{c_{BPP}c_{H_2}}{c_{CO}c_{TC}K_{dimer}} \right) \right] + \Omega_5 c_{CO}K_{5nCO}}$$

$$c_{S_{nHYFO}} = \Omega_{15} + \Omega_{16} + (\Omega_{13} + \Omega_{14})c_{H_2} + (\Omega_{11} + \Omega_{12})c_{CO}c_{H_2} \\ + (\Omega_{21} + \Omega_{41} + \Omega_{61})c_{CO}c_{H_2}c_{1D} + (\Omega_{22} + \Omega_{23} + \Omega_{31} + \Omega_{32})c_{H_2}c_{1D} \\ + (\Omega_{24} + \Omega_{25} + \Omega_{33} + \Omega_{34})c_{1D} \\ + (\Omega_{26} + \Omega_{35} + \Omega_{36} + \Omega_{46} + \Omega_{56} + \Omega_{66} + \Omega_{55})c_{nAld} \\ + (\Omega_{42} + \Omega_{43} + \Omega_{51} + \Omega_{52})c_{CO}c_{1D} \\ + (\Omega_{44} + \Omega_{45} + \Omega_{53} + \Omega_{54})c_{CO}c_{nAld} + (\Omega_{62} + \Omega_{63})c_{CO}c_{H_2}c_{nAld} \\ + (\Omega_{64} + \Omega_{65})c_{H_2}c_{nAld}$$

$$\Omega_1 = \Omega_{15} + \Omega_{16} + (\Omega_{13} + \Omega_{14})c_{H_2} + (\Omega_{11} + \Omega_{12})c_{CO}, c_{H_2} \quad (3.33)$$

$$\Omega_5 = (\Omega_{55} + \Omega_{56})c_{nAld} + (\Omega_{53} + \Omega_{54})c_{CO}c_{nAld} + (\Omega_{51} + \Omega_{52})c_{CO}c_{1D}$$

Finally, the constants are lumped together to form a manageable explicit equation suitable for parameter reduction and estimation. Thus, the following overall equation results for the reaction rate of the hydroformylation of the linear aldehyde:

$$r_{nHYFO} = \frac{(K_{nHYFO}^+ c_{H_2} c_{CO} c_{1D} - K_{nHYFO}^- c_{nAld}) C_{Rh,tot}}{K_1 + K_2 + K_3}$$

$$K_1 = 1 + K_{nHYFO}^I c_{H_2} + K_{nHYFO}^{II} c_{CO} c_{H_2} + K_{nHYFO}^{III} c_{CO} c_{H_2} c_{1D} + K_{nHYFO}^{IV} c_{H_2} c_{1D} + K_{nHYFO}^V c_{1D} \\ + K_{nHYFO}^{VI} c_{nAld} + K_{nHYFO}^{VII} c_{CO} c_{1D} + K_{nHYFO}^{VIII} c_{CO} c_{nAld} + K_{nHYFO}^{IX} c_{CO} c_{H_2} c_{nAld} + K_{nHYFO}^X c_{H_2} c_{nAld}$$

$$K_2 = K_{cat}^I c_{co} + K_{cat}^{II} \frac{c_{BPP}}{c_{co}} + K_{cat}^{III} \frac{c_{BPP}c_{H_2}}{c_{CO}c_{TC}} + K_{cat}^{IV} c_{H_2} c_{co} + K_{cat}^V \frac{c_{H_2}c_{BPP}}{c_{co}} + K_{cat}^{VI} \frac{c_{BPP}c_{H_2}^2}{c_{CO}c_{TC}} \\ + K_{cat}^{VII} c_{H_2} c_{co}^2 + K_{cat}^{VIII} c_{H_2} c_{BPP} + K_{cat}^{IX} \frac{c_{BPP}c_{H_2}^2}{c_{TC}}$$

$$K_3 = K_{inh}^I c_{nAld} c_{CO} + K_{inh}^{II} c_{1D} c_{CO}^2 + K_{inh}^{III} c_{nAld} c_{CO}^2 \quad (3.34)$$

Equation (3.34) illustrates the complexity and generality of mechanistic kinetic models for a single catalytic cycle with six intermediates. The derived model for the hydroformylation of the linear aldehyde consists of 22 free parameters. To have a complete description of the hydroformylation network in addition to the free parameter for the double-bond isomerization, the iso-selective hydroformylation and the hydrogenation must be considered. To decrease the complexity of a general model, there are several kinetic model reduction techniques available that support simplifications, as given in the introduction and discussed in detail in the following.

3.2.2.3 Reduction of Kinetic Models

In Section 3.2.2.2, it was illustrated that a general mechanistic kinetic model can be derived from the elementary steps of a catalytic cycle using the Christiansen mathematics. For several connected elementary steps and assumed equilibria, complex multiparameter kinetic models result, if no further simplifications are made. In the following, conceptionally different methods are presented, all of which help reduce the complexity of kinetic models:

- Quantum mechanics
- Mathematical model reduction exploiting experimentally determined kinetic data
- *Operando* spectroscopic techniques

Theoretical methods based on quantum chemistry enable calculating kinetic parameters and to identify rate-determining steps from first-principles calculations. The method will be illustrated below for three reactions, i.e., hydroesterification of methyl 10-undecenoate (10-UME), reductive amination of undecanal and hydroformylation of 1-decene. A second, mathematically based reduction method evaluates the identifiability of kinetic parameters for a given set of experimental input information and helps designing new and more selective experiments. The method is demonstrated for the Rh/BIPHEPHOS-catalyzed isomerization of 1-decene.

Furthermore, the structures of the Christiansen matrices are directly correlated with the concentrations of certain intermediates in the catalytic cycle. Thus, an improved mechanistic understanding of the catalyzed reaction by identification of organometallic intermediates and by analysis of rate-determining steps is of particular importance to reduce the complexity of the kinetic models, reasonably. For the Rh/BIPHEPHOS-catalyzed hydroformylation of 1-decene, selected results of an experimental spectroscopic investigation will be presented.

Quantum Chemistry

Transition metal catalysts are a challenge to computational approaches which are based on solving the electronic Schrödinger equation. Breaking and forming new

chemical bonds between (transition metal) catalyst and substrate/catalyst and intermediates/catalyst and products need to be described accurately by any quantum chemical approach to provide thermodynamic parameters such as Gibbs free energies of a reaction or barriers of chemical transformation steps during a reaction cycle. Those results provide chemical and physical data that are:

- Experimentally not available in literature
- Cannot be resolved experimentally
- Critically dependent on each system (transition metal, ligand, solvent composition, operating conditions)

Using quantum chemical calculations for complex reaction processes such as hydroesterification [116], hydroformylation [118, 145], or reductive amination [117] with large and bulky multidentate ligands is a challenge in terms of accuracy and the number of atoms and electrons that explicitly need to be treated.

Accurate Quantum Chemical Description of Catalytic Processes

Quantum chemical approaches rely on solving the electronic Schrödinger equation in the Born-Oppenheimer approximation:

$$\hat{H}\Psi = [\hat{T} + \hat{V} + \hat{U}]\Psi = \left[\sum_{i=1}^N \left(-\frac{\hbar^2}{2m_i} \nabla^2 \right) + \sum_{i=1}^N V(a_i) + \sum_{i<j}^N V(a_i, a_j) \right] \Psi = E\Psi \quad (3.35)$$

where for the N -electron system, \hat{H} is the Hamiltonian operator, E is the total energy, \hat{T} is the kinetic energy operator, \hat{V} is the potential energy operator from the external field due to positively charged nuclei, and \hat{U} is the electron–electron interaction energy operator. Kohn and Hohenberg first put the use of DFT in electronic structure calculations on a firm theoretical footing in the framework of the two Hohenberg–Kohn theorems [109]. DFT provides an alternative formulation to the Schrödinger equation. In DFT the key variable is the electron density, $\rho(a)$:

$$\rho(a) = N \int d^3 a_2 \dots \int d^3 a_N \Psi^*(a, a_2, \dots, a_N) \Psi(a, a_2, \dots, a_N) \quad (3.36)$$

with $\rho(a) = |\Psi(a)|^2$ as the square of the wavefunction, Ψ .

Thus, the total energy of the system can be formulated as a functional of the electron density alone. The effective single-particle potential is then expressed as the sum of the external potential, $V(a)$, the Coulombic term, and an exchange-correlation functional, E_{XC} , the latter of which is unknown and cannot be determined *a priori*.

$$E[\rho] = T_S[\rho] + J[\rho] + E_{XC}[\rho] + \int V(a)\rho(a)d^3a \quad (3.37)$$

Since eq. (3.37) is exact, the quest for an expression of E_{XC} has provided several useful approaches. The performance of those expressions of E_{XC} in terms of accuracy and error, however, is often non-systematic and can only be assessed by carefully benchmarking various types of exchange-correlation functionals against a wavefunction-based solution of the Schrödinger equation.

For typical reactions of rhodium transition metal complexes from the MOR41 benchmark set [54], a range of representatives of different classes of E_{XC} were calibrated against domain-localized pair natural orbital (DLPNO) coupled-cluster calculations (Figure 3.50).

Figure 3.50 gives the mean absolute deviation of DFT results of eight typical Rh-catalyzed reactions from DLPNO calculations which serve as the benchmark here. These are DFT single-point calculations at the PBE0-D3 optimized structures. For DLPNO, a tight PNO setting and a CBS (3/4) extrapolation scheme for aug-ccpVT(Q)Z basis sets were employed. For DFT calculations, we used a def2-TZVP basis set.

XTB calculations show the largest error, followed by the BP86 and TPSS (meta)-GGAs. The double hybrid PWPB95 results with a MAD of 13 kJ/mol are not superior to the meta-GGA TPSS. PBE0 with dispersion corrections gives the lowest MAD of 9 kJ/mol and was used in all further QM investigations of transition-metal catalysis. This choice corresponds to a versatile compromise between computational efficiency and the accuracy of the calculations.

Catalysis in Solvents: Thermodynamic and Kinetic Parameters – Identification of Rate-Determining Step

A solvent can play multiple roles in catalysis such as bringing catalyst and reactants into soluble forms, being itself a substrate, a co-catalyst, an inhibitor, or a stabilizing agent. This may significantly affect the thermodynamics and kinetics of the chemical process.

Accurate treatment of solvent effects is still a challenge to QM methods. Whereas energetics of reactions in the gas phase can be accurately described (see above). Bulk solvent effects such as polarity and solubility and the participation of explicit solvent molecules in catalytic steps are relevant.

Chemical reaction networks describe the interaction of all chemical species in a complex multi-component mixture. A large number of thermodynamic and kinetic parameters enter the equations to describe chemical equilibria and rate constants. Often, those parameters are not available from the literature or have to be estimated *a priori*, from a series of homologous compounds, solvents, or process conditions. Here, QM calculations are capable of generating missing or uncertain parameters regarding Gibbs free energies of a reaction and reaction rates, and to give their dependence on reaction conditions (temperature and pressure in addition to changes in solvent, ligand, and transition metal). From a complete coverage of possible side reactions, the catalyst's product selectivity and possible reactive branching points in a process can be rationalized. In kinetic network modeling, the rate-determining step (RDS) is decisive for

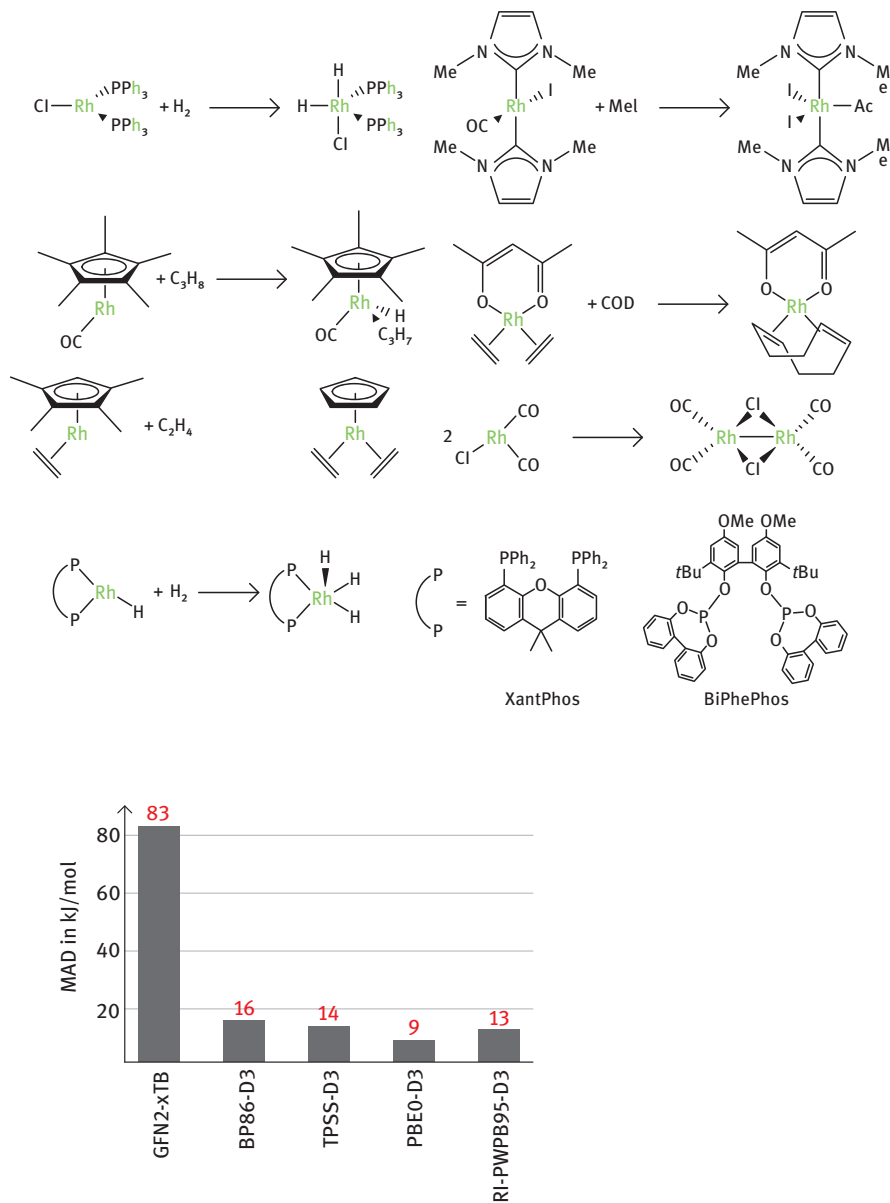


Figure 3.50: QM calculations for typical chemical reactions performed by rhodium(I) catalysts serve as benchmarks for the accuracy of common exchange-correlation functionals. The mean absolute deviation (MAD in kJ mol^{-1}) from coupled-cluster calculations is given.

substrate conversion and product formation and, in principle, can be identified from QM calculations and thus reduce the number of parameters and variables in a kinetic network model, as demonstrated in Section 3.2.2.2.

QM model reduction requires, at first, the identification of all chemical reactions in the complete reaction cycle (Figure 3.51) to provide the thermodynamics (Gibbs free energy) of each step and their respective activation energies (Figure 3.52). The free energy landscape reveals vital information about the thermodynamic driving force of each step, its solvent dependence, and also the solvent dependence of the transition state barriers.

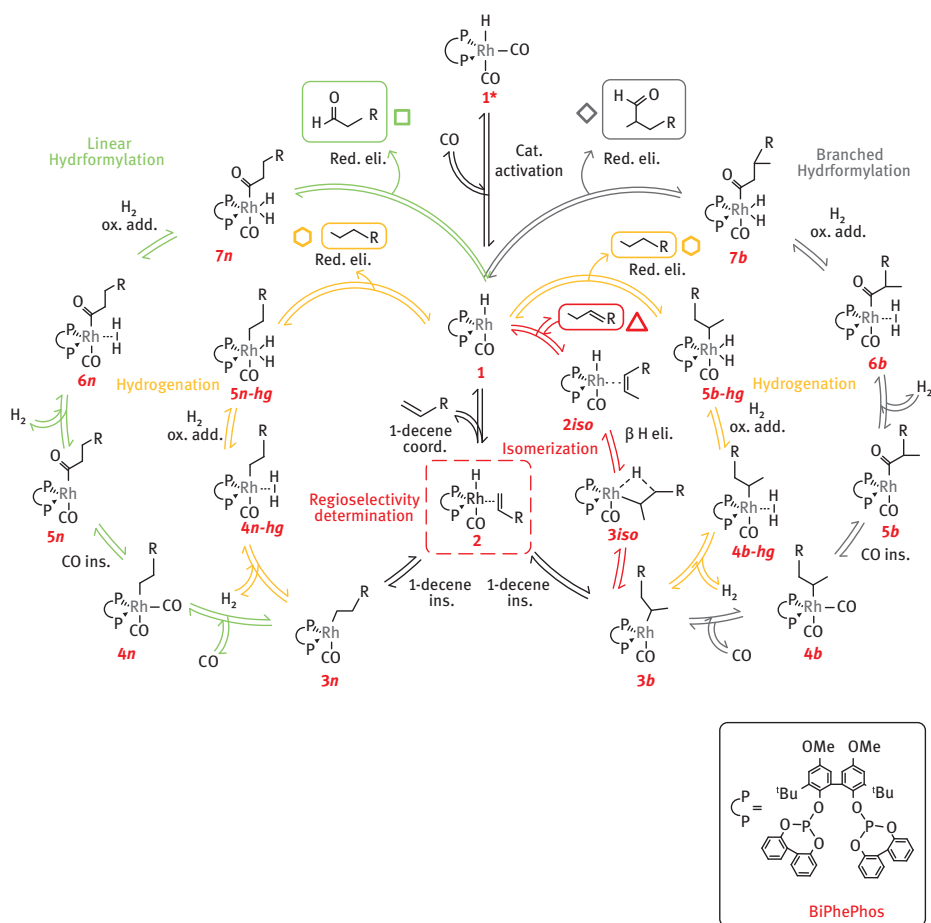


Figure 3.51: One example of the complexity of a chemical process. Catalytic cycle of the hydroformylation reaction of long-chain olefins (1-decene) to give the aldehydes (undecanal), using a bidentate phosphite rhodium(I) catalyst. Besides the desired linear hydroformylation pathway, side reactions such as isomerization, hydrogenation, and the branched hydroformylation are considered [118, 121, 122, 132, 162].

Once all the elementary reactions are characterized, the key chemical reactions influencing rate and selectivity are resolved. The complete reaction mechanisms of three industrially relevant complex reaction cycles, i.e., palladium(II) catalyzed hydroesterification [116], rhodium(I) catalyzed reductive amination [23, 115], and hydroformylation [118] with substrates from renewable resources in solution were elucidated in full mechanistic details. The DFT calculations can give reliable reaction free energies and thus chemical equilibria, which are used as starting parameters in reaction network simulations and global process optimizations [23, 133, 134, 145].

The relevant intermediates and transition states for all these systems are displayed as free energy profiles (Figure 3.52) in gas and solution. An increase of polarity of solvent has a positive effect on the thermodynamics of hydroesterification and hydroformylation, as the reaction equilibrium shifts towards the product side in polar compared to non-polar solvent. However, for the rhodium-catalyzed enamine hydrogenation in the reductive amination process (see the middle column in Figure 3.52), amine formation is more thermodynamically favorable in the non-polar decane, compared to the polar solvent methanol. Those critical reaction parameters can be used as initial guesses for the network model simulations and reduce the complexity of those reaction networks and the computational effort [78, 120, 132, 133].

The steric demand of bulky bidentate ligands coordinated to the transition metals is the major determinant of catalytic selectivity towards desired products, as the bite angle of the ligand dictates the ligand accessibility at the catalyst. In both hydroesterification [116] and hydroformylation [118], selectivity is determined very early in the catalytic cycle. The catalyst, in either case, needs to be activated via dissociation of a pre-coordinated ligand, a solvent in hydroesterification, and CO in hydroformylation. The catalyst activation is always a key step in kinetic parameter estimation, as it directly corresponds to the amount of active catalyst in the system and has a significant impact on the reaction rate [118, 119, 121, 123].

To ensure maximum productivities, possible side reactions must also be identified and their yield minimized. During hydroformylation, olefin double bond isomerization, the hydrogenation of olefins towards alkanes, and the formation of branched aldehydes are possible side reactions. CO, being a strongly coordinating ligand to transition metal catalysts, plays an important role in the suppression of isomerization and hydrogenation during hydroesterification and hydroformylation.

Once the complete reaction pathway is resolved, the RDS can now be identified. For hydroesterification, methanolysis is the RDS with an overall activation energy of 79 kJ mol^{-1} [116], which is in good agreement with the experimental activation energy of 72 kJ mol^{-1} [78]. In addition to direct methanolysis, we have also considered the possibility of a solvent-assisted proton transfer via a proton shuttle and showed that the activation energy of the rate-determining step slightly increases; however, methanolysis via explicit solvent molecules is less likely to occur due to geometric and steric hindrance by the ligand [116]. This further emphasizes the importance of quantum

mechanical calculations, as this kinetic influence of the solvent cannot be obtained experimentally.

In the case of the reductive amination reaction, the overall rate is determined by the reductive elimination of the final amine product [115], which was also confirmed by the experiments for the same catalytic system [133, 134].

QM studies have shown that in hydroformylation, both overall rate and product selectivity towards the desired linear product, are dictated by hydride insertion (RDS) into the olefin, with an overall activation energy of 95 kJ mol^{-1} , which can be used as an initial value for kinetic parameter estimation. The activation energy of the hydrogenation side reaction leading to the alkane is almost 30 kJ mol^{-1} higher than that for aldehyde formation which is in excellent agreement with the experimental kinetic study [122]. Double-bond isomerization of the terminal olefin reactant when coordinated to the catalyst, is a side reaction during the hydroformylation process. It lowers the overall yield and affords a mixture of internal olefins. This can be resolved by kinetic experiments and rationalized by DFT calculations [121].

Summarizing the results of resolving three complex reaction networks, it is now possible to devise a systematic strategy for reliable parameter identification, such as chemical equilibria and RDSs. From Gibbs free energy surfaces of the main and side reactions, the RDS can be identified and be used to reduce the complexity of kinetic reaction network models. In addition, the temperature and solvent dependence of thermodynamic and kinetic parameters can be investigated and inserted directly into network models.

Mathematical Methods for Model Reduction Exploiting Kinetic Data

The mathematical problem of quantifying kinetics in complex reaction networks corresponds with a large number of difficult-to-identify and, often, correlated parameters [136, 161]. As a consequence, the analysis of experimental data frequently leads to ill-posed inverse parameter estimation problems, causing large confidence intervals. Brun et al. [26] considered eigenvalues of sub-matrices of the Fisher-Information matrix, *FIM*, to quantify the identifiability of parameters. This approach inspired the development of the concept of parameter subset selection [30], exploiting singular value decomposition and rank-revealing matrix decomposition [QR factorization techniques, 16, 43, 67, 154, 212], which will be described below.

Parameter Subset Selection

For mathematical parameter identification and Design of Experiments (DoE) of the present complex reaction mechanism of the isomerizing hydroformylation (Figure 3.46), a three-step methodology was developed and applied [108]. The concept is illustrated in Figure 3.53c. In the first step, the reaction mechanism and rate approach are analyzed for identifiability. In particular, a parameter subset selection was carried out, applying the powerful sensitivity matrix, S_{sp} , formed by first experimental data, which

allows the separation of free model parameters into well- and ill-conditioned subsets, to exclude straightforwardly, the ill-conditioned ones from the estimation task. As a result, a reduced, not-overparametrized model can be suggested [132].

In the second step, new experiments will be suggested by a classical DoE. For unknowns with huge confidence intervals, the methodology was applied again, considering additionally the transient behavior of parameter sensitivities during the experiment in the third step. Thus, optimal dynamic control trajectories can be identified and experimentally realized to stimulate single reactions and parameters [73, 108, 120, 122].

The developed methodology using subset selection exploits parameter estimation, by solving an unconstrained nonlinear optimization problem. It is assumed, that the objective function, OF , is of the least square type for the model errors (eq. (3.38)). A standard Newton algorithm can be used to solve the problem with a quadratic approximation [51, 194], to obtain the minimum by optimizing parameters in the vector, $\bar{\Theta}$ (eq. (3.39)).

$$OF(\bar{\Theta}) = \sum_{i=1}^{N_c} \sum_{m=1}^{N_{Ex}} \sum_{n=1}^{N_{Sp}} (c_{i,m,n}^{Ex}(t_n) - c_{i,m,n}(\bar{\Theta}, t_n))^2 \quad (3.38)$$

$$O\nabla OF(\bar{\Theta}) = 0 \quad (3.39)$$

In eq. (3.38), measurements are denoted as a vector of experimental concentrations, $c_{i,m,n}^{Ex}$, at N_{Sp} sampling points for each of the N_{Ex} -analyzed batch/semi-batch experiments. The modeled concentrations from the mechanistic kinetic model are represented by $c_{i,m,n}(\bar{\Theta}, t_n)$, as a transient function of the parameters. An optimum can be found if the inverse of the Hessian $H(\bar{\theta})$ exists. To simplify the calculations, the Hessians were approximated using the Jacobian $J(\bar{\theta})$ (eq. (3.40)), which is possible for small curvatures and near the optimum [182].

$$\begin{aligned} \nabla^2 OF(\bar{\Theta}) &= 2J^T \cdot J = FIM \\ \rightarrow (\nabla^2 OF(\bar{\Theta}))^{-1} &\approx (2J^T J)^{-1} = \frac{1}{2} J^{-1} (J^T)^{-1} = \frac{1}{2} J^{-1} (J^{-1})^T = H^{-1} \end{aligned} \quad (3.40)$$

Optimal parameter values can be found only if the Jacobian of the objective function is invertible. Since the central sensitivity matrix, S_{Sp} (eq. (3.41)), is the inner derivation of J with respect to the parameters, $\bar{\theta}$ [136], it is sufficient to perform a transient singularity analysis regarding S_{Sp} , which depends on the related initial settings and the control profiles of each experiment. To obtain the time-dependent sensitivity matrix, S_{Sp} (eq. (3.41)), the sensitivities, \bar{s}_i , of all variables to all corresponding parameters, $\bar{\theta}_i$, for each point, $p=f(t)$, in each experiment have to be calculated. S_{Sp} depends strongly on the chosen initial conditions and the transient control profiles, (c_i, T, t) in the experiment. Thus, the sensitivities with respect to all

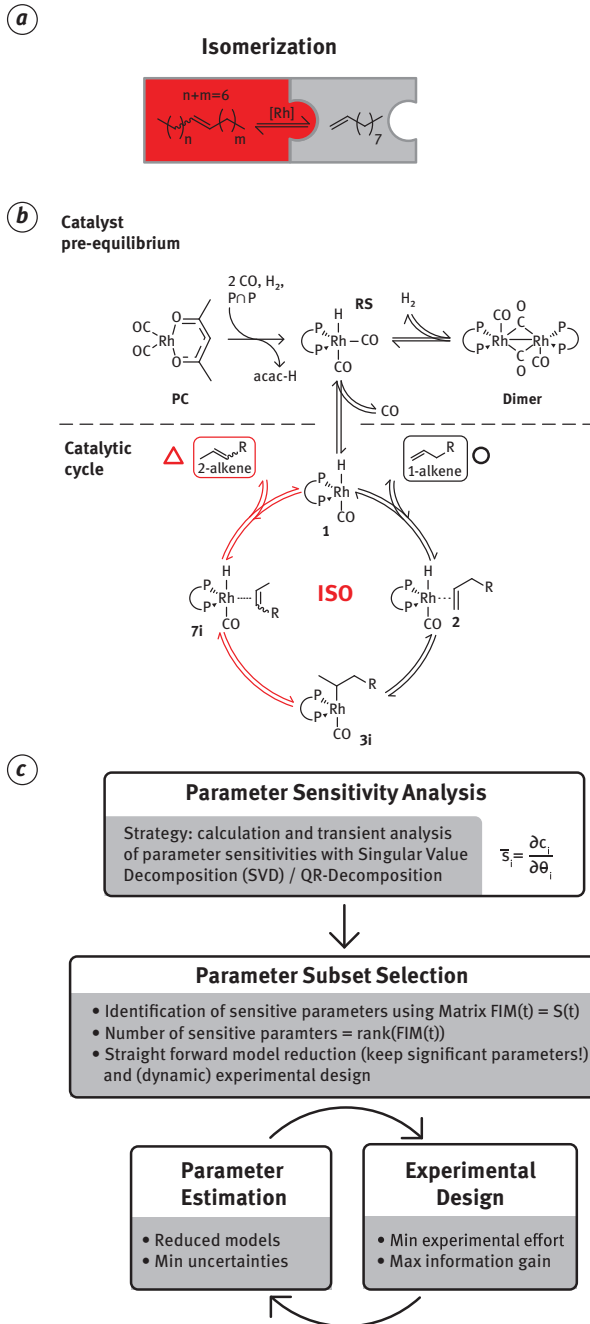


Figure 3.53: Rh/BIPHEPHOS-catalyzed isomerization of 1-decene: a) Simplified reaction network and b) proposed reaction mechanism for the derivation of a mechanistic kinetic model, c) Methodology of parameter subset selection and model reduction [120, 122, 132].

parameters are not constant. It is changing during the experiment, which was systematically used to improve parameter sensitivities by dynamically manipulating c_i and T , in the third step [108, 132].

$$S_{sp} = \begin{bmatrix} \left[\begin{array}{ccc} \bar{s}_1 & \dots & \bar{s}_{N_\theta} \end{array} \right]_{t_1} \\ \vdots \\ \left[\begin{array}{ccc} \bar{s}_1 & \dots & \bar{s}_{N_\theta} \end{array} \right]_{t_{N_p}} \end{bmatrix}_1 \in R^{N_c \cdot N_p \cdot N_{Ex} \times N_\theta} \text{ with } \bar{s}_i = \frac{\partial c_i}{\partial \theta_i}, i:1, \dots, N_\theta \quad (3.41)$$

$$\left[\begin{array}{ccc} \bar{s}_1 & \dots & \bar{s}_{N_\theta} \end{array} \right]_{t_1} \\ \vdots \\ \left[\begin{array}{ccc} \bar{s}_1 & \dots & \bar{s}_{N_\theta} \end{array} \right]_{t_{N_p}} \end{bmatrix}_{N_{Ex}}$$

The identification of well-conditioned parameters is performed in two steps. In the first step, the Fisher-Information matrix, FIM (eq. (3.40)), is decomposed by singular value decomposition (SVD), into a product of three matrices (eq. (3.42)). S_{sp} is expressed for the SVD by a product of orthogonal matrices, A and B , with the diagonal matrix, Υ , which is formed by the singular values of v_i :

$$S_{sp} = A\Upsilon B \quad \text{with } \Upsilon = \begin{bmatrix} v_1 & \dots & 0 \\ \vdots & \ddots & \vdots \\ 0 & \dots & v_{N_\theta} \end{bmatrix}, \quad v_1 > v_i > v_{N_p} \quad (3.42)$$

Subsequently, the parameters have to be ranked according to, e.g., their decreasing sensitivities, by a rank-revealing QR-decomposition (QRD) algorithm. The quantity required is now the condition number, κ_i , which evaluates the ratios of the maximum singular value, v_{max} , to any other singular values, v_i (eq. (3.43)). The rank of a matrix becomes the number of condition numbers, κ_i , with values less than a numerical tolerance. The latter depends on the largest dimension of the matrix, which is the number of parameters, N_p , and the square root of the machine precision provided [120].

$$\kappa_i = \frac{v_{max}}{v_i} \leq tol = \frac{1}{N_p \sqrt{\text{computer precision}}} \quad (3.43)$$

Finally, the remaining question is which of the parameters are well-conditioned. This can be answered in the next step, using the following rank-revealing QR-decomposition [111]:

$$S_{sp}P = QR \quad (3.44)$$

$$\psi_{p_1} \geq \psi_{p_2} \geq \dots \geq \psi_{p_{N_\theta}} \quad (3.45)$$

In eq. (3.44), $Q \in \mathbb{R}^{N_c \cdot N_{sp} \cdot N_{ex} \times N_\theta}$ is an orthogonal satisfying $Q^T Q = I_{N_\theta}$, $R \in \mathbb{R}^{N_\theta \times N_\theta}$ is an upper triangular matrix, and $P \in \mathbb{R}^{N_\theta \times N_\theta}$ is a permutation matrix [111]. The most important information is that P sorts the columns of S_{sp} in a way that the corresponding singular values, ψ_{p_i} , decrease sequentially (eq. (3.45)). If the graded sensitivity matrix, $S_{sp}P$ (eq. (3.44)), is reduced by taking only the first N'_θ columns of the matrix product, $S_{sp}P$, the corresponding parameters can be identified, and the parameter estimation problem becomes well-conditioned, with respect to the selected parameter subset.

Illustration of Model Reduction: Isomerization Kinetics

The introduced methodology for parametrizing the mechanistic kinetic model of the isomerization of 1-decene (Figure 3.53a) is illustrated in this section. Details can be found in [120]. The internal decenes were lumped into the pseudo component isodecenes. A reaction mechanism (Figure 3.53b) was proposed similar to Figure 3.46, which differs mainly in the catalyst pre-equilibrium. Herein, the formation of **RS** from the precursor, **PC**, was treated as a single irreversible reaction and a different Rh-Dimer was considered. The distribution of the total rhodium concentration over the species **RS**, **Dimer** and **1** were considered in eq. (3.46), and equilibrium constants were formulated (eq. (3.47)).

$$C_{Rh, tot} = C_{cat, RS} + C_{cat, Dimer} + C_{cat, 1} \quad (3.46)$$

$$K_{cat, 1} = \frac{C_{cat, RS}}{C_{cat, 1} C_{CO}^{n_{CO}}} \quad \text{and} \quad K_{cat, 2} = \frac{C_{cat, Dimer} C_{H_2}}{C_{cat, RS}^2} \quad (3.47)$$

Based on the reaction mechanism including the catalyst pre-equilibrium, a mechanistic kinetic model was derived for the isomerization (eq. (3.48) and eq. (3.49)), with eight unknown kinetic parameters as elements of the parameter vector, $\bar{\theta}_{ISO}$ (eq. (3.50)).

$$r_{ISO} = \frac{k_{ISO}(T) \left(c_{1D} - \frac{c_{isoD}}{K_{ISO}^{eq}} \right)}{\left(1 + K_{ISO}^I c_{1D} + K_{ISO}^{II} c_{isoD} + K_{ISO}^{III} \right)} \cdot C_{cat, 1} \quad (3.48)$$

$$C_{cat, 1} = - \frac{c_{H_2} (K_{cat, 1} C_{CO}^{n_{CO}} + 1)}{4K_{cat, 2} K_{cat, 1}^2 C_{CO}^{2n_{CO}}} + \left[\frac{c_{H_2} (K_{cat, 1} C_{CO}^{n_{CO}} + 1)}{4K_{cat, 2} K_{cat, 1}^2 C_{CO}^{2n_{CO}}} \right]^2 + \frac{C_{Rh, tot} c_{H_2}}{2K_{cat, 2} K_{cat, 1}^2 C_{CO}^{2n_{CO}}} \quad (3.49)$$

$$\bar{\theta}_{ISO} = \{ k_{ISO}^\infty, E_{ISO}^A, K_{ISO}^I, K_{ISO}^{II}, K_{ISO}^{III}, K_{cat, 1}, K_{cat, 2}, n_{CO} \} \quad (3.50)$$

Based on the publication of Hentschel et al. [106], an additional parameter for the reaction order with respect to CO (n_{CO}) was introduced to describe an observed, inhibiting influence of CO on the catalyst precursors.

The parameter subset selection was used to test the identifiability of the given kinetic parameter vector, $\bar{\theta}_{ISO}$ (eq. (3.50)). To analyze the kinetic model, numerical isomerization experiments were performed aiming at the analysis of the resulting sensitivity matrix. The resulting time-dependent sensitivity [120] of each parameter of vector, $\bar{\theta}_{ISO}$, is shown in Figure 3.54 for selected experiments. The sensitivity of each kinetic parameter depends on time and reveals maxima for certain conditions. Thus, the parameter sensitivities are significantly influenced by the experimental conditions and the duration of the experiments. Based on the sensitivities, the *FIM* was processed using SVD and QRD resulting in time-dependent condition numbers, κ_i (Figure 3.54e) and transient rank of *FIM* (Figure 3.54f). As the condition numbers, κ_i , of the *FIM* exceed the numerical tolerance at 25 min and 40 min, the rank of *FIM* decreases gradually. Consequently, the number of sensitive parameters in the subset decreases, as it is a function of the rank of the *FIM*. The transient information is condensed in Figure 3.54g for the individual parameters of the kinetic model of the isomerization. The parameters k_{ISO}^∞ , E_{ISO}^A , K_{ISO}^I and n_{CO} are sensitive over the entire duration of the experiment, while parameters K_{ISO}^I and $K_{cat,1}$ lose their sensitivity after 25 min and 40 min, respectively. Most importantly, the parameters, K_{ISO}^{III} and $K_{cat,2}$, do not have any sensitivity at all, which justifies a kinetic model reduction, as these parameters are not identifiable under the considered reaction conditions. Consequently, the kinetic parameters, K_{ISO}^{III} and $K_{cat,2}$, were fixed to physical meaningful values zero and unity, respectively. These values express a slow decoordination rate of 1-decene and the insignificance of the catalyst equilibrium, under H₂-excluding isomerization conditions. Finally, a reduced mechanistic kinetic model for the Rh/BIPHEPHOS-catalyzed isomerization of 1-decene can be formulated, leading to a reduced parameter vector:

$$r_{ISO} = \frac{k_{ISO}(T) \left(c_{1D} - \frac{c_{isoD}}{K_{ISO}^{2q}} \right)}{\left(1 + K_{ISO}^I c_{1D} + K_{ISO}^II c_{isoD} \right)} \cdot c_{cat,1} \quad (3.51)$$

$$c_{cat,1} = - \frac{c_{H_2} (K_{cat,1} c_{CO}^{n_{CO}} + 1)}{4K_{cat,1}^2 c_{CO}^{2n_{CO}}} + \left[\left\{ \frac{c_{H_2} (K_{cat,1} c_{CO}^{n_{CO}} + 1)}{4K_{cat,1}^2 c_{CO}^{2n_{CO}}} \right\}^2 + \frac{c_{Rh,tot} c_{H_2}}{2K_{cat,1}^2 c_{CO}^{2n_{CO}}} \right]^{0.5} \quad (3.52)$$

$$\bar{\theta}_{ISO} = \{ k_{ISO}^\infty, E_{ISO}^A, K_{ISO}^I, K_{ISO}^{II}, K_{ISO}^{III}, K_{cat,1}, K_{cat,2}, n_{CO} \} \quad (3.53)$$

In conclusion, based on applying the mathematical reduction method of subset selection, a complex mechanistic kinetic model was successfully reduced and

parameterized, exploiting the experimental data [120]. In further work not described here, the method was applied for the design of experiments, aiming at the optimization of experimental efforts to maximize the identifiability of kinetic parameters [120].

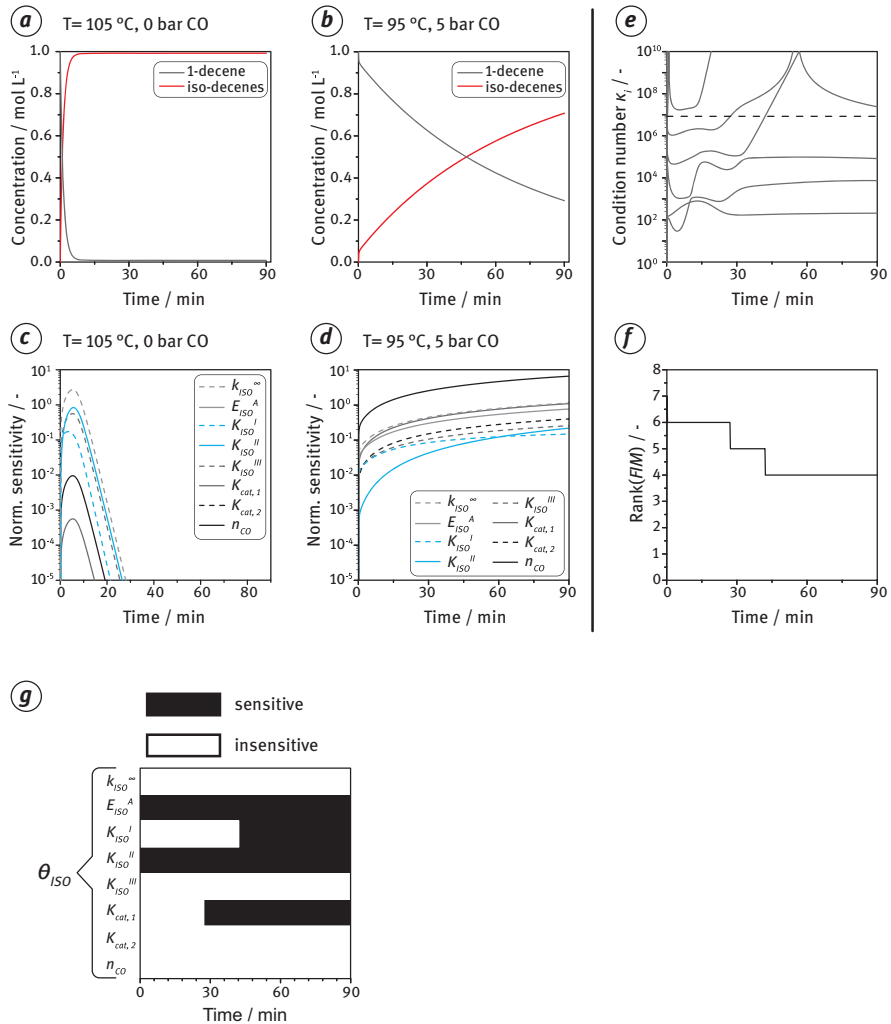


Figure 3.54: a-b) Numerical experiments of 1-decene isomerization at different conditions. c-d) Corresponding normalized transient parameter sensitivities for 1-decene concentration and dynamic sensitivity analysis: e) condition numbers κ_i , f) rank (*FIM*), g) dynamic sensitive parameter subset. Data from [120].

Model Reduction Based on Acquiring and Exploiting *Operando* Spectroscopic Data

Spectroscopic methods can contribute significantly to the mechanistic understanding of reactions. If a catalytic species in the catalytic cycle is a transition metal carbonyl complex, the strong CO vibrations of the same can be used to study intermediates [52]. An important spectroscopic method in this context is the Fourier-transform infrared (FTIR) spectroscopy for the identification of catalytic species.

Fourier-Transform Infrared Spectroscopy

To study the mechanism of the Rh/BIPHEPHOS-catalyzed hydroformylation of 1-decene (Figure 3.55a), a customized FTIR-system was used, which enabled studying the reaction under the same conditions as the kinetic experiments described in Section 3.2.2.1 [123]. Thus, information about catalytic species could be directly correlated to reaction products, under reaction conditions [*operando* spectroscopy, 130].

For this purpose, an autoclave was equipped with a Si-ATR-probe, which was attached to an FTIR spectrometer (Mettler Toledo, ReactIR, resolution 8 cm^{-1} , recorded wavelength $700\text{--}2280\text{ cm}^{-1}$) (Figure 3.43c). The reactor was filled with the solvent toluene and heated to $40\text{ }^\circ\text{C}$. Afterwards, the reaction was studied in different phases, with a particular focus on the metal-carbonyl region ($1900\text{--}2200\text{ cm}^{-1}$), by stepwise addition of catalyst precursor, ligand and substrates to the solution. All operations were performed under an inert gas atmosphere, using Schlenck technique.

In the initial catalyst pretreatment phase (Figure 3.55b), the catalyst precursor, $\text{Rh}(\text{acac})(\text{CO})_2$, was dissolved in toluene and fed into the reactor. Characteristic Rh-carbonyl bands were observed at 2085 cm^{-1} and 2014 cm^{-1} that corresponded to the precursor, $\text{Rh}(\text{acac})(\text{CO})_2$ (**PC1**). The subsequent dosing of diphosphite ligand BIPHEPHOS (Rh:ligand = 1:1.5) led to almost complete displacement of the two CO ligands at the Rh center, which was indicated by the disappearance of the Rh-carbonyl bands assuming the formation of $\text{Rh}(\text{acac})(\text{P} \cap \text{P})$ (**PC2**). By stepwise dosing of H_2 ($p_{\text{H}_2} = 5\text{ bar}$) and CO ($p_{\text{CO}} = 4\text{ bar}$), the Rh-hydrido-dicarbonyl species, **RS**, was formed with two characteristic Rh-carbonyl vibrational bands at 2077 cm^{-1} and 2017 cm^{-1} [123]. The observed bands are consistent with the literature [166, 207], indicating a bisequatorial coordination of the diphosphite ligand.

In the reaction phase (Figure 3.55b), upon addition of the substrate 1-decene (Rh/1-decene = 1:1000, $p_{\text{H}_2} = 5\text{ bar}$, $p_{\text{CO}} = 5\text{ bar}$), no significant change in the Rh-CO bands of **RS** was observed. No significant catalytic intermediates other than the Rh-hydrido-dicarbonyl species, **RS**, were detected during the reaction. Especially, no additional carbonyl bands of the assumed inactive species Rh-tetracarbonyl (**TC**), Rh-dimer (**Dimer**), and Rh-acyl carbonyl (**5nCO**) could be detected [123]. The n-selective hydroformylation to undecanal was monitored up to an alkene conversion of 75%, without significant isomerization or hydrogenation, under the applied reaction conditions.

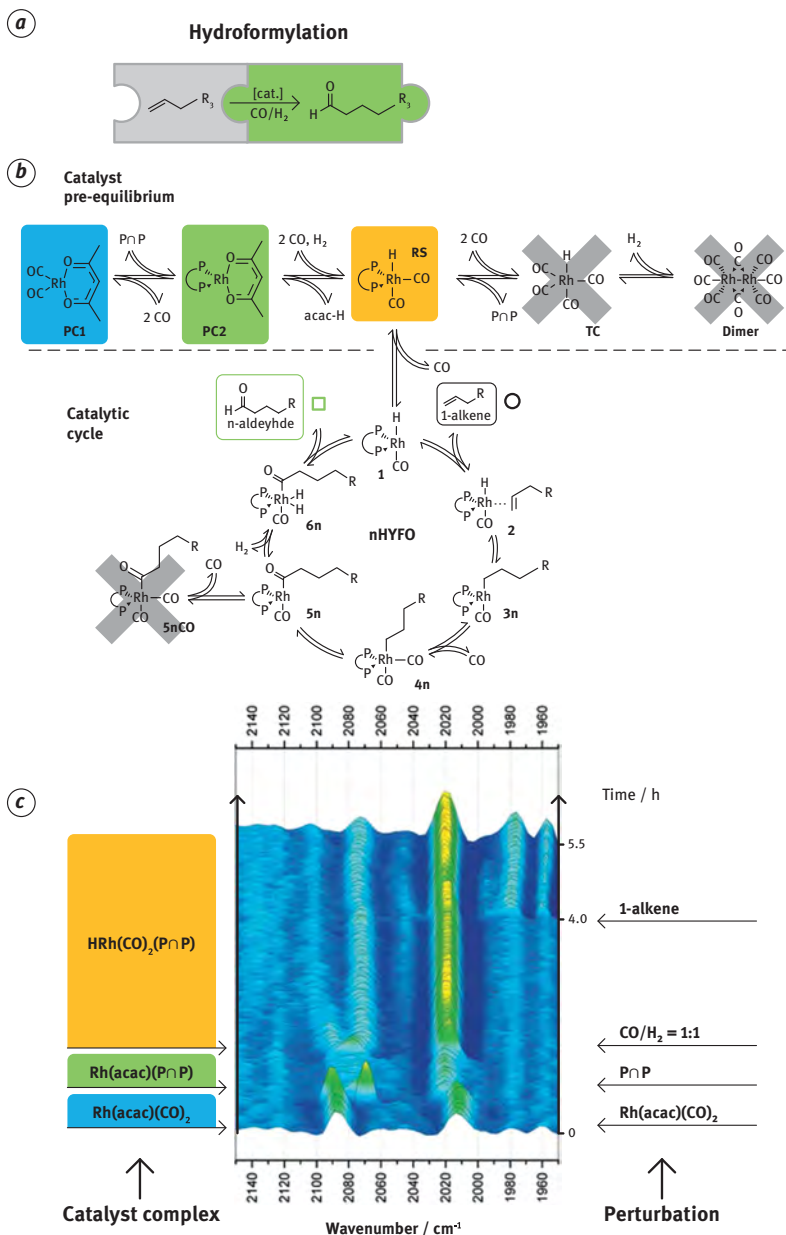


Figure 3.55: Rh/BIPHEPHOS-catalyzed hydroformylation of 1-decene: a) Simplified reaction network; b) proposed reaction mechanism for the derivation of a mechanistic kinetic model; and c) time-dependent *operando* FTIR spectra (Rh:ligand = 1:1.5 mol%, $T = 40^\circ\text{C}$, solvent toluene) of the Rh-CO vibration region for different perturbations to the reaction, revealing the transformation to different Rh-catalyst precursors connected to the proposed mechanism. The second derivative of the absorbance with respect to the wavenumber is shown. Data from [123].

The *operando* FTIR-spectroscopic hydroformylation results suggest the five-coordinated Rh(I)-hydrido-dicarbonyl complex, **RS**, as a stable resting state, which is in equilibrium with the active Rh-hydrido-carbonyl **1** via CO dissociation. Under the applied conditions, no Rh-carbonyl bands of **1** could be detected, pointing to an equilibrium, which is shifted towards the stable complex, **RS** [123]. As no changes in the Rh-CO-bands were detected and no erosion of the usual Rh/BIPHEPHOS chemo- and regioselectivity was observed, a deactivation by, e.g., hydroperoxides [77] could be excluded. This valuable spectroscopic information can be used to reduce the mechanistic kinetic model reasonably in Section 3.2.2.2, as no other significant inactive catalyst species were detected regarding the catalyst pre-equilibrium as well as external equilibria.

Furthermore, an analysis of the characteristic C = O stretching bands at 1729 cm^{-1} of undecanal (Figure 3.56a) and the C = C stretching band of 1-decene (Figure 3.56b) allowed a calculation of the 1-decene conversion as well as the calculation of the turnover frequency, *TOF*, by absorbance normalization [123].

$$TOF = \frac{r_{nHYFO}}{c_{Rh}} \quad (3.54)$$

$$r_{nHYFO} = -\frac{dc_{1D}}{dt} \approx -\frac{\Delta c_{1D}}{\Delta t} \quad (3.55)$$

$$c_{nAld}(t) = X(t) \cdot c_{1D}(t=0) \quad (3.56)$$

Thus, a linear correlation between the *TOF* and the normalized 1-decene concentration was found (Figure 3.56c). The spectroscopic results of a stable inactive **RS** outside of the catalytic cycle, before the start of the reaction sequences, point to an early elementary step to be rate-determining. In combination with the linear dependency of *TOF* on 1-decene concentration, the olefin coordination can be assumed to be the RDS [123].

Model Reduction for Total Hydroformylation Kinetics

The results of the spectroscopic investigations and quantum mechanical calculations allow a significant reduction of the complexity of the derived mechanistic kinetic models. The reduction will be exemplified rigorously for the *n*- and iso-selective hydroformylation, (**nHYFO**, **isoHYFO**), and summarized for the subnetworks of isomerization, (**ISO**), and hydrogenation, (**HYD**), according to the detailed reaction network of the Rh/BIPHEPHOS-catalyzed isomerizing hydroformylation of 1-decene (Figure 3.46). In particular, the 1-alkene coordination was identified as the most probable RDS for the Rh/BIPHEPHOS-catalyzed hydroformylation of 1-decene, which was concluded by both methods. In addition, only a single stable organometallic carbonyl species, **RS**, was identified that operated throughout the catalysis.

Despite the resting state, **RS**, no other inactive species could be detected that would potentially inhibit the catalysis by reducing the amount of available catalyst

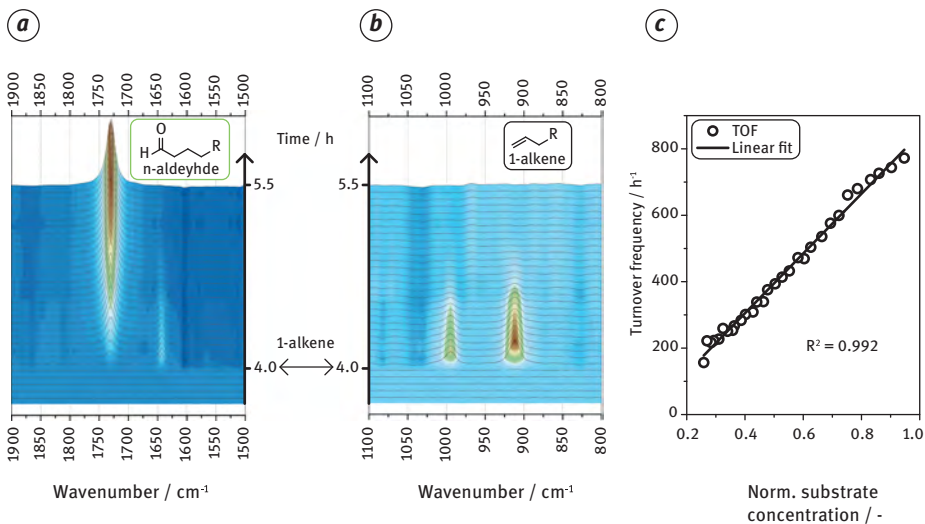


Figure 3.56: *Operando* FTIR spectra under hydroformylation conditions (Rh:ligand = 1:1.5 mol%, $T = 40^\circ\text{C}$, solvent toluene) until 75% conversion of 1-decene: a) C = O and C = C stretching vibrational region, b) C-H bending vibration region, c) Turnover frequency, *TOF* vs. normalized substrate concentration ($1 - X$). Data from [123].

material in the cycle. In the catalyst pre-equilibrium, the saturated inactive resting state $\text{HRh}(\text{BPP})(\text{CO})_2$ (**RS**, Figure 3.46) is assumed to be in quasi-equilibrium with the active unsaturated $\text{HRh}(\text{BPP})(\text{CO})$ (**1**, Figure 3.46) by a fast CO dissociation. Hence, the general eq. (3.28) can be reduced to

$$r_{\text{nHYFO}} = \frac{(\lambda_{12}\lambda_{23n}\lambda_{3n4n}\lambda_{4n5n}\lambda_{5n6n}\lambda_{6n1} - \lambda_{21}\lambda_{3n2}\lambda_{4n3n}\lambda_{5n4n}\lambda_{6n5n}\lambda_{16n})c_{\text{Rh,tot}}}{\mathcal{C}_{\text{S}_{\text{nHYFO}}} + D_{11}\left(\frac{c_{\text{CO}}}{K_{\text{RS},1}}\right)} \quad (3.57)$$

In the next step, the assumption of a rate-determining olefin coordination ($\mathbf{1} \rightarrow \mathbf{2}$, $\lambda_{12} \ll \lambda_{i,j} \rightarrow \lambda_{12} \approx 0$) is applied that leads to a simplification of the sum of the Christiansen matrix, $\mathcal{C}_{\text{S}_{\text{nHYFO}}}$, eq. (3.58). Additionally, the oxidative addition of hydrogen, ($\mathbf{5n} \rightarrow \mathbf{6n}$), as well as the reductive elimination, ($\mathbf{6n} \rightarrow \mathbf{1}$), can be treated as irreversible elementary steps [50, 76, 207], which results in the set of pseudo first-order rate coefficients given in Table 3.5.

In the Christiansen matrix, $\mathcal{C}_{\text{S}_{\text{nHYFO}}}$ (eq. (3.58)), all terms containing the pseudo first-order rate coefficient, λ_{12} (olefin coordination) become negligibly small as did the rate coefficients, λ_{6n5n} and λ_{16n} , resulting in the following equation:

$$\begin{aligned} \mathcal{C}_{\text{S}_{\text{nHYFO}}} = & \lambda_{23n}\lambda_{3n4n}\lambda_{4n5n}\lambda_{5n6n}\lambda_{6n1} + \lambda_{21}\lambda_{3n4n}\lambda_{4n5n}\lambda_{5n6n}\lambda_{6n1} + \lambda_{21}\lambda_{3n2}\lambda_{4n5n}\lambda_{5n6n}\lambda_{6n1} \\ & + \lambda_{21}\lambda_{3n2}\lambda_{4n3n}\lambda_{5n6n}\lambda_{6n1} + \lambda_{21}\lambda_{3n2}\lambda_{4n3n}\lambda_{5n4n}\lambda_{6n1} \end{aligned} \quad (3.58)$$

because $D_{22} = D_{33} = D_{44} = D_{55} = D_{66} = 0$.

Table 3.5: Reduced coefficients, λ , for the hydroformylation of the linear aldehyde including the assumptions of irreversible reactions and the olefin coordination to be rate-determining.

Forward reaction		Backward reaction	
Olefin coordination ($1 \rightarrow 2$)	$\lambda_{12} = k_{12}c_{1D} \approx 0$	Olefin decooordination ($2 \rightarrow 1$)	$\lambda_{21} = k_{21}$
Olefin insertion ($2 \rightarrow 3n$)	$\lambda_{23n} = k_{23n}$	β -H-elimination ($3n \rightarrow 2$)	$\lambda_{3n2} = k_{3n2}$
CO coordination ($3n \rightarrow 4n$)	$\lambda_{3n4n} = k_{3n4n}c_{CO}$	CO decooordination ($4n \rightarrow 3n$)	$\lambda_{4n3n} = k_{4n3n}$
CO insertion ($4n \rightarrow 5n$)	$\lambda_{4n5n} = k_{4n5n}$	CO extrusion ($5n \rightarrow 4n$)	$\lambda_{5n4n} = k_{5n4n}$
Oxidative addition of H ₂ ($5n \rightarrow 6n$)	$\lambda_{5n6n} = k_{5n6n}c_{H_2}$	Reductive elimination of H ₂ ($6n \rightarrow 5n$)	$\lambda_{6n5n} = 0$
Reductive elimination of prod. ($6n \rightarrow 1$)	$\lambda_{6n1} = k_{6n1}$	Oxidative addition of prod. ($1 \rightarrow 6n$)	$\lambda_{16n} = 0$

Finally, by introducing the catalyst equilibrium constant, the mechanistic rate equation (eq. (3.34)) reduces to:

$$r_{nHYFO} = \frac{(\lambda_{12}\lambda_{23n}\lambda_{3n4n}\lambda_{4n5n}\lambda_{5n6n}\lambda_{6n1})C_{Rh,tot}}{D_{11} + D_{11}(K_{cat}^I c_{CO})} \quad (3.59)$$

The application of Table 3.5 leads to the final explicit mechanistic rate equation (eq. (3.60)), after lumping the products of all elementary step rate constants in eq. (3.61):

$$r_{nHYFO} = \frac{k_{12}k_{23n}k_{3n4n}k_{4n5n}k_{5n6n}k_{6n1} c_{1D} c_{CO} c_{H_2}}{\left(\begin{array}{l} k_{21}k_{3n2}k_{4n3n}k_{5n4n}k_{6n1} + \\ (k_{21}k_{3n2}k_{4n5n}k_{5n6n}k_{6n1} + k_{21}k_{3n2}k_{4n3n}k_{5n6n}k_{6n1})c_{H_2} + \\ (k_{23n}k_{3n4n}k_{4n5n}k_{5n6n}k_{6n1} + k_{21}k_{3n4n}k_{4n5n}k_{5n6n}k_{6n1})c_{CO}c_{H_2} \end{array} \right)} \frac{C_{Rh,tot}}{(1 + K_{cat}^I c_{CO})} \quad (3.60)$$

$$r_{nHYFO} = \frac{k_{nHYFO}(T)c_{1D}c_{CO}c_{H_2}}{(1 + K_{nHYFO}^I c_{H_2} + K_{nHYFO}^{II} c_{H_2} c_{CO})} \cdot \frac{C_{Rh,tot}}{(1 + K_{cat}^I c_{CO})} \quad (3.61)$$

Similarly, the description of the formation of branched aldehydes from 1-decene (eq. (3.62)) and iso-decenes (eq. (3.63)) is done using the same structure of the kinetic equation, analogous with different kinetic parameters.

$$r_{isoHYFO,1} = \frac{k_{isoHYFO,1}(T)c_{1D}c_{CO}c_{H_2}}{\left(1 + K_{isoHYFO,1}^I c_{H_2} + K_{isoHYFO,1}^{II} c_{H_2} c_{CO} \right)} \cdot \frac{C_{Rh,tot}}{(1 + K_{cat}^I c_{CO})} \quad (3.62)$$

$$r_{isoHYFO,2} = \frac{k_{isoHYFO,2}(T) \sum_{i=2}^5 (c_{iD}) c_{CO} c_{H_2}}{\left(1 + K_{isoHYFO,2}^I c_{H_2} + K_{isoHYFO,2}^{II} c_{H_2} c_{CO} \right)} \cdot \frac{C_{Rh,tot}}{(1 + K_{cat}^I c_{CO})} \quad (3.63)$$

In principle, all elementary steps are the same, and the same simplifications concluded from the spectroscopic measurements can be applied.

Similar to the hydroformylation, the hydrogenation of 1-decene to decane involves two irreversible elementary steps: the oxidative addition of hydrogen ($3n \rightarrow 7n$), as well as the reductive elimination, ($7n \rightarrow 1$), can be treated as irreversible elementary steps [50, 76, 207]. Describing the elementary steps as mentioned with first-order rate coefficients, introducing the mechanistic rate equation and all subsequent simplifications, the following model results.

$$r_{\text{HYD}} = \frac{k_{12}k_{23n}k_{3n7n}k_{7n1}c_{1D}c_{H_2}}{\left(\frac{k_{21}k_{3n2}k_{7n1} + (k_{23n}k_{3n7n}k_{7n1} + k_{21}k_{3n7n}k_{7n1}) c_{H_2}}{1 + K_{\text{cat}}^I c_{CO}} \right)} \cdot \frac{C_{Rh, \text{tot}}}{(1 + K_{\text{cat}}^I c_{CO})} \quad (3.64)$$

The final mechanistic rate equation could be described by lumping the products of all rate constants in eq. (3.65).

$$r_{\text{HYD}} = \frac{k_{\text{HYD}}(T)c_{1D}c_{H_2}}{(1 + K_{\text{HYD}}c_{H_2})} \cdot \frac{C_{Rh, \text{tot}}}{(1 + K_{\text{cat}}^I c_{CO})} \quad (3.65)$$

In contrast to hydroformylation, isomerization is an equilibrium-limited reaction [119]; thus, all elementary steps are reversible and no simplifications could be made. Nevertheless, the assumption of rate-determining olefin coordination also holds for iso-decenes. This leads to the following final explicit mechanistic model.

$$r_{\text{ISO}, i, (i+1)} = \frac{k_{12}k_{23i}k_{3i7i}k_{7i1}c_{iD} - k_{21}k_{3i2}k_{7i3i}k_{17i}c_{(i+1)D}}{\left(\frac{k_{23i}k_{3i7i}k_{7i1} + k_{21}k_{3i7i}k_{7i1} + k_{21}k_{3i2}k_{7i1} + k_{21}k_{3i2}k_{7i3i}}{1 + K_{\text{cat}}^I c_{CO}} \right)} \cdot \frac{C_{Rh, \text{tot}}}{(1 + K_{\text{cat}}^I c_{CO})} \quad (3.66)$$

A simplified kinetic model for the isomerization used in later follow-up work is obtained, after lumping the products of all elementary step rate constants:

$$r_{\text{ISO}, i, (i+1)} = k_{\text{ISO}, i, (i+1)}(T) \left(c_{iD} - \frac{c_{(i+1)D}}{K_{i, (i+1)}^{\text{eq}}} \right) \cdot \frac{C_{Rh, \text{tot}}}{(1 + K_{\text{cat}}^I c_{CO})} \quad (3.67)$$

3.2.3 Demonstration of Concept for Coupled Networks

In the previous sections, the methodical approach of mechanistic kinetic model derivation and reduction was developed and “trained” for selected subnetworks of the Rh/BIPHEPHOS-catalyzed isomerization and hydroformylation of 1-decene (Figure 3.57a), individually. In this section, the developed methodical approach shall be applied for the isomerizing hydroformylation of decenes by consideration and interconnection of all subnetworks. Furthermore, the transferability and expandability of the developed

mechanistic kinetic models will be demonstrated by the example of Rh/SULFOXANTPHOS-catalyzed tandem HAM of 1-decene (Figure 3.41).

3.2.3.1 Isomerizing Hydroformylation

In order to estimate the parameters of the derived mechanistic kinetic models (eqs. (3.41)–(3.43), (3.45), (3.47)), the differences between experimental data obtained in batch and semi-batch reactor experiments and the corresponding modeling results were minimized, using a standard least-squares solver in Matlab[®]. The overall reaction network consisting of the hydroformylation, isomerization, and hydrogenation was studied individually by application of the individual subnetwork analysis strategy (Figure 3.57b). The control of the gas phase composition enabled “switching off” selected reactions. Thus, after the activation of the catalyst using syngas (CO:H₂ = 1:1), the gas phase composition

- a) was exchanged by CO to study the isomerization only
- b) was exchanged by H₂ to study the hydrogenation and isomerization only
- c) remained unchanged to study hydroformylation, hydrogenation and isomerization

The reaction network was studied with gradually increasing complexity [122, 132] (Figure 3.57b). The results presented below correspond to the most complex case, c).

To study the complex interrelation between hydroformylation and the migration of the double bond for isomerization, 1-decene (Feed 1) and a mixture of internal decenes (Feed 2) were used [122].

Isomerizing Hydroformylation, Feed 1: 1-decene

In the kinetic hydroformylation studies using 1-decene [122], following the kinetic procedures described in Section 3.2.2.1, the isomerization was the most dominant side reaction. At low syngas pressures (Figure 3.58a), high yields of internal decenes were observed. With increasing syngas pressure (Figure 3.58b, c), the chemoselectivity was significantly shifted towards the n-aldehyde undecanal, as the double bond isomerization is inhibited by CO. As clarified by the reaction mechanism, the inhibition by CO is caused by dragging the hydrido-alkene complex **2** (Figure 3.46) into the n-selective pathway by the formation of the Rh-acyl-complex, **5n**, by CO-insertion. The conversion of 1-decene and thus, the activity of the catalyst were independent of the pressure. The modulation of the temperature revealed a significant temperature dependency on chemoselectivity for the hydroformylation, which was shifted towards the isomerization with increasing temperature. In the case of the hydrogenation, only minor yields of decane were observed for all experimental conditions ($\approx 3\%$) for typical hydroformylation conditions using an equimolar mixture of CO and H₂.

The apparent activation energies for the n-selective hydroformylation, (r_{nHYFO}), and iso-selective hydroformylation, (r_{isoHYFO}), were recalculated to 30.3 kJ mol⁻¹

and 56.7 kJ mol^{-1} (eqs. (3.61)–(3.62)), respectively. Thus, to attain high regioselectivity of the hydroformylation, low temperatures should be applied. The local parameter subset selection presented in Section 3.2.2.3 was used additionally to prove high sensitivity and thus, the identifiability of all kinetic parameters for the chosen experimental design. All kinetic parameters revealed high sensitivity and were identifiable, despite the inhibition parameter, $K_{\text{isoHYFO}}^{\text{II}}$, of the iso-selective hydroformylation, $r_{\text{isoHYFO},1}$ and $r_{\text{isoHYFO},2}$ [122].

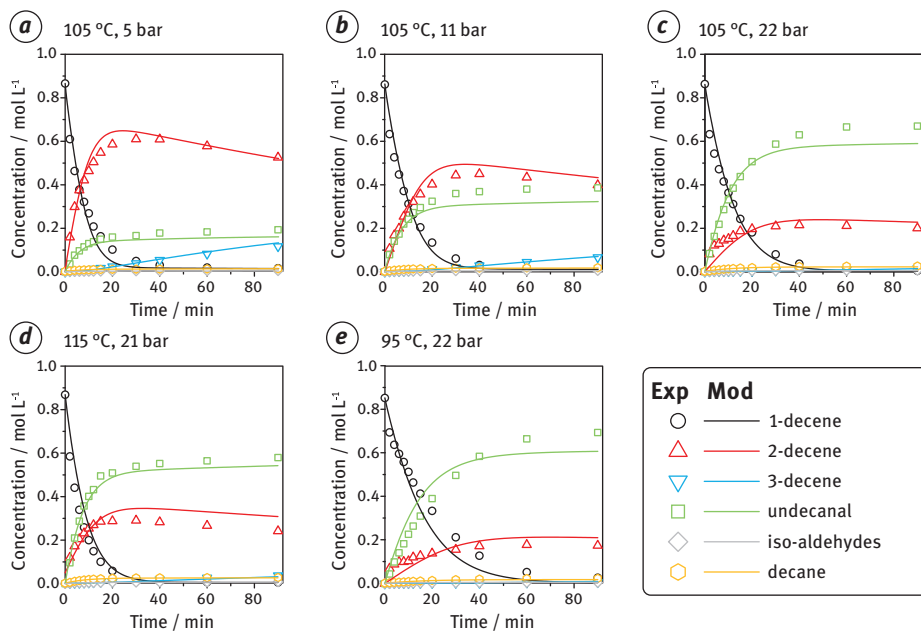


Figure 3.58: Time resolved experimental and modeling results for Rh/BIPHEPHOS-catalyzed isomerizing hydroformylation of 1-decene in batch mode. Additional experimental conditions: $\text{CO:H}_2 = 1:1$, $\text{Rh:1-decene} = 1:10,000$, $\text{Rh/BIPHEPHOS} = 1:3$. Data from [122].

Isomerizing Hydroformylation, Feed 2: iso-decenes

The kinetic experiments on the hydroformylation of 1-decene (Section 3.2.3.1) have shown that the isomerization essentially influences the chemoselectivity of the desired *n*-selective hydroformylation. For the terminal alkenes, this is an undesired side reaction, which can be prevented by an appropriate selection of reaction conditions (low temperatures, high synthesis gas pressure). On the other hand, for the most interesting renewable unsaturated substrates like methyl oleate with an internal double bond or the recycling of isomerized iso-decenes, this is the desired reaction to enable *n*-selective hydroformylation. For process optimization, the mechanistic kinetic models

should also be capable to describe and predict the complex isomerizing hydroformylation, starting from internal substrates like renewables in green chemistry.

The isomerizing hydroformylation of internal iso-decenes is a sophisticated reaction combining double bond isomerization and hydroformylation to achieve high regioselectivity and space–time yields of the desired n-aldehyde. In these experiments, a mixture of internal decenes was used [122]. The composition illustrated in Figure 3.59 corresponded to the equilibrium composition [119, 121] with a minor amount of 1-decene (<1%). Therefore, efficient coupling of isomerization and hydroformylation is necessary.

The dependence of isomerizing hydroformylation of internal decenes revealed an inverse behavior on synthesis gas pressure, compared to 1-decene [122]. The reason for this observation is the complex coupling between catalyst pre-equilibrium, isomerization and hydroformylation, in which CO constitutes a key role. The isomerization of the double bond is essential to achieve the desired n-selective hydroformylation: As 1-decene is converted, the equilibrium composition of internal decenes is disturbed. Consequently, 1-decene must be replenished via isomerization to ensure continuous hydroformylation. In this context, CO plays an ambivalent role in this reaction sequence. On the one hand, CO inhibits the formation of catalytically active species via the formation of the inactive stable resting state, **RS**, in the catalyst pre-equilibrium. On the other hand, CO accelerates the hydroformylation by “dragging” the catalyst mass into the hydroformylation cycle via the formation of the acyl species and, thus, into active species. This results in a negative reaction order for CO in the isomerization.

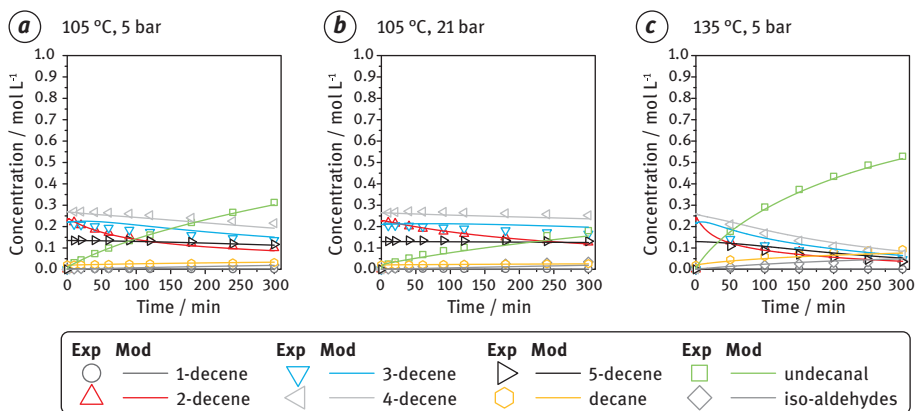


Figure 3.59: Time-resolved experimental and modeling results for Rh/BIPHEPHOS-catalyzed isomerizing hydroformylation of internal iso-decenes in semi-batch mode, with respect to the gas supply. Additional experimental conditions: CO:H₂ = 1:1, Rh:iso-decenes = 1:1000, Rh/BIPHEPHOS = 1:3 (a, b) = 1:5 (c). Data from [122].

To achieve high space–time yields of the desired n-aldehyde undecanal, it is advisable to perform the hydroformylation of terminal 1-decene at a high synthesis gas pressure to avoid isomerization, while low pressures are required for the isomerizing hydroformylation to ensure rapid re-isomerization of the double bond and an acceptable rate of hydroformylation. Furthermore, it could already be shown for the temperature dependence of hydroformylation of 1-decene that the isomerization increases with temperature. Thus, the yield of the undecanal could be increased from 30% to 53%, by elevating the temperature from 105 °C to 135 °C [122].

The good agreement between experimental data and the modeling results is illustrated in parity plots (Figure 3.60) for all performed experiments [122]. No significant systematic model errors can be recognized, even for minor side products of the hydrogenation and iso-selective hydroformylation.

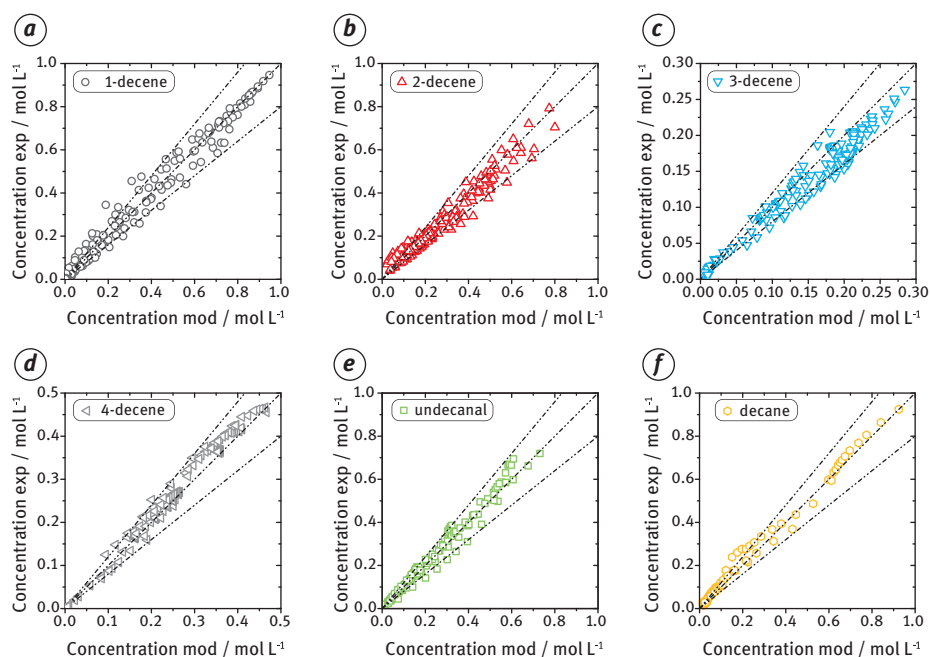


Figure 3.60: Agreement between experimental and modeled concentrations for all kinetic experiments summarized in parity plots for all detected species (experimental conditions similar to Figure 3.59). Data from [122].

In conclusion, the particularly good agreement between experimental data and the model confirms the applicability and broad validity of mechanistic kinetic models for complex catalyzed reactions. For the Rh/BIPHEPHOS-catalyzed hydroformylation of long-chain alkenes, the derivation of general mechanistic kinetic models and the

subsequent reasonable model reduction based on *operando* spectroscopic observations was successfully demonstrated.

3.2.3.2 Overall Reaction Network of Tandem Hydroaminomethylation

In the previous chapters, it could be shown that the application of mechanistic kinetic models is well suited to describe complex reactions. In the following section, the transferability and/or extrapolability of the kinetic model to other temperature and pressure ranges, as well as to other solvent systems and comparable bidentate ligands, will be examined for the total, most complex reaction network of the HAM. The reaction was previously illustrated in Figure 3.41 and is now presented in a reduced form in Figure 3.61. The main focus is on the coupling of hydroformylation with the subsequent reaction network of the reductive amination (RA). The validity of the kinetic mechanism structure, equations, and extrapolability of the derived and reduced mechanistic approaches to the overall reaction of the HAM (Figure 3.61) should be evaluated and proven.

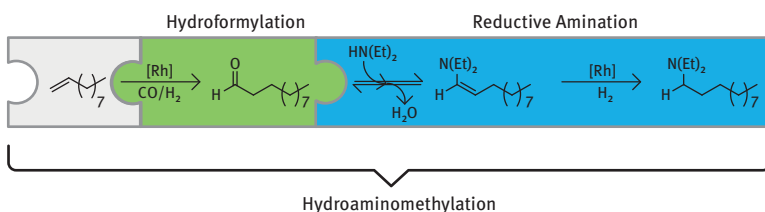


Figure 3.61: HAM reaction to the linear amine consisting of the single reactions hydroformylation and reductive amination.

The reaction conditions for the overall reaction HAM differ, in some essential points, from those of the individual reactions. In contrast to the hydroformylation, the hydroaminomethylation cannot be carried out with the polar solvent DMF [22], so that a TMS of methanol/dodecane must be used for the HAM [133; 134]. In addition, the ligand BI-PHEPHOS cannot be applied due to the by-product, water, so the water-soluble, water-stable bidentate ligand, SULFOXANTPHOS is used.

In addition to the main linear reaction, isomerization of the 1-alkene can also lead to branched by-products (iso-decenes, iso-aldehydes, iso-enamines, iso-amines) as well as the formation of decane and alcohols by hydrogenation of the terminal and internal decenes or the intermediate linear and branched aldehydes. Nevertheless, small amounts of aldols may also be formed as a result of an organo-catalyzed addition reaction of enamine and aldehyde. Consequently, for a simplified kinetic description, the branched by-products, as well as aldols and alcohols, can be neglected due to the insignificant amounts that were observed in preliminary experiments.

Only the isomers of the olefin and the formation of decane were considered, besides the linear main path.

The reaction rate equations for the hydroformylation, isomerization, and hydrogenation to decane were adopted in their structure from Section 3.2.3.2 (eqs. (3.61), (3.65), (3.67)), which are based on the catalytic cycle for the Rh/BIPHEPHOS-catalyzed isomerizing hydroformylation (Figure 3.46). In addition, for the non-catalyzed condensation step, eq. (3.68) can be used by assuming an equilibrium reaction with an equilibrium constant, K_{Cond}^{eq} . Furthermore, for the hydrogenation of the enamine to an amine, an additional catalytic cycle based on the elementary steps for olefin hydrogenation (**HYD**) in Figure 3.62 is postulated. Finally, a reduced mechanistic model is suggested (Figure 3.62(a)), eq. (3.69):

$$r_{Cond} = k_{Cond}(T) \left(c_{Ald} \cdot c_{DEA} - \frac{c_{En} \cdot c_{H_2O}}{K_{Cond}^{eq}} \right) \quad (3.68)$$

$$r_{Hyd, En} = \frac{k_{Hyd, En}(T) \cdot c_{En} \cdot c_{H_2}}{1 + K_{Hyd, En} \cdot H_2} \cdot c_{cat} \quad (3.69)$$

It is assumed that both cycles in Figures 3.46 and 3.62 start from the same resting-state catalytic species, so that the concentration of the catalyst can be described by the same equation.

An adaption of the kinetic models to the experimental data revealed that the structure of the mechanistic models for the hydroformylation (eq. (3.61)), isomerization (eq. (3.67)), and hydrogenation (eq. (3.65)) to decane are preserved and the change in the kinetics can be adapted by reparametrizing only the reaction rate constant (pre-exponential factor and the activation energies). Thus, the reaction rate constant includes the changes in the solvent system and the ligand, ($k_{reaction} = f(\text{solvent, catalyst})$). The influence of H_2 , CO, decenes, and aldehydes is described further by the mechanistic kinetic models derived before, without any changes. The condensation and the hydrogenation of the enamine were considered and adjusted in parallel.

A comparison of the experimental data and the simulation results in Figure 3.62 for the Rh/SULFOXANTPHOS-catalyzed hydroaminomethylation confirms the transferability of the mechanistic kinetic models that were derived and reduced for the Rh/BIPHEPHOS-catalyzed isomerizing hydroformylation by different methods. Furthermore, the extension of the mechanistic kinetic models by an additional catalytic cycle is absolutely confirmed, if the same active catalyst species is assumed. The temperature dependence (Figure 3.62b), as well as the pressure dependence (Figure 3.62c), can be successfully described over a wide range of operating parameters. Thus, the value, validity, and moreover, the extrapolability of mechanistic kinetic models are confirmed. Only the description of the influence of CO (Figure 3.62c) needs to be improved in the model. This can be realized by consideration of CO in the catalyst equilibrium or by further inhibiting species, such as Rh-dimers or Rh-dicarbonyls, which were neglected in the isomerizing hydroformylation reaction.

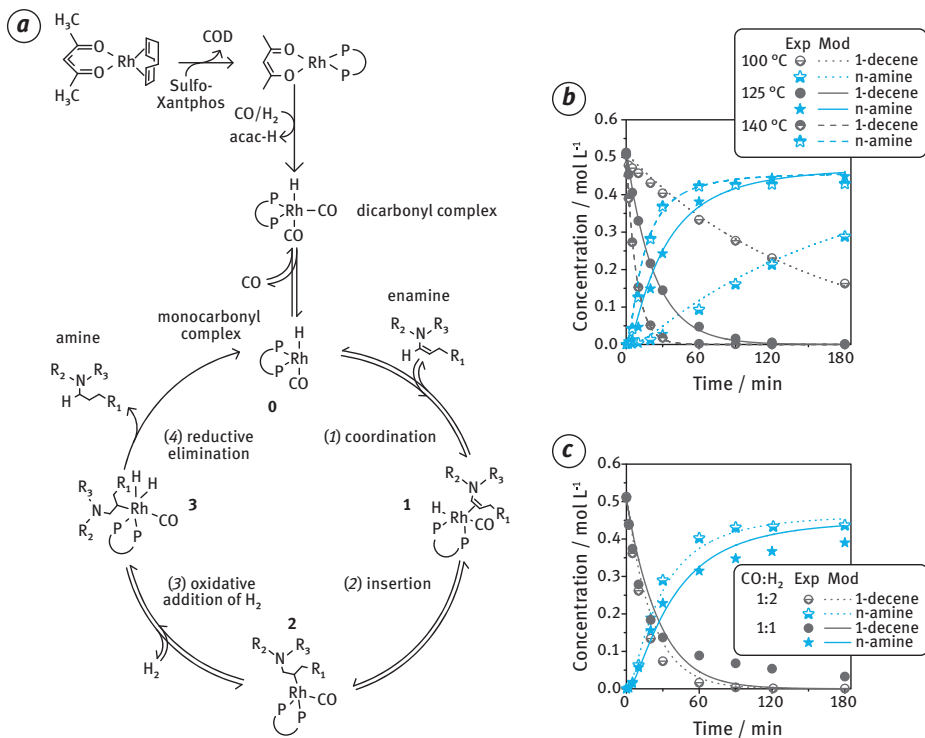


Figure 3.62: HAM results: (a) Proposed catalytic cycle for hydrogenation of enamines and experimental (symbols) and simulation results (lines) for temperature (b) and gas composition influence of CO:H₂ (c).

3.2.4 Thermodynamic Outlook

Solvents have a huge influence on the reaction equilibrium and can also significantly influence the kinetics of chemical reactions [199]. The drawback of the classical concentration-based kinetic modeling is the missing transferability between different solvent systems, since the kinetic parameters are only valid for the solvent system to which they were fitted. This means that for the same reaction new kinetic constants need to be determined, once the solvent changes. This limitation can be solved by using thermodynamic activities instead of concentrations for the kinetic modeling (compare Section 3.1.5 for the solvent influence on reaction equilibria).

The reaction rate, r , of a simple equilibrium reaction, $A + B \rightleftharpoons C + D$, can be expressed in a thermodynamic consistent way [147] according to eqs. (3.70)–(3.72).

$$r = \frac{dc_C}{dt} = k_1^* \cdot a_A \cdot a_B - k_{-1}^* \cdot a_C \cdot a_D \quad (3.70)$$

$$a_i = c_i \cdot \gamma_i^c = x_i \cdot \gamma_i^x \quad (3.71)$$

$$r = \frac{dc_C}{dt} = \underbrace{k_1^* \cdot \gamma_A^c \cdot \gamma_B^c}_{k_1} \cdot c_A \cdot c_B - \underbrace{k_{-1}^* \cdot \gamma_C^c \cdot \gamma_D^c}_{k_{-1}} \cdot c_C \cdot c_D \quad (3.72)$$

The thermodynamic activity, a_i , is defined as the product of concentration, c_i (or mole fraction x_i), and the activity coefficient, γ_i (eq. (3.71)). Activity coefficients depend on the concentrations of all components present in the mixture and account for all interactions among different species, including those between solvents and reactants or products. The intrinsic reaction rate constants, k_1^* and k_{-1}^* , of the forward reaction and the backward reaction, respectively, do not depend on the solvent, as long as the transition state is not affected. However, when using concentrations instead of thermodynamic activities for modeling the reaction kinetics (eq. (3.72)), the apparent reaction rate constants, k_1 and k_{-1} , also contain the activity coefficients and, thus, depend on the solvent. In turn, this means that intrinsic kinetic constants can be used for predicting the kinetics in different solvents, when accounting for the activity coefficients of the reactants.

To test the concept, the activity-based approach (eqs. (3.70-72)) was examined for an esterification reaction. The reaction is particularly suitable for this purpose, since it does not require a complex catalyst. Thus, the solvent influence on the reaction kinetics can be fully attributed to the solvent influence on the reactant/product activities. Figure 3.63 shows experimental results for the esterification kinetics of acetic acid with ethanol at 30 °C [146]. On the one hand, the influence of reactant concentrations on the reaction kinetics in the absence of a solvent was investigated for molar reactant ratios of 1:1, 3:1, and 1:3 (Figure 3.63a). On the other hand, the influence of the solvents DMF, ACN, and THF were examined, considering equimolar (1:1) reaction mixtures (Figure 3.63b). The experiments revealed a significant effect of the initial reactant ratio as well as of the solvents on the esterification kinetics. Compared to an initial reactant ratio of 1:1, both the reactant ratios of 1:3 and 3:1 resulted in a lower reaction rate. Among the used solvents, the highest reaction rate was achieved in THF, whereas the reaction rate was lowest in DMF.

The influence of both, reactant concentration and solvents, on the esterification kinetics could be predicted using PC-SAFT. For that purpose, only one kinetic parameter was fitted to the experimentally determined reaction kinetics in the solvent-free 1:1 system. By applying this intrinsic kinetic parameter and the activity coefficients of the reactants/products obtained from PC-SAFT, the reaction kinetics in all other systems could be predicted in very good agreement with the measured data, without fitting any additional parameters, as shown in Figure 3.63. The same approach was successfully used for quantifying the esterification kinetics of propionic

acid with methanol [146]. In conclusion, using an activity-based kinetic model accounting for the nonideal interactions between reactants/products and the solvent allows almost quantitative prediction of the solvent influence on the esterification kinetics.

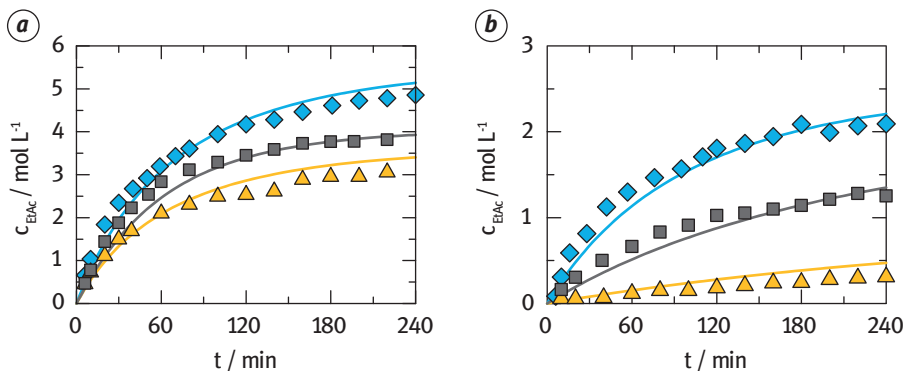


Figure 3.63: Reaction kinetics for the esterification of acetic acid and ethanol at 30 °C. (a) Symbols represent the experimental concentrations of the product ethyl acetate (EtAc) for initial acetic acid/ethanol ratios of 1:1 (diamonds), 3:1 (squares), and 1:3 (triangles). (b) Symbols represent experimental data for systems with an initial reactant ratio 1:1 in the solvents ACN (circles), THF (triangles), and DMF (squares). Lines are PC-SAFT results. The kinetic parameter was fitted only to the solvent-free 1:1 system; all other lines are full predictions using PC-SAFT [146].

To describe the solvent influence on the hydroformylation reaction kinetics, again the kinetics should be expressed in thermodynamic activities of the reactants (eq. (3.73)) instead of using concentrations (eq. (3.61)). Based on a reference solvent system (in this case 60 wt% n-decane and 40 wt% DMF), the apparent kinetic parameters k_{nHYFO} , K_{nHYFO}^I , and K_{nHYFO}^{II} that are only valid for this particular solvent system could be converted using reactant/product activity coefficients into the intrinsic kinetic parameters k_{nHYFO}^* , K_{nHYFO}^{I*} , and K_{nHYFO}^{II*} . These intrinsic kinetic parameters can again be reconverted into solvent-dependent apparent kinetic parameters for any solvent system (here 80 wt% n-decane and 20 wt% DMF, as well as 0 wt% n-decane and 100 wt% DMF) by calculating reactant/product activity coefficients in the new solvent system, e.g., via PC-SAFT. This procedure is exemplarily shown for k_{nHYFO} in eqs. (3.74) and (3.75).

$$r_{nHYFO} = \frac{k_{nHYFO}^* c_{ID}^c c_{CO}^c c_{H_2}^c \cdot \gamma_{D1}^c \gamma_{CO}^c \gamma_{H_2}^c}{\left(1 + K_{nHYFO}^{I*} c_{H_2}^c \cdot \gamma_{H_2}^c + K_{nHYFO}^{II*} c_{H_2}^c c_{CO}^c \cdot \gamma_{H_2}^c \gamma_{CO}^c\right)} \cdot \frac{c_{Rh} \cdot \gamma_{Rh}^c}{\left(1 + K_{nHYFO}^{I*} c_{CO}^c \cdot \gamma_{CO}^c\right)} \quad (3.73)$$

$$k_{nHYFO}^* = \frac{k_{nHYFO,60/40}}{\left[\gamma_{D1}^c \gamma_{CO}^c \gamma_{H_2}^c \right]_{60/40}} \quad (3.74)$$

$$k_{nHYFO,80/20} = k_{nHYFO}^* \left[\gamma_{D1}^c \gamma_{CO}^c \gamma_{H_2}^c \right]_{80/20} \quad (3.75)$$

The influence of the solvent composition on the activity coefficients of all reactants/products and solvents for the hydroformylation of 1-dodecene is depicted in Figure 3.64. The results show particularly that the DMF content of the solvent mixture has a significant influence on the activity coefficients, especially for the reactant 1-dodecene (1D). Thus, a substantial solvent influence on the hydroformylation reaction kinetics can be expected. Accounting for the remaining reactions in the global reaction network (Figure 3.46), it should be thus possible to obtain a complete picture of the solvent effects on the kinetics of the hydroformylation reaction.

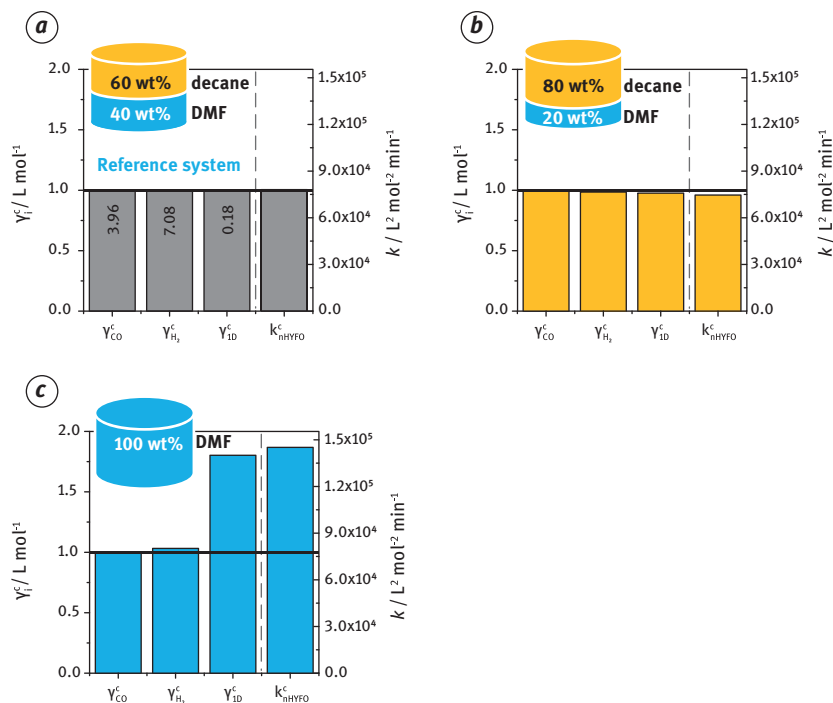


Figure 3.64: Activity coefficients of the reactants (CO, H₂, and 1D) of the hydroformylation (left axis) and the apparent kinetic constant, k_{nHYFO} , (right axis) obtained from PC-SAFT in different n-decane/DMF solvent mixtures (a–c) at 105 °C and 30 bar. Activity coefficients have been normalized to the reference solvent system of 60 wt% n-decane and 40 wt% DMF [145].

3.2.5 Summary

A methodical approach of mechanistic kinetic modeling for complex catalytic reactions in multiphase systems, based on detailed catalytic cycles and their reduction, utilizing different reduction techniques are described and successfully applied for quantifying the tandem reaction of the hydroaminomethylation of olefins. To provide a deeper understanding of such complex reaction networks, interdisciplinary cooperation in the fields of chemistry, thermodynamics, quantum mechanics and reaction engineering is required both theoretically and experimentally. In Section 3.2, the methodology for developing mechanistic kinetic models using the Christiansen mathematics, the Bodenstein approximation of quasi-stationarity of reaction intermediates, and “recipes” for model derivation and subsequent model reduction using three independent strategies were introduced.

A mechanistic kinetic model for the Rh/BIPHEPHOS-catalyzed hydroformylation, as a subnetwork of the HAM, was derived, based on a total catalytic cycle including all sub-reactions (isomerization and hydrogenation), inhibition effects, as well as the catalyst equilibrium. The resulting overparametrized kinetic models were subsequently reduced for the subnetworks of hydroformylation and isomerization, using three different approaches. First, quantum mechanical calculations were performed to verify the reaction mechanism and to identify RDS. This information can be used to perform model reductions and supports the estimation of kinetic parameters by providing reasonable estimate limits. A mathematical reduction method based on parameter sensitivity analysis that helps to increase the identifiability of kinetic parameters by designing dynamic perturbation experiments was presented. In addition, a spectroscopic method was demonstrated using *operando* FTIR spectroscopy for the experimental validation of postulated catalytic species and inhibition effects. In particular, the 1-alkene coordination was identified as the most probable RDS for the Rh/BIPHEPHOS-catalyzed hydroformylation of 1-decene. In addition, only a single organometallic carbonyl species was identified with a high abundance that operated throughout the catalysis.

The methodical approach of mechanistic kinetic model derivation and reduction was successfully applied for the Rh/BIPHEPHOS-catalyzed isomerizing hydroformylation of 1-decene and isomeric feed mixtures consisting of re-isomerization and subsequent hydroformylation. For the complex reaction network of isomerization, hydrogenation, and hydroformylation a particularly good agreement between simulated and experimental data was achieved in a broad region of operation conditions, using a single set of kinetic parameters. As a final result, for the total reaction network of HAM using a different bidentate ligand (Rh/SULFOXANTPHOS) as well as different compositions of the solvent system, the derived mechanistic kinetic model structures of the isomerizing hydroformylation (Rh/BIPHEPHOS) could be directly transferred and extended to the RA sequence. This reveals the significant potential of mechanistic kinetic modeling.

Since for multiphase reactions, the solvent selection is of ample importance, kinetic models and the corresponding parameters should be identified and applied, preferably independent of the solvent. A promising possibility to achieve this is the thermodynamically consistent formulation of kinetic models using activities, instead of the usually applied concentrations.

3.3 Mass Transfer Processes

Marc Petzold, Nona Afraz, Martin Gerlach, Kristin Hecht, Lutz Böhm, Matthias Kraume

3.3.1 Introduction

It is challenging to achieve high concentrations of poorly soluble reactants. This is especially true for multiphase reactions that involve immiscible phases. For reactions that occur between gases and liquids, the gas is often only slightly soluble in the liquid. For polar solvents, the solubility is typically even less at elevated temperatures [247]. However, elevated temperatures may be required for the reaction to occur. This difficulty may be overcome by increasing the pressure, which, in turn, increases the concentration of dissolved gas, but as the gas is consumed by the chemical reaction, sufficiently fast rates of mass transport are needed to replenish the gas that has been consumed.

For reactions involving immiscible organic and aqueous phases, the extremely limited solubility of the phases in each other represents a major challenge for developing processes that combine these materials. The use of novel phase systems including thermomorphic multiphase system (TMS), microemulsion systems (MES), and nanoparticle-stabilized Pickering emulsions (PE) has been investigated in the framework of this book to develop efficient chemical processes in liquid multiphase systems. These novel phase systems are an innovative idea for bringing immiscible organic and aqueous phases into contact for a chemical reaction. However, the properties of these materials, especially as they relate to mass transport, are largely unknown.

In this section, fundamentals of transport processes in novel phase systems are described. Rates of transport depend upon material properties such as the diffusion coefficient as well as the hydrodynamics of the multiphase flow. The rates of mass transfer exhibit a complicated dependence on temperature and the composition of the novel phase systems. The interfacial contact area plays an especially critical role. The rates of transport have been explored in different apparatuses. Investigations of the transport of gas into TMS and MES systems and of the transport of species among the liquids phases of MES and PE systems are reported.

3.3.2 Experimental Characterization of Multiphase Liquid–Liquid Mass Transport

To design reaction processes with interacting liquid phases, knowledge about the fluid dynamics and the mass transfer in these liquid–liquid systems is crucial. Rates of mass transfer are tightly coupled to the fluid dynamics of the system, which influence flow regimes, disperse phase velocities, and contact times. Each of these factors must be considered in all mass transfer processes. Due to the complex interaction of these parameters occurring in apparatuses such as stirred tanks and extraction columns (swarm behavior, holdup, counter-current flow, etc.), prediction is a challenging task. Furthermore, most processes do not use analytical-grade components, and, therefore, are influenced by impurities, which come into the process by contamination, as side products, or as deliberate additions. These impurities often accumulate at the interface. Since the transport occurs across the phase interface, interfacial effects influence both the fluid dynamics and the mass transfer. Even small traces of these often surface-active substances can alter the transport processes significantly. Small droplets are often intended to provide a large area for mass transfer, and the effect of surface-active substances is even stronger on small droplets [143]. To design extraction apparatuses considering all influencing factors, experiments are needed, and two approaches can be pursued [190]:

1. Experiments are done on the pilot scale. The results are achieved with the material system of interest and can be used directly for design. The downsides are the high costs as well as the lack of large amounts of the substances in the early project stages, and no insights into the effects of the impurities are gained.
2. Experiments performed on single drops. Single drop experiments offer a more cost-efficient and simple method for design. But, to use the results for designing the process, models for swarm effects, holdup, etc. must be applied.

In this section, both approaches were followed. Single drop experiments were conducted to determine the influence of the additives used in the various investigated solvent systems. Models were used to predict the effects of changes observed in a small scale at the scale of the process. Finally, the insights obtained from measurements with single drops were verified by experiments in a stirred tank reactor.

3.3.2.1 Single Drop Experiments

Single drop experiments were used to investigate the rising velocities and mass transfer for small amounts of the materials of interest. Knowledge of the terminal velocity of a falling or rising drop is a precondition to determining flow regimes, for correlations, and to calculate swarm effects (swarm velocity, holdup, etc.). The governing equation can be derived from a force balance applied to the drop including the forces of inertia, gravity, buoyancy and drag:

$$\frac{dw_p}{dt} = \frac{|\Delta\rho|}{\rho_d + \kappa \cdot \rho_c} \cdot g - \frac{3}{4} \cdot C_D \cdot \frac{\rho_c}{\rho_d + \kappa \cdot \rho_c} \cdot \frac{w_p^2}{d_p} \quad (3.76)$$

with the drag coefficient, C_D , and coefficient, κ , accounting for the accelerated ambient phase. For solid particles, the surface is immobile, while for fluid particles, momentum transfer takes place at the interface, inducing a flow field inside the drops. An analytical solution for eq. (3.76) was provided by Hadamard [97] and Rybczynski [211] for creeping flow conditions ($Re < 1$) only. Several authors have developed correlations for the drag coefficient to describe drop sedimentation velocities at higher Reynolds numbers. For rigid drops, the drag coefficient decreases with increasing Reynolds number, until reaching the turbulent regime at $Re > 3 \cdot 10^5$ and can be modeled, for example, by the correlation of Martin [163]. Fluid drops are spherical at low Reynolds numbers. Drop shapes become nonspherical due to deformation and oscillation at higher Reynolds numbers. In the spherical regime, the drag coefficient decreases with the Re . Different authors offer correlations for different ranges of applicability ($Re > 2$ [24]; $10 < Re < 100$ [39]; $10 < Re < 100$ [206]; $4 < Re > 100$ [98]; $Re < 400$ and $\mu^* < 1$ [213]; $5 < Re < 1000$ and $0 < \mu^* < \infty$ [66]), where μ^* corresponds to the ratio of disperse phase to continuous phase viscosity. Feng and Michaelidis [66] provide equations for the broadest range of Reynolds numbers and μ^* . With the start of deformation, the drag coefficient increases drastically. The onset was found to start at a critical Weber number of $We = 3.58-4.08$ [101, 113, 137, 244]. After deformation, oscillation starts, and because of the high drag, the drop velocity decreases. This behavior can be depicted, e.g., by a correlation of Thorsen et al. [233].

The mass transfer is strongly influenced by the flow regime around the drops, since at higher Reynolds numbers, oscillations increase convection around (and/or inside) the drops. Mass transfer equations exist mostly for the regime occurring at low Reynolds numbers, where drop shapes can be assumed to be spherical.

Correlations for mass transfer can be divided into solutions for stationary and nonstationary mass transfer. For solid and liquid drops without internal circulation in a quiescent liquid ($Re = 0$), mass transfer is controlled by diffusion alone, and the Sherwood number equals $Sh = 2$. Stationary mass transfer correlations express the Sherwood number:

$$Sh = \frac{k_L \cdot d}{D_{AB}} \quad (3.77)$$

as a product of Reynolds and Schmidt number for stagnant drops at $Re > 0$

$$Sh = C \cdot Re^m \cdot Sc^n \quad (3.78)$$

For different flow conditions and Peclet ($Pe = Re \cdot Sc$) numbers, values for C , m , and n have been suggested ($Re < 1$, $Pe > 100$: $m = n = 0.33$, $C = 0.991$ [69, 153]; $Re \gg 1$: $m = 0.5$, $n = 0.33$ [227], $C = 0.5-1$ [139, 153]). For fluid drops, nonstationary mass transfer

occurs, because the concentration of the transfer component changes due to the transport from continuous to disperse ($c \rightarrow d$) or vice versa ($d \rightarrow c$), until an equilibrium is reached. The equilibrium can be expressed by the partition coefficient, K , and, together with the ratio of diffusion coefficients in the dispersed and continuous phase, $D_{A,d}/D_{A,c}$, can be formed into the expression, $K \cdot \sqrt{D_{A,d}/D_{A,c}}$, to determine in which phase the mass transfer resistance mainly lies. The main resistance may occur in the external ambient phase ($K \cdot \sqrt{D_{A,d}/D_{A,c}} \gg 1$), in the internal disperse phase ($K \cdot \sqrt{D_{A,d}/D_{A,c}} \ll 1$), or both phases may provide similar mass transfer resistance, such that a conjugated problem arises ($K \cdot \sqrt{D_{A,d}/D_{A,c}} \approx 1$). Piarah [191] calculated the Sherwood number for the nonstationary problem with the main mass transfer resistance occurring in the external phase, and found that the Sherwood number decreases with rising Fourier number, a dimensionless number characterizing time, to the power of $Fo^{-1/2}$. Depending on the Peclét number, the curve asymptotically approaches the stationary solution for high Reynolds numbers, according to Clift et al. [44]. If the mass transfer resistance lies mainly inside the droplet, the internal concentration changes over time, until equilibrium is reached. The concentration can be expressed dimensionless as:

$$c^* = \frac{c_{A,d}(t) - K^* \cdot c_{A,c}(t \rightarrow \infty)}{c_{A,d}(t=0) - K^* \cdot c_{A,c}(t \rightarrow \infty)} \quad (3.79)$$

Since fluid dynamics have an impact on mass transfer, solid and liquid particles are usually referred to as limiting cases. The mass transfer to and from solid particles is slow and can be described by the correlation of Newman [175]. Faster rates of mass transfer are generally observed for fluid drops and can be described by the correlation of Kronig and Brink [138]. For turbulent internal circulation, the equation of Handlos and Baron [100] predicts even faster mass transfer. Calderbank and Korchinski [33] provided a correlation including an expression of the diffusion coefficient multiplied by the factor R . For $R = 1$, their equation coincides with the solution for solid particles from Newman [175], while for $R = 2.25$, the solution coincides with that for fluid particles of Kronig and Brink [138]. No correlations exist for conjugate problems due to their complexity. A brief overview of existing numerical solutions is given by Wegner et al. [243].

The basic behavior of drops changes in the presence of additives and surface-active substances. Surface-active substances accumulate at the interface and can lower the interfacial tension. In a flow field, the additives can accumulate at the back of the drop (stagnant cap) [41], leading to a local gradient of interfacial tension along the interface. Depending on which interfacial phenomenon dominates, the effects on mass transfer and fluid dynamics may differ. Additives leading to adsorption-dominated systems include surfactants and nanoparticles. Systems dominated by interfacial tension gradients occur in the presence of surfactants and amphiphiles and can be induced by transfer components alone. Due to the tight coupling of fluid dynamics and

mass transfer, even the fluid dynamics of single drops alone can be used to predict the mass transfer performance of systems with impurities [186, 223].

To uncover the effects of the additives used in the multiphase systems considered in this volume, single drop experiments were conducted. Figure 3.65 shows the single drop cell as it was configured for investigating rising drops. The cell consists of a glass pipe enclosed in a square heating jacket filled with glycerin (1). The heating jacket is made of acrylic glass with a similar refraction index as the glycerin inside, to avoid optical distortion. The jacket is heated using a circulating temperature bath (2). The dispersed phase is stored in a vessel (3a) and delivered via a syringe pump (4a) to a capillary (5). The capillary is connected to an electromagnet (6), which, when activated, pulls the capillary downwards to release the drop. The path of the drop is tracked with a high-speed camera (7). Picture quality is ensured by an appropriate light source (8). For mass transfer measurements, the drops are collected in a funnel (9). A second syringe pump (4b) delivers the disperse phase to a storage vessel (3b), from which samples are taken for analysis.

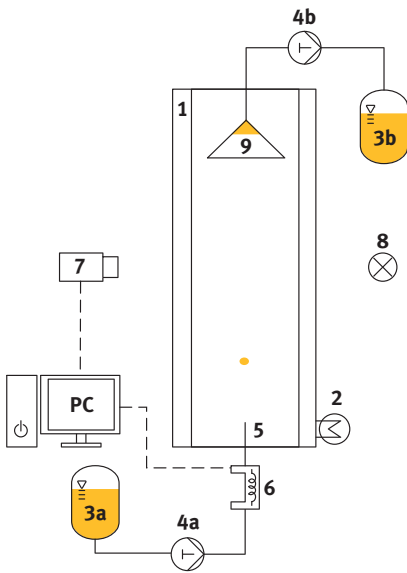


Figure 3.65: Apparatus used to investigate rising single drops.

3.3.2.2 Modified Nitsch Cell

The single drop experiments were extended using investigations in a modified Nitsch cell. In microemulsion systems, up to three liquid phases appear. Besides an aqueous and organic phase, a bicontinuous surfactant-rich middle phase is formed in specific temperature intervals. Due to the very low interfacial tensions between the bicontinuous and the other liquid phases [110], single drop experiments fail, since defined drop creation is difficult. Nevertheless, to quantify the mass transfer in this liquid–liquid

system and, especially, the mass transfer performance of the bicontinuous phase, stirred test cells with flat interfaces can be used. Lewis [149] provided a first design and analysis of a stirred mass transfer cell, which Nitsch et al. [181] and Waubke and Nitsch [242] improved upon. To investigate the mass transfer of the bicontinuous phase, a modified Nitsch cell was operated with three phases, as described by Paul et al. [187]. A schematic of the modified Nitsch cell is shown in Figure 3.66.

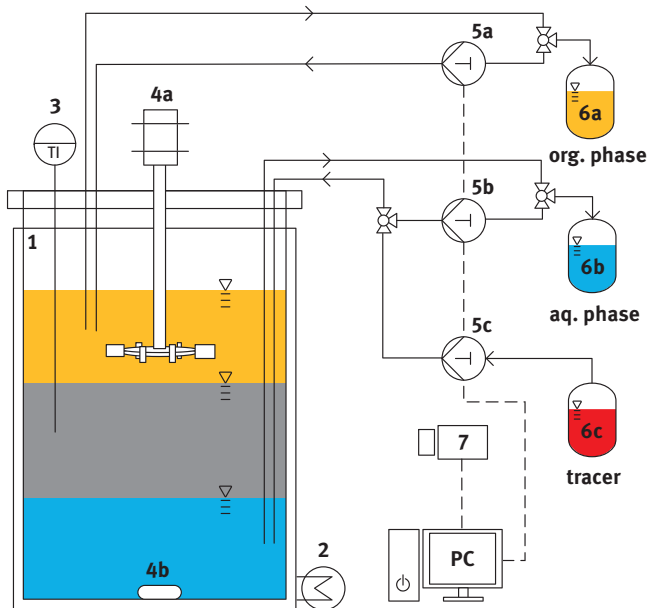


Figure 3.66: Modified Nitsch cell.

The modified Nitsch cell consists of a glass vessel with a flat bottom and a heating jacket (1), through which heat-transfer fluid is circulated using a circulating temperature bath (2). At a certain temperature, the microemulsion system separates into three distinct phases. The upper and lower phases are each stirred slowly by independent stirrers (4a, 4b). The stirrers are positioned in a manner such that the middle phase is undisturbed by the stirring process, while the other two phases are assumed to be perfectly mixed. The phase heights can be monitored by a camera (7). Three syringe pumps (5a, 5b, 5c) are connected to three containers (6a, 6b, 6c). At the start of the experiments, a specific amount of tracer (PADA = Pyridine-2-azodimethyl-aniline) is injected into the aqueous phase. At predetermined time intervals, samples are taken from the organic and aqueous phases for analysis. The setup allows for the determination of the temporal concentration profile in the organic and aqueous phases. Using the amount of tracer injected in the aqueous phase at the start of the experiment, together with the volumes of each phase and

knowledge about the physical properties of all liquids, the concentration in the bi-continuous phase can be calculated from a mass balance. The diffusion coefficient in the bicontinuous phase can be calculated assuming quasi-stationary transport by diffusion [187].

3.3.2.3 Stirred Tank Reactor

Investigations in a stirred tank reactor were used to examine mass transfer for complex flows consisting of multiple drops and phases at conditions similar to those used in the mini plants. To determine the general influence of swarm effects, experiments were conducted with microemulsion and Pickering systems in a stirred tank reactor, seen in Figure 3.67 and described by Paul [185] and by Petzold et al. [189]. The continuous phase was stirred in a double-walled glass reactor (1) with the wall temperature maintained using a circulating temperature bath (2) equipped with baffles and a Rushton turbine stirrer (3). The organic phase was stored in a container (4), above the reactor. At the start of the experiment, a valve was opened, and the organic phase was dispersed in the reactor. A conductivity probe (5) was used to monitor the electrical conductivity inside the dispersion. The drops in the dispersion were observed with an endoscope (7). The endoscope setup consists of

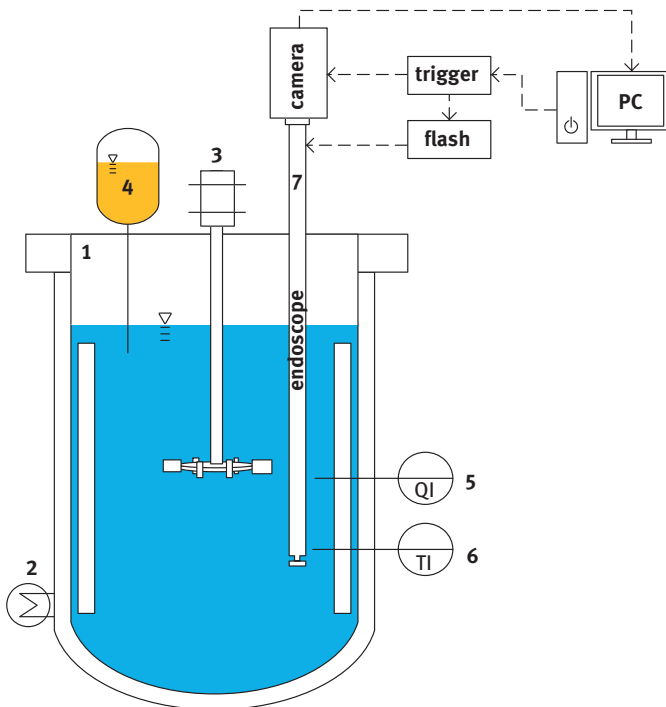


Figure 3.67: Stirred tank reactor with endoscope setup.

an endoscope lens attached to a camera and a stroboscope flashlight [155]. A computer-controlled trigger box enables the simultaneous triggering of camera and light. The pictures of recorded drops are automatically analyzed by software [156]. The drop size distributions from the pictures along with the volume of the disperse phase enable the calculation of the overall mass transfer area.

The rate of the rapid saponification of benzoyl chloride with sodium hydroxide was used to determine the mass transfer coefficient in the system [189]. A 0.1 M solution of benzoyl chloride in the organic phase was dispersed in a 0.5 M solution of sodium chloride in water. The reaction conversion was monitored with an electrical conductivity probe (5). The overall rate of the reaction is limited by the diffusion within the drop and, thus, the molar flux of benzoyl chloride in the system can be estimated from the measurements.

3.3.3 Experimental Characterization of Multiphase Gas-Liquid Mass Transport

In stirred tanks, the effect of an additional disperse liquid phase on the rate of mass transfer from the gas into the liquid is unclear and has only been reported in a handful of studies, of which most used water as continuous phase, adding carbon hydrates or perfluorocarbons as the dispersed liquid phase. Yoshida et al. [246] observed that the addition of kerosene to water reduced the rate of mass transfer. For the mass transfer of oxygen into the water with small amounts of dodecane added, an increase in the rate of mass transfer was found [176, 208]. Dumont et al. [56] found that an additional liquid disperse phase did not change the rate of mass transfer. Hassan and Robinson [102] found retardation of the rate of mass transfer. Similar contradicting results were found for the mass transfer of CO_2 into the water with small amounts of heptane [38, 176, 252]. Ngo and Schumpe [176] observed a dramatic increase in the rate of mass transfer when the continuous and disperse phases inverted, and the organic phase became the continuous phase. At the point of the phase inversion, an increase in the volumetric mass transfer coefficient, $k_L a$, of 189% was observed.

3.3.3.1 Determination of $k_L a$ from Pressure Decrease in a Closed System

The mass transfer involves the transport of a gaseous species from a gas phase to a liquid phase. The rate at which gas dissolves in a liquid (flux) at any particular time is proportional to the difference between the equilibrium concentration and the concentration at that time. This concentration difference can be considered as the “driving force” for the mass transfer. When the equilibrium concentration is reached, the liquid is saturated with the gas, and the rate of transfer is, therefore, zero. The proportionality factor between the concentration difference times interfacial area and the transfer rate

is called mass transfer coefficient, k_L . The equation of mass transfer can be written as follows:

$$\frac{dn_A}{dt} = -k_L \cdot A \cdot (c_A^* - c_A(t)) \quad (3.80)$$

where n_A is the moles of gas in the gas phase, c_A is the concentration of dissolved gas at the given time, c_A^* is the equilibrium concentration, A is the surface area between gas and liquid phase, and k_L is the liquid mass transport coefficient. The surface area A can be expressed in terms of volume-specific transport area, a , multiplied by the liquid volume.

$$\frac{dn_A}{dt} = -V_L \cdot k_L a (c_A^* - c_A(t)) \quad (3.81)$$

The concentration at the interface (c_A^*) is assumed to be in equilibrium with the gas phase, which can be described for poorly soluble gases by Henry's law:

$$c_A^* = H_A \cdot p_A \quad (3.82)$$

where p_A is the partial pressure of the gas in the gas phase, and H_A is the Henry constant. The gas phase is assumed to be saturated with the liquid component at its vapor pressure for the given temperature. The pressure and composition within the gas phase are assumed to be uniform. Referring to ideal gas law, the pressure of the gas is related to the amount of gas:

$$p_A = n_A \frac{RT}{V_G} \quad (3.83)$$

Applying eq. (3.82) and eq. (3.83) to eq. (3.81) leads to:

$$\frac{dp_A}{dt} \cdot \frac{V_G}{RT} = -V_L \cdot k_L a \cdot (H_A \cdot p_A - c_A(t)) \quad (3.84)$$

The concentration of the gaseous component in the liquid phase, $c_A(t)$, changes over time, as the gas dissolves in the liquid. The moles of gas leaving the gas phase must be the same amount arriving in the liquid phase, which can be expressed via:

$$\frac{dc_A}{dt} = -\frac{dn_A}{dt} \cdot \frac{1}{V_L} \quad (3.85)$$

$$\int_{c_{A0}}^{c_A} dc_A = -\frac{1}{V_L} \cdot \int_{n_{A0}}^{n_A} dn_A \quad (3.86)$$

$$c_A(t) - c_{A0} = -\frac{1}{V_L} \cdot (n_A(t) - n_{A0}) \quad (3.87)$$

Introducing eq. (3.83) into eq. (3.87) leads to an expression of the bulk concentration of gas dissolved in the liquid related to the partial pressure in the gas phase, p_A :

$$c_A(t) = c_{A0} - \frac{V_G}{V_L \cdot RT} \cdot (p_A(t) - p_{A0}) \quad (3.88)$$

The initial pressure at the beginning of an experiment is p_{A0} . The initial concentration of the gas in the liquid phase is c_{A0} . If the liquid is degassed beforehand, c_{A0} equals zero. Otherwise, the initial concentration of gas in the liquid phase is in equilibrium with the pressure in the system, which was present before the system pressure was raised to the starting pressure. The beforehand pressure, p_{Ab} , was usually 1 bar and can be described according to Henry's law with:

$$c_{A0} = H_A \cdot p_{Ab} \quad (3.89)$$

Introducing eq. (3.89) and (3.88) into eq. (3.84) gives the mass transfer represented by eq. (3.80) in terms of gas-phase pressure

$$\frac{dp_A}{dt} = - \frac{V_L \cdot RT}{V_G} \cdot k_L a \cdot \left(H_A \cdot p_A - H_A \cdot p_{Ab} - \frac{V_G}{V_L \cdot RT} \cdot (p_{A0} - p_A) \right) \quad (3.90)$$

Solving eq. (3.90) and considering the initial condition (for $t = 0$ is $p = p_{A0}$) results in:

$$\frac{p_A}{(p_{A0} - p_{Ab})} = \frac{1}{(1 + \Psi)} \cdot \left(\frac{p_{Ab}}{(p_{A0} - p_{Ab})} + \Psi \cdot \frac{p_{A0}}{(p_{A0} - p_{Ab})} + \exp\left(-\left(\frac{1}{\Psi} + 1\right) \cdot k_L a \cdot t\right) \right) \quad (3.91)$$

with

$$\Psi = \frac{V_G}{V_L \cdot RT \cdot H_A} \quad (3.92)$$

When rearranged, the equation matches the ones often found in the literature [53, 142]:

$$\ln\left(\frac{(p_{A0} - p_{Ab})}{(p_A - p_{Ab}) + \Psi \cdot (p_A - p_{A0})}\right) = \left(\frac{1}{\Psi} + 1\right) \cdot k_L a \cdot t. \quad (3.93)$$

If several liquid-disperse phases are present, for example in stirred systems, eq. (3.81) needs to be extended by a term for the mass transfer from the liquid continuous phase into the liquid-disperse phase. Assuming the transfer between liquid phases is instantaneous leads to:

$$\ln\left(\frac{(p_{A0} - p_{Ab})}{(p_A - p_{Ab}) + \frac{\Psi \cdot (p_A - p_{A0})}{(1 + \sum \varphi_{di} \cdot (K_{di} - 1))}}\right) = \left(\frac{1}{\Psi} + \frac{1}{(1 + \sum \varphi_{di} \cdot (K_{di} - 1))}\right) \cdot k_L a \cdot t. \quad (3.94)$$

Here, φ_{di} is the disperse phase fraction of the i -th liquid disperse phase and $K_{di} = c_{Adi}/c_{Ac}$ is the partition coefficient, when in contact with the continuous phase.

3.3.3.2 Stirred Tank Reactor

The gas–liquid mass transfer in multiphase systems is complex due to the multiple phases, complex fluid dynamics, and gradients occurring at the phase interfaces. To investigate the effects of the physical properties of the liquid on the mass transfer separately from the effects of the liquid properties on the bubble sizes and fluid dynamics, research was conducted in two different experimental setups. For thermomorphic and microemulsion multiphase systems, the phases were separated and individually investigated in a falling film contactor (Section 3.3.3.3). Important process parameters such as gas holdup, coalescence effects, disperse phase fraction, gas flow rate, bubble and drop interactions and further effects were investigated in a pressurized stirred tank reactor, as shown in Figure 3.68.

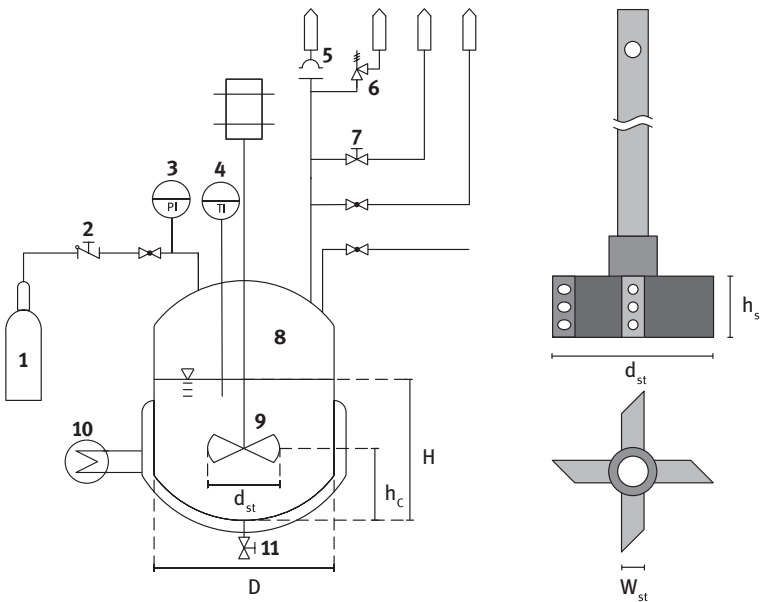


Figure 3.68: Gas-liquid stirred tank reactor, from Petzold et al. [188].

The stirred tank reactor consisted of a jacketed vessel (8, Halmosi, Germany, $D = 0.115$ m, $H = 0.115$ m, $h_c = 0.03$ m, $V = 1.393$ L) heated/cooled by a circulating temperature bath (10, VWR 1187P, Germany). Four baffles were placed in the reactor. Temperature and pressure were measured by a thermocouple (4) and a pressure sensor (3, WIKA S20, Germany), respectively. Different stirrers (9) could be used, such as a gas-inducing stirrer (Parr Instruments, USA, $d_{st} = 0.05$ m, $h_{st} = 0.019$ m, $w_{st} = 0.007$ m). To measure the volumetric mass transfer coefficient, the reactor is partly filled with the liquid, and the remaining volume is filled with gas with a pressure of up to 3–4 MPa. Starting the stirrer leads to a decrease in static pressure around the stirrer blades. Gas

is sucked through the opening in the stirrer shaft and dispersed through the orifices in the stirrer blades. The gas dissolves in the liquid, leading to a decrease in pressure, which can be evaluated to calculate the $k_L a$ value. The dispersion condition of drops and bubbles can be monitored with the same endoscope setup introduced in Section 3.3.2.3.

3.3.3.3 Falling Film Contactor

A falling film contactor consists of a flowing liquid as a film over wetted surfaces under the action of gravity. Thin liquid films can be less than 100×10^{-6} m in thickness with a high interfacial contact area [226]. In many processes, such as the absorption of CO_2 into alkaline solutions, the mass transfer of gas into the liquid film can limit the rate of the chemical reaction [248]. Due to the short distances through the thin liquid film, a falling film reactor is very effective for processes with the limiting mass transfer resistance in the liquid phase. The falling film contactor presented by Afraz et al. [3] was precisely constructed to produce a stable, annular falling film with a laminar velocity profile on the outside wall of a capillary. A schematic of the falling film experimental apparatus is illustrated in Figures 3.69 and 3.70. The falling liquid film was generated on the outer surface of a capillary from stainless steel, with an outer diameter of 1.588×10^{-3} m (1/16 inch) and a length of 0.18 m. The flow of the liquid film was gravity-driven and laminar. The liquid was continuously circulated between the liquid reservoir (Büchiglasuster A057875, stirred tank with a volume of 1×10^{-3} m³) and the falling film contactor using two syringe pumps (Cetoni, neMESYS1000N, 5×10^{-6} m³ heated stainless-steel syringes). The flow rate of the generated liquid film by the syringe pumps was 0.15×10^{-6} m³/s. The outer wall of the falling film contactor was surrounded by a cylindrical stainless steel tube, with an inner diameter of 8×10^{-3} m. A glass viewing window (Swagelok) was integrated into the surrounded tube around the capillary and on the top of the falling film contactor to enable observation of the falling film, before running the measurements. All tubing connections (gas and liquid tubes, falling film contactor) were heated using electrical resistance heating bands (Hillersheim Co. HT54 Pt). The inside of the stainless steel capillary and the liquid reservoir were heated with a circulating temperature bath thermostat (Huber Ministat 230). The inlet temperature at the gas and liquid was measured by thermocouples (Thermosensor Co., Type-K). The gas (with a volume of 50×10^{-6} m³) and liquid (with a volume of 1.185×10^{-3} m³) were introduced into the system before closing all valves to enable running the measurements in a closed system. As the gas molecules dissolved into the liquid, the pressure in the system decreased. The pressure decrease in the system was recorded with a pressure transducer (Labom CA1600).

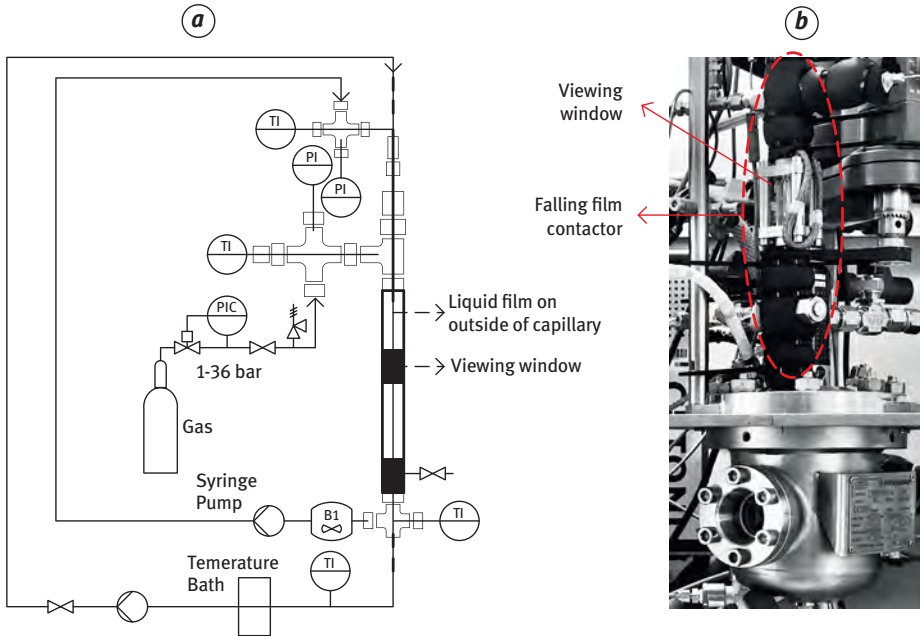


Figure 3.69: Schematic of the falling film apparatus for measuring mass transfer coefficients in a gas-liquid system (a), a photograph of the experimental setup (b) [3].

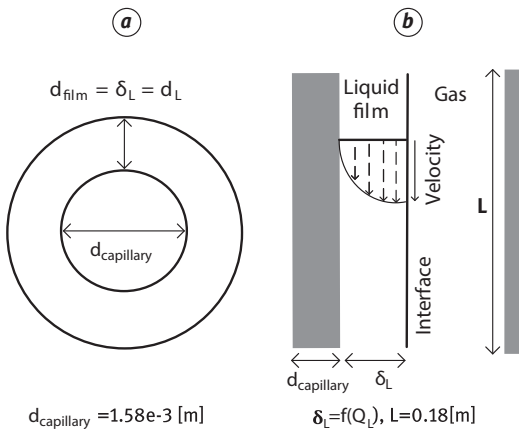


Figure 3.70: Schematic of the falling film geometry: top view of capillary surrounded by the liquid film (a), 2D geometry of the falling film, and velocity profile for a fully developed, laminar annular falling film (b) [3].

3.3.4 Gas–Liquid Mass Transfer

For chemical reactions between gases and liquids, forcing these distinct phases to mix is an engineering challenge. Different apparatuses have been developed to introduce the gases into the liquid system, with bubble columns or gassed stirred reactors being most common. Since the surface area of the introduced bubbles is often unknown, the mass transfer is measured in terms of volumetric mass transfer coefficient, $k_L a$, not differentiating between the influence of the liquid mass transfer coefficient, k_L , and the specific transfer area, a .

The mass transfer coefficient at a gas–liquid interface, whether it is in a stirred system or along with a falling film, may be described as proposed by film theory (eq. (3.95)) or penetration theory (eq. (3.96)) [107]:

$$k_L = \frac{D_{a,b}}{\delta} \quad (3.95)$$

$$k_L = 2 \cdot \sqrt{\frac{D_{a,b}}{\pi \cdot t_c}} \quad (3.96)$$

with the film thickness, δ , the contact time, t_c , and the diffusion coefficient, $D_{a,b}$. The temperature dependence of the diffusion coefficient can be expressed by the Stokes–Einstein equation [59]

$$D_{a,b} = \frac{k_b \cdot T}{6 \cdot \pi \cdot \eta \cdot r_H} \quad (3.97)$$

with Boltzman constant k_B , temperature T , dynamic viscosity η , and the hydrodynamic radius of the diffusing molecule, r_H . While the contact time can be straightforwardly calculated in a falling film by knowing the average velocity of the falling liquid and the film length, in stirred tank reactors, equations have been derived using the energy dissipation rate, which, in turn, is dependent on the power input, P/V_f [74]:

$$t_c = \sqrt{\frac{\eta_L \cdot V_L}{P}} \quad (3.98)$$

To determine the transfer area for a falling film on a capillary, the formula for calculating the surface of a cylinder can be applied, if the falling film is laminar (no waves) and the film thickness is known. In stirred systems, the average Sauter mean diameter of the bubbles,

$$d_{32} = 6 \cdot \frac{\sum V_{b,i}}{\sum A_{s,b,i}} \quad (3.99)$$

as well as the gas holdup inside the system must be known,

$$\varphi_G = \frac{V_G}{V_G + V_L} \quad (3.100)$$

with the volume of the i -th bubble, $V_{b,i}$, the surface area of the i -th bubble, $A_{s,b,i}$ the volume of the liquid, V_L , and the gas volume, $V_G = \sum V_{b,i}$. Both properties are often not available. The specific surface area can then be calculated via

$$a = \frac{6}{d_{32}} \cdot \varphi_G \quad (3.101)$$

Prediction of the gas absorption in stirred systems is usually presented in form of correlations for the volumetric mass transfer coefficient, $(k_L a)$, and is dependent on the power input, P/V_L , and superficial gas velocity, v_G , in the form of

$$k_L a = C \cdot \left(\frac{P}{V_L} \right)^a v_G^b \quad (3.102)$$

with the correlation constant, C , and the exponents, a and b . Poncin et al. [192] showed that these correlations can also apply to gas-inducing stirrers. It was not possible to measure the superficial gas velocity in the stirred tank experiments, directly. The superficial gas velocity was estimated using the correlation of Heim [105]. The gas holdup was measured for air at ambient pressure and temperature ($p = 1.013$ bar, $T = 20^\circ\text{C}$). To measure the gas holdup, the reactor was completely filled with the liquid. Upon starting the gas flow, the liquid was displaced from the tank by the gas, and the volume of displaced liquid was measured. A comparison of the values of the gas holdup predicted by the correlation to those of the experiments is shown in Figure 3.71. The comparison between the experiments and the correlation of Heim et al. [105]

$$\varphi_G = 28.96 \cdot Fr^{0.968} \cdot Re^{-0.354} \cdot Q^{0.644} \cdot \left(\frac{d_{st}}{H - h_c} \right)^{0.176}, \quad (3.103)$$

with the Froude number, $Fr = n^2 \cdot d_{st}/g$ and the dimensionless gas flow rate, $Q = \dot{V}_G/n \cdot d_{st}^3$, revealed that the correlation could predict the order of magnitude as well as the overall trend for different stirring frequencies and liquids (gas holdup dodecane > water) sufficiently accurate. The reasonable agreement in the measured and predicted values of the gas holdup supported the use of this correlation for estimating the gas superficial velocity.

To separate the effects of influencing parameters on the liquid mass transfer coefficient, k_L , from the effects on the transfer area, a in chemical reactors, the liquid mass transfer coefficient, k_L , was investigated in a falling film contactor, with a defined interfacial area available for mass transfer (Section 3.3.3.1). The mass transfer coefficient depends on both the physical properties of the materials and the hydrodynamics of the system. The dependence on the diffusion coefficient, a physical property of the liquid, is proposed differently in the film theory (eq. (3.95)) than in

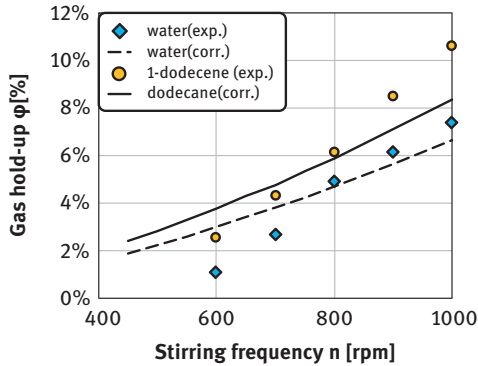


Figure 3.71: Values of gas holdup in water and dodecane at 20 °C from experiments (symbols) compared to the predictions from the correlation of Heim et al. [105] (lines). From Petzold et al. [188].

penetration theory (eq. (3.96)). The diffusion coefficient, ($D_{a,b}$) increases with increase in the temperature, and so does the mass transfer coefficient. Unlike gas solubility, which depends on temperature and pressure, the mass transfer coefficient and diffusion coefficient is not influenced by pressure. The rates of mass transfer for pure gases (hydrogen, oxygen, nitrogen, and helium) in water and n-dodecane were measured in the falling film contactor [3]. The values of the mass transfer coefficient obtained are shown in Figure 3.72, with respect to the diffusion coefficients of the systems, according to values given in the literature [237]. A comparison of the

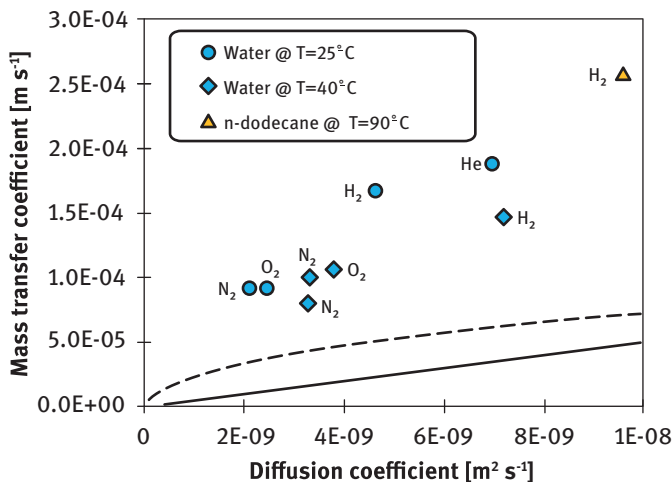


Figure 3.72: Relationship between measured values (symbols) of the mass transfer coefficient and the diffusion coefficient compared to the predictions according to the film theory (black solid line) and penetration theory (dotted line) (from Afraz et al. [3]).

experimental values to the values predicted for a laminar, falling film by film theory and penetration theory is shown, as well.

As shown in Figure 3.72, gases with higher diffusion coefficients have higher mass transfer rates. The diffusion coefficient increases with increasing temperature, and accordingly, the mass transfer coefficient increases, as well. For all gases and liquids investigated, higher rates of mass transfer were measured experimentally than predicted by models. Higher rates of mass transfer are essentially beneficial, since engineers are mostly involved with how to increase rates of mass transfer. However, this discrepancy limits the applicability of the theoretically predicted values. As a common rule of thumb, a k_L value of 1×10^{-4} m/s for water at ambient conditions is suggested [3]. This value gives an appropriate fit for nitrogen and oxygen gases at 295–313 K, which corresponds to diffusion coefficients of around 3.5×10^{-9} m²/s. This rule of thumb can be combined with the observed values of the interfacial area to give a rough approximation of the mass transport coefficient, $k_L a$, in a wide range of gas–liquid contacting apparatuses ranging from bubble columns to stirred tanks.

As an example, in the stirred tank reactor used in these investigations, bubbles with a Sauter mean diameter of 327×10^{-6} m were observed for hydrogen gas in water at a temperature of 76 °C, the pressure of 40 bar, and stirring speed of 1000 rpm. The diffusion coefficient of hydrogen in water at this temperature is about 7 times that of oxygen in water at ambient temperature. Thus, combining a general mass transport coefficient, k_L , for these conditions of 1.5×10^{-4} m/s with the interfacial area observed in the experiments would result in a volumetric mass transfer coefficient, $k_L a$ of 0.193 s^{-1} , for this system at 76 °C. Estimations of the volumetric mass transfer coefficient, $k_L a$, from measurements of the pressure decrease in the stirred tank reactor due to the absorption of hydrogen gave values of 0.14 s^{-1} at 80 °C and 0.17 s^{-1} at 90 °C. Thus, accounting for the diffusion coefficient in the system as suggested by Afraz et al. [3] and using direct observations of the interfacial area for transfer could be seen to give a reasonably good agreement in this system. The reason for this good agreement is that the interfacial area is the parameter that is highly relevant for the rate of mass transfer and tends to be influenced the most by changes in the system or operating parameters. Increasing the energy input to the system, e.g., through a higher power input or higher superficial gas velocity typically increases the interfacial area, and the rate of mass transfer can be predicted. But changes in the system – especially changing the liquid or gas from a model system to a technically relevant process – often affect the interfacial area in ways that cannot be predicted by changes in the physical properties (density, viscosity, surface tension) of the system alone but also depend upon the effect of these changes on the rates of bubble coalescence and breakup [103].

The determination of k_L from experiments in the falling film contactor revealed faster mass transfer than predicted by mass transfer theories. The predictions of correlations for mass transfer proposed in the literature were also evaluated. The values of the volumetric mass transfer coefficient, $k_L a$, derived from measurements in the stirred tank reactor were compared with common correlations following eq. (3.102). Since

most correlations are derived from measurements using model systems consisting of oxygen or air and water or aqueous solutions at ambient pressure and temperature, the mass transfer into the water was investigated. In all correlations, the superficial gas velocity was calculated according to the correlation of Heim et al. [105]. The volumetric mass transfer coefficients, $k_L a$, derived from measurements of the mass transfer of hydrogen in water at different stirring speeds and temperatures are compared to established correlations in Figure 3.73. Correlations derived from investigations using pure water were found to underpredict the experimental measured mass transfer of hydrogen in water at 90 °C. The correlations are closer to the prediction of the $k_L a$ at 20 °C, for which they were originally designed, with Linek et al. [152] giving the best fit. Only correlations for aqueous salt solutions of Smith et al. [228] and van Riet [236] gave better results for the 90 °C measurements, where the correlation of van Riet [236] overpredicted the experimental value. Thus, the predictive capabilities of correlations were already limited for measurements in pure water using hydrogen gas at elevated pressures. Correlations were able to predict the trend affected by changes in parameters such as the stirring speed but predicted a wide range of possible rates of mass transfer.

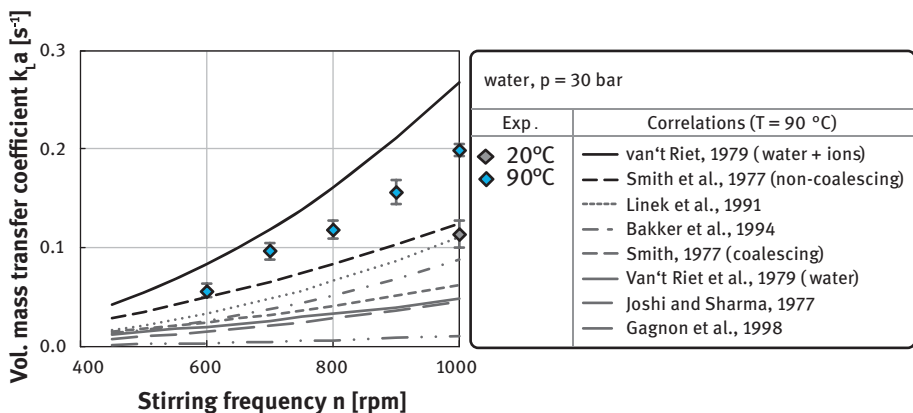


Figure 3.73: Comparison of experimental $k_L a$ values of hydrogen mass transfer into water with existing correlations from literature. References: Van't Riet, 1979 [236]; Smith et al., 1977 [228]; Linek et al., 1994 [152]; Bakker et al. 1994 [14]; Joshi and Sharma, 1977 [125]; Gagnon et al., 1998 [72].

The rate of mass transfer of a gas into mixtures of immiscible liquids was investigated in the stirred tank reactor. The influence of an additional dispersed phase on the gas absorption rate was investigated, using hydrogen gas and water and 1-dodecene as immiscible liquids; the measured $k_L a$ values for different volume fractions of 1-dodecene are shown in Figure 3.74. The volumetric mass transfer coefficient, $k_L a$, was derived from measurements of the pressure decrease in the system due to the physical absorption of hydrogen into the liquids, as explained in Section 3.3.3.2. At a volume fraction of $\varphi_d = 0$ vol.-%, pure water is present, while at $\varphi_d = 100$ vol.-%,

pure 1-dodecene makes up the liquid phase. The rate of mass transfer into pure 1-dodecene was higher than into water. Adding a second liquid was observed to decrease the rate of mass transfer, compared to the pure liquids. When adding 1-dodecene to water, the volumetric mass transfer coefficient decreases with the increasing volume fraction of 1-dodecene and reaches a minimum that is only 25% of the value observed in pure water. From a volume fraction of 1-dodecene of around $\varphi_d = 70$ vol.-%, the $k_L a$ value rises again, up to the value of pure 1-dodecene. Conductivity measurements reveal that phase inversion occurs at around 70 vol.-% of 1-dodecene. High amounts of disperse phase fraction, therefore, reduce the $k_L a$ drastically to 20–25% of the rates observed in the pure liquids, and this effect is observed when the continuous phase is aqueous as well as when the continuous phase is organic.

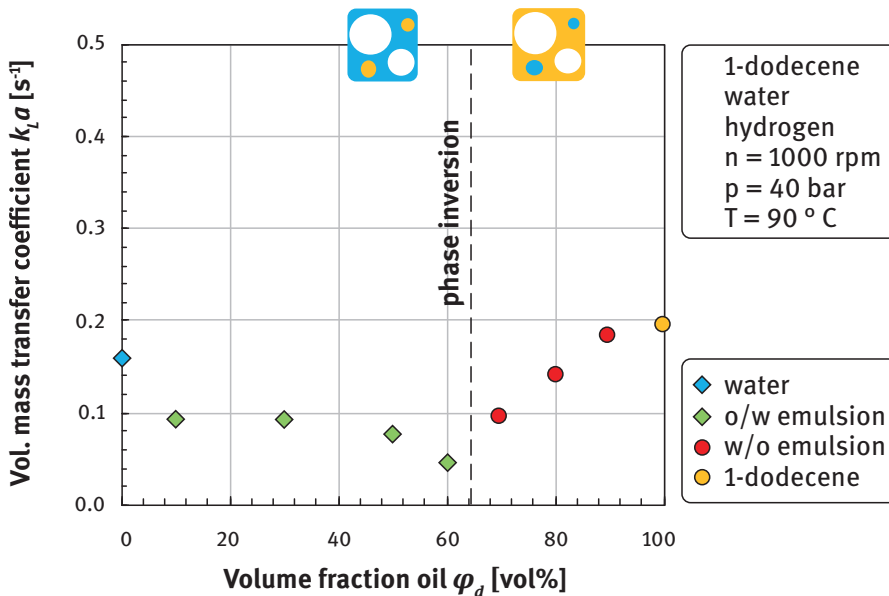


Figure 3.74: Volumetric mass transfer coefficients for the transfer of hydrogen into mixtures of different volume fractions of 1-dodecene in water. Symbols: blue diamond: water; green diamonds: oil in water emulsion; orange circles: water in oil emulsion; yellow circle: 1-dodecene. See also legend in Figure 3.76.

The gas–liquid mass transport depends upon the flux across the interface as well as the size of the interface. Changes in the interfacial area result in proportional changes of the mass transfer rate. Thus, the bubble sizes and interfacial areas for mixtures of immiscible liquids may contribute to the differences in the rates of mass transfer observed when adding an additional liquid, as shown in Figure 3.74. Bubble diameters were obtained with an endoscope imaging technique (Section 3.3.2.3 and Figure 3.75) and evaluated with an algorithm from SOPAT GmbH [156] for spherical

and convolutional neural network (Mask RCNN), as developed by [184] for deformed objects. Examples of photographs collected with the endoscope and the bubbles identified by the algorithm are shown in Figure 3.75. The Sauter mean diameter, d_{32} , for the bubble populations observed are shown in Figure 3.76. Higher liquid-disperse phase fractions shift the bubble size distribution to larger diameters and, therefore, larger Sauter mean diameters. Generally, a smaller bubble size corresponds to a higher interfacial area. The reason for this is twofold. First, smaller bubbles have a higher volume-specific interfacial area compared to larger bubbles. Second, larger bubbles have a smaller residence time in a liquid and leave the system more rapidly. This reduces the overall amount of gas in the system and, with it, the contact area between gas and liquid. Therefore, the interfacial area depends upon the amount of gas in the system (more gas leads to higher rates of mass transfer) as well as the dispersion of the gas (smaller bubbles offer a higher interfacial area). The gas holdup determined from the amount of liquid displaced from the tank by the gas is also shown for comparison, along with the Sauter mean bubble diameters, in Figure 3.76.

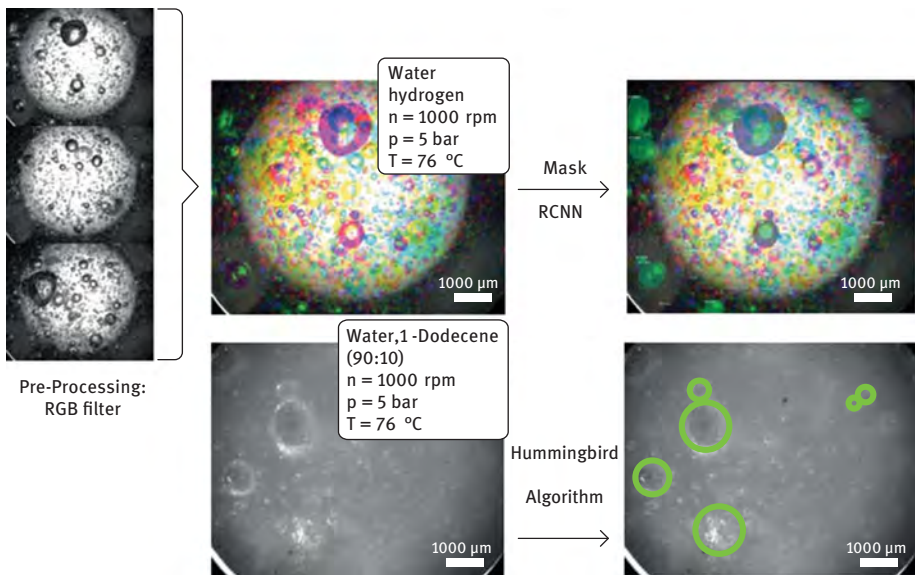


Figure 3.75: Top: particle detection of hydrogen bubbles in water via convolutional neural network Mask RCNN and RGB filter [184]. Bottom: bubbles in water/1-dodecene dispersion detected with SOPAT particle algorithm for spherical objects [156].

Bubbles in pure 1-dodecene were observed to be 25% smaller in diameter than in water. This is due to the interfacial tension of hydrogen in 1-dodecene being less than half the value (30 mN/m) of the interfacial tension in water (72 mN/m) [188]. The smaller bubbles corresponded to a higher gas holdup (Figure 3.76) in the system as well as offering a higher interfacial area and, thus, resulted in a higher rate

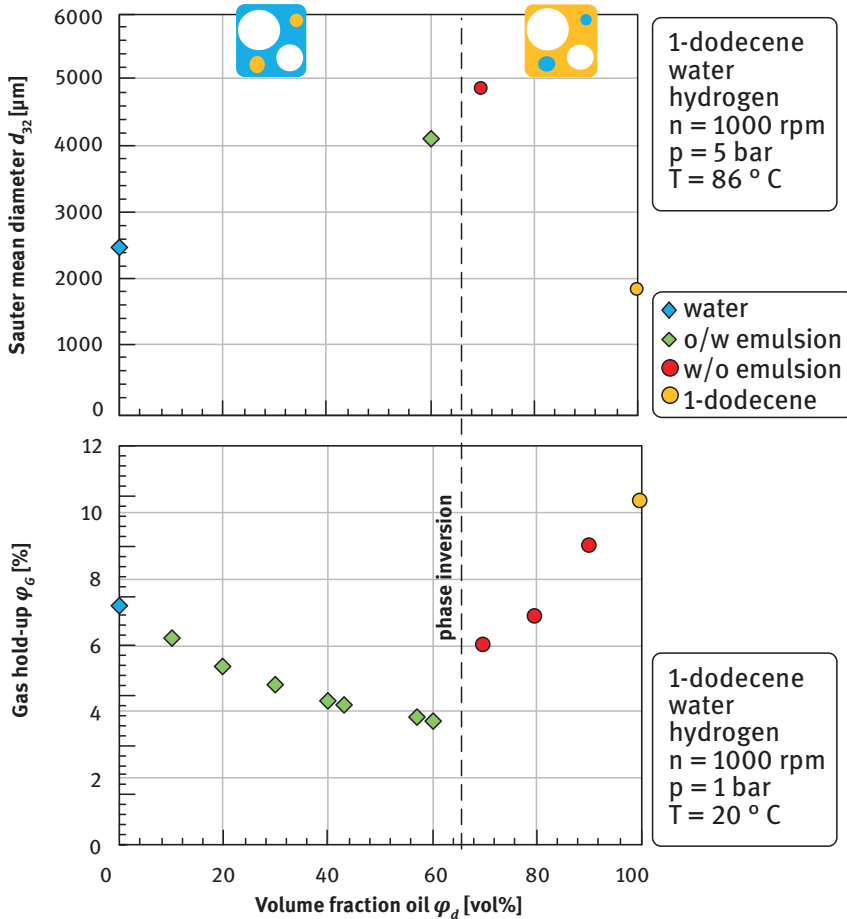


Figure 3.76: Top: Sauter mean diameter of gas bubbles in water/1-dodecene dispersions. Bottom: gas holdup measured with volume supersede method in water/1-dodecene dispersions.

of mass transfer (Figure 3.74). For high volume fractions of the liquid disperse phase close to the point where the continuous phase inverts, the Sauter mean diameter of the bubbles almost doubles. The larger bubble sizes correspond to a lower gas holdup (Figure 3.76) in the system as well as a smaller volume-specific interfacial area and can, thus, be used to understand the lower rates of mass transfer observed in these systems (Figure 3.74).

3.3.5 Effect of Mass Transfer on Reaction Selectivity

The mass transfer was investigated in systems involving homogeneously catalyzed gas–liquid reactions representing reactions starting from bio-based materials, in fulfillment of the aims of this book. The hydroformylation of 1-dodecene with hydrogen and carbon monoxide to form tridecanal as n-aldehyde was performed using a diphosphite ligand-modified rhodium-based catalyst (Rh/BIPHEPHOS). The reaction to form the n-aldehyde competes with other reactions such as the iso-selective hydroformylation to form branched iso-aldehydes (regioselectivity) and the isomerization of the terminal 1-alkene to form internal alkenes (chemoselectivity). To experimentally investigate the fundamental influence of mass transport on the chemo- and regioselectivity of Rh/BIPHEPHOS-catalyzed hydroformylation, two parameters were varied: the process pressure of synthesis gas, p_{CO/H_2} , and two different reactor geometries having different mass transport coefficients, $k_L a$, were compared. The first reactor geometry (R1) consisted of a 75 mL autoclave with a simple magnetic stirrer operated at 1,200 rpm. The second reactor geometry (R2) consisted of an 1,800 mL autoclave with a gas entrainment impeller, which was designed to incorporate gas into the liquid through surface entrainment, operated at 800 rpm. The thermomorphic multiphase system, consisting of 37 mol.-% decane, 49 mol.-% dimethylformamide (DMF), and 13 mol.-% 1-dodecene, forms a single phase at 105 °C. The mass transfer coefficients, $k_L a$, in this system were determined from the pressure decrease in the closed systems following a pressure step, as described in Section 3.3.3.1. The mass transfer coefficients determined for hydrogen and carbon monoxide gases are summarized in Table 3.6. For R2, significantly higher mass transfer coefficients were determined for CO and H₂, compared to R1. The different mass transfer coefficients for R1 and R2 are not only due to the stirrer geometry but also due to the entire reactor configuration and the differences in scale [151].

The local concentration of dissolved gas available for a hydroformylation reaction in this system is, thus, higher in R2, since it has a higher rate of gas–liquid mass transfer. The local concentration of dissolved gas is also influenced by the gas pressure in the system. The process pressure of the synthesis gas (CO:H₂ = 1:1, semi-batch) was varied between 5 bar and 40 bar for a fixed decane/DMF solvent composition. In the standard procedure for kinetic hydroformylation experiments, 1-dodecene was exposed to

Table 3.6: Mass transfer coefficients of different reactor configurations measured for hydrogen and carbon monoxide gases in a thermomorphic multiphase system consisting of decane/DMF/1-dodecene = 37/49/13 (mol%).

Reactor configuration	Stirrer speed (rpm)	$k_L a$ CO gas(s ⁻¹)	$k_L a$ H ₂ gas(s ⁻¹)
R1, magnetic stirrer	1200	0.04	0.04
R2, gas entrainment impeller	800	0.21	0.23

the corresponding process pressure of synthesis gas at room temperature, shortly before the kinetic experiment started and was injected afterwards. The kinetic experiments on hydroformylation at 5 bar ($\text{CO}:\text{H}_2 = 1:1$) show a significant influence of the reactor configuration on the chemoselectivity (Figure 3.77). For the reactor configuration R1, low yields of n-aldehyde of 39.9% were obtained after 90 min, whereas the yield of dodecene isomers was significantly increased by 53.4%. In contrast, for R2 with an increased mass transfer coefficient, an improvement could be achieved, shifting the chemoselectivity significantly from isomerization towards n-selective hydroformylation by approx. 10%.

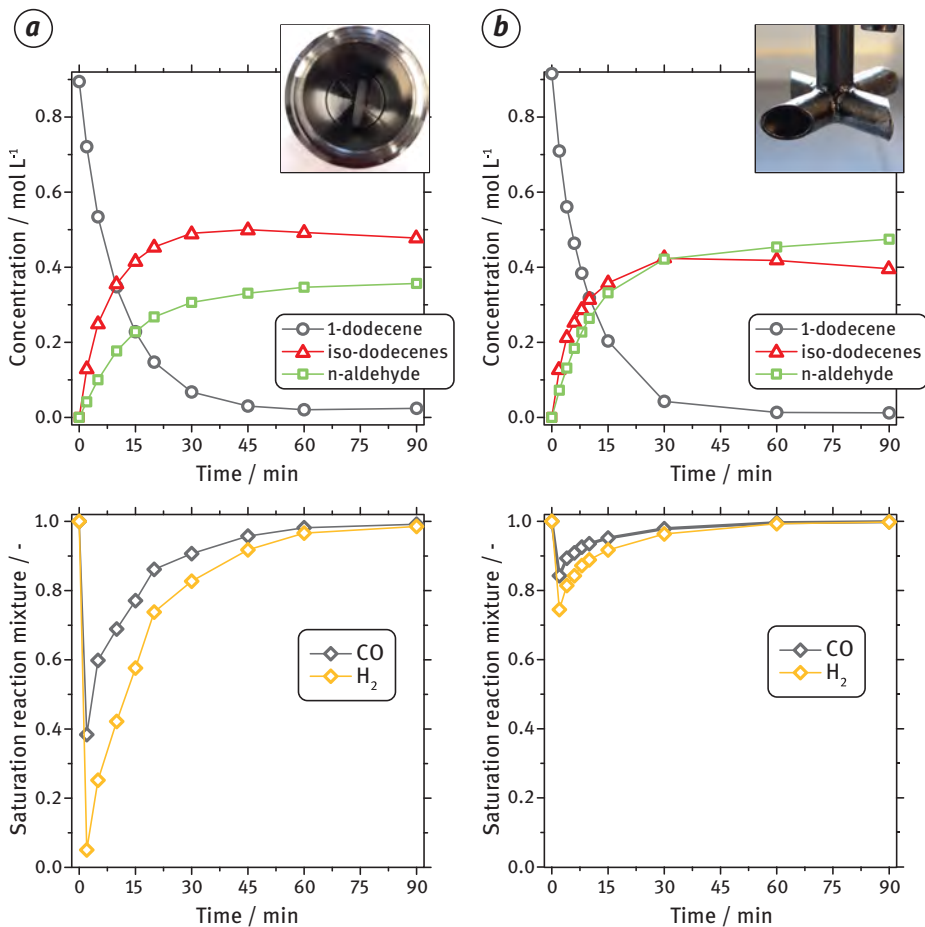


Figure 3.77: Comparison of the experimental values for the concentration of n-aldehyde and iso-dodecene (top) and the modeled saturation of the liquid phase with the dissolved gas species (bottom) for the hydroformylation of 1-dodecene performed in a mixture of decane and DMF at 5 bar at 105 °C in an autoclave with a slower rate of gas/liquid mass transfer (R1, left) and in an autoclave with more effective gas/liquid mass transfer (R2, right).

Using the formation rates of the CO and H₂ consuming reactions (hydroformylation, hydrogenation), an estimation of the time-dependent concentrations, c_A , of CO and H₂ in the reaction mixture was performed based on a semi-batch reactor model:

$$\frac{dc_A}{dt} = (k_L a)_A \cdot (c_A^* - c_A) + R_A \quad (3.104)$$

In the reaction network of hydroformylation (Section 3.2.2.1, Figure 3.45), n- and iso-selective hydroformylation (r_{nHYFO} , r_{isoHYFO}) and hydrogenation (r_{HYD}) were considered as relevant reactions with respect to CO and H₂. Thus, considering the stoichiometric coefficients, ν_A , the reaction terms, R_{CO} and R_{H_2} result in:

$$R_{\text{CO}} = -r_{\text{nHYFO}} - r_{\text{isoHYFO}} \quad (3.105)$$

$$R_{\text{H}_2} = -r_{\text{nHYFO}} - r_{\text{isoHYFO}} - r_{\text{HYD}} \quad (3.106)$$

The reaction rates were approximated based on experimental data for the products:

$$r_{\text{nHYFO}} = \frac{dc_{\text{nAld}}}{dt} \approx \frac{\Delta c_{\text{nAld}}^{\text{Exp}}}{\Delta t^{\text{Exp}}} \quad (3.107)$$

$$r_{\text{isoHYFO}} = \frac{dc_{\text{isoAld}}}{dt} \approx \frac{\Delta c_{\text{isoAld}}^{\text{Exp}}}{\Delta t^{\text{Exp}}} \quad (3.108)$$

$$r_{\text{HYD}} = \frac{dc_{\text{Alk}}}{dt} \approx \frac{\Delta c_{\text{Alk}}^{\text{Exp}}}{\Delta t^{\text{Exp}}} \quad (3.109)$$

To solve the differential equations eq. (3.104) numerically, the gas solubility in the reaction system at the gas–liquid equilibrium, c_A^* , and the experimentally determined mass transfer coefficients, $k_L a$ of CO and H₂ were used in addition. The gas solubilities of CO and H₂ in the reaction system at the gas–liquid equilibrium, c_A^* (Table 3.7), were calculated using PC-SAFT equation of state [238, 239]. As a result, the time-dependent saturation, $\eta_A = c_A(t)/c_A^*(t)$ for CO and H₂ in the reaction mixture could be simulated. The evolution in the extent of saturation of the liquid with the reactants from the gas phase over time is shown for the reaction at 5 bar in Figure 3.77 and at 30 bar in Figure 3.78.

Table 3.7: Gas solubilities for hydrogen and carbon monoxide gases at 105 °C for different pressures (CO/H₂ = 1:1) and a fixed decane/DMF solvent composition ($c_{1-\text{Dodecene}}^0 = 0.9 \text{ mol L}^{-1}$).

Decane/DMF (wt%/wt%)	Temperature (°C)	Pressure (bar)	c_{CO}^* (mol L ⁻¹)	$c_{\text{H}_2}^*$ (mol L ⁻¹)
60/40	105	5	0.020	0.011
60/40	105	30	0.119	0.067

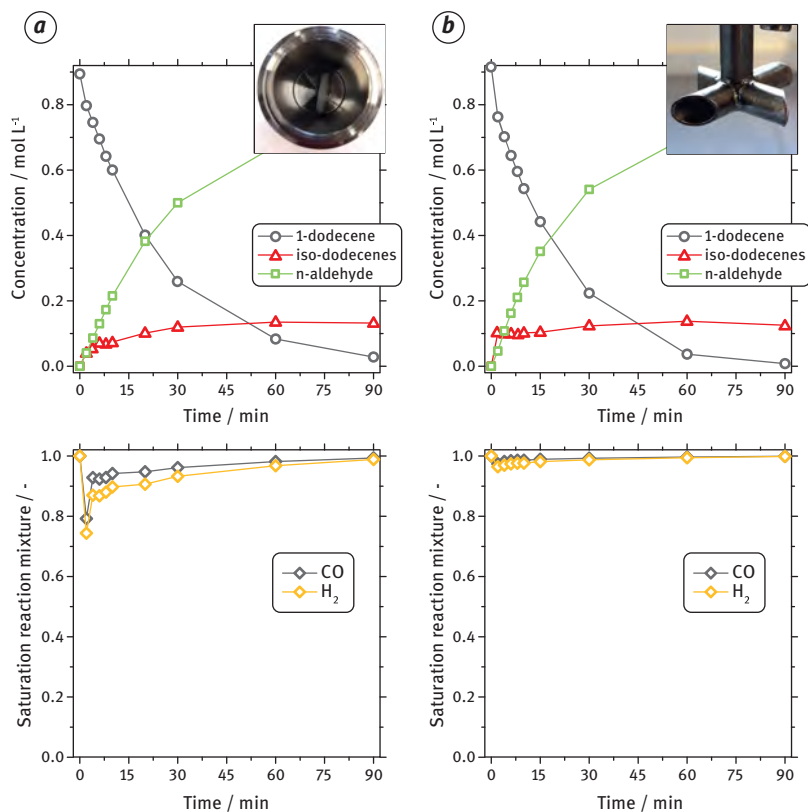


Figure 3.78: Comparison of the experimental values for the concentration of n-aldehyde and iso-dodecene (top) and the modeled saturation of the liquid phase with the dissolved gas species (bottom) for the hydroformylation of 1-dodecene performed in a mixture of decane and dimethylformamide at 30 bar at 105 °C in an autoclave with a slower rate of gas/liquid mass transfer (R1, left) and in an autoclave with more effective gas/liquid mass transfer (R2, right).

For the reactor configuration, R1, with lower mass transfer coefficients, a significant depletion of CO and H₂ in the reaction mixture is observed at 5 bar but not at 30 bar. For the reactor configuration R2, CO and H₂ are transferred much faster from the gas phase to the liquid phase, due to the increased rates of mass transfer. The dissolved concentrations in the liquid, C_A , are maintained to values of at least 70% of the equilibrium value (C_A)* at 5 bar and 95% of the equilibrium value at 30 bar. The kinetic hydroformylation experiments at 30 bar (CO:H₂ = 1:1) show that the chemoselectivity of the reaction is not significantly influenced by the reactor configuration, because the concentrations of dissolved gases are maintained at high levels in both systems due to the increased pressure. For R1 and R2, at 30 bar high yields of n-aldehyde of 82.4% and 80.5% were obtained, whereas low yields of dodecene isomers of 10.5% and 13.7% were observed, respectively. The analysis of the saturation for CO

and H₂ in the reaction mixture shows a stronger deviation for the reactor configuration, R1, compared to R2. Due to the higher process pressure of 30 bar and the resulting higher concentrations of dissolved CO and H₂ (Table 3.7), the relative deviations are significantly smaller, compared to the kinetic experiments at 5 bar. The relative deviation from the solubility equilibrium alone cannot explain the shift in chemoselectivity towards isomerization.

In summary, a basic influence of mass transport on the rate of the hydroformylation reaction and the resulting product distribution can be outlined. With respect to the reaction network and the reaction mechanism, the local depletion of CO and H₂ in the reaction mixture causes a shift of chemoselectivity from hydroformylation to isomerization, as the latter only needs the 1-alkene to proceed. This is achieved by low mass transfer coefficients and low synthesis gas pressures (low concentration of dissolved gases) and can be triggered additionally by increasing the 1-alkene and/or the catalyst concentration, leading to higher CO and H₂ consumption rates. The increase of mass transport leads to a higher saturation for CO and H₂ in the reaction solution, which reduces a local depletion of CO and H₂. Nevertheless, at low synthesis pressures, local depletion at the catalyst center cannot be excluded, so the additional increase in pressure increases the availability of CO and H₂. Chemoselectivity toward isomerization is desirable when the objective is *n*-selective hydroformylation of internal double bonds, as found in renewable feedstocks such as methyl oleate. Therefore, the migration of the double bond to the terminal end of the substrate is needed prior to the hydroformylation, which is applied in isomerizing hydroformylation reactions [73, 122].

The methods for investigating multiphase mass transfer detailed in this section have been used to investigate mass transfer in novel liquid phases including microemulsion systems, thermomorphic multiphase systems, and Pickering emulsions. All of them were investigated in the framework of this book for their use in combining organic molecules from renewable resources with aqueous and gas phases to create chemical products using sustainable, green chemical processes. Further details of these investigations are reported in the respective sections about each phase system. When investigating the mass transfer in microemulsion systems, thermomorphic multiphase systems, and Pickering emulsions, both the effects of these novel liquid phase systems on the mass transfer coefficient, k_L , as well as the influence of multiple phases on the specific transfer area, a , impact the observed rates of mass transfer and must be considered. The rate of mass transfer is important not only for the efficiency of the overall process but also for impacts on local reactant concentrations. This is accompanied by wide-ranging impacts varying from the rate of the chemical reaction to the selectivity of the chemical reactions, with decisive impacts on the purity of the chemical products and the overall feasibility of the process.

References

- [1] Abraham MH. 1984: Thermodynamics of solution of homologous series of solutes. *Water. J. Chem. Soc. Farad. Trans.* 1(80): 153–181.
- [2] Abraham MH, Matteoli E. 1988: The temperature variation of the hydrophobic effect. *J. Chem. Soc. Farad. Trans.* 1(84): 1985–2000.
- [3] Afraz N, Adi A, Hecht K. 2021: The effect of diffusion on mass transfer in a laminar falling film: Observation versus theory. *Chem. Eng. Sci.* 232: 116363.
- [4] Ahmed M, Seayad AM, Jackstell R, Beller M. 2003: Amines made easily: A highly selective hydroaminomethylation of olefins. *J. Amer. Chem. Soc.* 125: 10311–10318.
- [5] Ahmed M, Bronger RPJ, Jackstell R, Kamer PCJ, van Leeuwen PWNM, Beller M. 2006: Highly selective hydroaminomethylation of internal alkenes to give linear amines. *Chemistry*. 12: 8979–8988.
- [6] Ahmed M, Buch C, Routaboul L, Jackstell R, Klein H, Spannenberg A, Beller M. 2007: Hydroaminomethylation with novel rhodium-carbene complexes: An efficient catalytic approach to pharmaceuticals. *Chemistry*. 13: 1594–1601.
- [7] Antonelli ML, Bonicelli MG, Ceccaroni G, La Mesa C, Sesta B. 1994: Solution properties of octyl- β -D-glucoside. Part 2. thermodynamics of micelle formation. *Colloid Polym. Sci.* 272: 704–711.
- [8] Antosik M, Stafiej A, Stryjek R. 1990: Mutual solubility of binary trans-decalin +, and n-decane + polar component mixtures. *Fluid Phase Equilib.* 58: 325–333.
- [9] Aoudia M, Zana R. 1998: Aggregation Behavior of Sugar Surfactants in Aqueous Solutions: Effects of Temperature and the Addition of Nonionic Polymers. *J. Colloid Interface Sci.* 206: 158–167.
- [10] Astray G, Cid A, Manso JA, Mejuto JC, Moldes O, Morales J, Quintás J. 2011: N-alkylamines-based micelles aggregation number determination by fluorescence techniques. *J. Solution Chem.* 40: 2072–2081.
- [11] Aveyard R, Haydon DA. 1965: Thermodynamic properties of aliphatic hydrocarbon/water interfaces. *Trans. Faraday Soc.* 61: 2255–2261.
- [12] Baerns M, Behr A, Brehm A, Gmehling J, Hinrichsen KO, Hofmann H, Palkovits R, Onken U, Renken A. 2013: *Technische Chemie*. Second Edition, Weinheim, Wiley-VCH.
- [13] Bakeeva RF, Fedorov SB, Kudryavtseva LA, Belskii VE, Ivanov BE. 1984: Colloidal properties of aqueous solutions of partly protonated long chain amines. *Kolloidn. Zh.* 46: 755–757.
- [14] Bakker A, Van Den Akker HEA. 1994: Gas-liquid contacting with axial flow impellers. *Chem. Eng. Res. Des.* 72: 573–582.
- [15] Barcia PS, Silva JAC, Rodrigues AE. 2005: Adsorption equilibrium and kinetics of branched hexane isomers in pellets of BETA zeolite. *Microp. Mesop. Mat.* 79: 145–163.
- [16] Barz T, López Cárdenas DC, Arellano-García H, Wozny G. 2013: Experimental evaluation of an approach to online redesign of experiments for parameter determination. *AIChE J.* 59: 1981–1995.
- [17] Becker S, Werth S, Horsch M, Langenbach K, Hasse H. 2016: Interfacial tension and adsorption in the binary system ethanol and carbon dioxide: Experiments, molecular simulation and density gradient theory. *Fluid Phase Equilib.* 427: 476–487.
- [18] Behr A, Roll R. 2005: Hydroaminomethylation in thermomorphic solvent systems. *J. Mol. Cat A: Chem.* 239: 180–184.
- [19] Behr A, Neubert P. 2012: *Applied Homogeneous Catalysis*. Weinheim, Wiley-VCH-Verlag.
- [20] Beller M (Ed.) 2012: *Catalysis. From Principles to Applications*. Weinheim, Wiley-VCH-Verlag.

- [21] Bianga J, Künnemann KU, Gaide T, Vorholt AJ, Seidensticker T, Dreimann JM, Vogt D. 2019: Thermomorphic multiphase systems: Switchable solvent mixtures for the recovery of homogeneous catalysts in batch and flow processes. *Chemistry*. 25: 11586–11608.
- [22] Bianga J, Künnemann KU, Goclik L, Schurm L, Vogt D, Seidensticker T. 2020: Tandem catalytic amine synthesis from alkenes in continuous flow enabled by integrated catalyst recycling. *ACS Catal*. 10: 6463–6472.
- [23] Boz E, Tüzün NŞ, Stein M. 2018: Computational investigation of the control of the thermodynamics and microkinetics of the reductive amination reaction by solvent coordination and a co-catalyst. *RSC Adv*. 8: 36662–36674.
- [24] Brauer H. 1979: *Particle/Fluid Transport Processes*. Fortschritte in der Verfahrenstechnik. Düsseldorf, VDI Verlag.
- [25] Browarzik D. 2009: Calculation of excess functions and phase equilibria in binary and ternary mixtures with one associating component. *J. Mol. Liq*. 146: 95–104.
- [26] Brun R, Reichert P, Künsch HR. 2001: Practical identifiability analysis of large environmental simulation models. *Water Resour. Res*. 37: 1015–1030.
- [27] Budantseva LS, Lesteva TM, Nemtsov MS. 1975a: Liquid-vapor equilibrium in systems methanol-C7-8 hydrocarbons of different classes. *Zh. Fiz. Khim*. 49: 1844.
- [28] Budantseva LS, Lesteva TM, Nemtsov MS. 1975b: Liquid-vapor equilibria in methanol-C6 hydrocarbons of different classes. *Zh. Fiz. Khim*. 49: 260–261.
- [29] Bühl C, Enders S. 2016: Prediction of interfacial properties of ternary, sulfur containing mixtures. *J. Chem. Eng. Data*. 61: 4261–4269.
- [30] Burth M, Verghese GC, Velez-Reyes M. 1999: Subset selection for improved parameter estimation in on-line identification of a synchronous generator. *IEEE Trans. Power Syst*. 14: 218–225.
- [31] Butz J, Zimmermann P, Enders S. 2017: Impact of the equation of state on the calculated adsorption isotherm using DFT. *Chem. Eng. Sci*. 171: 513–519.
- [32] Cahn JW, Hilliard JE. 1958: Free energy of a nonuniform system. I. Interfacial free energy. *J. Chem. Phys*. 28: 258–267.
- [33] Calderbank PH, Korchinski JO. 1956: Circulation in liquid drops – A heat transfer study. *Chem. Eng. Sci*. 6: 65–78.
- [34] Carrillo E, Talanquer V, Costas M. 1996: Wetting transition at the liquid–air interface of methanol–alkane mixtures. *J. Phys. Chem*. 100: 5888–5891.
- [35] Casás LM, Touriño A, Orge B, Marino G, Iglesias M, Tojo J. 2002: Thermophysical properties of acetone or methanol + n -alkane (C9 to C12) mixtures. *J. Chem. Eng. Data*. 47: 887–893.
- [36] Castro G, Amigo A, Brocos P. 2014: Squeezing experimental measurements for a proper analysis of surfactant thermodynamics: octyl- β -d-glucopyranoside as a case study. *Fluid Phase Equilib*. 376: 31–39.
- [37] Cea-Klapp E, Míguez JM, Gómez-Álvarez P, Blas FJ, Quinteros-Lama H, Garrido JM. 2020: Molecular modelling techniques for predicting liquid-liquid interfacial properties of methanol plus alkane (n-hexane, n-heptane, n-octane) mixtures. *Phys. Chem. Chem. Phys*. 22: 27121–27133.
- [38] Cents AHG, Brillman DWF, Versteeg GF. 2001: Gas absorption in an agitated gas-liquid-liquid system. *Chem. Eng. Sci*. 56: 1075–1083.
- [39] Chao BT. 1962: Motion of spherical gas bubbles in a viscous liquid at large Reynolds numbers. *Phys. Fluids*. 5: 69–79.
- [40] Chen C, Dong XQ, Zhang X. 2016: Recent progress in rhodium-catalyzed hydroaminomethylation. *Org. Chem. Front*. 3: 1359–1370.
- [41] Chen J, Stebe KJ. 1996: Marangoni retardation of the terminal velocity of a settling droplet: The role of surfactant physico-chemistry. *J. Coll. Interf. Sci*. 178: 144–155.

- [42] Christiansen JA. 1953: The elucidation of reaction mechanisms by the method of intermediates in quasi-stationary concentrations. *Adv. Catal.* 5: 311–353.
- [43] Cintrón-Arias A, Banks HT, Capaldi A, Lloyd AL. 2009: A sensitivity matrix based methodology for inverse problem formulation. *J. Inverse Ill-posed Probl.* 2009(17): 545–564.
- [44] Clift R, Grace JR, Weber ME. 1978: *Bubbles, Drops, and Particles*. Academic Press.
- [45] Crozet D, Urrutigoity M, Kalck P. 2011: Recent advances in amine synthesis by catalytic hydroaminomethylation of alkenes. *Chem. Cat. Chem.* 3: 1102–1118.
- [46] Dahlmann U, Schneider GM. 1989: Liquid + liquid) phase equilibria and critical curves of (ethanol + dodecane or tetradecane or hexadecane or 2,2,4,4,6,8,8-Heptamethylnonane) from 0.1 to 120.0 MPa. *J. Chem. Thermodyn.* 21: 997–1004.
- [47] Danzer A, Enders S. 2018: Comparison of two modeling approaches for the interfacial tension of binary aqueous mixtures. *J. Mol. Liq.* 266: 309–320.
- [48] Danzer A, Enders S. 2019: Prediction of phase equilibrium and interfacial properties in the quaternary system water + 1-hexanol + hexylacetate + acetic acid. *Fluid Phase Equilib.* 493: 50–57.
- [49] Degiorgio V, Piazza R, Corti M, Minero C. 1985: Critical properties of nonionic micellar solutions. *J. Chem. Phys.* 82: 1025–1031.
- [50] Deshpande R. 1997: Effect of pH on rate and selectivity behavior in biphasic hydroformylation of 1-octene. *J. Mol. Cat A Chem.* 126: 133–140.
- [51] Deuffhard P, Hohmann A. 2019: *Numerische Mathematik*. 5. Auflage, Berlin, Boston, De Gruyter (De Gruyter Studium).
- [52] Diebolt O, van Leeuwen PWNM, Kamer PCJ. 2012: Operando spectroscopy in catalytic carbonylation reactions. *ACS Catal.* 2012(2): 2357–2370.
- [53] Dietrich E, Mathieu C, Delmas H, Jenck J. 1992: Raney-nickel catalyzed hydrogenations: gas-liquid mass transfer in gas-induced stirred slurry reactors. *Chem. Eng. Sci.* 47: 3597–3604.
- [54] Dohm S, Hansen A, Steinmetz M, Grimme S, Checinski MP. 2018: Comprehensive thermochemical benchmark set of realistic closed-shell metal organic reactions. *J. Chem. Theory Comp.* 14: 2596–2608.
- [55] Dudowicz J, Freed KF. 1991: Effect of monomer structure and compressibility on the properties of multicomponent polymer blends and solutions: 1. lattice cluster theory of compressible systems. *Macromolecules.* 24: 5076–5059.
- [56] Dumont E, Andrès Y, Le Cloirec P. 2006: Effect of organic solvents on oxygen mass transfer in multiphase systems: application to bioreactors in environmental protection. *Biochem. Eng. J.* 30: 245–252.
- [57] Ebner C, Saam WF, Stroud D. 1976: Density-functional theory of simple classical fluid. I. surfaces. *Phys. Rev. A.* 14: 2264–2273.
- [58] Eilbracht P, Bäracker L, Buss C, Hollmann C, Kitsos-Rzychon BE, Kranemann CL, Kranemann TR, Roggenbuck R, Schmidt A. 1999: Tandem reaction sequences under hydroformylation conditions: new synthetic applications of transition metal catalysis. *Chem. Rev.* 99: 3329–3366.
- [59] Einstein A. 1905: Über die von der molekularkinetischen Theorie der Wärme geforderte Bewegung von in ruhenden Flüssigkeiten suspendierten Teilchen. *Ann. Phys.* 322: 549–560.
- [60] Enders S, Häntzschel D. 1998: Thermodynamics of aqueous carbohydrate surfactant solutions. *Fluid Phase Equilib.* 153: 1–21.
- [61] Enders S, Quitzsch K. 1998: Calculation of interfacial properties of demixed fluids using density gradient theory. *Langmuir.* 14: 4606–4614.
- [62] Enders S. 2000: Phasen- und Grenzflächenverhalten von komplexen fluiden Systemen. Habilitation Thesis, University of Leipzig.

- [63] Enders S, Kahl H. 2007: Aggregation behavior of n-alkyl--D-glucopyranoside + water + alcohol mixtures. *Fluid Phase Equilib.* 261: 221–229.
- [64] Enders S, Langenbach K, Schrader P, Zeiner T. 2012: Phase diagrams for systems containing hyperbranched polymers. *Polymers.* 4: 72–115.
- [65] Evans D, Osborn JA, Wilkinson G. 1968: Hydroformylation of alkenes by use of rhodium complex catalysts. *J. Chem. Soc. A.* 3133–3142.
- [66] Feng ZG, Michaelides EE. 2001: Drag coefficients of viscous spheres at intermediate and high Reynolds numbers. *J. Fluids Eng. Trans. ASME.* 123: 841–849.
- [67] Fink M, Attarian A, Tran H. 2007: Subset selection for parameter estimation in an HIV model. *Appl. Math. Mech.* 7: 1121501–1121502.
- [68] Flory PJ. 1953: *Principles of Polymer Chemistry*. Ithaca, NY, USA, Cornell University Press.
- [69] Friedlander SK. 1961: A note on transport to spheres in Stokes flow. *AIChE J.* 7: 34–348.
- [70] Fu D, Gu F, Xie J. 2015: Effect of the quadrupolar contribution of CO₂ on the vapor-liquid equilibria and surface tensions of CO₂-hydrocarbon binary mixtures. *Fluid Phase Equilib.* 387: 146–153.
- [71] Fujimatsu J, Ogasawara S, Kuroiwa S. 1988: Lower critical solution temperature (LCST) and theta temperature of aqueous solutions of nonionic surface active agents of various polyoxyethylene chain length. *Colloid Poly. Sci.* 266: 594–600.
- [72] Gagnon H, Lounès M, Thibault J. 1998: Power consumption and mass transfer in agitated gas-liquid columns: A comparative study. *Can. J. Chem. Eng.* 76: 379–389.
- [73] Gaide T, Jörke A, Schlipköter KE, Hamel C, Seidel-Morgenstern A, Behr A, Vorholt AJ. 2017: Isomerization/hydroformylation tandem reaction of a decene isomeric mixture with subsequent catalyst recycling in thermomorphic solvent systems. *Appl. Cat. A General.* 532: 50–56.
- [74] Garcia-Ochoa F, Gomez E. 2004: Theoretical prediction of gas-liquid mass transfer coefficient, specific area and hold-up in sparged stirred tanks. *Chem. Eng. Sci.* 12: 2489–2501.
- [75] Garcia-Rio L, Leis JR, Mejuto JC, Mosquera V, Rodríguez-Dafonte P. 2007: Stability of mixed micelles of cetylpyridinium chloride and linear primary alkylamines. *Coll. Surf. A: Physicochem. Eng. Aspects.* 309: 216–223.
- [76] Garland M, Pino P. 1991: Kinetics of the formation and hydrogenolysis of acylrhodium tetracarbonyl. *Organometallics.* 10: 1693–1704.
- [77] Gerlach M, Abdul Wajid D, Hilfert L, Edelmann FT, Seidel-Morgenstern A, Hamel C. 2017: Impact of minor amounts of hydroperoxides on rhodium-catalyzed hydroformylation of long-chain olefins. *Catal. Sci. Technol.* 7: 1465–1469.
- [78] Gerlach M, Kirschtowski S, Seidel-Morgenstern A, Hamel C. 2018: Kinetic modeling of the palladium-catalyzed isomerizing methoxycarbonylation of 1-decene. *Chem. Ing. Tech.* 90: 673–678.
- [79] Gmehling J, Kleiber M, Kolbe B, Raray J. 2019: *Chemical Thermodynamics for Process Simulation*. Weinheim, Wiley-VCH.
- [80] Goetsch T, Zimmermann P, Van Den Bongard R, Enders S, Zeiner T. 2016: Superposition of liquid-liquid and solid-liquid equilibria of linear and branched molecules: Binary systems. *Ind. Eng. Chem. Res.* 55: 11167–11174.
- [81] Goetsch T, Zimmermann P, Van Den Bongard R, Enders S, Zeiner T. 2017a: Superposition of liquid-liquid and solid-liquid equilibria of linear and branched molecules: binary systems. *Ind. Eng. Chem. Res.* 56: 417–423.
- [82] Goetsch T, Danzer A, Zimmermann P, Köhler A, Kissing K, Enders S, Zeiner T. 2017b: Liquid-liquid equilibrium and interfacial tension of hexane isomers – Methanol systems. *Ind. Eng. Chem. Res.* 56: 9743–9752.

- [83] Goetsch T, Zimmermann P, Scharzec B, Enders S, Zeiner T. 2018: Liquid adsorption isotherms of isomeric mixtures. *Ind. Eng. Chem. Res.* 57: 11210–11218.
- [84] Gor GY, Paris O, Prass J, Russo PA, Carrott MMLR, Neimark AV. 2013: Adsorption of n-pentane on mesoporous silica and adsorbent deformation. *Langmuir*. 29: 8601–8608.
- [85] Gross J, Sadowski G. 2001: Perturbed-chain SAFT: an equation of state based on a perturbation theory for chain molecules. *Ind. Eng. Chem. Res.* 40: 1244–1260.
- [86] Gross J, Sadowski G. 2002: Application of the perturbed-chain SAFT equation of state to associating systems. *Ind. Eng. Chem. Res.* 41: 5510–5515.
- [87] Gross J, Vrabec J. 2006: An equation-of-state contribution for polar components: Dipolar molecules. *AIChE J.* 52: 1194–1204.
- [88] Grob S, Hasse H. 2005: Thermodynamics of phase and chemical equilibrium in a strongly nonideal esterification system. *J. Chem. Eng. Data*. 50: 92–101.
- [89] Haarmann N, Enders S, Sadowski G. 2018: Modeling binary mixtures of n-alkanes and water using PC-SAFT. *Fluid Phase Equilib.* 470: 203–211.
- [90] Haarmann N, Enders S, Sadowski G. 2019a: Heterosegmental modeling of long-chain molecules and related mixtures using PC-SAFT: 1. Polar compounds. *Ind. Eng. Chem. Res.* 58: 2551–2574.
- [91] Haarmann N, Enders S, Sadowski G. 2019b: Heterosegmental modeling of long-chain molecules and related mixtures using PC-SAF: 2. Associating compounds. *Ind. Eng. Chem. Res.* 58: 4625–4643.
- [92] Haarmann N, Sosa A, Ortega J, Sadowski G. 2019c: Measurement and prediction of excess properties of binary mixtures methyl decanoate + an even-numbered n-alkane (C₆–C₁₆) at 298.15 K. *J. Chem. Eng. Data*. 64: 2816–2825.
- [93] Haarmann N, Reinhardt A, Danzer A, Sadowski G, Enders S. 2020: Modeling of interfacial tensions of long-chain molecules and related mixtures using PC-SAFT and the density gradient theory. *J. Chem. Eng. Data*. 65: 1005–1018.
- [94] de Haan JW, van de Ven LJM. 1973: Configurations and conformations in acyclic, unsaturated hydrocarbons. A ¹³C NMR study. *Org. Magn. Reson.* 5: 147–153.
- [95] Hanna S, Holder JC, Hartwig JF. 2019: A multicatalytic approach to the hydroaminomethylation of α -olefins. *Angew. Chem. (Intern. Ed.)*. 58: 3368–3372.
- [96] Hansen JP, McDonald IR. 2013: *Theory of Simple Liquids*. 4th Edition. Academic Press/Elsevier.
- [97] Hadamard JS. 1911: Mouvement permanent lent d'une sphère liquide et visqueuse. *Comptes Rendus l'Académie Des Sci.* 152: 1735–1743.
- [98] Hamielec AE, Storey SH, Whitehead JM. 1963: Viscous flow around fluid spheres at intermediate Reynolds numbers (II). *Can. J. Chem. Eng.* 12: 246–251.
- [99] Hamerla T, Paul N, Kraume M, Schomäcker R. 2013: Aufklärung der Stofftransportwege in mizellaren Mehrphasenreaktoren am Beispiel der Hydroformylierung. *Chem. Ing. Tech.* 85: 1–11.
- [100] Handlos AE, Baron T. 1957: Mass and heat transfer from drops in liquid–liquid extraction. *AIChE J.* 3: 127–136.
- [101] Harper JF. 1972: The motion of bubbles and drops through liquids. *Adv. Appl. Mech.* 12: 59–129.
- [102] Hassan ITM, Robinson CW. 1977: Stirred-tank mechanical power requirement and gas holdup in aerated aqueous phases. *AIChE J.* 23: 48–56.
- [103] Hecht K, Bey O, Etmüller J, Graefen P, Friehmelt R, Nilles M. 2015: Effect of gas density on gas holdup in bubble columns. *Chem. Ing. Tech.* 87: 762–772.
- [104] Helfferich FG. 2004: *Kinetics of Multistep Reactions*. 2nd ed, Amsterdam, Boston, Elsevier.

- [105] Heim A, Krasawski A, Rzycki E, Stelmach J. 1995: Aeration of bioreactors by self-aspirating impellers. *Chem. Eng. J. Biochem. Eng. J.* 58: 59–63.
- [106] Hentschel B, Kiedorf G, Gerlach M, Hamel C, Seidel-Morgenstern A, Freund H, Sundmacher K. 2015: Model-based identification and experimental validation of the optimal reaction route for the hydroformylation of 1-dodecene. *Ind. Eng. Chem. Res.* 54: 1755–1765.
- [107] Higbie R. 1935: The rate of absorption of a pure gas into a still liquid during short periods of exposure. *AIChE J.* 31: 365–389.
- [108] Hoang MD, Wozny G, Brunsch Y, Behr A, Markert J, Hamel C, Seidel-Morgenstern A, Arellano-Garcia H. 2012: Model-based optimal design of experiments for determining reaction network structures. *Comp. Aided Chem. Eng.* 31: 705–709.
- [109] Hohenberg P, Kohn W. 1964: Inhomogeneous electron gas. *Phys. Rev.* 136: B864–B871.
- [110] Hohl L, Kraume M. 2018: The formation of complex droplets in liquid three phase systems and their effect on dispersion and phase separation. *Chemical Engineering Research and Design.* 29: 89–101.
- [111] Hong YP, Pan CT. 1992: Rank-revealing QR factorizations and the singular value decomposition. *Math. Comp.* 58: 213.
- [112] Hradetzky G, Hammerl I, Kisan W, Wehner K, Bittrich HJ. 1989: *Data of Selective Solvents*. Berlin, Verlag der Wissenschaften.
- [113] Hu S, Kinter RC. 1955: The fall of single liquid drops through water. *AIChE J.* 1: 42–48.
- [114] Huxoll F, Jameel F, Bianga J, Seidensticker T, Stein M, Sadowski G, Vogt D. 2021a: Solvent selection in homogeneous catalysis – Optimization of kinetics and reaction performance. *ACS Catal.* 11: 590–594.
- [115] Huxoll F, Schlüter S, Budde R, Skiborowski M, Petzold M, Böhm L, Kraume M, Sadowski G. 2021b: Phase equilibria for the hydroaminomethylation of 1-decene. *J. Chem. Eng. Data.* 66: 4484–4495.
- [116] Jameel F, Kohls E, Stein M. 2019: Mechanism and control of the palladium-catalyzed alkoxy-carbonylation of oleochemicals from sustainable sources. *Chem. Cat. Chem.* 11: 4894–4906.
- [117] Jameel F, Stein M 2021a: Mechanism and control of the rhodium catalyzed reductive amination of enamines from sustainable sources. [in preparation].
- [118] Jameel F, Stein M. 2021b: Solvent effects in hydroformylation of long chain olefins. *Molecular Catalysis.* 503: 111429.
- [119] Jörke A, Seidel-Morgenstern A, Hamel C. 2015a: Isomerization of 1-decene: estimation of thermodynamic properties, equilibrium composition calculation and experimental validation using a Rh-BIPHEPHOS catalyst. *Chem. Eng. J.* 260: 513–523.
- [120] Jörke A, Triemer S, Seidel-Morgenstern A, Hamel C. 2015b: Kinetic investigation exploiting local parameter subset selection: Isomerization of 1-decene using a Rh-Biphephos catalyst. *Chem. Ing. Tech.* 87: 713–725.
- [121] Jörke A, Kohls E, Triemer S, Seidel-Morgenstern A, Hamel C, Stein M. 2016: Resolution of structural isomers of complex reaction mixtures in homogeneous catalysis. *Chem. Eng. Proc. Process Intensif.* 102: 229–237.
- [122] Jörke A, Gaide T, Behr A, Vorholt A, Seidel-Morgenstern A, Hamel C. 2017a: Hydroformylation and tandem isomerization–hydroformylation of n-decenes using a rhodium-BiPhePhos catalyst: kinetic modeling, reaction network analysis and optimal reaction control. *Chem. Eng. J.* 313: 382–397.
- [123] Jörke A, Seidel-Morgenstern A, Hamel C. 2017b: Rhodium-BiPhePhos catalyzed hydroformylation studied by operando FTIR spectroscopy: catalyst activation and rate determining step. *J. Mol. Cat. A.* 426: 10–14.

- [124] Jörke A. 2018: Mechanisms and kinetics of petro- and oleochemicals in complex hydroformylation reaction networks. Dissertation. Magdeburg: Otto von Guericke University Magdeburg.
- [125] Joshi JB, Sharma MM. 1977: Mass transfer and hydrodynamic characteristics of gas inducing type of agitated contactors. *Can. J. Chem. Eng.* 55: 683–695.
- [126] Kahl H, Enders S, Quitzsch K. 2001: Experimental and theoretical studies of aqueous n-Decyl- β -D-maltopyranoside solutions. *Colloids Surf. A.* 183-185: 661–679.
- [127] Kahl H, Enders S. 2002: Thermodynamics of carbohydrate surfactant containing systems. *Fluid Phase Equilib.* 194–197: 739–753.
- [128] Kahl H, Wadewitz T, Winkelmann J. 2003: Surface tension and interfacial tension of binary organic liquid mixtures. *J. Chem. Eng. Data.* 48: 1500–1507.
- [129] Kalck P, Urrutigoity M. 2018: Tandem hydroaminomethylation reaction to synthesize amines from alkenes. *Chem. Rev.* 118: 3833–3861.
- [130] Kamer PCJ, Vogt D, Thybaut JW (Eds.) 2017: *Contemporary Catalysis. Science, Technology, and Applications*. London, Roy. Soc. Chem.
- [131] Kameyama K, Takagi T. 1990: Micellar properties of octylglucoside in aqueous solutions. *J. Coll. Interf. Sci.* 137: 1–10.
- [132] Kiedorf G, Hoang DM, Müller A, Jörke A, Markert J, Arellano-Garcia H, Seidel-Morgenstern A, Hamel C. 2014: Kinetics of 1-dodecene hydroformylation in a thermomorphic solvent system using a rhodium-biphephos catalyst. *Chem. Eng. Sci.* 115: 31–48.
- [133] Kirschtowski S, Jameel F, Stein M, Seidel-Morgenstern A, Hamel C. 2021: Kinetics of the reductive amination of 1-undecanal in thermomorphic multicomponent system. *Chem. Eng. Sci.* 230: 116187.
- [134] Kirschtowski S, Kadar C, Seidel-Morgenstern A, Hamel C. 2020a: Kinetic modeling of rhodium-catalyzed reductive amination of undecanal in different solvent systems. *Chem. Ing. Tech.* 92: 582–588.
- [135] Koch W, Holthausen MC. 2001: *A Chemist's Guide to Density Functional Theory*. 2nd ed, Weinheim, Wiley-VCH.
- [136] Körkel S. 2002: *Numerische Methoden Für Optimale Versuchsplanungsprobleme Bei Nichtlinearen DAE-Modellen*. Heidelberg University Library.
- [137] Krishna PM, Venkateswarlu D, Narasimhamurty GSR. 1959: Fall of liquid drops in water. *J. Chem. Eng. Data.* 4: 336–340.
- [138] Kronig R, Brink JC. 1949: On the theory of extraction from falling droplets. *Appl. Sci. Res.* A2: 142–154.
- [139] Kumar A, Hartland S. 1999: Correlations for prediction of mass transfer coefficients in single drop systems and liquid-liquid extraction columns. *Chem. Eng. Res. Des.* 77: 372–384.
- [140] Künnemann KU, Bianga J, Scheel R, Seidensticker T, Dreimann JM, Vogt D. 2020: Process development for the rhodium-catalyzed reductive amination in a thermomorphic multiphase system. *Org. Process Res. Dev.* 24: 41–49.
- [141] Langenbach K, Browarzik D, Sailer J, Enders S. 2014: New formulation of the lattice cluster theory equation of state for multi-component systems. *Fluid Phase Equilib.* 362: 196–212.
- [142] Ledakowicz S, Nettelhoff H, Deckwer WD. 1984: Gas–liquid mass transfer data in a stirred autoclave reactor. *Ind. Eng. Chem. Fundam.* 23: 510–512.
- [143] Leleu D, Pfennig A. 2020: *Drop-Based Modeling of Extraction Equipment*. In *Ion Exchange and Solvent Extraction*. Vol. 23, Boca Raton: CRC Press Taylor & Francis Group, p. 253–285.
- [144] Lemberg M, Sadowski G. 2016: Phase equilibria for the hydroesterification of 10-undecenoic acid methyl ester. *J. Chem. Eng. Data.* 61: 3317–3325.

- [145] Lemberg M, Sadowski G, Gerlach M, Kohls E, Stein M, Hamel C, Seidel-Morgenstern A. 2017a: Predicting solvent effects on the 1-dodecene hydroformylation reaction equilibrium. *AIChE J.* 63: 4576–4585.
- [146] Lemberg M, Sadowski G. 2017b: Predicting the solvent effect on esterification kinetics. *Chem. Phys. Chem.* 18: 1977–1980.
- [147] Lemberg M, Schomäcker R, Sadowski G. 2018: Thermodynamic prediction of the solvent effect on a transesterification reaction. *Chem. Eng. Sci.* 176: 264–269.
- [148] Levenspiel O. 1999: *Chemical Reaction Engineering*. 3rd ed., Hoboken, NJ, Wiley.
- [149] Lewis JB. 1954: The mechanism of mass transfer of solutes across liquid-liquid interfaces: Part I: The determination of individual transfer coefficients for binary systems. *Chem. Eng. Sci.* 3: 248–259.
- [150] Li C, Widjaja E, Chew W, Garland M. 2002: Rhodium tetracarbonyl hydride: The elusive metal carbonyl hydride. *Angew. Chem.* 114: 3939–3943.
- [151] Liepe F. 1998: *Rührwerke: Theoretische Grundlagen, Auslegung und Bewertung*. Köthen, Fachhochschule Anhalt.
- [152] Linek V, Sinkule J, Beneš P. 1991: Critical assessment of gassing in methods for measuring k_{La} in fermenters. *Biotechn. Bioeng.* 38: 323–330.
- [153] Lochiel AC, Calderbank PH. 1964: Mass transfer in the continuous phase around axisymmetric bodies of revolution. *Chem. Eng. Sci.* 19: 471–484.
- [154] López CDC, Barz T, Peñuela M, Villegas A, Ochoa S, Wozny G. 2013: Model-based identifiable parameter determination applied to a simultaneous saccharification and fermentation process model for bio-ethanol production. *Biotechn. Progr.* 29: 1064–1082.
- [155] Maaß S, Wollny S, Voigt A, Kraume M. 2011: Experimental comparison of measurement techniques for drop size distributions in liquid/liquid dispersions. *Exp. Fluids.* 50: 259–269.
- [156] Maaß S, Rojahn J, Hänsch R, Kraume M. 2012: Automated drop detection using image analysis for online particle size monitoring in multiphase systems. *Comp. Chem. Eng.* 45: 27–37.
- [157] Magazù S. 2000: NMR, static and dynamic light and neutron scattering investigations on polymeric aqueous solutions. *J. Mol. Struct.* 523: 47–59.
- [158] Mairhofer J, Gross J. 2018: Modeling properties of the one-dimensional vapor–liquid interface: application of classical density functional and density gradient theory. *Fluid Phase Equilib.* 458: 243–252.
- [159] Mączyński A, Wiśniewska-Goćłowska B, Góral M. 2004: Recommended liquid–liquid equilibrium data. part 1. binary alkane–water systems. *J. Phys. Chem. Ref. Data.* 33: 549–577.
- [160] Majhi PR, Blume A. 2000: Thermodynamic characterization of temperature-induced micellization and demicellization of detergents studied by differential scanning calorimetry. *Langmuir.* 17: 3844–3851.
- [161] Marin GB, Yablonsky GS. 2011: *Kinetics of Chemical Reactions. Decoding Complexity*. Weinheim, Wiley-VCH.
- [162] Markert J, Bruntsch Y, Munkelt T, Kiedorf G, Behr A, Hamel C, Seidel-Morgenstern A. 2013: Analysis of the reaction network for the Rh-catalyzed hydroformylation of 1-dodecene in a thermomorphic multicomponent solvent system. *Appl. Catal. A.* 462–463: 287–295.
- [163] Martin H. 1980: Wärme- und Stoffübertragung in der Wirbelschicht. *Chem. Ing. Tech.* 52: 199–209.
- [164] McBain JW, Richards PH. 1946: Solubilization of insoluble organic liquids by detergents. *Ind. Eng. Chem.* 38: 642–646.

- [165] Mitchell JD, Tiddy GJT, Waring L, Bostock T, McDonald MP. 1983: Phase behavior of polyoxyethylene surfactants with water mesophase structures and partial miscibility (cloud points). *J. Chem. Soc. Faraday Trans 1*. 79: 975–1000.
- [166] Moasser B, Gladfelter WL, Roe DC. 1995: Mechanistic aspects of a highly regioselective catalytic alkene hydroformylation using a rhodium chelating bis(phosphite) complex. *Organometallics*. 14: 3832–3838.
- [167] Murzin D, Salmi T. 2005: *Catalytic Kinetics*. Amsterdam, Elsevier.
- [168] Nagarajan R. 1985: Molecular theory for mixed micelles. *Langmuir*. 1: 331–341.
- [169] Nagarajan R. 1986: Micellization, mixed micellization and solubilization: the effect of interfacial interaction. *Adv. Coll. Interf. Sci.* 26: 205–264.
- [170] Nagarajan R, Ruckenstein E. 1991: Theory of surfactant self-assembly: A predictive molecular thermodynamic approach. *Langmuir*. 7: 2934–2969.
- [171] Nagarajan R. 1996: Solubilization in aqueous solutions of amphiphiles. *Curr. Opi. Coll. Interf. Sci.* 1: 391–401.
- [172] Nagarajan R, Ganesh K. 1996: Comparison of solubilization of hydrocarbons in (PEO–PPO) diblock versus (PEO–PPO–PEO) triblock copolymer micelles. *J. Coll. Interf. Sci.* 184: 489–499.
- [173] Nagarajan R. 2011: Amphiphilic surfactants and amphiphilic polymers: principles of molecular assembly. *ACS Symposium Series*. 1070: 1–22.
- [174] Nagarajan R. 2017: Constructing a molecular theory of self-assembly: interplay of ideas from surfactants and block copolymers. *Adv. Coll. Interf. Sci.* 244: 113–123.
- [175] Newman AB. 1931: The drying of porous solids: diffusion and surface emission equations. *Am. Inst. Chem. Eng.* 27: 203–220.
- [176] Ngo TH, Schumpe A. 2012: Absorption of CO₂ into alkane/water emulsions in a stirred tank. *J. Chem. Eng. (Japan)*. 45: 737–741.
- [177] Nilsson PG, Lindman B. 1983: Water self-diffusion in nonionic surfactant solutions. hydration and obstruction effects. *J. Phys. Chem.* 87: 4756–4761.
- [178] Nino-Amézquita OG, Enders S, Jaeger PT, Eggers R. 2010: Measurement and prediction of interfacial tension of binary mixtures. *Ind. Eng. Chem. Res.* 49: 592–601.
- [179] Nino-Amézquita OG, Putten D, Enders S. 2012: Phase behavior and interfacial properties of the system water + carbon dioxide. *Fluid Phase Equilib.* 332: 40–47.
- [180] Nino-Amézquita OG, Enders S. 2016: Phase equilibrium and interfacial properties of water + methane mixtures. *Fluid Phase Equilib.* 407: 143–151.
- [181] Nitsch W, Raab M, Wiedholz R. 1973: Zum Transportmechanismus der Wärme- und Stoffübertragung zwischen turbulent bewegten flüssigen Phasen. *Chem. Ing. Tech.* 45: 1026–1032.
- [182] Nocedal J, Wright SJ. 2006: *Numerical Optimization*. Second edition, New York, NY, Springer.
- [183] Otín S, Fernández J, Embid JM, Velasco I, Losa CG. 1986: Thermodynamic and dielectric properties of binary polar + non-polar mixtures I. Static dielectric constants and excess molar enthalpies of n-alkylamine + n-dodecane systems. *Ber. Bunsengesellschaft Phys. Chem.* 90: 1179–1183.
- [184] Panckow R, McHards C, Rudolph A, Muthig M, Kostova J, Wegener M, Rauh C. 2021: Characterization of fast-growing foams in bottling processes by endoscopic imaging and convolutional neural networks. *J. Food Eng.* 289: 110151.
- [185] Paul N. 2014: Theoretische und experimentelle Untersuchungen von Transport- und Grenzflächenphänomenen in mizellaren Flüssig/flüssig-Systemen (in German). Dissertation. Berlin: Technische Universität Berlin.
- [186] Paul N, Schulz JM, Kraume M. 2015: Fluid dynamics of droplets as a useful tool to determine coverage and adsorption kinetics of surfactants. *Chem. Eng. Technol.* 38: 1979–1984.

- [187] Paul N, Schulz JM, Kraume M. 2016: Determination of phase separation and mass transfer in complex micellar three phase systems. *Chem. Eng. Proc. Proc. Intensif.* 99: 143–148.
- [188] Petzold M, Paul N, Hohl L, Böhm L, Kraume M. 2021: Gas/liquid mass transfer phenomena in micellar multiphase systems. *Chem. Eng. Proc. Proc. Intensif.* 108547.
- [189] Petzold M, Röhl S, Hohl L, Stehl D, Lehmann M, Von Klitzing R, Kraume M. 2017: Mass transfer and drop size distributions in reactive nanoparticle-stabilized multiphase systems. *Chem. Ing. Tech.* 89: 1561–1573.
- [190] Pfennig A, Pilhofer T, Schröter S. 2006: *Flüssig-Flüssig-Extraktion*. Weinheim, WILEY-VCH Verlag GmbH, 907–992.
- [191] Piarah WH 2001: Numerische Untersuchung des instationären Stofftransports an und in umströmten Einzeltropfen (in German). Dissertation. Berlin: Technische Universität Berlin.
- [192] Poncin S, Nguyen C, Midoux N, Breyse J. 2002: Hydrodynamics and volumetric gas-liquid mass transfer coefficient of a stirred vessel equipped with a gas-inducing impeller. *Chem. Eng. Sci.* 57: 3299–3306.
- [193] Poser CI, Sanchez CI. 1981: Interfacial tension theory of low and high molecular weight liquid mixtures. *Macromolecules.* 14: 361–370.
- [194] Press WH. 2007: *Numerical Recipes. The Art of Scientific Computing*. 3rd ed, Cambridge, Cambridge Univ. Press.
- [195] Puvvada S, Blankschtein D. 1990: Molecular-thermodynamic approach to predict micellization, phase behavior and phase separation of micellar solutions. I. Application to nonionic surfactants. *J. Chem. Phys.* 92: 3710–3724.
- [196] Puvvada S, Blankschtein D. 1992: Thermodynamic description of micellization, phase behavior, and phase separation of aqueous solutions of surfactant mixtures. *J. Phys. Chem.* 96: 5567–5579.
- [197] Quitzsch K, Schrittmatter D, Geiseler G. 1969: On the thermodynamics of binary liquid mixtures with homologous formamides. VIII. The binary systems n-heptane-dimethylformamide and n-heptane-diethylformamide. *Z. Phys. Chem.* 240: 107–126.
- [198] Radke SJ, Prausnitz JM. 1972: Thermodynamics of multi-solute adsorption from dilute liquid solutions. *AIChE J.* 18: 761–768.
- [199] Reichardt C, Welton T. 2011: *Solvents and Solvent Effects in Organic Chemistry*. 4th ed, Weinheim, Wiley-VCH.
- [200] Reinhardt A, Haarmann N, Sadowski G, Enders S. 2020: Application of PC-SAFT and DGT for the prediction of self-assembly. *J. Chem. Eng. Data.* 65: 5897–5908.
- [201] Reinhardt A, Enders S 2021a: Modeling interfacial tension of binary mixtures of n-alkanes and water, (in preparation).
- [202] Reinhardt A, Enders S 2021b: The role of steric repulsion in modelling self-assembly of poly(oxyethylene) alkyl ethers in water. (in preparation).
- [203] Reinhardt A, Enders S. 2021c: Modelling the solubilization of weak polar components in aggregates formed by poly(oxyethylene) alkyl ethers. in preparation.
- [204] Reppe W, Vetter H. 1953: Carbonylierung VI. Synthesen mit metallcarbonylwasserstoffen. *Liebigs Ann. Chem.* 582: 133–163.
- [205] Riechert O, Husham M, Sadowski G, Zeiner T. 2015: Solvent effects on esterification equilibria. *AIChE J.* 61: 3000–3011.
- [206] Rivkind VY, Ryskin GM. 1976: Flow structure in motion of a spherical drop in a fluid medium at intermediate Reynolds numbers. *Fluid Dyn.* 11: 5–12.
- [207] van Rooy A, Kamer PCJ, van Leeuwen PWNM, Goubitz K, Fraanje J, Veldman N, Spek AL. 1996: Bulky diphosphite-modified rhodium catalysts: Hydroformylation and characterization. *Organometallics.* 15: 835–847.

- [208] Rols JL, Goma G. 1989: Enhancement of oxygen transfer rates in fermentation using oxygen-vectors. *Biotechn. Adv.* 7: 1–14.
- [209] Rost A, Müller M, Hamerla T, Kasaka Y, Wozny G, Schomäcker R. 2013: Development of a continuous process for the hydroformylation of long-chain olefins in aqueous multiphase systems. *Chem. Eng. Proc. Intensif.* 67: 130–135.
- [210] Rowane AJ, Gupta A, Gavaises M, McHugh MA. 2020: Experimental and modeling investigations of the interfacial tension of three different diesel + nitrogen mixtures at high pressures and temperatures. *Fuel.* 280: 118543.
- [211] Rybczynski W. 1911: Translatory motion of a fluid sphere in a viscous medium. *Bull. Int. l'Académie Des Sci. Cracovie.* 25: 40–46.
- [212] Saad Y. 2003: *Iterative Methods for Sparse Linear Systems*. Philadelphia, USA, Society for Industrial and Applied Mathematics.
- [213] Saboni A, Alexandrova S. 2002: Numerical study of the drag on a fluid sphere. *AIChE J.* 48: 2992–2994.
- [214] Schäfer E, Brunsch Y, Sadowski G, Behr A. 2012: Hydroformylation of 1-dodecene in the thermomorphic solvent system dimethylformamide/decane. Phase behavior–reaction performance–catalyst recycling. *Ind. Eng. Chem. Res.* 51: 10296–10306.
- [215] Schäfer E, Sadowski G. 2012: Liquid–liquid equilibria of systems with linear aldehydes. Experimental data and modeling with PCP-SAFT. *Ind. Eng. Chem. Res.* 51: 14525–14534.
- [216] Schäfer E, Sadowski G, Enders S. 2014a: Calculation of complex phase equilibria of DMF/alkane systems using the PCP-SAFT equation of state. *Chem. Eng. Sci.* 115: 49–57.
- [217] Schäfer E, Enders S, Sadowski G. 2014b: Interfacial tension of binary mixtures exhibiting azeotropic behavior. measurement and modeling with PCP-SAFT combined with density gradient theory. *Fluid Phase Equilib.* 362: 151–162.
- [218] Schäfer E, Horbach F, Enders S. 2014c: Modeling of liquid–liquid interfacial properties for ternary mixture. *J. Chem. Eng. Data.* 59: 3003–3016.
- [219] Schatzberg P. 1963: Solubilities of water in several normal alkanes from C7 to C16. *J. Phys. Chem.* 67: 776–779.
- [220] Schrader P, Culaguin-Chicaroux A, Enders S. 2013a: Phase behavior of the water + nonionic surfactant (C₁₂E₈) + 1-dodecene ternary system across a wide temperature range. *Chem. Eng. Sci.* 93: 131–139.
- [221] Schrader P. 2013b: Experimental investigation of the complex liquid-liquid equilibrium in the system pure/technical grade nonionic surfactant + water + oil. Ph.D. thesis, TU Berlin.
- [222] Schrader P, Paasche C, Enders S. 2014: Phase behavior of systems containing Genapol X0800 + technical 1-dodecene + water in comparison with the phase behavior of pure C₁₂E₈ + pure 1-dodecene + water. *Chem. Eng. Sci.* 115: 139–147.
- [223] Schulz JM, Petzold M, Böhm L, Kraume M. 2021: Tropfenbewegung und Stofftransport in technischen Flüssig/flüssig-Systemen. Teil 2: Auswirkung von Grenzflächeneffekten und Verunreinigungen. *Chem. Ing. Tech.* 93: 1214–1222.
- [224] Seayad A, Ahmed M, Klein H, Jackstell R, Gross T, Beller M. 2002: Internal olefins to linear amines. *Science.* 297: 1676–1678.
- [225] Shinoda K. 1970: Thermodynamic aspects of nonionic surfactant – Water systems. *J. Coll. Interf. Sci.* 34: 278–282.
- [226] Shvydkiv O, Jähnisch K, Steinfeldt N, Yavorsky A, Oelgemöller M. 2018: Visible-light photo oxygenation of α -terpinene in a falling film microreactor. *Catal. Today.* 308: 102–118.
- [227] Slater MJ. 1994: *Rate Coefficients in Liquid–Liquid Extraction Systems*. In *Liquid–liquid extraction equipment*. John Wiley & Sons, Ltd, 4594.
- [228] Smith JM, Van't Riet K, Middleton JC 1977: Scale-up of Agitated Gas–Liquid Reactors for Mass Transfer. In *Proceedings of 2nd European Conference on Mixing*. Cambridge, UK, F4. p. 51–66.

- [229] Srinivasan V, Blankschtein D. 2005: Prediction of conformational characteristics and micellar solution properties of fluorocarbon surfactants. *Langmuir*. 21: 1647–1660.
- [230] Steele WA. 1973: The physical interaction of gases with crystalline solids I. Gas-solid energies and properties of isolated adsorbed. *Atoms Surf. Sci.* 36: 317–352.
- [231] Stephan S, Becker S, Langenbach K, Hasse H. 2020: Vapor-liquid interfacial properties of the system cyclohexane + CO₂: Experiments, molecular simulation and density gradient theory. *Fluid Phase Equilib.* 518: 112583.
- [232] Stephenson RM. 1993: Mutual solubility of water and aldehydes. *J. Chem. Eng. Data.* 38: 630–633.
- [233] Thorsen G, Stordalen RM, Terjesen SG. 1968: On the terminal velocity of circulating and oscillating liquid drops. *Chem. Eng. Sci.* 23: 413–426.
- [234] Tian Y, Cao L, Qiu L, Zhu R. 2014: Comparison study on temperature dependence of the interfacial tension of n-alkane–water and n-alcohol–water two binary systems. *J. Chem. Eng. Data.* 59: 3495–3501.
- [235] Tolls J, van Dijk J, Verbruggen EJM, Hermens JLM, Loeprecht B, Schüürmann G. 2002: Aqueous solubility–molecular size relationships: A mechanistic case study using c 10- to C 19-alkanes. *J. Phys. Chem. A.* 106: 2760–2765.
- [236] Van't Riet K. 1979: Review of measuring methods and results in nonviscous gas–liquid mass transfer in stirred vessels. *Ind. Eng. Chem. Proc. Des. Dev.* 18: 357–364.
- [237] Verhallen P, Oomen L, Elsen A, Kruger J, Fortuin J. 1984: The diffusion coefficients of helium, hydrogen, oxygen and nitrogen in water determined from the permeability of a stagnant liquid layer in the quasi-s. *Chem. Eng. Sci.* 39: 1535–1541.
- [238] Vogelpohl C, Brandenbusch C, Sadowski G. 2013: High-pressure gas solubility in multicomponent solvent systems for hydroformylation. Part I: Carbon monoxide solubility. *J. Supercrit. Fluids.* 81: 23–32.
- [239] Vogelpohl C, Brandenbusch C, Sadowski G. 2014: High-pressure gas solubility in multicomponent solvent systems for hydroformylation. Part II: Syngas solubility. *J. Supercrit. Fluids.* 88: 74–84.
- [240] Vogl C, Paetzold E, Fischer C, Kragl U. 2005: Highly selective hydroformylation of internal and terminal olefins to terminal aldehydes using a rhodium-BIPHEPHOS-catalyst system. *J. Mol. Catal. A.* 232: 41–44.
- [241] Wadewitz T. 1995: Struktur und Grenzflächeneigenschaften binärer flüssiger Mischungen, diploma thesis, Martin-Luther-Universitaet Halle-Wittenberg.
- [242] Waubke M, Nitsch W. 1968: Zur Zweiphasenströmung in einer standardisierbaren Rührzelle. *Chem. Ing. Tech.* 58: 216–218.
- [243] Wegener M, Paul N, Kraume M. 2014: Fluid dynamics and mass transfer at single droplets in liquid/liquid systems. *Int. J. Heat Mass Transf.* 71: 475–495.
- [244] Winnikow S, Chao BT. 1966: Droplet motion in purified systems. *Phys. Fluids.* 9: 50–61.
- [245] Yaws CL. 1999: *Chemical Properties Handbook*. New York, McGraw-Hill.
- [246] Yoshida F, Yamana T, Miyamoto Y 1970: Oxygen Absorption into Oil-in-Water Emulsions: A Study on Hydrocarbon Fermentors. *Industrial Engineering Chemistry Process Design and Development.* 9: 570–577.
- [247] Young, CL, Editor. 1981: Hydrogen and Deuterium, in IUPAC Solubility Data Series. Pergamon Press Ltd.: Oxford, England. <http://dx.doi.org/10.18434/T4QC79>.
- [248] Zanfir M, Gavriilidis A, Wille C, Hessel V. 2005: Carbon dioxide absorption in a falling film microstructured reactor: experiments and modeling. *Ind. Eng. Chem. Res.* 44: 1742–1751.
- [249] Zeiner T, Browarzik D, Enders S. 2009: Calculation of the liquid-liquid equilibrium of aqueous solutions of hyperbranched polymers. *Fluid Phase Equilib.* 286: 127–133.

- [250] Zeiner T, Browarzik C, Browarzik D, Enders S. 2011: Calculation of the liquid-liquid equilibrium of solutions of hyperbranched polymers with the lattice-cluster theory combined with an association model. *J. Chem. Thermodyn.* 43: 1969–1976.
- [251] Zeppieri S, Rodriguez J, Lopez de Ramos AL. 2001: Interfacial tension of alkane + water systems. *J. Chem. Eng. Data.* 46: 1086–1088.
- [252] Zhang F, Cerato-Noyerie C, Woehl P, Lavric ED. 2011: Intensified liquid–liquid mass transfer in corning advanced-flow reactors. *Chem. Eng. Trans.* 24: 1369–1374.
- [253] Zimmermann P, Goetsch T, Zeiner T, Enders S. 2016: Prediction of adsorption isotherms of n-aldehydes using density functional theory in combination with Peng-Robinson equation of state. *Fluid Phase Equilib.* 424: 173–181.
- [254] Zimmermann P. 2017: Predicting Adsorption Isotherms of Systems Containing Isomers. Ph-D thesis, KIT.
- [255] Zimmermann P, Goetsch T, Zeiner T, Enders S. 2017a: Modelling of adsorption isotherms of branched molecules using density-functional theory. *Mol Phys.* 115: 1389–1407.
- [256] Zimmermann P, Walowski C, Enders S. 2018: impact of higher order diagrams on phase equilibrium calculations for small molecules using lattice cluster theory. *J. Chem. Phys.* 148: 094103.
- [257] Zoeller NJ, Blankschtein D. 1995: Development of user-friendly computer programs to predict solution properties of single and mixed surfactant systems. *Ind. Eng. Chem. Res.* 34: 4150–4160.

4 Phase Systems Characterization and Process Development

Anja Drews, Reinhard Schomäcker

After having elucidated and determined the thermodynamic and reaction fundamentals in Chapter 3, the challenge is to develop and demonstrate complete processes for each of the phase systems studied in this book. This involves both the reaction and the phase separation step in an integrated manner. To achieve this systematically, and to provide a basis for model-based process design and optimization, a thorough characterization of the physicochemical properties of the phase systems and their behavior in the different unit operations is required. For example, droplet sizes are likely to influence both the reaction rate (MES and PE) and the subsequent phase separation (TMS, MES, and PE), and properties deemed optimal for one process step might be unfavorable for the other.

The unit operations required to carry out the reactions, phase separation, and catalyst recovery together with their process engineering characterization are presented for each phase system in detail: thermomorphic multiphase systems (TMS, Section 4.1¹), microemulsion systems (MES, Section 4.2), and Pickering emulsions (PE, Section 4.3). Each section provides phase system characterization results, followed by a literature survey on their scope of application as reaction media, and finally by data obtained during the case studies on hydroformylation. Here, the process performances are evaluated in terms of conversion, space–time–yield, selectivity, and efficiency of catalyst recycling.

To conclude, obtained experimental results, observations and characteristic features of the three phase systems are summarized and compared in Section 4.4.

1 Parts of section 4.1 (4.1.3 and 4.1.5) are based on the previously published paper entitled “Thermomorphic Multiphase Systems: Switchable Solvent Mixtures for the Recovery of Homogeneous Catalysts in Batch and Flow Processes” in *Chemistry – A European Journal* [38]. For this publication parts of the content have been rewritten by the authors. All of the figures come from the previous publication and have been slightly altered for this article.

4.1 Thermomorphic Multiphase Systems

Fabian Huxoll, Gabriele Sadowski, Nona Afraz, Marc Petzold, Michael Jokiel, Kristin Hecht, Jonas Bianga, Kai Uwe Künnemann, Anna Kampwerth, Tom Gaide, Andreas J. Vorholt, Thomas Seidensticker, Jens M. Dreimann, Dieter Vogt, Stefan Schlüter, Mirko Skiborowski

4.1.1 Phase System Characterization

The general working principle of thermomorphic multiphase systems (TMS) is based on a temperature-dependent miscibility gap of the solvent system. As stated in Section 2.1, the TMS working point (WP) for the reaction is the monophasic region, whereas the WP for product/catalyst separation is the biphasic region [38]. Thus, knowing the LLE behavior of the solvent system provides a first idea about its applicability as TMS and allows a rough estimate of possible WPs for reaction and separation. However, the influence of the reactants and products on the LLE must also be accounted for. Depending on the interactions between the reacting species and the different solvents, the WPs during reaction and separation may differ significantly from the WPs derived from the phase diagram of the binary solvent system only. The tremendous effort would be necessary to experimentally scan the multicomponent reaction mixture at all relevant compositions and temperatures. Thermodynamic modeling of these phase diagrams as described in Section 3.1.3 is thus a very helpful tool to reduce the experimental effort to a minimum.

In the following, the effects of reactants/products on the phase behavior of the TMS are discussed for two example reactions, namely hydroformylation and reductive amination. Moreover, it is demonstrated that these effects can be modeled using PC-SAFT. As a first example, the influences of the reactant 1-dodecene and the product *n*-tridecanal on the phase behavior of the TMS *N,N*-dimethylformamide (DMF) + *n*-decane at temperatures ranging from 10 to 70 °C were investigated. Here, *n*-dodecanal was used instead of the product *n*-tridecanal, and similar phase behavior was assumed. The results are depicted in Figure 4.1 [229]. First, it reveals a significant temperature effect on the 1-dodecene + DMF + *n*-decane LLE as required for a TMS (Figure 4.1a). The miscibility gap changes from an open one at 25 °C to a closed one at 60 °C. Furthermore, 1-dodecene is acting as a moderate solubilizer with respect to system DMF + *n*-decane, leading to a shrinking miscibility gap between the DMF-rich phase and the *n*-decane-rich one with the increasing amount of 1-dodecene in the system. Thus, the presence of the reactant is beneficial toward reaching a homogeneous system during the reaction. As can be seen in Figure 4.1b, the product *n*-undecanal also acts as a strong solubilizer, leading to a significantly shrinking miscibility gap with rising *n*-undecanal concentrations. For the TMS concept, this behavior of the product *n*-undecanal is unwanted as the working window for the separation is

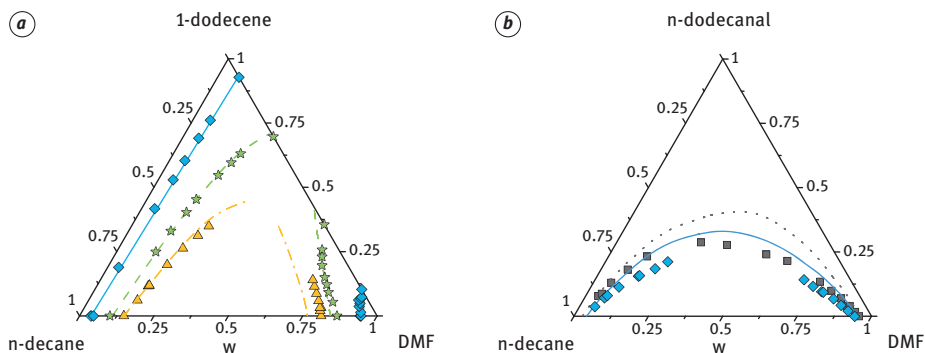


Figure 4.1: LLE of (a) DMF + *n*-decane + 1-dodecene and of (b) DMF + *n*-decane + *n*-dodecanal for different temperatures. Symbols represent experimental data at 10 °C (squares), 25 °C (diamonds), 60 °C (stars), and 70 °C (triangles). Lines are PC-SAFT modeling results [229].

reduced by the presence of the product. Nevertheless, implementing the TMS principle for this reaction system is still feasible

To predict the demixing behavior of the ternary systems using PC-SAFT, binary interaction parameters (k_{ij} s) were fitted to the LLEs of the binary systems (Section 3.1.3), whereas $k_{ij} = 0$ were assumed for the binary systems *n*-decane + dodecane and *n*-decane + *n*-dodecane. By doing so, the temperature-dependent miscibility gaps could be described in excellent agreement with the experimental data, including the switch from a closed miscibility gap to an open one for the 1-dodecene + DMF + *n*-decane system.

As a second example, the effect of the reactants of the reductive amination of *n*-undecanal with diethylamine as well as the product *N,N*-diethylundecylamine on a TMS consisting of methanol + *n*-dodecane was investigated at temperatures between 5 and 35 °C [116]. Figure 4.2a shows the experimental data for the ternary system methanol + *n*-dodecane + *n*-undecanal together with the modeling results. Again, the temperature dependence of the miscibility gap observed for this ternary system makes it suitable to be applied as TMS. Due to the solubilizing effect of *n*-undecanal, the homogeneous region and therewith the reaction working window is enlarged upon adding *n*-undecanal to the solvent system methanol + *n*-dodecane. PC-SAFT predicts the LLE behavior in very good accuracy with the experimental data. In contrast to the system DMF + *n*-decane + 1-dodecene discussed before, no open miscibility gap occurs in the considered temperature range as the subsystems *n*-dodecane + *n*-undecanal and methanol + *n*-undecanal are fully miscible at those temperatures.

Next to *N,N*-diethylundecylamine as the desired product of the reductive amination, the by-product water is formed. Due to its extremely low solubility in non-polar components, the presence of even small amounts of water has a significant influence on the phase behavior during the reaction [87]. Based on the k_{ij} s fitted to the LLEs of the binary systems (*n*-dodecane + water and *n*-dodecane + methanol)

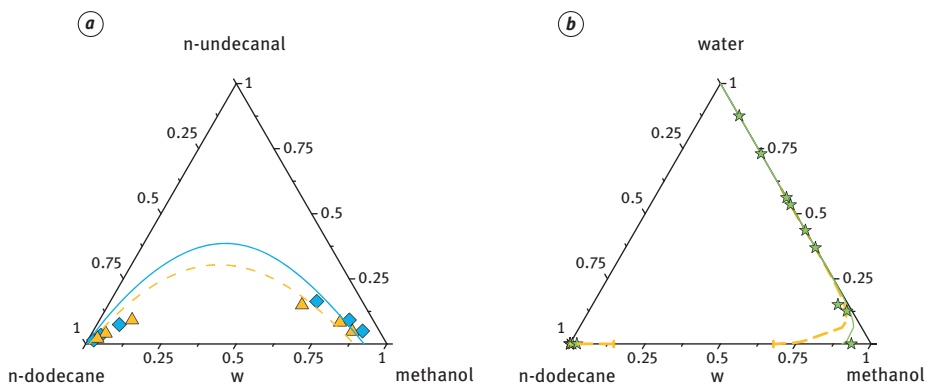


Figure 4.2: LLE of (a) *n*-dodecane + methanol + *n*-undecanal and of (b) *n*-dodecane + methanol + water at different temperatures. Symbols are experimental data at 5 °C (diamonds), 25 °C (stars), and 35 °C (triangles). Lines are PC-SAFT modeling results at 25 °C (solid line), 35 °C (dashed line), and 100 °C (dotted line) [116, 160].

and to VLE data (methanol + water), the LLE of the ternary system *n*-dodecane + methanol + water was predicted using PC-SAFT and compared to available literature data at 25 °C [160]. As can be seen in Figure 4.2b, already very small amounts of water formed during reaction lead to an open miscibility gap. Based on the phase behavior of *n*-dodecane + water (Figure 3.5), this behavior was expected and is predicted with PC-SAFT in very good agreement with the experimental data. Since the formation of a second phase during the reaction needs to be avoided, the working window strongly depends on the water content in the system emphasizing the importance of considering reactant/product effects on the TMS phase behavior.

These findings help to reduce the experimental effort for phase behavior investigations and thus allow faster and more reliable predictions about the operating windows of reaction and separation processes. Moreover, components that have a crucial impact on TMS phase behavior can be identified early in process development.

4.1.2 Mass Transfer in Thermomorphic Multiphase Systems

Thermomorphic phase systems consist of polar and nonpolar molecules in a single phase at temperatures relevant to a chemical reaction. A gas–liquid reaction in a thermomorphic phase system thus involves the transfer of a gas species into the liquid phase, where it may react. Gas–liquid mass transfer was investigated in thermomorphic phase systems using a falling film apparatus (Section 3.3.3.3) and a stirred tank (Section 3.3.3.2). The mass transfer rates measured in the falling film apparatus depend upon the rate of diffusion in the liquid, an intrinsic property of the system. The mass transfer rates measured in the stirred tank depend additionally upon the

dispersion of the gas phase in the liquid. The dispersion of the gas phase influences the interfacial area between the gas and liquid available for mass transfer. In a stirred tank, operating parameters such as the total pressure and the stirring frequency influence the rate of mass transfer. Correlations able to predict the influence of material and operating parameters on the rate of mass transfer are needed for designing processes using thermomorphic solvent systems.

The rate of mass transfer was measured in a thermomorphic system consisting of 25 wt% of *n*-dodecane and 75 wt% of methanol at a temperature of 363 K. Rates of mass transfer were also measured in the pure individual components. The mass transfer coefficient (k_L) is reported for the falling film apparatus, and the volumetric mass transfer coefficient ($k_L a$) is reported for the stirred tank. Measured values are summarized in Table 4.1.

Table 4.1: Rates of gas–liquid mass transfer measured for hydrogen gas into a thermomorphic liquid consisting of 25 wt% *n*-dodecane and 75 wt% methanol in a falling film apparatus (k_L) and a stirred tank ($k_L a$).

Gas	Liquid	T (K)	Solubility (Pa m ³ mol ⁻¹)	k_L (x10 ⁻⁴ m s ⁻¹)	$k_L a$ (s ⁻¹)
Hydrogen	<i>n</i> -dodecane	363	30,762	2.6	0.335
Hydrogen	Methanol	363	22,758*	0.6	0.341
Hydrogen	Methanol- <i>n</i> -dodecane	363	39,745	4.9	0.518

*Solubility value is taken from [57].

The rate of diffusion in the thermomorphic liquid is much higher than in either of the individual components. The measured rates of mass transfer listed in Table 4.1 show that the mass transfer coefficient k_L of the thermomorphic system is almost twice as high as in pure *n*-dodecane and more than 8 times the value of pure methanol. In the stirred tank the mass transfer rate $k_L a$ increases by a factor of 1.5 in the thermomorphic system compared to pure dodecane, comparable to the increase by a factor of 1.9 observed in the falling film apparatus. Since the volumetric mass transfer coefficient $k_L a$ is dependent not only on k_L but also on the interfacial area a , differences observed in the rate of mass transfer in the stirred tank may also be due to a reduction in the interfacial area, for example, the occurrence of larger bubbles and less gas holdup in the tank.

The effects of different stirring speeds and pressures on the rate of mass transfer in a stirred tank reactor were investigated for two thermomorphic systems. The thermomorphic system consisting of 20 wt% 1-dodecene and 48 wt% decane along with 32 wt% DMF to facilitate their mixing was studied for a hydroformylation reaction involving syngas (H₂:CO = 1:1). The solubility of synthesis gas needed for the calculation of $k_L a$ was taken from [273]. The thermomorphic system consisting of

25 wt% of *n*-dodecane and 75 wt% of methanol was studied for a reductive amination reaction using hydrogen gas. The rates of mass transfer measured into the two systems are shown for different stirring speeds and pressures in Figure 4.3. The reductive amination system was investigated in a stirred tank reactor of 1.4 L volume using a 4-blade gas-inducing stirrer ($d_{\text{stirrer}} = 50$ mm) as shown in Section 3.3.3.2. The hydroformylation system was investigated in a stirred tank reactor of 1.25 L volume ($d_{\text{reactor}} = 101.8$ mm), equipped with four baffles and a Rushton turbine gas-inducing stirrer ($d_{\text{stirrer}} = 45$ mm). The bubbles in the reactors were observed with an endoscope (Section 3.3.2.3). Most of the bubbles observed were spherical, and the bubble size distribution was derived from the endoscopic recordings.

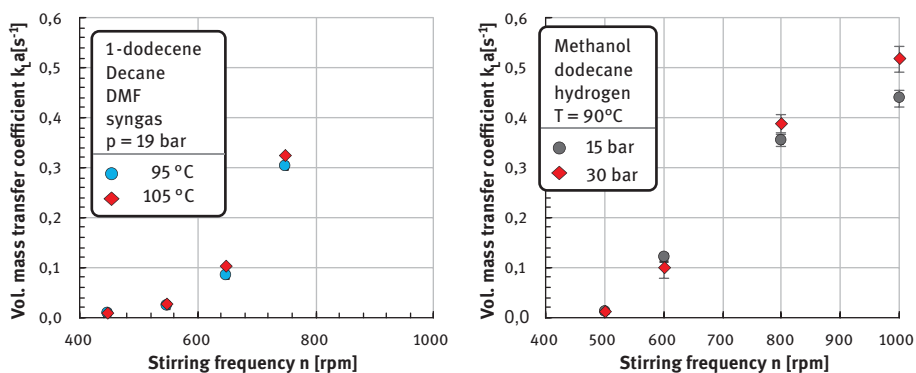


Figure 4.3: Influence of stirring frequency and temperature on the rate of mass transfer in a thermomorphic liquid for the hydroformylation system (left: 1-dodecene, decane, DMF) and for reductive amination system (right: dodecane, methanol) (unpublished).

The rate of mass transfer increased quadratically with stirring frequency. Higher rotational speeds lead to more gas being incorporated in the gas–liquid mixture by the gas-inducing stirrer. The gas flow depends on the pressure difference between the pressure above the liquid level and the static pressure around the stirrer blades [65, 177]. The static pressure around the stirrer blades is reduced for higher rotational speeds as the dynamic pressure increases. Since the dynamic pressure is proportional to $\rho/2 \cdot w_{\text{tip}}^2$, the static pressure shows a quadratic dependence on the tip speed as well, leading to a quadratic dependence of the gas flow and, therefore, a quadratic dependence of $k_L a$ on the rotational speed. Higher temperatures lead to an increase of the volumetric mass transfer coefficient as well. An increase in temperature lowers the viscosity of the liquid phase and enables faster diffusion (eq. 3.97) and results therefore in a higher value k_L . At the same time, the interfacial tension of the gas phase against the liquid phase decreases, which leads to smaller bubbles and higher interfacial areas available for mass transfer to occur.

Interestingly, similar rates of mass transfer were measured in both thermomorphic liquids (Figure 4.3, right and left). The stirred tanks used in investigating the two systems were similar but not identical. These results seem to indicate that mass transfer rates in thermomorphic systems are similar and that processes using thermomorphic liquids may be designed using correlations that can predict the effect of material and operating parameters. An increase in pressure leads to slightly higher volumetric mass transfer coefficients, which is especially apparent at higher stirring frequencies. With higher pressure, the gas density increases and bubble sizes decrease, which in turn leads to an enlarged transfer area [289].

The interfacial area in the thermomorphic system for the hydroformylation was estimated from the pictures of bubbles captured with the endoscope. Therefore, it was assumed, that the 2D projection of the bubbles in the small section seen by the endoscope represents the distribution and volume fractions in the whole reactor. The volumetric transfer area, a , is shown in Figure 4.4. The specific transfer area increases with stirring frequency. A higher stirring frequency leads to a higher gas flow rate through the system since the pressure difference between the stirrer blade tip and gas volume above the liquid increases. The higher amount of gas tends to produce larger bubbles, while the higher power input, due to increased rotational speed, reduces bubble sizes. The higher gas flow rate also increases the gas holdup [98], leading to a larger specific transfer area. A decrease in the specific mass transfer area was observed with rising temperatures. Since viscosity and interfacial tension decrease with rising temperature, the size of the bubbles decreases as well [187]. The smaller bubble sizes at constant power input should thus indicate a larger transfer area. But higher temperatures lead to lower densities and therefore to a slightly lower power input at the same stirring frequency. Nonetheless, the ca. 1.3% decrease in the liquid density does not explain the ca. 8% decrease in interfacial area. For the interfacial area to decrease while the bubble size decreases as well, the gas holdup in the system must decrease. The gas holdup was not measured separately but can be assumed according to correlations, for example, from [98], and could be a reason for the observed effect. To initiate the reaction, a rhodium precursor ($\text{Rh}(\text{acac})(\text{CO})_2$) and ligand (BIPHEPHOS) were added at a ratio of 1:3.3 as the catalyst at the start of experiments. The presence of the reaction increased the rate of gas absorption in the system. However, as seen in Figure 4.4, the interfacial area observed was nearly identical in the system with (a_{react}) and without reaction (a_{abs}). Due to the short residence time of a bubble in the liquid, the contact time with the reaction was not fast enough to change the bubble sizes significantly. The increase in the rate of gas absorption in the presence of the reaction indicates that the rate of gas–liquid mass transport limits the overall rate of reaction. Thus, increasing the amount of gas available for the reaction by increasing the pressure or the interfacial area can have a substantial impact on the rate of reaction and even on the reaction products formed through the reaction (Section 3.3.3).

The comparable rates of gas–liquid mass transfer observed in the different thermomorphic systems and similar stirred tank reactors indicate a possibility to use

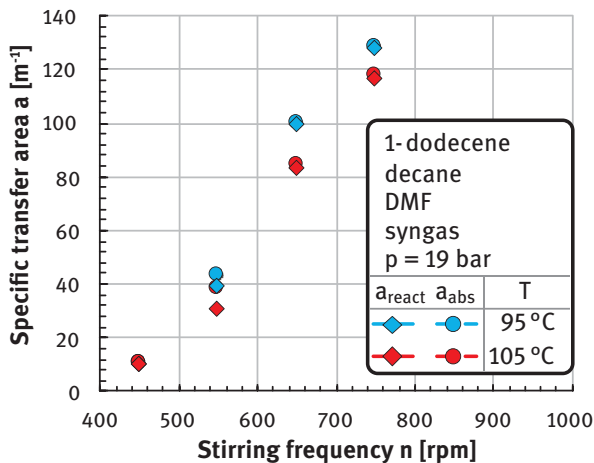


Figure 4.4: Specific transfer area at different stirring frequencies and temperatures of thermomorph system II in reactive and nonreactive conditions (unpublished).

correlations for predicting the rates of mass transport in thermomorph processes. However, as described in Section 3.3.4, empirical correlations predict widely varying rates of mass transfer and tend to be valid for the hydrodynamic and material systems for which they are developed. The measured rates of mass transfer in the thermomorph liquids and the pure liquids water and dodecane are compared to the values predicted by several correlations in Figure 4.5. The superficial gas velocity was estimated following the correlations of [98] as described in Section 3.3.4. The rates of mass transfer into the pure liquids were best predicted by the correlations of [249, 268]. However, considering the changes in the physical properties of the liquid, the correlations predict a lower rate of mass transfer in dodecane as well as in the thermomorph system than in water, but measurements showed higher rates of mass transfer. Since the physical properties of dodecane and the methanol/dodecane thermomorph liquid are similar, the correlations predict similar values of the mass transfer coefficient, but the rates of mass transfer measured experimentally were much higher in the thermomorph liquid compared to the pure substances. The correlation proposed by Baczkiewicz and Michalski [2] was based upon measurements in a nonaqueous solution (acetic acid in ethyl alcohol). This correlation was best able to predict the rate of gas absorption in the thermomorph systems, but not in the pure liquids. Thus, an approach using correlations to predict rates of mass transfer in thermomorph systems at other stirring speeds and sizes of equipment appears to be valid, but care must be taken since the bubble sizes and overall rates of transfer into thermomorph liquids deviate strongly from correlations meant for pure liquids. Most of the existing correlations for the gas absorption rate into liquids can, therefore, not be used to predict the mass transfer in thermomorph systems accurately.

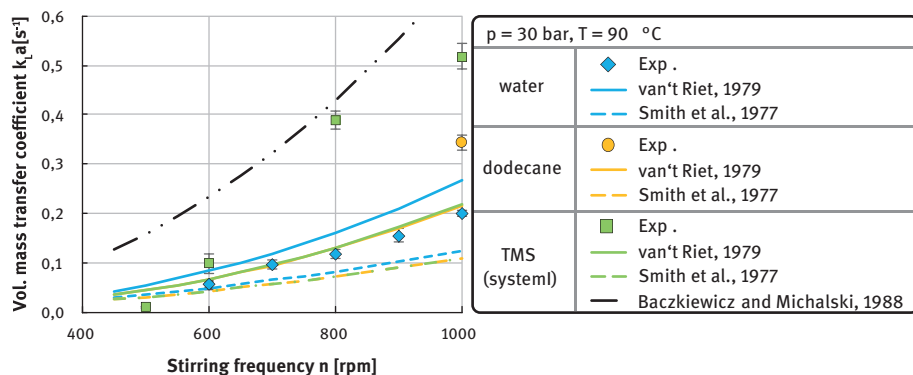


Figure 4.5: Comparison of experimental k_La of hydrogen in different liquids with the predicted k_La in those liquids according to the correlations of Smith et al. [249], Baczkiewicz and Michalski [2], and van't Riet [268] (unpublished data).

The rates of mass transfer measured in thermomorphic phase systems were much higher than the rates of mass transfer measured in the pure individual components. The high rates of mass transfer make thermomorphic liquids attractive systems for reactions combining gases and polar and less polar molecules. In addition to the benefits processes based on thermomorphic systems offer in terms of product separation, thermomorphic liquids can also reduce mass transport limitations and enable fast rates of the chemical reaction. Although thermomorphic liquids only consist of a single liquid phase, the rates of diffusion in these liquids are higher than in the pure liquid components. Thus, the observed rates of mass transfer are higher than those predicted by empirical correlations. Empirical correlations may still prove useful to predict incremental changes in the rate of the mass transfer due to changes in the stirred tank reactor, pressure, or physical properties of the liquids. Measurements in different thermomorphic liquids in similar stirred tank reactors exhibited similar rates of mass transfer, indicating the potential of thermomorphic phase systems to provide a highly effective reaction medium for a range of reactions involving typically immiscible liquids.

4.1.3 Applications

In this section, the state of the art of TMSs applied in homogeneous catalysis until early 2019 is outlined. Most research on TMSs was performed without the intention to establish a continuous process in the end. In some cases, the reaction itself was at the center of interest and in other general applicability was shown. Herein, special attention is given to the reaction indicators, which are only useful for the application of TMSs in homogeneously catalyzed reactions. Those given in the original reference are reported and discussed, and all results are presented as they were

described in the original publications. No calculations concerning the indicators were made by us, although, in some cases, available data would allow for reporting of additional reaction indicators. However, the calculation of some indicators is not useful, especially if the main focus of the research was not on the development of a recyclable catalyst system, for instance. This section is structured according to the reactions that contribute to investigations on TMSs sorted by the year of publication of the first implementation in a TMS. The reactions were investigated by several research groups (Table 4.2), using different solvent combinations. The development from reactions on laboratory scale to continuous-flow miniplant processes is shown with an integrated catalyst recycling based on TMSs to demonstrate their potential toward industrial processes.

Table 4.2 shows the reactions investigated in TMSs and indicates whether recycling of the catalyst was successful or not, and on which scale the reaction and recycling were performed. In the following, these reactions are presented by considering the problems that were faced; how these were tackled; and, if they still remain, why they have not yet been solved.

Table 4.2: An overview of reactions in TMS reported in the literature from laboratory-scale experiments to miniplants [38].

Reaction	First TMS	Investigating groups	Batch reaction ^(a)		Continuous reaction ^(a)	
			Reaction	Recycling	Reaction	Recycling
Hydrogenation	1998	Bergbreiter [32] Behr [19, 154, 155, 157] Jin and Wang [173]	✓	✓	–	–
Allylic substitution	1998	Bergbreiter [32] Kaneda [185]	✓	✓	–	–
Hydrosilylation	1999	Behr [7, 17]	✓	–	–	–
C–C cross-couplings	2000	Bergbreiter [33–35, 95] Kim [244] Chiba [97, 147]	✓	✓	✓	✓
Codimerization/ co-oligomerization	2002	Behr [8–11, 30, 96]	✓	✓/×	✓	×
Peptide synthesis	2002	Chiba [50]	✓	–	–	–
Telomerization	2003	Behr [13, 14, 22]	✓	–	–	–
Hydroacylation	2004	Jun [45]	✓	✓	–	–

Table 4.2 (continued)

Reaction	First TMS	Investigating groups	Batch reaction ^(a)		Continuous reaction ^(a)	
			Reaction	Recycling	Reaction	Recycling
Hydroformylation/ isomerizing hydroformylation	2005	Behr [44, 59, 61, 229, 308–310] Carpentier [263] El Ali [264] Dutta [241–243] Jin and Wang [302]	✓	✓/×	✓	✓
Hydroaminomethylation	2005	Behr [12, 25, 27, 275]	✓	✓/×	–	–
Hydroamination	2010	Behr [18, 20, 68, 69]	✓	✓	✓	✓
Ester hydrolysis (enzymatic)	2011	Behr [21, 23]	✓	✓	–	–
Cyclopropanation	2011	Chiba [150]	✓	–	–	–
Metathesis	2012	Behr [24] Fischmeister [112]	✓	✓	–	–
Methoxycarbonylation	2013	Behr [26, 76, 77]	✓	✓	–	–

(a) ✓ working; × not working; – not investigated; ✓/× depending on the reaction system.

Hydrogenation

Back in 1998, the group of Bergbreiter at the A&M Texas University (USA) was the first to apply the concept of TMSs for catalyst recycling in homogeneous catalysis [22]. Polymers were used in their “thermomorphic systems” as catalyst support to create phase-selective homogeneous catalysts that could be separated after reaction and upon cooling to room temperature. A TMS consisting of a mixture of water/ethanol (10/90 wt%) as a polar phase and *n*-heptane as a nonpolar phase was used. For proof of principle, leaching tests were performed by using a chromophore attached to the polymer backbone, which showed no leaching of the polymer into the nonpolar phase. For catalysis, rhodium-catalyzed hydrogenation of 1-dodecene was chosen as a model reaction (Figure 4.6). The rhodium(I) precursor $[\text{RhCl}(\text{C}_2\text{H}_4)_2]_2$ was complexed to a phosphine-substituted poly(*N*-isopropylacrylamide) (PNIPAM) polymer, and thus, only soluble in the aqueous ethanol phase (10% water), while the corresponding hydrogenation product *n*-dodecane was selectively dissolved in the *n*-heptane phase. At a reaction temperature of

70 °C, the aqueous mixture of ethanol/*n*-heptane (1:1) was monophasic. After lowering the temperature and subsequent phase separation, the catalyst was successfully recycled four times with stable conversions and catalyst activities, as shown through H₂-uptake of around 10 mL per run. However, neither TOF, TON, nor leaching was reported in this initial example, although the separated *n*-heptane phase did not show any catalytic activity [32].

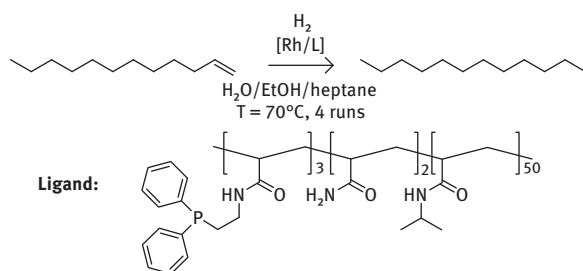


Figure 4.6: The first application of a TMS for rhodium-catalyzed hydrogenation [32].

Ruthenium-catalyzed hydrogenation of 1-octene in a TMS consisting of *n*-heptane and poly(ethylene glycol) (PEG) monoalkyl ether was reported in 2006 by Lu et al. [173] (Figure 4.7). The ruthenium catalyst was efficiently immobilized in the polar catalyst phase by modification with the PETPP ligand, which features the highest solubility in PEG. In ten consecutive runs, quantitative conversion of 1-octene was achieved after 3 h at a catalyst loading of 0.1 mol% at 50 bar. Ruthenium leaching was reported to be below a detection limit of 5 ppb, according to inductively coupled plasma (ICP)-atomic emission spectroscopy (AES) measurements.

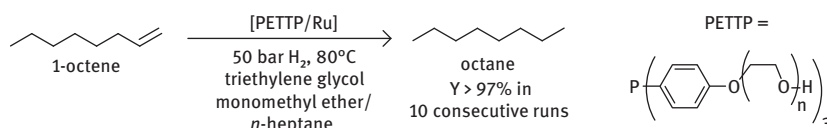


Figure 4.7: Hydrogenation of 1-octene in a TMS consisting of *n*-heptane and PEG monoalkyl ether with PETPP/Ru catalyst (PETPP = P-[*p*-C₆H₄O(CH₂CH₂O)_{*n*}H]₃, 3*n* = 14) [173].

After their first report on the recycling of homogenous ruthenium hydrogenation catalysts with a PEG/alkane-based TMS, in 2008, Huang et al. [115] reported on the application of palladium nanoparticles for the selective hydrogenation of 1,5-cyclooctadiene to cyclooctene in the TMS PEG 4000, toluene, and *n*-heptane was used as solvents in a ratio of 2:3:1, which formed a homogeneous mixture at 60 °C. At a catalyst loading of 0.1 mol%, in six consecutive recycling runs, the Pd nanoparticles could be separated from the product containing a nonpolar phase, with no evident loss in

activity and selectivity ($S = 98\%$ to cyclooctene). The Pd nanoparticles are reported to be very stable, according to their constant size during the recycling procedure.

The hydrogenation of 1-octene and 1-dodecene was investigated in 2008 by Behr et al. [19] in DMF/*n*-decane, *N*-methylpyrrolidone (NMP)/*n*-decane, and water/1-butanol TMSs by using Wilkinson's catalyst and $[\text{Rh}(\text{acac})(\text{CO})_2] + 3,3',3''\text{-phosphanetriyltris}(\text{benzenesulfonic acid}) \text{ trisodium salt (TPPTS; acac = acetylacetonate)}$ for the aqueous system. At conversions of $>95\%$, leaching of rhodium was reported to be <1 ppm and only 3 ppm for phosphorus in all systems; thus enabling recycling of the catalyst, as proven for all three systems through constant results. They used hydrogenation as a simple model reaction (only one liquid and one gaseous substrate) to show the potential of TMSs in homogeneous catalysis. The main focus was on the comparison of different solvents in TMSs and on the topic of catalyst recycling. Not only TMSs consisting of two solvents were investigated but also those with a third solvent as a mediator [19]. As a result, different types of TMS were defined, depending on the number of substrates and solvents used and the type of the formed miscibility gap (Section 2.1.2). Remarkably, test mixtures were prepared, for the first time, to test the effectiveness of catalyst immobilization in the polar phase by determining the leaching of an Rh/triphenylphosphine (TPP) system. Based on these results, different systems were compared.

A liquid–liquid biphasic solvent system consisting of water and 2-ethylhexanol for the synthesis of DMF through the hydrogenation of CO_2 in the presence of aqueous dimethylamine was used. DMF is soluble in the aqueous phase, while the applied ruthenium catalyst remains in the organic phase consisting of 2-ethylhexanol [154–157]. This approach is very interesting because it is a very rare example in which the catalyst is immobilized in the nonpolar phase, which is generally necessary in the production of rather polar products, such as DMF, in this case.

Allylic Substitution

After Bergbreiter et al. [32] demonstrated the idea of thermomorphic catalysis for the recycling of polymer-bound catalyst systems, the generality of this approach was illustrated by further experiments with a Pd^0 -PNIPAM (made of $\text{Pd}(\text{dba})_2$; dba = dibenzylideneacetone) catalyst in the coupling (allylic substitution) of cinnamyl acetate with dicyclohexylamine and dipropylamine in 1998 in their initial research on TMS. Interestingly, the product exhibited some solubility in the polar ethanol phase, and with the increasing number of recycling runs the polar phase was saturated. However, activity was not affected by the product, and thus, after the fourth recycling run with dipropylamine, 100% of the product formed in that run was successfully extracted into the *n*-heptane phase.

Mizugaki et al. [185] reported in 2002 on the recycling of dendrimer-bound Pd^0 by using $[\text{PdCl}_2(\text{PhCN})_2]$ as a precursor catalyst in a TMS system consisting of DMF and *n*-heptane (Figure 4.8). The allylic amination (allylic substitution) of *trans*-cinnamyl

acetate with dibutylamine was conducted in the homogeneous phase at 75 °C and the products were effectively separated from the catalyst-containing DMF phase. Yields for allylic amines in the nonpolar *n*-heptane phase were 66% in the initial run and 99% in three subsequent runs after 1 h reaction time each. In the initial run, the product was partially dissolved in the DMF phase. After this phase was saturated with the product, quantitative extraction was possible in the subsequent runs. Leaching of Pd metal was reported to be below the detection limit of 0.1 ppm, according to ICP measurements. The activity of the catalyst was, however, not reported.

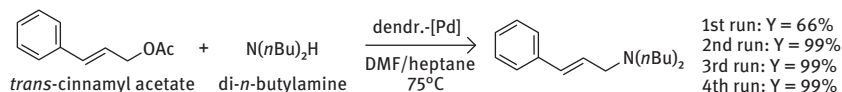


Figure 4.8: Allylic amination (allylic substitution) of *trans*-cinnamyl acetate with dibutylamine catalyzed by a dendrimer-bound Pd⁰ complex in TMS [185].

Hydrosilylation

One year after TMSs were initially presented by Bergbreiter, the group of Behr at the TU Dortmund University (Germany) picked up these systems in 1999. Behr and coworkers set themselves the goal of using only readily available precursors and ligands in commercially available solvents for creating TMSs. The first application they presented was the hydrosilylation of methyl 10-undecenoate with triethoxysilane in a propylene carbonate (PC)/cyclohexane/toluene (1:1:1) solvent system possessing a relatively low UCST of 40 °C (Figure 4.9). The performance of the H₂PtCl₆-catalyst (0.1 mol%) system in that monophasic TMS was compared with a biphasic system consisting only of cyclohexane and PC at an elevated reaction temperature of 80 °C. It was shown that much higher activities are reached in the TMS. This paper focused on the general proof that TMSs were a feasible catalyst recycling strategy in the hydrosilylation of alkenes and had huge potential for future research. Recycling itself was not investigated, nor were leaching values reported [7, 17].

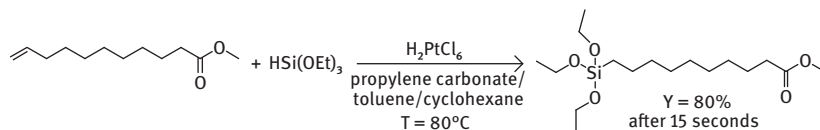


Figure 4.9: Hydrosilylation of methyl 10-undecenoate with triethoxysilane [7, 17].

C–C Cross-Couplings

After their initial publication on TMSs, Bergbreiter and coworkers extended the applicability of the polymer-supported catalysts in TMSs to other reactions, such as

Pd-catalyzed C–C cross-couplings in 2000 [33]. Two years after their introduction of TMSs, a PNIPAM-bound Pd catalyst was applied to Heck and Suzuki couplings. All reactions were conducted in a 90% aqueous *N,N*-dimethylacetamide (DMA)/*n*-heptane (2:1) thermomorphic system with 0.2 mol% of catalyst. Again, up to four recycling runs were successful with high yields [33]. In addition to the application of TMSs in C–C coupling reactions, the group presented different solvent combinations that formed a TMS, such as *n*-heptane/ethanol_{aq}, *n*-heptane/DMF, or triethylamine/water [34]. In 2003, they developed different phase-selective polymers, which could be used in these systems, for example, polyacrylamide-, polyisobutene, or polybutylstyrene-based polymers. Very low leaching values in the designated product phase (<0.1%) were reported. In future research, these polymers should be used as catalyst supports. At that time, the group wanted to show the concept of phase-selective polymers without the realization of reactions in these systems [35]. In 2016, the group of Bergbreiter [95] worked on hydrocarbon oligomers as alternatives to alkanes such as *n*-heptane to reduce the toxicity of alkane-based solvent systems. These oligomers are applicable, for example, in TMSs. All in all, the group of Bergbreiter did pioneering work and showed that TMSs were a very promising approach for the recycling of homogeneous catalysts. They mainly focused on polymer-supported catalysts, which were not commercially available, and the synthesis of which requires some effort. Hence, to date, no continuous-flow processes on the larger scale are known, in which these high-potential polymer-bound phases selective catalysts were implemented.

In 2006, the group of Chiba [97, 147] reported on the successful application of a palladium catalyst ([PdCl₂(dppf)], 5 mol%; dppf = 1,1'-bis(-diphenylphosphino)ferrocene) in a Suzuki–Miyaura reaction and extended their research to different C–C cross-coupling reactions (Sonogashira, Suzuki–Miyaura, and Mizoroki–Heck) and again reacted a substrate of lower polarity with coupling partners of higher polarity. By applying a TMS composed of cycloalkanes, such as cyclohexane and methylcyclohexane, in combination with NMP, DMA, or DMF, the reaction occurred with high efficiency at elevated temperature and efficient separation was achieved at room temperature. Recycling of the catalyst was also successfully demonstrated in three consecutive runs, with no significant loss of activity [97]. In 2008, they [149] used the same methodology with cycloalkane-based thermomorphic systems with propionitrile, acetonitrile, and methyl cyclohexane for the synthesis of oligosaccharides.

In 2014, Sharma et al. [244] presented one of the rare methods for “continuous recycling” with a TMS. In this case, a microfluidic loop system with different temperature zones for reaction and separation was developed for palladium-assisted isocyanide insertions (C–C cross-coupling) in a small-scale continuous-flow process. A polymeric *N*-heterocyclic carbene (NHC)-Pd catalyst was specifically synthesized to be retainable in the nonpolar *n*-decane phase, while the products and substrates were reported to be soluble only in the polar DMF phase. The catalyst showed stable catalytic activity in the continuous setup with yields of 82% for the synthesis of 2-amino-substituted quinazolinone with urea and tert-butyl isocyanide

within 18 h recycling runs. The TOF was 74 h^{-1} and the TTON was 1308. Palladium leaching into the product phase was not detected using ICP-AES ($<0.1 \text{ ppm}$). Afterward, the group successfully transferred their recycling system to other reactions, such as the copper-catalyzed click reaction of phenylacetylene with 4-bromobenzyl azide. The copper catalyst was immobilized by a phenanthroline ligand. Yields of 88% were reached over 10 h. No TON, TOF, or leaching values were calculated for this reaction. In addition, Sharma et al. [244] wanted to show the applicability of TMSs in pharmaceutical chemistry with a Heck reaction of methyl 2-iodobenzoate with allylic alcohol. Over a period of 6 h, stable yields of around 82% were obtained until the catalyst was exhausted. The reactions investigated by Kim and coworkers [244] are shown in Figure 4.10.

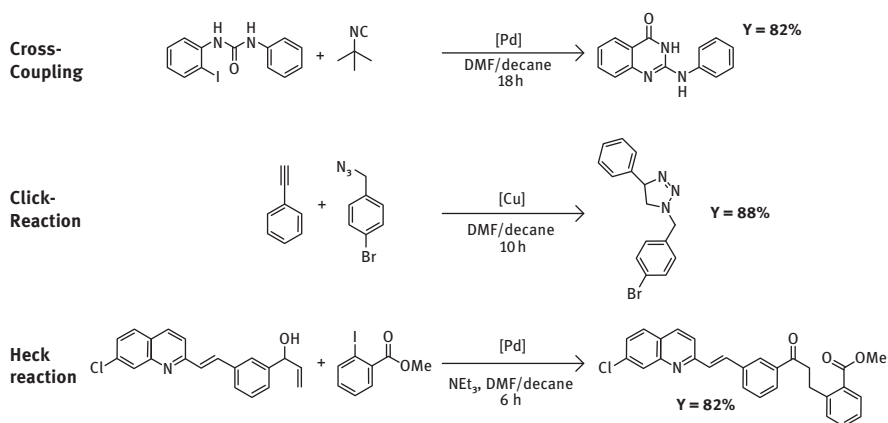


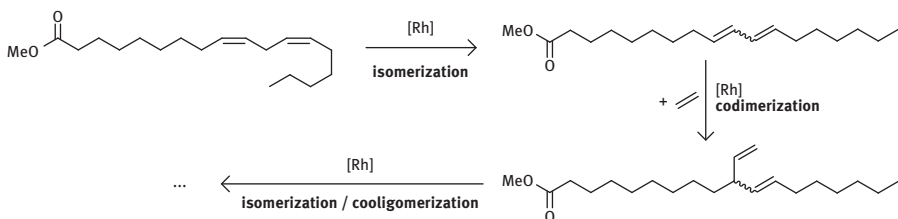
Figure 4.10: Different TMS approaches reported by Sharma et al. [244].

Codimerization/Co-oligomerization

In 2002, Behr and Fängewisch [8] coined the term “temperature-dependent solvent systems”. They compared these systems to other recycling concepts for homogeneous catalysts, such as liquid–liquid two-phase techniques or thermoregulated phase-transfer catalysis. Application possibilities and potentials of this new concept were presented and, for the first time, a general description of how these systems work was provided. Different TMSs consisting of three solvents and their temperature-dependent phase equilibria were investigated for the rhodium-catalyzed codimerization/co-oligomerization of sunflower fatty acid methyl esters (mainly consisting of methyl linoleate) with ethylene. Although the influence of the substrate was considered, the influence of the product on the phase behavior was neglected. To determine the composition of both phases after reaction, it would be more interesting to investigate the product and not the substrate.

In 2003, Behr et al. [9] investigated the rhodium-catalyzed co-oligomerization of methyl linoleate with ethylene in a TMS (Figure 4.11). The products of that transformation are branched fatty acid derivatives, which are, eventually after hydrogenation of the remaining double bonds, interesting as lubricants due to their lowered melting points. Different solvent systems were investigated. 1,4-Dioxane and tetrahydrofuran (THF) were tested with the polar solvent ethylene glycol, and 1,4-dioxane, anisole, toluene, and THF were tested with PC. In the end, they chose 1,4-dioxane and PC, in which product yields of around 70% were reached at a catalyst ($\text{RhCl}_3 \cdot 3\text{H}_2\text{O}$) loading of 2 mol%. Improved yields of around 90% were obtained by switching to the second TMS, consisting of polyethylene glycol (MW: 1000) and toluene, with 1 mol% of the same precursor and 2 mol% of TPP [10]. Later in 2014, the 1,4-dioxane/PC system was used in a continuous-flow miniplant [30]. The process consisted of a continuously stirred tank reactor and a phase separator and was run for a period of 100 h. A rhodium catalyst was used in combination with TPP. However, the very high leaching of Rh (0.08 n\%h^{-1}) and TPP (0.1 n\%h^{-1}) into the product phase led to a decreasing reaction rate over time and the yields were limited to 22%. The high leaching of the catalyst was attributed to the presence of a conjugated diene system in the fatty product phase. Presumably, rhodium is complexed and thereby extracted into the nonpolar phase to almost 40% of the initial rhodium content. However, in the absence of any double bonds in the product phase, leaching was suppressed by a factor of 100 and only 0.4% of the initial amount was extracted into the product phase. To finally obtain a working process, the reaction and miniplant system were extended in subsequent publications. In addition to the reaction and separation step, a trickle-bed reactor for the heterogeneously catalyzed (Pd/C) hydrogenation of the oligomerization products was installed. Upon hydrogenation of the product, the rhodium was successfully extracted from the hydrogenated product phase with a fresh PC. After the extraction step, the catalyst was recycled to the reaction. Through this combination of homo- and heterogeneous catalysis, the total yield of hydrogenated oligomerization products reached around 90%. However, neither TOF nor TON values for the process were calculated [96].

A solvent combination consisting of PEG 1000 and water was used for the rhodium-catalyzed codimerization of 1,3-butadiene with ethylene to *trans*-1,4-hexadiene (Figure 4.12) by Behr and Miao in 2005 [11]. The catalyst $\text{RhCl}_3 \cdot 3\text{H}_2\text{O}$ (0.07 mol%) was successfully recycled in ten sequential runs. Cinnamyl chloride had to be added for the reactivation of the rhodium catalyst in each recycling run. Surprisingly, very inconsistent conversions of ethylene of between 30 and 80% were reported. However, the selectivity to 1,4-hexadiene was always >90%. The influence of cinnamyl chloride on the product and catalyst separation was not reported [11]. Also, no information was given on whether the reaction system was homogeneous at a reaction temperature of 70 °C and spontaneously split up afterward.



conditions:

batch:

TMS: polyethylene glycol/toluene Promotor: cynammyl chloride, $T = 70^\circ\text{C}$, $p(\text{ethylene}) = 10 \text{ bar}$, $X = 95\%$, $S = 98\%$

continuous:

TMS: 1,4-dioxane/propylene carbonate Promotor: crotyl chloride, $T = 80^\circ\text{C}$, $p(\text{ethylene}) = 30 \text{ bar}$, $Y = 22\%$

Figure 4.11: Co-oligomerization of linoleic acid with ethylene [96].

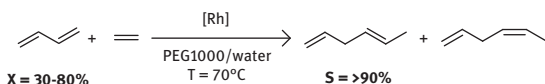


Figure 4.12: Codimerization of butadiene with ethylene in a TMS with PEG 1000 and water [11].

Peptide Synthesis

Inspired by the pioneering work of Bergbreiter et al. [32] Chiba et al. [50] applied cyclohexane-based thermomorphic systems in peptide synthesis in 2002. The aim was to obtain less polar reagents in a single phase together with fluorenylmethoxycarbonyl (Fmoc) amino acids for the reaction itself and then separate the product from excess reagents. In this case, different systems, such as nitromethane/nitroethane/cyclohexane (a homogeneous mixture between 25 and 45 °C), DMA/DMF/cyclohexane (a homogeneous mixture between 33 and 61 °C), and acetonitrile/propionitrile/cyclohexane (a homogeneous mixture between 18 and 47 °C), were investigated. The reaction took place at 35 °C and separation at 5 °C. Deprotection with a base and separation of the products from excess reagents was also accomplished by exploiting the thermomorphic behavior of the mixture.

Telomerization

Within the palladium-catalyzed telomerization, 1,3-dienes are functionalized with nucleophiles. Formally, telomerization is the dimerization of a 1,3-diene under the attack of a nucleophile. After initially failing to transfer butadiene telomerization with ethylene glycol into a TMS in 2003 [13, 14], the telomerization of β -myrcene with diethylamine was demonstrated in a TMS consisting of DMF and *n*-heptane in 2010 [22] (Figure 4.13). β -Myrcene conversions of up to 91% with a selectivity of 93% to the *tt*-telomer were achieved with palladium ($[\text{Pd}(\text{MeCN})_4](\text{BF}_4)_2$) catalyst (0.05 mol%) and the ligand TPP ($\text{Pd}/\text{P} = 1/8$) within 4 h at 100 °C. The leaching of palladium of

3 ppm and 4 ppm for the ligand was indicated to be very low. A promising TOF of 514 h^{-1} and a TON of 1800 were reached by using this system.

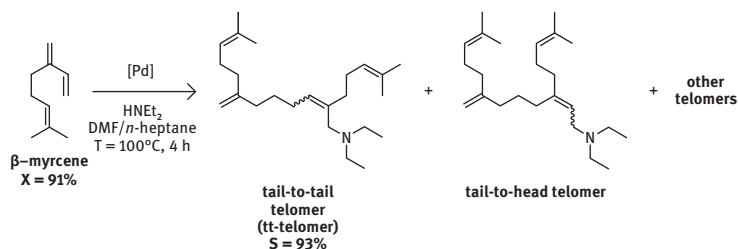


Figure 4.13: Telomerization of β -myrcene by Behr et al. [22] in TMS.

Hydroacylation

In 2004, Chang et al. [45] reported on the hydroacylation of different alkenes with different primary alcohols in a TMS (Figure 4.14). The general challenge is the opposite polarity of substrates employed. To ensure a single homogeneous reaction mixture without potential mass transport limitations, they compared TMSs to other approaches. For example, ionic liquids showed only low solubility of alkenes during reactions, leading to heterogeneity. This problem was successfully solved by using a TMS consisting of 4,4'-dipyridine and phenol. Rhodium-catalyzed hydroacylation of 1-hexene with benzyl alcohol was investigated as a model reaction. The ketone product separated from the catalyst-containing phase upon cooling to room temperature and was decanted. To quantitatively isolate the product, the catalyst phase was extracted three times with *n*-heptane. The polar phase was recycled and stable yields of 88–96% were observed within seven recycling runs at rhodium ($[(C_8H_{14})_2RhCl]_2$) loadings of 5 mol%. Only 0.005% and 0.01% in the first and second recycling runs of the rhodium catalyst and 2–5% of the ligand 4-DPBA were found in the product phase after separation. The concept was extended to differently substituted substrates, with almost identical performance.

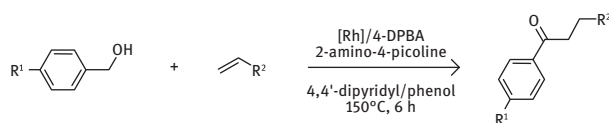


Figure 4.14: Rhodium-catalyzed hydroacylation of alkenes with benzyl alcohols [45]. 4-DPBA: 4-diphenylphosphinobenzoic acid.

Hydroformylation/Isomerizing Hydroformylation

Many detailed investigations on TMSs have been performed for hydroformylation reactions. As a model reaction, 1-dodecene was converted with a homogeneous $[\text{Rh}(\text{acac})(\text{CO})_2]$ (0.1 mol%) catalyst in a TMS consisting of DMF/*n*-decane (Figure 4.15). With the ligand 6,6'-[(3,3'-di-*tert*-butyl-5,5'-dimethoxy-1,1'-biphenyl-2,2'-diyl)bis(oxy)]bis(dibenzo[*d,f*] [1,3,2]dioxaphosphepin) (BIPHEPHOS; metal/ligand = 1/5), high regioselectivities of 99% for the desired linear aldehyde tridecanal were achieved [229]. Different solvents were investigated. DMF was compared with PC and acetonitrile in a TMS with *n*-decane. DMF was chosen due to the low leaching of the catalyst (7%) and its ligand (9%) in the nonpolar phase. For both acetonitrile and PC, significantly higher leaching (>34%) resulted for rhodium and phosphorus. Afterward, different alkanes were investigated as nonpolar compounds. It turned out that leaching decreased with the length of the carbon chain. The same trend resulted from the use of different alkene substrates with different carbon chains. In the system composed of DMF/*n*-decane, the catalyst was successfully used in 30 consecutive recycling runs. To achieve constant yields of around 80% of the linear aldehyde and regioselectivity of 99%, the ligand was replenished before each recycling run. Nevertheless, the yields decreased slightly to around 60% after 30 runs. Only leaching of the last recycling run was determined. In the product phase, 1% rhodium and 1% diphosphite ligand were present [44].

Hydroformylation has the same issue as other functionalization reactions of alkenes, namely, that a product is formed with slightly higher polarity than that of the substrate. Hence, with increasing substrate concentration, the concentration of the product also increases, assuming the same reaction performance. This could lead to the higher solubility of the polar solvent in the nonpolar phase, eventually resulting in higher catalyst and ligand leaching with increasing substrate loading. Additionally, the polar product has a higher affinity to the polar solvent, resulting in a decreased separation performance after the reaction.

A continuous-flow miniplant consisting of a continuously stirred tank reactor and a phase separator was developed for this reaction system and progressively optimized step by step in different works by Behr and coworkers (Figure 4.15) [59, 61, 308, 309].

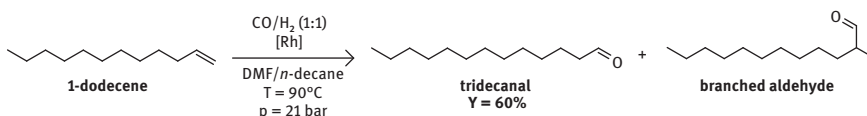


Figure 4.15: Hydroformylation of 1-dodecene in the TMS with DMF/*n*-decane [44].

The group of Seidel-Morgenstern performed detailed mechanistic and kinetic studies on the hydroformylation reaction, as well as on the associated isomerization

reaction to the internal alkenes [81, 129–133, 146, 176] (Section 3.3.2). Sadowski and coworkers carried out calculations on thermodynamics [163–165, 229, 230, 272, 273] (Section 3.3.1). For example, perturbed-chain statistical associating fluid theory (PC-SAFT) was used to make predictions on the solvents and to determine phase equilibria in TMSs. Sundmacher and coworkers, on one hand, developed concepts for an optimal reaction and process design (Section 5.3.1) and, on the other hand, used COSMO-RS for solvent selection based on DFT calculations [99–102, 138, 179–181, 324]. Engell and coworkers [103, 255, 256] supported the project with superior process modeling and optimization (Section 5.3.3). This collaboration helped to further fine-tune the design and operation parameters for the continuously operated miniplant process presented in Figure 4.16. This process shows the feasibility of continuously recycling and reusing the homogeneous catalyst in the loop I (grey area) through phase separation, but also the recycling and reuse of unconverted substrate in loop II (white area) through distillation.

Under steady-state operation, yields of 60% of the linear aldehyde and catalyst leaching of about $1\%h^{-1}$ of the initial loading (0.05 mol%) were achieved [61, 308–310]. Moreover, further downstream processing of the product phase was investigated: The efficient recycling of the nonpolar solvent *n*-decane and the unconverted alkenes in the reactor was accomplished by distillation [59]. Feeding the internal alkenes back into the reactor led to an increase in the overall selectivity of the reaction; thus demonstrating the necessity of evaluating the process as a whole. However, limitations of this process were uncovered. Catalyst leaching into the product phase was still high, and thus, a make-up stream of the ligand had to be installed. Later, it was shown that by applying an organic solvent nanofiltration (OSN) membrane separation, the catalyst content of the nonpolar phase, and thus, leaching could be efficiently reduced [62].

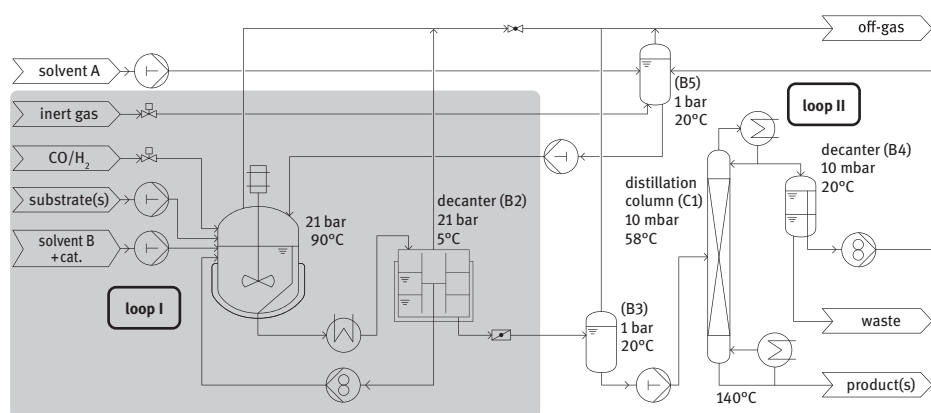


Figure 4.16: Process flow diagram for the continuous-flow process of the rhodium-catalyzed hydroformylation of 1-dodecene in a TMS with DMF and *n*-decane [59].

In 2006, Tijani and El Ali [264] investigated the hydroformylation of 1-octene and other olefins in a PC/*n*-heptane TMS with the catalyst [HRh(CO)(PPh₃)₃] (0.1 mol%) and a P(OPh)₃ ligand (0.6 mol%), which they named “thermomorphic biphasic hydroformylation”. Up to eight runs of catalyst recycling were reported with conversions of >86% of 1-octene within cycles 3–8, with high selectivities of >93% to the linear aldehyde. An additional ligand was required due to the relatively high leaching of the catalyst into the product phase, in analogy to studies by Behr et al. [310]. In this case, the temperature is used only for the reaction performance itself and not to achieve a homogeneous reaction system, and thus, a TMS is not represented in this case.

In 2007, Yang et al. [302] described a PEG-based TMS for the hydroformylation of 1-dodecene with the catalyst [Rh(acac)(CO)₂]/tri-(methoxypolyethylene glycol)phosphite (TMPGP; Rh/P ratio = 1/10). The TMS was composed of PEG-400/1,4-dioxane/*n*-heptane and high aldehyde yields of around 95% were achieved with 0.1 mol% of the catalyst. However, selectivity to the linear aldehyde, with a linear to branched (l/b) ratio of 1.1, was rather low and indicated the presence of unmodified Rh-carbonyl species. Nevertheless, a remarkable 23 recycling runs were possible with TOFs of around 160 h⁻¹ and rhodium leaching of 0.65% per run. Transfer to a continuous-flow reaction has not yet been performed.

The group of Dutta [241–243] used a PC/*n*-dodecane/1,4-dioxane (30:10:60) TMS for the hydroformylation of 1-octene with a [HRh(CO)(PPh₃)₃] catalyst. With 0.01 mol% of rhodium, high regioselectivities of about 10:1 in favor of the linear aldehyde were possible, with 3% rhodium leaching into the product phase at conversions up to 97%; thus representing a TON of 600 and a TOF of 400 h⁻¹. The group focused on kinetic studies for hydroformylation in a TMS, and thus, recycling experiments were not performed.

In 2005 [15, 16], a [Rh(acac)(CO)₂]/BIPHEPHOS (ratio 1/5) catalytic system was employed for the isomerizing hydroformylation of 4-octene to *n*-nonanal. The first reported TMS for this transformation consisted of PC (1,3-dioxolanone), *p*-xylene, and *n*-dodecane. Although with 0.5 mol% of the catalyst very high yields for the desired linear aldehyde of 90% at full conversion were reached, leaching of the catalyst system was around 50% due to the presence of the mediator *p*-xylene in the product phase [16]. Different compositions of a TMS consisting of cyclic carbonates (ethylene carbonate (EC), PC, and butylene carbonate) and *n*-dodecane were investigated with pyrrolidones (NMP and *N*-octylpyrrolidone (NOP)) as mediators, with the aim of substituting *p*-xylene, and thus, reducing catalyst leaching. In a mixture of EC (18 wt%) and PC (18 wt%) with NMP (54 wt%) as a mediator and *n*-dodecane (10 wt%) as an extraction agent, quantitative conversion of 4-octene with 80% yield of the linear aldehyde were observed (Figure 4.17) [16]. Leaching of initial rhodium (0.5 mol%) was reported to be <0.1% with phosphorous leaching of <0.6% at a separation temperature of 25 °C with a TON of 194. Despite these very promising results, the recycling of the catalyst phase was not investigated.

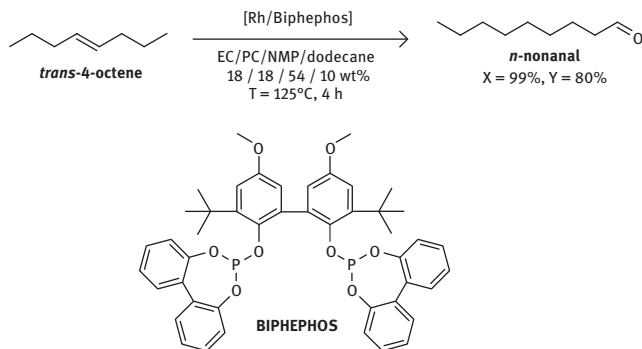


Figure 4.17: Isomerizing hydroformylation of 4-octene to *n*-nonanal with a Rh/BIPHEPHOS catalyst system in TMS [15, 16].

Ternel et al. [263] investigated different TMSs with organic solvents such as DMF/*n*-decane or PC/*n*-decane in the isomerizing hydroformylation of 10-undecenenitrile in 2013 (Figure 4.18). Promising yields were reached, but the TMS was limited by the relatively high product polarity and the resulting high product solubility in the polar catalyst phase. In a TMS, recycling was not possible. Carpentier and coworkers [263] decided to investigate catalyst recycling through vacuum distillation instead. For this, they used only a small amount of the solvent toluene to dissolve the [Rh(acac)(CO)₂]/BIPHEPHOS (ratio: 1/20) catalyst. At full conversion after 48 h, the solvent and pure aldehyde were removed through the vacuum distillation under inert conditions. Thus, the leaching of rhodium (initial: 0.002 mol%) in the product phase was not observed/investigated. Up to five recycling runs were possible with this procedure, with the addition of ligand in each run. In the last run, the conversion and l/b selectivities dropped slightly from >92% to 86% and 98:2 to 97:3, respectively. A TON value of up to 230,000 was possible in this system. Because the costs for the BIPHEPHOS ligand are relatively high, in comparison to ligands such as TPP, Carpentier and coworkers [263] calculated a TON not only for the metal but also for the ligand (5,750).

In 2016, Behr and coworkers [78] investigated a slightly different reaction to tackle the general limitation of a DMF/alkane TMS in the synthesis of bifunctional molecules. In rhodium-catalyzed hydroformylation, aqueous TMSs are an attractive alternative. They reported the hydroformylation of methyl 10-undecenoate with a [Rh(acac)(CO)₂]/4,5-bis(diphenylphosphino)-9,9-dimethyl-2,7-disulfoxanthene disodium salt (SULFOXANTPHOS; ratio 1/5) system in a mixture of water and 1-butanol. Although at reaction temperatures of 140 °C the system is not fully homogeneous, mutual solubilities of the solvents in each other are drastically increased, leading to catalytic activity that is still promising for this transformation. The water-soluble catalyst (0.05 mol%) was recycled in the aqueous phase, while the aldehydes were quantitatively extracted into the nonpolar 1-butanol phase. Constant yields of the linear

aldehyde ester of around 73% were reached with a TOF of 1500 h⁻¹. Catalyst leaching in the product phase was 15 ppm. Additionally, the system proved its feasibility on a continuous scale, with stable performance for over 20 h on stream in the miniplant already presented for 1-dodecene hydroformylation (Figure 4.16). Although this biphasic system is not fully homogeneous at the reaction temperature, it still shows thermomorphic behavior with regard to catalyst activity and enables efficient catalyst recycling. Accordingly, Behr and coworkers [78] defined this kind of reaction system as a “narrow TMS.”

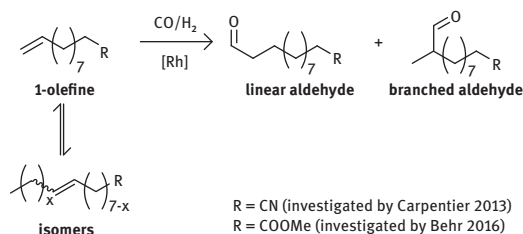


Figure 4.18: Hydroformylation of functionalized alkenes investigated by the groups of Carpentier [263] and Behr [78].

Hydroaminomethylation (HAM)

Behr and coworkers [12] also developed different TMSs for HAM. HAM is an autotandem reaction that consists of the rhodium-catalyzed hydroformylation of an alkene to an aldehyde, followed by reductive amination of the latter in the presence of an amine (Figure 4.19). The first example of HAM in a TMS was the reaction of morpholine and 1-octene presented in 2005, with PC and *n*-dodecane together with different mediators. These mediators were NMP, *N*-ethylpyrrolidone (NEP), *N*-cyclohexylpyrrolidone (NCP), NOP, ethyl lactate, and butyl lactate. These systems were compared to a system consisting of PC, *n*-hexane, and 1,4-dioxane. For this, a $[\{\text{Rh}(\text{cod})\text{Cl}\}_2]$ (0.1 mol%; cod = 1,5-cyclooctadiene) catalyst without any additional ligand was used. Within a reaction time of 2 h, amine yields of up to 96% were reached. Rhodium leaching observed in the product phase was less than 1.5%. However, this reaction protocol was limited due to a side reaction between PC and morpholine. Later in 2013 [25], investigations into an aqueous TMS with different mediators for the same reaction with a $[\{\text{Rh}(\text{cod})\text{Cl}\}_2]/\text{TPPTS}$ (ratio 1/64) system were conducted. A catalyst loading of 0.4 mol% concerning the olefin was used. The major problem of aqueous homogeneous catalysis consists of the low solubility of nonpolar substrates in the catalyst-containing water phase. To overcome this phase-transfer issue, a mediator is generally necessary. In the special case of a TMS, this mediator is usually a mid-polar solvent. Behr et al. [25] used the substrate 1-octene as the nonpolar phase and water as the polar phase. Different mediators, such as MeCN, ethanol, or NMP, were investigated. It was found that the mediator did not have a

negative effect on catalyst leaching into the product phase. In addition, the reaction performance in TMS was compared with a reaction under biphasic conditions without mediator. Lower leaching of rhodium (3–5 ppm) was observed in the TMS, in comparison to the investigated biphasic systems (7–13 ppm) [25]. The use of very low amounts of 1-octene in the reaction system with water shows TMS behavior without a mediator. Yields of up to 68% of the linear amine were obtained in this system. Neither in a TMS with a mediator nor in a biphasic reaction system were higher yields than 53% reached [25]. Surprisingly, no investigations into the recycling behavior for this reaction have been presented so far, and thus, it was not investigated in a continuous process.

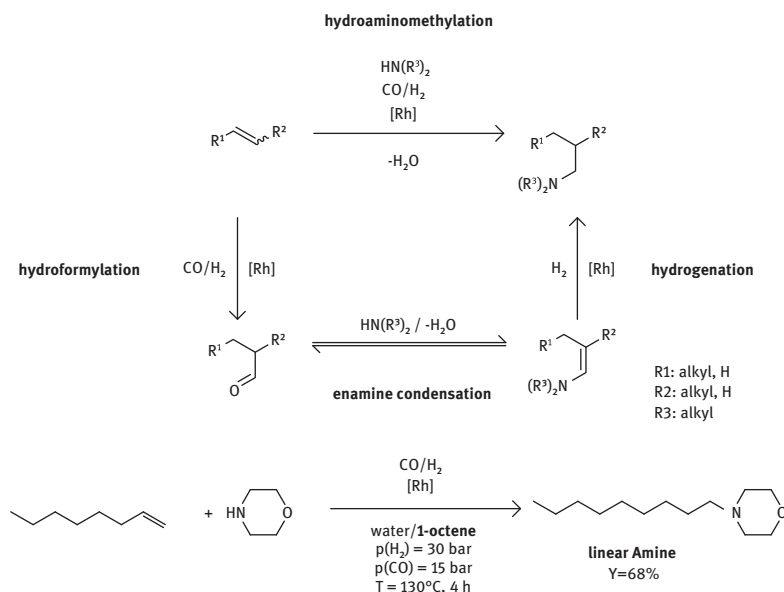


Figure 4.19: General scheme of the HAM and reactions of 1-octene with morpholine [25].

The group of Behr also investigated HAM of oleochemicals. In 2013 [274], HAM of oleyl alcohol with diethylamine (Figure 4.20) with a 0.5 mol% $[Rh(cod)Cl]_2$ /1,2-bis(di-tert-butylphosphinomethyl)benzene (1,2-DTBPMB) catalyst system was reported. Generally, this approach was reported to be problematic due to the relatively polar reaction product formed, which acted as a phase mediator to complicate phase separation after the reaction. Therefore, methanol and the alkanes cyclooctane, *n*-decane, and *n*-dodecane were used to create a highly temperature-dependent solubility gap between the polar catalyst phase and the nonpolar product phases. Although after the reaction a monophasic mixture resulted with cyclooctane at room temperature, the use of *n*-decane and *n*-dodecane led to very high rhodium and phosphorus leaching of >100 ppm. Thus, the recycling of this system was not investigated.

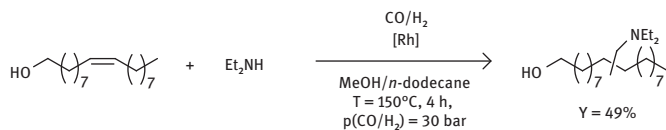


Figure 4.20: HAM of oleyl alcohol with diethylamine [274].

Between 2014 [27] and 2017 [275], rhodium-catalyzed HAM of methyl oleate with different amines was presented. Initially, the amino acid proline was employed as the amine component in a TMS consisting of methanol and an alkane. The presence of methanol led to the in situ esterification of proline, giving rise to a diester structure, of which up to 59% yield was achieved after 4 h of reaction time. The $[\{\text{Rh}(\text{cod})\text{Cl}\}_2]$ catalyst (2 mol%) could be recycled three times with slightly decreasing yields of bifunctional products from 46% to 33%. Rhodium leaching was between 8 and 9 ppm per recycling run [27]. Later [275], the solvents were changed to acetonitrile/*n*-heptane for HAM of methyl oleate in a 3:2 ratio of an amino nitrile compound to the branched nitrile ester (Figure 4.21). The ratios between the solvents were investigated. It was problematic that, for a higher *n*-heptane proportion, higher catalyst leaching resulted, whereas for a higher acetonitrile proportion higher product leaching into the catalyst phase resulted. The ratio of 3:2 (MeCN/*n*-heptane) used represents a compromise between these disadvantages. Without the use of a ligand for the $[\{\text{Rh}(\text{cod})\text{Cl}\}_2]$ (1 mol%) catalyst, 61–65% yield per run of the branched product was reached within three recycling runs. The catalyst leaching per run was around 0.9–1.1% of the rhodium catalyst. To finally obtain an amine ester, the nitrile ester formed was hydrogenated by using a heterogeneous Raney nickel catalyst after the reaction. The formed amine esters can be potentially used as monomers for polyamides [275].

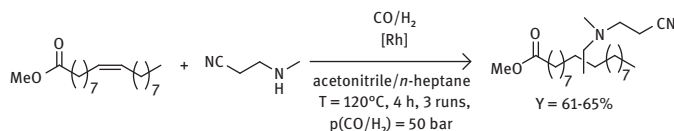


Figure 4.21: HAM of methyl oleate with amino nitriles [275].

In general, the examples show that the HAM represents a very complex reaction system. Two fluidic substrates and two different gases in nonequivalent amounts are used. In addition, water is formed as coproduct. Thus, the transfer of experience from preliminary reactions concerning catalyst and phase behavior into this multiphase system seems to be a very challenging task. As a result, no continuous process for HAM has been realized so far (Section 4.1.4 for latest developments).

Hydroamination

Another reaction investigated in a TMS is hydroamination, which usually occurs through the palladium-catalyzed addition of primary or secondary amines to 1,3-dienes. In 2010, Behr et al. [20] applied the renewable terpene β -myrcene, containing a 1,3-diene moiety, together with morpholine as a nucleophile in two different TMSs consisting of the polar compound DMF or MeCN together with the nonpolar compound *n*-heptane (Figure 4.22). In this case, a homogeneous $[\text{Pd}(\text{CF}_3\text{CO}_2)_2]$ (0.2 mol%) catalyst was used in combination with the ligand 1,4-bis(diphenylphosphino)butane (dppb) in a Pd/P ratio of 1/8. With a solvent mixture of 40:60 MeCN/*n*-heptane, 92% yield of 1,4-adducts was obtained after 5 h. The catalyst leaching was 1% Pd (5 ppm) and 0.3% P (3 ppm). In 2015 [68], a very detailed investigation into the optimal polar solvent to form a TMS was conducted for this reaction, which was supported by the thermodynamic model PC-SAFT. Again, DMF and acetonitrile emerged as the most promising candidates. The nonpolar solvent in both cases was *n*-heptane, which secured a monophasic mixture under reaction conditions. Yields of up to 85% terpenylamines, as the main product, were obtained. Based on these investigations, a continuous miniplant process was designed in 2015 and 2016 [18, 68, 69], consisting of a Taylor–Couette reactor and a phase separator. In further optimizations, in terms of reactivity and catalyst recovery, the TMS of *n*-heptane/DMF showed superior results. Herein, yields of the product of 80% were achieved over a continuous operating period of 6 h with 0.4 mol % $[\text{Pd}(\text{CF}_3\text{CO}_2)_2]$ and the ligand dppb (Pd/P = 1/8). Afterward the yields dropped significantly. Over the complete operation time of 24 h, the total loss of metal catalyst was 6%. In this example, the main focus was the use of a Taylor–Couette reactor in reactions with a TMS [18, 68, 69].

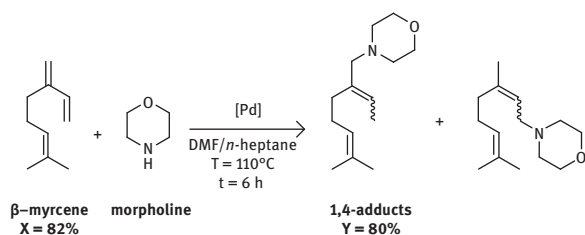


Figure 4.22: Hydroamination of β -myrcene with morpholine in a Taylor–Couette reactor [18, 68, 69].

Hydrolysis

In addition to homogeneous transition-metal catalysts, the concept of a TMS has also been used for enzymatic catalysts. To show the wide applicability of the concept, Behr et al. [21, 23] conducted the enzymatic hydrolysis of *p*-nitrophenyl palmitate with Amano lipase PS (Figure 4.23) as a model reaction. Moderate reaction temperatures of around 45 °C were required, and thus, a three-component TMS consisting of water, methanol, and 1-hexanol (52/35/13 wt%) was used. To achieve a homogeneous system

at this comparably low temperature, the exact composition of the ternary mixture was established by using the preliminary recorded ternary diagram. Finally, five recycling runs of the free enzyme with stable yields (98%) were achieved by the use of this system. To obtain a biphasic system for recycling of enzyme, the mixture was cooled to 5 °C after the reaction. Only 2% of the enzyme leached to the product phases within the five recycling runs.

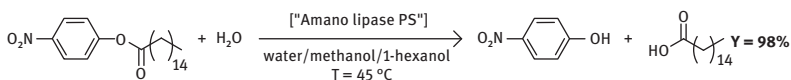


Figure 4.23: Enzymatic hydrolysis of *p*-nitrophenyl palmitate with amano lipase PS in a TMS [21, 23].

Cyclopropanation

The cycloalkane-based system was also applied in 2011 [150] for organocatalytic cyclopropanation (Figure 4.24). Under biphasic conditions, no complete reactions were observed. The first intention of the group was to demonstrate that homogeneous reaction conditions could be achieved with cycloalkane-based thermomorphic systems, which led to high yields of the target product of >90% for different substrates.

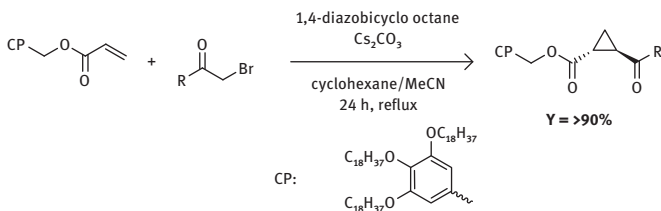


Figure 4.24: General scheme of cyclopropanation described by Kim et al. [150].

In addition to their organocatalytic research, in 2008 and 2012, the group of Chiba [148, 194] published articles on the application of TMSs in electrochemical reactions to separate nonpolar products from the polar electrolyte solution after electrochemical transformations.

Metathesis

In 2012, Behr et al. [24] reported on the first successful metathesis reaction in a TMS, including recycling of the ruthenium catalyst. The cross-metathesis of methyl oleate with 4-octene was performed in a solvent mixture consisting of methanol and ethylene glycol at 50 °C (Figure 4.25). With the Grubbs second-generation catalyst (0.5 mol%), the yield of the desired cross-metathesis product was 63% at 95% conversion, with Ru leaching of 14 ppm into the product phase, which consisted mainly of product and excess 4-octene, as revealed by ternary diagrams. A TMS

consisting of PC and 1,4-dioxane showed inferior results concerning catalyst leaching (158 ppm) because the ternary diagram showed the substantial presence of 1,4-dioxane in the product phase, which withdrew the catalyst from the polar PC phase. Despite promising results in the TMS (MeOH/glycol), recycling of the catalyst was only performed in a biphasic reaction regime by applying a mixture of *n*-dodecane and methanol, which surprisingly showed higher yields for the desired product of 75% at 90% conversion. Only a slight decrease in yield to 69% was detected in three consecutive runs at leaching values ranging from 29 to 22 ppm.

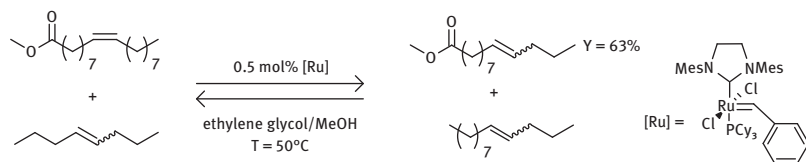


Figure 4.25: Cross-metathesis of methyl oleate with 4-octene in a TMS [24].

In close analogy to work by the group of Behr on the cross-metathesis of methyl oleate, Huang et al. [112] reported in 2015 on the cross-metathesis of the terminally unsaturated oleochemical methyl 10-undecenoate with methyl acrylate in a TMS based on PC and cyclohexane (Figure 4.26). Initially, they applied ethyl acetate to mediate between the polar PC and nonpolar cyclohexane phases and achieved higher yields of 88%, compared with the same reaction conducted in pure PC. Leaching of the catalyst was reported to be 62 ppm after extracting the polar phase three times with cyclohexane to sufficiently recover the product (initial catalyst content \approx 2,500 ppm). However, during investigations, it was revealed that both the substrate and product sufficiently mediated between the two phases, and a monophasic system was formed at an elevated reaction temperature of 80 °C. Under these conditions, the conversion of methyl 10-undecenoate was almost quantitative (97%) after 3 h with 0.5 mol% of catalyst. Unfortunately, recycling was not conducted with either system.

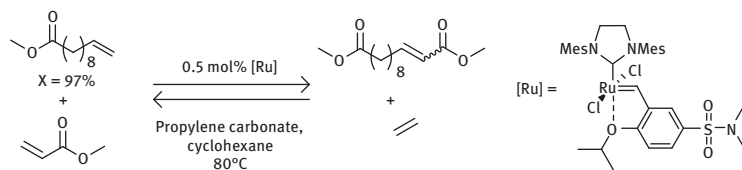


Figure 4.26: Cross-metathesis of methyl undecenoates with methyl acrylate by Huang [112].

Methoxycarbonylation

Another carbonylation reaction investigated in a TMS is palladium-catalyzed methoxycarbonylation, yielding methyl esters from alkenes, methanol, and carbon monoxide (Figure 4.27) [26].

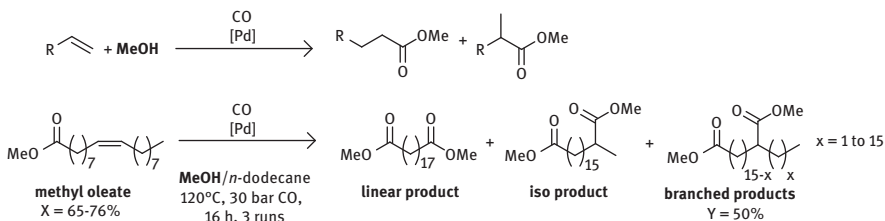


Figure 4.27: General scheme of the methoxycarbonylation of a terminal alkene (top) and methoxycarbonylation of methyl oleate in a TMS (bottom) [26].

Methoxycarbonylation is somewhat different from the other reactions discussed above because this reaction only proceeds with sufficient activity in methanol, which serves as a solvent and substrate at the same time. In particular, catalytic systems consisting of a palladium precursor and bidentate phosphine ligands proved their synthetic potential in recent years, for example, in the formation of diesters from unsaturated oleochemicals [53, 217, 219]. For instance, in 2013 [26], the first methoxycarbonylation investigated by Behr and coworkers in a TMS was that of methyl oleate. An alkane had to be used as the nonpolar solvent because only methanol was eligible as a polar component. Applying XANTPHOS (ligand/metal ratio of 1:4) as a ligand and methanesulfonic acid (MSA; 10 mol%) as a cocatalyst for [Pd(hfacac)₂] (1 mol%; hfacac = hexafluoroacetylacetonate), conversions of around 94% were reached with high selectivities of the branched diester products of up to 90%. Three recycling runs were successfully performed in MeOH/*n*-decane with very low palladium (<0.2%) and phosphorous (<0.1%) leaching. The conversion varied between 76 and 65%, while yields of up to 50% were observed for predominantly branched products.

Later, Behr and coworkers [76, 77] reported on the methoxycarbonylation of methyl 10-undecenoate (Figure 4.28), another unsaturated oleochemical. Their main focus was the development of a catalyst system for linear methoxycarbonylation, in which a linear C₁₂-diester is formed as a polymer precursor. Two catalyst systems differing in the applied ligand were compared: Xantphos showed higher activity than that of the ligand 1,2-DTBPMB. However, the latter showed, as expected, high selectivities toward linear methoxycarbonylation. Both systems showed their general recyclability in a TMS consisting of MeOH and *n*-dodecane, with leaching values of <1% of the initial [Pd₂(dba)₃] (0.05 mol%) content. Subsequently, the 1,2-DTBPMB catalyst system (metal/ligand = 1/20) was investigated in more detail. Again, the same solvent system

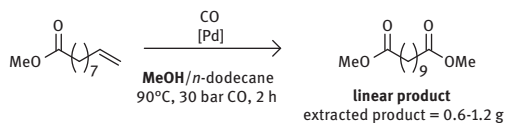


Figure 4.28: Methoxycarbonylation of methyl 10-undecenoate in a TMS [76, 77].

was used. Up to eight recycling runs were performed. The amount of extracted product was reported to decrease from 1.2 g in the beginning to 0.6 g in the last reaction. The addition of MSA ensured longer catalyst lifetimes [76, 77]. Kinetic models were described by Gerlach et al. [82], an investigation of the phase equilibria was performed by Sadowski and Lemberg [164], and Benski et al. [31] carried out an optimization of the reaction parameters. The application of a TMS to the methoxycarbonylation of oleochemicals seems to be principally limited because of the cross-contamination of the solvents in each other and the loss of catalyst activity with every run. To achieve reasonable activities, high concentrations of methanol are required. Thus, additional solvents, either polar ones for reducing leaching of the catalyst into the product phase or nonpolar ones for extraction of the product, inevitably result in reduced activity. Due to the high complexity of this system and highly sensitive catalyst complex, TMS does not seem to be the most promising strategy for catalyst recycling in methoxycarbonylation.

Figure 4.29 summarizes the presented examples according to the applied solvent combinations.

4.1.4 Recent Developments in TMSs

While some examples of recent work on TMSs were described briefly in the previous sections, some recent work that extends the TMS concept in different ways is presented in this section. Although some of these extensions are based on new design methodologies that were developed alongside the applications, this section only covers the application, while the respective methods are presented in the corresponding sections of this book. The extensions to the TMS concept that are covered in this section are:

- Combinations of the CSTR and decanter setup with new reactor types to increase the reaction performance
- Implementation of online analytics to track the concentration of different catalyst species, substrates, intermediates, and products
- Application of more complex homogeneously catalyzed reactions in TMSs and transfer to continuous operation for these reactions
- Improved catalyst recovery and process performance through the application of combined separation processes

	Water	Ethylene glycol / Polyethylene glycol	Methanol	Propylene Carbonate	Nitroalkanes (C1+C2)	Dimethyl formamide	
Reactants	1-Butanol (Behr et al. 2008; Gaide et al. 2016c) Polyethylene glycol 1000 (Behr and Miao 2005) Acetonitril N-Methyl pyrrolidone Ethanol (Behr et al. 2013a) Triethylamine (Bergbreiter et al. 2009)	1,4-Dioxane Tetrahydrofuran (Behr and Fängewisch 2003) Toluene (Behr and Miao 2004) Methanol (Behr et al. 2012)		1,4-Dioxane (Behr et al. 2014b; Behr et al. 2012) 1,4-Dioxane, Tetrahydrofuran, Ethanol, Anisole, Toluene (Behr and Fängewisch 2003)			
1-Hexanol	Methanol (Behr et al. 2011)						
Cyclohexane				Toluene (Behr and Tosli 1999; Huang et al. 2015) Ethyle Acetate (Huang et al. 2015)	Reactants (Chiba et al. 2002)	Dimethylacetamide (Chiba et al. 2002; Kim et al. 2008c; Kim et al. 2006a)	
Methyl cyclohexane						Dimethylacetamide (Chiba et al. 2002; Kim et al. 2008c; Kim et al. 2006a)	
n-heptane	Ethanol (Bergbreiter et al. 1998; Bergbreiter et al. 2000)	Toluene (Huang et al. 2008) 1,4-Dioxane (Yang et al. 2007) Reactants (Lu et al. 2006) *monoalkylether		Reactants (Tijani and El Ali 2006)		Reactants (Behr et al. 2010a; Mizugaki et al. 2002; Bergbreiter et al. 2003; Behr et al. 2010c; Behr and Färber 2015; Färber et al. 2016)	
n-decane			Reactants (Vorholt et al. 2013; Behr et al. 2014a; Vorholt et al. 2017; Behr et al. 2013b; Gaide et al. 2016a; Lemberg and Sadowski 2016; Bensi et al. 2017; Behr et al. 2012)	Reactants (Schäfer et al. 2012; Ternel et al. 2013)		Reactants (Brunsch and Behr 2013; Dreimann et al. 2016a; Zagajewski et al. 2014b; Zagajewski et al. 2016; Dreimann et al. 2017; Dreimann et al. 2016b; Zagajewski et al. 2014a; Behr et al. 2008; Sharma et al. 2014; Schäfer et al. 2012)	
n-dodecane			Reactants (Gaide et al. 2016a; Lemberg and Sadowski 2016; Bensi et al. 2017)	1, 4-dioxane (Shaharun et al. 2010) 1, 4-dioxane, Pyrrolidones (N-methyl, ethyl, octyl), Ethyl-lactate, Butyl-lactate, p-Xylene (Behr and Roll 2005a; Behr et al. 2005b; Behr et al. 2005a) + other carbonates		Reactants (Ternel et al. 2012)	

Figure 4.29: Reported TMSs for the recovery and recycling of homogeneous catalysts: Columns represent the polar (usually catalyst containing) solvents (blue), rows show the nonpolar (usually product containing) components, that is, reactants or solvents (yellow). Entries show the applied.

	Acetonitril	Dimethyl acetamide	<i>N</i> -Methyl pyrrolidone (s)	Propionitril	4,4'-dipyridin
Reactants					Phenol (Chang et al. 2004)
1-Hexanol					
Cyclohexane	Reactants (+Propionitril) (Hayashi et al. 2006; Kim et al. 2011; Kim et al. 2008c; Kim et al. 2008a)			Reactants (Hayashi et al. 2006; Kim et al. 2008c; Kim et al. 2008a)	
Methyl cyclohexane	Reactants (Hayashi et al. 2006; Kim et al. 2011; Kim et al. 2008c; Kim et al. 2008a)			Reactants (Hayashi et al. 2006; Kim et al. 2008c; Kim et al. 2008a)	
<i>n</i> -heptane	Reactants (Färber et al. 2015; Behr et al. 2010a; Vorholt et al. 2017)	Reactants (Bergbreiter et al. 2000)			
<i>n</i> -decane	Reactants (Schäfer et al. 2012; Vorholt et al. 2017)		Reactants (Behr et al. 2008)		
<i>n</i> -dodecane					

Figure 4.29 (continued)

mediator (if any) and the corresponding reference. Colors indicate the number of references applying the respective solvent combination (from light green = one to dark green = >5, cross-hatched: not reported so far) [38].

The reactions that are used as case studies in the following sections are the hydroformylation of long-chain alkenes as well as the reductive amination of aldehydes and the hydroaminomethylation of alkenes which combines the former two reactions in a tandem catalytic synthesis (Section 4.1.3).

4.1.4.1 Combination of TMSs with Other Reactor Types

While the reactor-decanter setup for continuous operation of a reaction in a TMS (Figure 4.16) captivates through simplicity, other more complex reactor variants could provide higher reaction rates or improved conversion, yield or selectivity, when they are coupled with a decanter for catalyst separation and recirculation. As the design and modeling of these reactor variants are quite complex, the interested reader is referred to Section 5.3.1, while this section focuses on the application for two examples in continuous processes.

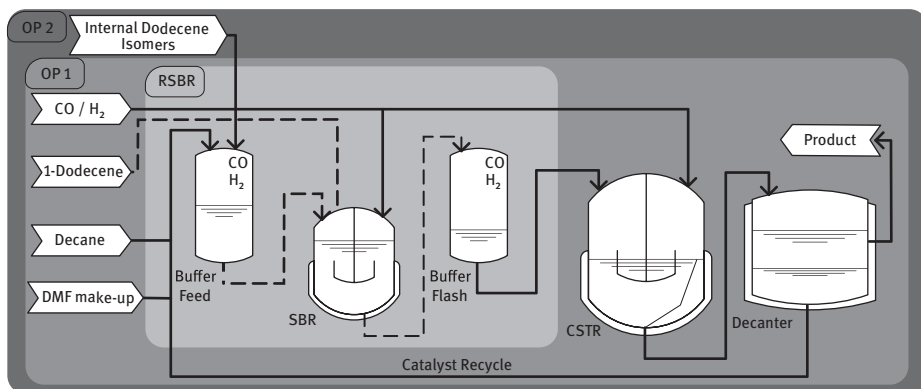


Figure 4.30: Combination of the conventional TMS setup (CSTR + decanter) with a repeatedly operated semibatch reactor. Adapted from [128].

Several theoretical reactor concepts and possible technical implementations of these concepts were developed by the framework of elementary process functions, with the goal of increased selectivity for the hydroformylation of 1-dodecene in a TMS consisting of *n*-decane and DMF by Sundmacher and coworkers [139]. The two suggested technical implementations for the theoretical concepts are the combination of either a helically coiled tubular reactor (HCTR) or a repeatedly operated semibatch reactor (RSBR) with a CSTR and a decanter. Both setups were subsequently realized and implemented in a continuously operated miniplant. The RSBR was implemented in an existing miniplant that consisted of a CSTR and decanter [128] as illustrated in Figure 4.30. The hydroformylation of 1-dodecene was performed in this tandem reactor setup operating continuously for more than 90 h. Compared to the standalone CSTR and decanter higher selectivity toward the product tridecanal was

achieved and the results could be predicted well with a process model that was previously published by the same group [218]. The HCTR was also combined with a CSTR and decanter for the same hydroformylation reaction [127], as illustrated in Figure 4.31. In addition to mass transfer investigations, the process was operated continuously for more than 100 h, and the reaction performance was slightly better than the CSTR and decanter setup regarding yield and conversion. Both examples show that more sophisticated reactor setups can be used to increase the reaction performance of TMSs.

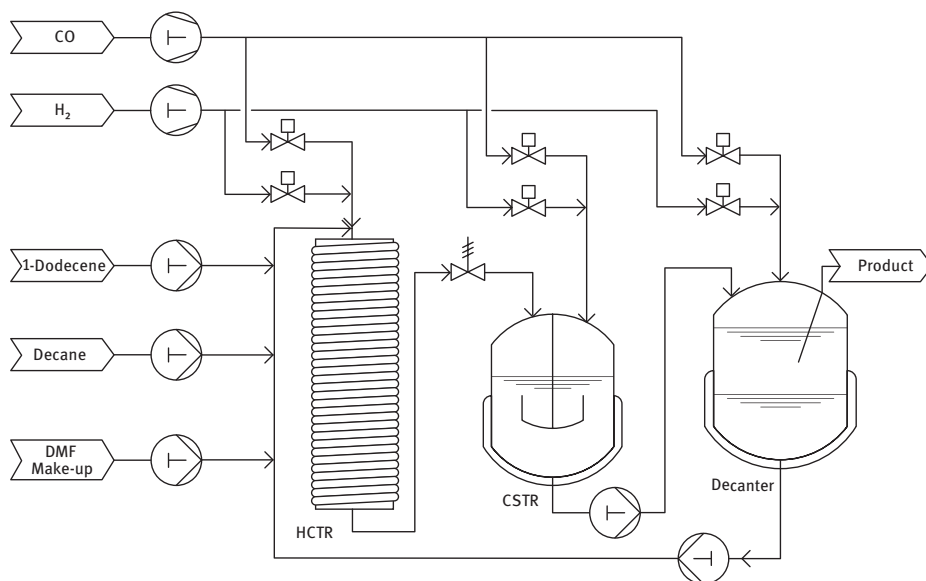


Figure 4.31: Combination of the conventional TMS setup (CSTR + decanter) with a helically coiled tubular reactor. Adapted from [127].

4.1.4.2 Improved Online Analytics

For the application of TMSs in miniplants, the most frequently used analytic technique is online gas chromatography to analyze the composition of the nonpolar product phase. While this is often sufficient to operate the process and identify steady states or unwanted behavior, additional information can enable further optimization of the reaction performance and improved process control. Furthermore, information about the polar catalyst phase can help to identify if components are accumulating or if the catalyst is still in its active form. This information can be obtained by analyzing samples of the catalyst phase offline. However, the drawback of offline analysis is that the information can have a large time delay and therefore cannot be used for process control. Additionally, for small-scale miniplant operation, the samples taken can significantly reduce the amount of catalyst phase over time. Thus, noninvasive online measurements of the concentration or type of species are an

important step to gain a deeper understanding of the process and to improve process control.

One possibility to determine the mixture composition and the catalyst species online is the use of in situ infrared (IR) spectroscopy. This technique was applied by Vorholt and coworkers [60] in batch and continuous reactions for the hydroformylation of 1-dodecene in toluene using a $\text{Rh}(\text{acac})(\text{CO})_2$ as the catalyst precursor and BIPHEPHOS as the ligand. They used two different modes of IR spectroscopy (attenuated total reflection and transmission mode) to determine the concentration of different components in the reaction mixture and, together with DFT calculations, different species of the catalyst could be distinguished. To deconvolute the measured spectra of the mixture into single component spectra, they used a method called band target entropy minimization (BTEM). Although the measurements were conducted in a single-phase system (not a TMS), this was a first step in evaluating the possibilities of in situ IR spectroscopy for the analysis of complex reactions mixtures in TMSs.

Vogt and coworkers [158] used in situ transmission Fourier-transform infrared spectroscopy with the BTEM approach to evaluate its potential for real-time process analysis in the reductive amination of decanal with diethylamine in a TMS consisting of DMF and *n*-dodecane. Due to a large number of IR active components present in the reaction mixture, this investigation focused on deriving pure component spectra from spectra of binary mixtures, by tuning different parameters of the BTEM algorithm. While spectra of mixtures consisting of DMF, *n*-dodecane, and decanal were successfully decomposed into single component spectra, especially mixtures with water showed a high variation in the quality of the decomposed spectra. Thus, this work serves as a step toward real-time process monitoring using infrared spectroscopy even for complex, homogeneously catalyzed reactions in TMSs.

4.1.4.3 Application of TMSs for Complex Reactions in Continuous Operation

Although many different reactions have been studied in TMSs (Section 4.1.3), only a few of these have been transferred to continuous operation, which is a major focus for the implementation in industrial processes. Thus, recent work has focused on the implementation of more complex reactions in continuous operation to broaden the applicability of TMSs. While the hydroformylation of long-chain alkenes was studied extensively during the first two funding periods of InPROMPT, the third funding period focuses on a more complex reaction. The selected model reaction is the hydroaminomethylation (HAM) of 1-decene with diethylamine. As explained in Section 4.1.3, HAM combines hydroformylation and reductive amination in a one-pot synthesis. Consequently, the reductive amination of decanal and undecanal with diethylamine were also studied as stand-alone reactions to combine the previously generated knowledge for the hydroformylation with that for the reductive amination, resulting in faster process development.

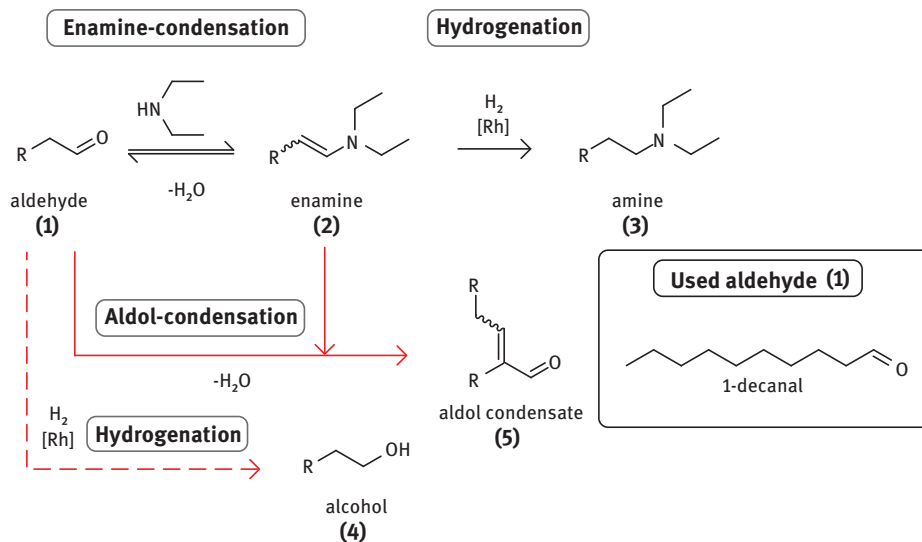


Figure 4.32: Reductive amination of 1-decanal with diethylamine. Adapted from [159].

Therefore, Vogt and coworkers [159] investigated the reductive amination of 1-decanal with diethylamine (Figure 4.32). They used a structured approach starting with catalyst and solvent selection, followed by the experimental determination of suitable reaction conditions in batch experiments, and concluding with the implementation in a continuous miniplant. DMF was chosen as a suitable polar solvent and *n*-dodecane as the nonpolar solvent to form the TMS. The separation temperature in the decanter and the separation efficiency were determined based on the solubility of the polar solvent in the nonpolar solvent, which results in a separation temperature of 5 °C. The catalyst precursor Rh(acac)cod and the ligand triphenylphosphine were selected based on literature data to obtain optimized reaction conditions. Therefore, reaction temperature, hydrogen pressure, and the aldehyde mass fraction in the feed were varied systematically in batch experiments. A reaction temperature of 100 °C, a hydrogen pressure of 30 bar, and an aldehyde mass fraction of 4 wt% resulted in the best yield (96%) and selectivity (76%) toward the desired product *N,N*-diethyldecylamine. The reaction was subsequently performed in a continuously operated miniplant to demonstrate the feasibility of the process concept. In several long-term experiments, a sensitivity analysis was conducted to optimize the residence time in the reactor, the ratio of diethylamine to *n*-decanal in the feed, and the hydrogen pressure (Figure 4.33).

With the optimized reaction conditions, a product yield of 93% was achieved while also reducing the amount of unconverted enamine and aldol by-products. Furthermore, the leaching of the catalyst into the nonpolar phase was lower than 1% of phosphorus as well as rhodium per hour of operation. Although water is produced as a

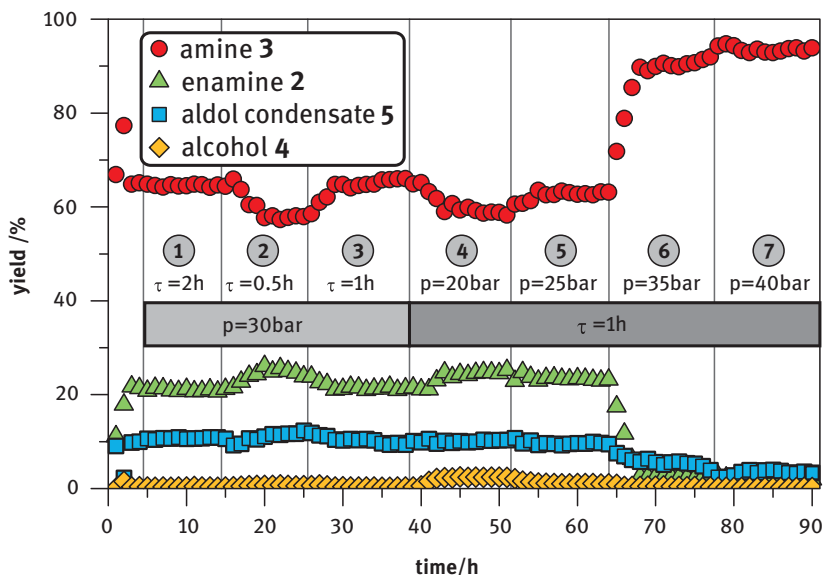


Figure 4.33: Variation of residence time and hydrogen pressure during the reductive amination of 1-decanal with diethylamine in a continuous miniplant experiment. Adapted from [159].

coproduct during the reaction and has a high affinity for the polar catalyst phase, no accumulation was reported in the continuous experiments.

Extending the previously described continuous process for the reductive amination to the hydroaminomethylation, was the scope of a different work in Vogt's group [39]. In this work the hydroaminomethylation of 1-decene with diethylamine to form *N,N*-diethylundecylamine was considered using $\text{Rh}(\text{acac})\text{cod}$ as the catalyst precursor and SULFOXANTPHOS as the ligand (Figure 4.34).

Again, a suitable polar reaction solvent and a nonpolar extraction solvent were selected. Interestingly, the tandem hydroaminomethylation reaction could not be performed in DMF, whereas its constituent reactions, hydroformylation, and reductive amination, were successfully performed in DMF. Consequently, methanol was identified as the best reaction solvent and was paired with *n*-dodecane to form the TMS. Bianga et al. [39] also investigated the influence of the coproduct water on the reaction performance and concluded that it has a negative but not detrimental effect on the reaction performance because its presence leads to an increase of byproducts that are formed (Figure 4.35). This was confirmed by recycling experiments in which the accumulation of water was also shown.

Finally, the reaction was transferred to continuous operation in a miniplant. Although the process was successfully operated for approx. 90 h with yields of up to 88% and only a small decline in reaction performance over time, severe water accumulation was demonstrated with a steady increase in water content that already

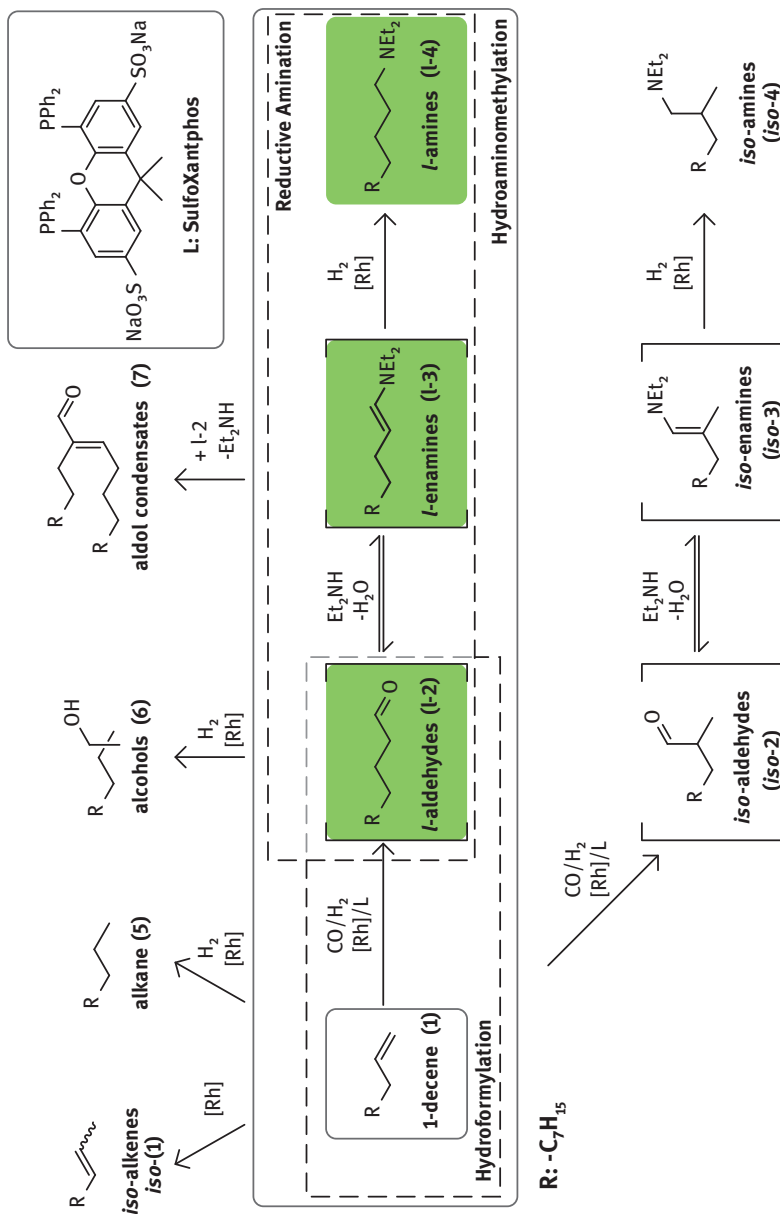


Figure 4.34: Hydroaminomethylation of 1-decene with diethylamine. Adapted from [39].

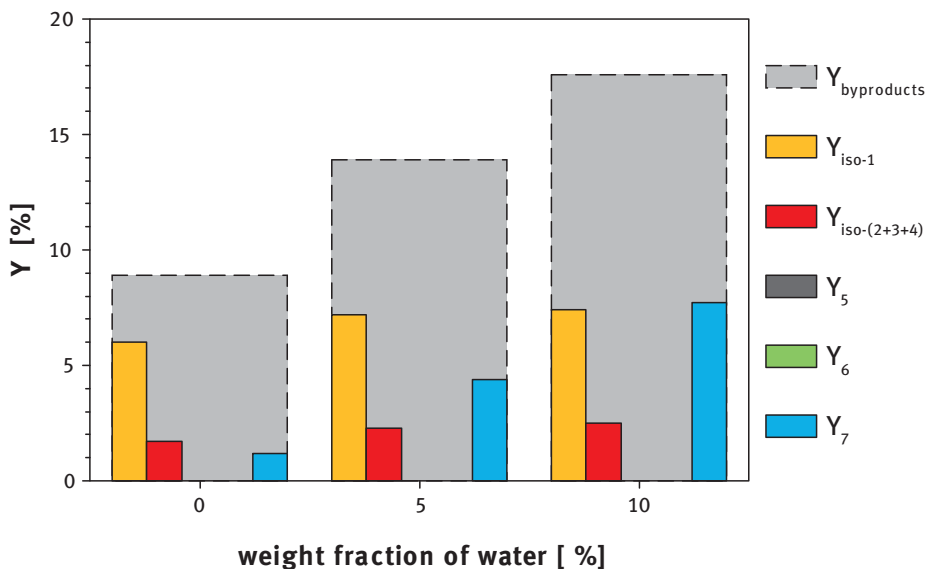


Figure 4.35: Formation of byproducts during the hydroaminomethylation of 1-decene with diethylamine in methanol with different amounts of water added at the start of the reaction. Adapted from [39].

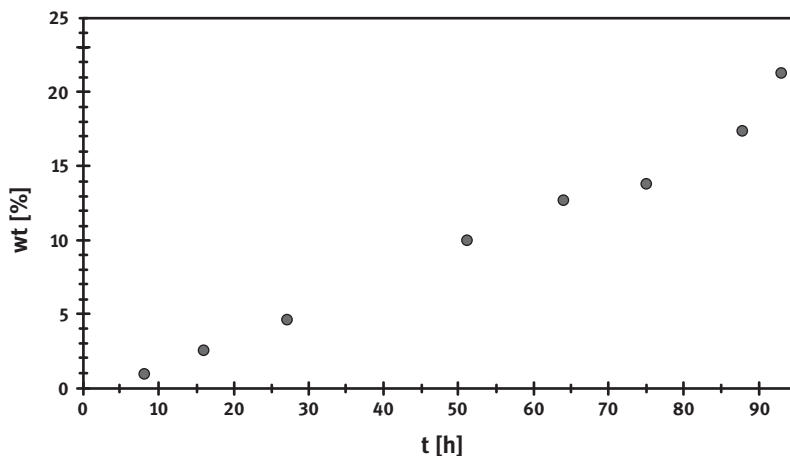


Figure 4.36: Weight fraction of water in the catalyst recycle stream during the hydroaminomethylation of 1-decene with diethylamine in a continuous miniplant. Adapted from [39].

reached 21 wt% in the recycle stream after approx. 90 h of operation (Figure 4.36). This demonstrates that accumulating components need to be removed from the system by additional separation steps. Thus, a combination of the TMS with other

separation techniques, such as membrane separations as discussed in Section 4.1.4.4, may be a necessary extension of the process concept for more complex reactions.

4.1.4.4 Combined Reaction Separation Processes

TMSs provide an elegant solution to efficiently separate the catalyst from the product in many homogeneously catalyzed reactions; however, two major challenges were identified in the previous work: catalyst leaching into the nonpolar phase and accumulation of by-products or coproducts with a high affinity for the polar catalyst phase. Both challenges can be addressed by combining the TMS with additional separation techniques. To allow for gentle separations, the combination of TMSs and organic solvent nanofiltration was considered by Skiborowski and coworkers [231], who illustrated several options to incorporate membrane-based separations into the TMS process. Depending on the specific limitation that is encountered by the standard TMS process, consisting of a CSTR and decanter, four limiting cases were specified based on atom economy (AE) and catalyst leaching (Figure 4.37):

1. AE = 100% and no or insignificant catalyst leaching
2. AE = 100% and significant catalyst leaching to the nonpolar phase
3. AE < 100% and coproduct distribution mainly to the nonpolar phase
4. AE < 100% and coproduct distribution mainly to the polar phase

For the first case, no adjustment of the conventional TMS process is necessary since there are no accumulating by-products and the separation efficiency of the catalyst in the decanter is sufficient. If catalyst leaching into the nonpolar product phase is significant (case 2) a membrane-based separation can be implemented in the nonpolar product stream to recover the leached catalyst while allowing for the permeation of the product and the nonpolar solvent. A similar setup applies for coproduct accumulation in the nonpolar phase (case 3), in order to separate the coproduct and the product. However, if the coproduct accumulates in the polar catalyst phase (case 4), a membrane-based separation can be implemented in the catalyst recycle stream, to selectively remove the coproduct while retaining the catalyst. Especially when the process is operated at high pressure, a gentle pressure-driven separation by OSN can exploit the pressure difference as the driving force for coproduct separation.

An example of case 2 has been given by Vorholt, Skiborowski and coworkers [62], who combined a commercially available, nonpolar OSN membrane with a TMS consisting of DMF and *n*-decane for the hydroformylation of 1-dodecene in a continuously operated miniplant (Figure 4.38).

Based on investigations on catalyst and ligand rejection [61], a process concept was developed that combines a CSTR and a decanter for the TMS followed by a buffer tank and a subsequent OSN membrane separation. The buffer tank was

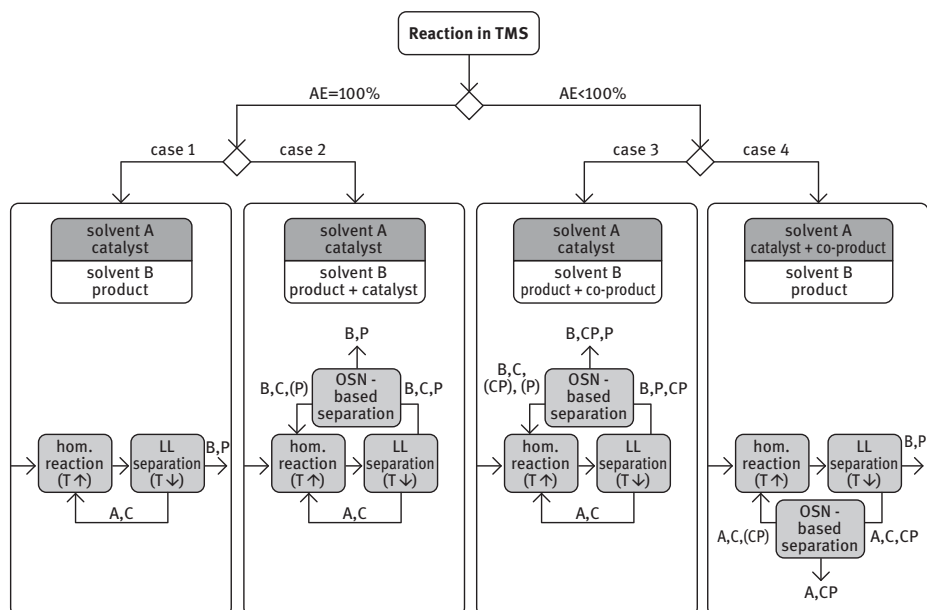


Figure 4.37: Process concepts that combine TMSs with an additional membrane-based separation for increased catalyst recovery or separation of byproducts or coproducts. Adapted from [231].

necessary to provide an ample flow rate for the membrane module and allow for easy recirculation of the retentate of the membrane back to the reactor. The combination of OSN and TMS with rejections of 80% and 87%, respectively, resulted in a total rejection of 97% of the catalyst. Additionally, the recycling of the catalyst to the reactor increased the product yield compared to the standalone TMS process (Figure 4.39). This demonstrates that high catalyst leaching can be overcome by combining the TMS with an OSN membrane.

While the coproduct accumulation to the nonpolar phase (case 3) has not been observed or investigated yet, Skiborowski's group [231] further evaluated a process concept according to case 4 which combines an OSN membrane in the polar recycle stream and subsequent separation of the coproduct from the remaining solvent by distillation (Figure 4.40).

Using the reductive amination, as published by Vogt and coworkers [159], as a case study but focusing on the membrane separation, a process design workflow that incorporates solvent selection, membrane screening and model-based evaluation of the membrane separation together with a subsequent distillation step was investigated. Several membranes were screened regarding high catalyst rejection and sufficient water removal from different polar solvents that were identified for use in a TMS (Section 6.3). For the two solvents DMF and methanol in combination with the DuraMem 150 membrane, it was demonstrated that OSN membranes can

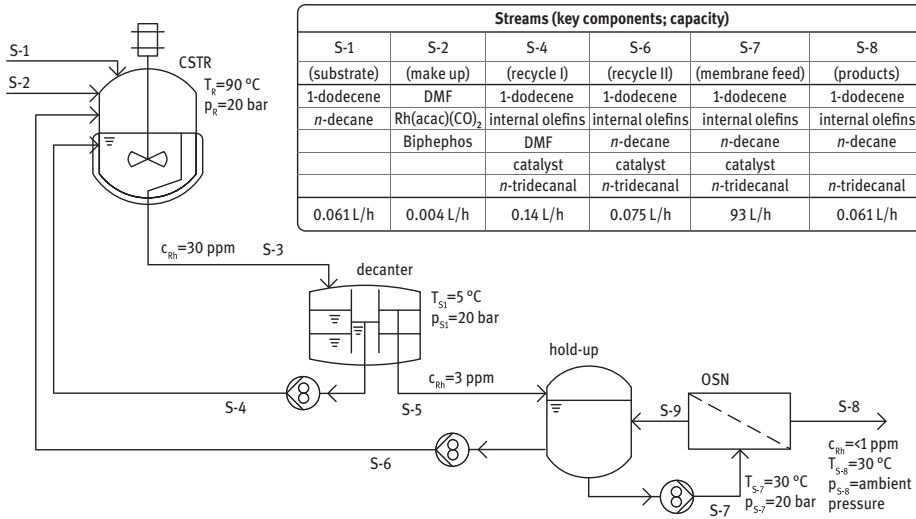


Figure 4.38: Process flow diagram for the hydroformylation of 1-dodecene with an additional organic solvent nanofiltration unit for enhanced catalyst recovery in a continuous miniplant. Adapted from [62].

be used to remove the coproduct water from the catalyst-rich recycle stream while retaining the catalyst. While this evaluation was based on model systems containing only the ligand, the polar solvent, and water, the study further evaluated the requirement of multistage membrane separations and a subsequent distillation step

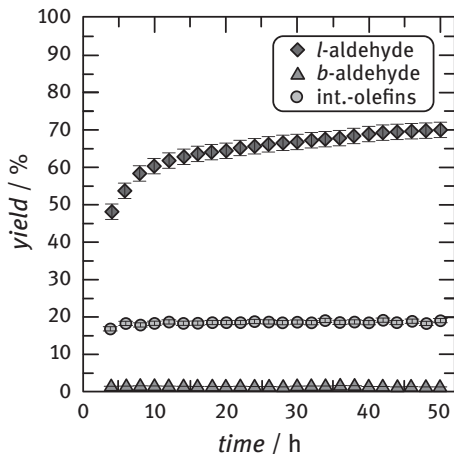


Figure 4.39: Product yields during the hydroformylation of 1-dodecene with an additional organic solvent nanofiltration unit for enhanced catalyst recovery in a continuous miniplant. Adapted from [62].

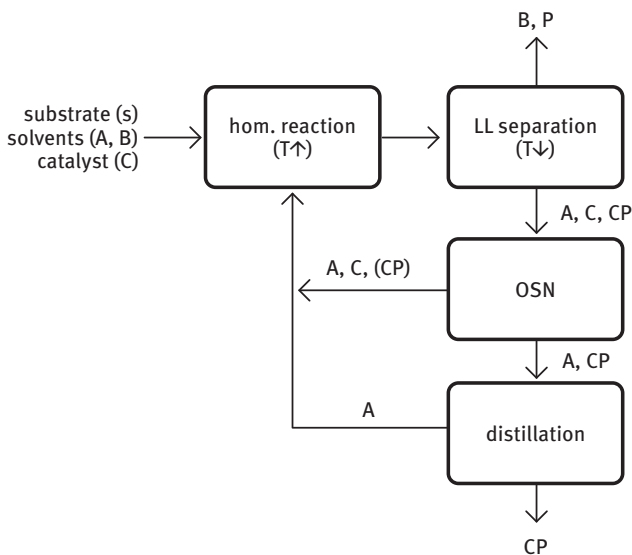


Figure 4.40: Process concept for coproduct removal from the polar catalyst phase of a TMS by organic solvent nanofiltration. Solvents (A, B), catalyst (C); coproduct (CP), product (P). Adapted from [231].

for selective removal of the water and recycling of the co-permeating solvent, while providing a sufficient catalyst recovery. Skiborowski and coworkers [231] concluded that process development for TMSs should also consider additional separation steps such as membrane separations or distillation, especially when solvents are selected, as they do not only influence the reaction and phase separation but also subsequent downstream processing and the total energy consumption.

To prove the feasibility of coproduct separation by OSN for the hydroaminomethylation in a TMS, Skiborowski, Vogt, and coworkers [236] experimentally investigated a continuous process incorporating the reaction, the decantation step, and the OSN membrane separation. The reaction conditions and the TMS were adapted from Vogt and coworkers [39]. Due to the different catalyst complex that was used, a different membrane was selected, compared to the previous work of Skiborowski's group [231]. The membrane selection was based on a thorough screening of several membranes and included membrane experiments with the actual catalyst phase from previous miniplant experiments. The selected membrane, the AMS NanoPro S-3012, showed very high catalyst rejection (>99%) while also enriching water in the permeate stream. Finally, the membrane separation was implemented in a continuous setup (Figure 4.41).

While the reaction performance was similar to the process without membrane separation [39], water accumulation reduced significantly (Figure 4.42). However, due to the direct coupling of membrane separation, decantation, and reaction, the

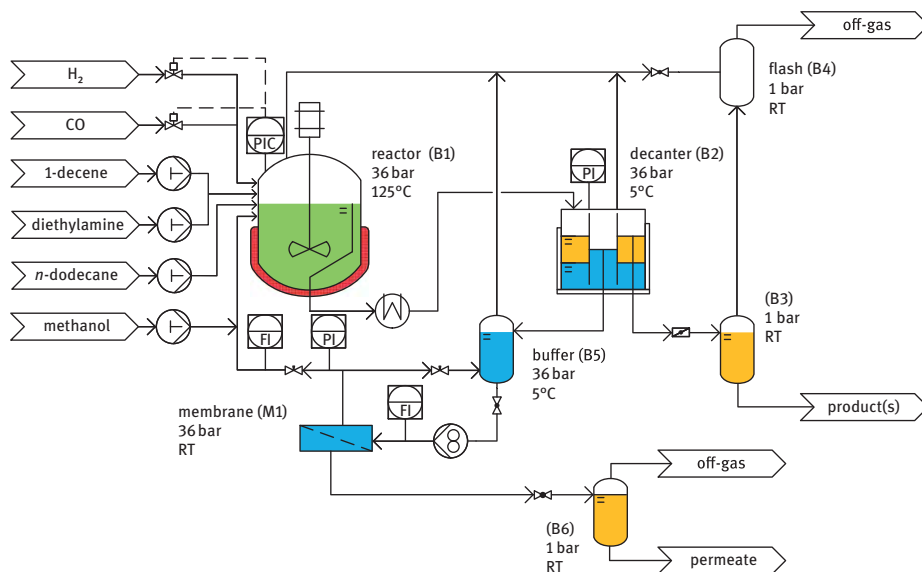


Figure 4.41: Process flow diagram for the hydroaminomethylation of 1-decene with diethylamine using a TMS for catalyst separation and organic solvent nanofiltration for coproduct separation. Adapted from [236].

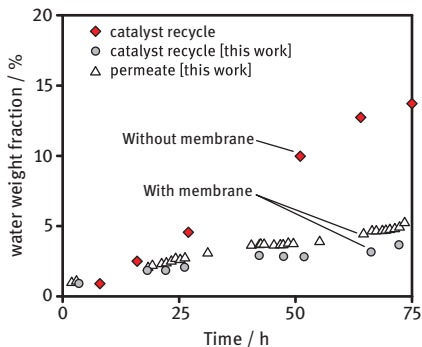


Figure 4.42: Weight fraction of water in the catalyst recycle stream during the hydroaminomethylation of 1-decene with diethylamine in a continuous miniplant with and without coproduct separation by OSN. Data without membrane is taken from [39]. Adapted from [236].

membrane was also in contact with the dissolved hydrogen and carbon monoxide, which led to a selective separation of carbon monoxide that necessitated a different feed gas ratio to the reactor. As the effect of dissolved gases in liquid phase membrane separation processes has received little attention in literature so far, the influence of the gas loss through the membrane on process performance and a more detailed investigation of the gas influence on OSN separations are still under investigation.

4.1.5 Summary and Outlook

As demonstrated by the results in Figure 4.29, a large number of successful examples exist, showing the suitability of TMSs in the context of homogeneous catalysis. Herein, three major objectives pursued by the researchers were identified: (1) separation of catalyst and product; (2) recycling of the separated catalyst; and (3) realization of continuously operated reaction, separation, and recycling.

In most of the presented results, the successful separation of catalyst and product was achieved; however, the recycling of the separated catalyst species was tackled and accomplished in only a small number of reports. Thereafter, only a few continuous processes were presented in the literature. The combination of thermodynamic fundamentals and homogeneous catalysis is a decisive, but mandatory, part for feasible reaction/separation combinations. So far, no industrial applications of TMSs are known.

As demonstrated in Figure 4.43, reports on TMSs in the context of homogeneous catalysis are available at different lower technology readiness levels (TRLs 1–5) [64, 224]. Most of the examples rather represent TRLs 1–2, whereas only a minor amount can be attributed to TRLs 4–5. Within TRL 5, the application of a TMS, compared with an industrially established process, is consequently the next step in TMS technology development. The construction of a pilot plant (TRL 6) that demonstrates large-scale operability would be a further step. Among the available data, a huge variety of indicators are presented, which can be used to calculate comparable data. In our opinion, it would be highly beneficial to have comparable data available in the literature with the aim of developing applications at higher TRLs, and therefore, pushing their application in the industry forward. Suggestions for common key indicators, which represent the reaction performance, on one hand, and separation efficiency, on the other hand, are summarized in Section 2.4.

We identified TMSs to be highly promising and outperform conventional catalyst recovery strategies if the following properties are met:

- 1) temperature dependency of the miscibility gap is as high as possible, in order to switch from a homogeneous reaction to biphasic separation with low energy consumption;
- 2) elimination of the liquid–liquid interface enables the unification of practical immiscible substrates in a homogeneous reaction mixture, and
- 3) only a single solvent is necessary to homogenize the catalyst and substrate, and preferentially a pure product phase forms upon cooling; thus, additional separation units for product purification and solvent recovery are dispensable.

In addition to highly promising features, the following inherent limitations of TMSs can be identified:

- 1) only single-stage separation is possible, which might lead to lower separation efficiency, relative to, for example, multistage extraction;

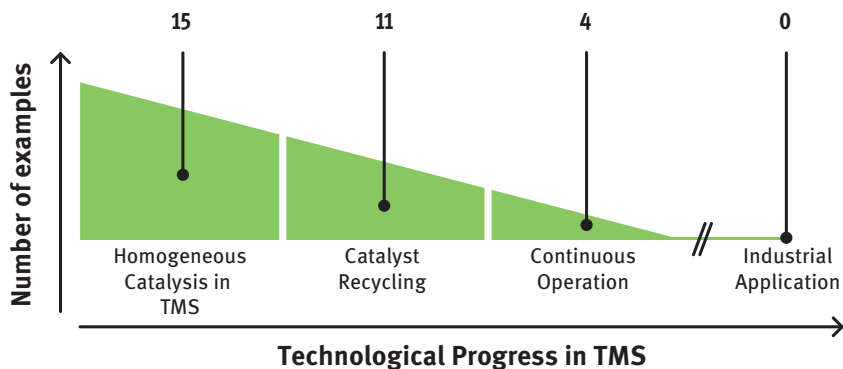


Figure 4.43: Technological progress in TMSs, as represented by the number of contributions reported in the literature [38].

- 2) limitations in substrate concentration need to be considered to maintain the TMS properties (temperature dependency of miscibility gap);
- 3) the molecular properties of substrate and product, particularly polarity, can differ considerably; hence, different LLEs before, during, and after the reaction may have a significant impact on the catalyst performance and/or its separation; and
- 4) from all known solvents, only a limited number of feasible solvent combinations exist that have a proper miscibility gap to form a TMS.

To apply promising features and overcome challenges, we identified certain gaps to pave the way toward industrial application. A harmonized database, including comprehensive TMS-data, should be accessible. These data and improved thermodynamic modeling of multicomponent LLE data would lead to reliable and predictable identification of TMSs, and, therefore, improve research into homogeneous catalysis. To estimate the suitability of TMSs in homogeneous catalysis, the phase behavior of all different mixtures potentially occurring during the reaction would be beneficial.

Additionally, challenges that affect TMSs in particular need to be tackled to overcome limitations. For optimization in catalyst utilization, precise differentiation between catalyst leaching throughout the catalyst-containing compartment and catalyst deactivation is mandatory. For TMS application in industry, larger demonstration processes and longer periods of operation than those presented in the literature are necessary, to overcome basic findings in batch operation in the lab (TRL 4) and feasibility under “real” continuous conditions (TRLs 6–9). Relevant data, in which the accumulation of certain compounds formed through side reactions, substrate impurities, or catalyst deactivation are presented, support the implementation of industrial TMS processes. In terms of developing catalyst recovery strategies, and therefore, proper

benchmarking, we suggest applying well-known homogeneously catalyzed reactions to find new TMSs and to use well-known TMSs to design catalyst recovery strategies for novel catalysis approaches.

As demonstrated herein, this tool for the recovery of transition-metal catalysts through switchable solvent mixtures is highly promising for the design of chemical production processes in the future. Beyond the presented work, the application of greener solvents will lead to sustainable chemistry. Also, the combination with other catalyst recovery approaches is highly promising because the inherent single-stage separation issue of TMSs will be overcome in that way. The first approaches in which TMSs were combined with other unit operations such as OSN were presented in Sections 4.1.3 and 4.1.4. We are also looking forward to reading about innovative approaches for TMSs apart from catalyst recovery.

4.2 Microemulsion Systems

Markus Illner, Ariane Weber, Lena Hohl, Marc Petzold, Nona Afraz,
Kristin Hecht, Lutz Böhm, Anja Drews, Jens-Uwe Repke, Reinhard Schomäcker

Microemulsions as multiphase media provide superior features for process application and utilization of sustainable resources such as long-chained unsaturated hydrocarbon starting materials. By designing suitable MESs and exploiting their switching functionality it is possible to overcome the two predominant contradicting design criteria for reaction media: perfect miscibility for high reaction rates and perfect separability for product extraction and recycling of additives.

This section hence provides an overview of the general concept of applying MES for homogeneous catalysis in continuously operating processes. Relevant steps for process development are outlined starting with the systematic design of microemulsions and choice of additives. Next, fundamental deliberations on mass transfer and coalescence behavior are given and merged into frameworks for the rigorous analysis of the phase separation behavior, as well as the augmentation of kinetic models to capture influences of the solvent system on the reaction kinetics. The main goal therein is to translate the inherent complexity of MES into easy to adapt workflows and decision guidelines, whose application yield a minimum of required physicochemical information on the MES for process development. This includes the identification of major challenges for process application regarding continuously operating systems by a minimum of systematically applied experimental studies. Based on this, the tailored development of solution approaches regarding process design and operation is possible.

This approach is outlined for a case study on the hydroformylation of 1-dodecene in MES and evaluated using long-term operation data from a technical miniplant system. The technical realization is assisted by strategies for advanced process analytics,

improved design of phase separation equipment, and the development of model-based soft sensors for relevant immeasurable process variables.

General Process Concept

The use of microemulsion reaction media aims at realizing switching functionalities regarding their solubility, internal mass transfer properties, and phase behavior for enabling efficient reaction performance and facilitated product separation and catalyst recycling. Focusing on process applications using homogeneous catalysis, this is obtained by immobilizing valuable organometallic catalysts in an aqueous phase. Polar ligands, such as TPPTS or SULFOXANTHOS [84], are used to modify the catalyst and provide water solubility. The resulting miscibility gap between aqueous catalyst solution and nonpolar substrates is then encountered by the addition of suitable surfactants, which cause the formation of a microemulsion [265]. Hence, a macroscopically homogeneous reaction mixture is obtained enabling a large interfacial area and high reaction rates (Section 2.2.2) using a reactor unit, as shown in Figure 4.44. For the separation of the reaction mixture, the specific temperature-dependent phase separation behavior of microemulsions can be exploited. After temperature adjustment, highly pure nonpolar phases containing reaction educts and products can be obtained using a gravity settler, while surfactant, catalysts, and additives can be recycled back to the reactor. Hence, the general process concept for reactive processes based on MES is represented by a mixer–settler system with internal recycles (Figure 4.44). Although high purity oil phase streams are obtained, the surfactant concentration is at least the CMC (Section 2.2.2.1) and could cause minor catalyst leaching. Hence, the process concept is augmented by a membrane separation for oil phase purification. Organophilic solvent nanofiltration and micellar-enhanced ultrafiltration are additional options to recover and recycle traces of surfactant and emulsified catalyst solution from the oil phase.

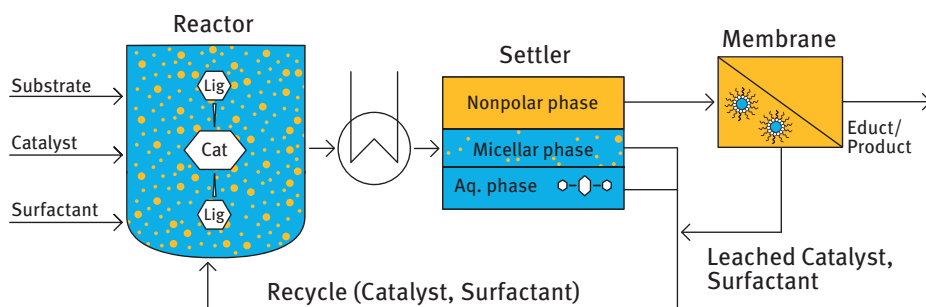


Figure 4.44: Concept for continuous processes using homogeneous catalysis in microemulsions.

The realization of such a process concept requires sufficient understanding of the considered MES including inherent phenomena and challenges. Thus, knowledge on the desired reaction with its kinetics (reactor), the specific phase separation behavior and dynamics (settler), as well as the interaction of both (recycle) and the potential need for further purification is to be collected. Despite extensive studies [134, 136, 137] on the thermodynamic properties of MES suitable modeling approaches or heuristics for process synthesis are scarce, as only equilibrium state calculations, partially applicable for ternary systems are available [80]. This is even complicated by ongoing chemical reactions, which constantly alter the chemical matrix of the microemulsion. Several additional influences on emulsion configuration and equilibrium states hence take action. As a consequence, industrial applications of MES for organic reactions are still very limited [237], and a significant deficiency of methodologies on how to realize such systems can be stated.

To overcome this situation, several systematic guidelines are presented in the following aiming at an early-stage proof of concept. The main idea is to break down the complexity of MESs as reaction media to a minimum number of required experimental studies, which provide sufficient information for process design and operation. It is hence not necessary to understand emulsion configurations, separation dynamics, and reaction routes on the micro-scale, but on the meso-scale or at the plant level. Key aspects are then:

- Phase separation behavior and dynamics concerning relevant influences present in process application
- Reaction performance and influence of microemulsion state on mass transfer and selectivity
- Identification and tracking of feasible operation regions (measurability)
- Requirements on design for reaction and separation steps
- Operability of a continuous process with internal recycles, process dynamics

When to Apply MES: Chemical Compatibility

For a successful implementation of a homogeneously catalyzed reaction in an MES, it must be ensured that all substrates and gases are chemically resistant to water and no additional side reactions occur. Special attention must be paid to the catalyst stability. High temperatures, especially for a long time, lead to the decomposition of the catalyst complex. This can be intensified using solvents. For example, water as a solvent is well known to cause catalyst deactivation or decomposition [54]. To increase the stability of a homogeneous catalyst system, the use of bidentate ligands such as Xantphos (X) or SULFOXANTPHOS (SX) should be preferred instead of using monodentate ligands like TPP or TPPTS [90] (Section 1.3). Another benefit of bidentate ligands is the enormous increase in regioselectivity.

4.2.1 Phase System Characterization and Systematic Analysis of MES for the Selected Reaction

As already described in Section 2.2.2, an MES may consist of up to three immiscible phases for a given composition [135]. When adding a gas, four distinct phases may be present. Mass transfer in MES, therefore, depends upon the distribution of each phase and the interaction among the distinct phases. In a stirred tank, the presence of a third liquid phase leads to the formation of two dispersed drop populations that are relevant for both liquid–liquid and gas–liquid mass transfer. Composition and temperature then also greatly affect phase state, interfacial tensions, phase volume fractions, interfacial rigidity, dispersion type, drop sizes, and interfacial area [108].

If homogeneous catalysis is performed in such a system, knowledge of the localization of the catalyst complex during reaction and separation is necessary for successful process operation. The distribution of the catalyst complex depends on the amount and hydrophobicity of the surfactant and the chemical structure of the catalyst complex [211]. As mentioned in Section 2.2, the reaction takes place at the interface and so the local concentrations of substrates, gases, and catalysts determine the reaction performance.

Each of these factors and the additional formation of (by-)products, in turn, influence the dispersion of a given phase [110] and its interaction with surrounding phases of the gas phase, which must be considered in elucidating the impact of surfactants on the mass transfer behavior in MESs. As a cornerstone for process development using MES the different dispersion types in MESs as well as an analysis on the impact of surfactant and phase behavior on mass transfer are outlined in the following. Based on this, systematic approaches for the development and analysis of reactive MES for process applications are presented. Their overarching aim is to identify all relevant effects and influences regarding phase behavior and the interaction of phase configuration and reaction performance by a minimum set of experimental studies. This can then be used for process design and the development of suitable strategies for process operation.

4.2.1.1 Dispersion Types in Micellar Multiphase Systems

The phase behavior described in Section 2.2 and Section 3.1.3 and especially the influence of the process parameters temperature and composition are important for a fundamental understanding of mass transfer phenomena and reactions taking place in MES. As one example, the temperature influence on phase behavior and dispersion type is depicted in Figure 4.45(a). At temperatures below $T = 88$ °C, a two-phase system with an o/w emulsion occurs, as determined via conductivity measurements and endoscope image analysis [108]. The electrical conductivity is near zero in the organic phase whereas high values can be measured in the aqueous

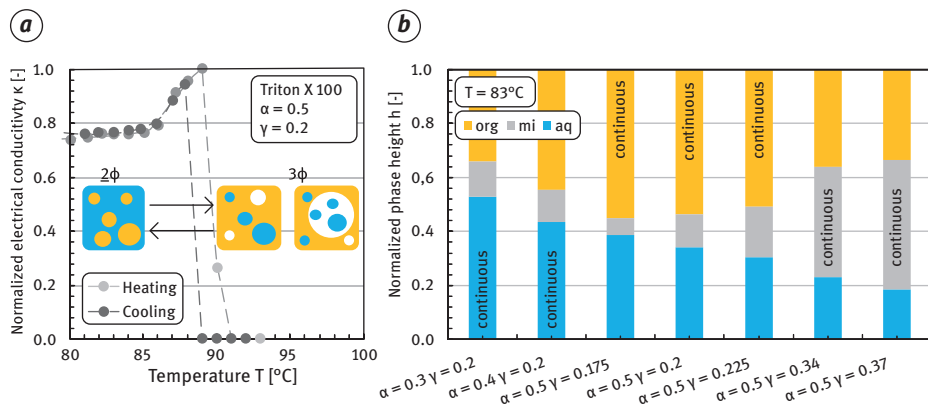


Figure 4.45: (a) Normalized conductivity measurements and dispersion type at the transition from two-phase to three-phase conditions over temperature in agitated systems with constant energy input (water, 1-dodecene, Triton X-100). (b) Phase volume fractions at a specific temperature in three-phase systems and resulting continuous phase (water, 1-dodecene, C_4E_2) [108].

phase. Due to the transition to three-phase conditions and corresponding change of phase volume fractions and surfactant solubility [136, 289], the organic phase becomes continuous at higher temperatures. Hence, an emulsion is formed where the aqueous and microemulsion phases are dispersed. Several hysteresis effects have been observed when the temperature was varied in agitated systems, as shown by the difference in conductivity during heating and cooling, which indicates a shift of the transition point from organic to aqueous continuous phase. While the dispersion types are usually obvious in two-phase conditions, the three-phase state leads to several new aspects that need to be considered. Which phase becomes the continuous phase at a certain temperature in three-phase conditions mainly depends on the phase volume fractions and composition as shown in Figure 4.45(b). At low water/oil ratios α , the aqueous phase is continuous, whereas the organic phase becomes continuous with rising oil content. Higher mass fractions of surfactant γ on the other hand lead to a larger microemulsion middle phase, which can also become the continuous phase. It should be noted, however, that also other aspects such as the positioning of the dispersion device (stirrer) within the reactor may affect the emulsion type.

In all cases, the two dispersed phases form two distinct drop populations which can interact with each other. In Figure 4.46 possible dispersion types occurring in micellar three-phase systems are summarized [109]. If one of the excess phases (aqueous or organic) is continuous, the two dispersed phases can interact by forming multiple emulsions, where the respective dispersed excess phase droplets are embedded in larger microemulsion droplets. Which state is formed, thereby, also depends on phase volume fractions and interfacial tensions. If one of the dispersed phases is clear and one turbid, the phases can be distinguished optically, as depicted

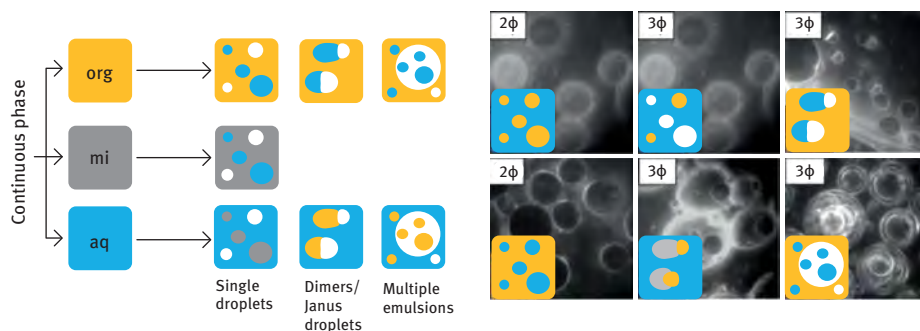


Figure 4.46: Summary of possible dispersion types in three-phase conditions (left) and corresponding appearance of drops determined via endoscope technique (right) [108].

in some of the example endoscope images. Further characteristics of multiple emulsions, such as number distribution of droplets per droplet or ratio of single-to-multiple emulsion droplets, are also a function of dispersion intensity, as shown by Hohl and Kraume [110].

4.2.1.2 Localization of the Catalyst Complex

The distribution of the catalyst between the individual phases depends on numerous factors like the chemical structure of the catalyst and the type of surfactant. In Figure 4.47, the schematic Rh distribution is shown. The use of a water-soluble ligand (e.g., TPPTS or SX) leads to a negligible amount of Rh in the organic phase. No catalyst can be detected in the aqueous phase when the pure Rh-precursor and the oil-soluble ligands (TPP and X) are used.

The choice of the amphiphile is also important for the localization of the catalyst complex. All determined amphiphiles showed a negligible concentration of Rh in the organic phase which is caused by the water-soluble ligand SX. The short-chained amphiphiles C_4E_1 and C_4E_2 are emulsifiers and do not form micellar structures. The distribution is caused by the partition coefficient and the polarity of each phase. In the C_4E_1 system, the aqueous phase has the highest polarity, but the middle phase is still too nonpolar to dissolve more than 34% of the catalyst. By using the amphiphile C_4E_2 , the polarity of the middle phase can be increased and about 83% of the catalyst complex is located in the middle-phase. The use of nonionic surfactants, for example, Marlipal 24-series, leads to a high Rh-amount (>96%) in the middle phase. Most of the catalyst follows the surfactant into the microemulsion phase, so it can be assumed that the catalyst has surface-active properties and adsorbs to the oil–water interface just like the nonionic surfactant, as shown in Figure 4.48. Based on this observation it can also be concluded that the reaction takes place at the interface and the local concentrations of the reactants and the catalyst complex are crucial for the reaction rate.

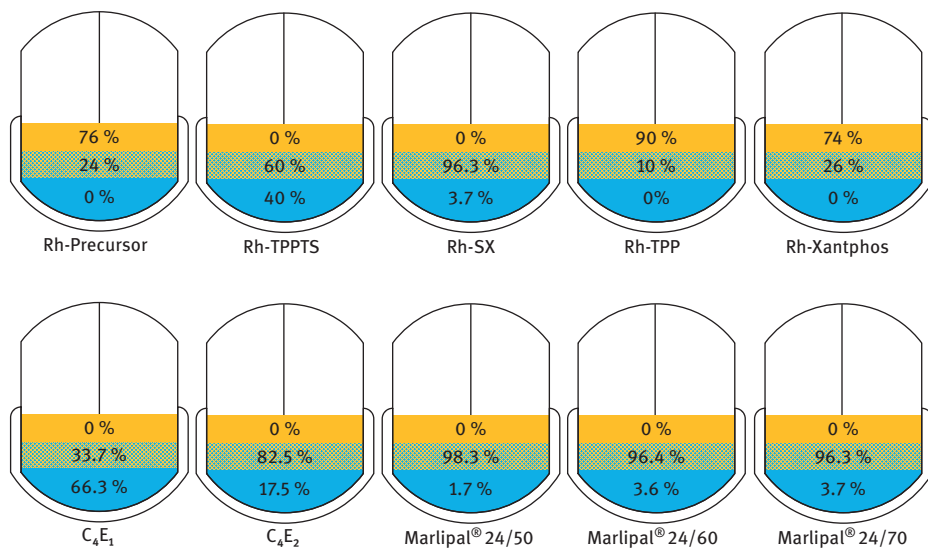


Figure 4.47: Rh distribution depending on the used surfactant and the chemical structure of the catalyst complex [212].

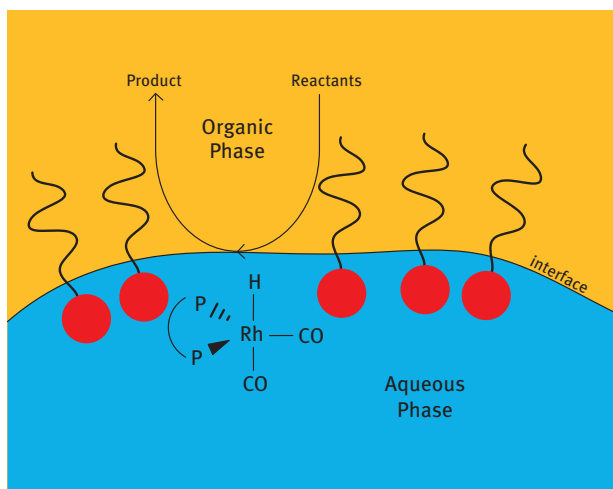


Figure 4.48: Schematic depiction of an Rh-catalyzed reaction at the interfacial area in an aqueous MES [214].

4.2.1.3 Mass Transfer in Microemulsion Systems

Mass transfer in multiphase systems is highly complex due to the number of phases and interfaces and corresponding transfer pathways. Especially in the case of the MES investigated, multiple liquid phases, each with different properties, create a

complex system of interacting phases that influence the mass transfer. Apart from phase behavior and dispersion types, mass transfer in MES is significantly influenced by the surfactant, which can also affect reaction rates. The adsorption of surfactant at the interface typically reduces the mobility of the interface and, therewith, the rate of mass transfer. The following paragraphs describe the mass transfer between the liquid phases as well as the gas–liquid mass transfer.

Transfer Between Liquid Phases in Microemulsion Systems

Fundamental mass transfer investigations can be performed by analyzing single droplets. Since the fluid dynamics influence the mass transfer, the drop sedimentation velocity must be known. Figure 4.49 shows results from single drop rising experiments in the system water(c)/1-octanol(d) with the addition of nonionic surfactant Triton X-100 to the continuous phase. The drop sedimentation velocity is displayed as a function of time. After an initial acceleration, the drop velocity passes through a maximum and decreases as the surfactants adsorb at the interface until the drops reach a terminal velocity.

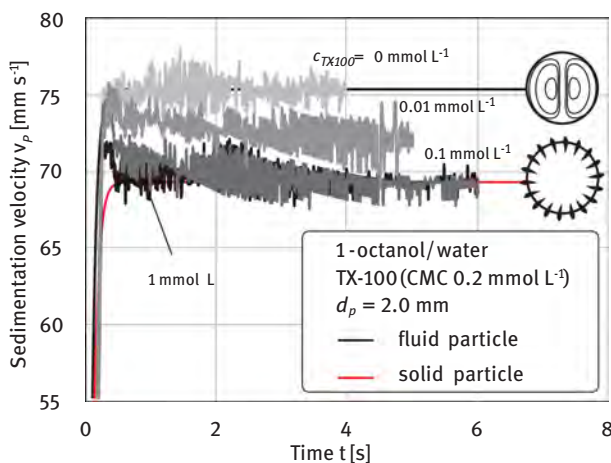


Figure 4.49: Drop sedimentation velocity of water/octanol with Triton X-100 from Paul et al. [201]. Theoretical velocities of fluid particles from Feng and Michaelides [70] and solid particles from Martin [178].

For the surfactant-free system, the terminal velocity matches the theoretical value of the fluid particle. With higher surfactant concentrations, the terminal velocity decreases to the velocity of the solid particle for surfactant concentrations of 0.1 mmol L^{-1} and higher, when no internal circulation is induced anymore. The behavior is similar in all adsorption-dominated systems. The same trend can be seen for example for water(c)/toluene(d) systems with SDS [284].

The mass transfer in these adsorption-dominated systems is reduced with increasing surfactant concentrations through reduced mobility of the interface and the change in fluid dynamics. The effect is accompanied by an additional mass transfer resistance because of steric hindrance of the adsorbed molecules and is often referred to as physico-chemical effect. This effect can be seen in Figure 4.50, where the dimensionless concentration is displayed against the contact time during sedimentation for the system water(c)/1-octanol(d). According to the definition of the dimensionless concentration c^* , an increase in concentration inside the drop is reflected by a decrease of c^* . For the mass transfer of the color-dye tracer pyridine-2-azo-dimethylaniline (PADA) from the continuous to the disperse phase ($c \rightarrow d$), with the main transfer resistance in the continuous phase, the concentration inside the drop increases as the drop rises.

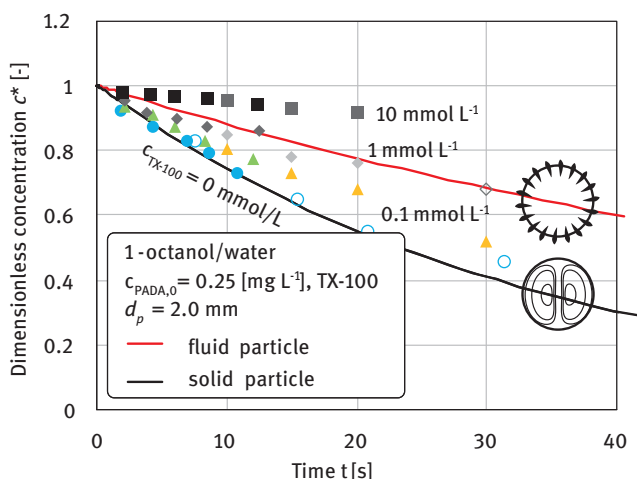


Figure 4.50: PADA concentration for different contact times of rising drops of octanol in water [197].

The surfactant-free system behaves as predicted by theory for fluid drops and shows the strongest rise in PADA concentration. As the surfactant concentration increases, the transferred tracer concentration is reduced and reaches the transfer rate of solid particles for 1 mmol L^{-1} . For higher surfactant concentrations an even further decrease in mass transfer below the limiting case of the solid particle was measured. Atomic force microscopy revealed that the rigidity of the interface increased for surfactant concentrations above the CMC, which indicates the formation of a new interface. Micelles form at the interface, solubilizing nanoscopic drops of the organic phase and forming a highly viscous liquid-crystalline layer that suppresses mass transfer further. For the system water/octanol with Triton X-100 the Sherwood correlation of Clift et al. [51] can be modified with a correction factor f^* , accommodating the effect of the liquid-crystalline layer to model the mass transfer [203]:

$$\text{Sh} = f^* \cdot \frac{2}{\sqrt{\pi}} \cdot \text{Pe}^{0.5} \quad (4.1)$$

$$f^* = \frac{1}{\eta_d/\eta_c} + \frac{(\eta_d/\eta_c)^2}{\text{Re}} \cdot \exp\left(\frac{c_{\text{TX-100}} - 100}{c_{A,0} \cdot \text{Re} \cdot \eta_d/\eta_c}\right) \quad (4.2)$$

In Figure 4.51 it is also evident, that the terminal velocity and consequently the characteristic mass transfer behavior of a solid particle is already reached at low surfactant concentrations. In Figure 4.51, the terminal velocity at different surfactant concentrations is linked to the surface coverage [201]. The terminal velocity in water/1-octanol/TX-100 systems decreases to the value of the solid particle at concentrations at which the surface is barely covered by surfactants ($\sim 0.1\%$). In conclusion, the fluid dynamic and mass transfer performance are reduced strongly, before being even detectable by interfacial tension measurements. The fluid dynamic

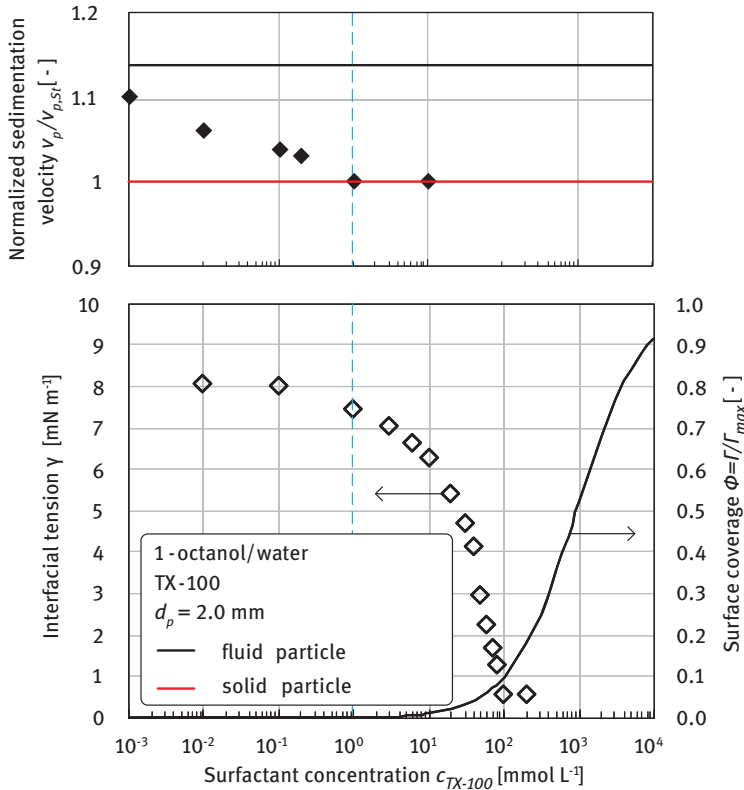


Figure 4.51: Normalized terminal velocity, interfacial tension, and surface coverage at different surfactant concentrations from Paul et al. [203]. Lines for fluid and solid particles from the correlations of Feng and Michaelides [70] and Martin [178].

determination of the terminal velocity, therefore, proves to be a sensitive tool and key experiment to predict the mass transfer performance [201].

Surfactants in the system do not always diminish the mass transfer. At the interface of a moving drop, the surfactant molecules move upstream through shear, which may lead to a pronounced accumulation at the rear end of the drop or a smooth concentration gradient along with the interface [48]. The gradient induces movement along with the interface, the so-called Marangoni effect, resulting in a turbulent flow field inside the drop and strongly enhanced mass transfer. Systems dominated by the Marangoni effect show a characteristic fluid dynamic behavior; see Wegner et al. [283] for a more detailed description. The overlapping of adsorption and the Marangoni effect is not yet fully understood and is still the subject of current research.

To verify the mass transfer behavior in surfactant adsorption-dominated systems in a droplet swarm, a mass transfer controlled reaction was employed in a stirred tank reactor using different dispersed phase volume fractions (Section 3.3.2.3). From the material balance, the effective reaction rate can be related to the overall surface area of the organic phase droplets (Figure 4.52 (left)), enabling the calculation of the mass transfer coefficient (Figure 4.52 (right)).

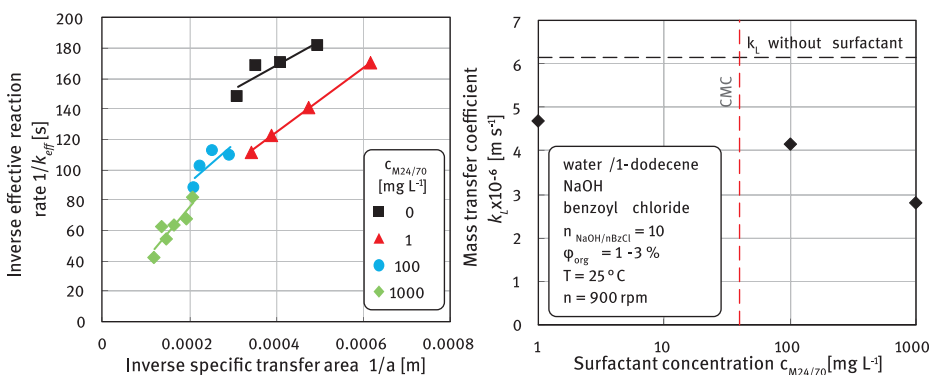


Figure 4.52: Mass transfer coefficients in a stirred tank reactor for different surfactant concentrations from Paul [197].

With increasing surfactant concentration, the transfer coefficient decreases. Above the CMC, the decline is even more drastic [197]. The results correspond to the observations from the single drop experiments. The liquid-crystalline/microemulsion structures in sedimenting drop experiments reflect Winsor I or Winsor II state in micellar emulsion systems, where two phases, one being a high surfactant-containing microemulsion, are in equilibrium. In between the upper and lower critical solution temperature (UCST, LCST), these systems enter the Winsor III state and form three liquid phases, with a bicontinuous microemulsion appearing [289]. Since single

drop experiments cannot be performed with the bicontinuous phase due to the low interfacial tension [110, 202], a modified Nitsch test cell was used instead (Section 3.3.2.2). After separation of the mixture into the three-layered liquid phases and determining their volumes optically, the tracer PADA was added to the bottom aqueous phase and its concentration was tracked over time in the aqueous and organic phase. In Figure 4.53 (left), typical concentration profiles of the tracer over time in the separate phases are displayed for the system 1-dodecene/water with the surfactant Marlipal 24/70. With a pseudo-steady-state mass transfer model of [202] and known physical properties [108], the diffusion coefficient can be calculated. The results in 1-dodecene/water systems with various types of surfactants can be seen in Figure 4.53 (right). For higher ethoxylation degrees (Marlophen NP7 ~ Marlipal 24/70 < Marlipal 24/90), the three-phase area moves to higher temperatures. The diffusion coefficients were calculated at the temperatures with the fastest separation speed between LCST and UCST. The diffusion coefficients of PADA in the bicontinuous phases were lower than in pure 1-dodecene or pure water at their respective temperatures due to the higher viscosities of the bicontinuous phases, which are inversely proportional to the diffusion coefficients according to the Stokes–Einstein equation [63]. The material systems with technical-grade surfactants showed even more complex behavior (Section 3.1.3). The viscosity rises toward the LCST and UCST in the three-phase region [108, 208] forming highly viscous layers in between the bicontinuous and aqueous respective organic phases (Figure 4.54). In the shown example, mass transfer was completely suppressed by this highly viscous phase.

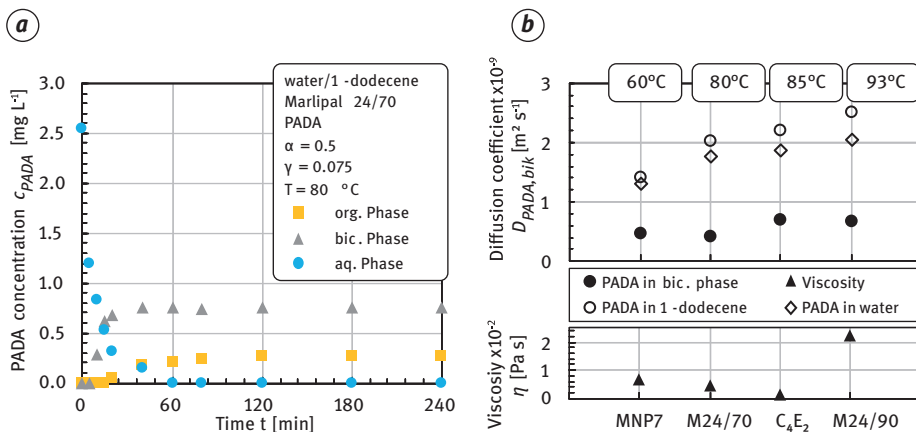


Figure 4.53: Left: Concentration of tracer PADA in the aqueous, organic, and bicontinuous liquid phases under Winsor III conditions of the system 1-dodecene/water/Marlipal 24/70. Right: Calculated diffusion coefficients in the bicontinuous phases and pure 1-dodecene and pure water. Diffusion coefficients in pure systems were calculated via the group method of Nakanishi [191] at 20 °C. Values at higher temperatures were extrapolated using the Stokes–Einstein equation [63] (unpublished).

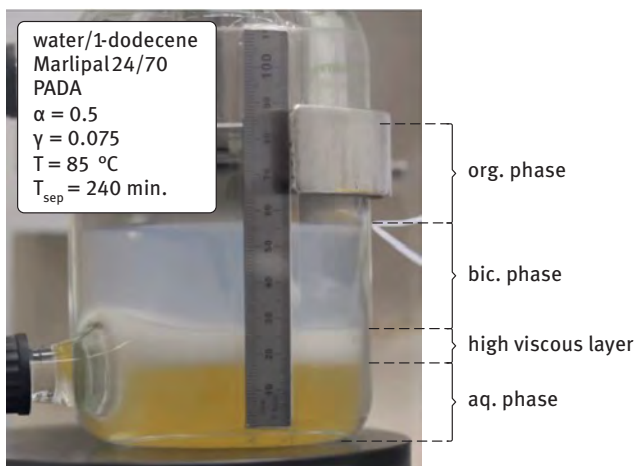


Figure 4.54: Highly viscous layer between the bicontinuous and aqueous phases at the upper critical solution temperature (UCST) in the system 1-dodecene/water with surfactant Marlipal 24/70; also see [208].

In conclusion, the addition of a nonionic surfactant to oil/water systems mostly reduces the mass transfer because of additional mass transfer resistance. Especially the transition temperatures between two- and three-phase conditions (LCST and UCST) should be avoided during the reaction since mass transfer can be limited by highly viscous layers.

Due to high surfactant concentrations, efficient reduction of interfacial tensions, and coalescence inhibition, drop sizes in MES usually are in the range of only a few micrometers if common surfactants such as Triton X-100 or the Marlipal and Marlophen series are used [108]. As can be seen from Figure 4.56 (left), Sauter mean diameters in agitated three-phase systems with water/1-dodecene/Marlipal 24–90 reach values below 50 μm even at low stirrer speeds, respectively, energy dissipation rate in the stirred tank.

Commonly used agitation speed or energy input of stirred tanks (Section 3.3.2.3) led to droplet sizes below the endoscope detection limit. At two-phase conditions, the coalescence hindrance is more effective than in three-phase conditions so *ex situ* optical microscopy could be used and revealed droplet sizes of 1–2 μm (Figure 4.55, right) [108]. Via analysis of electrical conductivity, phase volume fractions, endoscope images, and/or the analysis of phase separation behavior the type of dispersion and interfacial area available for mass transfer can be identified. Dispersion energy and the liquid–liquid interfacial area might not be a limiting factor despite the determined additional mass transfer resistance caused by surfactants if the transition temperatures (LCST and UCST) are avoided. It should be noted that other types of surfactants/amphiphiles such as C_4E_2 can lead to drop sizes up to two magnitudes

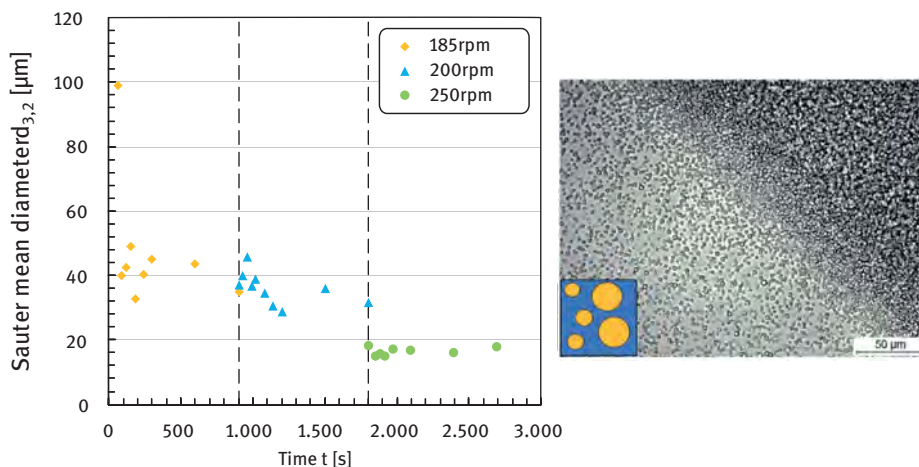


Figure 4.55: Left: Sauter mean diameters over time at different agitation speeds (water, 1-dodecene, Marlupal 24–90) in a three-phase system measured via endoscope technique. Right: Example image of a stable water/1-dodecene/Marlophen system at room temperature, taken via optical microscopy [108].

higher than the examples shown here. Agitation speed variations during reaction under otherwise identical conditions led to similar conclusions (Section 4.2.3.2). For gas–liquid mass transfer in MES, the choice of the optimal dispersion type can be used to shorten mass transfer routes.

Transfer Between Gas and Liquids in Microemulsion Systems

The gas–liquid mass transfer is affected by the phase behavior introduced in Sections 2.2 and 4.2.1.1, which is dependent on the temperature for a given mixture of a microemulsion system. A change in continuous phase also causes a change in disperse phase fraction if the present phases are volumetrically not equal, which was found to affect $k_L a$ itself (Section 3.3.4). In addition, the changing physical properties and interactions with the surfactant influence the mass transfer.

Figure 4.56 (left) displays the values of the volumetric mass transfer coefficient measured for the absorption of hydrogen in a MES comprised of 1-dodecene/water/butyldiglycole (C_4E_2) for two different surfactant concentrations. For a surfactant concentration of $\gamma = 0.2$, the rate of mass transfer is high until 79 °C, from which the volumetric mass transfer coefficient suddenly reduces by a factor of 7 before increasing again to half the value before 79 °C. At this temperature, the system changes from two practical immiscible phases to three practical immiscible phases, and the continuous phase switches from aqueous to organic. For a mixture with a higher concentration of surfactant ($\gamma = 0.34$), a similar trend can be observed as the

continuous phase changes from aqueous to bicontinuous from 81 °C on and the mass transfer rate decreases by a factor of 2. At both surfactant concentration levels, the $k_L a$ is highest with a continuous aqueous phase. However, which continuous phase yields the highest rate of mass transfer is system-specific.

The onset of the three-phase region does not always correspond to a change of the continuous phase. The volumetric mass transfer coefficient measured in the MES dodecane/water/Marlophen NP8 is shown in Figure 4.56 (right). At temperatures above 77 °C, the system separates into three liquid phases. However, the aqueous phase remains the continuous phase up to 87 °C above which the organic phase becomes continuous. The rate of mass transfer is, again, higher (more than three times) when an aqueous continuous phase is present compared to an organic continuous phase in this system.

To understand this phenomenon, the mass transfer coefficient and specific transfer area must be looked at individually. They are dependent on the properties of each phase and their interactions with each other. Properties of the pure liquids, as well as each of the three phases, are listed in Table 4.3. The surface tension was measured in a spinning drop tensiometer and the mass transfer coefficients k_L were measured in a falling film apparatus as discussed in Section 3.3.3.3. The addition of surfactant is seen to increase the mass transfer coefficient measured in both the aqueous and organic phases. The increase in the organic phase is much higher. Mass transport through the bicontinuous phase was much slower than in the other phases due to its high viscosity. Although the mass transfer coefficient in the organic phase was much higher than in the aqueous phase, the effect did not translate to the stirred system (Figure 4.56 (right)).

An explanation can be found when looking at the bubble size distributions in the stirred system. The bubble sizes were recorded using the optical endoscope measurements (Section 3.3) and shown in Figure 4.57(a) at 90 °C and in Figure 4.57 (b) at 84 °C. The bubbles were identified using a convolutional neural network algorithm. An example can be seen in Figure 4.57(c), where detected objects are highlighted in green. The resulting cumulative volume distribution is displayed in Figure 4.57(d).

The bubble sizes in the microemulsion system are significantly smaller at 84 °C when the aqueous phase is continuous than at 90 °C with an organic continuous phase. Although the interfacial tensions of the aqueous and organic phase are similar (the aqueous phase of the Winsor III state is in excess and contains amounts of surfactant in the range of the CMC [135]), the higher density and lower viscosity of the aqueous phase cause smaller bubble sizes, as predicted by correlations derived in terms of dimensionless groups [107, 187]. Smaller bubbles rise more slowly, which could imply a larger gas holdup and, therefore, a strongly enlarged overall specific transfer area, which would explain the higher $k_L a$ if an aqueous phase forms the continuous phase in any MES.

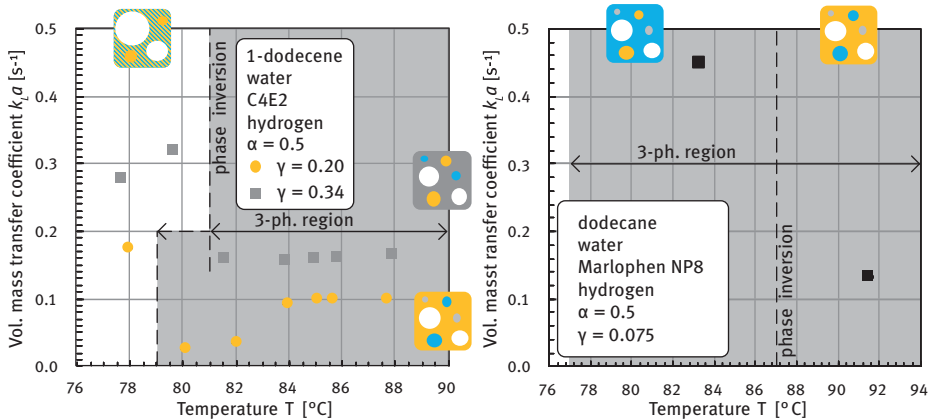


Figure 4.56: Left: Volumetric mass transfer coefficient at different temperatures for the system 1-dodecene/water/C₄E₂ for two surfactant concentrations. Right: volumetric mass transfer coefficient for the system dodecane/water/Marlophen NP8. The colors in the diagram represent yellow = organic phase, blue = aqueous phase, gray = bicontinuous phase, white = gas phase, blue/yellow stripes = aqueous phase microemulsion (unpublished).

Table 4.3: Properties of the pure liquids and the individual phases for the microemulsion system water/*n*-dodecane/Marlophen NP8 ($\alpha = 0.5$, $\gamma = 0.075$) at 90 °C.

Liquid	Density (kg m ⁻³)	Viscosity (mPa s)	Surface tension (mN m ⁻¹)	H ₂ solubility (Pa mol m ⁻³)	Mass transfer coeff. k_L (x10 ⁻⁴ m s ⁻¹)
<i>n</i> -dodecane	697.43 ^a	0.5686 ^b	19.16 ^c	30,212	2.6
Water	965.61 ^d	0.3217 ^d	60.82 ^e	174,848 ^f	1.0
Aqueous phase	964.84	0.2730	20.89	230,517	1.5
Organic phase	697.82	0.5854	21.73	38,886	5.9
Bicontinuous phase	906.78	8.2577	21.75	25,044	0.26

Surface tension was measured against air. ^a[162]; ^b[151]; ^c[122]; ^d[215]; ^e[269]; ^f[228].

In conclusion, the effect of the bubble interfacial area dominated the effect of the mass transfer in the phases themselves. Thus, the highest rate of mass transfer in microemulsion systems is not obtained if the continuous phase has the highest mass transfer coefficient, but rather in the system that happens to produce the smallest bubbles.

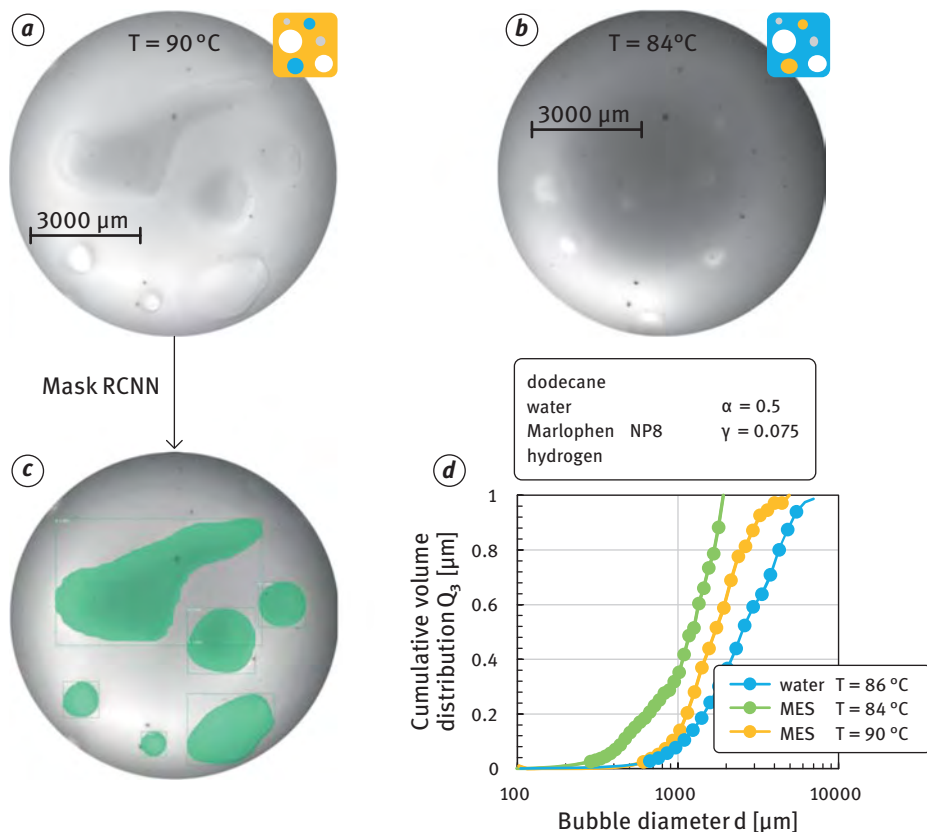


Figure 4.57: (a) and (b) Endoscope pictures of bubbles in a micellar emulsion system at 90 and 84 °C, respectively; (c) marked bubbles found by a trained convolutional neural network; (d) cumulative volume distribution of bubble sizes in water and the micellar emulsion system (water/dodecane/Marlophen NP8). The colors in the pictograms represent: yellow = organic phase, blue = aqueous phase, gray = bicontinuous phase, white = gas phase (unpublished).

4.2.1.4 Micellar-Enhanced Ultrafiltration and Organic Solvent Nanofiltration

The exploitation of microemulsion phase equilibria enables the capture oil phases with a minimum of impurities. However, traces of surfactant and thus also traces of emulsified polar substances and catalysts remain. This is connected to the CMC, which poses an attainable minimum largely depending on temperature (Section 2.2.2.2) [135]. Considering disturbances in operating a production plant, temporarily, higher surfactant concentrations ($\leq 5\text{ wt}\%$) and catalyst leaching are expected.

Hence, micellar-enhanced ultrafiltration (MEUF) of reverse micelles for catalyst recycle was investigated as an alternative or supplementary unit operation to phase separation but found not to be feasible for removal of the nonionic surfactant Marlophen NP5 from 1-dodecene. With neither hydrophobic (PTFE, PA, PES) nor

hydrophilic (PAN, TiO₂) membranes could retentions above 7% be achieved [193]. Below the CMC, irreversible adsorption of surfactant molecules on the membrane occurred which led to a strong flux decline, while above the CMC, reverse micelle formation competed with this adsorption and led to a high flux recovery. However, due to surface diffusion, surfactant or micelle retention was negligible in all cases [193]. These findings are in contrast to MEUF of reverse ionic surfactant micelles and MEUF of nonionic surfactants from aqueous streams which both resulted in reasonable performances [240].

However, organic solvent nanofiltration (OSN) was found to be a viable and robust option as in a membrane screening with four different polydimethylsiloxane (PDMS) membranes at different transmembrane pressures, temperatures, and Marlipal 24/70 mass fractions, fluxes of up to 40 L m⁻² h⁻¹ and surfactant retentions of up to 90% could be achieved (Figure 4.58). Even at high surfactant concentrations (up to 25 wt%), i.e., concentration factors, permeabilities remained in a range typical for OSN [312]. The influence of operating parameters could successfully be explained by physical phenomena such as swelling, compaction (Figure 4.58(c)) and sorption which were implemented in the modeling of fluxes J_i of 1-dodecene ($i = \text{dod}$) and surfactant ($i = \text{surf}$):

$$J_{\text{dod}} = \frac{D_{\text{dod}M} \cdot c_{\text{dod}M} \cdot V_{\text{dod}}}{R \cdot T \cdot \delta_{\text{eff}}} (\Delta p - \Delta \pi), \quad J_{\text{surf}} = \frac{D_{\text{surf}M} \cdot c_{\text{surf}M} \cdot V_{\text{surf}}}{R \cdot T \cdot \delta_{\text{eff}}} \Delta p \quad (4.3)$$

In contrast to available OSN transport models which depend on several fitting parameters, for example [58, 72], a more generally valid model which predicts the performance of several OSN membranes at different operating conditions was developed [313]. It contains only one fitting parameter in each equation: the diffusion coefficient D_{iM} through PDMS. Its obtained value was found to be in a plausible order of

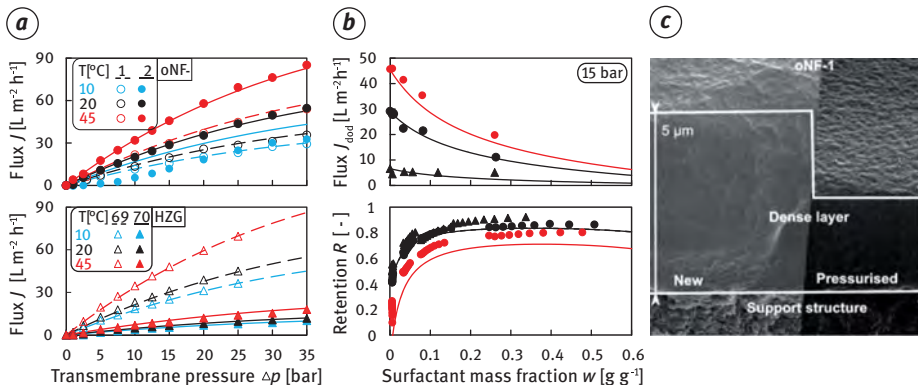


Figure 4.58: Experimental data (symbols [312]) and developed model (lines [313]) for Marlipal 24/70 removal by OSN: (a) influence of transmembrane pressure and temperature on pure 1-dodecene flux for four different PDMS membranes (cf. Section 4.3.1.6), (b) influence of surfactant mass fraction on retention and 1-dodecene flux, (c) SEM images of membrane oNF-1 before and after filtration [312].

magnitude. Other model parameters were estimated using measurements independent of filtration data. Dependencies of the diffusion coefficients and molar volume on temperature and pressure, as well as membrane compaction and different degrees of membrane swelling on contact with different surfactant concentrations, were implemented. With the diffusion coefficient fitted to filtration data of one membrane at one temperature only (oNF-2 at 20 °C, black filled circles (•) in Figure 4.58), it was possible to predict solvent flux with high accuracy for all used membranes in a range of 10–45 °C and at pressures between 15 and 35 bar. Retentions were also well predicted within experimental uncertainty [313].

4.2.1.5 Systematic Development and Analysis of Microemulsions for Process Application

To this point, major advances in understanding MESs have been made in the literature in recent years. Mass transfer phenomena regarding the application of homogeneously catalyzed reactions [89] (Section 4.2.1.3), the coalescence behavior of microemulsions [110] (Section 4.2.1.1), and influences of the emulsion on reaction performance and catalyst recycling [212] have been outlined. Despite these advances, the realization of stable operations of continuous processes using reactive MESs is still challenging. As shown by Illner et al. [120] for the hydroformylation of 1-dodecene, early-stage implementations suffer from unselective and unstable reaction performance with massive by-product formation and inoperable phase separation units. In this case, the causality between control actions, disturbances, and observed plant performance is unclear and needs to be resolved together with the complex phase behavior and high system dynamics of MES. Both are affected greatly by virtually every state variable of the system, meaning all components of the reaction mixture, formed by-products, and impurities (Section 4.2.1.1). Furthermore, strong interactions of the catalysis step and the emulsion are expected by simply looking at the coalescence behavior. This additionally complicates process operation, especially when multiple internal recycles have to be considered; see Figure 4.44.

To assist the development and successful realization of processes using MESs, this section thus discusses a holistic methodology for investigating such systems and the aligned derivation of strategies for process design and operation. Based on theoretical analyses of the system and the already shown phase system characterization a set of key experiments and systematic experimental studies is given. This way, a sufficient set of information for process development is to be obtained from a minimum of experiments. Following Figure 4.59, this systematic system analysis is ideally based on integrated lab-scale and miniplant experiments. As a prior step to this, the systematic formulation of microemulsions concerning optimized reaction performance and suitable operation regions for phase separation is discussed. The crucial steps of the process concept at hand (Figure 4.44) – homogeneously catalyzed reactions in MESs (reactor), the phase separation operation to obtain oily

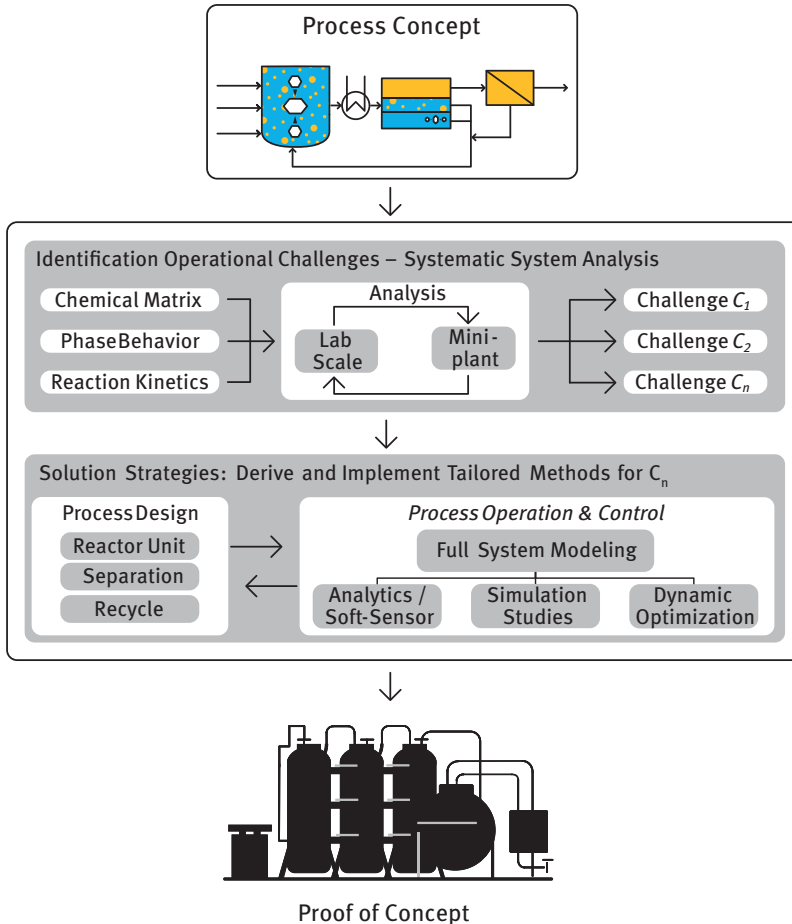


Figure 4.59: Workflow for the rigorous analysis of surfactant-based multiphase systems and derivation of process design and operation strategies [117].

products (settler), and the recycling of catalysts and additives (recycle) – are then systematically analyzed. Due to the complex nature of MES and its interaction with catalytic systems several requirements for such an analysis apply:

- Selection of microemulsion components and further additives must be the initial step. Applied substances then ideally must not change during further investigations.
- Reaction performance and phase separation behavior must be investigated considering all applied substances because significant influences are expected.
- Hence, interactions of the reaction and separation performance are also crucial.

- The analysis aims at the dynamic operation in a continuously operated plant with internal recycles. Possible disturbances like concentration shifts, mixing behavior, or accumulations of substances are possible.
- Special attention should be given to the measurability and controllability in the final application. Relevant state variables showing the significant influence on reaction performance and phase behavior should be measurable and controllable in larger plant systems.

As a major result, critical challenges C_n regarding process design and operation are identified. These enable the tailored design of solution strategies for the design of process units (reactor, settler) and process control at the second stage of the workflow. Especially for the latter, model-based methods from process systems engineering are to be considered to overcome the generally complex operation characteristics of microemulsion-based processes.

Systematic Choice of Components for MES

The most important component in an MES is the surfactant, which must be selected considering phase behavior, compatibility with the catalyst, reaction kinetics, and mass transfer properties as mentioned in Section 2.2. Not only the surfactant concentration is crucial for all these factors, but also its chemical structure. The surfactant family Marlipal 24/XX is a group of nonionic surfactants with C_{12} – C_{14} alkyl chains and certain numbers of ethoxylated groups, also called the degree of ethoxylation (EO), for example, Marlipal 24/70 has an average EO of 7. In Figure 4.60, the effect of surfactant concentration and degree of ethoxylation on the phase behavior is shown.

Higher surfactant concentrations lead to higher initial reaction rates caused by the increase of the interfacial area and a higher amount of the active catalyst species, resulting in a superposition of phenomena with different temperature dependencies. The influence of the EO is more complex and strongly dependent on the temperature. A higher degree of ethoxylation leads to a shift of the three-phase area to higher temperatures but without significant changes in the width of the three-phase region. At higher reaction temperatures, the turnover frequency (TOF) increases with increasing degree of ethoxylation but for a lower temperature at 80 °C, the TOF decreases with increasing EO of the surfactant (Figure 4.61). Therefore, the surfactants have a temperature range in which they work most efficiently [214].

In addition to the reaction performance, the subsequent phase separation is also decisive for the successful implementation of an MES. An important parameter for assessing the phase separation is, in addition to a complete separation into the corresponding phase states, the dynamics of this process. Investigations showed a fast phase separation for the three-phase area compared to the other possible two-phase states which make the three-phase area most attractive for the phase separation. Under certain conditions, there is no phase separation even after several hours for

the two-phase system, so that phase separation with the o/w MES is difficult to handle [211]. Furthermore, the addition of a lyotropic salt like sodium sulfate enhances the separation dynamics and the ionic strength of the added salt suppresses the stabilizing effects of the catalyst with its surface-active properties and the phase separation is much faster. However, too high amounts of salt lead to significantly lower reaction rates, which is due to the increasing destabilization of the microemulsion. As a result, the droplet size within the emulsion increases and the interfacial area decreases [214].

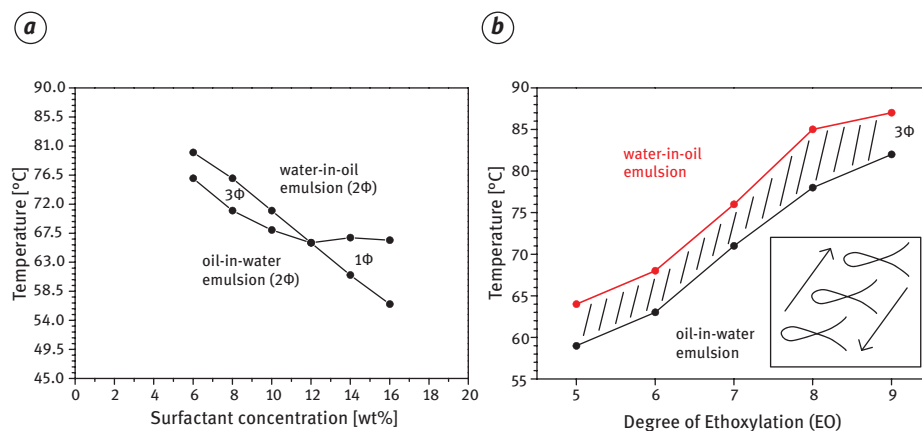


Figure 4.60: (a) Phase diagram of 1-dodecene/water/Marlipal(24/70) and (b) temperature shift of the three-phase area as a function of degree of ethoxylation with 1-dodecene/water/Marlipal (24/50 – 90) [214].

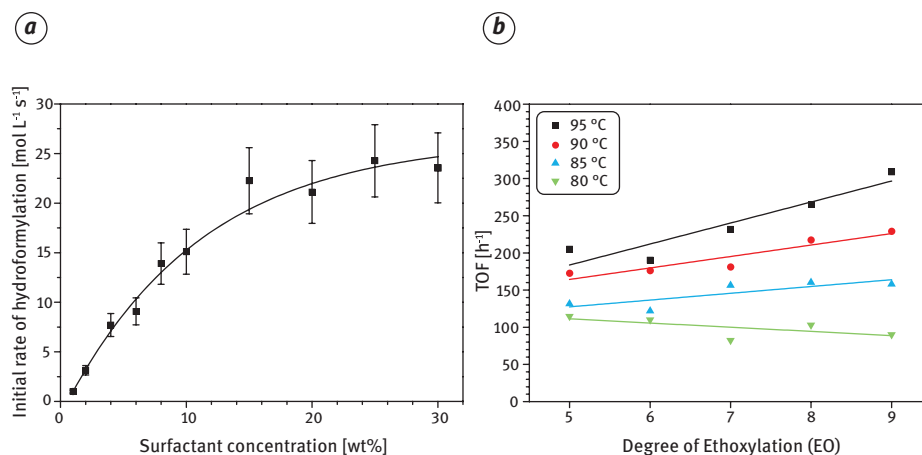


Figure 4.61: Effect of surfactant concentration and EO of surfactant on the Rh-catalyzed hydroformylation of 1-dodecene [214].

Reactions in MES – Influences on Kinetics and Adaption of Kinetic Models

To this point, methodologies for the development of detailed mechanistic kinetic models have been developed for several applications of homogeneous catalysis (Section 3.2). Therein, the combination of spectroscopic methods [37, 86] and quantum chemistry computational tools (Section 3.2.2.3; [36, 190]) enables the identification of catalyst equilibria, active compounds, and relevant reaction routes. Kinetic parameters are then typically estimated using experimental data from kinetic experiments.

However, the application of reactions in a MES requires knowledge of not only reaction kinetics but also its interaction with the phase system. Hence, a discrepancy exists between developed (micro)kinetic models and the desired application. The former usually is developed using idealized homogeneous reaction systems at given standardized reaction conditions. The latter, however, comprises additional influences on kinetics by the applied solvent system and the technological realization, such as trace compounds, side reactions, and mass transfer limitations in used reaction media. An adaption of available microkinetic models toward descriptions suitable for the desired process application is thus mandatory. This is covered by a systematic workflow presented by Pogrzeba et al. [210] and shown in Figure 4.62.

Initially, available data on the desired reaction and reaction conditions, as well as applied solvent system S_{theo} are collected in *Step 0* by reviewing literature or pre-screening experiments. Ideally, kinetic models (empirical or mechanistic) $Model_0$ already exist including kinetic parameters, yielding a suitable basis for the formulation of kinetic models. Also, physical properties and information on mass transfer are collected for the desired process application (typically a different solvent systems S_{real}). *Step 1* then tests the initial $Model_0$ for general suitability for the process application, the system S_{real} . Hence, kinetic experiments are performed using idealized laboratory conditions, which are constrained on the variation of model inputs I_0 and controls u_0 present in $Model_0$. The resulting kinetic data is used for the estimation of kinetic parameters of $Model_0$, and it is checked whether $Model_0$ is structurally suitable to describe the reaction kinetics in S_{real} concerning variations of I_0 and controls u_0 . If this can be verified, *Step 2* is used to identify additional relevant influences of S_{real} on the reaction performance. Systematic screening experiments are deployed here regarding the effect of the solvent system and required additives (co-solvents, emulsifiers, salts, buffer-systems), the catalytic system (applied ligand), and the desired technological realization (stirrer type and speed, pressure drop, recycling, and resting phases of the reaction mixture). Those influences with the highest sensitivity on the reaction performance are included in updated sets of inputs I_{real} and controls u_{real} and quantified by conducting additional kinetic experiments. This information is then used to perform a model adaption in *Step 3*. Respective rate equations of $Model_0$ are augmented with mathematical structures comprising the additional relevant influences of S_{real} and new kinetic parameters to obtain the adapted kinetic model $Model_{real}$. Next, the collected kinetic data for I_{real} and u_{real} are used to estimate all parameters of $Model_{real}$. Finally, model and parameter validity are checked with kinetic studies on variations

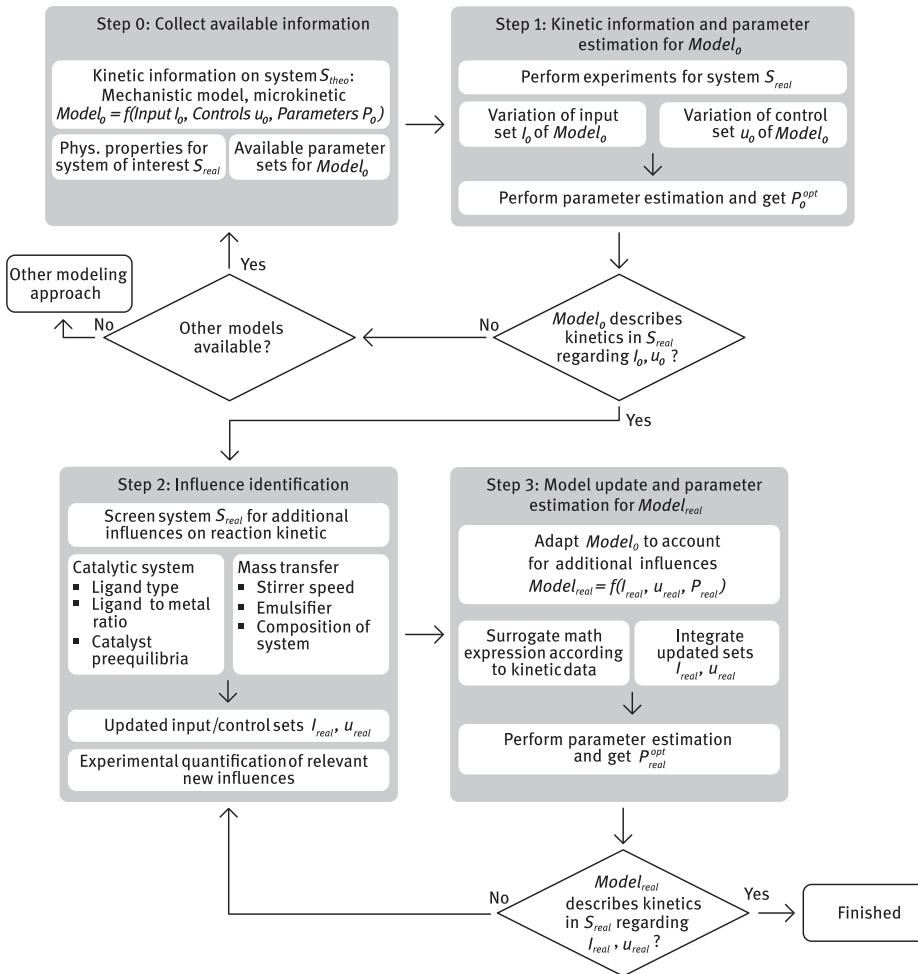


Figure 4.62: Workflow for the adaption of microkinetic or mechanistic models to describe the reaction performance for systems with inherent additional influences [210].

of I_{real} and u_{real} . If this is passed, an adapted kinetic model is obtained, which describes the reaction performance for a specified reaction system or solvent and the actual technical application. Otherwise, additional hidden effects are present and the framework is restarted at Step 2.

Phase Separation Behavior of MES – Systematic Analysis for Process Design and Operation

To capture the phase separation behavior and dynamics of MESs following the holistic workflow shown in Figure 4.59, a systematic procedure for the analysis of

surfactant-containing multiphase systems for process applications is highlighted. Key to that is the identification of *relevant* influences on the (dynamic) separation behavior based on theoretical considerations and fast prescreening experiments. Hence, a reduced set of key influences is derived, for which detailed investigations regarding the phase separation behavior and controllability are conducted. Obtained data is furthermore used to derive first designs of separation equipment and empirical models applicable for process control. Following this procedure, six successive steps are performed, while enforcing a reduction of the overall experimental effort (Figure 4.63):

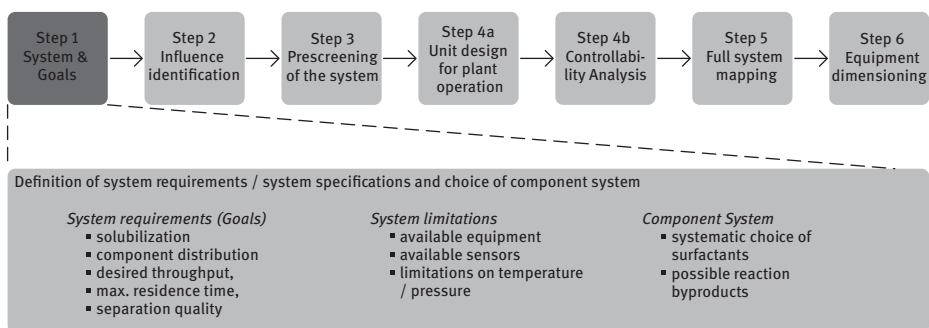


Figure 4.63: Systematic analysis of surfactant-containing multiphase systems; Step 1: system specification and goals for process operation (taken from [117], adapted and extended from Müller et al. [189]).

Step 1: As a starting point, requirements and constraints for the desired process application are defined. As already outlined, this includes the specification of the applied component system, microemulsion formulation, the catalyst system, possible products, applied gases, and possible additives. This is crucial since changes in the component system alter phase equilibria and separation dynamics significantly. After that, desired operation characteristics are specified. For the proposed mixer–settler concept, one may include efficient solubilization of reactant in the reactor and a suitable component distribution in the separated system. Finally, constraints on the desired technical application are gathered. This includes constraints on applicable pressures, temperatures, and available sensors or actuators.

Step 2: Based on theoretical considerations, possible influences on the phase behavior of MES are systematically listed and presorted for their relevance and applicable ranges of interest for process application. For multiphase systems with nonionic surfactants, deliberations in the literature [134, 136, 250] and Sections 2.2.2.1 and 3.1.3. are crucial for setting up guiding schemes and perform listings.

Step 3: Next, assorted influencing factors are qualitatively evaluated in prescreening experiments (Figure 4.64). If applicable, simplified *Shake&Wait* experiments are

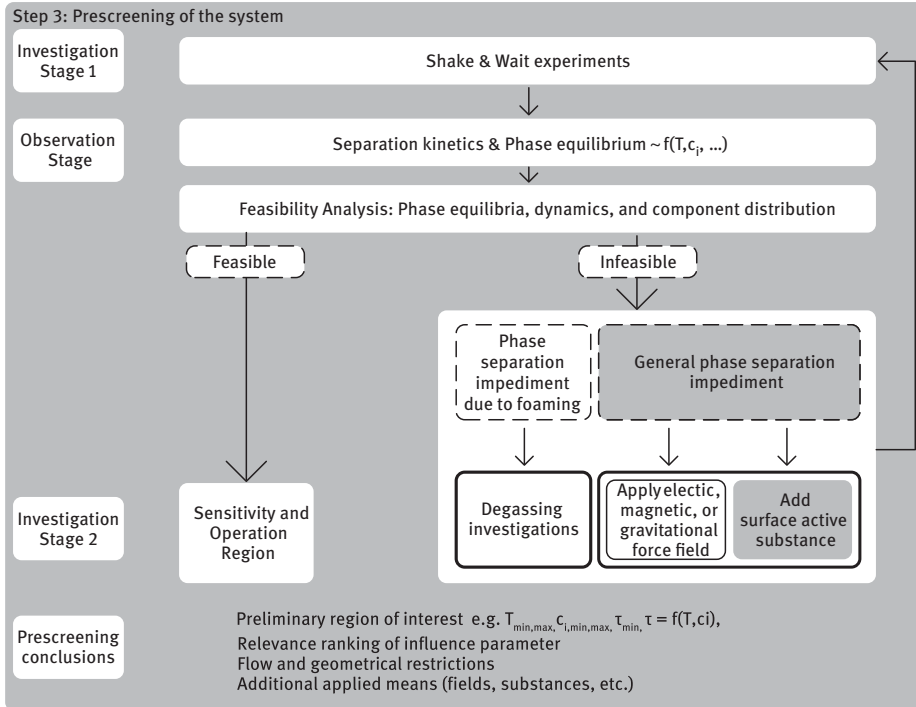


Figure 4.64: Systematic analysis of microemulsion systems; Step 3: prescreening and influence identification. Taken from Illner [117], which is an extension of Müller et al. [189].

proposed using multiple test tubes of varied compositions in thermostated baths [189]. At specified temperatures test tubes are taken from the bath, intensively shaken, returned to the bath, and observed for occurring phase separation (Investigation Stage 1). This way, the general phase separation dynamics, and occurring phase equilibria are tracked (Observation Stage 1).

A feasibility analysis is then performed on the results to identify suitable operation regions regarding dynamics (time for separation) and phase equilibria (e.g., quality of obtained oil phase) based on criteria from Step 1. If this is successful, a ranking of the sensitivity of relevant influence factors on the separation behavior, i.e., operation region and separation dynamics, as well as a specification of applicable lower and upper bounds is conducted (Investigation Stage 2 & Prescreening Conclusions). At this point, insensitive influences should be discarded for further detailed investigations to reduce the experimental effort. If the applicability of the current system is impeded by effects, such as foaming or emulsion stabilization due to components formed by ongoing chemical reactions, suitable counter measures are tested on Investigation Stage 2. If further modification of the component system or setup is required, Step 3 is restarted at Investigation Stage 1.

Step 4: To this point, suitable operation ranges, operation regions, and relevant sensitive influencing factors for the phase separation behavior have been specified. Step 4 then handles two aspects:

A preliminary separation unit design is conducted based on the obtained information. Design Stage 1 handles decisions on the type of equipment and phases to be handled. At Design Stage 2, additional equipment, such as internals to enhance phase separation or multiple heating zones, is discussed. Next, Step 4b analyses the operability and controllability of the system. Hence, identified key influencing factors are checked for measurability using available sensors or analytics of the technical system. Additionally, possible sampling rates should be evaluated with respect to the determined sensitivity of the respective influencing factor on the separation behavior. If a critical immeasurability is encountered, advanced process analytics or advanced process control methods, such as model-based soft sensing, should be checked for applicability. Furthermore, also controllability is investigated to ensure the availability of control elements for influencing factors. If this is not fulfilled, the design of the

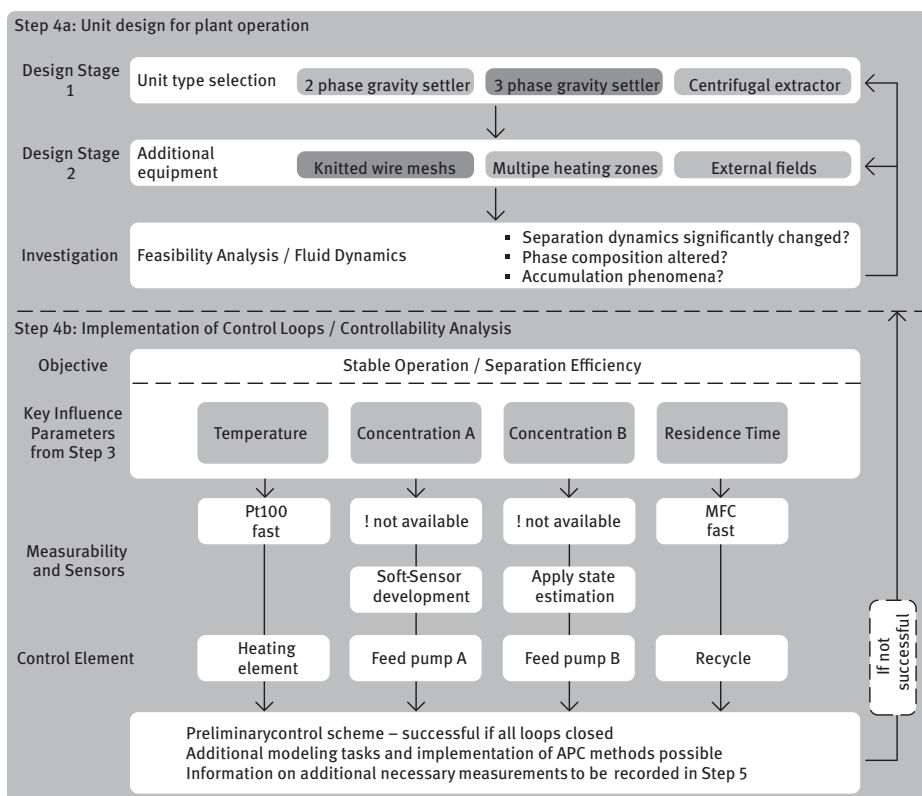


Figure 4.65: Systematic analysis of microemulsion systems; Step 4: unit design and operability analysis. Figure extended from [189] and taken from [117].

separation equipment (Design Stage 1) is to be adjusted by restarting Step 4. In general, this step yields a preliminary unit design and most important information on additional necessary measurements to quantify certain influence parameters.

Step 5: Based on the set of relevant influence parameters, data on operation regions for the separation of the multiphase system and corresponding mandatory measurements (to ensure controllability for process application) an appropriate experimental testing system can be designed, alongside an experimental plan. Hence, experimental mapping for the phase separation dynamics and states is conducted. Acquired information enables the development of empiric models for the phase separation behavior and component distribution while ensuring applicability regarding the measurability of relevant states. Furthermore, observations are used to set up design and dimensioning criteria for a detailed design of the separation equipment from **Step 6**.

4.2.2 Applications

Several reactions of interest for chemical engineering processes and the production of specialties have already been realized in MESs. Most applications aim for homogeneously catalyzed reactions using aqueous catalyst solutions. Following Table 4.4, most applications are based on kinetic experiments using (semi)-batch reactors on the lab-scale and recycling runs. Continuous operation of reaction and separation steps has been tested on the miniplant scale for the hydroformylation [119] and methoxycarbonylation [121] of 1-dodecene, resulting in successful proofs of concept.

Alkaline Hydrolysis

The alkaline hydrolysis of the methyl decanoate (Figure 4.66) in a surfactant-based system was investigated by Schomäcker and coworkers [232]. The influence of different surfactants (ionic and nonionic) on the reaction rate and the physicochemical behavior was studied. The use of surfactants improves the reaction rate of the alkaline hydrolysis in comparison with a reaction without a surfactant as a phase transfer agent. Especially the investigated cationic alkyl trimethylammonium bromide salts as surfactants enhance the reaction rate due to their electrostatic properties and behavior. Since this is a stoichiometric reaction, no metal catalyst is used and therefore catalyst recycling is unnecessary.

Hydroaminomethylation

The hydroaminomethylation (HAM) as a tandem reaction consisting of hydroformylation and reductive amination is of particularly great importance for the synthesis of long-chain amines (a general scheme is shown in Section 3.2.1). Luo and coworkers [278] described the HAM of long-chain alkenes with dimethylamine in an

Table 4.4: An overview of reactions in MES reported in the literature from laboratory-scale experiments to miniplants.

Reaction	Investigating groups	Lab scale		Continuous operation Miniplant	
		Reaction	Recycling		
Alkaline hydrolysis	Schmidt et al. [232]	✓	–	–	
Cross-coupling	Buchwald-Hartwig	Lipshutz et al. [169] and Salomé et al. [227]	✓	–	–
	Heck	Lipshutz and Taft [170] and Lipshutz et al. [169]	✓	–	–
	Negishi	Krasovskiy et al. [152] and Lipshutz et al. [169]	✓	–	–
	Sonogashira	Handa et al. [93] and Lipshutz et al. [169]	✓	✓	–
	Suzuki	Volovych et al. [270] and Handa et al. [92]	✓	✓/✓	–
Epoxidation	Colladon et al. [52]	✓	✓	–	
Hydroaminomethylation	Wang et al. [278] and Behr and Wintzer [28]	✓	–	–	
Hydroformylation	Illner et al. [120], Illner et al. [119], Pogrzeba et al. [213], Pogrzeba et al. [214], and Schwarze et al. [239]	✓	✓	✓	
Hydrogenation	Schmidt et al. [234]	✓	✓	–	
Hydroxycarbonylation	Weber et al. [282] and Schmidt et al. [235]	✓	✓	–	
Hydroxylation	Liu et al. [171]	✓	✓	–	
Olefin cross-metathesis	Lipshutz et al. [168] and Lipshutz et al. [169]	✓	✓	–	
Methoxycarbonylation*	Illner et al. [121] and Schmidt et al. [233]	✓	✓	✓	
Reductive amination	Behr et al. [29]	✓	–	–	
Reduction (enzymatic)	Orlich et al. [195]	✓	–	–	

✓ working; – not investigated; ✓/✓ depending on the reaction system; *biphasic system.

aqueous micellar system with the ionic surfactant CTAB and a water-soluble Rh/TPPTS catalyst complex. Good catalyst activity and selectivity for the tertiary amine were observed without the implementation of catalyst recycling experiments.

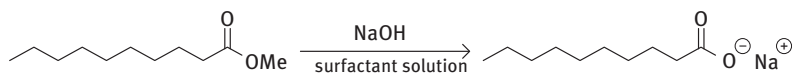


Figure 4.66: Alkaline hydrolysis of methyl decanoate with sodium hydroxide in an aqueous micellar system.

Of particular importance is the synthesis of primary amines from long-chain olefins with ammonia. The challenge here is to control the selectivity of the reaction to the primary amines. Behr and coworkers [28] investigated the hydroaminomethylation of limonene with ammonia in an aqueous micellar system (ionic surfactants) to give the desired primary amine with a yield of about 25%. Catalyst recycling would be possible due to the simple phase separation after reaction but was not carried out.

Hydroformylation

The hydroformylation of long-chain olefins in aqueous MESs was investigated by Schomäcker and coworkers [210, 214]. The reaction system can be compared with the thermomorphic solvent system from Section 4.1 with the difference that water as a solvent and a water-soluble ligand (SULFOXANTPHOS) were used and the addition of a nonionic surfactant like Marlipal 24/70 is necessary to improve the reaction rate. Batch experiments showed high conversions of the olefin and excellent linear-branched selectivities. Furthermore, recycling experiments showed the long-time stability of the catalyst complex. These results were transferred to continuous operation in cooperation with Wozny, Repke, and coworkers [119, 120]. They investigated the scale-up of this hydroformylation in a miniplant. They showed a stable operation for more than 100 residence times with a stable aldehyde yield of 21% and a low loss of catalyst (<0.1 ppm).

Hydrogenation

Schwarze and coworkers [234] described the enantioselective hydrogenation of itaconic acid (IA) and dimethyl itaconate (DMI) with an Rh/BPPM catalyst complex in an aqueous MES (Figure 4.67). The ionic surfactant SDS and the nonionic surfactant Marlophen NP8 showed good conversions of the substrates. Recycling experiments

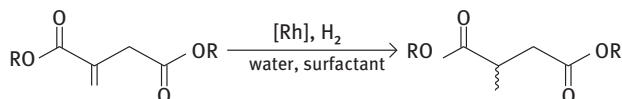


Figure 4.67: Rh-catalyzed hydrogenation of itaconic acid (R = H) or dimethyl itaconate (R = CH₃) in an aqueous micellar system.

showed a drastic catalyst deactivation after the second run for the hydrogenation of IA and a slight catalyst deactivation for the DMI.

Hydroxycarbonylation

The synthesis of fatty acids via the Pd-catalyzed hydroxycarbonylation of long-chain olefins in aqueous micellar systems was investigated by Schomäcker and coworkers (Figure 4.68). Nonionic surfactants from the Marlipal family [235] and ionic liquids (alkylmethylimidazolium bromides) as surfactants [282] were reported. Batch experiments showed good conversions for the olefin. The reaction performance of the Pd/SX catalyst complex has a strong temperature dependency so the balance between catalyst activity and stability is of great importance. Furthermore, the reaction performance can be controlled by the choice of surfactant. Recycling experiments with the ionic liquid surfactants (e.g., OMIM, octylmethylimidazolium bromide) were successfully carried out for four consecutive reactions with a stable yield of nearly 60% of the desired acid and a low catalyst leaching (<0.01 ppm Pd, <0.25 ppm P).

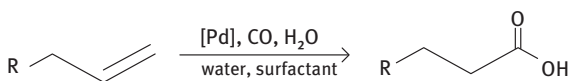


Figure 4.68: Pd-catalyzed hydroxycarbonylation of an olefin to acid in an aqueous micellar system.

Methoxycarbonylation

The same MES as described in Section 4.2.3.1 was used for the Pd-catalyzed methoxy-carbonylation of 1-dodecene, also investigated by Schomäcker and coworkers [233]. However, since methanol is required as a starting material, it turned out that the methoxycarbonylation does not require an MES for successful reaction performance. Also, the use of water as a solvent leads to a further side reaction, since the formed ester is hydrolyzed to the acid. This reaction is carried out in a two-phase system and was also transferred to a continuously operated miniplant in cooperation with Repke and coworkers [121].

Reductive Amination

Behr and coworkers [29] investigated the Rh-catalyzed reductive amination with ammonia for the synthesis of primary amines (Section 4.1.4) in an aqueous micellar system. The aqueous phase consists of the catalyst system Rh/TPPTS, the ammonia as an aqueous solution, and the ionic surfactant (quaternary ammonium salts). The aldehyde as the reactant and the desired amines are located in the oil phase. The use of ionic surfactants enhances the reaction performance, and the yield of the desired primary amine increases up to 45% but a very slow phase separation was observed.

This problem can be avoided by using Gemini surfactants like hexadeca-diylbis(dimethylammonium) bromide. The formation of a stable emulsion can be reduced, and high yields of primary amines (79%) can be obtained.

Cross-Couplings

Lipshutz and coworkers investigated several cross-coupling reactions in water under ambient conditions [92, 93, 152, 169]. To increase the reaction rates the use of ionic and nonionic surfactants as promoters was investigated with a special focus on the environmentally designer surfactant TPGS-750-M. All shown cross-couplings showed higher yields for the designer surfactant compared to cross-couplings with the first-generation surfactant PTS. Except for the Snogashira reaction, no catalyst recycling was investigated.

Schomäcker and coworkers investigated the Pd-catalyzed Suzuki coupling as part of a three-step Boscalid synthesis [270]. This coupling reaction was carried out in an aqueous MES (with nonionic surfactants) in which the hydrophilic catalyst is located in the aqueous phase and the coupling product is in the oil phase. Thus, the same principle is followed as already described in Section 2.2.2 and the catalyst can be separated and recycled. Recycling experiments showed high ligand and surfactant leaching which can be avoided by adding 30% of ligand and surfactant after each run. With this procedure, a stable yield of about 80–85% can be obtained for four consecutive runs.

Epoxidation

The Pt-catalyzed asymmetric epoxidation of terminal alkenes in an aqueous micellar system with hydrogen peroxide as oxidant was studied by Strukul and coworkers [52]. They tested different surfactant types with a wide range of the desired yield. Ionic surfactants like SDS or CTAB were not suitable for the described reaction (Figure 4.69). The screening of various nonionic surfactants showed a strong dependence on the structure and polarity of the surfactant. Good yields and enantioselectivity were obtained by using surfactants from the Triton family. Also, catalyst recycling could be carried out successfully with three consecutive runs and a stable yield and enantioselectivity.

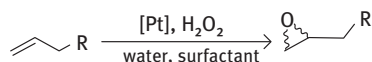


Figure 4.69: Pt-catalyzed asymmetric epoxidation of a terminal alkene with hydrogen peroxide as the oxidant in an aqueous micellar system.

Hydroxylation

The Fe-catalyzed hydroxylation of benzene with hydrogen peroxide was described by Fu and coworkers [171] (Figure 4.70). The catalyst system and the substrate benzene form the oil phase, water, and hydrogen peroxide form the aqueous phase in which the ionic surfactant sodium dodecylbenzene sulfonate (SDBS) is located. In addition to excellent conversions and selectivities (93% of phenol), an efficient catalyst recycling and recycling for unreacted benzene was realized.

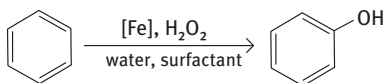


Figure 4.70: Fe-catalyzed hydroxylation of benzene to phenol with hydrogen peroxide as the oxidant in an aqueous micellar system.

Olefin Cross-Metathesis

Nonionic surfactants are also used to promote the olefin cross-metathesis in water at room temperature as is already reported by Lipshutz and coworkers [169, 170]. These vitamin E-based surfactants enhance the solubility of water-insoluble substrates in water, and high conversions and E-selectivities were observed. However, no attempts were made to recycle the Ru-catalyst system.

Enzymatic Reduction

In addition to the classic metal catalysis, biocatalysis can also take place in micellar systems. The enzymatic enantioselective reduction of ketones to alcohols was reported by Schomäcker and coworkers [195]. The water-soluble enzymes and the co-factor are located in the aqueous phase whereas the substrate and the products are located in the oil phase. The use of the nonionic surfactant Marlipal O13/60 at the described reaction conditions leads to an *o/w*-microemulsion with inverse micelles. A schematic sequence of the biocatalysis is shown in Figure 4.71.

4.2.3 Application Case Study: Hydroformylation of 1-Dodecene

The realization of microemulsions as switchable multiphase reaction media is demonstrated within a larger case study for the hydroformylation of 1-dodecene. The choice of this homogeneously catalyzed reaction and the long-chain alkene as a model substrate is motivated in Chapter 1. As relevant background information, the catalytic system and kinetic reaction network with relevant by-products are introduced in Section 3.2.

The global aim of this case study is to obtain a successful proof of concept (based on Figure 4.44) for the continuous operation of such a system in a larger miniplant system. As a fundamental basis to this, the present holistic guideline for

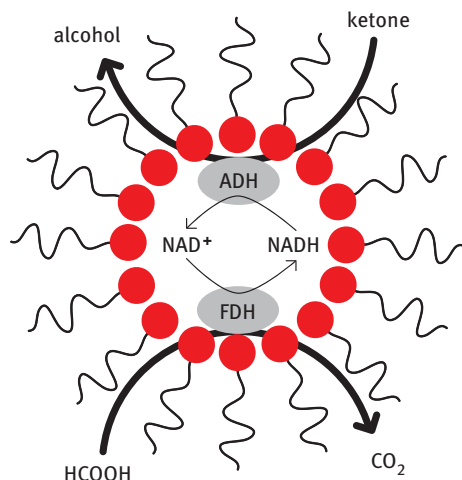


Figure 4.71: Scheme of the reaction during the enzymatic reduction of ketones to alcohols with cofactor regeneration.

system analysis, identification of crucial operational challenges is sequentially applied for the system at hand. Before this, information on applied substances, the technological realization of the miniplant system, as well as additionally implemented analytics is given. Required modification of process units of the miniplant and the development of strategies to enable process operation obtaining stable phase separation and desired reaction performance are shown. The cornerstone for the latter is a first-time model description of the three-phasic separation of MESs from which soft sensors for concentration tracking and advanced process control strategies are derived (Section 5.4.). Finally, miniplant operation results are presented to enable a proof of concept for the hydroformylation of 1-dodecene in microemulsions, while also emphasizing typical operational obstacles for MES.

4.2.3.1 Applied Substances and Miniplant Setup

Applied Substances

Applied substances are listed in Table 4.5. The aqueous catalyst solution is applied with a fixed composition of 98.96 wt% water, 6.48×10^{-2} wt% $[\text{Rh}(\text{acac})(\text{CO})_2]$, 0.98 wt% SULFOXANTPHOS throughout all experiments.

Miniplant Setup and Automation

The miniplant system is installed in a three-level housing and set up in a modular way to allow for easy reconfiguration and integration of new equipment. The total liquid hold-up of the plant's main section is 2.07 L with an additional gas hold-up of 0.90 L. According to Figure 4.72, the plant consists of three main sections, while the presented configuration is based on the setup used for hydroformylation experiments.

Table 4.5: Applied substances for lab experiments, plant operation, and analytics.

Substance	Purity	CAS no.	Supplier
1-Dodecene	≥94%	112-41-4	Merck KGaA
2-Propanol	≥99.9%	67-63-0	Carl Roth
Dodecane	≥99%	112-40-3	Merck KGaA
Marlipal [®] 24/70	–	68439-50-9	Sasol ¹
Nitrogen	≥99.8%	7727-37-9	Linde
[Rh(acac)(CO) ₂] ²	≥98%	14874-82-9	Umicore
Sodium sulfate	≥99%	7757-82-6	Carl Roth
SULFOXANTPHOS	– ³	215792-51-1	Molisa GmbH
Synthesis gas	CO 3.7	630-08-0	Linde
(CO:H ₂ 1: 1 mol%)	H ₂ 5.0	1333-74-0	Linde
Tridecanal	≥ 96% ⁴	10486-19-8	Alfa Aesar
Tridecanoic acid	≥99%	638-53-9	Sigma Aldrich
Water	Deionized	7732-18-5	–

1 Nonionic aliphatic surfactant provided as a donation from Sasol without further information on purity (technical grade).

2 Rhodium precursor (acetylacetonato)dicarbonylrhodium(I) donated by Umicore.

3 Purchased from Molisa GmbH without further information on batch quality.

4 Contains stabilizer α -tocopherol.

The **feed section** holds three 10 L feed tanks for substrate (B01), catalyst solution (B2), and surfactant (B03) as well as respective feed pumps. A maximum alkene feed of approx. 830 g h⁻¹ can be realized. The latter tank is additionally heated and stirred to ensure homogenization of the applied technical-grade surfactant. High-pressure gas containers are deployed for synthesis gas feed or individual mixtures of H₂ and CO.

For the **high-pressure section**, a stirred tank reactor of 1.5 L total and 0.6 L liquid volume, equipped with a heating jacket, stirrer (two Rushton turbines in gasing mode), and two baffles is deployed. The separation of the microemulsion is realized using a self-constructed modular settler, equipped with a tailored heating zone to avoid temperature gradients, a flow gauge glass, and multiple sensor ports for temperature, conductivity, or spectroscopic probes [117]. Three individual settler drains allow for the individual recycle of three developed phases of the emulsion back to the reactor. Both reactor and settler can be operated at pressures up to 35 bar and temperatures up to 120 °C, while individual recycle streams between 0.4 and 1.1 L h⁻¹ are applicable.

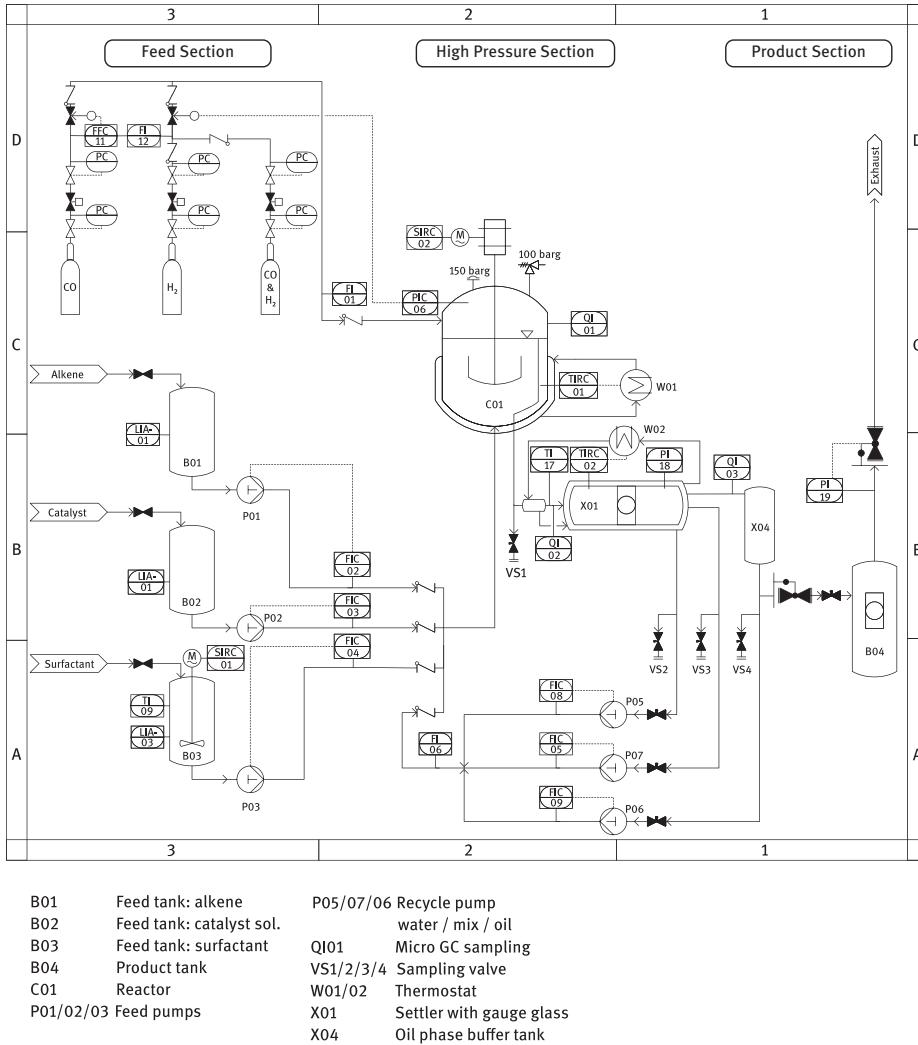


Figure 4.72: Simplified P&ID of the MES miniplant. Adapted from [117].

The **product section** then holds an intermediate buffer tank X04 for the oil phase. Using level control via a control valve, the oil phase is partially drained toward the product tank B04, enabling continuous operation of the miniplant.

The plant itself is designed and built according to ATEX Explosion Zone 2 specifications and based on detailed HAZOP analyses. Hence, all equipment used inside the plant complies with respective specifications and temperature classes for 1-dodecene and synthesis gas. The miniplant's housing is equipped with a ventilation system to avoid the accumulation of synthesis gas. The entire internal plant volume can be fully inerted with nitrogen. This is necessary since the catalyst decomposes

upon contact with oxygen and the formation of explosive mixtures of gas is to be avoided. Additionally, a vacuum pump is installed for purging gas from the system.

To enable reliable and safe operation, the miniplant is fully automated with the industrial-grade process automation controller system Siemens SIMATIC S7-400 and respective process control software Siemens SIMATIC PCS 7 V7.1. More than 40 sensors are deployed to track the plant's state, whereby generally temperature, pressure, flow rate, and level are captured. Process control is enabled using 20 actuators. High-pressure piston pumps are deployed in all major process streams, while W01 and W02 are used for temperature adjustment of reactor and settler respectively. Furthermore, control valves, stirrers, and switching valves are deployed. To track the reaction performance and obtain additional information on the plant's state, three liquid sampling positions are provided (reactor, oil/water phase recycle). Liquid samples are analyzed using gas chromatographs, while the gas phase composition of the reactor is tracked using an online GC. Additionally, a webcam with automated level detection is installed to observe the evolution of levels of liquid phases in the settler. All process data and external offline analytical data are merged on the process control system using an OPC UA server (<https://opcfoundation.org/>).

4.2.3.2 System Analysis and Operability

In this section, the systematic system analysis is performed for the given case study. Initially outlines on the choice of applied substances, respective concentration ranges, and applicable process conditions are given. The systematic influence identification for the reaction kinetics is then performed based on Figure 4.62 considering the technological realization and resulting limitations and process conditions. As the major aspect of this section, the guideline for the systematic analysis of multiphase media for process operation from Section 4.2.1.5 is applied, while critically discussing arising obstacles in the operation and control of MESs.

Formulation of MES for the Hydroformylation of 1-Dodecene

For the hydroformylation of 1-dodecene the mass fraction of oil is set to $\alpha = 0.5$, so the emulsion consists of 50 wt-% water and 50 wt-% substrate (1-dodecene), and no additional organic solvent is used. The concentration of the substrate is about 2.4 mol L^{-1} . An optimal surfactant concentration range (as defined in Section 2.2.2.1) is set to $0.06 < \gamma < 0.1$. The homogeneous catalyst is part of the aqueous phase. It contains a rhodium concentration of 2.5 mmol L^{-1} of Rh precursor. To ensure complete complexation with the ligand, 4 equivalents of the ligand should be added, which corresponds to a concentration of 0.01 mol L^{-1} .

Based on the chosen formulation of the MES and respective concentration ranges, an optimal reaction kinetic trajectory is obtained from lab-scale experiments (Figure 4.73). This marks the reference benchmark for realizations of the

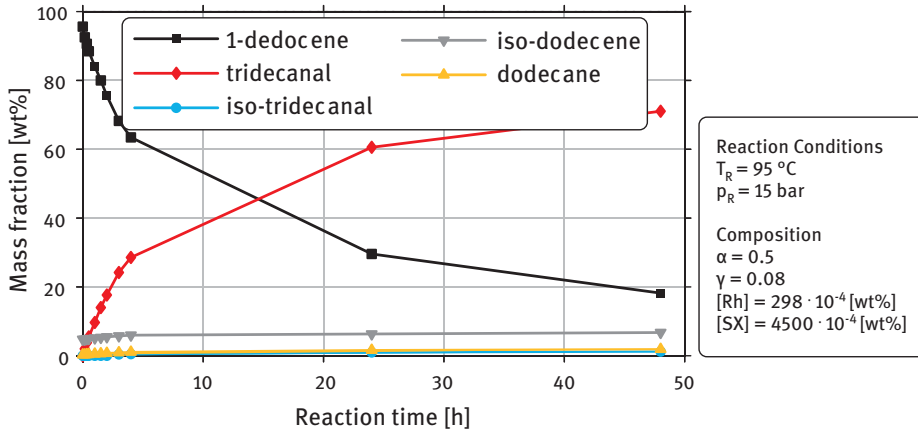


Figure 4.73: Reference kinetic trajectory for the hydroformylation of 1-dodecene. Experimental conditions: SX:Rh ratio = 4:1 with $[\text{Rh}(\text{acac})(\text{CO})_2] = 1 \times 10^{-3} \text{ mol L}^{-1}$; 2.4 mol L^{-1} 1-dodecene, 20 g water, 3.5 g Marlipal® 24/70, 1 wt% Na_2SO_4 , reaction volume = 50 mL, stirrer speed = 1,200 rpm. Maximum measurement error: $\pm 3\%$. Data generated by Tobias Pogrzeba, Technische Universität Berlin, Department of Chemistry.

reaction in the miniplant, while deviations from that especially regarding unwanted by-product formation and reduced catalyst activity can be assessed.

Reaction Performance and Influencing Factors

The transfer of the hydroformylation reaction from optimal lab-scale conditions into the miniplant requires analysis of several additional influences on the reaction performance. This is mandatory, because disturbances such as shifts in concentration of surfactant, catalyst, or substrate are prone to happen in a plant with three individual recycles. Furthermore, accumulations of substances during phase separation, as well as deficiencies in the reaction step may occur. To identify relevant influencing factors and the interaction of the MES and the reaction system, a comparison of the reaction conditions in the used laboratory-scale setup [214] and the miniplant has been conducted. Relevant influences were then tested and quantified regarding kinetic data at lab-scale to ensure reproducibility. Hence, close feedback of lab-scale investigations and pretesting in a miniplant system has been enforced. As a result of this analysis, Table 4.6 is provided, while selected results are discussed in the following. The presented experimental data are partly already published in our own contributions [210, 214].

Table 4.6: Identified influencing factors on reaction performance and interaction of reaction and MES for the miniplant system.

Influence	Affected by	Effect on reaction	Reference
Rhodium conc.	Feed, separation, and recycle operation	Available active catalyst and equilibria; reaction rates and selectivity	Figure 4.74
Ligand conc.	Feed, separation and recycle operation, decomposition	Cat. species equilibria; reaction activity and selectivity	Figure 4.74, left
Dissolved gases	System pressure, phase composition in reactor and settler	Cat. species equilibria; reaction activity and selectivity	Figure 4.75, left
Micelle structure, phase behavior	Mixture composition, temperature	None observed	Figure 4.74, right
Emulsification, interfacial area	Stirrer speed	None in the operation region	Figure 4.74
Surfactant Concentration	Feed, separation, and recycle operation, loss product stream	Reaction rates	Figure 4.75, right

Ligand Concentration

The influence of the ligand concentration is discussed by comparing the obtained reaction conversion and chemoselectivity at different ligand to rhodium ratios in the left of Figure 4.74. Interestingly, a distinct switch of the selectivity toward the target product tridecanal is visible at a ligand to metal ratio of approx. 2.3. Below this ratio, massive by-product formation (isomerization) occurs, lowering selectivity, while increasing total conversion. This behavior can be traced back to the catalytic cycle of the hydroformylation of 1-dodecene using SULFOXANTPHOS as a ligand introduced in Figure 3.46, which exhibits several catalyst pre-equilibria. Especially low ligand concentrations in the presence of CO are prone to promote the formation of the unselective unmodified Rh species (TC), featuring higher conversion but also increased formation of by-products [43]. This change in the catalytically active species is crucial for miniplant operations, as it can severely alter the reaction performance (accumulation of polar ligand in the settler's aqueous phase). Additionally, applied ligands are prone to degradation and require replenishing [73]. This is also discussed in Section 3.2 and by Gerlach et al. [81] using BIPHEPHOS in TMS, as hydroperoxides present in the substrate feed caused oxidation of the ligand. Despite high hydroperoxide amounts being present in 1-dodecene provided by Merck KGaA, this decomposition route was not observed in lab-scale

experiments nor long-term miniplant operation. Possibly, a stabilization of the ligand in the aqueous phase takes place in the case of MESs.

Emulsion State

Depending on the process conditions, several microemulsion structures are observed (Section 2.2). The type of continuous and disperse phases change dramatically and local concentrations of catalyst and substrate are prone to vary significantly. Nevertheless, the reaction performance is not affected by the present emulsion state, as can be seen in the right of Figure 4.74. The same behavior is even found for different stirrer speeds. In both cases, the feature of MES to form nano-scaled droplets due to the low interfacial tensions is the reason for that, as sufficiently high interfacial area even at low energy input is provided (Section 4.1.2). Consequently, it is assumed that mass transfer limitations are not relevant for the applied system in its operating region.

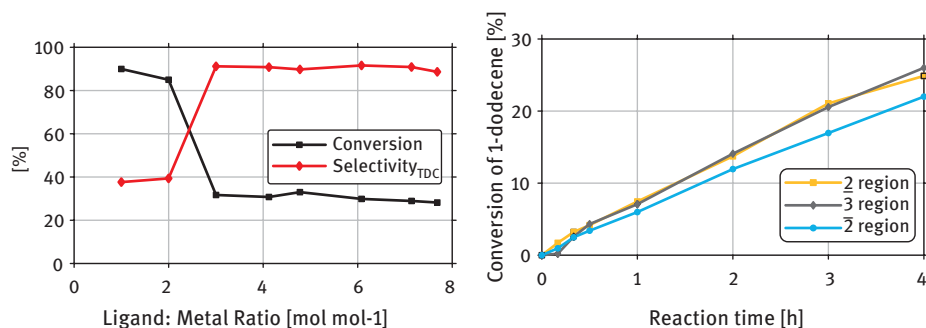


Figure 4.74: Left: Influence of ligand on conversion and selectivity. Experimental conditions: $[\text{Rh}(\text{acac})(\text{CO})_2] = 1 \times 10^{-3} \text{ mol L}^{-1}$, 2.4 mol L^{-1} 1-dodecene, 20 g water, 3.5 g Marlipal[®] 24/70 ($\alpha = 0.50$, $\gamma = 0.08$), 1 wt% Na_2SO_4 , reaction volume = 50 mL. $p = 15$ bar syngas, $T = 95$ °C, stirrer speed = 1,200 rpm, duration: 4 h. Right: Influence of phase behavior on conversion of 1-dodecene. Experimental conditions: $[\text{Rh}(\text{acac})(\text{CO})_2] = 1 \times 10^{-3} \text{ mol L}^{-1}$, molar ratio SX:Rh 4:1, 2.4 mol L^{-1} 1-dodecene, 20 g water, 3.5 g Marlipal[®] 24/70 ($\alpha = 0.50$, $\gamma = 0.08$), reaction volume = 50 mL. $p = 15$ bar syngas, $T = 95$ °C, stirrer speed = 1,200 rpm, duration: 4 h. Na_2SO_4 added to adjust phase behavior: 2: 0.1 wt%, 3:1 wt%, 2:3 wt%. Max. measurement error: $\pm 3\%$.

Concentrations of Dissolved Gases

Being reactants, carbon monoxide and hydrogen both affect the reaction kinetics directly. Furthermore, catalyst equilibria and thus the amount of available selective catalyst species is influenced by the concentration of CO (Figure 3.46). For the desired process application this becomes relevant for the separated phases in the settler. For long residence times, replenishing of dissolved gases is mainly limited to diffusion from the bulk gas phase through all liquid phases. Figure 4.75 (left) thus shows reaction kinetics for different resting phases. Here, the stirrer was stopped for specific time frames to allow for the separation of the reaction mixture in the

plant's settler and subsequent reentering into the reactor (restart stirrer after resting time). Significant decreases in chemoselectivity are observed for long resting times (2 h), while large amounts of iso-dodecene are formed. Interestingly, conversion increases by 22 percentage points, even for the separated system.

Stopping the stirrer, the phase separation occurs forming the $\bar{2}$ -system for high reaction temperatures (Section 2.2). Here, larger amounts of catalyst are present in the oil phase due to higher surfactant solubility. Since carbon monoxide shows high solubility in nonpolar substances and the ligand being preferentially located in the aqueous phase, the local concentrations around the catalyst promote the presence of the unmodified Rh species. Hence, increased isomerization is again observed despite the system being separated. A certain dead time is visible until this effect appears, and thus appropriate maximum residence times in the settler and recycle of a continuous plant system should be applied.

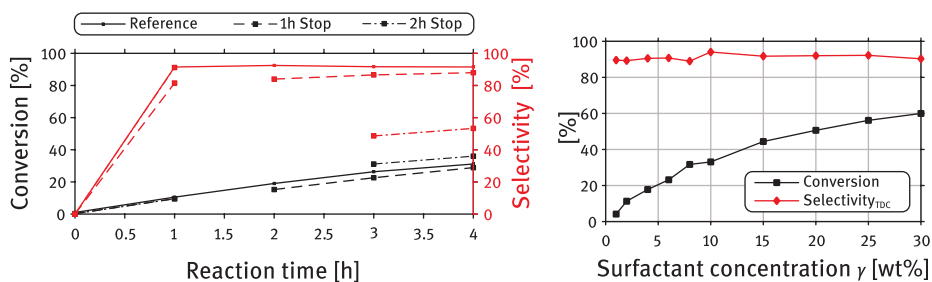


Figure 4.75: Left: Resting phases on conversion and selectivity for the hydroformylation of 1-dodecene. Experimental conditions: $[\text{Rh}(\text{acac})(\text{CO})_2] = 1 \times 10^{-3} \text{ mol L}^{-1}$, molar ratio SX:Rh 4:1, 2.4 mol L^{-1} 1-dodecene, 20 g water, 3.5 g Marlipal[®] 24/70 ($\alpha = 0.50$, $\gamma = 0.08$), 1 wt% Na_2SO_4 , volume = 50 mL. $p = 15$ bar syngas, $T = 95$ °C, stirrer speed = 1,200 rpm. Right: Influence of surfactant concentration on conversion and chemo selectivity toward the target product tridecanal for the hydroformylation of 1-dodecene. Experimental conditions: $[\text{Rh}(\text{acac})(\text{CO})_2] = 1 \times 10^{-3} \text{ mol L}^{-1}$, molar ratio SX:Rh 4:1, 2.4 mol L^{-1} 1-dodecene, 20 g water ($\alpha = 0.50$), 1 wt% Na_2SO_4 , reaction volume = 50 mL. $p = 15$ bar syngas, $T = 95$ °C, stirrer speed = 1,200 rpm, duration: 4 h. Maximum measurement error: $\pm 3\%$.

Surfactant Concentration

As an obvious consequence, the amount of surfactant directly affects reaction conversion for an MES, as the interfacial area is altered. This is verified in the right of Figure 4.75. The surfactant concentration thus should be tightly controlled to reliably track or predict the reaction performance. Chemoselectivity, however, is not affected by this and is constantly above 90%. It has to be mentioned, that the surfactant concentration exhibits an upper limit regarding the process concept since the formation of a stable emulsion (Winsor I system) at high γ should be avoided. Additionally, mass transfer limitation might take action at elevated surfactant concentrations due to the formation of high-viscosity surfactant agglomerates (Figure 4.54).

Systematic Analysis of Separation Behavior and Dynamics Regarding Process Design and Operation

The systematic guideline presented in Section 4.2.1.5 is applied and the system at hand focusing on the realization of a continuous process in the available miniplant. As relevant concentration measures, the oil to water ratio α and the surfactant concentration γ are chosen based on mass fractions. Y then represents the reaction yield calculated based on the oil phase composition:

$$Y = \frac{m_{\text{tridecanal}}^{\text{Oil}}}{m_{\text{total}}^{\text{Oil}}} \quad (4.4)$$

Step 1: Requirements and Process Constraints

Initially, desired performances of process application are collected focusing on reaction and separation performance:

- **Efficient emulsification** to enable high reaction rates
- **Fast separation** to keep required settler unit volume and residence times low, and avoid side reactions
- **Efficient separation** to enable acquisition of highly pure oil phases containing oily reactants (oil phase purity $\geq 95\%$) by applying simple gravity settlers
- **Minimal catalyst leaching** into the oil phase (≤ 1 ppm)
- **Operability** and stability of the phase separation even under transient operation conditions and expectable concentration shifts

Focusing on continuous operations in a miniplant, technical restrictions apply regarding deployed sensors. Standard continuous measurements of temperature, pressure, flows, and levels are available at their respective ranges. Concentration measurements are available for the gas phase composition regarding permanent gases and liquid sampling, which is mainly constrained to oily substances. Due to the presence of water and surfactant in analytical samples, gas chromatography measurements are only attainable for oily substances. Two configurations are used for liquid samples from the system: A Hewlett Packard HP6890 GC equipped with a 1 m fused silica precolumn with 0.32 mm inner diameter and a separation column Agilent HP-5 (cross-linked 5% PH ME Siloxan, 30 m length, 0.32 mm inner diameter, 0.15 μm) is used for aqueous and surfactant rich samples. Oil phase samples are analyzed with an Agilent 7890A GC without precolumn and the same HP-5 column. For both devices, a flame ionization detector operating at 300 °C and split/splitless injector working at 275 °C, 47.8 kPa, and 30:1 split ratio is used. The temperature program is set to 80 °C (3 min hold):10°C/min:130 °C (2 min hold), 10 °C/min:150 °C (5 min hold), 35 °C/min:270 °C (9.5 min hold). GC calibration was done for three measurements cases: oil phase, water phase, and reactor samples. Relative standard deviations in % of wt% are given by ≤ 0.4 , ≤ 2.0 , and ≤ 2.4 , respectively.

The specification of the component system to be applied is mainly given by the reaction system. An optimal composition has already been pointed out. It has to be mentioned, that the analysis of the phase separation behavior needs to consider product and by-product formation. Hence, tridecanal and iso-dodecene are found to be relevant, whereby the latter is waived for the discussion because its chemical structure is rather similar to 1-dodecene. Furthermore, catalytic species and the presence of syngas are to be considered for the general chemical matrix.

To ease the following discussion on the system analysis, microemulsion mixture compositions are denoted using the common indicators on oil to water ratio α , surfactant concentration γ , and yield Y (eq. (2.9), (2.10), (4.4)). Oil commonly indicates all organic reactants in the system, while water stands for the aqueous catalyst solution, applied with a fixed composition (Section 4.2.3.1).

Step 2: Influence Identification and Ranges of Interest

Following the theoretical background on MES (Section 2.2) as well as first deliberation on coalescence behavior (Section 4.2.1.1) and mass transfer (Section 4.2.1.3) in MES and constraints of the miniplant system, the initial set of influences is set up:

- **Trace compounds** and surface-active molecules likely affect the phase separation behavior and can alter interfacial tensions. Hence, the presence of different catalytic species is to be checked.
- **Pressure** typically has a negligible influence on liquid–liquid equilibria. However, gas solubility is directly affected.
- **Stirrer type and speed** should be analyzed because droplet size distribution and coalescence behavior and dynamics are affected (Section 4.2.1.1).
- **Temperature** is one of the most sensitive state variables for multiphase systems. Several physical properties are highly dependent on temperature.
- **Concentrations** of water, oily reactants, and surfactants directly affect phase equilibria (Sections 2.2 and 3.1.3)

These general influences are checked for relevance and effect on the phase behavior in prescreening. For this step, Table 4.7 lists relevant ranges of interest regarding a desired miniplant operation by defining a plant setpoint based on the identified optimal reaction conditions and variations thereof calculated from preliminary plant test runs.

Step 3: Prescreening and Feasibility Analysis

Prescreening tests are using either multiple test tubes, heated in a thermostat or via a stirred high-pressure glass reactor (see information on setups in [117]). General results on the prescreening are collected in Table 4.7. Initially, catalyst activation by syngas and the influence of pressure are investigated. A full impedance of the phase separation is found, if syngas is present in the system, in case no lyotropic salts, such as Na_2SO_4 , are present in the mixture. Catalyst activation renders the formed active species highly surface-active, leading to emulsion stabilization. This was the main reason to consider the addition of salt to the system to counter the

Table 4.7: Ranges of interest for influencing factors on phase separation behavior and prescreening results (steps 2 and 3).

Influence factor	Plant setpoint	Ranges	Prescreening result
Catalyst species (activation)	Activated	Activated/deactivated syngas on/off	Inhibited separation for catalyst activation; encountered by addition of 2.17 wt% Na ₂ SO ₄ in catalyst solution; with Na ₂ SO ₄ only negligibly slower separation dynamics
Pressure	15 bar	[1, 18] bar	Negligibly slower separation dynamics
Stirrer speed	1000 rpm	[800, 1,400] rpm	No influence observed
α	50%	[40, 60]%	Moderate influence on separation state
γ	8%	[6, 10]%	Very high influence on separation state
Y	40%	[0, 40]%	Moderate high influence on separation state
T	–	[25, 95] °C	Very high influence on separation state

ionic strength of the activated catalyst. Using this updated formulation, virtually no effect on the phase separation states is observed by catalyst activation or syngas pressure and the same respective phase volume fractions are observed. This is also true for experiments at varied pressures. However, phase separation dynamics are slightly altered and time until reaching stable phase levels increases for the active catalyst and elevated pressure. Since required separation times are still well below 5 min, this effect is considered irrelevant for process application. This is only true if pressure is kept constant. On depressurizing, massive foaming occurs and thus needs to be avoided for the main reaction and separation section of the miniplant. Additionally, the influence of stirrer type, speed, and gassing is found to be negligible, which is plausible considering microemulsions forming nanostructured emulsions configurations already at minimal energy input (Section 4.2.1.1).

The set of key influence factors for the separation behavior thus consists of temperature and system concentrations. In the next step, feasible separation states regarding the defined process goals are searched for. As a general requirement, phase separation should be completed within 30 min, to be applicable in a settler unit and avoid by-product formation (Figure 4.75). Also, suitable oil phase levels above 10% should apply. The feasibility analysis thus focuses on identifying applicable phase equilibria and emulsion types based on Figure 4.76. Results on performance criteria are summarized in Table 4.8 and concluded to the following statements:

- Feasible phase separation for applicable separation times are only observed for the three-phase region
- Separation time shows a distinct minimum for the three-phase region (Section 2.2)

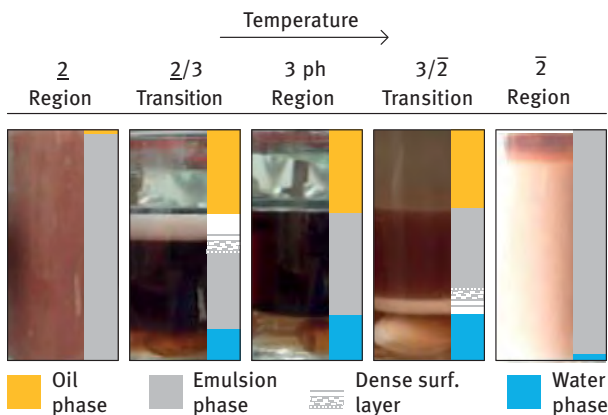


Figure 4.76: Observed phase behavior of the microemulsion for feasibility analysis. Mixture setpoint: $\alpha = 50\%$, $\gamma = 8\%$, and $Y = 0\%$. Connected performance criteria are listed in Table 4.8. Taken from [117].

Table 4.8: Collected performance criteria for observed phase states for a mixture setpoint: $\alpha = 50\%$, $\gamma = 8\%$, and $Y = 0\%$.

Phase state	$\underline{2}$	$\underline{2/3}$ boundary	3	$3/\bar{2}$ boundary	$\bar{2}$
Vol. fraction oil	<3%	$\leq 25\%$	$\leq 30\%$	$\leq 25\%$	<3%
Purity oil	–	$\geq 99.5\%$	$\geq 99.5\%$	$\geq 99\%$	–
Catalyst leaching	–	<1 ppm	<1 ppm	>1 ppm	–
Separation time	–	<30 min	<5 min	<30 min	–

- Feasible volume fractions of the oil phase $\geq 15\%$ are only observed for the three-phase region
- Oil phase purity is close to 100% for the three-phase region, but gradually decreases with temperature
- Likewise, catalyst leaching is lowest at low temperatures within the three-phase region
- Main impurities in the oil phase stem from the surfactant, especially at higher temperatures (solubility)
- Highly viscous surfactant layers are observed for the transition regions between two- and three-phase regions

Concluding, the three-phase region, avoiding metastable peripheral boundary areas is identified as the solely applicable operation region for phase separation operation.

Going beyond this region a stepwise transition of the phase separation behavior toward undesired unseparated states is found.

To support these findings, Figure 4.77 shows surface plots of the relative volume fractions of oil and water phase for a representative mixture depending on time and temperature. As expected, large volume fractions of the excess phases are only found for a constrained region – the three-phase region. Following the general pattern, a continuous shift toward lower oil phase fractions and increasing water phase levels are found for increasing temperature. Additionally, the water phase is formed faster than the oil phase at higher temperatures. Both effects are connected to the affinity of the surfactant switching from water to oil with temperature (Section 2.2). Considering phase separation operation in a settler, the temperature at a given composition should hence be adjusted toward the central area of the feasible three-phase region, ideally below the phase inversion temperature to obtain fast-developing pure oily excess phases.

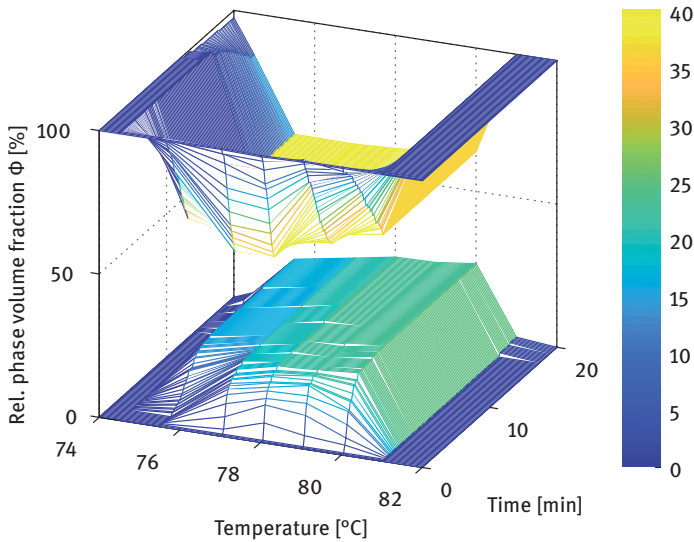


Figure 4.77: Experimental results on the relative phase volume fraction evolution over temperature and time for the mixture $\alpha = 50\%$, $\gamma = 8\%$, $Y = 0\%$. Top: oil phase; bottom: water phase [117].

As the last part of Step 3 of the systematic analysis of the surfactant-containing system, a sensitivity analysis is performed. Having already defined feasible phase separation operation regions, the aim is now to assess the influence of the remaining relevant influencing factors on the position of these operation regions. Sensitivity information can then be used in Step 5 to generate a suitable design of experiments. The result of this analysis is shown in Figure 4.78, highlighting the extent of the feasible three-phase separation region concerning temperature and surfactant

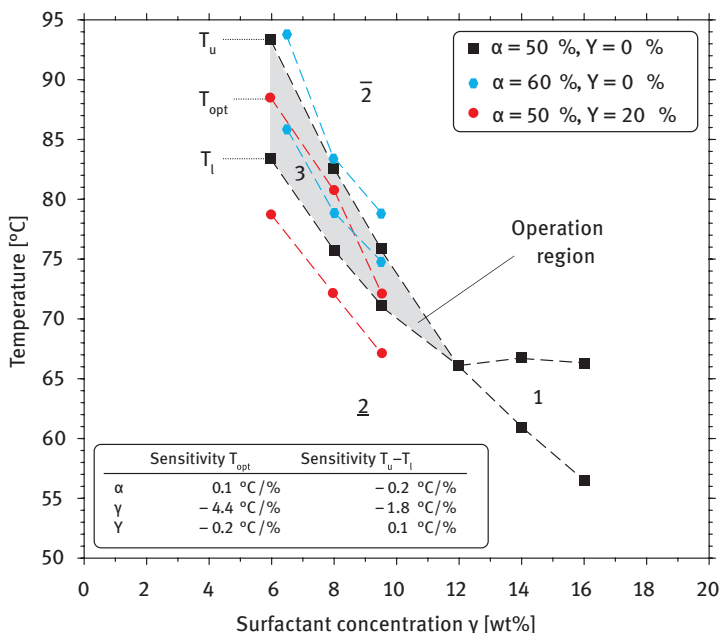


Figure 4.78: Phase diagram for the microemulsion system. Black squares mark the feasible operation region. Red dots show the shift at increased reaction yield, blue dots show a shift with changed α . Sensitivity information is provided for the temperature-wise position of the feasible region. Based on [117] and taken from [118].

concentration. Furthermore, shifts of this operation region with varied oil to water ratio α and product yield Y are highlighted. A drastic influence of the surfactant content is apparent, while the temperature-wise extent of the operation region is rather small and ranges between 5 and 9 °C. Respective sensitivities of the influencing factors are quantified by their impact on the position of the three-phase region, which is marked by the central optimal separation temperature T_{Opt} and the temperature-wise extent ($T_u - T_l$). Here, the surfactant shows the highest sensitivity, which is an order of magnitude higher, than for the oil to water ratio and product yield.

Step 4a: Preliminary Separation Unit Design

Given the previous findings, a preliminary design is proposed at this point. Given the feasible three-phasic separation, a standard gravity settler with three-phase drains is considered suitable, since settling times are found to be low and no general impedance of coalescence was observed. Detailed studies on the design of such a unit and the application of internals, like knitted wire meshes, have been conducted by Müller et al. [189]. However, a critical revision on the proposed application of coalescence enhancers is conducted in Figure 4.79.

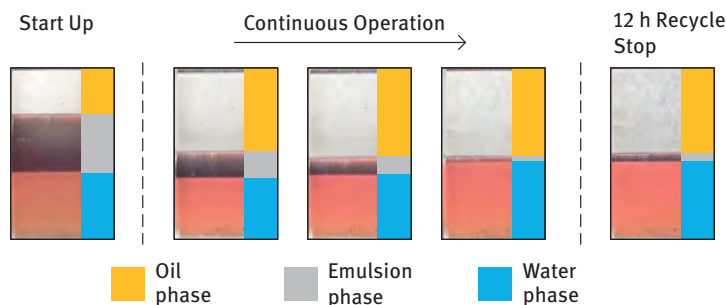


Figure 4.79: Test of the settler operation using knitted wire meshes as internals. The phase separation state is observed through a settler gauge glass. Test conditions: $\alpha = 50\%$ – $\gamma = 8\%$ – $Y = 0\%$, $T_{\text{Settler}} = 85\text{ }^{\circ}\text{C}$, $p_{\text{Settler}} = 15\text{ bar}$, 1 h residence time [117].

Preliminary experiments using a mixer–settler setup with total recycling were conducted in the miniplant. The continuous operation was performed, while knitted wire meshes and displacers were tested as the internals of the settler. After filling a reference microemulsion mixture into the plant, stable phase separation was established in a *start-up* phase. Subsequently, recycling was started and a long-term *continuous operation* was conducted. Via sight glass observations, a continuous shrinking of the middle emulsion phase was observed and an accumulation of a surfactant rich emulsion at the settler inlet before the internals was induced. To verify this, the recycling was stopped for 12 h, which led to a redistribution of the surfactant as the emulsion phase enlarged significantly in this resting phase. However, for process application, such an accumulation of surfactant is critical and severely impeded reaction and separation performance. It is thus proposed to omit any internals, which are prone to cause such accumulations for settler unit design.

Furthermore, the observed dense surfactant layers at the boundaries of the three-phase region (Figures 4.54 and 4.76) should be considered for unit design, since these structures are likely to cause pump failure and pipe clogging. Together with the rather small feasible operation area a very tight temperature control for the settler unit and avoidance of large radial temperature gradients is suggested.

Step 4b: Analysis of Controllability of Influencing Factors

For a stable and reliable process operation, the controllability of the identified relevant influences on the separation behavior is mandatory. To discuss this, Table 4.9 lists respective system variables, observed sensitivities on the phase separation, and available equipment for sensing and control.

If direct control of the settler is desired, the separation temperature needs to be adjusted according to the current microemulsion composition at the inlet of the settler. While temperature measurement and adjustment are fairly easy and typically fast, concentration measurements for the system at hand are critical. Only the oily reactants are measurable using offline GC sampling, which also exhibits a very

Table 4.9: Controllability analysis for influencing factors of the phase separation behavior, their sensitivity on the position of the separation operation region.

Influencing factor	Sensitivity	Measurement	Sampling rate	Control element
A	Moderate	Not possible	–	Pumps
γ	Very high	Not possible	–	Pumps
Y	Moderate	GC	1 h	Pumps, reaction conditions
T	High	Pt100	0.5 s	Heater unit settler

large sampling rate. Having high system dynamics especially at the border regions of the three-phase area, this situation is critical. Additionally, the most sensitive state, the surfactant concentration, is completely immeasurable given the deployed analytics, and hence the desired process concept is rendered infeasible.

To overcome this obstacle, the development of a model-based soft sensor is proposed. Key therein is the exploitation of the features of the three-phasic separation state of MES (Section 2.2). By using the optically accessible phase volume fraction information, a back-tracking to the current composition in the settler unit is possible and the critical immeasurability can be resolved. Hence, new measurements of phase levels must be considered for plant automation and respective model and soft sensor development must be considered to enable process operation.

Step 5: Full System Mapping

Finally, the full system mapping includes the actual empirical investigation of the phase separation behavior and data acquisition used for model formulation later on. With the performed influence and sensitivity analysis, the relevant factors and necessary levels for a full factorial design have been set to a $3^1 9^1 3^1$ design for the respective experimental parameters oil to water ratio α , surfactant concentration γ , and product yield Y . Of course, phase levels have to be included as additional measurements in the experimental procedure. Table 4.10 hence shows applied ranges of investigated influencing factors, increments, and required experimental observations.

Conclusion on System Analysis and Process Challenges

The conducted systematic analysis of the MES used as reaction medium for the hydroformylation of 1-dodecene revealed several severe obstacles, which render a realization of the desired process concept infeasible or at least very challenging. Hence, also common procedures for realizing reactor–separator systems with internal recycles, as presented by Biegler et al. [40], are not applicable. These challenges (C) stem from system inherent properties and are likely encountered for similar applications of MES. However, their systematic identification and quantification also

Table 4.10: Experimental ranges of parameters for the full system mapping and gathered observations [117].

Influencing factor	Range	Increment	Measurement
α	[40, 60]%	20%	Gravimetric
γ	[40, 60]%	0.5%	Gravimetric
Y	[40, 60]%	20%	Gravimetric
T	Adjustable	1–2 K	Pt100
Observation	Measurement		
Phase state	Qualitative optical evaluation		
Phase levels	Video capturing and level detection		

enabled the development of tailored solutions for process design and operation, outlined in Section 4.2.3.3.

C1: Severely small operation region for the phase separation step

C2: Very high sensitivity of the operation region regarding all concentrations

C3: Formation of viscous surfactant layers at the boundary of the operation region

C4: Immeasurability of crucial component concentrations

C5: Highly dynamic unstable operation in miniplant system, assuming frequent concentration fluctuations due to three recycles and ongoing reaction

4.2.3.3 Strategies for Process Design and Operation

As the second level of the holistic guideline for the realization of reactive MES, several tailored solution strategies are developed to counteract the above-stated operational challenges. As a fundamental basis for that, a dynamic miniplant model is required. Therein, the properties of the MES are to be integrated regarding the interaction of emulsion and reaction behavior, as well as the distinct phase separation behavior. Such a model then enables the connection of methods for an integrated process design and connects fundamentals (Section 2.2), actual process development, and the system analysis with advanced tools of superstructure optimization for process synthesis (Section 5.3.3), and optimization of process control using state estimation and dynamic real-time optimization (Section 5.4.2). For the given case study, generally, six major solution strategies (**S**) are outlined in this section and deployed to unlock the proof of concept for the desired process concept using MES for the hydroformylation of 1-dodecene.

S0: Development of a fully dynamic miniplant model with a detailed description of reaction macro-kinetics in MES and the three-phasic separation of MES.

S1: Design of a settler unit for precise control and observation of the phase separation.

S2: Soft sensing of immeasurable surfactant concentrations.

- S3:** Application of advanced process analytics to enhance (online) measurability of process states.
- S4:** A state estimation framework to efficiently track the plant's state and derive suitable model initials for process optimization, handling also multiple sampling rates (Section 5.4.4).
- S5:** A framework for dynamic real-time optimization and start-up optimization to handle the very high dynamics and nonsteady-state behavior of the system (Section 5.4.4).

Design of a Settler Unit for MES

The phase separation behavior for the system at hand is very complex due to its strong dependency on temperature and system composition. This is mainly due to very small operation regions, which are additionally greatly affected in the state space by several operational parameters or influences. Next to that, the critical immeasurability of surfactant concentrations and desired soft sensing via optical observation has to be considered. To ensure the description of the phase separation and the application of empirical models (based on the observations of the full system mapping), it is thus mandatory to perform the phase separation out of the fully mixed state at a given and constant separation temperature. This is realized by integrating a mixing zone and an optimized heating zone into a modular settler shown in Figure 4.80. First, a heated stirrer module is used for re-emulsification and heating of the entering liquid. Via an overflow weir, the mixture then enters the heating module. Here, a heating jacket and multiple internal heating coils are installed to reduce any radial or axial temperature gradients. Temperature control is possible via several deployed sensors. The volume of this module is chosen to meet a residence time of approx. 30 min. A flow sight glass is then installed to allow observation

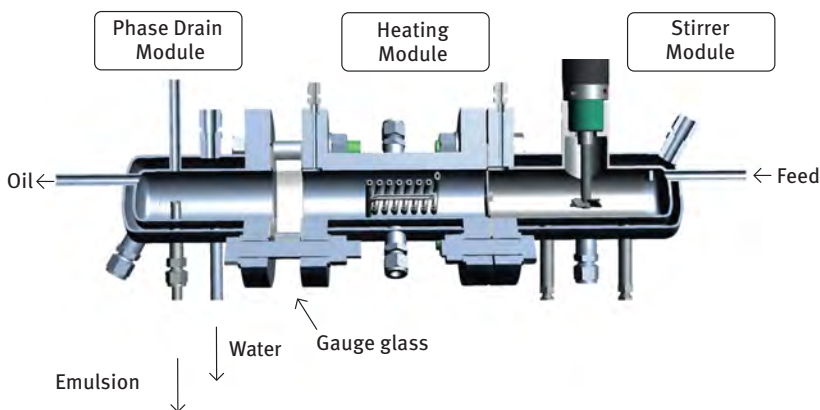


Figure 4.80: Developed settler design, combining mixing, heating, and separation zones.

of the phase separation state and measurements of phase volume fractions. Finally, the phase drain module allows for drawing off three liquids from the settler. The modular design enables easy adjustment of the internal volume and the addition of internals. Furthermore, the mixing zone is equipped with several ports for additional analytics, such as pH sensors or spectroscopic probes.

Analysis of Reaction Performance and Development of Adapted Kinetic Model

A detailed mechanistic model for the hydroformylation of 1-dodecene was developed and is presented in Section 3.2.2. However, the thermodynamic properties and dispersion types of MES greatly affect local concentrations around the catalyst and hence reaction performance. Although MES are considered homogeneous at a macroscopic level, this is not true on the molecular level. Hence, developed mechanistic models, which were developed for a fully homogeneous system, are only partially applicable. Sections 4.2.1.5 and 4.2.3 addressed this regarding systematic influence identification and quantification for microemulsions. The relevance for this is further emphasized using Figure 4.81.

Here the developed hydroformylation kinetics from Section 3.2.2 was taken and kinetic parameters were re-estimated based on kinetic experiments for the MES. However, the identified relevant influences, such as ligand-to-metal ratio (L:M) and surfactant concentration, are not varied in the experiments. Consequently, kinetic model predictions completely fail for variations of these additional influences (Figure 4.81), although adequate predictions of the reaction behavior for variations in, for example, temperature and pressure are found.

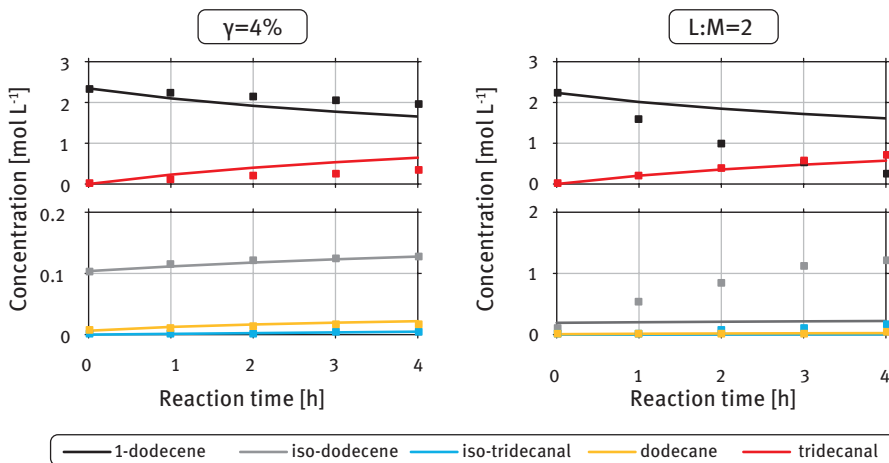


Figure 4.81: Comparison of experimental data (symbols) and initial kinetic model (lines) at ligand and surfactant concentrations different from standard mixture composition ($\gamma_0 = 8\%$, $L:M = 4$). Max. analytical error: $\pm 0.08 \text{ mol L}^{-1}$ [117].

An adaption of the initial kinetic model is thus performed by deploying suitable mathematical augmentations to capture the observed system behavior for relevant influences of the MES on the reaction kinetics (Section 4.2.1.5). Focusing on Figure 4.75 and the influence of the surfactant concentration, an enhancement of conversion while maintaining selectivity is observed. Taking the rate equations r_r^0 from the initial model, the insertion of a power law formulation for the surfactant concentration is suitable (eq. (4.5)).

Regarding the ligand to metal ratio (Figure 4.74), a stepwise transition on conversion and selectivity is found, while respective levels are rather constant. A detailed look at the experimental data shows that especially isomerization reactions and the formation of branched aldehydes is promoted. For respective rates in the initial model, a selectivity switch is inserted (eq. (4.5)). A sigmoidal function expression is used to allow for switching between 1 and $k_r^{Sx:Rh}$ at a specified value of the ligand-to-metal ratio, while maintaining twice-differentiability of the model. Finally, all model parameters are re-estimated using the collected experimental data.

$$r_r = \underbrace{C_{\text{Surfactant}}^{n_{\text{Surf}}}}_{\text{Enhancement emulsifier}} \cdot \left(1 + \frac{k_r^{Sx:Rh}}{1 + \exp\left(-\left(K^{Sx:Rh} - \frac{n_{Sx}}{n_{Rh}}\right) \cdot P_r^{\text{trig}}\right)}\right) \cdot r_r^0 \quad (4.5)$$

Selectivity switch ligand:metal ratio

Figure 4.82 shows a comparison of model predictions and experimental validation data for standard reaction conditions and variations of ligand to metal ratio and surfactant concentration. All plots demonstrate the successful adaptation of the initial kinetic model. The influences of surfactant and ligand to metal ratio are displayed adequately and deviations between model prediction and experiments are widely below 10%. Further details on the development and application of this model can be found in the literature [117, 210].

Detailed Model of Three-Phase Separation

The focus of modeling is laid on applicability for describing the separation operation in a settler and gaining access to the phase compositions. Figure 4.83 describes the general concept for this phase separation model and the fundamental principles of microemulsion thermodynamics it exploits. As a key aspect, the three-phasic separation of a ternary MES at constant temperature and pressure is considered (top left):

Setting up an initial microemulsion mixture within the three-phasic miscibility gap (feed composition in triangle diagram), three liquid phases with individual concentrations according to the corners of the inner triangle miscibility gap are formed. Changing the initial mixture within the three-phase miscibility gap while keeping temperature and pressure constant then results in the same individual phase compositions. However, the observed volume fraction of developed phases will differ. Thus, a correlation of the initial feed mixture composition with temperature T^* and

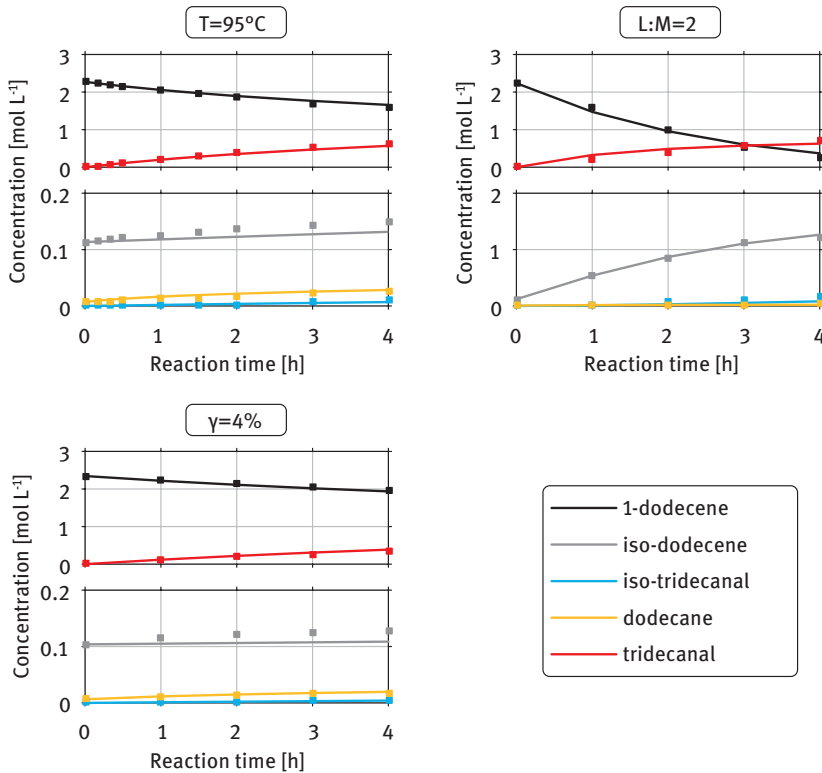


Figure 4.82: Comparison of experimental data (symbols) and the adapted kinetic model (lines) for experiments: $T = 95\text{ }^{\circ}\text{C}$ reference experiment, $L:M = 2$ variation of ligand-to-metal ratio, $\gamma = 4\%$ variation of surfactant concentration. Max. analytical error: $\pm 0.08\text{ mol L}^{-1}$ [117, 210].

with optically accessible phase level information is possible (phase state soft sensor). Combining this with empirical models describing the composition of the oily and aqueous excess phases (excess phase model), a valid formulation for all relevant composition variables in each phase is obtained via mass balances.

Phase State Model – Phase Volume Model

To implement such a model, first, an empirical description of the evolution of phase volume fractions in the domain of the influence factors on the separation state is required. The relevant experimental information for that is already available from the systematic system analysis. As key influences (and hence required input variables to the model) temperature T and the initial mixture given by oil to water ratio α , surfactant concentration γ , and yield Y are found. A polynomial model ϕ_{Phase} is deployed to capture observed phase levels according to the given total mixture composition. The model is furthermore restricted to the three-phasic separation

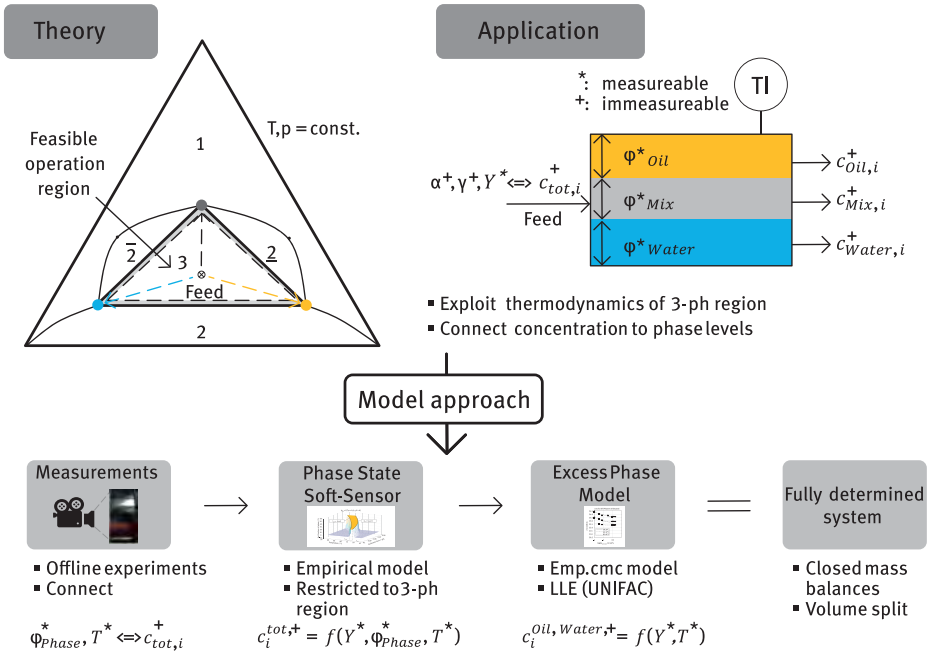


Figure 4.83: General approach for phase separation model [117].

region, being the feasible operation region regarding process application. Thus, confinement temperature functions $T_{upper/lower}$ are required for the three-phase region. Again, polynomial functions are deployed, while the applied experimental data for parameter fitting is classified for three-phasic separation showing a minimum of 10% volume fraction of the oil phase. This way, the feasible region is constrained to the inner part of the three-phase region, avoiding the rather unstable boundary region and observed critical emulsion states. To turn off phase separation at the boundaries, sigmoidal switching functions are used ($TRIG_{upper/lower}$). These compare the current temperature with the temperature boundary function $T_{upper/lower}$ based on the current composition. These functions are then multiplied on ϕ_{Phase} to form the finalized phase volume model:

$$\phi_{Phase} = f(\alpha, \gamma, Y, T) \quad (4.6)$$

$$T_{upper/lower} = f(\alpha, \gamma, Y) \quad (4.7)$$

$$TRIG_{upper} = \frac{1}{1 + \exp(500 \cdot (T - T_{upper}))}, \quad TRIG_{lower} = \frac{1}{1 + \exp(-500 \cdot (T - T_{upper}))} \quad (4.8)$$

$$\phi_{Phase}^{Model} = \phi_{Phase} \cdot TRIG_{upper} \cdot TRIG_{lower} \quad (4.9)$$

Figure 4.84 then shows a surface plot for the phase volume of the oil phase obtained from the model depending on surfactant concentration and temperature. Experimental data is provided for validation and is widely captured by the model. The switching functionality is furthermore emphasized and realizes a smooth shut down of the phase separation at the temperature boundaries.

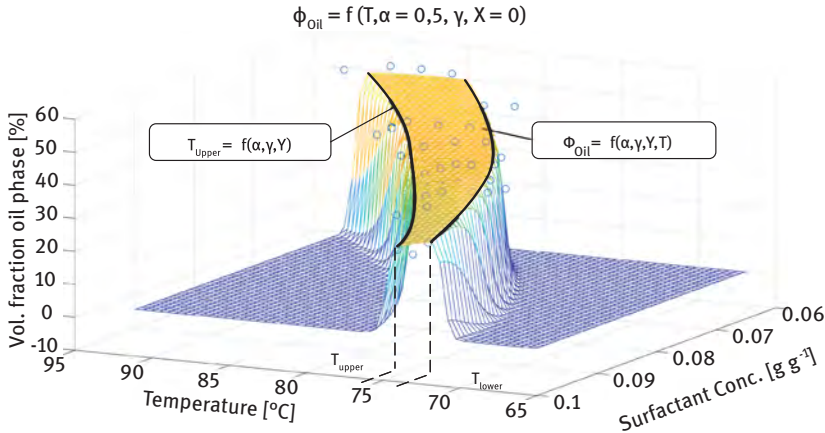


Figure 4.84: Surface plot for the model of oil phase volume fraction at constant oil to water ratio and yield. Marker show experimental data. Taken from [118].

Composition of Excess Phases

For MES two major observations are made for oily and aqueous excess phases: For the three-phase separation state, the surfactant concentration in the excess phases is at the level of the critical micelle concentration (Section 2.2.2). For nonionic surfactant and long-chained oily substrates, the CMC is typically at very low surfactant concentrations (5.59×10^{-5} g/g for pure substance equivalent of Marlipal[®], C12E8 in water [222]). Based on this, the assumption is made that the composition of the excess phases is mainly dictated by the binary miscibility gap for water and oil. Respective compositions depending on temperature can thus be calculated based on descriptions of the LLE of water, 1-dodecene, and the main reaction product tridecanal. Combined with a description of the temperature-dependent CMC, full concentration information on the excess phases is obtained.

The CMC is directly accessible via measurements of the surface tension. Representative mixtures of aqueous excess phases and oil phases containing 1-dodecene and tridecanal have thus been tested at different temperatures and varied surfactant content. The experimental information is then merged into an empiric model, which is exemplarily shown for an oily excess phase without tridecanal in Figure 4.85. For a fixed temperature, the CMC is obtained at the point, at which increasing the surfactant concentration does not cause a further decrease of the surface tension (saturated

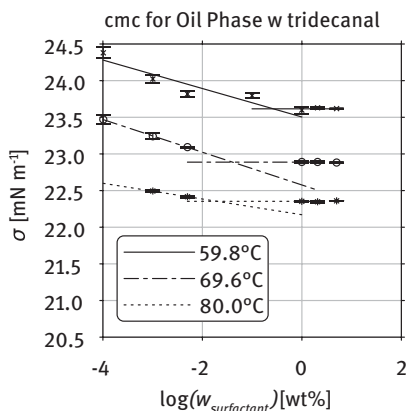


Figure 4.85: Surface tension measurements for a 1-dodecene-tridecanal mixture at different temperatures. A fit function is provided for the critical micelle concentration (CMC) depending on temperature. The CMC is obtained at the intersection of descending and constant parts of the surface tension. Image based on the diagram shown in [117].

surface and formation of micelles). For three different temperatures, a general trend for higher CMCs in oil at increasing temperatures is found. This is perfectly met with theoretical considerations on surfactant solubility.

$$w_{Surfactant}^{Phase} = P_{p=1}^{cmc,Phase} \cdot \exp\left(P_{p=2}^{cmc,Phase} \cdot T\right) \quad (4.10)$$

The LLE of water and oily reactant is then described using UNIFAC as g^E -model as no further measurements are required. However, to avoid the structural complexity of the g^E -model, evaluations of phase compositions at varied temperatures are calculated offline and merged into a polynomial surrogate model.

Soft Sensor for Surfactant Concentrations

Another challenge is the critical immeasurability of surfactant concentrations given the available standard analytics which renders process applications of MES infeasible. A general solution approach is developed by applying the phase separation model. Reformulated as an implicit function, it is used for the calculation or soft sensing of the composition of the microemulsion based on current temperature, observed fractions of phase volumes, and reaction yield traceable via GC sampling:

$$\alpha, \gamma = f(\phi_{Oil}, \phi_{mix}, \phi_{Water}, \alpha, \gamma, Y, T) \quad (4.11)$$

Measurements on the actual phase volume fractions ϕ_{Phase} are obtained using a webcam system on the settler's flow sight glass. Image processing is then used for level detection via an automated python-based script. The data is then transferred via OPC to a simulation/optimization station, which solves eq. (4.11) at given current plant measurements for the current microemulsion composition. To assist plant operation, an implementation of the soft sensor on the process control system has been developed and augmented with key performance indicators (KPI), as

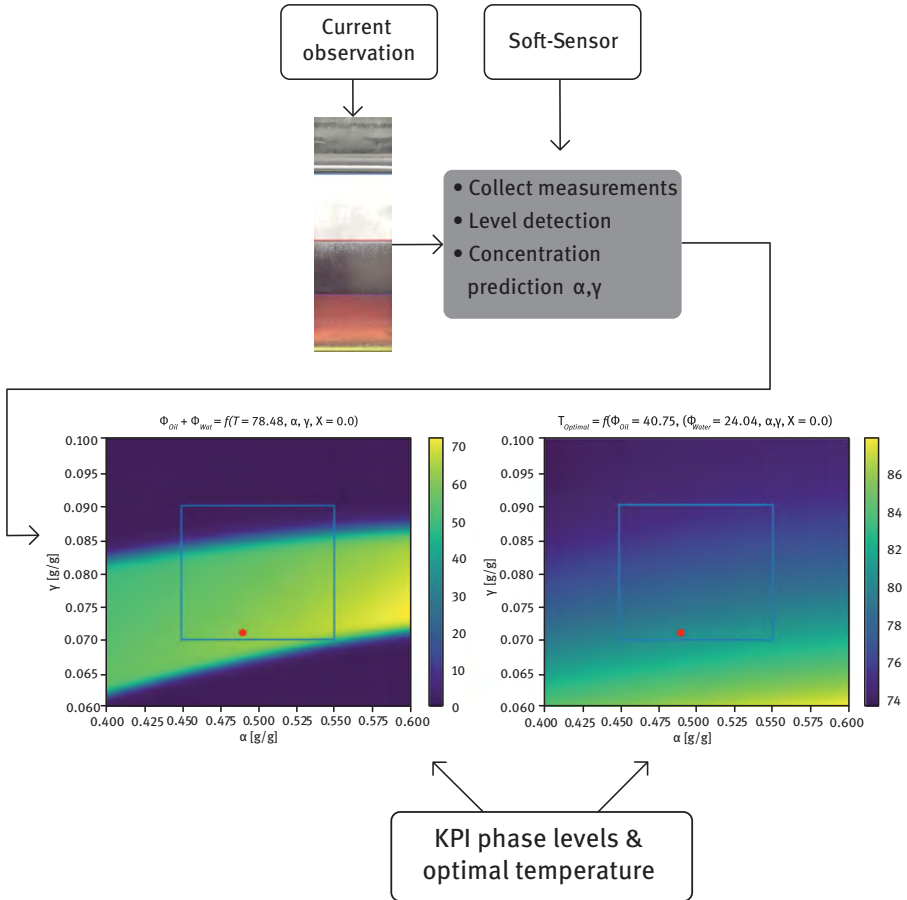


Figure 4.86: Integration of the concentration soft sensor and key performance indicators into the process control system. Picture adapted from [117].

shown in Figure 4.86. Given the current webcam image, calculated levels and concentration predictions are provided directly on the process control system. Based on this, two key performance indicators are generated. On the left, a surface plot of the cumulated levels of the oil and water phase with respect to α and γ is shown. Given the current plant state (red dot), the plant operator can choose control actions regarding feed of substances or adjustment of the recycling of phases to maintain a stable separation. Furthermore, a KPI for the optimal separation temperature depending on α and γ is provided to support controls actions on the settler temperature, especially, if a change in the composition of the feed to the settler is expected.

Implementation of Advanced Analytics

Successful plant operation and the application of model-based optimization methods depend to a large extent on fast and reliable concentration measurements. Since the typically deployed gas chromatography methods demand sampling times of more than 35 min and also significant sensitive concentrations, such as the surfactant concentration, cannot be detected, process monitoring is extremely difficult.

Hence, advanced process analytics have been evaluated for application in microemulsions. In collaboration with the Department 1.4 of the Federal Institute for Materials Research and Testing (BAM), Raman spectroscopy has been developed for online in situ concentration measurements in the miniplant. An integrated reaction autoclave and calibration test stand have been developed for this to enable the simultaneous collection of Raman spectra and reference measurements by high-field/low-field NMR, UV/vis, and GC for dynamic experiments under reactive conditions. Based on the collected data, suitable chemometric models have been obtained for the main reactants 1-dodecene, tridecanal, iso-dodecenes, and, with some limitations, Marlipal[®] 24/70. For model development, initial pretreatment of spectral data by standard normal variate transformation and detrending was conducted. Afterward, partial least squares regression models of respective compounds have been set up (RSME 1-dodecene 2.51 wt%, Tridecanal 2.93 wt%) [198]. Raman spectroscopy was tested online during several plant runs [184, 199]. It was shown that the operating conditions and thus also the configuration of the micelles (Section 4.2.1.1) have a considerable influence on the prediction and that the models are consequently

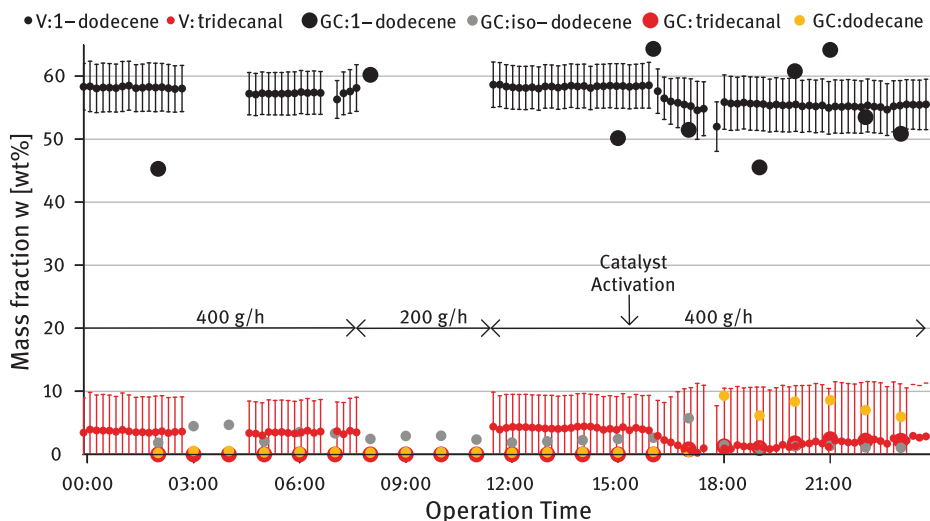


Figure 4.87: Results Raman spectroscopy (V) application for transient operation in miniplant and comparison to GC measurements (GC). Additional information on the total recycle to the reactor is given. Picture adapted from [117].

subject to a very limited validity. This is particularly evident in Figure 4.87, where an adequate prediction of the main reactants is achieved only after activation of the system with synthesis gas, as this represents the valid condition of the calibration experiments. In this case, a Raman probe was directly applied to the reactor outlet. Additionally, complete loss of model predictions is visible in enclosed cases (blank areas at 03:00 and 09:00). This is caused by changing properties of the microemulsion due to changes in the operation conditions, such as changed total recycle, recycle ratios, or surfactant feed. These affect the microemulsion structure, micelle configuration, and turbidity of the mixture. Hence, the optical properties of the mixture are severely altered, which again also affects Raman spectra. However, these obstacles could be overcome by including the microemulsion state into Raman calibration models by, for example, photon density wave spectroscopy and derivation of switchable model structures according to the present microemulsion state.

4.2.3.4 Miniplant Operation

This section outlines results from long-term miniplant operations to highlight the successful proof of concept for the hydroformylation of 1-dodecene in microemulsions. Additionally, also the operational complexity given by reactive MESs is outlined and linked to the successful application of methods presented in Section 4.2.3.3 to enable stable and reliable operation.

General Operation Conditions for Miniplant Campaigns

All miniplant operations follow a standard operating procedure regarding start-up, reaction initiation, and realization of a continuous operation. Basic preparation procedures encompass full inertization of the plant with nitrogen to ensure safe operation. Feed substances are then filled into feed tanks and the system is re-inertized. Since phase separation and reaction performance show very high dependency on the mixture concentration, the initial filling of reactor and settler is done via a gravimetrically premixed reaction mixture. This way an initial concentration set-point for the start-up is ensured. The start-up procedure is then started by heating the reactor and settler, as well as pressurizing the system with nitrogen while the recycling is turned off. Using predictions from the phase separation model, ideal separation conditions are applied on the settler and initial phase separation is awaited. When the desired three-phasic separation state is obtained, the recycle pumps are started at a precalculated ratio and operated while stabilizing phase separation in the settler. After that, the reaction is started by slowly reducing nitrogen pressure and deploying synthesis gas at reaction pressure. Generally, the miniplant can be operated in two basic operation modes: a continuous operation with an applied continuous feed of alkene and respective product drain toward the product tank; in case no feed is present, all separated phases from the settler are fully

recycled to the reactor. This (semi)-batch mode is applied for either stabilization of the phase separation or fast increase of reaction yield.

Reaction conditions are chosen according to the optimal reaction performance from lab-scale investigations and shown in Figure 4.73. Hence, the reaction pressure is fixed at 15 bar synthesis gas partial pressure (1:1 molar) and a reaction temperature of 95 °C. The stirrer speed is kept well above 750 rpm to ensure gassing and sufficient emulsification.

Operational Challenges for Conventional Miniplant Operation

Looking at the analysis of the applied MES, the operation of a continuous process has to be considered challenging. It is thus likely, that standard operating procedures for the start-up and operation of mixer settler systems [281] do not result in a desired steady state, and especially phase separation operation is disrupted. Analyzing plant operation characteristics based on miniplant test runs, two major operational issues are visible: first, no steady-state operation is attainable for the applied MES despite constant controls. Second, the reaction performance is severely dampened if the desired operational set-point is left. Severe by-product formation and a rather low target product concentrations are observed. This typically yields reduced chemoselectivities of only 33% compared to a reference of approx. 95% from lab results.

Both of these issues can be routed back to the phase behavior of the MES and the identified high system dynamics (challenge **C5**) and small feasible operation windows (**C1**). Operation set-points regarding separation temperature and recycle ratio (pumps) must meet the current phase separation state and steady state is only obtained if the recycle ratio is matched with the current fraction of the existing phase volumes in the settler. However, very high sensitivities of the separation state regarding all concentrations (**C2**) require frequent adjustment in presence of an ongoing chemical reaction and disturbances (pump operation, heating). If phase separation is lost or distorted, several undesired phenomena occur. Accumulations of the surfactant can be triggered if the feasible operation window for three-phasic separation is left (formation of highly viscous surfactant layers (Figure 4.54)). This leads to surfactant build-up in the settler and dropping reaction performance in the reactor (emulsifier is missing) (**C3**). Additionally, pump operation is affected by clogged pipes. Controlling the phase separation state is rather challenging because surfactant concentration measurements are not available (**C4**) and fast measurements would be required.

Incomplete phase separation and recycle operation furthermore lead to concentration shifts (and microemulsion configuration changes) in the reactor or long residence times of the aqueous catalyst-rich phase in the settler (**C5**). This directly affects the reaction performance, as local concentrations around the catalyst are altered and catalyst equilibria are likely shifted toward nonselective species. Hence, a close interaction of reaction and phase separation performance is encountered.

Successful Realization of Continuous Miniplant Operation

To encounter these operational challenges, the already presented systematic workflows for the analysis of MESs and the development of solution strategies are deployed to enable continuous process operation. The following results represent a validation case study to these methodologies regarding a successful realization of the hydroformylation of 1-dodecene in microemulsions.

An operation schedule is provided, which holds six operation modes to attain several goals (Table 4.11). To assist the critical start-up phase, an offline start-up trajectory for controller set-points is calculated from dynamic optimization based on the developed miniplant model (Section 5.4.4, solution approach **S0**). This results in **SP1**, which was used for plant start-up, feeding of substances, and obtaining and verify stable phase separation operation in full recycle mode. With **SP2**, the reaction was started by synthesis gas feed. For fast yield increase, the plant was initially operated in full recycle mode, before the continuous operation was started in **SP 3**. Finally, several step experiments were performed to investigate the controllability of the plant system. The response of reaction performance and phase separation were tested for the reduction of the residence time of the settler (**SP 4**), shifts in the recycle ratio (**SP 5**), and elevated reaction temperatures (**SP 6**). Besides these predefined operation modes, plant operation was assisted by several optimization-based tools to counteract disturbances from inaccurate flow control or sampling. Next to long-term optimized plant trajectories as a fall-back solution, dynamic real-time optimization (Figure 5.82, **S4, S5**) was applied based on plant measurements and concentration sampling. The phase separation soft sensor and deployed KPIs were used to derive operator actions in case the plant's state was highly disrupted (**S2**).

Table 4.11: Operation schedule for the miniplant operation and applied fixed controls for several operation modes (SP 1–SP 6) [117].

Controls	SP 1	SP 2	SP 3	SP 4	SP 5	SP 6
Operating hour/h	0–19	19–43	43–109	109–126	126–1254	154–172
Operation mode	Start-upfull recycle	Full recycle	Continuous	Continuous	Continuous	Continuous, $T_{Reactor} = 105\text{ °C}$
$T_{Reaction}/\text{h}$	–	7.1	7.1	8.0	7.4	7.1
$T_{Settler}/\text{h}$	0.64	0.48	0.34	0.90	0.47	0.34
Total recycle, g h^{-1}	600	800	1100	400	800	1,100

Table 4.11 (continued)

Controls	SP 1	SP 2	SP 3	SP 4	SP 5	SP 6
Recycle ratio oil:mix:water	0.25:0.50:0.25	0.25:0.50:0.25	0.18:0.5:0.32	0.25:0.50:0.25	0.4:0.2:0.4	0.18:0.5:0.32
Feed rate alkeneg h ⁻¹	0	0	28	28	28	28
Reaction status	Inactive	Active	Active	Active	Active	Active

Phase Separation and Catalyst Recycling

To this point, the highly dynamic and complex operation behavior of the three-phasic separation of the microemulsion proves to be one of the main obstacles for plant operation. As a key element of tools to improve control of the miniplant, a soft sensor for surfactant concentrations has been developed and tested for applicability using the start-up phase of the miniplant operation (**SP 1**). To meet the desired initial concentration set-point in reactor and settler, the plant was prefilled with a reaction mixture of $\alpha = 0.482 \text{ g g}^{-1}$ and $\gamma = 0.072 \text{ g g}^{-1}$. Using optimal start-up trajectories (Section 5.5.4) and soft sensor information, it was aimed at initializing phase separation in the settler and maintain a stable three-phasic separation for the start-up and stabilization of the recycle. Figure 4.88 shows observations from the settler's sight glass and results from soft sensor calculations including key performance indicator information. Starting from the prefilled system, initial phase separation was obtained showing the desired three-phasic state at 78.53 °C (first image).

Using the webcam image, the soft sensor predicts the corresponding mixture composition correctly (red dot), which matches the applied set-point perfectly (black diamond). Subsequently, recycling was initiated to homogenize the total high-pressure section of the plant and enforce full recycle operation. As expected, a shift of the phase separation state was encountered due to this. As can be seen from the second observation, the phase separation state approaches the boundary of the three-phase region (blue region, red dot), which is validated from the webcam observation. Here, the formation of dense surfactant layers is observed marking this state. Since the soft sensor correctly tracked this trend and optimal control trajectories were available, it was possible to deploy suitable actions regarding the adjustment of phase separation temperature and recycle ratio. This way, it was possible to already shift the settler composition toward the desired set-point for the third observation in Figure 4.88 and significantly improve the phase separation state, as larger excess phases are obtained. Further control actions resulted in a stabilization of the separation. Maintaining the three-phasic separation for **SP 1** and following dynamic plant operation was hence accessible using the soft sensor information.

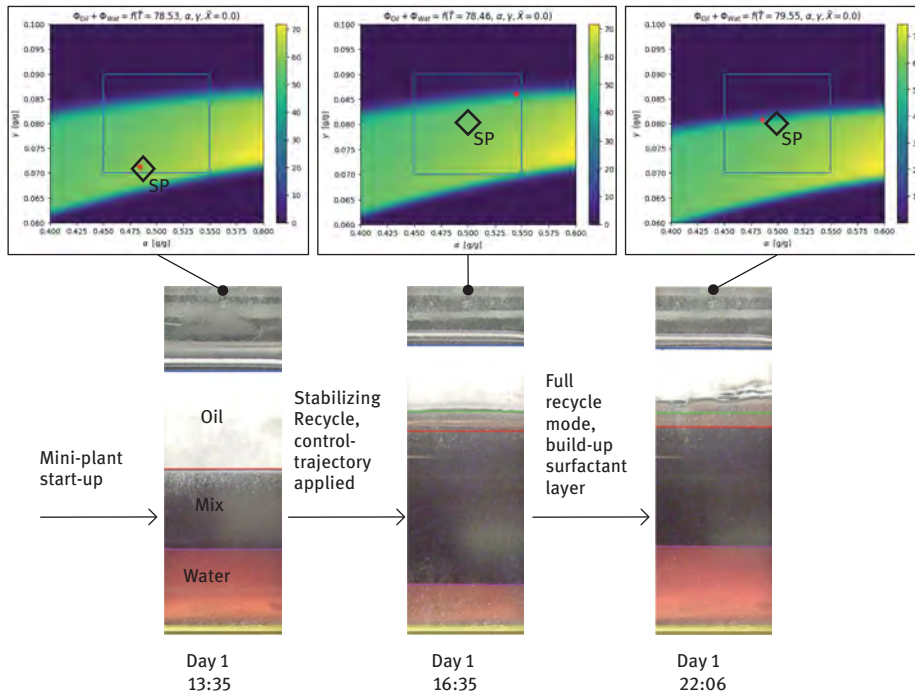


Figure 4.88: Soft sensor application for the start-up phase of the miniplant operation. Based on [117].

For the given plant operation this finally resulted in obtained oily product streams with an overall very good purity of 95–99 wt% (oily reactants in oil phase) and very low catalyst leaching of <0.1 ppm (detection limit of ICP-OES reached).

Product Phase Purification by Organic Solvent Nanofiltration

For further purification and full recycling of surfactant and catalyst, the applicability of OSN under process conditions for the organic product stream from the plant was checked using cross-flow filtration (Borsig oNF-1). Operating conditions were adjusted to miniplant operation conditions (40 °C, 15 bar) and are well within the range of performed lab experiments (Section 4.2.1.4). At a membrane cross-flow velocity of 0.7 m s^{-1} , fluxes of up to $13 \text{ L m}^{-2} \text{ h}^{-1}$ were achieved, which were within the range expected from pure substance tests by Zedel et al. [312]. Depending on the surfactant content in the retentate, even higher surfactant retentions of more than 95% could be demonstrated (within analytical accuracy). The selectivity for product and reactant was 85% so that only a low product accumulation has to be expected during long-term plant operation and OSN will not significantly compromise product yields.

Reaction Performance and Plant Operability

In the following, the reaction performance is discussed using conversion and yield depicted together with phase separation observations in Figure 4.89. Markups of the theoretically achievable yield are provided. Finally, Figure 4.90 depicts chemoselectivity toward tridecanal and n/iso-selectivity for tridecanal. Following the operation schedule, **SP 2** was used for reaction start and fast increase of yield in full recycle operation. This was successfully achieved for the shown plant operation and reaction yield Y matches its reference of 38.5% almost perfectly at the end of **SP 2** (duration of **SP 2** marks corresponding reaction residence time). Immediate activation of the rhodium catalyst in the desired resting state (Section 3.2) is achieved and validated with a chemoselectivity above 92%. For the continuous operation using the 1-dodecene feed in **SP 3**, conversion and yield initially decrease due to occurring surfactant accumulations in the settler. This was resolved until operation hour 70 (settler image in Figure 4.89) using soft sensor information and model-based control schemes. The reaction performance then stabilized in a steady state at a conversion of 38.8% and yield of 37.1%, which is again in very good agreement with the reference from the lab scale.

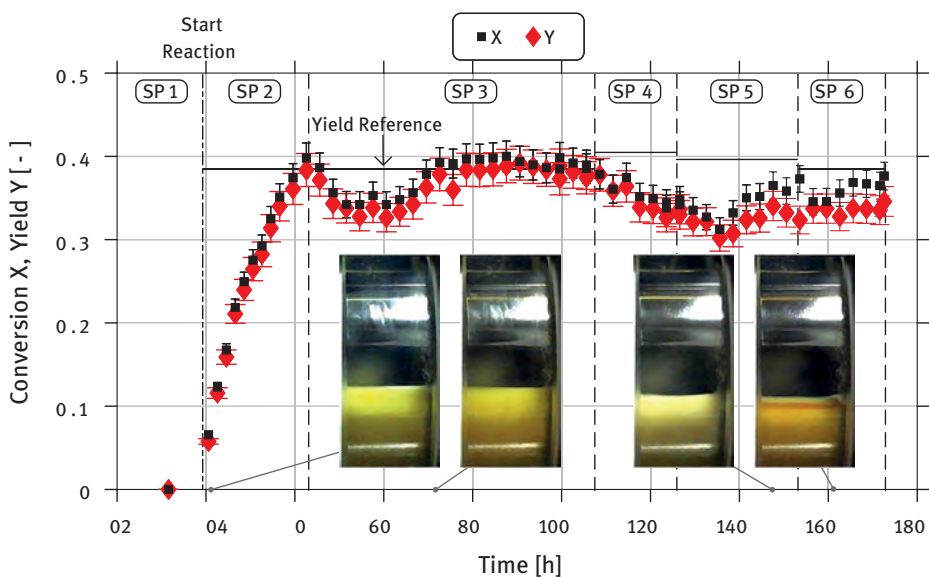


Figure 4.89: Operation results from the successful miniplant campaign: total conversion of 1-dodecene X and yield Y of tridecanal. Additionally, the visual observation from the settler is given at specific time points. Adapted from [117].

Starting with **SP 4**, the reaction performance significantly worsened and a drop in yield by more than 10 percentage points is visible. However, this behavior is rather

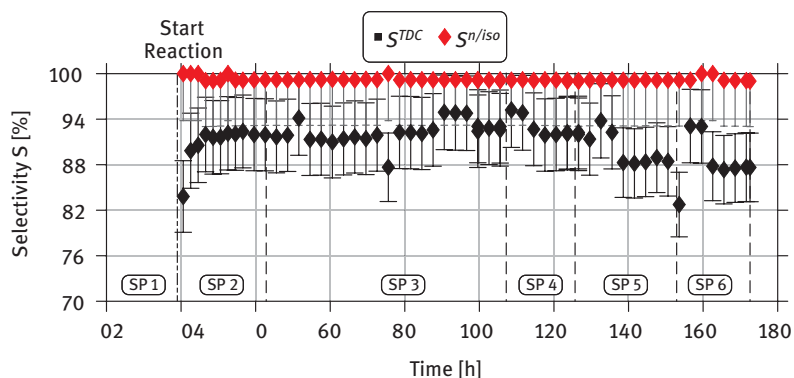


Figure 4.90: Operation results from successful miniplant campaign: reaction selectivity toward tridecanal S^{TDC} and n /iso selectivity $S^{n/\text{iso}}$ in the reactor. Taken from [117].

expected, since for **SP 4** the settler residence time was doubled to test the influence on the catalyst state and hence reaction performance. Comparing to the challenges for conventional plant operations significant by-product formation was expected. This could only partially be confirmed by a decrease in reaction activity. Chemoselectivity and n /iso-selectivity in contrast remained at desired high levels. In this case, a starting surfactant accumulation in the settler, which was further enforced for step experiments on the recycle ratio in **SP 5** is likely to have caused reduced surfactant concentrations in the reactor and hence reduced reaction rates. Seeing the webcam image from the settler sight glass at the end of **SP 5**, these accumulations were again resolved and stable phase separation was re-established, also leading to an improved reaction performance. Finally, **SP 6** shows the influence of an increased reaction temperature, expecting a reduction in chemo-selectivity (Section 3.2). This was partially confirmed in the miniplant, given a reduction of the selectivity toward tridecanal to 88%, despite re-establishing stable phase separation operation. Additionally, a persistent change in color of the catalyst solution was observed (last image in Figure 4.89), indicating changes in the catalytic system (pre-equilibria or decomposition).

Final Remarks

Concluding, a successful proof of concept for the hydroformylation of 1-dodecene in microemulsions was obtained for a continuously operated miniplant. Specifically, reaction conversion and product yield are in very good agreement with lab references and model predictions. All responses observed in the miniplant induced by step experiments on experimental controls resulted in the expected behavior of the system and can be explained based on the knowledge from the systematic system analysis. Additionally, exceptionally good results were obtained for chemo- and n /iso-selectivity, which remained above 91% and 99%, respectively, for desired

operating points. Using the model-based soft sensor and optimal offline and online control trajectories (Section 5.4.4), also a stabilization of the highly dynamic and transient phase separation of the microemulsion was obtained throughout all operational or transient states of the plant. No further operational limitations or challenges have been encountered and hence the application of microemulsion as liquid multiphase reaction media is generally encouraged.

4.2.4 Concluding Remarks

To this end, microemulsions are identified as a very promising switchable solvent system. They provide superior features enabling highly chemoselective homogeneously catalyzed reactions at high space–time–yields (Sections 3.2 and 4.2.3), while likewise showing remarkable separation efficiency. Catalyst and surfactant recycling are attainable to very high levels (Table 4.8 [212]) at minimal equipment and operating costs by simple means of gravity-driven phase separation. Additionally, the application of water as a solvent for the catalyst is enforced while co-solvents for liquid substrates are typically not required, both improving economic and ecologic viability. These properties can be implemented into a mixer–settler process scheme (Figure 4.44), for which a successful proof of concept has been shown for the hydroformylation of 1-dodecene.

However, these performance features are generally only unlocked if the following criteria are met:

- Substrates and catalysts have to be chemically inert regarding water and applied surfactants.
- Suitable surfactants regarding the polarity of water and structural properties of the substrate need to be available. Ideally, the usage of co-solvents is to be avoided.
- Formed value-added products have to provide inverse polarity compared to the catalyst (can be modified via ligands) to allow for suitable phase distributions.
- The phase behavior of formulated MESs must provide applicable states for catalyst and surfactant recycling.
- Catalyst or formed (by-)products must not trigger emulsion stabilization and impede phase separation.

To date, almost no applications of MES for reactive processes are visible. A major reason for that is the rather complex thermodynamic behavior of these systems combined with their complex physicochemical properties. Together with the challenging chemical matrix, MES do not provide intuitive access for the chemical engineering practitioner. Hence, designing MESs as reaction media and synthesizing processes using those appears highly challenging due to a large number of possible interactions between MES formulation, its phase behavior, and the performance of desired chemical reactions. Given the complex phase behavior operating continuous processes is

challenging especially if uncovered impacts on the phase behavior are prone to severely deteriorate plant operation. With lacking large-scale implementations, experience in operating such systems is severely limited and often only stems from lab-scale investigations ($\text{TRL} \leq 4$) omitting the crucial step of catalyst recycling.

To unlock the potential of MES for industrial applications, several advancements have been achieved within our studies, which tackle these critical challenges. First of all, the overall complexity of MES is broken down to the question: what is the minimum required amount of information to (1) design an MES for conducting chemical reactions and (2) transfer this reaction system into a continuous production plant and achieve stable steady-state operation? To obtain relevant information several, methodical frameworks and guidelines are deployed (Section 4.2.1.5) to enable:

- Systematic choice of components for MES based on key experiments
- Analysis of the reaction behavior and interplay of reaction and phase system and development of suitable kinetic models
- Systematic analysis of the phase behavior, identification of operation strategies, and possible drawbacks

These frameworks are merged into a holistic guideline for the systematic identification of operation challenges for processes using MES and the subsequent development of tailored solutions for equipment design and process operation (Figure 4.59). Its application on the presented case study for the hydroformylation of 1-dodecene in MES confirmed key operational obstacles: the complex chemical matrix with interactions of reaction and phase behavior, handling of the surfactant, as well as the complex phase behavior and resulting high system dynamics. Such characteristics are likely encountered for any application of MES but are technologically manageable if sufficiently analyzed. We already propose tailored solution approaches in a model representation for the three-phasic separation of MES, which can be readily adapted for the formulation of soft-sensors regarding (otherwise immeasurable) system concentrations and the phase state. Connected with model-based process control strategies (Section 5.4.4), process operability is thus attainable and has been demonstrated in a miniplant. MES as a switchable solvent system for continuous processes has hence been proven feasible on TRL 5.

To further encourage the application of MES in industry, larger-scale demonstration plants ($\text{TRL} \geq 6$) and long-term operations are required. Therein, especially long-term catalyst stability, accumulation of impurities or by-products, and chemical stability of surfactants are of interest.

In preparation for that, future academic research is advised to further generalize existing selection guidelines and analysis methods for the usage of ionic surfactants and cosurfactants. To further increase economic viability, the application of OSN for additional oil phase purification is found to be superior and should be covered in detailed studies regarding catalyst retention, long-term reactant accumulation in continuous processes, as well as possible surfactant

fractionation (if technical-grade surfactants are applied). Connected to this, also novel process concepts with fully integrated mixer–settler systems and membrane reactor systems are to be tested. Advances in thermodynamic descriptions of MES and solubilization of components of various polarities therein (Section 3.1.7) are prone to unlock partially rigorous model formulations for MES phase behavior. Based on that, quantitative selection guideline based on desired reactants and a further reduction in experimental effort is attainable.

4.3 Pickering Emulsions

Sebastian Stock, Maresa V. Kempin, Lena Hohl, Marc Petzold, Kristin Hecht, Regine von Klitzing, Anja Drews

As outlined in Section 2.3, Pickering emulsions (PEs) are the youngest and least understood of the three different phase systems discussed in this book. In order to design continuous reaction processes using PEs and to predict productivity and separation performance, thorough characterization and quantification of the properties and behavior of the system under process conditions are required and a better understanding of the underlying mechanisms has to be gained.

4.3.1 Phase System Characterization

In this section, investigated particle types and relevant characteristics of formulated PEs such as stability, drop size distributions, rheology, mass transfer, and filterability are described.

4.3.1.1 Particle Types and Characterization

For the application of PEs as reaction environments, the (nano)particle choice plays a significant role as it influences several relevant emulsion properties. In the following, the behavior of three different particle types (halloysite nanotubes (HNT, Figure 4.91 (a)), fumed silica (Figure 4.91(b)), and silica nanospheres (Figure 4.91(c))) are presented which were chosen for the following reasons: HNT are a natural product and are applied in large amounts already, for example, in the ceramic industry [174]. Fumed silica production is simple, cheap, and well established at a large scale [6]. Although silica nanospheres are very common in science [123], their large scale production has not been realized, yet. Nevertheless, spherical particles are easier to model and therefore better suited to predict and explain reaction results. Cheap and commercially available particle types were chosen as they can facilitate the profitability of the system. Silica spheres were applied in a bottom-up approach to explain the dominant mechanisms.

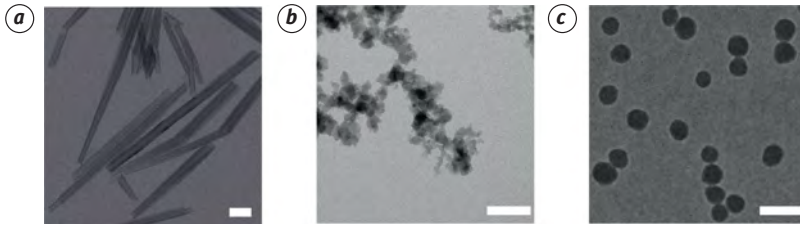


Figure 4.91: Transmission electron microscopy (TEM) images of different particle types used for PE stabilization. (a) HNT, (b) fumed silica, and (c) silica nanospheres. HNT and fumed silica are considered as commercial particles as they can be acquired at a low cost and in large amounts. White scale bars represent 100 nm [254, 258, 271].

Commercially Available Halloysite Nanotubes

HNT are found in almost every natural kaolin deposit [174]. The HNT presented in Table 4.12 have an aspect ratio of around 1:16 and an average length of 800 nm. The cylindrical lumen inside the HNT has a diameter of around 15 nm and the inner surface is charged positively while the presence of the silanol groups on the outer surface results in a negative surface charge. The silanol groups allow a surface modification via silanization. Positively charged HNT are not commercially available, yet, so they were made by modification using aminopropyltrimethoxysilane (APTES).

Table 4.12: Properties of pristine and modified HNT. The modification with APTES inverted their ζ -potential [251].

Particle type		HNT	HNT-NH ₃
Surface modification	[-]	Pristine	APTES
ζ -Potential	[mV]	-39	+50
Wettability	[-]	Hydrophilic	Hydrophilic

Commercially Available Fumed Silica

Fumed silica is manufactured by pyrolysis of chlorosilanes. In the reactor, the first nanometer-sized primary particles are formed which grow into larger aggregates and finally form a tertiary structure of micrometer size. Afterward, the surface properties are manipulated via silanization. In the following, results obtained with fumed silica purchased from Wacker (HDK series) are presented [276]. The particles differ in their shape (and thus tamped density) and their hydrophobicity (residual silanol and surface modification) but have a similar Brunauer-Emmet-Teller (BET) surface area (Table 4.13).

Table 4.13: Properties of the used commercially produced fumed silica [276].

Particle type		HDK [®] N20	HDK [®] H18	HDK [®] H2000	HDK [®] H20
Residual Si-OH	[%]	100	25	25	50
Specific particle surface area BET	[m ² g ⁻¹]	175–225	170–230	200	170–230
Tamped density	[g L ⁻¹]	40	50	100–250	40
Surface modification		Bare silica	Polydimethylsiloxyl	Trimethylsiloxyl	Dimethylsiloxyl

The hydrophobicity of the particles was measured by evaluating the contact angle of a water droplet on a particle layer deposited on a silicon wafer (Figure 4.92). Atomic force microscopy (AFM) studies of the particle layer were performed to prove a sufficient interfacial coverage by the particles and reproducible and low surface roughness. HDK[®]H18 was found to be the most hydrophobic particles followed by HDK[®]H2000 and HDK[®]H20. HDK[®]N20 are bare silica and very hydrophilic, thus, the droplet spreads fully on the particle layer.

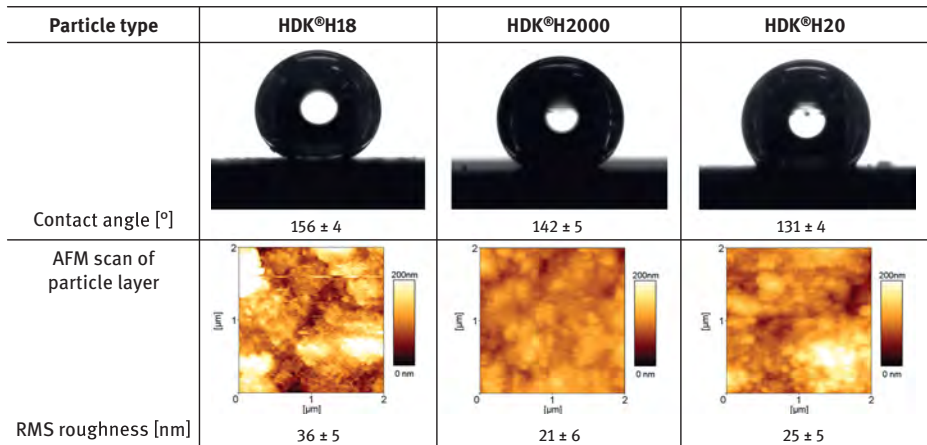


Figure 4.92: Investigation of the hydrophobicity of the different used commercial fumed silica particles. Contact angle errors were calculated from at least five drops and RMS roughness errors from four different spots [145].

Silica Nanospheres with Tailored Size and Surface Properties

For a quantitative understanding of the reaction process, it is helpful to use spherical instead of irregularly shaped particles. Besides composition and preparation method, the determining factors for the PE structure are the properties of the particles stabilizing it. The most important ones are the particles' wettability, their

size, and shape expressed by their specific cross-sectional area and their surface charge. The particles presented in the following were prepared via the Stöber process for silica nanospheres [257] and grown from the initial 50 nm spheres to 100 nm spheres using the method of van Blaaderen et al. [267] (Table 4.14).

Table 4.14: Determined particle properties of the tailored silica nanospheres (particle diameters were calculated from at least 10 TEM micrographs with at least 350 particles).

Aimed sphere diameter	50 nm	100 nm
Measured diameter (TEM) [nm]	45.7 ± 5	97 ± 5
Specific cross-sectional area [m ² g ⁻¹]	18.2 ± 0.4	8.0 ± 0.2
Specific surface area [m ² g ⁻¹]	72.7 ± 1.5	32.0 ± 0.5

Errors represent the standard deviation of the particle size distribution [258].

The particles were then surface modified using different silanes, and their wettability and ζ -potential were determined (Figure 4.93). The modification with ethoxy(trimethyl)silane (TMES) resulted in a contact angle on a particle layer of around 39° which shows their hydrophilicity. The modification with C18 chains (trimethoxy(octadecyl)silane and dimethyloctadecyl[3-(trimethoxysilyl)propyl]ammonium chloride) resulted in particle systems with similar hydrophobicity (around 110°). 50C18n⁻ are negatively and 50C18n⁺/100C18n⁺ are positively charged. The difference between 50C18n⁺ and 50C18n⁻ is only the sign in the surface charge and between 50C18n⁺ and 100C18n⁺ it is only the size.

Catalyst–Particle Interaction

The interaction between the particles and the catalyst plays a major role in the reaction behavior of a PE. The physical behavior of the catalyst is dominated by the properties of its ligand [253]. For the hydroformylation in PEs, the ligand SULFOXANTPHOS (SX) was used (Section 1.3). This ligand is soluble and negatively charged in water due to the dissociation of the Na⁺ ions from the sulfonate groups which make the ligand adsorb onto the positively charged surface of the modified particles. This can be seen in the ζ -potential curves (Figure 4.94) plotted against the amount of SX molecules per particle surface area k_N . SX had no influence on the ζ -potential of 50C18n⁻, but the ligand adsorbed onto the positively charged particles, decreased their ζ -potential, and reversed it to almost the same absolute value. This means, in the case of positively charged particles the adsorbed catalyst needs to be taken into account when evaluating the reaction results (Section 4.3.3.3).



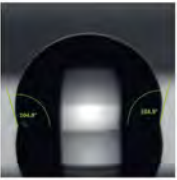

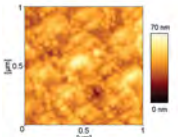
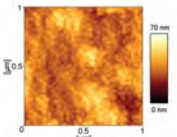
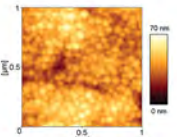
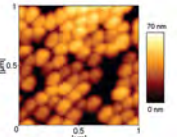
Particle type	50TMES	50C18n-	50C18n+	100C18n+
Surface modification	$\begin{array}{c} \text{H}_3\text{C} \\ \\ \text{H}_3\text{C}-\text{Si}-\text{O}-\text{CH}_2-\text{CH}_3 \\ \\ \text{H}_3\text{C} \end{array}$ ethoxy(trimethyl)silane	$\text{H}_3\text{C}-\left(\text{CH}_2\right)_{16}-\text{CH}_2-\begin{array}{c} \text{H}_3\text{CO} \\ \\ \text{Si}-\text{O}-\text{CH}_3 \\ \\ \text{H}_3\text{CO} \end{array}$ trimethoxy(octadecyl)silane	$\text{H}_3\text{C}-\left(\text{CH}_2\right)_{16}-\text{CH}_2-\begin{array}{c} \text{CH}_3 \\ \\ \text{N}^+-\text{CH}_2-\text{Si}-\text{O}-\text{CH}_3 \\ \quad \\ \text{Cl}^- \quad \text{OCH}_3 \\ \quad \quad \quad \\ \quad \quad \quad \text{OCH}_3 \end{array}$ dimethyloctadecyl[3-(trimethoxysilyl)propyl] ammonium chloride	
ζ -Potential [mV]	-44 ± 3	-50 ± 3	$+53 \pm 4$	$+53 \pm 4$
Contact angle [°]	 39 ± 2	 113 ± 3	 107 ± 4	 105 ± 3
AFM scan of particle layer				
RMS roughness [nm]	10 ± 2	13 ± 4	17 ± 4	29 ± 8

Figure 4.93: Particle properties of silica nanospheres after surface modification. The decoration with C18n chains is the reason for the hydrophobic character of the particles. Contact angle errors were calculated from at least five drops and RMS roughness errors from four different spots [258].

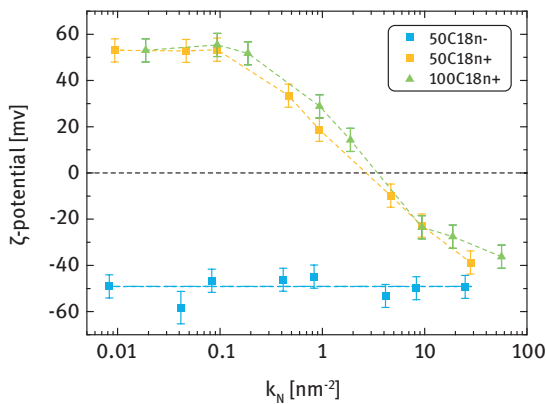


Figure 4.94: ζ -Potential against k_N (amount of SX molecules per particle surface area). At around three molecules per nm² surface area, a change in sign occurs for the curves of 50C18n+ and 100C18n+ [258].

4.3.1.2 Particles at the Liquid/Liquid Interface

During PE preparation, the particles occupy the emerging liquid/liquid (L/L) interface and not only the amount of particles [288] but also their arrangement determines the drop size. One of the optical techniques to observe particles directly at the interface is cryogenic scanning electron microscopy (cryo SEM). The different particle types showed disparate particle packing (Figure 4.95). HNT adsorbed laterally, fumed silica formed a thick layer on the droplet interface while silica nanospheres showed hexagonal packing.

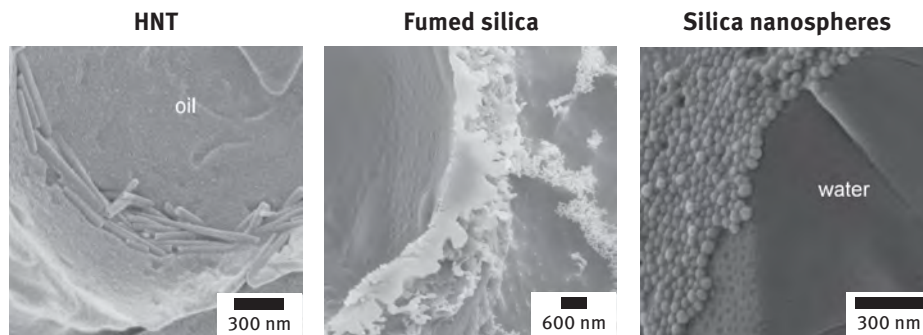


Figure 4.95: Cryo-SEM images of PEs prepared with different particles [251, 271].

The PE type (o/w or w/o) was determined by dyeing the water fraction of the PE with fluoresceine salt and analyzing the sample in a fluorescence microscope (Figure 4.96). The data show that no exceptions from the Bancroft rule were found for the investigated particles and compositions. The hydrophilic HNT and 50TMES formed an o/w PE, while the hydrophobized commercial H2O particles as well as the hydrophobized silica nanospheres formed a w/o emulsion. However, several particles such as H2O are able to stabilize both w/o and o/w emulsions (at very high water/oil ratios) [220]. For a continuous reaction process, where the catalyst is located in the aqueous phase, PEs need to be preferable of the w/o type and exhibit a high stability to enable the continuous separation of the catalyst containing water droplets from the product containing organic phase. Nevertheless, the o/w type is interesting for a batch approach, toward the design of a phase switchable system, and for reactions where the catalyst is located in the organic phase. A switch of the PE type, for example, for the intended removal of excess water in the reductive amination is possible by changing the hydrophobicity of the particles. This is either done by replacing the particles or by the use of responsive particles [287].

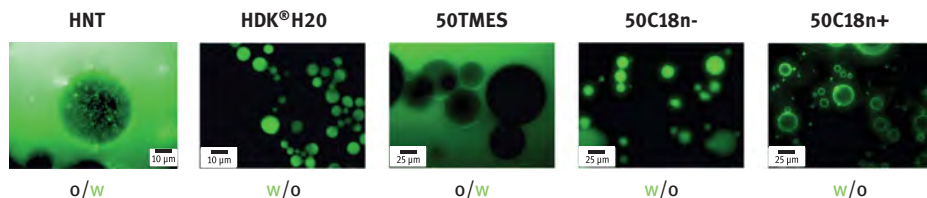


Figure 4.96: Fluorescence microscopy of PEs prepared with different particles (prepared with ULTRA-TURRAX® (UT), particle concentration 0.5 wt%, HNT: water:1-dodecene 3:1 w/w; other: water:1-dodecene 1:3 w/w). The water phase was dyed with fluorescein which is soluble in water but not in 1-dodecene. Green fluorescein dyed droplets prove w/o PE while black droplets confirm an o/w PE. Fluorescein also adsorbs at the positively charged particles [251, 252, 258].

4.3.1.3 Drop Size Distributions and Stability

Influence of Particle Type

As already described in Section 2.3, drop size distributions in PEs are governed by particle characteristics, fluid phase properties, and system composition (oil/water ratio, particle concentration). Furthermore, process conditions during emulsion preparation play an important role (dispersion device, energy input, temperature) [41, 266]. Although some general tendencies such as usually decreasing drop size with rising particle concentrations are well known, prediction of emulsion drop sizes is barely feasible due to the wide range of particle types and a lack of empirical correlations to describe the influence of preparation process conditions.

Figure 4.97 depicts representative cumulative drop size distributions of emulsions prepared using different fumed silica particles as shown in Table 4.13 at the same particle concentration of 1 wt%. Emulsions with H20 particles showed smaller drop sizes compared to H2000 and H18 and, therefore, a higher ability to stabilize emulsions, which is in agreement with, e.g., [105]. This is attributed to the higher residual silanol content and corresponding contact angle closer to 90° of H20 in comparison to H2000 particles (Figure 4.92) For the commercially available fumed silica nanoparticles, the contact angle seems to be the most important factor influencing drop sizes with a more pronounced effect than the BET area or tamped density [111, 145].

Influence of Particle Concentration

The influence of particle concentration of selected nonspherical particles such as the silica particle types H18 and H20 (w/o emulsions) as well as HNT (o/w emulsions) on Sauter mean diameters is shown in Figure 4.98 [253]. Drop sizes steadily decline with increasing particle concentration for both silica particles (Figure 4.98(a)) [42, 74, 182]. Below 0.25 wt%, no stable emulsions were created even if ultrasonication (US) at high energy dissipation rates was used. Between 0.25 and 0.75 wt%, the limited coalescence model applies, where droplets coalesce until their interface is fully covered by

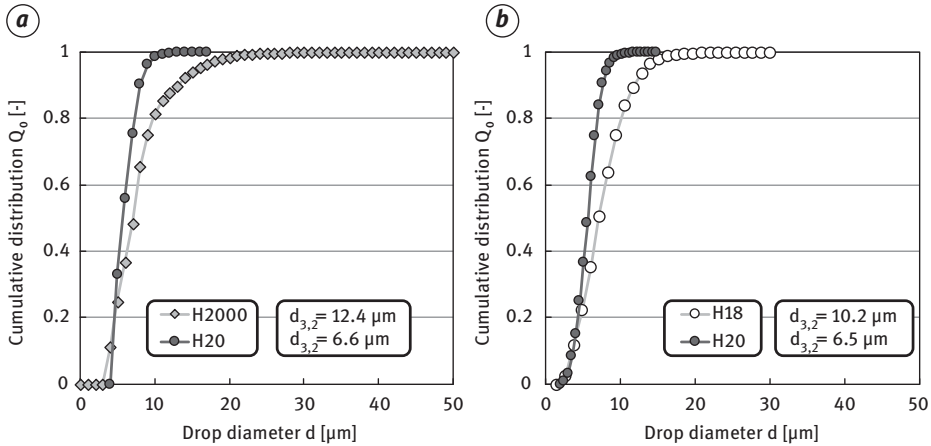


Figure 4.97: Drop size distributions of w/o PEs stabilized by 1 wt% of (a) H20 and H2000, water:1-dodecene 1:3 v/v, prepared with UT and (b) H20 and H18, water:dodecene 1:3 w/w, prepared with US. Distributions are a mean of triplicate measurements [111, 145].

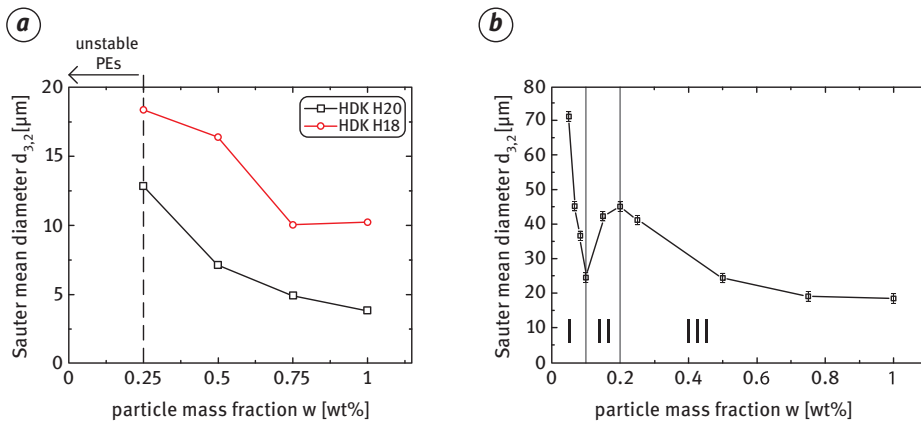


Figure 4.98: (a) Sauter mean diameters against particle concentration for silica particles H18, H20 with water:1-dodecene 1:3 w/w (w/o), created by US, and (b) of emulsions with HNT, water:1-dodecene 4.3:1 w:w (o/w), created by UT [251, 253].

nanoparticles. Above 0.75 wt% the drop sizes gradually seem to reach a plateau and are not a function of particle concentration anymore. The energy input or dispersion efficiency of the dispersion device becomes the limiting factor, which determines the corresponding minimum drop size that can be reached. Furthermore, a minimum drop size that can be stabilized by the available particles exists, based on the drop/particle size ratio [42, 266]. At high concentrations, particle multilayers can form at the interface (Section 4.3.1.5) or particles can remain in suspension instead of adsorbing at the

interface. Effects of such residual particles on rheology or of multilayers on mass transfer will be discussed in Sections 4.3.1.4 and 4.3.1.5. Differences between H18 and H20 in Figure 4.98(a) arise again from the different hydrophobicity and contact angle. For HNT particles shown in Figure 4.98(b), three regimes can be recognized: In regime I, the drop size decreased as the HNT concentration increased to 0.1 wt%. In regime II, a further increase in particle concentration resulted in rising drop sizes which decreased in regime III. The nonmonotonous change in the drop size indicates a change in the packing of HNT [251]. Isotropic orientation was observed, for example, for 0.083 wt% in contrast to 0.75 wt% with a preferred radial, side-to-side orientation. An analogous diagram for spherical particles is shown in Figure 4.111 in Section 4.3.3.1 where the impact of catalyst presence on drop sizes will be discussed.

Due to the larger interfacial area, smaller drop sizes are expected to be beneficial for mass transfer and reaction. Systems with H20 had the smallest Sauter mean diameter and narrowest distribution and were considered most suitable for the intended process due to their high stability against coalescence resulting in a large interfacial area [111, 143, 252]. Therefore, most further studies were carried out with H20 particles.

Influence of Preparation and Process Conditions

While the impact of emulsion composition on PE properties has been intensively studied in the literature, e.g., [111], knowledge about the impact of the homogenization process for PE preparation is surprisingly scarce. In contrast to dispersions or surfactant stabilized emulsions, where drop sizes are known to correlate with, for example, energy dissipation rate (e.g., [88]), no such correlations are available for PEs. Since the applicable dispersion devices vary in specific energy input and dispersion mechanism, a comparison of US and UT was performed, for example, by Skale et al. [248] with water/1-dodecene emulsions stabilized by H20 particles. Dispersion with US led to smaller drop sizes compared to UT, which is attributed to its higher energy input (Section 2.3). Furthermore, some emulsions with a lesser ability to hinder coalescence (e.g., with H18 particles) can be stabilized only with US, but not with UT at specific compositions and process conditions [145]. Furthermore, Skale et al. [247] showed that small emulsion drop sizes are crucial for stability during filtration; see also Section 4.3.1.6.

To develop correlations for drop sizes as functions of dispersion process characteristics (such as energy input or tip speed), a PE of constant composition (0.5 wt% H20, water:1-dodecene, 1:3 v/v) was prepared using two different dispersing heads of an UT (type S25N-10G vs. S25N-18G). The two devices differ in working volume, rotor-stator diameters, and gap width [143]. Additionally, different dispersing conditions were evaluated [142, 143]. High-speed rotor-stator homogenizers usually have energy dissipations in the range of 1,000 – 100,000 W kg⁻¹ [200]. For a given particle mass fraction, a minimum drop diameter was shown to exist which cannot further be reduced by an increase in dispersing speed or time [143]. Sauter mean diameters were

correlated using power-law models with energy density ($R^2 = 0.80$), energy dissipation rate ($R^2 = 0.85$), tip speed ($R^2 = 0.86$), and shear rate ($R^2 = 0.95$) [142, 143]. The correlation with energy dissipation rate yielded an exponent of -0.45 which is a bit higher than values reported for stirred L/L systems (between $-1/3$ and -0.4 for dissipation or inertial range, respectively [291]). As can be seen from the R^2 , a shear rate defined as the ratio of tip speed and the respective gap width between the rotor and stator was suited best to yield a coherent course of the curve, as indicated in Figure 4.99. This correlation can be used to predict the shear rate (and thus the tip speed for a given device) to obtain the desired Sauter mean diameter.

In stirred tanks, the energy dissipation rates are magnitudes lower than using US and UT (Section 2.3.2.2). Hence, larger drop sizes and a smaller interfacial area are achieved. To reach a better understanding of the dynamics of the dispersion process, dispersions in stirred tanks at comparatively low energy input were investigated. In stirred tanks with volumes around 0.5–2.5 L, drop sizes can be monitored in situ over time (Section 3.3.2.3). This is a significant advantage compared to the high energy dispersion in the small sample volumes used for dispersion with US and UT ($V \leq 0.1$ L), where only the resulting drop size after a specific dispersion procedure can be evaluated.

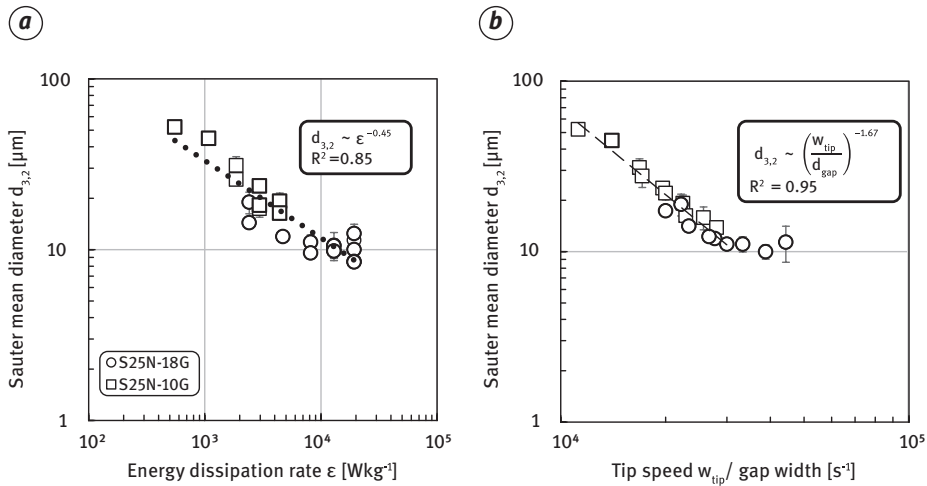


Figure 4.99: Sauter mean diameters of w/o PEs prepared with two different dispersing heads of an UT as a function of (a) energy dissipation rate and (b) shear rate = tip speed/gap width (0.5 wt% H₂O, water:1-dodecene, 1:3 v/v [142, 143]). All experiments were conducted in triplicate. Error bars represent the standard deviation.

For a stirred H₂O o/w emulsion, dynamic changes in drop size were monitored over time after agitation start at $t = 0$ s (see Figure 4.100) [220]. A steady state was achieved after approximately 700 s, when drop sizes stayed constant due to a balance between

drop breakage and coalescence processes. As shown in Figure 4.100(a), rising particle concentrations led to a reduction of drop sizes, similar to the effects shown in Figure 4.98. The reduction of agitation speed after 1,200 s led to a reduced energy dissipation rate and, therefore, shifted the ratio between breakage and coalescence events so that drop sizes increased for small particle mass fractions. At 1 wt% nanoparticle concentration related to the mass of dispersed phase (overall mass fraction of 0.152 wt%), the systems did not react to this change in energy input, indicating that coalescence was hindered.

In Figure 4.100(b), several characteristic diameters of the distributions such as the 10% and 90% quantile are shown for a particle concentration of 0.25 wt%. This comparison indicates that especially the smaller droplet fraction in the dispersed systems ($d_{n,10}$) is stabilized against coalescence at this intermediate particle concentration. The larger droplets in the systems, however, reacted to the changes in agitation speed and increased in size due to coalescence.

Especially at higher nanoparticle concentrations, the phase separation after stopping the stirrer was not always complete. Instead, a dense-packed zone formed with droplets remaining stable over a period of hours up to several days. In Figure 4.101, characteristic diameters of the drop size distribution of samples extracted from the dense-packed zone are shown. Within the first 24 h, the larger fraction of droplets within the dense-packed zone coalesced further ($d_{v,90}$), while the other fractions were barely affected. In the following hours, the drop size distributions became narrower in comparison, indicated by approaching values of $d_{v,90}$, $d_{3,2}$, and $d_{v,10}$. This also

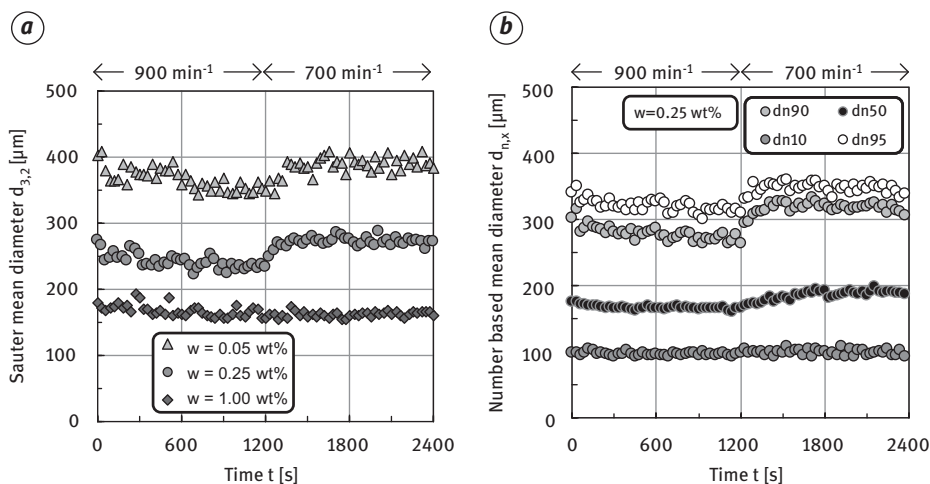


Figure 4.100: Sauter mean diameter for different particle concentrations (a) and number-based characteristic diameters for one concentration (b) in a stirred tank after agitation start at $t = 0$ s and with a change in energy input or stirrer speed, respectively, at 1,200 s (H₂O, *n*-heptane:water 1:5.67 w/w, $T = 20$ °C). Particle mass fractions are related to the mass of the dispersed phase and not the overall mass here [220].

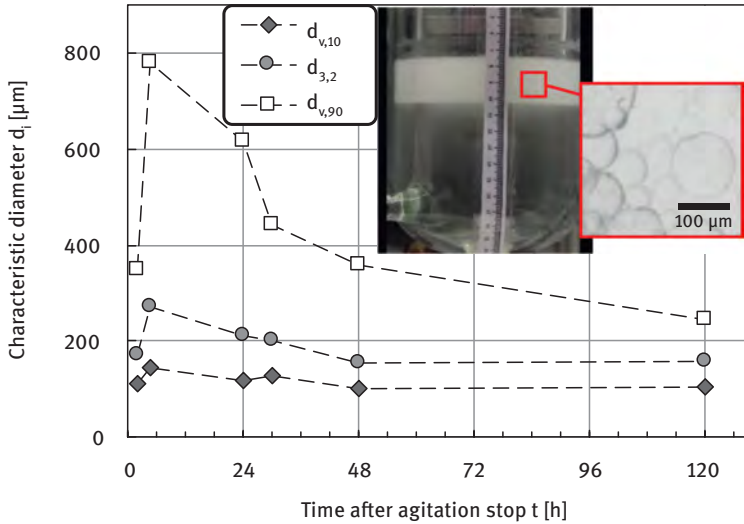


Figure 4.101: Characteristic diameters of the volume-based drop size distribution measured in samples extracted from the dense-packed zone in a stirred tank after agitation stop (1.0 wt% H₂O related to the mass of the dispersed phase, *n*-heptane:water 1:5.67 w/w, *T* = 20 °C, initial agitation speed $n = 700 \text{ min}^{-1}$) (unpublished data provided by Susanne Röhl, TU Berlin).

indicates that droplets above a certain size completely coalesced with their continuous phase. Eventually, drop sizes reached a constant value after 120 h which is close to the first value after 2 h. The resulting diameters represent the most stable fraction of the initial broader distribution generated in the stirred tank. In contrast to high-energy dispersion, parts of the organic phase always coalesced in these experiments. A further increase in drop size after 120 h due to Ostwald ripening is possible. For the size range generated by stirring, a decanter might be applicable to separate the larger droplets, followed by a filtration to recycle the smallest drop fraction. However, droplets of this size range created only via stirring might be too large for an efficient reaction and mass transfer. High energy input by US and UT and a subsequent filtration step seem to be the best option for application in the intended process (Sections 4.3.1.5, 4.3.1.6, and 4.3.2).

4.3.1.4 Rheology of Pickering Emulsions

Rheological behavior plays an important role concerning reaction as well as filtration, etc. and is, therefore, a crucial parameter for process design and operation.

Effect of Particle Concentration and Type on Suspension and Emulsion Rheology

Although the general effects of nanoparticles on suspension and emulsion rheology have already been discussed in the literature, quantification of the rheological

properties of the specific media is essential in terms of the fluid dynamic design of equipment for handling and mixing of both suspensions and emulsions as well as interpreting mass transfer and filtration results. Both suspensions and emulsions exhibit shear thinning and viscoelastic rheological behavior [140, 188, 286]. The nanoparticle type strongly influences the shear-thinning behavior of 1-dodecene/particle suspensions, as shown in Figure 4.102(a) for H20, H18, and H2000 particles at 0.5 wt%. Strong particle-particle interactions created by complex shapes and higher hydrophilicity in the case of H20 increase the shear thinning behavior in non-polar solvents. At high nanoparticle concentrations, the dynamic viscosity especially at low shear rates increases further [111, 140, 145, 188, 220]. Nanoparticle agglomerate orientation, breakup, and reconfiguration lead to a reduction of dynamic viscosity at high shear rates. A variation of fumed silica particle surface area only induced slight differences in viscosity, whereas particles with intermediate hydrophobicity (and consequently contact angles close to 90°) increased the dynamic viscosity and caused higher kinetic stability. In these cases, oscillatory measurements including amplitude and frequency sweep revealed a gel character ($G' > G''$) with little dependency on the angular frequency [111, 145, 245]. The ability to form a three-dimensional network structure is also an important characteristic for the filtration step (Section 4.3.1.6) [145]. Compared to suspensions, emulsions showed very similar behavior with rising viscosity at higher nanoparticle concentrations (Figure 4.102(b)). The extent of shear thinning and the apparent emulsion viscosity were further increased in comparison to suspensions by drop-drop interactions [5, 111, 196, 286].

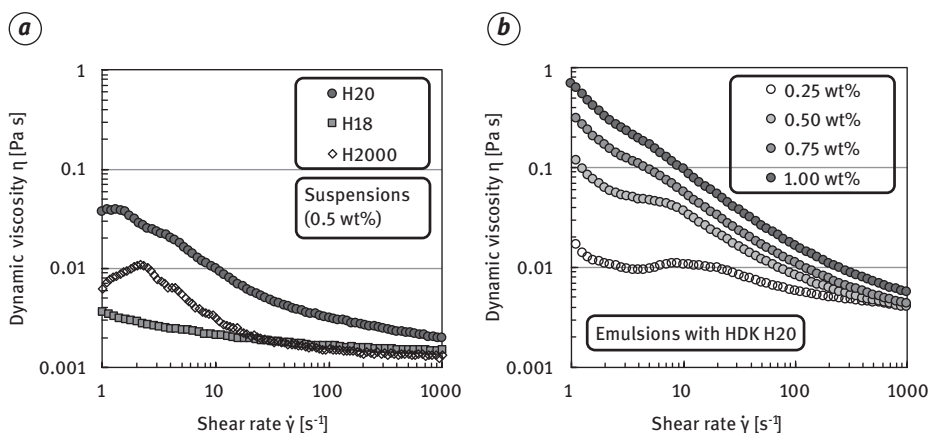


Figure 4.102: Impact of particle type on suspension rheology (a) (0.5 wt% silica particles in 1-dodecene, suspension prepared with US for H18 and H20, with UT for H2000). Emulsion rheology for H20 particles at different particle concentrations (b) (H20, water:1-dodecene 1:3 w/w, prepared with US). Triplicate measurements with a maximum relative error of 21% for small and 8% for high shear rates [111].

Effect of Dispersed Phase Fraction, Dispersion Mechanism, and Resulting Drop Size on Emulsion Rheology

Similar to high nanoparticle concentrations, high dispersed phase fractions and, therefore, high amounts of dispersed droplets increase the dynamic viscosity and pronounce shear thinning behavior due to drop-drop interactions. However, the dispersed phase fraction, particle concentration and type also directly influence the drop size, which was discussed for fumed silica nanoparticles in Hohl et al. [111].

An analysis of the effect of drop size on the viscosity without changing the other parameters was performed by Kempin et al. [143] and by Kempin and Drews [142] using different dispersion devices and dispersion intensities (Figure 4.103). The dynamic viscosity first decreased, passed through a plateau, and then increased with the tip speed/gap width ratio. This was attributed to the dominance of unbound particle networks at lower tip speeds and the stiffening of emulsions as drop sizes decreased at higher tip speeds [143].

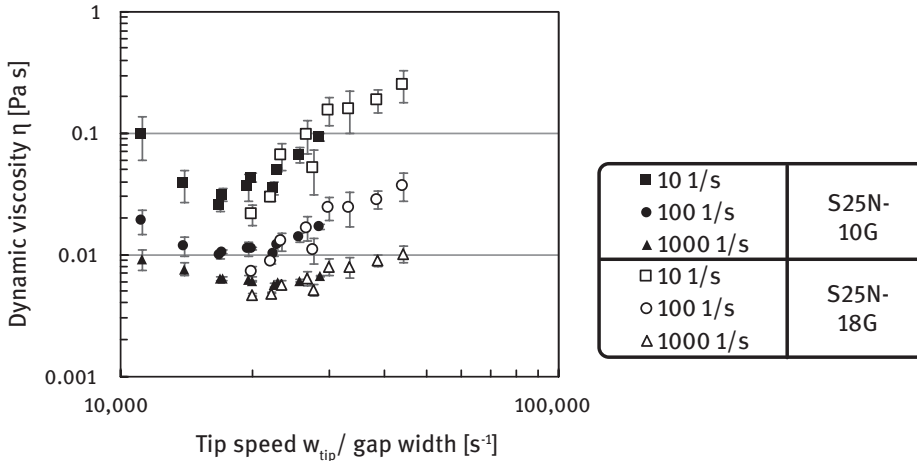


Figure 4.103: Apparent emulsion viscosity at different shear rates against tip speed/gap width, PEs prepared with two different UT dispersion heads S25N-10G and 18G (0.5 wt% H₂O, water:1-dodecene, 1:3 v/v) [142, 143]. All experiments were conducted in triplicate. Error bars represent the standard deviation.

4.3.1.5 Mass Transfer in Pickering Emulsions

Transfer Between Liquid Phases in Pickering Emulsions

As discussed before, the adsorption of nanoparticles at the interface hinders coalescence and will give rise to a mass transfer resistance. Thus, the mass transfer characteristics of PEs were studied to understand and optimize them for the application as reaction media. In contrast to surfactants, the effect of nanoparticles on interfacial

tension is less pronounced [41]. Some nanoparticles can even increase the interfacial tension by adsorbing impurities [41, 209, 253].

Investigations of the mass transfer of acetic acid from single toluene drop stabilized with nanoparticles in water [1, 85, 192, 225, 226] showed that the addition of nanoparticles up to a maximum of 0.003 wt% of the disperse phase increased the mass transfer rate by up to 83%, whereas higher amounts of nanoparticles led to a decline in mass transfer performance to below that of the nanoparticle free system. This general trend was demonstrated for nanoparticles of different materials (aluminum, titanium, silica), shapes (spherical, irregular), and sizes (5 – 150 nm). Smaller nanoparticles tend to show a stronger increase in mass transfer coefficient which is often attributed to micro convections, where the thermal motion of the particles enhances diffusion of the surrounding transfer component [153]. At higher particle concentrations, agglomeration leads to a reduction of thermal motion and the agglomerates more likely block the diffusion path of the transfer component [153]. The exact effect of nanoparticles on mass transfer at the interface remains unclear because the experiments were conducted with sedimenting drops that vary in size by up to 40% [225, 226]. The addition of nanoparticles also influences the movement of the drops. The presence of particles led to larger drops detaching from the capillary of the single drop cell (Section 3.3.2.1), with higher terminal velocities and enhanced convection. This alone increases the mass transfer coefficient and cannot be credited to the presence of nanoparticles at the interface or in the bulk. Additionally, the material system of toluene/water is known to show other fluid dynamic effects, like strong Marangoni convection behavior, for even the smallest concentrations of the transfer component acetic acid. This phenomenon is not considered in most publications and could influence the mass transfer results with nanoparticles as well [238].

Small drops created by dispersion promote high reaction rates. Nanoparticles further increase the interfacial area by inhibiting coalescence, but parts of this interface might not be available for mass transfer since nanoparticles can block the transfer of species [209].

To quantify the coverage of the interface and its influence on mass transfer, the effect of nanoparticles on the viscoelastic characteristics of droplets was investigated using the spinning drop technique for droplets of 1-dodecene in water; see Figure 4.104(a) [209]. For particle concentrations smaller than 0.5 wt%, only minor fluctuations of the viscoelasticity and viscous and elastic moduli were observed. With increasing concentrations up to 2.5 wt%, the viscous modulus remained almost unchanged, but the elastic modulus increased proportionally to the increase in nanoparticle concentration. The droplet developed solid-like viscoelastic properties and higher resistance against deformation [5]. This is attributed to the full coverage of the droplet by a solid layer of the entangled H2O nanoparticles [209]. Due to the irregular shape and heterogeneous size of H2O particles, an exact coverage of the interface cannot be calculated.

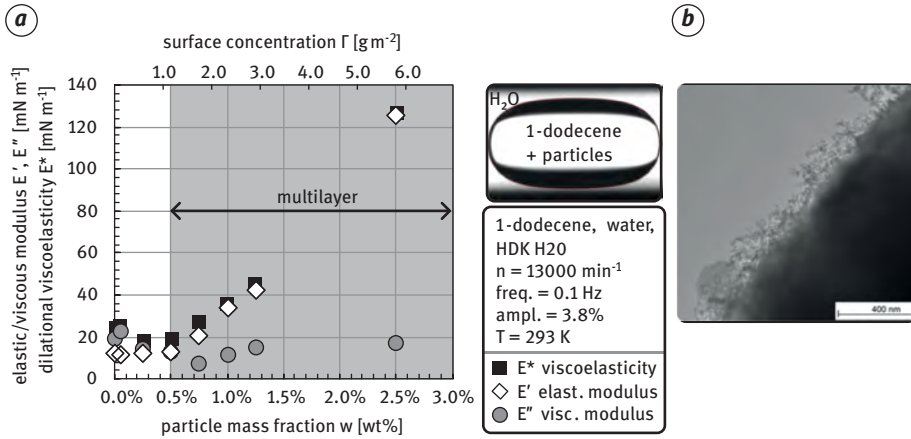


Figure 4.104: (a) Oscillatory spinning drop tensiometer measurements of the viscous and elastic moduli show that nanoparticle concentrations above 0.5 wt% tend to proportionally increase the rigidity of a liquid droplet in a PE, causing it to behave more like a solid particle. (b) SEM image of a L/L interface covered by H₂O nanoparticle agglomerates (water:1-dodecene) [209].

The effect of nanoparticles coverage on the mass transfer in stirred L/L systems was investigated using the saponification of benzoyl chloride to benzoic acid and sodium chloride as a fast model reaction, so the mass transfer is the limiting step (for details see [209]). In parallel, drop size distributions were determined using an in situ endoscope technique (Section 3.3.2.3) to calculate the L/L interfacial area and molar flow rates and Sauter mean diameters were determined at the time of 50% conversion. The mass flow of benzoyl chloride across the interface is governed by the area available for mass transfer. While the presence of nanoparticles, on the one hand, decreases the drop size and thus increases the interfacial area, its partial coverage and blockage by nanoparticles reduce the available area. Hence, an optimal nanoparticle concentration as assumed in Section 2.3.4.2 was found to exist, where mass flow across the interface is at a maximum (Figure 4.105). For higher particle concentrations and as soon as a maximum coverage of the L/L interface by particles is achieved, the decrease in drop size became less pronounced (Section 4.3.1.3). When drop sizes were barely affected or stayed constant at higher particle concentrations, the mass flow decreased to even below the value of a particle-free system [209]. Therefore, the choice of nanoparticle concentration plays a major role in the application of PEs as reaction systems.

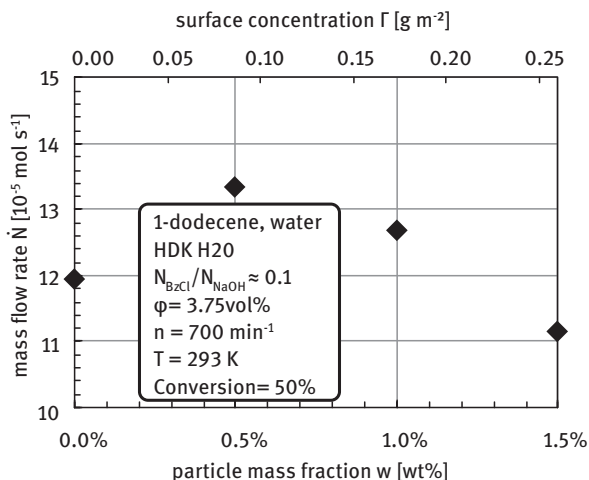


Figure 4.105: Overall mass flow rate of benzoylchloride across the L/L interface during saponification in a stirred tank for different particle concentrations, quantified using conductivity measurements (H₂O, water + NaCl in 1-dodecene + benzoyl chloride, w:o 1:25.67 w/w, stirrer speed 700 min⁻¹) [209].

Transfer Between Gas and Liquid Phases in Pickering Emulsions

For the reactions of interest, chemical species from the gas phase must be brought into contact with species both from an aqueous liquid phase and from an organic liquid phase. The mass transfer of the gas into the liquids depends not only upon the properties of the liquids but additionally on the transfer area of the gas bubbles in the PE. This, in turn, is influenced by the properties of the PE (emulsion type and continuous phase, particle type, and concentration).

G/L mass transfer was investigated in PEs made of water/1-dodecene/H₂O. A dramatic reduction in the rate of mass transfer can be seen in Figure 4.106(a) when the stirring frequency was reduced from 1000 to 615 min⁻¹. For gas-inducing impellers, decreasing the stirring speed does not only lead to larger bubble sizes but also decreases the overall amount of gas in the system which in turn results in a smaller overall transfer area and a slower mass transfer.

Mass transfer rates in PEs with low nanoparticle concentrations were very similar to the rates measured without the addition of nanoparticles at the same stirrer speed (1000 min⁻¹), and a similar decrease in the rate of mass transfer with an increasing volume fraction was observed (Figure 4.106(a)). The drop sizes in PEs, which were kept identical at the different phase fractions and are a magnitude smaller than those of the stirred emulsion without nanoparticles, therefore do not seem to influence the rate of G/L mass transfer. The effect of pressure was also negligible, although gas density and therefore bubble sizes were assumed to be affected. The solubility of hydrogen is much higher in the organic phase than in the

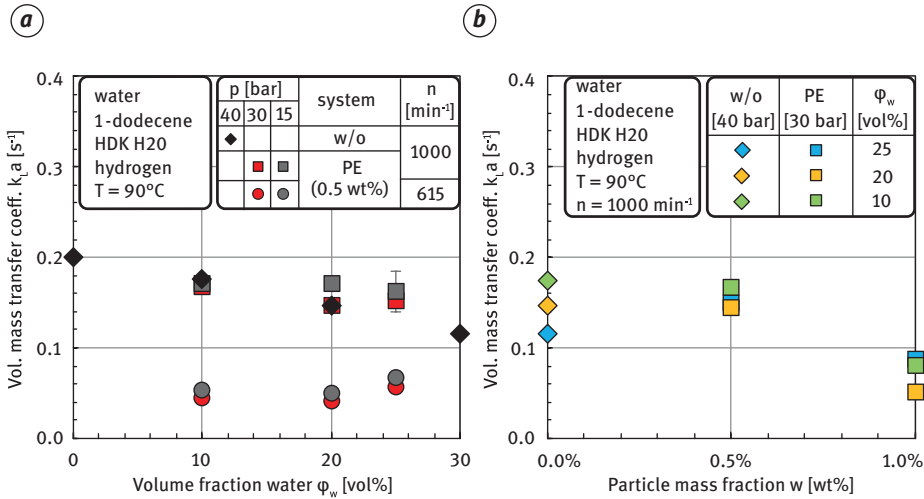


Figure 4.106: Volumetric mass transfer coefficient of a gas into a PE in a stirred tank: (a) influence of stirring frequency, water volume fraction, and pressure; and (b) influence of nanoparticle concentration for different water volume fractions (unpublished data).

aqueous phase. This effect is taken into account when considering the overall solubility of the gas in the system and the final resulting pressure (Section 3.1.3). A higher fraction of the organic phase in the system thus seems to slightly increase the rate at which the gas is dissolved in the emulsion. This observation raises interesting questions about how the emulsion interacts with the G/L interfaces surrounding the bubbles. As shown in Section 3.3.4, bubble sizes change with the disperse phase fraction, probably due to altered coalescence and breakage, leading to bigger bubble sizes for higher disperse phase fractions of water and ultimately reducing the mass transfer area and, therefore, $k_1 a$.

Adding a small concentration of nanoparticles (0.5 wt%) increased the rate of mass transfer rate in the PE with higher water volume fractions very slightly in comparison to the particle-free system (Figure 4.106(b)). Increasing the particle concentration further to 1 wt%, instead, reduced the mass transfer rate by 24–65%. This corresponds to the changes observed in the viscoelastic characteristics of the L/L interface of PEs. In this case, the G/L interface could be blocked and/or rigidified by adsorbing PE drops or residual particles. Additionally, the bubble sizes might be affected, since the PE drops are far smaller at higher nanoparticle concentrations and might affect bubble breakage differently.

Thus, PEs can be seen to provide comparable rates of G/L mass transfer to a stirred system without nanoparticles with the advantage that they eliminate the need for continual stirring to maintain the liquid emulsion and can therefore also be used in bubble column reactors.

4.3.1.6 Filterability of Pickering Emulsions

As outlined in Section 2.3, membrane filtration is a promising phase separation alternative to develop and realize genuine and economically feasible continuous reactions using PEs. Therefore, the possibility of drop retention and thus catalyst recycling via membrane filtration of w/o PEs was investigated. In the following, a membrane screening and selected results obtained with two different membranes are discussed. Finally, a PE filtration model is developed for process design and optimization.

Membrane Screening

For PE filtration, the micrometer-sized droplets of the catalyst containing dispersed (aqueous) phase as well as potentially freely suspended residual nanoparticles or nanoparticle aggregates (structures of micrometer size) have to be retained by the membrane, while the organic – educt and product containing – phase is continuously transported through the membrane. Therefore, only solvent-resistant ultrafiltration (UF) and organic solvent nanofiltration (OSN) membranes as listed in Table 4.15 were considered. Since most commercial UF membranes are still designed for aqueous applications the choice of possible membrane materials for the filtration of w/o PEs is limited [247].

Membranes that were not 1-dodecene permeable were not used in further trials. In the case of the DeltaMem membrane, no flux could be achieved in PE filtration trials. From the field of UF, only the ETNA01PP membrane was investigated further. For comparison, an OSN membrane of similar MWCO and similar pure 1-dodecene flux but different material was chosen. Although recommended operating pressures for the oNF-3 membrane are between 15 and 35 bar, significant flux levels could already be achieved at the lower applied pressures here. As seen in Section 4.2.1.4, oNF-1 and oNF-2 were also 1-dodecene permeable but were not used for the filtration of w/o PEs because their fluxes were significantly lower, as were those of the PuraMemFlux and the HZG PDMS membrane.

Filtration of Pickering Emulsions Using the Ultrafiltration Membrane ETNA01PP

The feasibility of w/o PE dead-end filtration was shown for the first time in 2016 [248]. The UF membrane ETNA01PP was used to separate w/o (1:3 w/w) PEs stabilized with 0.5 wt% H₂O particles. However, the washing fluxes J_{wash} of pure 1-dodecene during the pretreatment varied strongly between different membrane samples ($J_{\text{wash}} = 17.73 \pm 12.33 \text{ Lm}^{-2}\text{h}^{-1}$) [143, 145]. Retention of emulsion droplets and nanoparticles was 100% and the emulsions remained stable. However, an unexpected – but reproducible – filtration behavior was observed as the flux increased disproportionately with pressure and flux levels of the PEs were higher compared to flux levels of the pure solvent 1-dodecene (Figure 4.107(a)).

An abrasion of the membrane surface due to the particles could be ruled out as the reason as a comparison of SEM images of fresh and used membranes showed an

Table 4.15: List of investigated UF and OSN membranes (those selected for PE filtration studies are highlighted in bold). Molecular weight cut-off (MWCO) and materials according to manufacturers' information. Test conditions: pure 1-dodecene filtration at 4 bar for 90 min at room temperature and a stirring speed of 500 min⁻¹ in a Merck KGaA dead-end cell (working volume 91.5 mL). For a detailed description of the setup, see [145, 247].

Order no.	Manufacturer	MWCO	Type	Membrane material	Pure 1-dodecene flux	
		[Da]			[Lm ⁻² h ⁻¹]	Ref.
ETNA01PP	Alfa Laval	1,000	UF	PVDF (on PP)	17.7	[143, 145, 247]
ETNA10PP		10,000	UF		58.1	
GR81PP		10,000	UF	PES (on PP)	0.0	
GR90PP		5,000	UF		0.0	
GR95PP		2,000	UF		0.0	
PMUC	Microdyn Nadir	30,000	UF	Cellulose	93.7	unpublished data
PuraMem PMS600	Evonik	600	OSN	P84 [®] polyimide	0.0	
PuraMemFlux		/	OSN	Silicone-coated PAN	6.3	
DuraMem 900		900	OSN	Modified polyimide	0.0	
oNF-1	Borsig	600	OSN	Silicone polymer-based composite type	6.3	[313]
oNF-2		350	OSN		8.9	[313]
oNF-3		900	OSN		14.2	[141, 143, 144, 258]
DeltaMem	Sulzer Chemtech AG	20 nm	OSN	PAN	120 – 270	
SeIRO MPS-36	Koch Membrane Systems	1,000	OSN	PES	0.0	Unpublished data
HZG PDMS	Helmholtz Zentrum	/	OSN	PDMS (on PAN)	8.2	
HZG PIM	Geesthacht	/	OSN	PIM (on PAN)	0.0	

unharmful membrane surface structure after filtration; see Figure 4.107(b) [247]. Furthermore, a similar disproportionate flux increase was observed during filtration of PEs prepared with different organic solvents (decene, decane, and toluene) while the significant increase of PE fluxes compared to the pure solvent flux seemed to be specific for 1-dodecene. The drop size distributions changed differently during filtration depending on the solvent type, which suggests different coalescence behavior during

the filtration [247]. For 1-dodecene PEs, fluxes between 3 and 40 $\text{Lm}^{-2}\text{h}^{-1}$ were achieved for pressures between 1 and 4 bar. SEM images of the cross section of the membrane showed that the nanoparticles remain on the membrane surface and do not enter the pores, compare Figure 4.107(c).

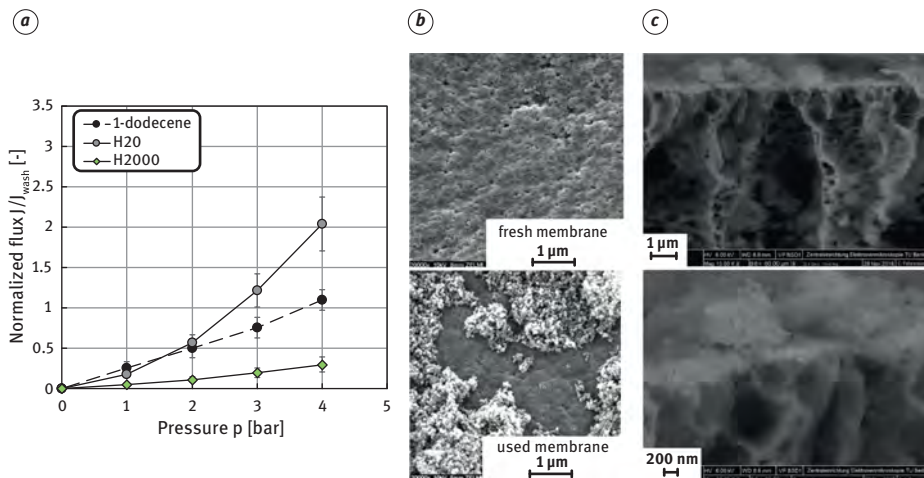


Figure 4.107: (a) Normalized steady-state fluxes as a function of pressure for w/o PEs prepared with different silica nanoparticles (0.5 wt% silica, water:1-dodecene, 1:3 v/v, prepared with UT) in comparison to pure 1-dodecene [145]. The flux J is normalized with respect to the flux J_{wash} from the membrane pretreatment to eliminate the impact of differences in membrane samples. All experiments were conducted in triplicate. Error bars represent the standard deviation. (b) SEM images of a fresh membrane in comparison to a membrane after w/o PE filtration (0.5 wt% H2O) [247]. (c) SEM images of the cross section of a membrane after w/o PE filtration (0.5 wt% H2O) (unpublished data).

The impact of different particle types on the filtration behavior is shown in Figure 4.107(a) [145]. PEs stabilized with H18 particles did not remain stable during the filtration process. The main differences were observed between PEs stabilized with H20 particles (intermediate hydrophobicity, $d_{3,2} \approx 10 \mu\text{m}$, shear-thinning rheological behavior, compare Sections 4.3.1.3 and 4.3.1.4) and H2000 particles (more hydrophobic, $d_{3,2} \approx 22 \mu\text{m}$, Newtonian rheological behavior). The H20 particles can form a three-dimensional network structure between particles and dispersed phase droplets, which was confirmed by rheological measurements and the formation of a several mm thick gel layer on the membrane surface after the filtration of suspensions without stirring [145]. Comparison of contact angles, as well as pure 1-dodecene fluxes of fresh membranes and membrane samples after the filtration of suspensions, revealed an increased dodecene wettability of the membrane surface after H20 particle contact. This effect led to an increase in the flux compared to the pure solvent. Due to the tendency to form a very loose network structure (calculated porosity >99%), the particles did not significantly add to the resistance. In contrast to that, H2000 particles

are unable to form such gel or network structures. Thus, freely suspended particles led to the formation of a dense filter cake (as confirmed by filtration of suspensions without stirring [145]) and a flux decline. This is in agreement with the UF of water-in-CPME PEs using a polyethersulfone (PES) membrane, where also higher fluxes were obtained using H₂O for PE stabilization in comparison to H₂O₀₀ [105, 106]. Hence, the interaction between particles, membrane, and solvent as well as the ability of the particles to form network structures significantly influence the filtration behavior of w/o PEs using the UF membrane ETNA01PP [145].

As reported in the literature, a suitable membrane pretreatment is necessary in order to apply (certain) membranes in nonaqueous systems [83]. Figure 4.108(a) shows that in comparison to just soaking (1 day) and washing (90 min, 4 bar) the membrane in 1-dodecene (“normal” pretreatment), successive soaking in water (3 h), 1 : 1 (v : v) mixtures of isopropanol/1-dodecene (3 h) and 1-dodecene (1 day) and subsequent washing (“specialized” pretreatment), led to higher fluxes and a linear increase of flux with pressure. This specialized membrane pretreatment seems to have opened up further pores or increased the already higher wettability due to the nanoparticle contact even further [145]. Filtration of w/o PEs prepared with CPME as the continuous phase and either spherical or colloidal silica nanoparticles using PES UF membranes resulted in constant permeability even without specialized membrane pretreatment [105, 106].

In contrast, during o/w PE filtration, compare Figure 4.108(b) – as relevant for the envisaged removal of polar phases – flux levels of all investigated PEs (stabilized with either H₂O or HNT) were comparable to the flux of pure deionized water and an almost linear behavior was observed. Hence, the presence of nanoparticle-covered oil droplets in water or unbound particle traces did not influence

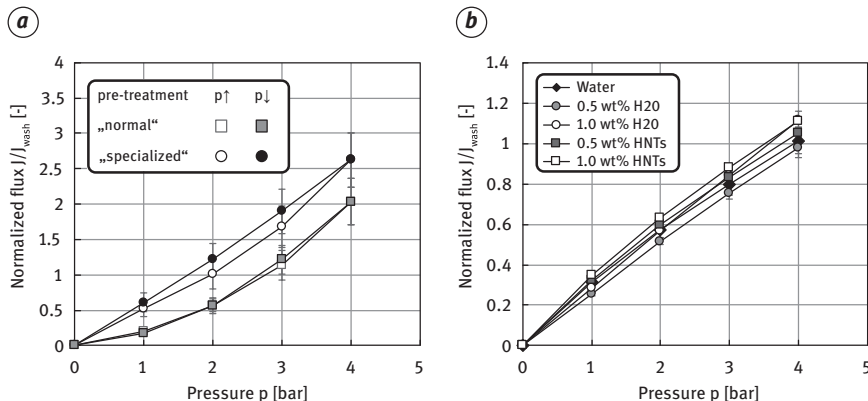


Figure 4.108: Normalized flux as a function of pressure for (a) w/o PEs (0.5 wt% H₂O, water: 1-dodecene, 1:3 v/v, prepared with UT) after normal and specialized membrane pretreatment and (b) o/w PEs (0.5 wt% and 1.0 wt% H₂O or HNT, water:1-dodecene, 3:1 w/w, prepared with UT). All experiments were conducted in triplicate. Error bars represent the standard deviation [145].

the filtration performance. As dispersed oil droplets tend to cream and residual (H₂O) particle traces should prevail within the organic phase, particle contact with the membrane at the bottom of the stirred cell and hence a potential change in membrane wettability is reduced in comparison to the filtration of w/o PEs. As shown in Figure 4.108 (b), the particle mass fraction did not significantly change the filtration performance.

Filtration of w/o Pickering Emulsions Using the Organic Solvent Nanofiltration Membrane oNF-3

The oNF-3 membrane showed high reproducibility of the filtration performance, the expected linear increase of flux with pressure and lower PE fluxes compared to flux levels of the pure solvent. In contrast to the ETNA01PP membrane, it is thus suited for a systematic parameter study to identify the main influencing parameters on the filtration of w/o PEs.

oNF-3 permeability remained unaffected by many potential influencing parameters (see Table 4.16) which shows that a stable and robust performance can be expected under different process conditions and that this membrane can be applied for a variety of stabilizing particles. The stirrer speed (stirring vs. no stirring) only had an impact when PEs stabilized by particles without the tendency to form network structures were filtered in long-term filtration experiments without stirring. The main influencing parameter was found to be the dynamic viscosity of the continuous organic phase – varied via the solvent type or the temperature.

Table 4.16: Overview of the main influencing parameters on w/o PE filtration using the oNF-3 membrane [141].

Investigated parameter	Impact on flux <i>J</i> ?
Particle type	No
Particle concentration	No
Dispersed phase fraction	No
Drop size distribution	No
Solvent type	Yes
Temperature	Yes
Stirrer speed	(Yes)
Hydroformylation products	No

From the acquired experimental data, for the first time, a mathematical model which describes the filtration of w/o PEs including the impact of temperature was established. A model based on the combination of the solution-diffusion model (pure 1-

dodecene flux through the membrane) and the resistance-in-series model was developed. The solution-diffusion model presented in Section 4.2.1.4 [313] could well be adopted for the prediction of temperature-dependent pure 1-dodecene fluxes through oNF-3 membranes with only slight modifications, compare Figure 4.109. Membrane compaction was not taken into account as the oNF-3 membrane was found to be incompressible within the experimentally investigated pressure range (up to 4 bar). Since the active layer thickness of the oNF-3 membrane was unknown, the ratio of diffusion coefficient and dry active layer thickness was taken as the only fitting parameter. To describe the temperature dependency of the diffusion coefficient, an exponential Arrhenius-type approach was used instead of the one used in [313]. Deviations between modeled (fitted and predicted) and experimental values were smaller than 10% indicating a high model accuracy even for extrapolation by 5 °C.

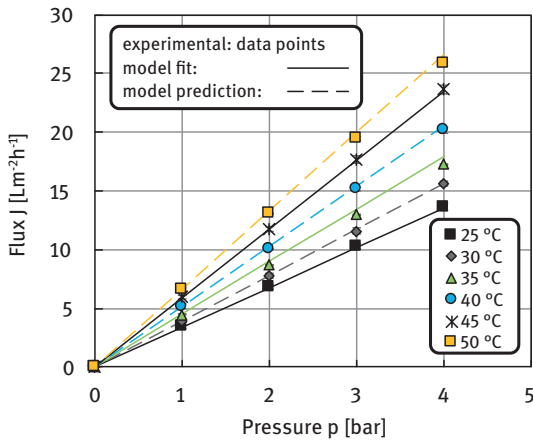


Figure 4.109: Experimental and modeled pure 1-dodecene flux at different temperatures as a function of pressure. For the model fit, experimental filtration data at 25, 35, and 45 °C were used. All experiments were conducted in duplicate. Error bars represent the standard deviation (where not visible, error bars are smaller than the symbol size) [144].

For w/o PE filtration, calculated filter cake resistances for both H2O and H2000 particles were found to be smaller than the membrane resistance and (almost) independent of temperature and pressure. No clear trend could be identified in the minor differences between filter cake resistances at different temperatures. Hence, the following equation (eq. (4.12)) to describe w/o PE fluxes as a function of temperature was used which includes a constant filter cake resistance R_c fitted only to data from the experimental run at 25 °C:

$$\frac{1}{J_i} = \frac{\eta_i R_M}{\Delta p} + \frac{\eta_i R_C}{\Delta p} = \frac{1}{J_{i,\text{SDM}}(T)} + \frac{\eta_i(T) R_{C,j}(25^\circ\text{C})}{\Delta p} \quad (4.12)$$

The index i represents the pure solvent 1-dodecene, while j stands for the particle type. As shown in Figure 4.110, deviations between modeled and experimental values from filtration of PEs using both particle types were smaller than 15%.

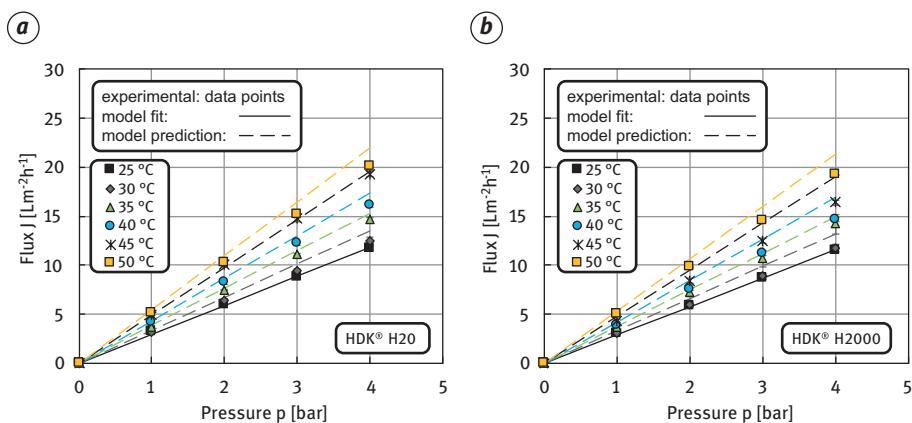


Figure 4.110: Experimental and modeled w/o PE flux (0.5 wt% silica, water:1-dodecene, 1:3 v/v, prepared with UT) at different temperatures as a function of pressure for (a) H2O and (b) H2000 nanoparticles. For the model fit, experimental PE filtration data at 25 °C were used. All experiments were conducted in duplicate. Error bars represent the standard deviation (where not visible, error bars are smaller than the symbol size) [144].

From a practical point of view, the model is beneficial as only a limited number of filtration experiments (here: pure solvent filtration at three distinct temperatures; w/o PE filtration for each particle type only at room temperature) were necessary to develop and fit a model which can predict solvent and PE fluxes over a wide temperature range.

The impact of dynamic viscosity of the pure continuous phase was also evident in trials with other solvents. Here, an increase of pure solvent flux as well as membrane resistances with decreasing molecular weight or dynamic viscosity, respectively, could be observed. The membrane could – again – be regarded as incompressible within the investigated pressure range. However, the membrane resistance presumably is influenced by different degrees of swelling. Again, cake resistances were smaller than membrane resistances and independent of pressure. An influence of solvent type on the cake resistance was observed. Clear tendencies with Sauter mean diameters could not be obtained [141].

4.3.2 Applications

Over the last decade, different catalytic reactions as shown in Table 4.17 have been performed in PEs at a laboratory scale (for a detailed overview over catalysis in PEs see the review articles by Bago Rodriguez et al. [3] or Chang et al. [46]).

Due to their biocompatibility as opposed to synthetic surfactants [207], traditionally, PEs have been employed in biocatalysis, but also acid/base or metal catalysts (e.g., Pd, Ru, Au, and Pt) have been studied [4]. A large variety of different liquid phases, including ionic liquids, and different particles were used with catalysts

Table 4.17: Overview of reactions in PEs reported in the literature (for details of chemical equations, see Section 4.1.3 or Section 4.2.2).

Reaction	Ref.	(Repeated) batch		Continuous reaction
		Reaction	Recycling	
Acetylation	[322, 297, 167]	✓	✓	–
Acylation	[261]	✓	✓	✓
Carboligation	[221]	✓	–	–
[Photocatalytic] degradation	[71, 186]	✓	–	–
Dehydration	[3, 311]	✓	✓	–
Epoxidation	[161, 175, 295, 316]	✓	✓	–
[<i>Trans</i> -] Esterification	[105, 106, 124–126, 205, 216, 277, 279, 280, 292, 300, 301, 305, 307, 315, 317]	✓	✓	✓
Hydro-deoxygenation	[55, 167, 303, 323]	✓	✓	–
Hydroformylation	[253, 254, 258, 262, 321]	✓	✓	(✓)
Hydrogenation	[67, 75, 91, 94, 104, 114, 166, 296, 306, 311, 314, 319]	✓	✓	–
Hydrolysis	[47, 49, 113, 172, 183, 204, 246, 285, 294, 307]	✓	✓	–
Knoevenagel condensation	[79, 223, 297, 299]	✓	✓	–
Oxidation	[56, 260, 304]	✓	–	–
Reduction	[66, 206, 259, 287, 316]	✓	✓	–
Other	[318] (three different types of reaction); [320] (methacrolein synthesis); [293] (fermentation of cholesterol)	✓	✓	✓

typically dissolved in the dispersed phase or anchored at/inside the stabilizing particles. For example, while Zhao et al. [321] and Tao et al. [262] used expensive mesoporous nanospheres which are tedious to make for the hydroformylation of long-chain olefins, Stehl et al. [253, 254] applied low-cost HNT and silica. As a result of this wide range of possible materials, PEs can be broadly applied and adapted, and have a large capacity for various industrial syntheses.

The potential to exceed the productivity of stirred dispersions and other investigated multiphase systems was demonstrated, for example, using catalytically active microbial whole cells for both PE stabilization and catalysis of a carbonylation reaction [221]. Reactions were performed in both w/o and o/w PEs and, where directly compared, a difference in selectivities and conversions was observed, i.e., the location of the catalyst seems to be important [3].

Published reactions in PEs are limited mainly to batch or repeated batch processes with demulsification/emulsification steps in-between reaction cycles [285, 307]. Apart from the possible damage to the catalyst, this strategy would require multiple energy inputs. In 2016, Zhang et al. [318] claimed a continuous w/o PE reaction in a packed bed. With around 100 h and more, however, the achieved residence times greatly exceeded those of typical industrial applications of continuous (bio)catalysis and were thus not industrially feasible. Tang et al. [260] and Zhao et al. [320] were able to reduce this to around 2–5 h in similar setups with drop sizes around 50 μm . With filtration being viable [247, 248], in the meantime, the first continuous biocatalysis in a w/o PE in a membrane reactor was successfully demonstrated by Heyse et al. [105, 106]. Over 8 hydraulic residence times, the process could reproducibly be run with economically feasible space-time-yields during which the PE remained stable and the enzyme did not suffer any activity loss.

4.3.3 Application Case Study

After fundamental investigations on individual phenomena, selected complete reacting systems were studied and applied to repeated reaction and filtration cycles to mimic the catalyst-containing droplet recycle in a continuous process. In the following, the influence of catalyst on emulsion drop sizes and available catalytically active area is discussed first and quantified using the tailored nanospheres presented in Table 4.14 and Figure 4.93. The decoration with C18n chains is the reason for the hydrophobic character of the particles. Contact angle errors were calculated from at least 5 drops and RMS roughness errors from 4 different spots [258]. Furthermore, selected results on reaction and filtration using HNT (o/w), silica nanospheres and commercial silica nanoparticles (w/o) are presented.

4.3.3.1 Influence of the Catalyst (Rh-SX) on the Pickering Emulsion Properties

The catalyst ligand SX was found to reduce the drop size for all used particles. The drop size $d_{3,2}$ against particle mass fraction w curve shows a reciprocal behavior (Figure 4.111) for both PEs with and without SX. The difference is found in the packing parameter s . Derived from eq. (2.3–2), eq. (4.13) describes this behavior and enables the determination of the packing parameter s under the assumption that all particles are located at the interface:

$$d_{3,2} = \frac{6sV_{PE,tot}}{a_{\emptyset} m_p} \varphi_w = \frac{6s\varphi_w V_{PE,tot}}{a_{\emptyset} m_{PE,tot} w} \quad (4.13)$$

φ_w is the volumetric water fraction, $V_{PE,tot}$ is the total PE volume, a_{\emptyset} is the specific particle cross-sectional area, $m_{PE,tot}$ is the total PE mass and m_p is the total mass of the particles. While all these parameters are known and kept constant, the packing parameter, s , is determined via a fit. In the case of the silica spheres, the packing parameter without SX was found to be close to the ideal hexagonal packing parameter of $s = 0.91$. The samples containing SX exhibited a smaller packing parameter of around $s = 0.69$. This implies that large particle-free voids form at the drop interface, which presumably is filled with SX.

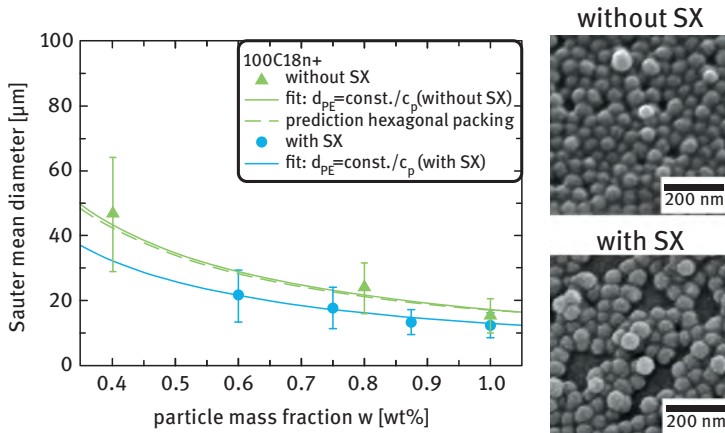


Figure 4.111: Drop size of PEs prepared with increasing mass fraction with and without SX (prepared with UT, water content 20 vol%). The presence of SX reduces the drop size. On the nanoscale this results in large voids in the hexagonal structure presumably filled with SX. On the right, the same effect is shown in cryo SEM for the 50 nm sized particles (50C18n+). When the PE was prepared with SX, large voids were visible between the particles at the drops surface [258].

Since SX adsorbs at the interface and on positively charged particle surfaces, the catalytically active surface area in the case of positively charged particles includes the particle area protruding into the oil phase. Since SX does not adsorb onto negatively charged particles, in the case of negatively charged particles only the voids between

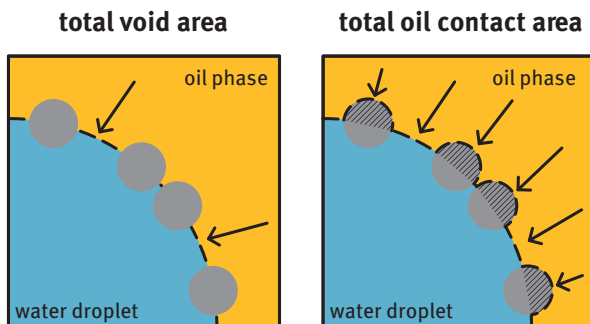


Figure 4.112: Total void area vs. total oil contact area. In the case of negatively charged particles, the reaction only takes place at the water–oil interface between the particles (left). For PEs stabilized by positively charged particles, catalyst adsorbs onto the particles and activates the particle–oil interface (right) [258].

the particles are catalytically active. The total void area (Figure 4.112, left, A_{void}) is calculated using eq. (4.14):

$$A_{\text{void}} = A_{\emptyset} \frac{1-s}{s} \quad (4.14)$$

A_{\emptyset} is the total cross-sectional area of the used particles. For positively charged particles, the particle area protruding into the oil needs to be included. This total oil contact area (Figure 4.112, right) is calculated for spheres with a contact angle of around 90° by eq. (4.15):

$$A_{\text{tot}} = A_{\emptyset} \frac{1+s}{s} \quad (4.15)$$

4.3.3.2 Emulsions Stabilized by HNT (o/w)

PEs stabilized by HNT are of o/w type. While this is not the ideal case for the subsequent catalyst retention intended here, reactions carried out in these systems provide new insights into the reaction process. Compared to PEs stabilized by pristine HNT, the yield of reactions in PEs prepared with positively charged HNT was increased by around 80% (Figure 4.113(a)) as the adsorption of the negatively charged catalyst complex onto the HNT particles facilitated the reaction. A more detailed analysis of this mechanism was investigated with the tailored silica spheres (Section 4.3.1.1). The yield was higher when a higher energy input was applied during preparation. The PE prepared with US exhibited a more than fourfold higher yield than the PE prepared with the UT at the expense of the n : iso ratio. A deeper investigation of the reaction process showed that the conversion stagnated after around 3 h (Figure 4.113(b)). This is explained by the increasing attachment of the particles onto the drops interface

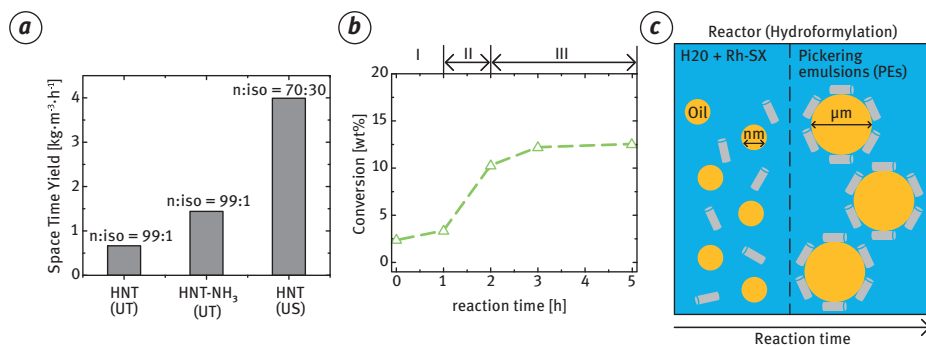


Figure 4.113: (a) Aldehydes space-time-yield (calculated after 24 h, $c_{\text{Rh(acac)(CO}_2)} = 3.9 \times 10^{-3} \text{ mol L}^{-1}$, $c_{\text{SX}} = 15.4 \times 10^{-3} \text{ mol L}^{-1}$, SX:Rh = 4:1, w:o = 3:1, 0.5 wt% HNT) in PEs stabilized by untreated and surface-modified (HNT-NH₃) HNT prepared with UT or US. (b) Conversion over reaction time for HNT particle-stabilized PEs prepared with UT. Conversion reaches a steady state after about 3 h. This is explained by the increasing amount of HNT adsorbed at the interface (c) [253].

over the reaction time (Figure 4.113(c)). SEM micrographs taken immediately after PE preparation by US show droplets in the nano-sized regime without particles attached. Later during the reaction, the interfacial coverage increased until a thick layer hindered the interfacial o/w contact. Membrane filtration (using the UF membrane ETNA01PP) of HNT stabilized PEs was successful – emulsions could be concentrated up to 90 vol % dispersed phase fraction [145, 254].

4.3.3.3 Reaction in and Filtration of Pickering Emulsions Using Tailored Nanospheres (w/o)

The space-time-yield after the hydroformylation of 1-dodecene with Rh-SX (Figure 4.114(a)) was higher for PEs with positively charged silica spheres than for PEs with the negatively charged ones. This is a result of the ability of the positively charged particles to attract the negatively charged catalyst complex as shown in Figure 4.94. This means, vice versa, that the amount of catalytically active interface is larger for PEs stabilized by positively charged particles (Section 4.3.3.1). In the case of the negatively charged particles, the reaction takes place only in the voids between the particles while in the case of the positively charged ones, additionally to the voids the reaction also takes place at the particle-oil interface. Normalizing the conversion (number of molecules) with the individual active surface area (Figure 4.114(b)) shows that the conversion rate per active area (CRAA) is almost identical for all three investigated systems. This implies that the catalyst is equally concentrated at the surface of particles and in the voids between the particles and is equally efficient on both. Comparing the results of the smaller 50C18n+ particles with larger 100C18n+ particles, the yield, as well as the CRAA is very similar since the drop sizes of both PEs are equal. It has to be noted that the experiments were

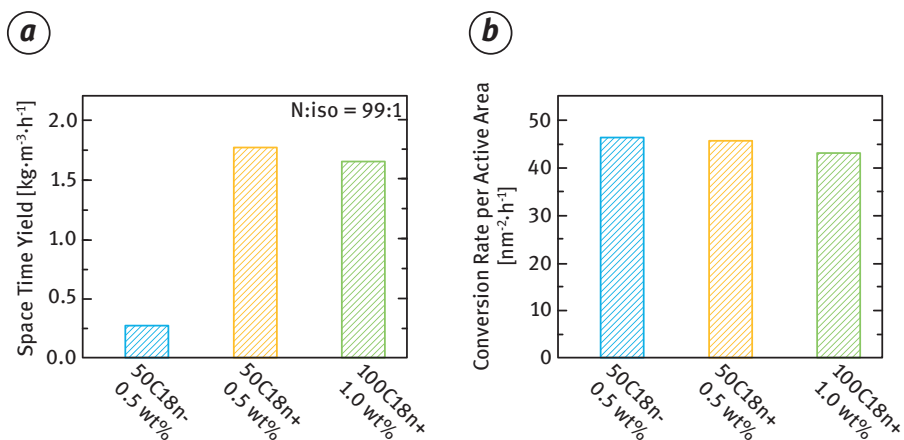


Figure 4.114: (a) Space-time-yield (calculated after 20 h) for PEs stabilized by spherical particles varying in size and surface charge ($c_{Rh(acac)(CO_2)} = 3.65 \times 10^{-3} \text{ mol L}^{-1}$, $c_{SX} = 15 \times 10^{-3} \text{ mol L}^{-1}$, SX:Rh = 4:1, w:o = 1:3). (b) The conversion rate per active area was calculated using eq. (4.14) for 50C18n- and eq. (4.15) for 50C18n+ and 100C18n+ [258].

designed to elaborate the particle-catalyst interaction, and that higher space-time-yields can be expected at optimized operating conditions.

To separate the catalyst containing dispersed phase droplets from the organic phase (consisting of 1-dodecene and the reaction products), filtration using the oNF-3 membrane described in Section 4.3.1.6 was applied. The flux shown in Figure 4.115(a) was normalized with respect to the pure 1-dodecene flux from the membrane pretreatment. A steady-state flux was reached after only a few minutes. The permeate was clear and colorless and no water breakthrough was observed. Neither particle size nor particle surface charge showed a significant influence on the filtration performance. Interestingly, the presence of catalyst and reaction products also did not influence the filtration behavior as the filtration of PEs prepared only with water, 1-dodecene and the tailored nanoparticles showed the same (normalized) flux level at a pressure of 4 bar. In general, w/o PEs could be concentrated up to a dispersed water phase fraction of about 80% (unpublished results for oNF-3, published for ETNAO1PP in [247]). The PEs remained stable during the whole process and also the drop size – measured for freshly prepared emulsions, after the reaction and after the filtration process, respectively – stayed constant. This proves the general applicability of the PEs in a larger scale separation process and paves the way to a continuous reaction and filtration system.

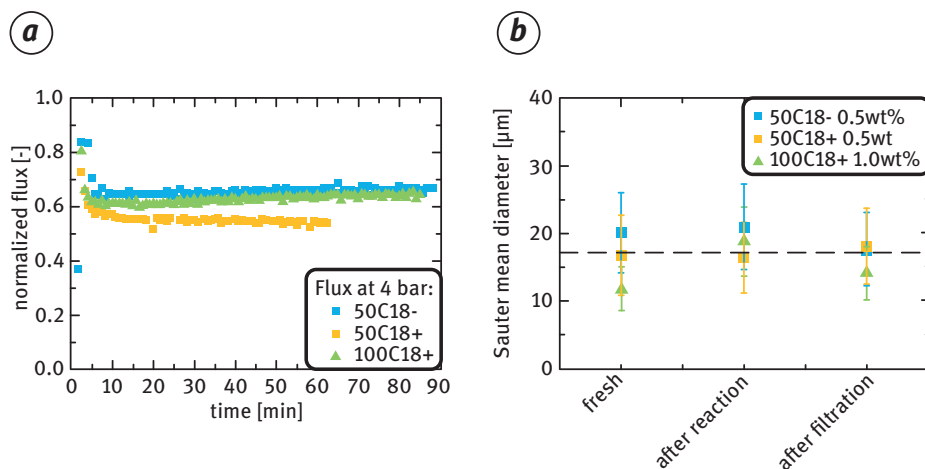


Figure 4.115: (a) Normalized flux during the filtration of PEs at 4 bar after the reaction. The flux was normalized with respect to the pure 1-dodecene flux from the membrane pretreatment. PE fluxes varied between 8.1 and 11.3 $\text{Lm}^{-2}\text{h}^{-1}$ for the different particle types. (b) Drop sizes of PEs stabilized by different particles. The PEs were stable over the whole process and no change in drop size was observed [258].

4.3.3.4 Reaction in and Filtration of Pickering Emulsions Using a Commercial Particle System (w/o)

The implementation of hydrophobic commercial particles is the essential step towards a large-scale industrial application. Figure 4.116 shows results obtained using the commercially available HDK[®]H2O fumed silica. Two 1-octene hydroformylation reaction cycles were carried out. In between, 50% of the oil phase was separated from the water droplets via membrane filtration (using the UF membrane ETNA01PP, Section 4.3.1.6). Flux at a pressure of 2 bar was approximately 30 $\text{Lm}^{-2}\text{h}^{-1}$. Since the permeate was colorless and clear, no catalyst leaching occurred. The separated volume was replaced with fresh 1-octene and a second batch reaction was carried out. The conversion in the second run was increased at the expense of the selectivity (Figure 4.116(a)). This indicates that a small portion of the TPPTS catalyst was deactivated or destroyed due to the exposure to oxygen when transferring the emulsion from the lab reactor to the lab membrane filtration unit. In a continuously operated process, this deactivation is easily avoided by using a sealed reactor/filtration loop and additionally flushing with a protective gas. The determined drop sizes in every stage (Figure 4.116(b)) showed the stability of the PEs over the whole process. The drop size stayed constant at around 13 μm and no excess water was observed (Figure 4.116(c)).

With HDK[®]N20 particles (o/w-PE), space-time-yields of around 7 $\text{kg m}^{-3} \text{h}^{-1}$ (calculated after 24 h) were achieved in batch experiments [253].

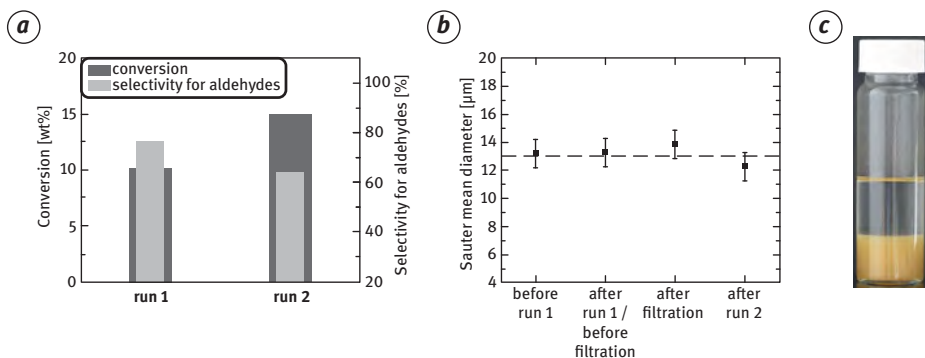


Figure 4.116: (a) Conversion after 24 h for the hydroformylation in water-in-1-octene PEs ($C_{\text{Rh(acac)}(\text{CO})_2} = 12.5 \times 10^{-3} \text{ mol L}^{-1}$, $C_{\text{TPPTS}} = 50 \times 10^{-3} \text{ mol L}^{-1}$, TPPTS:Rh = 4:1, w:o = 1:3) stabilized by HDK[®]H₂O (0.5 wt% and prepared with UT). (b) Sauter mean diameters d_{32} before and after reaction/membrane filtration. (c) PE after two reaction runs and after filtration [251].

4.3.4 Concluding Remarks

In summary, it could be shown that recent work has both advanced the state of the art of PE research in having characterized the system further and having explained fundamental influences and mechanisms, while it has also facilitated its application as reaction media in continuous processes.

In particular, the interaction of the catalyst with the particles was found to have a large impact on the reaction results. With the help of the defined spherical particles, it could be shown for the first time that the catalyst is equally effective adsorbed onto the particle surface protruding into the oil phase as it is independently attached to the w/o interface.

Apart from the PE composition, the impact of dispersing conditions during PE preparation on characteristic PE properties was investigated. Correlations between Sauter mean diameters, respectively, and energy dissipation rate or ratio of tip speed and rotor-stator gap width were developed. These now allow tailored preparation of PEs with optimum drop sizes.

With regard to L/L mass transfer, an optimum particle concentration was found to exist. At lower concentrations, drop sizes became too large for efficient mass transfer, while at higher concentrations, particles blocked parts of the available interface and even formed multilayers which changed the viscoelastic behavior of the interface and inhibited the L/L mass transfer further. Similarly, higher particle concentrations reduced the G/L mass transfer. This was accompanied by smaller PE drop sizes. While the effect of particle concentration was dominant, the liquid dispersed phase fraction played only a minor role and showed a slight mass transfer decrease with higher disperse phase fractions. Both effects are due to changed

bubble sizes caused by complex interactions during breakage and coalescence of liquid and gas phases.

The feasibility of PE filtration for efficient catalyst and additives recycle in a single step was demonstrated which enables the application of PEs in genuine continuous reaction processes as shown in continuous biocatalysis in a membrane reactor by Heyse et al. [105, 106]. It was found that interactions between the membrane material, nanoparticles, and the solvent can significantly influence the filtration performance of PEs with surprising results particularly for the investigated UF membrane (PVDF). The studied OSN membrane (silicone-based, similar MWCO to UF membrane), on the other hand, showed highly reproducible filtration performance with temperature and continuous phase viscosity having been identified as the only significant influencing parameters. Even at low pressures of only a few bars (lower than typical OSN applications), reasonable fluxes can be achieved. This indicates that w/o PE filtration is a very promising and robust technique with broad operation windows which allows the particle type and concentration to be optimized to meet the needs of the reaction. Since separation does not rely on phase changes, the membrane can even be integrated directly into the reactor if it can resist the reaction temperature. A model describing the permeability of w/o PEs stabilized by different particle types at different temperatures was successfully developed for the first time and can now be used for model-based optimization of this separation step.

Hydroformylations in PEs with commercially available fumed silica nanoparticles or silica nanospheres were found to be possible, and PEs remained catalytically active and stable with constant drop sizes after repeated reaction/filtration cycles. Naturally, available HNT are only able to stabilize o/w emulsions, which are not beneficial for the reactions studied here but potentially for other types of reactions. The same studied UF membrane can be used for the retention of oil droplets as well as for the removal of polar components after PE phase inversion.

The use of PEs is particularly beneficial in reactions that employ sensitive catalysts which suffer from surfactant or interfacial toxicity or shear-sensitivity and thus need to be protected from drop coalescence over the entire process chain. Even potentially moderate reaction yields or rates can be outweighed by the clear advantages of the phase system such as simple and robust catalyst and additive retention in an overall economic optimization of the entire integrated process. In line with Green Chemistry, environmentally benign additives can be applied [3] and only moderate operation energy is required for separation. Since no phase changes are involved, the system is quite insensitive to changes in pressure and temperature. The numerous degrees of freedom of the system such as particle type, catalyst and particle concentrations (i.e., drop sizes), and phase fractions offer a large optimization potential.

The advantages and disadvantages of PEs are summarized and compared to those of TMS and MES in Section 4.4.

4.4 Summary and Comparison of Phase Systems

Anja Drews, Reinhard Schomäcker

All three phase systems described in Sections 4.1 to 4.3 are suitable for a broad variety of chemical reactions performed with soluble catalysts, either typical homogeneous catalysts like metal complexes or biocatalysts. The different additives transfer the originally immiscible phases containing the catalysts and the reactants into well-dispersed systems that provide the required contact between them, enabling fast chemical reactions. Detailed knowledge of either their thermodynamics or phase behavior and characteristic properties is the basis for establishing a suitable phase separation that facilitates recycling of the catalysts and isolation of the products. A broad range of additives is available for all phase systems which provides enough degrees of freedom for the formulation of appropriate reaction media for various chemical reactions with many different catalysts. MES and PE require only small amounts of additives while TMS utilize larger quantities. On the other hand, water as the solvent for the catalyst requires a highly hydrophilic ligand. Still, water completely avoids the utilization of organic solvents, opening an approach to Green Chemistry.

In Table 4.18, a comparison of TMS, MES, and PE regarding the most important properties of the phase systems, their special features, and their performance as obtained for an example reaction is summarized. Building on the different fundamental approaches, homogeneous mixtures versus dispersions with large interfacial areas, the compared systems offer different intrinsic advantages and disadvantages. While the dispersion of two phases in MES or PE is possible with more chemical compounds than the establishment of a thermomorphic system, it is not suitable for water-sensitive catalysts or reactants/products. On the other hand, the use of water as a reaction medium is advantageous for highly polar reactants, like hydrogen peroxide as an oxidant or even ionic substances. The interfacial tensions in mixed solvent systems are usually higher than in surfactant-containing systems. This facilitates the phase separation of the TMS in comparison to MES. The differences in the composition and the polarity of the phases are larger in MES systems, causing a more pronounced partitioning of components between the phases. This facilitates catalyst recycling in MES systems, where larger distribution coefficients of catalyst complexes are observed than in TMS. While the phase separation behavior of MES with nonionic surfactants always depends on temperature, TMS specifically needs to be chosen to be temperature sensitive. If this temperature sensitivity conflicts with the selection of the reaction conditions, the less temperature-sensitive PE can be applied where the catalyst and additive retention can be accomplished in a single membrane filtration step in a simple and robust manner.

For the example of the hydroformylation of 1-dodecene with modified rhodium catalysts, the optimized reaction conditions and the results obtained are summarized in the lower part of Table 4.18. These results are described in detail in Sections 4.1 to

4.3. Differences in performance are largely due to distinct differences in the phase system states and mass transfer areas during the reaction, the used catalyst/ligand, or the type and amount of required additives but can partly also be explained by different phase system maturity and understanding of underlying mechanisms.

The results for TMS and MES were obtained in miniplant runs over several days using a CSTR as the reactor, continuous phase separation, catalyst phase recycling, and product extraction. The residence time in the reactor was adjusted in the range of 30 min. The experiments in PE were performed as repeated batch runs since although continuous phase separation and catalyst retention were realized, a catalyst recycling set-up was not available yet for hydroformylation. The *n*:*iso*-selectivity, as well as the selectivity toward aldehydes, is comparable in all these systems. Due to the different applied catalysts, the observed difference in reaction performance is more likely caused by the inherently less active Rh/XANTPHOS catalyst compared to Rh/BIPHEPHOS rather than by the type of phase system (see Sections 4.1 and 4.2 for choice of phase system-compatible ligands). This difference is partially compensated by the different maximum concentrations of 1-dodecene in the different phase systems, resulting in comparable space-time-yields. The difference in the leaching rates of the Rh-catalysts reflects the differences in the polarity of the separated phases since more similar phase properties cause increased cross-solubilization of the catalysts. The achieved results demonstrate the feasibility of the application of all three systems as reaction media for catalytic conversion reaction of hydrophobic substrates with homogeneous catalysts including efficient catalysts recycling. The technology readiness level (TRL) of the hydroformylation process in TMS and MES can be considered at level 5 since the continuous operation of the miniplants with the desired performance was successfully demonstrated in both cases. The PE hydroformylation can be considered to be at TRL 3 at the moment since it was operated only on the laboratory scale. The decision between these systems as reaction media for a hydroformylation process of a long chain olefin should be based on techno-economic analysis of the alternatives. In case of minor differences in the production costs of the product, the available expertise for the solution of the remaining technological challenges will be a key factor in this decision.

The selection of a multiphase system as a reaction medium is usually motivated by the advantage of a facilitated product isolation and catalyst separation for its recycling. In comparison to a single solvent, such systems introduce a substantial degree of complexity into the development process and their selection and design require detailed knowledge of the thermodynamics of nonideal liquid mixtures or of the surface activity of surfactants or particles in combination with their colloidal properties. For the separation, often additional nonstandard unit operations or advanced control procedures are required. This introduces additional complexity and additional design degrees of freedom and design parameters into the development process, which require the combination of experimental work with modeling, simulation, and optimization. Tools for solving these tasks within the process development are introduced in

Table 4.18: Overview of characteristics and achieved hydroformylation results for all three phase systems.

General:	TMS	MES	PE
Additives	Solvent	Water and surfactant	Water and solid or soft nano- or microparticles
State of phase system during reaction	Homogeneous liquid phase → no mass transfer limitation	Multiple (up to three) liquid phases → mass transfer potentially determining step	2 liquid phases → mass transfer potentially determining step
Product concentration	Moderate due to solvent dilution, depending on used solvent	High, since organic phase consists entirely of substrate and product/ does not need to be diluted	High, since organic phase consists entirely of substrate and product/ does not need to be diluted
Phase separation	Temperature-dependent phase behavior, decantation, simple control	Decantation is strongly influenced by surfactants and temperature, operation challenging	By low-pressure membrane filtration alone, insensitive to changes in composition, broad operation window.
Additives removal/catalyst recycle	Standard thermal separation, partly energy-intensive due to large amounts of additives (OSN, rectification)	Only small amounts need to be retained after decanter, can be accomplished by OSN or flotation, hampered by polydispersity of surfactants	No additional step required for additives/ catalyst removal since already accomplished along with phase separation
Types of products	Suited particularly for nonpolar reactants and products	Suited for polar and nonpolar products	Suited for polar and nonpolar products
Degrees of freedom for process optimization	Broad spectrum of polar and nonpolar organic solvents, adaptable to catalysts and ligands, p and T	Broad range of nonionic surfactants, volume fractions of phases and surfactant concentrations, p and T	Broad range of particle types and concentration, disperse phase fraction, drop sizes, p and T
Other	Versatile selection of suitable solvents according to compatibility and catalyst activity, in combination with phase equilibria for separation	Combination of aqueous catalyst phase and highly concentrated organic reactant/product phase by emulsification, tolerant against electrolytes, avoiding additional solvents	No additional solvents, high conc. (see MES); phase behavior insensitive to T and p changes; separation can be integrated into reactor if conditions compatible with membrane material; suited for sensitive catalysts

Table 4.18 (continued)

	TMS	MES	PE
Case studies for hydroformylation: achieved miniplant/lab results for hydroformylation of 1-dodecene:			
Olefin concentration	0.8 mol L ⁻¹	2.4 mol L ⁻¹	3.6 mol L ⁻¹ (depending on desired disperse phase fraction)
Residence time (reactor)	39 min	30 min	(Repeated) batch
Conversion	72% (CSTR + decanter)	40% (CSTR)	<40%
Selectivity	98% (CSTR + decanter)	95% (CSTR)	>95%
n:iso	>99:1	99:1	99:1 (iso below detection limit)
Space–time–yield	28.5 kg m ⁻³ h ⁻¹	27.5 kg m ⁻³ h ⁻¹	≈ 10 kg m ⁻³ h ⁻¹
Rh leaching	4 ppm (decanter) <1 ppm with additional OSN	<0.3 ppm	<0.2 ppm
TRL	5	5	3
References	[62, 117]	[212, 251]	[251, 253, 258]

the subsequent Chapter 5 on modeling, simulation, and optimization of reactors or entire processes. This includes experimental and computational tools for the analysis of fluid dynamics, the optimization of reaction systems, global optimization of entire processes for technological as well as economic objective functions, and methods for optimized process operation on the miniplant and later production scale. Finally, Chapter 6 discusses the integration of experimental and computational methods for the selection of an optimum phase system for a given reaction, the optimal components for the formulation of the reaction media with respect to the reaction kinetics, the separation of the product, and the catalyst as well as environmental assessments, and the choice of the process and equipment parameters.

References

- [1] Ashrafmansouri SS, Esfahany MN. 2015: The influence of silica nanoparticles on hydrodynamics and mass transfer in spray liquid–liquid extraction column. *Sep. Purif. Techn.* 151: 74–81.
- [2] Baczkiewicz J, Michalski M. 1988: Oxygen transfer during mixing of acetic acid fermentation medium with self-aspirating tube agitator. In Proceedings of the 6th European Conference on Mixing; Pavia, Italy; 24-26 May. Cranfield, BHRA Fluid Engineering.
- [3] Bago Rodriguez AM, Schober L, Hinzmann A, Gröger H, Binks BP. 2021: Effect of particle wettability and particle concentration on the enzymatic dehydration of n-Octanaloxime in Pickering emulsions. *Angew. Chem. (Int. Ed.)*. 60: 1450–1457.
- [4] Bago Rodriguez AM, Binks BP. 2020: Catalysis in Pickering emulsions. *Soft Matter*. 16: 10221–10243.
- [5] Barman S, Christopher GF. 2014: Simultaneous interfacial rheology and microstructure measurement of densely aggregated particle laden interfaces using a modified double wall ring interfacial rheometer. *Langmuir*. 30: 9752–9760.
- [6] Barthel H, Rösch L, Weis J. 1996: Fumed Silica – Production, Properties, and Applications. In Weis J, Auner N, (Eds.) *Organosilicon Chemistry II*. Weinheim and New York: VCH, p. 761–778.
- [7] Behr A, Toslu N. 1999: Einphasige und zweiphasige Reaktionsführung der Hydrosilylierungsreaktion. *Chem. Ing. Tech.* 71: 490–493.
- [8] Behr A, Fängewisch C. 2002: Temperature-dependent multicomponent solvent systems – an alternative concept for Recycling Homogeneous Catalysts. *Chem. Eng. Technol.* 25: 143–147.
- [9] Behr A, Fängewisch C. 2003: Rhodium-catalysed synthesis of branched fatty compounds in temperature-dependent solvent systems. *J. Mol. Catal. A: Chem.* 197: 115–126.
- [10] Behr A, Miao Q. 2004: A new temperature-dependent solvent system based on polyethylene glycol 1,000 and its use in rhodium catalyzed cooligomerization. *J. Mol. Catal. A: Chem.* 222: 127–132.
- [11] Behr A, Miao Q. 2005: Selective rhodium catalysed synthesis of trans-1,4-hexadiene in polyethylene glycol 1000-water solvent systems. *Green Chem.* 7: 617–620.
- [12] Behr A, Roll R. 2005: Hydroaminomethylation in thermomorphic solvent systems. *J. Mol. Catal. A: Chem.* 239: 180–184.
- [13] Behr A, Roll R. 2005: Temperaturgesteuerte Mehrkomponenten-Lösungsmittelsysteme für homogene Übergangsmetallkatalysierte Reaktionen. *Chem. Ing. Tech.* 77: 748–752.
- [14] Behr A, Urschey M. 2003: Palladium-catalyzed telomerization of butadiene with ethylene glycol in liquid single phase and biphasic systems: Control of selectivity and catalyst recycling. *J. Mol. Catal. A: Chem.* 197: 101–113.
- [15] Behr A, Obst D, Turkowski B. 2005: Isomerizing hydroformylation of trans-4-octene to n-nonanal in multiphase systems: Acceleration effect of propylene carbonate. *J. Mol. Catal. A: Chem.* 226: 215–219.
- [16] Behr A, Henze G, Obst D, Turkowski B. 2005: Selection process of new solvents in temperature-dependent multi-component solvent systems and its application in isomerizing hydroformylation. *Green Chem.* 7: 645–649.
- [17] Behr A, Toslu N. 2000: Hydrosilylation reactions in single and two phases. *Chem. Eng. Technol.* 23: 122–125.
- [18] Behr A, Färber T. 2015: Application of a Taylor-Couette reactor in homogeneous catalysis. *Chem. Eng. Trans.* 43: 835–840.
- [19] Behr A, Henze G, Johnen L, Awungacha C. 2008: Advances in thermomorphic liquid/liquid recycling of homogeneous transition metal catalysts. *J. Mol. Catal. A: Chem.* 285: 20–28.

- [20] Behr A, Johnen L, Rentmeister N. 2010: Novel palladium-catalysed hydroamination of myrcene and catalyst separation by thermomorphic solvent systems. *Adv. Synth. Catal.* 352: 2062–2072.
- [21] Behr A, Johnen L, Daniel B. 2010: Process for recycling a biocatalyst in a temperature-controlled multi-component solvent system, WO2012007023A1. 7/16/2010.
- [22] Behr A, Johnen L, Vorholt AJ. 2010: Telomerization of myrcene and catalyst separation by thermomorphic solvent systems. *Chem. Cat. Chem.* 2: 1271–1277.
- [23] Behr A, Johnen L, Daniel B. 2011: A liquid immobilisation concept for enzymes by thermomorphic solvent systems. *Green Chem.* 13: 3168–3172.
- [24] Behr A, Gomes-Jelonek J, Witte H. 2012: Katalysatorrecycling in der homogenkatalysierten Kreuzmetathese von Ölsäuremethylester und 4-Octen. *Chem. Ing. Tech.* 84: 2174–2181.
- [25] Behr A, Kleyensteiber A, Becker M. 2013: A novel approach to selecting thermomorphic multicomponent solvent systems (TMS) for hydroaminomethylation reactions. *Chem. Eng. Process.* 69: 15–23.
- [26] Behr A, Vorholt AJ, Rentmeister N. 2013: Recyclable homogeneous catalyst for the hydroesterification of methyl oleate in thermomorphic solvent systems. *Chem. Eng. Sci.* 99: 38–43.
- [27] Behr A, Seidensticker T, Vorholt AJ. 2014: Diester monomers from methyl oleate and proline via tandem hydroaminomethylation-esterification sequence with homogeneous catalyst recycling using TMS-technique. *Eur. J. Lipid Sci. Technol.* 116: 477–485.
- [28] Behr A, Wintzer A. 2015: Hydroaminomethylation of the renewable limonene with ammonia in an aqueous biphasic solvent system. *Chem. Eng. Techn.* 38: 2299–2304.
- [29] Behr A, Wintzer A, Lübke C, Müller M. 2015: Synthesis of primary amines from the renewable compound citronellal via biphasic reductive amination. *J. Mol. Cat. A: Chem.* 404-405: 74–82.
- [30] Behr A, Witte H, Kämper A, Haßelberg J, Nickel M. 2014: Entwicklung und Untersuchung eines Verfahrens zur Herstellung verzweigter Fettstoffe im Miniplant-Maßstab: development and investigation of the production of branched oleo derivatives in miniplant scale. *Chem. Ing. Tech.* 86: 458–466.
- [31] Bensi F, Nentwich C, Engell S. 2017: Optimization-based early phase design of a homogeneously catalysed process in a thermomorphic solvent system. In 27th Eur. Symp. Comp. Aided Process Eng. Amsterdam, Boston, Heidelberg: Elsevier, p. 715–720.
- [32] Bergbreiter DE, Liu YS, Osburn PL. 1998: Thermomorphic rhodium(I) and palladium(0) catalysts. *J. Am. Chem. Soc.* 120: 4250–4251.
- [33] Bergbreiter DE, Osburn PL, Wilson A, Sink EM. 2000: Palladium-catalyzed C–C coupling under thermomorphic conditions. *J. Am. Chem. Soc.* 122: 9058–9064.
- [34] Bergbreiter DE, Hughes R, Besinaiz J, Li C, Osburn PL. 2003: Phase-selective solubility of poly (N-alkylacrylamide)s. *J. Am. Chem. Soc.* 125: 8244–8249.
- [35] Bergbreiter DE, Sung SD, Li J, Ortiz D, Hamilton PN. 2004: Designing polymers for biphasic liquid/liquid separations after homogeneous reactions. *Org. Process Res. Dev.* 8: 461–468.
- [36] Besora M, Maseras F. 2018: Microkinetic modeling in homogeneous catalysis. *Wiley Interdiscip Rev: Comp. Mol. Sci.* 8: e1372.
- [37] Bhaduri S, Mukesh D. 2014: *Homogeneous Catalysis – Mechanisms and Industrial Applications*. Hoboken, John Wiley & Sons.
- [38] Bianga J, Künnemann KU, Gaide T, Vorholt AJ, Seidensticker T, Dreimann JM, Vogt D. 2019: Thermomorphic multiphase systems: switchable solvent mixtures for the recovery of homogeneous catalysts in batch and flow processes. *Chem. Eur. J.* 25: 11586–11608.
- [39] Bianga J, Künnemann KU, Goçlik L, Schurm L, Vogt D, Seidensticker T. 2020: Tandem catalytic amine synthesis from alkenes in continuous flow enabled by integrated catalyst recycling. *ACS Cat.* 10: 6463–6472.

- [40] Biegler LT, Grossmann IE, Westerberg AW. 1997: *Systematic Methods for Chemical Process Design*. Amundson NR, (Ed.) Pearson Education (US).
- [41] Binks BP. 2002: Particles as surfactants – similarities and differences. *Curr. Op. Coll. Interf. Sci.* 7: 21–41.
- [42] Binks BP, Lumsdon SO. 2000: Catastrophic phase inversion of water-in-oil emulsions stabilized by hydrophobic silica. *Langmuir*. 16: 2539–2547.
- [43] Börner A, Franke R. 2016: *Hydroformylation*. Weinheim, Wiley-VCH Verlag GmbH & Co. KGaA.
- [44] Brunsch Y, Behr A. 2013: Temperature-controlled catalyst recycling in homogeneous transition-metal catalysis: minimization of catalyst leaching. *Angew. Chem. Int. Ed. Engl.* 52: 1586–1589.
- [45] Chang DH, Lee DY, Hong BS, Choi JH, Jun CH. 2004: A new solvent system for recycling catalysts for chelation-assisted hydroacylation of olefins with primary alcohols. *J. Am. Chem. Soc.* 126: 424–425.
- [46] Chang F, Vis CM, Ciptonugroho W, Bruijnincx PCA. 2021: Recent developments in catalysis with Pickering emulsions. *Green Chem.* 23: 2575–2594.
- [47] Chen Z, Ji H, Zhao C, Ju E, Ren J, Qu X. 2015: Individual surface-engineered microorganisms as robust Pickering interfacial biocatalysts for resistance-minimized phase-transfer bioconversion. *Angew. Chem. (Intern. Ed.)*. 54: 4904–4908.
- [48] Chen J, Stebe KJ. 1996: Marangoni retardation of the terminal velocity of a settling droplet: the role of surfactant physico-chemistry. *J. Coll. Interf. Sci.* 178: 144–155.
- [49] Chen Z, Zhao C, Ju E, Ji H, Ren J, Binks BP, Qu X. 2016: Design of surface-active artificial enzyme particles to stabilize Pickering emulsions for high-performance biphasic biocatalysis. *Adv. Mater.* 28: 1682–1688.
- [50] Chiba K, Kono Y, Kim S, Nishimoto K, Kitano Y, Tada M. 2002: A liquid-phase peptide synthesis in cyclohexane-based biphasic thermomorphic systems. *Chem. Commun.* 16: 1766–1767.
- [51] Clift R, Grace JR, Weber ME. 1978: *Bubbles, Drops, and Particles*. New York, Dover Publications, Inc.
- [52] Colladon M, Scarso A, Strukul G. 2007: Towards a greener epoxidation method: use of water-surfactant media and catalyst recycling in the platinum-catalyzed asymmetric epoxidation of terminal alkenes with hydrogen peroxide. *Adv. Syn. Cat.* 349: 797–801.
- [53] Cole-Hamilton DJ. 2010: Nature's polyethylene. *Angew. Chem. Int. Ed. Engl.* 49: 8564–8566.
- [54] Crabtree RH. 2015: Reactivation in homogeneous transition metal catalysis: Causes, avoidance, and cure. *Chemical Rev.* 115: 127–150.
- [55] Crossley S, Faria J, Shen M, Resasco DE. 2010: Solid nanoparticles that catalyze biofuel upgrade reactions at the water/oil interface. *Science*. 327: 68–72.
- [56] Deng C, Xu M, Dong Z, Li L, Yang J, Guo X, Peng L, Xue N, Zhu Y, Ding W. 2020: Exclusively catalytic oxidation of toluene to benzaldehyde in an O/W emulsion stabilized by hexadecylphosphate acid terminated mixed-oxide nanoparticles. *Chin. J. Cat.* 41: 341–349.
- [57] Descamps C, Coquelet C, Bouallou C, Richon D. 2005: Solubility of hydrogen in methanol at temperatures from 248.41 to 308.20K. *Thermochim. Acta.* 430: 1–7.
- [58] Dijkstra MFJ, Bach S, Ebert K. 2006: A transport model for organophilic nanofiltration. *J. Membr. Sci.* 286: 60–68.
- [59] Dreimann JM, Warmeling H, Weimann JN, Künnemann K, Behr A, Vorholt AJ. 2016: Increasing selectivity of the hydroformylation in a miniplant: Catalyst, solvent, and olefin recycle in two loops. *AIChE J.* 62: 4377–4383.
- [60] Dreimann JM, Kohls E, Warmeling HFW, Stein M, Guo LF, Garland M, Dinh TN, Vorholt AJ. 2019: In situ infrared spectroscopy as a tool for monitoring molecular catalyst for hydroformylation in continuous processes. *ACS Cat.* 9: 4308–4319.

- [61] Dreimann JM, Lutze P, Zagajewski M, Behr A, Górak A, Vorholt AJ. 2016: Highly integrated reactor-separator systems for the recycling of homogeneous catalysts. *Chem. Eng. Process.* 99: 124–131.
- [62] Dreimann JM, Hoffmann F, Skiborowski M, Behr A, Vorholt AJ. 2017: Merging thermomorphic solvent systems and organic solvent nanofiltration for hybrid catalyst recovery in a hydroformylation process. *Ind. Eng. Chem. Res.* 56: 1354–1359.
- [63] Einstein A. 1905: Über die von der molekularkinetischen Theorie der Wärme geforderte Bewegung von in ruhenden Flüssigkeiten suspendierten Teilchen. *Ann. Physik.* 322: 549–560.
- [64] ESA. 2013: *Space Systems – Definition of the Technology Readiness Levels (Trls) and Their Criteria of Assessment (ISO 16290:2013)*. Berlin, Beuth Verlag GmbH.
- [65] Evans GM, Rielly CD, Davidson JF, Carpenter KJ. 1992: Hydrodynamic Characteristics of a Gas-Inducing Impeller. In *Fluid Mechanics of Mixing: Modelling, Operations and Experimental Techniques*. 10th ed. Dordrecht: Springer, p. 153–161.
- [66] Fang Z, Yang D, Gao Y, Li H. 2015: pH-responsible Pickering emulsion and its catalytic application for reaction at water–oil interface. *Coll. Polym. Sci.* 293: 1505–1513.
- [67] Faria J, Ruiz MP, Resasco DE. 2010: Phase-selective catalysis in emulsions stabilized by Janus silica-nanoparticles. *Adv. Syn. Cat.* 352: 2359–2364.
- [68] Färber T, Schulz R, Riechert O, Zeiner T, Górak A, Sadowski G, Behr A. 2015: Different recycling concepts in the homogeneously catalysed synthesis of terpenyl amines. *Chem. Eng. Process.* 98: 22–31.
- [69] Färber T, Riechert O, Zeiner T, Sadowski G, Behr A, Vorholt AJ. 2016: Homogeneously catalyzed hydroamination in a Taylor–Couette reactor using a thermomorphic multicomponent solvent system. *Chem. Eng. Res. Des.* 112: 263–273.
- [70] Feng ZG, Michaelides EE. 2001: Drag coefficients of viscous spheres at intermediate and high Reynolds numbers. *J. Fluids Eng.* 123: 841–849.
- [71] Fessi N, Nsib MF, Chevalier Y, Guillard C, Dappozze F, Houas A, Palmisano L, Parrino F. 2019: Photocatalytic degradation enhancement in Pickering emulsions stabilized by solid particles of bare TiO₂. *Langmuir.* 35: 2129–2136.
- [72] Fierro D, Boschetti-de-Fierro A, Abetz V. 2012: The solution-diffusion with imperfections model as a method to understand organic solvent nanofiltration of multicomponent systems. *J. Membr. Sci.* 413-414: 91–101.
- [73] Franke R, Selent D, Börner A. 2012: Applied hydroformylation. *Chemical Reviews.* 112: 5675–5732.
- [74] Frelichowska J, Bolzinger MA, Chevalier Y. 2010: Effects of solid particle content on properties of o/w Pickering emulsions. *J. Colloid Interface Sci.* 351: 348–356.
- [75] Fu L, Li S, Han Z, Liu H, Yang H. 2014: Tuning the wettability of mesoporous silica for enhancing the catalysis efficiency of aqueous reactions. *Chem. Comm.* 50: 10045–10048.
- [76] Gaide T, Behr A, Arns A, Benski F, Vorholt AJ. 2016: Hydroesterification of methyl 10-undecenoate in thermomorphic multicomponent solvent systems – process development for the synthesis of sustainable polymer precursors. *Chem. Eng. Process.* 99: 197–204.
- [77] Gaide T, Behr A, Terhorst M, Arns A, Benski F, Vorholt AJ. 2016: Katalysatorvergleich bei der Hydroesterifizierung von 10-Undecensäuremethylester in thermomorphen Lösungsmittelsystemen. *Chem. Ing. Tech.* 88: 158–167.
- [78] Gaide T, Dreimann JM, Behr A, Vorholt AJ. 2016: Overcoming phase-transfer limitations in the conversion of lipophilic oleo compounds in aqueous media – A thermomorphic approach. *Angew. Chem. Int. Ed. Engl.* 55: 2924–2928.
- [79] Gao Y, Sun C, Qi C. 2021: Ionic liquid-containing non-aqueous Pickering emulsions prepared with sterically-stabilized polymer nanoparticles: A highly efficient platform for Knoevenagel reaction. *Coll. Surf. A: Physicoch. Eng. Aspects.* 626: 126995.

- [80] García-Sánchez F, Eliosa-Jiménez G, Salas-Padrón A, Hernández-Garduza O, Ápam-Martínez D. 2001: Modeling of microemulsion phase diagrams from excess Gibbs energy models. *Chem. Eng. J.* 84: 257–274.
- [81] Gerlach M, Wajid DA, Hilfert L, Edelmann FT, Seidel-Morgenstern A, Hamel C. 2017: Impact of minor amounts of hydroperoxides on rhodium-catalyzed hydroformylation of long-chain olefins. *Catal. Sci. Technol.* 7: 1465–1469.
- [82] Gerlach M, Kirschtowski S, Seidel-Morgenstern A, Hamel C. 2018: Kinetic modeling of the palladium-catalyzed isomerizing methoxycarbonylation of 1-decene. *Chem. Ing. Tech.* 90: 673–678.
- [83] Giorno L, Mazzei R, Oriolo M, De Luca G, Davoli M, Drioli E. 2005: Effects of organic solvents on ultrafiltration polyamide membranes for the preparation of oil-in-water emulsions. *J. Colloid Interface Sci.* 287: 612–623.
- [84] Goedheijt MS, Kamer PCJ, van Leeuwen PWNM. 1998: A water-soluble diphosphine ligand with a large bite angle for two-phase hydroformylation of alkenes. *J. Mol. Catal. A: Chem.* 134: 243–249.
- [85] Goodarzi H, Esfahany MN. 2016: Experimental investigation of the effects of the hydrophilic silica nanoparticles on mass transfer and hydrodynamics of single drop extraction. *Sep. Purif. Techn.* 170: 130–137.
- [86] Grabow K, Bentrup U. 2014: Homogeneous catalytic processes monitored by combined in situ ATR-IR, UV-vis, and Raman spectroscopy. *ACS Catal.* 4: 2153–2164.
- [87] Haarmann N, Enders S, Sadowski G. 2018: Modeling binary mixtures of n-alkanes and water using PC-SAFT. *Fluid Phase Equilib.* 470: 203–211.
- [88] Hall S, Cooke M, El-Hamouz A, Kowalski AJ. 2011: Droplet break-up by in-line Silverson rotor-stator mixer. *Chem. Eng. Sci.* 66: 2068–2079.
- [89] Hamerla T, Paul N, Kraume M, Schomäcker R. 2013: Aufklärung der Stofftransportwege in mizellären Mehrphasenreaktionen am Beispiel der Hydroformylierung. *Chem. Ing. Tech.* 85: 1530–1539.
- [90] Hamerla T, Rost A, Kasaka Y, Schomäcker R. 2013: Hydroformylation of 1-dodecene with water-soluble rhodium catalysts with bidentate ligands in multiphase systems. *Chem. Cat. Chem.* 5: 1854–1862.
- [91] Han Z, Peng L, Li Q, Hao Y. 2017: An interfacially active Pd/C catalyst enhanced hydrogenation of aromatic compounds in Pickering emulsion. *Cat. Letters.* 147: 1615–1621.
- [92] Handa S, Andersson MP, Gallou F, Reilly J, Lipshutz BH. 2016: HandaPhos: A general ligand enabling sustainable ppm levels of palladium-catalyzed cross-couplings in water at room temperature. *Angew. Chem. (Intern. Ed.)*. 55: 4914–4918.
- [93] Handa S, Smith JD, Zhang Y, Takale BS, Gallou F, Lipshutz BH. 2018: Sustainable HandaPhos-ppm palladium technology for copper-free Sonogashira couplings in water under mild conditions. *Org. Letters.* 20: 542–545.
- [94] Hao P, Schwartz DK, Medlin JW. 2018: Effect of surface hydrophobicity of Pd/Al₂O₃ on vanillin hydrodeoxygenation in a water/oil system. *ACS Catal.* 8: 11165–11173.
- [95] Harrell ML, Malinski T, Torres-López C, Gonzalez K, Suriboot J, Bergbreiter DE. 2016: Alternatives for conventional alkane solvents. *J. Am. Chem. Soc.* 138: 14650–14657.
- [96] Haßelberg J, Behr A, Weiser C, Bially JB, Sinev I. 2016: Process development for the synthesis of saturated branched fatty derivatives. *Chem. Eng. Sci.* 143: 256–269.
- [97] Hayashi K, Kim S, Kono Y, Tamura M, Chiba K. 2006: Microwave-promoted Suzuki–Miyaura coupling reactions in a cycloalkane-based thermomorphic biphasic system. *Tetrahedron Lett.* 47: 171–174.
- [98] Heim A, Krasawski A, Rzyski E, Stelmach J. 1995: Aeration of bioreactors by self-aspirating impellers. *Chem. Eng. J. Biochem. Eng. J.* 58: 59–63.

- [99] Hentschel B, Peschel A, Xie M, Vogelpohl C, Sadowski G, Freund H, Sundmacher K. 2014: Model-based prediction of optimal conditions for 1-octene hydroformylation. *Chem. Eng. Sci.* 115: 58–68.
- [100] Hentschel B, Freund H, Sundmacher K. 2014: Modellbasierte Ermittlung der optimalen Reaktionsführung für integrierte Mehrphasenprozesse. *Chem. Ing. Tech.* 86: 1080–1087.
- [101] Hentschel B, Peschel A, Freund H, Sundmacher K. 2014: Simultaneous design of the optimal reaction and process concept for multiphase systems. *Chem. Eng. Sci.* 115: 69–87.
- [102] Hentschel B, Kiedorf G, Gerlach M, Hamel C, Seidel-Morgenstern A, Freund H, Sundmacher K. 2015: Model-based identification and experimental validation of the optimal reaction route for the hydroformylation of 1-dodecene. *Ind. Eng. Chem. Res.* 54: 1755–1765.
- [103] Hernández R, Engell S. 2016: Modelling and iterative real-time optimization of a homogeneously catalyzed hydroformylation process. In 26th Eur. Symp. Comp. Aided Process Eng.: Part A. Amsterdam, Netherlands: Elsevier Science, p. 1–6.
- [104] Herrera C, Fuentealba D, Ghampson IT, Sepulveda C, García-Fierro JL, Canales RI, Escalona N. 2020: Selective conversion of biomass-derived furfural to cyclopentanone over carbon nanotube-supported Ni catalyst in Pickering emulsions. *Cat. Comm.* 144: 106092.
- [105] Heyse A, Plikat C, Ansorge-Schumacher M, Drews A. 2019: Continuous two-phase biocatalysis using water-in-oil Pickering emulsions in a membrane reactor: Evaluation of different nanoparticles. *Cat. Today.* 331: 60–67.
- [106] Heyse A, Plikat C, Grün M, Delaval S, Ansorge-Schumacher M, Drews A. 2018: Impact of enzyme properties on drop size distribution and filtration of water-in-oil Pickering emulsions for application in continuous biocatalysis. *Proc. Biochem.* 72: 86–95.
- [107] Hinze J. 1955: Fundamentals of the hydrodynamics mechanisms of splitting in dispersion processes. *AIChE J.* 1: 289–295.
- [108] Hohl L. 2019: Dispersion and phase separation in liquid multiphase systems: Influence of three phase conditions on drop size distributions. PhD Thesis, Technische Universität Berlin; 2019.
- [109] Hohl L, Knossalla M, Kraume M. 2017: Influence of dispersion conditions on phase separation in liquid multiphase systems. *Chem. Eng. Sci.* 171: 76–87.
- [110] Hohl L, Kraume M. 2018: The formation of complex droplets in liquid three phase systems and their effect on dispersion and phase separation. *Chem. Eng. Res. Des.* 129: 89–101.
- [111] Hohl L, Röhl S, Stehl D, von Klitzing R, Kraume M. 2016: Influence of nanoparticles and drop size distributions on the rheology of w/o Pickering emulsions. *Chem. Ing. Tech.* 88: 1815–1826.
- [112] Huang S, Bilel H, Zagrouba F, Hamdi N, Bruneau C, Fischmeister C. 2015: Olefin metathesis transformations in thermomorphic multicomponent solvent systems. *Catal. Commun.* 63: 31–34.
- [113] Huang XM, Luo ZJ, Guo J, Ruan QJ, Wang JM, Yang XQ. 2020: Enzyme-adsorbed chitosan nanogel particles as edible Pickering interfacial biocatalysts and lipase-responsive phase inversion of emulsions. *J. Agricult. Food Chem.* 68: 8890–8899.
- [114] Huang J, Yang H. 2015: A pH-switched Pickering emulsion catalytic system: High reaction efficiency and facile catalyst recycling. *Chem. Comm.* 51: 7333–7336.
- [115] Huang TS, Wang YH, Jiang JY, Jin ZL. 2008: PEG-stabilized palladium nanoparticles: an efficient and recyclable catalyst for the selective hydrogenation of 1,5-cyclooctadiene in thermoregulated PEG biphasic system. *Chin. Chem. Lett.* 19: 102–104.
- [116] Huxoll F, Schlüter S, Budde R, Skiborowski M, Petzold M, Böhm L, Kraume M, Sadowski G. 2021: Phase equilibria for the hydroaminomethylation of 1-decene. *J. Chem. Eng. Data.* 66: 4484–4495.
- [117] Illner M. Rigorous analysis of reactive microemulsion systems for process design and operation. PhD Thesis, Technische Universität Berlin; 2020.

- [118] Illner M, Kozachynskiy V, Esche E, Repke J.-U. 2021: Fast-track realization of reactive microemulsion systems – Systematic system analysis and tailored application of PSE methods. *Chem. Eng. Sc.*: 117290.
- [119] Illner M, Müller D, Esche E, Pogrzeba T, Schmidt M, Schomäcker R, Wozny G, Repke JU. 2016: Hydroformylation in microemulsions: proof of concept in a miniplant. *Ind. Eng. Chem. Res.* 55: 8616–8626.
- [120] Illner M, Pogrzeba T, Schmidt M, Müller D, Esche E, Schomäcker R, Repke JU, Schomäcker R, Wozny G. 2016: Hydroformylation of 1-dodecene in microemulsions: operation and validation of lab results in a miniplant. *Tech. Trans – Mech Issue.* 1: 107–120.
- [121] Illner M, Schmidt M, Pogrzeba T, Urban C, Esche E, Schomäcker R, Repke JU. 2018: Palladium-catalyzed methoxycarbonylation of 1-dodecene in a two-phase system: The path toward a continuous process. *Ind. Eng. Chem. Res.* 57: 8884–8894.
- [122] Jasper JJ, Kring EV. 1955: The isobaric surface tensions and thermodynamic properties of the surfaces of a series of n-alkanes, C₅ to C₁₈, 1-alkenes, C₆ to C₁₆, and of n-Decylcyclopentane, n-Decylcyclohexane and n-Decylbenzene. *J. Phys. Chem.* 59: 1019–1021.
- [123] Jeelani PG, Mulay P, Venkat R, Ramalingam C. 2020: Multifaceted application of silica nanoparticles. *A Rev. Silicon.* 12: 1337–1354.
- [124] Jiang H, Li Y, Hong L, Ngai T. 2018: Submicron inverse Pickering emulsions for highly efficient and recyclable enzymatic catalysis. *Chem. – An Asian J.* 13: 3533–3539.
- [125] Jiang Y, Liu X, Chen Y, Zhou L, He Y, Ma L, Gao J. 2014: Pickering emulsion stabilized by lipase-containing periodic mesoporous organosilica particles: A robust biocatalyst system for biodiesel production. *Bioresour. Technol.* 153: 278–283.
- [126] Jiang H, Liu L, Li Y, Yin S, Ngai T. 2020: Inverse Pickering emulsion stabilized by binary particles with contrasting characteristics and functionality for interfacial biocatalysis. *ACS Appl. Mat. Interf.* 12: 4989–4997.
- [127] Jokiel M, Kaiser NM, Kováts P, Mansour M, Zähringer K, Nigam KDP, Sundmacher K. 2019: Helically coiled segmented flow tubular reactor for the hydroformylation of long-chain olefins in a thermomorphic multiphase system. *Chem. Eng. J.* 377: 120060.
- [128] Jokiel M, Rätze KHG, Kaiser NM, Künnemann KU, Hollenbeck JP, Dreimann JM, Vogt D, Sundmacher K. 2019: Miniplant-scale evaluation of a semibatch-continuous tandem reactor system for the hydroformylation of long-chain olefins. *Ind. Eng. Chem. Res.* 58: 2471–2480.
- [129] Jörke A, Seidel-Morgenstern A, Hamel C. 2015: Isomerization of 1-decene: Estimation of thermodynamic properties, equilibrium composition calculation and experimental validation using a Rh-BIPHEPHOS catalyst. *Chem. Eng. J.* 260: 513–523.
- [130] Jörke A, Triemer S, Seidel-Morgenstern A, Hamel C. 2015: Kinetic investigation exploiting local parameter subset selection: Isomerization of 1-decene using a Rh-biphephos catalyst. *Chem. Ing. Tech.* 87: 713–725.
- [131] Jörke A, Kohls E, Triemer S, Seidel-Morgenstern A, Hamel C, Stein M. 2016: Resolution of structural isomers of complex reaction mixtures in homogeneous catalysis. *Chem. Eng. Process.* 102: 229–237.
- [132] Jörke A, Gaide T, Behr A, Vorholt A, Seidel-Morgenstern A, Hamel C. 2017: Hydroformylation and tandem isomerization–hydroformylation of n-decenes using a rhodium-BiPhePhos catalyst: Kinetic modeling, reaction network analysis and optimal reaction control. *Chem. Eng. J.* 313: 382–397.
- [133] Jörke A, Seidel-Morgenstern A, Hamel C. 2017: Rhodium-BiPhePhos catalyzed hydroformylation studied by operando FTIR spectroscopy: Catalyst activation and rate determining step. *J. Mol. Catal. A: Chem.* 426: 10–14.
- [134] Kahlweit M. 1988: Microemulsions. *Science.* 240: 617–621.

- [135] Kahlweit M, Strey R, Busse G. 1990: Microemulsions: A qualitative thermodynamic approach. *J. Phys. Chem.* 94: 3881–3894.
- [136] Kahlweit M, Strey R, Firman P, Haase D, Jen J, Schomäcker R. 1988: General patterns of the phase behavior of mixtures of water, nonpolar solvents, amphiphiles, and electrolytes. 1. *Langmuir.* 4: 499–511.
- [137] Kahlweit M, Strey R, Haase D, Kunieda H, Schmeling T, Faulhaber B, Borkovec M, Eicke HF, Busse G, Eggers F, Funck T, Richmann H, Magid L, Söderman O, Stilbs P, Winkler J, Dittrich A, Jahn W. 1987: How to study microemulsions. *J. Coll. Interf. Sci.* 118: 436–453.
- [138] Kaiser NM, Flassig RJ, Sundmacher K. 2016: Probabilistic reactor design in the framework of elementary process functions. *Comput. Chem. Eng.* 94: 45–59.
- [139] Kaiser NM, Jokiel M, McBride K, Flassig RJ, Sundmacher K. 2017: Optimal reactor design via flux profile analysis for an integrated hydroformylation process. *Ind. Eng. Chem. Res.* 56: 11507–11518.
- [140] Kamibayashi M, Ogura H, Otsubo Y. 2006: Rheological behavior of suspensions of silica nanoparticles in associating polymer solutions. *Ind. Eng. Chem. Res.* 45: 6899–6905.
- [141] Kempin MV, Drews A. 2021: Organic solvent nanofiltration of water-in-oil Pickering emulsions – What influences permeability? *Membranes.* 11: 864.
- [142] Kempin MV, Drews A. 2021: What governs Pickering emulsion properties during preparation via batch rotor-stator homogenizers? *Chem. Ing. Tech.* 93: 311–317.
- [143] Kempin MV, Kraume M, Drews A. 2020: W/O Pickering emulsion preparation using a batch rotor-stator mixer – Influence on rheology, drop size distribution and filtration behavior. *J. Colloid Interface Sci.* 573: 135–149.
- [144] Kempin MV, Schroeder H, Hohl L, Kraume M, Drews A. 2021: Modeling of water-in-oil Pickering emulsion nanofiltration – Influence of temperature. *J. Membr. Sci.* 636: 119547.
- [145] Kempin MV, Stock S, von Klitzing R, Kraume M, Drews A. 2020: Influence of particle type and concentration on the ultrafiltration behavior of nanoparticle stabilized Pickering emulsions and suspensions. *Sep. Purif. Technol.* 252: 117457.
- [146] Kiedorf G, Hoang DM, Müller A, Jörke A, Markert J, Arellano-Garcia H, Seidel-Morgenstern A, Hamel C. 2014: Kinetics of 1-dodecene hydroformylation in a thermomorphic solvent system using a rhodium-biphephos catalyst. *Chem. Eng. Sci.* 115: 31–48.
- [147] Kim S, Yamamoto K, Hayashi K, Chiba K. 2008: A cycloalkane-based thermomorphic system for palladium-catalyzed cross-coupling reactions. *Tetrahedron.* 64: 2855–2863.
- [148] Kim S, Noda S, Hayashi K, Chiba K. 2008: An oxidative carbon-carbon bond formation system in cycloalkane-based thermomorphic multiphase solution. *Org Lett.* 10: 1827–1829.
- [149] Kim S, Tsuruyama A, Ohmori A, Chiba K. 2008: Solution-phase oligosaccharide synthesis in a cycloalkane-based thermomorphic system. *Chem. Commun.* 15: 1816–1818.
- [150] Kim S, Ikuhisa N, Chiba K. 2011: A cycloalkane-based thermomorphic system for organocatalytic cyclopropanation using ammonium ylides. *Chem. Lett.* 40: 1077–1078.
- [151] Koller TM, Klein T, Giraudet C, Chen J, Kalantar A, Von der Laan GP, Rausch MH, Fröba AP. 2017: Liquid viscosity and surface tension of n-dodecane, n-octacosane, their mixtures, and a wax between 323 and 573 K by surface light scattering. *J. Chem. Eng. Data.* 62: 3319–3333.
- [152] Krasovskiy A, Duplais C, Lipshutz BH. 2010: Stereoselective Negishi-like couplings between alkenyl and alkyl halides in water at room temperature. *Org. Letters.* 12: 4742–4744.
- [153] Krishnamurthy S, Bhattacharya P, Phelan PE, Prasher RS. 2006: Enhanced mass transport in nanofluids. *Nano Lett.* 6: 419–423.
- [154] Kuhlmann R, Prüllage A, Künnemann K, Behr A, Vorholt AJ. 2017: Process development of the continuously operated synthesis of N,N- dimethylformamide based on carbon dioxide. *J. CO₂ Util.* 22: 184–190.

- [155] Kuhlmann R, Schmitz S, Haßmann K, Prüllage A, Behr A. 2017: Synthesis of N,N-dimethylformamide from carbon dioxide in aqueous biphasic solvent systems. *Appl. Catal. A*. 539: 90–96.
- [156] Kuhlmann R, Nowotny M, Künnemann KU, Behr A, Vorholt AJ. 2018: Identification of key mechanics in the ruthenium catalyzed synthesis of N,N-dimethylformamide from carbon dioxide in biphasic solvent systems. *J. Catal.* 361: 45–50.
- [157] Kuhlmann R, Künnemann KU, Hinderink L, Behr A, Vorholt AJ. 2019: CO₂ based synthesis of various formamides in miniplant scale: A two-step process design. *ACS Sustainable Chem. Eng.* 7: 4924–4931.
- [158] Künnemann KU, Gumbiowski N, Müller P, Jirmann Y, Dreimann JM, Vogt D. 2020: Chemometrics in the homogeneously catalyzed reductive amination: combining in situ fourier-transform infrared spectroscopy and band-target entropy minimization. *Ind. Eng. Chem. Res.* 59: 9055–9065.
- [159] Künnemann KU, Bianga J, Scheel R, Seidensticker T, Dreimann JM, Vogt D. 2020: Process development for the rhodium-catalyzed reductive amination in a thermomorphic multiphase system. *Org. Process Res. Dev.* 24: 41–49.
- [160] Lasich M, Moodley T, Bhowanath R, Naidoo P, Ramjugernath D. 2011: liquid–liquid equilibria of methanol, ethanol, and propan-2-ol with water and dodecane. *J. Chem. Eng. Data.* 56: 4139–4146.
- [161] Leclercq L, Mouret A, Proust A, Schmitt V, Bauduin P, Aubry JM, Nardello-Rataj V. 2012: Pickering emulsion stabilized by catalytic polyoxometalate nanoparticles: A new effective medium for oxidation reactions. *Chem. Eur. J.* 8: 14352–14358.
- [162] Lemmon EW, Huber ML. 2004: Thermodynamic properties of n-dodecane. *Energy Fuels*. 18: 960–967.
- [163] Lemberg M, Sadowski G. 2016: Phase equilibria for the hydroesterification of 10-undecenoic acid methyl ester. *J. Chem. Eng. Data.* 61: 3317–3325.
- [164] Lemberg M, Sadowski G. 2017: Predicting the solvent effect on esterification kinetics. *Chem. Phys. Chem.* 18: 1977–1980.
- [165] Lemberg M, Sadowski G, Gerlach M, Kohls E, Stein M, Hamel C, Seidel-Morgenstern A. 2017: Predicting solvent effects on the 1-dodecene hydroformylation reaction equilibrium. *AIChE J.* 63: 4576–4585.
- [166] Li DD, Jiang JZ, Cai C. 2020: Palladium nanoparticles anchored on amphiphilic Janus-type cellulose nanocrystals for Pickering interfacial catalysis. *Chem. Comm.* 56: 9396–9399.
- [167] Li Y, Zhao G, Hong B, Zhao S, Han X, Pera-Titus M. 2020: Unraveling particle size and roughness effects on the interfacial catalytic properties of Pickering emulsions. *Coll. Surf. A: Physicochem. Eng. Aspects.* 599: 124800.
- [168] Lipshutz BH, Aguinaldo GT, Ghorai S, Voigtritter K. 2008: Olefin cross-metathesis reactions at room temperature using the nonionic amphiphile “PTS”: Just add water. *Org. Lett.* 10: 1325–1328.
- [169] Lipshutz BH, Ghorai S, Abela AR, Moser R, Nishikata T, Duplais C, Krasovskiy A, Gaston RD, Gadwood RC. 2011: TPGS-750-M: A second-generation amphiphile for metal-catalyzed cross-couplings in water at room temperature. *J. Org. Chem.* 76: 4379–4391.
- [170] Lipshutz BH, Taft BR. 2008: Heck couplings at room temperature in nanometer aqueous micelles. *Org. Lett.* 10: 1329–1332.
- [171] Liu H, Fu Z, Yin D, Yin D, Liao H. 2005: A novel micro-emulsion catalytic system for highly selective hydroxylation of benzene to phenol with hydrogen peroxide. *Cat. Comm.* 6: 638–643.
- [172] Liu J, Lan G, Peng J, Li Y, Li C, Yang Q. 2013: Enzyme confined in silica-based nanocages for biocatalysis in a Pickering emulsion. *Chem. Comm.* 49: 9558–9560.

- [173] Lu Y, Wang Y, Jin Z. 2006: Thermoregulated n-heptane/poly(ethylene glycol) monoalkyl ether biphasic system and its application in PETPP/Ru complex catalyzed hydrogenation. *J. Mol. Catal. A: Chem.* 252: 1–4.
- [174] Lvov Y, Wang W, Zhang L, Fakhrullin R. 2016: Halloysite clay nanotubes for loading and sustained release of functional compounds. *Adv. Mat.* 28: 1227–1250.
- [175] Lv G, Wang F, Zhang X, Binks BP. 2018: Surface-active hollow titanosilicate particles as a Pickering interfacial catalyst for liquid-phase alkene epoxidation reactions. *Langmuir.* 34: 302–310.
- [176] Markert J, Brunsch Y, Munkelt T, Kiedorf G, Behr A, Hamel C, Seidel-Morgenstern A. 2013: Analysis of the reaction network for the Rh-catalyzed hydroformylation of 1-dodecene in a thermomorphic multicomponent solvent system. *Appl. Catal. A.* 462–463: 287–295.
- [177] Martin GQ. 1972: Gas-inducing agitator. *Ind. Eng. Chem. Proc. Des. Dev.* 11: 397–404.
- [178] Martin H. 1980: Wärme- und Stoffübertragung in der Wirbelschicht. *Chem. Ing. Tech.* 52: 199–209.
- [179] McBride K, Sundmacher K. 2015: Data driven conceptual process design for the hydroformylation of 1-dodecene in a thermomorphic solvent system. *Ind. Eng. Chem. Res.* 54: 6761–6771.
- [180] McBride K, Gaide T, Vorholt AJ, Behr A, Sundmacher K. 2016: Thermomorphic solvent selection for homogeneous catalyst recovery based on COSMO-RS. *Chem. Eng. Process.* 99: 97–106.
- [181] McBride K, Kaiser NM, Sundmacher K. 2017: Integrated reaction–extraction process for the hydroformylation of long-chain alkenes with a homogeneous catalyst. *Comput. Chem. Eng.* 105: 212–223.
- [182] Melle S, Lask M, Fuller GG. 2005: Pickering emulsions with controllable stability. *Langmuir.* 21: 2158–2162.
- [183] Meng T, Bai R, Wang W, Yang X, Guo T, Wang Y. 2019: Enzyme-loaded mesoporous silica particles with tuning wettability as a Pickering catalyst for enhancing biocatalysis. *Catalysis.* 9: 78.
- [184] Meyer K, Ruiken JP, Illner M, Paul A, Müller D, Esche E, Wozny G, Maiwald M. 2017: Process spectroscopy in microemulsions – Setup and multi-spectral approach for reaction monitoring of a homogeneous hydroformylation process. *Meas. Sci. Techn.* 28: 035501.
- [185] Mizugaki T, Murata M, Ooe M, Ebitani K, Kaneda K. 2002: Novel catalysis of dendrimer-bound Pd(0) complexes: Sterically steered allylic amination and the first application for a thermomorphic system. *Chem. Commun.* 1: 52–53.
- [186] Mohaghegh N, Tasviri M, Rahimi E, Gholami MR. 2015: A novel p–n junction $\text{Ag}_3\text{PO}_4/\text{BiPO}_4$ -based stabilized Pickering emulsion for highly efficient photocatalysis. *RSC Adv.* 5: 12944–12955.
- [187] Momiroski V, Bhattacharya S, Davoody M, Abdul Raman AAB, Parthasarathy R. 2018: Size distribution of bubbles in agitated viscous newtonian and non-Newtonian solutions. *Asia-Pac. J. Chem. Eng.* 13: 1–21.
- [188] Mondragon R, Julia JE, Barba A, Jarque JC. 2012: Characterization of silica–water nanofluids dispersed with an ultrasound probe: A study of their physical properties and stability. *Powder Techn.* 224: 138–146.
- [189] Müller D, Esche E, Pogrzeba T, Illner M, Leube F, Schomäcker R, Wozny G. 2015: Systematic phase separation analysis of surfactant-containing systems for multiphase settler design. *Ind. Eng. Chem. Res.* 54: 3205–3217.
- [190] Murzin D, Salmi T. 2016: *Catalytic Kinetics*. 2nd ed. Murzin D, Salmi T, (Eds.). Elsevier Science.
- [191] Nakanishi K. 1978: Prediction of diffusion coefficient of nonelectrolytes in dilute solution based on generalized hammond-stokes plot. *Ind. Eng. Chem. Fund.* 17: 253–256.

- [192] Nematbakhsh G, Rahbar-Kelishami A. 2015: The effect of size and concentration of nanoparticles on the mass transfer coefficients in irregular packed liquid–liquid extraction columns. *Chem. Eng. Comm.* 202: 1493–1501.
- [193] Nguyen LAT, Minding M, Schwarze M, Drews A, Schomäcker R, Kraume M. 2013: Adsorption and filtration behaviour of non-ionic surfactants during reverse micellar-enhanced ultrafiltration. *J. Membr. Sci.* 2013(433): 80–87.
- [194] Okada Y, Kamimura K, Chiba K. 2012: Cycloalkane-based thermomorphic systems for organic electrochemistry: An application to Kolbe-coupling. *Tetrahedron.* 68: 5857–5862.
- [195] Orlich B, Berger H, Lade M, Schomäcker R. 2000: Stability and activity of alcohol dehydrogenases in W/O–microemulsions: Enantioselective reduction including cofactor regeneration. *Biotechn. Bioeng.* 70: 638–646.
- [196] Pal R. 1996: Effect of droplet size on the rheology of emulsions. *AIChE J.* 42: 3181–3190.
- [197] Paul N. 2014: Theoretische und experimentelle Untersuchungen von Transport- und Grenzflächenphänomenen in Mizellaren Flüssig/flüssig-Systemen (in German). PhD Thesis, Technische Universität Berlin.
- [198] Paul A, Meyer K, Ruiken JP, Illner M, Müller DN, Esche E, Wozny G, Westad F, Maiwald M. 2017: Process spectroscopy in microemulsions – Raman spectroscopy for online monitoring of a homogeneous hydroformylation process. *Meas. Sci. Techn.* 28: 035502.
- [199] Paul A, Ruiken JP, Meyer K, Westad F, Illner M, Müller D, Esche E, Maiwald M. 2015: Online spectroscopy in microemulsions – A process analytical approach for a hydroformylation miniplant II – calibration and prediction by Raman spectra. In *11. Kolloquium Arbeitskreis Prozessanalytik*. Wien, Austria.
- [200] Paul E, Atiemo-Obeng V, Kresta S. 2004: *Handbook of Industrial Mixing*. Hoboken, John Wiley & Sons.
- [201] Paul N, Schulz JM, Kraume M. 2015: Fluid dynamics of droplets as a useful tool to determine coverage and adsorption kinetics of surfactants. *Chem. Eng. Technol.* 38: 1979–1984.
- [202] Paul N, Schulz JM, Kraume M. 2015: Determination of phase separation and mass transfer in complex micellar three phase systems. *Chem. Eng. Proc.: Proc. Intensif.* 99: 143–148.
- [203] Paul N, Schön S, von Klitzing R, Kraume M. 2014: Transport processes at single droplets in micellar liquid/liquid systems. *AIChE J.* 66: 1092–1104.
- [204] Peng L, Feng A, Liu S, Huo M, Fang T, Wang K, Wei Y, Wang X, Yuan J. 2016: Electrochemical stimulated Pickering emulsion for recycling of enzyme in biocatalysis. *ACS Appl. Mat. Interf.* 8: 29203–29207.
- [205] Peng W, Hao P, Luo J, Peng B, Han X, Liu H. 2020: Guanidine-functionalized amphiphilic silica nanoparticles as a Pickering interfacial catalyst for biodiesel production. *Ind. Eng. Chem. Res.* 59: 4273–4280.
- [206] Peng F, Xu J, Zeng X, Feng G, Bao H. 2020: Metal-decorated Pickering emulsion for continuous flow catalysis. *Part. Part. Syst. Charact.* 37: 1900382.
- [207] Pera-Titus M, Leclercq L, Clacens JM, Campo F, Nardello-Rataj V. 2015: Pickering interfacial catalysis for biphasic systems: From emulsion design to green reactions. *Angew. Chem. (Intern. Ed.)*. 54: 2006–2021.
- [208] Petzold M, Paul N, Hohl L, Böhm L, Kraume M. 2021: Gas/liquid mass transfer phenomena in micellar multiphase systems. *Chem. Eng. Proc.: Proc. Intensif.* 108547.
- [209] Petzold M, Röhl S, Hohl L, Stehl D, Lehmann M, von Klitzing R, Kraume M. 2017: Mass transfer and drop size distributions in reactive nanoparticle-stabilized multiphase systems. *Chem. Ing. Tech.* 89: 1561–1573.
- [210] Pogrzeba T, Illner M, Schmidt M, Milojevic N, Esche E, Repke JU, Schomäcker R. 2019: Kinetics of hydroformylation of 1-dodecene in microemulsion systems using a rhodium sulfoxanthphos catalyst. *Ind. Eng. Chem. Res.* 58: 4443–4453.

- [211] Pogrzeba T, Müller D, Hamerla T, Esche E, Paul N, Wozny G, Schomäcker R. 2015: Rhodium-catalyzed hydroformylation of long-chain olefins in aqueous multiphase systems in a continuously operated miniplant. *Ind. Eng. Chem. Res.* 54: 11953–11960.
- [212] Pogrzeba T, Müller D, Illner M, Schmidt M, Kasaka Y, Weber A, Wozny G, Schomäcker R, Schwarze M. 2016: Superior catalyst recycling in surfactant based multiphase systems – Quo vadis catalyst complex? *Chem. Eng. Proc.: Proc. Intensif.* 99: 155–166.
- [213] Pogrzeba T, Schmidt M, Hohl L, Weber A, Buchner G, Schulz J, Schwarze M, Kraume M, Schomäcker R. 2016: Catalytic reactions in aqueous surfactant-free multiphase emulsions. *Ind. Eng. Chem. Res.* 55: 12765–12775.
- [214] Pogrzeba T, Schmidt M, Milojevic N, Urban C, Illner M, Repke JU, Schomäcker R. 2017: Understanding the role of nonionic surfactants during catalysis in microemulsion systems on the example of rhodium-catalyzed hydroformylation. *Ind. Eng. Chem. Res.* 56: 9934–9941.
- [215] Poling BE, Prausnitz JM, O’Connell JP. 2007: *The properties of gases and liquids*. New York, McGraw-Hill Inc.
- [216] Qu Y, Huang R, Qi W, Qu Q, Su R, He Z. 2017: Structural insight into stabilization of Pickering emulsions with Fe_3O_4 @ SiO_2 nanoparticles for enzyme catalysis in organic media. *Part. Part. Syst. Charact.* 34: 1700117.
- [217] Quinzler D, Mecking S. 2010: Linear semicrystalline polyesters from fatty acids by complete feedstock molecule utilization. *Angew. Chem. Int. Ed.* 49: 4306–4308.
- [218] Rätze KH, Jokiel M, Kaiser NM, Sundmacher K. 2019: Cyclic operation of a semi-batch reactor for the hydroformylation of long-chain olefins and integration in a continuous production process. *Chem. Eng. J.* 377: 120453.
- [219] Roesle P, Dürr CJ, Möller HM, Cavallo L, Caporaso L, Mecking S. 2012: Mechanistic features of isomerizing alkoxyacylation of methyl oleate. *J. Am. Chem. Soc.* 134: 17696–17703.
- [220] Röhl S, Hohl L, Kempin M, Enders F, Jurtz N, Kraume M. 2019: Influence of different silica nanoparticles on drop size distributions in agitated liquid-liquid systems. *Chem. Ing. Tech.* 91: 1640–1655.
- [221] Röllig R, Plikat C, Ansorge-Schumacher MB. 2019: Efficient and selective carbonylation with whole-cell biocatalysts in Pickering emulsion. *Angew. Chem.* 131: 13094–13097.
- [222] Rosen MJ, Cohen AW, Dahanayake M, Hua XY. 1982: Relationship of structure to properties in surfactants: 10. Surface and thermodynamic properties of 2-dodecyloxy poly-(ethenoxyethanol)s, $\text{C}_{12}\text{H}_{25}(\text{OC}_2\text{H}_4)_x\text{OH}$, in aqueous solution. *J. Phys. Chem.* 86: 541–545.
- [223] Sadgar AL, Deore TS, Jayaram RV. 2000: Pickering interfacial catalysis-Knoevenagel condensation in magnesium oxide-stabilized Pickering emulsion. *ACS Omega.* 5: 12224–12235.
- [224] Sadin SR, Frederick P, Povinelli RR. 1989: The NASA technology push towards future space mission systems. *Acta Astronautica.* 20: 73–77.
- [225] Saien J, Bamdadi H. 2012: Mass transfer from nanofluid single drops in liquid-liquid extraction process. *Ind. Eng. Chem. Res.* 51: 5157–5166.
- [226] Saien J, Bamdadi H, Daliri S. 2015: Liquid-liquid extraction intensification with magnetite nanofluid single drops under oscillating magnetic field. *J. Ind. Eng. Chem.* 21: 1152–1159.
- [227] Salomé C, Wagner P, Bollenbach M, Bihel F, Bourguignon JJ, Schmitt M. 2014: Buchwald–Hartwig reactions in water using surfactants. *Tetrahedron.* 70: 3413–3421.
- [228] Sander R. 2015: Compilation of Henry’s law constants (version 4.0) for water as solvent. *Atmospheric Chem. Phys.* 15: 4399–4981.
- [229] Schäfer E, Brunsch Y, Sadowski G, Behr A. 2012: Hydroformylation of 1-dodecene in the thermomorphic solvent system dimethylformamide/decane. phase behavior–reaction performance–catalyst recycling. *Ind. Eng. Chem. Res.* 51: 10296–10306.

- [230] Schäfer E, Vogelpohl C, Sadowski G, Enders S. 2013: Simultane Modellierung von Phasengleichgewichten und Grenzflächeneigenschaften mithilfe des PCP-SAFT-Modells. *Chem. Ing. Tech.* 85: 1512–1522.
- [231] Scharzec B, Holtkötter J, Bianga J, Dreimann JM, Vogt D, Skiborowski M. 2020: Conceptual study of co-product separation from catalyst-rich recycle streams in thermomorphic multiphase systems by OSN. *Chem. Eng. Res. Des.* 157: 65–76.
- [232] Schmidt M, Deckwerth J, Schomäcker R, Schwarze M. 2018: Alkaline hydrolysis of methyl decanoate in surfactant-based systems. *J. Org. Chem.* 83: 7398–7406.
- [233] Schmidt M, Pogrzeba T, Hohl L, Weber A, Kielholz A, Kraume M, Schomäcker R. 2017: Palladium catalyzed methoxycarbonylation of 1-dodecene in biphasic systems – optimization of catalyst recycling. *Mol. Cat.* 439: 1–8.
- [234] Schmidt M, Schreiber S, Franz L, Langhoff H, Farhang A, Horstmann M, Drexler HJ, Heller D, Schwarze M. 2019: Hydrogenation of itaconic acid in micellar solutions: catalyst recycling with cloud point extraction? *Ind. Eng. Chem. Res.* 58: 2445–2453.
- [235] Schmidt M, Urban C, Schmidt S, Schomäcker R. 2018: Palladium-catalyzed hydroxycarbonylation of 1-dodecene in microemulsion systems: does reaction performance care about phase behavior? *ACS Omega.* 3: 13355–13364.
- [236] Schlüter S, Künnemann KU, Freis M, Roth T, Vogt D, Dreimann JM, Skiborowski M. 2021: Continuous co-product separation by organic solvent nanofiltration for the hydroaminomethylation in a thermomorphic multiphase system. *Chem. Eng. J.* 409: 128219.
- [237] Schomäcker R, Holmberg K. 2009: Reactions in organised surfactant systems. In Stubenrauch C, (Ed.) *Microemulsions: Background, new Concepts, applications, perspectives.* John Wiley & Sons, Ltd, p. 148–179.
- [238] Schulz JM, Petzold M, Böhm L, Kraume M. 2021: Tropfenbewegung und Stofftransport in technischen flüssig/flüssig-Systemen. Teil 2: Auswirkung von Grenzflächeneffekten und Verunreinigungen. *Chem. Ing. Tech.* 93: 1214–1222.
- [239] Schwarze M, Pogrzeba T, Seifert K, Hamerla T, Schomäcker R. 2015: Recent developments in hydrogenation and hydroformylation in surfactant systems. *Cat. Today.* 247: 55–63.
- [240] Schwarze M, Schmidt M, Nguyen LAT, Drews A, Kraume M, Schomäcker R. 2012: Micellar enhanced ultrafiltration of a rhodium catalyst. *J. Membr. Sci.* 421–422: 165–171.
- [241] Shaharun MS, Mukhtar H, Dutta BK. 2008: Solubility of carbon monoxide and hydrogen in propylene carbonate and thermomorphic multicomponent hydroformylation solvent. *Chem. Eng. Sci.* 63: 3024–3035.
- [242] Shaharun MS, Dutta BK, Mukhtar H, Maitra S. 2010: Hydroformylation of 1-octene using rhodium–phosphite catalyst in a thermomorphic solvent system. *Chem. Eng. Sci.* 65: 273–281.
- [243] Shaharun MS, Mukhtar H, Dutta BK. 2011: Selectivity of rhodium-catalyzed hydroformylation of 1-octene in a thermomorphic solvent system. *J. Appl. Sci.* 11: 1157–1163.
- [244] Sharma S, Basavaraju KC, Singh AK, Kim DP. 2014: Continuous recycling of homogeneous Pd/Cu catalysts for cross-coupling reactions. *Org Lett.* 16: 3974–3977.
- [245] Sharma T, Kumar GS, Sangwai JS. 2015: Viscoelastic properties of oil-in-water (o/w) Pickering emulsion stabilized by surfactant–polymer and nanoparticle–surfactant–polymer systems. *Ind. Eng. Chem. Res.* 54: 1576–1584.
- [246] Shi J, Wang X, Zhang S, Tang L, Jiang Z. 2016: Enzyme-conjugated ZIF-8 particles as efficient and stable Pickering interfacial biocatalysts for biphasic biocatalysis. *J. Mat. Chem. B.* 4: 2654–2661.
- [247] Skale T, Hohl L, Kraume M, Drews A. 2017: Feasibility of w/o Pickering emulsion ultrafiltration. *J. Membr. Sci.* 535: 1–9.

- [248] Skale T, Stehl D, Hohl L, Kraume M, von Klitzing R, Drews A. 2016: Tuning Pickering emulsions for optimal reaction and filtration conditions. *Chem. Ing. Tech.* 88: 1827–1832.
- [249] Smith JM, Van't Riet K, Middleton JC. 1977: Scale-up of Agitated Gas-Liquid Reactors for Mass Transfer. In *Sec. Eur. Conf. On Mixing; St. John's College, Cambridge, England; March 30 – April 1*. Cranfield, U.K: BHRA Fluid Engineering, p. 51.
- [250] Sottmann T, Stubenrauch C. 2009: Phase behaviour, interfacial tension and microstructure of microemulsions. In: Stubenrauch C, (Ed.) *Microemulsions: Background, new concepts, applications, perspectives*. John Wiley & Sons, Ltd, p. 1–47.
- [251] Stehl D. 2020: Physico-Chemical Properties of pickering emulsions stabilized by different nanoparticles for hydroformylation of long-chain olefins. PhD Thesis, Technische Universität Darmstadt.
- [252] Stehl D, Hohl L, Schmidt M, Hübner J, Lehmann M, Kraume M, Schomäcker R, von Klitzing R. 2016: Characteristics of stable Pickering emulsions under process conditions. *Chem. Ing. Tech.* 88: 1806–1814.
- [253] Stehl D, Milojević N, Stock S, Schomäcker R, von Klitzing R. 2019: Synergistic effects of a rhodium catalyst on particle-stabilized Pickering emulsions for the hydroformylation of a long-chain olefin. *Ind. Eng. Chem. Res.* 58: 2524–2536.
- [254] Stehl D, Skale T, Hohl L, Lvov Y, Koetz J, Kraume M, Drews A, von Klitzing R. 2020: Oil-in-water Pickering emulsions stabilized by halloysite clay nanotubes toward efficient filterability. *ACS Appl. Nano Mat.* 3: 11743–11751.
- [255] Steimel J, Harrmann M, Schembecker G, Engell S. 2014: A framework for the modeling and optimization of process superstructures under uncertainty. *Chem. Eng. Sci.* 115: 225–237.
- [256] Steimel J, Engell S. 2016: Optimization-based support for process design under uncertainty: A case study. *AIChE J.* 62: 3404–3419.
- [257] Stöber W, Fink A, Bohn E. 1968: Controlled growth of monodisperse silica spheres in the micron size range. *J. Coll. Interf. Sci.* 26: 62–69.
- [258] Stock S, Schlander A, Kempin M, Geisler R, Stehl D, Spanheimer K, Hondow N, Micklethwaite S, Weber A, Schomäcker R, Drews A, Gallei M, von Klitzing R. 2021: The quantitative impact of fluid vs. solid interfaces on the catalytic performance of Pickering emulsions. *Phys. Chem. Chem. Phys.* 23: 2355–2367.
- [259] Tan H, Zhang P, Wang L, Yang D, Zhou K. 2011: Multifunctional amphiphilic carbonaceous microcapsules catalyze water/oil biphasic reactions. *Chem. Comm.* 47: 11903–11905.
- [260] Tang J, Cao S, Wang J. 2019: CO₂-switchable Pickering emulsions: Efficient and tunable interfacial catalysis for alcohol oxidation in biphasic systems. *Chem. Comm.* 55: 11079–11082.
- [261] Tang X, Hou Y, Meng QB, Zhang G, Liang F, Song XM. 2019: Heteropoly acids-functionalized Janus particles as catalytic emulsifier for heterogeneous acylation in flow ionic liquid-in-oil Pickering emulsion. *Coll.Surf. A: Physicochem. Eng. Aspect.* 570: 191–198.
- [262] Tao L, Zhong M, Chen J, Jayakumar S, Liu L, Li H, Yang Q. 2018: Heterogeneous hydroformylation of long-chain alkenes in IL-in-oil Pickering emulsion. *Green Chem.* 20: 188–196.
- [263] Ternel J, Couturier JL, Dubois JL, Carpentier JF. 2013: Rhodium-catalyzed tandem isomerization/hydroformylation of the bio-sourced 10-undecenenitrile: selective and productive catalysts for production of polyamide-12 precursor. *Adv. Synth. Catal.* 355: 3191–3204.
- [264] Tijani J, El Ali B. 2006: Selective thermomorphic biphasic hydroformylation of higher olefins catalyzed by HRhCO(PPh₃)₃/P(OPh)₃. *Appl. Catal., A.* 303: 158–165.
- [265] Tinucci L, Platone E. 1990: Process for the catalytic hydroformylation of olefins. Patent EP0380154A2.

- [266] Tsabet È, Fradette L. 2015: Effect of the properties of oil, particles, and water on the production of Pickering emulsions. *Chem. Eng. Res. Des.* 97: 9–17.
- [267] van Blaaderen A, van Geest J, Vrij A. 1992: Monodisperse colloidal silica spheres from tetraalkoxysilanes: Particle formation and growth mechanism. *J. Coll. Interf. Sci.* 154: 481–501.
- [268] Van't Riet K. 1979: Review of measuring methods and results in nonviscous gas-liquid mass transfer in stirred vessels. *Ind. Eng. Chem. Proc. Des. Dev.* 18: 357–364.
- [269] Vargaftik NB, Volkov BN, Voljak LD. 1984: International tables of the surface tension of water. *J. Phys. Chem. Ref. Data.* 12: 817–820.
- [270] Volovych I, Neumann M, Schmidt M, Buchner G, Yang JY, Wölk J, Sottmann T, Strey R, Schomäcker R, Schwarze M. 2016: A novel process concept for the three step Boscalid® synthesis. *RSC Adv.* 6: 58279–58287.
- [271] Von Klitzing R, Stehl D, Pogrzeba T, Schomäcker R, Minullina R, Panchal A, Konnova S, Fakhru'llin R, Koetz J, Möhwald H, Lvov Y. 2017: Halloysites stabilized emulsions for hydroformylation of long chain olefins. *Adv. Mat. Interf.* 4: 1600435.
- [272] Vogelpohl C, Brandenbusch C, Sadowski G. 2013: High-pressure gas solubility in multicomponent solvent systems for hydroformylation. part I: carbon monoxide solubility. *J. Supercrit. Fluids.* 81: 23–32.
- [273] Vogelpohl C, Brandenbusch C, Sadowski G. 2014: High-pressure gas solubility in multicomponent solvent systems for hydroformylation. part II: syngas solubility. *J. Supercrit. Fluids.* 88: 74–84.
- [274] Vorholt AJ, Neubert P, Behr A. 2013: Katalytische Funktionalisierungen von Oleylalkohol in thermomorphen Lösungsmittelsystemen zur Synthese potenzieller Biotenside und -monomere. *Chem. Ing. Tech.* 85: 1540–1547.
- [275] Vorholt AJ, Immohr S, Ostrowski KA, Fuchs S, Behr A. 2017: Catalyst recycling in the hydroaminomethylation of methyl oleate: A route to novel polyamide monomers. *Eur. J. Lipid Sci. Technol.* 119: 1600211.
- [276] Wacker Chemie AG. Pyrogenic Silica. [Online].; 2020. Available from: <https://www.wacker.com/cms/en-us/products/product-groups/pyrogenic-silica/pyrogenic-silica.html>.
- [277] Wang L, Liu X, Jiang Y, Liu P, Zhou L, Ma L, He Y, Li H, Gao J. 2019: Silica nanoflowers-stabilized Pickering emulsion as a robust biocatalysis platform for enzymatic production of biodiesel. *Catalysts.* 9: 1026.
- [278] Wang YY, Luo MM, Li YZ, Chen H, Li XJ. 2004: The catalytic hydroaminomethylation of long chain alkenes with dimethylamine in aqueous–organic two-phase system. *Appl. Cat. A: Gen.* 272: 151–155.
- [279] Wang M, Wang M, Zhang S, Chen J. 2019: Pickering gel emulsion stabilized by enzyme immobilized polymeric nanoparticles: A robust and recyclable biocatalyst system for biphasic catalysis. *React. Chem. Eng.* 4: 1459–1465.
- [280] Wang Z, van Oers MCM, Rutjes FPJT, van Hest JCM. 2012: Polymersome colloidosomes for enzyme catalysis in a biphasic system. *Angew. Chem. (Intern. Ed.)*. 51: 10746–10750.
- [281] Weber KH. 2007: *Inbetriebnahme verfahrenstechnischer Anlagen*. Springer-Verlag GmbH.
- [282] Weber A, Isbrücker P, Schmidt M, Schomäcker R. 2021: Ionic liquids as surfactants in aqueous multiphase systems for the Pd–catalyzed hydrocarboxylation. *Chem. Ing. Tech.* 93: 201–207.
- [283] Wegener M, Eppinger T, Bäumler K, Kraume M, Paschedag AR, Bänsch E. 2009: Transient rise velocity and mass transfer of a single drop with interfacial instabilities – Numerical investigations. *Chem. Eng. Sci.* 64: 4835–4845.

- [284] Wegener M, Paschedag AR. 2012: The effect of soluble anionic surfactants on rise velocity and mass transfer at single droplets in systems with Marangoni instabilities. *Intern. J. Heat Mass Transf.* 55: 1561–1573.
- [285] Wei L, Zhang M, Zhang X, Xin H, Yang H. 2016: Pickering emulsion as an efficient platform for enzymatic reactions without stirring. *ACS Sust. Chem. Eng.* 4: 6838–6843.
- [286] Whitby CP, Garcia PC. 2014: Time-dependent rheology of clay particle-stabilised emulsions. *Appl. Clay Sci.* 96: 56–59.
- [287] Wiese S, Spiess AC, Richtering W. 2013: Microgel-stabilized smart emulsions for biocatalysis. *Angew. Chem. (Intern. Ed.)*. 52: 576–579.
- [288] Wiley RM. 1954: Limited coalescence of oil droplets in coarse oil-in-water emulsions. *J. Coll. Sci.* 9: 427–437.
- [289] Wilkinson PM 1991: Physical Aspects and Scale-Up of High Pressure Bubble Columns. UB Stuttgart. PhD Thesis, Riksuniversiteit Groningen.
- [290] Winsor PA. 1948: Hydrotrophy, solubilisation and related emulsification processes. *Transact. Faraday Soc.* 44: 376–398.
- [291] Wollny S 2010: Experimentelle und numerische Untersuchungen zur Partikelbeanspruchung in gerührten (Bio-)Reaktoren. PhD Thesis, Technische Universität Berlin.
- [292] Wu C, Bai S, Ansoorge-Schumacher MB, Wang D. 2011: Nanoparticle cages for enzyme catalysis in organic media. *Adv. Mat.* 23: 5694–5699.
- [293] Xie H, Zhao W, Ali DC, Zhang X, Wang Z. 2021: Interfacial biocatalysis in bacteria-stabilized Pickering emulsions for microbial transformation of hydrophobic chemicals. *Cat. Sci. Techn.* 11: 2816–2826.
- [294] Xue LH, Xie CY, Meng SX, Bai RX, Yang X, Wang Y, Wang S, Binks BP, Guo T, Meng T. 2017: Polymer-protein conjugate particles with biocatalytic activity for stabilization of water-in-water emulsions. *ACS Macro Lett.* 6: 679–683.
- [295] Xue F, Zhang Y, Zhang F, Ren X, Yang H. 2017: Tuning the interfacial activity of mesoporous silicas for biphasic interface catalysis reactions. *ACS Applied Mat. Interf.* 9: 8403–8412.
- [296] Xue B, Xu T, Li D, Xu J, Li Y, Wang F, Zhu J. 2020: A Pickering emulsion of a bifunctional interface prepared from Pd nanoparticles supported on silicane-modified graphene oxide: An efficient catalyst for water-mediated catalytic hydrogenation. *Cat. Sci. Techn.* 10: 1096–1105.
- [297] Xue N, Zhang G, Zhang X, Yang H. 2018: A reinforced Pickering emulsion for cascade reactions. *Chem. Comm.* 54: 13014–13017.
- [298] Xu M, Richard F, Corbet M, Marion P, Clacens JM. 2020: Pickering emulsions assisted synthesis of fatty acetal over phenyl sulfonic groups grafted on activated charcoal. *Appl. Cat. A: Gen.* 597: 117543.
- [299] Yang H, Fu L, Wei L, Liang J, Binks BP. 2015: Compartmentalization of incompatible reagents within Pickering emulsion droplets for one-pot cascade reactions. *J. Am. Chem. Soc.* 137: 1362–1371.
- [300] Yang B, Leclercq L, Clacens JM, Nardello-Rataj V. 2017: Acidic/amphiphilic silica nanoparticles: New eco-friendly Pickering interfacial catalysis for biodiesel production. *Green Chem.* 19: 4552–4562.
- [301] Yang B, Leclercq L, Schmitt V, Pera-Titus M, Nardello-Rataj V. 2019: Colloidal tectonics for tandem synergistic Pickering interfacial catalysis: Oxidative cleavage of cyclohexene oxide into adipic acid. *Chem. Sci.* 10: 501–507.
- [302] Yang Y, Jiang J, Wang Y, Liu C, Jin Z. 2007: A new thermoregulated PEG biphasic system and its application for hydroformylation of 1-dodecene. *J. Mol. Catal. A: Chem.* 261: 288–292.

- [303] Yang X, Liang Y, Cheng Y, Song W, Wang X, Wang Z, Qiu J. 2014: Hydrodeoxygenation of vanillin over carbon nanotube-supported Ru catalysts assembled at the interfaces of emulsion droplets. *Cat. Comm.* 47: 28–31.
- [304] Yang X, Wang Y, Bai R, Ma H, Wang W, Sun H, Dong Y, Qu F, Tang Q, Guo T, Binks BP, Meng T. 2019: Pickering emulsion-enhanced interfacial biocatalysis: Tailored alginate microparticles act as particulate emulsifier and enzyme carrier. *Green Chem.* 21: 2229–2233.
- [305] Yang L, Zhao X, Lei M, Sun J, Yang L, Shen Y, Zhao Q. 2021: Facile construction of thermo-responsive Pickering emulsion for esterification reaction in phase transfer catalysis system. *Mol. Cat.* 500: 111335.
- [306] Yang H, Zhou T, Zhang W. 2013: A strategy for separating and recycling solid catalysts based on the pH-triggered Pickering-emulsion inversion. *Angew. Chem. (Intern. Ed.)*. 52: 7455–7459.
- [307] Yu S, Zhang D, Jiang J, Cui Z, Xia W, Binks BP, Yang H. 2019: Biphasic biocatalysis using a CO₂-switchable Pickering emulsion. *Green Chem.* 136: 7498.
- [308] Zagajewski M, Behr A, Sasse P, Wittmann J. 2014: Continuously operated miniplant for the rhodium catalyzed hydroformylation of 1-dodecene in a thermomorphic multicomponent solvent system [TMS]. *Chem. Eng. Sci.* 115: 88–94.
- [309] Zagajewski M, Dreimann JM, Behr A. 2014: Verfahrensentwicklung vom Labor zur Miniplant: Hydroformylierung von 1-Dodecen in thermomorphen Lösungsmittelsystemen. *Chem. Ing. Tech.* 86: 449–457.
- [310] Zagajewski M, Dreimann JM, Thönes M, Behr A. 2016: Rhodium catalyzed hydroformylation of 1-dodecene using an advanced solvent system: Towards highly efficient catalyst recycling. *Chem. Eng. Process.* 99: 115–123.
- [311] Zapata PA, Faria J, Pilar Ruiz M, Resasco DE. 2012: Condensation/hydrogenation of biomass-derived oxygenates in water/oil emulsions stabilized by nanohybrid catalysts. *Top. Catal.* 55: 1022–5528.
- [312] Zedel D, Drews A, Kraume M. 2016: Retention of surfactants by organic solvent nanofiltration and influences on organic solvent flux. *Sep. Purif. Techn.* 158: 396–408.
- [313] Zedel D, Kraume M, Drews A. 2017: Modelling and prediction of organic solvent flux and retention of surfactants by organic solvent nanofiltration. *J. Membr. Sci.* 544: 323–332.
- [314] Zhang Y, Ettelaie R, Binks BP, Yang H. 2021: Highly selective catalysis at the liquid–liquid interface microregion. *ACS Cat.* 11: 1485–1494.
- [315] Zhang M, Ettelaie R, Yan T, Zhang S, Cheng F, Binks BP, Yang H. 2017: Ionic liquid droplet microreactor for catalysis reactions not at equilibrium. *J. Am. Chem. Soc.* 139: 17387–17396.
- [316] Zhang W, Fu L, Yang H. 2014: Micrometer-scale mixing with Pickering emulsions: Biphasic reactions without stirring. *Chem. Sus. Chem.* 7: 391–396.
- [317] Zhang S, Hong B, Fan Z, Lu J, Xu Y, Pera-Titus M. 2018: Aquivion-carbon composites with tunable amphiphilicity for Pickering interfacial catalysis. *ACS Appl. Mat. Interf.* 10: 26795–26804.
- [318] Zhang M, Wei L, Chen H, Du Z, Binks BP, Yang H. 2016: Compartmentalized droplets for continuous flow liquid-liquid interface catalysis. *J. Am. Chem. Soc.* 138: 10173–10183.
- [319] Zhang Y, Zhang M, Yang H. 2018: Tuning biphasic catalysis reaction with a Pickering emulsion strategy exemplified by selective hydrogenation of benzene. *Chem. Cat. Chem.* 0: 5224–5230.
- [320] Zhao H, Li J, Wang L, Li C, Zhang S. 2021: Pickering emulsion stabilized by dual stabilizer: A novel reaction/separation system for methacrolein synthesis. *Chem. Eng. Sci.* 229: 116038.
- [321] Zhao Y, Zhang X, Sanjeevi J, Yang Q. 2016: Hydroformylation of 1-octene in Pickering emulsion constructed by amphiphilic mesoporous silica nanoparticles. *J. Cat.* 334: 52–59.

- [322] Zhou WJ, Fang L, Fan Z, Albela B, Bonneviot L, de Campo F, Pera-Titus M, Clacens JM. 2014: Tunable catalysts for solvent-free biphasic systems: Pickering interfacial catalysts over amphiphilic silica nanoparticles. *J. Am. Chem. Soc.* 136: 4869–4872.
- [323] Zhu Z, Tan H, Wang J, Yu S, Zhou K. 2014: Hydrodeoxygenation of vanillin as a bio-oil model over carbonaceous microspheres-supported Pd catalysts in the aqueous phase and Pickering emulsions. *Green Chem.* 16: 2636–2643.
- [324] Zinser A, Sundmacher K. 2016: Dynamische Methode zur Berechnung thermodynamischer Gleichgewichte in reaktiven Mehrphasensystemen. *Chem. Ing. Tech.* 88: 1617–1627.

5 Tools for Systems Engineering

Sebastian Engell

5.1 Overview

Sebastian Engell

The development of integrated chemical processes in liquid multiphase systems requires extensive knowledge about the reaction kinetics in the different phase systems, the thermodynamics of the phase systems that govern the phase separation, and the distribution of the reactants of the products and the catalyst in the different phases, as well as, e.g., the mass transfer coefficients and separation efficiencies. The methods for acquiring this deep knowledge and the results for different prototypical reactions were described in detail in the previous chapters. This step involves large amounts of experimental work, as ab initio predictions of the yield, the speed of reactions in complex media, and of the phase separation and distribution are not possible yet. Based on experimental investigations, detailed mathematical models of the kinetics and the phase separation can be developed, which help to guide and to speed up the experimental work to determine optimal phase systems and conditions for the reaction and separation steps. This combination of experimental work and mathematical modeling was also discussed in the previous chapters and successful examples were presented that highlight the potential of model-guided experimental investigations and homogeneously catalyzed reactions in multiphase systems.

Generally speaking, the design of chemical production processes consists of narrowing down the range of alternatives and, at the same time, removing uncertainty about the expected performance as well as about the best choice of the operating conditions, equipment parameters, etc. The search space comprises a huge number of possible alternatives, starting from the possible raw materials, over catalysts and ligands, solvent systems, types of equipment, to the sizing of the equipment, the ratios of the feed streams, residence times, temperatures, pressures, etc. It is not possible to deal with all these alternatives and their parameterization simultaneously. Therefore the design process proceeds in stages where some decisions are fixed sequentially (but may be revised if problems at subsequent stages are detected). In the beginning, the main goal is to single out promising options based on a preliminary evaluation of their potential, which necessarily has to be done with incomplete knowledge or under uncertainty. Traditionally, this step is very much based on the experience of the developers, gained in previous investigations. The goal is an economically viable, if possible economically optimal process that meets the sustainability criteria, as well as possible. A third, also very relevant criterion in the initial phase is the minimization of risk, i.e., to ensure that the product specifications are met and the economic viability is maintained under uncertainties about the precise properties of the raw materials, with limited

knowledge on the detailed behavior of the processes, and in the presence of uncontrolled influences. Hence, one faces a difficult multi-criteria optimization problem that cannot be treated rigorously in its full complexity.

A major challenge here is that, at the end, the real production process consists of a large number of processing steps, involving various pieces of equipment and, usually, including recycle streams. The individual decisions, e.g., on the catalyst, the phase system, the type and the sizing of the equipment, and the operating conditions of the reaction step and the separation processes involved, all influence the overall performance related to the three criteria mentioned above in a coupled manner. This makes it very difficult to take the right decisions based only upon experimental work, basic mathematical models for reaction kinetics and thermodynamics, and prior experience. Computer- and model-based (or systems engineering) methods can efficiently support this complex decision process. The toolkit that is available for this decision support is described in the different sections of this chapter, throughout with a focus on multi-phase processes. In Chapter 6, the application of the methods in the design process is then discussed in detail.

The first step in supporting the design of integrated processes is to build models of the different processing steps that include detailed models of the underlying phenomena and processes, to integrate these models in to a stationary or dynamic flowsheet simulation, and to simulate the equipment and the processes efficiently. This is discussed in Section 5.2. First, an integrated environment for process modeling is presented that enables teams of engineers to model complex processes transparently in collaborative work, to combine different sub-models, and to automatically translate the overall model into code that can be run by commercial simulation packages. Then, in Section 5.2.2, detailed fluid-dynamics models of key processing units for multiphase processes are presented that are necessary to ensure the performance and to investigate the influence of the operational parameters on the performance of the units. A major obstacle to using complex thermodynamic models, as they are described in Chapter 3, in process simulation and, even more so, in process optimization where the models are called many times, are the long computation times that are needed to evaluate the model equations iteratively. Approximating such models by surrogate models, i.e., by mathematical structures that can represent the input-output behavior of the rigorous models faithfully, provides a solution to this issue, as discussed in Section 5.2.3.

While simulation studies help the process designers to understand the options and the influence of the choice of different structures and parameters better and to narrow down the scope of promising options, they cannot explore the full design space and, also, they do not provide the exact best solution. In Section 5.3, the use of optimization methods for process design is presented. First, the optimization of reactors based on the Elementary Process Function Methodology is presented and demonstrated for the example of the hydroformylation of 1-dodecene in a thermomorphic solvent system. It is demonstrated that significant improvements over heuristically found solutions are possible. The scope of the optimization is then extended in Section 5.3.2

to the complete optimization of flowsheets, involving reactors and several separation units. As such problems are characterized by several local optima, global optimization methods for superstructures that involve discrete decision variables are presented and successfully applied to several examples of liquid multiphase processes.

Finally, as briefly discussed above, uncertainty about the real behavior of the real production plant is a major aspect of process design, even when relatively detailed process models are employed. In Section 5.3.3, an approach is presented to systematically deal with this uncertainty in the design process. Taking into account how production plants are operated in reality, i.e., counteracting the uncertainties by adapting the operational degrees of freedom to the real behavior of the process (by closed-loop control of key variables or by interventions of the operators), the approach searches for the best design degrees of freedom under the assumption that this adaptation is done in the best possible fashion.

Section 5.4 presents methods for process monitoring and control in the context of the development of multiphase processes. Such methods can make a substantial contribution to the efficiency of the development process in three ways: First, they are indispensable when it comes to the investigation of the processes at mini plant and pilot plant scale. Monitoring of process parameters that are not directly measurable, tight control of critical operating conditions, and guidance to the experimenters and operators with respect to starting up the processes and reacting to disturbances ensure reproducibility of the results, reduce experimental time and cost of materials, and prevent failures and the generation of useless data, thereby saving time and money. Second, by applying advanced methods for online optimization and control during the experiments, the best possible performance of the processes can be determined, thus providing a reliable basis for their evaluation and for further decisions in the design process. Third, the developed schemes can serve as the basis for the development of the automation systems of the real plant and hence speed up the detailed design and commissioning phase.

The methods described in this Chapter require that sufficiently accurate models of the different elements of the envisioned and investigated production process are available. The development of such models for key elements of multiphase processes is described in Chapters 3 and 4, where it is demonstrated that models with high predictive quality can be derived for such complex processes. These models were successfully used in the operation of plants at the miniplant and pilot plant scale, as described below and also reported in Chapter 4. However, this comes at a price: model development and validation is a costly and time-consuming process that requires expert knowledge. Hence, the effort for model building should ideally be focused on the most promising options, but to determine these options systematically requires the availability of models of sufficient predictive capability. To break this loop, iterative development processes consisting of (model-based) screening of alternatives, initial experimental work, model building, optimization, new experiments, model refinement, optimization with reduced uncertainty, experimental validation, etc.

up to the validation of a small number of remaining options at mini plant or pilot plant scale are needed. This is further discussed in Chapter 6 that builds upon the computational tools described in the following sections.

5.2 Modeling and Simulation

Modeling, simulation, and optimization are essential steps in process systems engineering for both process design and process operation [147]. Requirements for models vary strongly and depend heavily on the goal of a model's application and scale of the described system unit operation or phenomenon [58].

At a small scale, the physicality of models is usually quite high, while at a larger scale mechanistic descriptions are increasingly replaced by (semi-) empirical correlations. Reasons for this are diverse, but the model size and computational complexity are usually the main factors. Process intensification, e.g., the combination of reaction and separation in a single step, is a driving force toward more specialized models, compared to standard unit operation models [63]. At the same time, there is a more frequently arising desire to incorporate information from different scales into process models. This includes the lumping of results from molecular simulations [52] and the feedback of results of computational fluid dynamics [121] into process simulations. Inclusion of intensified unit operations or these novel approaches into standard software tools used for modeling, simulation, and optimization in process systems engineering is not straightforward, typically requires extensive manual work, and, frequently, cannot be achieved without the addition of new unit operation models, new thermodynamic property packages, or new user-defined components or correlations [147].

In Section 5.2.1, novel techniques to support process modeling with a focus on model documentation and exchange of models between different users will be looked at. Therein, insights into recent applications on reactive multi-phase systems will also be given. Afterward, in Section 5.2.2, fluid dynamics simulations of gas-liquid-liquid reactors will be discussed, before Section 5.2.3 turns toward surrogate-modeling to include complex thermodynamics into process synthesis problems.

5.2.1 A Framework for Process Modeling and Simulation

Erik Esche, Saskia Bublitz, Markus Illner, Volodymyr Kozachynskyi,
Jens-Uwe Repke, Günter Wozny

The state-of-the-art software tools for modeling and simulation of processes in chemical engineering, e.g., Aspen Plus, Aspen Hysis, ChemCAD, gPROMS, Pro/II, SimSci, are built around single-user settings: A user works by himself/herself on a model, performs simulation, and, thereon, optimization. As long as standard unit operations

are employed, these models are typically widely available and well documented within the software. However, as soon as the process at hand requires the implementation of specialized unit operations, the model usually breaks down.

Increasingly, industry and academia are moving into a different setting where co-workers within a team are spread out across locations, which has brought about new tools such as Google Docs [53] or Microsoft's Office integration into Teams [151]. These tools allow for simultaneous editing of texts, spreadsheets, and presentations across locations, while ensuring notification to all users about changes. For programming code, version control systems, e.g., git [19], are widely in use and support software development across locations.

To support collaboration regarding model development, simulation, and optimization, a number of initiatives have sprung up in the past 30 years. The Unit Operation interface specification within the CAPE-OPEN standard [23] supports the creation of unit operations within one tool, export, and reuse within a different flowsheeting environment. At the moment, this is limited to steady-state simulation problems and only works in sequential modular solution schemes, i.e., systems where individual unit operations are solved separately and in sequence. Moreover, the unit operations are black boxes, yielding little information to a user and cannot be modified. By contrast, the Modelica language [158] was created to allow for the creation of open model libraries with a primary focus on the automotive industry. Recently, this has led to the definition of the Functional Mock-up Interface FMI [40], which allows for the sharing of dynamic models. Herein, the system itself is provided as a precompiled binary and the accompanying documentation in XML form [182].

These initiatives have a number of shortcomings – shared model development is not envisioned and in the case of the black boxes, FMI and CAPE-OPEN unit operation are even impossible to achieve. Secondly, the documentation of models is separated from the implementation, leading to disparities and the need for maintaining both.

During engineering projects, models for novel equipment, processes, or components can undergo multiple iterations and evolutions, while already being used in connected projects. To further complicate this scenario, models are of course needed in a variety of implementations, i.e., in different modeling languages and programming code. This need is a frequently recurring situation in many disciplines, both in academia and in industry. Prior to the development of MOSAIC modeling, no technology or platform existed supporting such a form of modeling and model exchange.

5.2.1.1 Requirements for Collaborative Modeling

Beyond enabling simultaneous editing of models, collaborative modeling has a number of requirements that need to be addressed to allow for the design of a modeling platform for the exchange of models and model parts across locations and systems that is able to support a variety of applications and simulation tools.

Requirements Regarding Types of Models

The scope of modeling in process systems engineering tasks is quite wide. An overview can be found in literature [62]. Even if the range of applications is reduced to reactive liquid multiphase systems, a multitude of simulation and optimization tasks have to be carried out, for which mathematical models are required. An overview of the applications and the mathematical model types is given in Figure 5.1. In terms of applications, the design and operation of reactive liquid multiphase systems require basic simulation tasks, e.g., to support model validation against experimental data or to carry out sensitivity studies on specific model parameters. In addition, parameter estimation, optimal experimental design problems, and optimization problems regarding process synthesis or optimal operation trajectories have to be formulated and solved. In terms of models, this may range from steady-state to dynamic models, models of single phenomena, individual unit operations, and whole processes. Model types may, further, vary in terms of dynamic descriptions (e.g., flow-driven or pressure-driven) as well as a degree of detail (lumped models, description of temperature, and concentration fields, detailed reaction kinetics, etc.).

Based hereon, the scope for model formulation can be derived and is given in eqs. (5.1) to (5.6) [35]. This involves systems of equations, g , with state variables, x , including first- or second-order derivatives regarding time, t , and some spatial variables (e.g., z , r). The models may feature time-variant controls, u , parameters, p (with specific further subsets), and design variables, d . Besides, models could include inequality constraints, h , variable bounds as well as function definitions and function calls, f . To support optimization, formulation of objectives, Φ , and connection to measurement data, y , are implied. Examples for external function calls are connections to thermodynamic property packages to provide access to algorithmic solutions of complex flash calculations, equations of state, or activity coefficient models.

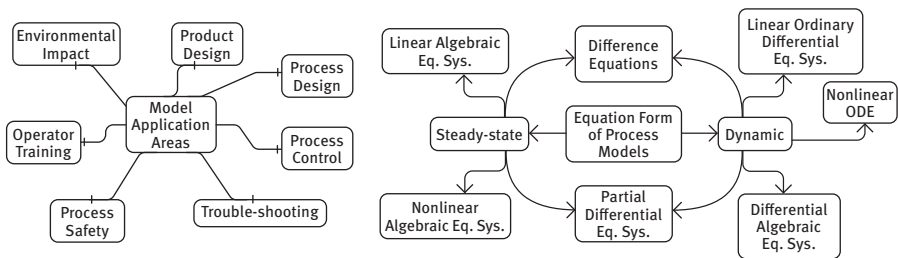


Figure 5.1: Types of application areas of models and mathematical forms of process models, based on Hangos and Cameron [62].

$$g\left(x, \frac{\partial x}{\partial t}, \frac{\partial x}{\partial z}, \frac{\partial x}{\partial r}, y, u, p, d, t, z, r\right) = 0 \tag{5.1}$$

$$h\left(x, \frac{\partial x}{\partial t}, \frac{\partial x}{\partial z}, \frac{\partial x}{\partial r}, y, u, p, d, t, z, r\right) \geq 0 \quad (5.2)$$

$$x^L \leq x \leq x^U \quad (5.3)$$

$$u^L \leq u \leq u^U \quad (5.4)$$

$$x := f(x, y, u, p, d, t) \quad (5.5)$$

$$\Phi(x, y, u, p, d, t) \quad (5.6)$$

Beyond mere classification of variable types, the scope of mathematical operators is, of course, also vital for describing complex systems in chemical engineering. Elementary binary mathematical operators (summation, subtraction, multiplication, division) and some of the most common unary operators (sine, cosine, exp, log, sqrt, power functions) are considered for g , h , f and Φ . Based on these operators, general algebraic equation systems, ordinary differential equation systems, or even partial differential-algebraic equation systems can be formed.

Requirements Regarding Documentation and Exchange of Models

In the aforementioned collaborative office tools, a number of requirements are already met, which arise from the specifics of multi-location teams. These are, tracking of changes and informing other users about those changes. For large models, this becomes even more important, e.g., changes in some thermodynamic properties can affect an entire flowsheet. With respect to storage, collaboration tools can follow two fundamentally different approaches. Either everything is stored in a single online location and all edits are directly implemented therein or local copies are created and, infrequently, changes are updated to and from other locations. In both cases, some form of cloud-based data management is required. Finally, the interaction of several researchers on the same mathematical model requires highly detailed documentation regarding symbols used, assumptions made, and changes implemented.

Requirements Regarding Model Structures and Hierarchies

During the design and investigation of reactive liquid multi-phase processes, individual phenomena, single unit operations, subprocesses, and large process flow sheets need to be modeled for simulation and optimization purposes. Hence, additional requirements regarding the structuring of models arise. These are identical to the general requirements realized in standard flow sheeting tools such as Aspen Plus, CHEMCAD, or gPROMS ProcessBuilder. A collaborative modeling framework should, hence, support modularity, meaning that repeating functions or model parts can be reused while being implemented only once. For example, this concerns the formulation of thermodynamic property packages and the creation of unit operations. Additionally, a model

hierarchy is desired with different levels of granularity, i.e., subprocesses can be masked within a large flow sheet.

Requirements Regarding Model Usage and Export

Further constraints for a collaborative modeling framework arise from the range of desired applications. Numerous tools for simulation and optimization exist. All these are dedicated to specific tasks with distinct advantages and disadvantages. By consequence, an export or compatibility of the modeling framework with a wide selection of tools is required. From the point of view of process systems engineering, this may include tools from operations research such as AMPL or GAMS; general mathematical or engineering tools, e.g., MATLAB, Scilab, Modelica, or Mathematica; as well as specific flow sheeting tools such as Aspen Plus, ChemCAD, gPROMS, etc.

Requirements vs. Existing Modeling Platforms

Comparing these four groups of requirements against the existing set of modeling platforms, simulation, and optimization environments, it quickly transpires that none of the existing solutions meet these requirements at all [147]. The largest hurdles by far are the desired collaboration and documentation functionalities. However, the required level of flexibility in mathematical complexity regarding model types is only fulfilled by a few solutions. PSE's gPROMS [180] comes closest in this regard but lacks collaboration capability.

Consequently, the following section builds a new data model based on the requirements above as a foundation for a completely new modeling platform. Afterward, functionality is detailed to put the requirements given above into practice.

5.2.1.2 Data Model for Modeling at the Documentation Level and Hierarchical Modeling

Based on the requirements listed above, a data model is derived, which supports both modeling at the documentation level, implements typical concepts from hierarchical modeling [147], and is fully functional in a multi-location collaborative setting.

When modeling new systems, engineers typically employ variable names with implied meaning, e.g., $p_{0,i}^{L,V}$ for the vapor pressure of a chemical component, i , and a connected unit of measure (engineering units), e.g., bar or Pa. The symbols, components, and units, of course, differ between disciplines and researchers. By consequence, the most essential model elements are definitions of units of measures and a nomenclature (here, notation). Once engineering units and nomenclature are defined and connected, equations (including inequalities and objectives), functions, and equation systems can subsequently be formulated. Figure 5.2 describes a possible decomposition structure for the model formulation that has been encoded in the data model for model formulation. While Figure 5.2 depicts the class relationships for the data model

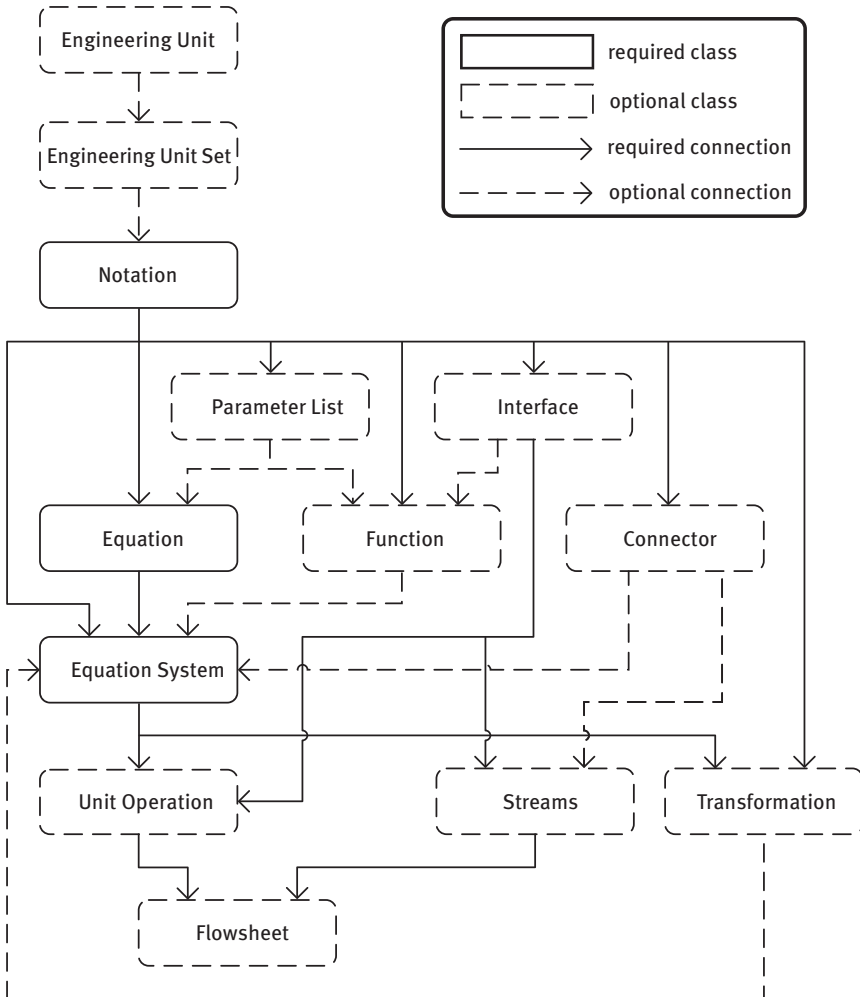


Figure 5.2: Decomposition of models into structural elements allowing for model formulation at the documentation level.

constructed, there are, of course, additional levels of complexity possible, e.g., equation systems can contain multiple hierarchy levels of equation systems themselves. Most elements of this data model have already been described in great detail elsewhere [35, 146, 147]. Here, the discussion is limited to the overall structure and the quintessential purpose of each element.

Each engineering unit specifies a symbol for a unit of measure, its dimensions in terms of length, mass, time, electric current, temperature, amount of moles, and light intensity, a description and conversion to the international system of units (SI). In addition, costs are included to also allow for economic quantifications. Engineering unit

sets are simply collections of units to be used for a model, which can then be referenced inside a model's notation. The latter specifies symbols, which may be used to construct variables. The aforementioned $p_{0,i}^{LV}$ is, here, assembled by a specification of p as a base name, 0 as a subscript, i as an index, and LV as a superscript. Its meaning and, with that, the desired documentation is ensured in the form of necessary descriptions for all model parts. The connection to engineering units may be established by assignment to templates of variables. While engineering units are optional from the perspective of the data model developed here, a notation is an essential starting point. With its help lists of parameters, symbols can be created, interfaces and connectors can be specified, functions can be implemented, and equations can be set up. The purpose of the parameter list is to pre-assign certain variables as parameters. Following this data model, equations and functions are then constructed based on the symbols given in the connected notation, and each is stored with the accompanying specification of a description. Similar to interfaces, connectors have multiple purposes. Their main goal is to connect variables with different names, which can occur under various circumstances and is detailed below.

This data model is the stringent implementation of the concept of “modeling at the documentation level” [120], which allows for the unity of model implementation and documentation. Of course, to achieve this implementation, the flat model perspective of eqs. (5.1) to (5.6) needs to be decomposed into its essential elements, and each element needs to be reconstructed as a model entity in accordance with the described data model.

Aspects of Hierarchical Modeling

Researchers working jointly on various model parts could initially agree on a single notation for the formulation of equations and equation systems. However, this is difficult, given that it is challenging early on to estimate which symbols might be required. Secondly, if two researchers work on two different model parts, the jointly-used number of variables is usually quite small. For example, let us assume researcher A works on reaction kinetics, while researcher B implements balances for mass and energy as well as transport equations. In this case, the shared variables would be temperatures, concentrations, and reaction rates, while the rest (kinetic parameters, diffusion coefficients, . . .) are usually used by only one of the two researchers.

To account for this situation and to ensure maximum flexibility, the data model foresees namespace policies. When constructing an equation system, three different namespace policies are available:

Integration: When elements are added to an equation system by “integration”, they share the same namespace, i.e., variables using the same set of symbols are identical. Naturally, this works best in case the added elements use the same notation as the equation system itself.

Encapsulation: Adding elements to an equation system by “encapsulation” ensures that each added element has its own unique namespace. Consequently, the variables of each added subsystem are unique and the subsystems would be completely disconnected. To connect them, each element added by encapsulation needs a connector (Figure 5.2), which specifies which variables of the subsystem relate to which variable in the superior system and, hence, also makes them available to one and another. In the example above, the connector would pair variables of both systems for temperatures, concentrations, and reaction rates. The rest of the variables that are not contained in the connector would retain their separate namespaces.

Streams: The third policy is an extension to encapsulation. Connectors and interfaces (Figure 5.2) can be used to turn equation systems into unit operations. Interfaces serve both, as type definitions for external functions, i.e., stating which input and output variables are exchanged, and as ports in unit operations and streams, i.e., which variables do an inlet or an outlet of a unit operation, present to the outside, and which variables do a stream of a flowsheet contain. Each inlet/outlet has a name and a specification of which, variables on the inside of the unit operation are visible to the outside. In case one or more unit operations are added to an equation system, the policy “streams” is activated. Ports of unit operations can be connected by streams. The variables of each stream and the variables inside each unit operation have their unique name spaces and are only connected by the connectors, specifying inlets and outlets as well as the streams. For the construction of larger flowsheets, this is the preferred naming policy, as it ensures the highest level of safety and also transparency regarding the origin of variables.

These namespaces ensure that models can safely be constructed by several researchers and various model parts can be simultaneously adjusted. At the same time, large flowsheet models with many hierarchy levels can also be easily transformed into the flat model view given in eqs. (5.1) to (5.6). For this purpose, the established namespaces are appended to the symbols constituting the variables to generate unique variable names.

As mentioned above, each model element detailed so far has its description. This way and through the linking of all model elements, the documentation of the whole model is always as up to date as its parts.

Set-based Formulation of Models and Reuse of Model Entities

As noted above, the notation may include named indices, e.g., i . Regarding the usage of these notations, a high level of flexibility is foreseen in the described data model:

- Specific instances of indices can be addressed by assigning a value to the index,
 $i: p_{0,i}^{LV}$

- A single variable can feature multiple named indices, e.g., as required for binary or ternary interaction parameters, $a_{i=1, j=2, k=3}$
- By default, all indices start at 1 and continue till an unspecified maximum value, e.g., N_i for index i .
- Indices can be employed for complex, nested summation expressions, including mappings of different indices, $\sum_{i=1}^{N_i} \left(\sum_{j=1}^{N_j} (a_i \cdot b_{i=j}) \right)$
- Beyond the default range of an index set, values below $i=1$ and above $i=N_i$ are accessible; creating new variable instances on the fly.
- Instances of indices can be associated identifiers, e.g., for chemical compounds, $i=1: \text{H}_2\text{O}$, $i=2: \text{N}_2$.
- Equations, such as the Antoine equation for obtaining the vapor pressure, are usually required for all components in a system. Hence, the data model allows for the completely generic formulation of equations: $\ln(p_{0,i=1}^{LV}) = (A_i - B_i / (C_i * T))^* \ln(10)$. At the time of formulation of the generic equation, the scope of index, i , is, of course, still unknown. Once it is specified, the generic equation is instantiated for each $i=1 \dots N_i$.
- The latter also applies to entire equation systems, e.g., sets of equations describing a tray in a distillation column with tray index, tr , and component index, i . The generic tray model can be formulated and added to an equation system that also describes the feed, condenser, and reboiler. Once the range of i and tr is known, the system is expanded into a large-scale nonlinear equation system with equations for each tray and each component.
- Generic indices can similarly be employed in function calls to later cause calls, e.g., for all components, all trays, etc.

Figure 5.3 shows an example of an excerpt of an equation system modeling the tray of a reactive distillation column. For a specific simulation case, the scope of the tray and component indices, tr and i , are selected and the respective generic terms and equations are expanded (right-hand side).

The data model describes an object-oriented structure regarding elements added to an equation system. Hence, the same element can be added to the same equation system multiple times as separate instances. While these are all connected to their original source, they receive a new separate namespace, depending on the chosen naming policy. This logic allows for a highly efficient modeling approach where recurring equations need to be formulated only once and can then be used anywhere, including in potential mappings with connectors. The same applies to equation systems extended as unit operations. Figure 5.4 takes a hierarchical view of an equation system, with a number of subsystems, connected equations, and function calls. For each added element, a naming policy needs to be chosen. In case different notations are used, a connector needs to be specified to tether the respective variables. Each function call is a connector or an instance of a generic connector itself, ensuring

**Simulation stage:
Excerpt of an instantiated equation**

$$(15) \quad \Delta p_{tr} = p_{tr+1} - p_{tr}$$

$$(16) \quad \Delta y_{tr=0} = p_{tr=1} - p_{tr=0}$$

$$(17) \quad 1 = \sum_{i=1}^{N_{tr}} x_{tr,i}$$

$$(18) \quad 1 = \sum_{i=1}^{N_{tr}} y_{tr,i}$$

$$(19) \quad 0 = F_{tr=NTR}^{L,n} - F_{tr=NTR+1}^{L,n}, \text{Reboiler,in}$$

$$(20) \quad 0 = F_{tr}^{F,n} \cdot h_{tr-1}^{L,n} + F_{tr-1}^{L,n} \cdot h_{tr}^{L,n} - F_{tr}^{L,n} \cdot h_{tr}^{L,n} - F_{tr}^{V,n} \cdot h_{tr}^{V,n} + Q_{tr}^{Loss}$$

$$(21) \quad 0 = F_{tr}^{F,n} \cdot x_{tr-1,i} + F_{tr-1}^{L,n} \cdot x_{tr+1,i} - F_{tr}^{L,n} \cdot x_{tr,i} - F_{tr}^{V,n} \cdot y_{tr,i} + r_{tr,i}^n$$

**Modeling stage:
Excerpt of a generic
equation system**

$$(245) \quad 0 = F_{tr=1}^{F,i} \cdot x_{tr=1}^i + F_{tr=2}^{D,L,Reboiler,n} \cdot x_{tr=1}^D + F_{tr=2}^{V,n} \cdot y_{tr=2,i=1} - F_{tr=1}^{L,n} \cdot x_{tr=1,i=1} - F_{tr=1,i=1}^{D,V,n} \cdot y_{tr=1,i=1}^D$$

$$(246) \quad 0 = F_{tr=2}^{F,i} \cdot x_{tr=1}^i + F_{tr=2}^{L,n} \cdot x_{tr=1,i=1} + F_{tr=3}^{V,n} \cdot y_{tr=3,i=1} - F_{tr=2}^{L,n} \cdot x_{tr=2,i=1} - F_{tr=2}^{V,n} \cdot y_{tr=2,i=1} + r_{tr=2,i=1}^n$$

$$(247) \quad 0 = F_{tr=3}^{F,i} \cdot x_{tr=1}^i + F_{tr=3}^{L,n} \cdot x_{tr=2,i=1} + F_{tr=4}^{V,n} \cdot y_{tr=4,i=1} - F_{tr=3}^{L,n} \cdot x_{tr=3,i=1} - F_{tr=3}^{V,n} \cdot y_{tr=3,i=1} + r_{tr=3,i=1}^n$$

$$(248) \quad 0 = F_{tr=4}^{F,i} \cdot x_{tr=1}^i + F_{tr=4}^{L,n} \cdot x_{tr=3,i=1} + F_{tr=5}^{V,n} \cdot y_{tr=5,i=1} - F_{tr=4}^{L,n} \cdot x_{tr=4,i=1} - F_{tr=4}^{V,n} \cdot y_{tr=4,i=1} + r_{tr=4,i=1}^n$$

$$(249) \quad 0 = F_{tr=5}^{F,i} \cdot x_{tr=1}^i + F_{tr=5}^{L,n} \cdot x_{tr=4,i=1} + F_{tr=6}^{V,n} \cdot y_{tr=6,i=1} - F_{tr=5}^{L,n} \cdot x_{tr=5,i=1} - F_{tr=5}^{V,n} \cdot y_{tr=5,i=1} + r_{tr=5,i=1}^n$$

$$(250) \quad 0 = F_{tr=6}^{F,i} \cdot x_{tr=1}^i + F_{tr=6}^{L,n} \cdot x_{tr=5,i=1} + F_{tr=7}^{V,n} \cdot y_{tr=7,i=1} - F_{tr=6}^{L,n} \cdot x_{tr=6,i=1} - F_{tr=6}^{V,n} \cdot y_{tr=6,i=1} + r_{tr=6,i=1}^n$$

$$(251) \quad 0 = F_{tr=7}^{F,i} \cdot x_{tr=1}^i + F_{tr=7}^{L,n} \cdot x_{tr=6,i=1} + F_{tr=8}^{V,n} \cdot y_{tr=8,i=1} - F_{tr=7}^{L,n} \cdot x_{tr=7,i=1} - F_{tr=7}^{V,n} \cdot y_{tr=7,i=1} + r_{tr=7,i=1}^n$$

Figure 5.3: Generic model formulation and instantiation for a specific simulation case. The excerpt shows component balances for trays, *tr* 1 to 7 for component, *i* = 1.

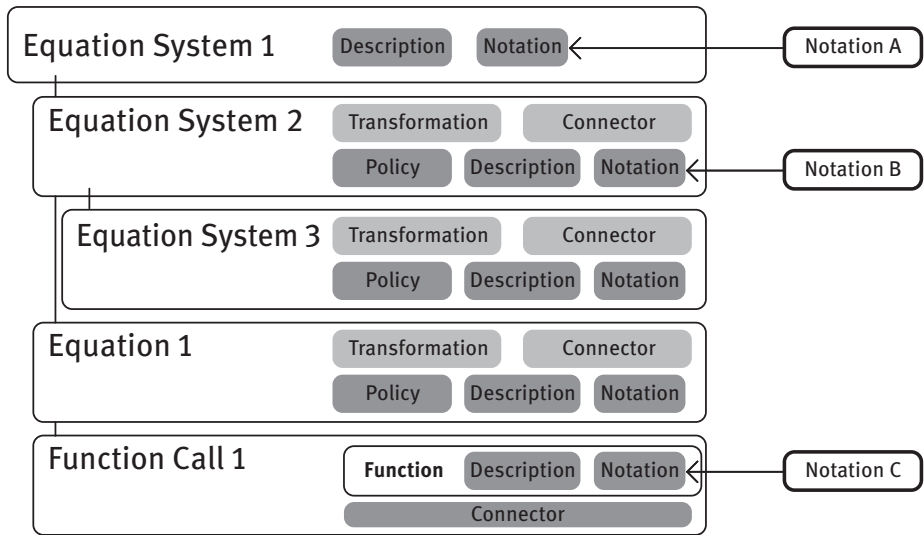


Figure 5.4: Levels of Complexity in Equation Systems.

separation of a function’s namespace and the equation system calling it, at all times. Descriptions for each element ensure proper documentation of all levels.

Transformation of Models

Regarding the scope described in Section 5.2.1.1, equation systems may contain partial differential algebraic equation systems in the form of initial value problems, boundary value problems, or combinations thereof. In case such an equation system is embedded directly or as a unit operation into a larger flowsheet, the connection to other model parts is of course not straightforward. For example, a fixed-bed reactor may be part of a larger flowsheet and described by a set of partial differential algebraic equation (PDAE) systems, including two spatial dimensions and respective boundary conditions. While the boundary conditions would serve as clear connecting points to the rest of the flowsheet, there is, at the moment, no general solver available that can solve arbitrary simulation or optimization problems involving PDAE subsystems. By consequence, the data model has been extended to include transformations, which can be applied on (sub-) systems of equations to partially or fully discretize these [37, 207]. For this purpose, a separate equation system needs to be established, which describes a discretization scheme.

Afterward, a transformation element can be set up, which connects the variables and indices of the discretization scheme with the original system to be discretized. Figure 5.5 shows an example of a simple PDAE system and its boundary conditions, the discretization system, the connection of both in the form of the transformation, and the resulting discretized system after application of the discretization. Note the

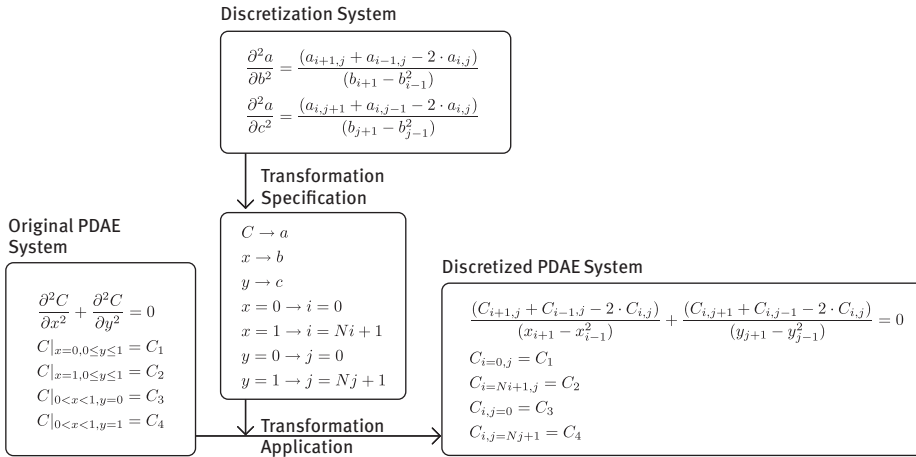


Figure 5.5: Example of full discretization of a PDAE system by the transformation of the symbolic expression.

generic nature of both the transformation specification as well as the resulting discretized equation system. Within both, N_i and N_j denote the maximum counter values for indices i and j , respectively. At the modeling stage of the PDAE system and integration into the larger flowsheet, several decisions will not have been made, e.g., on specific sizes of equipments, etc. During the later specification of a simulation problem, suitable choices regarding the meshing can be made, i.e., values for N_i and N_j as well as their spread in x and y . Beyond this rather simple system, more complex parabolic PDAE systems have also already been discretized, including boundary conditions involving derivatives. A major limitation has to be noted at this point. The logic and implementation described here are limited to rather simple spatial geometries (rectangular, cylindrical, or others). For more complex applications, manual interaction with dedicated software will become necessary.

With respect to the structure of equation systems given in the system of equations 3, e.g., a PDAE system could be used, where a Transformation is applied to fully discretize it into an algebraic equation system and a connector to tether its discretized variables to the variables of Equation System 2.

Implementation Aspects

A first implementation of the aforementioned data model has been achieved in the platform, MOSAICmodeling, and it has since been further developed. MOSAICmodeling serves as a backbone for model formulation, model development, management, and connection to simulation, as well as to optimization environments. MOSAICmodeling is a web-based collaborative platform for integrated model development and

data management, developed at the Process Dynamics and Operations Group at Technische Universität Berlin [35, 147, 207].

To best support the implementation of the concept of “modeling at the documentation level” and the data model described above, MOSAICmodeling pursues an XML-based [10] data structure, with symbolic expressions for variables, equations, and functions in MathML. The software tool is itself implemented in Java SDK 11 [169] in a modular and object-oriented fashion. Every single XML element of the data model has an equivalent java class and there is a bidirectional translation between java objects and instances in MathML/XML. By consequence, even some level of execution of symbolic expressions is possible on the java instances of equations. At runtime, all model modifications, instantiations, transformations, etc., are based on and translated back into the XML base. All model elements are stored separately as compressed XML files in a MariaDB [139] database (formerly mySQL). Only variables and parameters are stored in batches of specification lists. The connections between model elements, e.g., an equation connected to an equation system, takes place by reference, using a unique identifier. Hence, no copies of elements are created, but everything is reused by reference. Whenever any model is extended or corrected, all other model elements referencing it receive the updates.

While XML and MathML can easily be rendered into human-readable and human-editable forms, directly entering equations or function expressions in MathML is inadvisable. Hence, MOSAICmodeling offers a LaTeX [157] input including a variety of templates for complex structures for users. The LaTeX code is translated into XML expressions for storage and processing. However, the original LaTeX code is retained to allow for later modification.

5.2.1.3 Collaborative Modeling and Web Technologies

To meet the requirements regarding the model exchange, MOSAICmodeling uses a server-client structure, where all model elements are stored in a database on a web server. While the modification and construction of models are carried out on desktop clients, all storage and association of model parts take place on the web-based server. As all database elements are tethered by reference, all updates implemented are instantaneously propagated to all models referencing them. When opening or loading a model, users are informed about changes in referenced elements. To ensure fast model access, multiple servers in different locations exist with a master-slave configuration, which ensures synchronization across locations. The graphical user interface (GUI) is implemented in Java to ensure platform independence. From within the GUI, any user can grant read or read and write access to any other user. While all model elements are stored in a database, there is still a file-system-like hierarchy included between model elements, allowing users also to share whole folders, in turn ensuring access by inheritance. Based on the data model given above, the client software has a feature to export comprehensive documentation in XML, LaTeX, PDF, or plain text format.

In addition, MOSAICmodeling features a connection to a measurement database [107]. This way, experimental data can be directly loaded into a model for setting up simulation studies, parameter estimation, or similar studies. Finally, there is a model analysis feature, which allows for the automatic decomposition of square systems of nonlinear equations to find over- and underdetermined subsystems [108]. Based hereon, bad choices in design variables and structural issues in the formulated equations can be found more easily.

5.2.1.4 Specification of Simulation and Optimization Problems

Once a user has set up a model as described in Section 5.2.1.2, it still lacks important information for either simulation or optimization purposes. At this point, information on the scope of index sets, implementations of external functions, values for design variables and parameters, as well as initial values can be added to the model data in the form of variable and parameter specifications, simulation, and optimization elements. The involved workflows have already been published elsewhere [35, 147]. At this point, the description is limited to the basic functionality implemented in MOSAICmodeling, and the necessary information is presented to understand the “model-based model export”, subsequently introduced in Section 5.2.1.5.

Formulation and Solution of Simulation Problems

The most essential information when preparing a model for simulation is the specification of the scope of all indices, i.e., the number of components that need to be set, the number of trays in column models, the meshing for discretizations of PDAEs, etc. These directly influence the total number of variables, equations, and function calls. Once the index specification is completed, MOSAICmodeling expands all generic variables and equations automatically in the background to generate a comprehensive list of all variables and parameters and to determine the current degrees of freedom of the system. Based on the aforementioned parameter lists, the hence generated parameters are already pre-classified and separated from the rest of the variables. The rest of the variables need to be manually sorted by the modeler with respect to the definitions given in Section 5.2.1.2, into design variables d , control variables u , and measurement variables y . The remainder will stay as state variables, x , to be computed by the system equations, g . For differential algebraic equation systems, a further classification among the state variables, x , allows for signaling, for which these initial conditions are known. Additionally, (initial) values, and lower and upper bounds can be assigned to all variables and parameters at this point. The respective information is yet again stored in further XML structures, called “variable specification” and “parameter specification”, respectively.

In case the simulation problem is supposed to be solved stand-alone, a degree of freedom of zero needs to be achieved. In case this model shall subsequently be integrated into a flowsheet simulation, e.g., Aspen Plus, and inlets and outlets, need to be

defined and the inlets shall remain as degrees of freedom. At this stage, all the model information and additional specifications are still present as java objects and in XML form. Based hereon, the greatest benefit can be reaped from the data model. This highly generic model and simulation representation can be translated into virtually any modeling or programming language. For this purpose, MOSAICmodeling has its *CodeGeneration* engine, which, in combination with *LanguageSpecificator* classes, ensures export of simulations as code. Some dedicated *LanguageSpecificators* exist, which implement all necessary conversions of XML code into, e.g., MATLAB, AMPL, gPROMS, Aspen Custom Modeler, Scilab, python, C++, etc. In addition, a user-defined version exists (Section 5.2.1.5), which allows for the specification of further export languages. In both cases, MOSAICmodeling generates code in the specified language, including all necessary information, to compile and run the simulation problems [147, 207]. This ensures that any user of MOSAICmodeling can export the defined simulation problems to the tool of their choice and is provided with an error-free implementation, for example, a dedicated export for the flowsheet synthesis tool FSOpt [202] was created and used to export developed models.

Once the simulation problems have been generated and solved (either locally or on MOSAICmodeling's server), the results can be reimported and stored for other users alongside the model and simulation specifications.

Formulation and Solution of Optimization Problems

The starting point for the formulation of optimization problems is an existing simulation object. This might be amended by further inequality constraints and formulations of objective functions. Beyond that, the variable and parameter specification can simply be adjusted by classifying decision variables, controls, or parameters as decision variables, flagging certain variables as integers, and choosing upper and lower bounds for variables.

Depending on the structure of the underlying model, the resulting optimization problem could amount to a mixed-integer nonlinear program (MINLP) or even involve some differential equations. Similar to the simulation case, these hence specified problems are available in XML and can also be translated into executable code. For MINLPs, a direct connection to the NEOS server [28] exists, which allows for an online solution of the MINLP problems, formulated in GAMS or AMPL. For the latter, the mentioned user-defined export needs to be employed to generate code for a solution of dynamic optimization problems, e.g., by single shooting [64].

5.2.1.5 Model-Based Code Implementation of Models

The existence of all model parts, simulation, and optimization specifications in the form of the afore-described data model renders them highly accessible and allows a large array of pattern-based, string-based, or symbolic translations. This opens up a host of possibilities, which borrow from the hot topic in computer science “model-

driven development of complex software” [42], which essentially denotes that some form of a meta model is used to write code, which otherwise a programmer would have to manually develop. In terms of a mathematical model, this is sketched in Figure 5.6. The starting point is the “Abstract Model”, which describes the initial, e.g., pen and paper, deliberations of the modeler involving goal of the model, assumptions made, and derivation of the equations. In the conventional path, this abstract model is usually directly implemented in the form of some model, specific to a chosen target platform (Target Platform-specific Model). Alternatively, the data model sketched above represents a “High-Level Platform-independent Model”, which can be automatically translated into any “Platform-specific Model”. To support this path, the high-level model (here, XML/MathML representation) is first translated into a low-level platform-independent form (here, a model instance in Java), which contains primarily the mathematical functionality, i.e., variable definitions and equations. With the help of translators, such a low-level form can easily be transferred into a large variety of platform-specific models (e.g. Matlab code, C++ code, python code, etc.). This translation becomes especially versatile in case the translation mechanism itself can be modeled. Here, this is represented by the “Meta model”, which is essentially a specification of modeling or a programming language [207]. The “Language Specifier” class and its accompanying XML scheme describe how a generic simulation or optimization problem formulated in the abovedescribed data model can be translated into code.

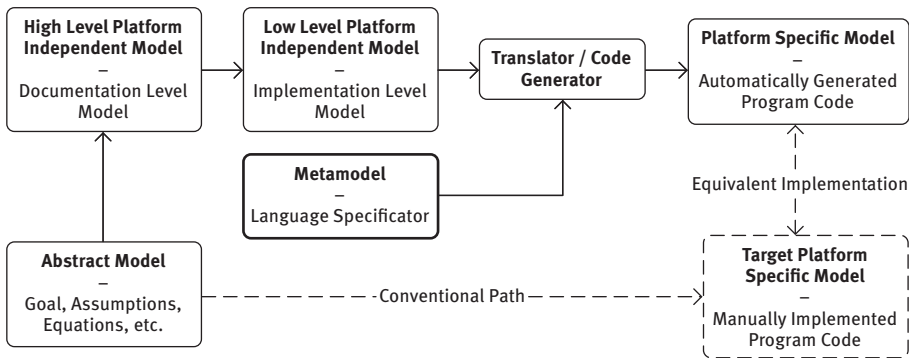


Figure 5.6: Abstract view of the translation procedure of the afore-described model structure into platform-specific code.

To this end, the meta model describing the code export needs to contain information regarding general language settings, i.e., how floating-point numbers and integers are described. Secondly, the mathematical operations allowed need to be adjusted to the needs of the target language, e.g., $(x)^{0.5}$ is turned into $\text{POW}(x,0.5)$. Thirdly, the symbolic variable names require a representation, either by using a flat structure

$(x(1), x(2), \dots)$, or a more legible version (e.g., *pOILV*). Furthermore, the representation of functions (including interfaces to external functions) needs to be defined. Finally, the core of the model describing the translation is a tree-based template, which builds the entire code export. This includes loops to enumerate or list equations, function calls, variable definitions. To ensure flexibility regarding the various options for problem definitions in simulation and particularly in optimization (optimal experimental design, parameter estimation, data reconciliation, . . .), this template contains a filter block to sample subsets of variables and parameters based on their properties, e.g., integer variables only.

With the help of this additional feature, models implemented in MOSAICmodeling's XML data model can be translated into virtually any modeling or programming language.

5.2.1.6 Examples of Models Developed and Managed in MOSAICmodeling

By now, a large variety of processes have been developed within MOSAICmodeling, ranging from superstructure formulations for distillation processes [109] and pressure-driven models for column start-up [69], to falling film absorbers [188].

In particular, the entire MES mini plant as described in Section 4.2 has been modeled in MOSAICmodeling. This includes reaction mechanisms for the hydroformylation of 1-dodecene as well as reductive amination. Regarding the MES mini plant, the main focus for the developed models lay on the support of the operation. To this end, a dynamic model has been developed for online state estimation (Section 5.4.3) and optimal operation (Section 5.4.4). Hence, the purpose of the developed mini plant model is to describe all operation modes, from “empty and cold”, via start-up, to full continuous operation.

The scope of the model for the MES mini plant is sketched in Figure 5.7. The light gray boxes therein describe the control volumes included in the balance equations and the blue hexagons the modeled streams. In the following paragraphs, the entire model will be discussed, focusing on the hydroformylation reaction. Boxes 1, 2, and 3 are the liquid feed tanks of 1-dodecene, catalyst solution, and surfactant. The synthesis gas feed is assumed to be an infinite reservoir with a constant pressure of 200 bar. Control volumes, 8 and 9, denote the gas and liquid phases in the reactor and 11, 12, 13, the three liquid phases in the settler. To mimic the plant behavior as closely as possible, a pressure-driven dynamic formulation is chosen. With regard to the reactor, this includes modeling of the overflow functionality, i.e., outflow occurs once the volume inside the reactor surpasses 500 mL and ceases once it is below that value. Such discrete switches are implemented into the dynamic model by sigmoidal switches to avoid discontinuities. Otherwise, the reactor model includes balances for all components, a gas solubility model, the full hydroformylation kinetics adjusted for the microemulsion system (Section 4.2.4), correlations for liquid and vapor densities

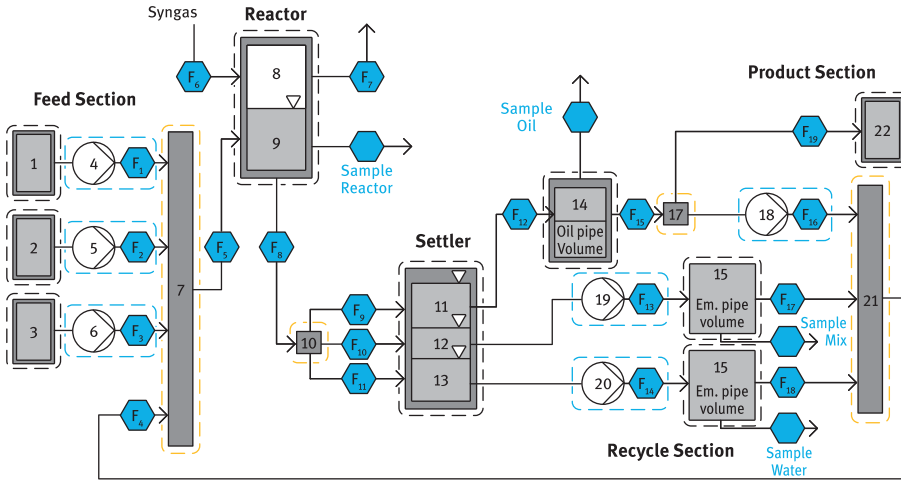


Figure 5.7: Scope of the dynamic model for the MSS mini-plant.

for connection of levels to molar hold-ups, as well as the controller equations for the basic PID control loops.

Within the settler's model, component mass balances for each of the three liquid phases are formulated separately and connected to the phase separation model described in Section 4.2.4. As described there, the model is able to predict the appearance and disappearance of each phase individually. For the mini plant model, this is then translated to compositions and sizes of the hold-ups, based on temperature and overall composition. Based on the individual phase heights, outflows via each of the three liquid outlets are then also (de-)activated using sigmoidal switches.

In case of the hydroformylation, the model describes 12 components overall, i.e., 1-dodecene, iso-dodecene, iso-tridecanal, n-tridecanal, H_2 , CO, water, rhodium precursor, and sulfoxanthphos ligand. All control loops contained within the actual mini plant are also represented by the respective PID controller equations in the model to fully mimic the plant behavior.

An excerpt of the full dynamic mini plant model is given in Figure 5.8. On the left-hand side, the hierarchical and modular structure of the model is displayed, while on the right-hand side the kinetic expressions, the six considered reaction rates are shown. The entire dynamic mini plant model consists of 544 differential algebraic equations. For various applications (Section 5.4.3), this model is automatically exported to Matlab and gPROMS [180], wherein several hours of plant operation can be solved within a few minutes.

As mentioned above, a strength of the model structure of MOSAICmodeling is to apply transformations on entire models or model parts. For the state estimation discussed in Section 5.4.3, a fully discretized version of the dynamic mini plant model is required. Here, orthogonal collocation on finite elements is applied to

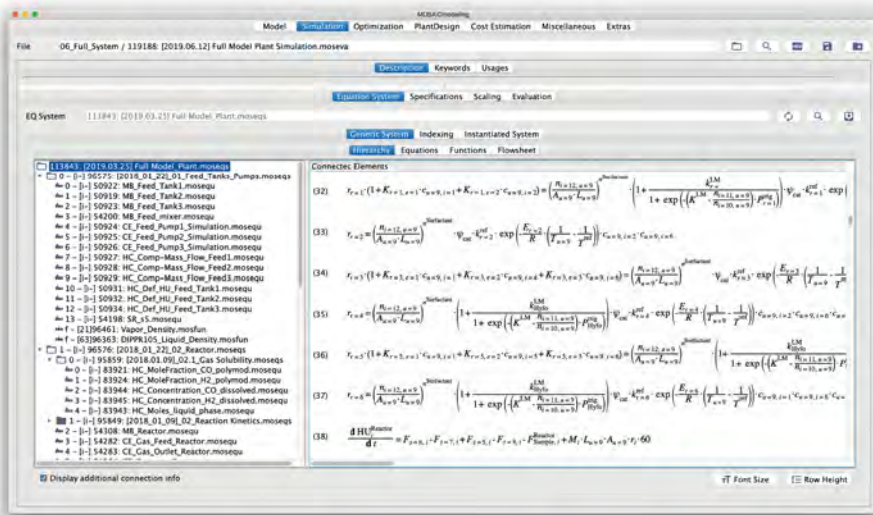


Figure 5.8: The dynamic model of the MES mini-plant within MOSAIC modeling.

discretize time [17]. To this end, the transformation module of MOSAIC modeling is used to automatically turn the differential algebraic formulation into a fully algebraic one, which is displayed in Figure 5.9.

$$\begin{aligned}
 (27) \quad r_{r=1,fc,cp} &= (1 + K_{r=1,e=1} \cdot c_{u=9,i=1,fc,cp} + K_{r=1,e=2} \cdot c_{u=9,i=2,fc,cp}) \cdot \left(\frac{n_{i=12,u=9,fc,cp}}{A_{u=9} \cdot L_{u=9,fc,cp}} \right)^{\text{Surfactant}} \cdot \left(1 + \frac{k_{r=1}^{LM}}{1 + \exp\left(-K_{r=1}^{LM} \cdot \frac{n_{i=11,u=9,fc,cp}}{n_{i=10,u=9,fc,cp}}\right)} \right) \\
 (28) \quad r_{r=2,fc,cp} &= \left(\frac{n_{i=12,u=9,fc,cp}}{A_{u=9} \cdot L_{u=9,fc,cp}} \right)^{\text{Surfactant}} \cdot \psi_{\text{cat,fc,cp}} \cdot k_{r=2}^{\text{ref}} \cdot \exp\left(-\frac{E_{r=2}}{R} \cdot \left(\frac{1}{T_{u=9,fc}} - \frac{1}{T_{\text{ref}}}\right)\right) \cdot c_{u=9,i=2,fc,cp} \cdot c_{u=9,i=6,fc,cp} \\
 (29) \quad r_{r=3,fc,cp} &= (1 + K_{r=3,e=1} \cdot c_{u=9,i=1,fc,cp} + K_{r=3,e=2} \cdot c_{u=9,i=4,fc,cp} + K_{r=3,e=3} \cdot c_{u=9,i=6,fc,cp}) \cdot \left(\frac{n_{i=12,u=9,fc,cp}}{A_{u=9} \cdot L_{u=9,fc,cp}} \right)^{\text{Surfactant}} \cdot \psi_{\text{cat,fc,cp}} \\
 (30) \quad r_{r=4,fc,cp} &= \left(\frac{n_{i=12,u=9,fc,cp}}{A_{u=9} \cdot L_{u=9,fc,cp}} \right)^{\text{Surfactant}} \cdot \left(1 + \frac{k_{Hyfo}^{LM}}{1 + \exp\left(-K_{Hyfo}^{LM} \cdot \frac{n_{i=11,u=9,fc,cp}}{n_{i=10,u=9,fc,cp}}\right)} \cdot P_{Hyfo}^{\text{sig}} \right) \cdot \psi_{\text{cat,fc,cp}} \cdot k_{r=4} \cdot \exp\left(-\frac{E_{r=4}}{R} \cdot \left(\frac{1}{T_{u=9,fc}} - \frac{1}{T_{\text{ref}}}\right)\right) \cdot c_i \\
 (31) \quad r_{r=5,fc,cp} &= (1 + K_{r=5,e=1} \cdot c_{u=9,i=1,fc,cp} + K_{r=5,e=2} \cdot c_{u=9,i=5,fc,cp} + K_{r=5,e=3} \cdot c_{u=9,i=6,fc,cp}) \cdot \left(\frac{n_{i=12,u=9,fc,cp}}{A_{u=9} \cdot L_{u=9,fc,cp}} \right)^{\text{Surfactant}} \cdot \left(1 + \frac{k_{Hyfo}^{LM}}{1 + \exp\left(-K_{Hyfo}^{LM} \cdot \frac{n_{i=11,u=9,fc,cp}}{n_{i=10,u=9,fc,cp}}\right)} \right) \cdot \psi_{\text{cat,fc,cp}} \\
 (32) \quad r_{r=6,fc,cp} &= \left(\frac{n_{i=12,u=9,fc,cp}}{A_{u=9} \cdot L_{u=9,fc,cp}} \right)^{\text{Surfactant}} \cdot \left(1 + \frac{k_{Hyfo}^{LM}}{1 + \exp\left(-K_{Hyfo}^{LM} \cdot \frac{n_{i=11,u=9,fc,cp}}{n_{i=10,u=9,fc,cp}}\right)} \cdot P_{Hyfo}^{\text{sig}} \right) \cdot \psi_{\text{cat,fc,cp}} \cdot k_{r=6}^{\text{ref}} \cdot \exp\left(-\frac{E_{r=6}}{R} \cdot \left(\frac{1}{T_{u=9,fc}} - \frac{1}{T_{\text{ref}}}\right)\right) \cdot c_i \\
 (33) \quad c_{u=9,i=7,fc,cp} \cdot A_{u=9} \cdot L_{u=9,fc,cp} &= \frac{n_{u=9,fc,cp}^L \cdot X_{i=7,fc,cp}}{1 - X_{i=7,fc,cp}}
 \end{aligned}$$

Figure 5.9: Discretized form of the dynamic mini-plant model.

Through the automatic discretization, the state variables within the models obtain two new indices: cp for the collocation position and fe for the number of the finite element. Control variables are assumed constant for each individual finite element and, hence, only receive the index, fe . For the usage in Section 5.4.3, the model is realized with 16 finite elements, each 15 min long, and a collocation order of 3. Hence, the fully discretized model amounts to 28,720 nonlinear equations. For simulation and optimization purposes, this model is exported to AMPL [41], wherein it can also be reliably solved within minutes.

Given MOSAICmodeling's modular model structure, the described model is easily adjusted for other applications. Regarding the reductive amination, the kinetics are replaced, gas solubilities adjusted, and a membrane module is added to the recycling.

5.2.1.7 Outlook on Model Development and Collaboration

With the afore-described data model and the corresponding implementation within MOSAICmodeling, a highly versatile platform for model development, management, and exchange has been created. By now, this is a mature technology and is widely in use. More than 2,000 users have accounts on MOSAICmodeling. Beyond the work described herein, MOSAICmodeling is in use for further research projects and teaching activities [38]. Drawing from the advances in dynamic models for complex chemical processes, MOSAICmodeling's model library now features a number of new process units to support a fully pressure-driven process simulation, which is, in general, beyond the scope of the state-of-the-art commercial tools. There are, of course, further interesting research paths to pursue to further extend the data model, e.g., to set-based algebra or the support of algorithmic solution paths. Besides, the master-slave configuration of the database servers needs to be continuously updated to account for the growing user base. The next step here will be research into asynchronous updates between servers, across many locations, building on modern web technologies.

5.2.2 Fluid-Dynamic Investigations of Multiphase Processes

Péter Kováts, Michael Mansour, Anurag Misra, Reddy Velagala,
Gábor Janiga, Dominique Thévenin, Katharina Zähringer

5.2.2.1 Introduction

Most processes considered in this book involve a very large number of coupled physicochemical processes. For all those taking place far above the molecular scale, the mesoscopic conditions found locally in space and time control both transport and reaction steps. For this reason, a better understanding of the hydrodynamic properties (velocity, possible fluctuations due to turbulence, but also in a more general sense temperature, pressure, concentrations, size distributions . . .) is essential to

identify the optimal process and operation conditions. Due to the complexity of the configurations considered here, combined studies involving a theoretical, numerical, and an experimental part are generally necessary. Theoretical and numerical models (the latter being denoted as CFD for Computational Fluid Dynamics) always require validation, best achieved by direct comparison with measurement data; on the other hand, experiments are complex and costly, and typically cannot provide all relevant fields. For this reason, the two following sections describe both, numerical flow simulations and detailed experimental investigations of flow and scalar fields, going hand in hand for the identification of optimal conditions.

5.2.2.2 Numerical Flow Simulations of Reactor and Settler for the MES Process

Introduction Regarding Numerical Flow Simulation

As already explained, when presenting the MES process in Section 2.2, a good separation of the aqueous phase, within which the valuable catalyst is dissolved, is highly desirable and forms a crucial aspect of process design. For this purpose, the gravity-driven separation of a multi-phase microemulsion system, consisting of water, oil, and a surfactant in a temperature-controlled stirred tank reactor (STR), is investigated. The main hydrodynamic features in the STR have been first investigated in detail, as explained next. Then, stirring is stopped and the separation process starts in the batch reactor. Droplet interaction processes are incorporated in the simulation using dedicated coalescence models. By comparison with experimental data regarding separation times [71], the free parameters of the coalescence model can be optimized with regard to the specific system considered in the project. The underlying idea is that a suitable model with adapted parameters will be able to accurately capture the separation kinetics and can be used for the later design and optimization of real separators, as considered at the end of this section. Figure 5.10 shows the strategy guiding this research project.

For all simulations, a numerical modeling method, combining the Euler-Euler multi-fluid framework with the Quadrature Method of Moments (QMOM), is employed on top of the standard equations, describing the conservation of mass and momentum (Navier-Stokes equation). An energy conservation equation based on the temperature variable is added to describe heat transfer processes, since the system is only stable for a narrow temperature window. The conservation equations of fluid dynamics being standard and found in many textbooks, for instance in Marchisio and Fox [135], they are not repeated here in the interest of space. Instead, the focus is on the QMOM approach and the very important coalescence model.

In order to get suitable boundary conditions and as a preparatory step for later simulations of the reactor, the hydrodynamic fields in the Stirred Tank Reactor used for the batch separation experiments have been first investigated in detail. Here, the flow conditions are turbulent, so that a suitable turbulence model must be selected.

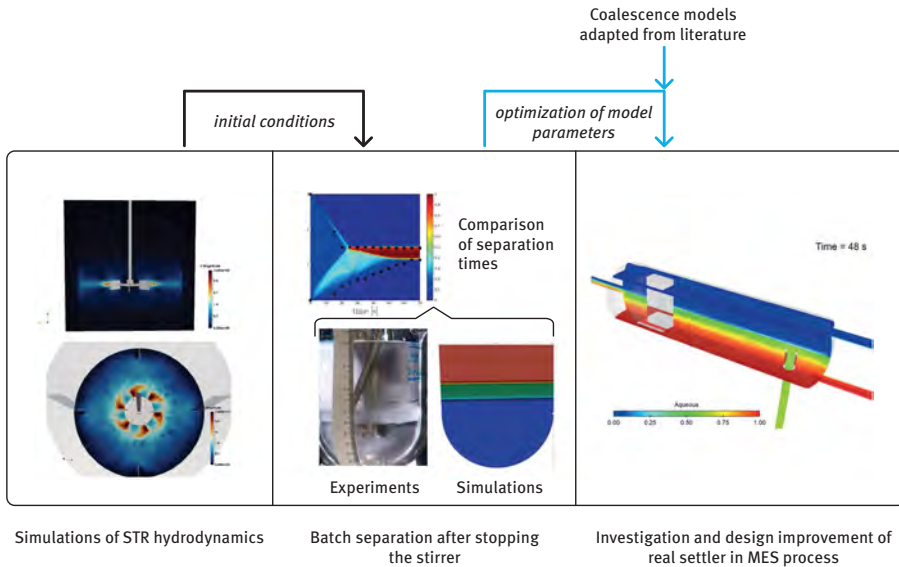


Figure 5.10: Strategy used during this research project.

Both the classical approach based on the Reynolds-Averaged Navier-Stokes Equations (RANS) using the standard k - ϵ model, and the advanced technique called the Large-Eddy Simulation (LES) have been compared for this purpose (Figure 5.11, left). These comparisons revealed that unsteady RANS simulations deliver in the present configuration, a sufficiently accurate description of the reactor hydrodynamics (for instance, a very good estimate of the power number, Figure 5.11, right), particularly so when taking into account the extremely long computing times required by LES, preventing any systematic studies. CFD simulations, based on unsteady RANS, can thus be used for analyzing the reactor, and to get the conditions before the batch separation experiments—starting from when the stirrer is stopped.

Numerical Modeling of a Separating Multiphase System

For cases involving non-homogeneous conditions in space, as found here, a comprehensive description of the separation process will, in general, be necessary to meet the accuracy requirements. For this purpose, Computational Fluid Dynamics can provide the starting point for the implementation of additional models, as explained above. While traditional CFD methods can readily deliver velocity, temperature, and concentration fields as a function of space and time for the continuous phase, the evolution of the dispersed population(s), i.e., of the microemulsion droplets, in the present case, must be described using additional approaches. The separation processes considered in this project are mainly controlled by buoyancy and take place at very low Reynolds numbers, Re . The numerical simulation of the settling process is implemented

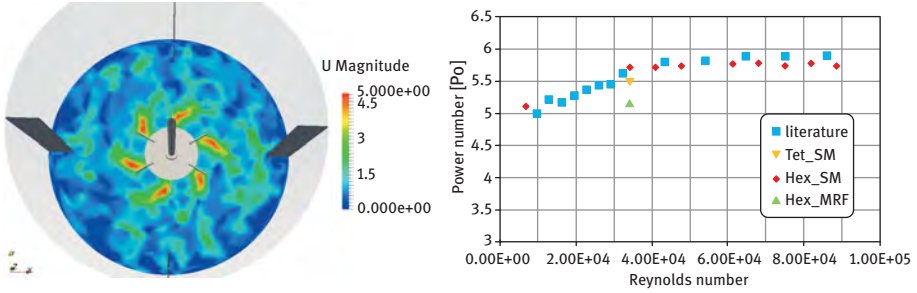


Figure 5.11: Left: Instantaneous velocity field in the STR tank, computed by LES; Right: comparison of the power number measured experimentally by Chapple et al. [20]; and of the numerical prediction obtained by the unsteady RANS simulations, using different grid types and rotation models.

using the Euler-Euler multi-fluid approach, which is well suited for flows containing a sufficiently large volume fraction of the disperse phase(s). The open-source OpenFOAM solver “multiphaseEulerFoam” (version 2012) was chosen for this purpose since it already contains a suitable multi-fluid model and can be freely extended.

Gravitation, drag, and surface tension are the dominating driving forces in the separation process under the aforementioned conditions. In the numerical model, the surface tension was assumed to be independent of flow conditions, with surface tension values for each phase pair obtained from companion experiments [71]. Drag on the disperse phase droplets of diameter d_k with respect to the continuous phase was evaluated using the following equation [215], where the subscripts c and d refer to the continuous and disperse phases, respectively, α denotes phase volume fractions, and u , the corresponding velocity:

$$\vec{F}_{D,k} = \frac{3}{4} \rho_c \alpha_d \alpha_c C_D \frac{|\vec{u}_d - \vec{u}_c| (\vec{u}_d - \vec{u}_c)}{d_k} \quad (5.7)$$

The drag coefficient, C_D , is estimated using the standard correlation of Schiller and Naumann [194] as a function of the (low) Reynolds number, Re . In order to track the time-evolution of the droplet size distribution $n(d,t)$ of the disperse phase(s), a population balance model (PBM) is coupled to CFD in order to describe a purely coalescing system, with the associated rates for birth, B_{coal} , and death, D_{coal} , under the consideration of a convective term with phase velocity, \vec{u}_α :

$$\frac{\partial n(d,t)}{\partial t} + \nabla \cdot (\vec{u}_\alpha n(d,t)) = S(d,t) = B_{coal} - D_{coal} \quad (5.8)$$

The corresponding set of equations is highly complex and a direct numerical solution is not possible within acceptable computational times. For this reason, a practical solution is achieved by transforming the PBM with the help of the moments of the distribution, $n(d,t)$. In the present case, the method called Quadrature Method of Moments

(QMOM), being generally more stable than other alternatives, has been selected [136, 137, 143, 144]. An implementation of this algorithm is available in the open-source library, OpenQBMM Version 6 [171], which was coupled with OpenFOAM and used for all subsequent simulations.

Using QMOM, the distribution, $n(d,t)$, is approximated by its first moments, μ_k :

$$\mu_k = \int_0^{\infty} d^k n(d) dd \quad (5.9)$$

In the present project, five moments have been systematically used, (μ_0 to μ_4). Then, a transport equation is solved to describe the evolution in time and space of these moments, in which the term on the right-hand side quantifies the importance of coalescence in the present application:

$$\frac{\partial \mu_k}{\partial t} + \nabla \cdot (\bar{\mathbf{u}} \mu_k) = \bar{S}_k \quad (5.10)$$

Two different coalescence models have been implemented to compute this term, and then compared with experimental data: 1) a simple model based originally on the work of Prince and Blanch [179], later extended by Lehr et al. [122] with a single free parameter, the critical velocity u_{crit} , as presented by Liao and Lucas [123]; 2) a simplified version of Grimes' model [56] with two free parameters, the binary coalescence parameter, K_{CE} , and the hindered sedimentation parameter, K_{SV} , both non-dimensional. In both cases, the computation of the coalescence kernel involves the product of a collision frequency (within square brackets) and a coalescence efficiency (after the \times -sign). This leads to:

- Buoyancy model adapted from Prince and Blanch, with u_{rel} , the relative velocity of the two droplets:

$$\beta = \left[\frac{\pi}{4} (d + d')^2 u_{rel} \right] \times \exp \left[\frac{-u_{rel}}{u_{crit}} \right] \quad (5.11)$$

- Simplified version of the Grimes' model, involving the Péclet number, Pe:

$$\begin{aligned} \beta = & \left[\frac{k_B T}{6\mu_c} \frac{(d + d')^2}{dd'} \left(1 + \text{Pe}(d, d') + 4.496 \text{Pe}(d, d')^{1/3} \right) \right] \\ & \times \exp \left[- \frac{1.046}{K_{CE}} \frac{|\rho_d - \rho_c| \mu_c g}{\Gamma^{3/2} B^{1/2}} \left(\frac{dd'}{d + d'} \right)^{9/2} \right] \end{aligned} \quad (5.12)$$

- with the Péclet number computed by:

$$\text{Pe}(d, d') = \left(\frac{3}{4\pi} \right)^{1/3} (1 - \alpha_d)^{K_{SV}} \frac{|\rho_d - \rho_c| g}{k_B T} \frac{dd'}{d^{2/3} - d'^{2/3}} \quad (5.13)$$

Finally, the implemented coupling between OpenFOAM and OpenQBMM, together with the exchange of information needed for the computational procedure, is illustrated in Figure 5.12.

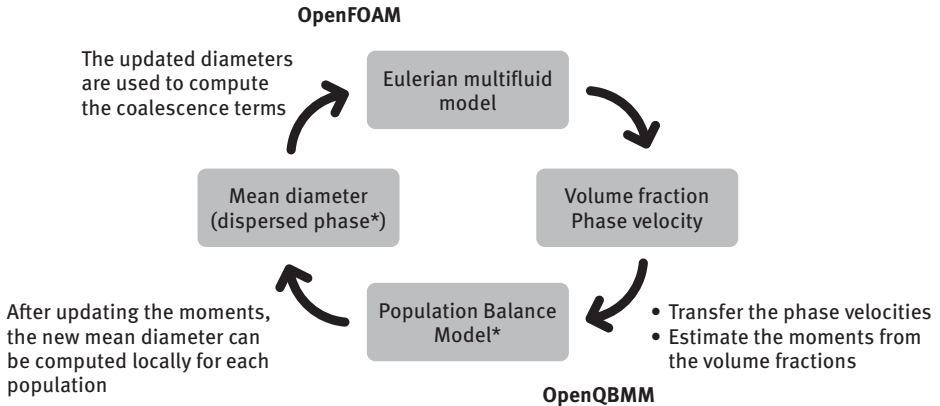


Figure 5.12: Working principle of the coupled numerical simulation between OpenFOAM and OpenQBMM used for all results described and discussed in this section concerning liquid-liquid separation.

Based on a series of separation experiments in a temperature-controlled glass tank (Figure 5.13, left) for a variety of process conditions [71], compared to our numerical predictions, optimal values of these parameters for the considered system have been finally identified as $u_{\text{crit}} = 0.21$ mm/s for the first model, and $K_{\text{CE}} = 0.65$ and $K_{\text{SV}} = 9.44$ for the second one. To identify the corresponding values, CFD-based optimization has been used—a technique widely employed in our group [206]. While varying freely the model parameters within a user-specified range using a Genetic Algorithm, the target function (to be minimized) is the mean difference between the experimentally measured separation times and the ones obtained numerically, tracking for this purpose, the contact surface between the aqueous and the organic phase in time (Figure 5.13, right). The optimal values determined, thanks to this procedure, are then employed for further computations.

Separation in the Real Settler

After having determined the optimal model parameters for the coalescence model and validated the coupled numerical approach (combining the two solvers, OpenFOAM and OpenQBMM) by direct comparisons for the batch settler experiments (Figure 5.14), the developed procedure can finally be applied to the target configuration—the continuous settler used for the mini plant experiments with the MES process.

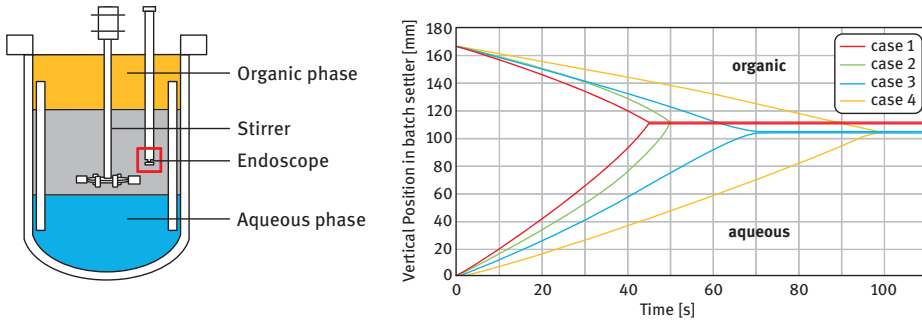


Figure 5.13: Left: Experimental set-up consisting of a temperature-controlled glass tank used in the investigation of a two-phase batch settling process [71], measuring the initial droplet-size distribution with the help of an endoscope. Right: Numerical prediction of the time-dependent separation process between organic and aqueous phase using the simplified Grimes model [56] for four different process conditions. The results shown here correspond to the finally identified, optimal model parameters.

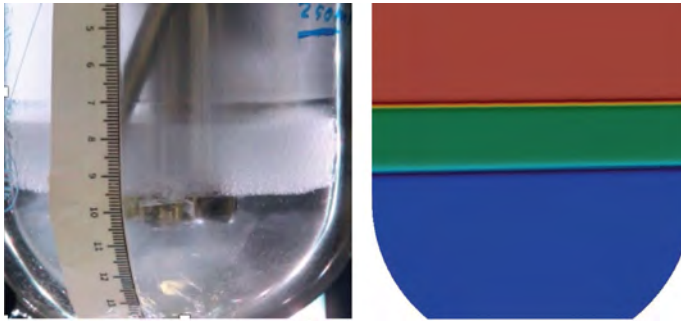


Figure 5.14: Direct comparison between the separation experiments in the batch settler (left) and own numerical simulations using the procedure described previously (right) at a given time during the process.

All the necessary details concerning the mini plant and its operation can be found in the literature [75–77] and in Section 4.2 of this book. For the simulations of the separation process, one strong but necessary hypothesis is that the optimal model parameters derived from the preliminary experiments in the batch settler can be kept identical for the much more complex, real settler geometry used for continuous phase separation and catalysis recycling after the reaction. One additional challenge is that the employed settler has been changed several times during the research project, leading to repeated simulations involving long computational times. Unfortunately, one single simulation of the full-scale three-dimensional settler for real process conditions takes at least days–up to weeks, even using parallelization on Linux clusters, depending on the physical time considered on the

particular geometry and the selected coalescence model. This is particularly true for the more detailed Grimes model, which requires additional computational power, compared to the simple buoyancy model. However, the model derived in this work, based on the original formulation by Grimes [56], is the only one that should be able to take into account the effects on separation due to surface tension as well as inhomogeneous distributions of temperature and surfactant concentration.

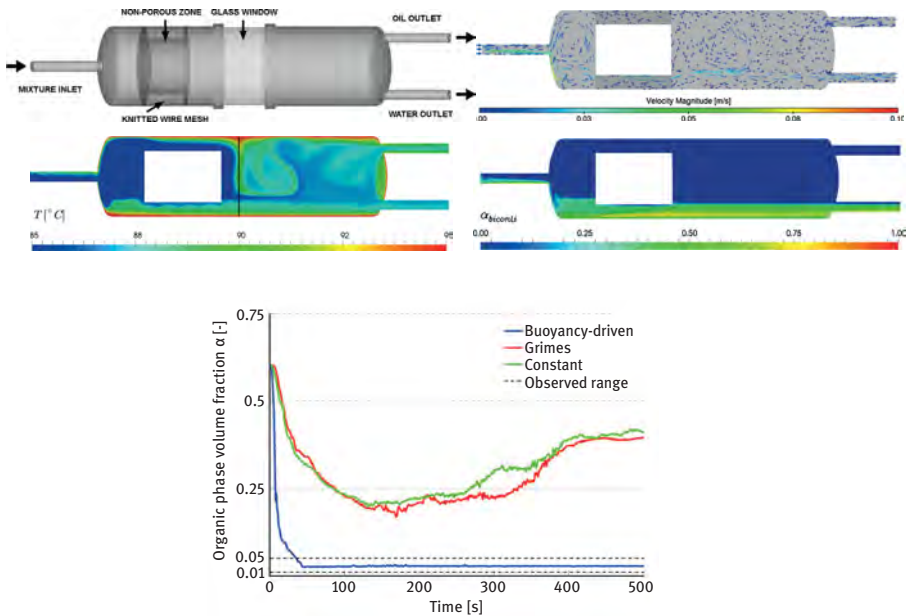


Figure 5.15: Top left: geometry of the settler. Top right: velocity field. Middle left: temperature field. Middle right: volume fraction of the bicontinuous phase, establishing itself between the organic and aqueous phases. Bottom: evolution of the volume fraction of organic phase at the bottom outlet of the settler (blue line), compared to the experimentally observed range (horizontal corridor delimited by thick dashed lines). Details can be found in Misra et al. [155].

First simulations considered the real geometry of the settler (as used at that time in the mini plant experiment) but simplified using a two-dimensional approximation [155]. The corresponding vertical cuts showing the different fields within the settler are shown in Figure 5.15.

As seen in this figure, the full Grimes model (red line) did not describe well the separation at that time, which was not due to the model itself, but to its numerical stiffness in the practical implementation. After checking this point further, the simplified version of this model, as described previously, has been implemented in OpenFOAM [154].

The later employed full-scale settler involving three outlets (one for each of the three phases; organic, aqueous, and bicontinuous) was finally simulated (Figure 5.16) in order to 1) better understand the separation process, and 2) identify bottlenecks, paving the way for a possible performance improvement in future studies. This investigation first revealed somewhat non-homogeneous velocity, temperature, and concentration fields, due to recirculation zones interacting with the temperature control through the external walls, impacting the separation. The porous zone existing in the first half of the settler noticeably impacts coalescence, as expected. The predicted time needed for a proper separation strongly depends on the employed coalescence model, but the final outcome of the simulation agrees well with experimental observations (as already shown in Figure 5.15). This reveals that, provided sufficient computational power is available, a detailed prediction of separation in complex systems can be achieved using CFD extended by suitable models, after properly calibrating the unknown model parameters, thanks to dedicated experiments.

A detailed analysis of the results obtained in the real settler revealed that the computation of the Péclet number appearing in the collision frequency for the Grimes' model can be numerically very stiff, depending on the local conditions; thus, often inducing numerical instabilities. For this reason, our current research concentrates on deriving a mixed model combining the collision frequency from the buoyancy-induced coalescence model from Prince and Blanch, together with a slightly modified expression for the coalescence efficiency, derived from the model of Grimes, still involving the same two model parameters, K_{CE} and K_{SV} . For this new model, the optimization procedure described previously must be repeated to identify suitable values for the parameters.

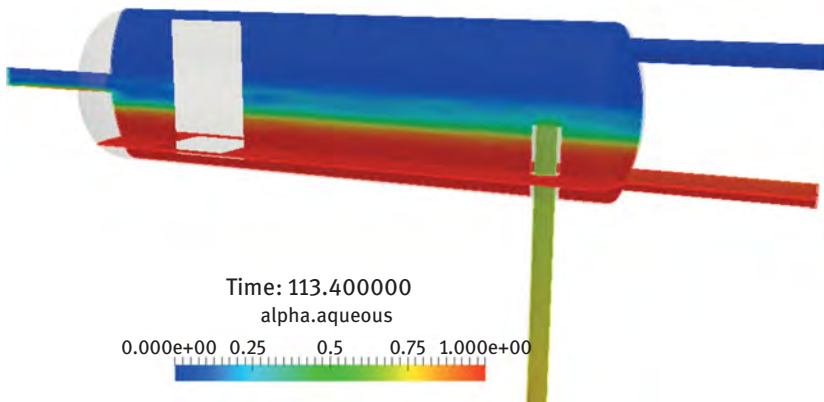


Figure 5.16: Volume fraction of the aqueous phase in the settler of the mini plant with three outlets, as obtained after 113.4 s of physical time with the simplified Grimes model, used in the coupled numerical procedure.

5.2.2.3 Fluid-Dynamic Investigation of Gas-Liquid-Liquid Continuous Helical Flow Reactors

For the hydroformylation of long-chain olefins in a thermomorphic multiphase system, Kaiser et al. [90], suggested a tandem reactor system consisting of a helically coiled tubular reactor (HCTR), connected to a continuous stirred tank reactor (CSTR) (Section 5.3.1). It was derived by an extensive model-based reactor synthesis and dimensioning study, for an already existing mini plant.

A hydrodynamic study of this reactor system, which is important for reactor modeling, dimensioning, and optimization, was necessary for the helically coiled tube reactor, as a special form of continuous flow reactors, since the performances of these reactors concerning mixing, heat and mass transfer are less known, than those of CSTR and plug-flow reactor (PFR).

For continuous processes, the most often used chemical reactors are stirred tank reactors, tubular reactors, and variations of these types. Due to their specific characteristics, they feature different mixing, especially back mixing, and heat and mass transfer properties. These properties are very important since they strongly influence the performance of the reactor, namely, the conversion and selectivity behavior in dependence on the underlying reaction kinetics. Moreover, if the reactants form a multi-phase flow, the operation of these reactors is completely different from a one-phasic operation, and the reactor geometry must be changed to enhance the performances.

It has been known for a long time that the axial back mixing and mass transfer behavior of tubular reactors can be enhanced by using coiled tubes (Figure 5.17, left), instead of straight ones [209]. Due to coiling, the centrifugal forces influence the flow, and a strong secondary flow forms in a radial direction, leading to Dean vortices (Figure 5.18, left). The development of these vortices enhances the radial mixing while keeping a low axial back mixing behavior. This increases heat and mass transfer, and leads to narrower residence time distributions [103, 209]. Other advantages of the coiled configuration are its higher compactness and relatively large surface area-to-volume ratio. Additionally, the laminar flow regime in coiled tubes is observed at larger Reynolds numbers, compared to straight tubes.

Helix Geometry

Although numerous studies were previously conducted to investigate the influence of different parameters on the advantages of helical pipes concerning heat and mass transfer, e.g. [51, 102, 159, 195], the characterization of pure mixing of miscible liquids in such apparatus, which is the basis of the aforementioned transfer processes, has rarely been undertaken. The group of Nigam [114, 198] experimentally and numerically investigated the influence of the Reynolds number, Schmidt number, and the curvature ratio on the mixing performances of different coiled geometries by determining the residence time. Saxena and Nigam [190] introduced a structured configuration



Figure 5.17: Coiled configurations: horizontal coil (left), Coiled Flow Inverter (center), Coiled Flow Reverser (right, European patent No. 19176360.6-1019, EP3741453 A1).

called the coiled flow inverter (CFI, Figure 5.17, center), in which the flow direction is inverted by bending the coils. In this way, the direction of the secondary flow is changed in order to improve mixing. The CFI can be simply constructed by fitting 90° bends at regular length intervals between the coils and it attracted, also due to its geometrical compactness, some more interest for industrial applications. In most CFI applications, the flow is usually inverted after at least 3 to 4 turns, e.g. [115, 160, 190], to ensure fully developed vortices, before changing the flow direction. Consequently, a considerable increase in pressure drop is unavoidable in most cases. Nevertheless, it was recently shown that mixing can even be improved by early flow inversion in the entrance region [98, 129]. This flow inversion can be provided by the use of a short CFI, which reverts the flow by 90° or a novel geometry, called coiled flow reverser (CFR, Figure 5.17, right), which leads to a 180° flow reversion [133].

The flow conditions leading to the apparition of secondary flow and symmetric vortices can be described by the Dean number, $De = Re \cdot \sqrt{\delta}$, which shows a dependency on the curvature ratio, $\delta = d/D$. A further parameter describing the geometry of a coil is its pitch, which is often represented as dimensionless pitch, $\gamma = P/(\pi D)$.

The influences of the helix geometry and the flow properties on mixing, heat and mass transfer were studied here on model geometries using Computational Fluid Dynamics (CFD) and locally and temporally resolved optical measurement techniques. Compared to the mini plant HCTR derived in Section 5.3.1, the model geometries had higher curvature ratios and bigger dimensionless pitches, due to the much smaller coil. For safety reasons and the fact that the TMS is two-phasic at temperatures $< 85^\circ\text{C}$, water was used in the model geometries instead of the TMS. However, as the outcomes of these studies confirm, the influence of these fluid parameters and geometrical differences between the mini plant HCTR and the smaller models on the examined processes are much less pronounced than the impact of the Reynolds number. Therefore, the results from the model geometries can be transferred to the mini plant HCTR as long as the same Reynolds number is respected. It ranges, in the studies presented hereafter, from $Re = 40$ to $Re = 1,000$; thus, a laminar flow regime is employed.

Mixing of the Liquid Phase

Using a helical pipe for mixing liquids may show noticeable advantages, compared to using a stirrer, since this is a robust solution (no moving parts), needs no additional

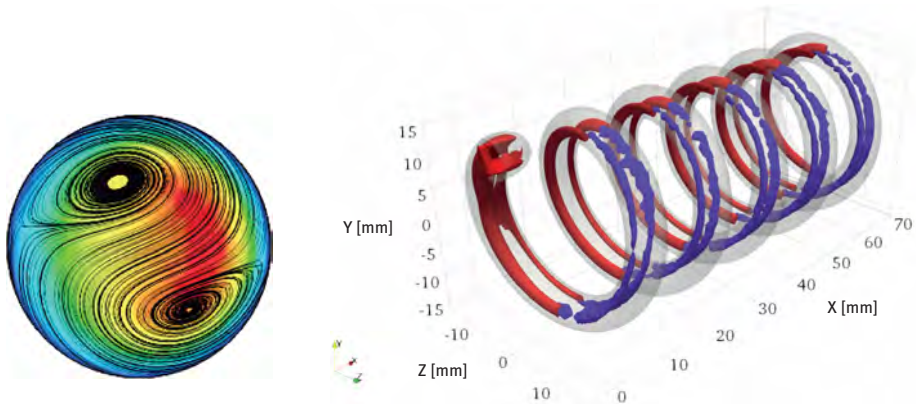


Figure 5.18: Left: Secondary flow structures (Dean vortices) for $Re = 200$ at the outlet of a 5-turn straight helical pipe. Calculations from [128]. Right: Dean vortices detected by 3D Q-criterion inside the helically coiled tube at $Re = 220$ and $De = 89$, as obtained from time-averaged measurements (purple isosurfaces) and simulation (red isosurfaces). Adopted from [104].

power source, and has a compact structure. Therefore, lower maintenance and energy consumption are usually required, compared to active mixers. Additionally, mixing in helical pipes can also take place efficiently in the laminar regime, avoiding energy losses associated with the generation of turbulence.

Liquid-liquid mixing was extensively examined here in different numerical and experimental configurations. The mini plant HCTR geometry (Section 5.3.1) was analyzed numerically and using the fluid properties of the TMS [86, 87]. In all configurations, the CFD code, Star-CCM+, was used for the calculations [128, 130], and planar laser-induced fluorescence (PLIF) and particle image velocimetry (PIV) were used to analyze the mixing and flow fields experimentally [103–105]. These studies showed a very good mixing behavior of the coiled reactors in the first 2–3 coils. Then, the established flow pattern with the secondary Dean vortices, which were visualized and quantified in three dimensions through tomographic PIV measurements and CFD calculations of the velocity fields inside the helical reactors (Figure 5.18, right), leads to only a slightly further mixing. This can be recognized in Figure 5.19 in the first row, where the mass fractions of two different liquids are represented in the cross-sections of a 6-coil straight helix reactor.

By varying the Reynolds number and looking at the outlet mixing efficiency for a variety of geometrical parameters (pipe diameter, d , coil diameter, D , and pitch, p), two maxima for the mixing efficiency were identified at about $Re \approx 35$ and $Re \approx 650$ (Figure 5.20) [130, 131]. Mixing shows a non-monotonic behavior with the change of Reynolds number, since the residence time, the vortex structure, and the vortex strength change simultaneously with Re . Here, it should be noted that the pressure drop in a helically coiled tube is generally higher, compared to a straight pipe of the

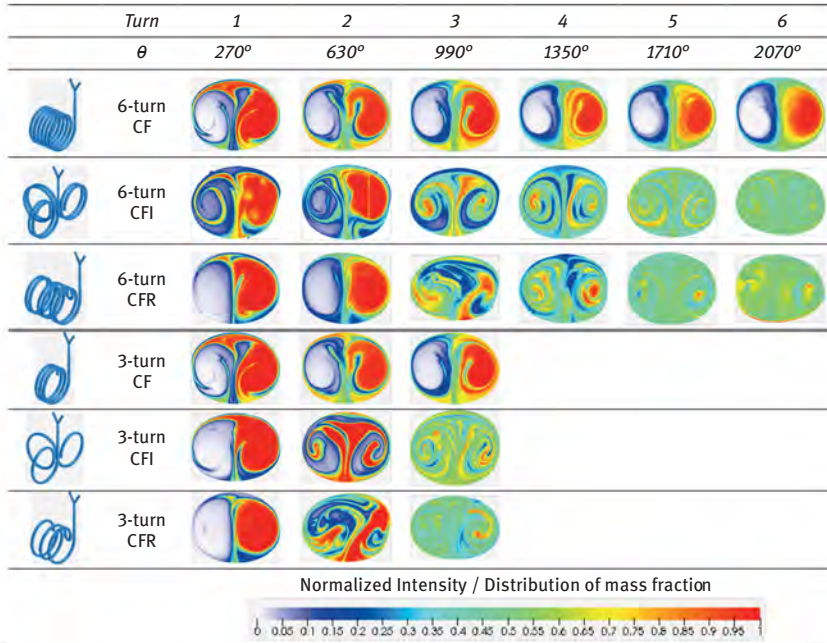


Figure 5.19: Mass fractions of two miscible liquids in cross-sections of different helically coiled reactor configurations at $Re = 500$. White and red regions correspond to the initial liquids; green regions show nearly complete mixing [105].

same length [78]. Accordingly, the first optimal Reynolds number should normally be preferred since the pressure drop is significantly lower, compared to the second optimal value. Only if the Reynolds number is smaller than 30 or bigger than 1,000, geometry has a major impact on the mixing efficiency. This shows that the transfer of the results obtained in the smaller model geometries to the bigger HCTR-geometry is possible since its Reynolds number ($Re \approx 100$) lies inside these limits.

In order to identify the most efficient helical geometry with the best mixing properties and lowest pressure drop, multi-objective numerical optimization for the flow of two miscible liquids in helical pipes was used in the aforementioned first optimal Reynolds number range [134], which also represented the range of Dean numbers in the mini plant HCTR (Section 5.3.1.4). The CFD simulations have been coupled with the optimization code, OPAL++, leading to an automatic evaluation loop, including geometry modeling, mesh generation, and post-processing. As a whole, 30 generations encompassing 1,226 CFD simulations have been completed during the optimization process. The resulting Pareto front involves 64 different individuals, in which good mixing and small pressure drop are found simultaneously. The first and last individuals of the Pareto front are represented together with the global optimum in Figure 5.21. Very low pipe diameters have been rejected in the

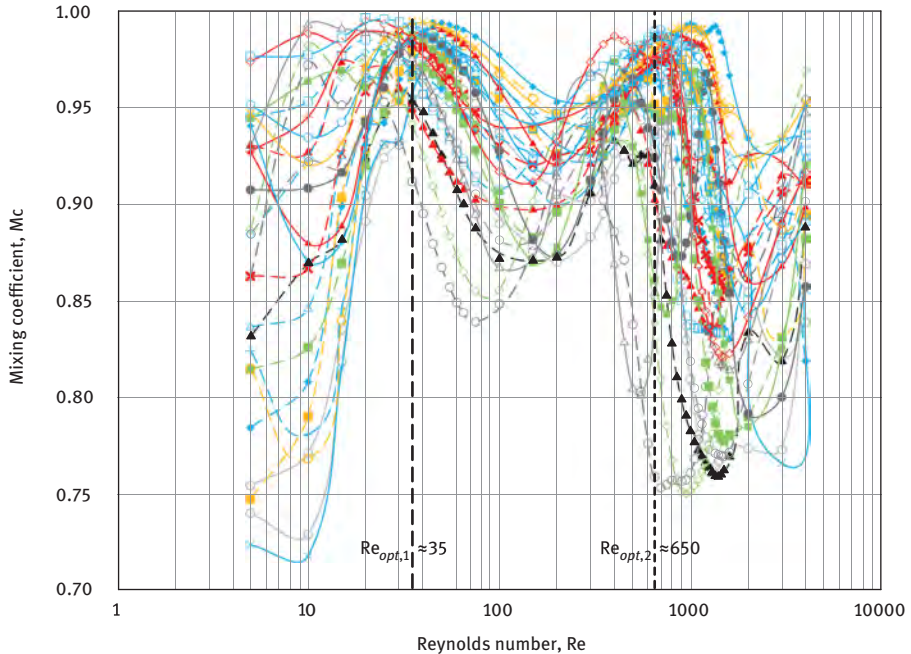


Figure 5.20: Outlet mixing coefficients of various helical geometries (G1–G27) as a function of the Reynolds number. For geometrical details, see Mansour et al. [130]. Two optimal regions for mixing can be identified at around $Re \approx 35$ and $Re \approx 650$.

optimization since they lead to unacceptably high-pressure losses. A low-to-moderate curvature ratio was found optimal. All optimal solutions correspond to low dimensionless pitch, torsion, and torsion number.

The results of all these numerical and experimental investigations showed the establishment of a stable vortex pair in the helical coils after 2–3 turns. Therefore, for heat and mass homogenization purposes, it is advantageous to disrupt this established flow field by early flow redirection, as it is done in coiled flow inverters, which have 90° bends after several turns (Figure 5.17, center). The effect of this bending can be even reinforced through a further redirection of the flow to 180° . These coiled flow reversers (CFR, Figure 5.17, right, European patent No. 19176360.6-1019, EP3741453 A1), were compared to straight helical coils (CF) and CFI, with the same diameters and lengths, in several numerical and experimental studies [98, 105, 133] concerning mass and heat transfer, respectively. These show the clear advantage of flow redirection for homogenization. CFI and CFR attain nearly complete mixing after only a few helical turns if the bending takes place after each first (rows 5–6 in Figure 5.19) or second (rows 2–3 in Figure 5.19) turn. The CFR performs even better than the CFI in the region of the second mixing optimum at $Re \approx 650$ [105].

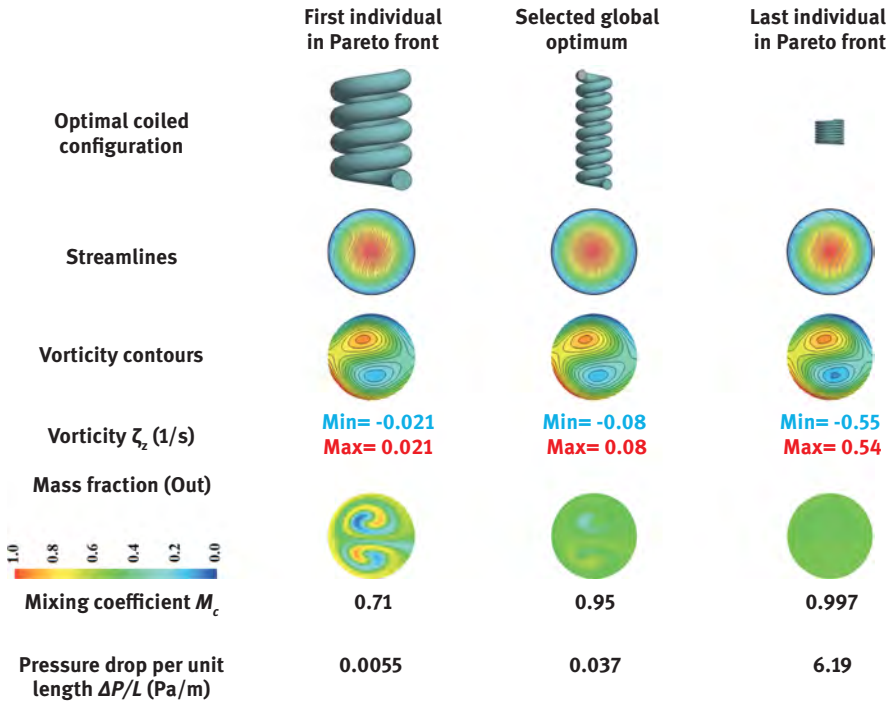


Figure 5.21: Results of numerical CFD helix geometry optimization: first and last individual of Pareto front, together with the global optimum. Their streamlines, vorticity, mass fractions, mixing coefficients, and pressure drop are also represented [134].

Heat Transfer

Due to the increased heat transfer coefficient, compared to straight pipes, the thermal properties and heat transfer in helical pipes have been extensively considered in early studies, e.g. [84, 112, 187, 196]. The effect of several process parameters was considered for different boundary conditions, such as constant wall flux, constant wall temperature, or convective heat transfer, e.g. [79, 178]. As a result, various correlations were proposed concerning Nusselt number, critical Reynolds number, and associated friction factor, based on experimental data or analytical solutions. However, no generally valid correlation has been developed covering all relevant geometrical parameters, boundary conditions, or flow characteristics. In addition, different correlations are sometimes inconsistent with each other, even for the same conditions. Therefore, additional studies are still useful to shed light on such issues. For practical applications, it is important to obtain a uniform fluid temperature as fast as possible after heat addition, to avoid inhomogeneity. Consequently, in the investigation presented hereafter, the homogenization performances were studied in terms of the coil length needed for reaching a homogenous temperature profile after heat addition.

This has been done numerically in two different studies [129, 133]. First, the thermal homogenization in a horizontally-coiled helical pipe was compared when heating either the entrance region or other locations within the fully-developed flow. Reynolds numbers between 2,000 and 16,000 were considered in a water flow. The heat was added to the flow by a constant-temperature wall, heating the first, third, or the fifth turn of a ten-turn coil individually. The average Nusselt number of the first-turn case was found to be noticeably higher than for the other two cases, increasingly so at higher values of the Reynolds number. Also, temperature homogenization is reached much earlier in that case, and the required homogenization length is almost independent of the Reynolds number. These results show, once more, the importance of the developing flow pattern for homogenization. Therefore, flow redirection, like in CFI or CFR, is advantageous for heat transfer as well.

For this reason, in the second numerical study, these reactors have been included and the heating of, initially, 27 °C warm water by 50 °C hotter reactor walls was examined. For low Reynolds numbers, the Nusselt numbers of the three reactors (straight coil, CFI, CFR) are comparable. However, for $Re > 1,000$, the Nusselt number of the CFR always shows the highest values. This can also be observed on the outlet temperature, shown in Figure 5.22; the values are constant and equal to the wall temperature for all geometries at low Reynolds numbers; in this case, perfect heat transfer was obtained, thanks to the long residence time. For higher Re , the CFI and the CFR can obviously lead to better heat transfer and higher averaged outlet temperatures. In all cases, the CFR shows the best heat transfer and thermal homogenization, which is reached much earlier, and the required homogenization length is almost independent of the Reynolds number.

Considering all these points, it is recommended to always select the first coil for controlling the temperature in a horizontally-coiled helical pipe. As a further consequence, reactors that are redirected after only a few coils should be preferred, as in short CFI and CFR.

Gas-Liquid Mass Transfer and Flow Regimes in Gas-Liquid Flows

Mass transfer has been considered in helically coiled tubes before, but most of these studies were executed by probe measurements, influencing the flow pattern inside the helix. Also, it should be mentioned that all these studies were performed in vertically orientated coils, which is different from the configurations used here.

The gas-liquid mass transfer of an annular flow has been studied in literature [7], with the determination of $k_L a$ -values. Similar measurements in the slug-flow regime were carried out in helically coiled tubes by Kulic and Rhodes [113]. The mass transfer in helically coiled tubes and straight horizontal tubes has been compared by Jespen [83]. In all these papers, $k_L a$ -values were found between 0.02 s^{-1} and 0.5 s^{-1} , depending on the flow regime employed. The comparison with straight tubes indicated a

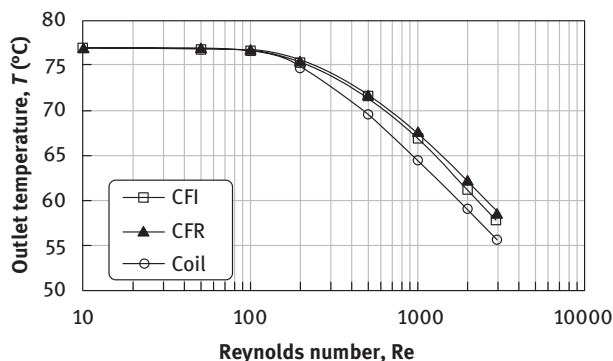


Figure 5.22: Surface-averaged outlet temperature of 3-turn coiled reactor configurations heated by a 77 °C hot wall at different Reynolds numbers [129].

higher mass transfer rate in the coiled tubes. The increased mass transfer rate found in coiled tubes was also confirmed by other studies [1, 60, 197] for liquid-liquid, solid-liquid, and gas-liquid situations.

In this study, the gas-liquid mass transfer in helical coils was examined experimentally and numerically in several model geometries [86, 103], since it is crucial for the reaction progress of the reactions considered within InPROMPT. Equivalent gas concentrations inside the liquid and also volumetric mass transfer coefficients were determined by laser-induced fluorescence of a tracer redox-reaction. The measurements showed that the saturation concentration was reached almost within the first 3–4 turns of the helix. The increase of the gas hold-up leads to higher mass transfer rates, whereas the liquid superficial velocity has no significant influence on the oxygen concentration in the liquid phase. The volumetric mass transfer coefficients were calculated from the measured oxygen concentrations and in the first turns of the helix, very high values of up to $k_L a = 3 \text{ s}^{-1}$ were obtained. When approaching saturation, these values decreased to around 0.2 s^{-1} for all examined conditions, which correspond to those of straight tubes. These findings underline the high impact of the Dean vortices on mass transfer processes. This effect is strongest during the very first turns of the helix.

The numerical and experimental analysis of the two-phase flow regimes in helical coils [132, 161] further showed that the velocity profiles and vortex structures are much more complex under two-phase flow conditions (Figure 5.23). The flow fields in the Taylor plug-flow regime show an additional vortex pair, counter-rotating in front of the bubbles. Compared to the Dean vortices, these are shifted to the outer side of the horizontal helix. With higher flow velocities, those secondary vortices extend deeper into the liquid slug and produce further tertiary vortices, rotating in the opposite direction. With small bubbles, no vortices, except the dominant Dean vortices, appear in the liquid slug. Therefore, mixing is favored by small liquid slug lengths with

Taylor bubbles, where the vortices generated by the bubbles dominate the flow behavior inside the slug.

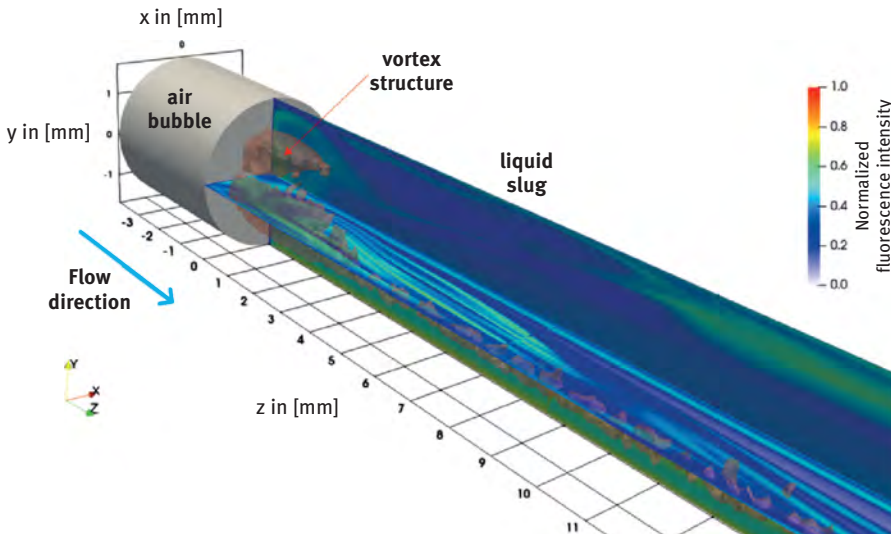


Figure 5.23: Mixing pattern and vortex structures (Q-criterion) in a liquid slug of a horizontal helically coiled gas-liquid reactor (unrolled visualization).

5.2.3 Surrogate Models for Thermodynamic Equilibria of Gas-Liquid and Liquid-Liquid Systems

Corina Nentwich, Stefanie Kaiser, Sebastian Engell

The first principle models are the methods of choice to describe chemical processes as they provide reliable results over a wide range of process conditions. In process synthesis, the thermodynamic models that describe the phase equilibria and compute the solubilities of the components in reaction systems are important building blocks of the flowsheets.

Equations of state, e.g., PC-SAFT, are powerful methods to predict the phase equilibria of complex systems (Section 3.1.1), but they are computationally expensive because iterative solutions of the density root problem and the phase equilibrium condition must be performed. The thermodynamic equilibrium conditions must be computed in each iteration of the solver, repeatedly. This leads to a very large number of equilibrium calculations and, therefore, such complex equations of state are difficult to use directly in optimization [163]. For example, in the case of the optimization of the layout and the operating parameters of distillation columns, the number of such calculations is very large because the thermodynamic equilibrium has to be

computed for each stage individually, leading to either a large number of calls to an external system of equations or a large increase in the number of equations that have to be solved simultaneously. A solution for this issue is the application of surrogate models. Surrogate models are black box models that can be evaluated fast and can replace more complex models. Examples of surrogate models are neural nets (ANNs), Kriging models, support vector machines (SVM), or other generic approximation functions.

Surrogate models are fitted by optimization of the free parameters of the surrogate models at a set of data points (sampling points) where the output values are obtained from querying the original model or from experiments. The selection of the sampling points has a strong influence on the quality of the final surrogate model.

A common sampling approach is space-filling or exploratory sampling, which covers the input space more or less equidistantly. Here, the location of all sampling points can be determined before any knowledge about the function has been generated. However, as all regions of the function are covered equally, no special emphasis is put on covering regions with more complex structures and, therefore, potentially larger errors of the surrogate model. An example that illustrates this problem is shown in Figure 5.24.

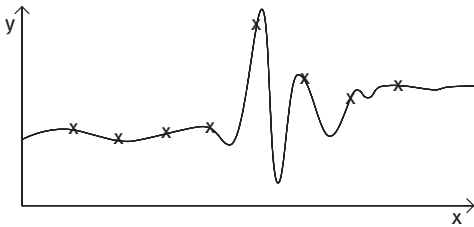


Figure 5.24: Example of a space-filling design.

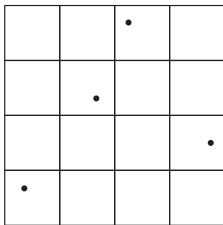


Figure 5.25: LHS design.

Examples of space-filling designs are full-factorial or partial factorial designs. The input space is divided into discrete levels and samples are taken at all combinations of these levels. Another variant that leads to fewer sampling points is the Latin-hypercube design (LHS). As for the factorial design, the input space is discretized, but the samples are not located at all combinations of all levels; only one sample is placed on each level and the distance between the sampling points is maximized

when distributing them. An example of the LHS design for a 2-dimensional space is shown in Figure 5.25. Space-filling sampling designs are widely used, but not efficient for complex structures or if discontinuities in specific regions exist. Space-filling sampling is an example of an explorative strategy as the entire region is equally covered. In contrast, exploitative strategies cover those parts of the input region more intensely that contribute most to the objective function value, i.e., where larger errors are expected or observed. Adaptive or sequential sampling seeks a compromise between exploration and exploitation and is, therefore, better suited for cases where large variations of the output are observed in some regions, whereas in other regions, the outputs are relatively smooth. In sequential sampling, additional points are added to the set of sampling points, iteratively, to improve the fit of the surrogate model. Sequential sampling approaches have been studied intensely in recent research [49, 85, 163, 165].

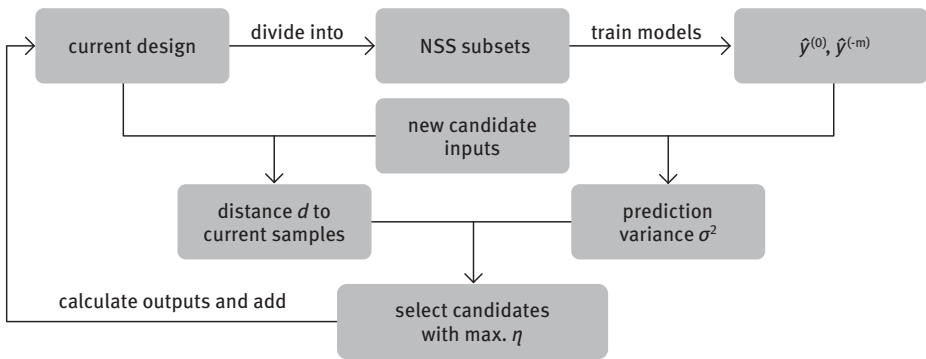


Figure 5.26: Graphical scheme of the sampling design update of the mixed adaptive sequential sampling [165].

Sequential designs originally mostly aimed at meeting the exploitative objective. Crombecq et al. [26] developed an algorithm, placing additional samples to explore regions with only a few points, and in the approach of Cozad et al. [25], the additional points are chosen such that the error between the true function value and the surrogate model prediction is maximized. This approach leads to a large number of expensive function evaluations, which can be overcome by the mixed adaptive sampling that was proposed by Eason and Cremaschi [33], and further developed by Nentwich and Engell [163], and Nentwich et al. [165]. This approach seeks a trade-off between a space-filling objective and exploitation. The principle is depicted in Figure 5.26. An initial current sampling design, e.g., a LHS design of small size, is divided into NSS subsets. These subsets are used to train surrogate models of the same structure: model $\hat{y}^{(0)}$ is based on the complete dataset and each model $\hat{y}^{(-m)}$ is based on all subsets

except for the subset m , which is left out. The next step is to propose a set of new sample candidates, for which only the input variables are proposed without calculating the output. This can be performed using a space-filling sampling design. Without knowing the actual output of the true function at the proposed input locations, the candidates can be assessed by calculating the distance of each candidate to all samples already present in the current design, which represents the explorative sampling criterion, and by calculating the prediction variance of all beforehand trained subset models, representing the exploitative sampling criterion. The minimum Euclidean or Manhattan distance d_j between the new candidate, j , and the N already existing points can be used as the distance measure. They are calculated as

$$d_j(\text{Euclidean}) = \min_{n \in \{1, \dots, N\}} \|x_j - x_n\|^2, \quad (5.14)$$

$$d_j(\text{Manhattan}) = \min_{n \in \{1, \dots, N\}} \|x_j - x_n\|. \quad (5.15)$$

The prediction variance can be calculated by the Jackknife variance as proposed by Eason and Cremaschi [33]; alternatively, bootstrapping can be used as shown by Nentwich et al. [165]:

$$s_j^2(\text{Jackknife}) = \frac{1}{N_{SS}(N_{SS} - 1)} \cdot \sum_{i=1}^{N_{SS}} (\tilde{y}_{ji} - \bar{y}_j)^2, \quad (5.16)$$

$$s_j^2(\text{Bootstrap}) = \frac{1}{B-1} \sum_{b=1}^B (\tilde{y}_j^{X_b} - \bar{y}_j)^2, \quad (5.17)$$

where \bar{y}_{ij} is the weighted average of the jackknife pseudo values (eq. (5.19)) of each candidate, j , predicted by the subset model, i , in the case of the Jackknife prediction variance. For the bootstrap prediction variance, random samples with replacement are drawn from the existing sampling design, resulting in a new sampling design X_b . Based on this design, a surrogate model $\tilde{y}_j^{X_b}$ is trained and the procedure is repeated B times. For the Jackknife prediction variance, Nentwich and Engell [163] proposed an alternative formulation, which is based on the number of samples N_i in subset i :

$$s_j^2 = \sum_{i=1}^{N_{SS}} \frac{1}{N(N - N_i)} (\tilde{y}_{ji} - \bar{y}_j)^2 \quad (5.18)$$

with

$$\bar{y}_j = \sum_{i=1}^{N_{SS}} \frac{N - N_i}{\sum_{l=1}^{N_{SS}} N - N_l} \cdot \tilde{y}_{ij} \quad (5.19)$$

and

$$\tilde{y}_{ij} = N\hat{y}^{(0)} - (N - N_i)\hat{y}^{(-1)}. \quad (5.20)$$

The more samples that are included in subset, i , the larger is the weight assigned to the subset model that is based on this subset. Both the exploitative and the explorative criterion are combined into one sampling criterion η :

$$\eta_j = \frac{d_j}{\max_j d_j} + \frac{s_j^2}{\max_j s_j^2}. \quad (5.21)$$

The candidates with the highest η -values are selected to be added to the sampling design. Only for those candidates, the true function is evaluated and the samples are added to the current design. In regions of the input space where currently no samples are located, the η_i -value might be very high. This may cause specific regions with significantly higher η_i -values than others, as shown for a 2-dimensional example in Figure 5.27. To avoid the selection of candidates that are close to each other, the peaks' candidate selection method developed in the literature [165] can be applied. All candidates are located in a grid and for neighboring points in the grid, the values η_i of the candidate selection criteria are compared. Candidates with all neighboring η_i -values being smaller are called local peaks (see cross and asterisk markers in Figure 5.27). Only local peaks are chosen to be added in this iteration.

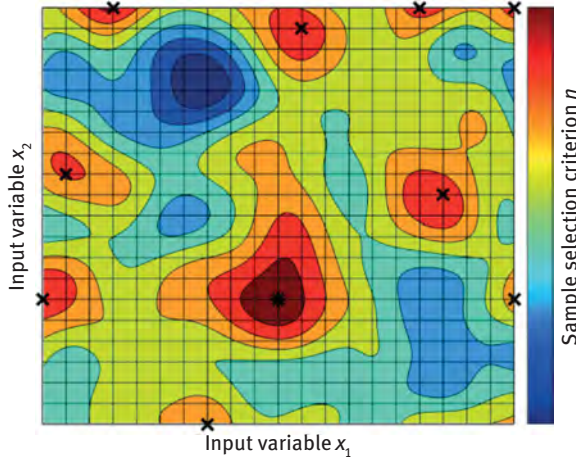


Figure 5.27: Illustrative 2D example for the peaks' candidate selection method [165].

The number of selected points c_{add} among the N candidates is determined by the selection factor SF :

$$c_{add} = SF \cdot N. \quad (5.22)$$

Thereby, the number of samples that are added increases in each iteration. To define a termination criterion, the cross-validation error (CVE) is used. Nentwich et al. [165] define the CVE by the squared error for each current sample, i , calculated as the deviation of the true value y_i and the prediction of the subset model y_i^{subset} , where the current sample i is missing:

$$CVE_i(y) = (y_i - y_i^{subset})^2. \quad (5.23)$$

As proposed by Eason and Cremaschi [33], the slope percentage criterion is used as a termination criterion:

$$\alpha_k = \frac{\text{CVE slope from iteration } k-1 \text{ to } k}{\max \text{ CVE slope from iteration } 1 \leq k} \leq \varepsilon. \quad (5.24)$$

The termination criterion is based on the cross-validation error in order to use all available information that was gained during the sampling procedure. To compare the different trained models, the use of measures with respect to a large test set is commonly used as the standard measure for comparable results. For regression models, the mean absolute error for the quantity i (MAE_i) or the mean squared error for the quantity i (MSE_i) can be used:

$$MAE_i = \frac{1}{N_{test}} \sum_{j=1}^{N_{test}} |\hat{y}_i(x_j) - y_i(x_j)|, \quad (5.25)$$

$$MSE_i = \frac{1}{N_{test}} \sum_{j=1}^{N_{test}} (\hat{y}_i(x_j) - y_i(x_j))^2, \quad (5.26)$$

where $\hat{y}_i(x_j)$ is the predicted value of quantity i at a sample location x_j and $y_i(x_j)$ is the true value of quantity i at a sample location x_j for $j=1, \dots, N_{test}$ test set samples. For classifiers, the percentage of misclassified test set samples ($MisC$) can be used:

$$MisC = \frac{100\%}{2N_{test}} \sum_{j=1}^{N_{test}} |\hat{y}_{class}(x_j) - y_{class}(x_j)|, \quad (5.27)$$

where $\hat{y}_{class}(x_j)$ is the classifier output at a sample location x_j and $y_{class}(x_j)$ is the true class at a sample location x_j for $j=1, \dots, N_{test}$ test set samples.

The choice of the inputs and outputs of the surrogate models is important and has to be made first. In the following paragraphs, we will present the surrogate-modeling of the liquid-liquid equilibrium of the ternary system n-decane, dimethylformamide (DMF), and 1-dodecene. By modeling this system the behavior in the decanter of the hydroformylation process of 1-dodecene can be predicted during optimization. The flowsheet of the process can be found in Figure 5.32. For the surrogate-modeling of thermodynamic models in process simulation and optimization, two different options exist. In the first option, called the direct surrogate-modeling approach, [163], the phase equilibrium condition is solved during the sampling and the composition of the

two phases is predicted using surrogate models. A classifier is trained to identify the biphasic region. Inside this region, a regression model is trained to model the compositions of the two phases. Because of the inclusion of a classifier, a modified mixed adaptive sampling strategy is applied. The term accounting for the exploitation criterion is changed to

$$\frac{s_j^2}{\max_j s_j^2} = \frac{1}{2} \frac{s_{class,j}^2}{\max_j s_{class,j}^2} + \frac{1}{2} \frac{s_{appr,j}^2}{\max_j s_{appr,j}^2}, \quad (5.28)$$

and the slope ratio in the termination criterion is a mixed criterion, calculated by the classifier and regression models, called the total slope criterion, α_{tot} :

$$\alpha_{tot} = \frac{1}{2} \frac{\alpha_{class}}{\max(\alpha_{class})} + \frac{1}{2} \frac{\alpha_{appr}}{\max(\alpha_{appr})}. \quad (5.29)$$

In the second option called the “indirect surrogate-modeling approach” that was presented by Nentwich et al. [165], the phase equilibrium condition is solved during the process simulation or optimization, and the fugacity coefficients that enter into this condition are approximated by surrogate models. In this approach, the phase equilibrium problem is explicitly formulated and solved simultaneously with all balance equations of the process model. Therefore, no classifier is needed to predict the biphasic region.

For the direct prediction of the composition of the two phases, the number of outputs can be reduced by the introduction of the distribution coefficients K_i instead of modeling the molar fractions $x_{j,i}$ of the component i in phase j . The distribution coefficient is defined as

$$K_i = \frac{\dot{n}_{i,A}}{\dot{n}_{i,in}} = \frac{x_{i,A} \cdot \dot{n}_A}{x_{i,in} \cdot \dot{n}_{in}}, \quad (5.30)$$

where $\dot{n}_{i,A}$ is the molar flow of the components i in phase A and $\dot{n}_{i,in}$ is the molar flow of the component i in the feed, respectively. \dot{n}_A and \dot{n}_{in} are the total molar flows of phase A and of the feed. Since the formulation of the distribution coefficient is only valid within the miscibility gap, a classifier that assigns a point to the biphasic region is used. If the classifier predicts a point to be in the biphasic region, a continuous regression model is used.

In the literature [163], a Support Vector Machine (SVM) is used for the classification problem, while ordinary Kriging models are chosen as regression models. To show the advantage of using mixed adaptive sequential sampling instead of the commonly applied purely space-filling design LHS, the performance of the trained models is compared to models of the same structure that were trained using LHS designs of the same sample size.

The performance of the mixed adaptive sampling and the space-filling LHS design are compared in Figure 5.28. For all sample sizes, the classifier trained with the

mixed adaptive sampling led to fewer misclassifications. Especially at medium sample sizes, the adaptive approach outperformed LHS significantly.

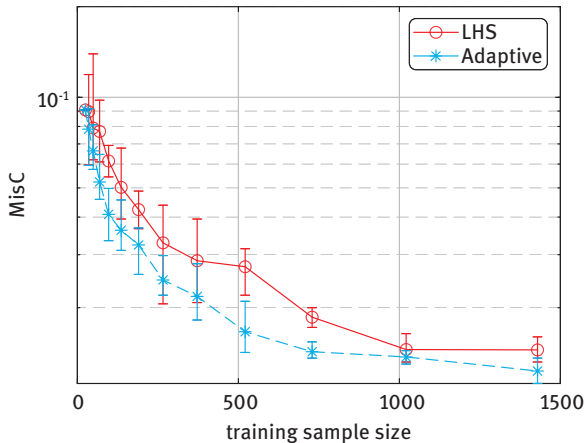


Figure 5.28: MisC over the classifier sample size of the sampling algorithm for $NSS = 18$ and $SF = 0.4$ and same-sized LHS design-based models showing the mean (markers), minimum, and maximum (bars) of each 5 runs [163].

The performance of the Kriging models that predict the distribution coefficients is depicted in Figure 5.29. It can be seen that the performance of the models using mixed adaptive sampling is better for the same number of sampling points. The difference of the mean absolute error is large for medium-sized sample sets of around 500 samples. For all components, a much smaller sample size is needed for the mixed adaptive sampling, in comparison to a LHS sampling, to reach a similar performance.

In the second option, the surrogate models were trained to predict the fugacity coefficients, and the equilibrium condition must be solved during optimization. Kriging models and Artificial Neural Networks (ANNs) were used to predict the fugacity coefficients [165]. The performance of the models trained using a LHS design, the mixed adaptive sampling with parameterization by Eason and Cremaschi [33] and, the mixed adaptive sampling with the best-found parameterization were compared (Figure 5.30) for ANNs as surrogate models. The model trained with LHS performed worst; it had the largest MSE and the largest spread of the prediction error. The best performance was obtained by the application of the peaks-candidate selection, and an optimal weighting of the exploratory and exploitative sampling objectives.

The miscibility gap that is predicted when using the surrogate models for the fugacity coefficients in the computation of the phase equilibrium is shown in Figure 5.31. The prediction of the gap and also of the compositions in the different phases is very accurate. Surrogate models were used in the literature [166] to predict the gas

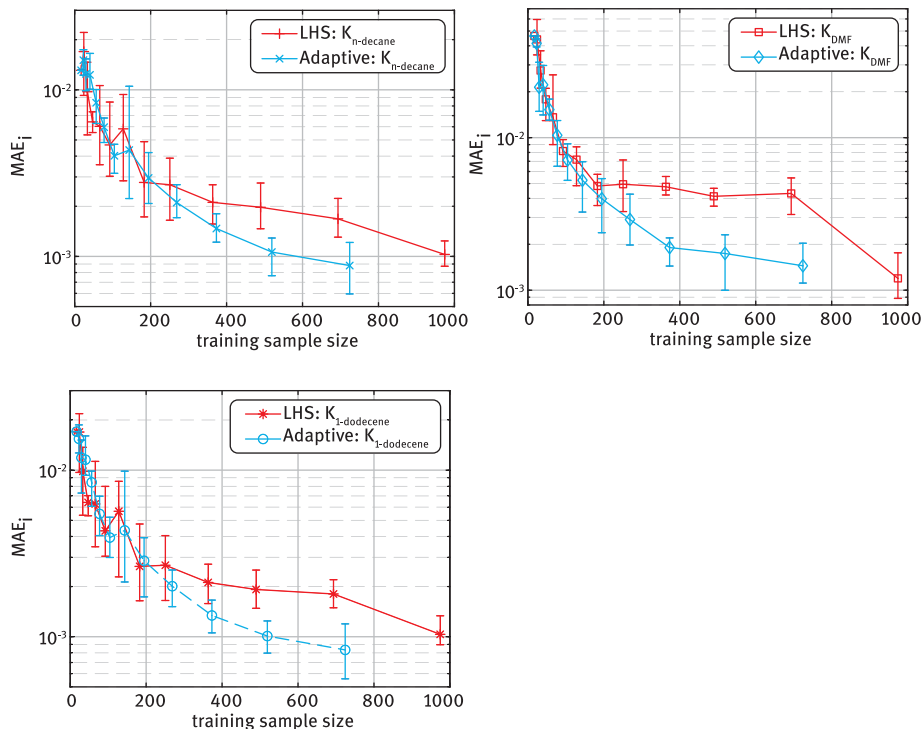


Figure 5.29: MAE_i for the K_i of the three components over the Kriging sample size of the sequential sampling algorithm for $NSS = 18$ and $SF = 0.4$ showing the mean (markers), minimum, and maximum (bars) of each 5 runs of the models, trained in the mixed adaptive sampling algorithm and the models based on LHS design [163].

solubilities, and the phase separation in the decanter of the hydroformylation process of 1-dodecene, as shown in Figure 5.2. As the original PC-SAFT model is computationally expensive, the optimization of the operating point of the process can only be performed using surrogate models. In this case, the results of the ternary system which are shown in Figure 5.31 had to be extended by the product component, 1-tridecanal, for describing the behavior of the system in the hydroformylation process.

For this quaternary system, both the indirect and the direct surrogate-modeling approach were applied. For the indirect method, Artificial Neural Networks (ANN) and Kriging models were trained as regression models. For the direct method, ANN classifiers were trained to describe the biphasic operating region in the decanter. The classifiers were combined with Kriging models (“direct Kriging”) and with ANN models (“direct ANN”) of the same structure, as in the case of the indirect method for regression. The test set errors of the four different model combinations for test sets of 10,000 samples each for the gas solubilities and for the phase separation are shown in Tables 5.1 and 5.2, respectively. Both for the gas solubilities and for the liquid-

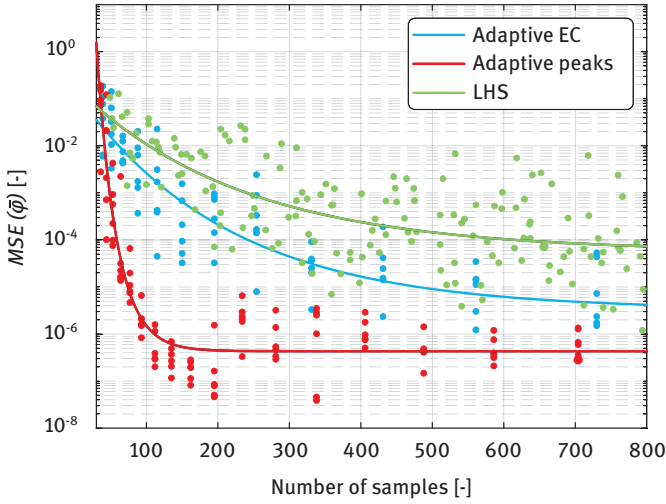


Figure 5.30: Comparative plot of the scaled MSE of the fugacity coefficients $MSE, \bar{\varphi}$, for the ternary system of 1-dodecene, DMF, and n-decane for the ANN models over the training sample size using the mixed adaptive sampling algorithm with the parameterization from Eason and Cremaschi [33] (blue), the peaks-candidate selection (red), and using LHS designs with exponential trend lines [165].

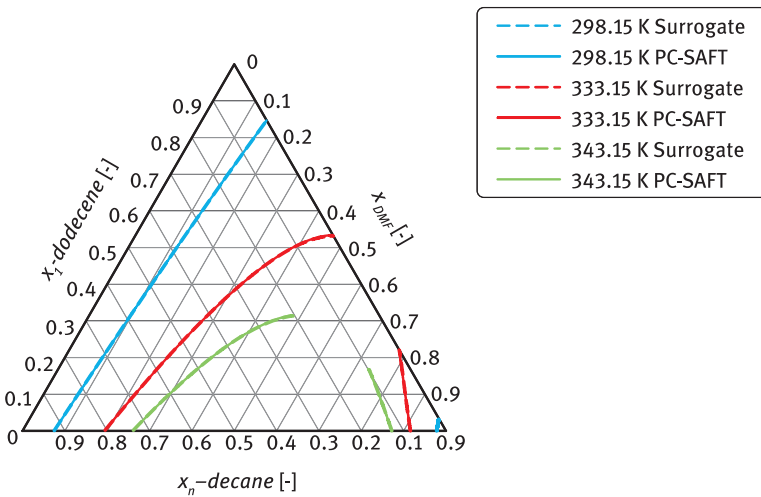


Figure 5.31: Liquid-phase compositions at different temperatures for the ternary system of 1-dodecene, DMF, and n-decane and predicted values using the surrogate models (dashed lines) compared to PC-SAFT (lines) (Section 4.1.1) [165].

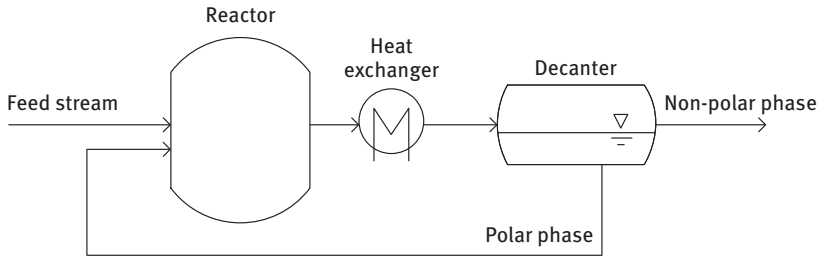


Figure 5.32: Flowsheet of the hydroformylation process of 1-dodecene [164]. The flowsheet corresponds to loop I presented in Figure 4.16.

liquid separation, the models applying the direct surrogate-modeling approach outperformed the surrogate models using the indirect surrogate-modeling approach. Especially for the liquid-liquid separation, for which the MAE of the product composition is shown in Table 5.2, the models using the indirect modeling approach show large errors of up to 3 mol% in composition. While for the indirect method, the chosen surrogate model structures were not able to approximate the behavior of the process with sufficient accuracy, the application of the direct method led to very accurate surrogate models, both for the gas solubilities and the liquid-liquid separation, with a maximum MAE in the product composition of 0.62 mol-% for the component DMF. The fraction of the misclassified samples was at most 1.90% in the direct Kriging case. As the classifier and the regression model were trained simultaneously for different adaptive samplings, the classification errors are also different.

Table 5.1: MAE of the predictions of the trained surrogate models [166].

MAE of	Indirect Kriging	Indirect ANN	Direct Kriging	Direct ANN
c_{H_2} [kmolm ⁻³]	1.914×10^{-3}	5.622×10^{-4}	1.962×10^{-6}	1.523×10^{-5}
c_{CO} [kmolm ⁻³]	3.077×10^{-3}	8.841×10^{-4}	2.607×10^{-6}	2.463×10^{-5}

Table 5.2: Misc and MAE of the predictions of the trained surrogate models for the molar fractions in the product phase of the decanter [166].

	Indirect Kriging	Indirect ANN	Direct Kriging	Direct ANN
MisC [%]	–	–	1.90	1.40
MAE $x_n^{product\ phase}$	0.0038	0.0187	0.0010	0.0004
MAE $x_{DMF}^{product\ phase}$	0.0075	0.0298	0.0062	0.0011
MAE $x_{1-dodecene}^{product\ phase}$	0.0029	0.0142	0.0010	0.0003
MAE $x_{1-tridecanal}^{product\ phase}$	0.0029	0.0183	0.0044	0.0006

A comparison of the computational expense of the different surrogate model options and the original model PC-SAFT for process simulations is shown in Table 5.3. The surrogate models provide a more than 90 times faster process simulation than using the original model PC-SAFT. As many process simulations are performed during optimization, this shows that the original model PC-SAFT is practically not applicable for process optimization.

Table 5.3: Simulation time for the hydroformylation process of 1-dodecene on a Windows 10 4.2/4.2 GHz dual Intel(R) Core™ i7 machine with 32 GB RAM using the SciPy-lm solver [166].

	PC-SAFT	Indirect Kriging	Direct Kriging	Direct ANN
Simulation time [s]	2963.9	31.7	18.4	13.1

As the indirect surrogate models were not sufficiently accurate, only the models trained using the direct surrogate-modeling method were used to optimize the operating point of the process: the feed composition (molar flow \dot{n} of component 1-dodecene, DMF, n-decane and catalyst), the reaction temperature (T), the reaction pressure (p_R), the carbon monoxide content of the synthesis gas (y_{CO}), and the separation temperature of the decanter (T_D). The cost function considered for the optimization is the production cost in Euro per ton t of n-tridecanal for a capacity ($\dot{m}_{nC_{13}al}$) constrained to 10,000 tons per year. Both operational costs C_{op} and investment costs C_{invest} were taken into account:

$$CPT = \frac{C_{op} + \frac{C_{invest}}{10}}{\dot{m}} \quad (5.31)$$

The resulting optimal operating points are shown in Figure 5.33. For these conditions, the process was also simulated with PC-SAFT [166]. The resulting errors in the objective function are shown in Table 5.4. Compared to the process simulation results using the original model PC-SAFT, the surrogate model approaches both results in a low relative error of the objective function—less than 3%. The ANN models that provided the best approximation accuracy for the test set for the liquid-liquid separation (Table 5.4) also showed the best result here.

In this section, two surrogate-modeling approaches for complex thermodynamic models that are used in process simulation and flowsheet optimization were presented. In the direct modeling approach, the thermodynamic equilibrium is solved during the sampling, the thermodynamic behavior is described by a classifier that predicts the number of phases, and a regression model describes the distribution coefficients in the biphasic region. In the indirect approach, the fugacity coefficients are predicted by the surrogate models; thus requiring a solution of equilibrium condition during the simulation or optimization of the process. In the ternary case, the

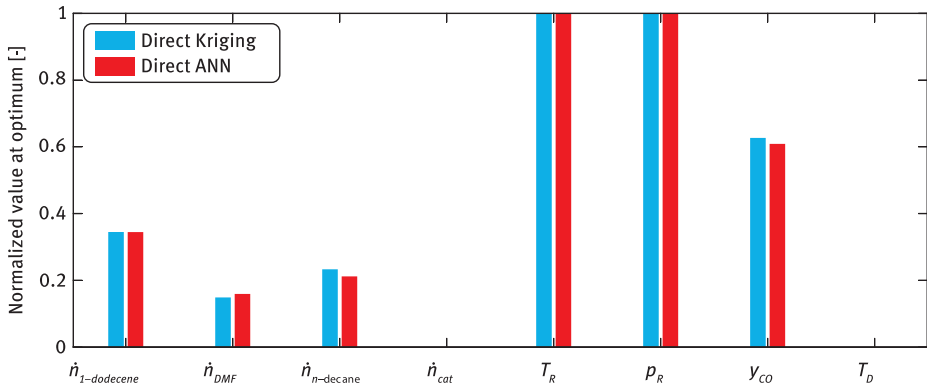


Figure 5.33: Normalized optimal operating points (normalized to the ranges of the variables) for the hydroformylation process of 1-dodecene using different surrogate models [166].

Table 5.4: Objective function values of the optimization using surrogate models compared to PC-SAFT simulations of the resulting optimal operating points [166].

	Direct Kriging	Direct ANN
CPT [€/t]	6547.17	6584.37
CPT PC-SAFT [€/t]	6730.32	6545.23
Absolute Error [€/t]	183.15	39.14

approximation of the LLE using both the indirect and the direct method was possible with small approximation errors. This shows that both approaches can provide accurate predictions of thermodynamic behavior. For the quaternary case, the indirect method showed an inferior performance, compared to the direct model. This could be overcome by using more complex surrogate-model structures.

The direct surrogate-modeling approach was successfully applied in the optimization of the operating point of the process for the hydroformylation of 1-dodecene, shown in Figure 5.32, by minimizing the production price per ton of the product. The relative error in the objective function in the best case is less than 1%, compared to PC-SAFT simulations using ANN regression models, which is certainly less than the uncertainty of the rigorous model. The results also show that the average quality of fit of the surrogate models over the test set is not necessarily a reliable indicator of the accuracy of the prediction of the process optimum; so the strategies that include the sensitivity of the optimum in the selection of the samples should be investigated, as shown by Winz and Engell [217]. The use of surrogate models in the global optimization of flowsheets is discussed in Section 5.2.3 and the application within the early-stage process design is demonstrated in Section 6.4.

5.3 Process Optimization

5.3.1 Optimal Design of Reactors for Complex Reaction Systems

Karsten H.G. Rätze, Michael Jokiel, Kai Sundmacher

The reactor unit(s) of a chemical production plant significantly influences the overall production costs since they determine the requirements for the subsequent, generally energy-intensive, downstream process. Efficient reactors that provide high selectivity towards the desired product are a prerequisite for a lean separation process. Therefore, the identification of optimal operation strategies for existing reactors and the synthesis of new processes in the form of conceptual design are topics of interest and subject to active research [156].

The design of new or the optimization of existing processes benefits from expert knowledge and from detailed, experimental investigations to develop a thorough understanding of various kinetic and thermodynamic effects. However, the optimization potential is generally limited due to the restriction to the reactive units in contrast to the overall process and/or constrained flexibility w. r. t. reactor designs and reactor operation strategies. Consequently, a holistic approach for the conceptual design of efficient chemical production processes is required, in which information from various sources is incorporated. An important tool that fosters an extended view on the reactor design task represents the utilization of reaction kinetic and process models, either in the form of mechanistic or data-driven models, in addition to experimental investigations. While mechanistic models are generally suited to achieve a detailed understanding of processes by providing reliable data for the investigation and analysis of operating windows/strategies that were not subject to any experimental investigations due to either limited resources or safety concerns (more information in this chapter), data-driven or surrogate models are particularly suitable for the aggregation, interpolation, and efficient access to information (Sections 5.2.3 and 5.3.2). As a consequence, both model types are indispensable for the state-of-the-art process design.

Despite these powerful, predictive tools, incomplete knowledge and uncertainty/randomness are inherent in process development; so the incorporation of these aspects in a quantitative manner in the design process allows for better decision making at early stages. Consequently, only a combination of model-based tools for process design with experimental investigations on multiple scales (lab and mini plant scale), can achieve reliable designs and, therefore, represents an essential part of process design. Especially, the investigation on different scales does not only serve the validation of simulative predictions but allows for the identification of unknown effects or unaccounted behavior – information that can be used to update process models and improve the process design. This interplay of process design and experimental validation already hints at an iterative and strongly interdisciplinary development that is mandatory for the modern and reliable design of chemical production processes.

This section provides a brief introduction to the systematic and model-based unit operation design in the process development cycle (Step 4a in Figures 4.63 and 4.65), with the emphasis on reactor design and optimization in the context of the entire production process. The next paragraphs touch upon the different strategies for reactor-network synthesis before reaching deeper into model-based reactor-synthesis via the methodology of Elementary Process Functions and its application to the hydroformylation of long-chain olefins. Subsequently, detailed simulative and experimental investigations are presented w. r. t. the reactor units as well as their interaction with the entire process.

5.3.1.1 Reactor-Network Synthesis

The selective synthesis of the desired product might require a careful adjustment of the different species concentrations inside the reaction unit for an optimal result. This optimal concentration profile is unique for each reaction and might change with external factors, like temperature and pressure. In reactor-network synthesis, the focus lies on the approximation of this optimal concentration profile using idealized reactor units with known behavior. These idealized reactor units are generally differentiated w. r. t. their internal mixing characteristics. The most common types are (i) the continuously stirred tank reactor (CSTR), (ii) the plug-flow reactor (PFR) and (iii) the distributed side-stream reactor (DSR). While the first two units represent edge cases with maximum and minimum axial dispersion, the last reactor unit enables the selective dosing of species and species mixtures along the reactor coordinate to achieve compromises between CSTR and PFR dispersion behavior [39].

Most of the approaches to reactor-network synthesis can be classified either as heuristics-, attainable region- (AR) or rigorous optimization-based, with the latter two representing model-based approaches. Especially, rigorous optimization-based approaches are relatively new, compared to the other categories, so that their full potential is still unexplored and are subject to active research. Superstructure optimization represents the most intensively studied sub-category of rigorous synthesis approaches in which the solver creates an optimal reactor network by using a list of predefined process units. While yielding high-performance reactor combinations and potentially unintuitive solutions for large-scale networks, high computational loads and the lack of innovative designs and process intensification led to the emergence of alternative approaches. One of these alternatives is the Elementary Process Functions methodology, which is based on dynamic optimization and tackles the synthesis problem via functional modules, instead of predefined process units. For a better understanding of the methodology, the general idea as well as a selected number of extensions and frameworks are discussed in the next section.

5.3.1.2 Elementary Process Functions Methodology

The Elementary Process Functions (EPF) methodology was introduced by Freund and Sundmacher [43] to shift the focus from connecting unit operations, e.g., *reactor, separator*, for the flowsheet generation to the consideration of functional modules, instead. These functional modules represent tasks, like *heating* and *separating*, which need to be performed in a process, without restricting the execution of these tasks to predefined apparatuses. This shift in perspective facilitates the generation of new process units and the direct consideration of integration potential in the process design.

In its original formulation, the reactor-network design task can be represented as a fluid element traversing the thermodynamic state space from the state at initial time $x(t_0)$ to the final state $x(t_f)$, where $x \in \mathcal{X} \subseteq \mathbb{R}^x$ represents the state vector, containing concentrations, temperature, pressure, etc. Its path is governed by process constraints, but can also be influenced by fluxes entering and leaving the fluid element, which act according to a predefined objective function (see Figure 5.34 for a schematic representation). This objective function can be defined in terms of the final state $x(t_f)$ or w. r. t. the fluid element's path in state space, leading to an Optimal Control Problem (OCP) of the form

$$\min_{u(t), \theta} \phi(x(t), u(t), \theta, c) \quad (5.32)$$

$$C(x(t), c) \frac{dx}{dt} = F(x(t), c) \quad J(x(t), u(t), c), x(t_0) = x_0, \quad (5.33)$$

$$h(x(t), u(t), \theta, c) = 0, \quad (5.34)$$

$$\tilde{h}(x(t), u(t), \theta, c) \leq 0, \quad (5.35)$$

$$x(t) \in \mathcal{X}, x_0 \in \mathcal{X}_0, u(t) \in \mathcal{U}, \theta \in \mathcal{P}, \quad (5.36)$$

with the Bolza type objective function ϕ , general equality h , and inequality constraints \tilde{h} , constants c , and bounds on the states $x^T(t) = (T(t), p(t), w^T(t), v(t), G(t))$, the static controls $\theta^T = x_0^T$ and the control profiles $u^T(t) = (\dot{m}_A(t), j_A^T(t), \dot{q}_A(t), \tau_A(t), f_V(t), w_t(t), g(t))$. Here, the state vector comprises the temperature T , pressure p , mass fractions w , velocity v , and geometrical state of the fluid element G , which is the fluid element's volume V , in the case of a batch process, or the volume flux vA_c for continuous processes, with A_c denoting the cross-sectional area of the fluid element. The control profile vector u contains the total mass flux \dot{m}_A , diffusion flux density vector j_A , surface stresses τ_A , volume forces f_V , heat fluxes \dot{q}_A , technical work w_t , and rates of the matter element's geometry variation g . For notational convenience, the time and state dependencies were neglected and all lower-case variables can be considered as vectors. The Ordinary Differential Equation (ODE) System eq. (5.33) is a compact representation of the balance equations that govern the feasible paths in the thermodynamic state space with the capacity matrix C , the weight factor matrix F , and the generalized flux vector $J^T(x(t), t) = (r_V^T(x(t)), u^T(t))$. In the case of a regular capacity

matrix, the eponymous linearly independent elementary vectors span the column space of $E = C^{-1}F$, which represents the attainable sub-space χ , according to the process constraints [204].

With the mathematical foundation of the EPF methodology in eqs. (5.32)–(5.36) describing the identification of controls that characterize the state trajectories in an optimal reactor, frameworks are required to create real-world reactor networks from these optimal control profiles. Two of these frameworks will be discussed in the next paragraphs, with both concepts approaching the approximation of the optimal control profiles from different perspectives.

Reactor-Network Synthesis Framework 1 – Successive Approximation

In eq. (5.33), it was already assumed that the internal reaction fluxes $r_V^T(x(t))$ and, consequently, $J^T(x(t), t)$ are dependent on the states $x(t)$. This is reasonable, since the standard reaction rate equations normally exhibit a concentration, temperature, and, sometimes, pressure dependency. Besides this simplification, solving eqs. (5.32)–(5.36) yields controls that optimally steer the fluid element in state space. However, this path might not be achievable in real life due to limitations on the fluxes in $u(t)$. In actuality, these fluxes result from driving forces that are dependent on the distance of the states to their respective equilibrium values, $x(t) - x^{eq}(x(t))$. Consequently, the introduction of rigorous flux models yields control profiles that approximate the ideal control profiles and are, therefore, closer to reality. A generalization of this approach was introduced by Peschel et al. [173], in which the successive refinement of the underlying model is formalized in a three-level procedure (Table 5.5), yielding a systematic approach for the synthesis of reactor networks. With each level, the complexity of the underlying process model increases, so that the maximum potential of the reaction without any limitations (Level 1) can be compared to a hypothetical reactor with (mass and energy) transport limitations and a limited number of controls (Level 2) and, eventually, to multiple technical approximations (Level 3).

Table 5.5: Three-level procedure for the design of optimal technical reactors using the EPF methodology [44, 173].

	Description	Characteristics
Level 1	Identification of the optimal route in state space	<ul style="list-style-type: none"> – Unlimited outer fluxes – Identification of the maximum potential of the reaction system (optimal route in state space)
Level 2	Identification of an ideal reactor concept	<ul style="list-style-type: none"> – Limited outer fluxes via transport kinetics – Selection of a suitable subset of $u(t)$ and θ
Level 3	Identification of an optimal technical reactor (network)	<ul style="list-style-type: none"> – Approximation of the controls using detailed reactor models – Consideration of non-idealities

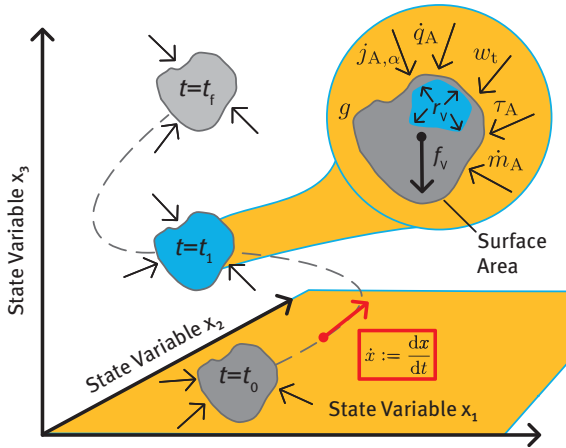


Figure 5.34: Schematic representation of a fluid element traversing the three-dimensional thermodynamic state space, from $x(t_0)$ to $x(t_f)$. The path of the fluid element is constrained by the internal reaction flux r_V and can be influenced by the volume forces f_V , diffusion flux of species α over the surface $j_{A,\alpha}$, the total mass flux \dot{m}_A , heat fluxes \dot{q}_A , technical work w_{ti} , the surface stress τ_A , and the rate of geometrical change of the fluid element g . Please note all V indices relate to volume-related fluxes and all A indices represent surface-related fluxes (adapted from [204]).

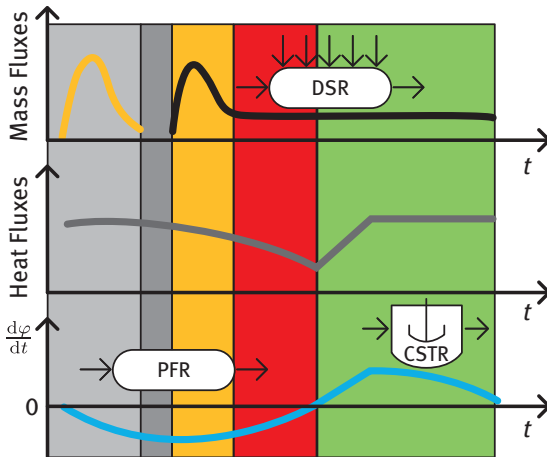
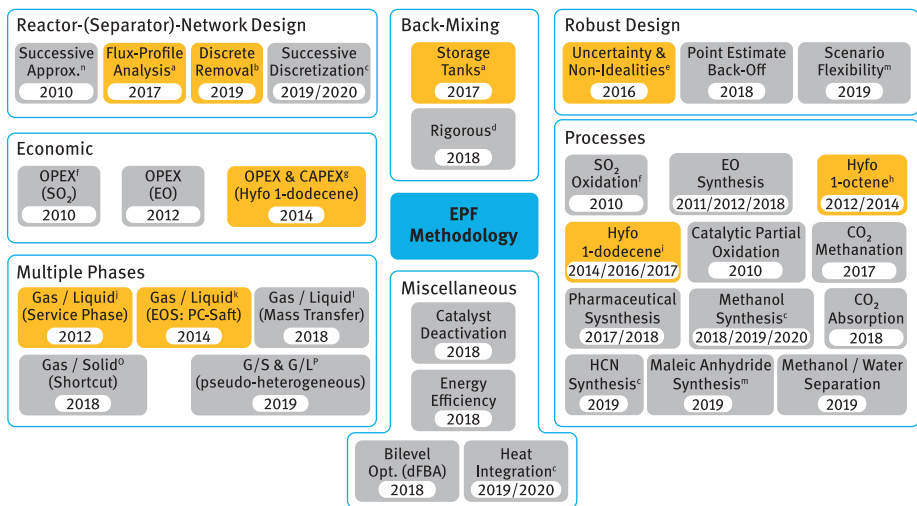


Figure 5.35: Division of control profiles $u(t)$ based on distinct patterns and subsequent interpretation via flux-profile analysis (FPA) and association to ideal reactor types CSTR, PFR, and DSR (adapted from [90]).

Table 5.6: Three-step procedure for the design of chemical reactor networks using the EPF methodology and flux-profile analysis [92].

Description	Characteristics
Step 1 Identification of the optimal route in state space	<ul style="list-style-type: none"> – Unlimited outer fluxes – Identification of the maximum potential of the reaction system (optimal route in state space)
Step 2 Subdivision of the time horizon into characteristic sections & Association with ideal reactor types	<ul style="list-style-type: none"> – The control profiles $u(t)$ are subdivided based on key characteristics of ideal reactor units – Each flux-profile section is associated with one ideal reactor type
Step 3 Evaluation of reactor network candidates	<ul style="list-style-type: none"> – The reactor networks from Step 2 are modeled rigorously – The reactor network candidates are evaluated and compared in terms of performance and economic feasibility

**Figure 5.36:** Derived approaches, extensions and applications of the EPF methodology since 2008. InPROMPT contributions highlighted. Selected contributions are: ^a[90] and [92], ^b[94], ^c[125, 126, 191–193], ^d[218], ^e[91], ^f[173], ^g[65], ^h[66, 175], ⁱ[65, 67, 90], ^j[65, 174], ^k[66], [219], ^m[141], ⁿ[173, 174, 176], ^o[177] and ^p[93].

Reactor-Network Synthesis Framework 2 – Flux-Profile Analysis (FPA)

While the successive approximation framework predominantly relies on the practitioners' knowledge, expertise, and intuition to select controls for the successful identification of suitable technical realizations, the Flux-Profile Analysis (FPA) emphasizes the design of reaction-networks and the selection of suitable classes of reactors before improving the technical feasibility [92].

After the initial identification of the maximum potential of the reaction system in Step 1 (Table 5.6) similar to Peschel et al. [173], all control profiles are approximated using a network of ideal reactor units. Here, the key idea lies in the observation that the optimized outer mass- and energy fluxes form specific patterns over the processing time. By subdividing or discretizing the time horizon according to these patterns, ideal reactor units, like a CSTR, PFR, or DSR, can be used to approximate the control profile and, consequently, the state trajectory of the fluid element. A schematic representation of this procedure can be found in Figure 5.35. For the accurate association of a control profile with an ideal reactor type, the consideration of axial dispersion or back-mixing is required.

In a first approach, axial dispersion can be rigorously considered by introducing internal fluxes $j_{\text{mix}}(t)$ alongside the diffusion fluxes in eqs. (5.32)–(5.36). These fluxes provide a connection of the fluid element with itself in time, allowing for the identification of additional integration potential, including process-wide recycles [218]. This is especially useful for the selection of suitable reactor units in which sections with high internal fluxes $j_{\text{mix}}(t)$ indicate a positive influence of axial dispersion on the reaction, while low internal fluxes hint at reactors with limited back-mixing behavior.

In complex reaction networks with many species, the rigorous consideration of internal fluxes becomes computationally challenging due to the temporal interconnection of the fluid element. For these cases, a simplified formulation of axial dispersion can be chosen with the introduction of storage tanks for each species, e.g., substrate, intermediates, and products, in the reaction network. Each storage tank contains a certain amount of initial fill volume at t_0 which the solver can use for dosing into the fluid element. With additional constraints to ensure dosing of the entire substrate amount and to prevent unsustainable insertion of (by-)product into the fluid element, axial dispersion and process-wide recycle streams can be approximated. As an indicator for the benefit or disadvantage of axial dispersion in the case of absent dosing fluxes in selectivity problems, the differential selectivity

$$\varphi = \frac{\text{moles of desired product formed}}{\text{moles of main reactant consumed}} = \frac{\frac{dn_{\text{Prod}}}{dt}}{\frac{dn_{\text{Sub}}}{dt}} \quad (5.37)$$

or rather its derivative w. r. t. time, the differential reaction flux, can be evaluated. Sections with a positive sign of the differential reaction flux indicate beneficial and

negative signs, disadvantageous influences on the selectivity toward the desired product [92].

EPF and Framework Extensions

Besides the extension of the EPF methodology towards reactor-network synthesis, many other extensions and applications can be found in the literature, with a selection of major advances depicted in Figure 5.36. All publications in the overview are grouped into categories, depending on either the methodological improvement, e.g., Reactor-(Separator)-Network Design and Back-Mixing, or the application, e.g., Processes and Economic. In the following paragraphs, each methodological category will be discussed, starting with the reactor-separator-network design as the natural yet complex evolution of reactor-network design.

The reactor-separator-network design requires the introduction of a concept for separation in the EPF methodology. This can be achieved by extending the bounds of the dosing and diffusion fluxes, j_A , toward the negative domain, making the withdrawal of species from the fluid element possible. Instead of considering the continuous withdrawal of (pure) components, which is only possible in special cases, discrete separation units are introduced at the transition points between profile patterns in Step 2 of the FPA [94]. The introduction of discrete separation points leads to a mixed-integer dynamic optimization (MIDO) problem, requiring specialized algorithms for solving or the reformulation by relaxing the integer variables and ensuring the convergence toward the integer solution via continuous switching functions. An alternative and more radical approach to the reactor-separator-network synthesis task aims at the discretization of the entire thermodynamic state space using predefined operations, like reacting, heating, separating analogous to the introduction of functional modules in the original EPF methodology [125]. This results in a separation of the evaluation of the (nonlinear) reaction model from the optimization of the trajectory in state space, leading to a graph-theoretical approach with a linear optimization problem. This approach even allows for simultaneous consideration of heat integration [126] and application to non-reactor units, like separators [191].

The extension toward multi-phase systems is crucial for the industrial application of the EPF methodology since numerous systems exhibit or require two or more phases during the reaction. In the simple case of one reactive and one auxiliary phase, like in the case of the homogeneously-catalyzed hydroformylation with the gas phase representing the auxiliary phase, the auxiliary phase can be modeled as a continuum enveloping the liquid fluid element. This continuum represents a service phase with an unlimited capacity and introduces an interphase driving force for species fluxes to and from the fluid element [175]. For an accurate description of the driving force, sophisticated equations of state (EoS), like PC-SAFT for liquid-liquid (L/L) and gas-liquid (G/L) equilibria [66], diffusion models for gas-solid (G/S) [177] and combinations of G/S and G/L [93] equilibria can be employed. An alternative, more rigorous representation of

multi-phase systems in the EPF methodology considers multiple fluid elements traversing state-space simultaneously [219]. In this formulation, each phase receives a separate fluid element with unique control fluxes. Consequently, mass transfer between both phases can be modeled accurately. The service phase and the rigorous modeling approach are visualized in Figure 5.37.

Most extensions of the EPF methodology introduce additional degrees of freedom or higher accuracy via rigorous representation of physicochemical phenomena, while assuming the process/reaction model to be accurate. However, this is not the case due to structural inaccuracies and uncertain parameters in the model as well as non-ideal reactor units and imperfect realizations of control profiles in the final plant. As a consequence, a probabilistic design framework is required to achieve robustness of the final reactor design. Since the direct consideration of the probability density function (PDF) of the uncertain variables in the optimization problem is not feasible from a computational perspective, an approximation of the PDF via the first and second statistical moments (mean and standard deviation/variance) in the unscented transformation or sigma point method represents a suitable trade-off between accuracy and applicability [91]. With the unscented transformation, both statistical moments can be mapped from the parameter to the criterion space of the objective function using the nonlinear process model. By formulating a bi-level optimization problem, the Pareto front comprising the expected value as well as the variance of the objective function can be calculated and used to identify the desired compromise of performance and robustness. An illustration of this procedure is shown in Figure 5.38. Due to the transition of the chemical industry toward sustainable feedstocks in chemicals production, changing sources of feedstock and fluctuating resource qualities become additional sources of uncertainty in the conceptual design. These uncertainties can be considered with the EPF methodology by taking a multi-scenario approach and solving, analogous to the unscented transformation, a multi-objective optimization problem in terms of performance, safety, and uncertainty of the reactor design [141].

5.3.1.3 EPF Application to the Hydroformylation of Long-Chain Olefins

Many advances in the EPF methodology from Section 5.3.1.2 are the result of the challenges in designing optimal reactor networks for the hydroformylation of long-chain olefins. While the derivation of accurate reaction-kinetic models for these example reactions is discussed in detail in Section 3.2, the following paragraphs provide a compact overview of the application of the EPF methodology to the reactor-network design for the homogeneously catalyzed hydroformylation reaction.

The biphasic nature of the hydroformylation reaction, in which a liquid phase is in contact with a gaseous phase containing the necessary substrates hydrogen (H_2) and carbon monoxide (CO), initiated the extension of the EPF methodology towards multiphase reactor design. With the introduction of the service phase approach, the first design of an optimal hydroformylation process was proposed for 1-octene in an

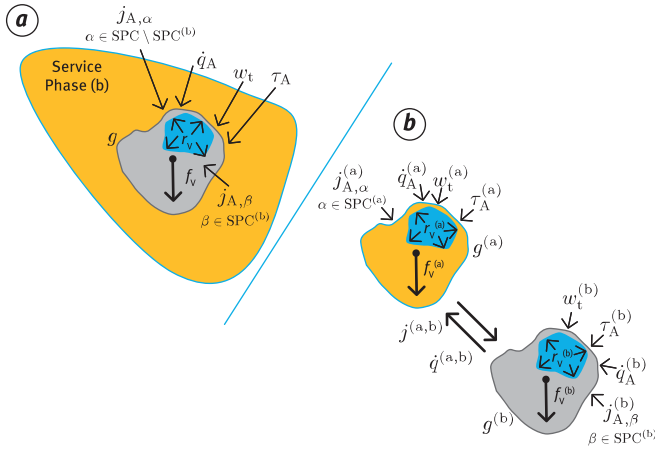


Figure 5.37: Consideration of multiple phases in the EPF methodology. a) Service phase and b) rigorous modeling of multiple fluid elements with interaction in terms of energy and mass transfer (adapted from [219]).

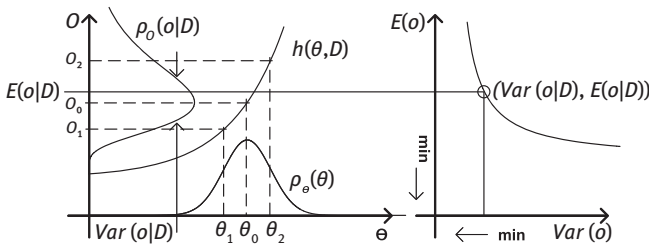


Figure 5.38: Robust reactor-separator-network design via sigma point approximation of the parameter uncertainty in the EPF methodology. Left: Mapping of the parameter space Θ via the nonlinear process model $h(\theta, D)$ into the criterion space O with $\theta \in \Theta$ denoting uncertain parameters and D representing the chosen process design. Right: Pareto front indicating the trade-off between the expected value and the variance of the criterion $o \in O$ (taken with permission from [91]).

ionic liquid (IL) [175]. By using reaction kinetics from the literature in the successive approximation three-level design [173], three reaction segments with distinct temperature profiles were identified in the technical approximation. The final reactor design is shown in Figure 5.39 and consists of a DSR comprising three temperature segments with discrete syngas dosing positions at the boundary of each segment. Additionally, two process-wide recycle loops, one for the IL and the second for unconverted substrates, are proposed, leading to an improved performance with selectivities of $S = 71.2\%$ to $S = 62.1\%$, in the CSTR reference case at comparable or higher space-time-yields (STY) [175].

Due to the importance of gas-liquid phase interactions in the hydroformylation, the influence of liquid phase CO and H₂ concentrations on the reaction performance was investigated in more detail. A simplified variant of the reaction network as in Figure 5.40 enabled the inclusion of the PC-SAFT EoS (Section 3.1.1) in the EPF methodology. After calibration of the EoS to literature data, this combination enabled the rigorous consideration of the G/L phase equilibrium during the reactor design. Multiple optimization studies with increasing degrees of freedom (DoF) revealed the importance of the gas phase composition on the selectivity towards the desired product. The investigations identified a decrease in solubility with progressing hydroformylation of the reactant. By optimally controlling the temperature, pressure, and the H₂ to CO ratio, this effect can be counteracted, leading to a differential selectivity $S > 90\%$, over the entire conversion interval [65]. These results were also confirmed for the hydroformylation of 1-dodecene using a rigorous reaction kinetic model in a flowsheet optimization, as shown by Hentschel et al. [65], with an “EPF reactor” at its core (Figure 5.41). The rigorous reaction kinetic model further revealed that recycling, not only of the unconverted terminal olefins but also of the olefin isomers, proves beneficial for the selectivity and conversion in the reactor. By shifting the equilibrium of the olefin isomerization reaction toward the terminal olefin, a selectivity of 94.2% at 97.3% conversion was achieved in contrast to the reference case of a CSTR with 93.4% selectivity at 51.6% conversion [65]. This represents a 90% increase in linear aldehyde yield in comparison to the reference case. While this increase in product yield significantly simplifies the downstream processing and reduces recycle streams, process profitability did not increase accordingly. An optimization of the entire reaction-extraction process of the homogeneously rhodium-catalyzed hydroformylation in a thermomorphic multiphase system (TMS) revealed that catalyst leaching, which occurs in the decanter for catalyst recovery while being on the ppm scale, represents the cost determining factor. As a remedy, a counter-current decanter cascade can be introduced, which effectively prevents catalyst leaching (Table 5.7) while simultaneously raising the temperature for the liquid-liquid separation to ambient conditions [142].

In addition to the performance optimization of the hydroformylation process, the influence of uncertainty on the process performance indicators was analyzed in the context of the EPF methodology. Different types of uncertainty, ranging from parameter uncertainty over uncertain residence time distributions to uncertain realizations of the control profiles, were considered. While the latter two sources of uncertainty mainly reduced the expected selectivity and increased the variance of the selectivity, a significant influence of the parametric uncertainty on the reactor performance was identified. For expected conversions $X \geq 97\%$, the concentration and control profiles revealed two distinct reaction zones across all realizations of the uncertain parameters. This formation of reaction zones became possible due to the increase in residence time, which was required to achieve high conversions. While the first reaction zone is characterized primarily by dynamic control trajectories, the second reaction zone, which was already identified in previous publications (e.g., [65]), exhibits constant, higher temperatures

and reduced carbon monoxide concentrations for the intensified re-isomerization of olefin isomers to terminal olefins and, consequently, linear aldehydes.

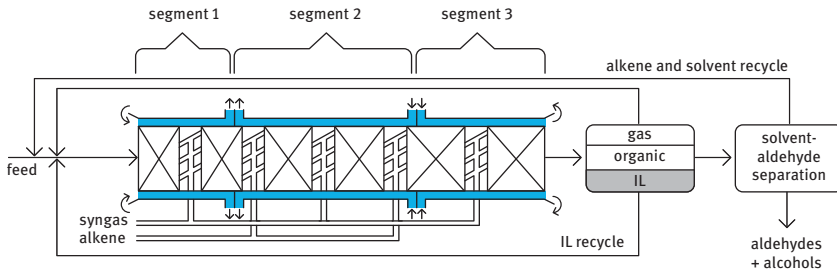


Figure 5.39: Technical approximation of the optimal reactor unit for the hydroformylation of 1-octene in an IL based on the EPF methodology (taken with permission from [175]).

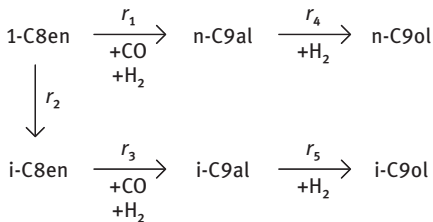


Figure 5.40: Simplified reaction network for the hydroformylation of 1-octene. 1-C8en: 1-octene, i-C8en: iso-octene, n-C9al: n-nonanal, i-C9al: iso-nonanal, n-C9ol: n-nonanol, i-C9ol: iso-nonanol (adopted from [175]).

However, with increased robustness of the reactor design, the percentage of the second zone of the total residence time is reduced to account for the increased sensitivity of the first reaction zone w. r. t. the parameter uncertainties [91]. This behavior leads to a pronounced Pareto front, as shown in Figure 5.42, and motivates experimental investigation. To capture not only microscopic but also process-wide effects, including long-term process stability, the process design needs to be built and evaluated in practice under mini plant-scale conditions.

5.3.1.4 Proof of Concept: Optimal Reactor-Design Hydroformylation of 1-Dodecene

For the hydroformylation of 1-dodecene (nC12en) in the TMS of N,N-dimethylformamide and n-decane, the optimal reactor configuration was sized and designed [90]. The goal of the design task was to maximize the selectivity towards the linear aldehyde tridecanal (nC13al) for high nC12en conversions between 90 % and 99 %. Additionally, the formation of undesired branched aldehydes should be avoided by

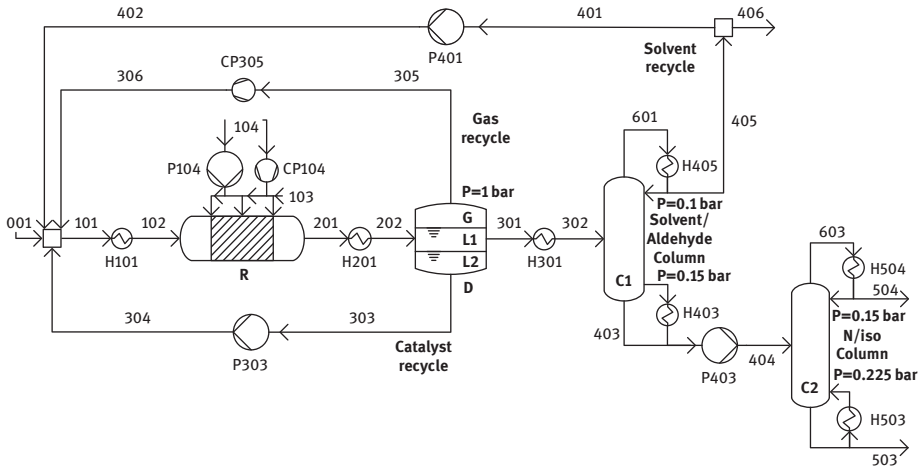


Figure 5.41: Hydroformylation of 1-dodecene flowsheet. R: “EPF reactor”, D: decanter, C1: solvent/product distillation column, C2: n/iso aldehyde distillation column. Heat exchanger units, pumps, and compressors are denoted as H, P, and CP, respectively (taken with permission from [65]).

Table 5.7: Percentage of catalyst cost of the total annual costs (TAC), total production costs, and the production costs without 1-dodecene for seven cases. Case one to six contain decanters in the counter-current decanter cascade. The reference case only contains one decanter [142].

Case	Catalyst Cost %		
	TAC	Production	Production w/o 1-dodecene
1	31.17	31.59	88.61
2	1.12	1.18	17.16
3	0.20	0.21	3.98
4	0.04	0.04	0.85
5	0.00	0.00	0.07
6	0.00	0.00	0.00
Ref.	70.50	71.39	98.06

employing a linear to branched (n/iso)-aldehyde ratio of $\geq 95:5$. To ensure that the reactor volumes are within the mini plant-scale, the total residence time was restricted to a maximum value of 300 min and the mass flow rate of the already existing mini plant [32] was considered. This also allows for a direct performance comparison between processes using a conventional stirred-tank reactor and optimal reactor designs.

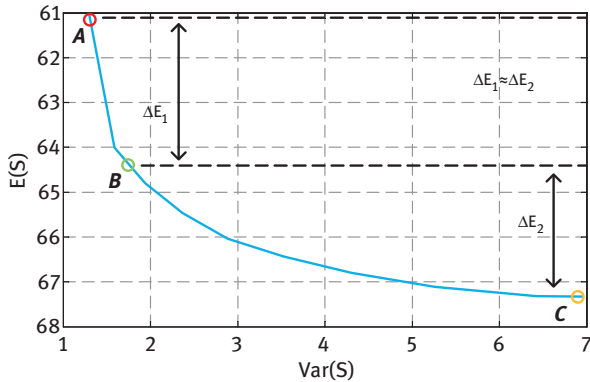


Figure 5.42: Pareto front of expected selectivity versus selectivity variance for parametric uncertainties at 99.5% expected conversion. Exemplary designs A, B, and C denote Pareto optimal points with low, middle, and high variance (taken with permission from [91]).

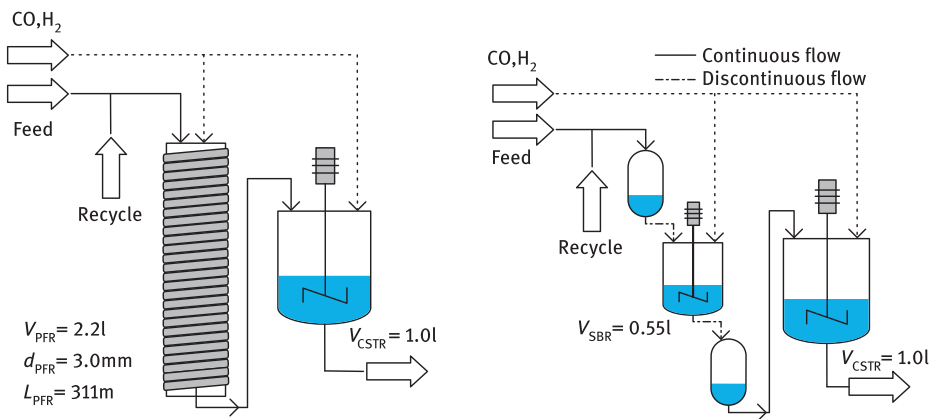


Figure 5.43: Optimal reactor designs from Kaiser et al. [90] for the hydroformylation of 1-dodecene (adopted from [89]).

Derivation of the Optimal Reactor Configuration via Flux-Profile Analysis

Four optimal reactor network candidates, comprising different DSR and CSTR combinations, were derived with the FPA for the hydroformylation of $nC_{12}en$ in a TMS [90]. The analysis of the conversion-selectivity behavior of these networks revealed that the combination of a DSR followed by a CSTR is the most robust design.

For the intended construction and continuous operation of the DSR-CSTR-tandem, the continuous control profiles along the DSR need to be approximated in a discrete manner. Therefore, the influence of different positions and numbers of dosing points along the DSR was evaluated, revealing only a slight loss of selectivity for

low conversions if gas and product dosing is performed only at the inlets of both reactors. This enables a rather simple construction of the DSR in the form of a PFR. In order to size this PFR, the determination of the flow regime is crucial to ensure high gas-liquid mass transfer rates and low axial dispersion, so that the reaction performance is not influenced by those parameters. After further analysis of both parameter limits and a literature search, the segmented Taylor regime was identified to enable those conditions. As this flow regime requires a rather small tube diameter ($d \leq 3$ mm) for the fluid properties of the TMS, a tube with a length of 300 m is needed for the necessary reactor volume of 2.2 L. To benefit from the positive effects of homogenization (low axial dispersion but intensive radial mixing, Section 5.2.2.3) and to allow for a compact design, the coiling of the tube was suggested. This design also enables simpler heating of the reactor via heating tapes through which four heating zones along the reactor can be realized. The flowsheet of the helically coiled tubular reactor (HCTR), followed by the CSTR, is depicted in Figure 5.43.

In addition to the continuously operated reactor design with approximated control profiles along the DSR, an alternative realization of the continuous control profiles is possible. By means of a repeatedly operated semi-batch-reactor (RSBR), the control profiles can be applied in time, in contrast to the length of the reactor, leading to simplified adjustments of the controls in the case of changing model structures and parameters. As the SBR and the subsequent CSTR differ w. r. t. their operation mode, two buffer vessels, before and after the SBR, are required so that the SBR can be operated repeatedly. Preservation of the catalyst activity and prevention of the liquid-liquid phase separation requires both buffer tanks to be heated and pressurized, leading to two additional reaction zones. While the feed buffer tank does not significantly contribute to the reaction progress because the substrate is dosed directly into the reactor, the flash buffer tank, which serves the reaction mixture to the CSTR, needs to be accounted for. In terms of the axial dispersion and adequate gas-liquid mass transfer, the SBR itself is free of axial dispersion and the stirrer intensifies the gas-liquid contacting, leading to the fulfillment of both requirements of a DSR. A flow chart of this repeatedly RSBR-CSTR-tandem is shown on the right of Figure 5.43.

After designing both reactor-tandems, their performance was evaluated by a more detailed process optimization (Figure 5.44). In contrast to the optimizations within the reactor design task, no ideal liquid-liquid separations were considered for the recovery of the TMS catalyst phase and the byproduct separation but the results show that both tandems have their selectivity and conversion optima at 95% and 98%, respectively, which indicates an enhancement of 24% and 40%, in comparison to a process with a single CSTR.

Reaction Condition Optimization of the Constructed Reactor Tandems

Based on the provided specifications from the design task, both reactor-tandems were constructed and operated with continuous catalyst recycling but without byproduct

separation via a distillation column [87, 88, 183]. In order to compare the results from the operation of both tandems, the catalyst concentration and the total residence time were fixed in accordance with a former study where a single CSTR was used [32]. The reaction conditions (temperature, pressure, and gas compositions) for the operation were determined with the help of process models optimization w. r. t. the selectivity towards the linear aldehyde nC13al.

For the HCTR-CSTR-tandem, the reaction conditions were derived with the help of the model from the reactor design task. However, the process model had to be modified to account for the approximations during the construction, i.e., the length of the HCTR had to be shortened due to the fixed residence time of the experiment. Therefore, only a reactor length of 80 m was used so that only two heating zones along the HCTR could be used for temperature control. The derived conditions of the HCTR-CSTR-tandem are depicted on the left of Figure 5.45. It can be observed that a slight excess of carbon monoxide and a temperature increase within the second heating zone of the HCTR are favorable in the first reactor. In the subsequent CSTR, which represents the second reaction zone, the temperature should stay the same but an excess of hydrogen is necessary.

For the second tandem, comprising the RSBR and CSTR, a more detailed dynamic model was developed to not only derive the necessary reaction conditions but also aid in the process start-up. With the model simulations, the operator receives valuable information on the time scale to reach the cyclic steady state of the reactor tandem. One particularly valuable piece of information for the RSBR-CSTR-tandem to ensure comparability between the different reactor networks involves the distribution of the fixed total residence time to each reaction unit. In addition to the residence time of the SBR $\tau_{\text{SBR}} = t_{\text{SBR}}$ and the CSTR $\tau_{\text{CSTR, PFR}} = V_L \dot{V}^{-1}$ with the liquid hold-up V_L and the volumetric flow rate \dot{V} , both buffer tanks as well as the preparation time or inactive time t_1 (see Figure 5.46 for a schematic representation) of the SBR need to be taken into account. Please note that the preparation time is a required, fixed time in which the charging and discharging of the SBR vessel is performed. While the feed buffer tank contains only traces of unconverted substrate and can, therefore, be neglected in the distribution of the total residence time, the flash buffer tank represents an additional, third reaction zone. With the approximated average residence time in the flash buffer tank, $\tau_{\text{DBuffer}} = 0.5V_L^{\text{DBuffer}}(t=0)\dot{V}_{\text{in}}^{\text{CSTR}^{-1}}$, with $t=0$ denoting the beginning of each process cycle, the available residence times for the SBR and CSTR can be computed with the distribution and coupling constraints

$$\tau_{\text{SBR}} + \tau_1 + \tau_{\text{DBuffer}} + \tau_{\text{CSTR}} - \tau_{\text{Total}} = 0, \quad (5.38)$$

$$\tau_{\text{SBR}} + \tau_1 - \tau_{\text{DBuffer}} - \tau_{\text{CSTR}} = 0. \quad (5.39)$$

Here, the coupling constraint ensures that the reaction in the SBR terminates and the reaction mixture can be transferred to the flash buffer tank shortly prior to the depletion of the liquid hold-up in the flash buffer tank, which supplies the continuous part

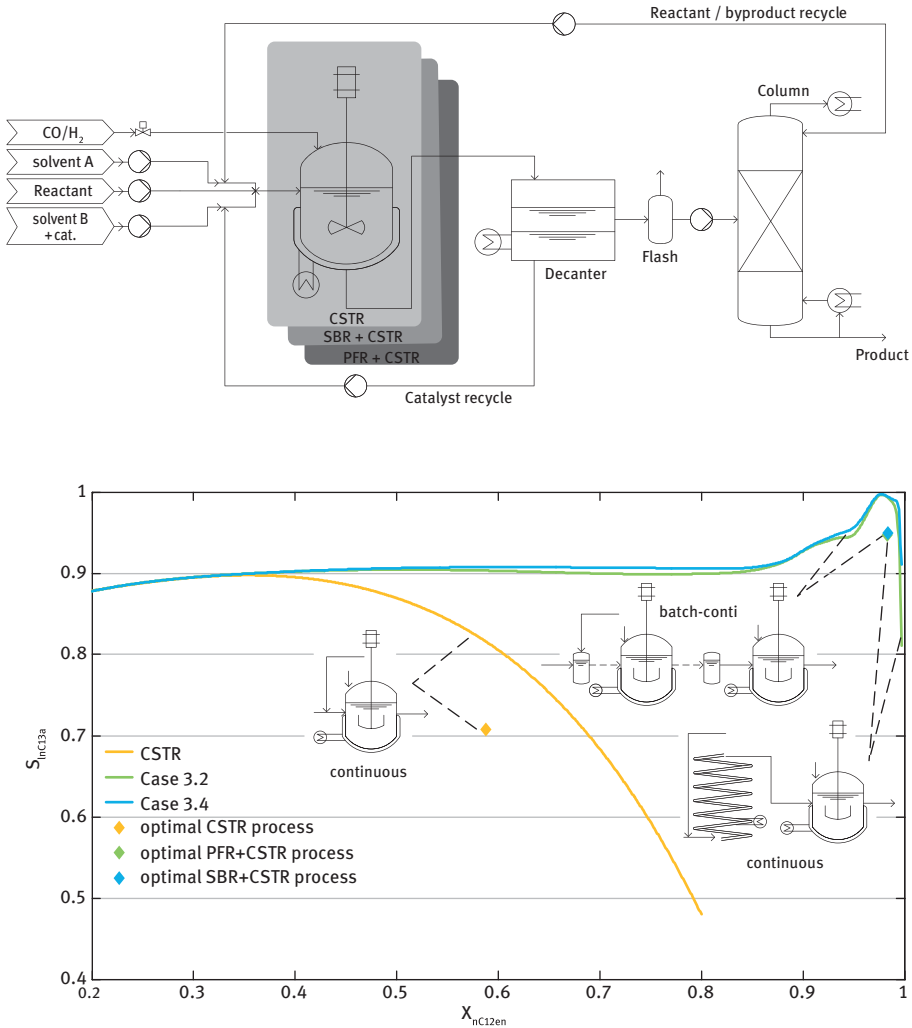


Figure 5.44: Flow chart of the overall process used for the process optimization (top) and performance comparison of the different reactor designs (bottom). The lines correspond to the maximum potential for ideal separations (taken with permission from [90]).

of the process [183]. Since τ_{DBuffer} and τ_{CSTR} are coupled via the constrained control parameter $\dot{V}_{\text{in}}^{\text{CSTR}}$, τ_{SBR} needs to be recalculated for each new cycle. This is especially important during process start-up due to concentration-induced changes in the reaction mixture density. Under ideal conditions, including the perfect realization of the controls and time-resolved adjustment of all fluxes in the process, the cyclic steady-state is achieved after approximately 30 h with n-dodecane (nC12an) being the rate-determining component (see Figure 5.47). In contrast, the concentration profiles of

the substrate (nC12en) and the product (nC13al) remain unchanged after 10 h of operation or 7 RSBR cycles [183].

In addition to the calculation of the start-up time, the residence time of each reactive unit and the process conditions, the dynamic RSBR model provided estimates of the flow rates in each pipe for each cycle in the experimental validation of the RSBR-CSTR-tandem [88]. The optimal control parameters for the SBR are depicted on the right side of Figure 5.45. The profiles for the CSTR are neglected since they are analogous to the corresponding profile in the HCTR-CSTR-tandem (Figure 5.45, left-hand side). Despite different operation modes and varying degrees of freedom, the optimal reaction conditions for both reactor tandems in Figure 5.45 are comparable approximations of the true optimal control profiles [89]. In terms of the hydroformylation reaction network, the low initial temperature and the slight excess of carbon monoxide causes a minor reduction of the catalyst activity through which all reactions and, especially, the isomerization of the terminal olefin as the main side reaction are inhibited. Subsequently, with increasing yield, a higher temperature and the hydrogen excess leads to higher catalyst activity and, therefore, faster reaction rates to compensate for the lower substrate concentration. Additionally, through those conditions, the back isomerization and hydroformylation of isomeric olefins are enhanced, which further enhances the nC13al selectivity.

For implementing the control trajectories of the RSBR in the process control system, smoothing was applied to the piecewise constant function and an additional delay of 1 – 2 min was added to account for the delay induced by the control action of the regulators. These minor adjustments and the direct applicability of the optimal control profiles in the experimental setup represent the major advantage of the RSBR over the HCTR process. While the number of control segments is limited and fixed for the HCTR after construction, fine-grained adjustments of the SBR controls are possible in the case of technical limitations or changes in the underlying model.

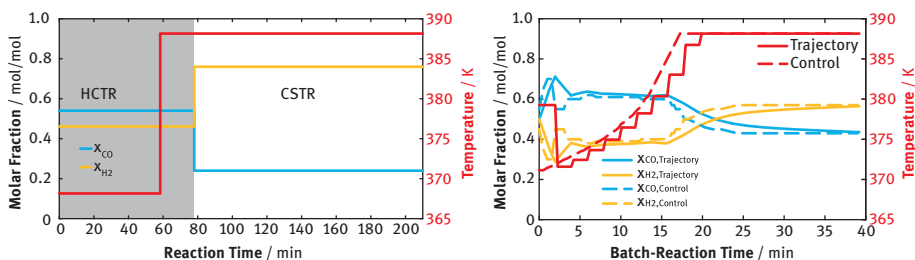


Figure 5.45: Optimal reaction control profiles for the HCTR-CSTR-tandem (left) (adopted from [87]) and the RSBR of the RSBR-CSTR-tandem (right) (adopted from [89]).

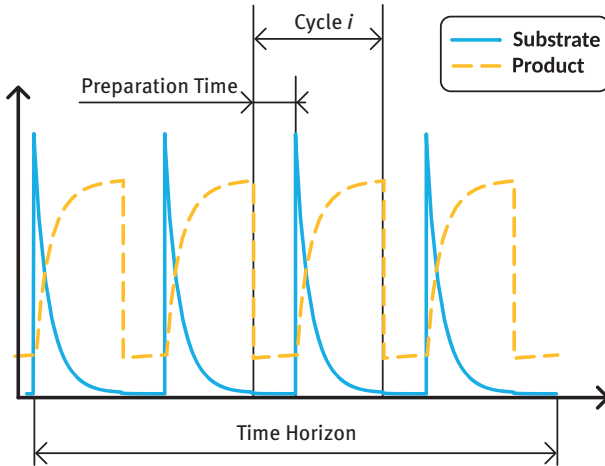


Figure 5.46: Operational cycles of the SBR in the RSBR-CSTR-tandem including the preparation time for emptying and filling of the reactor vessel (taken with permission from [183]).

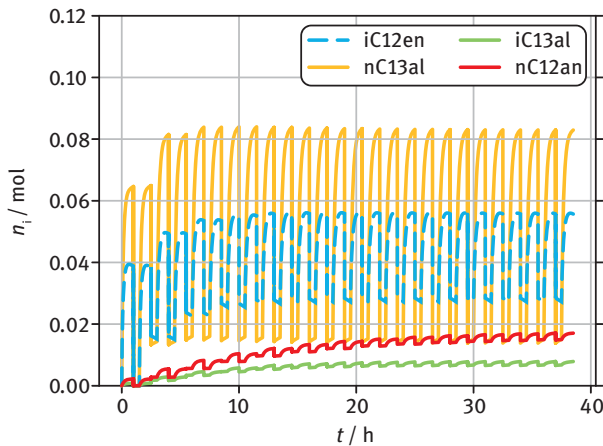


Figure 5.47: Start-up behavior of the RSBR-CSTR-tandem for selected species: dodecane isomers (iC12en), linear aldehyde (nC13al), branched aldehyde (iC13al), dodecane (nC12an). The accumulation of n-dodecane (nC12an) leads to a start-up time > 30 h for achieving a cyclic steady-state (taken with permission from [183]).

Comparison of both Reactor-Tandems

The results from all experimental campaigns of both reactor-tandems and the corresponding simulative studies are summarized in a conversion-yield-selectivity diagram in Figure 5.48. Here, the reference results from [32] are included. In comparison to the reference CSTR, which achieves a yield of 63% at 85% conversion, both reactor-

tandems surpass the reference case in both, conversion and product yield. With a conversion of over 94% and 100%, the RSBR-CSTR- and HCTR-CSTR-tandem achieve yields of 63% and 70%, respectively. In terms of STY, the HCTR-CSTR- and the RSBR-CSTR-tandem provide $2.75 \text{ kgL}^{-1} \text{ s}^{-1}$ and $2.58 \text{ kgL}^{-1} \text{ s}^{-1}$, respectively, in contrast to the single CSTR with $2.53 \text{ kgL}^{-1} \text{ s}^{-1}$, despite their approximately 1.6 times larger reaction volume [89]. In this comparison, the optimized reaction conditions were only applied to the HCTR-tandem. In a follow-up study, the optimized control profiles from Figure 5.45 were applied to the RSBR-tandem, alongside a 90 min increase of the total residence time, to remedy the effect of the preparation time on the reaction time [89]. With these adjustments, full conversion and a yield of 80% were achieved. Due to the optimized reaction parameters, the conversion and yield from [32] were already surpassed in the SBR after only 39 min.

The experimental results for the HCTR-CSTR-tandem are in excellent agreement with the simulative results. For the RSBR-CSTR-tandem, an error of approximately 4% between the simulation and the experiment occurred, which is slightly larger than the estimated error by the employed model. A comparison of the results from Figure 5.48 with the performance predictions by [90] in Figure 5.44 shows that the performance predictions were not reached in terms of selectivity. This is caused by the missing by-product separation and recycles into the reactor of the experimental set-up. With by-product recycling, the equilibrium of the isomerization reaction would be reached earlier in the reaction progress, leading to higher product selectivities.

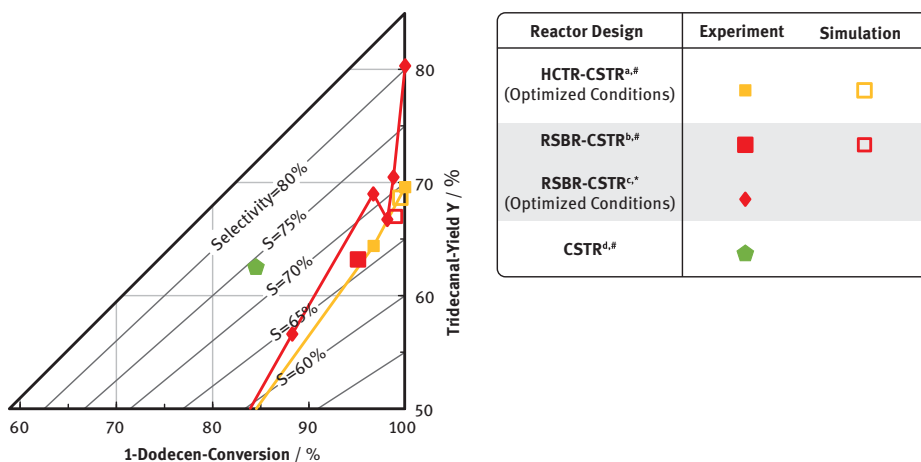


Figure 5.48: Comparison of the reactor performance for different reactor designs from ^a[87], ^b[88], ^c[89], and ^d[32]. In addition to the performance indicators that are generally evaluated at the outlet of the last reaction vessel, the experimental data from [87, 89] allow the depiction of the performance indicators over the reaction progress (solid lines). Similar residence times of 210 min are marked with # and the residence times of 300 min with *.

5.3.1.5 Summary

In systems engineering, the conceptual design of reactor networks and reactor optimization represents an indispensable tool for modern process development. Due to strong nonlinearities in the reaction kinetics and thermodynamic models, an intuitive identification of optimal operation strategies becomes impossible. As a consequence, systematic approaches, like the EPF methodology, which combines an intelligent formulation of the design problem with state-of-the-art algorithms and computation software enable the practitioner to make informed decisions.

The general idea of steering the path of a fluid element in state-space ensures a maximum number of DoF, preventing the prior restriction to conventional, potentially subpar process units. Extensions of this idea towards multiphase systems, the design of reactor-separator-networks and the robust design provide even more DoF, facilitating the consideration of more complex models and leading to a more accurate representation of real-world behavior.

The application of the EPF methodology to the homogeneously rhodium-catalyzed hydroformylation of long-chain olefins proves that complex reaction networks contain non-intuitive operation windows that can be achieved by combining the simultaneous reactor-network design and reactor optimization, leading to significant improvement in terms of selectivity and conversion. Besides reactor networks of conventional units, the perspective of functional modules also enables the consideration of alternative process operation modes, like the introduction of discontinuously operated reactors within a continuous process, to improve flexibility and enable precise control of the operating conditions.

The technical relevance of these advanced considerations is proven in experimental validations for the homogeneously rhodium-catalyzed hydroformylation of long-chain olefins in a thermomorphic multiphase system, which provides indisputable evidence for the feasibility of the methodology. Experimentally verified yields of over 80%, in contrast to the reference case with 63% without utilizing all available degrees of freedom, represent major improvements that await the transfer to industrial applications.

5.3.2 Global Optimization for Process Design

Christian Kunde, Achim Kienle

5.3.2.1 Introduction

Mathematical optimization is a powerful tool for designing processes. If a mathematical description of the considered process is available, including all relevant degrees of freedom and an objective function, gradient-based methods like steepest descent and randomized methods such as evolutionary algorithms can be used to identify promising new process designs or improve existing ones. Although there are powerful optimization tools available, most of them cannot guarantee to find the best possible process design or even provide any statement on the quality of solutions for general optimization

problems. This leads to the topic of deterministic global optimization. In addition to evaluating, for example, the annualized cost of an optimized process design, the quality of the solution is certified by calculating a lower bound for the cost. By definition, there is no process design with a lower cost than this bound. Therefore, if the cost of a process design is equal to the lower bound, that process design is guaranteed to be (one of) the best possible. Calculating lower bounds is computationally complex. A key to reducing the computational effort for global optimization lies in the use of process knowledge and problem-specific properties to improve algorithms as well as model formulations. This is demonstrated in this section for an exemplary set of processes, showing deterministic global optimization to be a useful tool for process design.

The challenge of global optimization in process design and some of the basic ideas for dealing with that challenge is introduced more thoroughly below, followed by the process examples and a short summary of this section.

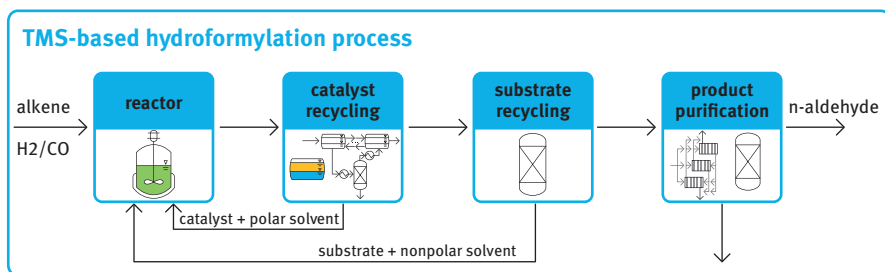


Figure 5.49: Hydroformylation process using a thermomorphic multiphase system: Efficient reaction and catalyst recycling by a temperature-switchable system that is homogeneous at the reaction temperature, and that exhibits a product-rich phase and a catalyst-rich phase at the separation temperature.

The overall synthesis of the processes employing complex phase systems includes the optimal design of the reaction step and the recycling of the catalyst-containing phase, as well as further processing of the product-containing phase. The TMS-based hydroformylation process illustrated in Figure 5.49 is a subset of the general model process introduced in Section 1.4. In short, linear aldehydes are produced from olefins in a homogeneously catalyzed reaction. The catalyst phase is then separated at lower temperatures by employing a TMS, and recycled to the reaction mixture. In a final purification step, the linear aldehyde product is separated from its isomers. This process was selected to provide case studies for the inherently model-based optimization methods presented in this section, due to the maturity of the available models. More detailed descriptions of this process are available in Sections 2.1 and 4.1.

The optimization of such nonlinear processes with structural and operational degrees of freedom typically leads to Mixed-Integer Nonlinear Programming (MINLP) problems

$$\begin{aligned}
 & \min_x && f(x) \\
 & \text{subject to} && c(x) \leq 0 \\
 & && x \in \mathbb{R}^N \\
 & && x_j \in \mathbb{Z} && \text{for all } j \in I \\
 & && l_i \leq x_i \leq u_i && \text{for all } i \in \{1, \dots, N\}
 \end{aligned} \tag{5.40}$$

where f is the objective function, c are constraints, x are variables, $I \subset \{1, \dots, N\}$ is the index set of integer variables, and l and u are lower and upper bounds for the variables, respectively. For non-convex objective functions or constraints, such problems may have multiple locally optimal solutions. In order to avoid making design choices based on poor local solutions, global optimization approaches that aim to cover the entire search space can be applied. Deterministic global optimization algorithms, in contrast to stochastic approaches, provide guarantees on the quality of solutions and are, therefore, able to certify globally optimal solutions [72].

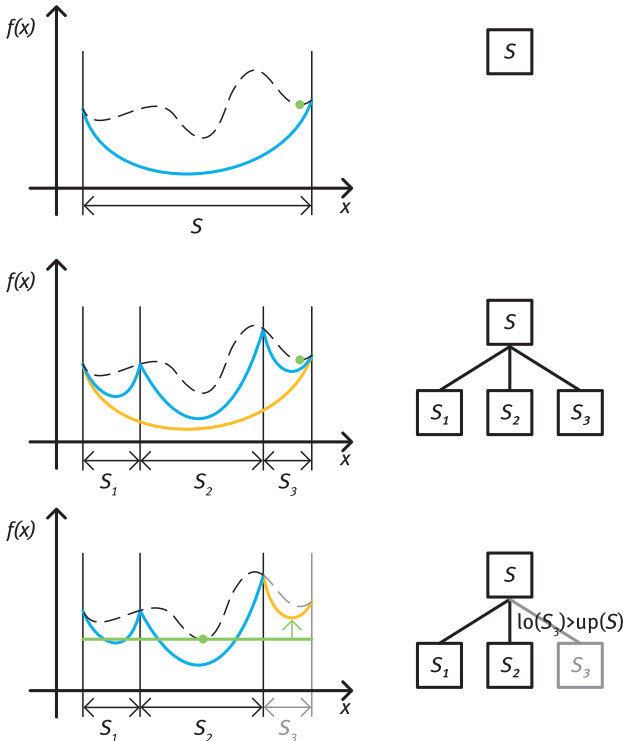


Figure 5.50: Basic principles of spatial branch-and-bound: Original function (dashed), convex relaxations for lower bounds (blue), local solutions for upper bounds (green), partitioning of the search space for refined relaxations, cutting of non-optimal branches from the search tree.

A general approach to deterministic global optimization of MINLP problems is spatial branch-and-bound, e.g. [72, 124], as illustrated Figure 5.50. Computationally tractable convex relaxations of the original non-convex problem, i.e. objective function and constraints, are solved in order to obtain globally valid lower bounds on the optimal objective function value. The search space is then recursively partitioned into smaller subdomains to refine the relaxations and, thus, obtain improved lower bounds. Non-optimal branches, i.e., those with lower bounds higher than a known local optimum, are cut from the search tree and not further considered. These steps are repeated until the lower bound is within a pre-defined tolerance margin of a feasible local solution.

The computational effort of this approach scales exponentially with the total number of variables and nonlinear expressions that need to be branched over, not only with the degrees of freedom of the problem, and easily grows to be intractable even for seemingly simple problems. Several general methods are typically employed to speed up the computations [181], e.g., by reducing the search space (less branching and better bounds) or by improving relaxations (better bounds). Examples are optimization-based bound tightening, i.e., maximizing and minimizing individual variables to obtain stronger bounds for those variables [124], or propagating strong bounds that are available for some variables to other variables that have weak a priori bounds by using interval arithmetic.

The area of deterministic global optimization has seen significant theoretical and algorithmic developments [9, 12] and several software packages are available, e.g., BARON [100], ANTIGONE [153], SCIP [50], COUENNE [9], and MAiNGO [11]. However, general-purpose solvers regularly fail to solve design problems that are relatively simple from a process design perspective in a reasonable time.

Process insight and solution strategies tailored to specific problems can lead the way to more efficient global optimization. Improved relaxations may be obtained by exploiting the specific structure of a problem or by adding efficient relaxations for problem-specific nonlinear expressions to general-purpose algorithms. Suitable model reformulations may reduce the number of variables and nonlinear expressions for an optimization problem.

Additional difficulty arises from process models that contain algorithmic solutions to black box functions or computationally highly expensive model equations, e.g., thermodynamic models, like PC-SAFT [57] and COSMO-RS [101]. In order to make such problems accessible for the algorithms discussed above, so-called surrogate modeling is used to approximate input-output relations $y=f(x)$ from the original model by computationally inexpensive approximations, $y \approx \hat{f}(x)$. Data-based surrogate modeling, in particular, fits surrogate functions \hat{f} to value pairs (x, y) that are obtained by sampling the original function, f . Choosing a structure for the surrogate function is non-trivial, with options that include polynomials, linear combinations of exponential functions, and mixed basis functions [13]. Once a suitable surrogate model is available, a certified globally optimal solution of the surrogate-based problem is obtained

by deterministic global optimization. Tailoring the surrogate modeling approach to the applied optimization algorithm and vice versa offers advances in this area.

This section summarizes a set of strategies that exploit problem-specific properties and process knowledge to significantly reduce the computational cost for solving process synthesis and design tasks globally. Problems to be considered are motivated by the process scheme in Figure 5.49. The spectrum is rather broad, including reaction and various separation processes. For the most complex models considered here, surrogates were successfully employed to reduce the computational effort and make the problems accessible for deterministic global optimization.

5.3.2.2 Distillation and Hybrid Separations

Distillation is a widely used unit operation in the chemical process industry and accounts for a significant share of its total energy consumption and costs. In the TMS-based hydroformylation process considered here, distillation is involved in catalyst recycling, recycling of unreacted substrate and the nonpolar solvent, and purification of the product. Although reliable design methodologies are available for distillation-based separation processes, new approaches are required for the branch-and-bound-based global optimization of flowsheets that also comprise other unit operations, e.g., hybrid separations or reactor-separator networks.

Rigorous stage-by-stage models used for the optimization of distillation columns require a large number of auxiliary variables and equations to describe the process states on each stage. This makes standard modeling approaches unsuitable for deterministic global optimization with general-purpose software [6]. The following approaches reduce the computational effort by orders of magnitude by exploiting the specific properties of the considered distillation models, ranging from ideal binary distillation to highly non-ideal multi-component distillation. This allows one to globally optimize distillation columns and hybrid separation processes that combine distillation with other process units in a feasible time.

The feed mixture for the product purification step in the TMS-based hydroformylation process, illustrated in Figure 5.49, contains an *n*-aldehyde and a corresponding iso-aldehyde. A straightforward approach for this separation is using a distillation column. This kind of separation can be described in good approximation using an equilibrium model with constant molar overflow (only material balances) and ideal thermodynamics. Important continuous decision variables are the heating rate and the column reflux. Important integer decision variables are the number of column stages and the number and position of feed stages. The integer decisions typically lead to MINLP problems with discrete variables in the model equations for each stage. For example, in some standard approaches for the MINLP implementation of distillation columns, e.g. [210], the optimal column length is determined with potential reflux to any column stage in the rectifying section multiplied by a

binary variable that is equal to one for the optimal top stage and zeroes for all others. This makes it difficult to obtain tight bounds for state variables in a branch-and-bound-based optimization approach without branching over each integer variable, especially for a large number of stages, and results in a high computational effort. In an alternative approach, separate fixed equation sets are used for the stripping section and the rectifying section of the column [6]. Additional equality constraints connect the feed stage with each of the two sections. For binary mixtures, this approach resembles the McCabe-Thiele method. Integer variables that determine whether a stage is included in the optimized design enter only the connecting constraints, but not the equation sets for each section. In the simplest case, the recursion formula reads

$$y_{n+1} = \left(1 - \frac{D}{V}\right) \frac{y_n}{\alpha + (1-\alpha)y_n} + \frac{D}{V}y_1, \quad y_1 \in [l_1, u_1] \quad (5.41)$$

for the vapor molar fraction of the low-boiling component, y , in the rectifying section of an ideal binary distillation column with total condenser and constant molar overflow. Here, D and V are distillate and vapor molar flows, respectively, α is the relative volatility of the low-boiling component, and n is the stage number. Bounds for y_n are then calculated recursively, starting from bounds for y_1 . This enables the propagation of bounds from states in the distillate and the bottoms, e.g., product specifications, through the column. Figure 5.51 illustrates these bounds, both for the rectifying section and the stripping section, by shaded areas that contain all possible concentration profiles in the column under given ranges for the product specifications and the molar flows.

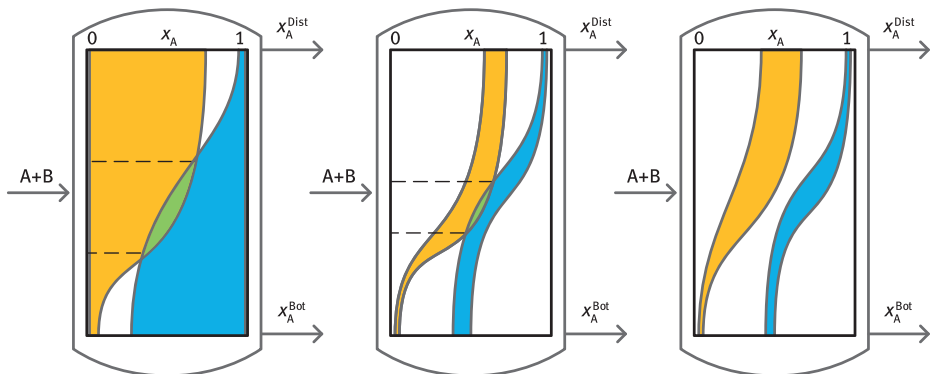


Figure 5.51: Search space reduction scheme for distillation. The shaded areas contain all possible concentration profiles. Feasible feed positions exist only for overlapping areas (between the dashed lines).

Once valid bounds on possible concentration profiles in each section are available, infeasible column designs can be removed from the search space very efficiently by probing the constraints that connect the feed stage to each section. In other words, it is checked whether there is any configuration with concentrations in the stripping section and in the rectifying section equal to that in the feed stage. In Figure 5.51, this is illustrated by overlapping areas for possible concentration profiles of stripping section and rectifying section that limit the range of feasible feed positions. If there are no overlapping concentration profiles, the column designs are infeasible and can be removed from the search space.

The bounds on concentration profiles were used in [6] to construct MINLP-relaxations of the distillation column model for optimization-based bound tightening in a custom branch-and-bound algorithm. The relaxed model comprises only the model equations for the column feed, head, and bottom stages, and uses the calculated bounds for concentration variables on all other stages. The solutions of the relaxed model still include all solutions of the original model. Therefore, if the relaxed model is found to be infeasible for a given configuration, the same is true for the original model. This was exploited by using the global optimization software, BARON, with the relaxed model to efficiently identify and remove infeasible nodes in the search tree, since the relaxed model is less complex and can be solved much faster. The resulting algorithm, combining the relaxed MINLP model with the modeling approach described above, reduced the computation time for deterministic global optimization of a simple distillation column to 5 min, as compared to over 100 h without bound propagation.

The isomers separated in the product purification step have very similar boiling points, potentially leading to unnecessarily high costs for separation by distillation alone. Melt crystallization, on the other hand, offers lower energy requirements than distillation, but the yield is limited in the case of eutectic systems. An optimal combination of distillation and melt crystallization potentially leads to reduced overall cost by exploiting the advantages of both separation methods [152].

In [116], a process containing distillation and two-stage countercurrent melt crystallization was globally optimized, directly with the general solver GAMS/BARON. In order to reduce the computational effort, the distillation column model described above was augmented with additional constraints that are redundant for the model description but can be used by the solver to substantially reduce the search space. Using the same example for the rectifying section of a binary distillation column as above, the additional constraints read

$$y_1 \geq y_2 \geq y_3 \geq \dots, \quad (5.42)$$

which follows from the monotonicity of the composition throughout the column, and

$$y^* = \left(1 - \frac{D}{V}\right) \frac{y^*}{\alpha + (1-\alpha)y^*} + \frac{D}{V} y_1,$$

$$y_n \geq y^*, n = 1, 2, 3, \dots,$$

where y^* is the fixed-point solution of the recursion formula introduced above. Various flowsheets comprising distillation and two-stage countercurrent melt crystallization were considered for the optimal design task; see Figure 5.52.

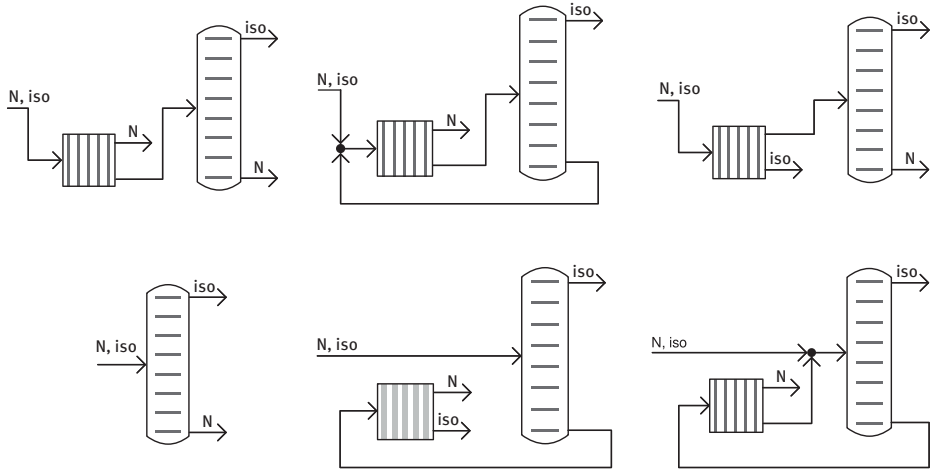


Figure 5.52: Flowsheet options and globally optimal objective function values for the hybrid distillation/melt-crystallization process considered by Kunde et al. [116]. The square symbol represents a two-stage countercurrent crystallizer cascade. Reprinted from [116], with permission from Elsevier.

A configuration that removes most of the n -aldehyde by melt-crystallization before separating only the remaining mixture via distillation was identified as the globally optimal solution. The optimal flowsheet contains a recycle from the distillation column to the crystallizer cascade. However, it was found that costs increase only marginally when using the less complex flowsheet obtained by removing this recycle.

The bound propagation strategy from Ballerstein et al. [6] relies on the monotonicity of composition profiles throughout the distillation column, which is not generally valid for multi-component ideal mixtures, as illustrated in Figure 5.53. In order to extend the bound propagation strategy to ideal multi-component mixtures, a linear transformation of variables was introduced in [148]. Replacing molar fractions x_i of components i , ordered by increasing volatility, with new variables \bar{x}_i , with $\bar{x}_1 = x_1$, $\bar{x}_2 = x_1 + x_2$, $\bar{x}_3 = x_1 + x_2 + x_3$, and so on, leads to monotonic concentration profiles in the new variables [149]. Accordingly, the model equations for the transformed variables were obtained by a summation of the component mass balances and the gas-liquid equilibrium equations. Since this transformation preserves the model structure,

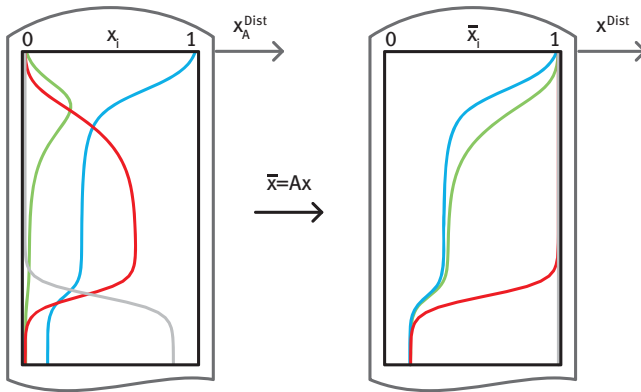


Figure 5.53: Composition profiles for ideal multi-component distillation. Left: original variables. Right: transformed variables.

the original bound-tightening strategy and related methods can also be applied to the transformed distillation column model. Reductions in computation time of orders of magnitude compared to the original model formulation without bound-tightening were observed for a test set of different multi-component global optimization problems; see Table 5.8.

Table 5.8: Running time in CPU minutes for selected test cases of multi-component ideal distillation, from Mertens et al. [149], each with different strategies to reduce the computational effort of global optimization. The original publication is referred to for computational details, software, and hardware.

	Test case 1	Test case 2	Test case 3
Original model	>1,440 min	1,373 min	1,038 min
Reformulation	51 min	462 min	97 min
Reformulation, bound tightening, and monotonicity	4 min	13 min	10 min

The substrate recycling step of the hydroformylation process, depicted in Figure 5.49, comprises the distillation of a non-ideal mixture with five main components, namely, dimethylformamide, decane, dodecane, dodecane, and tridecanal. Although strategies developed for ideal mixtures can, in principle, be extended to non-ideal mixtures with fixed order of volatilities [117], the transformation of variables from Mertens et al. [149] does not necessarily lead to composition profiles with the required properties for multi-component mixtures, with a variable order of the volatilities of its components [97]. The non-ideal behavior of such a mixture is depicted in Figure 5.54. Without the bound-tightening strategy, the MINLP formulation of the substrate recycling step was not solved by GAMS/BARON in a reasonable time. Therefore, a

surrogate-based optimization approach using Kriging interpolation for the distillation column model was employed in the literature [96]. The non-ideal multi-component distillation model was treated as a black box function, $y=f(x)$, for fixed feed conditions, with the design parameters, x , and the output flows of the column, y . The computationally expensive black box function was replaced by a series of simpler functions, $y \approx \hat{f}(x)$, using Kriging interpolation in order to reduce the computational effort of the optimization problem. Samples of the black box function for the initial surrogate model were obtained using a space-filling design. This strategy may introduce significant interpolation error to the model when trying to keep the number of function evaluations low. Therefore, the resulting optimization problem was repeatedly solved in order to refine the surrogate model in each iteration through additional sampling in a neighborhood of the current optimal solution. The optimization problems were solved by Keßler et al. [97] using deterministic global optimization with GAMS/BARON in each iteration step, in order to avoid constructing refined models around a poor local optimum and converging to a sub-optimal region of the search space. The adaptive Kriging approach was shown to reliably find solutions with significantly lower costs than a multi-start local optimization approach. A similar approach is implemented for general grey box problems in the optimization software ARGONAUT [13].

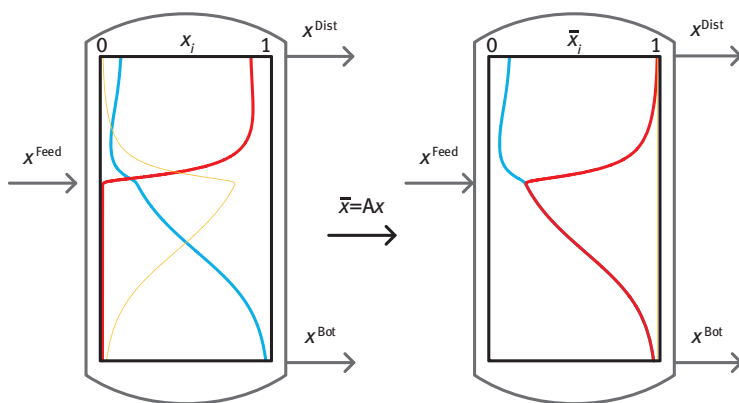


Figure 5.54: Composition profiles for strongly non-ideal distillation of a ternary mixture comprising toluene, methanol, and methylbutyrate. Left: original variables. Right: transformed variables.

Highly non-ideal mixtures may lead to input-output multiplicities for distillation columns, i.e., multiple steady-state solutions for the same set of feed conditions and parameters [30]. Standard surrogate modeling is not applicable in such a case, since the approach $y=f(x)$ is not suitable to describe input-output multiplicities. Instead, the surrogate problem was reformulated by Keßler et al. [97] in a way that the inputs as well as the outputs of the original model are inputs of a new implicit

function, $f(x, y) = 0$. Such an implicit function is able to describe input-output multiplicities and can be approximated by a surrogate, $\hat{f}(x, y) \approx 0$. The adaptive Kriging approach using global optimization in combination with implicit surrogate models was employed for the optimal design of a distillation column for the separation of a mixture comprising toluene, methanol, and methylbutyrate [97]. In the case study considered there, the Kriging-based approach found a solution with 30% less cost than a multi-start local optimization approach that was allowed to run for the same amount of computational time.

5.3.2.3 Multi-stage Separation Networks

Melt-crystallization and organic solvent nanofiltration play a substantial role in the downstream processing of the considered hydroformylation process. Melt-crystallization was shown to be beneficial for the separation of aldehyde isomers for product purification [8], whereas organic solvent nanofiltration was used to improve catalyst recycling [31] in TMS processes. In both separation processes, multiple stages are often required to achieve the desired purity. Conventional countercurrent cascades are a standard approach in this setup, but other configurations may be more profitable under certain conditions. Deterministic global optimization is a very useful tool to identify alternative configurations of multi-stage separation networks in a reliable way. Since the optimal solution is certified by a globally valid lower bound to the objective function value, a deterministic global solver will not fail to identify promising configurations due to the convergence to a suboptimal local solution. Superstructure models containing conventional and alternative configurations of multistage separation processes using either melt-crystallization or organic solvent nanofiltration were studied [117, 118]. Evaporative crystallization was also included here to study whether results are transferrable to further separation processes. Problem-specific model reformulations were employed to counter the increased computational effort required by global solvers and enable the solution development of the resulting challenging MINLP problems with GAMS/BARON. Extensive parameter studies were conducted to study the influence of key parameters on globally optimal solutions for these problems. The parameters studied for each type of process comprised the feed composition, a parameter characterizing the driving force of the separation, such as distribution factors, and the product specifications. The results can be categorized by the number of stages an optimal countercurrent configuration would require for a given separation task. If this number was high, i.e., more than three for the considered cases, there were no alternative configurations with lower cost. However, if this number was low, countercurrent cascades could be replaced by alternative configurations with substantially lower cost in certain parameter regions. Figure 5.55 includes an illustration of the results of the parameter study for multi-stage melt-crystallization that varies the feed composition and the differential distribution coefficient. The relative crystallization effort for alternative configurations is overlaid on a grid that marks the optimal countercurrent

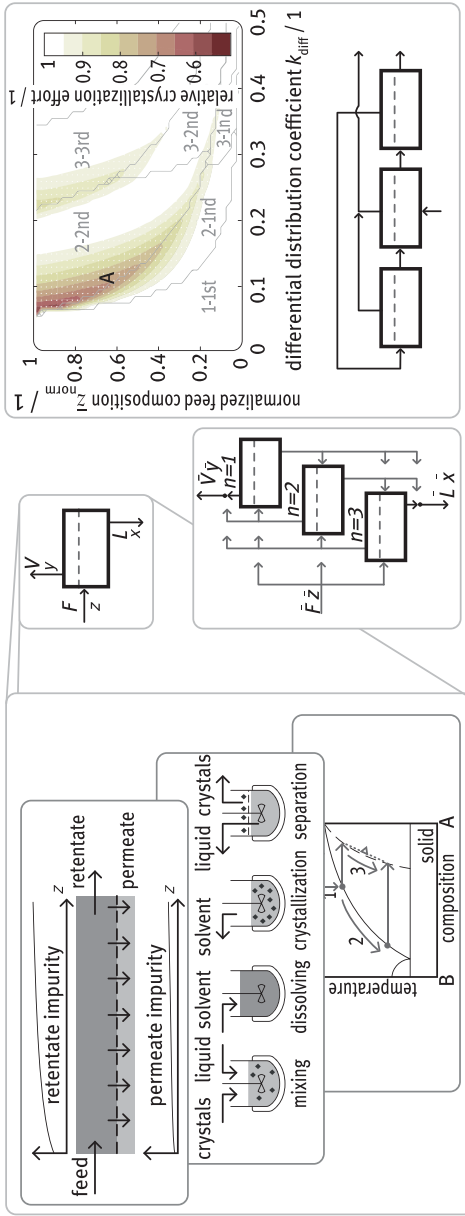


Figure 5.55: Deterministic global optimization of different multi-stage separation networks (left) leads to the same optimal multi-stage configuration in parameter region A (right). Reprinted from [118], with permission from Elsevier.

design, where e.g., 3-2nd stands for three stages and the feed on the second stage, counted from the top. The largest improvement for alternative configurations over countercurrent designs was observed in a parameter region where optimal countercurrent cascades have two stages and the feed switches from the first stage to the second stage. Notably, the same optimal alternative configuration was found for all three different separation processes (Figure 5.55). Although the globally optimal configuration has one more stage than the competing countercurrent design, the corresponding stages are smaller. Due to favorable concentration levels and a smaller recycle, enabled by the additional degrees of freedom, this ultimately reduces costs. Based on the results of the parameter studies, design guidelines for multi-stage binary separation processes could be extended by checking for alternative designs for low stage numbers only, and in particular, including the configuration in Figure 5.55 as a candidate [118].

5.3.2.4 Combined Reaction and Catalyst Recycling

The core of the TMS-based hydroformylation process comprises the homogeneous reaction and the subsequent phase separation at a lower temperature for catalyst recycling in a decanter (Figure 5.56). The computationally most expensive parts of the considered process model were identified to be the reaction kinetic model [67], an artificial neural network trained on PC-SAFT-based gas-liquid equilibrium data [167] and the catalyst recycle that included a liquid-liquid equilibrium model based on temperature-dependent equilibrium coefficients [201]. Although the model complexity was considered to be moderate from a process engineering perspective, standard approaches for deterministic global optimization lead to computation times of over 24 h. This could be reduced by orders of magnitude using the following methods [95].

Reformulations aimed at reducing the number of variables and nonlinear expressions were employed to obtain less complex models of the reactor and the decanter. This was especially effective for the decanter model: The original simulation model was designed to explicitly calculate output values from input values. Additional intermediate variables and nonlinear expressions were required for that purpose.

$$\dot{n}_I = \xi \dot{n}_{\text{feed}}, \quad \dot{n}_{II} = (1 - \xi) \dot{n}_{\text{feed}}, \quad \xi = K/(1 + K) \quad (5.44)$$

Here, \dot{n}_I , \dot{n}_{II} , and \dot{n}_{feed} are molar flows of a single component in phase I, phase II, and the feed, respectively, while K is the corresponding equilibrium coefficient. The intermediate variable, ξ , and most of the nonlinear expressions were removed in an equivalent implicit model formulation that was much more efficient for global optimization.

$$\dot{n}_I = K \dot{n}_{II} \quad \dot{n}_I + \dot{n}_{II} = \dot{n}_{\text{feed}} \quad (5.45)$$

Upper and lower bounds that were available for some variables prior to optimization were exploited to reduce the search space by calculating improved bounds for

every other variable in the model. The initial bounds resulted from e.g., the validity range of property, phase equilibrium, and reaction kinetic models for the reactor. Additional bounds were derived from operational restrictions, such as maximum temperature and pressure values or the condition of a single liquid phase.

Logarithmic reformulation was applied to the reaction kinetic model to further reduce the overall number of nonlinear expressions. By taking the logarithm of the reaction rate equations, products of exponential expressions that typically occur here were replaced by summation expressions.

Since certain reaction rate expressions of the considered model share the same argument, e.g., the temperature in Arrhenius expressions, using an independent convexification for each individual expression leads to an unnecessarily large search space. In contrast, simultaneous convexifications were calculated for these constraints using results from Ballerstein and Michaels [5]. Suitable linear combinations of the nonlinear expressions enable tighter convexifications that effectively reduce the search space. The resulting constraints were added to the model as inequalities that are redundant for the model description, but that are used by the solver for improved relaxations.

The artificial neural networks that modeled the gas-liquid equilibrium of the synthesis gas supplied to the reactor with the liquid reaction phase employed the hyperbolic tangent as the activation function. This introduced additional nonlinear expressions to the process model. Using ideas from Fügenschuh et al. [45], a piecewise linear approximation of the activation function was applied to eliminate these nonlinear expressions, but resulted in additional binary variables and reduced model accuracy. However, it was found that an approximation with three subdivisions of the activation function reduced the computation time significantly and only introduced an approximation error of 1% in the optimal objective function value.

Applying all of the methods discussed above reduced the computation time from over 24 h to approximately 5 min. Standard reformulations and bound propagation alone lead to a reduction of the computation time to 106 min. A further reduction to 34 min was achieved by using the logarithmic reformulation, and to 22 min by additionally employing simultaneous convexifications. The piecewise linear approximation of the activation function finally allowed one to solve the problem in 5 min.

5.3.2.5 Liquid-Liquid Extraction

The TMS-based hydroformylation concept enables efficient catalyst recycling by liquid-liquid extraction. However, due to the high cost of the employed catalyst, even small residual amounts of catalyst in the product phase may render the process unprofitable. Measures aimed at increasing the catalyst retention to increase profitability include additional organic solvent nanofiltration [31] and multi-stage liquid-liquid extraction [142]. Advanced thermodynamic modeling, e.g., for the optimal design of the liquid-

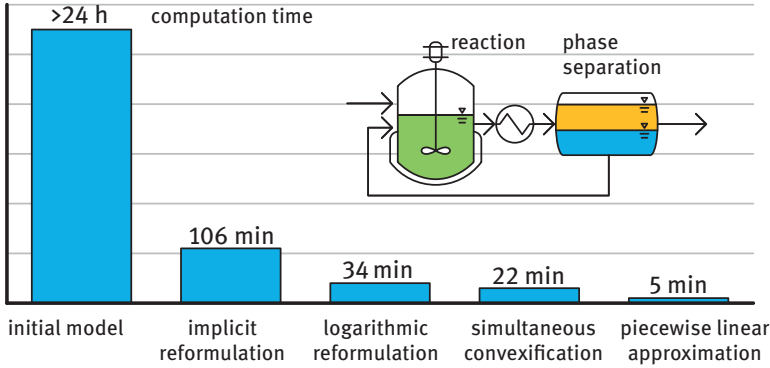


Figure 5.56: Influence of different speed-up strategies on the computation time required for the deterministic global optimization of an integrated reaction-separation process.

liquid extraction considered here, leads to increasing the predictive accuracy at the expense of increasingly complex models. Optimization problems with embedded iterative solution procedures for advanced thermodynamic models may lead to convergence problems and high computational effort. In the case of deterministic global optimization, these issues are even more pronounced. Instead of using advanced thermodynamic models directly for optimization problems, they can be replaced by computationally inexpensive surrogates that are accurate in the sense that the additional approximation error introduced by this step is small. Process models often contain multiple instances of the same thermodynamic model, e.g., the phase equilibrium on each stage of a multi-stage separation process. Using surrogates instead, therefore, substantially reduces model complexity, which justifies the additional effort of obtaining sufficient sample data for accurate surrogates and enables deterministic global optimization of such processes.

Surrogate modeling of liquid-liquid equilibria for simulation and local optimization is focused primarily on models that can be calculated in a sequence of explicit steps [142, 163]; see also Section 5.2.3. In the first step, a surrogate function, \hat{g} , acts as a classifier for the valid input domain, i.e., the biphasic region of a phase diagram. For feed conditions that lie in the biphasic region, a second surrogate function, \hat{f} , calculates the distribution of components between both phases. In the sequential approach, the resulting surrogate models, therefore, comprise two surrogate functions, e.g.,

$$\begin{pmatrix} K^{\text{I}} \\ K^{\text{II}} \end{pmatrix} = \hat{f}(x), \quad \hat{g}(x) \leq 0. \quad (5.46)$$

Here, feed conditions are denoted by x and the distribution coefficients from feed to phase I/II for all components, by $K^{\text{I/II}}$. For the sake of a simple notation, temperature is omitted here and only the molar fractions in the feed are considered, i.e., $x \in [0, 1]^{N-1}$, where N is the number of components in the mixture.

Since surrogates typically introduce nonlinear expressions to the process model, efficient global optimization requires the embedded surrogates to be as small as possible. This was achieved by an implicit model reformulation that only considers the binodal curve in order to reduce the model dimension, and a parameterization that allows removing the classifier model [119]. Value pairs on the binodal curve, i.e., the boundary of the biphasic region, are typically calculated by solving an implicit equilibrium model for compositions $x^{I/II}$ on both branches of the binodal curve, i.e., $h(x^I, x^{II}) = 0$. However, the solutions (x^I, x^{II}) of h can also be described by an explicit function $(x^I, x^{II}) = f(t)$ using a parameterization variable, $t \in [0, 1]^{N-2}$. Instead of using the unknown function $f(t)$, a surrogate $\hat{f}(t)$ is fitted to solutions of the equilibrium model.

$$\begin{pmatrix} x^I \\ x^{II} \end{pmatrix} = \hat{f}(t), \quad t \in [0, 1]^{N-2} \quad (5.47)$$

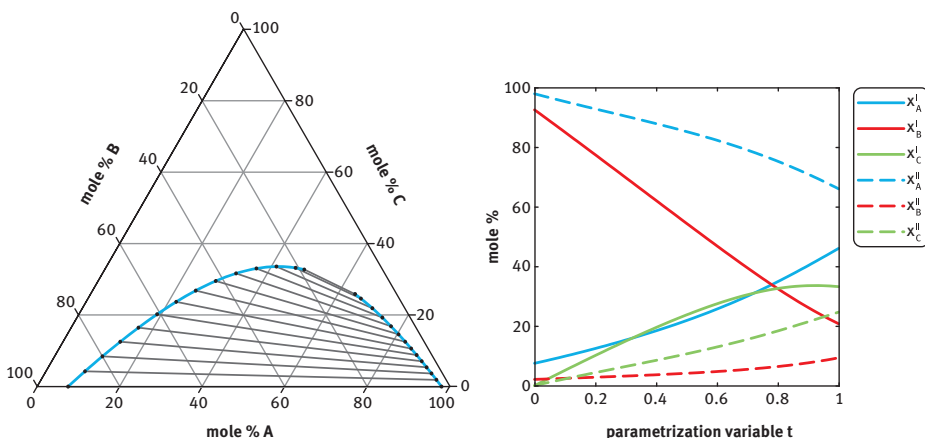


Figure 5.57: Parameterization of liquid-liquid equilibrium compositions on the binodal curve for a ternary mixture.

The resulting overall model is implicit with respect to the equilibrium compositions, (x^I, x^{II}) . However, the binodal curve has a smaller dimension than the interior of the biphasic region, and no additional classifier is required. For example, for a three-component mixture at a constant temperature as illustrated in Figure 5.57, this leads to a single one-dimensional surrogate, instead of two surrogates with two-dimensional inputs as in the sequential approaches. The extension of this strategy to mixtures with more components or a variable temperature is straightforward with a suitable parameterization of the data.

This surrogate modeling approach was applied to the deterministic global optimization of an extraction cascade employed for the catalyst recycling in the TMS-

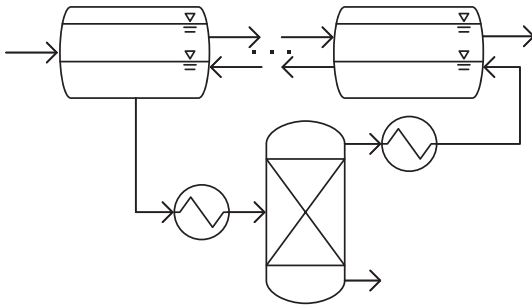


Figure 5.58: Catalyst recycling: decanter cascade with extraction solvent recycling using a distillation column.

based hydroformylation of 1-dodecene, see Figures 5.49 and 5.58. The feed mixture contained the substrate 1-dodecene, the product *n*-undecanal, the polar solvent dimethylformamide, the non-polar solvent dodecane, and small amounts of catalyst. The original model included a UNIFAC implementation for the liquid-liquid equilibrium calculation and COSMOtherm [24] to calculate the distribution of the catalyst between the phases. Even local optimization was challenging for this problem considering that a computation time of a couple of seconds was observed for a single evaluation of the catalyst distribution with COSMOtherm.

Replacing these complex models using the surrogate approach described above allows one to efficiently optimize this process, including with deterministic global solvers. The surrogate employed here was a combination of a second-order polynomial fitted using sparse optimization and an artificial neural network fitted to the residual between the polynomial and the data. The resulting model reproduced the data accurately, as illustrated in Figure 5.59 for data points of mixtures without 1-dodecene. Deterministic global optimization of the problem took less than 1 min of computation time for extraction cascades with up to five stages, using a shortcut distillation model for the solvent recycle. The results indicated a trade-off between higher solvent recycle and a larger number of stages for economical catalyst retention, with an optimal number of stages equal to four for the considered process.

5.3.2.6 Summary

The present section was concerned with the design of optimal reaction and separation processes. From the theoretical perspective, the focus was on deterministic global optimization for process design, which means that optimal solutions are proven to be the best possible ones, and subsequent design decisions are not based on suboptimal local solutions. It was shown that this can be computationally very challenging with available algorithms using standard model formulations. Tight integration of process knowledge, modeling strategies, and optimization algorithms was a key to reduce the computational effort by orders of magnitude, and thereby

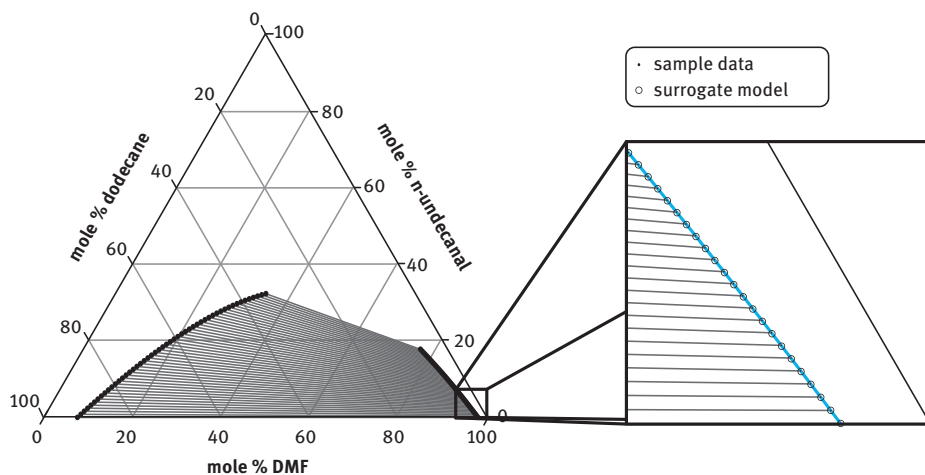


Figure 5.59: Surrogate modeling results. The displayed results show only mixtures without 1-dodecene. Reprinted from [119].

enable the global optimization of the considered processes within reasonable computation times. From the application perspective, a special focus was on the hydroformylation of long-chain olefins using a given thermomorphic multiphase system. Besides the reaction, separation processes also play an important role, i.e., for the efficient purification of products and the recycling of excess reactants and auxiliaries. Among the separation processes, distillation columns have a large impact on flowsheet optimization. Using monotonic reformulations, tailor-made bound-tightening, or surrogate models with iterative refinement, global optimization of distillation columns becomes feasible for the first time with moderate computational effort in the order of minutes up to a few hours, depending on the specific process (number of components, “difficulty” of separation). Further, global optimization was also applied to other multistage separation processes, including membrane separation, liquid-liquid extraction, evaporative and cooling crystallization, leading to novel insights. Substantial cost reductions were found for the novel process configurations, compared to classical countercurrent cascades, and some simple design rules were derived from the rigorous global optimization results.

Extended design problems that include the integrated molecular design of novel environmentally benign solvents, besides process structure and operating conditions, lead to a class of very challenging extended MINLP optimization problems. Since these problems could not be solved by deterministic global optimization algorithms with reasonable effort, a hierarchical approach was instead employed (Section 6.4).

5.3.3 Optimization under Uncertainties in Process Development

Tim Janus, Stefanie Kaiser, Jochen Steimel, Sebastian Engell

During the design phase of a chemical process, a team of experts generates and evaluates process alternatives in an iterative procedure. They choose production routes, interconnections of the underlying equipment, and promising resources, like solvents or catalysts. For these teams, computer-aided optimization can be an important part of their toolbox. Optimization in process design is challenging because of a large number of continuous and discrete decision variables, incomplete information, e.g., not exactly known reaction kinetics and physical properties, and the requirement of computation times that are in magnitudes such that are compatible with the design workflow. Incomplete or inaccurate information is an issue, especially when novel processes with several phases are designed, which largely increases the number of phenomena that have to be taken into account.

In this section, we present a framework for the selection and optimization of process designs (superstructure optimization) that takes the uncertainties explicitly into account. The approach helps to exclude designs, which are clearly suboptimal over the range of uncertainties considered and provides important information about which uncertain parameters must be determined more accurately before a final decision can be made. A core idea is to distinguish the degrees of freedom that must be fixed during process design from the degrees of freedom that can be adapted to the real behavior of the process during operation. The latter ones can be used to react to the observed behavior by automatic control (e.g., to achieve a specified purity by a higher reflux rate), real-time optimization (Section 5.4.2.1), or interventions of the operators (operational degrees of freedom). In the optimization of the fixed degrees of freedom, the presence of the adaptable parameters is included so that the best possible behavior of the given structure is considered.

Superstructure optimization is an approach to investigate structural design decisions on the choice of the unit operations and the pieces of equipment and their interconnections, and parametric decisions on the design variables in an integrated manner [145, 220]. A superstructure is a graph that represents a set of alternatives of a process structure and the related degrees of freedom (DoF). It includes all combinations of a set of processing routes and preselected unit operations, and the bounds of the associated degrees of freedom.

The DoFs can be categorized into design degrees of freedom (DDoF) and operational degrees of freedom (ODoF). DDoFs are decisions that define how a process is realized i.e., they define structural decisions that are fixed for a long period of time after the plant has been built. Examples of DDoFs are the number of reactors in a cascade, the number and connections of distillation columns, and the numbers of trays of the distillation columns, and the volumes of the vessels.

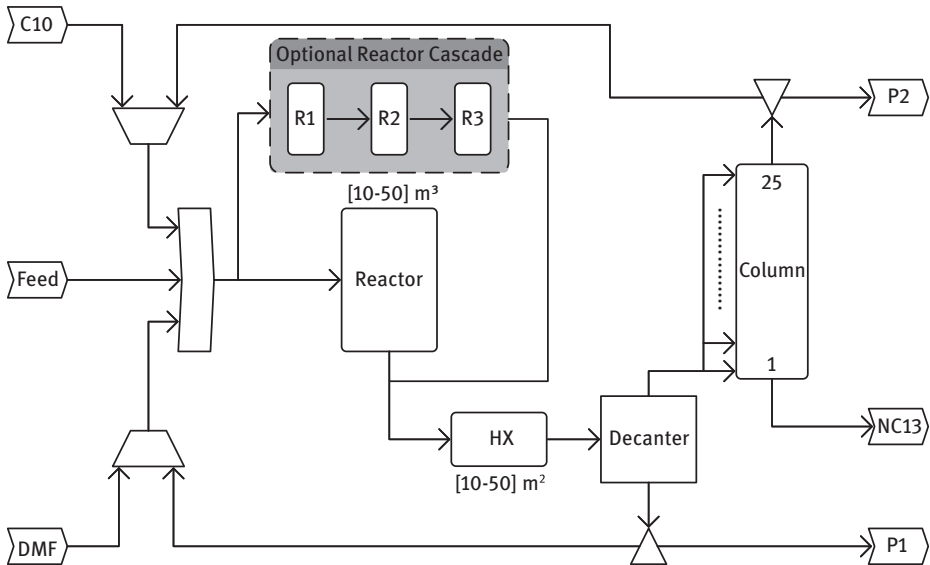


Figure 5.60: Superstructure of a process for the hydroformylation of 1-dodecene to tridecanal with either a reactor or a reactor cascade [203].

Figure 5.60 shows a superstructure for a chemical process that produces tridecanal by the hydroformylation of 1-dodecene. An important DDoF is the structure of the reaction section, which is represented as a binary decision between one continuous stirred-tank reactor or a cascade of three reactors. Further DDoFs are the volumes of the reactors [10–50 m³], and the area of the heat exchangers [10–50] m², the number of column stages [15–25], and the feed position [1–#no stages]. It is obvious that a manual “optimization by trial and error”, even of this relatively small number of degrees of freedom, is not very promising. For example, if we assume that the areas and volumes are discretized in full m² or m³, there is a total of $40^4 \cdot 10 \cdot (15 + \frac{10}{2}) = 512,000,000$ combinations of process alternatives that are represented by the instantiation of the superstructure for the reactor cascade.

Operational degrees of freedom (ODoFs), in contrast, are decisions that define how a process is operated; they define parameters that an operator or a control algorithm can change during operation. Examples of ODoFs are reactor or feed temperatures, pressures, feed amounts, and the distillate to feed ratio and the reflux ratio of a distillation column.

The superstructure (or flowsheet) optimization problem can be formulated as a mixed-integer nonlinear programming problem (MINLP). This kind of problem can be solved directly by suitable algorithms [59], but the computational effort is already very high for processes of medium size, and also the formulation of the underlying models requires a significant effort. In order to cope with the complexity, many authors proposed to decompose the superstructure optimization problem

[145]. Waltermann et al. [213] investigated the extension of superstructure optimization to complex separation processes. By formulating the superstructure based on elementary operations, the solution space also includes intensified processes, e.g., extractive distillations. The authors also included the selection of solvents in the optimization problem. Other works in this area aim at algorithms that find the global optimum when a large number of local optima is present; e.g. Urselmann et al. [208] used a hybrid algorithm that employs an evolutionary algorithm and a mathematical solver for local optimization of the continuous degrees of freedom to optimize a reactive distillation column. In the approach described in [81], the flowsheets are evaluated by a commercial process simulator that acts as a black box, and data-based models are trained during the optimization to speed up the search process that is based upon an evolutionary algorithm.

When optimization is used for the development of flowsheets, all units and processes must be described mathematically, and in the optimization, it is usually assumed that the models used are an exact description of the future reality, which of course is not true. Deviations between models and reality are always encountered, and the goal of process design is to develop a process that works sustainably and profitably in reality, not on a computer. Therefore, model uncertainties must be taken into account, which is traditionally done by adding margins (e.g., additional trays of a distillation column) ex-post to the design to ensure that the real plant can meet the specifications and can cope with disturbances, e.g., feed variations, external conditions, equipment and catalyst degradation, etc. By this approach, optimality is lost to some degree, and, therefore, the model-reality gap should be as small as possible. On the other hand, the more complex the physicochemical processes in the plant are, the more effort it takes to come up with mathematical descriptions that are accurate in the range of conditions where the (not yet known) optimal plant operates, and the necessary time and effort become a limiting factor. Therefore, it is desirable to exclude alternatives early, based on models of medium accuracy, and to concentrate the effort in model development, in particular, the required experimental work on plant structures and operating conditions that are promising. Therefore, there is a need to quantify the effect of the uncertainties on the optimum design. The interplay between the design of experiments and design optimization is discussed in more detail in Chapter 6. This section focuses on how to quantify the effect of the model uncertainties on the selection of the design degrees of freedom.

Model uncertainties can be classified into structural and parametric uncertainties. Structural uncertainties refer to neglecting certain effects or dependencies by the use of simpler mathematical expressions, e.g., Henry coefficients are used instead of the more complex descriptions of mass transfer. Parametric uncertainties reflect the lack of knowledge about the precise values of the parameters in models of a given structure. To some extent, parametric uncertainties can also describe structural uncertainties, e.g., if a parameter is temperature-dependent in reality, but is considered to be constant in the model; this can be expressed by a certain

range that its value may take, thus over-approximating the uncertainty. Of course, in this case, the optimization of the operating temperature based on other influences is only of limited reliability. In this section, we represent the model-reality mismatch by parametric uncertainties throughout, because this leads to computational tractability of the problem of process design under uncertainty. The assumed ranges of the parameters are understood to be approximations of the effect of all un-modeled influences on the relationships of interest.

As mentioned above, it is important to distinguish between the design degrees of freedom and the operational degrees of freedom in the design of processes under model uncertainty. While the DDoFs must be chosen such that the process tolerates the uncertainties for fixed values of the DDoF, the operational degrees of freedom can be adapted to the actual behavior of the process via automatic control, or real-time optimization (Section 5.4), or interventions by the operators.

We assume that for all uncertain parameters, ranges of their values are known, and we represent the uncertainty by Ω so-called scenarios – combinations of parameter values that represent the total uncertainty well enough. Each of these scenarios can have a certain probability, π_ω , which reflects an assumed likelihood of this scenario to happen, indicating, e.g., that the worst possible combination of all uncertain parameter values should be considered with respect to the feasibility of the operation (i.e., the plant can still produce the specified product), but the influence of this case on the expected production cost should be smaller than that of the nominal case.

The two-stage optimization procedure proposed in the literature [201, 203] formulates the optimization of a superstructure in the presence of model uncertainties as a two-stage mixed-integer optimization problem:

$$\min_{y_d, y_c, x_\omega} G(y_d, y_c) + \sum_{\omega=1}^{\Omega} \pi_\omega F_\omega(y_d, y_c, x_\omega, z_\omega) \quad (5.48a)$$

$$\text{s.t. } g(y_d, y_c, x_\omega, z_\omega) \leq 0 \quad (5.48b)$$

$$f(y_d, y_c, x_\omega, z_\omega) = 0 \quad (5.48c)$$

The objective function, eq. (5.48a), consists of two terms. The first term describes the cost that is incurred as a consequence of fixing the discrete (y_d) and continuous (y_c) design degrees of freedom (DDoF), which cannot be adapted to the realization of the uncertainties during plant operation. This is called the first stage cost. Usually, it represents the investment cost. The second term consists of the summation of the scenario-dependent costs for the Ω discrete scenarios (F_ω), weighted by their probabilities (π_ω). The scenario costs represent the operational costs and the revenues for the different instantiations of the uncertain model parameters (z_ω). In the calculation of the scenario costs, an optimal adaptation of the **operational** degrees of freedom (x_ω) (also called recourse variables) to the scenario-specific parameter realizations is assumed, which represents the optimal reaction of the control system or the plant operators to the uncertainties. This cost function represents the reality that

there is flexibility in the ODoF after the plant has been built. The formulation is “optimistic”, in the sense that an optimal reaction to the uncertainties is assumed.

The design problem is subject to inequality constraints, eq. (5.48b), e.g., product property constraints or operational limits, and is further constrained by equality constraints, eq. (5.48c), that result from the model equations that describe the unit operations and their possible connections. The discrete and continuous design decisions (y_d) and (y_c), and the recourse decisions (x_ω) have to be between the upper and lower bounds.

For the design problem shown in Figure 5.60, the degrees of freedom can be classified as shown in Table 5.9 [203].

Table 5.9: Degrees of freedom of the flowsheet in fig. 5.60 [203].

PROCESS STEP	VARIABLE	DESCRIPTION	TYPE	UNIT	MIN	MAX
REACTOR	Type		Design-binary	[-]	0	1
REACTOR	Volume		Design-continuous	m ³	10	50
HX	Area		Design-continuous	m ²	10	50
COLUMN	NStages	Number of stages	Design-discrete	[-]	15	25
COLUMN	Feed stage	Number of the feed stage	Design-discrete	[-]	10	NStages
REACTOR	T	Temperature	Recourse	K	353	383
REACTOR	p _{co}	CO partial pressure	Recourse	Bar	5	15
REACTOR	P _{h2}	H2 partial pressure	Recourse	Bar	5	15
COLUMN	R	Reflux ratio	Recourse	[-]	0	1
COLUMN	D2F	Distillate to feed ratio	Recourse	[-]	0	1
PURGE	P1.K	Split factor	Recourse	[-]	0	1
PURGE	P2.K	Split factor	Recourse	[-]	0	1
FEED	DECAN	Molar flow	Recourse	Kmol/h	5	17
FEED	DMF	Molar flow	Recourse	Kmol/h	0	2
FEED	Precursor	Molar flow	Recourse	Mol/h	0	1
FEED	Ligand	Molar flow	Recourse	Mol/h	0	1

The solution of this type of optimization problem, which is a two-stage optimization problem with nonlinear constraints and discrete and continuous variables (two-stage MINLPs), is computationally very demanding. In principle, the problem can be solved by representing it as a monolithic optimization problem and applying standard MINLP solvers; however, this often leads to excessive computation times and large integer gaps. A possible remedy is to apply decomposition techniques, which basically can be done either by solving the different scenarios independently and reinforcing the equality of the DDoF or by decomposing the problem according to the stages. The latter means optimizing the ODoF of the scenarios separately for fixed design parameters and iterating over the design parameters in an outer loop. The scenario optimization problems are NLPs and, therefore, relatively easy to solve, while the optimization of the DDoF includes discrete DoF and is computationally hard. Steimel and Engell [201, 203] proposed to employ an evolutionary algorithm for the optimization of the DDoF. The evolutionary algorithm fixes the design variables and generates Ω NLP sub problems of the form:

$$\min_{x_\omega} F(y_d, y_c, x_\omega, z_\omega). \quad (5.49)$$

In these sub-problems, the recourse variables are determined by rigorous equation-based optimization. This method has been implemented in the superstructure optimization framework FSOpt [201]. FSOpt provides an editor for the description of superstructures of chemical processes in the input language format Modelica. FSOpt translates the Modelica model to an intermediate object code that is an in-memory representation of the MINLP optimization problem. For each investigated set of DDoF, FSOpt transforms these subproblems into a formulation that is passed to the solver IPOPT [212].

In the following paragraphs, we show the results of the application of the superstructure optimization under uncertainties by FSOpt to the case study of the homogeneously catalyzed hydroformylation of 1-dodecene in a thermomorphic solvent system. Details about the process can be found in Section 4.1.3.8. The kinetic model is described in Section 3.2 (eqs. (3.61)–(3.63), (3.65), (3.67)).

The considered superstructure is shown in Figure 5.60. Table 5.9 contains all information of the resulting DoFs. There are five design variables and 11 operational degrees of freedom that can be used to counteract the effect of the uncertainties, i.e., as recourse variables. The eight parametric model uncertainties of the case study are described in Table 5.10. The ranges of the parameters resulted from lab experiments. Table 5.11 lists the values of the uncertain parameters for the nominal case and for 15 scenarios that were obtained by latin-hypercube sampling of the parameter space.

To illustrate the benefit of the adaptation of the operational degrees of freedom to the scenarios, we first present the results for a fixed design. In this design, there is one

Table 5.10: Uncertain parameters used in the case study.

UNCERTAINTY	DESCRIPTION	UNIT	MIN	MAX
H_{A,H_2}	Henry coefficient A of hydrogen	$MPa \cdot m^3/kmol$	819.00	1001.00
H_{B,H_2}	Henry coefficient B of hydrogen	J/mol/K	9155.70	11190.30
$H_{A,CO}$	Henry coefficient A of CO	$MPa \cdot m^3/kmol$	21950.00	39050.00
$H_{B,CO}$	Henry coefficient B of CO	J/mol/K	20677.50	25272.50
$U_{RR,1}$	Factor for reaction rate 1	[-]	0.90	1.10
$U_{RR,2}$	Factor for reaction rate 2	[-]	0.90	1.10
K_{Hex}	Heat-transfer coefficient	$kW/m^2/K$	540.00	660.00
$E_{Murphree}$	Murphree tray efficiency	[-]	0.75	0.85

Table 5.11: Scenarios considered in the case study.

SCENARIO	H_{A,H_2}	H_{B,H_2}	$H_{A,CO}$	$H_{B,CO}$	$U_{RR,1}$	$U_{RR,2}$	K_{Hex}	$E_{Murphree}$
S1	910.00	10173.00	35500.00	22975.00	1.00	1.00	600.00	0.80
S2	928.20	10783.38	39050.00	24047.17	1.05	0.98	540.00	0.76
S3	1001.00	9698.26	33370.00	22515.50	0.98	0.99	652.00	0.76
S4	964.60	9833.90	38103.33	21290.17	0.94	1.06	596.00	0.75
S5	988.87	9155.70	32896.67	23128.17	0.90	1.09	572.00	0.78
S6	819.00	10919.02	35736.67	25272.50	1.01	0.93	628.00	0.78
S7	952.47	10240.82	35263.33	23740.83	1.07	1.05	564.00	0.80
S8	843.27	10376.46	36210.00	24966.17	0.95	0.91	548.00	0.85
S9	867.53	9969.54	32423.33	20677.50	1.09	1.02	644.00	0.84
S10	855.40	11190.30	33843.33	21596.50	1.06	1.03	612.00	0.81
S11	903.93	10512.10	34790.00	22209.17	0.93	1.10	556.00	0.83
S12	940.33	10647.74	31950.00	20983.83	0.91	1.07	620.00	0.82
S13	831.13	10105.18	37630.00	22821.83	1.02	0.97	636.00	0.80
S14	891.80	9291.34	36683.33	24353.50	0.99	1.01	588.00	0.77
S15	879.67	9562.62	38576.67	24659.83	1.03	0.95	580.00	0.84
S16	976.73	9426.98	34316.67	21902.83	1.10	0.90	660.00	0.79

CSTR with a volume of 45 m^3 , a heat exchanger area of 25 m^2 , and the distillation column has 20 theoretical stages, with the feed on the 10th tray. We compare two cases: In the first case, only the feed rates of raw materials, solvents, and catalysts are adapted to the scenarios. In the full case, the operational parameters of the distillation column and the reactor were also adapted. Figure 5.61 shows the cost distribution for both cases on the left side and the normalized distribution of the recourse variables on the right side. In the first case, the disturbances introduced by the uncertainties are compensated by increasing the purge of the solvent recycle and by increasing the makeup streams of decane and DMF. This leads to large variations of the costs for the solvent, the catalyst, and the ligand.

In the full case, all parameters are adapted to the scenarios (full recourse). The optimal values of the partial pressures of the synthesis gases are adapted, depending on the changes in the uncertain reaction rates. In the distillation column, the reflux ratio is adapted to achieve a better separation of the incoming stream. Therefore, the purge and the make-up streams are considerably lower in the full recourse case, and there is nearly no variation in the optimal amount of the feed of ligand anymore. This leads to lower costs for the catalyst and ligand, and also to smaller variations of these costs. Without material costs, the annualized production costs for the most expensive scenario of the first case are 42.51 million Euro per year. The costs of the most expensive scenario of the full case are 38.5 million Euro per year, a reduction of 10 percent of the influenceable costs.

These adaptations of the operational degrees of freedom, in reality can be realized by the application of real-time optimization with uncertain process models, as discussed in Section 5.4.2.

The superstructure of the case study in Figure 5.60 was also optimized using FSOpt. The applied evolutionary algorithm uses κ -selection, with the maximum age of an individual of $\kappa = 10$ and to a generation size of 10. Infeasible individuals suffer a large penalty and, therefore, do not pass the survivor selection. The optimization was performed five times and terminated after 20 generations in each run. In each iteration, the local solver was invoked 150 times. The local solver calls contribute 99.99% percent of the total computational time.

Figure 5.62 (left) shows the dependency of the expected production cost on the yield of n-tridecanal with respect to 1-dodecene. Two clusters exist that correspond to a design with one reactor and to a design with a reactor cascade. The spreads of the clusters result from the explored values of the other design variables. In both clusters, there is a minimal cost at a specific yield and an increase of the yield results in an increase of the production cost. For larger values, the cost of energy, catalyst, and investments grow faster than the reduction of the cost of materials.

In Figure 5.62 (right), the production cost for the best design in each scenario is shown. The blue dots represent a design with one reactor and the red dots, a design with a reactor cascade. The scenarios are ordered by their production cost and it is

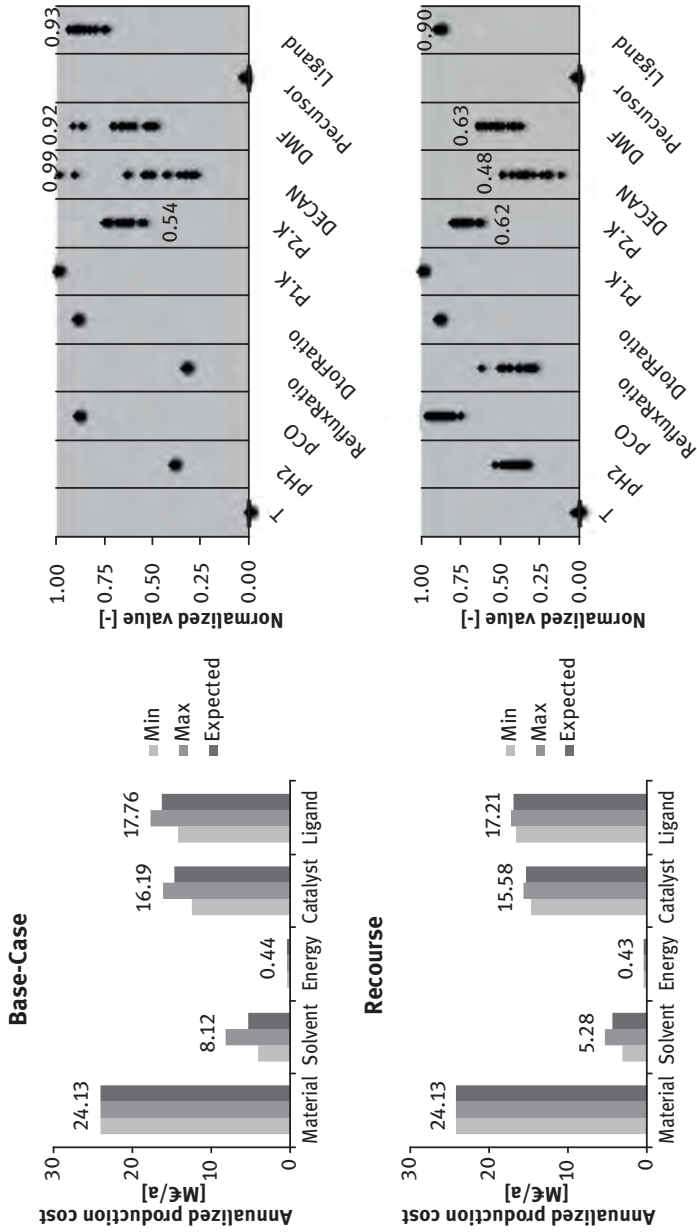


Figure 5.61: Cost and recourse variable distribution for two cases [203]. The variables are introduced in Table 5.9.

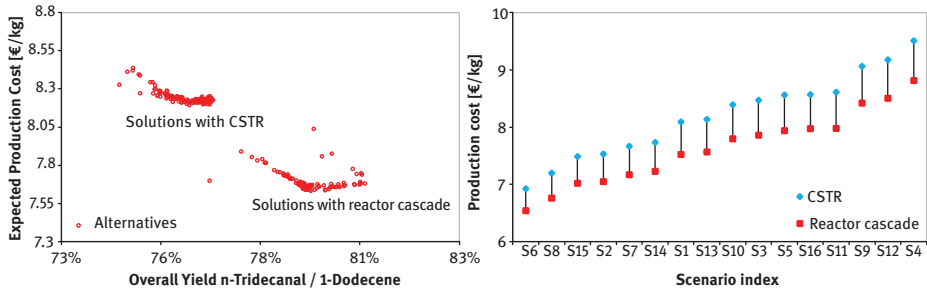


Figure 5.62: Solutions clustered according to the presence of a single CSTR or a reactor cascade (left) and best-found solutions for the single reactor and the cascade ordered by scenarios (right) [203].

visible that a cascade of reactors outperforms a single vessel in all cases; so this design decision can be fixed, as it is robust against the considered uncertainties.

The optimization framework FSOpt provides support for the difficult problem of superstructure optimization in the presence of uncertainties. The key idea of the approach is to model the operational degrees of freedom that can be adapted to the realization of the uncertainties (i.e., the real behavior of the process) after the plant has been built as so-called recourse variables in a two-stage optimization under uncertainty. It enables the design engineers to make decisions about different design alternatives in the presence of uncertain model parameters, taking into account that during operation, there is a potential to counteract the uncertainty. If there is no preferable design alternative, i.e., for some scenarios, design alternative A is preferable, and for other scenarios, design alternative B, it must be considered to first reduce the range of the uncertainty of some critical model parameters before returning to the design optimization. This is discussed in more detail in Section 6.5.

In this section, it was shown how the superstructure optimization under uncertainties can be used in the early stage of process development. Non-promising designs can be excluded early and it can also be analyzed which parameters are critical and must be determined more accurately. The operational flexibility of the process design is taken into account explicitly. When a miniplant, or pilot plant, or a full-scale production plant has been built to investigate or implement the chosen design, the operational degrees of freedom can be adapted to the real behavior. How to do this optimally even when the available process models are not accurate is discussed in Section 5.4.2.

5.4 Model-Based Process Monitoring and Operation

5.4.1 Online Monitoring and Online Optimization in the Development of Multiphase Processes

Sebastian Engell, Erik Esche

No matter how much effort is put into modeling, model-based design, and experimental validation of chemical production processes, their operation on industrial scale always requires continuous monitoring and control to counteract the influence of disturbances and changes in the processes. Nowadays, to a large extent – but not exclusively – this is performed by automatic, computer-based process control systems. Feedback control establishes the desired processing conditions (temperatures, pressures, flowrates, and filling levels) to operate production processes in a stable and reproducible manner as the basis for constant product quality and an economically and environmentally optimal operation.

In the last decades, model-based control schemes, in particular, model-predictive controllers have been increasingly applied in industrial production because they can handle many manipulated and controlled variables that interact with each other simultaneously, and they can also cope with nonlinear behavior much better than traditional controllers. A more recent trend is to not only maintain the controlled variables (e.g., temperatures, pressures, concentrations) at their set-points but to also use feedback control for optimizing the performance of processes online with respect to economic or economically motivated criteria, e.g., cost or energy efficiency [34].

A major challenge for controlling chemical processing plants is the fact that while basic variables, such as temperatures, pressures, flow-rates, levels, and pH values can be measured online relatively cheaply and reliably, the information about important variables of relevance for the stability and performance of the processes, e.g. concentrations of streams and temporal or spatial profiles of concentrations and temperatures inside large pieces of equipment, is scarce, if at all available. Such measurements are expensive, require frequent maintenance, and are often based on collecting samples and analyzing them, and, therefore, are usually only available at low frequencies, from minutes to hours. To provide information on these variables in between the sampling points or if they are not measured online at all, the so-called state estimation techniques can be used that employ dynamic models and infer from measurable quantities on the variables that are not measured, exploiting their mathematical relationship that is defined by the process model [3]. This technology can also be used to estimate process parameters, such as reaction rates or heat transfer coefficients during operation.

While the necessity and the potential of online monitoring and control in industrial production can hardly be questioned, it may not be immediately clear what the role of these techniques can be during process development. This is illustrated in

the following sections wherein the contribution of techniques for advanced online monitoring, control and optimization to the development of multiphase processes is demonstrated using several examples.

Due to their inherent complexity, the development of multiphase processes requires extensive experimental work, from lab scale to select and validate phase systems, catalysts, unit operations, and process windows, to the miniplant and pilot-scale, where the whole process including separation, recycling, and catalyst replenishing is tested over longer periods and sets of promising operational parameters are determined. To reduce the time and effort associated with the experiments and to provide reliable information and reproducible data, such plants also need to be controlled well; so a suitable monitoring and control structure has to be in place.

When a basic instrumentation and control system is in place, the potential of advanced monitoring and online optimization methods can be exploited to speed up the development and the experimental work. As mentioned in the beginning, models of multiphase processes are inevitably inaccurate, and it is of interest to determine the full potential of the real processes during the experimental work and to find the experimental conditions at which the best performance is observed with respect to their economic evaluation. While this can be done to some extent by trial and error by the staff at the mini plant or pilot plant, advanced techniques offer the potential to perform this task in a more systematic and faster manner. By iterative real-time optimization, as described exemplarily in Section 5.4.2 for the hydroformylation of 1-dodecene in a TMS phase system, the stationary operating point of a mini plant or pilot plant can be automatically adapted to realize the best possible operation of the real plant, in contrast to just implementing the nominally optimal operating point that was computed for a more or less reliable process model.

State estimation techniques provide insight into the behavior of the plant and its reaction to disturbances that inevitably happen during experimental work. They enable the integration of the information from various sources, to interpolate between infrequent measurements, and to provide the experimentalists with a full picture of what is going on in the mini plant or pilot plant at any point in time. A tailored solution for hydroformylation and reductive amination processes in microemulsion systems that are particularly sensitive to the correct choice of the operating conditions and need to be closely monitored is described in Section 5.4.3.

Processes with recycles often need a long period of time to reach their steady states, which means long periods of operation in which the plant is not operating at the designed conditions. Dynamic optimization of the start-up trajectories can significantly reduce the time to reach the desired steady states, saving large amounts of time and manpower, as described in Section 5.4.4. Finally, model-predictive control can be used to ensure the continuous operation of complex mini plants, and to implement the transitions between different set-points, while meeting the process constraints reliably and fast. This is demonstrated for a hydroformylation process

in an MES, in Section 5.4.4. This control strategy was employed in the successful experimental work reported in Section 4.2.

In summary, advanced online monitoring and optimization is an important tool to speed up process development and to obtain more information more reliably and faster during experimental trials in miniplant and pilot plant scale. They are indispensable in pilot plant operations whenever the speed or complexity of a process is beyond human decision-making capabilities [162]. Moreover, once developed and tested at the miniplant or pilot plant scale, the monitoring and control solutions presented in the following sections can be transferred easily to the industrial scale, to ensure process stability, the satisfaction of environmental constraints, and an economic and safe operation with only few interventions by the operating staff.

5.4.2 Iterative Real-Time Optimization Applied to a Hydroformylation Process on Miniplant Scale

Anwesh Reddy Gottu Mukkula, Reinaldo Hernandez, Sebastian Engell

In this section, we discuss the application of iterative real-time optimization, i.e., the online optimization of the operating conditions, to a miniplant for the hydroformylation of 1-dodecene in a TMS system. We demonstrate that the miniplant can be driven to optimal operating conditions despite the fact that the model that is used in the optimization is inaccurate. This is achieved by the combination of information that is obtained from online measurements with a model-based optimization scheme. By such an investigation on the miniplant scale, the true potential of a designed process can be evaluated under realistic conditions, in contrast to purely computer-based studies that have to rely on the assumption of an exact description of the real process by a model. Using this approach, the results of the optimization of the design under uncertainty, as discussed in Section 5.3.3, can be validated experimentally: the operating conditions (second-stage decisions or recourse variables) are adapted to the real behavior or the process while the design parameters (first-stage or here-and-now decisions) are fixed.

5.4.2.1 Real-Time Optimization and Approaches to Handle the Plant-Model Mismatch

The operating conditions of chemical production processes have to be chosen such that the processes are operated safely within their physical limits, the environmental regulations are satisfied, and the desired product quality is maintained. Furthermore, to compete in the market, it is desired to operate economically optimally, e.g., to minimize the production cost or maximize the difference between revenue

and cost, taking into account customer satisfaction such as, e.g., meeting deadlines for delivery. The optimal degrees of freedom for a process can be computed by formulating and solving an optimization problem, where the goal is to maximize or to minimize an objective function, taking into account the constraints, for example, the process, safety, quality, and environmental limitations. Maximization of product yield, minimization of production cost, etc. under changing feed and market conditions are examples of the goals of such an optimization.

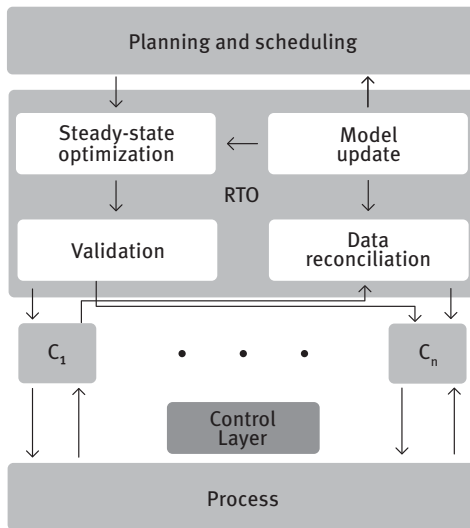


Figure 5.63: Hierarchical control structure with real-time optimization (RTO) [34]. $C_1 \dots C_n$ denote the local controllers.

Real-time optimization (RTO) denotes a model-based upper-layer optimization of the steady-state operating conditions of industrial processes, based on rigorous models to improve the profitability of the process, taking into account safety constraints, product quality specifications, and process limitations. It acts as a bridge between production planning and scheduling, and the regulatory control of the process. RTO has become a standard approach to improve the efficiency of industrial processes, in particular of large-scale processes in refineries and petrochemical plants [29]. Figure 5.63 illustrates the general structure of an RTO system. The parameters for the formulation of the optimization problem in RTO, e.g., the cost of raw materials, prices of the products, availability of raw materials and the demand for the products, and the minimum product quality requirements, are provided by the planning and scheduling layer. Within the RTO layer, usually a first principles-based steady-state process model is used. Steady-state measurements from the process are reconciled to reduce the measurement errors and to update key model parameters to ensure the validity of the nominal model. The updated nominal model, along with the information from the planning and scheduling layer, is used to formulate and solve a model-based optimization problem. The resulting set-points of the plant are validated

by the operating staff before they are passed to the control layer for implementation. In the control layer, conventional controllers or model-predictive controllers (MPC) perform the necessary moves to drive the process to the set-points computed by the RTO layer. After the process has stabilized in the new stationary point, the optimization is performed again, typically with sampling times in the order of magnitude of hours.

The performance of RTO schemes is dependent on the accuracy of the process model, and developing an accurate process model is expensive and time-consuming. Usually, despite the effort invested, the behavior of the process will deviate from the nominal model predictions due to differences in the model structure (because of the simplifications made in the modeling process) and due to parametric uncertainties. As a consequence, the optimum computed by solving the model-based optimization problem using a structurally or parametrically inaccurate nominal model will usually not match with the real process optimum, and in some cases even be infeasible because some constraints are not satisfied. It is, therefore, important to address model uncertainties, both structural and parametric, in the identification of the optimal operational degrees of freedom for a process.

The two-phase approach [21, 80] addresses the plant-model mismatch problem by iteratively updating some key model parameters using the available measurements from the process, as depicted in Figure 5.63. This approach, however, can only handle parametric uncertainties of the nominal model, but not cope with structural deficiencies of the model unless the adapted model is a reasonable local approximation.

Alternative RTO approaches to handle the plant-model mismatch are to adapt the model-based optimization problem by suitable correction terms (the modifier adaptation approach discussed in detail below) or to track optimality conditions by feedback control (direct input adaptation). In the direct input adaptation methods, e.g., self-optimizing control [199], tracking of necessary conditions of optimality [82], and extremum-seeking control [111], the RTO problem is transformed into a control problem and the optimization problem is solved indirectly online. An extensive survey of the existing RTO methods is reported in [138].

RTO, up to now, has been applied almost exclusively to large-scale petrochemical processes where accurate process models are available due to decades of investigations, and the large production volumes and often narrow margins provide a strong economic incentive. The advantage of schemes that can handle a significant mismatch between the model of the process and its true behavior, in particular of modifier adaptation schemes, is that they require less modeling effort and can still drive the process to its true optimum. Multi-phase processes are examples of processes that are difficult to model, and at the same time, the production volumes of long-chain products are orders of magnitude below those of the basic large-scale petrochemical processes. The issue of unmodeled variations of the process becomes even bigger when renewable resources are fed to the process due to the presence of many components and the varying composition of the feed stream.

In the context of process development, such techniques can play two roles: First, their application helps to explore the true potential of the processes when they are investigated on the miniplant or pilot plant scale, leading to a better characterization of the attainable performance under realistic conditions. This is shown below for the example of the homogeneously catalyzed hydroformylation of 1-dodecene in a thermomorphic solvent mixture realized in a miniplant. Second, referring to the optimization of processes in the early design stage as discussed in Section 5.3.3, the design under uncertainty should take into account the potential of adapting the operating conditions to improve the performance of the process when information about the real behavior of the plant is available. This adaptation can be realized in a systematic manner by using iterative RTO methods, in contrast to manual adaptation, which will only realize a certain fraction of the possible improvement.

In the following subsections, we will first briefly discuss the general problem of identifying a process optimum in the absence of an accurate process model and present the basic idea of modifier adaptation. Then, we introduce the MAWQA method proposed in [48], where the gradients for the formulation of the modifier adaptation problem are computed from fitting quadratic approximations to a selected set of observations. We then present the experimental results of applying MAWQA to a miniplant that realizes the hydroformylation of 1-dodecene in a TMS system, followed by conclusions and an outline of further developments.

5.4.2.2 Iterative Real-Time Optimization by Modifier Adaptation

Consider that the true mapping (mathematical model) of the operational degrees of freedom and the measured variables that enter into the cost function and the operating constraints of a continuous process is represented as:

$$\mathbf{y}_p = \mathbf{f}_p(\mathbf{u}), \quad (5.50)$$

where \mathbf{y}_p represents a vector of n_y measured variables of the process, \mathbf{u} represents a vector of n_u operational degrees of freedom, and the function $\mathbf{f}_p: n_u \rightarrow n_y$ is the true description of the underlying process. Our goal is to maximize an objective function, $J(\mathbf{y}_p, \mathbf{u})$, taking into account the process, safety, and quality constraints represented as $\mathbf{G}(\mathbf{y}_p, \mathbf{u})$. The optimal operational degrees of freedom of the process, \mathbf{u}_p^* , which must lie between the lower and upper bounds \mathbf{u}^L and \mathbf{u}^U can be (theoretically) computed by solving the following optimization problem:

$$\mathbf{u}_p^* = \max J(\mathbf{y}_p, \mathbf{u}) \quad (5.51a)$$

$$\text{s.t. } \mathbf{y}_p = \mathbf{f}_p(\mathbf{u}) \quad (5.51b)$$

$$\mathbf{G}(\mathbf{y}_p, \mathbf{u}) \leq 0 \quad (5.51c)$$

$$\mathbf{u}^L \leq \mathbf{u} \leq \mathbf{u}^U. \quad (5.51d)$$

However, the real plant mapping, \mathbf{f}_p , is not known but only a more or less accurate nominal model

$$\mathbf{y}_m = \mathbf{f}_m(\mathbf{u}) \quad (5.52)$$

is available. This model has to be used for the computation of the process optimum. In the nominal model, the vector, \mathbf{y}_m , represents the predictions of the n_y measured variables of the process by the nominal model. Using the nominal model, the nominal optimal operational degrees of freedom for the process, \mathbf{u}_m^* , can be computed by solving the following model-based optimization problem:

$$\mathbf{u}_m^* = \max_{\mathbf{u}} J(\mathbf{y}_m, \mathbf{u}) \quad (5.53a)$$

$$\text{s.t. } \mathbf{y}_m = \mathbf{f}_m(\mathbf{u}) \quad (5.53b)$$

$$\mathbf{G}(\mathbf{y}_m, \mathbf{u}) \leq 0 \quad (5.53c)$$

$$\mathbf{u}^L \leq \mathbf{u} \leq \mathbf{u}^U \quad (5.53d)$$

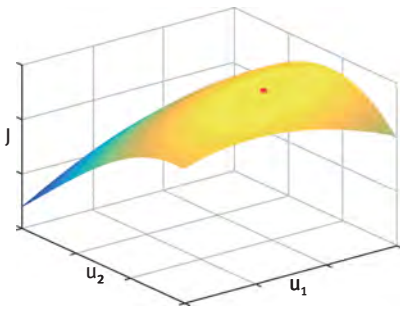


Figure 5.64: Illustration of the objective function of the nominal model and its optimum.

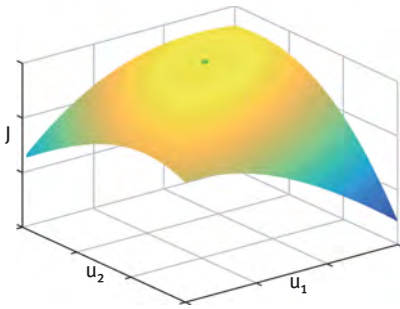


Figure 5.65: Illustration of the objective function of the real process and its optimum.

Due to the mismatch between the true process model (5.53b) and the nominal model (5.51b), $\mathbf{u}_m^* \neq \mathbf{u}_p^*$. This is illustrated in Figures 5.64 and 5.65. Figure 5.64 shows the objective function that has to be maximized, as computed using a nominal model with two operational degrees of freedom, and the nominal model optimum. Figure 5.65 shows the objective function of the true process and the optimum values of the

operational degrees of freedom. Due to the differences between the behavior of the real process model and the nominal model, the optimum computed using the nominal model-based optimization problem (\mathbf{u}_m^*) significantly differs from the process optimum (\mathbf{u}_p^*). The goal of modifier adaptation is to overcome this discrepancy by an iterative approach in which the plant model is repeatedly modified, based on the information that was gained in the previous optimization or exploration steps.

Modifier Adaptation

The optimum of an optimization problem is defined by the first- and second-order derivatives of the objective and constraint functions (generally referred to as the KKT conditions). At the optimum, the gradient of the Lagrangian of the problem is zero and the (reduced) Hessian is positive. The modifier adaptation method (MA) is an iterative RTO method where the gradients of the objective and of the constraint functions of the nominal model-based optimization problem are updated (modified) iteratively using correction terms called “bias terms” and “gradient correction modifiers”, to match the gradients of the real process and the values of the constraints. From the modified problem, a new model optimum is computed. The corrections (modifiers) are computed from available measurements of the response of the plant, either from the measurements obtained when the previously computed operating points were applied or from so-called probing moves. When the gradient of adapted optimization problem is zero, the gradients of the real process are also zero; so the process has been driven to the true optimum despite the plant-model mismatch.

Figure 5.66 shows a graphical representation of the effect of the gradient correction term in an iteration of modifier adaptation of an example process with one operational degree of freedom and with no constraints. In Figure 5.66, the red curve represents the objective function of the nominal model ($J(\mathbf{y}_m, \mathbf{u})$); the green curve represents the objective function of the true process ($J(\mathbf{y}_p, \mathbf{u})$); and the blue curve represents the modified objective function ($J_{ad}^k(\mathbf{y}_m, \mathbf{u})$), that results from the application of the bias and gradient correction modifiers at \mathbf{u}^k . The difference between $J(\mathbf{y}_m, \mathbf{u})$ and $J(\mathbf{y}_p, \mathbf{u})$ at \mathbf{u}^k is corrected by the bias modifier and the gradient difference between $J(\mathbf{y}_m, \mathbf{u})$ and $J(\mathbf{y}_p, \mathbf{u})$ at \mathbf{u}^k is corrected by the gradient modifier. In this way, the model-based optimization problem is corrected in each iteration, and the iterations converge to the true process optimum, \mathbf{u}_p^* , when the estimation of the gradient is perfect.

The modified objective and constraint functions of the nominal model-based optimization problem in the k^{th} iteration of modifier adaptation are:

$$J_{ad}^k(\mathbf{y}_m, \mathbf{u}) = J(\mathbf{y}_m, \mathbf{u}) + \varepsilon_J^k + \Psi_J^{kT}(\mathbf{u} - \mathbf{u}^k) \quad (5.54a)$$

$$\mathbf{G}_{ad}^k(\mathbf{y}_m, \mathbf{u}) = \mathbf{G}(\mathbf{y}_m, \mathbf{u}) + \varepsilon_G^k + \Psi_G^{kT}(\mathbf{u} - \mathbf{u}^k). \quad (5.54b)$$

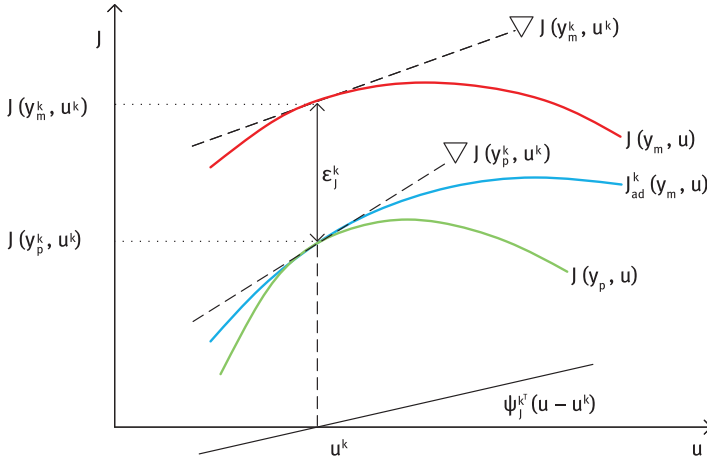


Figure 5.66: Illustration of the effect of the modifiers in modifier adaptation methods [138].

In eq. (5.54), the terms ε_j^k and ε_G^k are the bias modifiers, and Ψ_j^k and Ψ_G^k are the gradient correction modifiers. They are defined as:

$$\varepsilon_j^k := J(\mathbf{y}_p^k, \mathbf{u}^k) - J(\mathbf{y}_m^k, \mathbf{u}^k) \quad (5.55a)$$

$$\varepsilon_G^k := \mathbf{G}(\mathbf{y}_p^k, \mathbf{u}^k) - \mathbf{G}(\mathbf{y}_m^k, \mathbf{u}^k) \quad (5.55b)$$

$$\Psi_j^k := \nabla J(\mathbf{y}_p^k, \mathbf{u}^k) - \nabla J(\mathbf{y}_m^k, \mathbf{u}^k) \quad (5.55c)$$

$$\Psi_G^k := \nabla \mathbf{G}(\mathbf{y}_p^k, \mathbf{u}^k) - \nabla \mathbf{G}(\mathbf{y}_m^k, \mathbf{u}^k). \quad (5.55d)$$

Here, $\nabla J(\mathbf{y}_p^k, \mathbf{u}^k)$ and $\nabla \mathbf{G}(\mathbf{y}_p^k, \mathbf{u}^k)$ represent the gradients of the objective and constraint functions of the real process with respect to \mathbf{u} , evaluated at the operational degrees of freedom for the k^{th} iteration (\mathbf{u}^k). $\nabla J(\mathbf{y}_m^k, \mathbf{u}^k)$ and $\nabla \mathbf{G}(\mathbf{y}_m^k, \mathbf{u}^k)$ represent the gradients of the objective and constraint functions of the model-based optimization problem functions with respect to \mathbf{u} , evaluated at \mathbf{u}^k .

The modified optimization problem in the k^{th} modifier adaptation iteration to compute \mathbf{u}^{k+1} using the adapted objective and constraint functions in eq. (5.54a, b) is:

$$\mathbf{u}^{k+1} := \max_{\mathbf{u}} J_{\text{ad}}^k(\mathbf{y}_m, \mathbf{u}) \quad (5.56a)$$

$$\text{s.t. } \mathbf{y}_m = \mathbf{f}_m(\mathbf{u}) \quad (5.56b)$$

$$\mathbf{G}_{\text{ad}}^k(\mathbf{y}_m, \mathbf{u}) \leq 0 \quad (5.56c)$$

$$\mathbf{u}^L \leq \mathbf{u} \leq \mathbf{u}^U. \quad (5.56d)$$

The implementation of the MA scheme is shown in Figure 5.67. In each iteration of the scheme, first, an input \mathbf{u}^k is applied to the process. Once the process has reached a steady state, the measurements are reconciled to filter measurement noise to obtain \mathbf{y}_p^k . For systems with slow dynamics, a steady state identification method can be used to check if a system has reached a steady state or not. Upon obtaining the steady state measurements for \mathbf{u}^k , the modifiers ε_j^k , ε_G^k , Ψ_j^k , and Ψ_G^k are computed. Then, the cost function and the constraints are modified, as in eq. (5.54a, b), and the modified problem is solved to compute the optimal operational degrees of freedom for the next iteration \mathbf{u}^{k+1} .

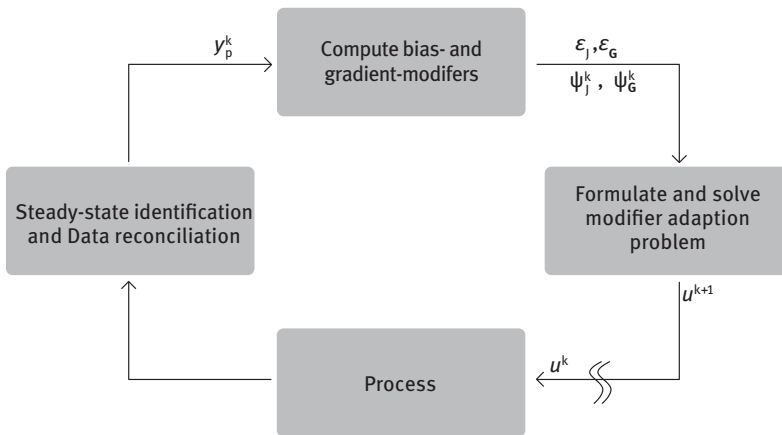


Figure 5.67: Implementation of modifier adaptation.

In Figure 5.68a–d, the evolution of the modified nominal model-based objective function $J_{ad}^k(\mathbf{y}_m, \mathbf{u})$ during the iterations of the modifier adaptation is shown for an example process with two operational degrees of freedom. Figure 5.68a is the surface plot of the objective function of the nominal model and Figure 5.68d is the surface plot of the adapted nominal model objective function upon convergence. It can be noted that the surface plot of the nominal model-based objective function upon convergence (Figure 5.68d) matches closely with the surface plot of the objective function of the real process shown in Figure 5.65. Figure 5.69 illustrates the iterative updates of the optimal operational degrees of freedom, obtained by solving the modifier adaptation problem, from the nominal model optimum (in red) to the real process optimum (in green).

While the modifier adaptation method can handle structural and parametric uncertainty, it is a prerequisite that the Lagrangian of the nominal model-based optimization problem at the process optimum has a positive definite Hessian matrix at the real process optimum, if the goal is to minimize the objective function, and a negative

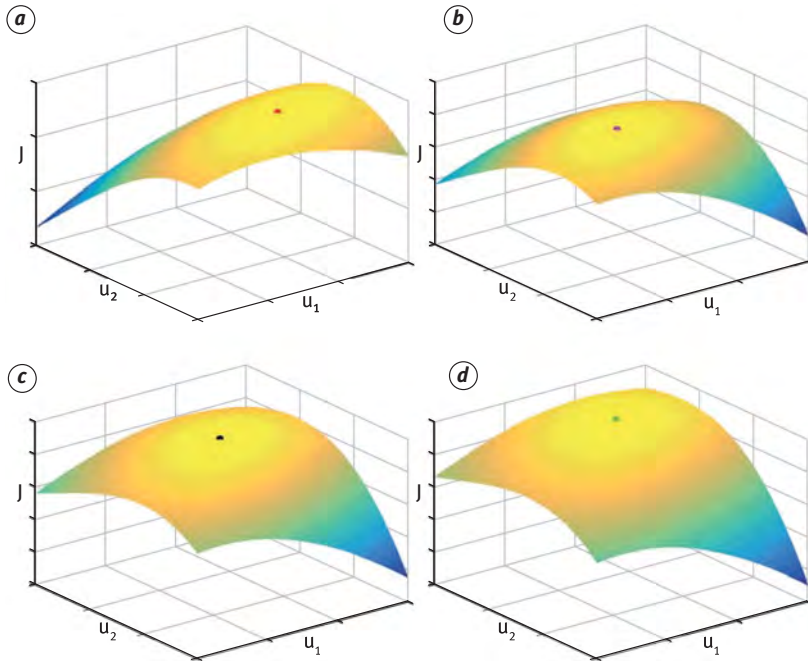


Figure 5.68: Illustration of the adaptation of the objective function of the nominal model by the modifier adaptation scheme from (a) to (d).

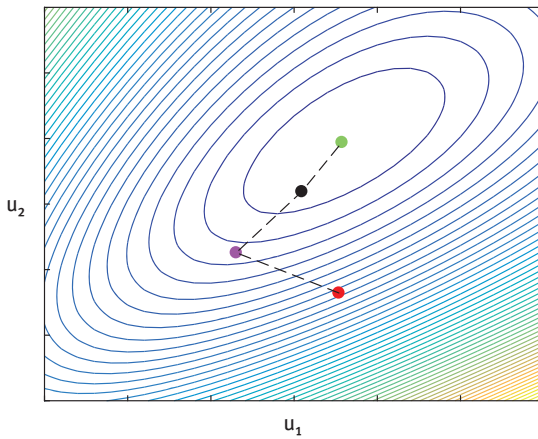


Figure 5.69: Illustration of the evolution of the inputs, u_m^* (red) to u_p^* (green), obtained from modifier adaptation.

definite Hessian, if the goal is to maximize the objective function. This condition is termed model adequacy and should be taken into account in MA [2, 55].

The main challenge in the implementation of the modifier adaptation method is to compute the gradient correction modifiers, Ψ_j^k and Ψ_G^k , for which the gradients of the plant objective function, $\nabla J(\mathbf{y}_p^k, \mathbf{u}^k)$, and of the plant constraint functions, $\nabla G(\mathbf{y}_p^k, \mathbf{u}^k)$, are required. The performance of the modifier adaptation scheme depends strongly on the accuracy of the estimated process gradients. As the process gradients usually cannot be measured, they have to be computed from the available process measurements. In the literature, several methods, e.g., finite differences and Broyden's formula are proposed to approximate the process gradients. However, these are sensitive to process noise. Recently, it was proposed to use quadratic approximation functions, along with elements from derivative-free optimization (DFO), for a robust and efficient estimation of the process gradients [48], leading to the MAWQA (modifier adaptation with quadratic approximation) scheme. The steady state process measurements obtained for various set-points of the process are used to fit quadratic approximation functions to the objective and the constraint functions. Then, the process gradients at \mathbf{u}^k ($\nabla J(\mathbf{y}_p^k, \mathbf{u}^k)$, $\nabla G(\mathbf{y}_p^k, \mathbf{u}^k)$) can be computed analytically by differentiating the fitted quadratic functions and evaluating them at \mathbf{u}^k . It was illustrated in [47] that the quadratic approximation is a more robust gradient approximation method in the presence of measurement noise when compared to other methods.

5.4.2.3 Application of Real-Time Optimization with Modifier Adaptation to the Hydroformylation of 1-Dodecene in a TMS-system on Miniplant Scale

The hydroformylation of 1-dodecene to produce tridecenal is considered here for the demonstration of the application of iterative RTO to a complex process that is difficult to model precisely due to its multiphase nature. The reaction is catalyzed using the precursor, (acetylaceto-nato)-dicarbonylrhodium(I) $\text{Rh}(\text{acac})(\text{CO})_2$, and the ligand Biphephos. It ensures high selectivity towards the linear isomer [211]. Further details about the hydroformylation reaction can be found in Section 4.1.3.8. Efficient recovery of the catalyst is necessary due to its high costs; therefore, a thermomorphic multiphase system (TMS) system is used. The TMS system is based on the principle of a temperature-dependent miscibility gap between the polar and nonpolar phases. A homogenous liquid phase is obtained at an elevated temperature of the mixture, and a decrease in the temperature leads to splitting the mixture into two phases, i.e., polar and nonpolar. See Section 2.1 for further details about the TMS system. In the reactor, the temperature in the reactor is maintained at a high value such that the reaction mixture is in a single phase to overcome the mass transfer limitations. Thereafter, the temperature of the mixture is reduced to separate the reaction mixture into two phases, a nonpolar phase containing the product and a polar phase containing the expensive catalyst, which is recycled to the reactor.

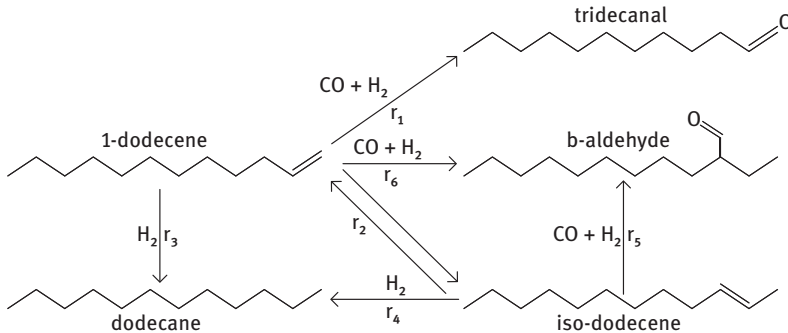


Figure 5.70: Reaction network of the hydroformylation process of 1-dodecene to produce tridecanal (adapted from [140]).

The full reaction scheme of the hydroformylation of 1-dodecene is shown in Figure 5.70. The strategy for deriving the reaction kinetics is discussed in detail in Section 3.2. In the reaction network, r_1 is the main reaction (hydroformylation), where 1-dodecene reacts with the dissolved CO and H_2 in the liquid phase of the reactor to produce tridecanal. In addition to the main reaction (r_1), several side reactions take place. A pseudo species of 1-dodecene, iso-dodecene is formed (reaction r_2). Hydrogenation of the reactant 1-dodecene and the formed pseudo species iso-dodecene react with H_2 (reaction r_3 and reaction r_4) to form dodecane. Additionally, the reactant 1-dodecene and the formed pseudo species iso-dodecene react with CO and H_2 (hydroformylation) to produce a b-aldehyde of tridecanal, i.e. 2-methyldodecanal (reaction r_5 and reaction r_6). Solvents, N,N-dimethylformamide (DMF), and n-decane, with a composition of 1:1 wt.%, are used to ensure high conversion and selectivity with minimum catalyst leaching [15]. The conversion of the reactant into the desired product, tridecanal, is influenced by the reactor temperature, reactor pressure, and the ratio of CO to H_2 in the gas fed to the reactor.

Iterative RTO with modifier adaptation is demonstrated for the realization of this process in a miniplant. The process flow diagram of the hydroformylation process is shown in Figure 5.71. The continuous-stirred tank reactor (B3) with a liquid holdup capacity of 330 mL is fed with a mixture of reactant 1-dodecene and solvent n-decane from the feed tank (B1), a mixture of the catalyst and solvent DMF from the feed tank (B2), CO gas, H_2 gas, and the recycled stream from the decanter. The temperature in the reactor is maintained by the heat bath WT1, by pumping heated silicone oil through the reactor jacket. The pressure in the reactor is controlled by feeding in high-pressure CO and H_2 gases in the desired ratio. It is desired to maintain the reactor temperature such that the liquid-phase components in the reactor are in a single phase to overcome the mass transfer limitations between the reaction components in the polar and the nonpolar phases. The reaction mixture from the outlet of the reactor is then passed to the decanter (B4), through the heat exchanger

WT3, where it is cooled down. In the decanter, the phase separation of the liquid into the polar and nonpolar phases happens due to the reduced temperature. The temperature in the decanter is maintained by circulating cooled glycol (WT2) through the jacket of the decanter. The liquid level in the decanter is maintained constant by regulating the flowrates of the recycle stream (polar phase), and of the product stream (nonpolar phase). The nonpolar stream from the decanter is then passed to the product tank via a flash tank (B5), where the pressure is reduced to atmospheric pressure. The nonpolar phase in the decanter is analyzed by gas chromatography.

The mathematical model of the process takes into account the following elements [68]:

a) Reactor model:

- material balance for the components in the liquid phase of the reactor
- material balance for the components in the gas phase of the reactor
- reaction kinetics [67, 99] (Section 3.2)
- mass transfer of CO and H₂ from the gas phase to the liquid phase in the reactor (Section 3.3.3)
- equilibrium between the active state and the inactive states of the catalyst [67]

b) Decanter model:

- material balance for the components in the polar and non-polar liquid phases of the decanter [14, 200]
- material balance for the components in the gas phase of the decanter.

The developed mathematical model was validated by comparing the model predictions with experimental data [32, 221].

The goal is to maximize the yield of the product, tridecanal, in the product stream of the miniplant shown in Figure 5.72 by manipulating the reactor temperature (T_R) and the molar fraction of CO in the gas fed to the reactor (y_{CO}) (operational degrees of freedom). The objective function of the optimization problem is the product yield, defined according to:

$$Y = \frac{w_{\text{tridecanal, product}} \dot{m}_{\text{product}} MW_{1-\text{dodecene}}}{w_{1-\text{dodecene, feed}} \dot{m}_{\text{feed}} MW_{\text{tridecanal}}}, \quad (5.57)$$

where $w_{\text{tridecanal, product}}$ and $w_{1-\text{dodecene, feed}}$ are the weight fractions of the desired tridecanal in the product stream and 1-dodecene in the fresh feed fed into the reactor. \dot{m}_{product} and \dot{m}_{feed} represent the mass flow rate of the product and the fresh feed streams. $MW_{\text{tridecanal}}$ and $MW_{1-\text{dodecene}}$ represent the molecular weights of the components, tridecanal and 1-dodecene. The optimization problem to identify the optimum operational degrees of freedom for the hydroformylation process is formulated as:

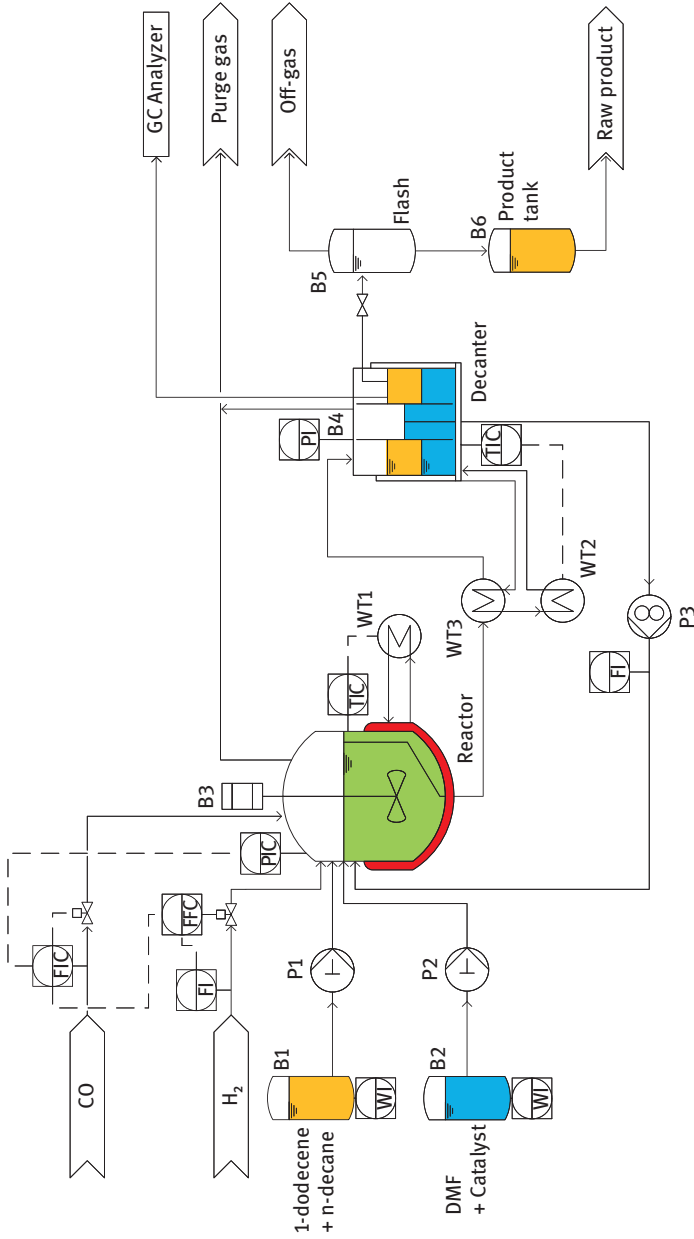


Figure 5.71: Process flow diagram of the hydroformylation process.

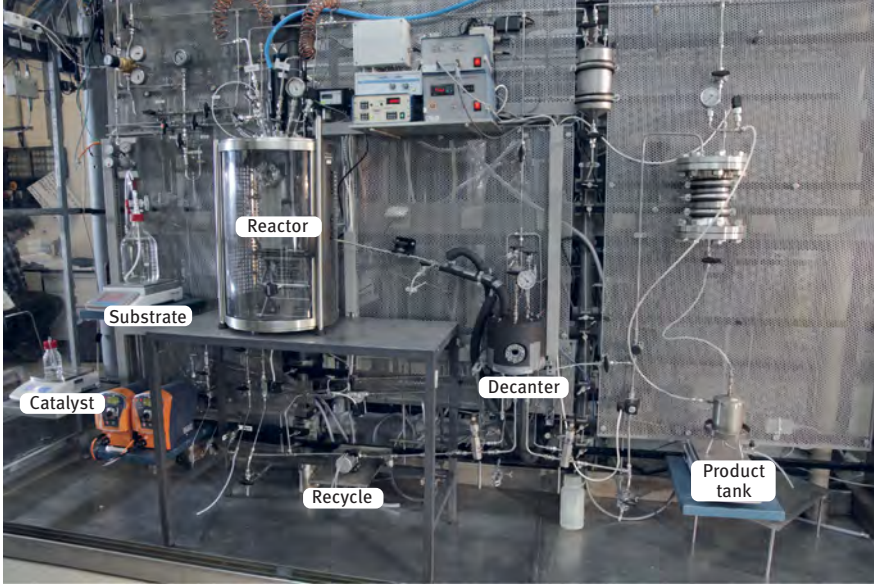


Figure 5.72: Miniplant setup for the hydroformylation process [68, 222].

$$\mathbf{u}^* = \max_{\mathbf{u}} Y \quad (5.58a)$$

$$\text{s.t. } \mathbf{H}(\mathbf{u}) = 0 \quad (5.58b)$$

$$\mathbf{u}^L \leq \mathbf{u} \leq \mathbf{u}^U, \quad (5.58c)$$

where $\mathbf{H}(\mathbf{u}) = 0$ represents the steady state model equations of the process, and $\mathbf{u}^L, \mathbf{u}^U$ represent the lower and upper bounds for the operational degrees of freedom. To illustrate the performance of the modifier adaptation scheme, structural and parametric plant-model mismatches are introduced. As a parametric mismatch, the value of the Henry coefficient used for computing the mass transfer of CO and H₂ from the gas phase to the liquid phase in the reactor is reduced by 50%. Simplifications are also made in computing the equilibrium between the active and inactive states of the catalyst, which leads to a structural mismatch. The equations of the nominal model are stated below:

1. Material balance for the liquid components in the liquid phase of the reactor:

$$\frac{dn_{i, \text{liq}}}{dt} = \dot{V}_{\text{in}} C_{i, \text{in}} - \dot{V}_{\text{out}} C_{i, \text{out}} + m_{\text{cat}} \sum_{l=1}^6 v_{i, l} r_l, \quad (5.59)$$

where i denotes the liquid components DMF, n-decane, and 1-dodecene. $n_{i, \text{liq}}$ represents the number of moles of the i^{th} component in the liquid phase of the reactor, and $\dot{V}_{\text{in}}, \dot{V}_{\text{out}}$ represent the volumetric flowrates at the reactor inlet and outlet. m_{cat} is the

mass of active catalyst in the reactor and $v_{i,1}$, r_1 are the molar coefficients and the reaction rates of the i^{th} component in reactions r_1 to r_1 (see Figure 5.70).

2. Material balance for the gas components CO and H₂ in the liquid phase of the reactor:

$$\frac{dn_{j,\text{liq}}}{dt} = V_{R,\text{liq}}J_j a - \dot{V}_{\text{out}}C_{j,\text{out}} + m_{\text{cat}} \sum_{l=1}^5 v_{j,1}r_l \quad (5.60)$$

where j denotes the gas components, J_j is the molar flux of the gas components into the liquid, and a is the specific G/L surface area in the reactor. $V_{R,\text{liq}}$ is the liquid volume in the reactor.

3. Material balance of the gas components CO and H₂ in the gas phase of the reactor:

$$\frac{dn_{j,\text{gas}}}{dt} = \dot{n}_{j,\text{in}} - V_{R,\text{liq}}J_j a, \quad (5.61)$$

where $\dot{n}_{j,\text{in}}$ is the molar inflow of the gas component into the reactor.

4. The rate equations for the reaction scheme are given as:

$$\begin{aligned} r_1 &= \frac{k_1 C_{1-\text{dodecene}} C_{\text{CO}} C_{\text{H}_2}}{1 + K_{1,1} C_{1-\text{dodecene}} + K_{1,2} C_{\text{tridecanal}} + K_{1,3} C_{\text{H}_2}} \\ r_2 &= \frac{k_2 \left(C_{1-\text{dodecene}} - \frac{C_{\text{iso-dodecene}}}{K_{e,2}} \right)}{1 + K_{2,1} C_{1-\text{dodecene}} + K_{2,2} C_{\text{iso-dodecene}}} \\ r_3 &= \frac{k_3 \left(C_{1-\text{dodecene}} C_{\text{H}_2} - \frac{C_{1-\text{dodecene}}}{K_{e,3}} \right)}{1 + K_{3,1} C_{1-\text{dodecene}} + K_{3,2} C_{\text{dodecane}} + K_{3,3} C_{\text{H}_2}} \\ r_4 &= k_4 C_{\text{iso-dodecene}} C_{\text{H}_2} \\ r_5 &= k_5 C_{\text{iso-dodecene}} C_{\text{H}_2} C_{\text{CO}} \\ r_6 &= k_6 C_{1-\text{dodecene}} C_{\text{H}_2} C_{\text{CO}}, \end{aligned} \quad (5.62)$$

where $K_{1,1}$, $K_{1,2}$, $K_{1,3}$, $K_{2,1}$, $K_{2,2}$, $K_{2,3}$, $K_{3,1}$, $K_{3,2}$, and $K_{3,3}$ are equilibrium constants. The rate constants, k_1 to k_6 , are computed according to the Arrhenius law

$$k_r = k_{r,0} \exp\left(\frac{-E_i}{R} \left(\frac{1}{T_{\text{reactor}}} - \frac{1}{T_{\text{ref}}}\right)\right), \quad r: = \{1, \dots, 6\}. \quad (5.63)$$

5. The material balances of the polar and nonpolar components in the liquid phase of the decanter are

$$V_{\text{polar}} \frac{dC_{i,\text{polar}}}{dt} = \zeta_i \dot{n}_{i,\text{in}} - \dot{V}_{\text{polar}} \dot{C}_{i,\text{out,polar}} - J_i a V_{\text{decanter}} \quad (5.64)$$

$$V_{\text{nonpolar}} \frac{dC_{i,\text{nonpolar}}}{dt} = (1 - \zeta_i) \dot{n}_{i,\text{in}} - \dot{V}_{\text{nonpolar}} \dot{C}_{i,\text{out,nonpolar}} + J_i a V_{\text{decanter}}, \quad (5.65)$$

where ζ_i denotes the split factor of i^{th} -component in the decanter.

6. The material balance of the gas components in the decanter is given by:

$$\frac{dn_{j,\text{gas}}}{dt} = \dot{n}_{j,\text{in}} - \dot{n}_{j,\text{off-gas}}. \quad (5.66)$$

All model parameters are available in [68].

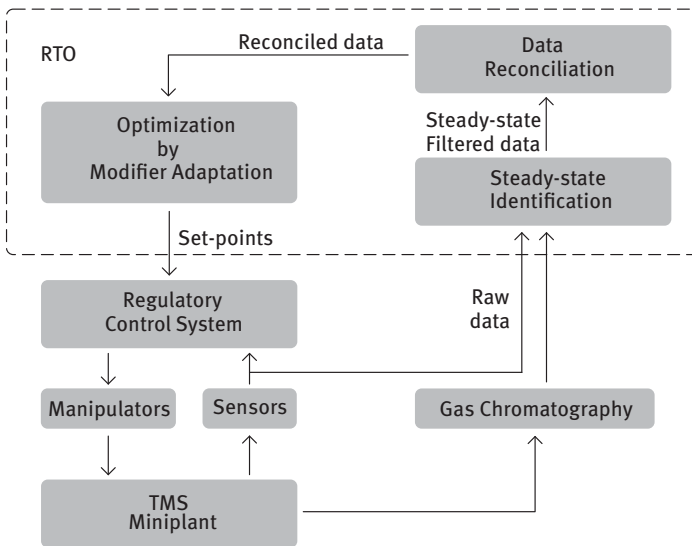


Figure 5.73: Framework for RTO of the TMS miniplant [68].

Figure 5.73 illustrates the monitoring and control framework that was developed for the application of iterative RTO to the hydroformylation process in the TMS miniplant. As the process requires between 2 h and 4 h to reach a steady state and as the gas chromatography requires approximately 30 min to analyze a sample, a steady state identification tool is required to identify a steady state as quickly as possible, to avoid operating the process sub-optimally for longer periods of time. In this work, the F-test [16] is used for steady state identification. As the correction of the plant model is based upon the measurements taken at the plant, the performance of the modifier adaptation scheme deteriorates in the presence of measurement errors. Therefore, data reconciliation is used to filter the errors. It adapts the

measurements such that the overall material balance of the process is obeyed before supplying them to the modifier adaptation scheme.

Figure 5.74 illustrates the communication framework used for the implementation of the iterative RTO scheme. The product sample from the miniplant is transported to the GC where it is analyzed by gas chromatography in an Agilent Gas Chromatography HP6890A with a capillary column (HP5, 30 m × 0.32 mm × 0.25 μm) and a flame ionization detector. The raw GC data is then sent to Computer-02. The raw GC data is processed using a Visual Basic script to compute the product composition. Computer-01 communicates with Computer-02 using a TCP/IP protocol to receive the product composition. Simultaneously, it receives other process measurements, for example the reactor temperature, reactor pressure, etc. from the miniplant. Upon receiving all measurement data, the RTO algorithm computes new set-points for the miniplant by formulating and solving the iterative modifier adaptation problem. It is implemented in MATLAB. The set-points computed are implemented via the Labview program, which directly passes the desired set-points to the regulatory controllers of the miniplant. The temperature in the reactor is controlled by a temperature controller and a desired molar fraction of syngas is maintained by a flow fraction controller.

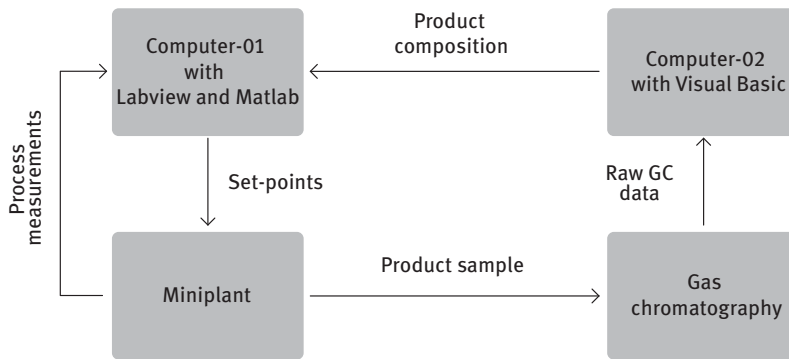


Figure 5.74: Illustration of the communication framework used for the implementation of iterative RTO at the miniplant.

The set-points of the hydroformylation process, computed by the iterative RTO scheme and the evolution of the objective function (Y) for an experiment are presented in Figures 5.75 and 5.76. The hydroformylation process was started at $t = 0$ with the input $\mathbf{u}_m^* = [95, 0.5]$ for the reactor temperature and the mole fraction of CO that was computed for the nominal model, which led to a product yield of 73%. The process reached its steady state approximately within 4 h. The process then was run at \mathbf{u}_m^* until $t = 15\text{h}$ to demonstrate the continuous operation of the process. The corresponding values of the objective function, computed using the process measurements, are shown in Figure 5.76. The iterative RTO scheme MAWQA was initiated at $t = 15\text{h}$, and from $t = 15\text{h}$, the RTO made six input moves to converge to an optimal set-point for

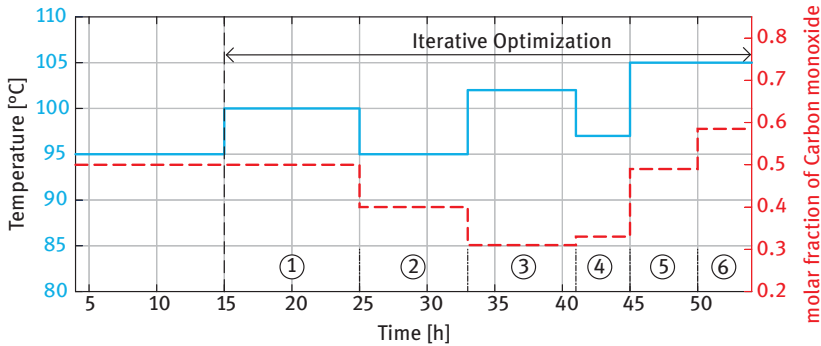


Figure 5.75: Experimental result: Inputs for the hydroformylation process computed by the iterative RTO scheme [68].

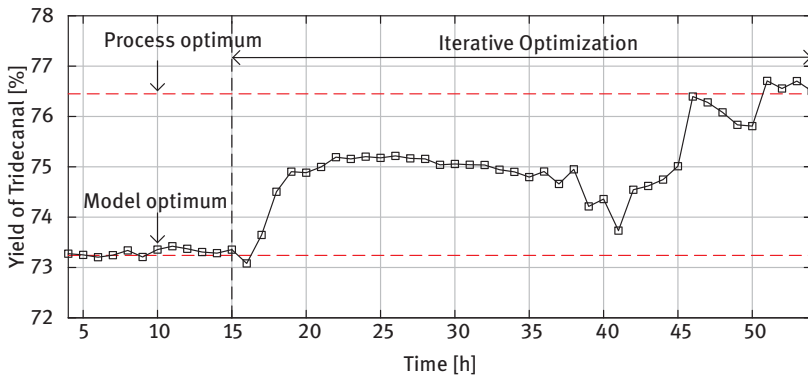


Figure 5.76: Experimental result: Evolution of the objective function for the iterative RTO scheme [68].

the process $\mathbf{u}_p^* = [105, 0.58]$ for the reactor temperature and the mole fraction of CO, which led to a yield of above 76% which is a remarkable improvement.

5.4.2.4 Conclusion and Outlook

The modifier adaptation scheme MAWQA was used successfully to identify the optimal operational degrees of freedom for the hydroformylation of 1-dodecene in a minilant, despite the fact that the nominal model deviates structurally and parametrically from the process model. The experimental results demonstrate the capabilities of modifier adaptation-based iterative RTO methods to overcome the deficiencies in the nominal model. Using MA-based iterative RTO methods, it is possible to optimally adapt the process operation to the realization of uncertain process parameters (Section 5.3.3) and disturbances or drifts. In the overall process development, this provides important information about the true potential of a process design: besides

the study of the long-term stability of the process, the best possible performance for a given phase system, catalyst, and plant sizing is determined under realistic experimental conditions, in contrast to purely model-based computer studies. Also, the real-time optimization approach can be scaled up with the plant, with reduced effort.

With regard to the application of the scheme that was demonstrated here in an industrial environment, some further issues that were not discussed here should be considered: Upon convergence to a process optimum, MA-based iterative RTO methods sometimes perform exploratory input moves which lead to a sub-optimal operation of the process. A strategy to turn off the RTO upon convergence to the process optimum and to turn it on again if a change in the process leads to a change in the process optimum detected, is proposed in [54]. This reduces unnecessary input changes, thereby improving the performance and avoiding upsets that will help to build confidence of the operators in the scheme.

Secondly, the modifier adaptation scheme may show oscillations in certain situations when there are significant structural differences between the model used for optimization and the behavior of the real plant, which is called model inadequacy in the literature. To handle this situation, a modification of the modifier adaptation-based methods was proposed to handle inadequate nominal models, i.e., the case when the nature of the computed solution where the gradient of the cost function with respect to the operating conditions vanishes is different between the true plant and the model; so instead of a minimum, a maximum is predicted, or vice versa. If the model adequacy condition is not satisfied, the inputs from the modifier adaptation oscillate [2]. In [55], a scheme that guarantees model adequacy was proposed, thereby avoiding oscillating inputs to the process.

To conclude, the application of modifier adaptation, an iterative RTO method, to the hydroformylation process in the miniplant demonstrated the maturity of the method and its readiness to be used in the process development process to determine the potential of a proposed process reliably and to be used in the process industries for improved process performance. Modifications leading to guaranteed model adequacy and concerning the start-up and shut-down phases can further improve its performance and reliability.

5.4.3 State Estimation for Reactions and Separations in a MES System in a Mini plant

Erik Esche, Markus Illner, Volodymyr Kozachynskyi, Karsten Duch,
Jens-Uwe Repke

Operating the complex miniplant shown in Figure 4.73 and carrying out experiments for the hydroformylation of 1-dodecene in an MES system is a challenge. The reaction system contains several chemical compounds – especially the surfactant – that are

not easily accessible by online measurements. Monitoring the performance of the miniplant, solely based on the available measurements is almost impossible without the help of models.

In the MES miniplant, the state estimation has three distinct tasks that are essential for the experimentation and the evaluation of the performance of the plant:

- The reaction progress needs to be tracked based on scarce concentration measurements, i.e., reaction yield and selectivity need to be continuously computed.
- The three-phasic separation in the decanter needs to be monitored and, particularly, the composition of the oily product phase needs to be estimated.
- An estimate of the state of the plant is needed for process control to implement adjustments whenever the process deviates from the desired operation.

Liquid multiphase systems as reaction media can present highly nonlinear and complex behaviors. This is especially the case for the MES miniplant (see Section 4.2). To minimize disturbances, samples for concentration measurements can be taken only on an hourly to three-hourly basis. However, the investigated reactive systems, i.e., the hydroformylation of 1-dodecene and reductive amination, display both fast and slow dynamics: Changes in the phase separation and the reactions can occur within seconds or minutes, while reaching steady state during start-up usually takes several hours (see Section 4.2).

The various approaches that are proposed for state estimation, such as the Kalman filter, particle filters, Moving Horizon Estimators, etc. [172], differ from each other with respect to how past and present measurement data is considered, how measurement errors (both noise and outliers) are treated, and whether or not a nonlinear process model is used.

Figure 5.77 visualizes the task of state estimation, as discussed in the following paragraphs. State estimation has to consider both continuously measured variables, y^c (e.g., temperatures, pressures, flows, levels) as well as infrequently measured data, y^d (e.g., concentration measurements). Gross error and measurement noise need to be removed from the measurement data. The control actions, u (i.e., all actions applied by pumps, valves, and other actuators), which affect the process need to be incorporated and the state variables, x , need to be estimated.

Measurements obtained from any process or any plant contain errors. These may stem from sensor failures, offsets, drifts of sensors, or stochastic measurement noise. Such errors are also present in the miniplant considered here. In order to apply methods of advanced process control to chemical plants, these errors need to be first reduced, and an as consistent as possible set of measurements needs to be computed. This is known as data reconciliation [27]. Consistency of measurement data is achieved with respect to process models. In general, the models involve material balances of process equipment and, sometimes, also energy balances. A major issue herein is the availability of sensors for all material streams and hold-ups. In most implementations, data reconciliation and state estimation are directly

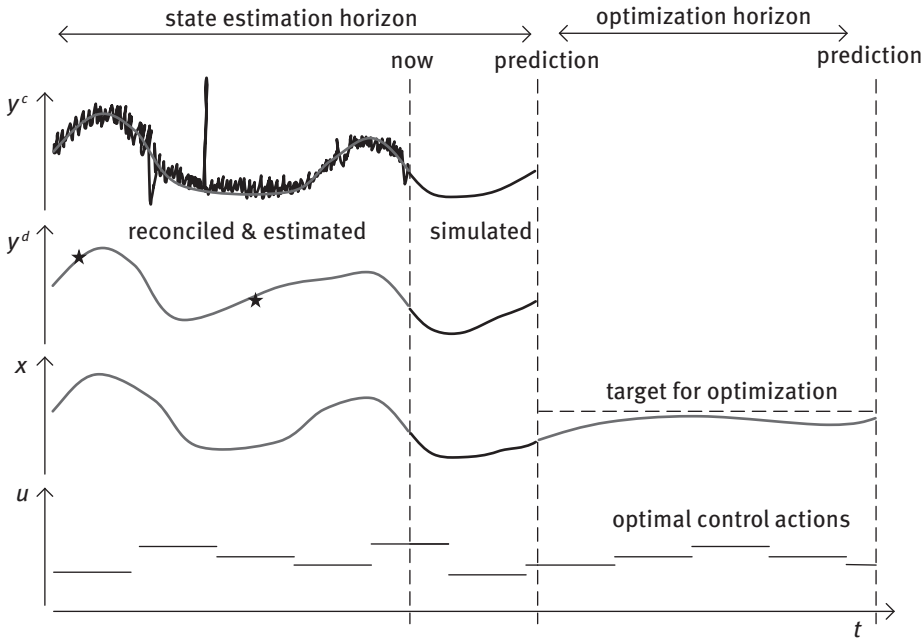


Figure 5.77: Visualization of the task of state estimation with state variables, x , control variables, u , continuous and discrete measurements, y^c and y^d .

integrated into a single state estimation framework. For state estimation, a dynamic model of the process is required, which is typically provided in a discrete-time formulation [168]:

$$x(k+1) = f(x(k), u(k)) + w(k), \quad (5.67)$$

$$y(k) = h(x(k)) + v(k), \quad (5.68)$$

$$w \sim \mathcal{N}(0, Q), v \sim \mathcal{N}(0, R), \quad (5.69)$$

wherein k denotes a discrete time point, $t(k)$, x are the estimated or predicted state variables, $u(k)$ the known control actions, and $y(k)$ denotes the measurements from the plant. The function f represents a discretized version of the system of differential equations that describes the system, and h are algebraic equations that relate the measurements y to the state variables. w and v are independent random Gaussian white noise variables, as indicated by eq. (5.69), and the covariance matrices Q and R represent the intensities of the process and measurement noise.

Among the available methods for state estimation that could be applied online to the mini plant, Moving Horizon Estimation (MHE) [150] was determined as the most suitable technique [216]. The two main factors here are the scarcity of the concentration measurements and, hence, the importance to use a model-based technique to

infer concentration trajectories in between measurements and secondly, the complexity of the behavior of the three-phasic separation in the MSE miniplant: The state estimation needs to be able to handle disappearing phases and to determine their compositions from ambiguous levels of the phases.

Most state estimation techniques employ Bayes' law to choose x , so that the probability, $p(x|y)$, is maximized for the given measurements, y . Herein, x and y usually entail an interval of $N+1$ time points, e.g., from $t(k-N)$ until $t(k)$. In MHE, this problem is solved in the form of a Nonlinear Program (NLP). Compared to other approaches, fewer simplifications are applied and constraints can be enforced, although these advantages come with the additional computational burden of solving an NLP to optimality. In the literature [216], a range of state estimation methods were evaluated regarding their applicability for highly nonlinear systems. It was found that most other methods overly rely on a very good guess of Q . Given that this process noise is, in practice, challenging to quantify reliably, we limit ourselves to the discussion and further development of MHE solutions for state estimation.

Development of MHE for the MES Miniplant

Based on Chen et al. [22], the basic statistical assumptions necessary for an MHE formulation are the following:

- The described system needs to be a first-order Markov process, i.e., the states $x(k+1)$ can be predicted solely from the current states, $x(k)$, and the current control actions, $u(k)$.
- The measurement noise is independent of the states.
- measurements used for MHE are mutually independent.
- All noise variables are assumed to be Gaussian with zero means.

The third assumption is, in practice, the most challenging, as hysteresis effects might occur. The final assumption necessitates that gross error and offsets have already been filtered from the measurements.

A formulation for MHE that is applicable online to problems in chemical engineering has been suggested by Nicholson et al. [168]:

$$\{\hat{x}_{k-N}, \dots, \hat{x}_k\} = \arg \min_{\{x_{k-N}, \dots, x_k\}} \left(\phi(k-N) + \frac{1}{2} \sum_{i=k-N}^k v_i^T R_i^{-1} v_i + \frac{1}{2} \sum_{i=k-N}^k w_i^T Q_i^{-1} w_i \right) \quad (5.70)$$

$$x_{i+1} = f(x_i, u_i) + w_i \quad (5.71)$$

$$y_i = h(x_i) + v_i, \quad (5.72)$$

$$x^L \leq x \leq x^U, \quad (5.73)$$

wherein $\phi(k-N)$ describes the arrival cost, which connects the current estimation horizon, $(t_{k-N} \dots t_k)$, to measurements prior to the current horizon. x^L and x^U are known lower and upper bounds to the state variables. This formulation ensures a smooth connection to the data that was obtained prior to the current horizon via the arrival cost and minimizes v and w by choosing the states, x , for the time step, $t_{k-N} \dots t_k$, while fulfilling the model, f , and the measurement relations, h . The arrival cost is especially important for short time horizons when little measurement data, y , is available [168].

As can be seen from eq. (5.70), the standard MHE formulation is highly sensitive to gross errors, because the measurement error, v_i , is squared and, hence, gross errors have a large influence. To overcome or dampen the influence of gross errors, data reconciliation techniques have been advanced for dynamic systems [170] and were introduced directly into the state estimation problem. Generally, this entails replacing $v_i^T R_i^{-1} v_i$ in eq. (5.70) by an alternative estimator. Of interest are Maximum Likelihood Estimators, e.g., the Fair function [170] or the Redescending estimator [61], which provide better robustness regarding gross errors [168]. In our experience [70], state estimation performs best in the presence of gross errors in case it is initialized with the Fair function and later solved with the Redescending estimator.

Apart from a suitable model, the success of MHE, of course, hinges on the availability of high-quality measurement data. While temperatures, pressures, flows, and levels are continuously measured in the MSE miniplant, this is in general not the case for quality measurements. As detailed in Section 4.2, very little quality measurement data is available in the MES miniplant, and the available data is only sampled infrequently (hourly rates or less) via offline GC measurements. There are various approaches toward extending MHE for measurements at different time scales. Among them, some pursue a fixed-structure approach. These make use of slow measurements, upon availability, else pursue linear or polynomial extrapolation of the slow measurements [106, 205]. This approach has its shortcomings when tackling highly nonlinear systems or in case there is a major improvement of the state estimation achievable through few quality measurements.

Alternatively, there are approaches with a variable structure, e.g., [127], which adjust the measurement model depending on the availability of measurement data. Nevertheless, we found that the assumptions in the available implementations are all too optimistic, compared to the actual availability ratios of measurement data in the case of the MES miniplant. Within the MES miniplant, significant dynamics can be observed in data in the range of seconds. On the other hand, GC measurements are available only once every two to three hours. Hence, the ratios of these two sampling rates are 1:10,000 compared to 1:10 or 1:100 in the literature [74].

Both for the application of the hydroformylation reaction as well as the reductive amination in the MES mini plant, the situation regarding the measurement data is similar. Information on all flows is available with sampling times in the range of seconds. The graphical analysis on the level inside the decanters is carried

out every two minutes to provide readings for the levels of the three liquid phases therein. The levels in all other vessels are available every few seconds as well. Concentration measurements from the reactor on the oily educts and products are obtained by GC measurements at least every two hours. The oil phase of the decanter is also sampled by GC and readings are available every 2 h to 4 h. Due to the danger of an increasing loss of catalyst, the water phase of the decanter is sampled every four hours. Because of its high content of surfactant, the middle phase is inaccessible by GC. For all three different GC samples, an additional delay of 45 min results from the manual sample preparation and processing by the GC [162].

Based on the available measurements, it is almost impossible to accurately measure the concentrations of surfactant, water, and catalyst in the system. The first two can only be inferred with large uncertainty from the level readings of the decanter.

Apart from continuous monitoring, the goal of state estimation for the MES miniplant is to ensure a safe and fast start-up as well as to optimize the continuous operation toward high reaction yields (Section 5.4.4). In consequence, it is essential for the state estimation to provide predictions of the concentrations, in both the reactor and the decanter of the miniplant, which highlights the importance of the slow GC measurements. Hence, the MHE framework has to operate on a horizon of at least 4 h of past measurement data in order to be able to provide any estimates at all. To implement the MHE at the miniplant, two different versions have been devised; the first is operating on fast and slow data simultaneously, and the second is based upon separating both problems.

First Implementation – Simultaneous Approach for Multi-rate MHE

For the first implementation, the full dynamic mini plant model, as discussed in Section 5.2.1, is implemented in MOSAICmodeling [35] and fully discretized by orthogonal collocation on finite elements. The discretized model is then exported to AMPL [41] for a solution by IPOPT [212] and CONOPT [4]. To account for the extremely different sampling rates, the terms inside the objective of the MHE are weighted to equalize rare and frequent measurements by their respective numbers. Apart from that, this first implementation is a rather standard one [168]. Full details, including details on the filtering steps to eliminate gross errors, can be found in [70].

Figure 5.78 shows results for this first implementation for a horizon of four hours for one fast measurement (level of the oil phase in the decanter) and a slow measurement (1-dodecene concentration at the reactor outlet). As can be seen from the lower half of Figure 5.78, the state estimation (SE) shows a persistent offset for the slow measurement, while the fast measurement is tracked almost perfectly. This situation was observed for all estimates based on slow measurements, which show a persistent positive or negative offset compared to the experimental data. It was attempted to overcome this issue by an adjustment of the weighting factors between the fast and slow measurements, but with no success.

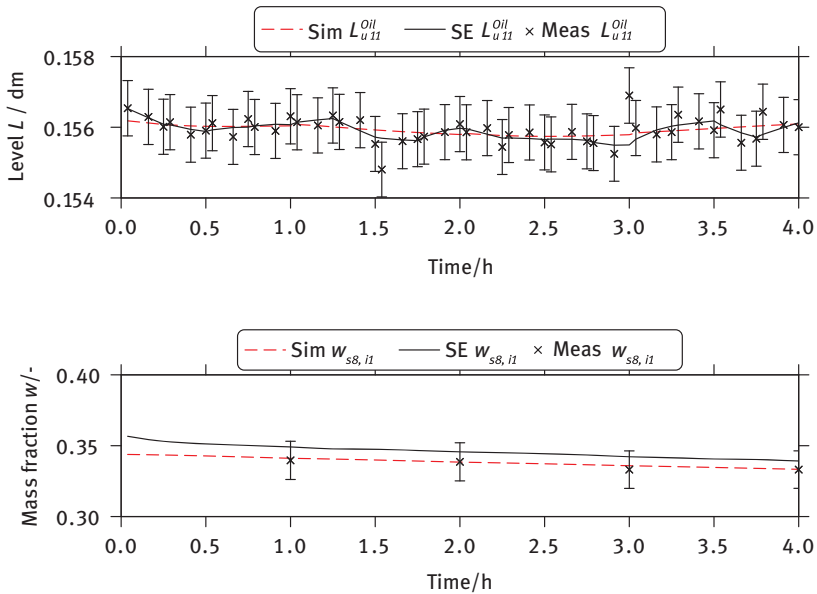


Figure 5.78: Simultaneous MHE Approach: Results of MHE applied to fast and slow measurement data on the MES mini plant. L_{u11}^{Oil} represents the level of the oil phase in the decanter, while $w_{s8,i1}$ is the weight fraction of 1-dodecene in the stream exiting the reactor. Image taken from [74].

Second Implementation – Two-stage Approach for Multi-rate MHE

Given the persistent offset between slow measurements and the state estimation results, a novel two-stage approach for the MHE was developed [74]. This approach handles fast and slow measurements separately. The first stage operates on the fast measurements only, i.e., flows, levels, temperatures, pressures, etc. Compared to the dynamic miniplant model presented in Section 5.2.1, this MHE implementation uses a slightly amended model formulation. Holdups and weight fractions of all oily components are summed up to form one oily pseudo component. This is done to handle the lack of continuous concentration measurements due to which it is not possible to distinguish between the individual oily components.

The second stage considers only the slow measurements and also employs the full plant model. Here, the individual component hold-ups are adjusted. In both stages, the Fair function is employed for the initial filtering of gross errors and the Redescending estimator is applied during the solution of the MHE problems. The two stages are complemented by several initialization and simulation steps to ensure proper initialization of all variables, and to ensure convergence. For the two-stage implementation, the same discretization scheme as above is used and the solution is also obtained via AMPL, IPOPT, and CONOPT. For full details on the framework, refer to [74].

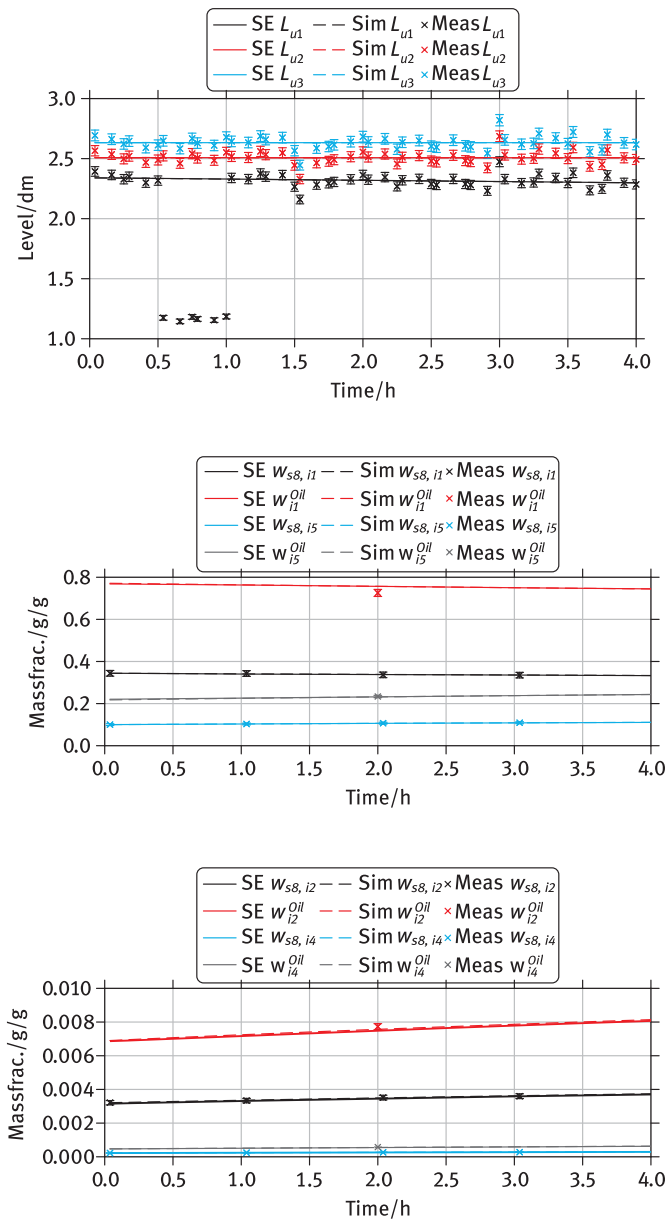


Figure 5.79: Two-stage MHE Approach: Results of MHE applied to fast and slow measurement data on the MES mini plant. L_{u1} , L_{u2} , and L_{u3} represent the levels of the three feed tanks. $w_{s8,i2}$ is the weight fraction of iso-dodecene in the stream exiting the reactor, w_{i2}^{Oil} is the weight fraction of iso-dodecene in the oil phase of the decanter, $w_{s8,i4}$ is the weight fraction of dodecene after the reactor and w_{i4}^{Oil} , respectively, in the oil phase.

Figure 5.79 depicts the results of the two-stage multi-rate MHE on fast and slow measurement data. It can be observed that the offset between the estimated states and the slow measurement data has disappeared. Especially important is the elimination of gross errors, which can be seen in the upper graph in Figure 5.79. The estimated level in the feed tank evolves smoothly despite the intermittent drop in the measurement data. There is, of course, a certain danger that this two-stage multi-rate MHE formulation applies an overly strong dependency on the quality of rare measurement data. It can, however, be assumed that the GC measurements will always be of a rather high accuracy as determined by validation samples.

The described multi-rate MHE framework has proven to work reliably when applied online in the MES miniplant [74]. This is the first multi-rate state estimation framework that we know of which can handle such extreme ratios of measurement frequencies. Despite the mentioned shortcoming that the approach might overly depend on rare concentration measurements, it shows a promising solution for how model-based state estimators can be applied in real-time on large-scale chemical production processes. However, a further generalization of this approach is required regarding the separation of the MHE into the two stages. In the case of the MES miniplant, this was rather straightforwardly achieved by the lumping of the oily components into a single pseudo-component. As of now, there is no obvious path to obtain a decomposition of the respective process models for both stages.

While the discussion in this section was largely problem-specific related to the MES miniplant, the issues tackled here are encountered frequently. In practice, large differences in sampling frequencies with rare quality measurements are often present. The multi-rate MHE approach presented here therefore is prototypical for other practical examples.

5.4.4 Optimal Operation of Reaction-Separation Processes in a MES Miniplant

Erik Esche, Markus Illner, Volodymyr Kozachynskyi, Karsten Duch,
Jens-Uwe Repke

The start-up and transition into continuous operation of the MES miniplant is a challenge, both for the hydroformylation of 1-dodecene and for the reductive amination. This is due to the critical influence of the surfactant and the complex three-phasic separation in the decanter. In case too much or too little surfactant is added during start-up, phase separation may not be achieved, which also has a detrimental effects on the selectivity of the reaction. It is essential to feed all components into the miniplant, in exactly the right ratios and composition, and also to quickly achieve a suitable temperature in the decanter to start the three-phasic separation.

Later on, during the initiation of the reaction, the addition of synthesis gas in the case of hydroformylation has an instantaneous effect on the phase separation, therefore the temperature in the decanter needs to be adjusted to retain the three-phasic separation. In case the three-phasic separation is lost, recovering it is not an easy matter and may cause a delay of several hours in the overall operation of the plant.

With the assistance of a dynamic process model, an operation trajectory can be computed which starts up the miniplant, fills all units, initiates the reaction, and moves the miniplant into continuous operation. Such a trajectory can be computed offline and then implemented as a detailed recipe. However, during the operation of any plant, the presence of disturbances and faults has to be considered. Regarding the MES miniplant, especially the feeding of the surfactant is an influential source of process disturbances – both too much and too little surfactant may have very negative effects on the operation of the process.

Given the complex nonlinear behavior of the MSE miniplant, devising countermeasures against such disturbances is not an easy task and several issues have to be considered: The catalyst and its ligand are the most expensive chemicals, despite their comparatively small amounts. Hence, minimizing catalyst loss, e.g., via the product stream is essential. At the same time, catalyst deactivation may occur, which leads to increased byproduct formation, in turn leading to a different and undesired phase-separation behavior. In the case where the phase separation is lost, no product phase should be siphoned off, as the associated catalyst loss would be large.

In Section 5.4.3, a state estimation framework was introduced which makes it possible to continuously determine the state of the mini plant throughout its operation and monitor key indicators, such as catalyst loss, reaction selectivity, and yield, as well as surfactant concentration within the decanter.

While, from the viewpoint of experimentation, maximizing the product yield of 1-tridecanal would be, of course, of strong interest, the issues discussed above imply that the operating window is strongly constrained and the stability of the phase separation is the most essential concern.

The start-up of chemical processes is a challenge, in general. The start-up of continuous processes and the operation of batch processes are still dominated by the implementation of recipes, i.e., human-designed sets of instructions to start-up complex equipment and entire processes. Some work has been carried out on achieving time-optimal start-up, using a combination of recipes and optimization, e.g., for reactive distillation [186]. The design of such recipes is based on experience and heuristics, and performing optimization within the frame of such recipes will most likely lead to sub-optimal results due to the constraints implied by the chosen base recipe. The full potential of optimization, e.g., regarding time optimality or resource efficiency, can be realized when a fully dynamic process model and rigorous optimization are employed [110, 214]. Here, a big challenge is the formulation of suitable dynamic process models that are able to describe all operation modes of the process, spanning from “empty and cold” to continuous operation [36].

Beyond start-up, the continuous (re-)optimization of processes regarding resource efficiency or costs [73, 162, 189] is of interest, given that demand, ambient conditions, and external disturbances change over time, and the behaviour of the process is continuously changing, e.g., due to aging of catalysts. For processes with slow dynamics that rarely reach steady state given external disturbances, this may be achieved by nonlinear model predictive control with economic cost functions, also called dynamic real-time optimization [34, 73, 184]. These methods compute optimal time-varying operating conditions that maximize the efficiency or minimize the cost over a certain prediction horizon. The control actions are either directly applied to the actuators within the processor, or realized via set-point updates to existing base control, such as PID controllers.

Regarding the operation of the MES miniplant, two specific tasks have to be achieved based on the initial experience from manual miniplant runs. The first task is to realize a fast start-up of the plant, including filling, initiation of the reactions, and, most importantly, initialization of a stable phase separation. The second task is concerned with achieving and stabilizing a high product yield in the presence of disturbances during the continuous operation.

Start-up Trajectories

Several challenges arise, especially during the start-up of the MES miniplant for the hydroformylation of 1-dodecene. Due to the long delay in obtaining reliable state estimates, the focus for the start-up optimization was on obtaining trajectories offline that are sufficiently robust to handle most disturbances that are encountered during start-up.

The feeding of all liquid components needs to be orchestrated in such a manner that separation inside the decanter succeeds and no blockages occur in the piping because of locally too high surfactant concentrations. This concerns both the control of the concentrations as well as the temperatures of the equipment and of the piping.

Considering these constraining factors, optimal start-up trajectories are computed for the entire time, from the beginning of the operation until a continuous stable operation of the reactive system is attained [162]. These trajectories were obtained by the formulation of a dynamic optimization problem, considering the entire miniplant model, as detailed in Section 5.2.1.6. The objective considers several aspects:

- Maximization of the product yield of 1-tridecanal in the reactor
- Maximization of the amount of 1-tridecanal collected in the product tank
- A quadratic penalty term for ensuring a desirable oil-to-water ratio of 50:50 in the reactor
- A quadratic penalty term for a surfactant concentration of 8 wt.-% in the reactor
- A penalty term for avoiding excessive residence times in the decanter.

In addition to the dynamic miniplant model, the optimization problem is further constrained by bounds on the allowed oil-to-water ratio and surfactant concentrations for which the phase-separation model described in Section 4.2 is valid. To

ensure a reliable phase separation even during startup, minimum relative phase heights of the oil and water phase in the decanter are required at any point in time. Doing so, even during the initial filling of the decanter, a separation into three phases is guaranteed. Furthermore, the residence time in the settler has to be greater than 12 min to ensure satisfactory separation quality (Section 4.2).

The MES miniplant is equipped with basic controls to realize a stable operation, in case no optimal trajectory can be obtained during continuous operation. The dynamic miniplant model includes these controllers, and the decision variables for the optimal startup problem include the set-points for all flow and level controllers (implemented by valves and pumps) as well as the set-points for the temperature controllers for the reactor and the settler.

The optimization problem was defined in MOSAICmodeling [35] and exported to gPROMS' Modelbuilder [180], where it was solved prior to operation. As an example of the optimization results, set-points for the three individual recycle streams and optimal temperatures for the settler and the reactor are shown in Figure 5.80 for the first 15 h of operation. The steadily decreasing settler temperature is in direct relation to the increasing product yield (Section 4.2).

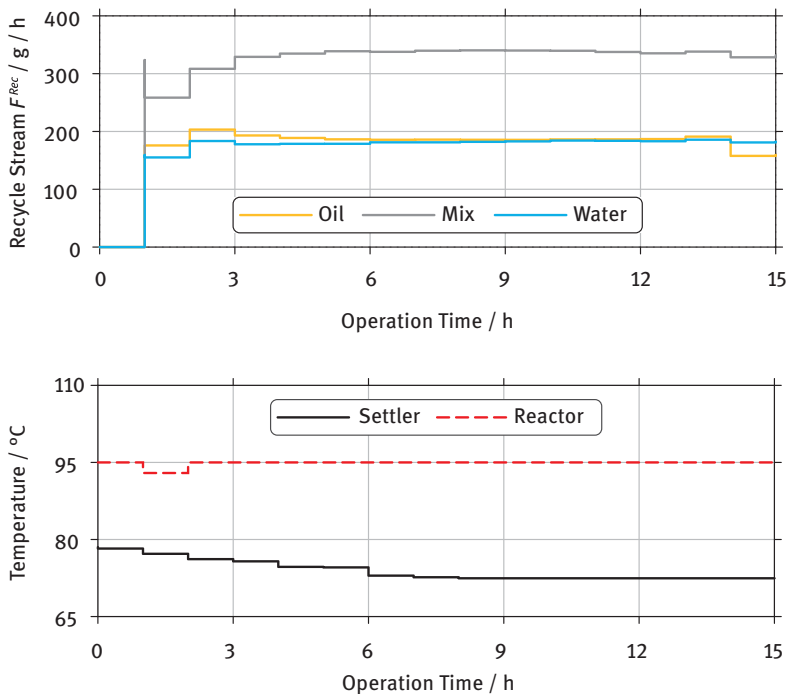


Figure 5.80: Optimal start-up trajectory for the MES miniplant.

Optimization of the Continuous Operation

Once the miniplant is at steady state, the multi-rate MHE (Section 5.4.3) is continuously applied to observe the plant state in the presence of disturbances: Sampling from various liquid phases causes considerable disruptions, compared to the overall miniplant holdup. Even greater issues arise from inaccuracies in flow control applied on pumps for feed and recycle. Further deviations from the desired operation may arise from by product formation due to the changing catalytic performance, which may be countered by adjusting the ratio of recycling streams to the reactor or the composition of synthesis gas in the reactor.

Under typical industrial circumstances, the optimization of the continuous operation would be implemented by real-time optimization [18, 48] (see Section 5.4.2), which employs an accurate steady-state model and implements the new operation conditions, either by model-predictive control or by basic PID controllers. However, considering the slow dynamics of the MES miniplant, in combination with the frequency of disturbances taking place during operation and the challenging issues involving the phase separation in the decanter, a different strategy is pursued here [46]. To ensure that all transients between the operation points are feasible [184] and to simultaneously ensure that even during the dynamic phases, the economic performance of the system is optimized, dynamic real-time optimization (D-RTO) or economics-based MPC [34], is applied, which is a nonlinear model-predictive control strategy with a partially economic objective. Here, the economics are represented as the maximization of the product yield and the minimization of the catalyst loss.

Accurate estimates of the multi-rate MHE are, of course, essential for a successful re-optimization of the plant operation. While meaningful updates on the oily reaction products are only obtained every four hours, the part of the MHE operating on the fast measurements yields estimates continuously. Considering the underlying dynamics of the system and the time it takes to reach a steady state after larger disturbances, the optimization horizon is set to two hours.

While the formulation of the D-RTO problem is similar to the start-up problem discussed above, the main differences lie in the implementation and in the interaction with the state estimation. For D-RTO, the optimization problem is fully discretized by orthogonal collocation on finite elements [17], exported to AMPL [41], and solved by IPOPT [212], as the MHE framework discussed above.

The schedule to orchestrate the interaction between MHE and D-RTO is presented in Figure 5.81. The difference between the marked time points relates to two hours in the real-life miniplant. The grey boxes mark the data considered for state estimation, wherein the crosses and boxes account for the fact that GC measurements arrive with a delay of 45 min. As noted before, the state estimation considers four hours in terms of measurement data to contain sufficient concentration measurements. The multi-rate state estimation problem usually converges reliably. Once the state estimation results are available, a simulation is initiated, which considers the currently planned set-point changes from the last computed trajectory, to predict the next initial point

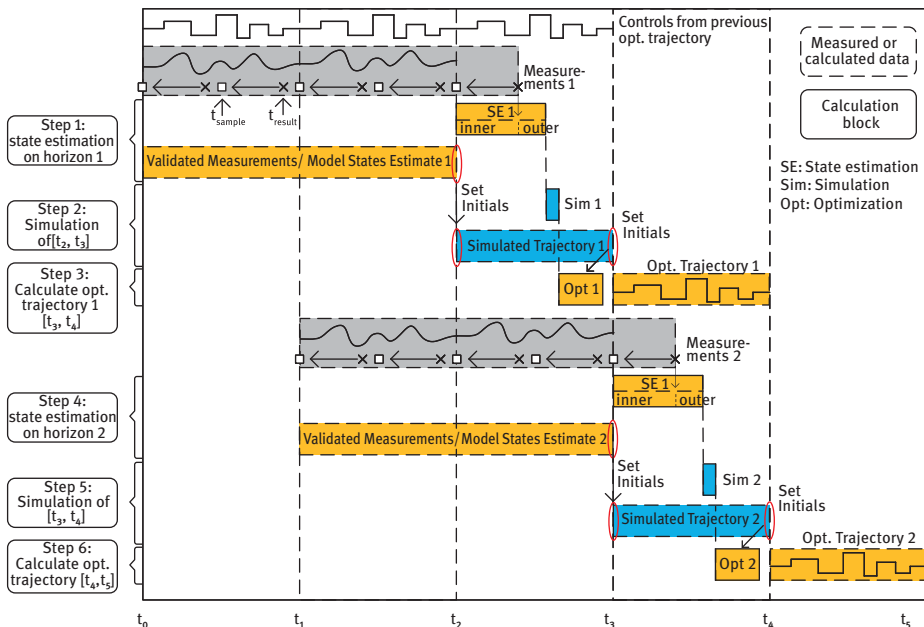


Figure 5.81: Continuous interaction between MES miniplant, multi-rate MHE, and dynamic real-time optimization.

of the optimization horizon, e.g., t_3 . Upon completion of the simulation, the optimization run is initiated for the next horizon of two hours (t_3 to t_4). This sequence of state estimation, simulation, and optimization is initiated every two hours.

For increased robustness of the overall framework, multiple instances of this framework are run in parallel with a shifted time horizon. In case of a failure of one of these instances to converge, it is still likely that there will be a fallback solution from another optimization run. Nevertheless, there can, of course, be major equipment failures or blockages that render optimal operation impossible. In these cases, the MHE-D-RTO cycle is discontinued and reinitialized, once the plant operators have regained the desired operation window. Further details on the technical implementation of this scheme in the process control system of the miniplant can be found in [74, 162].

Optimal Operation of the Miniplant

By now, MHE and D-RTO have been applied multiple times on the MES miniplant (Section 4.2). For both the hydroformylation of 1-dodecene and the reductive amination, high product yields were obtained. Throughout these miniplant runs, some disruptions occurred, which sometimes caused plant states from which the normal operation could only be recovered by manual interaction. In all cases, it was possible to pinpoint the origin of these disruptions to technical failures, e.g., damage to

stirrers, the disintegration of sealing material, which is due to the experimental nature of a miniplant.

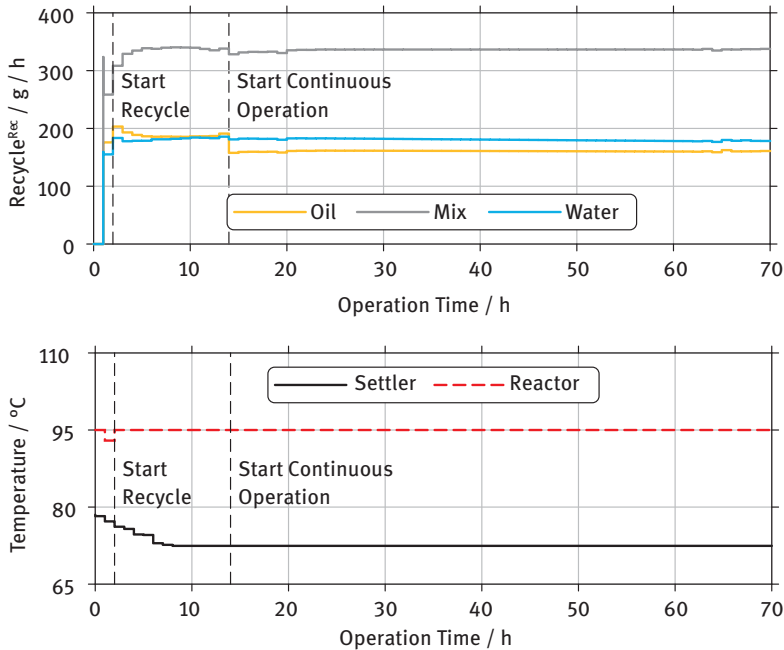


Figure 5.82: Optimal operation trajectories for the hydroformylation of 1-dodecene in the MES miniplant. Top: set-points for recycling flow rates, bottom: set-points for the temperatures in the settler and the reactor.

Figure 5.82 presents optimal recycle flows and temperatures profiles for the reactor and the decanter for 70 h of operation, obtained by the methodology described above and applied to the hydroformylation reaction. Especially during start-up, complex trajectories had to be implemented regarding both recycle flows as well as the temperature in the decanter. Regarding the former, particularly the abrupt changes at the start of the recycling and the switch over to continuous operation are noteworthy.

For the hydroformylation of 1-dodecene, a yield of up to 40% of the desired product 1-tridecanal was obtained, which is shown in Figure 5.83.

Therein, the black dots show the conversion of 1-dodecene and the red diamonds show the yield of 1-tridecanal. The horizontal black lines show the yield as predicted by the process model. The regions “start-up,” “full recycle,” and “continuous operation” denote different operation modes of the plant: “start-up” is the inertization and filling of the miniplant. At this point, only nitrogen gas is present; “full recycle” starts with the feeding of synthesis gas and contains an initial batch operation of the process, i.e., no 1-dodecene is fed during this period and the miniplant is in full recycle. Finally,

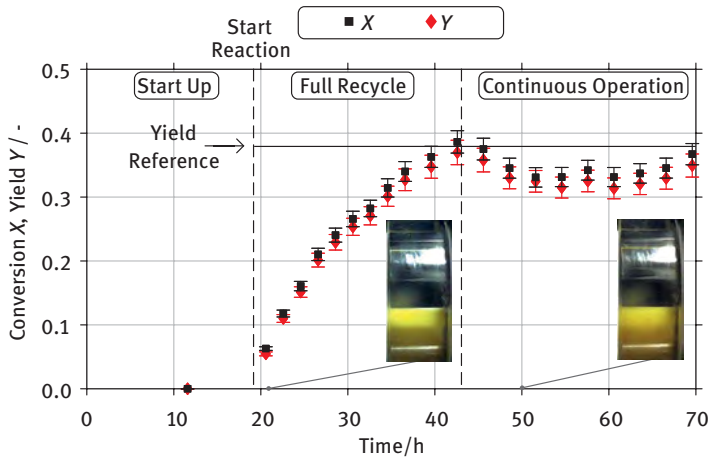


Figure 5.83: Yield and selectivity of a miniplant run of the MES system for the hydroformylation of 1-dodecene.

“continuous operation” describes the shift to continuous feeding of 1-dodecene and a corresponding continuous product stream with a high amount of 1-tridecanal. During “continuous operation”, an initial drop can be observed in the yield; this results from the start-up of the feed of 1-dodecene and is due to disturbances that had to be handled before the miniplant reaches steady state. Despite the strong disturbances, the plant was successfully operated continuously and the phase separation was retained. In the figure, snapshots from the corresponding three-phasic separation in the decanter are also shown. At the top, the clear oil phase is visible, which contains the product in high concentrations. An extended version of the evolution is shown in Figure 4.90, which shows results for a full campaign of 175 h.

The methodology described here is problem-specific as the formulation of the optimization has to be tailored to the specific needs of the process at hand. The general approach and the interplay of the MHE, the dynamic real-time optimization, and the plant as sketched in Figure 5.81 is very generic and can be applied to many similar situations.

The formulation of the model, including smooth reformulations to avoid discontinuities and the solution by full discretization via orthogonal collocation on finite elements, are highly useful building blocks for other applications. More specifically, the decanter model is a blueprint for other dynamic systems with two or more liquid phases. It could easily be adjusted to reductive amination and hydroaminomethylation reactions. The remaining hurdles are the manual decomposition of the process model for the MHE and the lack of ready-to-use systems for communication between the process control system, the MHE, and the dynamic optimization. While OPC UA has made great advances in recent years, no plug and play solutions are commercially available as of now.

References

- [1] Abdel-Aziz MH, Mansour IA, Sedahmed GH. 2010: Study of the rate of liquid–solid mass transfer controlled processes in helical tubes under turbulent flow conditions. *Chem. Eng. Proc.: Proc. Intensif.* 49: 643–648.
- [2] Ahmad A, Gao W, Engell S. 2019: A study of model adaptation in iterative real-time optimization of processes with uncertainties. *Comput. Chem. Eng.* 122: 218–227.
- [3] Alexander R, Campani G, Dinh S, Lima FV. 2020: Challenges and opportunities on nonlinear state estimation of chemical and biochemical processes. *Processes.* 8: 1462.
- [4] ARKI Consulting & Development A/S. 2021: Conopt Home Page. [Online].; cited 2021 03 14. Available from: <http://conopt.com/>.
- [5] Ballerstein M, Michaels D. 2014: Extended formulations for convex envelopes. *J. Global Opt.* 60: 217–238.
- [6] Ballerstein M, Kienle A, Kunde C, Michaels D, Weismantel R. 2015: Deterministic global optimization of binary hybrid distillation/melt-crystallization processes based on relaxed MINLP formulations. *Opt. Eng.* 16: 409–440.
- [7] Banerjee S, Scott DS, Rhodes E. 1970: Studies on concurrent gas-liquid flow in helically coiled tubes. II. Theory and experiments on turbulent mass transfer with and without chemical reaction. *Can. J. Chem. Eng.* 48: 542–551.
- [8] Beierling T, Micovic J, Lutze P, Sadowski G. 2014: Using complex layer melt crystallization models for the optimization of hybrid distillation/melt crystallization processes. *Chem. Eng. Proc.: Proc. Intensif.* 85: 10–23.
- [9] Belotti P, Kirches C, Leyffer S, Linderoth J, Luedtke J, Mahajan A. 2013: Mixed-integer nonlinear optimization. *Acta Numer.* 22: 1–131.
- [10] Bray T, Paoli J, Sperberg-McQueen CM, Maler E, Yergeau F. 2008: Extensible Markup Language (XML) 1.0 (Fifth Edition). [Online].; [cited 2021 01 03. Available from: <https://www.w3.org/TR/REC-xml/>.
- [11] Bongartz D, Naiman J, Sass S, Mitsos A. 2018: MAiNGO – McCormick-based Algorithm for mixed-integer Nonlinear Global Optimization. Tech. Rep. Process Systems Eng. (AVT.SVT), RWTH Aachen University.
- [12] Boukouvala F, Misener R, Floudas CA. 2016: Global optimization advances in Mixed-Integer Nonlinear Programming, MINLP, and Constrained Derivative-Free Optimization, CDFO. *Eur. J. Oper. Res.* 252: 701–727.
- [13] Boukouvala F, Floudas C. 2017: ARGONAUT: AlgoRithms for Global Optimization of coNstrAined grey-box compuTational problems. *Opt. Lett.* 11: 895–913.
- [14] Brunsch Y. 2013: Temperaturgesteuertes Katalysatorrecycling für die homogen katalysierte Hydroformylierung langkettiger Alkene. PhD Thesis. Technische Universität Dortmund.
- [15] Brunsch Y, Behr A. 2013: Temperature controlled catalyst recycling in homogeneous transition-metal catalyst: minimization of catalyst leaching. *Angew. Chem. (Int. Ed.)* 52: 1586–1589.
- [16] Cao S, Rhinehart R. 1995: An efficient method for on-line identification of steady state. *J. Process Control.* 5: 363–374.
- [17] Carey GF, Finlayson BA. 1975: Orthogonal collocation on finite elements. *Chem. Eng. Sci.* 30: 587–596.
- [18] Chachuat B, Srinivasan B, Bonvin D. 2009: Adaptation strategies for real-time optimization. *Comp. Chem. Eng.* 33: 1557–1567.
- [19] Chacon S, Git. 2021: [Online] cited 2021 2 23. Available from: <https://git-scm.com>.
- [20] Chapple S, Kresta A, Wall A, Afacan A. 2002: The effect of impeller and tank geometry on power number for a pitched blade turbine. *Chem. Eng. Res. Des.* 80: 364–372.

- [21] Chen CY, Joseph B. 1987: On-line optimization using a two-phase approach: an application study. *Ind. Eng. Chem. Res.* 26: 1924–1930.
- [22] Chen W, Bakshi BR, Goel PK, Ungarala S. 2004: Bayesian estimation of unconstrained nonlinear dynamic systems. *IFAC Proc.* 37: 263–268.
- [23] CO-LaN. 2021: COLN. CO-LaN – Unit Operation interface specification. [Online]; [cited 2021 02 23]. Available from: <https://www.colan.org/specifications/unit-operation-interface-specification/>.
- [24] COSMOlogic GmbH & Co. KG. 2015: COSMOtherm, C3.0, release 16.01.2015. <http://www.cosmologic.de>.
- [25] Cozad A, Sahinidis, NV, Miller DC. 2014: Learning surrogate models for simulation-based optimization. *AIChE J.* 60: 2211–2227.
- [26] Crombecq K, De Tommasi L, Gorissen D, Dhaene T. 2009: A novel sequential design strategy for global surrogate modeling. *Proceedings Winter Simulation Conference*, 731–742.
- [27] Crow CM. 1996: Data reconciliation – progress and challenges. *J. Proc. Contr.* 6: 89–98.
- [28] Czyzyk J, Mesnier MP, Moré JJ. 1998: The NEOS server. *IEEE J. Comp. Sci. Eng.* 5: 68–75.
- [29] Darby ML, Nikolaou M, Jones J, Nicholson D. 2011: RTO: an overview and assessment of current practice. *J. Process Control.* 21: 874–884.
- [30] Dorn C, Güttinger TE, Wells GJ, Morari M, Kienle A, Klein E, Gilles ED. 1998: Stabilization of an unstable distillation column. *Ind. Eng. Chem. Res.* 37: 506–515.
- [31] Dreimann JM, Hoffmann F, Skiborowski M, Behr A, Vorholt AJ. 2017: Merging thermomorphic solvent systems and organic solvent nanofiltration for hybrid catalyst recovery in a hydroformylation process. *Ind. Eng. Chem. Res.* 56: 1354–1359.
- [32] Dreimann J, Lutze P, Zagajewski M, Behr A, Górak A. 2016: Highly integrated reactor–separator systems for the recycling of homogeneous catalysts. *Chem. Eng. Proc., Proc. Intensif.* 99: 124–131.
- [33] Eason J, Cremaschi S. 2014: Adaptive sequential sampling for surrogate model generation with artificial neural networks. *Comp. Chem. Eng.* 68: 220–232.
- [34] Engell S. 2007: Feedback control for optimal process operation. *J. Proc. Control.* 17: 203–219.
- [35] Esche E, Hoffmann C, Illner M, Müller D, Fillinger S, Tolksdorf G, Bonart H, Wozny G, Repke, JU. 2017a: MOSAIC – Enabling large-scale equation-based flow sheet optimization. *Chem. Ing. Techn.* 89: 620–635.
- [36] Esche E, Repke JU. 2020: Dynamic process operation under demand response – A review of methods and tools. *Chem. Ing. Techn.* 92: 1898–1909.
- [37] Esche E, Müller D, Tolksdorf G, Kraus R, Wozny G. 2014: MOSAIC: an online modeling platform supporting automatic discretization of partial differential equation systems. In Eden MR, Sirola JD, Towler GP (Eds.) *Proceedings of the 8th International Conference on Foundations of Computer-Aided Process Design – FOCAPD 2014*, Elsevier: 693–698.
- [38] Esche E, Tolksdorf G, Fillinger S, Bonart H, Wozny G, Repke JU. 2017b: Support of education in process simulation and optimization via language independent modelling and versatile code generation. *Comp. Aided Chem. Eng.* 40: 2929–2934.
- [39] Feinberg M, Hildebrandt D. 1997: Optimal reactor design from a geometric viewpoint – I. Universal properties of the attainable region. *Chem. Eng. Sci.* 52: 1637–1665.
- [40] fmi. 2021: M. fmi – Functional Mock-up Interface. [Online], cited 2021 02 23. Available from: <https://fmi-standard.org>.
- [41] Fourer R, Gay D, Kernighan BW. 2002: *AMPL: A Modeling Language for Mathematical Programming*. 2nd ed. Duxbury.
- [42] France R, Rumpel B. 2007: Model-driven Development of Complex Software: A Research Roadmap. In *Future of Software Engineering (FOSE '07)*, IEEE: 37–54.

- [43] Freund H, Sundmacher K. 2008: Towards a methodology for the systematic analysis and design of efficient chemical processes. *Chem. Eng. Proc.: Proc. Intensif.* 47: 2051–2060.
- [44] Freund H, Maußner J, Kaiser M, Xie M. 2019: Process intensification by model-based design of tailor-made reactors. *Curr. Opi. Chem. Eng.* 26:46–57.
- [45] Fügenschuh A, Hayn C, Michaels D. 2014: Mixed-integer linear methods for layout-optimization of screening systems in recovered paper production. *Opt. Eng.* 15: 533–573.
- [46] Gao W, Engell S. 2016: Using transient measurements in iterative steady-state optimizing control. *Comp. Aided Chem. Eng.* 38: 511–516.
- [47] Gao W, Wenzel S, Engell S. 2015: Integration of Gradient Adaptation and Quadratic Approximation in Real-Time Optimization. *Proc. 34th Chinese Control Conference:* 2780–2785.
- [48] Gao W, Wenzel S, Engell S. 2016: A reliable modifier-adaptation strategy for real-time optimization. *Comput. Chem. Eng.* 91: 318–328.
- [49] Garud SS, Karimi IA, Kraft M. 2017: Smart sampling algorithm for surrogate model development. *Comp. Chem. Eng.* 96: 103–114.
- [50] Gamrath G, Anderson D, Bestuzheva K, Chen WK, Eifler L, Gasse M, Gemander P, Gleixner A, Gottwald L, Halbig K, Hendel G, Hojny C, Koch T, le Bodic P, Maher SJ, Matter F, Miltenberger M, Mühmer E, Müller B, Pfetsch M, Schlösser F, Serrano F, Shinano Y, Tawfik C, Vigerske S, Wegscheider F, Weninger D, Witzig J. 2020: The SCIP Optimization Suite 7.0. ZIB-Report. Zuse Institute Berlin.
- [51] Gelfgat AY, Yarin AL, Bar-Yoseph PZ. 2003: Dean vortices-induced enhancement of mass transfer through an interface separating two immiscible liquids. *Phys. Fluids.* 15: 330–347.
- [52] Gertig C, Fleitmann L, Schilling J, Leonhard K, Bardow A. 2020: Rx-COSMO-CAMPD: enhancing reactions by integrated computer-aided design of solvents and processes based on quantum chemistry. *Chem. Ing. Tech.* 92: 1489–1500.
- [53] Google. 2021: Google Docs. [Online], cited 2021 02 23. Available from: <https://www.google.com/docs/about/>.
- [54] Gottu Mukkula AR, Ahmad A, Engell S. 2019: Start-up and Shut-down Conditions for Iterative Real-Time Optimization Methods. 6th Indian Control Conference IEEE: 158–163.
- [55] Gottu Mukkula AR, Engell S. 2020: Guaranteed Model Adequacy for Modifier Adaptation With Quadratic Approximation. *Proc. 2020 Eur. Control Conf. (ECC), IEEE:* 1037–1042.
- [56] Grimes B. 2012. Population balance model for batch gravity separation of crude oil and water emulsions. Part I: Model formulation. *J. Disp. Sci. Technol.* 33: 578–590.
- [57] Gross J, Sadowski G. 2001: Perturbed-Chain SAFT: an equation of state based on a perturbation theory for chain molecules. *Ind. Eng. Chem. Res.* 40: 1244–1260.
- [58] Grossmann IE, Westerberg AW. 2004: Research challenges in process systems engineering. *AIChE J.* 46: 1700–1703.
- [59] Grossmann IE, Caballero JA, Yeomans H. 2000: Advances in mathematical programming for the synthesis of process systems. *Lat. Am. Appl. Res.* 30: 263–284.
- [60] Hameed MS, Saleh MM. 2003: Mass transfer into liquid falling film in straight and helically coiled tubes. *Intern. J. Heat Mass Transf.* 46: 1715–1724.
- [61] Hampel FR. 1974: The influence curve and its role in robust estimation. *J. Am. Stat. Assoc.* 69: 383–393.
- [62] Hangos K, Cameron I. 2007: *Process Modelling and Model Analysis*. London: Academic Press.
- [63] Harmsen GJ. 2007: Reactive distillation: the front-runner of industrial process intensification A full review of commercial applications, research, scale-up, design and operation. *Chem. Eng. Proc.* 46: 774–780.
- [64] Hartwich A, Marquardt W. 2010: Dynamic optimization of the load change of a large-scale chemical plant by adaptive single shooting. *Comp. Chem. Eng.* 34: 1873–1889.

- [65] Hentschel B, Peschel A, Freund H, Sundmacher K. 2014a: Simultaneous design of the optimal reaction and process concept for multiphase systems. *Chem. Eng. Sci.* 115:69–87.
- [66] Hentschel B, Peschel A, Xie M, Vogelpohl C, Sadowski G, Freund H, Sundmacher K. 2014b: Model-based prediction of optimal conditions for 1-octene hydroformylation. *Chem. Eng. Sci.* 15: 58–68.
- [67] Hentschel B, Kiedorf G, Gerlach M, Hamel C, Seidel-Morgenstern A, Freund H, Sundmacher K. 2015: Model-based identification and experimental validation of the optimal reaction route for the hydroformylation of 1-dodecene. *Ind. Eng. Chem. Res.* 54: 1755–1765.
- [68] Hernandez R, Dreimann J, Vorholt A, Behr A, Engell S. 2018: Iterative real-time optimization scheme for optimal operation of chemical processes under uncertainty: proof of concept in a miniplant. *Ind. Eng. Chem. Res.* 57: 8750–8770.
- [69] Hoffmann C, Weigert J, Esche E, Repke JU. 2020: A pressure-driven, dynamic model for distillation columns with smooth reformulations for flexible operation. *Comp. Chem. Eng.* 142: 107062.
- [70] Hoffmann C, Illner M, Müller D, Esche E, Wozny G, Biegler LT, Repke JU 2016: Moving-horizon state estimation with gross error detection for a hydroformylation miniplant. *Comp. Aided Chem. Eng.* 38: 1485–1490.
- [71] Hohl L, Paul N, Kraume M. 2015: Dispersion conditions and drop size distributions in stirred micellar multiphase systems. *Chem. Eng. Proc.* 99: 149–154.
- [72] Horst R, Tuy H. 1993: *Global Optimization: Deterministic Approaches*. 2nd ed. Springer-Verlag.
- [73] Huang R. 2010: Nonlinear model-predictive control and dynamic real time optimization for large-scale processes, Pittsburgh, PA: Carnegie Mellon University.
- [74] Illner M. 2020: Rigorous analysis of reactive microemulsion systems for process design and operation, Dr.-Ing. Dissertation, Technische Universität Berlin.
- [75] Illner M, Müller D, Esche E, Pogrzeba T, Schmidt M, Schomäcker R, Repke JU. 2016: Hydroformylation in microemulsions: proof of concept in a miniplant. *Ind. Eng. Chem. Res.* 55: 8616–8626.
- [76] Illner M, Esche E, Repke JU. 2018a. Optimal control of surfactant containing multiphase systems-challenges and solution strategies for a stable mini-plant operation. *Comp. Aided Chem. Eng.* 44: 739–744.
- [77] Illner M, Schmidt M, Pogrzeba T, Urban C, Esche E, Schomäcker R, Repke, JU 2018b: Palladium-catalyzed methoxycarbonylation of 1-dodecene in a two-phase system: the path toward a continuous process. *Ind. Eng. Chem. Res.* 57: 8884–8894.
- [78] Ito H. 1959: Friction factors for turbulent flow in curved pipes. *ASME J. Basic Eng.* 81: 123–134.
- [79] Jamshidi N, Farhadi M, Ganji DD, Sedighi K. 2013: Experimental analysis of heat transfer enhancement in shell and helical tube heat exchangers. *Appl. Therm. Eng.* 51: 644–652.
- [80] Jang SS, Joseph B, Mukai H. 1987: On-line optimization of constrained multivariable chemical processes. *AIChE J.* 33: 26–35.
- [81] Janus T, Cegla M, Barkmann S, Engell S. 2019: Optimization of a hydroformulation process in a thermomorphic solvent system using a commercial steady-state process simulator and a memetic algorithm. *Comp. Aided Chem. Eng.* 46: 469–474.
- [82] Jäschke J, Skogestad S. 2011: Nco tracking and self-optimizing control in the context of real-time optimization. *J. Proc. Control* 21: 1407–1416.
- [83] Jepsen JC 1970: Mass transfer in two-phase flow in horizontal pipelines. *AIChE J.* 16: 705–711.
- [84] Jeschke D. 1925: Heat transfer and pressure loss in coiled pipes. *Ergänzungsheft Z. VDI.* 68: 24–28.

- [85] Jin Y, Li J, Du W, Qian F. 2016: Adaptive sampling for surrogate modelling with artificial neural network and its application in an industrial cracking furnace. *Can. J. Chem. Eng.* 94: 262–272.
- [86] Jokiel M, Wagner LM, Mansour M, Kaiser NM, Zähringer K, Janiga G, Nigam KDP, Thevenin D, Sundmacher K. 2017: Measurement and simulation of mass transfer and backmixing behavior in a gas-liquid helically coiled tubular reactor. *Chem. Eng. Sci.* 170: 410–421.
- [87] Jokiel M, Kaiser NM, Kováts P, Mansour M, Zähringer K, Nigam KD, Sundmacher K. 2019: Helically coiled segmented flow tubular reactor for the hydroformylation of long-chain olefins in a thermomorphic multiphase system. *Chem. Eng. J.* 377: 120060.
- [88] Jokiel M, Rätze KHG, Kaiser NM, Künnemann KU, Hollenbeck JP, Dreimann JM, Vogt D, Sundmacher K. 2019b: Miniplant-scale evaluation of a semibatch-continuous tandem reactor system for the hydroformylation of long-chain olefins. *Ind. Eng. Chem. Res.* 58:2471–2480.
- [89] Jokiel M. 2020: Optimale Reaktionsführung durch Reaktor-Tandems am Beispiel der Hydroformylierung von 1-Dodecen. Dr.-Ing. Dissertation, Otto-von-Guericke Universität Magdeburg.
- [90] Kaiser NM, Jokiel M, McBride K, Flassig RJ, Sundmacher K. 2017: Optimal reactor design via flux profile analysis for an integrated hydroformylation process. *Ind. Eng. Chem. Res.* 56: 11507–11518.
- [91] Kaiser NM, Flassig RJ, Sundmacher K. 2016: Probabilistic reactor design in the framework of elementary process functions. *Comp. Chem. Eng.* 94:45–59.
- [92] Kaiser NM, Flassig RJ, Sundmacher K. 2018: Reactor-network synthesis via flux profile analysis. *Chem. Eng. J.* 335: 1018–1030.
- [93] Kaiser NM, Freund H. 2019: A multimodular pseudo heterogeneous model framework for optimal design of catalytic reactors exemplified by methanol synthesis. *Chem. Eng. Sci.* 206: 401–423.
- [94] Kaiser NM. 2019: Dynamic Optimization Based Reactor Synthesis and Design under Uncertainty for Liquid Multiphase Processes. Ph.D. Dissertation, Otto-von-Guericke-Universität Magdeburg.
- [95] Keßler T, Mertens N, Kunde C, Nentwich C, Michaels D, Engell S, Kienle A. 2017: Efficient global optimization of a novel hydroformylation process. *Comp. Aided Chem. Eng.* 40: 2113–2118.
- [96] Keßler T, Kunde C, Mertens N, Michaels D, Kienle A. 2018: Global optimization of distillation columns using surrogate models. *SN Appl. Sci.* 1: 11.
- [97] Keßler T, Kunde C, McBride K, Mertens N, Michaels D, Sundmacher K, Kienle A. 2019: Global optimization of distillation columns using explicit and implicit surrogate models. *Chem. Eng. Sci.* 197: 235–245.
- [98] Khot P, Mansour M, Thévenin D, Nigam KD, Zähringer K. 2019: Improving the mixing characteristics of coiled configurations by early flow inversion. *Chem. Eng. Res. Des.* 146: 324–335.
- [99] Kiedorf G, Hoang DM, Müller A, Jörke A, Markert J, Arellano-Garcia H, Seidel-Morgenstern A, Hamel C. 2014: Kinetics of 1-dodecene hydroformylation in a thermomorphic solvent system using rhodium-biphosphos catalyst. *Chem. Eng. Sci.* 115: 31–48.
- [100] Kılınç MR, Sahinidis NV. 2018: Exploiting integrality in the global optimization of mixed-integer nonlinear programming problems with BARON. *Opt. Methods and Software* 33: 540–562.
- [101] Klamt A. 1995: Conductor-like screening model for real solvents: a new approach to the quantitative calculation of solvation phenomena. *J. Phys. Chem.* 99: 2224–2235.
- [102] Kockmann N. 2020: Design and operation of a tubular reactor with narrow residence time distribution. *Chem. Ing. Techn.* 92: 685–691.

- [103] Kováts P, Pohl D, Thévenin D, Zähringer K. 2018: Optical determination of oxygen mass transfer in a helically-coiled pipe compared to a straight horizontal tube. *Chem. Eng. Sci.* 190: 273–285.
- [104] Kováts P, Martins FJ, Mansour M, Thévenin D, Zähringer K. 2020a: Tomographic PIV measurements and RANS simulations of secondary flows inside a horizontally positioned helically coiled tube. *Exp. Fluids*. 61: art. 117.
- [105] Kováts P, Velten C, Mansour M, Thévenin D, Zähringer K. 2020b: Mixing characterization in different helically coiled configurations by laser-induced fluorescence. *Exp. Fluids* 61: 203.
- [106] Krämer S, Gesthuisen R, Engell S. 2005: Fixed structure multirate state estimation. In *Proceedings 2005 American. Control Conf.*: 4613–4618.
- [107] Kraus R, Fillinger S, Tolksdorf G, Minh D, Merchan-Restrepo V, Wozny G. 2014: Improving model and data integration using MOSAIC as central data management platform. *Chem. Ing. Techn.* 86: 1130–1136.
- [108] Kraus R. 2015: Concepts and Implementation of Collaborative Modeling in MOSAIC. Dr.-Ing. Dissertation Technische Universität Berlin.
- [109] Krone D, Esche E, Asprión N, Skiborowski M, Repke JU. 2020: Conceptual design based on superstructure optimization in GAMS with accurate thermodynamic models. *Comp. Aided Chem. Eng.* 48: 15–20.
- [110] Kröner A, Kronseder T, Engl G, Stryk OV. 2001: Dynamic optimization for air separation plants. *Comp. Aided Chem. Eng.* 9: 433–438.
- [111] Krstić M, Wang HH. 2000: Stability of extremum seeking feedback for general nonlinear dynamic systems. *Automatica*. 36: 595–601.
- [112] Kubair V, Kuloor NR. 1966: Heat transfer to Newtonian fluids in coiled pipes in laminar flow. *Int. J. Heat Mass Transf.* 9: 63–75.
- [113] Kulic E, Rhodes E. 1974: Chemical mass transfer in co-current gas-liquid slug flow in helical coils. *Can. J. Chem. Eng.* 52: 114–116.
- [114] Kumar V, Aggarwal M, Nigam KD. 2006: Mixing in curved tubes. *Chem. Eng. Sci.* 61: 5742–5753.
- [115] Kumar V, Mridha M, Gupta AK, Nigam KD. 2007: Coiled flow inverter as a heat exchanger. *Chem. Eng. Sci.* 62: 2386–2396.
- [116] Kunde C, Michaels D, Micovic J, Lutze P, Górak A, Kienle A. 2016: Deterministic global optimization in conceptual process design of distillation and melt crystallization. *Chem. Eng. Proc.: Proc. Intensif.* 99: 132–142.
- [117] Kunde C. 2017: Global Optimization in Conceptual Process Design. Dr.-Ing. Dissertation. Otto-von-Guericke University Magdeburg.
- [118] Kunde C, Kienle A. 2018: Global optimization of multistage binary separation networks. *Chem. Eng. Proc. – Proc. Intensif.* 131: 164–177.
- [119] Kunde C, Keßler T, Linke S, McBride K, Sundmacher K, Kienle A. 2019: Surrogate modeling for liquid–liquid equilibria using a parameterization of the binodal curve. *Processes*. 7: 753.
- [120] Kuntsche S. 2013: Modular Model Specification on the Documentation Level. Concepts and Application in a Web-Based Modeling Environment. Technische Universität Berlin.
- [122] Lang Y, Malacina A, Biegler LT, Madsen JI, Zitney SE. 2009: Reduced order model based on principal component analysis for process simulation and optimization. *Energy Fuels*. 23: 1685–1706.
- [122] Lehr F, Millies M, Mewes D. 2002: Bubble-Size distributions and flow fields in bubble columns. *AIChE J.* 48: 2426–2443.
- [123] Liao Y, Lucas D. 2010: A literature review on mechanisms and models for the coalescence process of fluid particles. *Chem. Eng. Sci.* 65: 2851–2864.

- [124] Liberti L. 2008: Introduction to global optimization. Technical Report. Palaiseau: Ecole Polytechnique, LIX.
- [125] Liesche G, Schack D, Rätze KH, Sundmacher K. 2018: Thermodynamic Network Flow Approach for Chemical Process Synthesis. *Comp. Aided Chem. Eng.* 43: 881–886.
- [126] Liesche G, Schack D, Sundmacher K. 2019: The FluxMax approach for simultaneous process synthesis and heat integration: production of hydrogen cyanide. *AIChE J.* 65: 16554.
- [127] López-Negrete R, Biegler LT. 2012: A moving horizon estimator for processes with multirate measurements: a nonlinear programming sensitivity approach. *J. Proc. Control.* 22: 577–588.
- [128] Mansour M, Liu Z, Janiga G, Nigam KD, Sundmacher K, Thévenin D, Zähringer, K. 2017: Numerical study of liquid-liquid mixing in helical pipes. *Chem. Eng. Sci.* 172: 250–261.
- [129] Mansour M, Janiga G, Nigam KD, Thévenin D, Zähringer K. 2018: Numerical study of heat transfer and thermal homogenization in a helical reactor. *Chem. Eng. Sci.* 177: 369–379.
- [130] Mansour M, Thévenin D, Nigam KD, Zähringer K. 2019. Generally-valid optimal Reynolds and Dean numbers for efficient liquid-liquid mixing in helical pipes. *Chem. Eng. Sci.* 201, 382–385.
- [131] Mansour M, Khot P, Thévenin D, Nigam KD, Zähringer, K. 2020a: Optimal Reynolds number for liquid-liquid mixing in helical pipes. *Chem. Eng. Sci.* 214: 114522.
- [132] Mansour M, Landage A, Khot P, Nigam KD, Janiga G, Thévenin D, Zähringer, K. 2020b: Numerical study of gas–liquid two-phase flow regimes for upward flow in a helical pipe. *Ind. Eng. Chem. Res.* 59: 3873–3886.
- [133] Mansour M, Thévenin D, Zähringer K. 2020c: Numerical study of flow mixing and heat transfer in helical pipes, coiled flow inverters and a novel coiled configuration. *Chem. Eng. Sci.* 221: 115690.
- [134] Mansour M, Zähringer K, Nigam KD, Thévenin D, Janiga G. 2020d: Multi-objective optimization of liquid-liquid mixing in helical pipes using genetic algorithms coupled with computational fluid dynamics. *Chem. Eng. J.* 391: art. 123570.
- [135] Marchisio D, Fox R. 2007: *Multiphase Reacting Flows: Modelling and Simulation*. Springer Verlag.
- [136] Marchisio D, Fox R. 2013: *Computational Models for Polydisperse Particulate and Multiphase Systems*. Cambridge University Press.
- [137] Marchisio D, Vigil R, Fox R. 2003: Quadrature method of moments for aggregation-breakage processes. *J. Coll. Interf. Sci.* 258:322–334.
- [138] Marchetti AG, François G, Faulwasser T, Bonvin D. 2016: Modifier adaptation for real-time optimization-methods and applications. *Processes.* 4: Art. No. 55.
- [139] Maria DB Foundation. 2021: MariaDB Server: the open source relational database. [Online], cited 2021 03 01. Available from: <https://mariadb.org>.
- [140] Markert J, Brunsch Y, Munkelt T, Kiedorf G, Behr A, Hamel C, Seidel-Morgenstern A. 2013: Analysis of the reaction network for the Rh-catalyzed hydroformylation of 1-dodecene in a thermomorphic multicomponent solvent system. *Appl. Catal. A: General.* 462–463: 287–295.
- [141] Maußner J, Dreiser C, Wachsen O, Freund H. 2019: Systematic model-based design of tolerant chemical reactors. *J. Adv. Manuf. Proc.* 1:e10024.
- [142] McBride K, Kaiser NM, Sundmacher K. 2017: Integrated reaction-extraction process for the hydroformylation of long-chain alkenes with a homogeneous catalyst. *Comp. Chem. Eng.* 105: 212–223.
- [143] McGraw R. 1997: Description of aerosol dynamics by the quadrature method of moments. *Aerosol Sci. Technol.* 27: 255–265.
- [144] Medeiros de Souza L, Temmel E, Janiga G, Seidel-Morgenstern A, Thévenin D. 2021: Simulation of a batch crystallizer using a multi-scale approach in time and space. *Chem. Eng. Sci.* 232: 1–14.

- [145] Mencarelli L, Chen Q, Pagot A, Grossmann IE. 2020: A review on superstructure optimization approaches in process system engineering. *Comput. Chem. Eng.* 136: 106808.
- [146] Merchan VA, Tolksdorf G, Kraus R, Wozny G. 2014: Extending documentation-based models towards an efficient integration into commercial process simulators. *Chem. Ing. Techn.* 86: 1117–1129.
- [147] Merchan VA, Esche E, Fillinger S, Tolksdorf G, Wozny G. 2016: Computer-aided process and plant development. A review of common software tools and methods and comparison against an integrated collaborative approach. *Chem. Ing. Techn.* 88: 50–69.
- [148] Mertens N, Kunde C, Kienle A, Michaels D. 2016: A reformulation strategy for deterministic global optimization of ideal multi-component distillation processes. *Comp. Aided Chem. Eng.* 38: 691–696.
- [149] Mertens N, Kunde C, Kienle A, Michaels D. 2018: Monotonic reformulation and bound tightening for global optimization of ideal multi-component distillation columns. *Opt. Eng.* 19: 479–514.
- [150] Michalska H, Mayne DQ. 1995: Moving horizon observers and observer-based control. *IEEE Transact. Autom. Contr.* 40: 995–1006.
- [151] Microsoft. 2021: Microsoft Teams. [Online], cited 2021 2 23. Available from: <https://www.microsoft.com/de-de/microsoft-teams/collaboration>.
- [152] Micovic J, Beierling T, Lutze P, Sadowski G, Górak A. 2013: Design of hybrid distillation/melt crystallisation processes for separation of close boiling mixtures. *Chem. Eng. Proc.: Proc. Intensif.* 67: 16–24.
- [153] Misener R, Floudas CA. 2014: ANTIGONE: Algorithms for coNTinuous / Integer Global Optimization of Nonlinear Equations. *J. Global Opt.* 59: 503–526.
- [154] Misra A, Bonamy C, Medeiros de Souza L, Hohl L, Illner M, Kraume M, Repke JU, Thévenin, D. 2018: A multi-fluid approach to simulate separation of liquid-liquid systems in a gravity settler. *Comp. Aided Chem. Eng.* 43: 31–36.
- [155] Misra A, Medeiros de Souza L, Illner M, Hohl L, Kraume M, Repke JU, Thévenin D. 2017: Simulating separation of a multiphase liquid-liquid system in a horizontal settler by CFD. *Chem. Eng. Sci.* 167: 242–250.
- [156] Mitsos A, Aspiron N, Floudas CA, Bortz M, Baldea M, Bonvin D, Caspari A, Schäfer P. 2018: Challenges in process optimization for new feedstocks and energy sources. *Comp. Chem. Eng.* 113:209–221.
- [157] Mittelbach F. 2021: The LATEX Project. [Online], cited 2021 03 03. Available from: <https://www.latex-project.org/latex3/>.
- [158] Modelica. 2021: Modelica Association. [Online], cited 2021 02 23. Available from: <https://www.modelica.org>.
- [159] Moulin P, Rouch JC, Serra C, Clifton MJ, Aptel P. 1996: Mass transfer improvement by secondary flows: dean vortices in coiled tubular membranes. *J. Memb. Sci.* 114: 235–244.
- [160] Mridha M, Nigam KD. 2008: Coiled flow inverter as an inline mixer. *Chem. Eng. Sci.* 63: 1724–1732.
- [161] Müller C, Zähringer K, Thévenin D. 2021: Experimental characterization of mixing and flow field in the liquid slugs of a gas-liquid two-phase flow in a helically coiled reactor. *Experiments in Fluids* 62: 190.
- [162] Müller D, Illner M, Esche E, Pogrzeba T, Schmidt M, Schomäcker R, Biegler T, Wozny G, Repke JU. 2017: Dynamic real-time optimization under uncertainty of a hydroformylation mini-plant. *Comp. Chem. Eng.* 106: 836–848.
- [163] Nentwich C, Engell S. 2019: Surrogate modeling of phase equilibrium calculations using adaptive sampling. *Comp. Chem. Eng.* 126: 204–217.

- [164] Nentwich C, Varela C, Engell S. 2019a: Optimization of chemical processes applying surrogate models for phase equilibrium calculations. Proceedings 2019 Intern. Joint Conf. on Neural Networks: 1–8.
- [165] Nentwich C, Winz J, Engell S. 2019b: Surrogate modeling of fugacity coefficients using adaptive sampling. *Ind. Eng. Chem. Res.* 58: 18703–18716.
- [166] Nentwich C. 2021: Surrogate Modeling of Fugacity Coefficients Using Adaptive Sampling. Dr.-Ing. Dissertation, TU Dortmund, Fakultät Bio- und Chemieingenieurwesen. to be published in Shaker Verlag, Aachen.
- [167] Nentwich C, Engell S. 2016: Application of surrogate models for the optimization and design of chemical processes. Proc. 2016 Int. Joint Conf. on Neural Networks (IJCNN): 1291–1296.
- [168] Nicholson B, López-Negrete R, Biegler LT. 2014: On-line state estimation of nonlinear dynamic systems with gross errors. *Comp. Chem. Eng.* 70: 149–159.
- [169] Oracle. 2021: Java SE Development Kit 11 Downloads. [Online], cited 2021 03 01. Available from: <https://www.oracle.com/java/technologies/javase-jdk11-downloads.html>.
- [170] Özyurt DB, Pike RW. 2004: Theory and practice of simultaneous data reconciliation and gross error detection for chemical processes. *Comp. Chem. Eng.* 28: 381–402.
- [171] Passalacqua A, Heylmu J, Icardi M, Madadi E, Bachant P, Hu X, Weaver J. 2020: OpenQBMM/ doi:10.5281/zenodo.591651.
- [172] Patwardhan SC, Narasimhan S, Jagadeesan P, Gopaluni B, Shah SL. 2012: Nonlinear Bayesian state estimation: a review of recent developments. *Contr. Eng. Pract.* 20: 933–953.
- [173] Peschel A, Freund H, Sundmacher K. 2010: Methodology for the design of optimal chemical reactors based on the concept of elementary process functions. *Ind. Eng. Chem. Res.* 49: 10535–10548.
- [174] Peschel A, Hentschel B, Freund H, Sundmacher K. 2011: Optimal reactor design for the hydroformylation of long chain alkenes in biphasic liquid systems. 21st Europ. Symp. Comp. Aided Proc. Eng. 29: 1246–1250.
- [175] Peschel A, Hentschel B, Freund H, Sundmacher K. 2012a: Design of optimal multiphase reactors exemplified on the hydroformylation of long chain alkenes. *Chem. Eng. J.* 188: 126–141.
- [176] Peschel A, Jörke A, Sundmacher K, Freund H. 2012b: Optimal reaction concept and plant wide optimization of the ethylene oxide process. *Chem. Eng. J.* 207–208: 656–674.
- [177] Pietschak A, Kaiser M, Freund H. 2018: Tailored catalyst pellet specification for improved fixed-bed transport characteristics: a shortcut method for the model-based reactor design. *Chem. Eng. Res. Des.* 137: 60–74.
- [178] Prabhanjan DG, Rennie TJ, Raghavan GS. 2004: Natural convection heat transfer from helical coiled tubes. *Int. J. Thermal Sci.* 43: 359–365.
- [179] Prince M, Blanch H. 1990: Bubble coalescence and break-up in air-sparged bubble columns. *AIChE J.* 36: 1485–1499.
- [180] Process Systems Enterprise Ltd. 2021: gPROMS ModelBuilder. [Online], cited 2021 03 14. Available from: <https://psenterprise.com/products/gproms/modelbuilder>.
- [181] Puranik Y, Sahinidis NV. 2017: Domain reduction techniques for global NLP and MINLP optimization. *Constraints.* 22: 338–376.
- [182] Quin LRE. 2016: Extensible Markup Language (XML). [Online], cited 2021 2 23. Available from: <https://www.w3.org/XML/>.
- [183] Rätze KHG, Jokiel M, Kaiser NM, Sundmacher K. 2019: Cyclic operation of a semi-batch reactor for the hydroformylation of long-chain olefins and integration in a continuous production process. *Chem. Eng. J.* 377: 120453.
- [184] Rawlings JB, Bonne D, Jorgensen JB, Venkat AN, Jorgensen SB. 2008: Unreachable setpoints in model predictive control. *IEEE Transact. Automat. Control.* 53: 2209–2215.

- [185] Rawlings JB, Amrit R. 2009: Optimizing process economic performance using model predictive control. In: Magni L, Raimondo DM, Allgöwer F, (Eds.) *Nonlinear Model Predictive Control*. Berlin, Heidelberg: Springer: 119–138.
- [186] Reepmeyer F, Repke JU, Wozny G. 2004: Time optimal start-up strategies for reactive distillation columns. *Chem. Eng. Sci.* 59: 4339–4347.
- [187] Rogers GF, Mayhew YR. 1964: Heat transfer and pressure loss in helically coiled tubes with turbulent flow. *Int. J. Heat Mass Transf.* 7: 1207–1216.
- [188] Rosa LPS, Pontes KV, Costa GMN, Penteado AT, Esche E, Repke JU. 2020: An equation-oriented novel approach for modeling the falling film absorber using rigorous thermodynamic and transport description. *Chem. Eng. Res. Des.* 159: 179–194.
- [189] Sarabia D, de Prada C, Gómez E, Gutierrez G, Cristea S, Sola J, de Prada C. 2012: Data reconciliation and optimal management of hydrogen networks in a petrol refinery. *IFAC Proceed.* 20: 343–354.
- [190] Saxena AK, Nigam KD. 1984: Coiled configuration for flow inversion and its effect on residence time distribution. *AIChE J.* 30: 363–368.
- [191] Schack D, Liesche G, Sundmacher K. 2019: Simultaneous heat and mass flow optimization of a distillation column applying the FluxMax approach. *Chem. Eng. Trans.* 76: 337–342.
- [192] Schack D, Liesche G, Sundmacher K. 2020a: The FluxMax approach: simultaneous flux optimization and heat integration by discretization of thermodynamic state space illustrated on methanol synthesis process. *Chem. Eng. Sci.* 215: 115382.
- [193] Schack D, Jastram A, Liesche G, Sundmacher K. 2020b: Energy-efficient distillation processes by additional heat transfer derived from the FluxMax approach. *Front. Energy Res.* 8:134.
- [194] Schiller L, Naumann A. 1935: A drag coefficient correlation. *VDI Z.* 77: 318–320.
- [195] Schmidt EF. 1967: Heat transfer and pressure loss in pipe coils. *Chem. Ing. Techn.* 39: 781–789.
- [196] Seban RA, McLaughlin EF. 1963: Heat transfer in tube coils with laminar and turbulent flow. *Int. J. Heat Mass Transf.* 6: 387–395.
- [197] Shah AK, Sharma MM. 1973: Mass transfer in a liquid-liquid coil contactor. *Can. J. Chem. Eng.* 51: 772–775.
- [198] Sharma L, Nigam KD, Roy S. 2017: Single phase mixing in coiled tubes and coiled flow inverters in different flow regimes. *Chem. Eng. Sci.* 160: 227–235.
- [199] Skogestad S. 2000: Self-optimizing control: the missing link between steady-state optimization and control. *Comp. Chem. Eng.* 24: 569–575.
- [200] Steimel J. 2015: Model-based Conceptual Design and Optimization of Continuous Chemical Processes under Uncertainties. Dr.-Ing Dissertation, Technische Universität Dortmund, Shaker Verlag, Aachen.
- [201] Steimel J, Engell S. 2015: Conceptual design and optimization of chemical processes under uncertainty by two-stage programming. *Comp. Chem. Eng.* 81: 200–217.
- [202] Steimel J, Harrmann M, Schembecker G, Engell S. 2014: A framework for the modeling and optimization of process superstructures under uncertainty. *Chem. Eng. Sci.* 115: 225–237.
- [203] Steimel J, Engell S. 2016: Optimization-based support for process design under uncertainty: a case study. *AIChE J.* 62: 3404–3419.
- [204] Sundmacher K, Freund H. 2010: Chemical process design: moving matter elements along optimal travel routes in the thermodynamic state space. Talk presented at PSE Asia: The 5th Intern. Symp. on Design, Operation and Control of Chem. Proc. Singapore.
- [205] Tatiraju S, Soroush M, Ogunnaike BA. 1999: Multirate nonlinear state estimation with application to a polymerization reactor. *AIChE J.* 45: 769–780.

- [206] Thévenin D, Janiga G. 2008: *Optimization and Computational Fluid Dynamics*. Springer Verlag.
- [207] Tolksdorf G, Esche E, Wozny G, Repke JU. 2018: Customized code generation based on user specifications for simulation and optimization. *Comp. Chem. Eng.* 121: 670–684.
- [208] Urselmann M, Barkmann S, Sand G, Engell S. 2011: Optimization-based design of reactive distillation columns using a memetic algorithm. *Comput. Chem. Eng.* 35: 787–805.
- [209] Vashisth S, Kumar V, Nigam KD. 2008: A review on the potential applications of curved geometries in process industry. *Ind. Eng. Chem. Res.* 47: 3291–3337.
- [210] Viswanathan J, Grossmann IE. 1993: Optimal feed locations and number of trays for distillation columns with multiple feeds. *Ind. Eng. Chem. Res.* 32: 2942–2949.
- [211] Vogl C, Paetzold E, Fischer C, Kragl U. 2005: Highly selective hydroformylation of internal and terminal olefins to terminal aldehydes using a rhodium-BIPHEPHOS-catalyst system. *J. Mol. Catal. A: Chem.* 232: 41–44.
- [212] Wächter A, Biegler LT. 2006: On the implementation of an interior-point filter line-search algorithm for large-scale nonlinear programming. *Math. Program.* 106: 25–57.
- [213] Waltermann T, Grueters T, Muenchrath D, Skiborowski M. 2020: Efficient optimization-based design of energy-integrated azeotropic distillation processes. *Comp. Chem. Eng.* 133: 106676.
- [214] Wang L, Li P, Wozny G, Wang S. 2003: A start-up model for simulation of batch distillation starting from a cold state. *Comp. Chem. Eng.* 27: 1485–1497.
- [215] Wardle K, Weller H. 2013: Hybrid multiphase CFD solver for coupled dispersed/segregated flows in liquid-liquid extraction. *Int. J. Chem. Eng.* 128936.
- [216] Weigert J, Illner M, Esche E, Repke JU. 2018: Development of a state estimation environment for the optimal control of a mini-plant for the hydroformylation in microemulsions. *Chem. Eng. Trans.* 70: 973–978.
- [217] Winz J, Engell S. 2021. Optimization based sampling for gray-box modeling using a modified upper confidence bound acquisition function. *Comp. Aided Chem. Eng.* 50: 953–958.
- [218] Xie M, Freund H. 2018a: Fast synthesis of optimal chemical reactor networks based on a universal system representation. *Chem. Eng. Proc. – Proc. Intensif.* 123: 280–290.
- [219] Xie M, Freund H. 2018b: Rigorous design of multiphase reactors: identification of optimal conditions for mass transfer limited reactions. *Chem. Eng. Proc. – Proc. Intensif.* 124: 174–185.
- [220] Yeomans H, Grossmann IE. 1999: A systematic modeling framework of superstructure optimization in process synthesis. *Comp. Chem. Eng.* 23: 709–731.
- [221] Zagajewski M, Behr A, Sasse P, Wittmann J. 2014: Continuously operated miniplant for the rhodium catalyzed hydroformylation of 1-dodecene in a thermomorphic multicomponent solvent system (TMS). *Chem. Eng. Sci.* 115: 88–94.
- [222] Zagajewski M. 2015: Planung, Bau und Betrieb einer Miniplant zur kontinuierlichen Hydroformylierung von 1-Dodecen in thermomorphen Mehrkomponenten-Lösungsmittelsystemen. Dr-Ing.Dissertation, Technische Universität Dortmund.

6 Integrated Process Design

Kai Sundmacher

6.1 Introduction

Chemical process design is a complex task because many decisions have to be taken on different levels of the process system hierarchy, that is, the molecular level, the phase level, the process unit level, and the overall process system level. Moreover, the design procedure has to be performed based on increasing levels of detail and depth of information for the procedure, which starts from the first chemical synthesis idea and ends at the final process flow sheet equipped. While computer-aided methods and tools supporting individual decision-making procedures are discussed in Chapter 5, Chapter 6 aims at presenting frameworks and workflows that enable the integration of these methods along the chemical process design pathway with a special focus on processes with liquid multiphase systems.

Section 6.2 is dedicated to general selection criteria for multiphase systems suitable for given target products or reactions to be performed. A methodology is presented that allows quantitative comparison of various types of phase systems during different stages of process design, without the need for extensive experts' knowledge. The complexity of the considered phase systems is reduced by the systematic application of questionnaires and key experiments. Thereby, process engineers are guided stepwise from the initial formulation of the problem and identification of constraints over the selection of required substrates, solvents, and additives to suitable process candidates. The whole procedure is cast into the modular computer-aided phase system selection (caPSS) framework which integrates several important aspects of process development: data acquisition, model generation, conceptual process design, flow sheet optimization, and evaluation regarding economic feasibility as well as Green Chemistry criteria.

The most important part of a liquid multiphase system, suitable for a specific homogeneously catalyzed reaction, is the identification of solvents wherein this reaction proceeds at both a high rate and high selectivity. Thus, the choice of one or multiple reaction solvent(s) is a key step in composing a powerful liquid multiphase system. Section 6.3 presents different approaches from quantum chemistry (QM) and thermodynamics to support the identification of reaction solvents. Screening of chemical equilibria or transition state barriers as a function of solvent polarizability provides insights into the reaction thermodynamics and kinetics, respectively. The methodologies presented in this section are well suited to generate a set of potential reaction solvent candidates that are combined with further solvents to obtain mixtures featuring a thermomorphic multiphase systems (TMS) behavior.

Section 6.4 discusses the integration of solvent design and process design. Usually, these two design tasks are performed sequentially, that is, first, a solvent is selected based on a limited number of desirable thermodynamic properties, and then a process is developed for this specific solvent. While computer-aided molecular design (CAMD) can aid in the selection of solvents that possess process-relevant solvent properties, only the simultaneous consideration of solvent and process design in an integrated computer-aided molecular and process design (CAMPD) framework ensures the identification of optimal process designs and operation points. In the last two decades, this realization led to the publication of several methodological developments in the scientific literature for which Section 6.4 provides an overview and illustrates key aspects in CAMD/CAMPD via selected examples.

According to the caPSS framework, one of the most important integration steps is the combination of phase system selection with model-based process synthesis. For this purpose, an integrated model-based process design methodology is presented in Section 6.5 which combines both aspects by making use of various sources of knowledge. The methodology involves an iterative workflow wherein suitable models are identified and calibrated, prior to the evaluation of the final process design, in terms of reaction and separation performance, sustainability, and economic potential. This iterative procedure repeatedly creates intermediate process design candidates based on the available information. In the case of high levels of uncertainty, model-based optimal experimental design (mboED) is used to improve the available data basis successively via carefully designed experiments.

6.2 Selection Criteria for Liquid Multiphase Systems

Karsten H. G. Rätze, Steffen Linke, Ariane Weber, Maresa Kempin,
Markus Illner, Reinhard Schomäcker, Anja Drews, Kai Sundmacher

6.2.1 Introduction

To this point, the potential of innovative liquid multiphase solvent systems for conveying chemical reactions have been demonstrated. Based on this, the development of novel chemical processes adhering to the principles of Green Chemistry is attainable. However, the adequate selection of the type of multiphase solvent system, the choice of respective compounds or additives, as well as process synthesis based on such systems remains challenging. This is mainly caused by the inherent complexity of multiphase solvent systems regarding thermodynamics, physicochemical properties, and strong interactions with reactive species. Furthermore, the selection and design of liquid multiphase systems directly affects process design in terms of required reaction equipment, separation unit sequences, and operation conditions.

Even though the reaction performance might be superior for a chosen phase system, the actual product separation and recycling of additives might hold severe obstacles, rendering a process economically infeasible or inoperable.

Considering the rather large chemical matrix of liquid multiphase systems, the necessity of an integrated process development already considering the feasibility of reaction and separation steps at an early stage and given economic and environmental constraints (Green Chemistry), process development expands to a large combinatorial problem. Given a desired target product or reaction, it is a priori unclear which multiphase solvent system is suited best. Finding optimal process variants is thus only attainable when profound knowledge on *all* considered rather complex phase systems as well as extensive comparative experimental studies is provided. This situation greatly inhibits process development and the application of such systems.

To overcome this hurdle, a holistic guideline for the systematic selection of liquid multiphase systems as reaction media and process design is presented in the following. As a major innovation, this methodology allows a quantitative comparison of multiple types of phase systems at all stages of process design, without demanding the contribution of or application by experts in the respective fields. Its application is thus designed for the industrial practitioner in the field of reaction engineering and process development, which demands fast and robust solution approaches at minimal use of resources.

To achieve this, the complexity of the considered phase systems is broken down to the systematic application of simplified questionnaires and easy to perform key experiments. The user is thus guided from the initial formulation of the problem and constraints over the selection of required substrates, solvents, and additives toward suitable process candidates in a stepwise manner at a possible minimum of required experimental effort. Simultaneously, questionnaires and key experiments already aim at identifying critical obstacles regarding the desired reaction performance, product separability, chemical stability, and operability of process candidates.

Regarding a holistic guideline, this is merged into a modular framework for the computer-aided Phase System Selection (caPSS), which systematically deploys the relevant steps for process development: data acquisition, model generation, conceptual process design, flow sheet optimization and evaluation regarding economic feasibility as well as Green Chemistry criteria. caPSS is fundamentally based on the developed methodologies and tools for the analysis, modeling, and application of phase systems. Based on these methodologies, the wrapping or deconstruction of the complex phase and reaction behavior of the investigated phase systems regarding process development is enabled and usability is increased.

The following outlines are hence restricted to the application of thermomorphic multiphase systems (TMS), microemulsion systems (MES), and Pickering emulsions (PE), which only represent a subset of possible reactive liquid multiphase systems. However, caPSS presents a major starting point for a holistic selection and design workflow for such systems and can readily be extended by adding information and

methods from respective experts for other solvent systems. As a major competing phase system, ionic liquids are mentioned by way of example for which several guidelines on their selection as solvents [19, 81] as well as for process design [63] are already available.

6.2.2 General Criteria for Phase System Selection

The general selection criteria are the first considerations after the problem statement and the chemical system definition. Independent of the selected phase system, these criteria or constraints need to be fulfilled so that they need to be evaluated in the first step. The constraints can be ordered from low effort for evaluation to higher expenditures, leading to four major steps as shown in Figure 6.1.



Figure 6.1: Steps for the general criteria for phase system selection.

First, the operation windows of temperature and pressure must be determined for both reaction and separation. Here, all chemicals involved in the chemical reaction are considered, that is, reactants, products, catalysts, and, if present, a ligand. Solvents are not of interest at this stage since solvent considerations are inherently phase system-specific. Melting points, boiling points, and the thermal decomposition temperature should be checked. The first lead for this information is material and safety data sheets (MSDSs). If this information is not available in the MSDSs, it should be checked if the pure components can be purchased commercially at an acceptable price to perform these rather simple experiments. If this is not possible, at least the boiling point and the melting point for reactants and products may be estimated using group contribution (GC) methods [23], while for common ligands the decomposition temperature is more relevant. Based on these data, a temperature window for operation can be roughly derived. Of course, this window may be varying for different unit operations: in a reactor, solid reactants may be unwanted, while for separation, crystallization could be an option. Regarding the pressure, the most important objective is to check the state of the reactants. The homogeneous catalyst is by definition dissolved in a liquid; therefore, all reactants need to be present in a liquid phase. Vaporous reactants may be condensed by pressure increase, or at least the gas solubility is increased for gaseous components such as synthesis gas. Deriving a pressure window from this consideration can be only done based on the expert's experience or by considering similar reactions.

Second, the miscibility of reactants should be investigated. If only one reactant is liquid within the operation window, this step can be skipped. Otherwise, it is worth studying the mutual solubilities preferably experimentally, or, if not possible, computationally using GC methods for activity coefficients (e.g., universal functional activity coefficient (UNIFAC)) or a quantum-chemical-based method such as conductor-like screening model for real solvents (COSMO-RS) [51].

Third, potential separation operations are screened for feasibility. The challenge is to separate desired products and side products from reactants and catalyst species. The simplest case is probably when the products are gaseous and can be withdrawn from the top of the reactor, as in the Ruhrchemie/Rhône-Poulenc process. This might be also achievable by distillation for some specific postreaction mixtures. If such a separation concept is worthy of consideration, the user of the methodology takes a shortcut to the systematic process design presented in Section 6.2.4. In many cases, however, this approach will not be possible, for example, due to temperature-sensitive components, and other separation techniques must be considered. Since, in the scope of this book, only liquid–liquid-based phase systems are considered, other separation techniques such as crystallization are not discussed here. In liquid–liquid-based separation, a “polarity check” must be performed for the components of interest. The goal is to estimate whether the components can be generally separated via splitting into two liquid phases. Such an estimation can be done using solubility parameters or COSMO σ -profiles. With respect to the catalyst, this polarity analysis can lead to the need to modify the ligand in order make a liquid–liquid separation feasible. A more detailed investigation cannot be conducted at this point because solvents have not yet been considered. The phase-system-specific considerations are presented in the following sections.

Finally, a rough economic analysis should be performed based on material prices. The prices P per mole for all N_{rea} reactants (rea), all N_{pro} products (pro), the catalyst (cat), and the ligand (lig) are identified in order to estimate an upper limit for the margin m per mole key reactant (key) via

$$m = X_{\text{key}} \cdot \sum_{j=1}^{N_{\text{pro}}} S_j \cdot \frac{|v_{\text{pro},j}|}{|v_{\text{key}}|} \cdot P_{\text{pro},j} - \sum_{i=1}^{N_{\text{rea}}} \frac{|v_{\text{rea},i}|}{|v_{\text{key}}|} \cdot P_{\text{rea},i} - L_{\text{cat}} \cdot P_{\text{cat}} - L_{\text{lig}} \cdot P_{\text{lig}}. \quad (6.1)$$

Here, the conversion X_{key} and the selectivity S for the desired product can be set to unity as best-case scenario or be guessed based on experience while the stoichiometric coefficients v are taken from the reaction scheme and one reactant is chosen as a key reactant for reference. The loss of the catalyst components L_i with $i \in \{\text{cat}, \text{lig}\}$ describes the amount of catalyst components which need to be replaced due to bleeding, deactivation, and decomposition. This replacement is done by a make-up stream in a steady-state process. Hence, the losses can be calculated from the make-up mole flux of the catalyst components and the mole flux of the key reactant using

$$L_i = \frac{\dot{n}_i}{\dot{n}_{\text{key}}}, \quad i \in \{\text{cat, lig}\}. \quad (6.2)$$

Of course, these losses cannot be determined with high certainty since they are highly dependent on the phase system and the specific process configuration applied. However, typical recovery rates for different phase systems can be found in the literature and in the case of TMS, MES, and PE, Table 4.18 provides such data. Eq. (6.1) is useful to estimate the economic potential of the selected reaction and indicates if catalyst recycling is economically necessary. Second, if the margin m is set to zero indicating a cost-covering performance, eq. (6.2) can be used to determine the order of magnitude needed for the recycling of the catalyst components. After deriving this order of magnitude, some phase systems could be discarded before advancing toward a more detailed investigation.

6.2.3 Feasibility and Constraints for Phase Systems Application and Key Experiments

The evaluation of the general criteria from the previous section limits the number of possible phase systems so that a finite set of phase system types can be investigated in more detail. Due to specific requirements for each phase system, the inclusion of a phase system in the set of feasible phase systems requires the preliminary consideration of key constraints as exemplified in Figure 6.2 and the execution of key experiments. In this section, possible preliminary considerations are discussed for three example phase systems, TMS, MES, and PE.

6.2.3.1 Thermomorphic Multiphase System

Some critical aspects must be considered for using TMS in homogeneous transition metal-catalyzed reactions. The chemical resistance of all components, especially the catalyst complex, toward the solvents and the substrates is essential. Of course, the solvents used must also be inert. The TMS technique has limitations regarding substrate concentration, amount of extractant, and limited ranges of reaction and separation temperatures (see Section 4.4). Additionally, the reaction mixture is rather diluted due to the presence of a second solvent, potentially lowering the space–time–yield. In some cases, the phase separation in the decanter is slow, leading to long residence times. In addition, the heating/cooling procedure of the reaction mixture is relatively energy-intensive.

Nevertheless, since homogeneous catalysis offers high selectivities and high catalyst activities under mild reaction conditions, it holds enormous future potential for the chemical industry. Provided an efficient recovery of the homogeneous

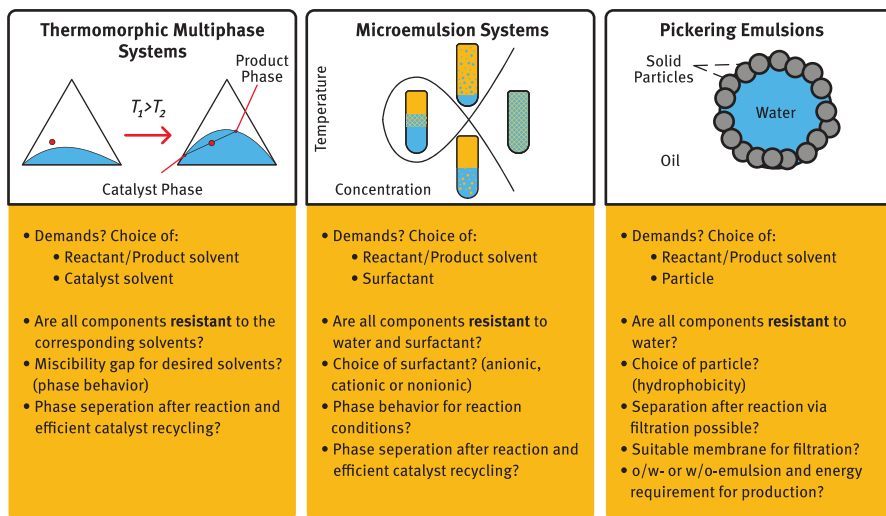


Figure 6.2: Overview of specific criteria of the considered phase systems.

catalyst, energy and waste treatment costs can be significantly reduced. The TMS technology offers an efficient way to carry out reactions under homogeneous conditions and simultaneously separate the catalyst while simultaneously being able to enable catalyst separation in a subsequent processing step.

Research on concepts such as TMSs requires significant experimental effort, implying high costs for a company in the chemical industry. The introduction of suitable key experiments can be essential to reduce the effort.

The initial point for the key experiments represents a homogeneously catalyzed reaction with an already known catalyst system. The first task is to find a suitable solvent for the reaction itself. Instead of performing experiments in the laboratory, the solvent can be found, on the one hand, by calculating the activity coefficients of the used substrates (via e.g., UNIFAC) and, on the other hand, by density functional theory (DFT) calculations of the catalyst system in different solvents. It is advisable to reduce the number of possible solvents to a minimum for this initial investigation, for instance, by a short list of suitable solvents. In the next step, the second solvent for separating catalyst and product has to be found. This solvent should not inhibit the reaction itself. Predictive calculations should be used to identify miscibility gaps between at least two compounds to reduce laboratory work. Furthermore, the solubility parameters of the used catalyst and ligand have to be calculated in the different phases along with their respective partition coefficients. These data are used to evaluate whether the solvent system found is potentially suited for separating catalyst and product in the respective system.

Finally, the TMS developed by predictive methods must be verified in the laboratory along with key parameters for its complete description. The first point should be

to map out the temperature-dependent miscibility gap before and after catalytic conversion. It needs to be proven whether the mixture is indeed homogeneous under reaction conditions with a high amount of substrate and also with a high amount of product present. In addition, a separation temperature should be determined by simple extraction experiments. If the miscibility gap fits the required reaction conditions, the next step is to carry out the reaction in the TMS. An initial reaction followed by separation should be conducted in a TMS to obtain as much information as possible with minimal laboratory effort. In this way, information on the reaction, such as yield, selectivity, and TOF, and the phase compositions after the reaction can be obtained with the aid of analytics, for example gas chromatography. In addition, the catalyst leaching into the product phase can be determined by inductively coupled plasma (ICP)-optical emission spectroscopy (OES)/MS (mass spectroscopy), so that the catalyst retention in the TMS can be confirmed. To further verify the feasibility of catalyst reuse using the TMS technique, the catalyst phase should be reused in a further reaction.

Overall, predictive work cannot replace experiments in the laboratory but it can significantly reduce the effort and, thus, the cost. The provided key experiments should form an iterative process. For example, if it is impossible to find a second solvent for the separation, the first solvent can be changed again. The concept is designed to verify the feasibility of a catalyst separation for a particular reaction via TMS. The aim is to evaluate whether further research, considering kinetic data, long-term studies, mechanistic investigations, and the selection of more environmentally friendly solvents would be appropriate. For all presented steps, specific basic knowledge is required, for example, to create a list of suitable solvents.

6.2.3.2 Microemulsion Systems

In order to carry out a homogeneously catalyzed reaction in a MES, some aspects are not predictable and need to be investigated experimentally. The chemical stability of all components, especially of the catalyst complex, to water and surfactant plays a decisive role in this application, as already described in Section 4.2.1. Probably the most important component in a MES is the surfactant. The type of surfactant, surfactant concentration, and temperature can have an enormous influence on the phase behavior and, thus, on the reaction performance as explained in Section 4.2. Furthermore, the choice of surfactant is described in Section 4.2.3.1. It must be noted that the given temperature range for the reaction already imposes a certain restriction on the choice of surfactant since not every surfactant is suitable for every temperature. Therefore, the desired three-phase area cannot always be achieved. To determine the phase behavior, it is necessary to have a look at the influence of the individual components as well as at the influence of the entire reaction mixture on the phase behavior, because the occurring effects can overlap. At the same time, the phase separation can be examined, and a suitable separation

temperature can be found in which the phases are completely and quickly separated. Inevitably, some key experiments are required to evaluate the suitability of the chosen surfactant or the concentrations and parameters. Such key experiments and suited conditions are suggested in Table 6.1.

Table 6.1: Key experiments for homogeneously catalyzed reactions in an aqueous microemulsion system.

	Changed parameter	Reaction conditions
Choice of surfactant	Type of surfactant and surfactant concentration Standard concentrations: 1 wt% ionic surfactant (e.g., CTAB and SDS) 8 wt% nonionic surfactant (e.g., Marlipal and Marlophen)	0.25 mol% metal precursor 1.0 mol% ligand 30 mmol substrate T, p , from literature $\alpha = \frac{m_{oil}}{m_{oil} + m_{water}} = 0.5$
Variation of substrate concentration	Adding a cosolvent, for example, octane, decane, dodecane, . . . for example: $m(oil) = 25$ wt% substrate + 75 wt% cosolvent	0.25 mol% metal precursor 1.0 mol% ligand 15 mmol substrate T, p , from literature

With the help of the key experiments, a rough estimation of whether the reaction can be carried out in the MES can be made. However, first, the desired yields and selectivities should be defined in the key experiments for a successful implementation. Then, if necessary, reaction conditions can be adjusted, and new key experiments can be carried out. The reaction can be optimized using various parameters such as temperature, concentrations, or a dosing strategy. However, the MES approach should not be pursued if the key experiments do not provide sufficient results.

It must be noted that the surfactants leach into the other phase, for example, into the organic phase. As a result, the catalyst complex can leach, too. Once the key experiments have been carried out successfully, the extent of catalyst leaching must be determined. This is usually done with ICP-OES but can also be done with any other common method for elemental analysis.

6.2.3.3 Pickering Emulsions

Nanoparticle-stabilized droplets and their high stability allow a robust mechanical separation of additives and catalyst via filtration in a single step and, consequently, a simpler flow sheet (Section 2.3). Also, catalysts being sensitive to mechanical stress (e.g., enzymes) can be protected [31, 92].

In order to apply PE for liquid–liquid multiphase reactions, the choice of the particle type is crucial. As introduced in Sections 2.3 and 4.3.1.1, numerous different nanoparticles are commercially available, but particle synthesis and design are also possible, which opens up several alternatives for the user, compare Table 6.2.

Table 6.2: Possible particle candidates and typical compositions for Pickering emulsion stabilization.

Alternative 1	Alternative 2	Alternative 3
Commercially available fumed silica nanoparticles of intermediate hydrophobicity (e.g., HDK series by Wacker Chemie AG)	Other commercially available particles (e.g., clay, natural emulsifiers, and spherical silica)	Particle synthesis, modification or design (e.g., Section 4.3.1.1)
Well-proven emulsion composition:		
0.5 wt% particle mass fraction		
0.2–0.3 dispersed phase (dp) fraction		
(e.g., 100 mL w/o PE, 0.5 wt% nanoparticles, 0.25 dispersed phase fraction → 0.412 g nanoparticles or 16.5 g L_{dp}^{-1})		

We recommend starting with fumed silica particles as their impact on characteristic PE properties (such as drop size distribution, stability, rheology, and mass transfer) has intensively been studied in literature and Section 4.3.1. To obtain PEs with superior long-term stability, particles have to be partially wetted by the organic and the aqueous phase (Section 2.3) and, hence, need to be of intermediate hydrophobicity. Typical emulsion compositions are given in Table 6.2. The preliminary investigation of the drop size distribution gives important information about the interfacial area available for the catalytic reaction as well as the emulsion stability. Sauter mean diameters in the low micrometer range are desirable. In a simple “drop test,” in which a drop of emulsion is added to both water and the organic phase, the desired emulsion type (oil-in-water or water-in-oil) can be checked. For continuous reactions employing hydrophilic catalysts and hydrophobic substrates and products, such as the hydroformylation, with a subsequent PE filtration as investigated in Section 4.3.3, a water-in-oil emulsion is needed. In general, different dispersion devices (Section 2.3) can be applied for PE preparation. The impact of homogenization conditions using an Ultra-Turrax® on drop size distribution and rheology was investigated in Section 4.3.1.3 and 4.3.1.4.

Being the least mature of the investigated phase systems (Section 2.3), a systematic or theoretical selection of reaction conditions is not possible for PE, yet. Therefore, reaction conditions were adopted from the MES system in a first step (Table 6.1) and feasibility was demonstrated in Section 4.3.3.

PEs are known for their superior stability and are, thus, less sensitive to changes in the emulsion composition or operating conditions compared to MES and TMS. As long as the “rules” for particle choice and PE preparation (as introduced at the beginning of this section) are followed, PE stability is maintained. Sedimentation or creaming of droplets does not mean instability of the PE as simple hand-shaking or gentle stirring can redisperse the droplets. Stability against coalescence exists when the drop size distribution does not change with time.

A membrane can be chosen, for example, from the list of suitable ultrafiltration and organic solvent nanofiltration membranes (retention of micrometer-sized droplets and possibly freely suspended nanoparticle aggregates) presented in Section 4.3.1.6. Typical operating windows for these membranes are given by the manufacturers. In Section 4.3.1.6, it was shown that PE filtration is a robust process and the temperature as well as the type of the continuous phase were identified as the main influencing parameters. The PE filtration behavior was insensitive to, for example, changes in the emulsion composition (e.g., presence of reaction products) and drop sizes. This allows PEs to be optimized for the actual reaction without compromising the feasibility of PE membrane filtration.

As the catalyst should be immobilized within the dispersed aqueous phase droplets which are in turn retained 100% by the membrane, catalyst leaching is supposed to be much lower compared to MES and TMS systems (see Section 4.4). Standard methods for the quantification of catalyst and particle leaching in the permeate can be applied by the user.

6.2.4 Systematic Phase System Selection and Process Design

The general and phase system specific criteria for the TMS, MES, and PE systems represent a toolbox or heuristic to check the feasibility of these distinct phase systems for a reaction system. However, due to the limited number of considered phase systems, a generalization of these criteria is necessary as well as a systematic framework that encompasses the heuristics but allows an extension toward alternative solvent systems and their optimal application in process development.

In the initial stage of process development, information on the chemical reaction in terms of accurate thermodynamic information and reaction kinetics is limited. Nevertheless, the selection of suitable solvents or solvent systems, especially in homogeneous catalysis, is mandatory at this early stage. These solvents need to be compatible with the catalyst while simultaneously being inert to the reaction, provide favorable characteristics with respect to product separation and catalyst recovery and, ideally, possess traits that are compliant with the movement towards Green Chemistry. Due to all of these constraints, the phase system selection has significant consequences on the final process costs. Yet, this important decision is still based on expert knowledge and reference processes in contrast to systematic, model-based investigations in the

majority of cases. To systematize the selection of phase systems while retaining and embracing expert knowledge and mechanistic insight in the process, this section introduces a new and, to the best of the authors' knowledge, the first framework for computer-aided phase system selection (caPSS).

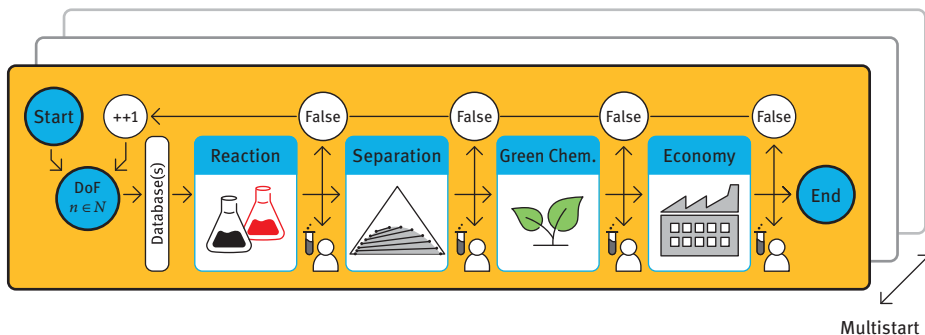


Figure 6.3: Computer-aided phase system selection (caPSS) framework. N denotes the set of auxiliary degrees of freedom (DoF), in particular auxiliary substances, which may be added to the reaction system. These auxiliary substances comprise catalyst ligands, solvents, surfactants, particles, and many more.

The caPSS framework aims at systematizing the process development by incorporating the steps of data acquisition, model generation, conceptual process design, flow sheet optimization, and evaluation with respect to economic feasibility and fulfillment of the goals of Green Chemistry. The practitioner is guided step by step from the initial specification of the substrates and target products to the final process or process candidates which adhere to the constraints provided. A visualization of this procedure is given in Figure 6.3. This procedure is heuristics based and favors simple processes with a minimum of auxiliary substances which are assumed to be more robust and cost-efficient. Since this heuristic may lead to suboptimal solutions in cases where increased process complexity yields significantly better economic performance, caPSS incorporates a mechanism through which the practitioner is able to override the heuristic based on prior knowledge. However, before introducing this exception, a formalization of the heuristic procedure is required. For this, we borrow the idea of the elementary process functions (EPF) methodology (Section 5.3.1.2) and express the entire process including the downstream process via an optimal control problem (OCP) in accordance with eqs. 5.32–5.36. The feasibility of this representation was already proven by Kaiser [37] in the reactor–separator network synthesis. In the OCP, $u(t) \in \mathcal{U} \subseteq R^{n_u}$ and $\theta \in R^{n_\theta}$ denote the dynamic and static control vectors, respectively, which represent the degrees of freedom (DoF) of the process. Originally, the time coordinate was used to describe the reaction progress within the fluid element. In this generalization which encompasses the downstream process as well, the time can be considered as the

progress of the fluid element through the process or flow sheet. For the heuristic, the DoF are partitioned into inherent (inh) $u_{\text{inh}}, \theta_{\text{inh}}$ and auxiliary (aux) $u_{\text{aux}}, \theta_{\text{aux}}$ DoF. Examples for inherent DoF are heat fluxes \dot{q}_A and diffusion fluxes j_α of all species which are part of the reaction network $\alpha \in \text{SPC}_{\text{inh}}$, while auxiliary DoF comprise diffusion fluxes j_α of species which are not native to the reaction network and, therefore, represent auxiliary substances like solvents $\alpha \in \text{SPC}_{\text{aux}}$. Of course, all inherent and auxiliary substances form the set of all species in the process $\text{SPC} = \text{SPC}_{\text{inh}} \cup \text{SPC}_{\text{aux}}$. As the name suggests, the inherent species are inherent to the reaction and process so that they can always be considered as DoF. Auxiliary DoF, on the other hand, can be added to the process to achieve a certain goal, that is, process performance, improved separability, and so on. In caPSS, this partition is used in the set N denoting the number of auxiliary DoF which can be added to the process. For example, if $N = \{1, 2\}$ process configurations are tested with one or two auxiliary DoF, considering the incorporation of a catalyst ligand in case of processes which face selectivity problems or, for $n = 2$, the addition of a solvent, surfactant, or particles when facing heat or mass transfer issues. With a sufficient number of auxiliary DoF, all phase systems can be composed including TMS, MES, and PE (see Table 6.3). Additionally, this concept facilitates the incorporation of prior knowledge since the practitioner defines N and ensures extensibility due to the parallel or sequential execution of multiple framework instances using multiple sets N_i as indicated in Figure 6.3.

With the introduction of auxiliary substances, substance databases are required from which suitable candidates are selected. These databases are categorized with respect to substance polarity, molecular weight, chemical activity, and so on, and provided as default databases in caPSS. However, the databases can also be extended by user-defined databases including data from literature or the key experiments (see Section 6.2.3). Depending on the allowed number of auxiliary DoF $n \in N$, the algorithm iterates through all substances from the databases in each block in Figure 6.3 to form candidate systems and test them in terms of feasibility of the reaction and separation as well as process-wide Green Chemistry and economic constraints. It is important to mention at this point that the customization of the databases allows for an initial screening with respect to Green Chemistry and economical objectives so that only promising candidates are evaluated in the framework. As already mentioned, reaction system candidates which are formed based on the substances of the initially known reaction network and the auxiliary substances are evaluated in four blocks or stages. After each block, the results comprising the set of all reaction systems passing the stage are passed to the user with additional information like distances to the constraints against which the reaction system is evaluated. In case of an empty set which is equivalent to no reaction system passing the requirements, the algorithm starts anew from the beginning with the number of auxiliary substances incremented by one according to N . This ensures that simple processes which pass all stages are preferred while allowing for the investigation of additional potential by adjusting N .

Table 6.3: Example of associations of auxiliary DoF with substance categories for a homogeneously catalyzed reaction system with selectivity problems and catalyst recovery.

Number of auxiliary DoF n	Exemplary substance categories
0	–
1	Ligand
2	Ligand + solvent
3	Ligand + two solvents (extraction, TMS)
4	Ligand + two solvents + surfactant/particles (MES/PE)

In the first stage, the feasibility of the reaction is evaluated. With the operation window (T, p) specified by the user, the reaction system is tested with respect to temperature, pressure, conversion, and selectivity constraints. The evaluation of the candidate system in each block is performed on multiple levels. For instance, if pre-implemented or user-defined models are available, simulation-based analyses are performed before experimental investigations to focus the time- and cost-intensive experiments on promising candidates. Likewise, simple models and simulations precede investigations with more sophisticated models. This allows an efficient selection process.

All auxiliary substances that pass the first stage are combined to new, reduced databases and evaluated in the second stage for checking the feasibility of the product and catalyst separation. Many homogeneously catalyzed processes require an efficient recovery of the catalyst for economic feasibility. For this task, multiple separation procedures are possible, such as liquid–liquid extraction, distillation, crystallization, and filtration via membranes to name just a few. Therefore, multiple separation technologies are investigated by simulation as well as experimentally at this stage (see Section 6.2.3 for possible key experiments for liquid–liquid separation). This can be summarized by analyzing the G/L/S-phase diagrams and evaluating constraints on the product purity and mass flow as well as catalyst recovery.

Even though Green Chemistry considerations can be included in the database creation, the entire process needs to be evaluated as well. This is necessary since substances that should not be used according to the Green Chemistry guidelines might be encapsulated in the process so that their harmful potential is drastically reduced.

Similar to the Green Chemistry considerations, the economic evaluation is performed in multiple steps. If a set of reaction system candidates is found which passes the previous stages, the operating expenses, in particular the material and energy costs, need to be estimated since they indicate trade-offs in reaction and separation performance. If the process revenue exceeds a user-defined lower limit, process development (e.g., by using the framework from Section 6.5) with the remaining

reaction system candidates commences. These rigorously modeled process candidates are then compared in terms of economic measures and Green Chemistry indicators, leading to a Pareto-front from which the user chooses a suitable final process configuration. If no candidate process suffices the user criteria, caPSS may start again with an incremented number of auxiliary DoF and/or relaxed constraints.

This procedure systematically analyzes multiphase system candidates, including various analysis techniques like model-based approaches as well as experimental investigations and focuses on the development of simple, robust, and economic processes with the inherent potential for increasing the sustainability and safety of chemicals production.

6.3 Solvent Selection for Reactions in Liquid Phases

Froze Jameel, Fabian Huxoll, Matthias Stein, Gabriele Sadowski

The choice of solvent is critical for the overall process performance with high rates and selectivity, as discussed in Section 6.2. Very often, the main emphasis when aiming at improving catalyst performance (in terms of rate, yield, and selectivity) is on modifications of the ligand. However, the many roles that solvents play in catalytic processes are receiving less attention but are equally important if not of higher relevance. The environmental impact is often considered by the incorporation of health, safety, and environment (HSE) solvent parameters into process design. The use of organic-immiscible solvents is frequently addressed with respect to catalyst recovery, product isolation, and recycling and may lead to the design and choice of a temperature-switchable solvent (a TMS).

The direct role of solvents in reactions is, however, often overlooked. The choice of solvent may affect solubilities, reaction equilibria, and transition state barriers and thus may alter kinetics and pathways and also act as a co-catalyst. The solvent molecules interact directly with the catalyst, substrates, products, and transition states, and all these interactions can increase or decrease the process rate and/or selectivity. When considering the role of solvents in catalysis, we illustrate their critical role viewed from a mechanistic approach. Physical solvent properties such as polarity and hydrogen-bond donating/accepting abilities of solvent molecules strongly influence the rate and reaction mechanism. Although frequently observed, the underlying fundamentals behind solvent effects are often not rationalized in detail. In this section, methods and tools from QM, plus the sequential incorporation of solvent effects to give the thermodynamics in ideal and non-ideal solutions, are presented.

6.3.1 Standard Gibbs Energies of Chemical Reactions and Transition State Barriers

The difference in Gibbs energies between products and reactants of a chemical reaction at standard-state conditions is the standard Gibbs energy of a reaction $\Delta_R G^\circ$ which is directly related to the thermodynamic equilibrium constant K_a :

$$K_a = e^{-\frac{\Delta_R G^\circ}{RT}} \quad (6.3)$$

Thus, a negative standard Gibbs energy of a reaction refers to a chemical equilibrium on the product side, whereas a positive $\Delta_R G^\circ$ indicates that the unreacted substrates are preferred. Standard Gibbs energies of reactions, and thus chemical equilibrium constants, for a particular reaction, are often not available experimentally. Qualitative and quantitative approaches to obtain $\Delta_R G^\circ$ for a new type of reaction from a theoretical perspective are then an attractive alternative to time-consuming and difficult experiments.

The standard Gibbs energy of a reaction $\Delta_R G^\circ$ is introduced here to describe the reaction of two compounds “A” and “B” forming the product “C” (Figure 6.4) as the difference in standard Gibbs energies between product “C” and reactants “A” and “B”. Before reaching the product state “C”, reactants “A” and “B” form a transition state $[A-B]^\ddagger$ which further reacts toward the product “C”. The transition state theory treats the transition state as a quasi-equilibrium state (eq. (6.4)). Thermodynamics and kinetics of a chemical reaction cannot be treated separately since they are closely related by changes in standard Gibbs energies, the latter by that of the formation of the transition state $[A-B]^\ddagger$, for example, the transition state barrier $\Delta_R G^\ddagger$:

$$k = \left(\frac{k_B T}{h} \right) \kappa(T) e^{-\frac{\Delta_R G^\ddagger}{RT}} \quad (6.4)$$

Here, k is the reaction rate constant, $\kappa(T)$ represents the collision factor, k_B is Boltzmann’s, and h is Planck’s constant.

6.3.2 Introducing a Three-Level Description of Chemical Reactions in Solution

In the following, we are introducing a three-level description for systematic incorporation of solvent effects on the thermodynamics, here the standard Gibbs energy of a reaction $\Delta_R G^\circ$, and the kinetics, here the Gibbs energy of the transition state barrier $\Delta_R G^\ddagger$ (Figure 6.4). The top level is the chemical reaction when treated in the absence of any solvent. $\Delta_R G^{\circ, id}$ can be obtained from various theoretical approaches. Reactants $A_{(g)}$ and $B_{(g)}$ form a transition state $[A-B]^\ddagger_{(g)}$ and the product $C_{(g)}$, where (g) denotes

the neglect of any chemical environment, commonly referred to as the “ideal-gas phase”. Even for the gas phase, a careful benchmarking of computationally efficient DFT methods versus wave function-based solutions of the electronic Schrödinger equation may reveal systematic or non-systematic deficiencies of the former (Section 3.2). Standard Gibbs energies of reacting species (reactants, transition states, and products) are obtained by adding thermodynamic corrections to electronic energies via partition functions from statistical thermodynamics, for example, based on the rigid rotor and harmonic oscillator assumptions. QM calculations in the gas phase (g) are able to provide transition state barriers (e.g., the thermodynamics of activation) and the thermodynamics (standard Gibbs energies; chemical equilibria) of the overall reaction in an ideal gas phase with an uncertainty of 5–10 kJ mol⁻¹.

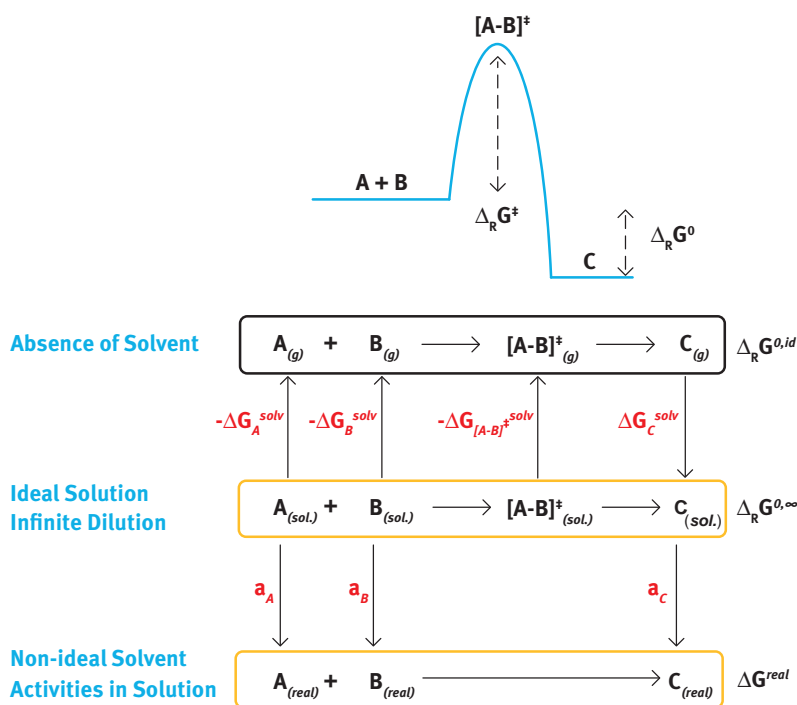


Figure 6.4: Three-level workflow of the treatment of chemical reactions in condensed phases. QM calculations of standard Gibbs energies of activation and standard Gibbs energies of reactions $\Delta_R G^{0,id}$, in the gas phase (g) are corrected by solvation terms ΔG_i^{solv} in order to describe the reaction at infinite dilution ($\Delta_R G^{0,\infty}$). Thermodynamic activities a_i of the reactant and product species are used to obtain the standard Gibbs energy of a reaction in a real (liquid) solvent (ΔG^{real}).

6.3.2.1 Taking Quantum Chemical Calculations from the Gas Phase to Infinitely Diluted Solution

The second level is the incorporation of solvation effects into the QM approach to obtain the Gibbs energies of the individual species $A_{(\text{sol})}$, $B_{(\text{sol})}$, and $C_{(\text{sol})}$ in solution, but also the one of the transition state $[A-B]_{(\text{sol})}^{\ddagger}$ (Figure 6.4). Solvation effects can be incorporated using various approaches (Figure 6.5). The accuracy of QM methods to calculate standard Gibbs energies of reactions in condensed-phase environments is still a challenge and ongoing research. The simplest and computationally most efficient one is the description of solvent effects by a dielectric continuum such as in COSMO (conductor-like solvation model) [52]. Polarization of the solute by surrounding solvent molecules is described by an unspecific term depending on the dielectric constant ϵ . Continuum solvent models represent an appealing approach for the calculation of Gibbs energies of solvation, in particular for relative effects upon change of solvent or temperature.

Such a consideration of solvation gives the infinitely diluted solution of non-interacting species in which molecular solute–solute and solvent–solvent interactions are not incorporated. This state refers to an “ideal solution at infinite dilution” to give $\Delta_R G^{0,\infty}$ or the respective transition state barrier $\Delta_R G^{\ddagger,\infty}$. Going from accurate QM calculations in the absence of a solvent to chemical reactions in solution is performed via a Born–Haber cyclic approach. For the thermodynamics and kinetics of the reaction to be calculated in solvents, reactants A and B are (de)solvated from an infinitely diluted solution to the gas phase (by $-\Delta G_{A,B}^{\text{solv}}$), and subsequently, the transition state $[A-B]^{\ddagger}$ ($\Delta G_{[A-B]^{\ddagger}}^{\text{solv}}$) and the product C (by ΔG_C^{solv}) are solvated to yield the standard Gibbs energy at infinite dilution but also the effect of (de)stabilization of the transition state (Figure 6.4).

Figure 6.5 shows different levels of representations of solute–solvent interactions in QM calculations. The dielectric continuum representation (left) is a computationally affordable approach to incorporate polarization effects into the electronic Schrödinger equation. The most realistic one is the full explicit atomistic QM treatment of all solute, solvent, and catalyst species in a large simulation box with periodic boundary conditions. The mixed cluster-continuum model (hybrid; right) is an intermediate level representation in which solvent molecules close to the solute are treated in full atomistic detail whereas further distant solvents are a dielectric medium.

6.3.2.2 From Infinite Dilution to Real Solutions with Thermodynamic Activities of Reacting Species

The third level of solvent treatment is a correction for the “non-ideality” of the previous stages. The “real solvent” description, which explicitly considers intermolecular interactions among all species in solution, is obtained from experimentally parameterized

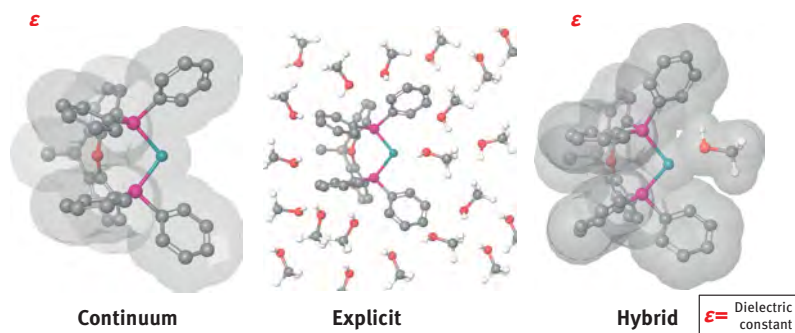


Figure 6.5: Different levels of solvent representations in QM calculations. Left: continuum solvent model with a specific dielectric constant ϵ ; center: the explicit atomistic picture of all solute and solvent molecules; right: mixed cluster-continuum model in which the solute (here a catalyst) and directly interacting solvent molecules are embedded in a dielectric medium.

coarse-grained analytical models, for example, perturbed-chain statistical associating fluid theory (PC-SAFT, Section 3.1.1) or the group-contribution method modified UNI-FAC-Do. This computationally efficient treatment of chemical species in solution yields the thermodynamic activities a_i of the reactants and products in different solvents (Figure 6.4). However, this does not include the transition state.

The solvent influence on reaction equilibria in real solutions was already discussed in Section 3.1.5. The reaction rate r of an equilibrium reaction $A + B \rightleftharpoons C + D$ is defined in a thermodynamic-consistent way using thermodynamic activities instead of concentrations (eqs. (3.70)–(3.72)). At the beginning of the reaction ($t = 0$), k_{-1} can be neglected if no products are present in the mixture. Thus, eq. (3.70) can be simplified to

$$r = k_1^* \cdot a_A \cdot a_B \quad (6.5)$$

As solvent effects on the reactants are accounted for by the thermodynamic activities a_i , the intrinsic reaction rate constant k_1^* does not depend on the solvent as long as the transition state is not affected by the solvent. In these cases, it is possible to predict the solvent influence on the reaction kinetics from the reactant thermodynamic activities only. The highest reaction rates and turnover frequencies are obtained in solvents that cause high reactant thermodynamic activities, that is, large activity coefficients of the reactants. Thus, potential solvents were screened toward their effect on the thermodynamic activity of the reactants in a reaction mixture.

Examples of high practical relevance are the hydroformylation of olefins and the subsequent reductive amination of aldehydes. These are homogeneously catalyzed liquid-phase reactions with the gases CO and/or H₂ as reactant(s). Thus, the thermodynamic activity of these gaseous components in the liquid also needs to be accounted for. However, it could be shown that – except for very high pressure – the

thermodynamic activity of gaseous components in the liquid phase does only depend on the composition of the gas phase which is in equilibrium with that liquid [34]. Consequently, in contrast to their solubility, the thermodynamic activities of the gases CO and H₂ neither depend on the solvent nor on the composition of the liquid phase. Thus, as long as liquid-phase reactions are performed in the presence of an equilibrium gas phase, the solvent influence on the reaction is only determined by the solvent influence on the thermodynamic activities of the reactants in the liquid solution.

6.3.3 Solvent Selection for Chemical Equilibria and Reaction Rates

The rationale to suggest an optimal solvent for a given chemical reaction is based on the many roles a solvent may play. Differences in Gibbs energies of solvation between substrates and products affect the standard Gibbs energy of the reaction $\Delta_R G^\circ$ and thus the chemical equilibrium. The transition state barrier of the rate-determining step $\Delta_R G^\ddagger$ should be minimal to yield fast kinetics of the chemical reaction. Likewise, high thermodynamic activities for reactants (a_i) are in favor of a swift catalytic turnover. There may also be direct molecular interactions between solvent molecules and a catalyst to (i) act as a cocatalyst, (ii) stabilize the transition state structure, or (iii) inhibit catalytic performance. Here, we present selected examples of the different roles that solvents may play in catalysis.

6.3.3.1 Modeling Solvent Effects on Standard Gibbs Energies and Chemical Equilibria

The solvent effects on the hydroformylation reaction of 1-dodecene to *n*-tridecanal were investigated at different decane/DMF ratios and different temperatures [55]. Solvent effects were described using those two apparently different approaches: first, a qualitative prediction and, second, a quantitative prediction, whereas the qualitative prediction is based on the standard Gibbs energy of reaction at infinite dilution in liquid solvents. The standard Gibbs energy of reaction at infinite dilution in liquid solvents was also calculated using the fugacity coefficients at infinite dilution calculated from PC-SAFT.

Quantum chemically calculated standard Gibbs energies of reaction in absence of any solvent $\Delta_R G^{0,id}$ were calculated using various levels of theory, and a high level of electron correlation was required to obtain results of chemical accuracy (within 4 kJ mol⁻¹). Thermochemical properties for the hydroformylation reaction of 1-dodecene were calculated at various levels of accuracy to critically assess their performance. DFT calculations and wave function-based methods with different levels of electron correlation were used for those tasks. Calculation of second derivatives was performed to consider thermodynamic corrections to the energies at 298 and 378 K.

Solvent effects were treated using an implicit solvation model to estimate the effect of solvents on the standard Gibbs energy of reaction at infinite dilution in liquid solvents. The consideration of solvents at infinite dilution in liquid decane/DMF solvent mixtures ($\Delta_R G^{0,\infty}$) allowed a qualitative prediction of the solvent effect on the equilibrium concentrations (Table 6.4). Based on the standard Gibbs energy of reaction at the ideal-gas standard state and on fugacity coefficients φ_i calculated using PC-SAFT, the equilibrium concentrations of reactants and products for the 1-dodecene hydroformylation performed in decane/DMF mixtures at different compositions could be predicted in very good agreement with experimental data (Section 3.1.5).

Table 6.4: Standard Gibbs energies for the hydroformylation of 1-dodecene at infinite dilution in liquid solvent mixtures decane/DMF at 378.15 K.

<i>w/w</i> (decane/DMF)	<i>p</i> (bar)	$\Delta_R G^{0,\infty}$ (kJ mol ⁻¹)	
		MP2/COSMO	PC-SAFT
80/20	0.74	-36.48	-68.76
0/100	0.57	-37.72	-79.18

The values obtained from the two methods agree qualitatively, but differ in absolute values and also regarding the magnitude of the solvent effect. While PC-SAFT explicitly accounts for binary interactions among the solvents and the reacting species, COSMO is an implicit solvation model in which the reacting species are embedded in a dielectric continuum surrounding the molecular cavity. COSMO, in contrast to PC-SAFT, does not explicitly include solvent molecules. Nevertheless, the standard Gibbs energies of reaction at infinite dilution decrease with increasing DMF content for both MP2/COSMO and MP2/PC-SAFT, which leads to increasing K_a . This is in qualitative agreement with the experimental observations. This shows that the solvent effect on the reaction equilibria can be predicted qualitatively via QM calculations alone as well as via a combination of QM calculations and PC-SAFT without using any experimental reaction data.

Table 6.5: Thermodynamic equilibrium constants for the hydroformylation of 1-dodecene at ideal-gas standard state.

<i>T</i> (K)	$K_{f,MP2}$	$K_{f,exp}$
368	848.85	973.08
378	292.97	322.82
388	106.65	129.34

A quantitative prediction of the solvent effect on K_x requires the thermodynamic equilibrium constant K_f . K_f was calculated at different temperatures using the reaction enthalpy and the Gibbs energy of reaction at the ideal-gas standard state. The standard Gibbs energy of reaction was used to determine the thermodynamic equilibrium constant K_f at 378 K. K_f values at 368 K and at 388 K were determined using the standard reaction enthalpy at 373 K and 383 K, respectively. For comparison, thermodynamic equilibrium constants $K_{f,\text{exp}}$ were calculated using the experimentally determined mole fractions of the reactants/products at the solvent composition 60%/40% ($w_{\text{decane}}/w_{\text{DMF}}$) and the respective fugacity coefficients obtained from PC-SAFT (Section 3.1.5). The resulting two sets of values for the thermodynamic equilibrium constant from both, MP2 ($K_{f,\text{MP2}}$) and experimental data combined with PC-SAFT ($K_{f,\text{exp}}$) are presented in Table 6.5. As can be seen, the values obtained from MP2 calculations and experimental data/PC-SAFT are in very good agreement, particularly keeping in mind the complexity of the reaction system and that QM is purely predictive. The solvent effect observed could not have been described at all neglecting the fugacity coefficients, as these are the only physical properties that depend on the solvent and therewith enforce the change in K_x .

6.3.3.2 Model-Based Screening to Predict Solvent Effects on Reaction Kinetics

Here, we present two examples of the application of the combined solvent screening using QM and UNIFAC-Do. Both refer to complex reaction systems in homogeneous catalysis using substrates from renewable sources.

According to the above-defined criteria, the optimum solvent must simultaneously provide high thermodynamic activities of the liquid reactants (eq. (6.5)) and low activation barriers according to eq. (6.4).

Hydroformylation

For the Rh(I)-BIPHEPHOS catalyzed hydroformylation, 12 commonly used polar and non-polar industrial solvents were screened in terms of their effect on the thermodynamics and kinetics of the reaction (Figure 6.6a). The thermodynamics of the reaction is significantly affected by the choice of solvent. A COSMO screening of the effect of polarity on the Gibbs energy of the reaction $-\Delta_R G^{0,\infty}$ was $\sim 12 \text{ kJ mol}^{-1}$ [36]. Polar media, such as DMF, NMP, and methanol, appear to be beneficial for the thermodynamics of the hydroformylation reaction.

The solvent polarity can also affect the activation energy of the rate-determining step (Figure 6.6a) when the stabilization of the transition state is more pronounced than that of the preceding intermediate. In Figure 6.6a, the reduction of the transition state barrier $-\Delta\Delta G_{[\text{A-B}]^\ddagger,(\text{sol})}$ upon screening of the dielectric constant ϵ relative to that in the absence of solvent is given. The activation energy of the rate-determining step

in the hydroformylation reaction, that is, the hydride insertion into the olefin double bond, is not significantly affected by the polarity of solvent (only by $\sim 4 \text{ kJ mol}^{-1}$) which is in good agreement with the experiment.

UNIFAC-Do calculations were performed to obtain the thermodynamic activity of 1-decene in reactions mixtures for the same solvents at experimental reaction conditions (100 °C, 13 wt% 1-decene). The results are depicted in Figure 6.6a, emphasizing a significant solvent effect on the thermodynamic activity of 1-decene in various solvents.

Based on these calculations, DMF, NMP, and short-chain alcohols, especially methanol, are predicted to be promising solvent candidates for hydroformylation. Performing the reaction in one of these solvents should lead to a fast conversion from the reactants to the desired product. In contrast, solvents like THF, toluene, or *n*-heptane are expected to result in lower reactant-conversion rates.

Reductive Amination

As a second example, we present results for the reductive amination of undecanal with diethylamine (DEA) in the presence of Rh(I)-XANTPHOS. While the chemical equilibrium is hardly affected by the polarity of solvent (only by $\sim 2 \text{ kJ mol}^{-1}$) [7, 34], the rate of reduction of the enamine is critically dependent on the solvent polarity. Polar media accelerate the rate of the reaction by lowering the transition state barrier and thus increase the overall yield of the reaction. The rate constant of the rate-limiting reduction step increases by an order of magnitude depending on the polarity of solvent (Figure 6.6b), which is in good agreement with the experiment [34].

UNIFAC-Do screening of the solvent effect on the reaction kinetics of the reductive amination of undecanal was performed. The reductive elimination of the tertiary amine was found to be the rate-determining reaction step [49]. Thus, the thermodynamic activity of the enamine intermediate in various solvent candidates was evaluated. UNIFAC-Do calculations were performed for the thermodynamic activity of the enamine in the reaction mixture, considering 12 different solvents and fixed initial reactant concentration (4 wt% undecanal, and fourfold excess DEA). Short-chain alcohols, NMP, and DMF are predicted to lead to high reactant-conversion rates, similar to the results of the hydroformylation. THF, toluene, and *n*-heptane, again, perform inadequately for this reaction and should, if possible, not be considered as solvents for these reactions.

When combining results from QM and UNIFAC-Do solvent screening of the hydroformylation and reductive amination reactions, the two, apparently contradictory approaches give a consistent picture. The combined results are shown in Figure 6.6a for the hydroformylation and in Figure 6.6b for the reductive amination. As a result of initial screening, polar solvents are preferred candidates compared to non-polar solvents for both example reactions. DMF, NMP, and methanol show similar performance in

terms of reduction of activation energy for the rate-determining step making the recommendation of a single most appropriate solvent not possible at this state. However, as a result of swift solvent screening, the number of solvents to be considered in a subsequent step is significantly reduced.

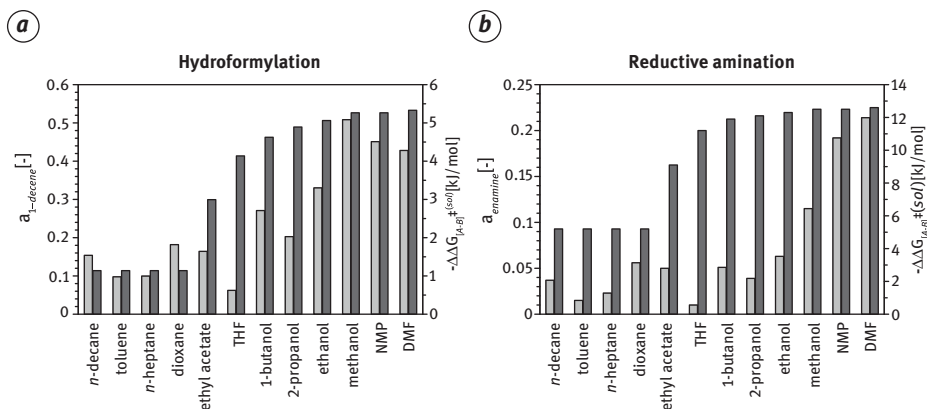


Figure 6.6: Solvent effects on (a) the rate-determining step of the hydroformylation (b) and the reductive amination. Thermodynamic reactant activities were calculated using UNIFAC-Do (left axis, light gray bars) and reduction of the transition state barrier relative to those in absence of solvent (right axis, dark gray bars) in 12 different solvents [34].

6.3.3.3 Beyond Implicit Solvation: The Many Roles of Solvent Molecules

Accelerating and Promoting Catalysis

The Pd(II)-catalyst hydroesterification of 1-decene with methanol and 1,2-bis(di-tert-butylphosphinomethyl)benzene is a prime example for the promotion of catalysis by solvent molecules (Figure 6.7). In the pre-catalyst, a methanol solvent molecule is coordinating to the central metal atom and blocking the site of catalytic turnover. Here, methanol plays three different roles in this catalytic process: first, its dissociation is necessary to activate the pre-catalyst; second, it is the substrate to form methoxy esters; third, it coordinates to the Pd(II)-hydride intermediate complex and occupies the vacant coordination site. In the rate-limiting final step of methanolysis, the coordination of two additional methanol molecules was investigated in a mixed cluster/continuum model. The cyclic arrangement of these two additional solvent molecules is the optimal coordination geometry to form a network of three hydrogen bonds in addition to the substrate–Pd interaction. The thermodynamically unfavorable single methanol coordination (Gibbs energy of reaction step $+31 \text{ kJ mol}^{-1}$) becomes thermodynamically feasible (by -3.4 kJ mol^{-1}). The explicit solvent methanol molecules form a cyclic ring cluster which enables an efficient concerted proton transfer from methanol to the palladium center to regenerate the hydride [35].

One prime example for explicit solvent stabilization of the transition state is the amination step of undecanal with DEA using methanol as a solvent (Figure 6.7). The Gibbs energy of the transition state barrier of the hemiaminal formation by the nucleophilic addition of DEA to undecanal is critically dependent on an assisted proton transfer by explicit solvent coordination. The transition state barrier is +137 kJ mol⁻¹ in the absence of any explicit solvent coordination and reduces to +41 and +19 kJ mol⁻¹ when one or two methanol molecules, respectively, are assisting the proton transfer from the amine to form the hemiaminal intermediate [34].

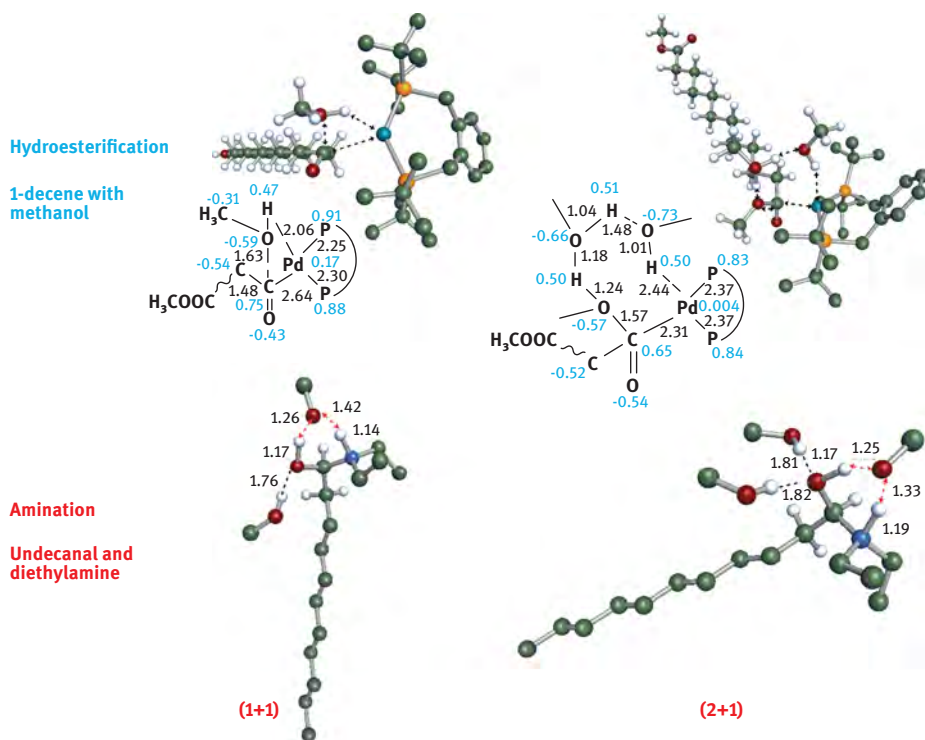


Figure 6.7: Two examples of explicit solvent involvement in catalysis (top). Explicit methanol solvent molecules acting as proton transfer agents in methanolysis of the acyl species (rate-determining step) in the hydroesterification of methyl 10-undecenoate (bottom). Hydrogen bond-forming methanol solvent molecules in the amination reaction of undecanal with diethylamine. One methanol molecule is acting as a proton transfer mediator, two methanol molecules from hydrogen bonds with the carbonyl oxygen and thus assist the nucleophilic addition of the amine.

Catalyst Inhibition

Solvents in chemical reactions have a multitude of roles: solubilizing substrates, catalysts, and products; stabilizing intermediates and transition states; enabling a facile separation of catalyst and products, and so on. An aspect that has not received much

attention yet is the inhibition of catalysts by solvent molecules, and the thermal decomposition of solvents.

Methanol, NMP, and DMF were top-ranked candidate solvents for the reductive amination (Section 6.3.3.2). Methanol and DMF were chosen for further investigations as representatives of polar media with and without hydrogen bonding abilities. The active transition metal catalyst has a vacant binding site where the substrate must coordinate for the reaction to proceed. This site is, in principle, also solvent accessible and solvent molecules may approach the central metal atom and thus occupy the site of catalytic turnover. If such binding is overstabilized, solvent coordination competes with substrate binding. Since the concentration of active transition metal catalysts in solution may be lower than estimated, overall turnover and reaction yields will be affected.

Table 6.6 shows the DFT calculated binding energies of various species to the active catalyst for the reductive amination reaction. Enamine is the substrate and also has high binding energy to the Rh(I) catalyst. Carbon monoxide is an inhibitor and shows the highest binding energy. For the reduction of the enamine, H₂ must coordinate to Rh(I) and undergo an oxidative addition. DMF, as a frequently used solvent, has higher binding energy to the active catalyst than hydrogen and is thus a competitor. Methanol, as an alternative solvent candidate, has lower binding energy and does not obstruct hydrogen coordination. It is not competitive with either substrate or H₂ binding and is not expected to inhibit the catalytic performance. As discussed above, the hydrogen bonding ability of methanol also significantly reduces the activation barrier for enamine formation.

At elevated temperature and pressure, DMF is not an inert solvent but is also susceptible to decomposition into dimethylamine and carbon monoxide. These DMF decomposition products can also potentially bind to the catalytic center, further reducing the catalytic activity of Rh(I) (Table 6.6). Hence, the use of DMF as a solvent is not recommended for the hydrogenation of the enamine.

Table 6.6: Calculated binding energies of various species during reductive amination to the Rh(I)XANTPHOS catalyst in kJ mol⁻¹.

Enamine	H ₂	MeOH	DMF	DMA	CO
-125	-61	-50	-81	-97	-183

The reaction performance was confirmed by experiments comparing methanol, DMF, toluene, *n*-heptane, and 1-butanol as solvents. The reductive amination of undecanal with DEA in different solvent systems showed that methanol gave the highest product yields and lowest side-product formation [34].

6.3.4 Conclusions

The multifaceted roles of solvents in integrated process design need adequate computational treatment. As outlined above, the development of a generally applicable thermodynamic multistep workflow allows a fast solvent screening without the need for *a priori* experimental reaction data. The presented approach can be a powerful tool in selecting optimal solvents for catalytic transformations and significantly reduce time-consuming experimental solvent screening.

Different methods and levels of treating solvent effects in catalytic reactions give different levels of information. Screening of chemical equilibria or transition state barriers as a function of solvent polarizability gives initial valuable insight into reaction thermodynamics and kinetics, respectively. Calculating the thermodynamic activity of reactants in (mixed) solvents is a complementary approach. Solute–solute, solvent–solute, and solvent–solvent interaction parameters are included in this “real solvent” representation whereas the catalyst is not considered.

Ideally, both approaches give a consistent set of solvent candidates of which only the top-ranked might be evaluated experimentally. Only when explicit coordination of solvent molecules, their active involvement in transition state stabilization, or reaction mechanism appear possible, a final full atomistic representation of solvent molecules in QM is required. However, for integrated process design, the methodologies presented in this section are very well-suited to create a list of reasonable solvent candidate molecules.

6.4 Integrated Solvent and Process Design

Steffen Linke, Tobias Keßler, Christian Kunde, Achim Kienle, Kai Sundmacher

As one part of the procedure for selecting an appropriate phase system for homogeneously catalyzed reactions, as proposed in caPPS in Section 6.2, the specific problem of selecting a solvent or a solvent mixture for a particular phase system must be investigated. Traditionally, in chemical process development, solvents are selected based on preliminary studies, considering some desirable thermodynamic properties for decision-making. Subsequently, a process is developed for the selected solvent. This sequential procedure can lead to suboptimal decisions since complicated trade-offs must be made between different thermodynamic properties that can only be rationally weighted at the process level for each solvent individually. Therefore, it is recommendable to develop and establish methodologies that combine very closely solvent selection with the process design procedure. This integrated approach and the related frameworks published in the scientific literature are discussed in the following section and are illustrated by specific examples from the authors' research works.

6.4.1 Introduction to Integrated Solvent and Process Design

Integrated solvent and process design, or CAMPD, means selecting a solvent by evaluating its performance at the process level so that all interdependencies, for example, between different unit operations, are considered. This performance can usually be defined as economic profit as a rule, but exergetic considerations, ecological criteria, or even multiobjective trade-offs are also possible. Besides the decision criterion, engineers must choose the solvent design space, a method to predict thermodynamics, unit operation models, the process flow sheet, an optimization algorithm, and the degree of decomposition. The solvent design space defines what kind and type of molecules are considered and studied as solvent candidates; in other words, the design space is the pool of molecular possibilities for the solvent. Property estimation models are necessary to predict the thermodynamic behavior of the molecules in mixtures. Therefore, the process performance of a solvent can be calculated without experimental data, and a selection can be made in the early stage of process design. Besides physical properties, HSE criteria are also very important in decision-making, and thus, predictive methods are needed for these properties as well. Regarding the process, models for the unit operations must be chosen describing, for example, reactors, separators, and heat exchangers. Obviously, these unit operations need to be connected resulting in a process flow sheet. If an economic analysis is performed, cost models for the apparatus and the utilities must be formulated as well. Since individual process simulations for each solvent candidate are not sufficient for fair decision-making, an optimization algorithm must be applied. Such an algorithm must be able to handle and solve the system of equations representing the process flow sheet for each solvent candidate under investigation.

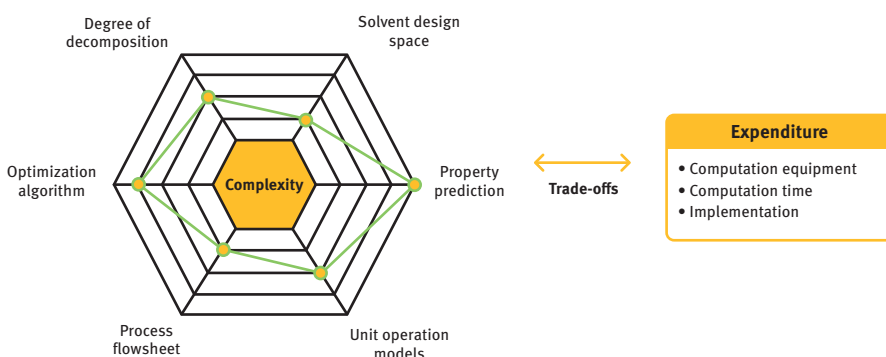


Figure 6.8: Trade-offs in the context of integrated solvent and process design between the scope of the results, their accuracy, and the effort required to solve the optimization problem.

In total, engineers face a bundle of different trade-offs between accuracy, reliability, the scope of the results, and the expenditure required including man and computational power, which are summarized in Figure 6.8. To give an example, a huge process network consisting of fully spatially resolved unit operations, applying complex quantum mechanical (QM) calculations for the solvent, and solved to global optimality is conceivable but not practically viable nowadays. Therefore, reasonable trade-offs must be made by the expertise of the engineers involved, such as the use of shortcut models for unit operations. A common technique to make the problem feasible is to apply decompositions, that is, to reduce the level of integration, and, thus, the complexity. This leads to smaller or simpler problems, which are solved to identify promising solvent candidates and starting values for the more complex, fully integrated solvent-process problem.

If these challenges are met, unexpected and highly efficient solvent and process configurations may be found that lead to benefits on a major scale. However, from a practical point of view, it must be considered that a solvent is always an auxiliary component, which must be cheap and easily available in large quantities. Secondly, new components being considered for large-scale use must be carefully studied from a regulatory perspective resulting in costly experiments and authorization processes. Thirdly, all side effects that occur in chemistry are up to now not predictable, so that complex solvents and mixtures may be predicted to be beneficial but will not work in practice. The experimental validation of the prediction is consequently essential, as well as the initial restriction to predictable chemistry. Therefore, the direct impact of integrated process and solvent design in practice may finally be more in the direction of identifying generally useable solvent structures for many applications, rather than designing one specific solvent for each process, or, on the other hand, to replace widely used solvents which have drawbacks due to their HSE properties and are becoming more strictly regulated.

Mathematically spoken, an integrated solvent-process design problem can be formulated as optimization problem as shown in eqs. (6.6)–(6.14) adapted from Austin et al. [3]:

$$\min C(n, p, \mu) \quad (6.6)$$

$$p = f(n, \mu) \quad (6.7)$$

$$h_1(p, \mu, n) \leq 0 \quad (6.8)$$

$$h_2(p, \mu, n) = 0 \quad (6.9)$$

$$s_1(n) \leq 0 \quad (6.10)$$

$$s_2(n) = 0 \quad (6.11)$$

$$p_k^L \leq p_k \leq p_k^U \quad \forall k \quad (6.12)$$

$$n_d^L \leq n_d \leq n_d^U \quad \forall d \quad (6.13)$$

$$\mu_w^L \leq \mu_w \leq \mu_w^U \quad (6.14)$$

Hereby, the objective function C describing the performance metric depends on the solvent's structural information n (e.g., a vector containing several groups when a GC method is employed), a set of estimated properties p , and the process variables μ . The molecular properties p are predicted using the model f as shown in eq. (6.7). General constraints are denoted by h , such as the process model, while structural constraints for feasible solvent structures are represented by s (e.g., valency). Upper and lower bounds, denoted by superscripts U and L, are given in eqs. (6.12)–(6.14), which limits each property in p , the size, structure, and/or the complexity of the solvent identifier n , and the process variables μ . The minimal value of the performance metric will be determined by choosing the optimal solvent identifier n accompanied by the optimal process conditions μ . This integration of solvent and process decision variables makes the optimization problem more complex than either a pure CAMD problem or a pure process optimization problem. Moreover, due to the solvent decision variables, the integrated problem usually contains integer variables, resulting in a challenging mixed-integer nonlinear problem (MINLP). Several solution frameworks have been proposed for this challenging optimization problem, whereby some approaches avoid such a mixed-integer formulation to obtain a less complicated nonlinear optimization problem (NLP).

General overviews of the field of integrated solvent-process design can be found in review articles discussing CAMD methodologies. Detailed reviews summarizing the state of the art in this field of research were published in the last few years [3, 69]. Shorter communications complete the overview articles with new developments addressing the field of integrated design directly [11, 99]. Hereby, Gertig et al. focus on CAMD methods based on quantum chemical approaches, especially discussing the solvent design for reactive systems and the design of catalyst structures [25]. Recently, the perspective of process systems engineering on material design in general, including CAMPD, was discussed by Adjiman et al. [1] in an overview article.

6.4.2 Survey of Integrated Solvent and Process Design Methodologies

The various frameworks for integrated solvent and process design can be classified into manifold categories. These categories may be, for example, the method used to solve the optimization problem, the thermodynamic prediction method, or the technical application considered in the case study. However, all of these categories are not fully selective, and, therefore, hybrid approaches that belong in more than one category can always be found. It should be noted that within the scope of this chapter,

only a selection of contributions to the field of integrated design can be presented, which are discussed in the following.

The idea of integrated solvent and process design emerged in the late 1990s. Pistikopoulos and Stefanis presented a solvent design methodology in which the overarching postulated goal was to minimize the environmental impact. To this end, a three-step framework was proposed consisting of identification of agent-based process operations, generation of suitable solvent candidates satisfying environmental and processing constraints, and verification on the process level to determine economic costs. The prediction of the molecular properties was done by use of GC methods, and the methodology was successfully applied to two gas adsorption tasks as case studies. Trade-offs between economic and ecological criteria were analyzed and discussed. The stepwise approach was evaluated as a suitable tool for reducing the combinatorial complexity, later denoted as the decomposition approach. Although the scope of this initial work was even more holistic, the general idea of CAMPD was born: predictive thermodynamics is used to evaluate a process so that the solvent selection is based on the process performance [71]. In follow-up work, this methodology was extended to design binary mixtures used as solvent systems [9].

On that ground, Hostrup and coworkers [33] proposed an integrated solvent and process design strategy for separation processes by combining heuristics and mathematical optimization. A superstructure of alternative separation technologies was suggested, which was reduced by the application of task specific constraints. Afterward, solvent candidates were generated for the remaining separation technologies. The final MINLP was solved by enumeration. Two case studies were presented. One was the generation of a flow sheet for the separation of an azeotropic mixture, and the other was a water treatment problem [33]. Marcoulaki et al. applied stochastic simulated annealing for the optimization and exemplified their method for liquid–liquid extraction, extractive distillation, retrofit design, and absorption processes [59]. Two years later, a multiobjective integrated solvent and process design were published determining Pareto optimal solutions. Environmental criteria and uncertainties were considered for the design of the solvents. The application, the recovery of acetic acid, was modeled and optimized using Aspen Plus [47]. Eden et al. [17] came up with a different solution strategy: The problem was reformulated into two reverse problems by decoupling the balance equations and constitutive equations. The resulting problem could be visualized and solved using a property clustering technique, which allowed the projection into a ternary diagram. The information from the property cluster diagram was used for a CAMD to identify solvents that correspond to the desired cluster values [17]. This strategy has been expanded to the use of GC methods for molecular design [18], and finally, for the identification of properties that provide optimal process performance [10]. Cheng and Wang [14] developed a two-stage computational scheme for the solution of integrated design problems. First, a feasible solution was determined using a

mixed-integer hybrid differential evolution algorithm, which is a genetic algorithm (GA) for the global optimization of MINLPs. Second, the identified feasible solution was numerically validated to be optimal using a quadratic programming algorithm. The approach was used to identify a biocompatible solvent for a fermentation–separation process for ethanol production consisting of a two-phase fermenter, an extractive distillation, and a distillation column for solvent recovery [14]. First et al. [20] dealt with an integrated material and process design by investigating a zeolite for the separation of methane and CO₂. Hereby, the architecture including shape, size, and pore selectivity was part of a screening step, followed by a process optimization to determine the costs. In order to make the partial differential algebraic equation system manageable in optimization, a Kriging surrogate model was developed to describe the pressure swing adsorption [20].

A broad framework, which was extended over many years, was developed by Papadopoulos et al. In a first contribution, a multiobjective CAMD method was presented to determine a Pareto-optimal set of molecules with respect to desired thermodynamic and/or environmental properties using GC methods such as UNIFAC. The Pareto optimal candidates were evaluated on the process level. Suboptimal decision-making due to the use of a single objective optimization was avoided at the cost of an increased number of process optimizations [65]. This drawback was tackled by introducing a property clustering approach in which one molecule was selected as representative for a cluster of molecules with similar properties in the Pareto set [66]. The framework was applied to liquid–liquid extraction, extractive distillation, and a gas adsorption process. A subsequent study investigated problems of industrial complexity involving reactive systems [67] workflow [68]. Since a dynamic model was not available, controllability was verified by calculating the variations of the steady state of the system due to small manipulations of some control variables. Besides the controllability assessment, a second process design stage for the most promising candidates was suggested using rigorous process models.

6.4.2.1 Approaches Using Alternative Thermodynamic Models

As an alternative to UNIFAC for describing activity coefficients, Keskes et al. [42] proposed the use of the SAFT-VR model for CO₂ capture from methane in a conference contribution, which was studied in detail afterward [42, 70]. Burger et al. [8] proposed a hierarchical framework using a GC method for SAFT- γ Mie. In the framework, reduced unit operation models were considered at the first stage and surrogate models were developed to estimating contributions to the objective function. The Pareto optimal candidates were defined via multiobjective optimization, and the detailed problem was solved for these candidates [8]. SAFT- γ Mie was also applied for the working fluid selection of an organic Rankine cycle process including transport properties [91]. Another thermodynamic model was used by Sioungkrou

et al. [82]. GC-VTPR was applied to investigate a Diels–Alder reaction using experimental kinetic data considering three solvent candidates.

A novel methodological approach was proposed by Scheffczyk et al. using the method COSMO-RS in combination with pinch-based shortcut models [76]. The use of COSMO-RS eliminated the need for GC methods, thereby increasing the complexity of the molecules in the solvent design space. For the evaluation of the shortcut models, NRTL parameters were regressed using COSMO-RS generated activity coefficients for solvent mixtures with candidates that passed a prescreening step. In the case study, a databank of molecules was screened for a solvent with minimum energy for a hybrid extraction distillation process that reduces the minimum energy demand by 63%. This concept was further developed to generate new molecules using a GA that overcomes the limitations of employing a database as solvent design space [77]. Fleitmann et al. [21] applied this methodology to the CO production from CO₂ captured from natural gas. Hereby, a storage molecule was generated as an intermediate so that excess energy from renewable energy sources could be stored chemically [21]. Additionally, a second level for the process design was introduced that evaluates solvent candidates using rigorous process models.

6.4.2.2 Most Recent Contributions

Recently, a multistage design methodology for extractive distillation processes was proposed. It used a multiobjective CAMD method to identify Pareto-optimal candidates, followed by rigorous thermodynamic calculations and analysis using residue curves, and final process optimization [98]. Chen et al. [12] published an integrated ionic liquid and process design approach exemplified by azeotropic separation processes. UNIFAC-IL was applied to predict thermodynamics. Ten et al. [86] integrated safety and health aspects into the integrated design and applied the method to a gas adsorption problem. In terms of the prediction of reaction kinetics, Gertig et al. presented approaches to calculate kinetics using DFT and COSMO-RS to select the optimal reaction solvent or respectively catalyst based on process performance [24, 26]. Zhang et al. [93] also predicted reaction kinetics using DFT. However, the design objective was the identification of an optimal reaction solvent for an antioxidant [93]. Both contributions point to a novel direction in CAMPD.

6.4.2.3 Direct Optimization of Thermodynamic Parameters: Continuous Molecular Targeting

The continuous molecular targeting approach addresses the integrated solvent and process design optimization problem in a conceptually different way and is therefore presented in a separate section. Hereby, the parameters describing the solvent in the thermodynamic model are treated as optimization variables chosen by the optimizer. This means that the process is optimized together with the solvent parameters, resulting in an ideal reference case for a virtual solvent. A second step is

to search for real solvents that exhibit similar thermodynamic behavior to the virtual solvent. To this end, a Taylor approximation can be performed to evaluate the loss in the objective functions due to deviations from the optimal, virtual parameters. Alternatively, an integer-programming problem is solved using GC methods to design solvents having the same parameters as the virtual solvent as far as possible. Since this second step is a matching step for the thermodynamic parameters of the virtual solvent, the methodology requires a thermodynamic model in which the parameters are physically meaningful. The advantage of this technique is that the optimization needs to be performed only once and not repeatedly for all suitable solvent candidates. The price of this advantage is, of course, the increasing number of optimization variables and the verification of the validity of the matching decomposition step.

The continuous molecular targeting technique was first presented for the design of an adsorption solvent for carbon capture and storage [4, 5]. PC-SAFT was used as a thermodynamic model since it has a sound physical basis by considering repulsion, dispersion, association, and multipole interactions. Detailed information on this modeling approach is discussed in Section 3.1.1. The process flow sheet for the CO₂ adsorption took into account a high-pressure adsorption unit, a pressure valve with a subsequent flash unit for desorption, and a pump to close the solvent recycle connected to the adsorption unit. The objective function to be minimized was the amount of solvent makeup needed to compensate for solvent losses. For the mapping step, the Taylor approximation method was used and a database with PC-SAFT parameters was evaluated to find real-world solvents with minimal deviations from the optimal, virtual solvent. The method identified dimethyl sulfoxide as the solvent with the lowest predicted solvent loss, representing a reduction of more than factor 1,000 compared to the reference adsorption solvent methanol.

The general continuous molecular targeting framework has been refined in various ways over the last few years: The integrated working fluid and process design for an organic Rankine cycle was successfully investigated and the mapping using GC methods was introduced [53, 54]. Besides equilibrium thermodynamics, transport properties were included for the process design, and the potential of mixtures as working fluids instead of pure components was investigated [78, 80]. The approach was successfully applied to an antisolvent crystallization process using PC-SAFT and a convex hull method to reduce the solvent design space [89]. For the crystallization application and the organic Rankine cycle each, a superstructure optimization approach was developed using continuous molecular targeting [79, 90].

6.4.2.4 Integrated Solvent and Process Design for the Kinetics of Chemical Reactions

While solvent selection for reaction kinetics has already been considered in CAMD approaches [84], the first contribution for selecting a reaction solvent in a CAMPD was proposed by Zhou et al. [95] and is presented more in detail below. The approach aims at maximizing the total process profit, as is schematically shown in Figure 6.9. The prediction of reaction rates can be done on a theoretical basis by searching for the transition states and their QM calculation as presented in Sections 3.2.2.3 and 6.3. However, since these investigations are time consuming, a data-based approach was chosen for the integrated design: Experimentally determined reaction rates were fitted to a linear quantitative structure–property relationship (QSPR) model using quantum chemically based descriptors derived from σ -profiles. The σ -profile of a molecule is a histogram of the electric charges on the surface of the molecule, which is embedded in an ideal electrical conductor [51]. These σ -profile-based descriptors were derived by dividing the histogram into six sections and integrating each section resulting in six descriptors representing each solvent candidate. Eq. (6.15) shows the structure of the QSPR, where k denotes the reaction rate, S_i are the six descriptors, and a denotes the fit parameters. The model enabled the prediction of reaction rates in unknown solvent candidates by using the candidate's sigma profile:

$$\log(k) = a_0 + \sum_{i=1}^6 a_i S_i \quad (6.15)$$

However, the σ -profiles must be available for all potential candidates. In general, this means that a geometry optimization and a single point energy calculation must be performed using the continuum solvation model COSMO [51]. Since the full σ -profile was not needed, but only the six descriptors representing sections of the profile, a GC method was established for predicting these six descriptors. Molecules were encoded into UNIFAC groups, and the contribution of each group to one of the sections was regressed using molecules with available σ -profiles. In this way, the time-consuming QM calculation could be avoided. In addition to predicting the reaction rate, GC models from the literature were taken to estimate the boiling point, critical point, enthalpy of vaporization, density, and heat capacity of the solvent candidates. This approach was applied to a Diels–Alder reaction evaluated on a simple process configuration including a CSTR, a distillation column, and a recycle of unreacted reactants and solvent. The best performing solvent in experiments, acetic acid, was outperformed by isopropanol, with a 20% increase in total process profit, highlighting the potential of integrated solvent and process design.

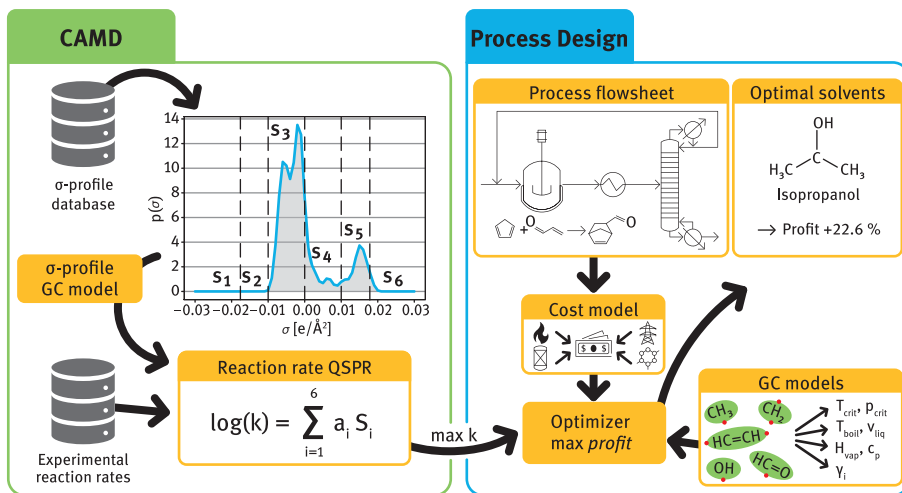


Figure 6.9: Overview of the reaction solvent design approach [95].

This selection approach was refined by applying a robust optimization method to account for uncertainties in the predictions [94]. The case study was adjusted to consider a competitive Diels–Alder reaction that distinguishes between the desired product and an undesired isomeric by-product. Consequently, two reaction constants k_1 and k_2 were regressed for the desired and the side reaction, respectively, to receive two QSPR models. The 14 parameters describing the two reactions were considered in a sensitivity analysis. Hereby, the 90% confidence interval of each parameter was taken separately without changing the other parameters, and it was sampled uniformly in this uncertainty region. For each sample point in these regions, the solvent leading to the highest reaction rate was computed. It was assumed that the most sensitive parameters would yield many different solvents with the highest reaction rate when the uncertainty region was sampled. It turned out that the fit parameters a_3 and a_4 for the side reaction are the most uncertain parameters according to eq. (6.15). Due to computational limitations, only these two parameters were included in the robust optimization framework. The objective of the robust optimization was to find the solvent that maximizes the average concentration difference between the desired and the side product over all scenarios considered. The final optimal solvent was the one that showed the largest concentration differences in most scenarios. The framework suggested new solvent candidates; however, since the first three most promising solvent candidates contain fluorine, the inclusion of HSE properties in the solvent design process were suggested for future work.

6.4.2.5 Genetic Optimization Approach for Complex Solvent-Process Optimization Problems

This inclusion of HSE criteria was one aspect in a CAMD approach for a reactive multiphase system exemplified by an extractive reaction, where biocompatibility was included as a constraint in the solvent design [96]. This study was a preliminary work, the results of which were used for an integrated design presented afterward. A new methodology was developed to calculate the combined reactive and liquid–liquid equilibrium simultaneously. To this end, the problem was treated as a system of ordinary differential equations (ODEs) describing a mass transfer problem within several phases. The ODEs were solved until the steady state was reached, indicating that the equilibrium compositions were achieved in all phases. This algorithm was shown to provide robust and efficient solutions for complex phase equilibria including equilibrium reactions and was an important achievement for the calculation of phase equilibria in the following integrated design works. Despite these achievements, the calculation of phase equilibria was still time-consuming in the context of optimization, therefore, a GA was applied for the solvent design step instead of solving the MINLP deterministically. Hereby, a set of solvent candidates is chosen as starting generation, their performance in the objective function is calculated, and the most efficient candidates are used with a higher probability for genetic operations. In this context, genetic operations were alterations of the structure of the molecules, such as the replacement of a group in a molecule or the creation of a new molecule from two existing ones. To perform these operations easily, the molecules had to be encoded flexibly. In the proposed method, molecules were represented as a tree graph. UNIFAC structural groups served as nodes of the tree and were connected to form molecules with physically feasible structures. In the case study, the GA showed its ability to design suitable molecules that maximize the equilibrium conversion of the reactant.

Since these achievements were encouraging in the CAMD, the methods were applied in an integrated solvent and process design as well. The objective was to develop a solvent for a coupled adsorption–desorption process to remove acetone from the air [97]. For each solvent generated by the GA, the NLP describing the process conditions was solved. Using this hybrid solution strategy enabled the solution of such a complex optimization problem, which was practically not possible with state-of-the-art MINLP solvers like branch-and-reduce optimization navigator (BARON). This hybrid framework is schematically shown in Figure 6.10.

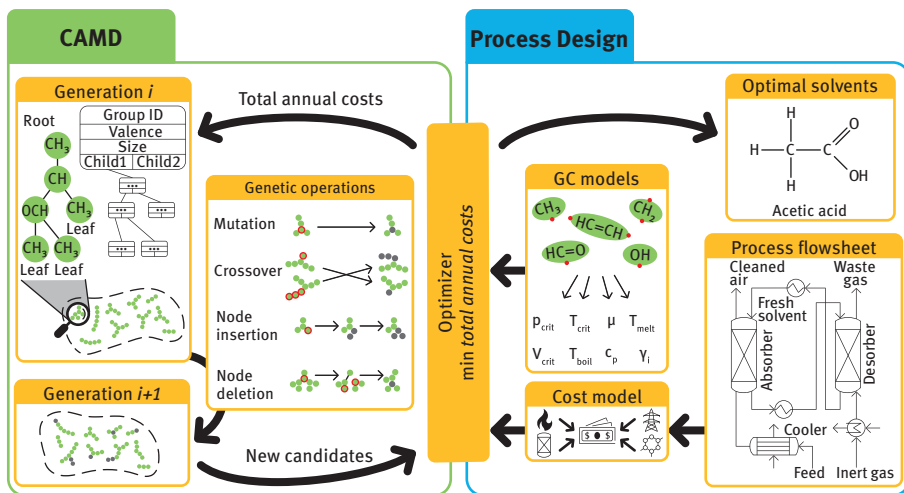


Figure 6.10: Hybrid stochastic-deterministic optimization approach for an integrated solvent and process design [97].

6.4.3 Integrated Solvent and Process Design for Thermomorphic Multiphase Systems

While the works described above are dedicated to the design of single molecular components, McBride et al. [60] studied the potential to design novel multicomponent TMS. The hydroformylation of long-chain alkenes was considered as reaction example of practical relevance. The design methodology is based on COSMO-RS since a predictive thermodynamic model for the catalyst–ligand complex of rhodium and BIPHEPHOS was needed. A database approach of successive screening steps was proposed to identify promising catalyst carrier solvents and product extraction agents before these candidates were composed to multicomponent solvent systems. The results confirmed that the state-of-the-art TMS, consisting of dimethylformamide (DMF) and *n*-decane was very efficient from a thermodynamic point of view and was predicted to outperform other TMS. Consequently, a process optimization scheme was set up for the hydroformylation using the DMF-based TMS [61]. Since the cost caused by the leaching of the catalyst complex was included in the objective function, a multistage extraction cascade with solvent regeneration by distillation was considered. The investigation revealed that the optimal number of extraction stages is five. In particular, it was found that a classical TMS-based process with only a single decanter is significantly inferior, making such a process design economically infeasible. This finding opened the door for further solvent-based considerations, as DMF is on the list of very high concerns of the REACH legislative for being developmental toxic, and thus should be replaced. When multistage extraction is unavoidable, solvents with

lower extraction power but “green” properties, that is, appropriate HSE properties, can be used if an increased number of extraction stages is used to compensate for the lower extraction power.

For this purpose, a refined solvent screening was established considering HSE criteria such as fish toxicity, carcinogenicity, or flash point. These properties were predicted using QSPR models published in the literature and are also applied in authorization processes for novel chemical compounds under REACH [6, 87]. By evaluating these models, potential solvents could be excluded from the candidate list. Preliminary results of this procedure were published, and the most promising solvent candidates were successfully experimentally validated [62]. The final methodology involved 15 different green properties predicted by more than 30 different models. Besides that, the methodology included conformers, was completely automated, and databases for the prediction results were established so that fast relaxations of the green screening criteria could be made and examined [56]. Hereby, diethylsulfoxide (DESO) was identified as a particularly efficient replacement candidate for DMF, as it showed a remarkably similar thermodynamic behavior. The identified candidates were used below for an integrated solvent and process design, as shown later.

First, systematic process optimization was performed for the candidates identified in the preliminary screening study, namely dimethylsuccinate (DMSU), tetrahydropyranone (THPO), and, for reference purposes, DMF, which are all shown in Table 6.7 [43]. The process flow sheet is shown in Figure 6.11 along with the overall approach. The sequence of screening and process design can be seen as strong decomposition, but the restriction to three solvents offered the chance for rigorous process optimization. The main contribution of this study was the automated generation of surrogate models to efficiently perform the process optimizations for the different solvents. To this purpose, the techniques presented in Section 5.3.2 were applied. In order to efficiently calculate the liquid–liquid equilibrium and the partition of the catalyst in the decanter, the surrogate model technique of reduced dimensionality was used [48]. Next, a surrogate model for the solvent regeneration by distillation was developed that computes the costs directly from the feed composition [44]. The resulting set of equations was solved using the multistart local optimization of BARON to determine the optimal process cost. The analysis of the different processes revealed that THPO can compete with DMF within the uncertainty range of the economic objective function, while DMSU was less efficient due to its reduced catalyst extraction power. Therefore, THPO was successfully identified as a green alternative solvent with sufficient efficiency.

However, when this approach is applied, the solvent design space is limited to molecules available in the screening database. To overcome this limitation, a novel strategy for the integrated solvent design was introduced to expand the solvent design space to a region around promising solvents from the screening using QM-based descriptors. In a preliminary study, a CAMD problem was formulated using a

Table 6.7: Successfully identified solvent candidates by the screening of McBride et al. [62], which served as a candidate pool for rigorous process optimization [43].

Name (abbreviation)	Structure
Dimethylsuccinate (DMSU)	
Tetrahydropyranone (THPO)	
Dimethylformamide (DMF)	

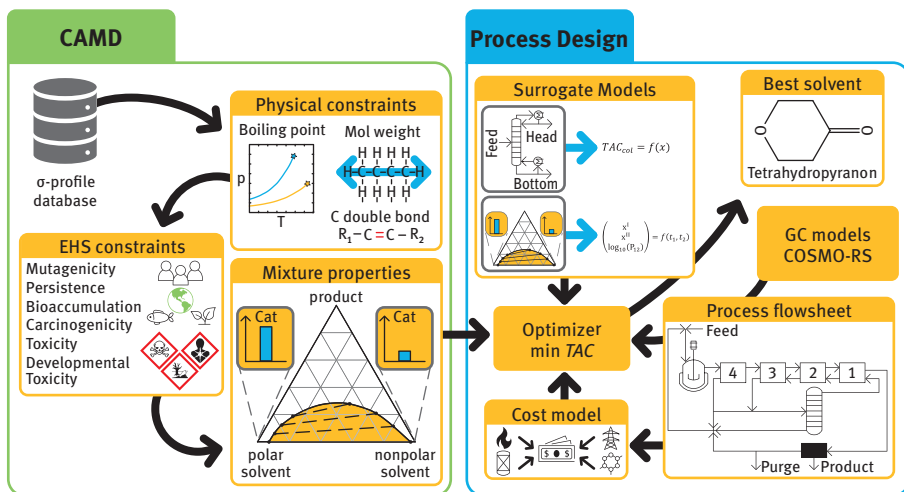


Figure 6.11: Integrated solvent and process design strategy for homogeneously catalyzed reactions using a decomposition consisted of a solvent screening for the molecular design and subsequent process optimization.

GC method to predict σ -profiles and two green properties, while the conductor-like screening model segment activity coefficient (COSMO-SAC) was applied to predict equilibrium thermodynamics [45]. The goal was to generate green solvent candidates that form a liquid–liquid equilibrium in the post-reaction mixture of hydroformylation and separate the catalyst. In a first step, solvents with low boiling points and appropriate green properties were generated by minimizing a weighted sum of the boiling point, the permissible exposure limit, and oral rat toxicity. Hereby, 20

candidates were identified. Secondly, these candidates were evaluated by maximizing the difference of the molar amount of the catalyst in the coexisting liquid phases.

This design approach yielded feasible green solvents suitable for catalyst separation and was therefore extended to an integrated design approach [46] as shown in Figure 6.12. A set of 17 promising solvents was determined by the final screening approach. On the one hand, the σ -profiles $h(\sigma)$ of these candidates were analyzed based on their first, second, and third σ -moments, which are the k th moments known from statistics and defined as $M^k = \int \sigma^k \cdot h(\sigma) d\sigma$. On the other hand, a moment for the ability of a solvent to act as acceptor for hydrogen bonding was chosen as characteristic: $M_{\text{acc}} = \int h(\sigma) f_{\text{acc}}(\sigma) d\sigma$, where f_{acc} describes the part of the σ -profile where the charge σ is larger than the threshold value σ'_{hb} of 0.01 e \AA^{-1} . Interestingly, these moments laid in distinct domains or bands for the solvent candidates from the screening, except from two outliers. It was concluded that other relevant solvent candidates, which were not included in the solvent design space of the screening, will also lay in these bands. Therefore, a solvent design was introduced, and only the solvents whose σ -moments were in the target domain were considered in process design. The CAMD problem to generate solvents within the desired σ -bands was solved using a GC method for σ -profiles [57] and a set of appropriate molecular feasibility constraints [15, 74]. It should be noted that numerous candidates of the screening were not included in the solvent design space since only groups containing hydrogen, carbon, and oxygen were considered. This reduction was made under the assumption that molecules from these elements tend to be less hazardous. At the same time, the number of candidates was lowered decisively. Six suitable molecules were obtained from the CAMD problem solution and evaluated at the process level. The process configuration remained unchanged as shown in Figure 6.11, and again the process conditions were solved using the multistart local optimization option provided by BARON.

For four of the solvent candidates, feasible process operation conditions were found that meet all constraints in terms of molar flow rates, reactor model validity, and so on. Table 6.8 shows these four candidates, of which EMM and DMG outperform the reference solvent DMF regarding the total annualized costs. It is particularly encouraging that DMG is already known as a harmless solvent in the cosmetic industry, which proves its general suitability as a solvent. In total, this integrated solvent and process design approach showed its potential to identify new solvent candidates and to overcome the problem of a limited solvent design space if suitable databases are involved.

In conclusion, various approaches ranging from screening to CAMPD can be used for TMS design. The screening-based methodologies often can provide very valuable input for the optimization-based methods. It is important to note that different methodologies often lead to different solvent candidates for the same process.

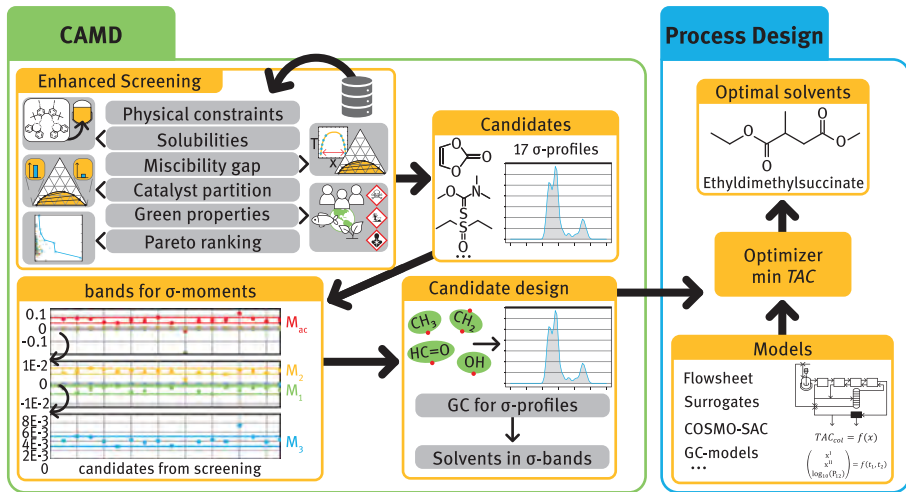


Figure 6.12: σ -Bands approach for integrated solvent and process design. First, a screening procedure identifies promising molecular structures. The σ -moments of these solvents are used to define general target domains for newly created solvents using a group contribution method. The final generated candidates are evaluated at the process level to determine their economic performance [46].

Table 6.8: Final solvent candidates identified by the integrated solvent and process design approach according to Figure 6.12 and proposed by Kefler et al. [46].

Name (abbreviation)	Structure	Name (abbreviation)	Structure
1-Ethyl 4-methyl 2-methylsuccinate (EMM)		Ethyl levulinate (ELL)	
Dimethyl glutarate (DMG)		Methyl 2-ethylacetoacetate (MEA)	

This is due to different solvent design spaces considered, different strictness of HSE criteria applied, different thermodynamic models used, and/or different decision criteria applied for ranking the candidates. Concerning the latter decision-making aspect, CAMPD has clear advantages over screening approaches since trade-offs between different thermodynamic properties are rationally made on cost. However, evaluation on the process level requires some effort and can be tedious. For the hydroformylation example discussed here, numerous candidates of the screening were not included in

the solvent design space of the σ -band-based CAMPD (Figure 6.12), which explains the appearance of different candidates. However, from a physical point of view, the results obtained from the different methods point in a similar direction, namely that mid-polar solvents are best suited as catalyst carriers. To answer the question, which of all molecules proposed is finally the best, it must be noted that such a rigorous answer cannot be given in terms of green solvents since the weighing of green properties is, inherently, highly subjective. For example, a rational, clear trade-off between fish toxicity and carcinogenicity is not possible. Such decisions must be made based on legal regulations and company policy, but also depend on the opinion of the individuals taking decisions. In terms of economy, the identification of an optimal solvent is clearer because all decisions can be finally boiled down to cost. The next step in this identification is the reduction of uncertainty for promising solvent candidates. Experimental data, in particular on the kinetics of a reaction to be performed in these solvents and the phase equilibria of the most important separation steps in the process, must be collected. The experiments will also reveal whether unforeseen complications may arise, such as unwanted reactions of the candidate solvent, or, related to a TMS process, the formation of an emulsion under separation conditions, either of which would result in the rejection of the candidate. However, the candidates evaluated successfully in experiments can subsequently be compared in a more detailed process optimization study based on the data obtained, so that the best candidate can be selected on a secure knowledge base. Generally, CAMD/CAMPD methods are not recommended to be used for final decision making of a solvent, but for isolating a manageable set of very promising candidates which then should be assessed in detail experimentally.

6.4.4 Conclusions

The concept of integrated solvent and process design is known for its potential to find novel solvents that are more efficient by making decisions based on process performance. This approach helps to avoid wrong decisions in solvent selection since all complex, hidden interactions at the process level are considered – at least within the assumptions and simplifications made. Since the optimization problems involved in combined solvent-process design decisions are very challenging to solve, various solution strategies and frameworks can be found in the literature. Different approaches tackling the same task may lead to different solvent candidates due to different design spaces, constraints, optimization algorithms, decompositions steps, or because of uncertainties in the thermodynamic prediction methods. Finally, experimental validation is required due to these uncertainties and possible unforeseen chemical effects.

Overall, integrated solvent and process design are in line with the trend to consider molecular DoF in the design of chemical processes. The levels from molecule to process addressed in Section 6.1 are more strongly interwoven to overcome the

classical heuristic-hierarchical design approach. Despite significant progress of computer-aided solvent-process design, carefully collected and evaluated experimental data remain an indispensable element for designing a final process at the lowest possible uncertainty. Where measurements need to be made and how the increasing experimental knowledge should be embedded in the final process design, is discussed in Section 6.5.

6.5 Integrated Model-Based Process Design Methodology

Stefanie Kaiser, Karsten H. G. Rätze, Fabian Huxoll, Gabriele Sadowski,
Kai Sundmacher, Sebastian Engell

The computer-aided solvent selection and process design approach presented in Section 6.4 represents one possible formulation of the algorithmic part of caPSS (Section 6.2, Figure 6.3). Nevertheless, it is based on the assumption that the phase system and the process structure have been selected before and reliable information on thermodynamics and kinetics is available. In reality, however, this is part of an iterative selection and design process in which there is significant uncertainty about the quantitative description of the underlying phenomena. In this section, we discuss the interaction between algorithms and process developers including experimental work that is done to reduce the model uncertainties. This builds on the computer-based tools that are described in Chapter 5. Due to the complex nature and the multitude of viable approaches to the realization of each block in the caPSS framework, this section can only discuss a limited set of options for integrated design approaches.

One of the most important integration steps in the caPSS framework concerns the combination of experimental work with model-based process synthesis (Section 5.3). Model-based procedures require a thorough understanding of the underlying thermodynamics (Section 3.1), knowledge about the reaction networks and kinetics (Section 3.2), insight into the mass transfer mechanisms (Section 3.3) as well as experience in the development and operation of chemical production processes (Chapter 4). Therefore, this integration exemplifies the combination of different sources of knowledge in the integrated design of multiphase chemical processes.

Instead of assuming the availability of accurate models of the thermodynamics, reaction kinetics, mass transfer coefficients, and separation efficiencies at the beginning of the process design workflow, an additional loop is added to the caPSS framework in which suitable models are identified and calibrated iteratively during the evaluation of the final process design in terms of reaction and separation performance, sustainability and economic potential (Section 6.2.4). This iterative process contains the repeated creation of intermediate process design candidates based on all information that is available at this point in time but taking into account the model uncertainties. To reduce

the uncertainty, mbOED is integrated into the design procedure to improve the available data efficiently via systematic and carefully selected experiments.

After a short introduction to experimental design and, in particular, mbOED, the integrated process design in which process designs under uncertainty and experimental design are combined is presented. Then, approaches to the integration of additional tools which are described in Chapter 5 are introduced and discussed.

6.5.1 Experimental Design for Efficient and Accurate Parameter Identification

One crucial aspect in integrated process design is the bridge between fundamental knowledge and its utilization in process development in the form of mathematical models as shown in Figure 6.13. These models not only have to accurately represent the physicochemical phenomena but also require a form and implementation which keeps the computational load in simulation and optimization to a minimum. If the general structure of a model is fixed, either based on first-principles or via surrogate approximations, the identification of the associated model parameters using experimental data is required. Due to significant efforts in terms of time, manpower, and money that are necessary to generate such data, the generation of data that is most useful with respect to the design decisions is desired.

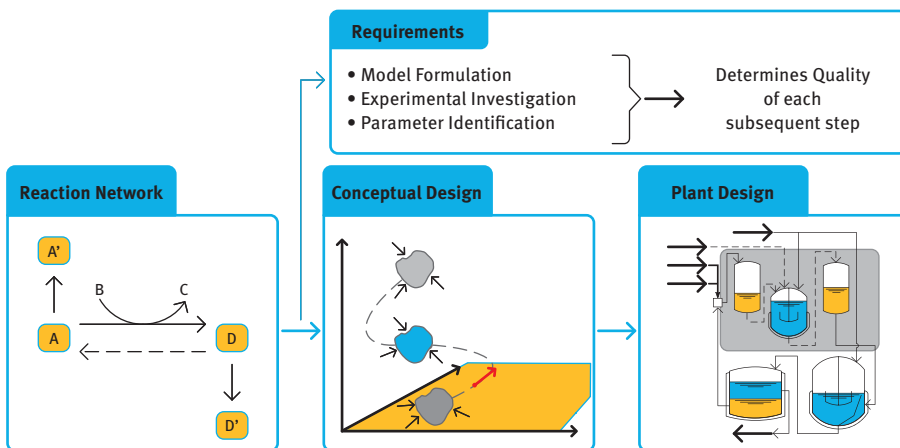


Figure 6.13: Schematic representation of the process development procedure for chemical production plants. Conceptual design: Figure 5.34 adopted from [85]. Plant design: Adopted from [72].

Experimental design approaches encompass heuristics, statistical design of experiments (DoE) and mbOED. For better differentiation, Figure 6.14 provides a schematic representation of the different design approaches. Whereas heuristics, in

particular the “one-factor-at-a-time” (OFAT) approach, are not well suited for parameter identification for nonlinear models, statistical designs like factorial or Latin hypercube designs as well as tailor-made mBOED approaches are able to capture nonlinear process behavior and multifactor interactions [88]. Especially, mBOED is subject to active research because of its wide applicability in model discrimination and parameter identification [32] via the design of sequential and/or simultaneous, potentially dynamic, experiments [22]. For parameter identification, mBOED is usually based on the Fisher information matrix (FIM)

$$F_{\theta} = F_{\theta, \text{prior}} + \sum_{j=1}^{n_{\text{Exp}}} \sum_{i=1}^{n_{\text{sp}}} \left(\frac{dy_{j,i}}{d\theta} \Big|_{\theta^*} \right)^{\top} \Sigma_y^{-1} \frac{dy_{j,i}}{d\theta} \Big|_{\theta^*}, \quad (6.16)$$

with the sensitivities $dy_{j,i}/d\theta \in \mathcal{R}^{n_y \times n_{\theta}}$ denoting the derivative of the measured variables y of experiment j and sampling point i with respect to the uncertain parameters θ . Here, all lowercase variables represent vectors while all uppercase variables denote matrices. In nonlinear process models, these sensitivity matrices may depend on the parameters so that they should be evaluated at the true parameter values θ^* . Since the true parameter values are usually unknown, they can be approximated by the current best guess $\hat{\theta}$. Eq. (6.16) also contains the measurement variance–covariance matrix Σ_y and available prior information $F_{\theta, \text{prior}}$. The inverse of the FIM F_{θ}^{-1} defines a confidence hyperellipsoid and provides an approximation of the nonlinear parameter confidence region. According to the Cramér–Rao lower bound, this confidence ellipsoid presents a lower bound to the true confidence region Σ_{θ} [58].

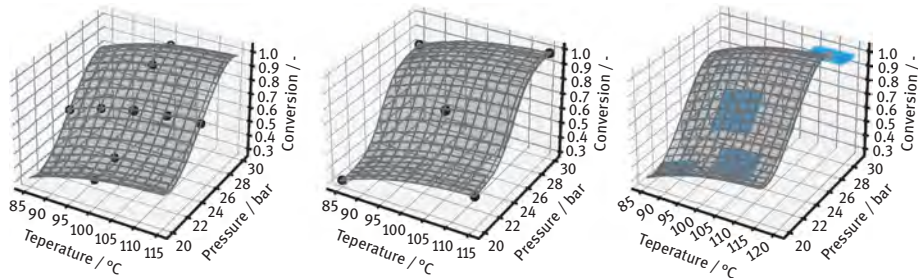


Figure 6.14: Schematic representation of the OFAT approach (left), factorial design with center point experiments (middle), and mBOED (right) for an exemplary two-factor (T, p) system. While the OFAT and factorial design provide a-priori schemata for optimally sampling the decision space, mBOED uses derivative information of the model output with respect to the parameters for a local approximation of the response surface (blue) to identify a sampling point with high sensitivity and decorrelating properties.

With this representation of the resulting parameter uncertainty, an optimization problem can be formulated as

$$\begin{aligned}
& \min_{u_1, u_2, \dots, u_{n_{\text{Exp}}}} \phi(F_\theta) \\
& \left. \begin{array}{l} \text{Process model,} \\ \text{FIM definition: eq. (6.16),} \\ \text{Variational equations,} \\ \text{Path constraints,} \\ x \in \mathcal{X}, \\ u \in \mathcal{U} \end{array} \right\} 1, 2, \dots, n_{\text{Exp}} \quad (6.17)
\end{aligned}$$

where a scalar metric of the FIM is minimized. In this formulation, the simultaneous design of n_{Exp} experiments are assumed with static control vectors $u_j \in \mathcal{U}$. The states $x_j \in \mathcal{X}$ may be constrained via additional path constraints and represent the solution to the process model while the sensitivity matrices in eq. (6.16) follow the variational equations.

In mbOED, various metrics ϕ are commonly used to scalarize the FIM. The most prominent of these are summarized in Table 6.9. In order to focus the experiments to identify specific parameters, weights can be introduced into the FIM yielding the modified FIM [73]:

$$\tilde{F}_\theta = W^{\frac{1}{2}} F_\theta W^{\frac{1}{2}}, \quad (6.18)$$

The combination of mbOED according to eq. (6.17) and process design via superstructure optimization will be discussed in the following.

Table 6.9: Subset of FIM optimality criteria for experiment design [22].

Criterion	Definition
A	$\phi(F_\theta) = \text{trace}(F_\theta^{-1})/n_\theta$
D	$\phi(F_\theta) = \det(F_\theta^{-1})^{1/n_\theta}$
E	$\phi(F_\theta) = \max(\text{eig}(F_\theta^{-1}))$

6.5.2 Integrated Process Design

In the early stage design of new chemical processes, the most cost influencing decisions are taken, which makes it a crucial phase of process development. The pressure to reduce the development time is increasing due to shorter product cycles in the chemical industry and hence new strategies for fast, efficient, and risk-aware process development are needed. The established methodologies for process design can be classified into hierarchical or knowledge-based methods and optimization-

based methods. In knowledge-based process design, the design problem is divided into smaller subproblems which are then solved by the use of expert knowledge as introduced by Douglas [16]. Although the use of knowledge-based methods is still common in the process industries, it may fall short in terms of finding synergies between the different process units.

Optimization-based methods on the other hand find the optimal process configuration by solving an optimization problem [13]. The setup of this optimization problem however requires reliable process models. These models rely on experimental data to identify model parameters and physical properties. Sequentially performing laboratory experiments, identifying all model parameters and physical properties, and simulating and optimizing the process leads to long development cycles. To speed up the development and to reduce the experimental effort, a new methodology is proposed that integrates these steps.

Only a few works have been reported that focus on the integration of model identification and process simulation of optimization. Asprion et al. [2] integrated optimal experimental design in a flow sheet simulator. However, the framework focuses on model improvement and a good parameter estimation only and does not include a process design method. Marquardt and coworkers [73] developed integration of process optimization and optimal DoEs. By weighting the FIM as shown in Equation 6.18 in the optimal experimental design, they focus the experiments on the relevant parameters. However, in their approach uncertainties in the process optimization are neglected.

In this section, we integrate superstructure optimization under uncertainties (Section 5.3.3) with sensitivity analysis and optimal DoEs. After describing the proposed methodology and the sensitivity analysis as part of the methodology, we apply it to two case studies. The first case study is the hydroaminomethylation of 1-decene. In this case study, we show the results of a superstructure optimization under uncertainties and use these results to design a new experiment that reduces the variation in the prediction of the production costs. In the second case study, the hydroformylation of 1-dodecene, we will expand the methodology by global sensitivity analysis and show the improvements that are possible compared to a design methodology that is not focused on the identification of the cost-driving parameters.

6.5.2.1 Methodology

When first experiments have been performed and the most important elements of the process, for example, the phase system and the catalyst system, have been identified, the integrated process design starts. A schematic representation of the proposed methodology is depicted in Figure 6.15.

Starting with the first screening experiments, kinetic and thermodynamic models are developed that in the beginning will have significant parametric uncertainties.

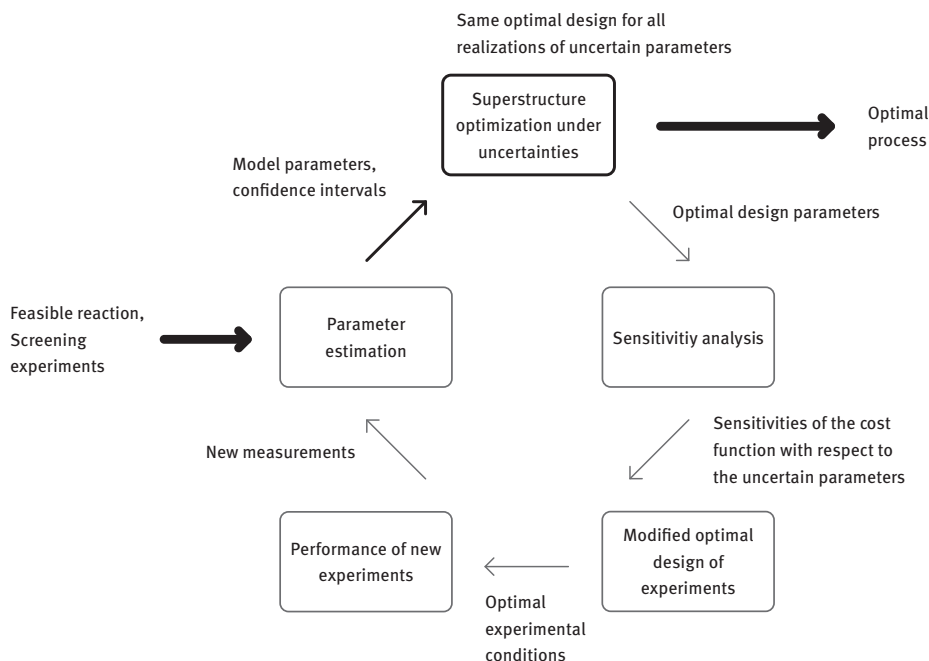


Figure 6.15: Schematic representation of the main elements of the integrated process design methodology.

These models are used in a subsequent step for superstructure optimization under uncertainties as explained in Section 5.3.3. At this point, it is checked if one or few process alternatives can be already identified as optimal. This would be the case if for all realizations the value of the cost function is lower for one design or a few designs compared to all other design alternatives. For large parametric model uncertainties, this is rather unlikely to happen. If no design could be identified as optimal, a sensitivity analysis of the cost function with respect to the uncertain parameters is performed to identify the parameters that have the largest impact on the cost function which will be explained in Section 6.5.2.2. The computed sensitivities are used as weights in the optimal DoEs to plan experiments that are focused on the determination of the most cost-relevant parameters.

6.5.2.2 Methods for Sensitivity Analysis in Process Synthesis

As lab experiments are expensive, process engineers want to identify those uncertain parameters that contribute most to the cost function of interest, for example, the production cost. For this, methods of local or global sensitivity analysis can be used. Local methods are computationally less expensive but provide reliable information

only in a small range around the nominal values of the parameters. Global methods require more computational effort but provide information for the entire parameter space [75].

Local sensitivity analysis can be performed by linear regression. Here, n uncertain parameters x_i are correlated to the regressed value \hat{Z}_j :

$$\hat{Z}_j = \beta_0 + \sum_{i=1}^n \beta_i x_i \quad (6.19)$$

The intercept β_0 and the regression coefficients β_i are determined via the least squares method. To standardize the regression coefficients with 0 mean and a standard deviation of 1, the standardized regression coefficients (SRC) are computed for N samples as follows [27]:

$$\text{SRC}_j = \frac{\beta_j \hat{S}_i}{\hat{S}} \quad (6.20)$$

with

$$\hat{S} = \left[\sum_j \frac{(Z_j - \bar{Z})^2}{N-1} \right]^{1/2} \quad (6.21)$$

and

$$\hat{S}_i = \left[\sum_j \frac{(x_i - \bar{x})^2}{N-1} \right]^{1/2} \quad (6.22)$$

Since the SRCs are independent of the regressor, they can be used to compare the effect of the parameters on the objective function. Large SRCs correspond to a large impact on the objective. The samples are generated via perturbation from their corresponding nominal value. Thus, a linear approximation of the objective function in this region is generated.

In global sensitivity analysis, samples are taken from the entire parameter space. The sampling points should be distributed evenly. For this, Latin hypercube sampling can be used which is explained in Section 5.2.3. According to Sobol [83], the effect of a single parameter x_i can be computed via

$$S_i = \frac{\text{var}(y|x_i)}{\text{var}(y)} \quad (6.23)$$

Here, $\text{var}(y|x_i)$ is the conditional variance of the output y with respect to the i th parameter. $\text{var}(y)$ is the general variance of y . The total effect, which takes additionally nonlinear and interaction effects into account, can be computed as

$$S_{T,i} = 1 - \frac{\text{var}(y|x_{\sim i})}{\text{var}(y)} \quad (6.24)$$

where $\text{var}(y|x_{\sim i})$ is the conditional variance of y with respect to all parameters except parameter i .

6.5.2.3 Case Study I: Hydroaminomethylation of 1-Decene

The approach presented above is applied to the hydroaminomethylation of 1-dodecene in a TMS [40]. The process includes unit operations for the reaction, phase separation, and the removal of the byproduct, water. As hydroaminomethylation can be considered as the sequence of the steps of hydroformylation and reductive amination, the kinetic models described in Hentschel et al. [29] and Kirschtowski et al. [50] (Section 3.2) are combined in order to get a first structure of the kinetic model. The parameters were fitted to experimental data of the hydroaminomethylation in a solvent system of methanol and dodecane. 12 different batch experiments where the concentration profiles were measured over time were used for the initial parameter estimation.

For the prediction of the solubilities of the components of syngas in the reaction medium and the phase separation in the decanter, thermodynamic models are needed. The gas–liquid and the liquid–liquid equilibrium can be predicted with PC-SAFT. The required parameters for the syngas, the solvents, and the main components are available in Huxoll [34]. Since the equations of PC-SAFT have to be solved iteratively, it is not suitable to use them directly in optimization [64]. Therefore, artificial neural networks were trained to predict the concentrations of hydrogen and carbon monoxide in the liquid phase depending on the temperature, the partial pressures, and the solvent composition. For describing the liquid–liquid equilibrium, the distribution coefficients defined as $K_i = \dot{n}_{i, \text{polar}} / \dot{n}_{i, \text{feed}}$ are fitted by artificial neural networks with respect to the temperature and the composition of the inlet of the decanter. The removal of water is modeled by a membrane model, using a solution-diffusion model.

The objective of the superstructure optimization is the minimization of the production cost per ton of the long-chain amine. The prediction of the costs includes the costs of the raw materials, the investments, and the utilities. As it is assumed that the solvents can be recovered in a further separation step, they are not included in the cost function.

The uncertainties considered here are the pre-exponential factors $k_{0,i}$ and the activation energies $E_{A,i}$ of the kinetic model resulting in 31 uncertain parameters. 35 different combinations of the uncertain parameters within their 95% confidence regions are used in the superstructure optimization under uncertainties. As described in Section 5.3.3, a two-stage optimization is performed where the design parameters are the

same for each scenario and are optimized under the assumption that the operating parameters (called recourse variables) are adapted to the actual values of the parameters in each scenario by control or online optimization during operation. Here, the design decisions include the binary decisions if the reaction is performed as a tandem reaction, meaning that all reactants and the catalyst are added into one reactor for the hydroaminomethylation, or if the hydroformulation and the reductive amination are performed in two subsequent reaction steps. The second binary decision is the choice if the polar and the unipolar solvent are added to the reactor forming a TMS system or if the nonpolar solvent is added after the reaction for phase separation and catalyst recycling. The recourse variables are the temperatures and partial pressures in the reactor, the solvent ratio, the temperature in the decanter, and the catalyst concentration.

The results for the four best designs that are structurally different are shown in Figure 6.16.

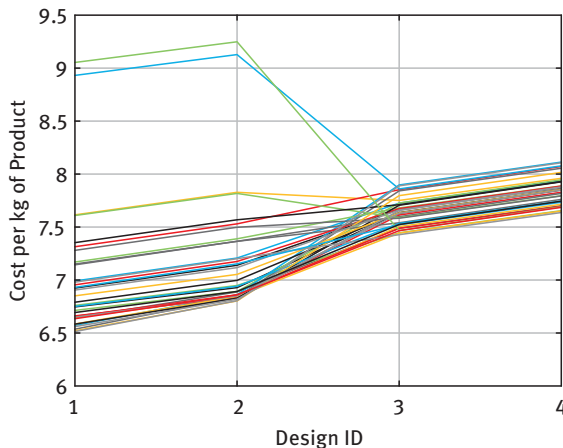


Figure 6.16: Costs for the four best process designs for different combinations of the uncertain parameters from the first superstructure optimization.

From Figure 6.16, it can be seen that no decision about the best design can be made at this point, which makes further model improvement necessary. The operating conditions can be adjusted depending on the realization of the uncertain parameters. The scaled operating conditions for design 1 are shown in Figure 6.17. It can be seen that the optimal operating conditions strongly depend on uncertain parameters.

The results of the sensitivity analysis after the first superstructure optimization that are presented in Figure 6.18 show that the reaction rate constants of the isomerization have the largest impact on the cost function. This can be explained by the fact that the reaction toward the side product *iso*-decene only occurs to a small extent and therefore this parameter is the most uncertain. The large variation of the side reaction leads to a large variation in the yield and hence in the production cost.

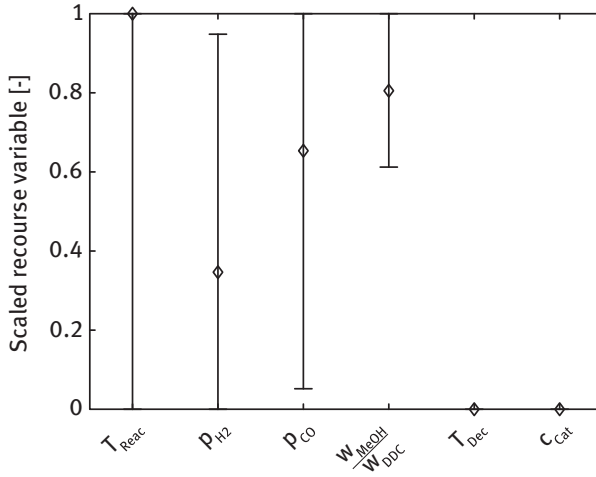


Figure 6.17: Recourse variables scaled with respect to their bounds.

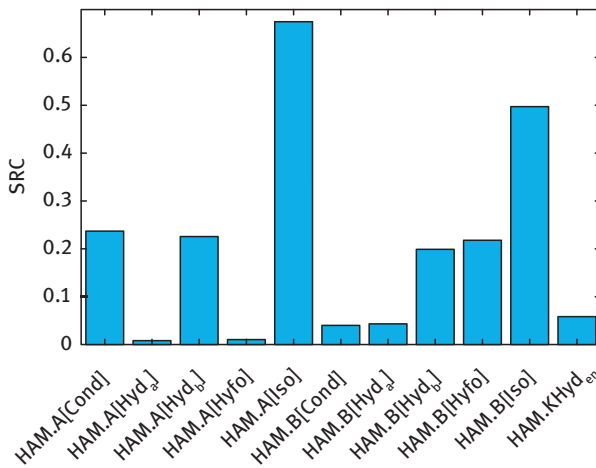


Figure 6.18: Standardized regression coefficients (SRC) for the kinetic parameters. Reproduced from [40].

The results of the weighted mboED with the temperature, the pressure, the ratio of H_2 and CO , the catalyst concentration, and the sampling times as DoF are presented in Table 6.10. The optimal sampling times were identified as 6.5, 40.4, 40.4, 60, and 60 min.

The iterative process design is then applied using simulation experiments. The measurements are generated using a simulation model with the true parameters, corrupted by white noise with a standard deviation of 5%. In each iteration, the model parameters are updated using the new measurements, a superstructure optimization

Table 6.10: Optimally designed experiment for the hydroaminomethylation of 1-decene.

Temperature (K)	Pressure (bar)	Catalyst concentration ($\text{mol}_{\text{Cat}}/\text{mol}_{\text{Substrate}}$)	Gas composition (CO: H ₂) (mol/mol)
136.4	50	0.002	0.5

is performed, the most relevant parameters are identified and a new experiment is planned. This procedure is repeated until one structurally different design is superior to the others for all discrete scenarios. For this desired result, eight additional experiments are needed if they are iteratively planned. The comparison of the iterative procedure and a model refinement using a full-factorial design with 16 additional experiments is shown in Figure 6.19. It can be seen that for the factorial design no decision about the best design can be made because the order is different for different scenarios although the number of experiments is twice as large as for the iterative procedure. Therefore, it can be concluded that the proposed model-based iterative process design can reduce the experimental effort and hence the time and costs for process development.

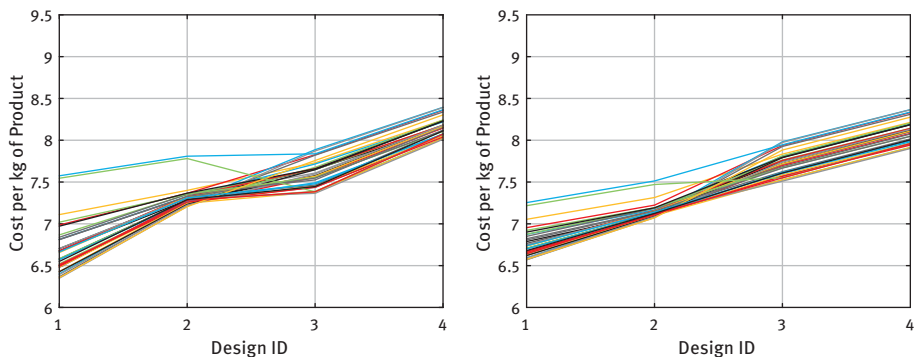


Figure 6.19: Comparison of the costs for the four best process designs for different combinations of the uncertain parameters after model refinement using 16 experiments planned by a full-factorial design on the left and after 8 iteratively designed experiments on the right.

6.5.2.4 Case Study II: Hydroformylation of 1-Dodecene

In this section, we show the benefits of using global sensitivity analysis in the integrated process development by applying it to the hydroformylation of 1-dodecene [41]. Here, we focus on the combination of sensitivity analysis and mbOED.

The process model that was used is described in detail by Hernandez et al. [30]. The pre-exponential factors and the activation energies of the hydroformylation and the isomerization of 1-dodecene of the kinetic model developed by Hentschel et al. [29]

are considered as uncertain parameters. All other parameters of the kinetic model have been observed as less influencing and are hence fixed to their predefined values.

In the mBOED, isothermal batch experiments are planned that measure the concentration profile over the batch time. The reaction temperature, the initial concentrations of 1-dodecene and *iso*-dodecene, the ratio of H₂ to CO, the catalyst concentration, and the sampling times of the concentration measurements are considered as DoF. The number of measurements taken during each batch experiment is fixed to six. The cost function is the yield of tridecanal in the product stream with respect to the 1-dodecene in the feed stream. Simulation results of a kinetic model with the true parameters, corrupted by white noise with a standard deviation of 5% are used as measurements of the batch experiments.

Three methods are compared: mBOED with unweighted FIM (normal), mBOED with the FIM weighted by local sensitivity analysis (local), and mBOED with the FIM weighted by global sensitivity analysis (global). For the first parameter estimation, the experiment is performed at two different temperatures and the measurements are taken equidistantly. In iterative steps of parameter estimation, mBOED, and a new experiment, planned according to the applied methods, a sequence of 25 new experiments was planned. The predicted yield over the number of experiments is evaluated and compared to a benchmark of a static factorial design where in total 32 experiments are performed at the lower and upper bounds of 5 DoF. In each iteration, the minimum and maximum yields are computed for the values of the uncertain parameters within the 95% confidence interval. To reduce the effect of random noise in the predictions, the mean values of 10 runs are considered. The evolution of the predicted yield is shown in Figure 6.20.

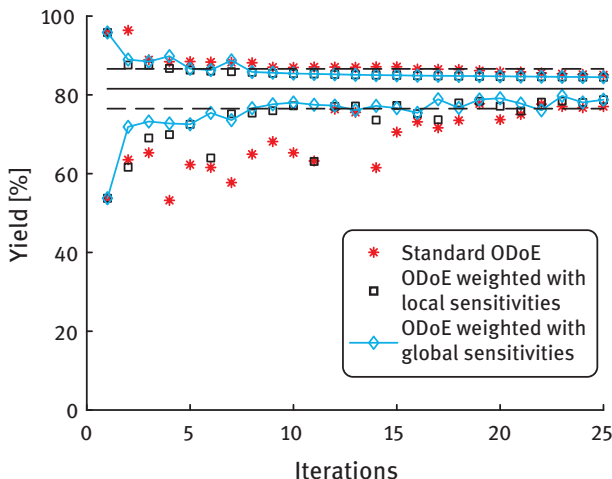


Figure 6.20: Evolution of the predicted intervals of the yield of tridecanal. The solid line represents the true yield and the dashed line represents the yield predicted with parameters obtained from a full factorial design of 32 experiments reproduced from [41].

The minimum and maximum predicted yields for all three cases are presented together with the true yield and the yield predicted using factorial sampling. After only 9 experiments, the prediction of the minimum yield is better compared to the factorial design in the case of the global sensitivity analysis and after 15 iterations in the case of the local sensitivity analysis. The standard mbOED performs erratically in comparison. This can be explained by the fact that in this case, it can happen that experiments are planned that improve a parameter with a low impact on the yield. It shows that by using weights on the parameters with a large impact on the cost function, more efficient experiments can be planned. As the global sensitivity analysis also takes nonlinear effects into account, it performs even better than the local sensitivity analysis.

It was shown how the integration of the DoEs and optimization under uncertainty can be used to accelerate the early design phase. Superstructure optimization under uncertainties helps to identify promising process alternatives and the variation of the predicted cost over the range of the uncertain parameters of a process design. Sensitivity analysis was applied to identify the model parameters that have a high impact on the final production costs. These parameters should then be determined by further experiments. An optimal DoE, in which the FIM is weighted by either local or global sensitivities, leads to fewer experiments that are required to reduce the variation in the cost function.

6.5.3 Advanced Integration Potential for Systematic Multiphase Process Design

The methodology presented in Section 6.4.2 can be extended to include further aspects in process design. Although only some applications were shown so far, the approach allows for many future applications. First, the integration in the methodology proposed for the selection of the phase system is possible. Simplified process models can be generated for each possible phase system and can be included in the superstructure optimization. As stated in Section 6.2, phase systems with the least possible number of additional substances are preferable. The two objectives – minimizing the process costs and using the least possible number of additional substances – can be evaluated by drawing the Pareto front, a curve of all results where one objective cannot be improved without worsening the other. Based on this evaluation, a decision about the best process can be made.

Moreover, methods for model-based solvent selection and optimal reactor design have been presented in Sections 6.3 and 5.3.1. As these methods are also part of the process design, the possibilities to include them in the integrated approach will be discussed in more detail in the following sections.

6.5.3.1 Model-Based Solvent Selection

Solvent selection is an important issue in the design of processes with liquid multi-phase systems. Therefore, it is desirable to include solvent selection in the methodology for integrated process design. The proposed integration in the existing methodology is shown schematically in Figure 6.21.

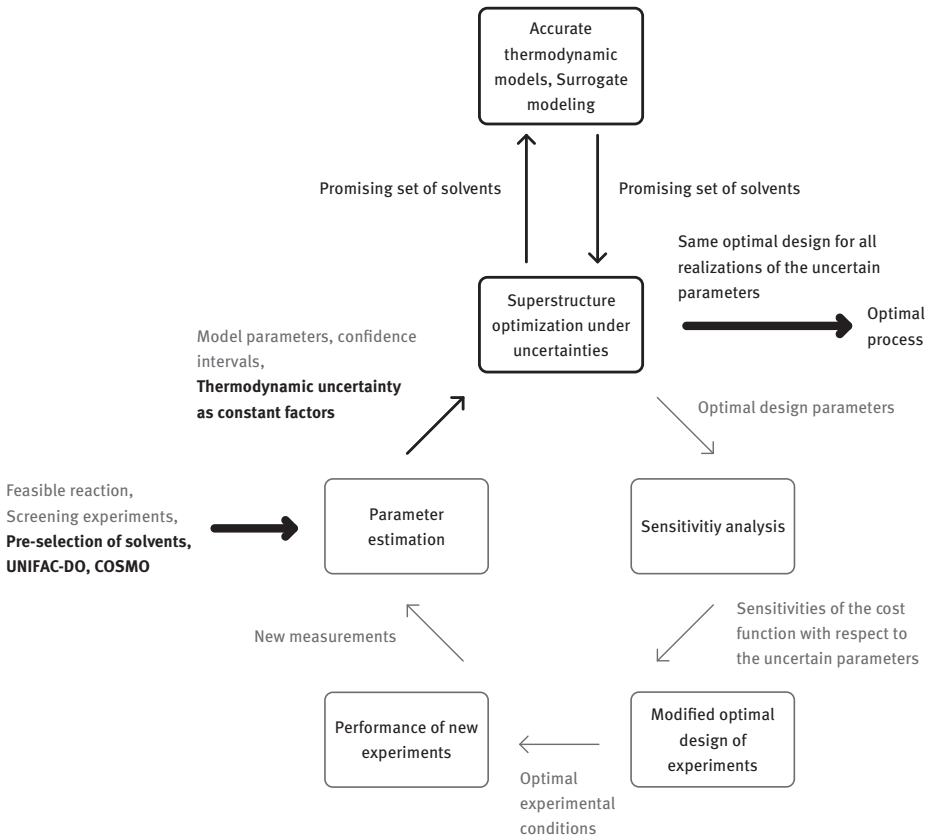


Figure 6.21: Proposed integration of solvent selection in process design. Blocks that are not part of the solvent selection procedure are marked in light gray.

The superstructure can be extended by thermodynamic models of all potential solvent candidates that have been selected based on expert's knowledge or by computer-aided solvent design as presented in Section 6.4. As the number of solvents that have to be considered might be large at this stage and accurate thermodynamic models will not be available for all of them, group contribution methods such as UNIFAC-Do can be used for a first approximation of the thermodynamic behavior (Section 6.3.3). Other options are, for example, the prediction by COSMO-RS as it was explained in Section 6.3.3.

The selection of solvents can be modeled in the superstructure optimization by binary variables, that is, one for each solvent. The maximum number of solvents that are allowed can be restricted using an inequality constraint. Constraints may have to be formulated to ensure that the desired behavior is reached. For example, the number of phases during reaction and separation can be predefined, for example, to ensure a single-phase reaction medium and a two-phase separation if a TMS system is used, as it was done in the case study presented in Section 6.5.2.3.

After a first superstructure optimization of the process, more detailed thermodynamic models can be derived for the most promising solvents. As described in Section 3.1, the application of PC-SAFT provides an accurate prediction of complex phase behavior, accounting for non-ideal interactions between the reactants/products and the solvents.

If such accurate models are not suitable for optimization, surrogate models as discussed in Section 5.2.3 can be applied. These models are used to replace the equations for the thermodynamic behavior in the process model. Following the methodology discussed in Section 6.4.2, the uncertainties in these thermodynamic models can then be reduced further until they do not influence the decision of the optimal process anymore.

This procedure enables not only to identify one optimal solvent but also to consider different numbers and combinations of solvents. Since the complete flow sheet is considered and optimized, it is possible to select a solvent system that provides the best overall performance.

6.5.3.2 Model-Based Optimal Reactor Design

While superstructure optimization in process design is able to identify the optimal interconnection and operation of elements from a set of preestablished, usually manually selected, unit operations, the EPF methodology from Section 5.3.1 represents an approach to the design of optimal reactor–(separator) networks without the necessity of a-priori knowledge about specific process units. This enables the identification of non-intuitive, non-standard reactor networks and operation strategies which might greatly improve the process performance.

While both approaches can be used for process development sequentially, a combination of superstructure optimization with the EPF methodology as one building block in the process design cycle represents a powerful addition to the integrated process design framework. Figure 6.22 contains a schematic representation of the interaction between mbOED and superstructure optimization including reactor network design via EPF. Two scenarios with different degrees of integration are possible.

Scenario 1: The flux-profile analysis (Section 5.3.1) is able to create reactor network candidates which need to be implemented and analyzed rigorously in terms of performance and cost [39]. Instead of manually comparing each of the reactor network candidates, these candidates can be used directly as unit operations in the

superstructure optimization. This integration enables the systematic evaluation of all candidates not only with respect to the reaction performance but also on the process scale, taking into account the downstream process (Figure 6.22).

Scenario 2: Instead of integrating reactor network candidates in the superstructure optimization, an “EPF reactor” with the extensions of axial dispersion, as discussed in Section 5.3.1, can be used as the sole reaction unit as shown by Hentschel et al. [28]. The simultaneous optimization of the operating conditions of the EPF reactor in the superstructure optimization replaces the inclusion of other reactor candidates which have fewer DoF and, therefore, show inferior performance. As a consequence, the superstructure is mainly used to identify the optimal downstream process and auxiliary process units. To incorporate the three-level approach to reactor network design of the EPF methodology, an additional iteration loop around the superstructure optimization is necessary to include realistic technical approximations.

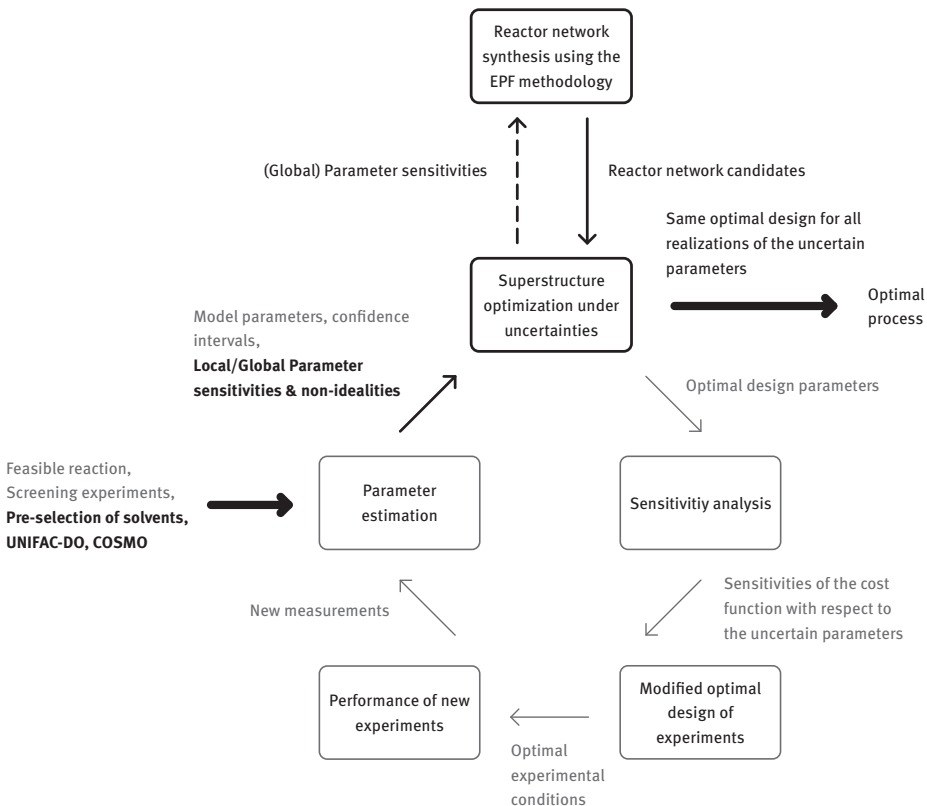


Figure 6.22: Integration of EPF-based reactor network candidates in the integrated process design framework. The interactions between superstructure optimization and EPF calculations are highlighted in dark gray. Global parameter sensitivities are only available in the second iteration cycle and therefore visualized with a dashed arrow.

The integration of the EPF methodology in this framework also enables synergistic effects. Consideration of uncertainty, especially parameter uncertainty, is of major importance in reactor design and leads to a more robust reactor and process performance. While Kaiser et al. [38] only considered the influence of uncertainty on the reactor performance, the combination of the probabilistic reactor design using sigma points with weights in the form of the global sensitivities with respect to the entire flow sheet allows for improved robustness of the process with optimally designed and operated reactor networks.

6.5.4 Summary

In this section, an integrated approach for model-based process development has been discussed. Model-based Optimal Experimental Design is a useful tool to identify model parameters with minimal experimental effort. However, usually, it does not focus on specific parameters, for example, parameters that are relevant for the uncertainty in the prediction of the final process costs. This can be overcome by using the integrated approach. By performing superstructure optimization under uncertainties, promising process designs can be identified and the impact of the model uncertainties on the production costs can be estimated via sensitivity analysis. Applying the computed sensitivities as weights in the mbOED enables focusing the experiments on the cost-relevant parameters to get a faster decrease of the parameter uncertainty. In this section, the application of this methodology was presented for two different processes, namely the hydroformylation of 1-dodecene and the hydroaminomethylation of 1-decene.

Finally, options for the extension of the methodology to further important aspects of the process development, for example, optimal solvent selection and optimal reactor design have been sketched briefly which are interesting fields for further research.

References

- [1] Adjiman CS, Sahinidis NV, Vlachos DG, Bakshi B, Maravelias CT, Georgakis C. 2021: Process systems engineering perspective on the design of materials and molecules. *Ind. Eng. Chem. Res.* 60: 5194–5206.
- [2] Asprión N, Böttcher R, Mairhofer J, Yliruka M, Höller J, Schwientek J, Vanaret C, Bortz M. 2019: Implementation and application of model-based design of experiments in a flowsheet simulator. *J. Chem. Eng. Data.* 65: 1135–1145.
- [3] Austin ND, Sahinidis NV, Trahan DW. 2016: Computer-aided molecular design: An introduction and review of tools, applications, and solution techniques. *Chem. Eng. Res. Des.* 116: 2–26.

- [4] Bardow A, Steur K, Gross J. 2009: A continuous targeting approach for integrated solvent and process design based on molecular thermodynamic models. 10th Intern. Symp. Proc. Sys. Eng. 813–818.
- [5] Bardow A, Steur K, Gross J. 2010: Continuous-molecular targeting for integrated solvent and process design. *Ind. Eng. Chem. Res.* 49: 2834–2840.
- [6] Benfenati E, Manganaro A, Gini G. 2013: VEGA-QSAR: AI inside a platform for predictive toxicology. *CEUR Workshop Proceedings*.
- [7] Boz E, Tüzün NŞ, Stein M. 2018: Computational investigation of the control of the thermodynamics and microkinetics of the reductive amination reaction by solvent coordination and a co-catalyst. *RSC Adv.* 8: 36662–36674.
- [8] Burger J, Papaioannou V, Gopinath S, Jackson G, Galindo A, Adjiman CS. 2015: A hierarchical method to integrated solvent and process design of physical CO₂ absorption using the SAFT-γ Mie approach. *AIChE J.* 61: 3249–3269.
- [9] Buxton A, Livingston AG, Pistikopoulos EN. 1999: Optimal design of solvent blends for environmental impact minimization. *AIChE J.* 45: 817–843.
- [10] Chemmangattuvalappil NG, Eden MR. 2013: A novel methodology for property-based molecular design using multiple topological indices. *Ind. Eng. Chem. Res.* 52: 7090–7103.
- [11] Chemmangattuvalappil NG. 2020: Development of solvent design methodologies using computer-aided molecular design tools. *Curr. Op. Chem. Eng.* 27: 51–59.
- [12] Chen Y, Gani R, Kontogeorgis GM, Woodley JM. 2019: Integrated ionic liquid and process design involving azeotropic separation processes. *Chem. Eng. Sci.* 203: 402–414.
- [13] Chen Q, Grossmann IE. 2017: Recent developments and challenges in optimization-based process synthesis. *Ann. Rev. Chem. Biomol. Eng.* 8: 249–283.
- [14] Cheng HC, Wang FS. 2010: Computer-aided biocompatible solvent design for an integrated extractive fermentation–separation process. *Chem. Eng. J.* 162: 809–820.
- [15] Churi N, Achenie LE. 1996: Novel mathematical programming model for computer aided molecular design. *Ind. Eng. Chem. Res.* 35: 3788–3794.
- [16] Douglas JM. 1985: A hierarchical decision procedure for process synthesis. *AIChE J.* 31: 353–362.
- [17] Eden MR, Jørgensen SB, Gani R, El-Halwagi MM. 2004: A novel framework for simultaneous separation process and product design. *Chem. Eng. Proc. Proc. Intensif.* 43: 595–608.
- [18] Eljack FT, Eden MR, Kazantzi V, Qin X, El-Halwagi MM. 2007: Simultaneous process and molecular design – A property based approach. *AIChE J.* 53: 1232–1239.
- [19] Ferro VR, Ruiz E, de Riva J, Palomar J. 2012: Introducing process simulation in ionic liquids design/selection for separation processes based on operational and economic criteria through the example of their regeneration. *Separ. Purif. Techn.* 97: 195–204.
- [20] First EL, Hasan MM, Floudas CA. 2014: Discovery of novel zeolites for natural gas purification through combined material screening and process optimization. *AIChE J.* 60: 1767–1785.
- [21] Fleitmann L, Scheffczyk J, Schäfer P, Jens C, Leonhard K, Bardow A. 2018: Integrated design of solvents in hybrid reaction-separation processes using COSMO-RS. *Chem. Eng. Trans.* 69: 599–564.
- [22] Franceschini G, Macchietto S. 2008: Model-based design of experiments for parameter precision: State of the art. *Chem. Eng. Sci.* 63: 4846–4872.
- [23] Gani R. 2019: Group contribution-based property estimation methods: Advances and perspectives. *Curr. Opi. Chem. Eng.* 23: 184–196.
- [24] Gertig C, Fleitmann L, Schilling J, Leonhard K, Bardow A. 2020b: Rx-COSMO-CAMPD: Enhancing reactions by integrated computer-aided design of solvents and processes based on quantum chemistry. *Chem. Ing. Tech.* 92: 1489–1500.

- [25] Gertig C, Leonhard K, Bardow A. 2020a: Computer-aided molecular and processes design based on quantum chemistry: Current status and future prospects. *Curr. Opi. Chem. Eng.* 27: 89–97.
- [26] Gertig C, Fleitmann L, Hemprich C, Hense J, Bardow A, Leonhard K. 2021: CAT-COSMO-CAMPD: Integrated in silico design of catalysts and processes based on quantum chemistry. *Comp. Chem. Eng.* 153: 107438.
- [27] Harrmann M. 2019. Contribution to the management of laboratory experiments in early phases of process development. Dissertation TU Dortmund.
- [28] Hentschel B, Peschel A, Freund H, Sundmacher K. 2014: Simultaneous design of the optimal reaction and process concept for multiphase systems. *Chem. Eng. Sci.* 115: 69–87.
- [29] Hentschel B, Kiedorf G, Gerlach M, Hamel C, Seidel-Morgenstern A, Freund H, Sundmacher K. 2015: Model-based identification and experimental validation of the optimal reaction route for the hydroformylation of 1-dodecene. *Ind. Eng. Chem. Res.* 54: 1755–1765.
- [30] Hernandez R, Dreimann J, Vorholt A, Behr A, Engell S. 2018: Iterative real-time optimization scheme for optimal operation of chemical processes under uncertainty: Proof of concept in a miniplant. *Ind. Eng. Chem. Res.* 57: 8750–8770.
- [31] Heyse A, Plikat C, Grün M, Delaval S, Ansorge-Schumacher M, Drews A. 2018: Impact of enzyme properties on drop size distribution and filtration of water-in-oil Pickering emulsions for application in continuous biocatalysis. *Proc. Biochem.* 72: 86–95.
- [32] Hoang MD, Barz T, Merchan VA, Biegler LT, Arellano-Garcia H. 2013: Simultaneous solution approach to model-based experimental design. *AIChE J.* 59: 4169–4183.
- [33] Hostrup M, Harper PM, Gani R. 1999: Design of environmentally benign processes: Integration of solvent design and separation process synthesis. *Comp. Chem. Eng.* 23: 1395–1414.
- [34] Huxoll F, Jameel F, Bianga J, Seidensticker T, Stein M, Sadowski G, Vogt D. 2021: Solvent selection in homogeneous catalysis-optimization of kinetics and reaction performance. *ACS Catal.* 11: 590–594.
- [35] Jameel F, Kohls E, Stein M. 2019: Mechanism and control of the palladium-catalyzed alkoxy carbonylation of oleochemicals from sustainable sources. *Chem Cat Chem.* 11: 4894–4906.
- [36] Jameel F, Stein M. 2021: Solvent effects in hydroformylation of long-chain olefins. *Mol. Cat.* 503: 111429.
- [37] Kaiser NM. 2019: Dynamic Optimization Based Reactor Synthesis and Design under Uncertainty for Liquid Multiphase Processes. Ph.D. Thesis. Otto-von-Guericke-Universität Magdeburg.
- [38] Kaiser NM, Flassig RJ, Sundmacher K. 2016: Probabilistic reactor design in the framework of elementary process functions. *Comp. Chem. Eng.* 94: 45–59.
- [39] Kaiser NM, Flassig RJ, Sundmacher K. 2017: Reactor-network synthesis via flux profile analysis. *Chem. Eng. J.* 335: 1018–1030.
- [40] Kaiser S, Engell S. 2020: Integrating superstructure optimization under uncertainty and optimal experimental design in early stage process development. *Comp. Aided Chem. Eng.* 48: 799–804.
- [41] Kaiser S, Menzel T, Engell S. 2021: Focusing experiments in the early phase process design by process optimization and global sensitivity analysis. *Comp. Aided Chem. Eng.* 50: 899–904.
- [42] Keskes E, Adjiman CS, Galindo A, Jackson G. 2006: Integrating advanced thermodynamics and process and solvent design for gas separation. 16th Eur. Symp. on Comp. Aided Proc. Eng. and 9th Int. Symp. on Proc. Systems Eng. 743–748.

- [43] Keßler T, Kunde C, Linke S, McBride K, Sundmacher K, Kienle A. 2019a: Systematic selection of green solvents and process optimization for the hydroformylation of long-chain olefines. *Processes*. 7: 882.
- [44] Keßler T, Kunde C, McBride K, Mertens N, Michaels D, Sundmacher K, Kienle A. 2019b: Global optimization of distillation columns using explicit and implicit surrogate models. *Chem. Eng. Sci.* 197: 235–245.
- [45] Keßler T, Kunde C, Linke S, McBride K, Sundmacher K, Kienle A. 2020: Computer aided molecular design of green solvents for the hydroformylation of long-chain olefines. 30th Eur. Symp. Comp. Aided Chem. Eng. 745–750.
- [46] Keßler T, Kunde C, Linke S, Sundmacher K, Kienle A. 2022: Integrated computer-aided molecular and process design: Green solvents for the hydroformylation of long-chain olefines. *Chem. Eng. Sci.* 249: 117243.
- [47] Kim KJ, Diwekar UM. 2002: Integrated solvent selection and recycling for continuous processes. *Ind. Eng. Chem. Res.* 41: 4479–4488.
- [48] Kunde C, Keßler T, Linke S, McBride K, Sundmacher K, Kienle A. 2019: Surrogate modeling for liquid–liquid equilibria using a parameterization of the binodal curve. *Processes*. 7: 753.
- [49] Kirschtowski S, Jameel F, Stein M, Seidel-Morgenstern A, Hamel C. 2021: Kinetics of the reductive amination of 1-undecanal in thermomorphic multicomponent system. *Chem. Eng. Sci.* 230: 116187.
- [50] Kirschtowski S, Kadar C, Seidel-Morgenstern A, Hamel C. 2020: Kinetic modeling of rhodium-catalyzed reductive amination of undecanal in different solvent systems. *Chem. Ing. Tech.* 92: 582–588.
- [51] Klamt A, Jonas V, Bürger T, Lohrenz JC. 1998: Refinement and parametrization of COSMO-RS. *J. Phys. Chem. A.* 102: 5074–5085.
- [52] Klamt A, Schüürmann G. 1993: COSMO: A new approach to dielectric screening in solvents with explicit expressions for the screening energy and its gradient. *J. Chem. Soc. Perkin Trans. 2*: 799–805.
- [53] Lampe M, Stavrou M, Bücker HM, Gross J, Bardow A. 2014: Simultaneous optimization of working fluid and process for organic rankine cycles using PC-SAFT. *Ind. Eng. Chem. Res.* 53: 8821–8830.
- [54] Lampe M, Stavrou M, Schilling J, Sauer E, Gross J, Bardow A. 2015: Computer-aided molecular design in the continuous-molecular targeting framework using group-contribution PC-SAFT. *Comp. Chem. Eng.* 81: 278–287.
- [55] Lemberg M, Sadowski G, Gerlach M, Kohls E, Stein M, Hamel C, Seidel-Morgenstern A. 2017: Predicting solvent effects on the 1-dodecene hydroformylation reaction equilibrium. *AIChE J.* 63: 4576–4585.
- [56] Linke S, McBride K, Sundmacher K. 2020: Systematic green solvent selection for the hydroformylation of long-chain alkenes. *ACS Sust. Chem. Eng.* 8: 10795–10811.
- [57] Liu Q, Zhang L, Liu L, Du J, Meng Q, Gani R. 2019: Computer-aided reaction solvent design based on transition state theory and COSMO-SAC. *Chem. Eng. Sci.* 202: 300–317.
- [58] Ljung L. 1999: *System Identification: Theory for the User*. Prentice Hall.
- [59] Marcoulaki EC, Kokkosis AC. 2000: On the development of novel chemicals using a systematic optimisation approach. Part II. Solvent Design. *Chem. Eng. Sci.* 55: 2547–2561.
- [60] McBride K, Gaide T, Vorholt A, Behr A, Sundmacher K. 2016: Thermomorphic solvent selection for homogeneous catalyst recovery based on COSMO-RS. *Chem. Eng. Proc. Proc. Intensif.* 99: 97–106.
- [61] McBride K, Kaiser NM, Sundmacher K. 2017: Integrated reaction–extraction process for the hydroformylation of long-chain alkenes with a homogeneous catalyst. *Comp. Chem. Eng.* 105: 212–223.

- [62] McBride K, Linke S, Xu S, Sundmacher K. 2018: Computer aided design of green thermomorphic solvent systems for homogeneous catalyst recovery. 13th Intern. Symp. Proc. Sys. Eng. 1783–1788.
- [63] Meindersma GW, de Haan AB. 2008: Conceptual process design for aromatic/aliphatic separation with ionic liquids. Chem. Eng. Res. Des. 86: 745–752.
- [64] Nentwich C, Engell S. 2019: Surrogate modeling of phase equilibrium calculations using adaptive sampling. Comp. Chem. Eng. 126: 204–217.
- [65] Papadopoulos AI, Linke P. 2005: A unified framework for integrated process and molecular design. Chem. Eng. Res. Des. 83: 674–678.
- [66] Papadopoulos AI, Linke P. 2006: Efficient integration of optimal solvent and process design using molecular clustering. Chem. Eng. Sci. 61: 6316–6336.
- [67] Papadopoulos AI, Linke P. 2009: Integrated solvent and process selection for separation and reactive separation systems. Chem. Eng. Proc. Intensif. 48: 1047–1060.
- [68] Papadopoulos AI, Seferlis P, Linke P. 2017: A framework for the integration of solvent and process design with controllability assessment. Chem. Eng. Sci. 159: 154–176.
- [69] Papadopoulos AI, Tsvintzelis I, Linke P, Seferlis P. 2018: Computer-aided molecular design: fundamentals, methods, and applications. In: *Reference Module in Chemistry, Molecular Sciences and Chemical Engineering*. Elsevier.
- [70] Pereira FE, Keskes E, Galindo A, Jackson G, Adjiman CS. 2011: Integrated solvent and process design using a SAFT-VR thermodynamic description: High-pressure separation of carbon dioxide and methane. Comp. Chem. Eng. 35: 474–491.
- [71] Pistikopoulos EN, Stefanis SK. 1998: Optimal solvent design for environmental impact minimization. Comp. Chem. Eng. 22: 717–733.
- [72] Rätze KHG, Jokiel M, Kaiser NM, Sundmacher K. 2019: Cyclic operation of a semi-batch reactor for the hydroformylation of long-chain olefins and integration in a continuous production process. Chem. Eng. J. 377: 120453.
- [73] Recker S, Kerimoglu N, Harwardt A, Tkacheva O, Marquardt W. 2013: On the integration of model identification and process optimization. Comp. Aided Chem. Eng. 32: 1021–1026.
- [74] Sahinidis NV, Tawarmalani M, Yu M. 2003: Design of alternative refrigerants via global optimization. AIChE J. 49: 1761–1775.
- [75] Saltelli A, Ratto M, Andres T, Campolongo F, Cariboni J, Gatelli D, Tarantola S. 2008: *Global Sensitivity Analysis*. The Primer. John Wiley & Sons.
- [76] Scheffczyk J, Redepenning C, Jens CM, Winter B, Leonhard K, Marquardt W, Bardow A. 2016: Massive, automated solvent screening for minimum energy demand in hybrid extraction–distillation using COSMO-RS. Chem. Eng. Res. Des. 115: 433–442.
- [77] Scheffczyk J, Schäfer P, Fleitmann L, Thien J, Redepenning C, Leonhard K, Marquardt W, Bardow A. 2018: COSMO-CAMPD: A framework for integrated design of molecules and processes based on COSMO-RS. Mol. Systems Des. Eng. 3: 645–657.
- [78] Schilling J, Tillmanns D, Lampe M, Hopp M, Gross J, Bardow A. 2017: From molecules to dollars: Integrating molecular design into thermo-economic process design using consistent thermodynamic modeling. Mol. Sys. Des. Eng. 2: 301–320.
- [79] Schilling J, Horend C, Bardow A. 2020: Integrating superstructure-based design of molecules, processes, and flowsheets. AIChE J. 66: e16903.
- [80] Schilling J, Entrup M, Hopp M, Gross J, Bardow A. 2021: Towards optimal mixtures of working fluids: integrated design of processes and mixtures for organic rankine cycles. Renew. Sust. Energy Rev. 135: 110179.
- [81] Schuur B. 2015: Selection and design of ionic liquids as solvents in extractive distillation and extraction processes. Chem. Papers. 69: 16.

- [82] Sioukrou E, Galindo A, Adjiman CS. 2014: On the optimal design of gas-expanded liquids based on process performance. *Chem. Eng. Sci.* 115: 19–30.
- [83] Sobol I. 2001: Global sensitivity indices for nonlinear mathematical models and their Monte Carlo estimates. In: *Mathematics and Computers in Simulation*. p. 271–280.
- [84] Struebing H, Ganase Z, Karamertzanis PG, Sioukrou E, Haycock P, Piccione PM, Armstrong A, Galindo A, Adjiman CS. 2013: Computer-aided molecular design of solvents for accelerated reaction kinetics. *Nature Chem.* 5: 952–957.
- [85] Sundmacher K, Freund H. 2010: Chemical process design: Moving matter elements along optimal travel routes in the thermodynamic state space. *PSE Asia 2010: The 5th Intern. Symp. on Design, Operation and Control of Chem. Proc.*
- [86] Ten JY, Hassim MH, Chemmangattuvalappil NG. 2020: Integration of safety and health aspects in a simultaneous process and molecular design framework. *Chem. Eng. Res. Des.* 153: 849–864.
- [87] US EPA. 2017: Estimation Programs Interface Suite for Microsoft Windows.
- [88] Van Derlinden E, Mertens L, Van Impe JF. 2013: The impact of experiment design on the parameter estimation of cardinal parameter models in predictive microbiology. *Food Control.* 29: 300–308.
- [89] Wang J, Lakerveld R. 2018: Integrated solvent and process design for continuous crystallization and solvent recycling using PC-SAFT. *AIChE J.* 64: 1205–1216.
- [90] Wang J, Zhu L, Lakerveld R. 2020: A hybrid framework for simultaneous process and solvent optimization of continuous anti-solvent crystallization with distillation for solvent recycling. *Processes.* 8: 63.
- [91] White MT, Oyewunmi OA, Haslam AJ, Markides CN. 2017: Industrial waste-heat recovery through integrated computer-aided working-fluid and ORC system optimisation using SAFT- γ Mie. *Energy Conv. Manag.* 150: 851–869.
- [92] Wu C, Bai S, Ansorge-Schumacher MB, Wang D. 2011: Nanoparticle cages for enzyme catalysis in organic media. *Adv. Mat.* 23: 5694–5699.
- [93] Zhang L, Pang J, Zhuang Y, Liu L, Du J, Yuan Z. 2020: Integrated solvent-process design methodology based on COSMO-SAC and quantum mechanics for TMQ (2,2,4-trimethyl-1,2-H-dihydroquinoline) production. *Chem. Eng. Sci.* 226: 115894.
- [94] Zhou T, Lyu Z, Qi Z, Sundmacher K. 2015b: Robust design of optimal solvents for chemical reactions – A combined experimental and computational strategy. *Chem. Eng. Sci.* 137: 613–625.
- [95] Zhou T, McBride K, Zhang X, Qi Z, Sundmacher K. 2015a: Integrated solvent and process design exemplified for a Diels-Alder reaction. *AIChE J.* 61: 147–158.
- [96] Zhou T, Wang J, McBride K, Sundmacher K. 2016: Optimal design of solvents for extractive reaction processes. *AIChE J.* 62: 3238–3249.
- [97] Zhou T, Zhou Y, Sundmacher K. 2017: A hybrid stochastic–deterministic optimization approach for integrated solvent and process design. *Chem. Eng. Sci.* 159: 207–216.
- [98] Zhou T, Song Z, Zhang X, Gani R, Sundmacher K. 2019: Optimal solvent design for extractive distillation processes: A multiobjective optimization-based hierarchical framework. *Ind. Eng. Chem. Res.* 58: 5777–5786.
- [99] Zhou T, McBride K, Linke S, Song Z, Sundmacher K. 2020: Computer-aided solvent selection and design for efficient chemical processes. *Curr. Opi. Chem. Eng.* 27: 35–44.

7 Résumé

Matthias Kraume

This volume presents the results obtained in the DFG Collaborative Research Center/Transregio 63 integrated chemical processes in liquid multiphase systems between 2010 and 2022. The overarching objectives of the research were a better understanding, detailed modeling, technical realization, and optimal design of liquid multiphase systems for the homogeneously catalyzed conversion of long-chain molecules. Substrates such as dodecene and unsaturated oleochemicals were selected to mimic biogenic feedstocks that are expected to increasingly replace conventional petrochemicals as raw materials in the near future. The physical properties of long-chain molecules call for specific solutions for an efficient contact between the reacting components and the catalysts used, as well as efficient separation of products, feeds, and catalysts to recycle the expensive catalysts and unconverted feedstock. To optimally meet the conflicting requirements of the chemical reaction and the subsequent separation steps, multiphase systems are a very promising option. Hydroformylation, hydroesterification, and hydroaminomethylation were selected as model reactions because they exhibit specific properties of industrially relevant reactions.

To use such unconventional multiphase systems in as environmentally friendly as possible processes, an innovative path that has not yet been implemented industrially was pursued: using phase systems with partially tunable properties. Three different phase systems (thermomorphic multiphase systems (TMS), microemulsion systems (MES), and Pickering emulsions (PE)) were selected from several possible options, as they represent a broad spectrum from highly dispersed and switchable to stable and easily separable. In these systems, different additives transform the originally nearly immiscible phases that contain the catalysts on the one hand and the reactants on the other into well-dispersed systems that provide the required contact between them, enabling fast chemical reactions by improved mass transport. The advantages of homogeneous catalysis were utilized while minimizing the problems usually associated with it, namely the recovery and recycling of the highly efficient but generally very expensive catalyst complexes.

The research on the example processes covered all levels of chemical process development, from the elementary steps of the reaction and the interaction with the reaction medium, the characterization of the investigated phase systems to the design and optimization of the individual processing steps to the design and operation of entire plants on the miniplant scale. Besides process and systems technology, investigations of physicochemical fundamentals constituted the scientific backbone of the research.

The thermodynamic and chemical fundamentals, as well as mass transfer phenomena, were elucidated and quantified as a preliminary step of process development and operation for the investigated phase systems. The determination of thermodynamic

data for process design usually requires a high experimental effort. Therefore, significant attention was paid to increasing the predictive power of the thermodynamic models. Two physically based models, the perturbed-chain statistical associating fluid theory (PC-SAFT) and the lattice cluster theory (LCT), were applied and complemented by new approaches developed for the description of TMS. As a result, both thermodynamic models could describe the phase equilibria of the studied TMS mixtures with an excellent agreement with the experimental data.

Regarding PC-SAFT, a new heterosegmented approach led to noticeable improvements in the prediction power. Furthermore, some model parameters could be correlated with the number of carbon atoms within a homologous series of molecules. Regarding LCT, an improvement in the description of small molecules could be achieved. Besides the phase behavior, the interfacial properties, such as interfacial tension, surface tension, and adsorption isotherms, could be modeled in good agreement with experimental data. This predictive power was achieved by combining the thermodynamic models with the density functional theory (DFT) for inhomogeneous systems. Additionally, PC-SAFT was also used to investigate chemical reactions. Precisely, the impact of solvents on the reaction equilibrium could be predicted in excellent agreement with experimental findings.

The phase behavior of mixtures that contain surfactants cannot be modeled in full detail because nanostructures are formed. Therefore, for mixtures containing surfactants, experimental investigations were performed that led to reliable phase diagrams. In addition, the aggregation model could be improved by replacing empirical correlations with PC-SAFT in combination with density gradient theory (DGT).

Due to the importance of reaction kinetics for reactor design and optimization, a general strategy was developed for deriving and parametrizing mechanistically based kinetic models for reactions in multiphase systems. This methodical approach is based on detailed catalytic cycles and their subsequent simplification utilizing different reduction approaches. To provide a deeper understanding of such complex reaction mechanisms and reaction networks, an interdisciplinary collaboration of chemistry, thermodynamics, quantum mechanics, and reaction engineering was required, both theoretically and experimentally. The developed method was successfully applied to the Rh/BIPHEPHOS-catalyzed isomerizing hydroformylation of 1-decene and isomeric feed mixtures consisting of re-isomerization and subsequent hydroformylation. Considering a complex reaction network of isomerization, hydrogenation, and hydroformylation, an excellent match between simulated and experimental data was achieved in a broad range of operating conditions using a single set of kinetic parameters.

In liquid multiphase systems, incompletely miscible organic and aqueous phases are brought into contact for a chemical reaction. In addition, gaseous feed components often occur, for example, in hydroformylation. In phase systems with partially tunable properties, this leads to complex mass transport phenomena which had not been described before. Therefore, the liquid–liquid and the gas–liquid mass transfer were characterized for the three different phase systems experimentally using different

devices. In addition to material properties such as diffusion coefficients and operating conditions, in particular fluid dynamics and temperature, the composition of the phase systems influences the transfer rates in a complex manner.

Complete processes for all three investigated phase systems were developed and successfully demonstrated based on the thermodynamic models and reaction kinetics. These processes include the chemical reaction, a phase separation step, and catalyst recovery and recycling in an integrated manner.

All three investigated phase systems were shown in the literature to be suitable for various chemical reactions using soluble catalysts, either typical homogeneous catalysts like metal complexes or enzymes. For all phase systems, detailed knowledge of their thermodynamics, separability, and physical properties was the basis for establishing a suitable phase separation that enables recycling of the catalysts and isolation of the products. Each phase system has its own advantages and disadvantages, rendering them the best-suited choice for different reactions and tasks. A broad range of additives is available for all phase systems, providing enough freedom to formulate appropriate reaction media for various chemical reactions with many different catalysts. MES and PE require only small amounts of additives, while TMS utilize larger quantities. On the other hand, water as the solvent for the catalyst requires a highly hydrophilic ligand. Still, water completely avoids the utilization of organic solvents, opening an optimal approach to Green Chemistry. Challenges in phase separation and catalyst recycling that had so far limited a more comprehensive application of the three phase systems were overcome, thus paving the way for continuous operation. Decantation (TMS and MES) was combined with other unit operations such as organic solvent nanofiltration for improved recycling of catalyst and additives and the removal of by-products. The combination of PE with membrane filtration has been shown to be a very promising and robust technique for efficient catalyst and additives recycling in a single step. For both MES and PE, models that describe the separation accurately were developed and can be used for model-based optimization and control of such processes.

For the example of the hydroformylation of 1-dodecene with modified rhodium catalysts, experimental investigations were carried out with TMS and MES in miniplant runs over several days using a CSTR as the reactor, continuous phase separation, catalyst phase recycling, and product withdrawal. The experiments in PE were performed as repeated batch runs. Although continuous phase separation and catalyst retention were achieved, catalyst recycling was not realized yet for hydroformylation in PE. The *n*:*iso* selectivity and the selectivity toward aldehydes were comparable in all three phase systems. Due to the different applied catalysts, the observed difference in reaction performance is probably caused by the inherently less active Rh/XANTPHOS catalyst compared to Rh/BIPHEPHOS rather than by the type of phase system. Lower reaction yields of a phase system can be outweighed by the ease of separation in an overall economic optimization of the entire integrated process. The achieved results demonstrate the feasibility of applying all three systems as reaction media for the

homogeneously catalyzed conversion of hydrophobic substrates, including efficient catalyst recycling.

The selection of a multiphase system as a reaction medium is motivated by the advantages for facilitated product isolation and catalyst separation and recycling. However, compared to a single solvent, such systems introduce substantial complexity into the development process. Their selection and design require detailed knowledge of the thermodynamics of nonideal liquid mixtures or the surface activity of surfactants or particles in combination with their colloidal properties. For the separation, often additional nonstandard unit operations and advanced control procedures are required. This introduces additional complexity and design degrees of freedom into the development process, requiring the best possible combination of experimental work with modeling, simulation, and optimization.

A significant challenge in designing a chemical production process is that the real production process consists of several unit operations involving various pieces of equipment, usually including recycle streams. This complexity makes it challenging to make the right decisions based only on experimental work, basic mathematical models for reaction kinetics and thermodynamics, and prior experience. However, computer and model-based (or systems engineering) methods can efficiently support this complex decision process. In this research project, a toolkit was developed for this decision support and successfully demonstrated for multiphase processes.

As a first step in the systematic design of integrated processes, models of the different process steps are set up that include detailed models of the underlying phenomena and processes. These models can be incorporated into a stationary or dynamic flowsheet simulation of the overall process. To support this step, an integrated environment for transparent and collaborative process modeling was developed that facilitates combining different submodels and supports the automatic translation of the overall model into code that commercial simulation packages can run. Additionally, detailed fluid dynamics models of critical processing units for multiphase processes were developed, which are necessary to investigate the performance and the influence of the operational parameters on their performance. When complex thermodynamic models are used for simulation and optimization, this may lead to unacceptably long computation times due to the iterative solution of the model equations. Approximating the result from these models by surrogate models, that is, mathematical structures that can faithfully represent arbitrary input–output data, was shown to be efficient in solving this issue.

The scope of using optimization methods to explore the entire design space for process development was extended in several directions. The optimization of reactors based on the elementary process function methodology showed significant improvements over heuristically found solutions as demonstrated by experimental validation for the hydroformylation of 1-dodecene in a TMS. Global optimization methods for superstructures that involve discrete decision variables were developed and successfully applied to several examples of liquid multiphase processes. In the

early stages of the design process, the model parameters often can only be determined with limited accuracy. To deal with these uncertainties, an approach was developed which distinguishes between design degrees of freedom that have to be fixed when a plant is built and operational degrees of freedom that later are adapted to the real behavior in the best possible fashion. Finally, advanced control and real-time optimization techniques were developed for and demonstrated at the miniplants and pilot plants. So, the plants could be operated optimally, thus providing reliable information for assessing the potential of the different phase systems, catalyst systems, and plant designs.

The methods used here for process design require sufficiently accurate models of the different elements of the investigated production process. It was demonstrated that models with high predictive quality could be derived for such complex processes. These models were successfully used in the operation of plants at the miniplant and pilot plant scale. However, this comes at a price: model development and validation are costly and time-consuming processes requiring expert knowledge. Hence, the effort for model building should ideally focus on the most promising options, but determining these options systematically involves the availability of models of sufficient predictive capability. To overcome this contradiction, iterative development processes consisting of (ideally model-based) screening of alternatives, initial experimental work, model building, model-based optimization, design of new experiments, further model refinement, optimization with reduced uncertainty, additional experiments, and so on up to the validation of a small number of remaining options at miniplant or pilot plant scale are needed.

Therefore, workflows to integrate the methods for process design along the chemical process development pathway were developed with a particular focus on processes with liquid multiphase systems. Vital elements for integrated process design are general selection criteria for multiphase systems suitable for the given target products or reactions. A methodology was established that allows quantitative comparison of various types of phase systems during different process design stages, without the need for extensive experts' knowledge. The complexity of the considered phase systems is reduced by the systematic application of questionnaires and key experiments. The whole procedure was cast into the modular computer-aided phase system selection (caPSS) framework, which integrates several essential aspects of process development: data acquisition, model generation, conceptual process design, flowsheet optimization, and evaluation regarding economic feasibility as well as Green Chemistry criteria.

For TMS, the choice of solvents in which a specific homogeneously catalyzed reaction proceeds with both a high reaction rate and a high selectivity is crucial. Different approaches were derived from quantum chemistry and thermodynamics to support the identification of suitable solvents. Screening of chemical equilibria or transition state barriers as a function of solvent polarizability provides insights into the reaction thermodynamics and kinetics. The developed methodologies are

well suited to generate a set of potential solvent candidates that are combined with other solvents to obtain mixtures featuring a TMS behavior.

Integrated process development requires the combination of solvent design and process design. Usually, these two design tasks are performed sequentially. While computer-aided molecular design (CAMD) can aid in selecting solvents that possess process-relevant solvent properties, only the simultaneous consideration of solvent and process design in an integrated computer-aided molecular and process design (CAMPD) framework ensures the identification of optimal process designs and operation points. Examples illustrated key aspects in CAMD/CAMPD. Nonetheless, experimental validation is still required due to uncertainties and possible unforeseen chemical effects.

According to the caPSS framework, one of the essential integration steps is the combination of phase system selection with model-based process synthesis. For this purpose, an integrated model-based process design methodology was developed, combining both aspects, using various sources of knowledge. The methodology involves an iterative workflow wherein suitable models are identified and calibrated before evaluating the final process design regarding reaction and separation performance, sustainability, and economic potential. In the case of high levels of uncertainty, model-based optimal experimental design was used to improve the available data basis successively via carefully designed experiments. As a result, critical model parameters can be identified with minimal experimental effort.

Overall, the research program of the SFB/TR 63 resulted in an elaborated, integrated toolkit for the rapid development of liquid multiphase processes. The work has significantly advanced the technology readiness level of each of the three phase systems. All steps in process design, starting from the first theoretical concept to the overall process selection, process simulation, and optimization, were covered. Numerous methodological innovations were proposed, tested, and validated using the representative sample reactions. The whole development chain from the first reaction-related investigations in the laboratory up to the technological realization in automatically controlled miniplants and pilot plants was implemented. Based on the experiences gained during the entire duration of the SFB/TR 63, a classification was developed for an efficient selection of a suitable phase system for a broad spectrum of homogeneously catalyzed reactions based on carefully selected key experiments and the assessment of fundamental properties of substances and mixtures.

Even after 12 years of research, it also became clear that, as in every scientific project, more research is still necessary to validate and extend the derived knowledge base. In general, the various methods should be applied and checked for other reactions and especially different phase systems. Models must be tested for their accuracy and possibly sharpened. The tools for systems engineering and integrated

process design should be applied for other practical examples. So, the selection criteria for liquid multiphase systems must be further tested. Finally, methodologies like model-based process development still need to be extended. However, all methods developed in this collaborative program may pave the way for a more sustainable chemical production in the future based on liquid multiphase processes.

Index

- 2-phase region 34
3-phase region 35
- activity coefficient 28, 145
adsorption isotherms **78–80**, 82, 100
advanced fluids 5
aggregation behavior 101
aggregation formation model **55**, 101
artificial neural networks 407–408
atomic force microscopy **244**, 306
attainable region 414
axial back mixing 392
axial dispersion 419
azeotropic phase behavior 58, 67
- back-mixing. see axial dispersion 431
benchmarking 119
binodal curve 27
BIPHEPHOS 208, 210
Bodenstein approximation 109
branch-and-bound 436
– bound propagation 440
– convex relaxation 436
branched 69–70
branching **58**
breakage **314**
bubble sizes **167**, 194, **250**, **320**
- cake resistances 327
CAPE-OPEN standard 365
catalysis promotion **532**
catalyst inhibition **534**
catalyst leaching 45–46, 209, **229**, 299, **339**
catalyst pre-equilibrium **133**
catalyst recycling 198, 210, 212, 234
catalyst rejection 229, 232
catalytic cycle **108**, 110, 143
CFD-based optimization 388
chemoselectivity **170**
Christiansen matrix 110
 $C_i E_j$ 95
class relationships 368
classifier 406, 408
- coalescence 248, 254, 282, **310**, **314**, 323, 384
coalescence model 387
code generation 378
coiled flow inverter (CFI) 393
coiled flow reverser (CFR) 393, 396
collocation position 383
communication framework 479
Computational Fluid Dynamics (CFD) 384
computer-aided molecular and process design **536**
computer-aided molecular design **538**
computer-aided phase system selection 511, **520**
conceptual design. see process synthesis 425
contact angle 40, 306
continuous molecular targeting **541**
continuous operation 198, 203, 205, 208, 212, 215, 219, 234, 263, 330
continuum solvent models **526**
conversion 45, 341
COSMO 513, 526, **529**, 543, **546**
coupled-cluster calculation 119
coverage of the interface 41
critical micelle concentration 33, 91, 95, 97–98, 100, 237, 244, 252, 261
cryo SEM 309
- data model 368, 380
data reconciliation 478, 482, 485
Dean number 393
Dean vortex 392
decanter 408, 445, 474, 486
decanter model 474, 496
degrees of freedom 377
density functional theory (DFT) 55, 78, 528
design degrees of freedom 451
design of chemical production processes 361
design variables 366
density gradient theory (DGT) 55, 71, 75, 93, 101
diffusion coefficient **165**, **247**, 327
direct surrogate modeling approach 405
discretization 383

Note: Page numbers in bold refer to passages in the text with a detailed discussion of the respective index term.

- dispersion types **240**
- distillation 209, 230, 437
 - equilibrium model 437
- distributed side-stream reactor
 - DSR 414
- documentation 367
- documentation level 368
- drag coefficient 386
- drop sedimentation velocity **243**
- drop size distribution 41, **310**, 314, 323
- dynamic real-time optimization 493

- elementary process functions 520, 566
- elementary process functions (EPF)
 - methodology 415
- encapsulation 371
- endoscope **194, 241**
- enzymatic catalysts 215, 268, 330
- Euler-Euler multi-fluid framework 384
- evolutionary algorithm 456
- extensible markup language (XML) 367

- falling film **160, 193**
- feedback control 461
- finite element 383
- Fisher information matrix **554**
- flowsheet optimization 440
- fluid element. *see* Elementary
 - Process Functions (EPF) Methodology 430
- fluorescence microscopy 310
- flux profile analysis 566
- flux profile analysis (FPA). *see* elementary
 - process functions (EPF) methodology 429
- free energy profile 122
- functional mock-up interface 365

- gas hold-up **163, 168**
- gas solubilities 408
- gas/liquid mass transfer **159**, 320, 398
- global optimization 433
- gradient correction 472
- gravity-driven separation 384
- Green Chemistry 1, 338, 511
- group contribution 512

- halloysites **304–305**
- heat transfer coefficient 397
- helically coiled tubular reactor (HCTR) 222,
 - 392, 427

- Henry coefficient 476
- hetero-azeotrope 68
- hetero-segmental PC-SAFT 62
- heterosegmented 100
- hierarchical modeling 368
- homo-azeotrope 68
- homogeneous transition-metal catalysts 23
- hybrid separation process 437
- hydroamination 215
- hydroaminomethylation **142**, 212, 224, 263,
 - 559
- hydroesterification **122**
 - isomerizing hydroformylation **140**
- hydroformylation 42, **122**, 137, 208, 222, **272**,
 - 307, 333, 335, 478, **530**, 546, 562
- hydroformylation of 1-dodecene 380, 408, 424,
 - 452, 456, 472, 480, 491, 495
- hydroformylation of long-chain olefins 421
- hydrogenation 199, 265, **329**

- indirect surrogate modeling approach 406
- InPROMPT 2
- integrated process design **555**
- integrated solvent and process design
 - 536**
- interfacial area **195**
- interfacial coverage **245**, 306, **318**, 333
- interfacial tension **71**, 74, 94, 100
- ionic liquid (IL) 422
- isomerizing hydroformylation 210
- iterative real-time optimization 463, 478
- iterative RTO method 480

- Kahlweit's fish diagram 34
- kinetic modeling 13
- Kriging models 406, 408

- laboratory scale 198
- laser-induced fluorescence 399
- latin-hypercube design 401
- latin-hypercube sampling 456
- lattice cluster theory (LCT) **55**, 57, 63, 78–79, 100
- liquid-liquid equilibrium 26, 405
- liquid-liquid extraction 446
 - binodal curve 448
- liquid-liquid separation 410

- Marangoni effect **246**
- mass transfer 44, **192**, **242**, **317**, 319–320

- mass transfer coefficient **162, 193, 249–250,**
 318, 321, 399
 mechanistic kinetic model
 – hydroformylation 117, 135
 – hydrogenation 136
 – isomerization 128, 136
 – reductive amination 143
 melt crystallization 443
 membrane filtration 44, 252, **322, 333, 335**
 membrane screening **230, 253, 322**
 MES miniplant 482, 486, 489
 meta-model 379
 MHE implementation 487
 micellar-enhanced ultrafiltration **252**
 micelles 33
 microemulsion phase separation model 288
 microemulsion prescreening 261
 microemulsion system 7, 33, **236, 338, 516**
 microkinetic models 258
 miniplant 19, 205, 208, **212, 215, 222–223,**
226, 269, 295, 341, 473
 miscibility gap **61, 190, 234, 407**
 mixed adaptive sampling 402
 mixed micelles 101
 mixed-integer nonlinear problem 538
 mixed-integer nonlinear programming 452
 mixing efficiency 394
 mixing in helical pipes 394
 model hierarchy 368
 model of permeability 253, 326
 model process 11
 model uncertainties 465
 model-based design methodology 15
 model-based optimal experimental design
553
 Modelica 365
 model-predictive control 465, 493
 modified Nitsch cell **154**
 modifier adaptation **466, 473, 480**
 modifier adaptation with quadratic
 approximation 472
 modularity 367
 monophasic systems 23
 MOSAIC modeling 365, 375, 378, **382, 486, 492**
 moving horizon estimation 483
 multi-objective numerical optimization 395
 multi-phase microemulsion system 384
 multiphase systems 23
 multi-rate MHE 489, 493
 N,N-diethyldecylamine 225
 N,N-diethylundecylamine 226
 N,N-dimethylformamide 208, 225
 nanoparticle 40, **304**
 n-decane 208
 n-dodecane 225
 neural network **168**
 non-ideal distillation 437
 nonlinear optimization problem 538

 object-oriented structure 372
 oil-to-water ratio 34
 operando spectroscopy
 – FTIR 103, 133
 operational degrees of freedom 451, 454,
 467, 474
 optical measurement techniques 393
 optimal control problem (OCP) 415, 520
 optimal operating point 411
 optimization 378
 – mixed-integer nonlinear programming 434
 optimization under uncertainties **556**
 organic solvent nanofiltration 209, **229, 253,**
 299, 322, **326, 443**
 orthogonal collocation on finite elements 381

 packing parameter 331
 palladium 122
 parameter identification 125, 127
 – Fisher-information matrix 127
 – parameter sensitivity 127, 129
 – parameter subset selection 124
 – singular value decomposition 127
 parametric mismatch 476
 parametric model uncertainties 456
 Pareto front 395
 partial differential algebraic equation
 systems 374
 particle image velocimetry (PIV) 394
 PC-SAFT **55–59, 60, 61, 62, 63, 67–68, 74,**
 84–87, 89–90, 92–93, 100–101, 145, **190,**
 209, 215, 400, 408, **528, 559**
 phase behavior **239**
 phase behavior microemulsions **34**
 phase configuration 239
 phase equilibrium 29
 phase inversion **167**
 phase separation 209, 213, 252, **259, 277, 322**
 phase systems **338**

- physico-chemical effect **244**
- Pickering emulsion 7, 40, **304**, 338, 517
- planar laser-induced fluorescence (PLIF) 394
- plant-model mismatch 465, 468
- population balance model 386
- probabilistic design 421
- process concept 230, 237
- process design 535
- process development 2
- process synthesis 413
- product yield 474, 480, 491
- production cost 458, **559**

- quadrature method of moments 384, 386
- quantitative structure–property relationship **543**
- quantum chemistry **523**
- quantum mechanical (QM) calculation **87**

- Raman spectroscopy 294
- rate equations 477
- rate-determining step 133
- reaction equilibrium **144**
- reaction indicators 45
- reaction kinetic 145
- reaction mechanism
 - hydroformylation 106
- reaction network
 - hydroformylation 104
- reaction performance 208, 219, 273, 300, 336, 339
- reactor 380
- reactor model 474
- reactor operation 413
- reactor setup 103
- reactor-network synthesis 414
- reactor-tandems 431
- real-time optimization **463**
- recourse variables 454
- reductive amination **89**, 98, **142**, 212, 380, **531**
- reductive elimination **124**
- regioselectivity **170**
- renewable raw materials 9
- repeatedly operated semibatch reactor (RSBR) 222, 427
- residence time distribution 392
- reuse of model entities 371

- rheology, see viscosity
 - shear thinning 41, 316
- rhodium **122**

- Sauter mean diameter **168**, 248, **310–311**, **314**
- scenarios 454
- Schrödinger equation 118
- selectivity **45**, 341
- self-assembly **90**
- sensitivity analysis **557**
- sensitivity matrix **554**
- separation behavior 277, 286, 338
- separation network 443
- separation of isomers **78**
- separator 384
- sequential sampling 402
- settler 389
- settler unit design 287
- SFB/TR 63 2
- shear thinning **316**
- sigma point method. see unscented transformation 433
- silica particles 304–**305**, **310**
- soft sensor for surfactant concentrations 292
- solid-liquid equilibrium (SLE) **68**
- solubilization **56**
- solvent decomposition 534
- solvent effect **119**, 146, 527–**528**
- solvent selection **523**, 535
- specific transfer area **162**
- stability 40, 309, 312
- stagnant cap **152**
- start-up 491, 495
- start-up trajectories 491
- state estimation 482
- steady state identification 478
- strategies process design 285
- structural mismatch 476
- subnetwork analysis 137
- SULFOXANTHOS 211, 226, 307
- superstructure optimization 451, 456, 460
- support vector machine 406
- surface modification **305**
- surface tension **73–74**, 94, 100, 386, 390
- surface-active substances **152**
- surrogate modeling 436
 - artificial neural network 445
 - Kriging interpolation 442

- piecewise linear approximation 446
- switchable solvents 5
- syngas **59**
- systematic development of MES 254

- T,x diagram 27
- Taylor bubble 400
- Taylor–Couette reactor 215
- technology readiness level 234, 303, **339**
- temperature homogenization 398
- temperature-dependent miscibility gap **25**
- ternary diagram 30
- ternary system **191**
- thermodynamic activity **84**, 145, 527
- thermodynamic equilibrium constant **84**
- thermodynamic equilibrium data 13
- thermomorphic multiphase system (TMS) 6,
24, **190**, 197, 338, 423, 472, 514, 546
- three-phase region 35
- tip speed 194, **317**
- TMS-miniplant 478
- total annual costs (TAC) 425
- transition state barrier 524
- transition state theory **524**
- triphenylphosphine 201, 205–206, 225

- tunable solvents 5
- turbulence model 384
- turnover frequency **45**
- turnover number **45**
- two-phase approach 465
- two-stage optimization 454

- ultrafiltration 252, 322
- uncertain parameters 454
- uncertainties 451, 453
- UNIFAC **530**, 543
- unscented transformation 421
- upper critical solution temperature 60

- viscosity 194, 247, **316–317**, 326
- volumetric mass transfer coefficient **162**, 399

- water accumulation 226, 232

- XANTPHOS 218

- yield 45, 341, 480

- zeta potential 305, 307

